Vasant Matsagar   *Editor*

Advances in Structural Engineering

Materials, Volume Three

Springer

Advances in Structural Engineering

Vasant Matsagar

Editor

Advances in Structural Engineering

Materials, Volume Three

Springer

Editor
Vasant Matsagar
Department of Civil Engineering
Indian Institute of Technology (IIT) Delhi
New Delhi, Delhi
India

Foreword

Structural Engineering Convention (SEC-2014) is organised by IIT Delhi at Delhi during 22–24 December 2014. Its proceedings are published in three volumes. The first and second volumes contain papers dealing with the themes of Mechanics of Structures and Structural Dynamics, respectively. The present third volume contains research papers dealing with Structural Materials and Structural Behaviour.

On Structural Materials

In contrast to plant-manufactured materials like steel and cement, and naturally occurring materials like wood, concrete is designed and produced by civil engineers in the concrete plants or even at the construction site itself. Designing concrete mixes for achieving the specified strength, durability and economy requires considerable knowledge about the physical, chemical and mechanical properties of concrete. Perhaps, this is why most of the papers on structural materials presented here deal with concrete and its constituent materials.

Extended cost–benefit analysis of infrastructural projects demands that their negative environmental impacts should be included in the estimation of their costs. On this score, energy-intensive process of cement manufacture is known to make substantial contribution to global warming. Use of waste pozzolanic mineral matter as part replacement of cement for producing concrete is credited to be an attempt towards reducing such negative impacts. In this context, geopolymers promise to be a substitute for cement in concrete. Geopolymers are composed of alkali-activated silicon molecular chains similar to carbon-based polymers. As in the case of cement hydration, polymerisation of geopolymers results in the development of cohesive and adhesive properties. These papers deal with the mix design and properties of geopolymer materials and its applications in concrete structures and masonry blocks. For achieving the same purpose, search is on for cement clinker

replacements. Of course, research on the pozzolanic cement concrete continues. Because of their environmental friendliness, 10 papers are devoted to the production and properties of these materials.

It is worth remembering that the consumption of aggregate in concrete is about three to four times that of the cement. This is why their continued availability in the coming decades is a matter of concern. Many potential substitutes for the currently popular crushed aggregate have been explored. These substitutes include river and marine sand, quarry dust, marble powder, recycled aggregate, demolished concrete, rubber particles, polyethylene terephthalate (PET) granules, etc. Some papers in these proceedings deal with these alternatives to aggregates in concrete.

Fibre-reinforced concretes (FRC) exhibit higher impact resistance and better cracking control. Here, some papers explore the effectiveness of biofibres, polypropylene and nanocarbon fibres in addition to the more popular steel and glass fibres. Bamboo concrete has also been explored as an alternative structural material.

About seven papers report investigations dealing with the durability of concrete and corrosion of rebars. Chemically deteriorating effect of sea water, rain, etc., on the properties of concretes containing high-volume fly ash and rice husk ash, high strength concrete and fibrous mortars is investigated. Also, the vulnerability of reinforcement steel bars to corrosion on exposure to marine as well as to chloride and sulphate-bearing ambient environment is delineated. A model for the prediction of service life of concrete structures is also presented.

Mix design procedures for pozzolanic, high performance, fibrous and self-compacting concrete are continuously being upgraded. Of course, new concrete constituents like geopolymers, aggregate substitutes and fibres demand the acquisition of the required empirical database as well as the development of appropriate concrete mix design procedures. Most of these papers present the results of experimental investigations. The absence of any papers on the constitutive models simulating the damage, elastoplastic, viscoelastic and viscoplastic response of concrete is noted.

On Structural Behaviour

Perhaps, because of considerable seismic risk to public life and property, the discipline of structural dynamics is dominated by seismic analysis and design. This observation is confirmed by the almost total absence of the papers, in this conference, on the other sources of dynamic loading on structures. It is well known that the classical theory of linear elastic vibrations is not valid for nonlinear elastoplastic concrete structures. Because of the complexity of seismic behaviour of concrete structures, the present methods of their seismic analysis and design are predominantly empirical–computational in nature. Many papers, about one-third of those on structures, in this volume are devoted to their static, quasi-static and dynamic response.

Structural performance of concrete non-ductile frames as well as frames with infills and shear walls is investigated. Static response of concrete structures with welded rebars, shear-deficient concrete beams, fibre-reinforced concrete beams, partially prestressed concrete, slabs, precast structures, etc., is reported. Pushover analysis as an essential input to seismic analysis is presented. Effect of exposure to elevated temperatures or fire is determined. Behaviour of precast member connections and concrete members under fatigue and load reversal is also investigated. The effectiveness of metallic dampers in enhancing the lateral capacity is evaluated. The progressive collapse of buildings and the cyclic response of concrete shear walls are presented. One paper each is devoted to the determination of the natural period of infilled concrete frames and to the dynamic stability of concrete beam columns. Effect of buoyancy on rafts of a building with five basements is determined. At least 15 papers report their findings on these issues.

Failure of concrete frames is catastrophic when it is triggered by the column failure than by beam failure. Perhaps, this is why there are about four papers on the performance of concrete columns. Most of these papers deal with the behaviour of concrete-filled steel tube (CFST) columns. Tension stiffening in torsion as well as cyclic behaviour of reinforced concrete (RC) columns is also studied.

Concrete structures partially damaged by moderate earthquakes need to be strengthened or retrofitted. Also, structures may have to be strengthened to satisfy the more stringent design requirements of the revised design code or to enhance their load carrying capacity. Such retrofitting is carried out by jacketing the structural members with glass or carbon fibre-reinforced plastic (GFRP or CFRP) sheets. The bond–slip relations for such FRP sheets have been studied. The performance of the FRP columns and beams in flexure and shear is evaluated. One-way spiral ties and ultra-high performance concrete overlay have been explored for retrofitting. Also, the effectiveness of glass reinforced plastic fibre (GRPF) rebars as potential replacement for steel rebars is evaluated. Nine papers are devoted to search for effective retrofitting measures.

Behaviour of steel and masonry structures beyond the linear elastic range is not so well understood. The effectiveness of braced steel frames in enhancing their seismic resistance is evaluated. Other problems dealt with here include stress concentration in tubular member connections, fatigue life of welded and bolted connections, complex behaviour of fillet welds, etc. Strength values exhibited by LDSS columns with different section details are compared. Low-cycle fatigue resistance and fatigue-induced damage of bridges upon overloading as well as performance of FRP-strengthened bridges are evaluated. Performance of concrete block masonry, compressed earth blocks, rammed earth columns and soft brick and strong mortar masonry is reported. In-plane and out-of-plane behaviour of masonry walls is explored. Seven and five papers are devoted to steel and masonry structures, respectively. A paper is presented which identifies the challenges posed by the tall buildings to the profession.

Uncertainties in the structural properties as well as the loading details demand probability-based approaches to structural analysis and design. Risk and confidence levels associated with even well-designed structures are to be evaluated. Reliability

analysis may demand stochastic simulation. An attempt to establish the relation between the damage index and fragility curve of concrete structures is reported. The reliability of petroleum and geotechnical structures is reported. About five papers address these research issues.

Considerable research attention is currently being focused on the development of economical non-destructive testing (NDT) methods for evaluating the performance of structures. Vibration-based as well as wave-based methods are being developed for the purpose of damage detection and structural health monitoring. Sensitivity of piezo material lead zirconate titanate (PZT) patches is determined. New areas, like piezoelectric energy harvesting, beyond structural engineering are being explored. Degradation of concrete strength upon exposure to fire can be quantified by using NDT methods.

Dr. Gurmail S. Benipal
Associate Professor
Department of Civil Engineering
Indian Institute of Technology (IIT)
Hauz Khas, New Delhi, India

Preface

I am delighted that the Department of Civil Engineering, Indian Institute of Technology (IIT) Delhi has hosted the eagerly awaited and much coveted 9th Structural Engineering Convention (SEC2014). The biennial convention has attracted a diverse range of civil and structural engineering practitioners, academicians, scholars and industry delegates, with the reception of abstracts including more than 1,500 authors from different parts of the world. This event is an exceptional platform that brings together a wide spectrum of structural engineering topics such as advanced structural materials, blast resistant design of structures, computational solid mechanics, concrete materials and structures, earthquake engineering, fire engineering, random vibrations, smart materials and structures, soil-structure interaction, steel structures, structural dynamics, structural health monitoring, structural stability, wind engineering, to name a few. More than 350 full-length papers have been received, among which a majority of the contributions are focused on theoretical and computer simulation-based research, whereas a few contributions are based on laboratory-scale experiments. Amongst these manuscripts, 205 papers have been included in the Springer proceedings after a thorough three-stage review and editing process. All the manuscripts submitted to the SEC2014 were peer-reviewed by at least three independent reviewers, who were provided with a detailed review proforma. The comments from the reviewers were communicated to the authors, who incorporated the suggestions in their revised manuscripts. The recommendations from three reviewers were taken into consideration while selecting a manuscript for inclusion in the proceedings. The exhaustiveness of the review process is evident, given the large number of articles received addressing a wide range of research areas. The stringent review process ensured that each published manuscript met the rigorous academic and scientific standards. It is an exalting experience to finally see these elite contributions materialise into three book volumes as SEC2014 proceedings by Springer entitled "Advances in Structural Engineering". The articles are organised into three volumes in some broad categories covering subject matters on mechanics, dynamics and

materials, although given the diverse areas of research reported it might not have been always possible.

SEC2014 has ten plenary speakers, who are eminent researchers in structural engineering, from different parts of the world. In addition to the plenary sessions on each day of the convention, six concurrent technical sessions are held every day to assure the oral presentation of around 350 accepted papers. Keynote speakers and session chairmen for each of the concurrent sessions have been leading researchers from the thematic area of the session. The delegates are provided with a book of extended abstracts to quickly browse through the contents, participate in the presentations and provide access to a broad audience of educators.

A technical exhibition is held during all the 3 days of the convention, which has put on display the latest construction technologies, equipment for experimental investigations, etc. Interest has been shown by several companies to participate in the exhibition and contribute towards displaying state-of-the-art technologies in structural engineering. Moreover, a pre-convention international workshop organised on "Emerging Trends in Earthquake Engineering and Structural Dynamics" for 2 days has received an overwhelming response from a large number of delegates.

An international conference of such magnitude and release of the SEC2014 proceedings by Springer has been the remarkable outcome of the untiring efforts of the entire organising team. The success of an event undoubtedly involves the painstaking efforts of several contributors at different stages, dictated by their devotion and sincerity. Fortunately, since the beginning of its journey, SEC2014 has received support and contributions from every corner. I thank them all who have wished the best for SEC2014 and contributed by any means towards its success. The edited proceedings volumes by Springer would not have been possible without the perseverance of all the committee members.

All the contributing authors owe thanks from the organisers of SEC2014 for their interest and exceptional articles. I also thank the authors of the papers for adhering to the time schedule and for incorporating the review comments. I wish to extend my heartfelt acknowledgment to the authors, peer-reviewers, committee members and production staff whose diligent work put shape to the SEC2014 proceedings. I especially thank our dedicated team of peer-reviewers who volunteered for the arduous and tedious step of quality checking and critique on the submitted manuscripts. I am grateful to Prof. Tarun Kant, Prof. T.K. Datta and Dr. G.S. Benipal for penning the forewords for the three volumes of the conference proceedings. I wish to thank my faculty colleagues at the Department of Civil Engineering, Indian Institute of Technology (IIT) Delhi, and my Ph.D. Research Scholars for extending their enormous assistance during the reviewing and editing process of the conference proceedings. The time spent by all of them and the midnight oil burnt is greatly appreciated, for which I will ever remain indebted. The administrative and support staff of the department has always been extending their services whenever needed, for which I remain thankful to them. Computational

laboratory staff of the department had handled the online paper submission and review processes, which hardly had any glitch therein; thanks to their meticulous efforts.

Lastly, I would like to thank Springer for accepting our proposal for publishing the SEC2014 conference proceedings. Help received from Mr. Aninda Bose, the acquisition editor, in the process has been very useful.

<div align="right">

Vasant Matsagar
Organising Secretary, SEC2014

</div>

About the Editor

Dr. Vasant Matsagar is currently serving as an Associate Professor in the Department of Civil Engineering at Indian Institute of Technology (IIT) Delhi. He obtained his doctorate degree from Indian Institute of Technology (IIT) Bombay in 2005 in the area of seismic base isolation of structures. He performed post-doctoral research at the Lawrence Technological University (LTU), USA in the area of carbon fibre reinforced polymers (CFRP) in bridge structures for more than 3 years. His current research interests include structural dynamics and vibration control; multi-hazard protection of structures from earthquake, blast, fire, and wind; finite element methods; fibre reinforced polymers (FRP) in prestressed concrete structures; and bridge engineering. He has guided students at both undergraduate and post-graduate levels in their bachelor's and master's projects and doctoral research. Besides student guidance, he is actively engaged in sponsored research and consultancy projects at national and international levels. He has published around 40 international journal papers, 60 international conference manuscripts, a book, and has filed for patents. He is also involved in teaching courses in structural engineering, e.g. structural analysis, finite element methods, numerical methods, structural stability, structural dynamics, design of steel and concrete structures, to name a few. He has organised several short- and long-term courses as quality improvement programme (QIP) and continuing education programme (CEP), and delivered invited lectures in different educational and research organisations.

Dr. Matsagar is the recipient of numerous national and international awards including "Erasmus Mundus Award" in 2013; "DST Young Scientist Award" by the Department of Science and Technology (DST) in 2012; "DAAD Awards" by the Deutscher Akademischer Austausch Dienst (DAAD) in 2009 and 2012; "DAE Young Scientist Award" by the Department of Atomic Energy (DAE) in 2011; "IBC Award for Excellence in Built Environment" by the Indian Buildings Congress (IBC) in 2010; "IEI Young Engineer Award" by the Institution of Engineers (India) in 2009; and "Outstanding Young Faculty Fellowship" by the Indian Institute of Technology (IIT) Delhi in 2009. He has also been appointed as "DAAD Research Ambassador" by the German Academic Exchange Programme since the academic session 2010.

About Structural Engineering Convention (SEC) 2014

The ninth structural engineering convention (SEC) 2014 is organised at Indian Institute of Technology (IIT) Delhi, for the first time in the capital city of India, Delhi. It is organised by the Department of Civil Engineering during Monday, 22nd December 2014 to Wednesday, 24th December 2014. The main aim towards organising SEC2014 has been to facilitate congregation of structural engineers of diverse expertise and interests at one place to discuss the latest advances made in structural engineering and allied disciplines. Further, a technical exhibition is held during all the 3 days of the convention, which facilitates the construction industry to exhibit state-of-the-art technologies and interact with researchers on contemporary innovations made in the field.

The convention was first organised in 1997 with the pioneering efforts of the CSIR-Structural Engineering Research Centre (CSIR-SERC), Council of Scientific and Industrial Research, Chennai and Indian Institute of Technology (IIT) Madras. It is a biennial event that attracts structural engineers from India and abroad, from both academia and industry. The convention, as much as it did in its history, is contributing to scientific developments in the field of structural engineering in a global sense. Over the years, SEC has evolved to be truly international with successive efforts from other premier institutes and organisations towards the development of this convention.

Apart from the 3 days of the convention, an international workshop is also organised on "Emerging Trends in Earthquake Engineering and Structural Dynamics" during Saturday, 20th December 2014 to Sunday, 21st December 2014. Eleven experts in the areas of earthquake engineering and structural dynamics delivered keynote lectures during the pre-convention workshop. The convention includes scholarly talks delivered by the delegates from academia and industry, cultural programmes presented by world-renowned artists, and visits to important sites around the historical National Capital Region (NCR) of Delhi.

Composition of Committees for SEC2014

Structural Engineering Convention 2014
9th Biennial Event, Under the Auspices of Indian Association for Structural Engineering (IASE)
Department of Civil Engineering, Indian Institute of Technology (IIT) Delhi

Organizing Committee		
Patron	R.K. Shevgaonkar Director, IIT Delhi	Areas of Interest: Fiber Optic Communication, Photonics, Nonlinear Fiber Optics, Antennas, Image Processing, Radio Astronomy. E-mail: rks@ee.iitd.ac.in director@admin.iitd.ac.in Phone: +91-11-2659-1701

(continued)

(continued)

Organizing Committee		
Organizing Chairman	 A.K. Jain Professor Civil Engineering Department, IIT Delhi	Areas of Interest: Earthquake Resistant, Analysis of Structures, Wind load, Dynamic Behaviour of Offshore Structure. E-mail: akjain@civil.iitd.ac.in Phone: +91-11-2659-1202
Mentor	 Tarun Kant Institute Chair Professor Civil Engineering Department, IIT Bombay, Mumbai	Areas of Interest: Solid Mechanics, Finite Element and Other Numerical Methods, Polymer Composites, Composite and Computational Mechanics. E-mail: tkant@civil.iitb.ac.in Phone: +91-22-2576-7310

(continued)

Organizing Committee		
Members	 A.K. Nagpal Dogra Chair Professor Civil Engineering Department, IIT Delhi	Areas of Interest: Structural Engineering, Tall Buildings, Bridges, Earthquake Engineering. E-mail: aknagpal@civil.iitd.ac.in Phone: +91-11-2659-1234
	 Abhijit Ganguli Assistant Professor Civil Engineering Department, IIT Delhi	Areas of Interest: Non-destructive Evaluation of Structures, Subsurface Imaging, Ultrasonics, Wave Scattering Problems, Structural Dynamics, Active Control of Structural Vibration Mechatronics. E-mail: abhijit.ganguli@civil.iitd.ac.in Phone: +91-11-2659-6426

(continued)

Organizing Committee

 Alok Madan Professor Civil Engineering Department, IIT Delhi	Areas of Interest: Structural Engineering, Nonlinear Structural Dynamics, Concrete Structures, Computing in Structural Engineering, Structural Masonry. E-mail: madan@civil.iitd.ac.in Phone: +91-11-2659-1237
 Ashok Gupta Professor Civil Engineering Department, IIT Delhi	Areas of Interest: Structural Engineering, Artificial Intelligence, Technology Enhanced Learning, Web Based Courses. E-mail: ashokg@civil.iitd.ac.in Phone: +91-11-2659-1194

(continued)

Organizing Committee	
 B. Bhattacharjee Professor Civil Engineering Department, IIT Delhi	Areas of Interest: Durability of Concrete, Rebar Corrosion, Cement-Based Composites, Construction Technology, Building Science. E-mail: bishwa@civil.iitd.ac.in Phone: +91-11-2659-1193
 D.R. Sahoo Assistant Professor Civil Engineering Department, IIT Delhi	Areas of Interest: Earthquake Engineering, Large-Scale Testing, Supplemental Damping and Energy Dissipation Devices, Performance-Based Seismic Design, Steel-Fiber Reinforced Concrete. E-mail: drsahoo@civil.iitd.ac.in Phone: +91-11-2659-1203

(continued)

Organizing Committee

  G.S. Benipal Associate Professor Civil Engineering Department, IIT Delhi	Areas of Interest: Concrete Mechanics, Constitutive Modeling, Nonlinear Elasto-Dynamics and Stability. E-mail: gurmail@civil.iitd.ac.in Phone: +91-11-2659-1207
  J. Uma Maheswari Assistant Professor Civil Engineering Department, IIT Delhi	Areas of Interest: Design Management, Matrix-Based Design Techniques, Construction Project Management, Automation. E-mail: umapaul@civil.iitd.ac.in Phone: +91-11-2659-1189

(continued)

Organizing Committee

<table>
<tr>
<td></td>
<td>K.C. Iyer
Professor
Civil Engineering Department,
IIT Delhi</td>
<td>Areas of Interest: Financial Management, Project Risks, Legal Issues in Business, Infrastructure Project Management.

E-mail: kciyer@civil.iitd.ac.in
Phone: +91-11-2659-1209</td>
</tr>
<tr>
<td></td>
<td>K.N. Jha
Associate Professor
Civil Engineering Department,
IIT Delhi</td>
<td>Areas of Interest: Construction Project Management, Project Success Factor, Asset Management, Schedule Cost Quality and Safety.

E-mail: knjha@civil.iitd.ac.in
Phone: +91-11-2659-6255</td>
</tr>
</table>

(continued)

Organizing Committee		
	Shashank Bishnoi Assistant Professor Civil Engineering Department, IIT Delhi	Areas of Interest: Experimental and Numerical Studies into Hydration of Cement and Supplementary Cementitious Materials, Sustainability, Durability, Repairs and Life-Cycle Costs of Concrete Structures. E-mail: shashank.bishnoi@civil.iitd.ac.in Phone: +91-11-2659-1185
	Supratic Gupta Assistant Professor Civil Engineering Department, IIT Delhi	Areas of Interest: Concrete Mechanics, Self-Compacting Concrete, Constitute Modeling, Analytical and Experimental Research of RC and Prestressed Concrete Bridges, Bamboo Concrete Composites. E-mail: supratic@civil.iitd.ac.in Phone: +91-11-2659-6307

(continued)

Organizing Committee		
	Suresh Bhalla Associate Professor Civil Engineering Department, IIT Delhi	Areas of Interest: Smart Material and Structures, Structural Health Monitoring, Non-destructive Evaluation, Biomechanics, Engineered Bamboo Structures. E-mail: sbhalla@civil.iitd.ac.in Phone: +91-11-2659-1040
	T.K. Datta Emeritus Professor Civil Engineering Department, IIT Delhi	Areas of Interest: Earthquake Engineering, Wind Engineering, Offshore Dynamics, Structural Control. E-mail: tkdatta@civil.iitd.ac.in Phone: +91-11-2659-1184

(continued)

Organizing Committee		
Organizing Secretary	Vasant Matsagar Associate Professor Civil Engineering Department, IIT Delhi	Areas of Interest: Multi-Hazard Protection of Structures, Earthquake, Wind, Blast and Fire Engineering, Fiber Reinforced Polymer Composites. E-mail: matsagar@civil.iitd.ac.in Phone: +91-11-2659-1225

Sub-Committee		
Members	Arun Kumar Assistant Professor Civil Engineering Department, IIT Delhi	Areas of Interest: Human Health Risk Assessment, Nanoparticles, Water Treatment, Uncertainty Analysis. E-mail: arunku@civil.iitd.ac.in Phone: +91-11-2659-1166
	Aravind K. Swamy Assistant Professor Civil Engineering Department, IIT Delhi	Areas of Interest: Modeling Behaviour of Asphaltic Material, Continuum Damage Modeling, Pavement Engineering, Rheology, Recycling of Pavement Materials. E-mail: akswamy@civil.iitd.ac.in Phone: +91-11-2659-1191

(continued)

(continued)

Sub-Committee		
	Bappaditya Manna Assistant Professor Civil Engineering Department, IIT Delhi	Areas of Interest: Dynamics Soil-Pile Interaction, Pile Foundation, Machine Foundation, Stability of Reinforced Slopes. E-mail: bmanna@civil.iitd.ac.in Phone: +91-11-2659-1211
	C.T. Dhanya Assistant Professor Civil Engineering Department, IIT Delhi	Areas of Interest: Hydro-Climatological Modeling, Nonlinear Dynamics and Chaos Theory, Stochastic Hydrology, Optimization in Water Resource Systems, Data Mining in Hydrology, Water Resources Management. E-mail: dhanya@civil.iitd.ac.in Phone: +91-11-2659-7328

(continued)

(continued)

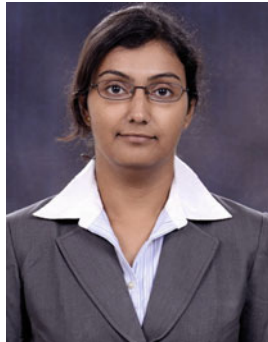| Sub-Committee		
	 Gazala Habib Assistant Professor Civil Engineering Department, IIT Delhi	Areas of Interest: Aerosol Monitoring Characterization and Modeling, Local Air Quality, Health and Climate Effects. E-mail: gazala@civil.iitd.ac.in Phone: +91-11-2659-1192
	 R. Ayothiraman Associate Professor Civil Engineering Department, IIT Delhi	Areas of Interest: Soil Dynamics and Earthquake Engineering, Pile Foundations, Deep Excavations in Urban Areas, Problematic Soils and Ground Improvement. E-mail: araman@civil.iitd.ac.in Phone: +91-11-2659-1188

(continued)

Sub-Committee		
	Sumedha Chakma Assistant Professor Civil Engineering Department, IIT Delhi	Areas of Interest: Settlement in Landfills, Gas Generation from Landfills, GIS Based Landfill Management, Bioreactor Landfill, Infiltration Characteristics of Different Vegetation and Land Use, Watershed Management, Water Contamination and Remediation, Open Channel Hydraulics, Contaminant Hydrology. E-mail: chakma@civil.iitd.ac.in Phone: +91-11-2659-1263
	Tanusree Chakraborty Assistant Professor Civil Engineering Department, IIT Delhi	Areas of Interest: Foundation Engineering, Blast Loading in Soil, Soil Plasticity and Constitutive Modeling, Soil-Structure Interaction and Underground Construction in Soil and Rock. E-mail: tanusree@civil.iitd.ac.in Phone: +91-11-2659-1268

Contents

Volume 2

Part VIII   Seismology and Ground Motion Characteristics

**Part IX   Earthquake Response of Steel, Concrete and Masonry
                    Structures**

Part XIV   Wind Induced Vibration Response of Structures

**Part XV   Statistical, Probabilistic and Reliability Approaches
in Structural Dynamics**

Volume 3

Part XVI   Geopolymers

Part XVII   Cement and Pozzolana

Part XVI
Geopolymers

Mix Design of Fly Ash Based Geopolymer Concrete

Subhash V. Patankar, Yuwaraj M. Ghugal and Sanjay S. Jamkar

Abstract Geopolymer is a new development in the world of concrete in which cement is totally replaced by pozzolanic materials like fly ash and activated by highly alkaline solutions to act as a binder in the concrete mix. For the selection of suitable ingredients of geopolymer concrete to achieve desire strength at required workability, an experimental investigation has been carried out for the gradation of geopolymer concrete and a mix design procedure is proposed on the basis of quantity and fineness of fly ash, quantity of water, grading of fine aggregate, fine to total aggregate ratio. Sodium silicate solution with $Na_2O = 16.37$ %, $SiO_2 = 34.35$ % and $H_2O = 49.28$ % and sodium hydroxide solution having 13 M concentration were maintained constant throughout the experiment. Water-to-geopolymer binder ratio of 0.35, alkaline solution-to-fly ash ratio of 0.35 and sodium silicate-to-sodium hydroxide ratio of 1.0 by mass were fixed on the basis of workability and cube compressive strength. Workability of geopolymer concrete was measured by flow table apparatus and cubes of 150 mm side were cast and tested for compressive strength after specified period of oven heating. The temperature of oven heating was maintained at 60 °C for 24 h duration and tested 7 days after heating. It is observed that the results of workability and compressive strength are well match with the required degree of workability and compressive strength. So, proposed method is used to design normal and standard geopolymer concrete.

Keywords Geopolymer concrete · Mix design · Fly ash · Alkaline solution · Flow · Heat-cured · Compressive strength

S.V. Patankar (✉)
Department of Civil Engineering, SRES'S College of Engineering,
Kopargaon 423 603, Maharashtra, India

Y.M. Ghugal
Department of Applied Mechanics, Government College of Engineering,
Karad 431 416, Maharashtra, India

S.S. Jamkar
Department of Applied Mechanics, Government College of Engineering,
Aurangabad 431 005, Maharashtra, India

1 Introduction

Use of concrete is globally accepted due to ease in operation, mechanical properties and low cost of production as compared to other construction materials. An important ingredient in the conventional concrete is the Portland cement. Production of Portland cement is increasing due to the increasing demand of construction industries. Therefore the rate of production of carbon dioxide released to the atmosphere during the production of Portland cement is also increasing. Generally for each ton of Portland cement production, releases a ton of carbon dioxide in the atmosphere [1]. The green house gas emission from the production of Portland cement is about 1.35 billion tons annually, which is about 7 % of the total greenhouse gas emissions [2]. Moreover, cement production also consumes significant amount of natural resources. Therefore to reduce the pollution, it is necessary to reduce or replace the cement from concrete by other cementitious materials like fly ash, blast furnace slag, rice husk ash, etc.

Fly ash is a by-product of pulverized coal blown into a fire furnace of an electricity generating thermal power plant. According to the survey, the total fly ash production in the world is about 780 million tons per year but utilization is only about 17–20 % [2, 3]. In India more than 220 million tons of Fly ash is produced annually [4]. Out of this, only 35–50 % fly ash is utilized either in the production of Portland pozzolana cement, workability improving admixture in concrete or in stabilization of soil. Most of the fly ash is disposed off as a waste material that covers several hectares of valuable land. The importance of using fly ash as a cement replacing material is beyond doubt. Malhotra [5, 6] recommended replacing cement by fly ash up to 60 % known as high volume fly ash concrete. But it was observed that the pozzolanic action of fly ash with calcium hydroxide formed during the hydration of cement is very slow. The particles of size less than 45 μm are responsible for pozzolanic reaction. Higher size particles present in fly ash acts as filler.

Therefore for complete replacement of cement by fly ash and to achieve the higher strength within a short period of curing, Davodavits [7, 8] suggested the activation process of pozzolanic material that are rich in silica and alumina like fly ash with alkaline elements at certain elevated temperature. Fly ash when comes in contact with highly alkaline solutions forms inorganic alumino–silicate polymer product yielding polymeric Si–O–Al–O bonds known as Geopolymer [7–9].

To produce concrete of desired strength, various mix proportioning methods are used on the basis of type of work, types, availability and properties of material, field conditions and workability and durability requirements. Rangan [10] have proposed the mix design procedure for production of fly ash based geopolymer concrete whereas Anuradha et al. [11] have presented modified guidelines for mix design of geopolymer concrete using Indian standard code.

As geopolymer concrete is a new material in which cement is totally replaced by fly ash and activated by alkaline solutions. Chemical composition, fineness and density of fly ashes are different from cement. Similarly, in cement concrete, water

plays main role during hydration process while water come out during polymerisation process as in case of geopolymer concrete. Therefore it is necessary to develop a new mix design procedure for geopolymer concrete to achieve desired strength at required workability.

So, in the present investigation, geopolymer concrete mix design procedure is proposed on the basis of quantity and fineness of fly ash to achieve desired strength [12], quantity of water to achieve required degree of workability [13], grading of fine aggregate [14] and fine-to-total aggregate ratio by maintaining solution-to-fly ash ratio by mass of 0.35 [15], water-to-geopolymer binder ratio of 0.35 [16], sodium silicate-to-sodium hydroxide ratio by mass of 1 [17] and tested after oven heating at a temperature 60 °C for duration of 24 h and tested after test period of 7 days [13].

2 Experimental Work

2.1 Materials

In the proposed mix proportioning method, low calcium processed fly ash of thermal power plant was used as source material. The laboratory grade sodium hydroxide in flake form (97.8 % purity) and sodium silicate (50.72 % solids) solutions are used as alkaline activators. Locally available river sand is used as fine aggregate and locally available 20 and 12.5 mm sizes crushed basalt stones are used as coarse aggregates.

2.2 Parameters Considered for Mix Proportioning of Geopolymer Concrete

For the development of fly ash based geopolymer concrete mix design method, detailed investigations have been carried out and following parameters were selected on the basis of workability and compressive strength.

A. **Fly ash**

Quantity and fineness of fly ash plays an important role in the activation process of geopolymer. It was already pointed out that the strength of geopolymer concrete increases with increase in quantity and fineness of fly ash [12]. Similarly higher fineness shows higher workability and strength with early duration of heating. So, the main emphasis is given on quantity and fineness of fly ash in the development of mix proportioning procedure of geopolymer concrete. So, in the proposed mix design procedure, quantity of fly ash is selected from Fig. 1 on the basis of fineness of fly ash and target strength [12].
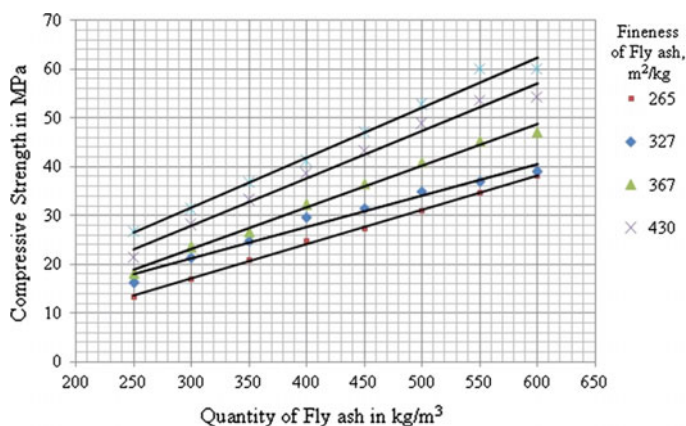
Fig. 1 Effect of quantity of fly ash on compressive strength for different fineness at solution-to-fly ash ratio of 0.35 [12]

B. **Alkaline Activators**

In the present investigation, sodium based alkaline activators are used. Single activator either sodium hydroxide or sodium silicate alone is not much effective as clearly seen from past investigation [17]. So, the combination of sodium hydroxide and sodium silicate solutions are used for the activation of fly ash based geopolymer concrete. It is observed that the compressive strength of geopolymer concrete increases with increase in concentration of sodium hydroxide solution and or sodium silicate solution with increased viscosity of fresh mix. Due to increase in concentration of sodium hydroxide solution in terms of molarity (M) makes the concrete more brittle with increased compressive strength. Secondly, the cost of sodium hydroxide solid is high and preparation is very caustic. Similarly to achieve desired degree of workability, extra water is required which ultimately reduce the concentration of sodium hydroxide solution. So, the concentration of sodium hydroxide was maintained at 13 M while concentration of sodium silicate solution contains Na_2O of 16.37 %, SiO_2 of 34.35 % and H_2O of 49.72 % is used as alkaline solutions. Similarly, sodium silicate-to-sodium hydroxide ratio by mass was maintained at 1 which set cubes within 24 h after casting and gives fairly good results of compressive strength [17].

C. **Water**

From the chemical reaction, it was observe that the water comes out from the mix during the polymerization process. The role of water in the geopolymer mix is to make workable concrete in plastic state and do not contribute towards the strength in hardened state. Similarly the demand of water increases with increase in fineness of source material for same degree of workability. So, the minimum quantity of water required to achieve desired workability is selected on the basis of degree of workability, fineness of fly ash and grading of fine aggregate [13].

D. **Aggregates**

Aggregates are inert mineral material used as filler in concrete which occupies 70–85 % volume. So, in the preparation of geopolymer concrete, fine and coarse aggregates are mixed in such a way that it gives least voids in the concrete mass. This was done by grading of fine aggregate and selecting suitable fine-to-total aggregate ratio. Workability of geopolymer concrete is also affected by grading of fine aggregate similar to cement concrete. So, on the basis of grading of fine aggregate, fine-to-total aggregate ratio is selected in the proposed mix proportioning method which is given in Fig. 2 [14].

E. **Degree of Heating**

For the development of geopolymer concrete, temperature and duration of heating plays an important role in the activation process. In the present investigation, cubes were demoulded after 24 h of casting and then place in an oven for heating at 60 °C for a period of 24 h. After specified degree of heating, oven is switched off and cubes are allowed to cool down to room temperature in an oven itself. Then compression test is carried out on geopolymer concrete cubes after a test period of 7 days. Test period is the period considered in between testing cubes for compressive strength and placing it in normal room temperature after heating. Table 1 shows the effect of duration of heating and test period on compressive strength of geopolymer concrete. It is observed that the compressive strength of geopolymer concrete increases with increase in duration and test period. From the design point of view, 24 h of oven curing at 60 °C and tested after a period of 7 days was fixed as per past research [13].

F. **Water-to-geopolymer binder ratio**

The ratio of total water (i.e. water present in solution and extra water if required) to material involve in polymerization process (i.e. fly ash and sodium silicate and sodium hydroxide solutions) plays an important role in the activation
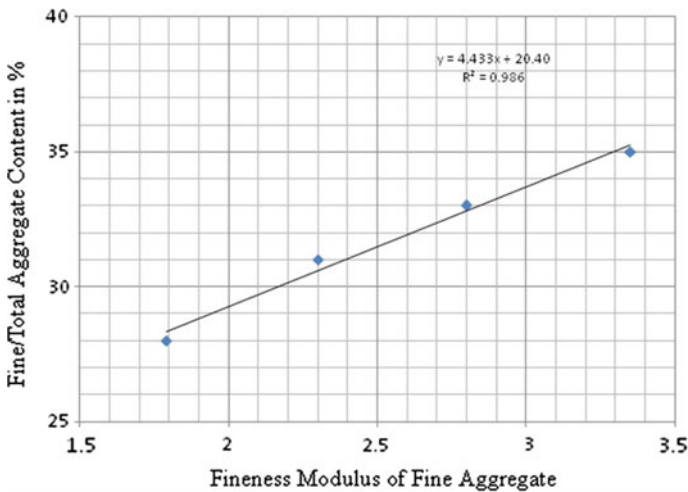
Fig. 2 Relation between fineness modulus of fine aggregate and fine-to-total aggregate content [14]

Table 1 Effect of heating temperature, duration and test period on compressive strength of geopolymer concrete [13]

S.No.	Temperature (°C)	Duration of heating (h)	Compressive strength in MPa				
			Tested after heating @				
			1 day	2 days	3 days	7 days	28 days
1	2	3	4	5	6	7	8
4	60	8	–	–	11.56	17.76	38.78
5		12	5.67	9.11	15.67	22.56	40.22
6		24	13.11	19.67	26.78	36.00	42.33

process. Rangan [10] suggested the water-to-geopolymer solid ratio in which only solid content in solution and fly ash is considered. But the calculation is tedious and water present in solution indicates the concentration of solution itself. So, in the present investigation, water-to-geopolymer binder ratio is considered. From the investigation, it is observed that the compressive strength reduces with increase in water-to-geopolymer binder ratio similar to water-to-cement ratio in cement concrete. At water-to-geopolymer binder ratio of 0.25, the mix was very stiff and at 0.40, the mix was segregated. Similarly water come out during polymerisation process and does not contribute anything to the strength. So, water-to-geopolymer binder ratio is maintained at 0.35 which gives better results of workability and compressive strength [16].

G. **Solution to fly ash ratio**

As solution (i.e. sodium silicate + sodium hydroxide) to fly ash ratio increases, strength is also increases. But the rate of gain of strength is not much significant beyond solution to fly ash ratio of 0.35. Similarly the mix was more and more viscous with higher ratios and unit cost is also increases. So, in the present mix design method, solution-to-fly ash ratio was maintained at 0.35 [15].

2.3 Preparation of Geopolymer Concrete Mixes

Preparation of geopolymer concrete is similar to that of cement concrete. Two types of coarse aggregates, sand and fly ash were mixed in dry state. Then add prepared mixture solution of sodium hydroxide and sodium silicate along with extra water based on water-to-geopolymer binder ratio and mix thoroughly for 3–4 min so as to give homogeneous mix.

It was found that the fresh fly ash based geopolymer concrete was viscous, cohesive and dark in color. After making the homogeneous mix, workability of fresh geopolymer concrete was measured by flow table apparatus as per IS 5512-1983 and IS 1727-1967. Concrete cubes of side 150 mm are casted in three layers. Each layer is well compacted by tamping rod of diameter 16 mm. All cubes were place on table vibrator and vibrated for 2 min for proper compaction of concrete. After compaction of concrete, the top surface was leveled by using trowel.

After 24 h of casting, all cubes were demoulded and then placed in an oven for thermal curing (heating). To avoid the sudden variation in temperature, the concrete cubes were allowed to cool down up to room temperature in an oven. Three cubes were cast and tested for compressive strength for each curing period.

3 Method Proposed for Mix Proportioning

Based on the experimental investigation carried out in the present study the following mix proportioning method is proposed.

3.1 Data Required for Mix Design

1. Characteristic compressive strength of Geopolymer Concrete (f_{ck})
2. Fineness of fly ash in terms of specific surface in m^2/kg
3. Workability in terms of flow
4. Oven curing (heating) 60 °C for 24 h and tested after 7 days
5. Fineness modulus of fine aggregate
6. Water absorption and water content in fine and coarse aggregate

Following design steps are used to select the suitable mix proportion of fly ash based geopolymer concrete.

3.2 Design Steps

1. **Target Mean Strength (F_{ck}) for Mix Design**

$$F_{ck} = f_{ck} + 1.65 \times S \tag{1}$$

The standard deviation, S for each grade of geopolymer concrete shall be calculated, separately on the basis of minimum 30 test samples. With reference to IS 456-2000, the value of S is assumed as per Table 1 in the first instant as mentioned in clause 9. 2. 4. 2. [18].

2. **Selection of Quantity of Fly ash (F)**
   Quantity of fly ash selected based on target mean strength and fineness of fly ash at solution-to-fly ash ratio of 0.35 from Fig. 1.

3. **Calculation of the Quantity of Alkaline Activators**
   Based on the quantity of fly ash (F) determined in the previous step, the amount of total solution is obtained using solution-to-fly ash ratio of 0.35 by mass. After that, quantity of sodium silicate and sodium hydroxide is decided using sodium silicate-to-sodium hydroxide ratio of 1 by mass.

4. **Calculation of Total Solid Content in Alkaline Solution**

   Calculate solid content in sodium silicate and sodium hydroxide solution on the basis of percentage solid present in each solution.

5. **Selection of Quantity of Water**

   Workability of geopolymer concrete is depending on total quantity of water including water present in both alkaline solutions and the degree of workability. Select the total quantity of water required to achieve desired workability based on fineness of fly ash as per Table 2.

6. **Correction in Water Content**

   In concrete, volume occupied by fine and coarse aggregate is about 70–85 % of total volume. Similarly, finer particles have large surface area as compared to coarser one and hence required more water to produce workable mix. IS 10262 [19] suggested some correction in water content for the mix proportioning of cement concrete on the basis of grading of fine aggregate. In geopolymer concrete, the role of water is to make workable concrete. So, it is recommended to apply same correction to geopolymer concrete in the proposed mix design on the basis of grading zones of fine aggregate [15]. Table 3 shows the correction in water content per cubic meter of concrete on the basis of grading zones of fine aggregate.

7. **Calculation of Additional Quantity of Water**

   In geopolymer concrete, alkaline solutions are used which contains certain quantity of water on the basis of their concentration. But to meet workability requirements, additional water may be added in the mix externally which is calculated as:

$$\text{Additional quantity of water, if required} = [\text{Total quantity of water}]$$
$$- [\text{Water present in alkaline solutions}]$$

Table 2 Water content per cubic meter of concrete [14]

Degree of workability	Flow in percentage	Quantity of water required in kg/m^3			
		Fineness of fly ash in m^2/kg			
		<300	300–400	400–500	>500
Low	0–25	80	85	100	110
Medium	25–50	90	95	110	120
High	50–100	100	110	120	135
Very high	100–150	120	130	140	160

Table 3 Correction in water content per cubic meter of concrete

Grading zone of fine aggregate as per IS 383 [20]	Correction in water content (%)
Zone-I	−1.5
Zone-II	–
Zone-III	+1.5
Zone-IV	+3

8. **Selection of Wet Density of Geopolymer Concrete**
   Select wet density of geopolymer concrete based on fineness of fly ash as per Fig. 3.
9. **Selection of Fine-to-Total Aggregate Content**
   Fine-to-total aggregate content is taken from Fig. 2 on the basis of grading (fineness modulus) of fine aggregate [15].
10. **Calculation of Fine and Coarse Aggregate Content**
    Fine and Coarse Aggregate Contents is obtained using following relations:

$$
\begin{aligned}
\text{Total quantity of aggregate} &= [\text{Wet Density of Geopolymer concrete}] \\
&\quad - [\text{Quantity of Geopolymer Binder} + \text{Additional water, if any}] \\
\text{Sand content} &= [\text{Fine-to-total aggregate content in \%}] \\
&\quad \times [\text{Total quantity of aggregate}] \\
\text{Coarse aggregate content} &= [\text{Total quantity of aggregate}] - [\text{Sand content}]
\end{aligned}
$$

11. **Actual Quantity of Materials Required on the Basis of Field Condition**
    The above mix proportion has been arrived on the assumption that aggregates are saturated and surface dry. For any deviation from this condition i.e. when aggregates are moist or air dry or bone dry, correction has to be applied on quantity of mixing water as well to the aggregates.
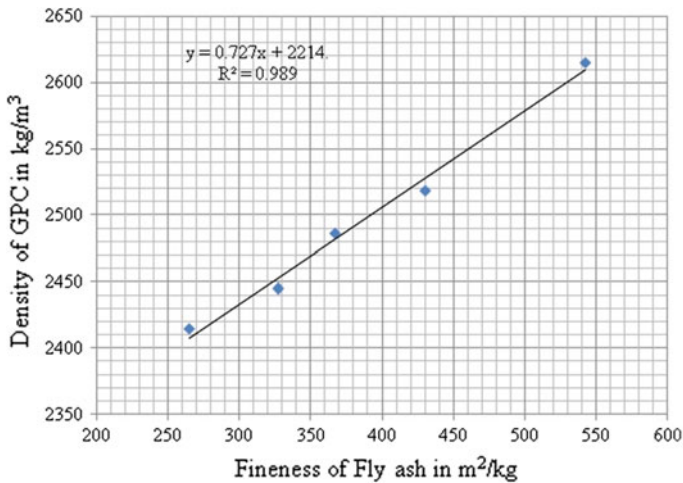
Fig. 3 Relation between fineness of fly ash and density of geopolymer concrete [15]

4 Mix Design for M30 Grade of Geopolymer Concrete Using Proposed Method

Based on the mix design steps discussed in preceding section, a sample mix proportioning for M30 grade of geopolymer concrete is carried out using proposed method. Following preliminary data is considered for the mix design:

1. Characteristic compressive strength of Geopolymer Concrete (f_{ck}) = 30 MPa.
2. Type of curing: Oven curing at 60 °C for 24 h and tested after 7 days
3. Workability in terms of flow: 25–50 % (Degree of workability—Medium)
4. Fly ash: Fineness in terms of specific surface: 430 m^2/kg
5. Alkaline activators (Na_2SiO_3 and NaOH)

   (a) Concentration of Sodium hydroxide in terms of molarity: 13 M
   (b) Concentration of Sodium silicate solution: 50.32 % solid content

6. Solution-to-fly ash ratio by mass: 0.35
7. Sodium silicate-to-sodium hydroxide ratio by mass: 1.0
8. Fine aggregate

   (a) Type: Natural river sand confirming to grading zone-I as per IS 383 [20], F.M. = 3.35
   (b) Water absorption: 3.67 %
   (c) Water content: Nil

9. Coarse aggregate

   (a) Type: Crushed/angular
   (b) Maximum size: 20 mm
   (c) Water absorption: 0.89 %
   (d) Moisture content: Nil.

5 Design Steps

1. Target mean strength
   Fck = 38.25 MPa
2. Selection of quantity of fly ash
   From Fig. 1, the quantity of fly ash required is 405 kg/m^3 for the target mean strength of 38.25 MPa at solution-to-fly ash ratio of 0.35 and for 430 m^2/kg fineness of fly ash
3. Calculation of the quantity of alkaline activators

Calculate the quantity of alkaline activators considering:

$$\text{Solution/Fly ash ratio by mass} = 0.35$$
$$\text{i.e. Mass of } (Na_2SiO_3 + NaOH)/\text{Fly ash} = 0.35$$
$$\text{Mass of } (Na_2SiO_3 + NaOH)/405 = 0.35$$
$$\text{Mass of } (Na_2SiO_3 + NaOH) = 141.75 \text{ kg/m}^3$$

Take the sodium silicate-to-sodium hydroxide ratio by mass of 1
Mass of sodium hydroxide solution (NaOH) = 70.88 kg/m^3
Mass of sodium silicate solution (Na_2SiO_3) = 70.88 kg/m^3

4. Calculation of total solid content in alkaline solution

$$\text{Solid content in sodium silicate solution} = (50.32/100) \times 70.88$$
$$= 35.67 \text{ kg/m}^3$$
$$\text{Solid content in sodium hydroxide solution} = (38.50/100) \times 70.88$$
$$= 27.29 \text{ kg/m}^3$$
$$\text{Total Solid content in both alkaline solutions} = 62.96 \text{ kg/m}^3$$

5. Selection of water content
   For medium degree of workability and fineness of fly ash of 430 m^2/kg, water content per cubic meter of geopolymer concrete is selected from Table 2
   Water content = 110 kg/m^3

6. Adjustment in water content
   For sand conforming to grading-I, correction in water content is taken from Table 3

$$\text{Adjustment in water content} = -1.5\%$$
$$\text{Total quantity of water required} = 110 - (1.5/100) \times 110$$
$$= 108.35 \text{ kg/m}^3$$

$$\text{Water content in alkaline solutions} = 141.75 - 62.96$$
$$= 78.79 \text{ kg/m}^3$$

7. Calculation of additional quantity of water
   = [Total quantity of water] − [Water present in alkaline solutions]
   = 108.35 − 78.79 = 29.46 kg/m^3

8. Selection of wet density of geopolymer concrete
   From Fig. 3, wet density of geopolymer concrete is 2,528 kg/m^3 for the fineness of fly ash of 430 m^2/kg

9. Selection of fine-to-total aggregate content

Table 4 Materials required for M30 grade geopolymer concrete

Ingredients of geopolymer concrete	Fly ash	NaOH	Na$_2$ SiO$_3$	Sand	Coarse aggregate	Total water (W/GPB)	Extra water
Quantity (kg/m^3)	405	70.88	70.88	683.13	1,268.66	108.35	29.46
Proportion	1	0.35		1.82	3.37	0.211	0.07

From Fig. 2, Fine-to-total aggregate content is 35% for fineness modulus of sand of 3.35

10. Calculation of fine and coarse aggregate content

$$\begin{aligned} \text{Total aggregate content} &= [\text{Wet density of GPC}] - [\text{Quantity of fly ash} \\ &\quad + \text{Quantity of both solutions} + \text{extra water, if any}] \\ &= 2{,}528 - [405 + 141.75 + 29.46] \\ &= 1{,}951.79 \text{ kg/m}^3 \end{aligned}$$

$$\begin{aligned} \text{Sand content} &= [\text{Fine} - \text{to} - \text{total aggregate content in } \%] \\ &\quad \times [\text{Total quantity of all-in-aggregate}] \\ &= (35/100) \times 1{,}951.79 \\ &= 683.13 \text{ kg/m}^3 \end{aligned}$$

$$\begin{aligned} \text{Coarse aggregate content} &= [\text{Total quantity of all-in-aggregate}] - [\text{Sand content}] \\ &= 1{,}951.79 - 683.13 \\ &= 1{,}268.66 \text{ kg/m}^3 \end{aligned}$$

Quantity of materials required per cubic meter for M30 grade of geopolymer concrete is shown in Table 4.

6 Results and Discussions

Geopolymer concrete mix is prepared using mix proportion calculated in preceding section and shown in Table 4. It was found that the fresh fly ash-based geopolymer concrete was viscous, cohesive and dark in colour and glassy appearance. After making the homogeneous mix, workability of fresh geopolymer concrete was measured by flow table apparatus as per IS 5512-1983 and IS 1727-1967. Freshly mixed geopolymer concrete is viscous in nature and water comes out during polymerization process, methods like slump cone test is not suitable to measure workability as concrete subside for long time while in compaction factor test, concrete cannot flow freely. So, flow table test is recommended for workability measurement of

Table 5 Results of M30 grade geopolymer concrete

Observation	Data considered in mix design	Results obtained
Workability (flow)	25–50 %	44.15 %
Degree of workability	Medium	Medium
Temperature/duration	60 °C/24 h	60 °C/24 h
Mass density	2,528 kg/m^3	2,601.48 kg/m^3
Compressive strength @ 7 days after heating	38.25 MPa (target strength)	37.22 MPa

geopolymer concrete. From Table 5, it is observed that the result of workability in terms of flow is 44.15 % which is in between 25 and 50 % which was considered for the design mix. That means the degree of workability is lies within considerable limit.

After measuring workability, concrete cubes of side 150 mm were cast in three layers and each is properly compacted similar to cement concrete. Then after 24 h of casting, all cubes were demoulded and weight was taken for the calculation of mass density. Average weight of three cubes was considered for calculation of mass density. It is observed that the average mass density obtained by proposed method is 2,601.48 kg/m^3 which is 3.33 % higher than that considered in design method.

Then cubes were placed in an oven for thermal curing at 60 °C for 24 h. To avoid sudden variation in temperature, the concrete cubes were allowed to cool down up to room temperature in an oven itself. Three cubes were cast and tested for compressive strength after 7 days of test period. Here, test period is the period considered after removing the cubes from oven till the time of testing for compressive strength. It is observed that the compressive strength of M30 grade geopolymer concrete is 37.22 MPa tested after 7 days of test period which is 2.69 % less than the target strength (38.25 MPa) considered in proposed mix design method which is within the limit of +/−15 % as per IS 456-2000.

In the previous design mixes provided by Rangan [10] and Anuradha [11], the major parameters such as fineness and quantity of fly ash, quantity of water, grading of aggregates and fine-to-total aggregate ratio were not considered. These parameters are also considered in the proposed method. The results of workability and compressive strength as per the proposed method match well with the targeted values. Present method also provides, comparatively, economical mix.

7 Mix Proportions for Various Grades of Geopolymer Concrete

Table 6 shows the quantities of all ingredients of fly ash based geopolymer concrete calculated using proposed method of mix proportioning. Also Table 7 shows the comparison between the theoretical result expected for M20–M40 grade geopolymer concrete and the experimental results of the workability and compressive strength obtained in the laboratory.

Table 6 Geopolymer concrete mixes for different grades

Grade	Quantity of water (kg/m^3) (W/GPB)[a]	GPB (kg/m^3)	Fine aggregate (kg/m^3)	Coarse aggregate (kg/m^3)
M20	118.20	378	727.40	1350.88
	0.313	1	1.92	3.57
M25	118.20	445.50	707.53	1313.97
	0.265	1	1.59	2.95
M30	108.35	513	690.54	1282.43
	0.211	1	1.35	2.5
M35	108.35	594	667.19	1239.07
	0.182	1	1.12	2.08
M40	98.50	661.50	649.37	1205.97
	0.149	1	0.98	1.82

[a] *W* Quantity of water including extra water if any. *GPB* Geopolymer binder i.e. Fly ash + (NaOH + Na$_2$SiO$_3$) solution

Table 7 Test results of present mix proportioning method for different grades of geopolymer concrete

Grade of concrete	M20	M25	M30	M35	M40
Workability in terms of flow, (%)	77.86	61.61	44.15	29.17	21.20
Degree of workability	High	High	Medium	Medium	Low
Wet density, kg/m^3	2558.52	2582.22	2601.48	2610.37	2597.04
Compressive strength, MPa	28.67	33.33	37.22	43.56	44.78

8 Conclusions

This paper proposed the guidelines for the design of fly ash based geopolymer concrete of ordinary and standard grade on the basis of quantity and fineness of fly ash, quantity of water and grading of fine aggregate by maintaining water-to-geopolymer binder ratio of 0.35, solution-to-fly ash ratio of 0.35, and sodium silicate-to-sodium hydroxide ratio of 1 with concentration of sodium hydroxide as 13 M. Heat curing was done at 60 °C for duration of 24 h and tested after 7 days after oven heating. Experimental results of M20, M25, M30, M35 and M40 grades of geopolymer concrete mixes using proposed method of mix design shows promising results of workability and compressive strength. So, these guidelines help in design of fly ash based geopolymer concrete of Ordinary and Standard Grades as mentioned in IS 456: 2000.

References

1. Davidovits J (1995) Global warming impact on the cement and aggregate industries. World Res Rev 6(2):263–278
2. Hardjito D, Wallah SE, Sumjouw DMJ, Rangan BV (2004) On the development of fly ash based geopolymer concrete. ACI Mater J 101:467–472
3. Mullick AK (2005) Use of fly ash in structural concrete: part I—why? Indian Conc J 79:13–22
4. Kumar V, Mathur M, Sinha SS, Dhatrak S (2005) Fly Ash: an environmental savior. Fly Ash Utilisation Programme (FAUP), TIFAC, DST, Fly Ash India, New Delhi, IV, pp 1.1–1.4
5. Malhotra VM, Ramezanianpour AA (1994) Fly Ash in concrete. Canada Centre for Mineral and Energy Technology (CANMET), Canada
6. Malhotra VM (1999) Making concrete greener with fly ash. ACI Conc Int 21(5):61–66
7. Davidovits J (1991) Geopolymers: inorganic polymeric new materials. J Therm Anal 37:1633–1656
8. Davidovits J (1994) Geopolymers: man-made geosynthesis and the resulting development of very early high strength cement. J Mater Edu 16(2, 3):91–139
9. Davidovits J (1988) Geopolymer chemistry and properties. In: Proceedings of 1st European conference on soft mineralurgy. Geopolymere, vol 88, France, pp 25–48
10. Rangan BV (2008) Mix design and production of fly ash based geopolymer concrete. Indian Concr J 82:7–15
11. Anuradha R, Sreevidya V, Venkatasubramani R, Rangan BV (2012) Modified guidelines for geopolymer concrete mix design using Indian standard. Asian J Civ Eng (Build Hous) 13 (3):353–364
12. Patankar SV, Jamkar SS, Ghugal YM (2012) Effect of sodium hydroxide on flow and strength of fly ash based geopolymer mortar. J Struct Eng 39(1):7–12
13. Jamkar SS, Ghugal YM, Patankar SV (2013) Effect of fineness of fly ash on flow and compressive strength of geopolymer concrete. Indian Concr J 87(4):57–61
14. Patankar SV, Jamkar SS, Ghugal YM (2014) Selection of suitable quantity of water, degree and duration of heat curing for geopolymer concrete production. In: Proceedings of 3rd international conference on recent trends in engineering and technology, ICRTET'2014. Supported by Elsevier
15. Patankar SV, Jamkar SS, Ghugal YM (2014) Effect of grading of fine aggregate on Flow and compressive strength of geopolymer concrete. In: UKEIRI concrete congress-innovations in concrete, pp 1163–1172
16. Patankar SV, Jamkar SS, Ghugal YM (2012) Effect of solution-to-fly ash ratio on flow and compressive strength of geopolymer concrete. In: Proceedings of 8th biennial conference on structural engineering convention (SEC–2012) at S.V.N.I.T., Surat, pp 161–166
17. Patankar SV, Jamkar SS, Ghugal YM (2013) Effect of water-to-geopolymer binder ratio on the production of fly ash based geopolymer concrete. Int J Adv Technol Civ Eng 2(1):79–83
18. IS 456-2000 Plain and reinforces concrete-code of practice (forth revision). Bureau of Indian Standards, New Delhi
19. IS 10262-1970 Recommended guidelines for concrete mix design on for coarse and fine aggregates from natural sources for concrete. Bureau of Indian Standards, New Delhi
20. IS 383-1970 Specification for coarse and fine aggregates from natural sources for concrete. Bureau of Indian Standards, New Delhi

Bibliography

21. Hardjito D, Wallah SE, Sumjouw DMJ, Rangan BV (2004) On the development of fly ash-based geopolymer concrete. ACI Mater J 467–472
22. Fernandez Jiminez AM, Lachowski EE, Palomo A, Macphee DE (2004) Microstructural characterisation of alkali-activated PFA matrices for waste immobilization. Cement Concr Compos 26:1001–1006
23. Hardjito D, Wallah SE, Sumjouw DMJ, Rangan BV (2004) Brief review of geopolymer concrete. Invited paper, George Hoff symposium, American Concrete Institute, Los Vegas, pp 1–14
24. Barbosa VF, MacKenzie KJ, Thaumaturgo C (2000) Synthesis and characterisation of materials based on inorganic polymers of alumina and silica: sodium polysialate polymers. Int J Inorg Mater 2(4):309–317
25. Palomo A, Fernandez-Jimenez A (1999) Alkaline activation of fly ashes: manufacture of concrete not containing Portland cement. In: Proceeding of international conference in Institute Eduardo Torroja (CSIC), Madrid, Spain, pp 1–8
26. Ranganath RV, Mohammed S (2008) Some optimal values in geopolymer concrete incorporating fly ash. Indian Concr J 82:26–34

Effect of Delay Time and Duration of Steam Curing on Compressive Strength and Microstructure of Geopolymer Concrete

Visalakshi Talakokula, R. Singh and K. Vysakh

Abstract Ordinary Portland cement (OPC) is conventionally used as a primary binder to produce concrete. The amount of carbon dioxide released during the manufacture of OPC is a matter of great environmental concern in view of global warming. Thus, alternative concrete technologies have become an area of increasing interest in research community. On the other hand, fly ash (FA), abundantly available by-product of coal fired thermal power plants poses great environmental problems in terms of its safe disposal. Therefore, use of FA as a replacement of cement in concrete production is one alternative, which is being widely used in the construction field. Geopolymer is a type of amorphous alumino-silicate cementitious material. This paper reports the results of an experimental study on the effect of delay time and duration of steam curing on the compressive strength and microstructure development of FA based geopolymer concrete specimens prepared by thermal activation of FA with sodium hydroxide and sodium silicate solution.

Keywords Compressive strength · Concrete · Geopolymer · Microstructure · Steam curing

1 Introduction

Concrete with 100 % fly ash (FA) replacement can be obtained through Geopolymerization, which can be synthesized by polycondensation reaction of geopolymeric precursor and alkali polysilicates. Geopolymerization is an innovative technology that can transform several alumino-silicate materials into useful products

V. Talakokula (✉)
Department of Civil Engineering, Galgotia's University, Greater Noida, India
e-mail: basavishali@gmail.com

R. Singh · K. Vysakh
Department of Civil Engineering, Amity University, Noida, India

called inorganic polymers. Materials rich in silica such as fly-ash, slag, rice husk and alumina such as clay are the primary requirements for geopolymerization.

Addition of FA to concrete has become a common practice in recent years. FA is a fine residue from powdered coal combustion that acts as a pozzolanic material [1] i.e. the particles react with water and lime to produce cementitious products [2, 3]. Reasons for FA replacements of cement in various proportions include economy and enhancement of certain properties of fresh concrete (workability and pumpability) as well as hardened concrete [3]. Studies have been published concerning the effect of FA on concrete porosity and resistivity, pore solution chemistry, oxygen and chloride ion diffusivity [3–6], carbonation rates [7, 8] and passivation [9], mechanical properties of concrete [10, 11]. In order to produce fly ashes with stable properties and adequate quality, many power plants have implemented their own sophisticated quality control measures. The property improvement of FA blended cements has been extensively studied and it is found that their physical and mechanical properties match those of OPC [6, 12–14].

2 Details of FA Utilized

Figure 1 shows the scanning electron microscopy (SEM) image of FA in which the spherical shape of the FA particles can be clearly seen in the SEM image. The major components of FA are silica, alumina, ferric oxide and calcium oxide. The current standard, ASTM C-618 [15] defines two classes of FA based on bulk chemical composition and, specifically, in terms of the sum $Al_2O_3 + SiO_2 + Fe_2O_3$. As per the standard, this sum is between 50 and 70 % for Class C FA and 70 % or greater for Class F FA. The higher percentage of more reactive calcium oxide in Class-C FA makes it advantageous to use for higher strength gain. To know the class of FA used in the present study, the sample was characterized by X-ray diffraction (XRD), composition analysis. XRD is a non-destructive analytical
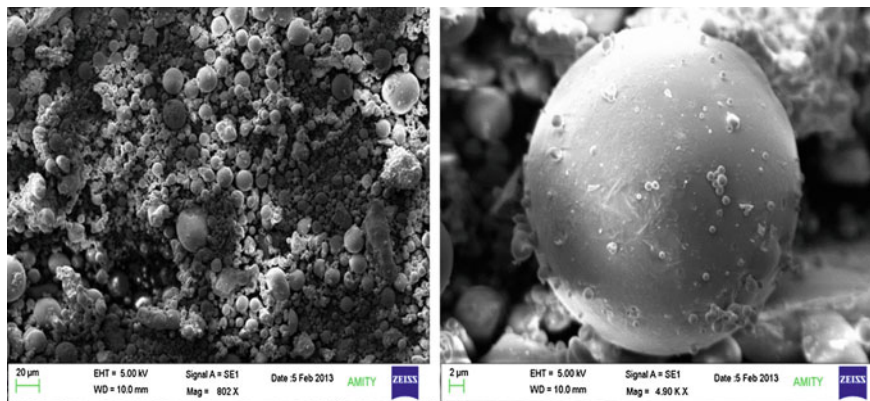
Fig. 1 SEM images of FA
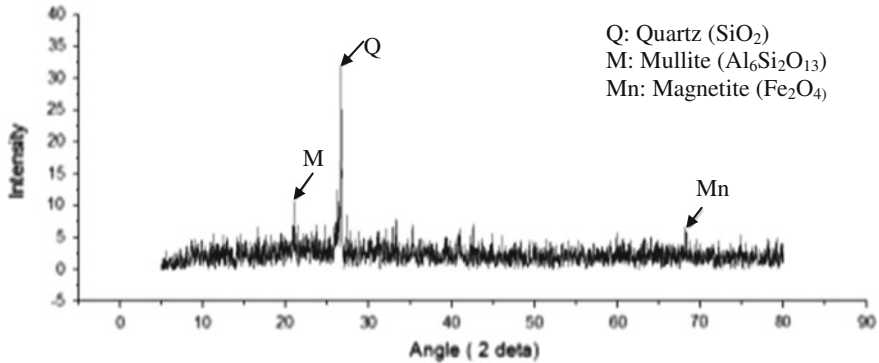
Fig. 2 XRD spectrum of FA

technique which reveals information about the crystal structures, Fig. 2 shows the XRD diffractograms of the investigated sample. The figure presents the comparative diffractograms of a sample of FA. The symbols on figures indicate the positions and peak intensities of the powder diffraction standard from international centre for diffraction database. As seen from the figure, XRD analysis indicates predominance of Quartz (SiO_2), along with Mullite ($Al_6Si_2O_{13}$) and Magnetite (Fe_2O_4), which confirms that the sample of FA analysed belongs to Class C FA.

3 Experimental Procedure

In this investigative study six cubes were made of M30 grade concrete mix with 100 % replacement of cement with FA. The alkaline liquid required for the mix preparation is prepared by mixing sodium hydroxide (NaOH) and sodium silicate (Na_2SiO_3) at room temperature. The mixture of chemicals is left at room temperature for 24 h before being used for the concrete mix preparation. Cubes of size $150 \times 150 \times 150$ mm^3 were casted as per IS: 516-1959 [16] using the chemical mixture. Table 1 shows the details of mix proportions adopted. After casting, steam curing was done for two different cycles (i) 2 h delay and for 18 h at 100 °C and (ii) 2 h delay and for 3 h 100 °C.

4 Steam Curing at Atmospheric Pressure

The temperature during curing is very important, and depending upon the source materials and activating solution, often heat must be applied to facilitate polymerization, although some systems have been developed that are designed to be cured at room temperature. In this study, two aspects of a steam-curing cycle is adopted.

Table 1 Details of mix proportions

Characteristic compressive strength	M30
Maximum size of aggregate	20 mm
Specific gravity of FA	2.2
Specific gravity of fine aggregate	2.6
Specific gravity of coarse aggregate	2.6
Zone of sand	Zone I
Specific gravity of NaOH	1.46
Specific gravity of sodium hydroxide	1.6

5 Results

After steam curing, the specimens were tested as per IS: 516-1959. The compressive strength results obtained are as shown in Fig. 3. It can be clearly seen from figures that the compressive strength of the cubes is found to be lower for a curing period of 3 h as compared to the curing period of 18 h. The maximum compressive strength attained is only about 50 % of the design strength.

6 Microstructural Study

To understand the microstructural changes occurring during these curing periods, SEM images were obtained before and after curing. Figures 4, 5 and 6 show clear variation in the microstructure of the samples. For the samples before curing (Fig. 4), a gel medium is formed due to the addition of the alkaline liquid with dispersion of FA particles can be seen.

Figure 5 shows the image of a sample with 2 h delay followed by 18 h cycle of steam curing at 100 °C, the fly ash particles are seen to be broken and the structure of it is destroyed due to the prolonged steam curing cycle. It can also be observed that the structure has a large number of disintegrated particles leading to the reduction in compressive strength. Figure 6 showing the sample after 2 h delay

Fig. 3 Results of compressive strength for two different curing regimes
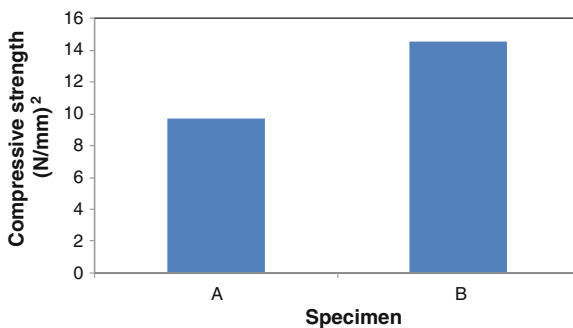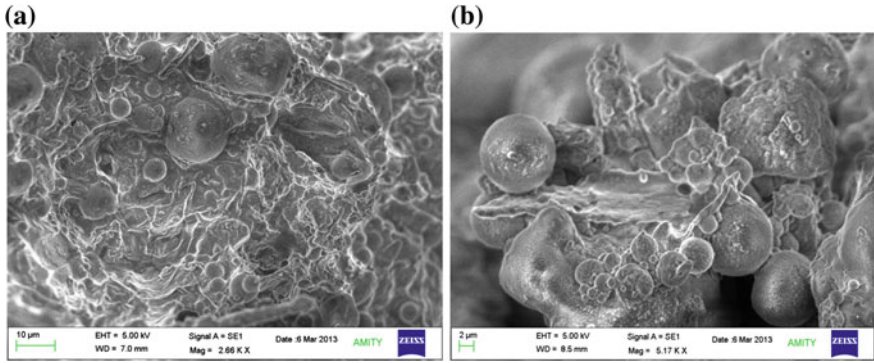
Fig. 4 SEM image of 100 % fly ash concrete sample before curing at different magnifications **a** 10 μm, **b** 2 μm
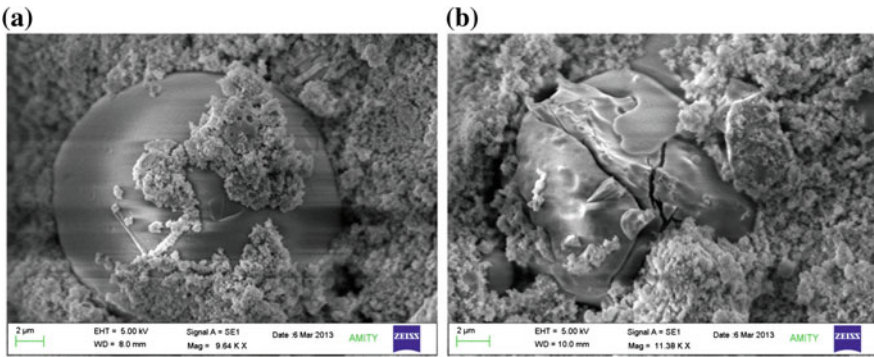
Fig. 5 SEM image of 100 % fly ash concrete sample after 2 h delay and 18 h steam curing cycle at 100 °C **a** 10 μm, **b** 2 μm
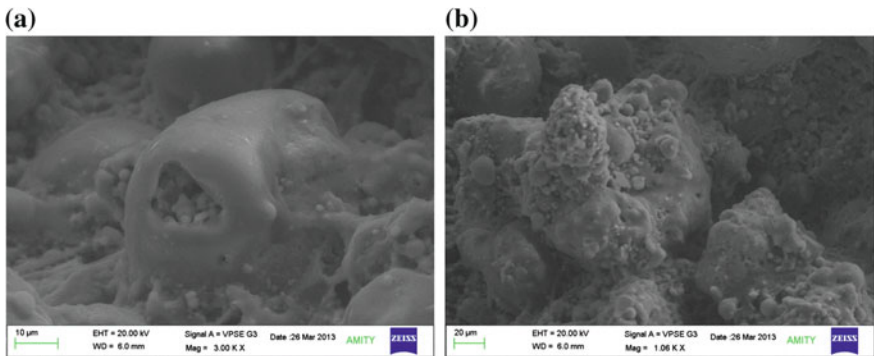
Fig. 6 SEM image of 100 % fly ash concrete sample after 2 h delay and 3 h steam curing cycle at 100 °C at different magnifications **a** 10 μm, **b** 2 μm

followed by 3 h steam curing at 100 °C. In this image the fly ash particles are seen to be well bonded. The granular particles form a continuous mass, and this fact combined with the better bonding between fly ash particles leads to a higher compressive strength.

7 Conclusions

The experimental results concluded that FA based geopolymer specimens has greater compressive strength for a steam curing cycle of 2 h delay followed by 3 h curing at 100 °C as compared to steam curing cycle of 2 h delay followed by 18 h curing at the same temperature. When the curing period is prolonged the FA particles were found to be broken.

References

 1. Fraay ALA, Bijen JM, Haan YMD (1989) The reaction of fly ash in concrete a critical examination. Cem Concr Res 19(2):235–246
 2. ACI Committee 226.3 R (1987) Use of fly ash in concrete. ACI Mater J 84:381–409
 3. Thomas MDA, Matthews JD (1992) The permeability of fly ash concrete. Mater Struct 25:388–396
 4. Preece CM, Gronvold FO, Frolund T (1983) Corrosion of reinforcement in concrete. In: Construction. Halstel, London
 5. Mangat PS, Gurusamy K (1987) Chloride diffusion in steel fibre reinforced concrete. Cem Concr Res 17:385–396
 6. Salta MM (1994) Corrosion and corrosion protection of steel in concrete. In: International conference, University of Sheffield, UK
 7. Montemor MF, Simoes AMP, Salta MM, Ferreira MGS (1993) The assessment of the electrochemical behaviour of fly ash containing concrete by impedance spectroscopy. Corros Sci 35(5):1571–1578
 8. Montemor MF, Simoes AMP, Salta MM (2000) Effect of fly ash on concrete reinforcement corrosion studied by EIS. Cement Concr Compos 22:175–185
 9. Montemor MF, Simoes AMP, Ferreira MGS (1998) Analytical characterization of the passive film formed on steel in solutions simulating the concrete interstitial electrolyte. Corrosion 54 (5):347–353
10. Paya J, Monzo J, Borrachero MV, Peris-Mora E (1995) Mechanical treatment of fly ashes-part-i: physicochemical characterization of ground fly ashes. Cem Concr Res 25:1469–1479
11. Paya J, Monzo J, Borrachero MV, Peris-Mora E, Gonzalez Z, Lope E (1996) Mechanical treatment of fly ashes-part-ii: particle morphologies in ground fly ashes (GFA) and workability of GFA-cement mortars. Cem Concr Res 26:225–235
12. Ampadu KO, Toril K, Kawamura M (1999) Beneficial effect of fly ash on chloride diffusivity of hardened cement pastes. Cem Concr Res 29:585–590
13. Bai J, Sabir BB, Wild S, Kinuthia JM (2000) Strength development in concrete incorporating PFA and metakaolin. Mag Concr Res 52:153–162
14. Behera JP, Sarangi B, Nayak BD, Ray HS (2000) Investigations on the development of blended cements using activated fly ash. Indian Concr J 74:260–269

15. ASTM C-618 (2006) Standard specification for coal fly ash and raw or calcined natural pozzolan for use in concrete. ASTM International, PA
16. IS: 516 (1959) Indian standard methods of tests for strength of concrete. Reaffirmed 2004, Bureau of Indian Standard, New Delhi

Behaviour of Geopolymer Concrete Under Static and Cyclic Loads

Sulaem Musaddiq Laskar, Ruhul Amin Mozumder and Biswajit Roy

Abstract The behaviour of plain and reinforced geopolymer concrete under static compressive, static tensile, static flexural and cyclic flexural load was investigated by means of laboratory tests. For the comparison of test results, similar type of tests were performed on Portland cement concrete, polymer Portland cement concrete and latex modified concrete. It was observed that geopolymer concrete exhibited better properties than Portland cement concrete and latex modified concrete when tested under static load and cyclic load. However, Polymer Portland cement concrete exhibited similar properties under static load but inferior properties under cyclic load than geopolymer concrete. Performance of latex modified concrete was inferior compared to the others under both static and dynamic loads.

Keywords Geopolymer concrete · Ground granulated blast furnace slag · Reinforced concrete · Cyclic flexural load

1 Introduction

Geopolymer is an emerging material that has strong potential for replacing Portland cement in concrete. Geopolymer is a chain or network of mineral molecules formed by geopolymerization. Geopolymerization is a reaction that chemically integrates naturally occurring silicon and aluminum that are ready to dissolve in alkaline solution. The alkali component which acts as an activator is a compound from the element of first group in the periodic table, therefore the material formed as a result of geopolymerization is also called as alkali activated alumino-silicate binder or alkali activated cementitious material. Silicon and aluminum atoms react to form molecules that are chemically and structurally comparable to the building natural rocks [1].

The geopolymer binder shows good bonding properties, better abrasion and impact resistance and is less susceptible to chemical attack. Geopolymer binder

S.M. Laskar (✉) · R.A. Mozumder · B. Roy
National Institute of Technology Silchar, Silchar, Assam, India

uses by-product materials such as flyash, blast furnace slag, etc. and when activated with alkaline solution, form an amorphous material i.e., alkaline alumino-silicate with high structural strength [2]. The hardening and strength gain in geopolymer occurs due to the formation of polymeric Si–O–Al bonds [3]. The geopolymer binder shows good bonding properties, better abrasion, erosion and impact resistance and is less susceptible to chemical attack [4]. Thus, the use of geopolymer can reduce CO_2 emission that is resulted during the manufacture of Portland cement. This may help in minimizing the environmental impact caused due to CO_2 emission by the construction industry.

Investigation on the properties of Geopolymer concrete was performed by combination of flyash and granulated blast-furnace slag and it was found that such concrete have similar strength development as that of PCC and better durability properties [5]. Geopolymer concrete can also be used at elevated temperatures without significant deterioration of the mechanical properties of the concrete [6]. Several works were performed to assess the behaviour of Portland cement concrete. Mathematical models were also proposed for this purpose [7]. Such models and formulations contributed to the evaluation of many properties in plain and reinforced concrete due to static and cyclic loadings [8–10].

Review of literature reveals that reports on mechanical, rheological, dynamic properties, etc. of plain and reinforced PCC, LMC and PPCC are abundant. However, the static and cyclic behaviour of reinforced GPC are yet to be reported. Such results may contribute to the further use of reinforced GPC in the structures subjected to seismic loads, dynamic loads, fatigue loads, wind loads, etc. Thus, an attempt has been made in the present study to experimentally evaluate the behaviour of GPC plain and reinforced under static and dynamic loadings. Similar type of tests were performed on plain and reinforced Portland cement concrete, polymer Portland cement concrete and latex modified concrete for comparing the test results.

2 Experimental Program

Behaviour of geopolymer concrete (GPC) under both static and cyclic load was assessed and compared with that of Portland cement concrete (PCC), polymer Portland cement concrete (PPCC) and latex modified concrete (LMC). Tests such as static compressive strength test, static tensile strength test, static flexural strength test and cyclic flexural load tests were performed for assessing the behaviour.

2.1 Materials

Ordinary Portland (43 Grade) Cement (OPC) was used for preparation of PCC. Fine aggregates (FA) of 4.75 mm maximum size having specific gravity 2.55 and coarse aggregates (CA) of 20 mm maximum size having specific gravity 2.6 obtained from

nearby sources were used. Commercially available epoxy resin (ER), natural rubber latex (NRL) and ground granulated blast furnace slag (GGBS) based geopolymer having initial and final setting time as 10 and 22 min respectively were used for the preparation of the concretes. Reinforcing bars and mild steel bars having f_y = 570 and 270 MPa respectively, were also used for reinforcing the beam specimens.

2.2 Mix Proportions and Concrete Preparation

Mix proportion of 1:1.47:2.9 having 28-day compressive strength of 24.295 MPa was selected for preparing PCC specimens. PPCC and LMC specimens were prepared by replacement of 10 % of OPC by weight with ER and NRL respectively. GPC specimens were prepared by replacement of 100 % of OPC by weight with GGBS and also by replacement of 100 % of water by weight with NaOH solution of 12 Molar (M) strength. Water/cement ratio and alkali/binder ratio was kept same for all the types of concrete to investigate the effect of different types of binders in concrete when other parameters were unchanged. Table 1 presents the details of the tests and test specimens. The PCC specimens were prepared in accordance with Indian Standard Specifications [11]. The other concretes were prepared as per the procedures mentioned in the literature.

2.3 Test Procedure and Setup

The static compressive strength test, static splitting tensile strength test and static four point flexural strength test were performed in the 1,000 kN capacity automated UTM as per Indian Standard Specifications [11, 12]. The cyclic flexural strength test was performed in the 25 kN capacity automated servo controlled actuator by applying displacement controlled loading. The specimens were subjected to cyclic displacements with a frequency of 0.25 Hz. Specific amplitude was applied in a set of three cycles consisting of downward and upward flexure before its next increment as in Fig. 1. The initial amplitude applied was ±1 mm. This amplitude was

Table 1 Details of the tests and test specimens

Specimen type			
Plain concrete			Reinforced concrete
Compressive strength test	Splitting tensile strength	Static four point flexural strength test	Cyclic flexural strength test
Cubes of 150 × 150 × 150 mm	Cylinders of 150 mm diameter and 300 mm height	Prisms of 150 × 150 × 700 mm	Beam of 115 × 150 × 1,200 mm
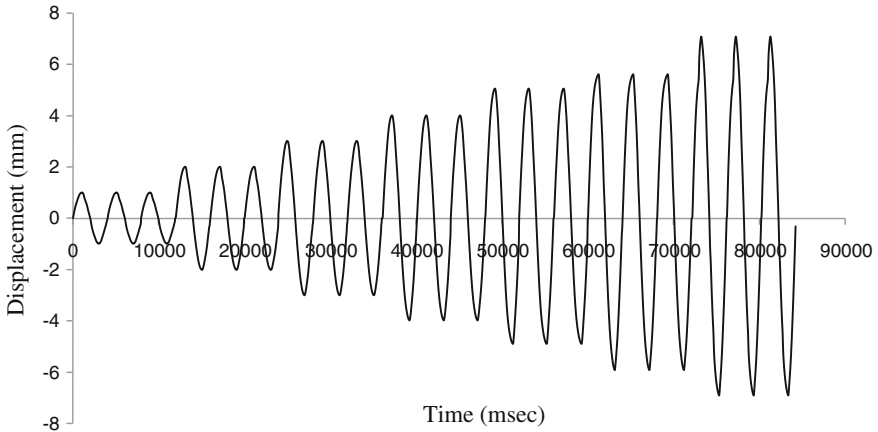
Fig. 1 Displacement history

kept very low to arrest the appearance of the first crack. The next amplitude was increased by 1 mm. The test was stopped at a stage when the load came down to a range of 75–85 % of the ultimate load carrying capacity of the specimen. The mentioned protocol was maintained for all the specimens. The details of the test setup for cyclic flexural strength test on the beams along with reinforcement are in Fig. 2.
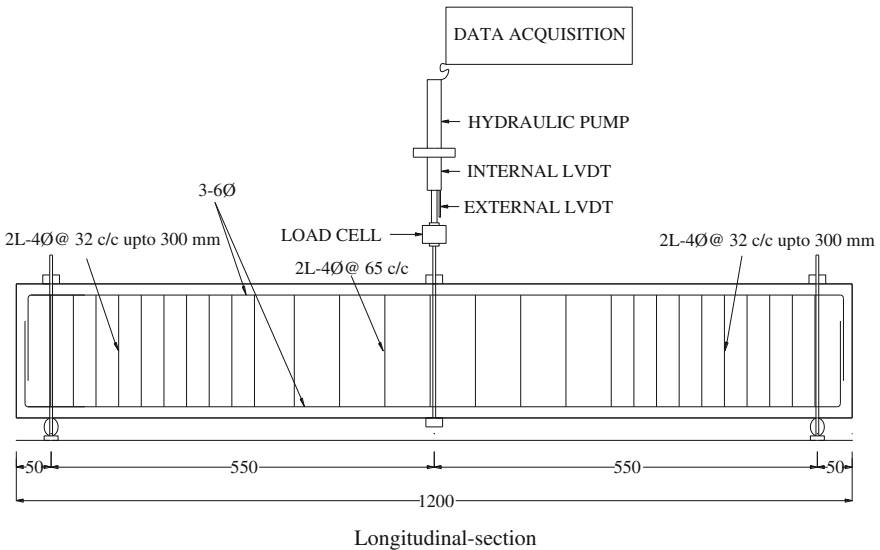
Fig. 2 Details of the specimen reinforcement and cyclic flexural strength test setup

3 Results and Discussions

3.1 Compressive Strength

Test results of the compressive strength are reported in Table 2. GPC exhibited greater compressive strength then PCC and LMC. However, lesser compressive strength was exhibited when compared to PPCC. The cracks in GPC, PCC-1 and PPCC developed due to the failure of the binder matrix and debonding at ITZ.

3.2 Flexural Strength

Figure 3 shows load-deflection behaviour for each type of concrete specimens. GPC showed an increase in strength compared to PCC and LMC. However, the strength of GPC decreased and compared to PPCC. This strength pattern is similar to that of

Table 2 Compressive strength test results

Concrete type	Compressive strength test	
	Ultimate stress (N/mm^2)	Strain at ultimate stress
PCC	24.295	0.0250
PPCC	26.020	0.0328
LMC	18.716	0.0223
GPC	25.650	0.0309
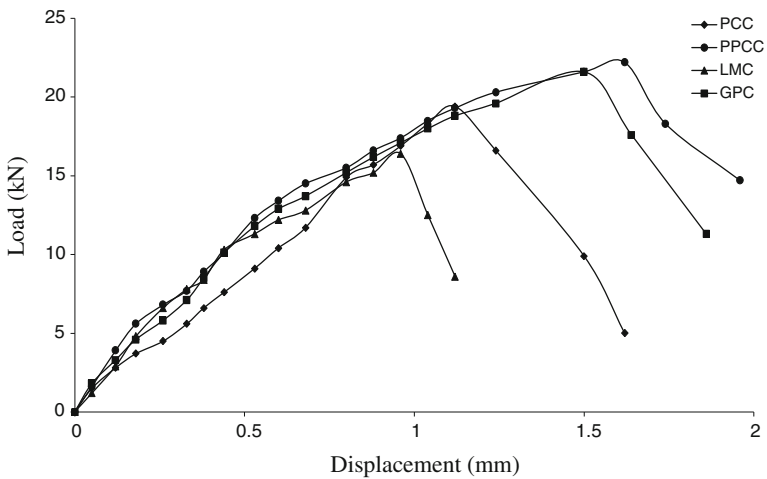
Fig. 3 Load-displacement plot from four point flexural strength test on unreinforced concrete specimens

the results from the compressive strength test. The initial stiffness of all the specimens were almost the same, with PCC showing small amount of decrease in initial stiffness compared to the others.

3.3 Splitting Tensile Strength

From the results of splitting tensile strength test as in Table 3, it was found that GPC exhibited higher tensile strength than PCC and LMC. Moreover, the strength was comparable to that of PPCC. From the observation of the failed specimen, it was concluded that the failure in GPC, PCC and PPCC happened primarily due to debonding at ITZ.

3.4 Response Due to Cyclic Flexural Load

Figures 4, 5, 6 and 7 present the load-deflection behaviour of each type of concrete beam due to cyclic flexural load. From the failure envelop in Fig. 8, it was observed that the maximum load attained by GPC due to downward flexure was 24.15 kN and due to upward flexure was 21.28 kN at 5 mm displacement. Compared to PCC, GPC showed increase in maximum load by 30.68 % in downward flexure and by 26.29 % in upward flexure. Moreover, GPC also showed increase in maximum load by 2.59 % in downward flexure compared to PPCC. Increase in maximum load in upward and downward flexure in GPC was also observed when compared with LMC.

3.5 Stiffness Degradation

To obtain the stiffness (K) of the specimen, the secant stiffness corresponding to a specified displacement is considered as given

$$K = (F_D^+ - F_D^-)/(D_D^+ - D_D^-) \tag{1}$$

Concrete type	Splitting tensile strength (N/mm^2)
PCC	2.05
PPCC	2.27
LMC	1.56
GPC	2.21

Table 3 Splitting tensile strength test results
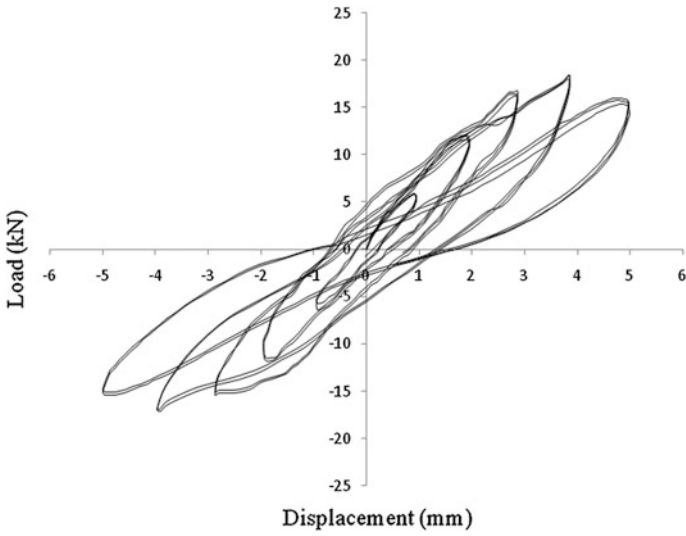
Fig. 4 Hysteretic response of PCC beam
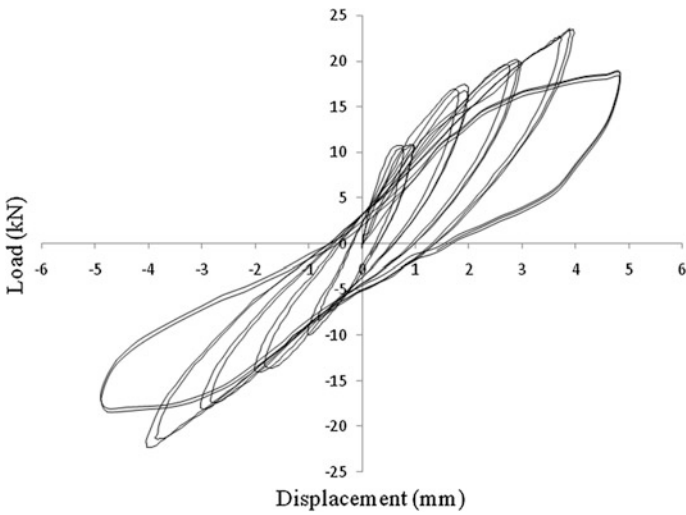
Fig. 5 Hysteretic response of PPCC beam

where D_D^+ and D_D^- are the displacement for a particular amplitude due to downward and upward flexure respectively and F_D^+ and F_D^- are their corresponding loads. Stiffness degradations of the concrete specimens are presented in Fig. 9. The stiffnesses of GPC and PPCC were more than PCC corresponding to any displacement. Though the initial stiffness of PPCC was higher than that of
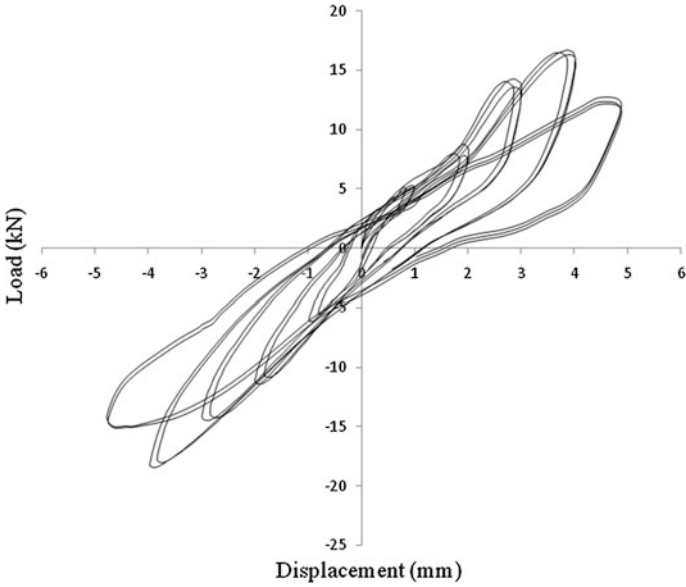
Fig. 6 Hysteretic response of LMC beam
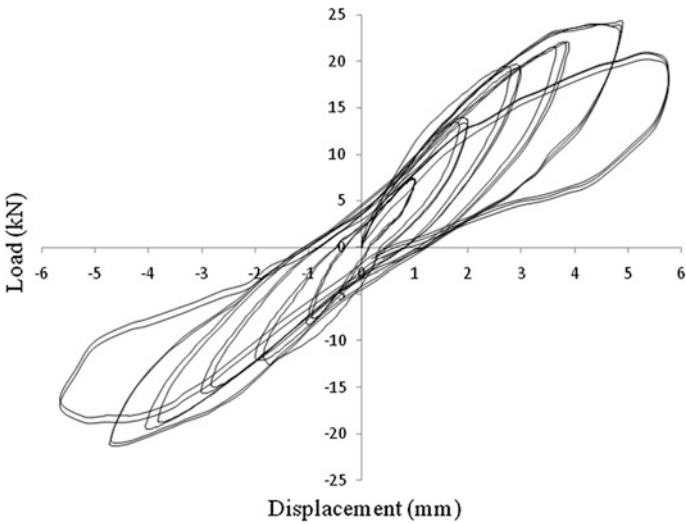
Fig. 7 Hysteretic response of GPC beam

GPC, the degradation occurred very rapidly leading to lowering of stiffness at ±3 mm displacement compared to GPC. The stiffness of GPC corresponding to the first applied amplitude of ±1 mm was 8.14 kN/mm, while that of PCC was
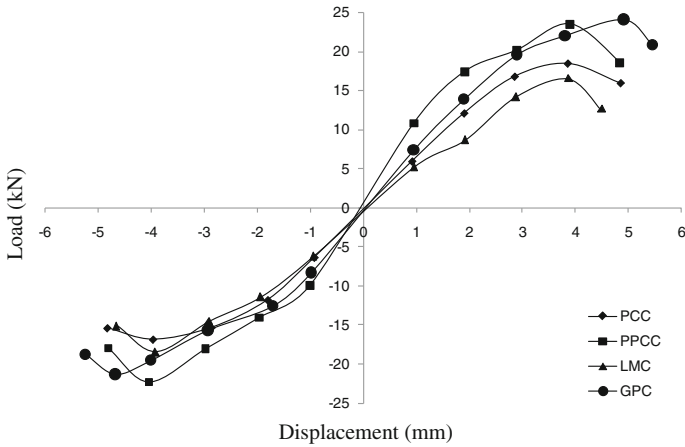
Fig. 8 Failure envelop of the specimens

Fig. 9 Stiffness versus amplitude plot for the specimens
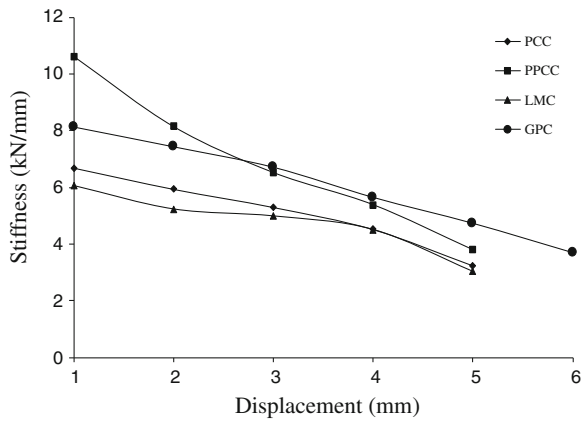
6.7 kN/mm. Thus, the gain in initial stiffness in GPC compared to PCC was found to be 21.49 %. At the second amplitude of ±2 mm, the stiffness of GPC and PCC got reduced by 8.48 and 11.19 % respectively. PCC showed fastest degradation while GPC showed slowest stiffness degradation among all. LMC showed lowest stiffnesses at any amplitude.

3.6 Energy Dissipation Capacity

It is known that the ability of a structural member to sustain the effects of earth-quake depends largely on its capacity to dissipate the energy. This energy dissipated

Fig. 10 Cumulative energy
dissipation versus amplitude
plot for the specimens
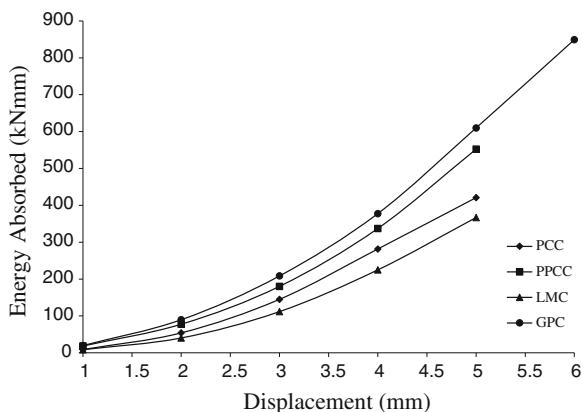
is determined by measuring the area of the hysteresis loop. The cumulative energy
dissipated at each amplitude by the specimens is presented in Fig. 10. It is calcu-
lated by summing up the energy dissipated by each specimen in all the preceeding
amplitudes including that particular amplitude.

When compared to PCC, gain in cumulative energy dissipation at failure stage in
GPC was found to be 1.45 times. The gain in the capacity in GPC was also exhibited
when compared with PPCC and LMC at any displacement. The increase in stiffness
and straining capacity attracted more load at any displacement for GPC specimen in
comparison to the other specimens. Thus, the total area enclosed by the plot of load
versus displacement was more for GPC specimen. This was the reason for gain in
cumulative energy dissipation in GPC and hence the structure built with GPC can
have better capability to resist cyclic load due to earthquake, wind storm, etc.

4 Conclusions

The following general conclusions may be derived from the present study:

1. GPC showed higher strength than PCC and LMC but lower strength than PPCC
   under static loading condition.
2. The strain corresponding to ultimate compressive strength of GPC was also
   found to be higher than PCC and LMC but lower than that of PPCC.
3. However, under cyclic load GPC showed higher strength than PCC, PPCC and
   LMC.
4. The stiffness degradation and energy dissipation capacity of GPC was found to
   be better than PCC, PPCC and LMC.

References

1. Khale D, Chaudhary R (2007) Mechanism of geopolymerization and factors influencing its development: a review. J Mater Sci 42:729–746
2. Alonso S, Palomo A (2001) Alkaline activation of metakaolin and calcium hydroxide mixtures: influence of temperature, activator concentration and solids ratio. Mater Lett 47:55–62
3. Davidovits J (1994) Properties of geopolymer cements. In: Alkaline cements and concretes, pp 131–149
4. Lloyd NA, Rangan BV (2010) Geopolymer concrete: a review of development and opportunities. In: Proceedings, 35th conference on our world in concrete and structures, Singapore Concrete Institute, Singapore, pp 25–27
5. Li G, Zhao X (2003) Properties of concrete incorporating fly ash and ground granulated blast-furnace slag. Cem Concr Res 25:293–299
6. Siddique R, Kaur D (2012) Properties of concrete containing ground granulated blast furnace slag (GGBFS) at elevated temperatures. J Adv Res 3:45–51
7. Carpinteri A, Carpinteri A (1984) Hysteretic behavior of RC beams. J Struct Eng 110 (9):2073–2084
8. Hwang TH, Scribner CF (1984) R/C member cyclic response during various loadings. J Struct Eng 110(3):477–489
9. Darwin D, Nmai CK (1986) Energy dissipation in RC beams under cyclic loadings. J Struct Eng 112(8):1829–1846
10. Fang IK, Yen ST, Wang CS, Hong KL (1993) Cyclic behavior of moderately deep HSC beams. J Struct Eng 119(9):2573–2592
11. IS: 516 (1959) Methods of tests for strength of concrete. Bureau of Indian Standard, New Delhi
12. IS: 5816 (1999) Splitting tensile strength of concrete—method of test. Bureau of Indian Standard, New Delhi

Biofibre Reinforced Concrete

**T. Manasa, T. Parvej, T. SambaSiva Rao, M. Hemambar Babu
and Sunil Raiyani**

Abstract This paper presents the outcomes of the experimental program conducted to study the mechanical properties of concrete homogeneously reinforced with biofibres like *Sida cordifolia* plant fibre (SICOF), Pineapple leaf fibre (PALF), Banana fibre (MUSAF) and Bagasse (BAGAF). The optimum content of fibre to be used is determined by conducting an experimental study on MUSAF and it is found to be 0.25 % by weight of concrete. The performance of this biofibre reinforced concrete (BFRC) is evaluated by conducting strength tests like compressive, split tensile and flexural strength tests in accordance to Indian standards. The results when biofibres are used in concrete individually shows that MUSAF and SICOF are good in improving compressive strength and split tensile strength, respectively. Scanning Electron Microscopy (SEM) images indicate that there is good bonding between these biofibres and concrete matrix. In this study, also an attempt has been made to check the performance of biofibres when used in combination. The combinations tried are SICOF-PALF (SP), SICOF-MUSAF (SM), SICOF-BAGAF (SB) and PALF-MUSAF (PM). Out of these, the combination SM gave excellent results both in improving compressive and split-tensile strengths of concrete.

Keywords Biofibres · *Sida cordifolia* · Pineapple leaf fibre · Optimum fibre content · BFRC

1 Introduction

Concrete is the most widely used construction material for permanent structures throughout the world since the last few decades and it is the second largest consumable material after water. However, this extremely versatile material suffers

T. Manasa (✉) · T. Parvej · T.S. Rao · M.H. Babu · S. Raiyani
Department of Civil, Rajiv Gandhi University of Knowledge Technologies,
Nuzvid Campus, Gachibowli 521202, Andhra Pradesh, India
e-mail: manasathalluri@gmail.com

from certain intrinsic deficiencies like low tensile specific modulus, limited ductility and little resistance to cracking. To compensate, steel is added to concrete which distributes the tensile strain forces that causes concrete to crack and ultimately fail. Although this method has been used successfully for many years, there are few associated drawbacks. Steel is expensive to purchase, transport and store. The placement of steel consumes time and labour costs and often requiring placement in difficult and dangerous locations. Most serious of all, steel is highly corrosive in nature leading to failure of structure which is expensive to repair and even requiring demolition of the structure. Hence, researchers are aiming at sustainable and eco-friendly structures and to develop a material which could replace steel.

Since 1960, efforts have been made by scientists and engineers to develop concrete composites, devoid of the basic drawbacks of concrete, culminating in the development of fibre reinforced concrete (FRC). This FRC is a new material in which fibres are randomly oriented and homogeneously distributed. These fibres can be natural or manmade. The proven properties of Natural/Biofibres like renewability, lightweight, non-corrosive nature, high toughness etc. makes them stand in lieu of synthetic fibres. Inclusion of biofibres as reinforcement in concrete have proved to improve resistance to fatigue, impact, thermal shock and spalling and also supports the concept of sustainability and green building. Although several researchers have done investigation on biofibres, very limited or no work has been done on biofibres like SICOF (*Sida cordifolia* fibre), PALF (Pineapple leaf fibre), MUSAF (Banana fibre) and BAGAF (Bagasse). In this study, SICOF is the fibre which is used entirely new exclusively in this work and SICOF and PALF are used as reinforcement in concrete for first time thus finding their new application. This paper presents a summary of findings of the study conducted to investigate the properties of this biofibre reinforced concrete (BFRC). In this study, the biofibres SICOF, PALF, MUSAF and BAGAF are used as reinforcement both individually and also in combinations like SICOF-PALF, SICOF-MUSAF, SICOF-BAGAF and PALF-MUSAF. The present study aims to develop a new class of concrete by analyzing the mechanical properties of BFRC experimentally including compressive, split-tensile and flexural strength. This study is useful for further research on BFRC which helps in developing a sustainable and ecofriendly structures.

2 Background

2.1 History of FRC

The concept of using fibres as reinforcement dates back to biblical times when straws were used in mud brick manufacture [1]. The first modern alternative was the use of asbestos in concrete in the early 19th century, to protect it from crack formation. The need to replace asbestos fibres due to associated health risks in the early 1950s gave rise to the development of composite materials and by 1970s steel

fibre reinforcement had been accepted as a viable alternative to traditional reinforcement. Steel fibre however suffered the same problems as traditional steel. In addition, steel fibre reinforced concrete required high dosage rates and handling steel fibres often resulted in puncture wounds [2, 3]. Hence, research still continues on the use of different types of fibres in concrete.

2.2 Literature Review

The use of biofibres in cementitious materials is widely reported in the literature. In 1990, Wafa [4] in his paper showed that upon addition of fibres to the concrete matrix alters the mechanical properties like compressive strength, modulus of elasticity, flexure, toughness, fatigue strength and impact resistance [4]. In 1999, Toledo Filho et al. [5], studied the performance of sisal fibre as reinforcement in cement based composites which increased tensile stress at splitting failure. In 2005, Ramakrishna and Sundararajan [6, 7] made an investigation on the resistance to impact loading of cement mortar slabs reinforced with four natural fibres, coir, sisal, jute and kenaf out of which coir reinforced slabs gave best results. Li et al. [8], studied the mechanical and physical properties of hemp fibre reinforced concrete (HFRC) with variables of experiment as (1) mixing method; (2) fibre content by weight; (3) aggregate size; and (4) fibre length. In 2006, Teo et al. [9] presented a paper investigating the flexural behavior of reinforced concrete beams produced from oil palm shell (OPS) aggregates. In 2011, Elsaid et al. [10] conducted out an experimental research program to study the mechanical properties of a natural fiber reinforced concrete (FRC) which is made using the bast fibers of the kenaf plant. In 2012, Majid [11] presented a paper on the properties of different natural fibres which were investigated by different researchers as a construction material to be used in composites (such as cement paste, mortar and/or concrete). All the above works supports the use of biofibres in cement matrix. The present study is intended to find the potential biofibres which can be used as construction material.

2.3 SICOF Plants and Fibres

Sida cordifolia is a perennial subshurb of the *Malvaceae* family, which grows up to 1.5 m tall with hairy, long and slender yellow-green stems and dark yellow flowers (Fig. 1a). It is widely distributed along with other species throughout tropical and sub tropical plains all over India and Srilanka, growing wild along the road side. This plant has various medicinal uses as it is used in the treatment of respiratory related troubles [12]. This study discovers the latent use of this plant by extracting fibre from the stem and as reinforcing material with concrete, thus finding the new use of this fibre.

Fig. 1 **a** *Sida cordifolia* plant (*inset* showing its flower). **b** Retting of sida stems. **c** SICOF

Fibre from this plant (SICOF) can be obtained by a process called retting. The stems of SIDA are placed for retting in concrete tank as shown in Fig. 1b. Retting is a process of obtaining natural fiber in which the stalks are submerged in water

where there will be action of micro-organisms to dissolve or rot away much of the cellular tissues and pectins surrounding bast-fibre bundles, and so facilitating separation of fibre from the stem [13]. The fibre is obtained by manual separation of outer bark from the stem and it is washed for several times to get clean fibre. The obtained fibre is pale yellow in color (shown in Fig. 1c). It is dried in air and then cut into pieces of length of 35 mm.

2.4 PALF Plants and Fibres

Pineapple (*Ananas comosus,* L. family *Bromeliaceae*) is a perennial tropical plant with edible fruits. This is an herb which grows to 1.0–1.5 m tall and has a short, stocky stem with tough, waxy leaves. The fruit of pineapple is known to have good nutritional value and health benefits [14]. After the first fruit is produced, the entire crop is removed leaving behind a lot of biological waste. The leaf of pineapple (shown in Fig. 2a) has fibre and its major use is to make textiles (Barong Tagalog). This study recognizes the new use of PALF by reinforcing it in concrete.

The pineapple leaves are decorticated manually by beating, rasping and stripping using wooden hammers. The scraped leaves are immersed in retting tank containing 1:20 substrate (urea): liquor (water) ratio. 0.5 % urea or di-ammonium phosphate (DAP) was added for quick retting [15]. Pineapple leaves placed for retting in concrete tank is shown in Fig. 2b. The leaves from retting tank are regularly checked by pressing them with finger tips to see whether the fibres are loosened and can be extracted. At the end of retting the leaves were taken out and fibres were mechanically extracted by washing in water. The extracted fibres are pale green to cream white in color (shown in Fig. 2c) and then dried in air and cut to a length of 35 mm.

2.5 MUSAF Plants and Fibres

Banana plant (*Musa sapientum,* L. family *Musaceae*) is a perennial herb with trunk-like pseudo stems growing mostly in humid tropical regions. Figure 3a shows the Banana plants used for this study. These are vigorously growing, monocotyle-donous herbaceous plants which attain height up to 7 m and leaves up to 2.7 m length [16]. The mother plant is cut off after the harvest and usually, entire stem is thrown out as waste. The fibre obtained from stems after harvest is finding its commercial use now a days, as it is used to produce doormats, carpets, yarn, rope, interior decorative items etc. In this study, this fibre is used as reinforcement in concrete.

To obtain fibre, the stems stroked against floor repeatedly until the stems become loose and are separated into thinner ones. They are then placed in retting tank with

Fig. 2 **a** Pineapple leaves (*inset* showing Pineapple fields). **b** Retting of Pineapple leaves. **c** PALF

urea (1:20 substrate:liquor ratio) as shown in Fig. 3b for 10 days. After retting, the fibres are washed thoroughly in water and dried in air. The fibre which is cream white in color (shown in Fig. 3c) is cut into pieces of length 35 mm.

Fig. 3 **a** Banana plants. **b** Retting of Banana stems. **c** MUSAF

Fig. 4 a Sugar Cane fields. **b** Bagasse

2.6 BAGAF Plants and Fibres

Sugarcane (*Saccharum officinarum*, L. family *Poaceae*) shown in Fig. 4a is a member of grass family, which is widely cultivated all over the globe mainly in tropics, providing around 70 % of world's sugar. It is a tall grass which looks rather like a bamboo cane, grows to 3–6 m high with stems 20–45 mm in diameter and leaves 70–150 cm long, 6 cm wide [17].

Crushed Sugarcane stalks (Bagasse) are taken and dried in sunlight for 3–5 days as shown in Fig. 4b. During nights, the stalks are kept in room or covered with tarpaulin covers to keep away from moisture/dew. After drying, the inner soft portion of the stalk is scrapped with knife and they are cut into length of 35 mm.

3 Experimental Program

An experimental program has been conducted to evaluate the mechanical properties of concrete reinforced with biofibres. Four types of biofibres (SICOF, PALF, MUSAF and BAGAF) are used in concrete both as individual and in combination. The combinations are SICOF-PALF (SP), SICOF-MUSAF (SM), SICOF-BAGAF (SB) and PALF-MUSAF (SM). Compressive, split-tensile and flexural strength tests are conducted on concrete with biofibre and the results are compared with that

of plain concrete. In each case, three specimens are casted and tested to get compressive, split-tensile and flexural strength values. Casting, curing and testing procedures are done as per IS standards.

3.1 Materials

The cement used for concrete is 53 grade ordinary Portland cement confirming to IS: 12269-1987 [18]. The physical properties are shown in Table 1. River sand confirming to zone II as per IS: 383-1970 [19] is used and crushed granite coarse aggregate of sizes 12 and 20 mm are used. Ordinary portable water confirming to IS: 456-2000 [20] is used to prepare concrete specimens. The physical properties of fine aggregate are given in Table 2 and that of coarse aggregates are given in Table 3. The grade of concrete used is M30 and the mix proportions are 1:1.5:2.72:0.45 (cement:fine aggregate:coarse aggregate:w/c ratio).

Table 1 Physical properties of 53 grade ordinary Portland cement

Physical property	Value of OPC used	Requirement as per IS 12269-1987
Standard consistency	31.5 %	–
Initial setting time	110	Maximum of 30 min
Final setting time	210	Maximum of 600 min
Specific gravity	3.14	–
Compressive strength in N/mm^2 at 7 days (MPa)	33.7	Not less than

Table 2 Physical properties of fine aggregate

Physical properties	Values
Specific gravity	2.64
Fines modulus	2.57
Water absorption (%)	3.35

Table 3 Physical properties of coarse aggregate

Physical properties	Values	
	12 mm	20 mm
Specific gravity	2.71	2.73
Water absorption (%)	1.13	0.3
Bulk density (kg/m^3)	1,575	1,587
Impact value (%)	19.12	11.37

3.2 Specimens

Cubes of size 150 mm × 150 mm, cylinders of size 150 mm × 300 mm and beams of size 100 mm × 100 mm × 500 mm are used for compressive, split-tensile and flexure strength tests. The sizes are selected according to IS 516-1999 [21].

3.3 Items of Investigation

The optimum fibre content is determined by conducting compressive and split-tensile strength tests on concrete with biofibres. Also, the BFRC specimens and control specimens are tested for compressive, split-tensile and flexure strength test at the age of 7 and 28 days. The tests are done as per Indian standard codes (IS: 516-1999 and IS: 5816-1999) [21, 22].

3.4 Mixing Procedure

The mixing procedure followed for casting is explained below. The procedure is same for all types of biofibres (both individual and combination).

 (i)   The calculated quantity of water is measured and then poured in the pan mixer.
 (ii) The required amount of cement and sand is weighed added into mixer with water.
(iii) Similarly, coarse aggregate is added into mixer and mixed for 2–3 min until a homogeneous mix is obtained.

Fig. 5 Mixing of biofibres while casting

(iv) The calculated quantity of fibre is carefully added to the mixture and mixed until the fibres are uniformly distributed. The addition of fibres is shown in Fig. 5.

(v) The concrete thus made is casted into cube, cylinders and beam specimens.

4 Results and Discussion

4.1 Optimum Fibre Content Determination

The amount of fibre to be added into concrete is an important factor to be determined as it directly affects the compressive and tensile strength of concrete. The designed grade of concrete is M30 and the age of testing is 3 days. The concrete cube of size 150 mm × 150 mm and cylinder specimens of size 150 mm × 300 mm are tested with fibre contents of 0.2, 0.25, 0.3 and 0.35 % with MUSAF as reinforcement material. The compressive and split-tensile strength results are shown in Fig. 6a, b respectively.

From the results of compressive strength test, the stress values increased upon adding fibre up to 0.25 % and then showed a decreasing pattern. Similar behavior can be observed with split-tensile strength test, but the peak value is at 0.3 %. It can be noted that the split-tensile stress at 0.25 % is 2.51 MPa which is very close to the stress at 0.3 % fibre content i.e., 2.59 MPa. Hence, fibre content of 0.25 % is taken as optimum, for this study.

4.2 Strength Tests

Mechanical strength properties on concrete with single type of fibres are evaluated by conducting compressive, split-tensile and flexure strength test. The results are presented below. The identity of specimens, represent R, S, P, M and B for Reference, SICOF, PALF, MUSAF and BAGAF respectively.
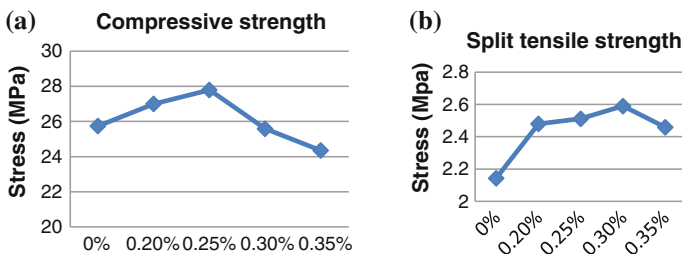
Fig. 6 a Compressive strength. b Split tensile strength

4.2.1 Compressive Strength Test

The 7 and 28 days compressive strength results are presented in Table 4. The specimens with biofibres are compared with that of plain control specimens. The control specimens showed very little cracking prior to failure. Brittle failure is observed with the sudden spalling of concrete. Whereas, BFRC specimens showed ductile type of failure with more distributed cracking.

The observation of table shows that the stress at 1st crack of BFRC (excluding BAGAF) increased in comparison with reference specimens. Among these biofibres, BAGAF showed very inferior compressive strength values. The 7 days results in comparison with 28 days results are shown in Fig. 7.

From the figure, it can be observed that, all types of specimens showed an increase in compressive strength at 28 days compared with 7 days. Eventhough PALF showed inferior compressive strength at 7 days testing compared with reference, its value increased significantly in comparison with reference at 28 days. Among all fibres, MUSAF is found to give good compressive strength values. The failure specimens of BFRC are taken and observed under SEM to study its bonding property. The images as shown in Fig. 8 indicates that there is good bonding between fibre and cement matrix.

Figure 9 shows the compressive strength results of BFRC with biofibres used in combinations. The results reveal that the combination SM showed good results at 7 and 28 days testing as well. While the combination SB showed peculiar behavior at

Table 4 Compressive strength test results of individual fibres at the age of 7 days

Type of fibre used	Stress at 1st crack (MPa)	7 days compressive strength (MPa)
R	16.69481481	31.06
S	26.88667	35.52
P	18.93556	28.97
M	26.06815	34.02
B	–	6.14

Fig. 7 Compressive strength test results of BFRC with single type of biofibres
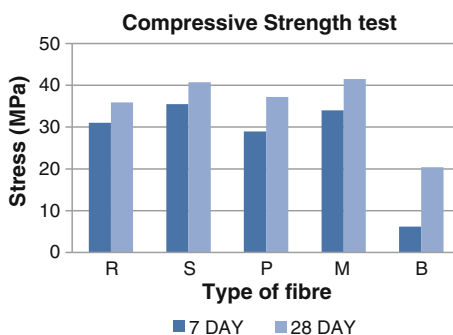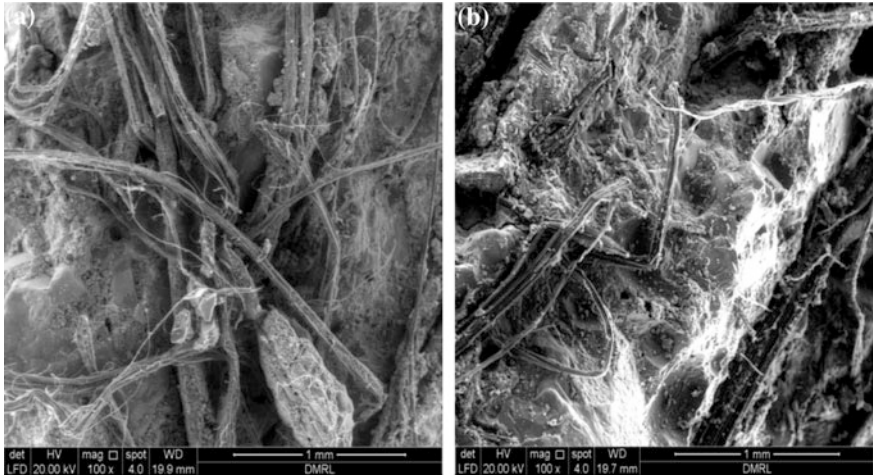
Fig. 8 a PALF. **b** SICOF

Fig. 9 Compressive strength results of BFRC with biofibre used in combinations
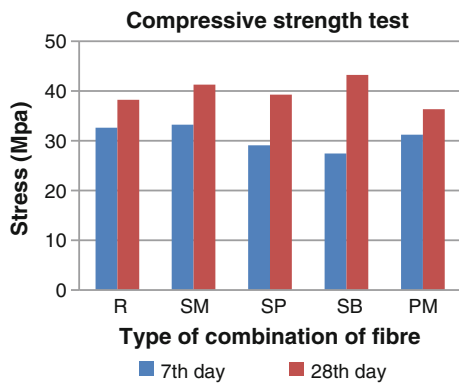
28 days testing. A further more investigation is needed to study the nature of SB, perhaps material characterization.

Figure 10 shows the comparison of BAGAF and SICOF with combination SB. In this case, the combination SB shows sudden increase in strength at 28 days compared with 7 days. This pattern is observed in BAGAF. SB also gives highest compressive strength showing the dominant behavior of SICOF. From this, we can observe that both the characteristics of biofibres is seen in their combination.

The observation of cube specimens after testing of compressive strength revealed that the specimens of BFRC are intact. The control specimens showed brittle kind of failure and the pieces just stripped off. Figure 11 the specimens of BFRC and plain control specimens. The failure angle of both the BFRC specimens and control specimens are observed. It is 70° for control and 38° for BFRC
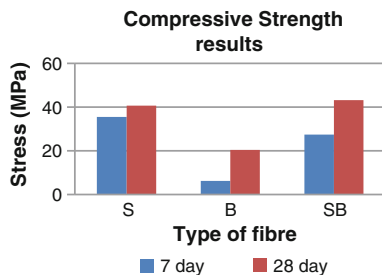
Fig. 10 Compressive strength results showing the comparison of SICOF and BAGAF with combination SB

Fig. 11 **a** BFRC specimen. **b** Control specimen

specimens. This clearly shows that the failure of control specimens is due to both axial and shear forces. Whereas, BFRC specimens failed under axial force only showing that the biofibres are successful at absorbing shear forces. The failure of specimens under compressive load showed that the BFRC specimens showed bulging type of failure.

4.2.2 Split-Tensile Strength Test

The 7 and 28 days split-tensile strength test is conducted to evaluate the BFRC specimens and compared to the behavior of plain concrete specimens. The plain specimens showed sudden failure with a single crack along the vertical diameter of the specimen. Unlike this, the BFRC specimens showed ductile type of failure.

The 7 and 28 days test results of BFRC specimens with single type of biofibre is given in Fig. 12. The results indicate that SICOF showed an increase in split tensile strength compared with reference and rest of the biofibres. Also in this case, BAGAF showed inferior characteristics at both 7 and 28 days. Figure 13 shows the

Fig. 12 Split tensile strength test results of fibres with single type of biofibre
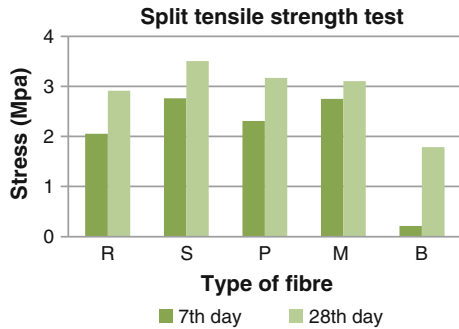
Fig. 13 Split tensile strength results of BFRC specimens with combination of fibres
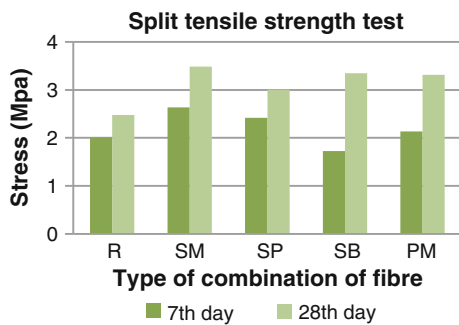
split-tensile strength results of BFRC specimens with biofibres in combination. The results indicate that the combination SM gave good results both at 7 and 28 days.

The BFRC specimens showed more ductile mode of failure. An inspection of failure specimens show the bridging of cracks by biofibres (Fig. 14). The specimens could take extra load even after failure due to the presence of biofibres.

4.2.3 Flexural Strength Test

Four-point bending tests are conducted on BFRC specimens to evaluate the flexural strength and compare with that of control specimens. Figure 15 shows the 7 and 28 days results of BFRC specimens with single type of fibre. The results show that there is no significant increase in flexure strength of BFRC specimens when compared with that of control specimens. An increase of flexure strength could be observed with increasing in biofibre content and its length.

The 7 and 28 days flexural strength results of BFRC specimens with combination of fibres are in Fig. 16. The results indicate that the combinations SP and PM showed an increase in the value of modulus of rupture compared with control specimens. This may be due to the enhanced performance of PALF with SICOF and MUSAF.

Fig. 14 Cylinder specimen of BFRC showing bridging of cracks by fibre

Fig. 15 Flexure strength test results of BFRC specimens with single type of fibre
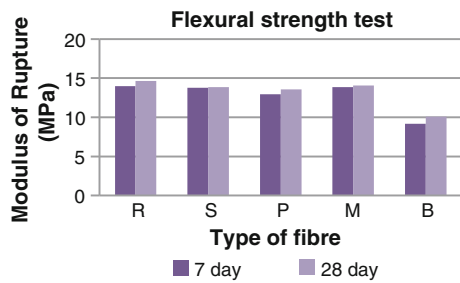
Fig. 16 Flexure strength test results of BFRC specimens with combination of fibres
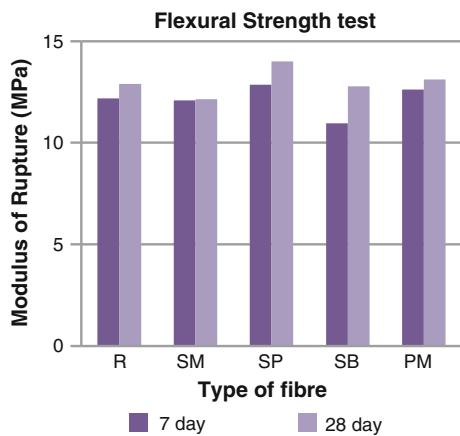
5 Conclusions

This paper presents the findings of an experimental program conducted to evaluate the mechanical properties of biofibre reinforced concrete (BFRC). The optimum biofibre content to be added into the concrete is found to be 0.25 %. Upon addition of biofibres to plain concrete, the compressive and split-tensile stress increased drastically (excluding BAGAF). A significant increase in flexural strength is not observed. This could be improved upon increasing the biofibre content and its length. Optimizing fibre content should also include the consideration of length of fibre and flexure strength results should also be included to come to final decision.

Among all fibres, SICOF and MUSAF gave good results; the former in increasing split-tensile strength and the later in improving compressive strength values. In this study, these two are identified as potential biofibres. Biofibres when used in combination also gave good results in compressive and split-tensile strength tests. The combination SM showed excellent increase in compressive and split tensile stresses. The behavior of the combination SB is peculiar and needs a further study.

The BFRC specimens showed very ductile kind of failure unlike control specimens. The specimens also remained intact even after failure indicating bridging of cracks by biofibres. The compressive strength tests showed the BFRC specimens showed bulging kind of failure. The angle of failure for BFRC specimens was found out to be 70° which is the indication of the restriction of shear failure.

This study helps to form a foundation for further research on BFRC specially when biofibres are used in combination.

References

1. Exodus 5:7. The Holy Bible
2. World Wide Web. http://en.wikipedia.org/wiki/Fiber-reinforced_concrete
3. World Wide Web. http://www.elastoplastic.com/index.php/fibre-facts/the-history-of-fibre-reinforcement-70141
4. Wafa FF (1990) Properties and applications of fiber reinforced concrete. Eng Sci 2:49–63
5. Tolêdo Filho RD, Kuruvilla J, Khosrow G, George LE (1999) The use of sisal fibre as reinforcement in cement based composites. Rev Bras de Engenharia Agrícola e Ambiental 3 (2):245–256
6. Ramakrishna G, Sundararajan T (2005) Impact strength of a few natural fibre reinforced cement mortar slabs: a comparative study. Cem Concr Compos 27(5):547–553
7. Ramakrishna G, Sundararajan T (2005) Studies on the durability of natural fibres and the effect of corroded fibres on the strength of mortar. Cem Concr Compos 27(5):575–582
8. Li Z, Wang X, Wang L (2006) Properties of hemp fibre reinforced concrete composites. Compos A Appl Sci Manuf 37:497–505

9. Teo DCL, Mannan MA, Kurian JV (2006) Flexural behaviour of reinforced lightweight concrete beams made with oil palm shell (OPS). J Adv Concr Technol 4(3):459–468

10. Elsaid A, Dawood M, Seracino R, Bobko C (2011) Mechanical properties of kenaf fiber reinforced concrete. Constr Build Mater 25:1991–2001

11. Ali Majid (2012) Natural fibres as construction materials. J Civil Eng Constr Technol 3 (3):80–89

12. Jain A, Choubey S, Singour PK, Rajak H, Pawar RS (2011) *Sida cordifolia* (Linn)—an overview. J Appl Pharm Sci 01(02):23–31

13. Paridah MT, Ahmed AB, Saiful Azry S, Ahmed Z (2011) Retting process of some bast plant fibres and effect on fibre quality: a review. BioResources 6(4):5260–5281

14. World Wide Web. http://en.wikipedia.org/wiki/Pineapple

15. Banik S, Nag D, Debnath S (2011) Utilization of pineapple leaf agro-waste for extraction of fibre and the residual biomass for vermicomposting. Indian J Fibre Text Res 36:172–177

16. World Wide Web. http://en.wikipedia.org/wiki/Banana

17. World Wide Web. http://www.kew.org/science-conservation/plants-fungi/saccharum-offici-narum-sugar-cane

18. IS: 12269-1987. Specification for 53 grade ordinary portland cement. Indian Standard Institute, New Delhi, India

19. IS: 383-1970. Specification for coarse and fine aggregates from natural sources for concrete. Indian Standard Institute, New Delhi, India

20. IS: 456-2000. Code of practice for plain and reinforced concrete. Indian Standard Institute, New Delhi, India

21. IS: 516-1999. Methods of tests for strength of concrete. Indian Standard Institute, New Delhi, India

22. IS: 5816-1999. Splitting tensile strength of concrete—method of test. Indian Standard Institute, New Delhi, India

Bibliography

23. Uzomaka OJ (1976) Characteristics of akwara as reinforcing fiber. Mag Concr Res 28 (96):162–167

24. Weerasinghe ALSD (1977) Fundamental study on the use of coir fiber board as a roofing material. M Eng Thesis. The Asian Institute of Technology, Bangkok

25. Mohanty AK, Misra M, Drzal LT (2005) Natural fibers, biopolymers, and biocomposites. CRC Press, Taylor and Francis group, New York

26. Rancines PG, Pama RP (1978) A study of bassage fiber-cement composite as low-cost construction materials. In: Proceeding international conference materials for developing countries. Bangkok, pp 191–206

27. Aggarwal LK (1992) Studies on cement-bonded coir fibre boards. Cem Concr Compos 14 (1):63–69

28. Agopyan V, Savastanojr H, John V, Cincotto M (2005) Developments on vegetable fibre-cement based materials in Sao Paulo, Brazil: an overview. Cem Concr Compos 27(5):527–536

Experimental Investigation and Numerical Validation on the Effect of NaOH Concentration on GGBS Based Self-compacting Geopolymer Concrete

J.S. Kalyana Rama, N. Reshmi, M.V.N. Sivakumar and A. Vasan

Abstract The construction sector is booming all over the world with an increase in the demand for the production of cement. Cement produced by India by the end of the financial year 2012–2013 was about 8 % of the global production. Cement production accounts for 7 % of total CO_2 emission into the atmosphere. It's high time for a sustainable replacement for cement in order to prevent greenhouse effect and global warming and other environmental impacts. In the present study, laboratory tests were conducted to investigate the effect of sodium hydroxide concentration on the fresh properties and compressive and flexural strength of self-compacting geopolymer concrete (SCGC) incorporating ground granulated blast slag (GGBS). The experiments were conducted for five different molarities of NaOH varying between 3 and 11 M with an increment of 2 M. In order to investigate the fresh concrete properties of SCGC, slump flow, V-Funnel, and T_{50} tests were carried out. The workability of GGBS based self-compacting geopolymer concrete showed an evident decrease with the increase in sodium hydroxide concentration. Standard cubes and beams were casted and cured in the open atmosphere. Its 28 days compressive strength and flexural strength were found to be decreasing with the increase in sodium hydroxide concentration. Using ABAQUS numerical modeling for compressive strength and flexural strength was determined and the results obtained were found to be similar to that of the experimental results.

J.S. Kalyana Rama (✉) · N. Reshmi · A. Vasan
Birla Institute of Technology and Science (BITS) Pilani, Hyderabad, India

M.V.N. Sivakumar
National Institute of Technology (NIT), Warangal, India

1 Introduction

Cement is one of the most important portions of concrete. However, its production is causing serious damage to the atmosphere due to the emission of huge amount of carbon di-oxide (CO_2) into the atmosphere. This emission of CO_2 into the atmosphere will increase the greenhouse effect which in turn causes global warming. In order to eliminate this environmental hazardous effect supplementary cementitious materials (SCM) are being experimented. These SCMs are usually materials of geological origin or by-products. Ground granulated blast furnace slag (GGBS) is a by-product obtained from the blast furnace used to make iron. In this work, experimental and numerical investigation of self-compacting geopolymer concrete with varying molarity of sodium hydroxide is carried out and presented.

It was in 1986 that self-compacting concrete was first introduced in Japan as the necessity for durable concrete increased. Okamura and Ouchi [1] carried out the pioneering work in the development of SCC. The geopolymer concrete is found to be an excellent way to reduce the usage of cement. It uses supplementary cementitious material which is either of geological origin or by-products from power plants and steel plants. Komnitsas in his paper [2] studied the sustainability of geopolymer concrete. It briefly outlines the potential of using geopolymer technology towards green buildings and future sustainable cities with a reduced carbon footprint. The basic concept of geopolymer concrete is the alkali activation of aluminum and silica rich source material [3]. The end product of the reaction is an amorphous alumino-silicate gel which has a structure similar to that of zeolitic precursors. The mineral admixture considered in their work is fly ash. Chindaprasirt et al. [4] investigated the basic properties such as workability and strength of coarse lignite high calcium fly ash geopolymer mortar. Sodium hydroxide (NaOH), sodium silicate and heat were used to activate the geopolymer. Sengul and Tasdemir [5] incorporated finely ground fly ash and finely ground granulated blast furnace slag in concrete and investigated its effects on compressive strength and chloride permeability. Hardjito et al. [6] studied the factors influencing the compressive strength of fly ash based geopolymer concrete. Temuujin et al. [7] studied the physical and mechanical properties of geopolymer mortars with varying levels of sand aggregate. Khater [8] investigated the effect of calcium hydroxide on the mechanical and microstructural characteristics of geopolymer produced from alkaline activation of alumino-silicate wastes produced from demolition works on geopolymerization of alumina silicate. Li et al. [9] investigated the mechanical properties and microstructure of class C fly ash based geopolymer paste and mortar at mass ratios of water to fly ash between 0.30 and 0.35; the fluidity of pastes and mortars were in the range of 145–173 and 131–136 mm, respectively. Tho-in et al. [10] evaluated the properties of pervious concrete made of high calcium fly ash geopolymer binder. The fly ash (FA) to coarse aggregate (CA) ratio was taken as 1:8. A constant ratio of 0.5 was considered for sodium silicate to sodium hydroxide. Influence of aggregate content on the behavior of fly ash based geopolymer concrete was studied by Joseph and Mathew [11]. Vora and Dave [12] also conducted

parametric study on the compressive strength of geopolymer concrete. The influence of elevated temperature on the thermal behavior and mechanical performance of fly ash geopolymer paste, mortar and light weight concrete was investigated by Abdul-Kareem et al. [13]. Pangdaeng et al. [14] investigated the influence of curing conditions on the properties of high calcium fly ash geopolymer containing Portland cement as additive. Kupwade-Patil and Allouche [15] studied the impact of alkali silica reaction on fly ash based geopolymer concrete. Brouwers and Radix [16] conducted an extensive study on experiments and theories on self-compacting concrete. The features of "Japanese and Chinese Methods" are discussed, in which the packing of sand and gravel plays a major role. Demie et al. [17] conducted an extensive study on the effect of curing temperature and superplasticizer on the workability and compressive strength of self-compacting geopolymer concrete. Anuradha et al. [18] optimized the molarity on workable self-compacting geopolymer concrete. Two kinds of system were considered in this study: 100 % replacement of cement by fly ash and 100 % replacement of river sand by manufactured sand.

In the present study, the usage of sustainable material GGBS with a 100 % replacement of cement was used in self-compacting concrete to study its behavior corresponding to compressive and flexural strength for different molarities of sodium hydroxide (NaOH). The same been validated using computational tool ABAQUS.

2 Preparation of Self-compacting Geopolymer Concrete

In order to study the effect of molarity of alkaline solution on the fresh and hardened self-compacting geopolymer concrete compressive test and flexural test were conducted on self-compacting geopolymer concrete with five different mix designs by varying the molarity of the alkaline solution. In this case, the cement is completely replaced by ground granulated blast furnace slag (GGBS) obtained from JSW Cement Plant. Also, the fresh concrete properties were studied using slump flow and V-funnel testing. The source material (GGBS) and the alkaline solution are the two main components of geopolymer. Usually, the alkaline solutions used are either sodium or potassium based. A combination of sodium hydroxide (NaOH) and sodium silicate (Na_2SiO_3) or potassium hydroxide (KOH) and potassium silicate (K_2SiO_3) is used to react with the alumina and silica content in the source material.

In this work, combination of sodium hydroxide (NaOH) and sodium silicate (Na_2SiO_3) is used at a specific ratio. The molarity of sodium hydroxide is varied between 3 and 11 M (3, 5, 7, 9 and 11 M).

2.1 Physical Properties of GGBS

Color: Off white
Relative Density: 2.92
Bulk Density: 1.2–1.3 ton/m^3.

2.2 Chemical Composition of GGBS

The Chemical Composition of GGBS are presented in Table 1 (Fig. 1).

2.3 Catalytic Liquid System

The alumina and silicate in the source material is made to react with the alkaline solution which is a combination of sodium hydroxide solution and sodium silicate solution. This solution has to be prepared 24 h before the experiment. It becomes semi-solid mass beyond 36 h and hence has to be used within the time limit. Sodium hydroxide solution is prepared by dissolving sodium hydroxide pellets in distilled water according to the required concentration. For different concentrations the mass of the NaOH to be dissolved in the water varies.

2.4 NaOH Molarity

The quantity of NaOH required for the preparation of 1 L NaOH solution of each molarity is given in Table 2.

2.5 Superplasticizer

The superplasticizer used in the research work is Glenium B233 [18]. It is an admixture based on modified polycarboxilic ether. It was developed in order to

Table 1 Chemical constituents of GGBS

Chemical constituents	Percentage
CaO	40
Al$_2$O$_3$	35
SiO$_2$	10
MgO	8

Fig. 1 GGBS from JSW
cements
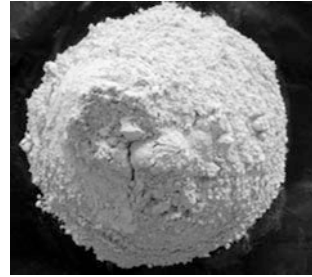
Table 2 Mass of NaOH per
liter

Sl. No.	Molarity (M)	Quantity of NaOH (g/L)
1	3	120
2	5	200
3	7	280
4	9	360
5	11	440

enhance the durability and performance in high performance concrete. It is compatible with any kind of cement as it is free from chlorides and alkali. Its relative density is around 1.09. The quantity of Glenium added was based on that reported in the literature [18]. Upon addition of up to 4 % by mass of binder, there was significant increase in the compressive strength [17]. Hence, for this study 4 % by mass of binder is considered.

2.6 Aggregates

Fine aggregate of specific gravity of 2.6, passing through 4.75 mm sieve was used in GGBS based self-compacting geopolymer concrete. Coarse aggregate of specific gravity 2.66, passing through 16 mm and retained in 12 mm was used.

2.7 Mix Design

The mix design of self-compacting concrete is done based on EFNARC guidelines [19], which is presented in Table 3.

Table 3 GGBS based SCGC mix design for different NaOH molarity

Mix	Molarity NaOH (M)	GGBS (kg/m^3)	CLS/ GGBS	CLS (L)	Fine aggregate	Coarse aggregate	Sodium hydroxide (kg)	Sodium silicate (L)
M1	3	500	0.65	325	532.5	745	1.2	3
M2	5	500	0.65	325	532.5	745	2	3
M3	7	500	0.65	325	532.5	745	2.8	3
M4	9	500	0.65	325	532.5	745	3.6	3
M5	11	500	0.65	325	532.5	745	4.4	3

3 Experimental Evaluation of SCGC

3.1 Fresh SCGC

Self-compacting concrete is highly workable concrete due to its properties like passing ability, filling ability and resistance to segregation. In order to find the properties of fresh SCGC, slump flow test and V funnel test were conducted. The test results of fresh concrete property are presented in Table 4.

It is seen from the results that the workability of self-compacting geopolymer concrete using GGBS is reducing as the molarity is increased. The results are graphically represented as in the Figs. 2, 3 and 4.

3.2 Hardened SCGC

In order to find the effect of NaOH molarity on the strength of SCGC, compressive test and flexural test was conducted on cubes and beam specimens cured in the room temperature. Standard 150 mm × 150 mm × 150 mm cubes were casted and 28 days compressive strength test was conducted in compressive testing machine of

Table 4 Workability test results

Mix	Slump flow (mm)	T 50 (mm)	V funnel flow time (s)
M1–3M	750	2.5	7
M2–5M	728	3	8
M3–7M	693	3.3	9.5
M4–9M	668	5	11.5
M5–11M	633	6	13
EFNARC recommended values			
Min.	650	2	6
Max.	850	5	12

Fig. 2 Graphical representation of slump flow versus molarity
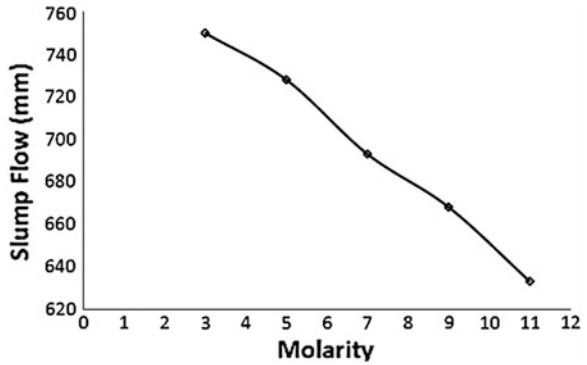
Fig. 3 Graphical representation of T_{50} slump flow versus molarity
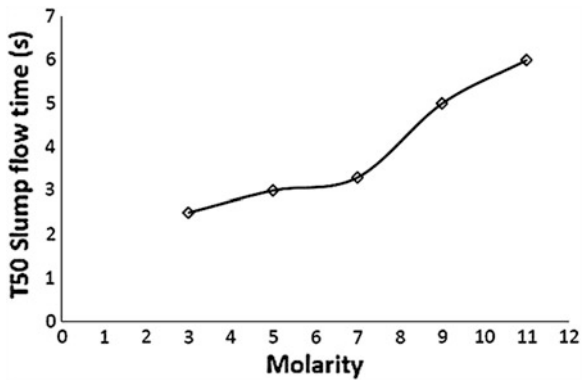
Fig. 4 Graphical representation of V funnel flow time versus molarity
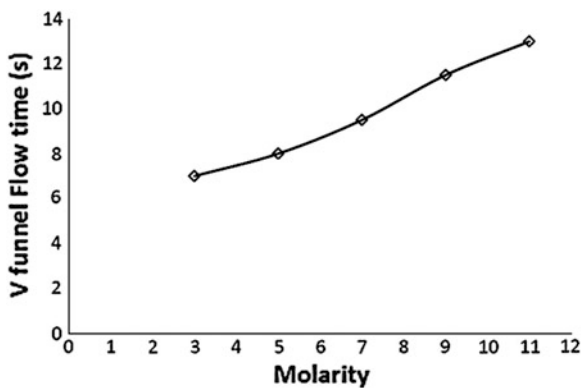
capacity 2,000 kN; six cubes were casted for each mix. The results obtained for compressive strength are graphically represented in Fig. 5. From the results obtained it was seen that the compressive strength was reduced with the increase in molarity.

Fig. 5 Effect of NaOH molarity on 28 days compressive strength
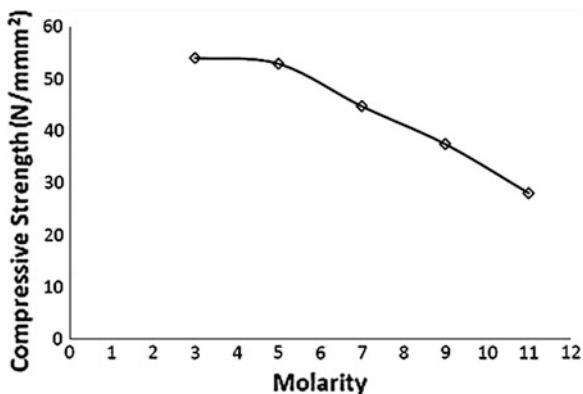
Fig. 6 Effect of NaOH molarity on flexural strength
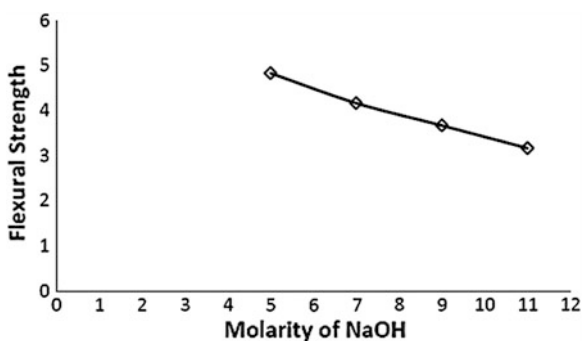
Three standard beam specimens of dimension 500 mm × 100 mm × 100 mm was used to conduct flexural test (Fig. 6). From the results obtained, it is seen that the flexural strength is decreasing with the increase in molarity of NaOH.

4 Numerical Evaluation of SCGC

The results obtained from experimental studies were compared by modeling the same specimen using ABAQUS CAE 6.10. Cubes of sizes 150 mm × 150 mm × 150 mm were modeled. Two steel plates of thickness 10 mm were considered on sides perpendicular to the loading plane. The interaction between the steel plates and concrete cubes is defined as tie constraint. The material properties for steel and SCGC with different molarities are defined. The Young's modulus for each mix was different. The Poisson's ratio was considered to be 0.15 for all the specimens. Similarly, material properties of steel plates were also defined. The Young's modulus for different mixes were as given in Table 5.

Table 5 Young's modulus

Sl. No.	Mix	Molarity of NaOH (M)	Young's modulus (N/mm^2)
1	M1	3	36742.35
2	M2	5	36362.37
3	M3	7	33433.18
4	M4	9	30586.85
5	M5	11	26457.51

4.1 Modeling of Cube

Different mesh sizes were considered for the concrete cube and the steel plate. As the concrete cube was the interest of our study, it was given coarser mesh and the steel plates were given finer mesh. The element used was C3D8R which was an 8-node linear brick with reduced integration, hourglass control. The FE model and mesh of the cube specimen are shown in Figs. 7 and 8, respectively. Uniform pressure was applied on the top of steel plate and the bottom portion of the plate was fixed (Fig. 9).

Though concrete is a brittle material, here only linear elastic analysis was considered. The stress-strain graph was obtained from ABAQUS. The results obtained were slightly less than that of the experimental results. The Strain contour is

Fig. 7 Model of 150 mm × 150 mm × 150 mm SCGC in ABAQUS/CAE 6.10
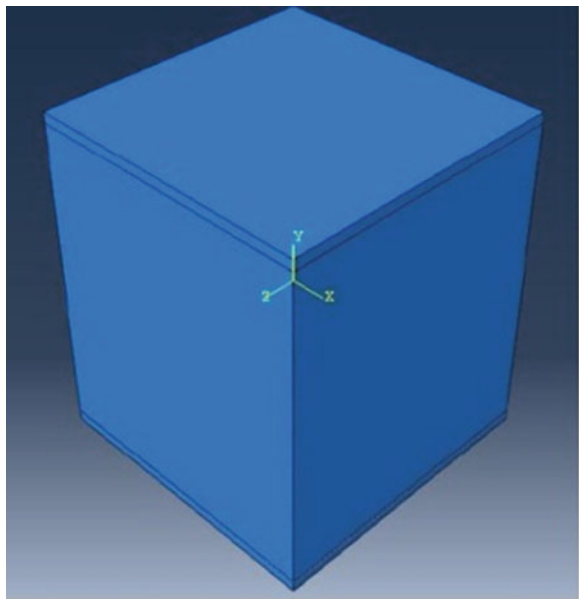
Fig. 8 Meshed specimen
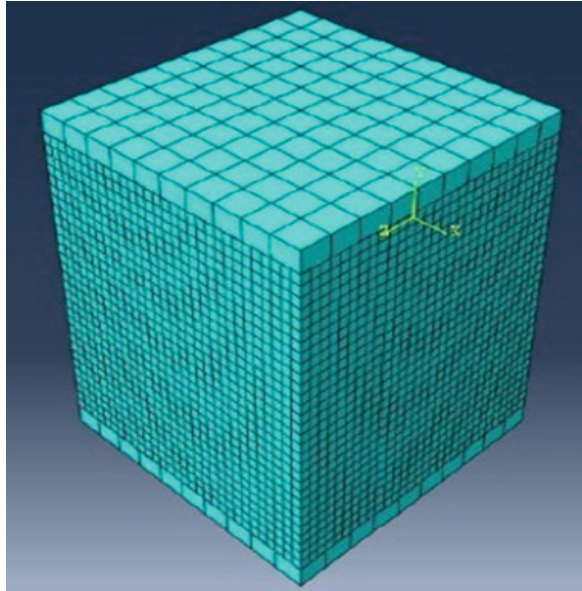
shown in Fig. 10. The results are presented in Table 6 and are plotted in Figs. 11, 12 and 13. From Figs. 11 and 12, it can be seen that the stress-strain behavior of self-compacting geopolymer concrete varies linearly.

Fig. 9 Load and boundary condition applied
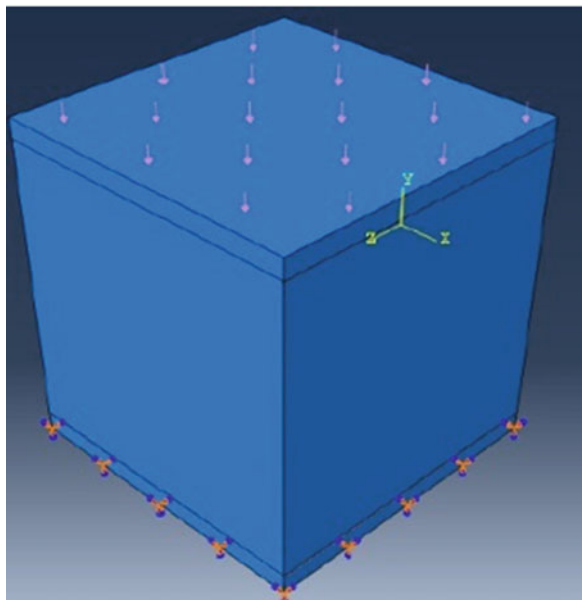
Fig. 10 Strain contour
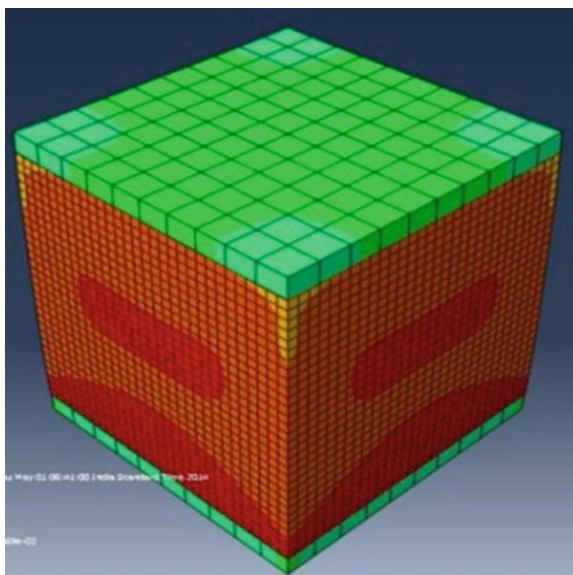
Table 6 Compressive strength obtained from ABAQUS

Sl. No.	Mix	Molarity of NaOH (M)	Compressive strength (N/mm^2)
1	M1	3	53.31
2	M2	5	52.13
3	M3	7	44.05
4	M4	9	36.73
5	M5	11	27.3

4.2 Stress–Strain Graphs for 3 and 5 M

See Figs. 11 and 12.

4.3 Comparison of Experimental and Numerical Results

See Fig. 13.

Fig. 11 Stress-strain curve obtained from ABAQUS for 3 M mix
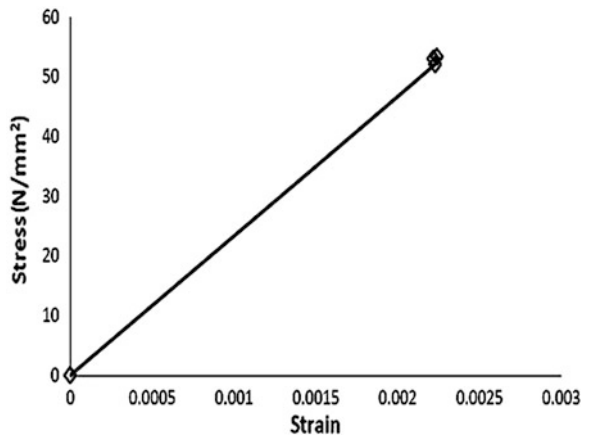
Fig. 12 Stress-strain curve obtained from ABAQUS for 5 M mix
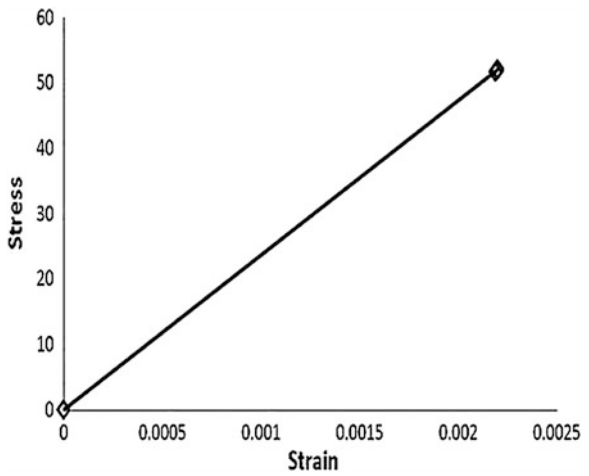
Fig. 13 Experimental and numerical result comparison
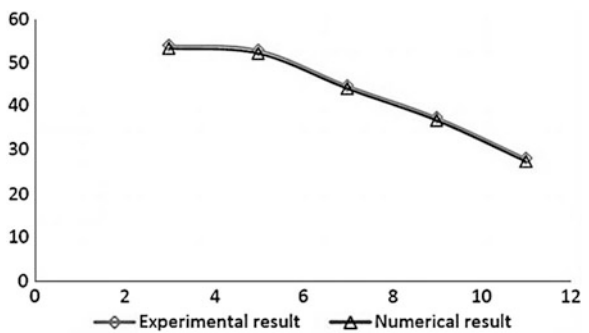
5 Conclusions

In this research work, the effect of sodium hydroxide concentration on the compressive and flexural strength of self-compacting geopolymer concrete with ground granulated blast furnace slag and binder was studied. Also, the effects of concentration on fresh concrete properties were investigated. Hence, the variable considered in this work is the concentration in terms of molarity of sodium hydroxide. Five different mix designs with varying molarity were considered. The molarity was varied between 3 and 11 M with an increment of 2 M.

- To study the properties of fresh concrete slump flow test and V-funnel test were conducted. The results obtained shows that,

  - Workability of self-compacting geopolymer concrete is decreasing with the increase in the molarity of sodium hydroxide.
  - When the concentration of sodium hydroxide increases, the viscosity of the alkaline solution further increases which in turn reduce the workability.

- To study the properties of hardened concrete compressive and flexural strength tests were conducted. The results obtained shows that,

  - Compressive and flexural strengths were decreasing with the increase in sodium hydroxide concentration because of flow properties of SCC in which polymerization effect hasn't had the significant effect on the mix.

References

1. Okamura H, Ouchi M (2003) Self-compacting concrete. J Adv Concr Technol 1(1):5–15
2. Komnitsas KA (2011) Potential of geopolymer technology towards green buildings and sustainable cities. Procedia Eng 21:1023–1032
3. Palomo A, Grutzeck MW, Blanco MT (1999) Alkali-activated fly ashes a cement for the future. Cem Concr Res 29:1323–1329
4. Chindaprasirt P, Chareerat T, Sirivivatnanon V (2007) Workability and strength of coarse high calcium fly ash geopolymer. Cem Concr Compos 29(3):224–229
5. Sengul O, Tasdemir MA (2009) Compressive strength and rapid chloride permeability of concretes with ground fly ash and slag. J Mater Civil Eng 21(9)494–501
6. Hardjito D, Wallah SE, Sumajouw DMJ, Rangan BV (2007) Factors influencing the compressive strength of fly ash-based geopolymer concrete. Civil Eng Dimension 6(2):88–93
7. Temuujin J, van Riessen A, MacKenzie KJD (2010) Preparation and characterization of fly ash based geopolymer mortars. Constr Build Mater 24(10):1906–1910
8. Khater HM (2012) Effect of calcium on geopolymerization of aluminosilicate wastes. J Mater Civil Eng 24: 92–101
9. Li X, Ma X, Zhang S, Zheng E (2013) Mechanical properties and microstructure of class C fly ash-based geopolymer paste and mortar. Materials (Basel) 6(4):1485–1495
10. Tho-in T, Sata V, Chindaprasirt P, Jaturapitakkul C (2012) Pervious high-calcium fly ash geopolymer concrete. Constr Build Mater 30(325):366–371

11. Joseph B, Mathew G (2012) Influence of aggregate content on the behavior of fly ash based geopolymer concrete. Sci Iran 19(5):1188–1194
12. Vora PR, Dave UV (2013) Parametric studies on compressive strength of geopolymer concrete. Procedia Eng 51:210–219
13. Abdul-Kareem OA, Al AMM, Kamarudin H, Nizar IK, Saif A (2014) Effects of elevated temperatures on the thermal behavior and mechanical performance of fly ash geopolymer paste, mortar and lightweight concrete. Constr Build Mater 50:377–387
14. Pangdaeng S, Phoo-ngernkham T, Sata V, Chindaprasirt P (2014) Influence of curing conditions on properties of high calcium fly ash geopolymer containing portland cement as additive. Mater Des 53:269–274
15. Kupwade-Patil K, Allouche EN (2013) Impact of alkali silica reaction on fly ash-based geopolymer concrete. J Mater Civil Eng 25(1):131–139
16. Brouwers HJH, Radix HJ (2005) Self-compacting concrete: theoretical and experimental study. Cem Concr Res 35(11):2116–2136
17. Demie S, Nuruddin MF, Ahmed MF, Shafiq N (2011) Effects of curing temperature and superplasticizer on workability and compressive strength of self-compacting geopolymer concrete. National Postgraduate Conference, pp 1–5
18. Anuradha R, Thirumala RB, John PN (2014) Optimization of molarity on workable self-compacting geopolymer concrete and strength study on SCGC by replacing fly ash with silica fume and GGBFS. Int J Adv Struct Geotech Eng 03(01)
19. EFNARC (2002) Specification and guidelines for self-compacting concrete. European Federation of National Associations Representing for Concrete (EFNARC), ISBN 0 9539733 4 4

Performance Studies on Geopolymer Based Solid Interlocking Masonry Blocks

M. Sudhakar, George M. Varghese and C. Natarajan

Abstract Hydraform interlocking blocks were developed in industrial site from the optimum mix obtained by factorial design of experiment using alumino-silicate rich industrial waste materials like fly ash (FA), ground-granulated blast-furnace slag (GGBS) and bottom ash (BA). A strong alkaline mixture of sodium silicate (Na_2SiO_3) and sodium hydroxide (NaOH) in seawater was used as the activator liquid for geopolymerization to carry out. The physical and mechanical properties of the blocks were studied and proved to be superior. The present paper evaluates the masonry design strength from prism test and also discusses the influence of the variation of height-to-thickness ratio and loading direction on the strength. The prisms and panels subjected to loading applied at eccentricities of 0, t/6, and t/3, generally experienced by arches, vaults and pillars, showed good results. Wallettes tested for Flexural strength, under horizontal bending, performed better than that tested under vertical bending and gave the orthogonal ratio as 0.556, useful in wall design. The failure mechanism patterns are also discussed briefly. The paper concludes that the geopolymer blocks are sustainable and a structurally viable option for the construction industry.

Keywords Geopolymer blocks · Compressive strength · Prism test · Eccentric capacity · Flexural strength

1 Introduction

A sustainable development has to cater to the needs of the present without compromising the ability of future generations to meet their own needs. The technologies for the industrial waste utilization, especially in building construction sector have given considerable worldwide attention as it paves the way for reducing greenhouse gases emission leading to sustainable development. Present trends and

M. Sudhakar (✉) · G.M. Varghese · C. Natarajan
National Institute of Technology, Tiruchirappalli, Tiruchirappalli, India

development in industrial sectors pose a big challenge to maintaining low energy consumptions and CO_2 emissions leading to global warming and climate changes.

Coal-powered power stations generate 41 % of world's electricity. Some countries show higher dependence on coal electricity production ranging around 43 % in US, 68 % in India and 94 % in South Africa [1]. Globally, it is estimated that 750 million tons of FA is generated each year including the Indian contribution of 180 million tons from its 90 thermal power plants. Current gainful utilization of FA figures is 39 % in US and 47 % in Europe [2] and 43 % in India [3]. Also due to the variations in the composition coal, the resultant by-product FA also varies not only from region to region but also within the region. Approximately 316 individual minerals and 188 mineral groups have been identified in different FAs [4] throughout the world.

The ever increasing volume of fly ash quantities in the world has not been properly matched by its utilization. The problem of FA disposal, BA in particular, is more challenging. Recent studies [5] concluded that fly ash application to agricultural soil even at a small scale of 5 % is not suitable for leafy vegetable growth and reduces biomass and yield. These openly dumped ashes also pose radiation hazard due to the leachability of radio nuclides (atoms with unstable nucleus) into the ground water stream, ultimately contaminating the drinking water sources [6]. As such, there is an urgent need to find more possible ways of effective utilisation of Fly ash. It requires a lot of efforts to achieve 95–100 % utilization as the energy demand is also increasing rapidly. Hence the only sustainable option left may be the brick/block manufacture due to bulk consumption of BA.

Masonry is a field assembled product, handcrafted by people who are not necessarily highly skilled, with materials that are not exact and designs that are not always specific despite the fact that 70 % of world's existing construction includes masonry. The inherent advantage of masonry is that the same "form" can perform multiple functions like providing structure, subdivision of space, thermal and acoustical insulation, fire and weather protection simultaneously. It is relatively cheap, durable and can make elegant external appearance. It is the oldest and arguably the best building system known to man so far. Bricks are widely used as a building material throughout the world. But their smaller size with higher number of mortar joints ends in relatively slower execution. Also in the manufacturing of clay bricks, the average embodied energy is approximately 2.0 kWh and release about 0.41 kg of carbon dioxide (CO_2) per brick. The clay brick industry also consumes more than 24 million tons of coal and emits more than 42 million tons of CO_2 to the atmosphere [3].

As per BS6073-1:1981 clause 3.1.2 "a brick masonry is a unit not exceeding 337.5 mm length, 225 mm in width, or 112.5 mm in height". Any unit with a dimension that exceeds any one of those specified above is termed as blocks [7]. Block construction is well accepted as a building system in many countries of the world today. Usage of blocks in place of bricks reduces construction speed when mortar is used. Hence the search for a more rapid and less labour intensive building system has led to the development of interlocking dry stackable block masonry units which can be laid without mortar layers. Quality variation in mortar, and other

problems associated due to mortar joints such as inadequate bond and cracking of mortar are eliminated. Handling and positioning are simple and can be done by semiskilled and unskilled labour with proper guidance. The wall is also more ductile; not rigid. Dry stacked wall construction will reduce the labour cost by as much as 80 % [8]. The system provides aesthetic and affordable building walls that may be left exposed, plastered or finished with cement paint.

Most of the commercially available interlocking blocks vary in geometry, material, and dimensional characteristics and invariably are proprietary systems. Blocks masonry systems can be categorized as those that ensure two-way inter-locking (vertical and horizontal) or those that provide only one-way (vertical) interlocking [9]. Many of the developed systems did not progress beyond the design stage because of the complicated configurations [10]. This technology is not yet regulated by code of practice. Several countries are now involved in the develop-ment of this technology; however, the emphasis so far has been on the development of the geometrical properties of the dry-stack masonry units with very little attention on the analytical investigation. This is likely due to the fact that the development of interlocking dry-stack masonry units requires continuous extensive modifications through experimental investigations before satisfactory geometry is achieved. There is a great diversity among the existing dry-stack masonry systems because of the unique nature of the interlocking mechanism of the units. Each interlocking system is unique with regard to structural behaviour [11].

The alumino-silicate rich materials like fly ash, GGBS along with bottom ash were bonded together in a high alkaline medium called geopolymerization. Geo-polymer, a term coined by a French chemist, Dr. Joseph Davidovits in 1978, is a class of materials formed by the polymerization of silicon, aluminum, and oxygen species to form an amorphous three-dimensional framework structure. The primary course of reaction is dissolution, condensation, polymerization and resulting in the formation of three-dimensional semi-crystalline amorphous structure [12]. The chemical bonds of Si–O and Al–O are among the most stable covalent bonds in nature and the polycondensation degree of geopolymer is much higher than cement-based materials. Hence, they possess many advanced properties such as the excellent compressive and bond strength, long-term durability, low shrinkage, better resistance to fire, acid, sulphate, freeze-thaw and corrosion [6]. Besides, it is also a "Green Material" for its low manufacturing energy consumption and low waste gas emission. Because of these prominent characteristics, geopolymer is considered as one of the potential candidates to solve the conflict between social development and environmental pollution from binder.

The compressive strength of masonry is the most important parameter in the design of masonry structures and it primarily depends on the strength of the indi-vidual block units. Masonry design values for the geopolymer binder based masonry are estimated by the prism test as mentioned by IS 1905-1987 [13], and the influence of height-to-thickness ratio and loading direction on those prisms are worth studying. The paper also focuses on the eccentric load carrying and flexural capacities of the Geopolymer based masonry.

2 Experimental Program

2.1 Materials

The chemical composition of the industrial effluents utilized in the mix is presented in Table 1. These wastes and other ingredients like Sodium Silicate, Sodium Hydroxide and sea water were collected from various places in and around Tiruchirappalli, Tamil Nadu.

2.2 Methodology

Compressive strength test of the Hydraform interlocking block should be done in compression testing machine in accordance with IS 3495 Part I-1976 after 28 days of curing was recorded [14]. To apply the load to the flanged portion of the blocks, two steel plates of sizes 50 mm × 230 mm and thickness 10 mm are placed on top flange and gradual load is applied over the plates till failure occurs and the maximum load at failure is noted. The compression test was conducted on thirty blocks and the schematic arrangement of the test setup is shown in Fig. 1. The flexural strength test on the blocks is done in accordance with ASTM C67 [15] given for clay bricks and the test setup is presented in Fig. 2.

Table 1 Chemical composition of industrial waste materials used

Material	Specific gravity	Composition, %				
Fly ash	2.05	SiO_2	Al_2O_3	Fe_2O_3	CaO	SO_3
		53.30	29.50	10.70	7.60	1.80
GGBS	2.20	SiO_2	Al_2O_3	FeO	CaO	MgO
		35.47	19.36	0.80	33.25	8.69
Bottom ash	2.05	SiO_2	Al_2O_3	Fe_2O_3	CaO	SO_3
		56.76	21.34	5.98	2.88	0.72

Fig. 1 Compressive strength test setup
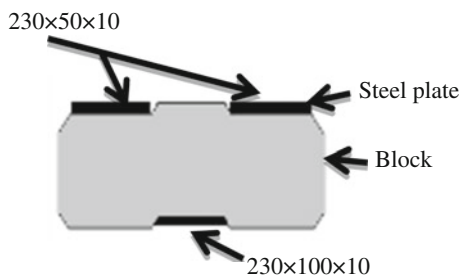
Fig. 2 Flexure strength test setup

The Indian masonry design standard (IS 1905-1987) does not deal with interlocking block masonry, but Appendix B clause 5.4.4 describes prism tests which are small assemblages representing the actual construction, to determine the masonry ultimate compressive strength. Accordingly, the h/t should not be less than 2, with minimum height 40 cm and given the correction factors up to 5 (h/t). With respect to the dimensions of the blocks studied a minimum of four layers were required. For h/t ratio 2.3, a correction factor of 1.06 is applied. The prism must be built of similar material under the same conditions with the same bonding arrangement as that of the structure. The test was done on ten specimens and schematic arrangement of the test setup is shown in Fig. 3, with a bonding arrangement similar to the structure using half and full blocks. The influence of variation in h/t ratios and the loading direction are indicated in the figures below.

The figures for the test setup of eccentric and flexural load carrying capacity are presented in Figs. 4 and 5. The eccentricity is applied at 0, t/6 and t/3 positions with rods at top and bottom of the prism and panel specimens. The calculations of the

Fig. 3 Prism test setup indicating different h/t and loading direction arrangements

Fig. 4 Different eccentric compression test arrangements

Fig. 5 Loading arrangement of masonry **a** parallel **b** perpendicular to bed joint

strengths are done according to IS 1905 and BS 5628. Conventional masonry is not isotropic and therefore does not provide the same resistance to bending in both directions. The difference in resistance to bending when spanning vertically (load parallel to bed joints) and horizontally (line of load perpendicular to bed joints), the orthogonal ratio, is used primarily for the calculation of bending moments in wall design.

3 Results and Discussions

The results including physical and mechanical properties of the masonry units, prisms and panel specimens are presented in tabular form separately in Tables 2, 3 and 4 respectively.

The water absorption property and density were observed to be within the permissible limit of as per IS 1725-1982 [16]. The results of strength are very much encouraging with the geopolymerization in sea water, due to the formation of semi-crystalline polymeric structures. Cost of the block is little high mainly due to the lack of transportation network and Na_2SiO_3 and NaOH is responsible for 68 % of the cost.

The tensile and shear stress values can be derived for interlocking block masonry using prism test in same way as Clauses 5.4.2 and 5.4.3 of the code and are presented in Table 5.

Table 2 Test results of individual masonry units

Parameters	Results
Density	1635.16 kg/m^3
Water absorption	11.95 %
Compressive strength	15.81 MPa
Flexural strength	5.99 MPa
Total cost per block	Rs. 15.45

Table 3 Test results of masonry prisms

Parameters	Results		
Prism Strength, MPa	Loading perpendicular to bed joint		Loading parallel to bed joint
	6.54		3.62
Eccentric compressive strength, MPa	e = 0	e = t/6	e = t/3
	6.81	10.72	11.01

Table 4 Test results of individual masonry units

Parameters	Results		
Eccentric compressive strength, MPa	e = 0	e = t/6	e = t/3
	2.54	4.25	5.02
Flexural strength, MPa	Loading perpendicular to bed joint		Loading parallel to bed joint
	0.9		0.5

Table 5 Design values [13] for interlocking geopolymer masonry from prism test

Stress type	Permissible value, MPa
Basic compressive stress	1.63
Permissible tensile stress	0.14
Permissible shear stress	0.37
Modulus of elasticity	1,180
Modulus of rigidity	475
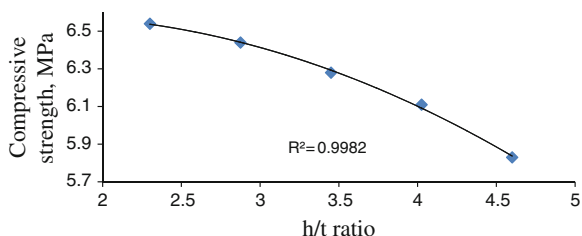
Fig. 6 Plot between h/t ratio and compressive strength

The reduction in the compressive strength of the prism compared to the individual block unit was due to the effect of the slenderness of the prism specimen. The reduction in strength with increase in h/t (Fig. 6) observed in the prism specimens may have been due to the interlocking interaction between the different block units. The increase in the number of interlocking joints adversely affects the strength. The in-plane strength of the infill wall rely on the strength of the masonry when loaded in the direction parallel to the bed joint. The factor $\chi = 0.55$ (ratio of parallel to perpendicular loading directions) is useful in the design of infill masonry in combination with the diagonal strut approach.

Wallettes tested under horizontal bending performed better than those tested under vertical bending. The orthogonal ratio is about 0.556 is required for the wall design. The load-deflection curves of the prism specimens under eccentric loading and panels loaded parallel and perpendicular to the bed joints are presented in Figs. 7 and 8.

Fig. 7 Load-deflection plot of prism specimens under eccentric loading case for eccentricities 0, t/6 and t/3 (not to full failure)
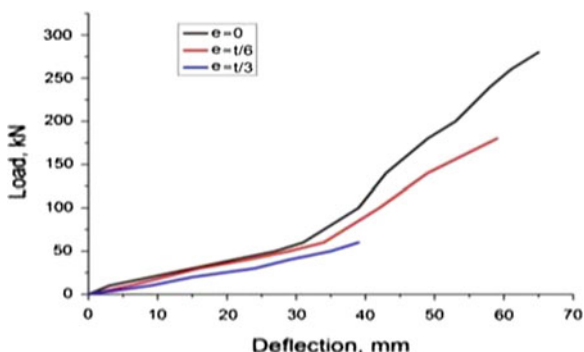
Fig. 8 Load-deflection plot for the interlocking masonry wallette (not to complete failure) under horizontal and vertical bending
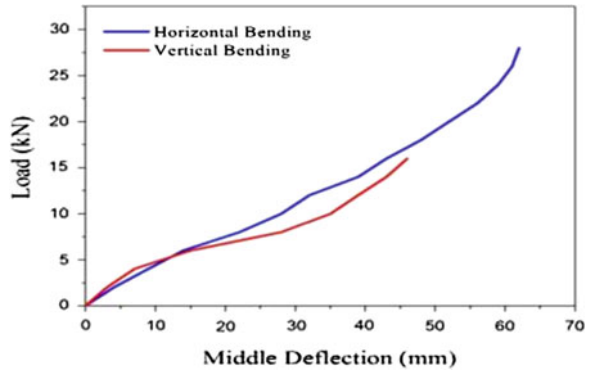
4 Failure Mechanism

The failure pattern of individual block is visible from Fig. 9 is by crushing while the flexural failure is shown in Fig. 10. The failure modes observed for masonry prisms under compression, loaded in the direction perpendicular to bed joint are of two kinds. One is masonry crushing for the weak units or a complete collapse (Fig. 11) and the other is the vertical cracking through the interlock portion of the prism (Fig. 12). Due to the low tensile strength of the masonry, cracking through the flange or web of the units is formed which results in the final failure of the prism. The longitudinal cracking was observed from top to bottom throughout the prism specimen loaded in a direction parallel to bed joint, due to splitting tensile stresses. This may be the reason for low ultimate strength observed in the specimen. Also the confinement effects of the loading table may force the interlocking parts of the prisms to fail in shear. The use of different effective areas in the calculation of strength adds discrepancy to the results.

Fig. 9 Crushing under compression

Fig. 10 Failure under flexure

Fig. 11 Failure patterns observed in prism test for different h/t ratios

As expected, at an eccentricity of t/6, crushing failure occurred on the compression side along the interface between successive blocks, whereas at t/3, separation was observed along the interface of successive blocks on the tension side together with spalling on the compression face as shown in Figs. 13 and 14.

The failure of the wallettes under horizontal bending, where loading was in the direction perpendicular to the bed joint, was characterised by the gradual rotation of the units around the vertical axis with load increase leading into opening of the vertical joints in the area between the loading points accompanied by the formation of uniform curvature to the entire section (Figs. 15 and 16). The average lateral load

Fig. 12 Failure patterns when loaded parallel to the bed joint
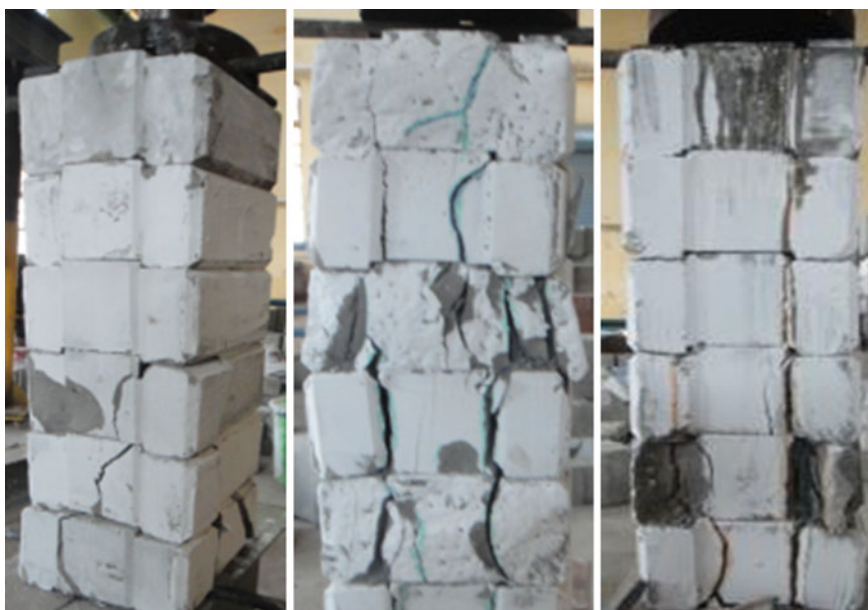
Fig. 13 Failure patterns in prisms when loaded with eccentricities 0, t/6 and t/3

Fig. 14 Failure patterns in panels when loaded with eccentricities 0, t/6 and t/3

Fig. 15 **a** Top view of flexural loading arrangement of masonry perpendicular to bed joint and **b** its failed view

Fig. 16 Failure patterns of flexure loading under horizontal loading
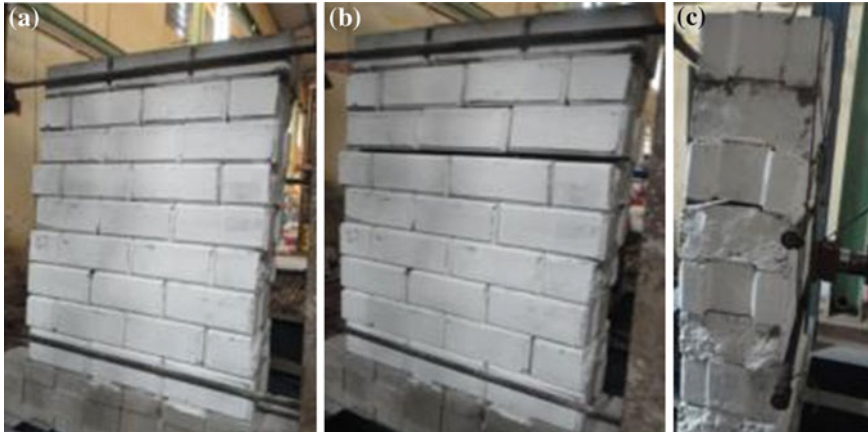
Fig. 17 Typical mode of failure of wallette under vertical bending **a** before failure **b** after failure **c** side view

at failure was 28 kN. Failure of the interlocking mechanism by shear was also observed. The bed joints remained very tightly closed.

The failure under vertical bending accompanied by the gradual opening of the bed joints above the mid-section stretching across the entire length of the specimen was clearly visible from the Fig. 17. The average ultimate load at the point of failure was 16 kN. The opening of the bed joint due to the rotation of the units along vertical axis was observed, which eventually resulted in the sliding of the units out of the interlocking mechanism. The entire vertical joints practically remained closed.

5 Conclusions

Test results and the sustainable characteristics indicate that the geopolymer-based interlocking block system has great potential to be adopted in building or housing construction. The geopolymer binder blocks prepared with sea water showed very good physical and mechanical properties. Prisms, loaded parallel to the bed joint, were found to exhibit lower strength than prisms loaded normal to the bed joint and the horizontal-to-vertical ratio was found to be 0.55.

The geopolymer-based interlocking prisms and panels posses superior eccentric load carrying capacity ensuring its use as arches, vaults, pillars and out-of-plane loaded masonry panels. Wallettes, tested under horizontal bending, performed better than those tested under vertical bending and the flexural strength perpendicular to bed joints was about two times that parallel to bed joints. The orthogonal ratio, primarily used for the calculation of bending moment resistance in panel wall design is estimated to be 0.556. The mortarless interlocking dry-stack masonry

Fig. 18 Bar chart representation of allowable stress in flexure for equivalent mortar masonry systems and the dry-stack masonry system
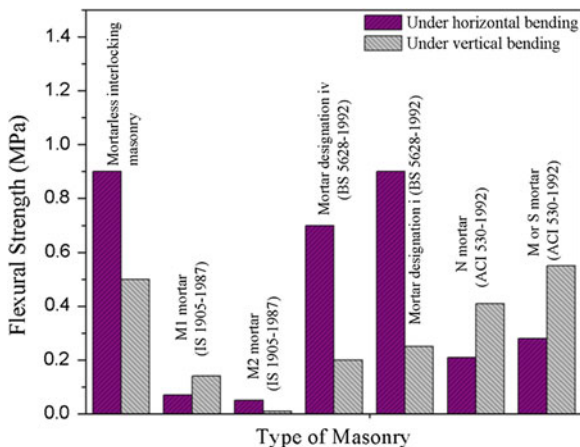
when compared for the allowable stress in flexure is equivalent to the conventional masonry with mortar designation (i), given by BS 5628-1992, having mortar strength greater than 14 MPa and unit block strength 16 MPa. The bar chart representation of the comparison is shown in Fig. 18.

References

1. World Coal Association (2014) World coal statistics. http://www.worldcoal.org/resources/coal-statistics. Accessed on 28 Feb 2014
2. Vassilev SV, Vassileva CG (2005) Methods of characterization of composition of fly ashes from coal-fired stations: a critical review. Energy Fuels 19(3):1084–1098
3. TERI Report No 2006 RD25 Policy, Institutional and legal barriers to economic utilisation of fly ash
4. Blisssett RS, Rowson NA (2012) A review of the multi-component utilisation of coal fly ash. Fuel 97:1–23
5. Singh A, Sharma RK, Agrawal SB (2008) Effects of fly ash incorporation on heavy metal accumulation, growth and yield responses of *Beta vulgaris* plants. Bioresour Technol 99:7200–7207
6. Pandit GG, Sahu SK, Puranik VD (2011) Natural radionuclides from coal fired thermal power plants—estimation of atmospheric release and inhalation risk. Radioprotection 46(6):173–179
7. British Standards Institution (2005) BS 5628: Part 1. The structural use of unreinforced masonry, UK
8. Harris HG, Oh K, Hamid AA (1992) Development of new interlocking and mortarless block masonry units for efficient building systems. In: Proceedings of the 6th Canadian masonry symposium, vol 2, Saskatoon, Saskatchewan, Canada pp 723–734
9. Anand KB, Ramamurthy K (1999) Techniques for accelerating masonry construction. Int J Hous Sci Appl 23.4
10. Crofts FS (1993) State of the art of mortarless concrete masonry in South Africa. In: Proceedings of the 6th north American masonry conference, Pennsylvania, pp 875–884
11. Bansal D (2011) Masonry from stabilized earth blocks-sustainable and structurally viable option. Int J Earth Sci Eng 4(6):772–779. ISSN 0974-5904

12. Davidovits J (1994) Inorganic polymers and methods of making them. J Mater Educ 16:91–139
13. Bureau of Indian Standards: IS 1905 (1987) Code of practice for structural use of unreinforced masonry, New Delhi
14. Bureau of Indian Standards: IS 3495 (1976) Method of tests on burnt-clay building bricks. New Delhi
15. American Society for Testing and Materials: ASTM C67, Standard test methods for sampling and testing brick and structural clay tile
16. Bureau of Indian Standards: IS 1725 (1982) Specification for soil based blocks under general building construction. New Delhi

Part XVII
Cement and Pozzolana

A Review on Studies of Fracture Parameters of Self-compacting Concrete

J. Sri Kalyana Rama, M.V.N. Sivakumar, A. Vasan, Chirag Garg and Shubham Walia

Abstract In the recent past, the use of self-compacting concrete (SSC) as a primary structural material in complex structures such as tall buildings, submerged structures, bridges, dams, liquid and gas containment structure has increased enormously. Proper understanding of the structural behavior of SCC is absolutely necessary in designing complex concrete structures. Due to the presence of micro-cracks and other inherent flaws, the strength of the concrete structure decreases. Engineering fracture mechanics can deliver the methodology to compensate the inadequacies of conventional design concepts. It might be expected that SCC would exhibit more brittle behavior than normal/conventional concrete. The improved pore structure and better densification of matrix have great influence on the fracture characteristics of SCC. It is widely agreed that the strength, elastic modulus and fracture resistance of SCC decreases slightly with increased paste content. Increasing the volume of paste tends to make SCC brittle. Due to the quasi-brittle nature of concrete; various computational fracture models have been developed to study the crack characterizing parameters in concrete structures, such as fictitious crack model, crack band model, two parameter fracture model, size effect model, smeared crack model, cohesive crack band model and effective crack model. Compared to conventional vibrated concrete, self-compacting concrete often has a higher susceptibility to crack due to different mixture design, material properties and construction practices. Many studies have addressed the SCC fracture properties using different computational models. As mentioned above, all these studies are purely computational and there is no support or evidence from the experiments. This paper deals with presenting the various models as well as experimental investigations that have already been conducted by some of the researchers to study the exposure of self-compacting concrete to crack.

J. Sri Kalyana Rama (✉) · A. Vasan · C. Garg · S. Walia
Department of Civil Engineering, Birla Institute of Technology and Science (BITS) Pilani, Hyderabad, India
e-mail: jskr.publications@gmail.com

M.V.N. Sivakumar
Department of Civil Engineering, National Institute of Technology (NIT), Warangal, India

1 Introduction

1.1 History of SCC

The concept of self-compacting concrete originated in the 1970s when researches were carried on underwater [1–11]. The first model of SCC mix design was developed by Okamura and Ozawa et al. in 1989, as mentioned in Gaimster and Dixon [11]. The mix design of SCC was simultaneously studied in Europe, Japan and North America at the same time between 1970 and 1990. All the initial studies revolved around developing the best mix design for self-compacting concrete. Figure 1 compares the content difference between SCC and a regular mix. SCC is preferred over normal concrete as it offers several advantages over the later one which can be namely classified into economical, technical and environmental. The technical advantages of SCC mainly comprised of the benefits like concreting in heavily reinforced sections, with the help of SCC, thin section precast units could be manufactured and also structures of any geometry could casted. Economically too, SCC was preferred due to its reduced construction time and reduced labour costs because of safe operations. Because SCC had a reduced level of carbon foot-printing and had a large scope for use of waste materials, it had environmental advantages as well.

Several researchers worked hard to develop the most efficient and effective design mix of SCC. Many methods for mix were coined by people, the primary
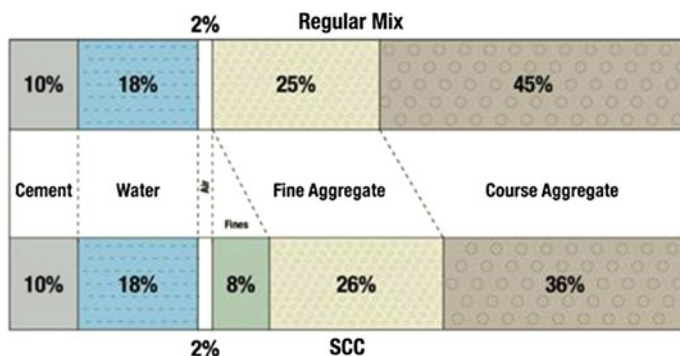
Fig. 1 SCC mix versus regular mix [1, 2]

methods being [12–23]: Power method, Admixture method and Combination method. After the study of mix design and workability mixes of this type of concrete, studies were carried on to explore the fracture parameters of SCC.

2 Fracture Parameters of SCC

The first study to explore about the fracture mechanics and the parameters of SCC was carried out by Bourdette et al. [24] in 1995. In this research, the ion diffusion process in different mortars has been studied. The diffusion process arises due to the presence of transition zones in the mortar paste. With the help of mercury, these transition zones were studied and it was concluded that this zone depends upon the mortar composition and degree of hydration.

Further studies carried out by Prokopskia and Halbiniakb [25] in 2000 demonstrated the critical values of stress intensity factors, K, and the critical values of crack tip opening displacement, CTOD as per RILEM specifications. The samples with aggregates used directly and aggregates coated with paraffin were tested. The different transition zones in both the cases showed difference in the mechanical strengths of both the samples as well. The crack tip opening displacement dropped when the aggregates with coating were used. In 2002, Jefferson [26] produced a model to demonstrate the formed cracks in concrete. The main aim of the model was to understand the interlocking of aggregates and crack closing behaviour. Three contact states were observed for experimental data with the help of a contact function. These states were named open, where there is no contact, interlock, for which the stresses depend upon the nearest distance to the contact surface and closed, for which the stresses depend upon the relative displacements directly. Jefferson concluded that the interlocking of aggregates plays a crucial role in the fracture behaviour of SCC. This behaviour had not been accounted for in the previous studies.

In the very same year, Toumi and Bascoul [27] studied the crack propagation in concrete under fatigue. They observed the mode 1 crack in a notched beam specimen by carrying out a three-point bending test. Microscopic observations and FEM modelling were both used to understand the propagation of the crack. It was concluded through this study that cohesive force distribution can be assumed at various loading stages. This study was extended by Hanson and Ingraffea [28] in 2003 when the size-effect, two-parameter, and fictitious crack models were developed to predict crack growth in materials like concrete that experience tension softening. They studied the crack mouth opening displacement of a specimen by plotting a graph against specific loading.

3 Discrete and Smeared Crack Model

In 2004, de Borst et al. [29] made an attempt to bridge the gap between discrete and smeared crack model for concrete fracture. They challenged the conventional belief of the two models being very different from each other by exploiting the partition of unity property of finite element shape functions. The study concluded that both approaches have their domain of application: discrete crack models are appropriate for modelling one or more dominant cracks, while smeared crack models can simulate the diffuse cracking patterns that arise due to the heterogeneity of concrete and the presence of reinforcement. Figure 2 represents the crack propagation as studied in 2004 by Rene de Borst et al. But in 2006, Cervera and Chiumenti [30] carried out a study to show the difference between the discrete and smeared crack model. The paper focuses on the smeared approach, identifying as its main drawbacks the observed mesh-size and mesh-bias spurious dependence when the method is applied 'straightly'. This paper shows the application of standard finite elements with continuous displacement fields, such as linear triangles, to the solution of problems involving the propagation of tensile cracks using the classical smeared crack approach; in this case, via a local isotropic continuum damage model with strain softening regularized using the classical fracture energy regularization technique. Figures 3 and 4 represent the difference as indicated by M. Cervera and M. Chiumenti between the discrete and smeared crack approach. Both the approaches were tested with and without remeshing.
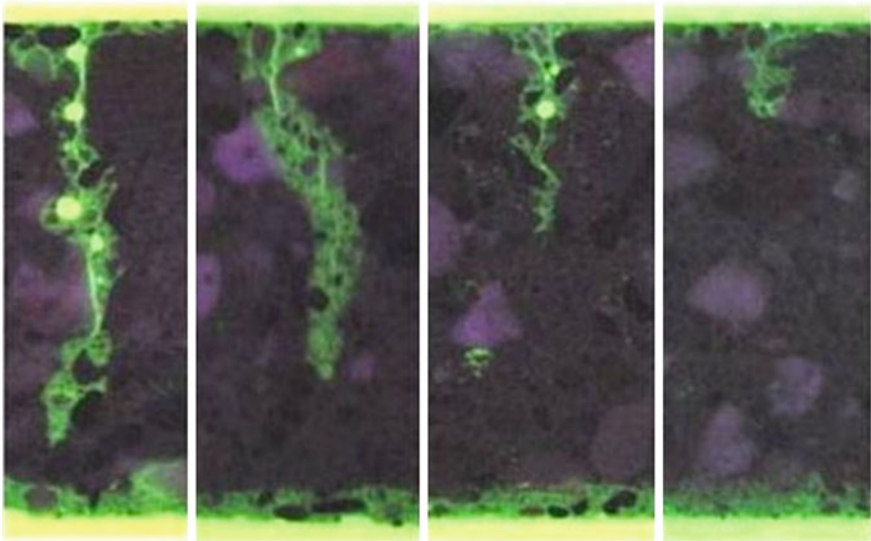
Fig. 2 Crack propagation [29]

Fig. 3 Discrete crack approach **a** without remeshing **b** with remeshing [30]
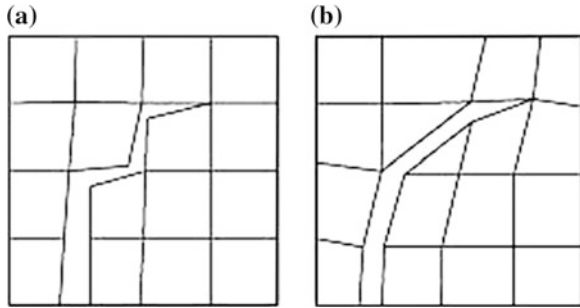
Fig. 4 Smeared crack approach **a** without remeshing **b** with remeshing [30]
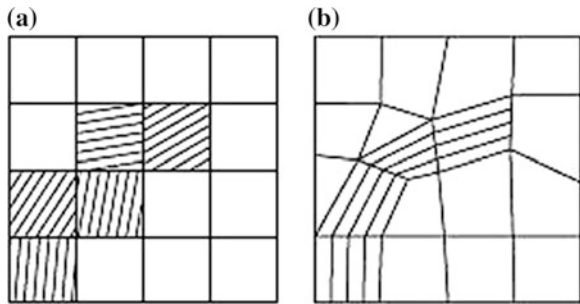
4 Fracture Energy and Softening Curve

In 2008, Zhao et al. [31] further extended the study on effects of specimen size on the fracture energy and softening curve of concrete. With the help of a three point test on a notched beam, they studied if the fracture energy changed with variation in size of specimen. They concluded through their tests results that the fracture energy increases with an increase in specimen size in both the beam and wedge splitting tests. They asserted that the fracture energy increases with an increase of the specimen size, especially in the wedge tests, and asymptotic behaviour over the size is observed in some concretes. Additionally, it was shown that the fracture energy increases with an increase of the maximum aggregate size, but there was no systematic trend with the water to binder ratio and the test method. They continued their research by representing the relationship between the crack opening and the gradual stress drop after tensile strength by an inverse analysis [32]. In this extended research work, they have discussed about the fracture process zone with respect to the size effect. The fracture analysis of concrete was therefore done in two-fold stages, first being the fracture energy analysis and the second being the inverse analysis.

Again in 2008, Seleem et al. [33] observed the effect of coarse aggregate type, crack-depth ratio (a/w) and area of tensile steel reinforcement (As) on the fracture toughness of SCC. This was an extension to the previous research work done on the

size effect of aggregated on the fracture properties of SCC. This study covered the coarse aggregate type and reinforcement with steel is the main criteria of change from the previous works. At the end of this research, it was concluded that the fracture toughness self-compacting concrete decreased with increasing crack—depth ratio and that the presence of steel reinforcement in the cracked section created a closing effect to the crack propagation. Another observation they made was in 2012, when they studied the fracture parameters by varying the depth of the notch and increasing the area of reinforced bars [34]. Eskandari et al. [35] also concluded almost similar results but they also compared the results between beam specimens with and without notches.

4.1 Studies in the Recent Past

Valentini and Hofstetter [36], in 2011, studied the plasticity model and a damage-plasticity model of a 3D concrete specimen with the help of finite element analysis. They observed and studied the variation between the predicted and actual material behaviour. As a result of their study, they developed an efficient stress update algorithm in a finite element program for performing large-scale 3D numerical simulations of concrete structures.

In 2012, Aslani and Nejadi [37] developed three new models for the fracture study on SCC and conventional concrete both. These models included elastic model, tensile strength model and a compressive stress-strain model. These models were also verified against the experimental results. Upon verification against experimental results, they concluded that the three models could accurately predict the branches of the stress-strain curves. The models also predicted the descending curves with a minimum range of deviation with a reasonable accuracy, which helped to study the fracture parameters. On a similar basis, in 2013, Grégoire et al. [38] compared experimental results with numerical simulations performed with reference to an integral non local model. The shortcomings of this classical formulation were also illustrated, which failed to describe size effect over the investigated range of geometries and sizes. Experimental results were also compared with the universal size effect law.

Cifuentes and Karihaloo [39] analysed the wedge splitting results obtained for normal- and high-strength self-compacting concrete and by comparison with the available results previously obtained under similar conditions for normal- and high strength vibrated concrete, and concluded that the specific fracture energy of self-compacting concrete mixes is lower than that of vibrated mixes of the same strength and the ductility of vibrated concrete mixes as measured by their characteristic length is only marginally higher than that of self-compacting concrete mixes.

5 Flexural Behavior of SCC

Pająk and Ponikiewski [40] investigated the flexural behavior of self-compacting concrete reinforced with straight and hooked end steel fibres at levels of 0.5, 1.0 and 1.5 % and compared it to normally vibrated concrete (NVC). They concluded that the type of steel fibres affects much the post-peak behavior of SCC and generally SCC indicates similar flexural behavior to NVC where the increase of fibres volume ratio increases the flexural tensile strength. They also concluded that the fracture energy increases with the increase of fibre dosage and is higher for hooked end steel fibres than for straight ones.

Erdem and Blankson [41] quantitatively determined the fractal character and texture of fracture surfaces investigated their influence on the fracture-related properties in different types of concrete having different interfacial bonding properties and coarse aggregate characteristics. They produced various conclusions on the interfacial zone, texture and aggregate characteristics of the concrete. Muralidhara et al. [42] made an attempt is made to obtain size independent fracture energy from fracture energy release rate. The new method using the relationship between RILEM fracture energies and un-cracked ligament lengths seem gave size independent fracture energy comparable with other methods and the method seemed to give good results when adopted for varying depths of beam.

Beygi et al. [43] researched experimentally on fracture characteristics of self-compacting concrete. Three point bending tests conducted on 154 notched beams with different water to cement (w/c) ratios. The specimens were made from mixes with various w/c ratios from 0.7 to 0.35. For all mixes, common fracture parameters were determined using two different methods, the work-of-fracture method (WFM) and the size effect method (SEM). Investigation major mechanical properties of SCC for twelve SCC mixes with wide spectrum of different variables i.e. maximum coarse aggregate size, coarse aggregate volume and aging was performed [44]. They made various conclusions relating the size of coarse aggregate, volume of coarse aggregate, SCC age, to parameters of compressive and tensile strength of the concrete.

In the experiment performed in order to determine the effect of coarse aggregate volume on fracture behavior of self-compacting concrete [45], a series of three point bending tests as shown in Fig. 5 were carried out on 58 notched beams. SCC
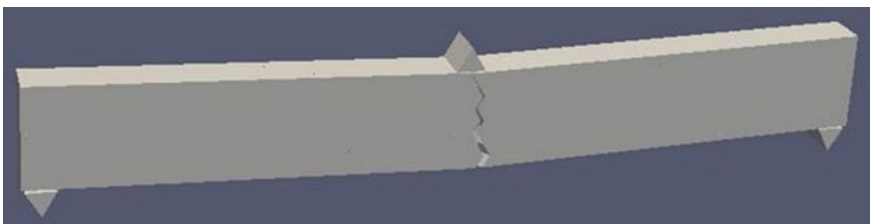
Fig. 5 Three point test for crack propagation study [45]

was prepared with coarse aggregate in varying percentages of 30, 40, 50 and 60 % (as the percentage of the total aggregate volume). For all mixes, the fracture parameters were analysed by the work-of-fracture method (WFM) and by the size effect method (SEM) to obtain a suitable correlation between these methods which is used to calibrate fracture numerical models. On evaluating the effect of maximum aggregate size on fracture behavior of self-compacting concrete [46], the parameters were analysed by the work-of-fracture method (WFM) and by the size effect method (SEM) and consequently a correlation between these methods was obtained which is used to calibrate cracking numerical models.

Korte et al. [47], compared the results of static and dynamic three-point bending tests and wedge-splitting tests on specimens, made from vibrated concrete (VC) and two types of self-compacting concrete (SCC). Different fracture parameters were derived from the experimentally obtained load–CMOD curves (load vs. crack mouth opening displacement) and the softening curve was extracted using inverse analysis. In 2014, Huang et al. [48] investigated the physico-chemical process of self-healing in blast furnace slag cement paste. The physico-chemical process of self-healing in slag cement paste was simulated with a reactive transport model and the effect of carbonation on self-healing was studied by using thermodynamic modelling. Pacheco et al. [49], studied bending cracks in reinforced concrete specimens by measuring the electrical resistance across the crack. Cracks have a major influence on the durability measurements of concrete. This effort was made to relate crack width to the electrical resistance across the crack.

6 Digital Image Correlation Technique

In 2010, Shah and Kishen [50] started the use of Digital Image Correlation Technique to observe the fracture properties such as mode I and mode II fracture toughness and the critical strain energy release rate for different concrete-concrete jointed interfaces. The set-up for DIC technique is shown in Fig. 6. Images were captured at several intervals of the loading process and then they were correlated and the surface displacements were computed from which the surface strains, crack opening displacements, load-point displacement, and crack length and crack tip location were also computed as shown in Fig. 7. They concluded that the image correlation technique is an effective method to study the crack propagation and other fracture properties of a concrete specimen. The use of Digital Image Correlation further gained a stronghold when Hemalatha et al. [51] again studied the crack propagation in a SCC specimen under three point loading test but this time using a scanning electron microscope (SEM). They again concluded that DIC technique is very helpful in determining the fracture toughness by observing the crack tip location and crack lengths.
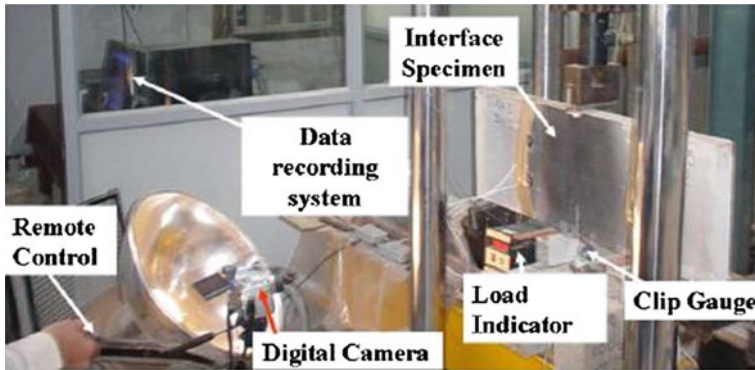
Fig. 6 Experimental setup for DIC technique [50]
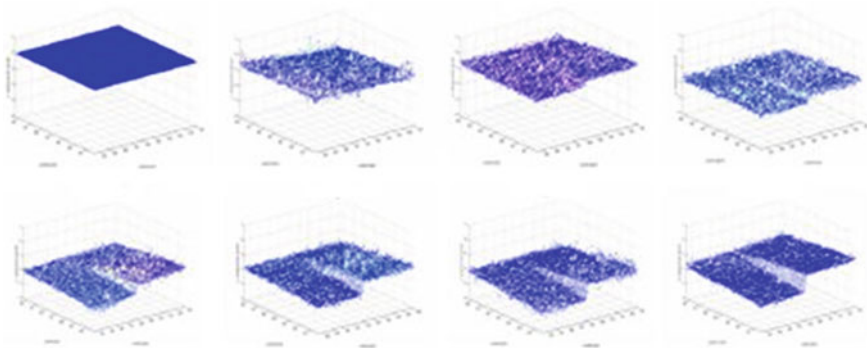
Fig. 7 Displacement and cracking pattern obtained from DIC [50]

7 Summary

The self-compacting concrete (SSC) was initially characterized by the study of mix design. With the progress in time, researchers shifted towards studying the fracture parameters. The study of fracture mechanism in the SCC began with the fracture zone and crack mouth opening displacement studies. Different models of fracture mechanics such as smeared crack model and discrete model were studied and compared. Fracture energy and fracture energy release rate were also among the parameters that formed the basis of study along with the softening point curve and stress-strain curve of concrete. The study further extended to the use of digital image correlation techniques and the use of other optical devices for precise and accurate results. Next, researchers started to explore the three-point test results and the use of notched beam to observe the crack development and crack propagation through the specimen. This led to the initiation of flexural behavior of the SCC.

8 Scope for Further Extension

Though finite element approach was studied by several researchers, there is still scope for the study of fracture parameters by analyzing the crack initiation, propagation, energy release rate, and crack displacement by studying the specimen both experimentally and by modeling. Further extension in this field can be done to find out the most effective method for studying the fracture parameters. There are several methods available for the study however it has not yet been stated which among these is the most effective under certain circumstances.

References

1. Okamura H, Ouchi M (2003) Self compacting concrete. J Adv Concr Technol 1(1):5–15
2. Ozawa K, Maekawa K, Kunishima M, Okamura H (1989) Development of high performance concrete based on the durability design of concrete structures. In: Proceedings of the second east-Asia and pacific conference on structural engineering and construction (EASEC-2), vol 1, Jan 1989, pp 445–450
3. Gołaszewski J, Szwabowski J (2004) Inluence of superplasticizers on rheological behaviour of fresh cement mortars. Cement Concr Res 34:235–248
4. Neville AM, Brooks JJ (2010) Concrete technology. Prentice Hall (Pearson), Essex, pp 408–410
5. Türkel S, Kandemir A (2010) Fresh and hardened properties of SCC made with different aggregate and mineral admixtures. J Mater Civ Eng 22:1025–1032
6. Sideris K (2007) Mechanical characteristics of self-consolidating concretes exposed to elevated temperatures. J Mater Civ Eng 19:648–654
7. Ghafoori N, Diawara H (2010) Inluence of temperature on fresh performance of self-consolidating concrete. Constr Build Mater 24:946–955
8. Naik TR, Kumar R, Ramme BW, Canpolat F (2012) Development of high-strength, economical self-consolidating concrete. Constr Build Mater 30:463–469
9. Kwan AKH, Ng IYT (2010) Improving performance and robustness of SCC by adding supplementary cementitious materials. Constr Build Mater 24:2260–2266
10. Al-Tamimi AK, Sonebi M (2003) Assessment of self-compacting concrete immersed in acidic solutions. J Mater Civ Eng 15:354–357
11. Gaimster R, Dixon N (2003) Self compacting concrete. In: Newman J, Choo BS (eds) Advanced concrete technology, process. Elsevier Butterworth Heinemann, Oxford, pp 9/1–9/23
12. European Federation of National Associations Representing Producers and Applicators of Specialist Building Products for Concrete (EFNARC) (2005) The European guidelines for self compacting concrete—specification, production and use, pp 1–63
13. Domone PL (2007) A review of the hardened mechanical properties of self-compacting concrete. Cement Concr Compos 29:1–12
14. Domone PL (2006) Self-compacting concrete: an analysis of 11 years of case studies. Cement Concr Compos 28:197–208
15. Wallevik OH, Wallevik JE (2011) Rheology as a tool in concrete science: the use of rheographs and workability boxes. Cem Concr Res 41:1279–1288
16. Banill PFG (2011) Additivity effects in the rheology of fresh concrete containing water-reducing admixtures. Constr Build Mater 25:2955–2960

17. Zhang M-H, Sisomphon K, Ng TS, Sun DJ (2010) Effect of superplasticizers on workability retention and initial setting time of cement pastes. Constr Build Mater 24:1700–1707
18. Li Z (2007) State of workability design technology for fresh concrete in Japan. Cem Concr Res 37:1308–1320
19. Vikan H, Justnes H, Winnefeld F, Figi R (2007) Correlating cement characteristics with rheology of paste. Cem Concr Res 37:1502–1511
20. Felekoðlu B, Tosun K, Baradan B, Altun A, Uyulgan B (2006) The effect of fly ash and limestone illers on the viscosity and compressive strength of self-compacting repair mortars. Cement Concr Res 36:1719–1726
21. Li Z, Ohkubo T, Tanigawa Y (2004) Flow performance of high-fluidity concrete. J Mater Civil Eng 588–596
22. Hodgson D III, Schindler AK, Brown DA, Stroup-Gardiner M (2005) Self-consolidating concrete for use in drilled shaft applications. J Mater Civil Eng 17:363–369
23. Mehta PK, Monteiro PJM (2006) Concrete microstructure, properties and materials. McGraw Hill, San Francisco, pp 475–476
24. Bourdette B, Ringot E, Ollivier JP (1995) Modelling of the transition zone porosity. Cem Concr Res 25(4):741–751
25. Prokopskia G, Halbiniakb J (2000) Interfacial transition zone in cementitious materials. Cem Concr Res 30:579–583
26. Jefferson AD (2002) Constitutive modelling of aggregate interlock in concrete. Int J Numer Anal Meth Geomech 26:515–535
27. Toumi A, Bascoul A (2002) Mode I crack propagation in concrete under fatigue: microscopic observations and modelling. Int J Numer Anal Meth Geomech 26:1299–1312
28. Hanson JH, Ingraffea AR (2003) Using numerical simulations to compare the fracture toughness values for concrete from the size-effect, two-parameter and fictitious crack models. Eng Fract Mech 70:1015–1027
29. de Borst R, Remmers JJC, Needleman A, Abellan MA (2004) Discrete vs smeared crack models for concrete fracture: bridging the gap. Int J Numer Anal Meth Geomech 28:583–607
30. Cervera M, Chiumenti M (2006) Smeared crack approach: back to the original track. Int J Numer Anal Meth Geomech 30:1173–1199
31. Zhao Z, Kwon SH, Shah SP (2008) Effect of specimen size on fracture energy and softening curve of concrete: part I. Experiments and fracture energy. Cement Concr Res 38:1049–1060
32. Zhao Z, Kwon SH, Shah SP (2008) Effect of specimen size on fracture energy and softening curve of concrete: part I. Inverse analysis and softening curve. Cement Concr Res 38:1061–1069
33. Seleem MH, Sallam HEM, Attwa AT, Heiza KT, Shaheen YB (2008) Fracture toughness of self compacting concrete. MesoMechanics. HBRC
34. Seleem MH, Sallam HEM, Attwa AT, Heiza KT, Shaheen YB (2012) Behavior and analysis of cracked self-compacted reinforced concrete beams. Concr Res Lett, ISSR J 3(1):373–385
35. Eskandari H, Muralidhara S, Raghuprasad BK, Venkatarama Reddy BV (2010) Size effect in self-consolidating concrete beams with and without notches. Sadhana, Indian Acad Sci 35 (3):303–317
36. Valentini B, Hofstetter G (2013) Review and enhancement of 3D concrete models for large-scale numerical simulations of concrete structures. Int J Numer Anal Meth Geomech 37:221–246
37. Aslani F, Nejadi S (2012) Mechanical properties of conventional and self-compacting concrete: an analytical study. Constr Build Mater 36:330–347
38. Grégoire D, Rojas-Solano LB, Pijaudier-Cabot G (2013) Failure and size effect for notched and unnotched concrete beams. Int J Numer Anal Meth Geomech 37:1434–1452
39. Cifuentes H, Karihaloo BL (2013) Determination of size-independent specific fracture energy of normal- and high-strength self-compacting concrete from wedgesplitting tests. Constr Build Mater 48:548–553
40. Pająk M, Ponikiewski T (2013) Flexural behavior of self-compacting concrete reinforced with different types of steel fibers. Constr Build Mater 47:397–408

41. Erdem S, Blankson MA (2013) Fractal–fracture analysis and characterization of impact-fractured surfaces in different types of concrete using digital image analysis and 3D nanomap laser profilometery. Constr Build Mater 40:70–76
42. Muralidhara S, Raghu Prasad BK, Singh RK (2013) Size independent fracture energy from fracture energy release rate in plain concrete beams. Eng Fract Mech 98:284–295
43. Beygi MHA, Kazemi MT, Nikbin IM, Amiri JV (2013) The effect of water to cement ratio on fracture parameters and brittleness of self-compacting concrete. Mater Des 50:267–276
44. Nikbin IM, Beygi MHA, Kazemi MT, Vaseghi Amiri J, Rahmani E, Rabbanifar S, Eslami M (2014) A comprehensive investigation into the effect of aging and coarse aggregate size and volume on mechanical properties of self-compacting concrete. Mater Des 59:199–210
45. Nikbin M, Beygi MHA, Kazemi MT, Vaseghi Amiri J, Rahmani E, Rabbanifar S, Eslami M (2014) Effect of coarse aggregate volume on fracture behavior of self-compacting concrete. Constr Build Mater 52:137–145
46. Beygi MHA, Kazemi MT, Vaseghi Amiri J, Nikbin IM, Rabbanifar S, Rahmani E (2014) Evaluation of the effect of maximum aggregate size on fracture behavior of self-compacting concrete. Constr Build Mater 55:202–211
47. Korte S, Boel V, De Corte W, De Schutter G (2014) Static and fatigue fracture mechanics properties of self-compacting concrete using three-point bending tests and wedge-splitting tests. Constr Build Mater 57:1–8
48. Huang H, Ye G, Damidot D (2014) Effect of blast furnace slag on self-healing of microcracks in cementitious materials. Cement Concr Res 60:68–82
49. Pacheco J, Šavija B, Schlangen E, Polder RB (2014) Assessment of cracks in reinforced concrete by means of electrical resistance and image analysis. Constr Build Mater 65:417–426
50. Shah SG, Kishen JMC (2010) Determination of fracture parameters of concrete interfaces using DIC. Fracture mechanics of concrete and concrete structures—assessment, durability, monitoring and retrofitting of concrete structures. Korea Concrete Institute
51. Hemalatha T, Kishen JMC, Ramaswamy A (2011) Fracture processes of self compacting concrete using image analysis. Sadhana, Indian Academy of Sciences

Use of Marble Dust as Clinker Replacement in Cements

Vineet Shah and Shashank Bishnoi

Abstract Around 6 million tonnes of marble dust, which is a waste product of marble polishing and grinding, is currently being dumped annually in three states in India. Though previous studies have investigated the use of this material as a replacement of fine-aggregate, since its particle size distribution is closer to that of cement, it could be more suitable as a clinker replacement. As the primary molecule in marble dust is calcium carbonate, the same as limestone, this study looks at the possible use of marble dust in ways similar to crushed limestone. Blends of ordinary Portland cement (OPC) with marble dust, with and without fly-ash and calcined clays as sources of alumino-silicates, were prepared and tested in the laboratory. The role of activators such as gypsum and sodium sulphate was also studied. The results show that although marble dust may be less reactive in such systems than limestone, it offers the advantage of better workability in concretes using these blends.

Keywords Carboaluminates · Compressive strength · Fly-ash · Portland cement · Marble dust

1 Introduction

Cement is the basic ingredient of concrete, a fundamental building material for society's infrastructure around the world. Concrete consumption is second only to water in total volumes consumed annually. The Indian cement industry's share was around 7 % of the country's total man-made CO_2 emissions as in 2010. India's population is set to rise from 1.2 billion to 1.7 billion by 2050 and by the same time, 50 % of India's population will be residing in urban areas leading to rapid

V. Shah (✉) · S. Bishnoi
Department of Civil Engineering, Indian Institute of Technology (IIT) Delhi,
New Delhi 110016, India
e-mail: vineet.shah9@gmail.com

urbanisation [1]. Large-scale infrastructure development such as dams in the northern mountainous regions, ports on the western coast, dedicated freight corridors and airports in the growing metropolitan areas are planned for the growth of country. All the above factors collectively will drive up concrete demand in the construction sector. Per capita cement consumption will increase somewhere between 465 and 810 kg/capita from 188 kg/capita [1].

Increased production of cement will have a strong impact on the overall energy utilization of the cement industry. More energy input required to meet the demand in various processes will result in increased fuel consumption leading to higher emissions of CO_2 and other greenhouse gases raising concern over the security of supplies and people. Enormous efforts are being made in the cement industries to bring down the carbon dioxide emission during cement production by using alternate fuel and raw material, waste heat recovery, clinker substitution etc. Clinker substitution by supplementary cementitious materials (SCM's) like fly-ash, metakaolin, silica fume, slag and natural pozzolana material is being used since many years. But due to every rising emissions and need, efforts are being made to optimize and use combination of SCM's together as clinker replacement.

Nearly 960 million tonnes of solid waste is generated every year in India. The waste produced is mainly by-product of mining, agricultural, municipal, industrial and other processes [2, 3]. Due to unavailability of proper disposal method, the waste generated is released into the nearby environment creating health and environmental related issues. Due to various economic, social and environmental restraints, identification of suitable disposal method remains a top priority.

Use of limestone powder as partial cement replacement material is well known. Limestone act as a filler material and increase the rate of reaction and to some extent it participates in cement hydration process to form carboaluminate which is more stable form as compared to monosulfoaluminate present in the system [4, 5]. The ordinary Portland cement (OPC)-limestone reaction is not so prominent due to limited availability of aluminate ions from clinker and limestone [6]. Use of fly-ash as a binder material is now known for a long time. Fly-ash initially does not take part in the reaction and hence the initial strength development is less in cement containing fly-ash. After sufficient quantity of CH is present in the system the fly-ash starts reacting with it and form cementitious material [7]. Limestone and fly-ash produces synergic effect when used together as a constituent for ternary cement containing clinker and form carboaluminate phases in the system and reduces conversion of Aft to Afm phase. Around 6 million tonnes of Marble dust, which is a waste product of marble polishing and grinding, is currently being dumped annually in three states in India. Though previous studies have investigated the use of this material as a replacement of fine-aggregate, since its particle size distribution is closer to that of cement, it could be more suitable as a clinker replacement [7, 8]. As the primary molecule in marble dust is calcium carbonate, the same as limestone, this study looks at the possible use of marble dust in ways similar to crushed limestone.

2 Methodology

The experiments were carried out in two sets. In first set of experiments chemical composition of constituent materials were analysed and different blends with varying proportion of the constituent materials using fly-ash as a source of alumina-silicate was tested for compressive strength. The variation in blends was done in such a way that when one of the constituent material proportions was altered then all the remaining constituent materials proportion was decreased or increased in the same proportion to have the same mass fraction among materials and in order to establish a common evaluation basis. The water to binder ratio was fixed to 0.4 and aggregate to binder ratio was fixed to 1:3 for all the blends. The materials were added directly into the mixture at the time of casting no prior inter blending or inter grounding was done. Figure 1 shows the thermal gravimetric analysis (TGA) result of raw marble dust.

In the second set of experiment, metakaolin was used in place of fly-ash for the blends which gave consistent compressive strength results from the first set of experiments. Along with that casting was carried out by using sodium sulphate as an activator in the system instead of gypsum for the selected blends. In order to understand the reactivity of different constituents in the blends, the materials were replaced by quartz one at a time and effect of it was studied. Along with that inter-blending and inter-grounding of the constituent materials was carried out prior to mixing with water to create homogenous blend. Mortar specimens of size of $70.6 \times 70.6 \times 70.6$ mm^3 were cast for compressive strength measurement cured at 27 °C and tested after 3, 7, 28, 56 and 90 days. Chemical analysis of constituent materials, using XRF, and the experimental matrix are shown in Tables 1 and 2, respectively.
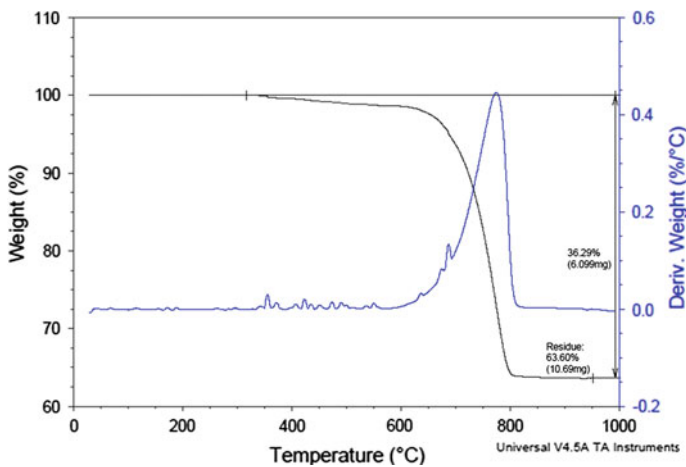
Fig. 1 Raw marble dust TGA

Table 1 Chemical analysis of constituent materials using XRF

	OPC	Fly-ash	Marble dust	Gypsum
SiO_2	20.7	64.5	5.97	3.22
Al_2O_3	5.68	27.4	0.35	0.22
Fe_2O_3	4.23	3.45	2.87	0.16
TiO_2	0.423	1.15	0.083	0.033
CaO	62.2	1.14	36.5	31.3
MgO	0.88	0.245	11.86	0.23
Na_2O	0.174	0.184	0.081	0.135
K_2O	0.322	0.778	0.094	0.035
SO_3	1.94	0.066	0.041	44.2
P_2O_5	0.023	0.165	0.038	0.101
MnO	0.045	0.039	0.302	0.011
Cl	0.03	0.025	0.008	0.06
LOI	3.12	0.71	41.6	20.2

Table 2 Experimental matrix

Notations	Ratio			
	Cement	Fly-ash	Marble dust	Gypsum
C50F30M15G5	0.50	0.30	0.15	0.05
C57F20M15G6	0.57	0.20	0.15	0.06
C53F32M10G5	0.53	0.32	0.10	0.05
C47F28M20G5	0.47	0.28	0.20	0.05
C51F32M16G2	0.51	0.32	0.16	0.02
C57K20M15G6	0.57	0.20	0.15	0.06
C53K32M10G5	0.53	0.32	0.10	0.05
C47K28M20G5	0.47	0.28	0.20	0.05
C50F30M15N5	0.50	0.30	0.15	0.05
C57F20M15N6	0.57	0.20	0.15	0.06
C53F32M10N5	0.53	0.32	0.10	0.05
C47F28M20N5	0.47	0.28	0.20	0.05
C100	1.00	0.30	*	*
C70F30	0.70	0.30	*	*

3 Results

3.1 Compressive Strength

Compressive strength results for blends containing fly-ash and marble dust with gypsum as activator at different ages is presented in Table 3.

Table 3 Compressive strength (N/mm^2) results at different age

	3 days	7 days	28 days	56 days	90 days
C50F30M15G5	3.42	10.81	17.61	22.58	24.97
C57F20M15G6	10.77	12.84	17.36	22.37	28.68
C53F32M10G5	10.84	12.53	16.81		28.11
C47F28M20G5	9.52	11.95	12.34	19.6	22.81
C51F32M16G2	5.46	10.45	20.62	25.41	30.45
C57K20M15G6	13.19	18.70	31.88	28.34	31.98
C53K32M10G5	14.82	24.08	24.84	27.98	20.44
C47K28M20G5	13.36	20.01	26.28	33.07	26.58
C50F30M15N5	5.90	13.45	18.67	23.19	28.84
C57F20M15N6	11.79	13.76	21.84	25.29	27.96
C53F32M10N5	10.95	13.79	20.01	23.74	29.38
C47F28M20N5	9.52	11.56	16.08	18.49	23.25
C100	20.25	31.13	27.49	44.61	55.65
C70F30	6.94	14.85	25.89	34.17	41.23

3.2 Consistency

The results of the standard consistency tests are presented in Table 4.

Table 4 Standard consistency test

Consistency	Percentage of water required to get penetration of 5–7 mm
C100	27.5
C65F35	26.5
C50F30M20	25.5

4 Discussion

4.1 Compressive Strength

With increasing marble dust content in the mix the compressive strength decreases at all ages. The maximum compressive strength was obtained for the blends containing 15 % marble dust of the total binder system as shown in Fig. 2.

Blends containing sodium sulphate gained higher compressive strength as compared to the blends containing gypsum. The increase in strength is obtained due to faster dissolution of ions from sodium sulphate. But at the later age strength this effect tends to mitigate and equivalent strengths were observed for gypsum and sodium sulphate blends. When metakaolin was used as aluminate source instead of
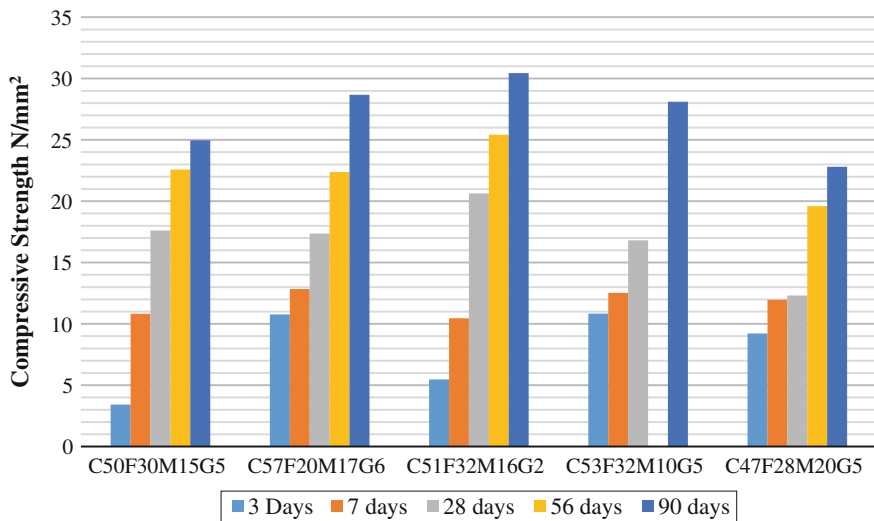
Fig. 2 Compressive strength results for blends containing combination of marble dust and fly-ash

fly-ash high early strength was obtained but at the later age strength loss was observed as shown in Fig. 3. The compressive strength results of OPC and Portland pozzolana cement (PPC) are shown in Fig. 4. It can be inferred from the results that the compressive strength of all the blends containing fly-ash and marble dust together is less as compared to OPC and PPC.

From the results discussed it can be inferred that compressive strength of the blends decreases on replacing clinker with marble dust. 30 % strength loss was observed in blends comprising of marble dust and fly-ash when compared to PPC.
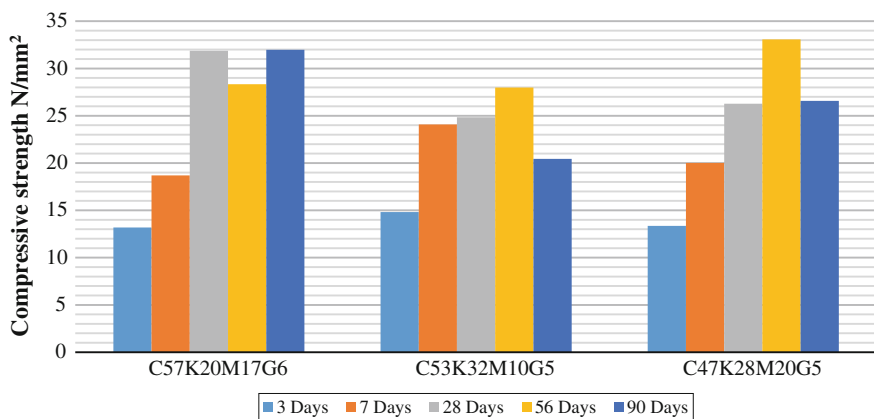
Fig. 3 Compressive strength results for blends containing combination of marble dust and metakaolin
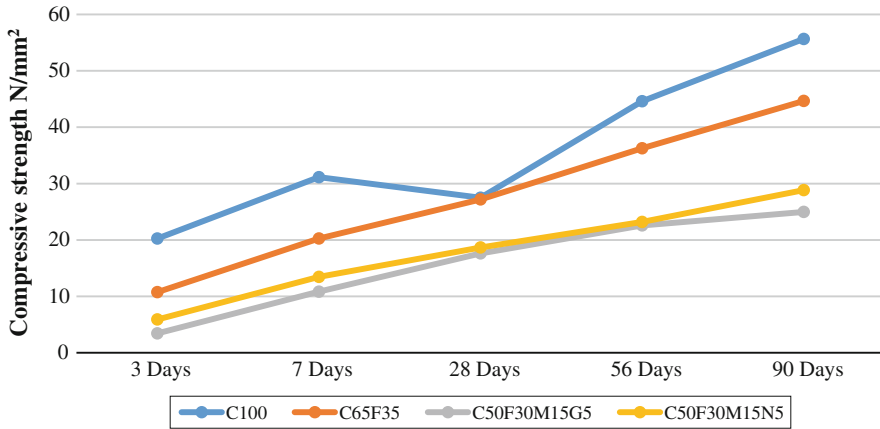
Fig. 4 Comparison of compressive strength results with respect to control mixes

Using metakaolin, higher initial strength was observed but strength loss at later stage is observed indicating formation of meta-stable phases which get transformed into stable phase with time or due to leaching. Higher reactivity of metakaolin is attributed mainly due to its arrangement of penta-coordinated alumina ions formed during the dehydroxylation process and higher specific surface area. Slight increase in early age strength is observed when sodium sulphate was used as an activator. At later ages, the effect tends to mitigate and in most cases it gives lower strength as compared to gypsum. Moreover, presence of sodium sulphate in the system can lead to formation of gypsum in presence of CH in later age leading to expansion of the system. On increasing marble dust and fly-ash in the system in place of clinker a general trend of decrease in strength is observed but it helps to improve the workability of the mix.

4.2 Consistency

The standard consistency test was carried out in accordance to IS: 4031 (Part 4) [9]. From the results shown in Table 4 it can be inferred that in order to achieve the same flow-ability the amount of water required for blend containing marble dust is less as compared to OPC and PPC, indicating marble dust helps to improve the workability of system.

5 Conclusions

 (i) 30 and 45 % strength loss was observed when 50 % of clinker was substituted
      and replaced by combination of marble dust and fly-ash as compared to PPC
      and OPC respectively.
 (ii) With increasing percentage of marble dust in the system, the strength
      decreases.
(iii) Marble dust helps to improve the workability.
(iv) Higher percentage of gypsum in the blends did not have any significant
      influence on the formation of additional ettringite in the system. No substantial
      change was observed when sodium sulphate was used as an activator. Using
      sodium sulphate increase in early strength was observed as compared to
      gypsum but at later age the effects tend to mitigate.
 (v) The reaction between pozzolanic minerals and marble dust is sluggish in
      nature. Determination of appropriate activator and its subsequent effect on the
      system along with other parameters should be analysed.

References

 1. Technology roadmap, low-carbon technology for Indian Cement Industry (2012). International
    Energy Agency, Paris
 2. Patel AN, Jayesh P (2013) Stone waste in India for concrete with value creation opportunities.
    Int J Latest Trend Technol 2(3):113–120
 3. Pappu A, Saxena M, Asolekar RS (2007) Solid wastes generation in India and their recycling
    potential in building materials. Build Environ 42(6):2311–2320
 4. Bonavetti VL, Rahhal VF, Irassar EF (2001) Studies on the carboaluminates formation in
    limestone filler blended cements. Cem Concr Res 31(6):853–859
 5. Charles HF (1985) Hydration of carbo-aluminous cement at different temperatures. Cem
    Concr Res 15(4):622–630
 6. Matschei T, Lothenbach B, Glasser F (2007) The role of calcium carbonate in cement
    hydration. Cem Concr Res 37(4):551–558
 7. Peter CH (2004) Lea's chemistry of cement and concrete, 4th edn. Butterworth-Heinemann,
    Oxford
 8. Bacarji E, Toledo R, Koenders E, Figueiredo E, Lopes JLMP (2013) Sustainability perspective
    of marble and granite residues as concrete fillers. Constr Build Mater 45:1–10
 9. IS: 4031 (part 4) (1998) Indian standard for methods of physical tests for hydraulic cement
    (part 4). Bureau of Indian Standards, New Delhi, India

Bibliography

10. Bahar D (2010) The effect of the using waste marble dust as fine sand on the mechanical
    properties of the concrete. Int J Phys Sci 8(3):193–203
11. Nutan P, Amit R, Jayesh K (2013) Marble waste: opportunities for development of low cost
    concrete. Global Res Anal 2(2):94–96

High Level Clinker Replacement in Ternary Limestone-Calcined Clay-Clinker Cement

Sreejith Krishnan and Shashank Bishnoi

Abstract Cements with 50 % clinker contents were produced in a pilot scale using low grade crushed limestone and low grade calcined clays. The clays were calcined in a static pottery unit and blending was carried out at a grinding unit in West Bengal. A total of 40 tonnes of 4 blends of the cement were produced and tests were carried out in the laboratory. The results show that despite the production being carried out by untrained personnel and the low clinker factor, relatively high strengths were obtained from the cements. Results show that it is possible to improve the economy and eco-friendliness of concrete production through the use of these new blended cements. The cement also holds the promise to improve the life of limestone quarries through the utilisation of material that was earlier discarded.

1 Introduction

Ordinary Portland cement is one of the most versatile building materials available today. It can be manufactured locally, with available local raw materials. It is estimated that around 3 tonnes of concrete is produced per capita per year in the world today [1]. This makes concrete one of the most produced and consumed material in the world. However, the major criticism faced by the cement industry is that manufacturing of Portland cement results in the emission of carbon dioxide leading to global warming and associated climate change. One of the possible solution to this problem is to lower the clinker factor with supplementary cementing

S. Krishnan (✉) · S. Bishnoi
Department of Civil Engineering, Indian Institute of Technology (IIT) Delhi, Hauz khas, New Delhi 110016, India
e-mail: sree1111@gmail.com

materials (SCM) like fly ash, Ground Granulated Blast furnace Slag (GGBS), Rice Husk Ash, metakaolin etc. However, substitution rates beyond 30 % using various SCMs have been observed to adversely affect the performance of concrete. In this study, the possibility of reducing the clinker factor up to 50 % using a mix of limestone and calcined clay and its effect on mechanical properties of cement is being investigated.

The kaolinite clay available in India has been found to have pozzolanic properties [2]. The kaolinite clay on being heated up to 800 °C undergoes dehydroxylation and converts into reactive pozzolana [3]. Monocarboaluminates have been observed as a hydration product in limestone blended cements [4]. Monocarboaluminate is found to be more stable than monosulphoaluminate in the presence of limestone. Lothenbach et al. [5] observed that formation of monocarboaluminate indirectly stabilised ettringite which leads to an increase in the volume of hydration products and a reduction in porosity.

The metakaolin present in the calcined clay contains aluminates which will react with limestone to produce calcium monocarboaluminate and calcium hemicarboaluminate. The carboaluminates formed will fill out the concrete pore structure and improve the compressive strength. Antoni et al. [6], suggests that a MK/Limestone mix of the ratio of 2:1 by weight can be used for the purpose of clinker replacement. The chemical reaction that takes place is represented by Eq. 1.

$$A + C\bar{C} + 3CH + H \Rightarrow C_3A \cdot C\bar{C} \cdot H_{12} \tag{1}$$

2 Experimental Programmes

2.1 Raw Materials

Two different type of kaolinitic clay samples were obtained from the state of West Bengal in eastern India for the purpose of this study. First clay contained around 80 % kaolinite (Type 1 clay) while the second clay (Type 2 clay) contained around 20 % kaolinite. The clays were calcined at a temperature of 800 °C in a down draft kiln using static calcination and a soaked for a period of 8 h. The two limestone samples were identified, of which one was of cement grade quality (Limestone A) while the other was of a lower quality with high dolomite content (Limestone B). The clinker and the gypsum were obtained from Bansal Cement Plant located at Kharagpur district of West Bengal, where the inter-grinding of raw materials was carried out. The raw materials were ground together at ratio of 50 % clinker, 30 % calcined clay, 15 % limestone and 5 % gypsum. Four blends of cement were produced and used for carrying out the various tests. In addition to these four blends, a laboratory cement blend was produced using industrial grade metakaolin, MetaCem 85 and limestone A with same clinker and gypsum as the trial blends. Table 1 summarizes the cement blends that were produced.

Table 1 Cement blends and compositions

Cement blend	Clay	Limestone
LC3 A	Type 1	LSA
LC3 B	Type 1	LSB
LC3 C	Type 2	LSA
LC3 D	Type 2	LSB
LC3 E	MetaCem 85	LSA

2.2 Tests on Calcined Clay

The calcined clays were tested for their lime reactivity as per IS 1727-1967 [7].

2.3 Tests on Cements

The cement blends produced were tested as per IS 4031 [8] to measure the standard consistency, initial and final setting times and Blaine's fineness. Mortar cubes of size 70.6 mm × 70.6 mm × 70.6 mm were cast using the cement blends and standard sand at a ratio of 1:3. A fixed w/c ratio of 0.45 was used for preparing the mortar cubes so as to compare the performances of each blend at same water cement ratio.

2.4 Tests on Concrete

A fixed water content of 160 kg/m^3 of concrete were used and compressive strength was tested at four different water cement ratios of 0.425, 0.45, 0.475 and 0.5. A constant slump of 75 mm was achieved using BASF MetaGlenium Sky 8777 super-plasticizer. 150 mm × 150 mm × 150 mm size cubes of concrete were cast and de-moulded after 24 h. They were cured continuously under water till the time of testing. The strengths results were compared with that obtained from OPC and PPC with 30 % fly ash replacement. The PPC used was not a commercial PPC but made by blending fly ash with OPC in the laboratory.

3 Results

3.1 Lime Reactivity

The lime reactivity tests of the calcined clays showed that the fully calcined Type 1 clay was nearly as reactive as MetaCem 85. Type 2 clay showed poor lime reactivity as compared to Type 1 clay. It was observed that the calcination process used

Table 2 Lime reactivity of clays

Clay	Lime reactivity (MPa)
Fully calcined Type 1 clay	9.25
Fully calcined Type 2 clay	1.38
Partially calcined Type 1 clay	6.30
MetaCem 85	10.01
IS 1344-1981 limiting value	4

resulted in partially calcined clays as shown from the lime reactivity of clays. This was due to the inefficient distribution of heat in the kilns. It is also interesting to note that the poor lime reactivity of Type 2 clay makes it ineligible to be used as Supplementary Cementing Material in the manufacturing of Portland Pozzolana Cement as per IS 1344 [9]. The lime reactivity results are represented in Table 2.

3.2 Tests on Cements

The standard consistencies of the LC3 blends were found to be higher than OPC. The initial setting times for all the blends were found to be lower than that of OPC with the blends containing Type 1 clay setting faster than blends containing Type 2 clay. From Table 3 it can be observed that both initial and final setting times were found to be within the limits prescribed by the standards. It was observed that the LC3 blends produced were finer than the OPC as the Blaines fineness values of the blends were higher. The LC3 blends gave good strength performance with the blends containing Type 1 clay obtaining greater strengths than both OPC and PPC. The blends containing inferior clay provided equivalent performance to that of OPC and PPC even at a low clinker factor of 0.5 as seen from Fig. 1.

Table 3 Properties of the LC3 blends measured in laboratory

Cement blends	Standard consistency (%)	Initial setting time (min)	Final setting time (min)	Blaine's fineness (m^2/kg)
LC3 A	32.5	34	290	534
LC3 B	33	33	335	534
LC3 C	34	101	330	520
LC3 D	34	105	400	462
OPC	29	190	–	290

Fig. 1 Compressive strengths (MPa) of mortar cubes @ w/c —0.45
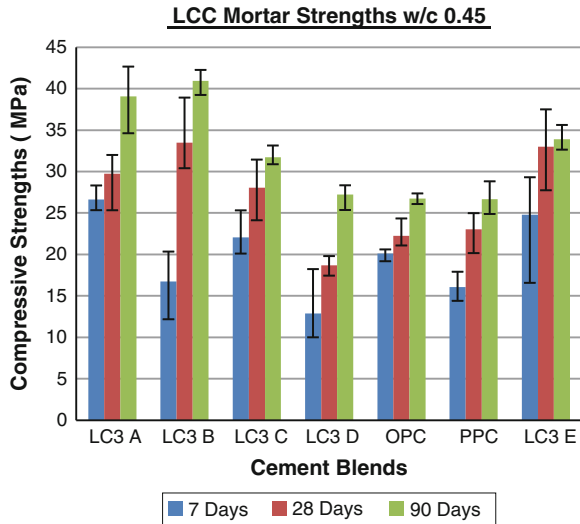
3.3 Tests on Concrete

The LC3 blend A provided the best compressive strengths at 28 days at all the four different water ratios. The concrete prepared using blends C and D, which contained low quality clay, gave strengths comparable with that of PPC. It was observed that variations in strength of concrete cubes were large which was due to the inefficient calcination process which resulted in the addition of uncalcined clays to the cement. The lab blend prepared E produced using commercial metakaolin was found to give strengths comparable to blends A and B. The compressive strength obtained at different water cement ratios have been shown in Figs. 2, 3, 4 and 5.

Fig. 2 Strength comparisons of LC3 blends @ w/c—0.425
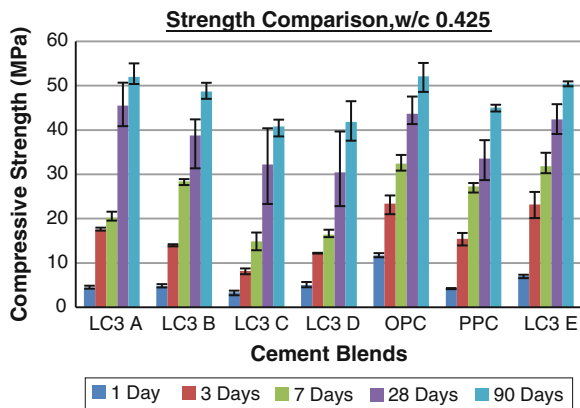
Fig. 3 Strength comparisons of LC3 blends @ w/c—0.45
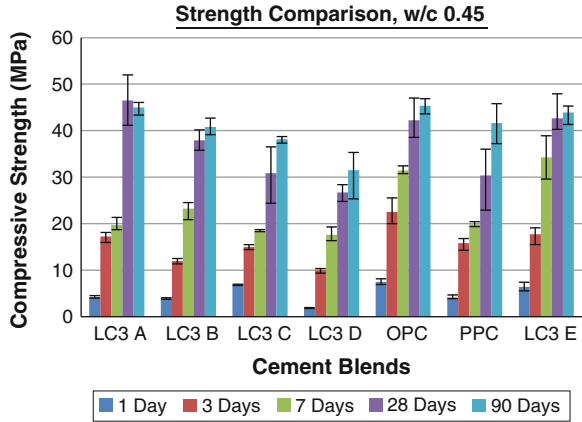
Fig. 4 Strength comparisons of LC3 blends @ w/c—0.475
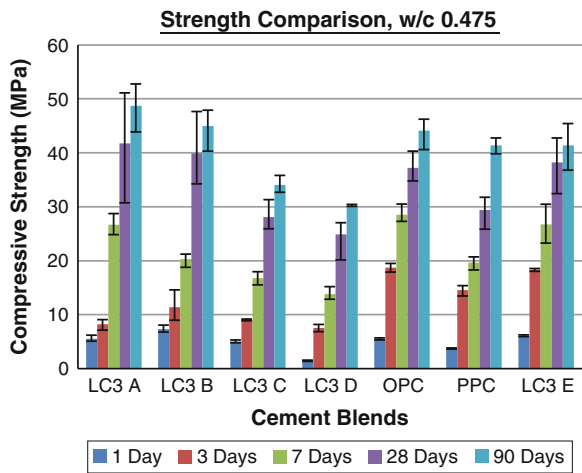
Fig. 5 Strength comparisons of LC3 blends @ w/c—0.5
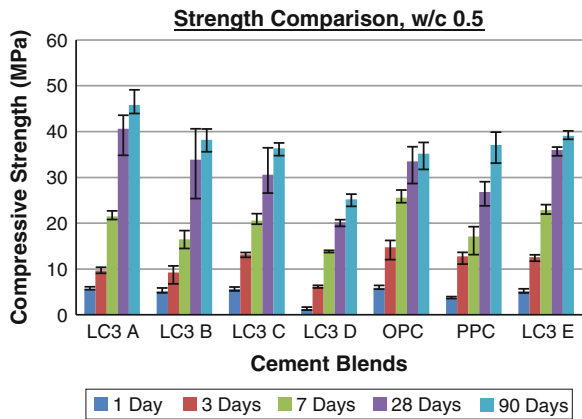
4 Conclusions

The possibility of reducing the clinker factor by 50 % using calcined clay and limestone was explored in this study. The LC3 blends produced using clay containing high metakaolin content gave strength performance equivalent to that of OPC while the blends containing low quality clay gave performance equivalent to that of PPC. It was observed that LC3 blends gave high early age strengths as compared to both OPC and PPC. The variability in the strengths was due to the improper calcination of clays which resulted in the addition of un-reactive clay in the cement. It was seen that reduction of clinker factor up to 50 % is possible without the loss of strength using limestone and calcined clay.

References

1. Technology Roadmap, Low-Carbon Technology for Indian Cement Industry (2012). In: Conference proceedings. International Energy Agency
2. Singh M, Garg M (2006) Reactive pozzolana from Indian clays—their use in cement mortars. Cem Concr Res 36(10):1903–1907
3. Bich C, Ambroise J, Pera J (2009) Influence of degree of dehydroxylation on pozzolanic activity of metakaolin. Appl Clay Sci 44:194–200
4. Bonavetti VL, Rahhal VF, Irassar EF (2001) Studies of carboaluminate formation in limestone blended cement. Cem Concr Res 31:853–859
5. Lothenbach B, Saout GL, Galluci E, Scrievner K (2008) Influence of limestone on hydration of cement. Cem Concr Res 38:848–860
6. Antoni M, Martinera F, Scrievner K (2012) Cement substitution by a combination of metakaolin and limestone. Cem Concr Res 42:1579–1589
7. IS 1727 (1967) Methods of tests for pozzolanic materials. Bureau of Indian Standards
8. IS 4031 (1999) Methods of physical tests for hydraulic cements, parts 1–5. Bureau of Indian Standards
9. IS 1344 (1981) Specification for calcined clay pozzolana. Bureau of Indian Standards

Development of Mix Proportions for Different Grades of Metakaolin Based Self-compacting Concrete

Vaishali G. Ghorpade, Koneru Venkata Subash and Lam Chaitanya Anand Kumar

Abstract Concrete is the most widely used construction material because of its mouldability into any required structural form and shape due to its fluid behavior at early ages. Thorough compaction, using vibration, is normally essential for achieving workability, the required strength and durability of concrete. Inadequate compaction of concrete results in large number of voids, affecting strength and long-term durability of structures. Self-compacting concrete (SCC) provides a solution to these problems. As the name signifies, it is able to compact itself without any additional vibration or compactive effort. However, widespread applications of self-compacted concrete have been restricted due to lack of standard mix design procedure and testing methods. Self-compacted concrete is used as a special concrete in place of standard concrete due to lack of mix design procedures. It is gaining wide acceptability because no vibration is needed and noise pollution is eliminated thereby. The construction process is safer and more productive. This paper presents the performance of self-compacted concrete by using ordinary Portland cement, metakaolin (MK) as a mineral admixture and Glenium B233 as a superplasticizer. Metakaolin is produced by heating kaolin, one of the most abundant natural clay minerals, to temperatures of 700–850 °C. The performance of metakaolin in self-compacting concrete is not well documented, particularly over a wide range of grades. In particular, the effects of metakaolin as a high surface area mineral addition on the workability as well as mechanical properties of self-compacting concrete need to be fully recognized. Therefore, the present study is an effort to characterize the fresh and hardened properties of self-compacting concrete containing metakaolin. Glenium B233 is an admixture of a new generation based on modified poly carboxylic ether. It is free from chloride and is compatible with all types of cements. This experimental study demonstrates that metakaolin can be

V.G. Ghorpade
Jawaharlal Nehru Technological University (JNTU), Anantapur, India

K.V. Subash (✉)
PVP Siddhartha Institute of Technology, Vijayawada, India
e-mail: koneruvenkatasubash@gmail.com

L.C. Anand Kumar
VR Siddhartha Engineering College, Vijayawada, India

1733

successfully used as an admixture in the preparation of self-compacting concrete (SCC). In order to prepare suitable mix proportions for different grades of metakaolin based self-compacting concrete, investigations were undertaken replacing cement with 0, 10, 15, 20, 25 and 30 % of metakaolin and with different percentages of superplasticizer (Glenium B233). As per the European guidelines for self-compacting concrete, slump flow test, V-funnel test and L-box test have been carried out on fresh properties of metakaolin based self-compacting concrete. The compressive strength, split tensile strength and flexural strength of the specimens have been analyzed for 7 and 28-days curing. In addition, finally mix proportions have been recommended for low, medium and high strength grades of metakaolin based self-compacting concrete. The fresh concrete test results revealed that by substituting different percentages of metakaolin in self-compacting concrete, satisfactory workability and rheological properties could be achieved, even though no viscosity-modifying agent was needed. In general, it seems that metakaolin can be considered as suitable replacement regarding to the economic efficiency, fresh and hardened properties of metakaolin based self-compacting concrete. The test results for acceptance characteristics of self-compacting concrete such as slump flow test, V-funnel test and L-Box test were satisfactory as per EFNARC for developed mix proportions of M60, M40 and M20 grade self-compacting concrete mixes. Further, compressive strength, tensile strength and flexural strength at the ages of 7 and 28 days were also determined and 10–15 % replacement of metakaolin can be regarded as a suitable replacement and mix proportions have been recommended for low (M20), medium (M40) and high (M60) strength grades of metakaolin based self-compacting concrete from this study.

1 Introduction

The development of specifying a concrete according to its performance requirements, rather than the constituents and ingredients has opened innumerable opportunities for producers of concrete and users to design concrete to suit their specific requirements. One of the most outstanding advances in the concrete technology over the last decade is "self-compacting concrete" (SCC). Self-compacting concrete is a high flowable concrete, which can be placed and compacted without any vibration in complex or dense reinforced formworks. In order to achieve such behavior, the main requirements of fresh self-compacting concrete are filling ability, passing ability and very high segregation resistance. The first two properties can be achieved by using a superplasticizer admixture. To secure stability/cohesion of the mix, a large quantity of powder materials and/or viscosity-modifying admixture (VMA) is required. The hardened self-compacting concrete is

dense, homogeneous and has the same engineering properties and durability as that of traditional vibrated concrete. The use of self-compacting concrete eliminates the need for compaction thereby saves time, reduces labor costs and conserves energy. Furthermore, use of self-compacting concrete enhances surface finish characteristics.

According to EFNARC [1], the term powder is defined for materials of particle size smaller than 0.125 mm, which includes fraction of aggregate, additions and cement. Portland cement is a highly energy-intensive product. On the other hand, CO_2 emanations are produced by the cement industry. In addition, some disadvantages in the properties of concrete have been reported as the cement content exceeded a specified value [2]. To minimize these negative effects, the requirement to increase powder content in self-compacting concrete is usually met by the use of additions. For this purpose, substantial studies have been performed on the usage of different additions for partially replacement of cement in self-compacting concrete or self-compacted mortar such as marble powder, limestone powder, basalt powder, fly ash and slag.

Metakaolin (MK) can also be considered as addition in the production of self-compacting concrete. Metakaolin (commercially available since the mid-1990s [3]) is a thermally activated alumino-silicate material mostly produced by calcination of kaolin clay at temperature ranging from 700 to 850 °C [4] without production of CO_2 [5, 6]. Metakaolin processing involves lower temperatures than Portland cement, which may yield a lower cost on metakaolin production. However, due to the low production of metakaolin, the price will be raised up [6]. Nonetheless, the usage of metakaolin in concrete can be reasonable due to its environmental benefits [5, 6] and positive effect on the both short- and long-terms strength of concrete.

However, different aspects of normal concrete containing metakaolin have been reported in literature, but the performance of metakaolin in self-compacting concrete is not well documented, particularly over a wide range of grades. In particular, the effects of metakaolin as a high surface area mineral addition on the workability as well as mechanical properties of self-compacting concrete need to be fully recognized. Therefore, the present study is an effort to characterize the fresh and hardened properties of self-compacting concrete (SCC) containing metakaolin. For this purpose, several tests concerning slump flow, V-funnel and L-box were conducted to assess the workability of the matrix. Furthermore, hardened properties were evaluated by compressive strength, splitting tensile strength and flexural strength.

2 Experimental Plan

2.1 Materials

The 53 grade ordinary Portland cement (OPC) and metakaolin (brought from 20 Microns Ltd., Gujarat) were used as binder materials in the production of self-compacting concrete mixes. The chemical compositions and physical characteristics of binders are given in Table 1. The fine aggregate was natural river sand. The particle size distribution of metakaolin, cement and fine aggregate are listed in Table 2. The nominal maximum size of 10 mm gravel was used as coarse aggregate. Poly-carboxylic ether based admixture namely Glenium B233 (brought from BASF) with relative density 1.08 (at 25 °C) was used to enhance the flowability of the mixtures. In addition, viscosity-modifying agent namely Glenium stream2 was used in self-compacting concrete mixes without metakaolin.

Table 1 Chemical compositions and physical characteristics of binders

Chemical composition (%)	Cement	Metakaolin
Silicon dioxide (SiO_2)	17–25	60–65
Aluminum oxide (Al_2O_3)	3–8	30–34
Iron oxide (Fe_2O_3)	0.5–6	1
Calcium oxide (CaO)	60–67	0.2–0.8
Magnesium oxide (MgO)	0.1–4.0	0.2–0.8
Sodium oxide (Na_2O)	0.4–1.3	0.5–1.2
Potassium oxide (K_2O)	–	0.5–1.2
Sulphur	1.3	–
Physical properties		
Specific surface (m^2/kg)	0.33	2.54
Specific gravity	3.15	2.6

Table 2 Particle size distribution of cement, metakaolin and fine aggregate

Characteristics (mm, %)	Cement	Metakaolin	Fine aggregate
Retained at 1	0.75	7.13	0.05
Retained at 0.600	0.91	65.12	10.26
Retained at 0.425	8.10	14.17	34.39
Retained at 0.300	21.07	4.91	29.21
Retained at 0.150	66.91	6.81	24.96
Retained at 0.075	2.27	1.86	1.14

2.2 Mixture Proportion

Self-compacting concrete mixtures were designed in three groups, which were defined as M60, M40 and M20 and are shown in Tables 4, 5 and 6, respectively. In each group, the reference concrete was prepared by only Portland cement while in the remaining mixtures Portland cement was partially replaced with the metakaolin. On the basis of preliminary experimental investigation, metakaolin was partially replaced at 10, 15, 20, 25 and 30 % by weight of cement. Moreover, in the mixes without metakaolin, VMA has been used to achieve proper viscosity and controlling the rheological properties of the concrete mixtures. In all mixes, the dosage of superplasticizer was adjusted in order to obtain a suitable flowability without segregation.

For mix preparation, the process for free-fall mixer stated in EFNARC [1] was employed to produce self-compacting concrete with metakaolin. In this way, approximately two thirds of the mixing water is added to the mixer. This is followed by the aggregates and cement. When a uniform mix is obtained, the remaining mixing water and the superplasticizer are added. Where VMA is used, this should be added after the superplasticizer and just prior to final consistence adjustment with water.

2.3 Test Procedure

2.3.1 Fresh Concrete Tests

In the present study, the slump flow, V-funnel and L-box tests were performed according to the procedure recommended by EFNARC committee [1]. Slump flow test has been proposed to assess filling ability of concrete in the absence of obstructions. According to EFNARC [1], there are typically three slump flow classes for a range of applications, which are given in Table 3. Slump flow is not a suitable factor to exactly exhibit the fresh characteristic of self-compacting concrete. However, if the slump flow is kept within a desirable range, it is possible to evaluate the requirements of self-compacting concrete. Self-compacting concrete

Table 3 Slump flow, viscosity and passing ability classes with respect to EFNARC [1]

Class slump flow (mm)
Slump flow classes
SF1550–650
SF2660–750
SF3760–850
ClassT50 (s) V-funnel (s)
Viscosity classes
VS1/VF1 ≤ 2 ≤ 8
VS2/VF2 > 29 − 25
Passing ability classes
PA1 and PA2 ≥ 0.8 with two rebar

containing metakaolin with slump flow values between 660 and 750 mm were proposed in the present study. Viscosity can be assessed by the T50 or V-funnel times. On the basis of EFNARC [1], there are two viscosity classes, which were determined by V-funnel, and T50 flow times (Table 3). The L-box test is utilized to determine passing ability of self-compacting concrete when flowing through confined or reinforced areas. The passing ability classifications according to EFNARC [1] were presented in Table 3. The workability test results were presented in Tables 4, 5 and 6, respectively.

Table 4 Mixture proportions and fresh properties of SCC-M60

	Mix No.	H-1	H-2	H-3	H-4	H-5	H-6
Mixture proportions	Metakaolin, %	0	10	15	20	25	30
	Cement, kg	600	540	510	480	450	420
	C.A., kg	660	660	660	660	660	660
	F.A., kg	810	810	810	810	810	810
	Water, kg	190	190	190	190	190	190
	Metakaolin, kg	0	60	90	120	150	180
	S.P., %	1.3	1.5	1.4	1.3	1.3	1.2
Slump test	Slump, mm	725	690	710	705	700	685
	T-50, s	4.28	4.93	4.95	5.11	5.24	6.13
V-funnel	T0, s	7.01	6.08	6.28	7. 95	10.54	12.02
	T5 min, s	8.56	8.86	8.90	10.12	12.67	14.14
L-box	H2/H1	0.86	0.84	0.97	0.95	0.96	0.98

Table 5 Mixture proportions and fresh properties of SCC-M40

	Mix No.	M-1	M-2	M-3	M-4	M-5	M-6
Mixture proportions	Metakaolin, %	0	10	15	20	25	30
	Cement, kg	500	450	425	400	375	350
	C.A., kg	800	800	800	800	800	800
	F.A., kg	800	800	800	800	800	800
	Water, kg	190	190	190	190	190	190
	Metakaolin, kg	0	50	75	100	125	150
	S.P., %	1.3	1.5	1.4	1.4	1.2	1.1
Slump test	Slump, mm	660	680	690	685	670	660
	T-50, s	3.22	3.89	3.95	4.00	4.65	5.05
V-funnel	T0, s	11.95	9.34	10.25	12.01	12.60	12.99
	T5 min, s	14.26	12.95	13.50	15.24	15.67	16.14
L-box	H2/H1	0.89	0.81	0.83	0.90	0.81	0.80

Table 6 Mixture proportions and fresh properties of SCC-M20

	Mix No.	L-1	L-2	L-3	L-4	L-5	L-6
Mixture proportions	Metakaolin, %	0	10	15	20	25	30
	Cement, kg	400	360	340	320	300	280
	C.A., kg	780	780	780	780	780	780
	F.A., kg	844	844	844	844	844	844
	Water, kg	180	180	180	180	180	180
	Metakaolin, kg	0	40	60	80	100	120
	S.P., %	0.80	0.85	0.82	0.76	0.70	0.62
Slump test	Slump, mm	690	700	710	700	690	620
	T-50, s	3.33	3.68	3.55	4.22	5.92	6.84
V-funnel	T0, s	6.36	6.94	7.81	9.84	12.64	13.64
	T5 min, s	8.95	9.65	11.24	12.63	16.01	16.73
L-box	H2/H1	0.96	0.94	0.97	0.96	0.89	0.86

2.3.2 Hardened Concrete Tests

After the completion of initial fresh concrete tests, the fresh concrete was poured into the molds. Specimens were de-molded one day after casting and were placed under water curing regime until the testing day. The average compressive strength, split tensile strength and flexural strength of cubes, cylinders and beam specimens at the age of 7 and 28 days (denoted as 7d and 28d) were observed and tabulated in Tables 7, 8 and 9.

3 Results and Discussions

3.1 Fresh Concrete Results

The fresh characterizations of self-compacting concrete containing metakaolin were studied and the results were summarized in Tables 4, 5 and 6.

3.1.1 Slump Flow Diameter and T50 Time

As can be seen in Tables 4, 5 and 6, the slump flow values for different concrete mixes were measured in the range of 660–750 mm. According to EFNARC (Table 3), all concrete mixtures under investigation can be categorized as slump flow class 2 (SF2). The concrete mixture at this class of slump flow is suitable for many normal applications such as walls and columns. The flowability of the

Table 7 Hardened properties of SCC-M60

Properties (N/mm^2)	H-1		H-2		H-3		H-4		H-5		H-6	
	7d	28d	7d	28d	7d	28d	7d	28d	7d	28d	7d	28d
Compressive strength	55.2	61.2	54.2	61.6	59.3	64.7	47.5	56.2	45.0	50.3	43.6	48.7
Split tensile strength	3.6	4.2	5.2	5.6	6.5	6.9	4.3	5.3	3.9	4.8	3.8	4.1
Flexural strength	4.6	4.7	5.1	5.3	4.9	5.8	4.3	4.5	4.1	4.4	3.7	4.0

Table 8 Hardened properties of SCC-M40

Properties (N/mm^2)	M-1		M-2		M-3		M-4		M-5		M-6	
	7d	28d	7d	28d	7d	28d	7d	28d	7d	28d	7d	28d
Compressive strength	34.3	46.6	38.1	48.4	39.2	52.5	35.4	42.0	31.2	37.1	28.7	29.6
Split tensile strength	3.0	4.8	4.2	6.3	4.6	6.8	3.9	4.6	3.7	4.9	3.5	4.5
Flexural strength	5.2	7.7	7.9	9.2	8.5	9.9	6.9	8.5	5.4	7.3	5.1	6.8

Table 9 Hardened properties of SCC-M20

Properties (N/mm²)	M-1		M-2		M-3		M-4		M-5		M-6	
	7d	28d	7d	28d	7d	28d	7d	28d	7d	28d	7d	28d
Compressive strength	20.1	29.4	29	33.2	30.5	34.3	21.3	24.0	20.4	22.7	19.7	20.1
Split tensile strength	2.0	2.1	1.9	2.1	2.2	3.1	1.6	1.8	1.5	1.7	1.4	1.6
Flexural strength	2.3	2.6	2.6	3.1	2.7	3.2	2.4	2.6	2.3	2.4	1.9	2.1

mixtures was reduced with the higher proportion of metakaolin replacement, as indicated in Tables 4, 5 and 6. For instance, at a given superplasticizer dosage, the slump flow of SCC-M20 was measured to be 690 mm while this could be decreased to 620 mm when metakaolin introduced to 30 %. This could be explained by the higher surface area of the metakaolin particles compared to Portland cement.

During the slump flow test, the aggregate segregation and bleeding was visually inspected. In addition, uniformity in the distribution of coarse aggregate can be visually observed by inspecting the broken split tensile test specimens, which indicate proper segregation resistance of mixtures. As presented in Tables 4, 5 and 6, the T50 flow times was measured in the range of 3–7 s. The incorporation of metakaolin increased T50 flow time of the self-compacting concrete.

3.1.2 V-Funnel Time

The V-funnel times of different concrete groups were presented in Tables 4, 5 and 6. From this table, it can be seen that the V-funnel times for M60, M40 and M20 concrete groups were in the range of 6.08–12.02 s, 9.34–12.99 s and 6.94–13.64 s, respectively.

Regarding to the EFNARC [1], a V-funnel flow time higher than 25 s did not recommended (Table 3). As presented in Tables 4, 5 and 6, the V-funnel flow times of all mixtures satisfy this requirement. The results presented in Tables 4, 5 and 6, the V-funnel time shows a distinct tendency to increase with increasing metakaolin content. From the results, it can be concluded that in the self-compacting concrete based metakaolin, no viscosity-modifying agent was needed.

3.1.3 Blocking Ratio (L-Box Test)

From Tables 4, 5 and 6, self-compacting concrete mixtures containing metakaolin mostly showed satisfactory blocking ratio as per EFNARC recommendation (Table 3).

An overview on the fresh properties of self-compacting concrete containing metakaolin of low (M20), medium (M40) and high (M60) grade self-compacting concrete reveals that metakaolin replacement generally satisfy the fresh-state behavior requirements related to high segregation resistance, deformability, passing and filling abilities.

3.2 Hardened Concrete Results

The hardened concrete tests such as compressive strength, splitting tensile strength and flexural strength were performed for all mixtures since they were molded without any compaction and tabulated in Tables 7, 8 and 9.

3.2.1 Compressive Strength

The compressive strength for M60, M40 and M20 concrete groups are respectively shown in Tables 7, 8 and 9. The early age compressive strength of all mixtures enhanced with usage of chemical admixture (Glenium B233). Among different metakaolin replacement level at M60, M40 and M20 self-compacting concrete groups, the most remarkable strength development was found to attain for metakaolin replacement at the levels of 10–15 %. Nonetheless, concerning the economic efficiency, it seems that 10 % metakaolin can be regarded as a suitable replacement to get the desired strength class.

3.2.2 Splitting Tensile Strength

In a similar trend to that observed in compressive strength, self-compacting concrete mixtures containing 10–15 % metakaolin provided better performance in terms of splitting tensile strength for M60, M40 and M20 concrete groups respectively shown in Tables 7, 8 and 9.

3.2.3 Flexural Strength

The same tendency as observed in compressive strength and split tensile strength, self-compacting concrete mixtures containing 10–15 % metakaolin provided better performance in terms of flexural strength for M60, M40 and M20 concrete groups respectively shown in Tables 7, 8 and 9.

4 Conclusions

This study was carried out to evaluate the fresh and hardened properties of self-compacting concrete containing metakaolin for developing different grades of self-compacting concrete. The following conclusions can be drawn:

1. Self-compacting concrete containing metakaolin with slump flow values between 660 and 750 mm can be produced by adjusting the high range water reducer dosage. Self-compacting concrete with this range of slump flow can practically be used in many applications.
2. Self-compacting concrete with metakaolin can be produced with proper workability without using viscosity-modifying agent.
3. Splitting tensile strength and flexural strength development followed the same pattern as compressive strength for different desired grades of self-compacting concrete, though the tensile and flexural strengths development is rather small.

4. Based on the overall effects of metakaolin, it seems that 10–15 % replacement of metakaolin can be regarded as a suitable replacement and have been recommended for low, medium and high strength grades of metakaolin based self-compacting concrete, which provides good workability and achieved desired strength grade.

5. The powder content was chosen as indicated in guidelines of EFNARC [1] for producing different grades of self-compacting concrete.

References

1. The European guidelines for self-compacting concrete; specification production and use. EFNARC, May 2005
2. Neville AM (1995) Properties of concrete, 4th edn. Longman, London
3. Al-Akhras NM (2006) Durability of metakaolin concrete to sulfate attack. Cem Concr Res 36:1727–1734
4. Sabir BB, Wild S, Khatib JM (1996) On the workability and strength development of metakaolin concrete. In: Dhir RK, Dyer TD (eds) Concrete for environmental enhancement and protection. E&FN Spon, London, pp 651–656
5. Vejmelkova E, Keppert M, Grzeszczyk S, Skalinski B, Cerny R (2011) Properties of self-compacting concrete mixtures containing metakaolin and blast furnace slag. Constr Build Mater 25:1325–1331
6. Vejmelkova E, Pavlikova M, Keppert M, Kersner Z, Rovnanikova P, Ondracek M (2010) High performance concrete with Czech metakaolin: experimental analysis of strength, toughness and durability characteristics. Constr Build Mater 24:1404–1411

Evaluating the Efficiency Factor of Fly Ash for Predicting Compressive Strength of Fly Ash Concrete

Khuito Murumi and Supratic Gupta

Abstract Fly ash is used as a supplementary cementitious material in concrete. In order to determine the strength of fly ash concrete similar to ordinary Portland cement concrete at a required age, one of the methods of designing concrete mix is by using efficiency factor (*k*-value) concept. This paper presents the utility of this concept for predicting the strength of fly ash concrete. The 28 days strength-based efficiency factor is 0.54 for 25 % fly ash and 0.35 for 45 % fly ash. The proposed efficiency factor is applicable to wide range of strength and fly ash percentage.

1 Introduction

Fly ash is used as a supplementary cementitious material worldwide. It is generally collected using electrostatic precipitators in thermal power stations. Fly ash can be either siliceous or calcareous and is used in concrete as pozzolanic material or mineral admixture or both. The reaction of active silica in the fly ash with calcium hydroxide produced during cement hydration contributes an additional strength to concrete [1]. Concrete gets better durability on proper curing as fly ash decreases the pores of concrete [2].

Although it is well-documented in literature that fly ash improves the workability, strength and durability, there is no established method for predicting the strength of concrete and design such that 28 days strength is assured. Among the research group, Pusa [3] presented certain efficiency factor (*k*-values) for design of

K. Murumi · S. Gupta (✉)
Indian Institute of Technology (IIT), Delhi, Hauz Khas 110 016, New Delhi, India
e-mail: supratic@yahoo.com

K. Murumi
e-mail: khuitomurumi@gmail.com

fly ash concrete with limited experimental data. In this research, further experimental results are presented to support this theory.

2 The Formulation

The first step in designing concrete is based on the assumption that strength of concrete depends on water cement (w/c) ratio. Research to project porosity as the controlling factor [4] does exist, this is difficult to be measured. Hence, it is assumed that the w/c ratio is the most important factor deciding the strength of concrete. The second consideration is the definition of water in the numerator. The aggregates or any particle capable of absorbing water would absorb water in the mixing stage provided there is enough time for the absorption, and therefore, this excess water should be subtracted from the design water content. Also, any extra adsorbed water trapped around any particle like sand should also be taken care of while calculating water content. When supplementary cementitious materials like fly ash is used, the cementitious material, c in Eq. 1 is considered as binder, B (Eq. 2). In this research, it is assumed that the compressive strength is a unique function of water to binder (w/B) ratio and that the k-value is a function of fly ash percentage, F at a given age. The assumed relations are given as,

$$f_c = \mathrm{f}(w/c) \tag{1}$$

$$f_c = \mathrm{f}(w/B) \tag{2}$$

$$B = c + kf \tag{3}$$

$$k = \mathrm{f}(F) \tag{4}$$

where
f_c compressive strength to be achieved (MPa)
c   cement content (kg/m^3)
f   fly ash content (kg/m^3)
B   effective binder or equivalent cement content (kg/m^3)
K   efficiency factor or k-value of fly ash
F   fly ash percentage of total cementitious material (kg/m^3)

To explain this concept, three cases are shown for mix proportioning of fly ash concrete, when fly ash is used to partially replace an ordinary Portland cement (OPC) (Eq. 5). The first case represents a control mix with water and cement contents, denoted by w_0 and c_0, respectively. The second case represents a mix with same water quantity, but by decreasing cement content from c_0 to c_1 and introducing fly ash, f_1 and efficiency factor, k_1. The denominator, that is, effective binder or equivalent cement content, remains equal in the first two cases. The third case

represents any other case with different water (w_2), cement (c_2) and fly ash (f_2). A new efficiency factor, k_2 is used with fly ash, f_2 in order to obtain same w/B ratio as the other two cases.

$$\frac{w_0}{c_0 + 0} = \frac{w_1(= w_0)}{c_1 + k_1 f_1} = \frac{w_2}{c_2 + k_2 f_2} \tag{5}$$

It is assumed that all these three cases would give similar compressive strength as they have same w/B ratio as per Eqs. 2–4. In this paper, a combination of only fly ash and OPC is considered.

3 The Efficiency Factor (*K*-Value) Concept for Design of Fly Ash Concrete

Smith [5] first presented the concept of efficiency factor of fly ash. Since then, similar work had been carried out by several researchers such as Dunstan [6], Bijen and Selst [7], Hassaballah and Wenzel [8], Babu and Rao [9–11], Papadakis and Tsimas [1], Papadakis et al. [12], Oner et al. [13], Vollpracht and Brameshuber [14], Yildirim et al. [15], Cho and Jee [16], Cho et al. [17] and Dinakar [18]. Babu and Rao [9–11] developed "overall efficiency factor" that depends on fly ash percentage and age at which the strength is required to be equal. Therefore, one may have efficiency factor for 7, 28, 90 days or even 365 days.

BS EN 206 [19] specifies *k*-value of 0.4 for fly ash conforming to BS EN 450-1 [20]. This is for fly ash up to a maximum of 25 % by mass of total cementitious material for CEM I conforming to BS EN 197-1 [21]. If one re-calculates the efficiency factor for fly ash usage greater than 25 % by adjusting the amount of fly ash usage, a decreasing graph would be obtained. A comparison of these are provided in Fig. 1. This shows that this relationship would be conservative and therefore provide higher strength.

Fig. 1 Efficiency factor comparison
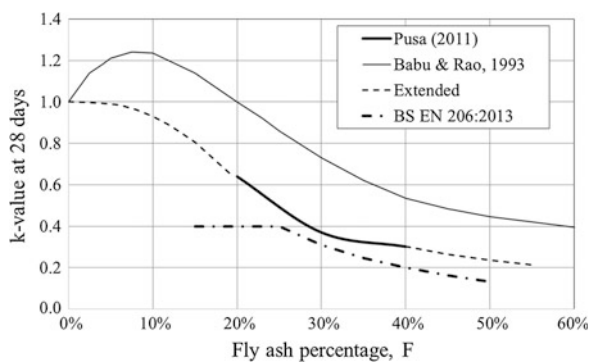
Pusa [3] conducted experiments to compute *k*-values for fly ash percentage in the range of 20–40 %. The values were significantly lower than the one proposed by Babu and Rao [9]. This paper presents the efficiency factor of fly ash for 25 and 45 % fly ash at 28 days. One limitation of this work is that this method needs verification for different types of fly ash. This was tested only for fly ash produced in northern India.

4 Materials Used

Cementitious materials: The cementitious materials used were ordinary Portland cement of grade 43 conforming to the specifications of IS 8112: 2013 [22] and siliceous fly ash conforming to the specifications of IS 3812 (Part 1) [23] procured from a thermal power plant in northern India. The fly ash was equivalent to class *F* fly ash of ASTM C618-12a [24] with low amount of calcium oxide. Tables 1 and 2 show the chemical properties and physical properties of cement and fly ash used, respectively.

Aggregates: River sand having a specific gravity of 2.62 was used as fine aggregate while the coarse aggregate had specific gravity of 2.67 (for 10 mm size) and 2.80 (for 20 mm size). The fine and coarse aggregates conformed to IS 383 [25]. The sand was of grading zone II of IS 383 [25].

Water: The water used in the experiment was potable. The test results conformed to the requirements of IS 456 [26].

Admixture: The admixture was a polycarboxylate ether (PCE)-based super-plasticiser with pH value exceeding 6 and specific gravity of 1.08 at 25 °C. The admixture conformed to the specifications of IS 9103 [27].

Table 1 Chemical and physical properties of OPC

S. No.	Chemical properties	Test result	S. No.	Physical properties	Test result
1	$(CaO - 0.7\ SO_3) \div (2.8\ SiO_2 + 1.2\ Al_2O_3 + 0.65\ Fe_2O_3)$	0.88	1	Blaine's fineness (m^2/kg)	290
2	$Al_2O_3 \div Fe_2O_3$	1.43	2	Soundness	
3	Insoluble residue (% by mass)	1.94		(a) Le Chatelier expansion (mm)	1.0
4	Magnesia (% by mass)	0.95		(b) Autoclave expansion (mm)	0.05
5	SO_3 (% by mass)	1.8	3	Compressive strength (MPa), at 28 days	56.3
6	Loss on ignition (% by mass)	1.82			
7	Total chlorides (% by mass)	0.014			

Table 2 Chemical and physical properties of fly ash

S. No.	Chemical properties	Test result	S. No.	Physical properties	Test result
1	$SiO_2 + Al_2O_3 + Fe_2O_3$ (% by mass)	93.8	1	Blaine's fineness (m^2/kg)	343
2	SiO_2 (% by mass)	62.4	2	Particle retention on 45 μm sieve, wet sieving (% by mass)	29
3	Reactive silica (% by mass)	26			
4	MgO (% by mass)	0.70	3	Lime reactivity (MPa)	5.1
5	SO_3 (% by mass)	0.18	4	Compressive strength of neat cement mortar (% of plain cement mortar cubes)	90.3
6	Na_2O (% by mass)	0.21			
7	Cl (% by mass)	0.03			
8	Loss on ignition (% by mass)	1.3	5	Soundness by autoclave test (%)	0.08

5 Casting Methodology and Testing

The coarse aggregates (10 and 20 mm) were used in saturated surface dry (SSD) condition. SSD moisture content of the natural sand was 1.2 %, determined using a frustum cone as per ASTM C128—07a [28]. The sand was usually in moist condition and therefore appropriate water correction was done before casting.

A tilting drum-type mixer was used to prepare the concrete. Aggregates were first dry-mixed. Cement and fly ash were then added along with approximately 70 % of the design water. After few minutes of mixing, admixture was added to the remaining water and used in the mix. Table vibrators were used to vibrate the moulds for full compaction. The admixture dosage was so as to maintain similar workability with slump range of about 80–150 mm. 100 mm cube specimens were used. Test was carried out at 7 and 28 days for compressive strength. The specimens in the moulds were covered with plastic sheets to minimise evaporation of water and removed after 24 h and then cured in water tank until the testing day. The curing water temperature varied from 25 to 29 °C.

6 Mix Design, Results and Discussion

Table 3 shows the mix design and results of control concrete, that is, without fly ash. Figure 2 correspondingly shows the plot of compressive strength versus *w/c* ratio for this case.

Table 3 Mix proportioning details and strength results for control concrete

Mix No.	F (%)	k-value	w/B	Mix proportioning: weight of materials (kg/m³)						Admixture kg/m³	Slump (mm)	Strength (MPa) 7 d	28 d
				w	c	f	s	10 mm	20 mm				
1	0	1.00	0.31	160	516	0	670	490	580	1.5	85	56.3	67.0
2	0	1.00	0.30	145	483	0	700	457	680	2.4	120	51.5	64.9
3	0	1.00	0.35	150	430	0	670	485	640	3.4	130	44.4	55.9
4	0	1.00	0.35	150	430	0	768	720	441	4.3	100	44.9	55.0
5	0	1.00	0.35	150	430	0	768	469	703	4.3	100	50.6	61.5
6	0	1.00	0.40	160	400	0	710	480	680	1.8	80	36.4	46.5
7	0	1.00	0.40	160	400	0	708	484	618	6.0	110	33.1	44.0
8	0	1.00	0.40	155	390	0	710	485	590	3.1	110	34.5	45.9
9	0	1.00	0.45	165	370	0	800	460	630	4.1	100	34.0	42.0
10	0	1.00	0.45	148	330	0	715	602	671	4.6	100	32.9	39.4
11	0	1.00	0.45	170	380	0	670	480	695	1.5	130	29.6	37.5

Fig. 2 Compressive strength versus *w/B* ratio: 0 % fly ash
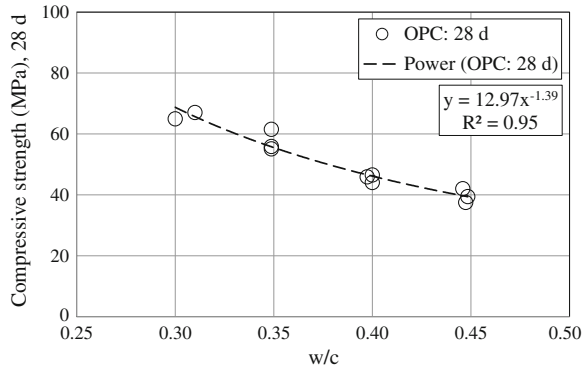
Table 4 shows the mix design and results for 25 and 45 % fly ash content. In this, the efficiency factor (*k*-value) of fly ash is varied and used in calculating the *w/B* ratio until the compressive strength of the fly ash concrete coincides with the plot of the control concrete. Figures 3 and 4 are the plots of strength versus *w/B* ratio for 25 and 45 % fly ash cases, respectively. For 0 % fly ash, it is calculated as 1.0 as per the definition of efficiency factor. After several trials, *k*-values of 0.54 and 0.35 were found to be appropriate for 25 and 45 % fly ash, respectively, that matched well with 0 % fly ash case.

Figure 5 shows combined data and compared with an equation in Popovics [4] indicating similarity with the present result. It may be noted that 45 % fly ash case approaches the high volume fly ash category. But because of the efficiency factor used in the design of concrete, the 28 days compressive strength remains almost equal to that of OPC concrete. The popular belief that use of higher fly ash would lead to lower strength is negated when appropriate efficiency factor is used and strength is logically compared with the appropriate *w/B* ratio.

With increase in fly ash percentage *F*, the powder content increases. This increase is very beneficial at low strength range as one can use lower cement content and still maintain sufficient powder ensuring a good mix. But at higher strength, *w/B* is low, thus resulting in lower water content and usually higher cement content. In such condition, using higher fly ash percentage *F* results in excessively high powder content and the mix becomes cohesive and increases admixture demand.

Further, even at cement content of 350 kg/m^3 (mix no. 19; *w/B* = 0.29), a strength of 73.7 MPa could be achieved, which is an M 65 concrete of IS 456 2000 and qualifies "standard concrete" criterion. This could be achieved comfortably in 45 % fly ash case. Concrete grade of M30 up to M65, could be therefore achieved by using appropriate efficiency factor.

Table 4 Mix proportioning details and strength results of fly ash concrete

Mix No.	F (%)	k-value	w/B	Mix proportioning: weight of materials (kg/m³)							Admixture kg/m³	Slump (mm)	Strength (MPa)	
				w	c	f	s	10 mm	20 mm				7 days	28 days
12	25	0.54	0.32	125	330	110	600	504	761	4.0	90	45.4	65.0
13	25	0.54	0.35	171	417	139	768	362	514	2.2	160	41.9	55.9
14	25	0.54	0.36	155	365	120	700	385	635	2.4	160	33.2	51.4
15	25	0.54	0.40	170	365	120	655	449	595	3.9	110	29.8	43.6
16	25	0.54	0.40	182	388	129	778	357	516	2.3	115	36.8	47.3
17	25	0.54	0.45	176	334	111	855	364	515	2.2	120	36.0	40.2
18	25	0.54	0.45	175	330	110	600	420	745	4.4	140	27.3	41.1
19	45	0.35	0.29	130	350	290	600	451	676	6.4	180	48.2	73.7
20	45	0.35	0.29	125	330	270	640	458	687	7.2	230	46.7	67.5
21	45	0.35	0.33	167	392	321	699	319	428	5.0	160	44.6	64.9
22	45	0.35	0.38	179	368	301	665	325	470	3.3	200	40.2	56.1
23	45	0.35	0.40	170	330	270	640	397	595	2.1	170	34.0	45.2
24	45	0.35	0.41	160	304	249	647	388	582	3.0	180	30.6	42.4
25	45	0.35	0.43	174	318	260	763	318	487	2.6	210	29.1	46.3

Fig. 3 Compressive strength versus w/B ratio: 25 % fly ash
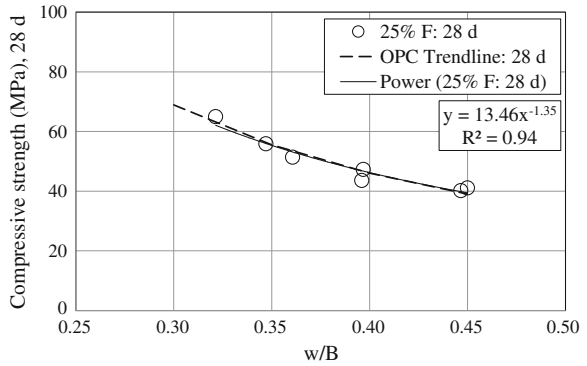
Fig. 4 Compressive strength versus w/B ratio: 45 % fly ash
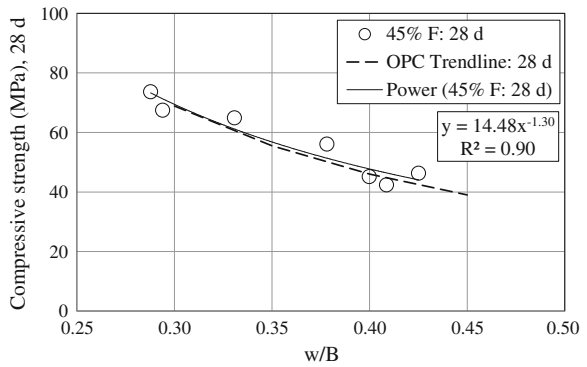
Fig. 5 Compressive strength versus w/B ratio: 0, 25 and 45 % fly ash
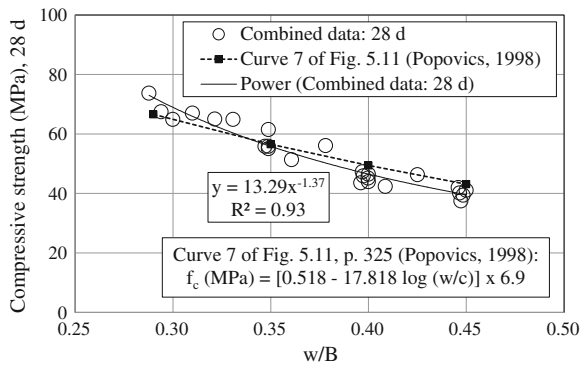
7 Conclusions

Fly ash has become an important constituent material in present concrete. Use of this material would not only reduce cement, but also reduce fine and coarse aggregates requirement thereby making the construction process more sustainable. The proposed efficiency factors are based on fly ash percentage, F. The following conclusions can be drawn based on this research.

1. Use of efficiency factor is effective to predict compressive strength of concrete. However, minor adjustment and detailed experimental verification are necessary.
2. The 28 days strength-based efficiency factor is 0.54 for 25 % fly ash and 0.35 for 45 % fly ash.
3. Even at 45 % fly ash, which approaches high volume fly ash range, there would be no reduction in strength if appropriate efficiency factor is used.
4. The proposed efficiency factor is applicable to wide range of strength and fly ash percentage.
5. A "standard concrete" of M65 grade could be achieved with cement content of 350 kg/m^3 only ($w/B = 0.29$).

References

1. Papadakis VG, Tsimas S (2002) Supplementary cementing materials in concrete, part I: efficiency and design. Cement Concr Res 32(10):1525–1532
2. Aïtcin P-C (1998) High-performance concrete. E & FN Spon, London
3. Pusa V (2011) Study on mechanical and durability properties of concrete with specific reference to fly ash. Indian Institute of Technology, Delhi
4. Popovics S (1998) Strength and related properties of concrete, a quantitative approach. Wiley, New York
5. Smith IA (1967) The design of fly-ash concretes. In: Institution of civil engineers proceedings, vol 36(4), pp 769–790
6. Dunstan ER Jr (1986) A concrete proportioning odyssey—the optimum/pessimum fly ash percentage. A paper presented at the ACI fall meeting, ACI, Baltimore
7. Bijen J, Selst VR (1993) Cement equivalence factors for fly ash. Cem Concr Res 23 (5):1029–1039
8. Hassaballah A, Wenzel TH (1995) A strength definition for the water to cementitious materials ratio. ACI SP 153–24 153:417–438
9. Babu KG, Rao GS (1993) Efficiency of fly ash in concrete. Cement Concr Compos 15 (4):223–229

10. Babu KG, Rao GS (1994) Early strength behaviour of fly ash concretes. Cem Concr Res 24 (2):277–284
11. Babu KG, Rao GS (1996) Efficiency of fly ash in concrete with age. Cem Concr Res 26 (3):465–474
12. Papadakis VG, Antiohos S, Tsimas S (2002) Supplementary cementing materials in concrete, part II: a fundamental estimation of the efficiency factor. Cement Concr Res 32 (10):1533–1538
13. Oner A, Akyuz S, Yildiz R (2005) An experimental study on strength development of concrete containing fly ash and optimum usage of fly ash in concrete. Cem Concr Res 35(6):1165–1171
14. Vollpracht A, Brameshuber W (2010) Performance-concept, k-value approach-which concept offers which advantages? In: International RILEM conference on material science. RILEM Publications SARL, Bagneux, France
15. Yildirim H, Sumer M, Akyuncu V, Gurbuz E (2011) Comparison of efficiency factors of F and C types of fly ashes. Constr Build Mater 25(6):2939–2947
16. Cho HB, Jee NY (2011) Prediction model for cementing efficiency of fly ash concrete by statistical analyses. Adv Mater Res 250–253:1293–1296
17. Cho HB, Jee NY, Shin NY (2012) Strength prediction of fly ash concrete using cementing efficiency by statistical analysis. Adv Mater Res 374–377:1774–1777
18. Dinakar P (2012) Design of self-compacting concrete with fly ash. Mag Concr Res 64 (5):401–409
19. BS EN 206 (2013) Concrete-specification, performance, production and conformity. British Standards Institute (BSI), London
20. BS EN 450-1 (2012) Fly ash for concrete. Definition, specifications and conformity criteria. British Standards Institute (BSI), London
21. BS EN 197-1 (2011) Cement: composition, specifications and conformity criteria for common cements. British Standards Institute (BSI), London
22. IS 8112 (2013) Ordinary Portland cement, 43 grade-specification (second revision). Bureau of Indian Standards (BIS), New Delhi, India
23. IS 3812 (Part 1) (2013) Pulverized fuel ash-specification, Part 1, for use as pozzolana in cement, cement mortar and concrete (third revision). Bureau of Indian Standards (BIS), New Delhi, India
24. ASTM C618-12a (2012) Standard specification for coal fly ash and raw or calcined natural pozzolan for use in concrete. ASTM International, West Conshohocken
25. IS 383 (1970) Specification for coarse and fine aggregates from natural sources for concrete (second revision). Reaffirmed 2002, Bureau of Indian Standards (BIS), New Delhi, India
26. IS 456 (2000) Plain and reinforced concrete—code of practice (fourth revision). Up to Amendment No. 4, 2013, Bureau of Indian Standards (BIS), New Delhi, India
27. IS 9103 (1999) Concrete admixtures-specification (first revision) (incorporating amendment nos. 1 and 2). Reaffirmed 2004, Bureau of Indian Standards (BIS), New Delhi, India
28. ASTM C128-07a (2007) Standard test method for density, relative density (specific gravity), and absorption of fine aggregate. ASTM International, West Conshohocken

Part XVIII
Aggregates for Concrete

Use of Efficiency Factors in Mix Proportioning of Fly Ash Concrete

Santanu Bhanja

Abstract In the first revision of IS: 10262, 2009 an illustrative example of concrete mix proportioning using fly ash as one of the ingredients has been added. Merely a numerical example without theoretical backup leads to number of queries in the mind of the designer, who has no other option but to follow the steps empirically. To incorporate fly ash @ 30 % of total binder content an increase of 10 % has been envisaged on the binder content of control concrete. This does not seem to be justified as the fly ash used can have a wide variation in properties, which has not been taken into consideration at all. On the other hand, if some guidelines are provided on the basis of the efficiency factor of fly ash, at least a good first hand estimate of the fly ash content equivalent of the cement replacement percentage can be obtained. Even if such relationships are available for one type of fly ash, whose properties are known, an estimate of the cement equivalence of fly ash can be obtained for the fly ash used. This will help in reducing the number of trial mixes needed to arrive at the desired concrete mix. The present paper is a humble effort in this direction and deals with fly ash concrete mixes having water binder ratios ranging from 0.4 to 0.6, binder contents varying from 300 to 450 kg/m^3 and fly ash binder ratios ranging from 0.0 to 0.5. Efficiency factors have been derived and parameters affecting the efficiency values have been identified. Typical ranges of efficiency values with respect to those parameters have been provided which can act as useful tools in the mix proportioning of fly ash concrete.

Keywords Fly ash · Mix proportion · Efficiency factor · Water-cement ratio · Compressive strength

S. Bhanja (✉)
Department of Civil Engineering, National Institute of Technical Teachers' Training and Research, Block-FC, Sector-III, Salt Lake, Kolkata 700106, West Bengal, India
e-mail: san244in@yahoo.com

1 Introduction

There is a growing realization throughout the world that the raw material resources used in the production of cement are finite and non-renewable and need to be conserved for the future generations. With the objective of attaining sustainable construction, a strong trend favoring the increased use of mineral admixtures, which are basically the waste products of industrial processes, in concrete is emerging throughout the world. Indian coals are very rich in ash content and hence ash is abundantly produced in India as a waste product in thermal power plants but its consumption is still quite limited. It is well documented that the use of fly ash, as a partial replacement for cement results in a significant improvement in concrete properties. Efforts have been made to quantify the effect of fly ash in concrete by determining the cementing efficiency factors. The cementing efficiency of a pozzolana is defined as the number of parts of cement that could be replaced by one part of the pozzolana without affecting the property under consideration (mainly strength). According to Papadakis and Tsimas [1], the efficiency factor (k-value) is defined as the part of the pozzolanic material which can be considered as equivalent to Portland cement having the same properties as the concrete without the pozzolanic material (k = 1 for Portland cement).

Quantification of the contribution of fly ash in concrete has been under study for many years and a brief review of some of the important works is presented below. Ho and Lewis [2] have observed that the k value of fly ash with respect to 28-day compressive strength varies over a wide range depending on the amount of fly ash added, type of cement, incorporation of chemical admixture and the particular strength level chosen. Gopalan and Haque [3] have reported that the efficiency factor depends on the quantity of fly ash in the mix. Fraay et al. [4] have reported that the reaction of fly ash in concrete is only initiated after one or more weeks and during this incubation period; the fly ash behaves more or less as an inert material. Hence, the efficiency values of fly ash can be very low or even negative at early ages. Bijen and van Selst [5] have reported that the contribution of fly ash to concrete strength is strongly dependent on the water cement (w/c) ratio, type of cement and fly ash and age of concrete. Ganesh Babu and Nageswara Rao [6] have reported that the overall efficiency factor of fly ash (k) is the combination of general efficiency factor (k_e) depending on age and an additional percentage efficiency factor (k_p) depending on replacement percentage. It has been reported that the overall efficiency factor ($k = k_e + k_p$) varies from 1.25 to 0.35. The authors have inferred that the efficiency of fly ash increases with decrease in w/c, whereas it decreases with increase in replacement percentages. Ganesh Babu and Nageswara Rao [7] have reported that k value has been suggested as 0.25 for replacements up to 25 %, German standards recommend a value of 0.3 for replacements between 10 and 25 %, British code refers to a value of 0.4 for replacements up to 25 %, CEB-FIP model code proposes a value of 0.4 for replacements between 10 and 25 %. It has also been reported that for concrete with different types of fly ash and cement (up to 28 % replacement and w/c between 0.5 and 0.65) a value of 0.5 is

appropriate. It has been mentioned that cementing efficiency factor of fly ash depends on the physical and chemical characteristics of fly ash and cement, mix design parameters, strength range, age, w/cm ratio and replacement level. Hanehara et al. [8] have reported that hydration of cement is accelerated with increase in the water-cement ratio. It has been mentioned that the pozzolanic reaction of fly ash proceed from the age of 28–91 days and the reaction ratio of fly ash decreases with increase in the substitution rate.

It is observed from the above reporting that the efficiency of fly ash in concrete depends on a number of parameters such as type of cement and fly ash, replacement level, age, w/cm, strength level etc. where 'cm' is the cementitious material content. Hence, efficiency of fly ash should not be considered as an intrinsic or fundamental property of the material as it depends on a host of parameters. Since, the efficiency value is not a constant one evaluation of the same requires a considerable amount of judgment and understanding on the part of the designer. However, efficiency factors can be very useful for effective utilization/quantification of fly ash in concrete. However, the literature is rich in reporting on cementing efficiency of fly ash there is still a dearth of guideline as how to judiciously choose the efficiency values while proportioning fly ash mixes. The present paper is directed in this direction.

2 Significance of the Present Research Work

The aim of concrete mix design is to achieve the desired strength at a specified age satisfying the requirements of workability, durability and economy. For control concrete guidelines for mixture proportioning are readily available in the standards and specifications. Though the process of mix design incorporating fly ash involves more variables and is more complicated, guidelines are available nowadays and in the latest version of the Indian standard on concrete mix proportioning (IS: 10262, 2009) [9], a guideline in the form of a numerical example has been incorporated. Though mix design is still an empirical procedure and is mostly arrived at by adopting the method of trial mixes some inherent drawbacks regarding assessment of some parameters in the Indian standard (IS) method have been identified and based on the present research work some simple tips are proposed. The aim is not to propose a new mixture proportioning method but to suggest some improvement in the existing IS method, which may result in some value addition to the existing methodology.

3 Materials Used

The constituent materials used in the program were tested to comply with the relevant Indian standards. To assure uniformity of supply, the materials were subjected to periodical control tests. The cement used was ordinary Portland

cement, having a 28-day compressive strength of 43 MPa with a Blaine's fineness of 325 m^2/kg. Fly ash, containing 60.78 % SiO$_2$ (out of which reactive silica by mass was 23.1 %) and having a Blaine's fineness of 250 m^2/kg, from a thermal power plant in West Bengal was used. Hence, the reactivity or pozzolanic effect of the fly ash was quite low and its filler effect insignificant. Natural river sand having a fineness modulus of 2.94 was used. The specific gravity and water absorption values were obtained as 2.6 and 0.58 %, respectively. Crushed, angular, graded coarse aggregates of nominal maximum size 20 mm were used in the investigation. The specific gravity and the water absorption of the aggregates were 2.87 and 0.9 %, respectively. Potable water was employed for the mixing [10].

4 Experimental Procedure

The experimental program included five sets of concrete mixtures at w/cm ratios of 0.4, 0.45, 0.5, 0.55 and 0.6 prepared by partial replacement of cement by equal weights of fly ash. Each set had mixtures at five fly ash replacement percentages—0 (control mix), 20, 30, 40 and 50 % of the total binder content. In order to evaluate the effect of fly ash incorporation at different binder contents three total binder contents were selected—300, 375 and 450 kg/m^3. Thus, the scheme of experimentation spanned over 5 water-binder ratios, 5 fly ash replacement percentages at each of the three binder contents [10, 11]. For the present investigation, the proportions of the coarse and fine aggregates were determined in the laboratory by trial and error so that the resultant aggregate mix yielded maximum packing density. This proportion has been kept constant for all the mixes. The volume of voids in the system was calculated as (1 − Packing Density). The paste contents of all the mixes were determined and compared with the volume of voids within the aggregate particles. In order to fill up the voids within the aggregate particles (so as to drive off the air voids in the concrete mix), the volume of cement paste must be larger than the volume of voids within the aggregate particles. This was verified by actual casting whereby mixes having paste contents less than the volume of voids resulted in unworkable mixes and hence they were rejected. The mixes at higher binder contents and with high values of water-binder ratios were not stable rather they exhibited high bleeding and segregation and thus were rejected. Thus, a total number of 55 mixes, which were cohesive and workable, were only investigated. The amount of coarse and fine aggregates used were 42 and 58 % by mass of total aggregates and the amounts of the different ingredients were determined by using the absolute volume formula [12]. Thereafter, only cement was replaced by fly ash (by equal weights). Due to change in the volumes of cement and fly ash necessary changes in the masses of the ingredients were calculated using the absolute volume method keeping all other mix proportion parameters constant. Since, the water contents of the mixtures varied over a wide range, workability of the mixtures also varied over a wide range. The workability of the mixes were carefully observed and measured to ensure that all the mixes were workable. To minimize variations in

workability, the compaction energy was varied for obtaining proper compaction. Cube specimens of 150 × 150 × 150 mm were used for compressive strength determination. All the specimens were moist cured under water at room temperature until testing. Since, the curing condition was uniform for all the specimens no adverse effect on the subsequent test results is expected due to temperature variations. Each strength value was the average of five specimens [10, 11].

5 Results and Discussions

5.1 Determination of Efficiency Factor Values of Fly Ash

The 28-day strengths of 55 concrete mixes have been determined. It has been observed that with increase in fly ash contents concrete strengths have been reduced [10, 11]. In order to determine the efficiency factors of fly ash, a simple methodology has been adopted [13]. As postulated by Abrams' there exists a hyperbolic relation between strength and w/c ratio. Hence, the relationship between $\log_e$ (compressive strength) and w/c should be a linear one. A typical relationship between $\log_e$ (strength) at 28-days and w/c for control concrete at binder content of 375 kg/m^3 is presented in Fig. 1.

Using the method of least squares the equation of the best fit line for this data set has been obtained as,

$$\log_e(S) = 5.4164 - 3.142 \, (w/c) \tag{1}$$

where S is the strength and w/c is the water-cement ratio of the control concrete. Using this equation and the $\log_e$ (strength) of fly ash concrete mix at any

Fig. 1 Typical relationship between log (compressive strength) of control concrete and water-cement (w/c) ratio at binder content of 375 kg/m^3
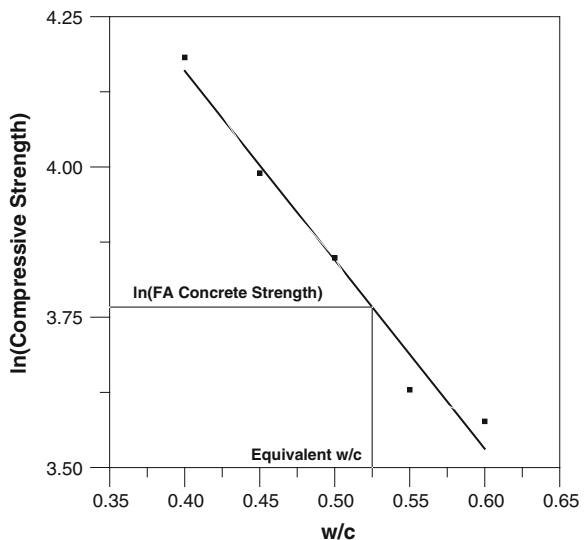
replacement percentage at the corresponding binder content the value of the equivalent w/c can be calculated [13]. From the value of the equivalent w/c ratio, efficiency factor has been estimated by the following expression,

$$(w/c)_{Equivalent} = \frac{w'}{c' + kf} \tag{2}$$

where w', c' and f are the water, cement and fly ash contents (kg/m^3), respectively in the fly ash concrete; k is a parameter known as cementing efficiency factor for the fly ash. The values of the efficiency factors for all the 44 fly ash concrete mixes have been calculated in a similar way and are presented in Table 1.

5.2 Mix Proportioning of Fly Ash Concretes Using Efficiency Factors

Bharatkumar et al. [14] have reported that the strength and workability of fly ash concrete with effective w/b [w/(c + kf)] is comparable to that of conventional concrete without fly ash having same w/b − water/binder ratio and water content. Constant water content yields constant workability of fresh concrete irrespective of w/b ratio. For achieving similar strength level for control and fly ash concrete the following expression, which is similar to Eq. (2), may be considered,

$$(w_1/c)_{Control\ Concrete} = \left(\frac{w_2}{c_1 + kf}\right)_{Fly\ ash\ concrete} \tag{3}$$

where, w_1 and c are respectively the water and cement content in kg/m^3 of control concrete; w_2, c_1 and f refer to water content, cement content and fly ash contents in kg/m^3 of fly ash concrete and k is the efficiency factor of fly ash with respect to compressive strength.

For obtaining the specified workability, water contents of the control as well as fly ash concrete should be the same. For this condition,

$$w_1 = w_2 \tag{4}$$

After considering that the water contents in both the mixes are same, the Eq. (3) takes the form,

$$(c)_{control\ concrete} = (c_1 + kf)_{fly\ ash\ concrete} \tag{5}$$

Equation (5) relates the binder contents of control and fly ash concretes. If the k values at different fly ash replacement levels are known, the total binder content of the fly ash concrete, which is equivalent to the cement content of the control concrete, can be determined.

Table 1 Efficiency factors of fly ash at 28-days

w/cm	20 % FA Binder (kg/m³)			30 % FA Binder (kg/m³)			40 % FA Binder (kg/m³)			50 % FA Binder (kg/m³)		
	300	375	450	300	375	450	300	375	450	300	375	450
0.4		0.484	0.630		0.498	0.643		0.401	0.541		0.316	0.501
0.45		0.601	0.658		0.546	0.513		0.443	0.484		0.393	0.424
0.5	0.244	0.831	0.836	0.312	0.575	0.394	0.256	0.519	0.500	0.125	0.408	0.403
0.55	−0.092	0.508		0.064	0.510		0.084	0.530		−0.029	0.428	
0.6	0.275	0.532		0.007	0.617		0.073	0.709		0.079	0.552	

Table 2 Average values of efficiency factors

Age (days)	Up to 30 % Fly ash			>30 % Fly ash		
	Binder (kg/m^3)			Binder (kg/m^3)		
	300	375	450	300	375	450
	w/cm (0.5–0.6)	w/cm (0.4–0.6)	w/cm (0.4–0.5)	w/cm (0.5–0.6)	w/cm (0.4–0.6)	w/cm (0.4–0.5)
28	0.14 (25–38)	0.57 (26–55)	0.61 (31–56)	0.10 (16–31)	0.47 (19–43)	0.48 (22–46)

Compressive strength values based on 150 mm cubes (MPa) are given in brackets

A comparatively poor quality of fly ash, coarser than cement and having a low value of reactive-silica content was selected for the present research work. This was done with the apprehension that even if these values are used for estimating the efficiency factors of fly ashes conforming to IS 3812 (Part 1), 2003, which should have a Blaine's fineness of 320 m^2/kg and reactive silica of 20 % by mass, conservative values of cement equivalence factors will be obtained.

Efficiency of fly ash is dependent on the replacement percentage and decreases with increase in the replacement percentage. Efficiency values beyond 30 % replacements reduce almost drastically (13). Instead of using the actual numerical values, some form of averaging has been performed to obtain more or less representative values of the efficiency factors. Hence, the values up to and beyond 30 % have been added and divided by the number of observations to obtain representative values of the efficiency factors and are presented in Table 2.

The average values of 28-day efficiency factors of the fly ash used in the present work have been tabulated at different ranges of water-binder (w/b) ratios, binder contents and fly ash replacement percentages. It is the primarily the quality of fly ash which will determine what should be the replacement level and how much increase is needed in the total cementitious material content. If some means of assessment of the quality of fly ash is available, reasonable assessment of these parameters can be achieved instead of arbitrarily choosing these values. Such guidelines can lead to effective intelligent assessment and thereby reduce the number of trial mixes necessary to arrive at the desired mix. It is neither expected nor claimed that the efficiency values obtained for the type of ash used in the present research can cater to all types of fly ashes under all concreting conditions. However, the values can help in finding a reasonably good first hand estimate of the cement equivalence factors of fly ash. These can be used to determine the replacement level and increase in total binder content needed instead of arbitrarily choosing them only on the basis of experience and skill of the designer. This will reduce the number of trial mixes needed to arrive at the desired mix.

5.3 Illustrative Example

Suppose, for a specified strength and workability of control concrete, w/c ratio and water content have been determined as 0.5 and 187.5 kg/m^3, respectively. It is required to design a fly ash concrete mix, using similar type of fly ash, to meet the above requirements and the specified age of design is 28-days.

For the control concrete, cement content $= \frac{187.5}{0.5} = 375$ kg/m^3

For the present study, two sets of efficiency factors have been proposed—one for replacements up to 30 % and the other for replacements beyond 30 %. Since, the quality of fly ash used has been comparatively poor, it may be considered that replacements will lie within 30 %. Total binder content should preferably be selected based on the efficiency values as indicated in Table 2. Corresponding to binder content of 375 kg/m^3 and fly ash content of 30 %, efficiency value at 28-day age level is 0.57 as per Table 2. For the present problem Eq. (5) takes the form,

$375 = c_1 + kf$

Here, f = 30 % of the cement content of control = $375 \times 0.3 = 112.5$ kg/m^3

k = 0.57

Hence, $375 = c_1 + 0.57 \times 112.5$

Therefore, $c_1 = 310.9$ kg/m$^3 \cong 311$ kg/m^3

Hence, total binder content = $c_1 + f = 423.5$ kg/m^3

Fly ash as a percentage of total binder $= \frac{f}{c_1 + f} \, 100\% = 26.6\% \approx 27\%$

Increase in binder content $= \frac{423.5 - 375}{375} \, 100 = 12.9\% \approx 13\%$

Thus, it can be inferred that in order to achieve similar compressive strength as control, Fly ash @ 30 % of the cement content or 27 % of the total binder content can be replaced with a subsequent 13 % increase in the total binder content. The quantities of cement, fly ash, water contents being known, amounts of coarse and fine aggregates can be calculated using absolute volume formula [12]. In this way, compound composition of fly ash concrete can be determined and trial mixes may be performed to arrive at the desired mix. In the current version of Indian standard (IS 10262, 2009), for mixture proportioning of fly ash concrete, the binder content has been arbitrarily increased by 10 % of the cement content of control concrete for 30 % replacement of binder content by fly ash. No back up calculation has been provided to justify this step. Since, the physical and chemical characteristics of fly ash are widely variable such arbitrary generalizations does not seem to be justified. Based on the results of the present investigation, a simplified methodology of modifying the binder content of fly ash concrete with respect to the control concrete has been developed based on the evaluation of efficiency factors. The uniqueness of this approach lies in the fact that even if these numerical values, which have been developed for only one type of fly ash, are considered to calculate the total binder content of fly ash concrete at a specified cement replacement level, it can act as an intelligent guess instead of assuming or arbitrarily choosing the modified binder content.

6 Conclusions

Extensive experimentation was performed over a wide range of w/cm ratios ranging from 0.4 to 0.6, binder contents varying from 300 to 450 kg/m^3 and fly ash replacement percentages from 20 to 50 %. On the basis of the results of the present investigation a table featuring the representative values of efficiency factors at 28-days have been furnished. The proposed values of efficiency factors, if used in conjunction with the Indian standard (IS) method, can lead to proper quantification of the ash used without merely relying on the experience and discretion of the designer. It may be expected that the findings of the present work may serve as a useful guideline for judiciously applying the concept of efficiency factors to optimize the effect of fly ash in concrete and lead to improvement in the IS method of mix design of fly ash concretes.

References

1. Papadakis VG, Tsimas S (2005) Greek supplementary cementing materials and their incorporation in concrete. Cement Concr Compos 27:223–230
2. Ho DWS, Lewis RK (1985) Effectiveness of fly ash for strength and durability of concrete. Cem Concr Res 15:793–800
3. Gopalan MK, Haque MN (1989) Mix design for optimal strength development of fly ash concrete. Cem Concr Res 19:634–641
4. Fraay ALA, Bijen JM, De Haan YM (1989) The reaction of fly ash in concrete. A critical examination. Cem Concr Res 19:235–246
5. Bijen J, van Selst R (1993) Cement equivalence factors for fly ash. Cem Concr Res 23:1029–1039
6. Babu KG, Rao GSN (1996) Efficiency of fly ash in concrete with age. Cem Concr Res 26 (3):465–474
7. Babu KG, Rao GSN (1993) Efficiency of fly ash in concrete. Cement Concr Compos 15:223–228
8. Hanehara S, Tomosawa F, Kobayakawa M, Hwang K (2001) Effects of water/powder ratio, mixing ratio of fly ash, and curing temperature on pozzolanic reaction of fly ash in cement paste. Cem Concr Res 31:31–39
9. IS: 10262 (2009) Indian Standard, concrete mix proportioning—guidelines (first revision). Bureau of Indian Standards (BIS)
10. Bhanja S (2012) Project report entitled—"development of modified law for high performance concrete with fly ash". Department of Science and Technology (DST), Government of India, New Delhi, India
11. Pan S (2013) Effect of fly ash as a cement replacement material on the characteristics of concrete. PhD thesis, Jadavpur University, Kolkata, India
12. Neville AM (1996) Properties of concrete, 4th edn. ELBS with Addison Wesley Longman Limited, England

13. Bhanja, S, Pan S (2013) Predictor models for evaluation of efficiency factors of fly ash in concrete. In: First international conference on concrete sustainability (ICCS13), Tokyo, Japan, 27–29 May 2013
14. Bharatkumar BH, Narayanan R, Raghuprasad BK, Ramachandramurthy DS (2001) Mix proportioning of high performance concrete. Cement Concr Compos 23:71–80

Study on Some Engineering Properties of Recycled Aggregate Concrete with Flyash

M. Surya, P. Lakshmy and V.V.L. Kanta Rao

Abstract Any landfill in urban India is generally comprised of 45–55 % demolished masonry and concrete. In addition, with urbanization, the demand for construction aggregates is increasing year after year and in India, it is estimated to be 5.07 billion metric tons in the year 2020. High quantity of demolition waste in landfill and increasing demand for aggregates can be reduced by extracting aggregates from the demolition waste and utilising the same in construction. Research to evaluate the properties of the aggregates extracted and concrete made there from has been in progress globally. Present study is aimed at studying the load versus deflection behaviour of reinforced recycled aggregate concrete (RAC) beams under flexural loading and bond strength of RAC by rebar pullout test. The recycled concrete aggregate (RCA) for this study was obtained by crushing concrete cubes of strength 35–45 MPa, cast at various bridge construction sites and tested in CSIR-CRRI. The properties of RCA produced were studied and an appropriate method for design of RAC mixes was proposed. RAC mixes with 50 and 100 % RCA with 20 % flyash i.e., R50 and R100, were prepared and their mechanical properties such as compressive strength, split tensile strength, flexural strength and elastic modulus were evaluated and compared to those of natural aggregate concrete with flyash (NAF). In addition, the bond strength of the above three mixes was investigated by performing rebar pullout test. For the study of flexural behaviour, 150 × 250 × 2,000 mm reinforced beams were cast and tested under simply supported conditions and one third point loads. The mechanical properties of RAC were comparable to that of NAF. The bond strength of RAC mixes has been found to be about 35 % lower than that of NAF. The modulus of elasticity of RAC mix decreased, by up to 34 %, with increase in percentage of RCA. Consequently, the deflections of RAC beams were found to be 10–35 % greater than NAF beam. However, the ultimate loads of the RAC beams were found to be 84–89 % of NAF beam and greater than the theoretical ultimate loads. It has been concluded that the strength properties of RAC are encouraging for

M. Surya (✉) · P. Lakshmy · V.V.L. Kanta Rao
Bridges and Structures Division, CSIR-Central Road Research Institute (CRRI), Mathura Road, New Delhi 110 025, India

M. Surya · P. Lakshmy · V.V.L. Kanta Rao
Academy of Scientific and Innovative Research (AcSIR), CSIR, New Delhi, India

use in new concrete. However, the use of RAC in structural concrete can be recommended with more confidence when low value of elastic modulus and its influence in the flexural behaviour of RAC beams are suitably addressed.

Keywords Recycled aggregate · Flyash · Concrete · Flexural strength · Bond strength

1 Introduction

With the increased emphasis on the environmental protection, solid waste management has moved to the forefront of the environmental agenda. Waste reduction and resource recovery are considered to be the most effective methods to address this problem. As any landfill in India contains 45–55 % [1] of demolished masonry and concrete, its reuse plays an important role in solid waste management. In addition, with urbanization the demand for construction aggregates is increasing year after year. The estimated construction aggregate demand in India for the year 2020 is 5.07 billion metric tonnes. It has been recognised that the dual concerns of high quantity of demolition waste in landfills and increasing demand for aggregates can be addressed by extracting aggregates from the demolition waste and utilising the same in construction. Research to evaluate the properties of the aggregates extracted and concrete thus produced has been in progress all over the world. However, only a few studies have been carried out with an aim to explore the structural performance of recycled aggregate concrete (RAC).

This paper discusses the results of a research aimed at studying the load versus deflection behaviour of RAC under flexural loading and bond strength of RAC by rebar pullout test.

2 Experimental Program

2.1 Materials

The recycled aggregate for this study was obtained by crushing concrete cubes cast at various bridge construction sites and tested at CSIR-CRRI. These cubes were of 35–45 MPa strength and age of the cubes varied from 2 to 3 years. A mini laboratory jaw crusher was used for producing the recycled concrete aggregate (RCA). Crushed granite natural aggregate (NA) was used in the study. The properties of aggregate were studied and are presented in Table 1. Crushed stone sand, of specific gravity 2.63 and water absorption 0.72 % conforming to zone I of IS 383 [2],

Table 1 Properties of coarse aggregate used in the present study

Property	RCA	NA
Fineness modulus	6.65	6.52
Specific gravity	2.501	2.675
Water absorption (%)	2.76	0.42
Abrasion loss (%)	29.24	26
Crushing value (%)	28.87	27.12
Impact value (%)	16.04	21.77
Bulk density (kg/m^3)	1,340	1,630

available in Delhi region was used as fine aggregate in the study. Tap water of pH 7.2 was used for mixing the concrete. The plasticizer used in the present study was Glenium SKY 777.

2.2 Concrete Mixes

A modified mix design method was developed and adopted for RAC mixes [3]. The method involves modification of coarse aggregate content obtained using IS 10262 [4], multiplying the same by the ratio of specific gravity of RCA to the specific gravity of NA. Concrete mixes with 0, 50 and 100 % RCA with flyash, viz. NAF, R50 and R100 respectively, were prepared using this mix design and their proportions are given in Table 2.

2.3 Casting and Curing

The concrete mixes were prepared in a drum mixer of capacity 300 kg. Triple mixing method, developed by Kong et al. [5], for NAF and RAC mixes were adopted for the production of concrete. The steps in triple mixing method are as

Table 2 Details of mix proportions

Mix designation		NAF	R50	R100
Cement (kg/m^3)		410	410	410
Water (kg/m^3)		164	164	164
Flyash (kg/m^3)		82	82	82
Fine aggregate (kg/m^3) (SSD condition)		706	706	706
Coarse aggregate (SSD condition) (kg/m^3)	NA	1,172	568	–
	RCA	–	568	1,119
Super plasticizer (percentage by weight of cement)		0.6	0.6	0.6
Slump (mm)		61	63	68

follows: coarse (RCA and NA) and fine aggregates were initially mixed for 15 s. A part of water was then added to the aggregate mixture and mixed for 15 s, and to this wet aggregate, the flyash was added and further mixed for 15 s to facilitate coating of the surface of aggregate with flyash. Cement was then added to the surface coated aggregate, the remaining water was added, and the mixing was continued for further 60 s. The oiled moulds were filled with concrete in layers and vibrated on a table vibrator. The cast specimens were water cured until the age of test.

3 Results and Discussions

3.1 Mechanical Properties

Mechanical properties such as compressive strength, split tensile strength, flexural strength and elastic modulus were determined at 28 and 56 days. The results of the tests are as given in Table 3 from which it can be seen that the density decreased with increase in percentage of RCA and, compressive strength, split tensile and flexural strength of RAC were comparable to that of NAF. The modulus of elasticity of RAC mix decreased with increase in percentage of RCA; the reduction for R100 mix was about 34 % [6]. Similar trend in the test results were observed by other researchers also and a reduction of up to 35 % was reported [7].

3.2 Rebar Bond Strength

The bond strength of the three mixes was investigated by performing rebar pullout test. The pullout test was performed as per the procedure given in IS 2770–Part I,

Table 3 Mechanical properties of NAF, R50 and R100 mixes

Mix designation		NAF	R50	R100
Density, kg/m^3 (dry)		2,396.7	2,309.7	2,257.3
Compressive strength, MPa	3 days	33.33	28.89	30.15
	7 days	41.03	37.49	43.11
	28 days	47.25	47.40	48.89
	56 days	57.77	54.02	57.33
Split tensile strength, MPa	28 days	3.74	3.49	3.68
	56 days	4.15	3.53	4.15
Flexural strength, MPa	56 days	5.46	4.78	5.72
Elastic modulus, GPa	28 days	29.15	24.07	19.38
	56 days	35.20	27.17	25.03

Fig. 1 Comparison of load versus slip curve for NAF, R50 and R100 specimens
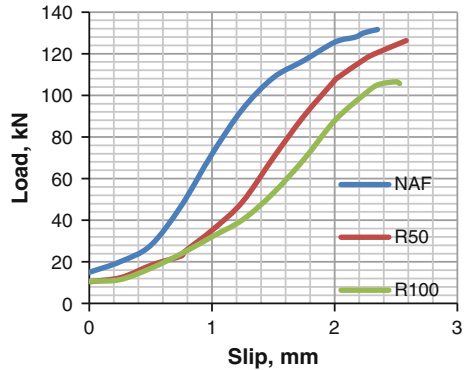
2007 [8] using $150 \times 150 \times 150$ mm^3 with 20 mm deformed high yield strength deformed bars (HYSD) bars embedded for a length of 140 mm. The load at a specified slip was recorded until the total slip was 2.5 mm or rebar failure or concrete crushing, whichever occurred first. During the pullout test, it was observed that, in the case of NAF, crack formation on concrete surface could be clearly seen as the load is applied to the rebar, whereas in case of RAC mixes, there has been no development of measurable/significant crack on the concrete surface. On the other hand, a fine powdery material was seen falling from the concrete-rebar interface in the RAC mixes during the test. This may be due to crushing of the adhered mortar (which is porous and comparatively weaker than aggregate) in the RAC mixes which could be preventing transfer of load from the rebar to the adjacent concrete as the rebar was pulled. Thus, appearance of crack on concrete surface, which normally happens in the NA mixes, was not found in RAC mixes. The effect of this localized crushing of mortar in the interface between RAC and rebar can be observed in the load versus slip curves given in Fig. 1.

Test specimen of NAF mix displayed comparatively steeper curves than R50 and R100. The steeper curves of NAF show that the increase in slip was lower for equal increase in load. This indicates that the rate of slip of the bar in RAC specimens is comparatively greater than the rate of slip in NAF. This may be because in case of NAF the slippage of bar is resisted by the strong rebar-concrete interface as the load is transferred, whereas in the case of RAC mix the rebar-concrete interface becomes weak due to crushing of the mortar at the interface. The bond strength was determined using the load corresponding to a slippage of 0.025, 0.25 mm and at failure of specimen as obtained from the load versus slip curve. Three specimens have been tested for each mix and the average bond strength is plotted in Fig. 2, from which it is seen that at a slippage of 0.025 and 0.25 mm the bond strength of RAC mixes were about 2–26 % less than that of NAF, however, the bond strength at failure was almost similar for all the mixes with the maximum difference in bond strength being 2 % between NAF and RAC, with R100 having the maximum bond strength. The results of the present study are similar to the results observed earlier. Mixes with 100 % RA exhibited higher bond strength at failure load and it was

Fig. 2 Variation in bond
strength for various mixes
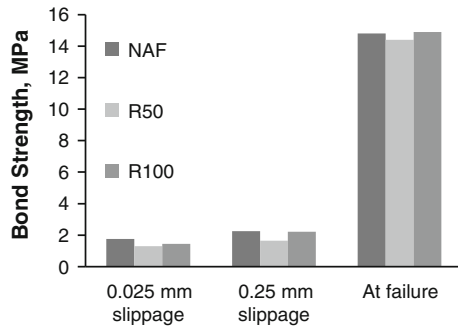
concluded that the bond strength of RAC would be similar to the bond strength of
NAC concrete when the compressive strength of the mixes are comparable. The
same is applicable in the present study as well, as the compressive strength of the
mixes is in similar range.

3.3 Flexural Behaviour

For the study of flexural behaviour, reinforced beams of size $150 \times 250 \times 2,000$ mm
were cast and tested under simply supported conditions of span 1,800 mm and loads
were applied at one third points (two-point loading). The deflections of the beams
were monitored at the centre point and one third points with increase of load on the
beam and the loading was stopped at ultimate load of the beam. Figure 3 gives the
test setup for flexure test of RCC beams and Fig. 4 gives the details of reinforcement.

3.3.1 Load Versus Deflection

The comparison of load versus deflection curves for beams of concrete mixes NAF,
R50 and R100 are presented in Fig. 5 for mid span location and in Fig. 6 for one
third span location. It is seen from Figs. 5 and 6 that the beam of NAF mix showed
the least deflection when compared to the other beams of different concrete mixes,
during the application of same load. Similarly, beams of R50 and R100 exhibited
similar deflection values up to an applied load of 30 kN, thereafter the R50
exhibited a lower deflection than R100.

Figure 7 gives the comparison between the deflection values of RAC and NAF
beams, where reference indicates the deflection equal to that of NAF. It may be seen
from Fig. 7 that the beams of R50 and R100 mixes exhibited deflections 13–36 %
and 16–46 %, respectively greater than NAF throughout the test. The higher
deflection in RAC can be attributed to the lower elastic modulus of RAC. Similarly,
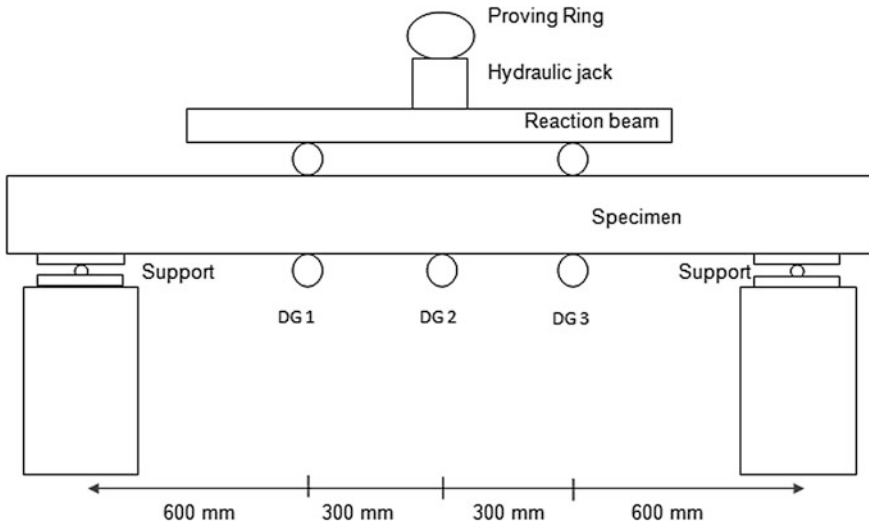
Fig. 3 Test set up of RCC beam under flexure
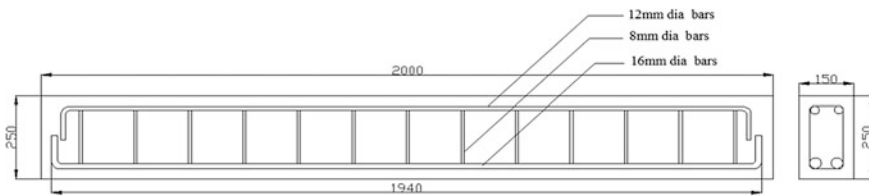
Fig. 4 Details of reinforcement

Fig. 5 Load versus deflection curve of RC beams for mid span section
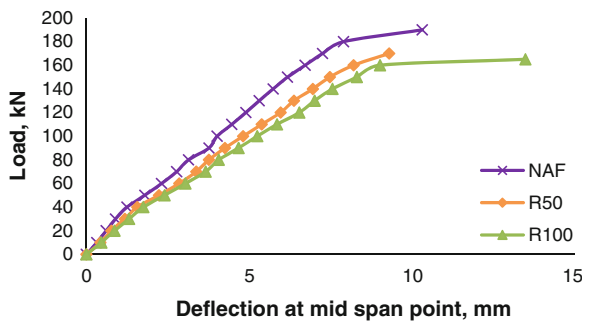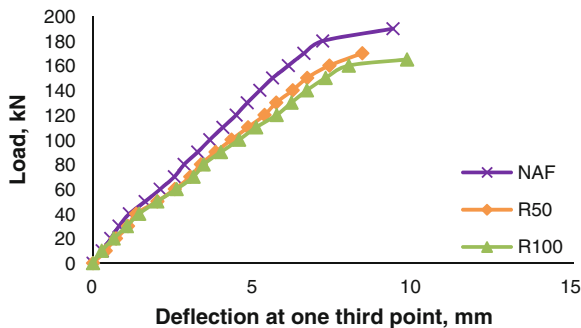
Fig. 6 Load versus deflection curve of RC beams for one third span section
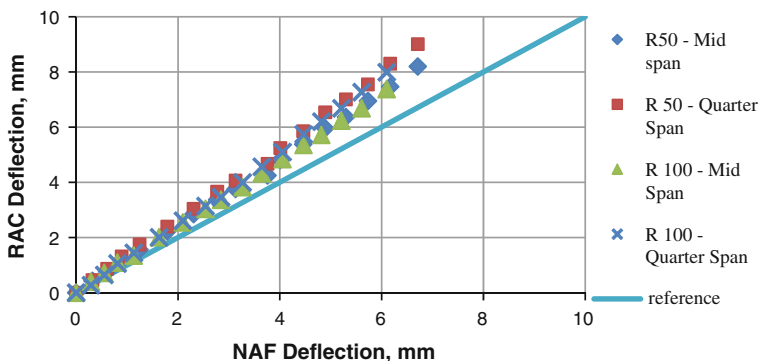
Fig. 7 Variation in deflection of RAC from NAF

Maruyama et al. [9], Kishore [10] reported that the deflection of RAC was about 43 % greater than that of NA concrete.

Though the deflections of RAC beams were greater than the NAF it can be seen from Fig. 8, the same were found to be lower than the theoretically estimated deflection values obtained, using standard deflection formulae for simply supported beams.

3.3.2 Crack Pattern and Measured Crack Width

During the application of load, initiation of cracks has been observed on both faces of beams tested under flexure. It was observed during testing that the number of cracks has increased and crack spacing has decreased with increase in percentage of RCA, similar to the observation made by Maruyama et al. [9]. Since crack width for different cracks were varying in each of RAC and NAF beams, only the maximum crack widths on these beams have been measured at different loading stages and the values are given in Table 4.
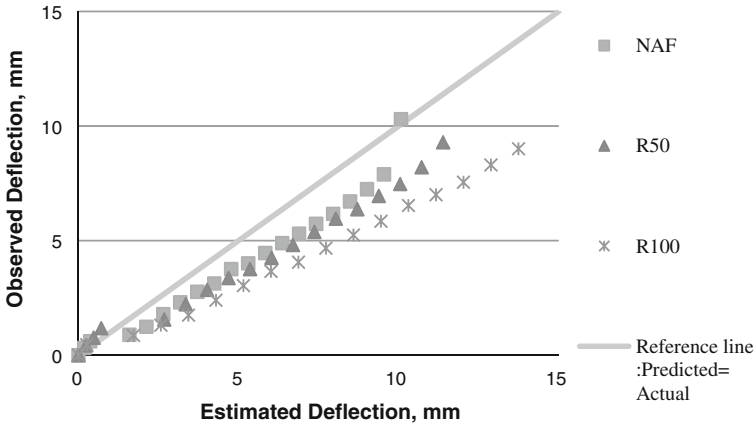
Fig. 8 Estimated deflection and observed deflection—a comparison

Table 4 Maximum measured crack width on RC beams at various loading stages

Load (kN)	Crack width (mm)		
	NAF	R50	R100
0	–	–	–
10	–	–	–
20	–	–	0.02
30	0.02	–	0.02
40	0.02	0.02	0.03
50	0.02	0.02	0.05
60	0.03	0.02	0.07
70	0.05	0.03	0.10
80	0.10	0.05	0.15
90	0.15	0.10	0.20
100	0.18	0.15	0.25
110	0.20	0.18	0.30
120	0.23	0.20	0.35
130	0.25	0.30	0.40
140	0.28	0.32	0.45
150	0.30	0.35	0.50
160	0.33	0.45	2
170	0.35	0.5	–
180	0.37	–	–
190	0.40	–	–

It is seen from Table 4 that the maximum measured crack width for the five RC beams of different mixes are different for both NAF and RAC beams at a same applied load. The measured crack width is found to be higher for R100 beam in

Table 5 Ultimate load of RCC beams tested

Mix designation	Ultimate load obtained from flexure test (kN)	Theoretical ultimate load (kN)
NAF	195	93.28
R50	175	92.63
R100	165	93.21

comparison to other beams. To satisfy the serviceability limit state, when the concrete structure is subjected to very severe exposure condition IRC 112 [11] has limited the crack width as 0.2 mm. Considering the maximum load at which a crack width of 0.2 mm is developed on all the five beams, it is seen from Table 4 that a crack of 0.2 mm is observed on NAF, R50 and R100 beams at a load of 110, 120, and 90 kN, respectively.

3.3.3 Ultimate Load

During the experimental studies, it has been observed that the five RC beams of different concrete mixes have failed at different ultimate loads and these values are given in Table 5. Also, using the cross-sectional and reinforcement details of these beams the ultimate load for these have been estimated using the expressions given in IS 456 [12]. It is observed that the ultimate loads of R50 and R100 beams were 89.7 and 84.6 % of ultimate loads of NAF beams. However, the ultimate load of RAC was found to be 77–89 % greater than that of theoretical ultimate load.

4 Conclusions

From the experimental results presented and the discussions made in the paper, the following conclusions can be drawn.

1. The properties of RCA were menial compared to NA but were well within the limiting values of the specifications.
2. The mechanical properties of RAC were comparable with NAF, except for elastic modulus, which decreased with increase in percentage of RCA.
3. The bond strengths of RAC mixes were lesser than that of NAF initially but the same were similar to the bond strength of NAF at failure.
4. The flexural properties of RAC beams though inferior to NAF, were still satisfactory. The deflections of RAC beams were lesser than the estimated values and the ultimate loads were greater than the theoretical ultimate loads.
5. It has been concluded from the results of the study that the strength properties of RAC are encouraging for use in new concrete. However, the use of RAC in structural concrete can be recommended with more confidence when low value

of modulus of elasticity and the influence of which is reflected in the flexural behaviour of RAC beams are suitably addressed.

References

1. Mullick AK (2013) Recycled concrete aggregate processing using and specifications. Indian concrete institute—central public works department workshop on C&D waste recycling in New Delhi, 28 Feb–1 Mar 2013, 20 p
2. IS 383 (1997) Specification for coarse and fine aggregate from natural sources of concrete. Bureau of Indian Standards (BIS), New Delhi, India
3. Surya M (2013) Experimental studies on structural properties of recycled aggregate concrete. M. Tech. dissertation, submitted to Academy of Scientific and Innovative Research (AcSIR), CSIR-Central Road Research Institute (CRRI), New Delhi, 125 p
4. IS 10262 (2009) Concrete mix proportioning—guidelines. Bureau of Indian Standards (BIS), New Delhi
5. Kong D, Lei T, Zheng J, Ma C, Jiang J, Jiang J (2010) Effect and mechanism of surface-coating pozzalanic materials around aggregate on properties and microstructure of recycled aggregate concrete. Constr Build Mater 24(5):701–708
6. Etxeberria M, Vázquez E, Marí A, Barra M (2007) Influence of amount of recycled coarse aggregates and production process on properties of recycled aggregate concrete. Cem Concr Res 37:735–742
7. Rao MC, Bhattacharya SK, Barai SV (2011) Influence of field recycled coarse aggregate on properties of concrete. Mater Struct RILEM 44:205–220
8. IS 2770 (2007) Methods of testing bond in reinforced concrete. Bureau of Indian Standards (BIS), New Delhi, India
9. Maruyama I, Sogo M, Sogabe T, Sato R, Kawai K (2004) Flexural properties of reinforced recycled beams. In: Proceedings of international RILEM conference on the use of recycled materials in buildings and structures, vol 1, pp 525–535
10. Kishore R (2007) Influence of recycled aggregates on flexural behaviour of reinforced beams. In: Proceedings of international conference on sustainable construction materials and technologies, University of Wisconsin, Milwaukee, US, June 2007, pp 36–44
11. IRC 112 (2011) Code of practice for concrete road bridges. Indian Roads Congress, New Delhi, India
12. IS 456 (2000) Plain and reinforced concrete—code of practice. Bureau of Indian Standards (BIS), New Delhi, India

Influence of Rubber on Mechanical Properties of Conventional and Self Compacting Concrete

M. Mishra and K.C. Panda

Abstract   The present study is carried out an experimental investigation on both fresh and hardened properties of conventional and self compacting concrete (SCC) containing waste tyre rubber. A comparison study between conventional rubberised concrete (CRC) and self compacting rubberised concrete (SCRC) is carried out. In both CRC and SCRC, the replacement of rubber varies from 0 to 20 % with coarse aggregate. The rubber chips of size 5 and 10 mm are used. The total volume of rubber chips are replaced in coarse aggregate i.e. 40 % from 5 mm size and 60 % from 10 mm size. The mix design of conventional concrete was targeted for M30 grade of concrete. The mix proportion of the concrete was 1:1.03:2.37 with water cement ratio of 0.375. CERA HYPERPLAST XR-W40 high end super plasticisers are used for the production of SCRC. The test results indicate that there was a reduction in the strength of CRC as compared with the SCRC. However, in both CRC and SCRC the replacement of 5 % rubber chips with coarse aggregate gives more strength than other replacement.

Keywords Tyre rubber · Conventional rubberised concrete (CRC) · Self compacting rubberised concrete (SCRC) · Compressive strength · Flexural strength · Split tensile strength

1 Introduction

Solid waste disposal is a major environmental issue on cities around the world. The volume of polymeric waste like tyre rubber is increasing at a fast rate. The waste tyre rubber becomes an environmental problem due to its non-biodegradable nature. Up to now a small part is recycled and millions of tyres are just stockpiled; land

M. Mishra (✉) · K.C. Panda
Department of Civil Engineering, ITER, SOA University, Bhubaneswar 751 030, Odisha, India
e-mail: mishramadhumita1986@gmail.com

K.C. Panda
e-mail: kishoriit@gmail.com

filled or buried and used as fuel in many industries. Aiello and Leuzzi [1] investigated on tyre shreds to replace fine and coarse aggregates and found that the sizes of the rubber particles have a major influence on the compressive strength. When coarse aggregates are replaced by the tyre particles the compressive strength loss is much more profound when compared to the compressive strength loss of concrete in which fine aggregates were replaced by rubber particles. Ei-dieb et al. [2] reported that by adding less than 10 % rubber through the replacement of coarse aggregate does not significantly find the performance of concrete reducing strength by around 10–15 %. Eldin and Senouci [3] used a different size of rubber aggregate and their rubber aggregate contained steel wires. The large displacement and deformation which were observed are due to the fact that rubber aggregate has the ability to withstand large deformations. Rubber aggregate particles seem to act as springs and cause a delay in widening the cracks and preventing the catastrophic failure which is usually experienced in plain concrete specimens. Ghaly and Cahill [4] studied the use of different percentage of rubber in concrete i.e. 5, 10 and 15 % by volume also noticing that as rubber content increase leads to a reduction of compressive strength. Herrnandez-Olivares et al. [5] investigated the dynamic characteristics of rubberised concrete material. Because of the unique elasticity properties of rubber material, the rubberised concrete showed potential advantages in reducing or minimizing vibration and impact effect. Khatib and Bayomy [6] studied the influence of adding two kinds of rubber crumb and chipped rubber. They made three groups of concrete mixtures, in group A: crumb rubber was used to replace fine aggregate, in group B: chipped rubber was used to replace coarse aggregate and in group C: both types of rubber were used in equal volumes. All the three groups had eight different rubber contents in the range of 5–100 %. It was found that there was a decrease in slump with increase in rubber content and mixtures made with fine crumb rubber were more workable than those with coarse tyre chips or a combination of tyre chips and crumb rubber. The objective of this experiment is to study the strength comparison between conventional rubberised concrete (CRC) and self compacting rubberised concrete (SCRC).

2 Experimental Work

2.1 Material Used and Properties

In this experimental study, ordinary Portland cement 43 grade (OPC), Ramco cement, zone I fine aggregate, natural coarse aggregate (20 mm passing), waste tyre rubber (5 and 10 mm), high end super plasticiser (SP) i.e. CERA HYPERPLAST XR-W40, new generation polycarboxylate base water reducing admixture provided by CERA-Chem India Ltd. Chennai and tap water were used. The rubber is replaced with coarse aggregate i.e. 0–20 % of its weight in both CRC and SCRC. The properties of fine aggregate and coarse aggregate are presented in the Table 1. The sample of waste tyre rubber chips in 10 and 5 mm size as shown in Fig. 1.

Table 1 Properties of fine and coarse aggregates

Characteristics	Fine aggregate value obtained experimentally as per IS 383-1970 [7]	Coarse aggregate value obtained experimentally as per IS: 383-1970 [7]
Abrasion value (%)	–	27.02
Bulk density (kg/m^3)	1,568	1,418
Crushing value (%)	–	28.70
Fineness modulus	3.48 (zone 1)	7.95
Impact value (%)	–	24.00
Specific gravity	2.63	2.84
Water absorption (%)	0.30	0.10

Fig. 1 Waste tyre rubber chips (10 and 5 mm)

2.2 Mix Proportion and Identifications

The adoptable mix design of CC is 1:1.03:2.37 with W/C ratio of 0.375. The mix design of SCC is conducted in a trial basis. With 34 % increase in fine aggregate and 34 % decrease of coarse aggregate in CC mix with same W/C ratio and the addition of 0.4 % of super plasticiser satisfied EFNARC (The European Federation of Specialist Construction Chemicals and Concrete Systems) specifications of SCC mix [8, 9]. SP increases the flowing, filling and passing ability of concrete.

Five concrete mixes are prepared for both the CRC and SCRC with variation of rubber from 0 to 20 %. Two sizes of rubber chips are used for this experiment i.e. 5 and 10 mm. 40 % of rubber used from 5 mm size and 60 % of rubber used from 10 mm size as the replacement of coarse aggregates. The detail mix proportion along with their identification is designated according to their replacement as given in Table 2. The detail mix quantities per cubic meter of concrete are presented in Table 3.

Table 2 Details of CC and SCC mix proportion along with identification

Concrete mix proportion	Mix identity
C concrete mix with 100 % NCA + 0 % rubber chips + w/c 0.375	CRC0
C concrete mix with 95 % NCA + 5 % rubber chips + w/c 0.375	CR0C5
C concrete mix with 90 % NCA + 10 % rubber chips + w/c 0.375	CRC10
C concrete mix with 85 % NCA +15 % rubber chips + w/c 0.375	CRC15
C concrete mix with 80 % NCA + 20 % rubber chips + w/c 0.375	CRC20
SC concrete mix with 100 % NCA + 0 % rubber chips + w/c 0.375 + SP 0.4 %	SCRC0
SC concrete mix with 95 % NCA + 5 % rubber chips + w/c 0.375 + SP 0.4 %	SCRC5
SC concrete mix with 90 % NCA +10 % rubber chips + w/c 0.375 + SP 0.4 %	SCRC10
SC concrete mix with 85 % NCA + 15 % rubber chips + w/c 0.375 + SP 0.4 %	SCRC15
SC concrete mix with 80 % NCA + 20 % rubber chips + w/c 0.375 + SP 0.4 %	SCRC20

Table 3 Details of CC and SCC mix quantity per m^3 of concrete

Mix identity	Mix quantity of different constituents m^3 of concrete						
	Cement (kg)	Sand (kg)	NCA (kg)	Rubber chips (kg)		Super plasticiser (kg)	Water (kg)
				5 mm (40 %)	10 mm (60 %)		
CRC0	511.00	527.00	1209.27	–	–	–	191.6
CRC5	511.00	527.00	1148.81	24.18	36.28	–	191.6
CRC10	511.00	527.00	1088.34	48.37	72.56	–	191.6
CRC15	511.00	527.00	1027.88	72.56	108.83	–	191.6
CRC20	511.00	527.00	967.42	96.74	145.11	–	191.6
SCRC0	511.00	706.18	798.12	–	–	2.044	191.6
SCRC5	511.00	706.18	758.21	15.96	23.95	2.044	191.6
SCRC10	511.00	706.18	718.31	28.25	42.37	2.044	191.6
SCRC15	511.00	706.18	678.40	47.89	71.83	2.044	191.6
SCRC20	511.00	706.18	638.50	63.85	95.77	2.044	191.6

3 Test Program

3.1 Fresh Concrete Test

The fresh concrete tests are conducted to know about the workability of CC. The test is conducted using slump cone. For SCC fresh concrete tests are conducted to know the details about flow, filling and passing ability of concrete. Six tests conducted for fresh concrete such as slump flow, T_{500}, J-ring, V-funnel, L-box and U-box. Slump test is conducted to know about the filling and flow ability, T_{500} and V-funnel tests are conducted to know the flow ability and J-ring, L-box and U-box tests are conducted to know the passing ability of concrete. The slump cone test,
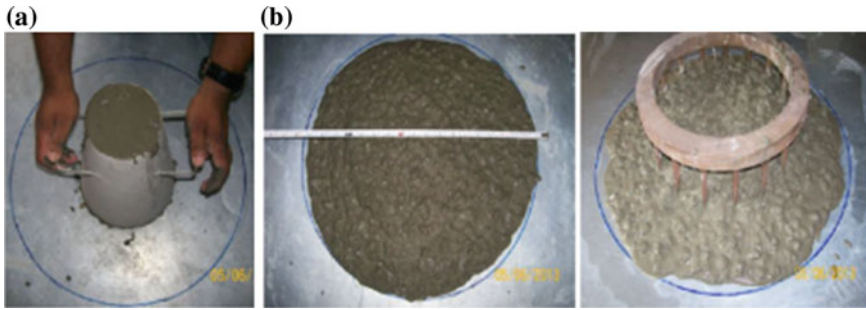
Fig. 2 **a** Slump cone test and T_{500} test, **b** J-ring test
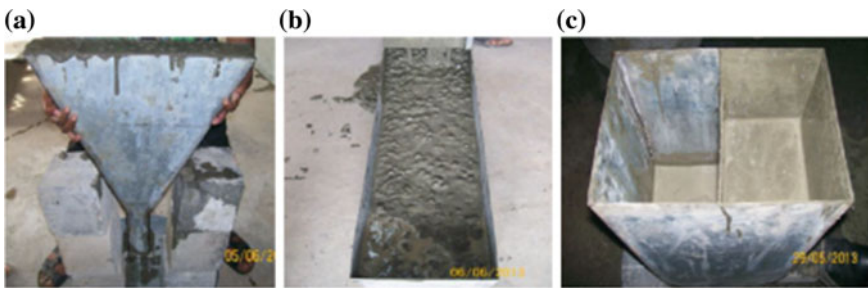
Fig. 3 **a** V-funnel test, **b** L-box test, **c** U-box test

T_{500} test and J-Ring test is presented in Fig. 2a, b. The V-funnel test, L-box test, U-box test are presented in Fig. 3a–c respectively.

3.2 Hardened Concrete Test

The hardened concrete test is conducted for both CC and SCC in 7, 28 and 90 days. After casting the specimens (cube, cylinder and prism) the curing has been done properly to achieve the target strength. Compressive strength, flexural strength and split tensile strength test were conducted to know the hardened properties of the specimens.

4 Test Results

The fresh concrete test results of workability for CC mix are obtained from slump flow test and the slump values for CRC0, CRC5, CRC10, CRC15 and CRC20 are 36, 25, 20, 18 and 15 mm respectively. In SCC the fresh concrete test results for

SCRC0, SCRC5, SCRC10, SCRC15 and SCRC20 are presented, for slump flow test the values are 570, 650, 690, 710 and 730 mm, for T_{500} test the values are 8, 7, 6, 5 and 5 s, for J-ring test the step height results are 12, 10, 8, 6 and 5 mm, for V-funnel test the values are 15, 13, 12, 10 and 9 s., for U-box test the values are 78,70, 60, 55 and 50 mm, for L-box test the passing ability values are 0.76, 0.78, 0.80, 0.82 and 0.90.

The hardened concrete specimen are obtained by testing the specimens at the time specified that is after 7, 28 and 90 days. Compressive strength, flexural strength and split tensile strength test were conducted to know the hardened properties of the specimen. The compressive strength verses age in days test results for CRC and SCRC are presented in Figs. 4 and 5. The flexural strength verses age

Fig. 4 The compressive strength verses age in days for CRC
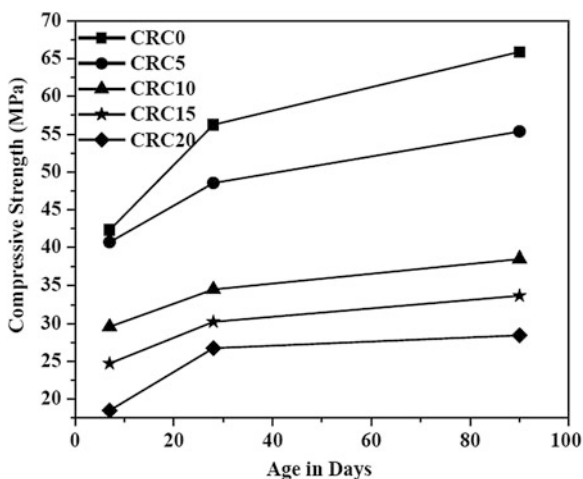
Fig. 5 The compressive strength verses age in days for SCRC
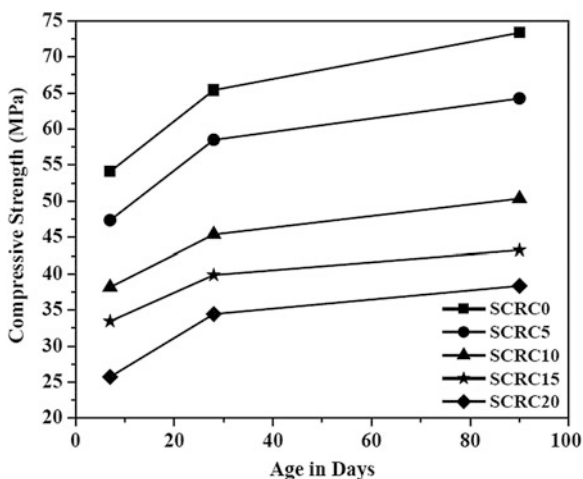
in days test results for CRC and SCRC are presented in Figs. 6 and 7. The split tensile strength verses age in days test results for CRC and SCRC are presented in Figs. 8 and 9.

From figures, without any replacement of rubber having more compressive, flexural and split tensile strength in both CRC and SCRC. As replacement of rubber amount increases the strength decreases at all age. Among all replacement, CRC5 and SCRC5 having more strength at all age. In CRC the flexural strength difference between CRC5 and control mix is very less.

Fig. 6 The flexural strength verses age in days for CRC
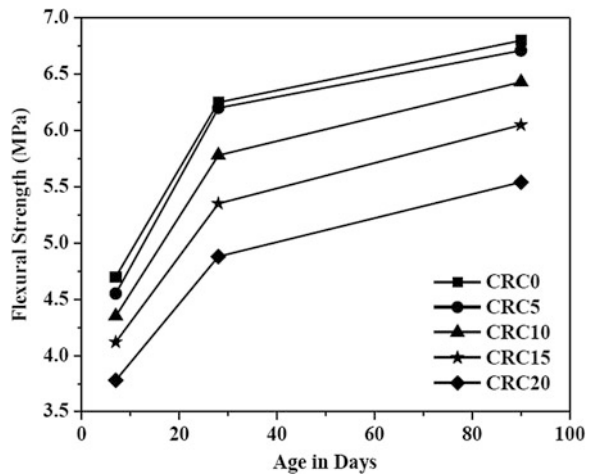
Fig. 7 The flexural strength verses age in days for SCRC
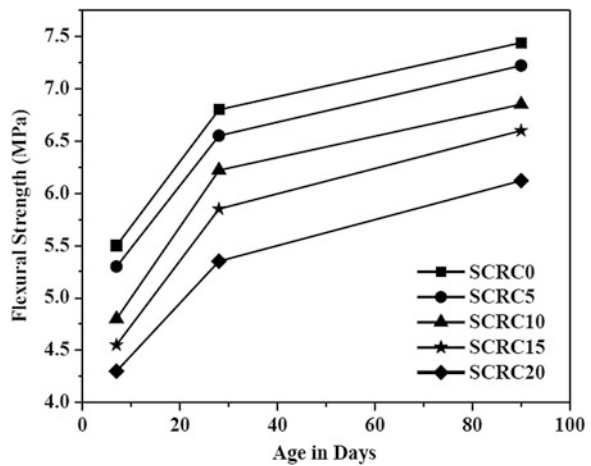
Fig. 8 The split tensile strength verses age in days for SCRC
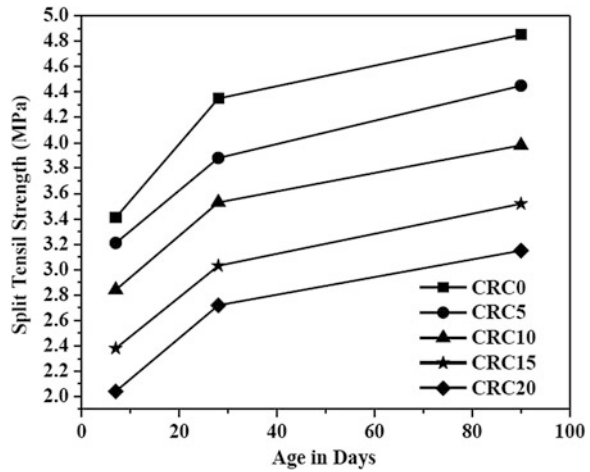
Fig. 9 The split tensile strength verses age in days for SCRC
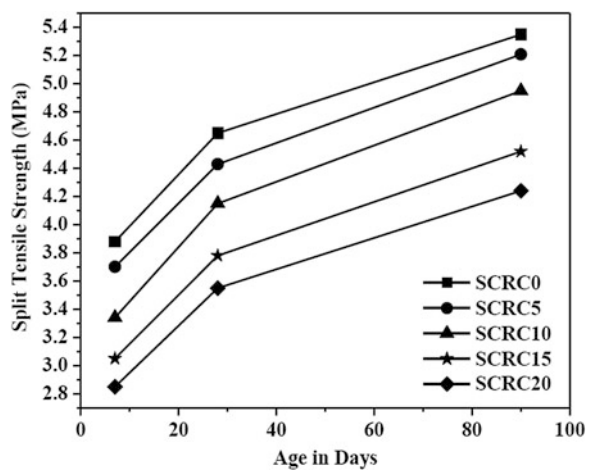
4.1 Comparison Between CRC and SCRC

The comparision graph of CRC and SCRC for compressive strength, flexural strength and split tensile strength are presented in Figs. 10, 11 and 12 respectively. From figures it is observed that in SCRC the strength is more than CRC. In SCC the superplasticiser helps to get maximum strength. The replacement of 5 % rubber having more strength than other replacement at all age of curing. As rubber replacement increases the strength decreases in both CRC and SCRC. The strength of CRC20 is very low at all age whereas in SCC at same replacement of rubber the strength comparatively higher.

Fig. 10 Comparison of compressive strength for different curing condition
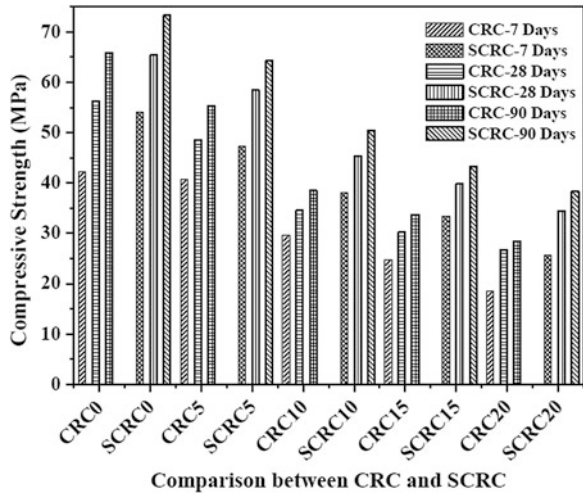
Fig. 11 Comparison of flexural strength for different curing conditions
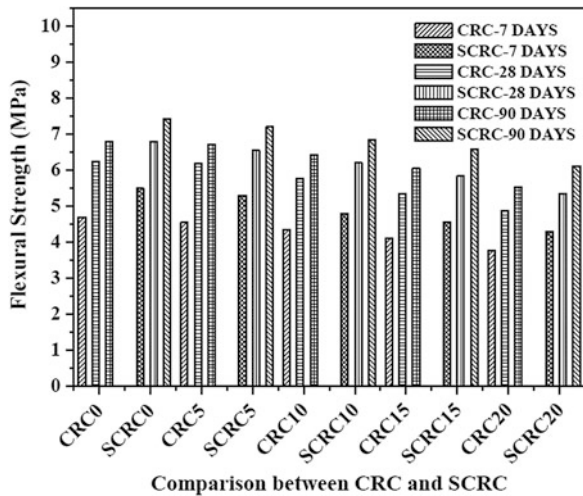
5 Concluding Remarks

- As rubber chips amount increases in SCRC the flow, filling and passing ability are more in less time period.
- In slump flow test, the replacement of rubber chips from 0 to 5 % satisfy the first class criteria and 10, 15 and 20 % replacement satisfy the second class criteria as per EFNARC guidelines.
- The addition of super plasticiser in SCC gives more strength in early age.
- The compressive strength, flexural strength and split tensile strength of SCRC is more than CRC at all age of curing.
- In SCC, 5 % replacement of rubber has more strength than other rubber replacement.

Fig. 12 Comparison of split
tensile strength for different
curing conditions
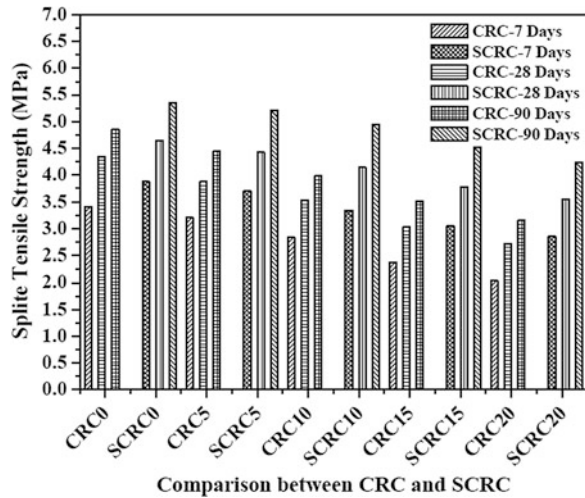
- The strength is more in 5 % replacement of rubber in CRC than 10, 15 and 20 % replacement at all age.
- The strength variation between 5 % replacement of rubber and control mix is very less in both CRC and SCRC.

References

1. Aiello M, Leuzzi F (2010) Waste tyre rubberised concrete: properties at fresh and hardened state. Waste Manage 30:1696–1704
2. Ei-dieb AS, Abdelw MM, Abdel-Hameed ME (2001) Concrete using tyre particles as aggregate. In: Proceedings of the international symposium, concrete technology unit, ISBN:0 7277 2995 0. Thomas Telford Publishing, London, pp 251–259
3. Eldin NN, Senouci AB (1993) Rubber-tire particles as concrete aggregate. J Mater Civ Eng 5:478–496
4. Ghaly A, Cahill J (2005) Correlation of strength, rubber content, and water to cement ratio in rubberised concrete. Can J Civ Eng 32:1075–1081
5. Hernandez-Olivares F, Barluenga G, Bollati M, Witoszek B (2002) Static and dynamic behavior of recycled tyre rubber-filled concrete. Cem Concr Res 32:1587–1596
6. Khatib ZK, Bayomy FM (1999) Rubberised portland cement concrete. J Mater Civ Eng 11 (3):206–213
7. IS 383-1970 Specification for coarse and fine aggregates from natural sources for concrete. Bureau of Indian Standards, New Delhi
8. EFNARC (2002) Specification and guidelines for self-compacting concrete. EFNARC, Association House, Farnham, Surrey
9. EFNARC (2005) The European guidelines for self-compacting concrete specification, production and use

Investigation of the Behaviour of Concrete Containing Waste Tire Crumb Rubber

R. Bharathi Murugan and C. Natarajan

Abstract In the concrete preparation 70–80 % occupying natural aggregates like crushed rock and river sand, the most commonly used coarse and fine aggregate is likely become scarcer the it is today. Now construction people need the alternatives to natural aggregates. Therefore, finding alternatives to naturally available materials is important to sustaining construction industry. On other hand a large quantity of waste materials are being produced by various industries and the governments are seeking ways to reduce the problem of disposal and to control the health hazard from the accumulation of waste materials. Some of the waste materials, such as coal fly ash, bottom ash, glass granules, plastic granules, copper slag, and crushed rock dust were used in the concrete. So in such waste materials are used to modify the mechanical and durability properties of concrete so as to make it suitable for any situation, this would also additional benefits in terms of reduction in cost, energy savings, promoting ecological balance and conservation of natural resources. In this study, the production of concrete was obtained by partially replacing the fine aggregate with crumb rubber. The main advantages of crumb rubber utilization in concrete to give the lower density, higher impact and toughness resistance, enhanced ductility, and better sound insulation etc. Crumb rubber is made by shredding waste tires. In the shredding process the steel wires are removed from the discard tires. The crumb rubber particle size ranging from 0.075 mm to not exceeding 4.75 mm, similar to the fine aggregates. Experimental investigations were carried out to study the behaviour of concrete with and without crumb rubber. The replacement of crumb rubber contents varying 5–25 % of river sand by volume. The test results indicated that the addition of waste tire crumb rubber substitution increases, the density, compressive strength and static modulus of elasticity was decreased. At the same time the flexural strength was increased up to 15 % of crumb rubber replacement. The relationship between static modulus of elasticity

R. Bharathi Murugan (✉) · C. Natarajan
Department of Civil Engineering, National Institute of Technology, Tiruchirapalli 625015, Tamil Nadu, India
e-mail: rbmmecivil@gmail.com

C. Natarajan
e-mail: nataraj@nitt.edu

and flexural strength with compressive strength of concrete with and without crumb rubber was analyzed and compared the experimental results with the empirically calculated values by using design codes.

Keywords Rubberized concrete · Crumb rubber · Compressive strength · Flexural strength · Static modulus of elasticity

1 Introduction

Utilization of waste tire is very difficult to handle because the waste tire is not biodegradable even after long period [1–3]. Solving this problem the main three ways of waste handling techniques can be used: Reuse, Burning and Dumping. The above three ways reuse only very opted and good solution for environmental issues. It has been determined that burning of waste tire will emit large amounts of Co, NoX and SO_2. Dumping the waste tire into the land create serious land hazardous and settlement effects [4, 5].

Reuse of waste tire has been used in different applications. In recent years the waste tire crumb into the small particles then used as a construction materials. Many articles are mentioned the utilization of waste tire crumb rubber as a aggregate in the concrete preparation, asphalt pavement mixture, playground matt and noise barriers [5, 6].

Waste tire crumb rubber is a very good alternative construction material in the construction industry due to its low specific gravity, more elasticity, very good energy and sound absorption.

In this paper, waste tire crumb rubber partially replaces the fine aggregate by volume with different percentage (5, 10, 15, 20 and 25 %) and study the main properties of the concrete with crumb rubber and the test results are compared to the normal concrete (without rubber).

The compressive strength, flexural strength and static modulus of elasticity are the main properties of concrete. In fact, these are very important properties for designing and analyzing the concrete structures. The bureau of Indian standards [7] recommends the empirical relation between the static modulus of elasticity and compressive strength of concrete,

$$Ec = 5000\sqrt{fck} \qquad (1)$$

Further IS 456 [7] also recommends the flexural strength of concrete,

$$fr = 0.7\sqrt{fck} \qquad (2)$$

where Ec = Static modulus of elasticity in MPa, fr = Flexural strength in MPa and fck = Characteristic compressive strength of concrete at 28 days in MPa.

2 Objectives

The main objectives of the experimental program were:

- To study the properties of concrete with and without waste tire crumb rubber.
- To compare the experimentally obtained results with empirical relationships suggested by IS codes.

3 Experimental Program

3.1 Material Properties

Ordinary Portland cement 53 grade (OPC 53) confirming to IS 12269 [8] was used throughout the investigation. The properties of cement determined and the test results are tabulated in Table 1. Properties of cement test results satisfied the requirements.

Locally available river sand was used as a fine aggregate. The properties are confirmed as per IS 383 [9]. River sand confirms grading Zone II with specific gravity of 2.65 and fineness modulus of 2.45 were used.

Crushed granite stone having maximum size of 20 mm and down with specific gravity of 2.63 and fineness modulus of 7.2 were used. The properties are confirmed to IS 383 [9].

Shredding of waste tires were to produce crumb rubber passing through 4.75 mm IS sieve and specific gravity as 0.689. Crumb rubber was added into the concrete as a replacement for fine aggregate.

3.2 Casting and Testing of Specimens

Cement concrete cubes (150 mm × 150 mm × 150 mm) were cast for compressive strength. Cylinders (150 mm diameter and 300 mm height) were cast for static modulus. Concrete prisms were cast for flexural strength. M20 grade concrete had

Table 1 Properties of cement

Sl. No	Property	Results	Requirements as per IS 12269 [8]
1	Normal consistency	31 %	–
2	Specific gravity	3.14	–
3	Initial setting time and final setting time	65 min 280 min	Not less than 30 min Not more than 600 min
4	Fineness (m^2/kg)	320	225
5	Compressive strength 7 days (N/mm^2) 28 days (N/mm^2)	38.60 56.96	37.00 53.00

Table 2 Concrete mix proportion

Sl. No	Mix ID	Replacement of crumb rubber (%)	Mix ratio C:S:CA:CR	Slump (mm)	28 day compressive strength of concrete cubes (MPa)
1	R0	0	1:1.89:2.88:0.00	48	34.77
2	R5	5	1:1.78:2.88:0.09	50	32.07
3	R10	10	1:1.71:2.88:0.18	52	30.13
4	R15	15	1:1.62:2.88:0.27	56	27.15
5	R20	20	1:1.53:2.88:0.36	61	24.62
6	R25	25	1:1.44:2.88:0.45	69	18.62

Note C cement, S river sand, CA coarse aggregate and CR crumb rubber

cement, fine aggregate and coarse aggregate in the ratio 1:1.89:2.88 with water-cement ratio was 0.5. The mix was designed as per IS 10262:2009 [10] and the target strength was found 26.60 MPa. Fine aggregate partially replaced with crumb rubber by volume (5, 10, 15, 20 and 25 %). Concrete specimen mixing and curing has been carried out room temperature and potable water confirming to IS 456 [7] was used for both mixing and curing. Compaction of fresh concrete in the mould was carried out 2 min by using table vibrator. Three set of specimens were cast to each test. The identification of concrete mix is given in Table 2.

4 Result and Discussion

4.1 Workability of Fresh Concrete

Table 2 shows that the addition of crumb rubber increased the slump of the concrete. The analysis of slump values the rubberized concrete mixes give high workable concrete compared to normal concrete. The crumb rubber were not absorbing the water compare to river sand so the rubber content increases in the concrete the workability also increased and gives required slump for various conditions of placement and compaction of concrete.

4.2 Compressive Strength

Compressive strength of concrete with and without crumb rubber was given in Table 2 and graphical representation represented on Fig. 1. It was observed that the compressive strength of concrete was decreased with percentage of rubber content increased in the concrete mix. The decrease in compressive strength of concrete with addition of 5, 10, 15, 20 and 25 % waste tire crumb rubber was observed 7.85, 13.34, 21.92, 29.9 and 46.44 % at 28 days respectively compared to normal

Fig. 1 Variations in the compressive strength of the concrete
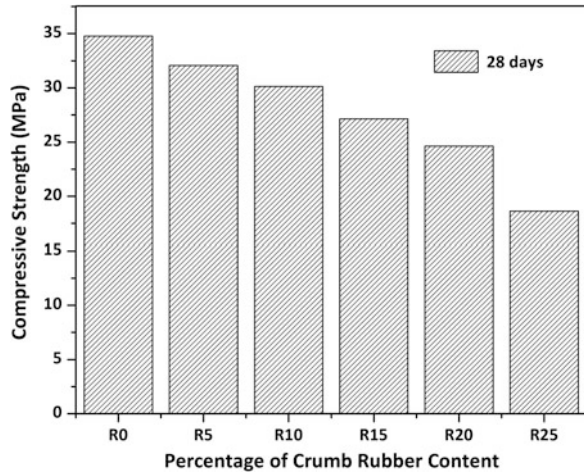
concrete (without rubber). At the same time up to 15 % of crumb rubber added concrete strength was increased as compared to target strength (26.60 MPa) of the concrete mix. For that up to 15 % of crumb rubber added concrete was suitable for any construction work.

The strength reduction of crumb rubber added concrete due to two reasons are reported; first, normally the rubber particles are much softer than cement paste, on loading cracks propagation are very fast around the rubber particles which leads the failure of the rubber-cement matrix. Secondly, due to lack of adhesion between crumb rubber particles and other concrete materials can be disturbed, because the rubber particles having more air content it may increase the voids in the concrete [11, 12].

4.3 Modulus of Elasticity

Figure 2 shows the measured values of modulus of elasticity at 28 days and calculated values from the empirical equation given in the IS 456 [7] code for both normal and rubberized concrete. The figure clearly shows the measured modulus of elasticity is lower than the calculated one. In this test 150 mm × 300 mm size cylinder specimens were used. The gauge length of cylinder was marked on the central height of specimens. Longitudinal extensometer was attached to the specimen such that gauge length is 200 mm, placed the cylinder with longitudinal extensometer on the compression testing machine and adjusted the deflectometer reading to zero. The load will be increased in increment up to failure of the specimen. The deflectometer readings are tabulated and the static modulus of elasticity was found and the stress strain curve was plotted. The reading of one unit

Fig. 2 Variations in the static modulus of elasticity of the concrete
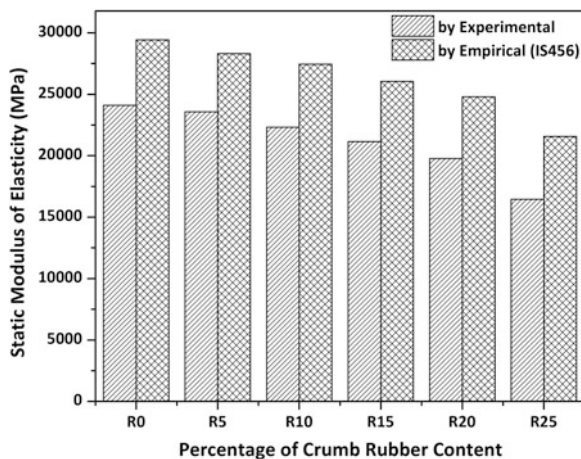
in the extensometer is equal to $\frac{1}{100}$ mm, and also checked Static modulus of elasticity value as per IS 456 [7]. Static modulus of elasticity of normal concrete was about 29.43 MPa at the age of 28 days. Figure 3 showed that the modulus of elasticity decreased with increasing rubber content it is similar to that observed in compressive strength. Increasing rubber contents 5, 10, 15, 20 and 25 % of the fine aggregate volume, the static modulus reduced to 2.44, 7.38, 12.19, 18.01 and 31.74 % respectively.

4.4 Flexural Strength

Comparison of experimentally obtained values of flexural strength and empirically obtained values given by IS 456 [7] code for both normal and rubber added concrete shown in Fig. 3. Two point load was applied to the specimens and the breaking load for the specimens were measured. From the breaking load the flexural strength was calculated.

The result shows that the flexural strength was increased up to 15 % replacement. The improvement of flexural strength is limited to relatively small rubber contents. Modulus of elasticity was decreased when rubber content increased. Generally the normal concrete behaves brittle when the modulus of elasticity was higher and concrete mixed with large volumes of rubber behave more ductile or flexible when modulus of elasticity values were lower [13].

Therefore it can be explained that the addition of lower volume of rubber into the concrete significantly increased the modulus of elasticity. Accordingly, in this study the flexural strength was increased with low volume of rubber (5, 10 and 15 %) and strength was decreased higher volume of rubber (20 and 25 %).

Fig. 3 Variations in the flexural strength of the concrete
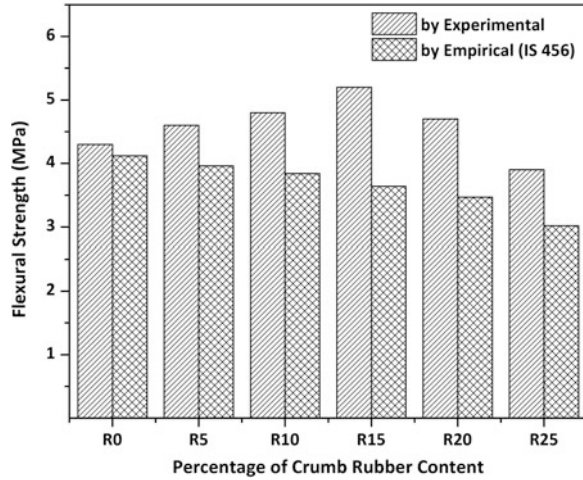
5 Conclusions

A series of test has been carried out to investigate the behaviour of concrete containing waste tire crumb rubber. The following conclusions were drawn based on the test results of this study.

The test results showed that there was increasing in slump values when crumb rubber content increased up to 25 %. Meaning that the workability of rubberized concrete an acceptable in terms of ease of handling, placing and finishing as compare to normal concrete.

The compressive strength was reduced with increasing in rubber content. Acceptable compressive was recorded at crumb rubber lower than 15 % replacement of fine aggregate by volume.

Static modulus of elasticity of rubberized concrete was lower than normal concrete but there was withstanding large displacement and deformation due to the properties of rubber. Normally rubber having more ductile or flexible in that it has the ability to withstand large deformation.

Flexural strength of concrete was increased up to 15 % of crumb rubber replacement. It the percentage of crumb rubber replacement increases over 15 % the flexural strength was decreased.

As compared to experimentally obtained flexural strength was higher than the predicted strength of all concrete mix by using IS 456 [7] code. In the static modulus, experimental values are lower than the empirical values.

References

1. Azmi NJ, Mohammed BS, Al-Mattarneh HM (2008) Engineering properties of concrete containing recycled tire rubber. ICCB B 34:373–382
2. Issa CA, Salem G (2013) Utilization of recycled crumb rubber as fine aggregate in concrete mix design. J Constr Build Mater 42:48–52
3. El-Gammal A, Abdel Gawad AK, El-sherbini Y, Shalaby A (2010) Compressive strength of concrete utilizing waste tire rubber. J Emerg Appl Sci (JETEAS) 1(1):96–99
4. Ozbay E, Lachemi M, Sevim UK (2011) Compressive strength, abrasion resistance and energy absorption capacity of rubberized concretes with and without slag. J Mater Struct 44 (7):1297–1307
5. Guneyisi E (2010) Fresh properties of self-compacting rubberized concrete incorporated with fly ash. J Mater Struct 43(8):1037–1048
6. Gunneyisi E, Gesoglu M, Ozturan T (2004) Properties of rubberized concrete containing silica fume. J Cem Concr Res 34:2309–2314
7. Indian standard code for plain and reinforced concrete for general building construction, IS 456:2000. Bureau of Indian Standards, New Delhi
8. Indian standard specification for 53 grade ordinary Portland cement, IS 12269:1987. Bureau of Indian Standards, New Delhi
9. Indian standards specification for coarse and fine aggregate from natural sources of concrete, IS 383:1970. Bureau of Indian Standards, New Delhi
10. Indian standard code for concrete mix proportioning—guidelines, IS 10262:2009. Bureau of Indian Standards, New Delhi
11. Najim KB, Hall MR (2013) Crumb rubber aggregate coatings/pre-treatments and their effects on interfacial bonding, air entrapment and fracture toughness in self-compacting rubberised concrete. J Mater Struct 46(12):2029–2043
12. Khatip ZK, Bayomy FM (1999) Rubberized portland cement concrete. J Mater Civ Eng ASCE 11(3):206–213
13. Ling TC, Nor HM, Hainin MR (2009) Properties of crumb rubber concrete paving blocks with SBR latex. J Road Mater Pavement 10(1):213–222

Bibliography

14. Al-Mutairi N, Al-Rukaibi F, Bufarsan A (2010) Effect of micro silica addition on compressive strength of rubberized concrete at elevated temperatures. J Mater Cycles Waste Manage 12 (1):41–49
15. Kizinievic O, Maciulaitis R, Kizinievic V (2006) Use of rubber waste in the ceramic. J Mater Sci 12(3):237–242
16. Shariq M, Prasad J, Masoold A, Ahuja AK (2013) Modulus of elasticity, modulus of rupture and compressive strength relationships of concrete containing GGBFS. Indian Concr J 53–60
17. Li Y, Wang M, Li Z (2010) Physical and mechanical properties of crumb rubber mortar (CRM) with interfacial modifiers. J Wuhan Univ Technol-Mater Sci Ed 25(5):845–848

Study on the Properties of Cement Concrete Using Manufactured Sand

M.R. Lokeswaran and C. Natarajan

Abstract Fine and coarse aggregate constitute about 75 % of total volume of concrete. The most commonly used fine aggregate is natural river sand. Nowadays the demand for river sand is increasing due to its lesser availability. Sand quarrying has resulted in scarcity and poses environmental problems such as loosing water retaining sand strata, deepening of the river courses and causing bank slides, loss of vegetation on the bank of rivers, disturbs the aquatic life as well as affects agriculture. So there is an immediate need to control the sand quarrying and provide a sustainable replacement of river sand. Properties of aggregate affect the durability and performance of concrete, so fine aggregate is an essential component of concrete. Manufactured sand in concrete not only acts as replacement for concrete but also leads to the development of eco-friendly construction as well as reduction in cost of construction. Manufactured sand offers viable alternative to natural sand and it is purposely made fine aggregate produced by crushing and screening or further processing. This experimental investigation was performed to evaluate the grading and strength properties of M20 grade of concrete mixes, in which natural sand was replaced with manufactured sand. The properties of river sand and manufactured sand such as specific gravity, sieve analysis, fineness modulus and water absorption were determined through test as per IS 383-1970 and compared. Specimens were cast to compare the strength properties of concrete with river sand and manufactured sand as fine aggregate. Specimens for compressive strength, tensile strength and flexural strength were casted and tested up to failure to evaluate the strength properties of concrete at the age of 7 and 28 days. Test results showed that the grading of manufactured sand fall in the Zone II gradation as per the specifications provided in IS 383-1970. Test results showed that there is only a marginal decrease in compressive strength, splitting tensile strength and flexural strength for M20 concrete mixes on ages of 7 and 28 days in comparison to the river sand concrete

M.R. Lokeswaran (✉) · C. Natarajan
National Institute of Technology, Tiruchirappalli, India
e-mail: lokescivil@gmail.com

C. Natarajan
e-mail: nataraj@nitt.edu

but the strength is more than the target mean strength for which the mix was designed. These studies reveal that the test results are in conformation with the river sand concrete and hence manufactured sand can be used as fine aggregate in concrete.

Keywords Manufactured sand · Sustainable replacement · Concrete · Fine aggregate · Strength

1 Introduction

The global consumption of natural sand is very high, due to the extensive use of concrete or mortar.

Properties of aggregate affect the durability and performance of concrete, so fine aggregate is an essential component of concrete and cement mortar. The most commonly used fine aggregate is natural river sand. Fine and coarse aggregate constitute about 75 % of total volume. It is therefore, important to obtain right type and good quality aggregate at site, because the aggregate forms the main matrix of concrete or mortar [1].

Increasing extraction of natural sand from river beds causing many problems, loosing water retaining sand strata, deepening of the river courses and causing bank slides, loss of vegetation on the bank of rivers, exposing the intake well of water supply schemes, disturbs the aquatic life as well as affecting agriculture due to lowering the underground water table are few examples [2, 3].

Manufactured sand offers viable alternative to natural sand and it is purpose made fine aggregate produced by crushing and screening or further processing i.e. washing, grading, classifying of quarried rock, cobbles, boulders or gravels from which natural fine aggregate had been removed [3].

Now a day's sand is becoming a very scarce material, in this situation research began for inexpensive and easily available alternative material to natural sand. Some alternatives materials have already been used as a part of natural sand e.g. fly-ash, slag limestone and siliceous stone powder are used in concrete mixtures as a partial replacement of natural sand [4, 5]. However, scarcity in required quality is the major limitation in some of the above materials. Now a day's sustainable infrastructural growth demands the alternative material that should satisfy technical requisites of fine aggregate as well as it should be available abundantly [6].

Based on review, work is carried out on strength properties of cement concrete with full replacement of natural sand by manufactures sand. Also strength of cement concrete is determined for ages of 7 and 28 days.

2 Material Properties

(i) Cement

The ordinary Portland cement was classified into three grades, namely 33 grades, 44 grades and 53 grades depending upon the strength of cement at 28 days when tested as per IS 4031-1988. If 28 days strength is not less than 53 N/mm^2, it is called 53 grade cement. In this research M20 concrete is selected for the study, 43 grade (OPC) cement has been used for this research.

(ii) Fine Aggregate

Natural river sand with fraction passing through 4.75 mm sieve and retained on 60 µm sieve is used and will be tested as per IS 2386. The sieve analysis of fine aggregates is presented in Table 1 and the grading zone is shown in Fig. 1.

(iii) Coarse aggregate

Coarse aggregates of maximum size of 20 mm we used and the physical properties will be tested as per IS 2386-1963.

Table 1 Sieve analysis of fine aggregates

IS sieve designation	River sand % passing	Manufactured sand % passing
4.75 mm	97.25	98.52
2.36 mm	94.01	77.83
1.18 mm	80.65	57.24
600 µm	61.61	47.65
300 µm	26.46	31.51
150 µm	4.32	13.37
Fineness modulus	2.35	2.63
Specific gravity	2.65	2.52

Fig. 1 Grading of fine aggregates
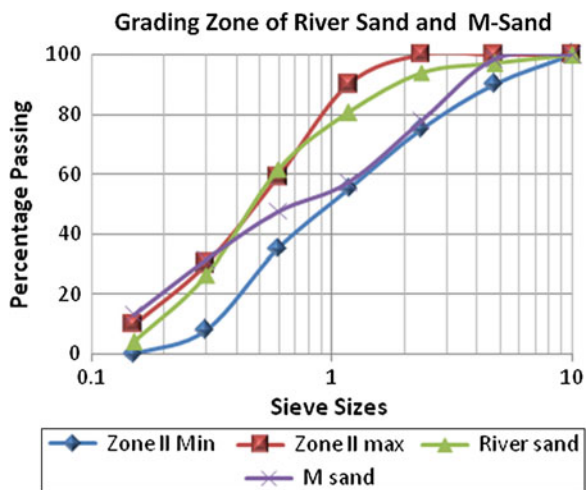
Table 2 Mix design ratio of concrete

Type of concrete	Cement	F.A.	C.A.	W/C
Normal concrete	1	1.660	2.90	0.5
M-sand concrete	1	1.648	2.90	0.5

3 Experimental Investigation

The mix ratio is prepared for M20 grade concrete for both conventional sand and also M-Sand. Detailed mix ratio of each grade of concrete is given in Table 2. The cube sizes of (150 × 150 × 150) mm Specimen are prepared for compressive strength. The cylinder of height 30 cm and 15 cm diameter are prepared for tensile strength. The specimens of size (100 × 100 × 500) mm are used for flexural strength test. The specimens are tested for 7 and 28 days. Totally there are 12 cubes, 12 cylinders and 12 flexural beams casted. All the specimens are de-moulded after 24 h, and curing is done in water for 7 and 28 days.

4 Results and Discussion

(a) **Compressive Strength of Concrete**
The compression test was conducted as per IS 516-1959. Compressive strength of concrete mixes made with and without manufactured sand was determined at 7 and 28 days. The test results are given in Table 3 and Fig. 2. The strength of manufactured sand concrete with respect to their compressive strength at the age of 7 and 28 days was 92 and 98 % of M20 grade when compared to same grade of conventional concrete. Therefore, the ultimate strength were taken at the peak load which was considered to represent the material strength of the manufactured sand concrete. Figure 2 shows the gradual and good increase of compressive strength of manufactured sand concrete when but marginally low strength compared to controlled concrete specimens. The variation in fine aggregate has affected the concrete to a minimal extent. Since the properties of the fine aggregate are similar to that of the river sand, the compressive strength was not influenced predominantly.

(b) **Split Tensile Strength of Concrete**
The split tensile test was conducted as per IS 516-1959. Tensile strength of concrete mixes made with and without manufactured sand was determined at 7 and 28 days. The test results are given in Table 4 and Fig. 3. The strength of manufactured sand concrete with respect to their tensile strength at the age of 7 and 28 days was 92 and 94 % of M20 grade when compared to same grade of

Table 3 Average compressive strength value

Tested on	Normal concrete	Manufactured sand concrete
7th day	19.07	17.63
28th day	31.03	30.44

Fig. 2 Compressive strength versus age
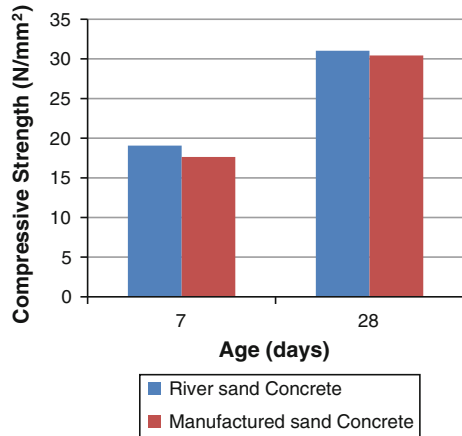
Table 4 Average tensile strength value

Tested on	Normal concrete	Manufactured sand concrete
7th day	2.30	2.11
28th day	3.07	2.87

Fig. 3 Split tensile strength versus age
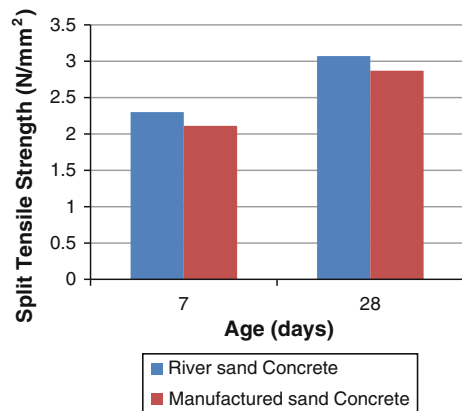
conventional concrete. Therefore, the ultimate strength were taken at the peak load which was considered to represent the material strength of the manufactured sand concrete. Figure 3 shows the gradual and good increase of tensile strength of manufactured sand concrete but marginally low strength when compared to controlled concrete specimens. The discussions for the behaviour of the compressive strength of the concrete with manufactured sand holds good for the results of splitting tensile strength of the concrete.

(c) **Flexural Strength of Concrete**

The flexure test was conducted as per IS 516-1959. Flexural strength of concrete mixes made with and without manufactured sand was determined at 7

Table 5 Average flexural strength value

Tested on	Normal concrete	Manufactured sand concrete
7th day	3.675	3.60
28th day	4.8	4.65

Fig. 4 Flexural strength versus age
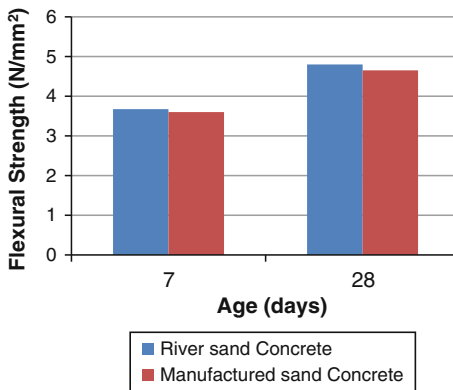
and 28 days. The test results are given in Table 5 and Fig. 4. The strength of manufactured sand concrete with respect to their flexural strength at the age of 7 and 28 days was 98 and 97 % of M20 grade when compared to same grade of conventional concrete. Therefore, the ultimate strength were taken at the peak load which was considered to represent the material strength of the manufactured sand concrete. Figure 4 shows the gradual and good increase of flexural strength of manufactured sand concrete but marginally low strength when compared to controlled concrete specimens. The presence of more micro fines in manufactured sand is responsible for the very less decrease in flexural strength, when compared to the splitting tensile strength and compressive strength values of concrete.

5 Conclusions

- From the research following conclusions were obtained Compressive strength, Splitting tensile strength and Flexural strength of Manufactured sand concrete specimens were in conformation with the control concrete specimens at all the ages.
- The concrete containing manufactured sand had strength higher than the target mean strength, for which the mix design was made.
- The decrease in 7 days strength of concrete to the conventional concrete was more in comparison with the 28 days strength, which implies there is good increase in strength of concrete with age.

- From this experimental investigation, it was also observed that replacement of natural sand by manufactured sand will reduce the strength of concrete marginally.
- The effect of the specific gravity, grading and fineness modulus on the compressive and splitting tensile strength of concrete was considerably low, since the difference of the aggregate properties of manufactured sand was moreover similar to the river sand.
- The presence of more fines in manufactured sand gave good flexural strength results at 7 and 28 days on comparison with compressive and splitting tensile strength of concrete. But the presence of fines did not increase the flexural strength of manufactured sand concrete more than the conventional concrete.
- From the following studies, we can conclude that manufactured sand is a good alternative for river sand in concrete.

References

1. Hudson BP (1997) Manufactured sand for concrete. Indian Concr J 71:237–240
2. Ahmad S, Mahmood S (2008) Effects of crushed and natural sand on the properties of fresh and hardened concrete. In: 33rd conference on our world in concrete and structures, Singapore, article ID 100033006
3. Elavenil S, Vijaya B, Hariharan K (2005) Manufactured sand, a solution and an alternative to river sand and in concrete manufacturing. J Eng Comput Appl Sci (JEC&AS) 2(2):20–24
4. Guide to the specification and use of manufactured sand in concrete. Cement concrete & aggregates Australia (CCAA), T60, Nov 2008
5. Shanmugapriya T, Uma RN (2012) Optimization of partial replacement of M-S and by natural sand in high performance concrete with silica fume. Int J Eng Sci Emerg Technol 2(2):73–80
6. Chitlange MR, Pajgade PS (2010) Strength appraisal of artificial sand as fine aggregate in SFRC. ARPN J Eng Appl Sci 5(10):34–38

Bibliography

7. SyamPrakash V (2007) Ready mixed concrete using manufactured sand as fine aggregate. In: 32nd conference on our world in concrete and structures, Singapore, article ID 100032053
8. Nanthagopalan P, Santhanam M (2010) Fresh and hardened properties of self-compacting concrete produced with manufactured sand. J Cem Concr Compos 33:353–358
9. IS 516-1959 Indian standard code of practice-methods of test for strength of concrete. Bureau of Indian standards, New Delhi, India
10. IS 383-1970 Indian standards specification for coarse and fine aggregate from natural sources of concrete. Bureau of Indian Standard, New Delhi, India
11. IS 456-2000 Indian Standard code of practice for plain and reinforced concrete. Bureau of Indian standards, New Delhi, India
12. IS 10262-2009 Recommended guidelines for concrete mix design. Bureau of Indian standard, New Delhi, India
13. IS 4031 (Part V) (1988) Methods of physical tests for hydraulic cement (compressive strength other than masonry cement). Bureau of Indian standard, New Delhi, India
14. IS 2386-1963 Methods of test of aggregates for concrete. Bureau of Indian standard, New Delhi, India

Part XIX
Concrete, Steel and Durability

Characterization of Recycled Aggregate Concrete

S.R. Suryawanshi, Bhupinder Singh and Pradeep Bhargava

Abstract The effects of using crushed waste concrete as coarse aggregates upon fresh and hardened properties of concrete were investigated through series of testing concrete cylinder specimens to failure. The coarse recycled concrete aggregate (RCA) used in this investigation was sourced from the tested concrete specimens like cubes, cylinders, prisms and beam specimens originally tested for various purposes in the concrete testing laboratory of IIT Roorkee. Total six numbers of concrete mixtures were prepared. These mixtures were differing only in amount of coarse RCA used. The mixture without any RCA was referred as control mixture. Considerable effect of replacement level on compressive strength was observed. Moreover increase in peak strain and significant decrease in static modulus was observed. Stress-strain curves generated during testing were utilized to evaluate normalized toughness and ductility index. Higher value of replacement level found decreasing normalized toughness and ductility index.

Keywords Recycled concrete aggregate (RCA) · Recycled aggregate concrete (RAC) · Natural aggregate concrete (NAC) · Stress-strain curve (SSC) · Replacement level

1 Introduction

The European Environmental Commission (EEC) envisages that there will be enormous increase in the available quantities of construction and demolition concrete waste from 55 million tons in 1980 to 302 million tons by the year 2020 in the EEC member countries. In other part of the world, rather in India the picture is not so different. The Central Pollution Control Board has estimated current quantum of solid waste generation in India is to the tune of 48 million tons per annum out of which, waste from construction industry only accounts for more than 25 % [1].

S.R. Suryawanshi (✉) · B. Singh · P. Bhargava
Department of Civil Engineering, IIT Roorkee, Roorkee, India

Usually most of the waste materials produced by demolished structures dumped on open spaces creating nuisance to the environment. This becomes serious issue in urban areas, already facing the shortage of land due to the industrialization, globalization and commercialization. Management of such a high quantum of waste puts huge pressure on the solid waste management system.

With the objective to protect the environment, to control endless consumption of natural aggregate and to use the potential of C&D waste, many governments adopted the policy to support the programs promoting the reuse of recycled aggregate. Pilot studies [2], have shown that, use of RA in concrete can result in a 20 % saving in cement consumption and a 35 % saving in the consumption of coarse aggregates without compromising the mechanical strength of concrete. Some of the organizations are one step ahead in setting up the standards to quantify the quality of recycled aggregates like BCSJ, RILEM, DIN4226.1000 and prEN13242:2002. As a result, the use of recycled aggregates have gained momentum in some of practical applications of civil engineering projects, however, hardly used in RCC structures due to the prejudice of that RCA had inferior quality to that of NA. In reality, few purported inferior properties like higher water absorption capacity of RCA compare to NA are because of only adhered mortar, which can be improved by suitable treatment.

This study aims to increase the insight of the effects of replacement level of the recycled aggregate on hardened concrete properties so as to promote the practical application of recycled aggregates in structural concrete. A test program was carried out to determine the mechanical properties of concretes prepared with natural and recycled concrete aggregates. The influence of RCA on the peak stress and the peak strain, the shape of SSC, and on the elastic modulus were analyzed. Moreover, effect of RCA content on ductility index and normalized toughness of RAC also experimentally evaluated.

2 Experimental Program

2.1 Materials Used

2.1.1 Cement

Locally produced ordinary Portland cement confirming to IS 1489 [3], was used in this study. The specific gravity of cement was 3.12 and fineness was 3,082.4 cm^2/g. The use of admixtures was avoided.

2.1.2 Fine Aggregate

Natural river sand confirming to IS 383 [4] and grading zone II, was used as fine aggregates. Basic properties such as specific gravity was determined as per IS 2386 [5].

Table 1 Physical properties of natural and recycled concrete aggregate

Type	Nominal size (mm)	Attached mortar (%)	Moisture content (%)	Water absorption (%)	Specific gravity	Aggregate crushing value
NA	20–4.75	–	0.05	0.5	2.65	18.33
RCA	20–10	25.2	2.50	3.5	2.37	24.43
RCA	10–4.75	52.0	3.62	6.0	2.34	26.64

2.1.3 Coarse Aggregates

The crushed aggregates as per IS 383 [4] of nominal size of 20 mm were used as natural coarse aggregates. Recycled concrete aggregates were extracted from laboratory tested concrete specimens crushed by light weight hammers. All relevant properties of natural and recycled concrete aggregates are summarized in Table 1. For consistency, the gradation of the recycled concrete aggregate was kept the same as that of the natural aggregate.

2.2 Preparation of Concrete Mixture

The concrete mixtures were prepared with the use of natural and recycled coarse aggregates in six combinations; i.e., 100 % natural, 80 % natural + 20 % recycled, 60 % natural + 40 % recycled, 40 % natural + 60 % recycled, 20 % natural + 80 % recycled and 100 % recycled. The mix proportion of control mix was done using the absolute volume method by assuming the aggregates were at a saturated surface-dried condition in accordance to IS 10262 [6]. In other mixes NA was just replaced by RCA with specified percentage. All the mixes have the free water-to-cement (w/c) ratio of 0.50 and a fine aggregate to total aggregate ratio of 0.37. As the densities of the natural and recycled coarse aggregates were different, the actual amounts of recycled coarse aggregates in the mixes were slightly different.

To capture the effect of replacement level on the compressive strength all other factors must be kept the same as that of control mix. Even addition of extra water meant to control the slump loss also was avoided. Further, gradation of the RCA must match the gradation of the NA as the water absorption capacity of the RCA depends upon the aggregate size. It was observed that small size RCA aggregate has more water absorption capacity due to more amount of adhered residual mortar compare to large size RCA aggregate. It is important to note that the term RCA content, percentage replacement or replacement level used hereafter really means relative residual mortar content in that particular mix. Because all the purported inferior mechanical and elastic properties of the RAC compared to the NAC are the result of adhered mortar only. The amount of water and materials used in these 6

Table 2 Mixture composition (kg/m^3)

ID	Cement	Water	FA	NCA	RCA (20–10) mm size	RCA (10–4.75) mm size	% RCA (R)
R00	378.60	189.37	692	1,145	0	0	0.00
R20	378.60	189.37	692	916	141	85	20.00
R40	378.60	189.37	692	687	289	169	40.00
R60	378.60	189.37	692	458	433	254	60.00
R80	378.60	189.37	692	229	577	339	80.00
R100	378.60	189.37	692	0	721	424	100.00

mixes and there designations are given in Table 2. All the concrete mixtures were mixed mechanically before casting into moulds and compacted on a vibrating table.

2.3 Testing of Concrete Specimens

Each set representing certain concrete mixture consisted of three cylinder specimens of 150 mm diameter and 300 mm height. All the test specimens were caste and cured for 28 days as per guidelines specified in IS 516-1959 [7]. In order to get the complete load displacement behavior, micro computer controlled electro-hydraulic servo tester INSTRON of 2,500 kN capacity was used. The strain rate was kept constant in accordance to IS 2854-1964 [8]. To capture accurate strain, additional LVDTs were employed at selected locations within specified gauge length of the specimen as shown in Fig. 1. In order to reduce the influence of improper seating if it was, each specimen was preloaded before actual loading.

Fig. 1 Test set up for axial compression test to determine compressive stress and stress-strain curve

3 Results and Discussions

The main parameters used in this investigation to characterize mechanical properties of RAC were compressive strength, peak strain, ultimate strain at prescribed stress level (0.67 f_c', in this case) and static modulus of elasticity. Table 3 reveals the experimentally obtained values of considered parameters. The values in Table 3 represent the average of each set consisting of three nominally identical specimens.

3.1 Compressive Strength

The compressive strength is the peak stress of the test specimen under uniaxial compression. It was evaluated after 28 day of wet curing according to IS 516-1959 [7], on cylindrical concrete specimens. The mean values are obtained from at least three specimens. The test results indicated the RCA content has remarkable influence on the compressive strength of the concrete. Average values of results for the compressive strength of RAC were plotted against percentage replacement in Fig. 2. The trend in decreasing compressive strength on increased RCA content is found in good agreement with trends compiled by Tam [9]. Similar trend of reduced compressive strength with increasing replacement level of RCA was obtained by Poon [10], Xiao [11], Etxeberria [12], Gonzalez et al. [13] and Kishore [14]. However, results obtained by Ridzuan [15] showed opposite trend. Ridzuan [15] recorded increase in compressive strength with increase in replacement level. Rao [16] reported that strength of RCA concrete was depend upon the type of RCA, replacement ratio, water cement ratio and moisture state of the RCA. Rao [16] observed that the strength of RAC and reference concrete was comparable even at 100 % replacement, provided that the water cement ratio was higher than 0.5 and at water cement ratio 0.4 the strength of RAC was only 75 % of the reference concrete.

Table 3 Summary of the compression test results

Set no.	Percentage replacement (R) (%)	Compressive strength f_c' (MPa)	Peak strain ε_0	Ultimate strain ε_u	Static modulus E_c (MPa)	Normalized toughness T_n	Ductility index μ
Set I	00	38.19	0.0019	0.0036	35,360	1.3426	0.6416
Set II	20	36.65	0.0020	0.0037	31,610	1.3521	0.6757
Set III	40	35.82	0.0021	0.0034	28,674	1.2104	0.6877
Set IV	60	35.36	0.0023	0.0039	24,654	1.2250	0.6396
Set V	80	34.69	0.0024	0.0036	28,296	1.1351	0.6944
Set VI	100	34.10	0.0025	0.0037	20,152	1.1441	0.5820

Fig. 2 Variation of compressive stress with percentage replacement of RCA
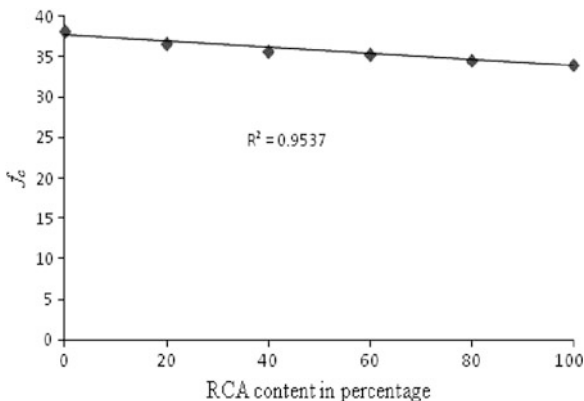
3.2 Modulus of Elasticity

Modulus of elasticity was determined in compression on cylindrical specimens according to IS 2854 [8]. The mean values obtained after 28 days for each set are reported in Table 3 and plotted as a function of the RCA content in Fig. 3. The values of modulus of elasticity were affected by the use of recycled aggregate, since considerable decreases with percentage of replacement have been detected. This decrease is caused by the use of recycled aggregate with lower Young modulus than conventional aggregate. Various authors show greater decrease in modulus of elasticity than those obtained for compressive strength, and more pronounced as replacement percentage was increased. There exists fair degree of diversity in values regarding percentage reduction of static modulus with replacement ratio. However, all experimental investigations reporting reduced modulus of elasticity as compiled by Tam [9]. Values obtained in this investigation are in good agreement with the values found by Xiao [11].

Fig. 3 Variation of modulus of elasticity with RCA content
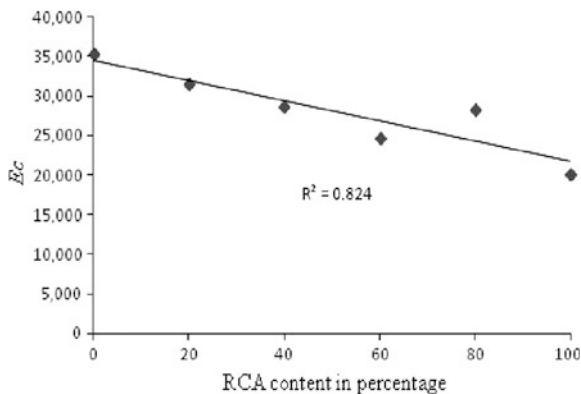
3.3 Stress-Strain Curves

Figure 4 reveals typical stress strain curves for different percentages of replacements. All the concretes present very similar stress-strain curves regardless of the recycled aggregate replacement ratio. The shape is linear up to 0.4 fc, and then it becomes parabolic. However, a considerable shift of the curve was observed. At the same stress level, the strain in recycled aggregate concrete is higher compare to the strain in control concrete. The presence of mortar adhered to the recycled aggregate, which is more compliant than the conventional aggregate, allows the increase of strains in the ascending branch [13]. Consequently this increase leads to an increase in the peak strain value which is particularly significant when the recycled aggregate is used with replacement ratio of 100 %.

The shape of the descending branch of recycled aggregate concrete is similar that of natural aggregate concrete. However, an increase in slope is detected when the percentage of recycled aggregate is increased in the contrast of the results obtained by Belen [13]. This implies decreased rate in increase of ultimate strain (strain at which failure is defined, in this case 0.67 $f_c' fc$). In other words $\varepsilon/\varepsilon_0$ ratio decreases on increase of RCA content as shown in Fig. 5, which in turn indicate that the recycled aggregate concrete behaves in more brittle manner than conventional concrete. This is in fair agreement with results obtained by Xiao et al. and Li et al.

3.4 Normalized Toughness and Ductility Index

In addition to strength, as reported by Sahoo [17], structural members can also be characterized on the basis of their deformation behavior. Normalized toughness and

Fig. 4 Experimental stress-strain curves of different RCA content
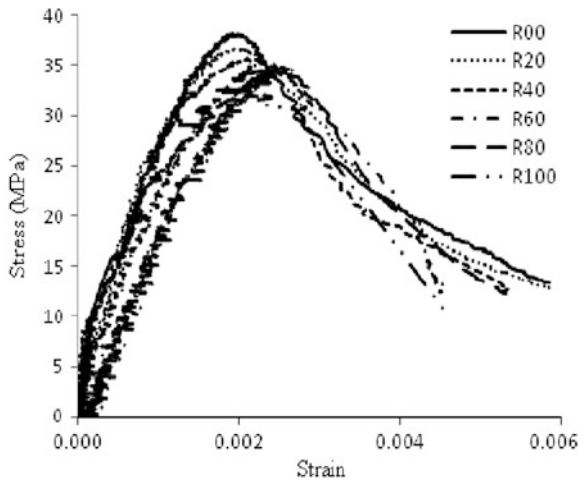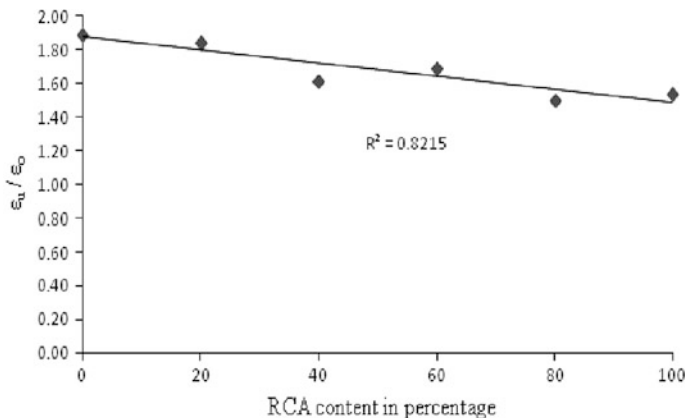
Fig. 5 Normalized ultimate strain vis-à-vis RCA content

ductility index are key indicators of deformation response and the structure may be evaluated in terms of two parameters normalized toughness (T_N) and Ductility index (μ). The parameter T_N is an indicator of the energy absorption capacity and represents the work done for a specified deformation in a member. The mentioned ductility index, μ, is a measure of the structure to undergo inelastic deformations beyond the initial yield deformation while retaining at least a specified minimum load resistance, and adapted from Xie et al.

The parameter normalized toughness, T_N, is evaluated as the area under normalized stress versus normalized strain curve up to two third of the peak stress in the post peak region, showed in Fig. 6. The ratio of area under post peak region up to two third of peak stress to area under complete curve up to two third of peak stress in post peak region was treated as ductility index, μ. The two third limit has been selected since it corresponds to maximum usable compressive strength in

Fig. 6 Evaluation of toughness and ductility of concrete
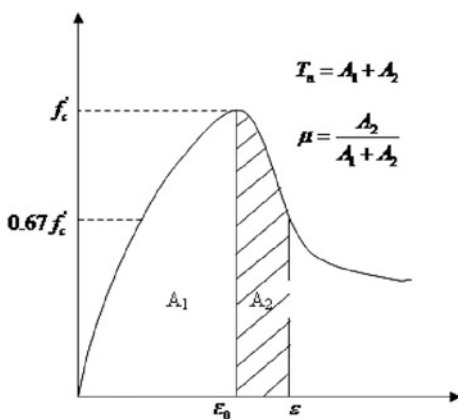
concrete specified by the Indian Standard, IS 456:2000 [18]. It was found that increased replacement level reduced the normalized toughness (T_N) as well as the ductility index (μ) of recycled aggregate concrete as revealed in Table 3.

4 Conclusions

1. The test results indicated significant reduction in compressive strength as well as in elastic modulus at higher level of RCA content in RAC.
2. The shape of stress-strain curves of the recycled concretes is similar to that of conventional concrete but not identical. A shift to the right in the stress-strain curve of the recycled concrete was detected.
3. The slope of stress-strain curve found reduced in pre-peak region of SSC and found increased in post-peak region of SSC at higher replacement level of RCA. This implies the relative decrease in elastic modulus and relative increase in brittleness of RAC.
4. Not much vivid difference was noticed in the ultimate strain value of NAC and RAC. However, the ratio of ultimate strain and peak strain reduced significantly at higher replacement level of RCA indicating RAC was more brittle.
5. The increase in replacement level of recycled concrete aggregate reduced the normalized toughness (T_n) as well as the ductility index (μ) of recycled aggregate concrete.

References

1. Bhattacharyya SK, Barai SV, Chakradhar Rao M (2011) Recycled coarse aggregates and its use in concrete. ICI J 11(4):27–40
2. Singh SK & Sharma PC (2007) "Use of recycled aggregates in concrete—A paradigm shift". J N Build Mater Constr World 13(4):173–183
3. Bureau of Indian Standards, IS 1489 Part (I), 43 grade ordinary Portland cement-specification (reaffirmed 2005). Bureau of Indian standards, New Delhi (India)
4. Bureau of Indian Standards, IS 383-1970, Specification for coarse and fine aggregate from natural sources for concrete. Bureau of Indian standards, New Delhi (India)
5. Bureau of Indian Standards, IS 2386-1967 Part (III), Method of test for aggregates for concrete. Bureau of Indian standards, New Delhi (India)
6. Bureau of Indian Standards, IS 10262-1982, Guidelines for concrete mix design. Bureau of Indian Standards, New Delhi (India)
7. Bureau of Indian Standards, IS 516-1959, Method of tests for strength of concrete. Bureau of Indian standards, New Delhi (India)
8. Bureau of Indian Standards, IS 2854-1964, Method of test for determining modulus of elasticity. Bureau of Indian standards
9. Vivian WY, Tam CM, Le KN (2007) Removal of cement mortar remains from recycled aggregate using pre-soaking approaches. Resour Conserv Recycl 50(1):82–101

10. Poon CS, Shui ZH, Lam L, Fok H, Kou SC (2004) Influence of moisture states of natural and recycled aggregates on the slump and compressive strength of concrete. Cem Concr Res 34 (1):31–36

11. Xiao J, Li J, Zhang C (2005) Mechanical properties of recycled aggregate concrete under uniaxial loading. Cem Concr Res 35(6):1187–1194

12. Etxeberria M, Vázquez E, Marí A, Barra M (2007) Influence of amount of recycled coarse aggregates and production process on properties of recycled aggregate concrete. Cem Concr Res 37(5):735–742

13. González-Fonteboa B, Martínez-Abella F, Carro López D, Seara-Paz S (2011) Stress-strain relationship in axial compression for concrete using recycled saturated coarse aggregate. Constr Build Mater 25:2335–2342

14. Bhikshma V, Kiskore R (2011) Development of stress block and design parameters for recycled aggregate concrete members. Asian J Civ Eng (Build Hous) 12(2):179–195

15. Ridzuan ARM (2001) The influence of recycled aggregate concrete on the early compressive strength and drying shrinkage of concrete. In: Proceeding of the international conference on structural engineering, mechanics and computation, 2001, pp 1415–1421

16. Rao A, Jha KN, Misra S (2007) Use of aggregates from recycled construction and demolition waste in concrete. Resour Conserv Recycl 50(1):71–81

17. Sahoo DK (2009) An investigation of the strength of bottle-shaped struts. Ph.D thesis, Indian Institute of Technology Roorkee, Roorkee (India), 2009

18. Bureau of Indian Standards, IS 456, Plain and reinforced concrete-code of practice. Bereau of Indian Standards, New Delhi (India)

Durability of High Volume Flyash Concrete

M. Vaishnavi and M. Kanta Rao

Abstract Concrete is by far the most widely used construction material worldwide. First, it consumes huge quantities of virgin materials. Second, the principal binder in concrete is cement, by these production the greenhouse gas is increased which causes effects the global warming and climatic changes. Many structures suffer from lack of durability that has an adverse effect on the resource productivity of the industry. The supplementary cementing materials like natural materials, by-products or industrial wastes are used. The cement is replaced with high volumes of fly ash (>40 %) for M30 and M40 grades with % variation of flyash used in this grades and also finding the durability of high volume fly ash concrete (HVFC). The compressive strength test to be conducted to justify the strength properties of HVFC. Few durability properties like resistance to 2 and 5 % sulfuric acids and resistance to 2 and 5 % hydrochloric acids, resistance to 5 % magnesium sulfate solution and resistance to 5 % sodium chloride solution were studied. The mass variation of the specimens are also to be studied for M30 and M40 grades of concrete for HVFC when immersed in acids, the strength tests of the specimens that are immersed in acid solutions to be found. The deterioration effect of sulphuric acid and hydrochloric acid are to be compared. The strength parameters of fly ash replacing will be compared with the nominal mix of HVFC.

Keywords CO_2 · HVFC · Flyash · Durability · Pozzolanaic reaction

1 Introduction

Energy conservation in the building industry is a worldwide concern, by taking this into consideration the engineers and scientists have taken this as a challenge and exploring new ways of producing building materials with minimum energy unit.

M. Vaishnavi (✉) · M. Kanta Rao
V.R. Siddhartha Engineering College, Vijayawada, Andhra Pradesh, India

1.1 Flyash

Flyash is a by-product of coal-fired from thermal power plants, it is approximately 80 million tons each year, and its percentage utilization is less than 10 % during last few years [1]. Any concrete containing flyash that is greater than 50 % by mass of the total cementitious materials is considered as high volume flyash concrete (HVFC). The production of Portland cement is not only costly and energy-intensive, but it also produces large amounts of carbon dioxide (CO_2). Flyash is commonly used in concrete in replacements ranging from 0 to 30 % by mass of the total cementitious material. However, research has shown that using a 50 % or greater replacement of flyash can have a wide range of benefits. Flyash exits in a number of different chemistries and classes, but it is primarily the particle size that is important. The average particle size of flyash is about 20 μm, which is similar to the average particle size of Portland cement. Particles below 10 μm provide the early strength needed in concrete, while particles between 10 and 45 μm react more slowly. Depending on the lime content, flyash is categorized as low lime flyash (CaO < 10 %) and high lime flyash (CaO > 10 %). Low lime flyash corresponding to class 'F' and high lime flyash corresponding to class 'C' Flyash properties are hollow spherical glassy particles of size between 1 to 150 μm in diameter and also passes through the 45 μm sieve. Flyash used supplementary cementitious materials in the concrete. The specific gravity of flyash particles ranges between 2.0 and 2.4 depending on the source of coal. The fineness of flyash is typically in the range of 250–600 m^2/kg.

Flyash is a by-product and therefore less expensive than Portland cement; it is also known to improve workability and reduce internal temperatures. With large quantities of flyash available around the world at low costs, the use of HVFA seems to offer the best short-term solution to rising cement demands. It improves the durability when used as replacement of cement, as an admixture in concrete and increases the strength of the concrete [2]. There is advantage in adding flyash to concrete products cured at normal atmospheric conditions or in the autoclave at high temperatures and pressures. Recently, flyash has been increasingly used in the concrete industry. In some cases, large volume of (>40 %) flyash is used to achieve desired concrete properties and lower the cost of concrete production. This limits the wide use of high-volume flyash concrete by engineers. As flyash is more complex than silica, however, and contains CaO, Al_2O_3, Fe_2O_3 and other impurities, its composition is dependent on the source and operational conditions at each power plan. Different approaches are used to accelerate the pozzolanic reaction, these approaches include (i) mechanical treatment (grinding), (ii) accelerated curing and autoclaving, and (iii) chemical activating. Chemical activating involved using alkali activation and sulfate activation. However, alkali activation used in concrete may lead to alkali-silica reaction, and sulfate activation may decrease the durability of concrete due to the large ettringite contents. If the materials show high pozzolanic activity, the heat produced during hydration is higher [2].

It is well known that the service life of a concrete structure is strongly dependent on its material properties, which are controlled by the microstructure characteristics of concrete. It is generally recognized that the incorporation of pozzolanic materials

as a partial replacement for Portland cement in concrete is an effective means for improving the properties of concrete [3]. Concrete containing flyash as partial replacement of fine aggregate will have no delayed early strength development, but rather will enhance its strength on long-term basis [1]. The size of the pores of crystalline hydration products, make the microstructure of concrete more uniform and improve the impermeability and durability of concrete. These improvements can lead to an increase in the service life of a concrete structure.

1.2 Water-Tightness and Durability

In general, the resistance of a reinforced concrete structure to corrosion, alkali aggregate expansion, sulfate and other forms of chemical attack depends on the water-tightness of the concrete.

The water-tightness is greatly influenced by the amount of mixing-water, type and amount of supplementary cementing materials, curing, and cracking resistance of concrete. High-volume flyash concrete mixtures when properly cured, are able to provide excellent water-tightness and durability.

1.3 Pozzolanaic Reaction

A pozzolanic reaction occurs when a siliceous or aluminous material reacts with calcium hydroxide in the presence of humidity to form compounds exhibiting cementitious properties. In the cement hydration development, the calcium silicate hydrate (C–S–H) and calcium hydroxide [Ca(OH)$_2$ or CH] are released within the hydration of two main components of cement namely tricalcium silicate (C3S) and dicalcium silicate (C2S) where C, S represent CaO and SiO$_2$. Hydration of C3S, C2S also C3A and C4AF (A and F symbolize Al$_2$O$_3$ and Fe$_2$O$_3$), respectively, is important. Upon wetting, the following reactions occur.

$$2(3CaO \cdot SiO_2) + 6H_2O \rightarrow 3CaO \cdot 2SiO_2 \cdot 3H_2O + 3Ca(OH)_2 \qquad (1)$$

$$2(2CaO \cdot SiO_2) + 4H_2O \rightarrow 3CaO \cdot 2SiO_2 \cdot 3H_2O + Ca(OH)_2 \qquad (2)$$

$$3CaO \cdot Al_2O_3 + 31H_2O + 3CaSO_4 \rightarrow 3CaO \cdot Al_2O_3 \cdot 3CaSO_4 \cdot 31H_2O \qquad (3)$$

$$4CaO \cdot Al_2O_3 \cdot Fe_2O_3 + 10H_2O + 2Ca(OH)_2 \rightarrow 6CaO \cdot Al_2O_3 \cdot Fe_2O_3 \cdot 12H_2O \qquad (4)$$
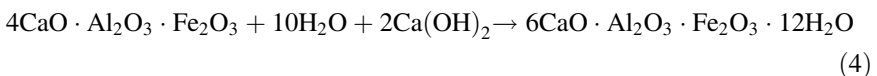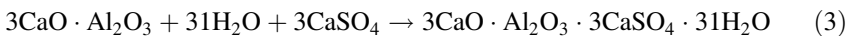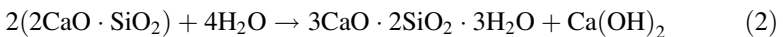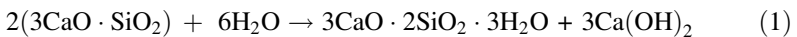
The crystallized compound of C–S–H and C–A–H, which are called cement gel, hardened with age to form a continuous binding matrix with a large surface area and are components responsible for the development of strength in the cement paste Pozzolana-lime reactions are slow, generally starting after one or more weeks. The

behavior of the delay in pozzolanic reaction will result in more permeable concrete at early ages and gradually becomes denser than plain concrete with time. This behavior is due to two reasons: Firstly, pozzolana particles become the precipitation sites for the early hydration C–S–H and CH that hinders pozzolanic reaction. Secondly, the strong dependency of the breaking down of glass phase on the alkalinity of the pore water that could only attain the high pH after some days of hydration. Pozzolana can partially replace cement in mortar or concrete mix without affecting strength development. The effect of the pozzolanic reaction produces more cement gel (i.e. C–S–H and C–A–H) reducing the pore size, blocks the capillary and produces denser concrete thus making it stronger and more durable [4].

2 Durability

Durability is the ability to endure. According to American Concrete Institute (ACI) Committee 201, durability of Portland cement concrete is defined as its ability to resist weathering action, chemical attack, abrasion, or any other process of deterioration; that is, durable concrete will retain its original form, quality, and serviceability when exposed to its environment. No material is inherently durable; as a result of environmental interactions the microstructure and, consequently, the properties of materials change with time. A material is assumed to reach the end of service life when its properties under given conditions of use have deteriorated to an extent that the continuing use of the material is ruled either unsafe or uneconomical. Durability of concrete can be defined as the ability to perform satisfactorily in the exposure condition to which it is subjected over an intended period of time with minimum of maintenance. Materials related failures in concrete deterioration could be caused by: the use of inappropriate materials, poor construction practices, environmental related causes of concrete durability problems etc.

The inferior durability characteristics of concrete may be caused by the environment that the concrete is exposed to. The following environmental condition can affect the concrete durability: temperature, moisture, physical factors, chemical factors, and biological factors. These factors may be due to weathering conditions (temperature, and moisture changes), or to abrasion, attack by natural or industrial liquids and gases, or biological agents. Durability problems related to environmental causes include the following: steel corrosion, delamination, cracking, carbonation, sulfate attack, chemical attack, scaling, spalling, abrasion and cavitation.

3 Experimental Program

The experimental program consisted of arriving at suitable mix proportions for M30 and M40 grade high volume flyash concrete (HVFC) that satisfies the fresh properties as per American code specifications in replacement of flyash in cement. The

objective of the study is to study the strength parameters, study the durability of HVFC short-term and long-term, study the flow behavior of HVFC. Investigations on performance of HVFC concrete are found such as preliminary investigations of cementitious blends, optimization of flyash concrete mixes and influence of durability of HVFC concrete.

For durability studies of M30 and M40 grade HVFC concretes, a total of 120 cubes were casted. Out of which, 60 cubes were of M30 grade and 60 cubes were of M40 grade. Of these 60 cubes, 6 cubes each were tested for resistance to 2 % sulphuric acid attack, resistance to 2 % hydrochloric acid attack, resistance to 5 % sulphuric acid attack resistance to 5 % hydrochloric acid attack and out of the remaining 6 cubes 3 cubes each were tested for 5 % magnesium sulfate attack and 5 % sodium chloride attack.

3.1 Materials

A brief description of the materials used and their physical properties are discussed below.

Cement: Ordinary Portland cement of 53 grade confirming to IS: 12269-1987.

Fine Aggregate: Locally available riverbed sand confirming to Zone-2 according to IS: 383 were used. The physical properties of fine aggregate were tested in accordance with IS: 2386-1963.

Coarse Aggregate: Locally available crushed granite metal of sizes 12, 16 and 20 mm was used in the present investigation work and tested as per IS: 383-1970.

4 Tests on Hardened Concrete

4.1 Determination of Compressive Strength

The compression test on cubes was carried out according to the procedure given in IS: 516-1959. The cubes were cured under water for 28 days, then placed in acids for 3, 7 and 28 days later they were tested for compression strength.

4.2 Non-destructive Tests

Rebound hammer test and ultrasonic pulse velocity test were conducted as per IS: 13311 (Part 2)-1992 and IS: 13311 (Part 1)-1992 to find out the compressive strength and assess the quality of concrete.

4.3 Acid Attack Study

The chemical resistance of the concrete was studied through chemical attack by immersing them in an acid solution. After 28 days period of curing twelve specimens each of two grades M30 and M40, the initial mass, body diagonal dimensions, ultrasonic pulse velocity, rebound hammer value were measured. Six specimens of each grade of concrete were immersed in 2 and 5 % H_2SO_4 solution and 2 and 5 % hydrochloric acid solutions. For preparing 2 % acid solution 2 l of concentrated acid is mixed in 98 l water and 5 % acid solution is prepared by mixing 5 l concentrated acid in 95 l of water.

4.4 Sulfate Attack and Chloride Attack Study

The chemical resistance of the concrete was studied through chemical attack by immersing them in 5 % magnesium sulfate solution and 5 % sodium chloride solution. 5 % magnesium sulfate solution and 5 % sodium chloride solution are prepared by mixing 5 kg of magnesium sulfate salt in 100 l of water and 5 kg of sodium chloride salt in 100 l of water. After 28 days period of curing six specimens each of two grades M30 and M40, the initial mass, ultrasonic pulse velocity, rebound hammer value were measured. Three specimens of each grade of concrete were immersed in 5 % magnesium sulfate solution and 5 % sodium chloride solution. After 7 and 28 days of immersion, change in mass, change in ultrasonic pulse velocity (UPV) and change in rebound number are recorded. After 28 days of immersion, change in average compressive strength is also observed.

5 Results and Discussions

5.1 Compressive Strength of Flyash

The compressive strength of flyash concrete mixes with 20, 30, 40, and 50 % fine aggregate replacement with flyash, was higher than the control mix at all ages. Compressive strength of all mixes continued to increase with the increase in age. However, the rate of increase of strength decreases with the increase in flyash content. This trend is more obvious between 40 and 50 % replacement level. However, maximum strength at all ages occurs with 50 % fine aggregate replacement. This increase in strength due to the replacement of fine aggregate with flyash is attributed to the pozzolanic action of flyash. In the beginning (early age), flyash reacts slowly with calcium hydroxide liberated during hydration of cement and does

not contribute significantly to the densification of the concrete matrix at early ages. Concrete with flyash shows higher strength at early ages because inclusion of flyash as partial replacement of sand starts pozzolanic action and densification of the concrete matrix, and due to this strength of flyash concrete is higher than the strength of control mix even at early ages.
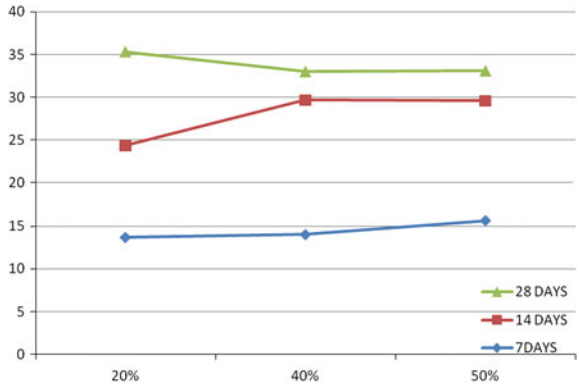
Compressive strength (ordinate) of flyash versus % replacement of flyash (abscissa) for M30 grade of concrete
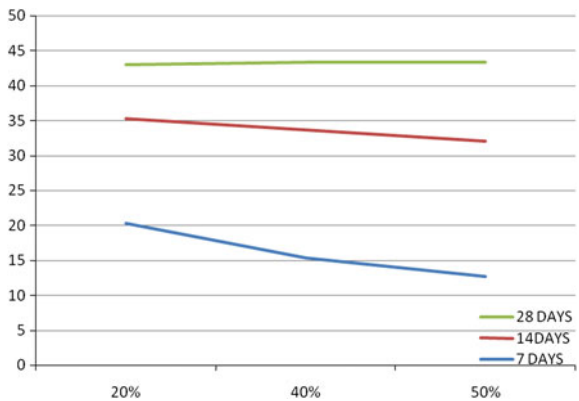
Compressive strength (ordinate) of flyash versus % replacement of flyash (abscissa) for M40 grade of concrete

6 Acid Attack Test

6.1 Visual Appearance

It has been observed that in specimens immersed in 5 % sulfuric acid, after 28 days of immersion the cement mortar from the surface was badly eaten up and aggregates are clearly visible. The specimens in 2 % sulfuric acid solution were not that much damaged when compared to those of 5 % sulfuric acid. In both the solutions even after 7 days immersion time only efflorescence was observed.

For the specimens immersed in 2 % hydrochloric acid solution, there was no change in the physical state and only micro-cracks were observed on the surface of the specimens. For the specimens immersed in 5 % hydrochloric acid, cracks were observed on the surface and edges were lost after 28 days.

6.2 Mass Loss

The change in the mass of the specimens was observed and the results are shown in the Table 1.

It can be observed that the mass loss in M70 and M40 grade HVFC after 28 days immersion in 2 % sulfuric acid are 4.6 and 5.71 %. Similarly, in 5 % sulfuric acid the values are 10.93 and 11.89 %, respectively. In case of hydrochloric acids, the mass loss in M40 and M30 grade HVFC after 28 days immersion in 2 % hydrochloric acid are 1.25 and 1.92 %. Similarly, in 5 % hydrochloric acid the values are 2.33 and 2.11 %, respectively.

It was observed that in all the acid solutions, the mass loss is more in M30 grade HVFC when compared to that of M40 grade HVFC. This might be because of higher content of pozzolanic material in M40 grade HVFC than M30.

6.3 Average Compressive Strength

The variation of average compressive strength in the two grades of HVFC when immersed in acid solutions is shown in Figs. 1, 2, 3 and 4.

Table 1 Percentage mass losses when immersed in acid solutions

No. of days of immersion	Percentage mass loss (%)							
	2 % H_2SO_4		5 % H_2SO_4		2 % HCl		5 % HCl	
	M40	M30	M40	M30	M40	M30	M40	M30
0	0	0	0	0	0	0	0	0
3	1.25	3.39	3.45	4.14	0.67	0.87	1.5	1.84
7	1.89	5.12	5.01	6.4	0.69	1.1	1.54	1.89
28	4.6	5.71	10.93	11.89	1.25	1.92	2.33	2.11

Fig. 1 Average compressive strength variation when immersed in 2 % H_2SO_4 solution
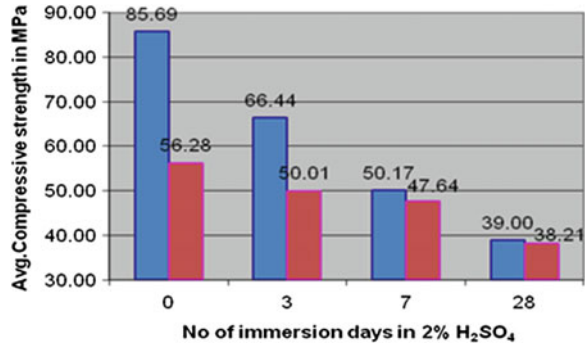
Fig. 2 Average compressive strength variation when immersed in 5 % H_2SO_4 solution
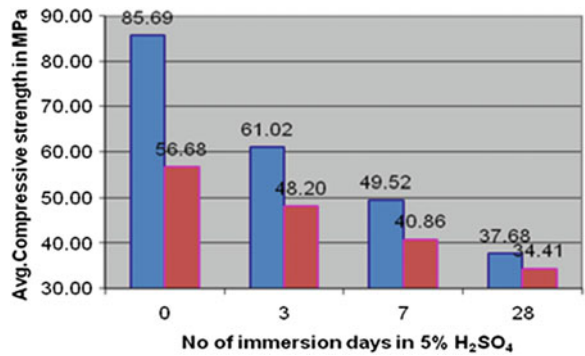
Fig. 3 Average compressive strength variation when immersed in 2 % HCl solution
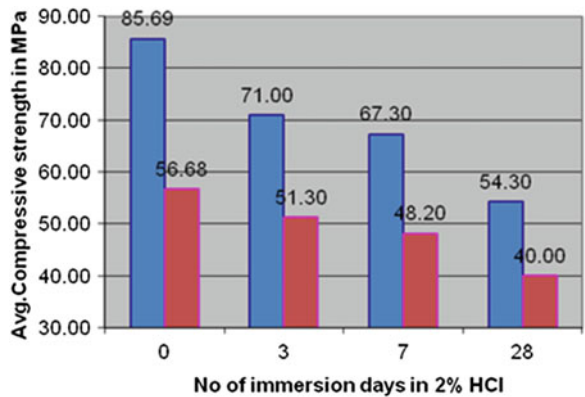
The observations made are that the decrease in the average compressive strength in M40 and M30 grade HVFC after 28 days immersion in 2 % sulfuric acid are 55 and 33 %. Similarly, in 5 % sulfuric acid the values are 57 and 40 %, respectively. In case of hydrochloric acids, the decrease in average compressive strength in M40

Fig. 4 Average compressive
strength variation when
immersed in 5 % HCl solution
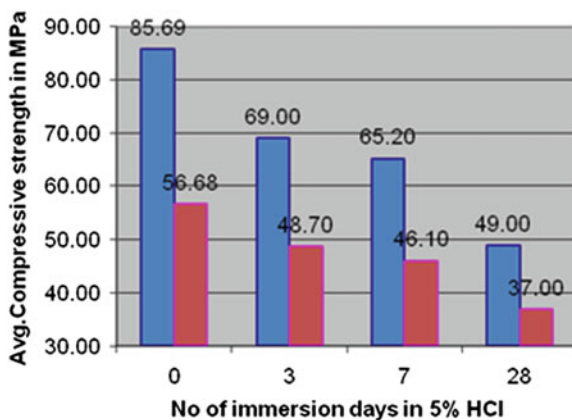
and M30 grade HVFC after 28 days immersion in 2 % hydrochloric acid are 37 and
30 %, respectively. Similarly, in 5 % hydrochloric acid the values are 43 and 35 %,
respectively. It was observed that the decrease in the average compressive strength
and rate of decrease is more in M40 grade HVFC than that in M30 grade. This
might be due to the usage of higher amount of powder and less coarse aggregates in
M40 grade HVFC.

6.4 Non-destructive Tests

The variation in the pulse velocity and rebound hammer was observed thereby
observing the rate of deterioration of concrete. The variation in the UPV and RH
values for the specimens immersed in different acid solutions is presented in the
Tables 2 and 3.

Table 2 Ultrasonic pulse velocity (UPV) values when immersed in acid

No. of days of immersion	UPV values (m/s)							
	2 % H_2SO_4		5 % H_2SO_4		2 % HCl		5 % HCl	
	M40	M30	M40	M30	M40	M30	M40	M30
0	4,472	4,253.5	4,426	4,192	4,513	4,367	4,413	4,252
3	3,985	3,816	3,836	3,680	4,446	4,131	4,114.5	4,037.5
7	3,792	3,592	3,880	3,509	4,149	4,043	3,994.5	3,900
28	3,452	3,151	3,086	3,046	3,836	3,640	3,398	3,086

Table 3 Rebound hammer values when immersed in acid

No. of days of immersion	Rebound hammer (RH) number							
	2 % H_2SO_4		5 % H_2SO_4		2 % HCl		5 % HCl	
	M40	M30	M40	M30	M40	M30	M40	M30
0	48	37	48	37	49	39	47	38
3	38.33	35	34.5	33	40.5	36	38.5	35
7	35.67	32.33	31.83	29	37.17	31	36	30
28	32.99	29.33	25	24	29.5	25	26.5	23

7 Magnesium Sulfate Attack

7.1 Visual Observation

There was no change in the dimensions of the specimens but efflorescence was observed on the surface of the specimens and it increased with increase in the immersion time.

7.2 Mass Loss

It was observed that there was no change in the mass of the specimens even after 28 days immersion in 5 % magnesium sulfate solution.

7.3 Average Compressive Strength

Change in the average compressive strengths was studied after 28 days immersion in 5 % magnesium sulfate solution. It was observed that there is 6 % decrease in the compressive strength after 28 days immersion in both the grades of concrete. Table 4 shows the values of compressive strength after immersion in acid at the end of 28 days.

Table 4 Average compressive strength values when immersed in acid

No. of days of immersion	Average compressive strength (MPa)	
	M40	M30
0	85.69	56.68
28	81.21	53.41
% loss in strength	6 %	6 %

8 Sodium Chloride Attack

In sodium chloride attack, there was no considerable difference in the mass loss, non-destructive test (NDT) values and average compressive strength was observed.

9 Conclusions

After the analysis of the results of the experimental program, the following conclusions were arrived.

1. Early age strength of concrete, i.e. for 7 and 14 days is decreasing with increase in percentage replacement of flyash.
2. 28 days strength of concrete increasing with increase in percentage replacement of flyash up to 50 %.
3. Flexural strength of concrete is decreasing with increase of percentage replacement of flyash.
4. The visual appearance, mass change, UPV variation, rebound hammer number variation, average compressive strength variation after certain exposure periods were studied to assess the deterioration of HVFC when subjected to 2 and 5 % sulfuric acid and hydrochloric acid solutions.
5. The surface of the specimens was badly damaged and cement mortar was completely eaten up and coarse aggregates were clearly visible in case of sulfuric acid attack. It was not found in hydrochloric acid attack.
6. The mass loss is more in M30 grade HVFC when compared to that of M40 grade HVFC when immersed in acids due to higher content of pozzolanic material in M40 than in M30 grades HVFC.
7. The decrease in the average compressive strength and rate of decrease is more in M40 grade HVFC than that of in M20 grade when immersed in acid solutions.
8. The deterioration effect of sulfuric acid was found more severe when compared to hydrochloric acid.
9. When HVFC is subjected to 5 % magnesium sulfate attack, the mass variation was not observed and the average compressive strength decreased by 6 % after 28 days of immersion.
10. When HVFC is subjected to 5 % sodium chloride attack, there was no change in mass and average compressive strength even after 28 days of immersion.
11. A decrease in the ultrasonic pulse velocity and rebound hammer number values was observed for HVFC subjected to acid attack and an increasing pattern was observed in case of sulfate attack.

References

1. Arezoumandi M, Wolfe MH, Volz JS (2013) A comparative study of the bond strength of reinforcing steel in high-volume flyash concrete and conventional concrete. J Constr Build Mater 40:919–924
2. Yazici S, Arel HS (2012) Effects of flyash fineness on the mechanical properties of concrete. J Indian Acad Sci 37(3):389–403
3. Yang E-H, Yang Y, Li VC (2007) Use of high volumes of flyash to improve ECC mechanical properties and material greenness. J ACI 104:6
4. Celik O, Damci E, Piskin S (2008) Characterization of flyash and its effects on the compressive strength properties of Portland cement. Indian J Eng Mater Sci 15:433

Bibliography

5. Hardjito D, Wallah SE, Sumajouw DMJ, Vijaya Rangan B (2004) On the development of flyash-based geopolymer concrete. J ACI 101:6
6. Yoshitake I, Komure H, Nassif AY, Fukumoto S (2013) Tensile properties of high volume flyash (HVFA) concrete with limestone aggregate. J Constr Build Mater 49:101–109
7. Ramezanianpour AA, Malhotra VM (1995) Effect of curing on the compressive strength, resistance to chloride-ion penetration and porosity of concretes incorporating slag, flyash or silica fume. J Cem Concr Compos 17(2):1995
8. Crouch LK, Hewitt R, Byard B (2007) High volume flyash concrete. J World Coal Ash (WOCA) 1–14
9. Bazzar K, Bouatiaoui MR, Hafidi Alaoui A (2013) Performance approach the durability of high volume flyash concrete. Int J Eng Sci Innovative Technol (IJESIT) 2:2
10. Siddique R (2002) Effect of fine aggregate replacement with class F flyash on the mechanical properties of concrete. Department of Civil Engineering, Thapar Institute of Engineering and Technology, Deemed University, Patiala
11. Shetty MS (2005) Concrete technology. S. Chand Publisher, New Delhi

Numerical Estimation of Moisture Penetration Depth in Concrete Exposed to Rain—Towards the Rationalization of Guidelines for Durable Design of Reinforced Concrete in Tropics

Kaustav Sarkar and Bishwajit Bhattacharjee

Abstract Moisture imbibed within the porous matrix of concrete during the course of service plays a critical role in causing its degradation. Under tropical climatic conditions structural concrete elements often get exposed to spells of rainfall which result in a conspicuous ingress of moisture and subsequently to conditions amenable for corrosion of embedded steel reinforcement—the most prevalent cause of premature durability failure of reinforced concrete (RC) elements. The estimation of associated moisture penetration depth in concrete is thus pivotal for delineating the near surface zone of a RC element which remains susceptible to durability damage. Such an estimate also enables in ascertaining rationally the cover depth to be provided to RC elements intended to serve under tropical conditions which is otherwise adopted as per to the prescriptive standards currently in vogue. The present work numerically investigates the aspect considering the probable extremes of rainfall scenarios pertaining to the composite tropical climate of New Delhi (India). The associated exposure traits have been ascertained by statistically analyzing 15 years' rainfall data obtained from the archives of Indian Meteorological Department. The moisture transport phenomenon in concrete has been represented using a modified form of Richards' equation constituted using dimensionless terms to achieve computational efficiency. The material properties which serve as inputs to the analysis have been adopted from published experimental literature.

Keywords Concrete · Moisture ingress · Rainfall exposure · Finite element analysis · Durable design

K. Sarkar (✉) · B. Bhattacharjee
Department of Civil Engineering, Indian Institute of Technology Delhi,
Hauz Khas, New Delhi 110016, India
e-mail: srkrkaustav@gmail.com

B. Bhattacharjee
e-mail: bishwa@civil.iitd.ac.in

1 Introduction

The application of concrete as a structural material subjects it to the concomitant influence of ambient environment. The exposure provides a sustained impetus to the hygro-thermal state of exposed concrete, often rendering the pore moisture condition conducive for the propagation of degradation mechanisms [1]. The concurrent action of reactive entities inherent to concrete and of those which invade its porous matrix from external sources disrupts the physiochemical character and causes gradual degradation of concrete [2]. The progressive deterioration of material integrity renders the structural components susceptible to the loss of serviceability and eventual impairment, begetting consequently, the need for costly repairs.

Most commonly, the ambient action leads to the corrosion of steel reinforcement in structural elements implicating thereby the adequacy of the prescriptively adopted concrete cover to resist the effect of ambient exposure over a desired period of service [3–5]. This in turn necessitates the design of cover thickness based on the rational consideration of mechanisms leading to corrosion. Of special significance in this regard is the estimation of moisture penetration depth in concrete which delineates the zone within which the onset and propagation of corrosion mechanism owing to its moisture dependence remains viable. The provision of a cover thickness higher than the penetration depth of moisture thus keeps the embedded steel protected from corrosion. The pertinence of such an evaluation is especially critical for those exposure conditions which influence the state of pore moisture over significant depths, thus aggravating the extent of impending degradation—the action of rainfall being a typical instance of such exposure type.

Under tropical climatic conditions, rains prevail over a considerable spell of the year. Exposed concrete, during this wet period, imbibes conspicuous amount of water through capillary action. During the subsequent dry spell, a fraction of the imbibed water is lost through evaporation rendering the medium unsaturated and hence susceptible to the attack of rebar corrosion. Despite of its eminent influence in regulating the corrosion induced degradation of structural concrete, the study of moisture transport in concrete subjected to rain induced wetting has been very limited. In a pioneering effort, Andrade et al. [6] experimentally recorded the variation of average relative humidity and temperature within the near surface zone of concrete samples exposed to natural rainfall. Lately, Ryu et al. [7] have also reported observations on the evolution of humidity and saturation states at different depths in a concrete specimen subjected to artificially created rainfall and summertime conditions. In a more recent study on wet-dry cycles, albeit not simulating a natural exposure condition, Zhang et al. [8], have investigated the variation of pore humidity caused due to the action of ponding and subsequent drying of specimen surface. These studies have provided valuable insights into the hygro-thermal behavior of concrete exposed to wetting-drying cycles, however, the complexities of controlling several influencing factors and measuring moisture distribution in concrete render the implementation of such experimental pursuits less tractable for a vivid investigation. On the other hand,

a model based investigation requires the appropriate consideration of exposure conditions and a robust numerical analysis of the moisture transport phenomena to facilitate a useful and efficient solution of the problem.

The present work numerically investigates the extent of rain induced moisture penetration in concrete subjected to the action of tropical monsoon spells. The exposure scenarios adopted for the study have been constituted to simulate the annual wet period of New Delhi (28.61°N, 77.23°E), based on the statistical analysis of 15 years' (1990–2005) rainfall data obtained from the archives of Indian Meteorological Department. The phenomenon of moisture transport in concrete has been represented using a modified form of Richards' equation constituted using a set of dimensionless variables and subsequently analyzed using a one dimensional, nonlinear FE scheme [9]. Typical values of material properties have been adopted from published experimental literature.

2 Characteristics of Rainfall Exposure

The occurrence of rainfall in New Delhi is primarily a seasonal phenomenon. The constitution of a representative rainfall model has therefore to be based on the analysis of meteorological characteristics pertaining to this particular period of the year referred to as the "annual wet spell" in present study. The method implemented for identification of annual wet spell and statistical exploration of associated rainfall data to ascertain the exposure traits of (i) total duration of the monsoon spell, (ii) duration of rainfall on a rainy day and (iii) average rainfall intensity on a rainy day have been duly elaborated in the following sections.

2.1 Identification of Annual Wet Spell

Figure 1 depicts the distribution of daily average rainfall over the period of a year. The pattern shows a rise in the amount of rain roughly during the period between 100–300 days indicating the disposition of the wet spell. A more clear representation of the distribution can be obtained by classifying each day of the year into three discrete categories [10]: (1) Rainy day (rain $\geq$ 2.5 mm), (2) Wet day (2.5 mm > rain $\geq$ 0.1 mm) and (3) Dry day (rain < 0.1 mm). Figure 2 presents the resulting classification with the period of 140–267 days appearing to be eminently wet with only two dry days and 94.19 % of the total number of rainy days of the year occurring in this interval. This period is thus selected to be the annual wet spell for New Delhi.

Fig. 1 Distribution of daily average rainfall data
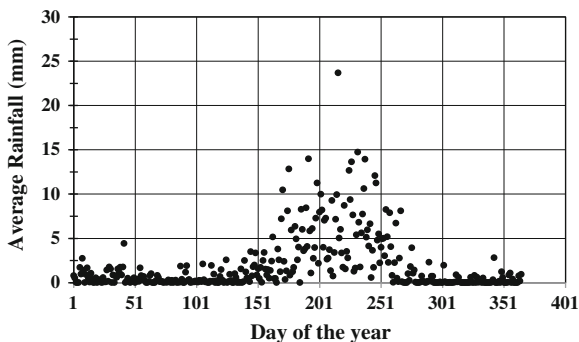
Fig. 2 Distribution of dry, wet and rainy days over the spell of a year
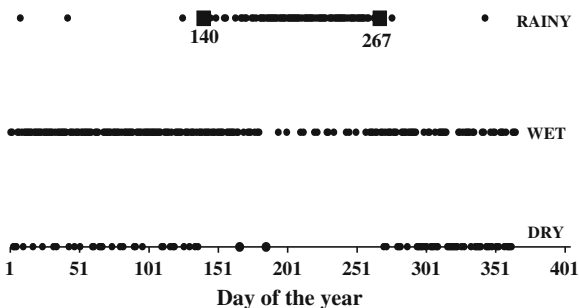
2.2 Duration of Annual Wet Spell

Figure 3 shows the variation of total rainfall duration occurring during the identified wet spell for fifteen consecutive years (1991–2005). The observed values are seen to vary widely in the range of 144.91–55.94 h with an average value of 95.37 h. In the present study, analysis for moisture ingress has been carried out for the upper, middle and lower points of 125.63, 83.16 and 66.14 h respectively.
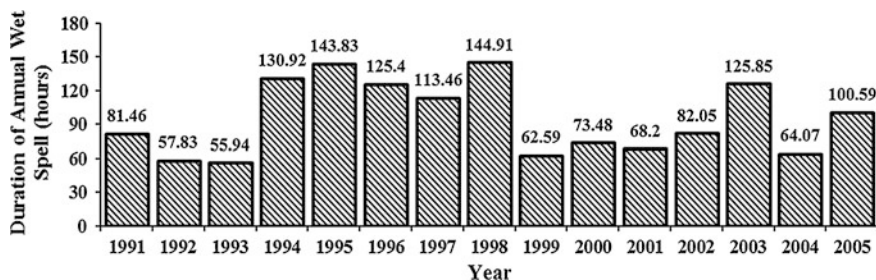
Fig. 3 Distribution of total duration of annual wet spell during 1991–2005

2.3 Duration and Average Intensity of Rainfall

Rainfall during the course of annual wet spell manifests in discrete spells of random durations with time varying intensities. However, to achieve simplicity in modeling of the exposure, the present study considers that only a single rainfall event takes place on a given rainy day and that it occurs with a constant intensity equaling the average value i.e., (total quantity/total duration) of rainfall recorded for the day. The simplifying assumption is reasonable in light of the fact that the quantity of moisture that ingresses a porous building material has been reported to be dependent on the duration of exposure rather than the intensity of incident flux [6].

To facilitate the selection of characteristic rainfall duration and average intensity values, the underlying probability distribution models have been determined based on the analysis of available data. Figure 4 presents the density histogram plot of rainfall duration pertaining to the rainy days of annual wet spell. An inspection of the plot reveals its asymmetric nature with a skew towards the right. A similar trend can be observed in Fig. 5 which corresponds to the distribution of average rainfall
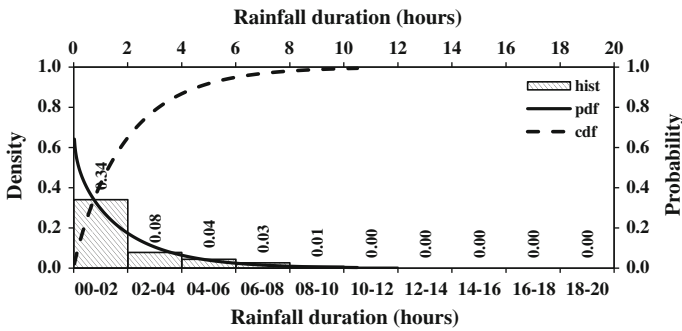
Fig. 4 Density histogram, probability density and cumulative probability distribution plots for daily rainfall
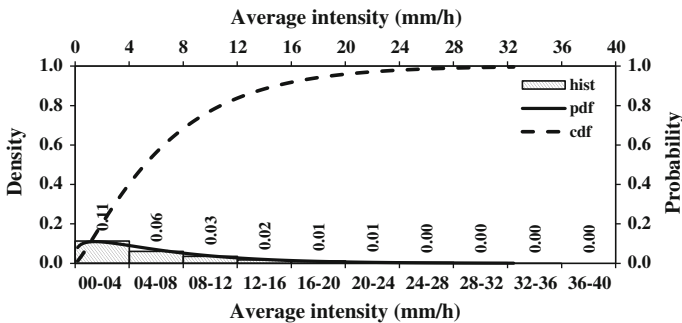
Fig. 5 Density histogram, probability density and cumulative probability distribution plots for average rainfall intensity

intensity values. The nature of these plots suggests the suitability of gamma probability density function to describe the observed variation of data. Using the method of maximum likelihood estimates [8], the shape and scale parameters in the density function are estimated to be (0.91, 2.14) and (1.27, 5.37) for rainfall duration and average intensity respectively. The corresponding duration and intensity values which have a 95 % chance of not being exceeded are 6.03 h and 18.85 mm/h respectively. The same have been adopted as characteristic values for the moisture ingress analysis presented in a subsequent section.

3 Modeling of Moisture Ingress

The phenomenon of moisture flow in an unsaturated porous medium is conventionally represented using the extended Darcy's law, stated as,

$$\partial\theta/\partial t = \nabla(D(\theta)\nabla\theta) \tag{1}$$

For a one dimensional domain, the governing equation reduces to,

$$\partial\theta/\partial t = \partial/\partial x(D(\theta)\partial\theta/\partial x) \tag{2}$$

with the term, $D(\theta) \cdot (\partial\theta/\partial x)$ representing a flux acting in the direction of outward normal to the exposed surface. Here, $\theta(\mathrm{m^3/m^3})$ is the moisture content, $t(\mathrm{s})$ is the time variable, $x(\mathrm{m})$ is the space variable and $D(\theta)(\mathrm{m^2/s})$ is the moisture dependent hydraulic diffusivity function.

The distribution of moisture in a porous medium is characterized by the nature of hydraulic diffusivity function which is known to assume typical trends for wetting and drying conditions respectively. Absorption of rain water in building materials is primarily caused due to the action of capillary forces and the associated hydraulic diffusivity has been successfully represented using an exponential function of the form [11–13],

$$D_r(\theta_r) = D_{d\_wet}\exp(n\theta_r) \tag{3}$$

where, D_{d_wet} ($\mathrm{m^2/s}$) is the wetting diffusivity corresponding to totally dry state of the medium. The value of n in the stated equation ranges between 6 and 8 for building materials [14] and for concrete in an initially dry state a value of $n = 6$ has been suggested [15]. For an initial condition of partial saturation, the value of n can be approximated using a simplified form of Brutsaert's model [16],

$$n = \frac{\left[1 - (S/S_0)^2\right] / \left[2(\theta_s - \theta_o)\theta_{r,ini}\right]}{\left\{\left[1 - (S/S_o)^2\right] / \theta_{r,ini} - 1\right\}} \tag{3a}$$

where, $\theta_{r,ini}$ is the reduced initial moisture content calculated as per Eq. (4a), θ_o(m^3/m^3) and θ_s(m^3/m^3) are the moisture contents corresponding to the completely dry and saturated states of concrete, S(m/√s) and S$_o$(m/√s) are the sorptivities corresponding to the initial partial saturation and dry states respectively. Having determined the value of n, the parameter D_{d_wet}(m^2/s) can be estimated using the function [15],

$$D_{d\_wet} = \frac{n^2 \cdot (S/\theta_s)^2}{e^n(2n - 1) - n + 1} \tag{3b}$$

The strong dependence of hydraulic diffusivity on moisture content renders the unsaturated flow problem highly non-linear. A plausible analysis of the problem is therefore dependent on the application of a robust numerical scheme. Being of first order in time and second order in space, the solution of the problem relies on the specification of an initial condition and two boundary conditions. The boundary condition may either be provided as the value of moisture content θ (Dirichlet/ Essential boundary condition) or as the value of moisture flux stated as, $D(\theta) \cdot (\partial\theta/ \partial x) = -V_o$ (Neumann/Natural boundary condition) where, V_o is boundary rain flux acting opposite to the direction of outward normal to surface (m/s). The initial moisture content across the physical domain of analysis is generally described by an initial moisture profile.

3.1 Modified Governing Equation

Since the parameters constituting the given problem range over several orders of magnitude, restating Eq. (2) using the following dimensionless terms, aids in minimizing the computing errors.

$$\text{Reduced moisture,} \quad \theta_r = (\theta - \theta_o)/(\theta_s - \theta_o) \tag{4a}$$

$$\text{Reduced distance,} \quad x_r = (V_o/D_{d\_wet})x \tag{4b}$$

$$\text{Reduced time,} \quad t_r = \left(V_o^2/D_{d\_wet}\right)t \tag{4c}$$

Restating Eq. 2 in terms of the non-dimensional parameters gives,

$$\frac{\partial\theta_r}{\partial t_r} = \frac{1}{D_{d\_wet}}\frac{\partial D_r(\theta_r)}{\partial\theta_r} \cdot \left(\frac{\partial\theta_r}{\partial x_r}\right)^2 + \frac{1}{D_{d\_wet}}D_r(\theta_r)\frac{\partial^2\theta_r}{\partial x_r^2} \tag{5}$$

A scrutiny of these terms reveals their appropriateness in reducing the range of orders involved in computation; the most prominent aspect in the modified model

represented by Eq. (5) is the normalization of the diffusivity function $D_r(\theta_r)$ with the term, D_{d-wet}. Moreover, expressing the model in terms of these parameters enables adaptation of results to determine the behaviour of all hydraulically similar materials. Considering a simplified representation for hydraulic diffusivity function, $D_r(\theta_r) = D_{d-wet} f_w(\theta_r)$, where $f_w(\theta_r)$ is a function of reduced moisture content and subsequently equating the modified boundary flux term, $V_o(\theta_s - \theta_o)(D_r(\theta_r)/D_{d-wet})$ $\partial\theta_r/\partial x_r$ to wetting flux yields the following condition, $f_w(\theta_r) \, \partial\theta_r/\partial x_r = -1/(\theta_s - \theta_o)$.

3.2 Finite Element Formulation

Using the governing differential equation stated in Eq. 5, the FE formulation can be carried out using Galerkin's weighted residual technique [17]. For a linear element or reduced length l, the element level governing equation can be obtained as,

$$\frac{l}{6}\begin{bmatrix} 2 & 1 \\ 1 & 2 \end{bmatrix}\frac{\partial\{d^e\}}{\partial t_r} + \frac{f_w(\theta_r)}{l}\begin{bmatrix} +1 & -1 \\ -1 & +1 \end{bmatrix}\{d^e\} = \begin{Bmatrix} +\left(\frac{1}{\theta_s-\theta_o}\right)_{x_r=0} \\ -\left(f_w(\theta_r)\frac{\partial\theta_r}{\partial x_r}\right)_{x_r=l} \end{Bmatrix} \tag{6}$$

An inspection of the Eq. (6) reveals its dependence on the function $f_w(\theta_r)$ which as described earlier is known to follow characteristic exponential form for the case of wetting. Also, as the term $1/(\theta_s - \theta_o)$ is relative in nature, the derived expression can be considered to represent the behavior of all hydraulically similar materials. Equation (6) is semi discrete and can be represented in the matrix form as,

$$[m]\{\dot{d}^e\} + [k]\{d^e\} = \{q\} \tag{7}$$

where, {m}, {k} are element level mass and diffusivity matrices, $\{d^e\}$ is the vector of elemental degrees of freedom, $\{\dot{d}^e\}$ is the vector of time derivatives of elemental degrees of freedom and {q} is the vector of elemental nodal fluxes. In order to obtain a fully discretized system of equations, the time derivatives of the field variable in these equations are to be further approximated using the method of finite difference. Adopting the Crank–Nicolson scheme, a completely discrete system of equations is obtained as,

$$\left([m] + 0.5\Delta t \, [k]^{n+1}\right)\{d^e\}^{n+1} = ([m] - 0.5\Delta t \, [k]^n)\{d^e\}^n + 0.5\Delta t\left(\{q\}^{n+1} + \{q\}^n\right) \tag{8}$$

where, the superscripts n and $(n + 1)$ denote the previous and present time levels.

4 Moisture Ingress Simulation

The simulation has been carried out for the extreme cases of rainfall exposure to estimate the maximum penetration depth of moisture in concrete. In the most severe scenario conceptually possible, the annual wet spell has been considered to occur as a single rainfall event. Three exposure durations of 125.63, 83.16 and 66.14 h corresponding respectively to the upper, middle and lower quartile values of recorded data have been adopted for analysis. In another scenario, the total rainfall duration of 125.63 h has been taken to occur in a series of successive rainfall events each of 6.03 h duration i.e. a total of 125.63/6.03 = 20.8–21 rainfall events. All the rainfall events have been considered to be incident with a constant intensity of 18.85 mm/h.

The proportions and properties of concrete considered for the analysis are presented in Table 1 and have been adopted from the experimental work of Wong's et al. [18].

The moisture content of concrete corresponding to the state of full saturation has been assumed to be equal to its capillary porosity determined using the well-known Power's model [19] for curing age of 28 day,

$$\phi_c = \frac{\frac{w}{c} - 0.36h + \frac{a}{C}}{0.317 + \frac{A_f}{\rho_f C} + \frac{A_c}{\rho_c C} + \frac{w}{c} + \frac{a}{C}} \tag{9}$$

Here, ϕ_c (m³/m³) is the capillary porosity of concrete, h is the degree of hydration of cement, w/c is the water to cement ratio by mass, a (m³/m³) is the volume of entrapped air in concrete, C, A_f and A_c are the parts of cement, fine and coarse aggregates by mass, ρ_f and ρ_c are the specific gravities of fine and coarse aggregate respectively.

The degree of hydration determined at a curing age t_{cure} (days) estimated using the empirical expression proposed by [20],

$$h = C_1 \cdot \ln(w/c) + C_2 \cdot \ln(t_{cure}) + C_3 \tag{9a}$$

For OPC 43 [21] grade cement, $C_1 = 0.217$, $C_2 = 0.07$, $C_3 = 0.591$. Using the mix proportion data presented in Table 1 and for a curing age of 28 days, the values of h and ϕ_c have been computed to be 0.67 and 0.11 m³/m³ respectively.

Table 1 Mix proportions and properties of concrete

w/c	0.5
Cement (kg/m³)	374
Fine agg. (kg/m³)	856
Coarse agg. (kg/m³)	924
Water (kg/m³)	187
Air (%)	1.64
S_o (m/√s)	2.711×10^{-5}
D_{d-wet} of dry concrete (m²/s)	4.704×10^{-10}

The domain considered is of length, $L = 0.50$ m in an initially dry state i.e., $\theta_r = 0$ at $t_r = 0$ and $x_r \geq 0$. The finite element mesh has been constituted using linear elements of reduced size, $l = 0.5$ and the reduced time step size has been varied corresponding to 0–300 s.

In the case of wetting in successive spells, the values of diffusion equation parameters (n and D_{d_wet}) at the commencement of each of the spells have been estimated using Eqs. (3a) and (3b) respectively. For this purpose, the initial moisture content of the medium $\theta_{r,ini}$ has been determined by averaging the moisture content values of all those nodes into which the water has already penetrated (numerically taken to be $\theta_r > 0.01$). The corresponding sorptivity values have been estimated using the following relation applicable to the concrete under study [18],

$$S = S_o\left(-\theta_{r,ini} + 1\right) \tag{10}$$

The obtained moisture profiles corresponding to each of the two scenarios are presented in Fig. 6a, b. It becomes evident from Fig. 6a that for a given intensity of rainfall the depth of penetration of moisture in an initially dry concrete medium increases with the duration of exposure. Figure 6b which presents the simulated results of a more realistic exposure scenario aids in delineating the thickness of an

Fig. 6 a Moisture distribution profiles for the case of total annual rainfall manifesting as a single event. b Evolution of moisture distribution in concrete during the manifestation of annual wet spell through successive rainfall events
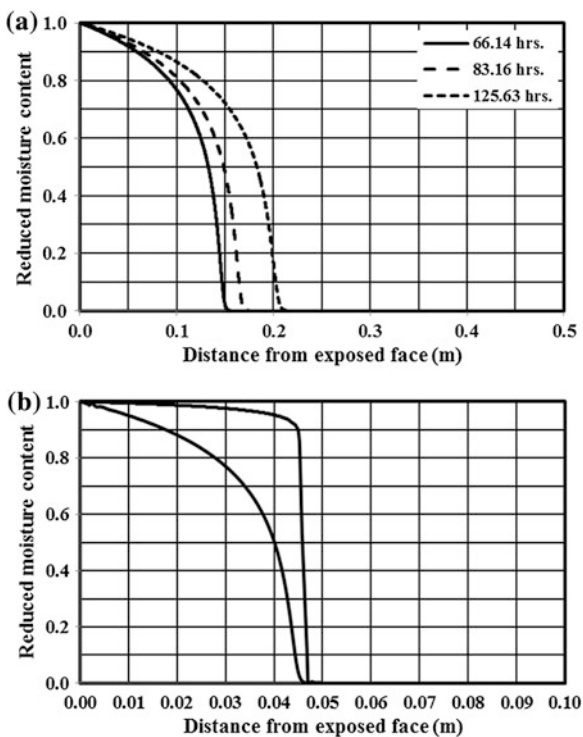
exposed concrete medium which remains available to the ingress of moisture and hence to subsequent gradual degradation. The results reveal that a conspicuous ingress of moisture takes place in the outer 45–50 mm thickness which almost attains a near saturation condition. It is worth noting that after the end of the first rain spell the moisture front penetrates up to a depth of 45.7 mm and the ingress further extends only up to 47.0 mm at the end of the last spell. The observation establishes the significance of the duration of first rainfall event which occurs during the course of annual wet spell as it largely governs the depth in an exposed concrete medium which remains amenable to the ingress of moisture.

5 Summary and Conclusions

The subject of this paper relates to the modelling of moisture ingress in concrete exposed to rains. The considered exposure type is typical of tropical climates and is potentially critical in aggravating the evolution of reinforcement corrosion by causing substantial ingress of water in near surface zone of concrete.

In its discourse, the paper has described the characteristics of tropical rainfall exposure relevant for its pragmatic modelling namely, the period of annual wet spell, total duration of rainfall in wet spell, the duration and average intensity of rainfall events pertaining to the rainy days of the spell. Based on the statistical analysis of 15 years' rainfall data, the delineated exposure traits have been quantified for the station of New Delhi. On the basis of the explored characteristics, probable extreme rainfall scenario have been constituted and subsequently implemented for the estimation of maximum moisture penetration depth in concrete.

Using a modified Richards' equation to describe the moisture transport phenomena and a one dimensional nonlinear finite element scheme to numerically analyse the model, the evolution of moisture distribution in a typical ordinary concrete medium has been simulated. The results reveal that the outer 50 mm layer of exposed concrete attains a near saturated condition during the course of annual wet spell. It is worth mentioning here that the Indian standard design code [22] currently in vogue recommends a nominal cover depth of 45 mm for concrete members exposed to the action of severe rains. This invaded zone on subsequent drying becomes susceptible to the action of carbonation induced corrosion of embedded steel. The availability of adequate water in the concrete pores during the post rainy period of the year enables the steady propagation of carbonation and corrosion mechanisms. It has also been observed in the simulation that, the depth which remains amenable to moisture ingress in an initially dry concrete medium is largely governed by the duration of the first rainfall event. The successive spells on the other hand have a relatively minimal contribution in propagating the moisture front further into the medium. However, during the course of these spells, the saturation level of the already invaded depth continues to rise.

To conclude, it is reiterated that the pragmatic modelling of rainfall exposure and concomitant moisture ingress in concrete facilitates the estimation of cover

thickness necessary to offset corrosion damage of reinforced concrete elements. Similar studies should thus to be carried out for the different climatic zones of tropical belt.

References

1. Nilsson L (1996) Interaction between microclimate and concrete—a prerequisite for deterioration. Const Build Mater 10(5):301–308
2. Glasser FP, Marchand J, Samson E (2008) Durability of concrete—degradation phenomena involving detrimental chemical reactions. Cem Concr Res 38(2):226–246
3. Stewart MG, Xiaoming W, Nguyen MN (2011) Climate change impact and risks of concrete infrastructure deterioration. Eng Struct 33(4):1326–1337
4. Stewart MG, Xiaoming W, Nguyen MN (2012) Climate change adaptation for corrosion control of concrete infrastructure. Struct Saf 35:29–39
5. Talukdar S, Banthia N (2013) Carbonation in concrete infrastructure in the context of global climate change: development of a service lifespan model. Const Build Mater 40:775–782
6. Andrade C, Sarria J, Alonso C (1999) Relative humidity in the interior of concrete exposed to natural and artificial weathering. Cem Concr Res 29(8):1249–1259
7. Ryu DW, Ko JW, Noguchi T (2011) Effects of simulated environmental conditions on the internal relative humidity and relative moisture content distribution of exposed concrete. Cem Concr Comp 33(1):142–153
8. Zhang J, Gao Y, Han Y (2012) Interior humidity of concrete under dry-wet cycles. J Mater Civ Eng 24(3):289–298
9. Sarkar K, Bhattacharjee B (2014) Wetting and drying of concrete: modeling and finite element formulation for stable convergence. Struct Eng Int 24(2):192–200
10. Singh N, Ranadae AA (2009) Climatic and hydro climatic features of wet and dry spells and their extremes across India. Research report no. RR-122, Indian Institute of Tropical Meteorology, Pune
11. Lin SH (1992) Nonlinear water diffusion in unsaturated porous solid materials. Int J Eng Sci 30(12):1677–1682
12. Hall C (1994) Barrier performance of concrete: a review of fluid transport theory. Mater Struct 27(5):291–306
13. Pel L (1995) Moisture transport in porous building materials. Doctoral thesis, Technische Universiteit Eindhoven, Netherlands
14. Hall C (1989) Water sorptivity of mortars and concretes: a review. Mag Concr Res 41 (147):51–61
15. Leech C, Lockington D, Dux P (2003) Unsaturated diffusivity functions for concrete derived from NMR images. Mater Struct 36(6):413–418
16. Hall C, Hoff WD, Skeldon M (1983) The sorptivity of brick: dependence on the initial water content. J Phys D: Appl Phys 16:1875–1880
17. Reddy JN (2005) An introduction to the finite element method, 3rd edn. TMH, New Delhi
18. Wong SF, Wee TH, Swaddiwudhipong S, Lee SL (2001) Study of water movement in concrete. Mag Concr Res 53(3):205–220
19. Neville AM, Brooks JJ (1987) Concrete technology. Pearson Education Ltd., New Delhi
20. Kondraivendhan B, Bhattacharjee B (2010) Effect of age and water-cement ratio on size dispersion of pores in ordinary portland cement paste. ACI Mater J 107(2):147–154
21. IS 8112 (1989) Specification for 43 grade ordinary portland cement. Bureau of Indian Standards, New Delhi, India
22. IS 456 (2000) Plain and reinforced concrete-code of practice. Bureau of Indian Standards, New Delhi, India

Acid, Alkali and Chloride Resistance of Early Age Cured Silica Fume Concrete

A.P. Shetti and B.B. Das

Abstract Research investigations were carried out on silica fume concrete with respect to its workability, compressive strength, and durability and are reported in this paper in detail. The quantity of silica fume was varied from 1 to 6 %. Workability of the silica fume admixed concrete mix was found to decrease by 30 mm with an increase in silica fume content (2 %) and beyond the use of 3 % silica fume, it necessitated the use of super plasticizers for maintaining the workability level as compared to control concrete. 28 days compressive strength of the silica fume concrete showed a significant increase with increase in the silica fume content from 1 to 6 %. Durability studies were carried out by immersing the cubes in sulphuric acid, sodium sulphate solution and in sodium chloride solution. Further, water absorption test was also carried out to check concrete's ability to resist water penetration. It is found that the loss in weight of the concrete cubes in acidic media is found to be decreasing with increase in silica fume content. Further, it is also observed that the loss in weight of silica fume concrete is found to be almost nil in against to alkali media. Water absorption is also found to be reducing with the increase in silica fume content.

Keywords Concrete · Silica fume · Workability · Compressive strength · Durability

A.P. Shetti

National Institute of Construction Management and Research (NICMAR), Goa Campus, Farmagudi, Ponda 403 401, India

B.B. Das (✉)

Indore Centre, National Institute of Construction Management and Research (NICMAR), Indore 452 016, India

e-mail: bibhutibhusan@gmail.com; bdas@nicmar.ac.in

1 Introduction

Concrete is the preferred construction material in India. The cement production has increased, thanks, mainly to the renewed thrust on infrastructure development across the world. There is an increased thrust in the use of supplementary cementitious materials such as fly ash, ground granulated blast-furnace slag (GGBS), silica fume and metakaolin. As per the estimates, fly ash generation is expected to increase to about 170 million tons by 2012 and 225 million tons by 2017 [1].

The experiments indicate that an addition of fly ash, while retaining the water-binder ratio, gives a lower rate of diffusion for chloride compared with pure Portland cement paste. The rate of diffusion also decreases markedly when the water-binder ratio is reduced. The lowest diffusion rate is obtained for specimens with 40 % fly ash and a water-binder ratio of 0.40 [2].

It is seen that GGBS can greatly increase the chloride binding capability and also improve the pore structure of the concrete thereby reducing chloride diffusion coefficient of GGBS concrete [3]. GGBS reacts with water in alkali environment and then with $Ca(OH)_2$ to form hydrated product of cement through pozzolanic reaction to form extra CSH gel. Studies have revealed that structural members with GGBS concrete show higher resistance to corrosion [4]. It has also been reported that as GGBS content increases, water cement ratio decreases for the same workability. However, it is also reported that the compressive strength of GGBS concrete increases as the GGBS content is increased up to an optimum point after which the compressive strength decreases [5]. GGBS gives high early stage resistance against chloride penetration, which may be important in severe marine environment [6].

Silica fume concrete (SFC) is also emerging as one of the new generation construction material. The use of pozzolanic admixtures like condensed silica fume, because of its finely divided state and very high percentage of amorphous silica, proved to be the most useful if not essential for the development of very high strength concretes and/or concretes of very high durability. From the research reported by some authors it is understood that silica fume in concrete essentially reduces the size of pores in the 50–500 µm range [7]. It is reported that as silica fume improves both mechanical characteristics and durability characteristics of concrete, both the chemical and physical effects are significant. Physical effect of silica fume in concrete is that of filler, which, because of its fineness, fit into spaces between cement grains in the same way that sand fills the spaces between particles of coarse aggregate and cement grains fill the spaces between sand grains. As for chemical reactions of silica fume is concerned, because of high surface area and high content of amorphous silica, this highly active pozzolan reacts more quickly than ordinary pozzolans [3].

It is also reported that silica fume inclusion to the concrete design is primarily dictated by project performance specifications aiming to minimize corrosion concerns and maximizing concrete strength performance, abrasion, impact or chemical resistance, while some uses are non-project specific addressing improvement to

other occasional shortcomings in concrete technology such as limiting aggressive alkali activity, reduction of heat of hydration generation, optimizing viscosity modifying properties and limiting drying shrinkage potentials [7]. Silica fume concrete has an increased resistance to sulphate attack due to its dense and impermeable matrix which inhibits the movement of water and alkalis and by binding free alkalis in calcium silicate hydrates or by adsorption on their large specific surface area thereby reducing the hydroxyl ion concentration of the pore solution [8].

This study was conducted on a tropical environment like India and the results were presented and discussed in an exhaustive manner in this paper. This research will be of great relevance to the researchers and the engineers in understanding the durability of early age cured concrete subjected to alkali, acid and chloride attack.

2 Material Characterization

Ordinary Portland Cement (OPC) of 43 grade that conforms to IS 8112 [9] cement is used in this study. Fine-aggregates used in this study conform to Zone-I of IS 383 [10]. Coarse-aggregates used in this study are of maximum size 20 mm. Specific gravity of these materials was determined as per the procedure mentioned in IS 2386-3 [11] and the results are found to be 2.7 and 2.58 for the coarse and fine aggregates, respectively. However, specific gravity of cement is determined as per specifications of IS 4031-11 [12] and found to be 3.09. Water absorption test was carried out as per IS 2386 part-3:1963 [11] and found to be 1.1, 1.4 and 2 % for 20 mm coarse aggregate, 10 mm coarse aggregate and fine aggregate, respectively. Chemical admixture used as plasticizer conforming to IS 9103 [13] and having its specific gravity 1.1.

3 Testing Methodology

The details of the mix design were carried out as per the guidelines of IS 10262 [14] and IS 456 [15] and designation of concretes is presented in Table 1. For the sake of uniformity of concretes, mixing was done in a rotary mixer for about 2 min. The desired compaction of concrete was achieved with the help of a table vibrator. These samples were stored in a humidity chamber by maintaining 95 ± 5 % relative humidity and a temperature of 27 ± 2 °C. After 24 h of storage, the cubes were de-molded and stored in a submerged condition in a controlled curing tank.

Cubes of 150 mm size were cast and at the end of 7 and 28 days, their compressive strength was determined by employing an automatic compression testing machine, and the results are presented in Table 2.

Additional cubes were cast for testing the durability resistance of control as well as silica fume concretes. All the durability tests were carried out at the end of 7 days

Table 1 Mix proportions

Concrete mix	Cement (kg/m^3)	Silica fume (kg/m^3)	Fine aggregates (kg/m^3)	Plasticizer (% by mass of cement)	Coarse aggregates, kg/m^3 (20 mm)	Coarse aggregates, kg/m^3 (10 mm)	Water (kg/m^3)
Control	438	0	665	0	599	490	197
M1	433.6	4.4	665	0	599	490	197
M2	429.4	8.6	665	0	599	490	197
M3	425.2	12.8	665	1	599	490	197
M4	421.1	16.9	665	1	599	490	197
M5	417.1	20.9	665	1	599	490	197
M6	413.2	24.8	665	1	599	490	197

Table 2 Fresh and hardened properties of concrete

Concrete mix	Slump	Compaction factor	Compressive strength	
			7 days	28 days
Control	50	0.94	24.00	36.60
M1	30	0.89	33.20	45.42
M2	20	0.87	35.36	47.10
M3	210	0.99	38.04	54.89
M4	160	0.97	41.96	55.20
M5	150	0.96	45.73	56.35
M6	145	0.95	48.27	60.13

Table 3 Compressive strength of cubes after immersion in acid, alkali and chloride solution

Concrete mix	Compressive strength (MPa)		
	Acid solution	Alkaline solution	Chloride solution
Control	19.2	23.6	29.15
M1	24.5	30.4	30.22
M2	25.2	31.38	33.27
M3	29.7	37.87	34.89
M4	30.7	45.24	38.18
M5	32.5	52.84	44.44
M6	33.4	58.62	51.16

curing period with respect to acid (concentrated sulphuric acid) attack, alkali (sodium sulphate) attack and chloride resistance (sea water). Further, the water absorption test was also carried out for controls as well as the silica fume concretes. Compressive strength of the cubes after certain durability was also determined and the results are reported in Table 3.

4 Test Procedures for Durability Resistance Measurement

After 7 days of curing, all specimens subjected to various levels of durability test (acid and alkali attack, chloride content and water absorption test) were kept in ambient atmosphere for two days for achieving a constant weight.

4.1 Acid Attack

The specimens were then weighed and immersed in 5 % sulphuric acid (H_2SO_4) solution for 60 days. The pH value of the acidic media was kept at 0.3 and it was periodically checked and maintained. After 60 days of immersing in acid solution,
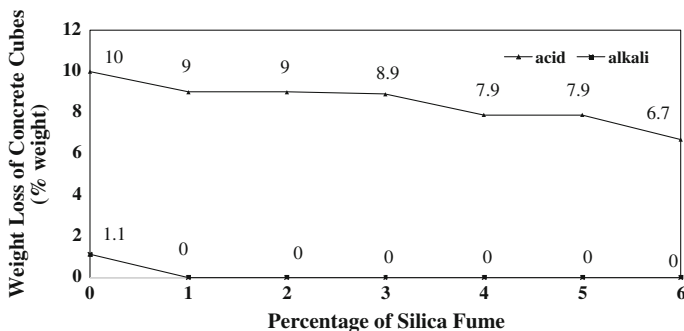
Fig. 1 Percentage loss in weight of concretes replaced with different levels of silica fume and subjected to acid and alkali attack

the specimens were taken out and are washed in water and kept in atmosphere for 2 days for achieving constant weight. Further, the specimens were weighed and the loss in weight and the percentage loss of weight were calculated and is presented in Fig. 1.

4.2 Alkali Attack

The specimens were then weighed and immersed in 5 % sodium sulphate (Na_2SO_4) solution for 60 days. The pH value of the alkaline media was kept at 12.0 and periodically checked and maintained. After 60 days of immersing in alkaline solution, the specimens were taken out and were washed in water and kept in atmosphere for 2 days for constant weight. Further, the specimens were weighed and loss in weight and the percentage loss of weight was calculated and is presented in Fig. 1.

4.3 Chloride Content Test

The specimens were then weighed and immersed in saline water for 60 days. After 60 days of immersing in saline water, the specimens were taken out and kept in atmosphere for 2 days for constant weight. Further, the specimens were tested for chloride content and the results are presented in Fig. 2.
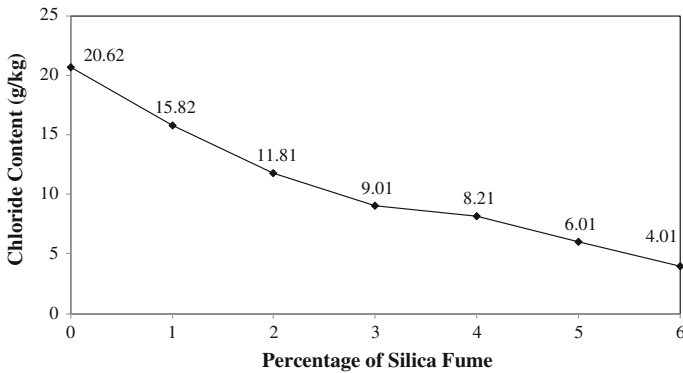
Fig. 2 Chloride content of concretes replaced with different levels of silica fume after immersion in saline water

4.3.1 Determination of Chloride Content

Chloride content was determined as per the guidelines presented in IS 14959-2 [16]. Silver nitrate solution of 0.0141 N was prepared by dissolving 2.38 g of $AgNO_3$ in 1 l of distilled water. 10 g of pulverized concrete sample passing through 2.38 mm sieve in a beaker was weighed and 100 ml of distilled water (chloride free) was added to it. It was then kept for 24 h dissolution. The sample was filtered through Whatman filter paper. 25 ml of sample was then transferred to a conical flask. A couple of drops of $K_2Cr_2O_4$ indicator was added to it. It was titrated against 0.0141 N $AgNO_3$, till colour changed from yellow to brick red. The volume of titrant used was noted. Chloride content was determined based on the following formula: [(FR − IR) × 35.5 × 1,000 × 0.0141]/ml of sample.

4.4 Water Absorption Test

The specimens were then weighed and immersed in water for 30 days. The cubes were weighed again and the change in weight was noted. Water absorption of the cubes is determined and is presented in Fig. 3.

5 Results and Discussions

5.1 Slump

The results of the slump tests are presented in Fig. 4. It can be noted from the figure that slump reduced by 30 mm when silica fume content was increased from 0 to
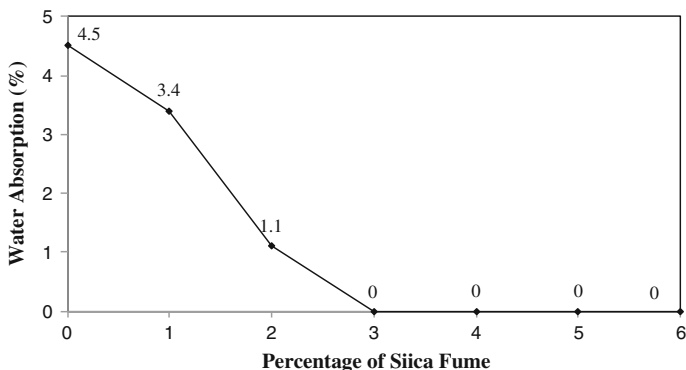
Fig. 3 Water absorption of concretes replaced with different levels of silica fume

Fig. 4 Slump obtained for various percentage levels of silica fume
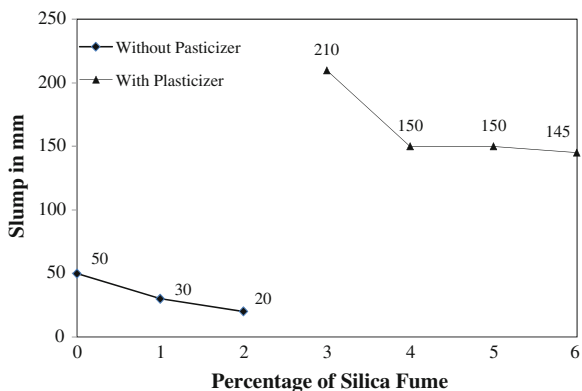
2 % without adding any superplasticizer. It was also observed that silica fume concrete did not show any tendencies for segregation and bleeding. This is due to the fact that as the percentage of fine materials (silica fume) increases the mixture of concrete forms a cohesive paste. However, the decrease in workability necessitated the use of plasticizer from M3 mix (silica fume replacement in this mix is 3 %) onwards. The silica fume concrete was found to become cohesive with increase in silica fume content.

5.2 Compaction Factor

The results of the compaction factor test are presented in Fig. 5. Compaction factor showed a decreasing trend as silica fume content in concrete was increased. Compaction factor reduced by 0.07 when silica fume content was increased from 0

Fig. 5 Compaction factor obtained for various percentage levels of silica fume
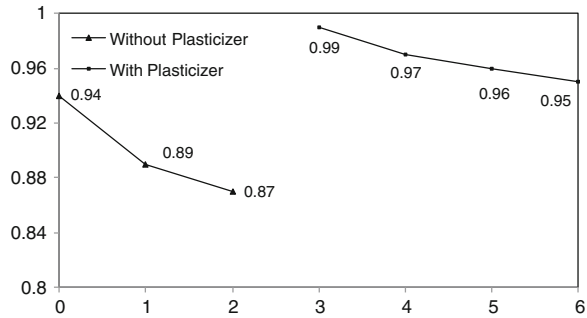
to 2 % without adding any plasticizer. With the addition of plasticizer, the consistency became good and compaction factor achieved a definite value.

5.3 Compressive Strength

The results of the compressive strength tests before and after subjected to durability tests are presented in Figs. 6 and 7, respectively. It can be observed from the Fig. 6 that the compressive strength of concrete showed an increasing trend as silica fume content was increased from 0 to 6 %. This is due to the fact that silica fume acts as a pozzolanic material and additions of the same to concrete results in high early age strength as compared to strength at latter stages. 7 days compressive strength increased by 24.27 MPa with percentage of silica fume was increased from 0 to 6 %. Similarly, 28 days compressive strength increased by 23.53 MPa with percentage of silica fume was increased from 0 to 6 %.

5.4 Acid Attack Test

The resistance against acid attack increased as the silica fume content was increased in concrete from 0 to 6 %. The percentage weight loss, which is an indication of durability in acidic media was found to decrease as the percentage of silica fume in concrete was increased. It can be observed from Fig. 1 that loss in weight reduced by 3.3 % when percentage of silica fume was increased from 0 to 6 %.

Further, the 60 days compressive strength of concrete is significantly reduced when concrete is subjected to acid attack as compared to the strength attained after 28 days of curing under normal conditions. The 60-day compressive strength of control concrete subjected to acid attack was found to be 52 % of the 28-day compressive strength under normal curing conditions as presented in Fig. 8. However, with inclusion of silica fume, concrete attains resistance even cured for only 7 days.
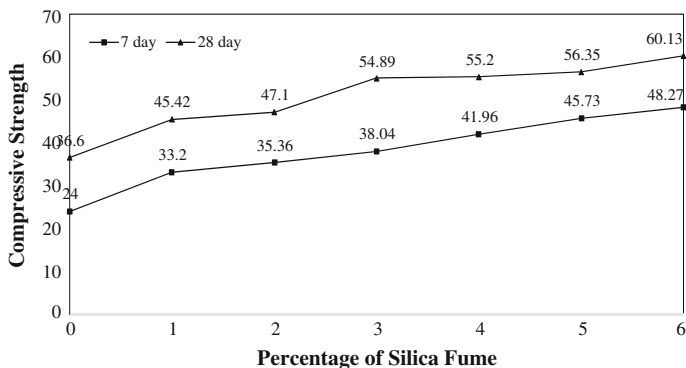
Fig. 6 At 7 and 28 days compressive strength for various percentage levels of silica fume
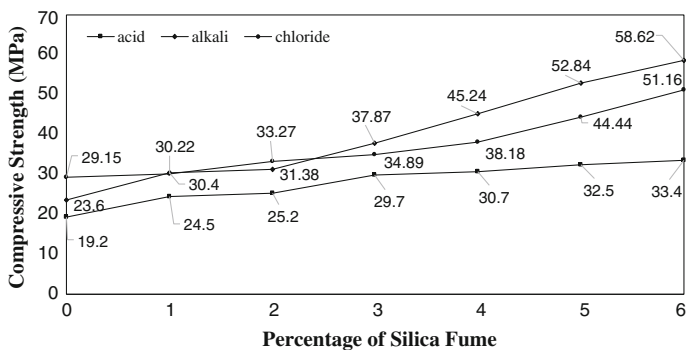
Fig. 7 Compressive strength of cubes after immersion in acid, alkali and chloride solution for 60 days
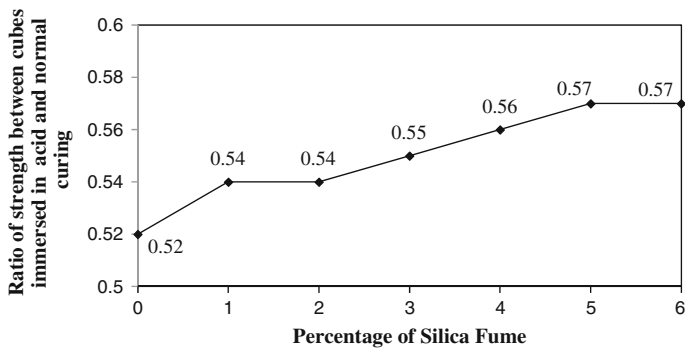
Fig. 8 Ratio of compressive strength between cubes immersed in acid solution and normal curing at 28 days
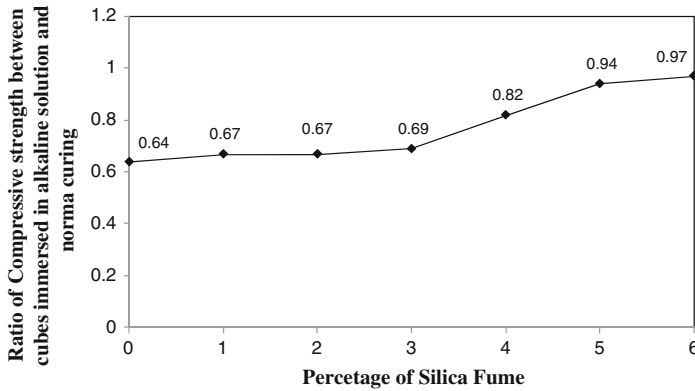
Fig. 9 Ratio of compressive strength between cubes immersed in alkaline solution and normal curing at 28 days

5.5 Alkali Attack Test

From the Fig. 1, it can be observed that addition of 1 % silica fume in concrete is good enough to counter any kind of alkali attack. The percentage loss of weight of cubes for control concrete was 1.1 % and it becomes virtually zero from 1 % of silica fume replacement in concrete.

The 60 days compressive strength of concrete subjected to alkali attack is found to be comparatively less as compared to that obtained under normal curing conditions. The 60 days compressive strength of control concrete, subjected to alkali attack was found to be 64 % of the 28 days compressive strength under normal curing conditions. However, the 60-day compressive strength of concrete with 6 % silica fume, subjected to alkali attack was found to be 97 % of the 28 days compressive strength under normal curing conditions and is presented in Fig. 9. This attack is related to the ettringite formation by reaction of internal or external sulphate with the hydrated calcium aluminate of the hardened cement matrix.

Since the concrete is rigid and if there are insufficient voids to accommodate the ettringite volume increase, expansion and cracks can occur. Silica fume because of its increased impermeability, significantly retards the alkali penetration into the concrete thereby reducing the ettringite related damage.

5.6 Chloride Attack Test

From the Fig. 2, it can be observed that chloride content of concretes replaced with different levels of silica fume shows a decreasing trend with increasing percentage of silica fume. The chloride ion penetration in case of control concrete (without any

Table 4 Ratio of compressive strength between cubes immersed in chloride solution and normal curing

Concrete mix	Ratio
Control	0.79
M1	0.66
M2	0.70
M3	0.63
M4	0.69
M5	0.78
M6	0.85

addition of silica fume) is the highest as compared to concretes replaced with various levels of silica fume content. Further, it can also be noted that the chloride content reduced by 16.61 g/kg of concrete when percentage level of silica fume was increased from 0 to 6 %.

Compressive strength of concrete when cured in saline water for 2 months was found to be comparatively less than the 28 days compressive strength obtained under normal water curing. The compressive strength for control concrete, after 60 days immersion in saline water was found to be 79.6 % of the 28 day compressive strength under normal curing conditions. The results are presented in Table 4. Further, the compressive strength for concrete with 6 % silica fume, after 60 days immersion in saline water was found to be 85.1 % of the 28 days compressive strength under normal curing conditions. This can be attributed to the chloride ions penetration into concrete pores and chloride salts such as sodium chloride may crystallise within the pores inducing internal cracks, which badly affect the compressive strength of concrete. For reinforced concrete, the condition will be much worse as the presence of chloride ions de-passive the concrete around, thus making it possible to initiate reinforcement corrosion.

5.7 Water Absorption Test

Based on the data presented in Fig. 3, it can be noted that the amount of water absorbed decreases with increase in silica fume content. The amount of water absorbed reduced by 3.4 % when percentage of silica fume is increased from 0 to 2 % (control, M1 and M2) and is almost found to be zero from concrete mix M3 (silica fume replaced by 3 %) onwards. This can be attributed to increased impermeability of the silica fume concrete. Silica fume has an average particle size of less than one micron (100 times finer than cement). In concrete, these fine particles fill the gaps between cement grains and react with free lime released during cement hydration. This produces strong calcium silicate hydrates to replace weak lime and voids found in normal concrete. The effect on the water penetrability

is related to the pores size. It has been shown that water does not penetrate pores less than 6 Å nominal diameter. On the other way, it can be defined as silica fume reduces absorption of concrete by reducing the pore size.

6 Conclusions

Workability of concrete decreases with increase in silica fume content. This can be attributed to the percentage increase of fine materials (silica fume) in the mixture of concrete. Therefore use of plasticizer or superplasticizer is almost necessary for having desired workability to concrete. Loss in weight in acidic media decreases with increase in silica fume content. It is found that loss in weight in alkaline media is almost nil for silica fume concrete. Water absorption decreases with increase in silica fume content. This fact is attributed to the increase in impermeability. Chloride content decreases with increase in silica fume content which is also due to increase in impermeability of the concrete. Compressive strength of concrete immersed in saline water is comparatively less as compared to normally cured concrete which can be due to the internal cracking caused by the chloride ions which leads to a loss in strength.

References

1. Kumar V, Mathur M, Sinha S, Dhatrak S (2005) Fly ash: an environmental saviour. Fly Ash India, New Delhi, TIFAC, DST
2. Mccarter WJ, Ben-Saleh AM (2001) Influence of practical curing methods on evaporation of water from freshly placed concrete in hot climates. Build Environ 36:919–924
3. Byfors K (1987) Influence of silica fume and fly ash on chloride diffusion and pH values in cement paste. Cem Concr Res 17(1):115–130
4. Luo R, Cai Y, Wang C, Huang X (2003) Study of chloride binding and diffusion in GGBS concrete. Cem Concr Res 33(1):1–7
5. Cheng A, Huang R, Wu J, Chen C (2005) Influence of GGBS on durability and corrosion behaviour of reinforced concrete. Mater Chem Phys 93(2–3):404–411
6. Oner A, Akyuz S (2007) An experimental study on optimum usage of GGBS for compressive strength of concrete. Cem Concr Compos 29(6):505–514
7. Delage P, Aitcin PC (1983) Influence of condensed silica on the pore size distribution of concrete. Ind Eng Chem Prod Res Dev 22(2):286–290
8. Buhler ER (2007) Two decades of ready-mixed high performance silica fume concrete—a US project review. NRMCA Concrete Technology Forum, Proceedings, Dallas, p 22
9. IS 8112 (1989) Specification for 43 grade Ordinary Portland Cement. Indian Standard Institute, New Delhi, India
10. IS 383 (1970) Specification for coarse and fine aggregates from natural sources for concrete. Indian Standard Institute, New Delhi, India
11. IS 2386-3 (1963) Methods of test for aggregates for concrete, part 3-specific gravity, density, voids, absorption and bulking. Indian Standard Institute, New Delhi, India
12. IS 4031-11 (1988) Methods of Physical Tests for Hydraulic Cement: Part 11—determination of Density. Indian Standard Institute, New Delhi, India

13. IS 9103 (1999) Specifications for admixtures for concrete. Indian Standard Institute, New Delhi, India
14. IS 10262 (2009) Indian standard concrete mix proportioning-guidelines. Indian Standard Institute, New Delhi, India, pp 22–28
15. IS 456 (2000) Code of practice for plain and reinforced concrete. Indian Standard Institute, New Delhi, India
16. IS 14959-2 (2001) Indian standard determination of water soluble and acid soluble chlorides in mortar and concrete—method of test. Indian Standard Institute, New Delhi, India

Influence of Sea Water on Strength and Durability Properties of Concrete

T. Jena and K.C. Panda

Abstract This paper presents the results of an experimental investigation carried out on strength and durability properties of plain and blended cement concrete exposed to sea water. The mix design is targeted for M30 grade concrete. The plain cement concrete samples made 0 % replacement of fly ash (FA) with cement and the blended concrete samples made 10, 20, 30, 40 and 50 % replacement of FA with cement. Another blended cement concrete samples also made with 10 % replacement of FA and 10, 20, 30, and 40 % replacement of silpozz (silica fume) (SF) with cement. Two set of samples (cube) have been prepared. One set of sample, after 28 days of normal water curing (NWC) was being immersed in sea water for 7, 28 and 90 days and the other set of samples have been cured in normal water for 7, 28 and 90 days and their compressive strength measured. The investigation reflects that the percentage increase in compressive strength for blended cement concrete in NWC is better than the samples in sea water curing (SWC) after 28 days of NWC. The water soluble chloride and acid soluble chloride were found less for blended cement concretes up to 10 % replacement of FA and 30 % replacement of SF with cement.

Keywords Sea water · Blended cement · Compressive strength · Acid soluble chloride · Water soluble chloride · Fly ash (FA) · Silpozz (Silica fume) (SF)

1 Introduction

Concrete durability is a subject of major concern in many countries. Numbers of international seminars are held on concrete durability and numerous papers written on failures of concrete structures are discussed and state-of-the-art reports are written and disseminated, regularly. In the recent revision of IS 456-2000 [1], one

T. Jena (✉) · K.C. Panda
Department of Civil Engineering, ITER, SOA University, Bhubaneswar 751030,
Odisha, India
e-mail: trilochanjena@soauniversity.ac.in

of the major point discussed, deliberated and revised is the durability aspects of concrete, in line with codes of practices of other countries, which have better experiences in dealing with durability of concrete structures. One of the main reasons for deterioration of concrete in the past is that too much emphasis is placed on concrete compressive strength. As a matter of fact, advancement in concrete technology has been generally on the strength of concrete. It is now recognized that strength of concrete alone is not sufficient, the degree of harshness of the environmental condition to which concrete is exposed over its entire life is equally important. Therefore, both strength and durability have to be considered explicitly at the design stage.

Some of the researchers have investigated the issue of strength and chloride diffusion in concrete. Guerrero et al. [2] and Bouzoubaa et al. [3] carried out the main deterioration mechanisms in reinforced concrete (carbonation and chloride penetration) and the use of SF with high volume FA significantly lengthened the chloride-induced corrosion initiation stage. Sunil [4] studied the compressive strength and strength reduction factor for the period of 1 year of exposure both in normal water and sea water after 28 days of NWC and the effect of marine environment on concrete is to decrease its compressive strength and this loss increases with age of exposure. Prince and Gagne [5] studied the effect of the type of solutions used in accelerated chloride migration tests for concrete. Basheer et al. [6] monitored the electrical resistance of concretes containing alternative cementitious materials to assess their resistance to chloride penetration. Meck and Sirivivatnanon [7] studied field indicator of chloride penetration depth by using conventional concrete and FA. Lay et al. [8] developed a new method to measure the rapid chloride migration coefficient of chloride-contaminated concrete. Chindaprasirt et al. [9] experimentally studied the resistance to chloride penetration of blended Portland cement mortar containing palm oil fuel ash, rice husk ash and FA. Andrade et al. [10] conducted the testing and modeling of chloride penetration into concrete. Present study focuses on strength deterioration phenomena and chloride content in concrete exposure to sea water.

2 Experimental Study

2.1 Material Used and Properties

The material used in the present study is ordinary Portland cement (OPC), class F fly ash (FA), Silpozz (SF), fine aggregate, coarse aggregate, normal water and sea water. The physical properties of OPC obtained from experimentally and the value specified by IS 8112:1989 [11] are presented in Table 1.

The sand was procured from Daya river bank, Bhubaneswar. The sand is used as fine aggregate which is passing through IS 4.75 mm sieve. The coarse aggregate was supplied by the crusher at Tapanga, near Khurda. The size of aggregate is used

Table 1 Physical properties of ordinary Portland cement

Specifications	Value obtained experimentally	Value specified by IS 8112:1989
Setting time (min)		
Initial setting time	165	30 min (minimum)
Final setting time	360	600 min (maximum)
Standard consistency (%)	34 %	NA
Specific gravity	3.15	3.15
Compressive strength (MPa)		
(a) 3 days	28 MPa	23 MPa
(b) 7 days	42 MPa	33 MPa
(c) 28 days	48 MPa	43 MPa
Fineness (m^2/kg)	333	225 (minimum)

Table 2 Properties of aggregates

Specifications	Value obtained experimentally as per IS:383-1970	
	Coarse aggregates	Fine aggregates
Fineness modulus	7.0	3.03 (zone-3)
Specific gravity	2.86	2.67
Water absorption (%)	0.2	0.4
Bulk density (kg/m^3)	1,424	1,568
Abrasion value (%)	34.78	–
Impact value (%)	24	–
Crushing value (%)	23.3	–

below 20 mm size. The properties of aggregates obtained experimentally as per IS: 383-1970 [12] and the values are presented in Table 2. Sea water is collected from Puri Beach, Bay of Bengal, Konark, Odisha.

In this work, class F fly ash was supplied by NALCO, Angul, Odisha. Silpozz is used as substitute material of silica fume and was supplied from N. K. Enterprises, Singhania House, Jharsuguda, Odisha. The properties of FA and silpozz (SF) are specified by the supplier is presented in Tables 3, 4 and 5.

2.2 Mix Proportion and Identifications

A concrete mixture of M30 was designed as per standard specification of IS 10262-2009 [13] to achieve target mean strength 39 MPa. The concrete mix proportion was (1:1.44:2.91), w/c 0.43. The concrete mix proportion along with their mix

Table 3 Physical properties of fly ash

Characteristics	Physical properties
Specific gravity	2.12
Plasticity	Non-plastic
Proctor compaction	Maximum
Dry density (g/cc)	1.2
Optimum moisture content (%)	28.5
Cohesion (kg/cm^2)	Negligible
Compression index	0.18
Permeability (cm/s)	104.6

Table 4 Physical properties of silpozz (SF)

Characteristics	Average value
Specific surface (m^2/g)	15
Oversize percent retained on 45 μ IS sieve	10
Oversize percent retained on 45 μ IS sieve variation from average percent	5
Compressive strength at 7 days as percent of control sample	85
Bulk density	0.23 g/cc
Physical state	Solid-non-hazardous
Colour	Grey
LOI	<6.0 %

Table 5 Chemical composition of fly ash and silpozz (SF)

Oxides (%)	Chemical composition of silpozz (SF)	Chemical composition of FA
SiO$_2$	88.18	58.13
Al$_2$O$_3$	1.61	31.00
Fe$_2$O$_3$	0.56	4.10
Carbon	2.67	–
CaO	1.59	0.60
MgO	1.63	0.10
K$_2$O	1.67	0.90
Na$_2$O	–	0.05
SO$_3$	–	0.12
TiO$_2$	–	1.63
Others	2.09	0.011
Moisture	0.79	–
LOI		2.90

identification was designated according to their replacement ratio as given in Table 6. Workability of fresh concrete was measured by slump test immediately after mixing. It was found that the slump value varied between 25 and 40 mm.

Table 6 Mix proportions and identity for plain and blended cement concrete

Concrete mix proportion	Mix identity
Contains 100 % cement + 0 % fly ash	MC100F0
Contains 90 % cement + 10 % fly ash	MC90F10
Contains 80 % cement + 20 % fly ash	MC80F20
Contains 70 % cement + 30 % fly ash	MC70F30
Contains 60 % cement + 40 % fly ash	MC60F40
Contains 50 % cement + 50 % fly ash	MC50F50
Contains 80 % cement + 10 % fly ash + 10 % silica fume	MC80F10S10
Contains 70 % cement + 10 % fly ash + 20 % silica fume	MC70F10S20
Contains 60 % cement + 10 % fly ash + 30 % silica fume	MC60F10S30
Contains 50 % cement + 10 % fly ash + 40 % silica fume	MC50F10S40

3 Experimental Results and Discussion

The hardened concrete property such as compressive strength was tested in the laboratory using compression testing machine (CTM). The results are presented along with their graphical plots and discussions. Also, a comparative study of samples in NWC and SWC after 28 days of NWC is presented. The water soluble chloride and acid soluble chloride of samples are also presented in graphical form.

3.1 Compressive Strength

The compressive strength is measured using cube specimens. The size of the cube specimen is 150 mm × 150 mm × 150 mm. Nine cubes were casted for each mix and cured in normal water for 90 days and another nine cubes were casted in normal water and cured in sea water after 28 days of NWC. Figures 1 and 2 show the plot between the compressive strength of cube in MPa and age in days for FA based concrete samples in NWC and SWC respectively. Figure 1 indicates that as percentage of FA increases, the compressive strength decreases. As the number of days of curing increases the compressive strength of cube increases. The percentage of increment of compressive strength is more up to 28 days, thereafter the percentage of increment of compressive strength decreases up to 90 days. In later age, the compressive strength of concrete is almost same up to 20 % replacement of FA with cement. From Fig. 2 it is observed that the compressive strength of concrete specimen is almost same up to 28 days in SWC. In later age the compressive strength of concrete in SWC increases for all mixes, whereas up to 20 % replacement of FA with cement, there is no significant difference with control

Fig. 1 Compressive strength versus age in days (NWC)
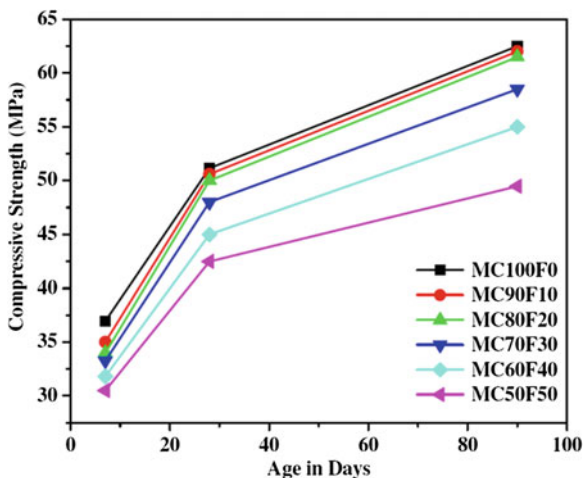
Fig. 2 Compressive strength versus age in days (SWC)
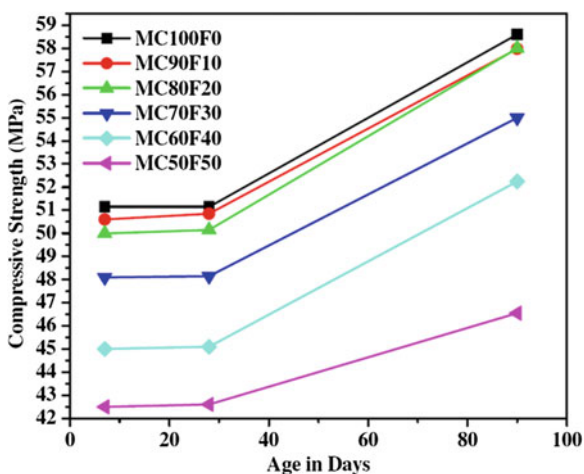
specimen. The compressive strength of SWC samples is also relatively lower as compared to NWC samples in later age.

Figures 3 and 4 represent the compressive strength in MPa versus age in days for 10 % FA and SF based concrete samples in NWC and SWC respectively. Figure 3 indicates that with 10 % of FA and up to 20 % SF, the compressive strength is comparatively more with respect to control specimen at 90 days. It is observed from Fig. 4 that the compressive strength of concrete specimens in SWC is almost same up to 28 days and in later age the strength increases in all the specimens. The compressive strength of specimen with 10 % replacement of FA and up to 20 % SF with cement gives higher value as compared with control specimen in later age. The compressive strength of SWC samples is relatively lower as compared to NWC samples.

Fig. 3 Compressive strength versus age in days (NWC)
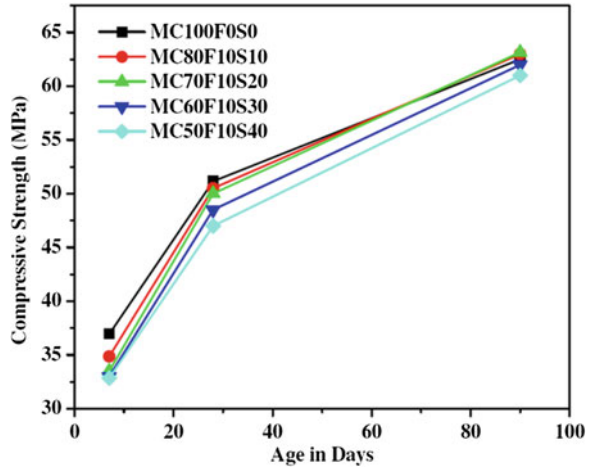
Fig. 4 Compressive strength versus age in days (SWC)
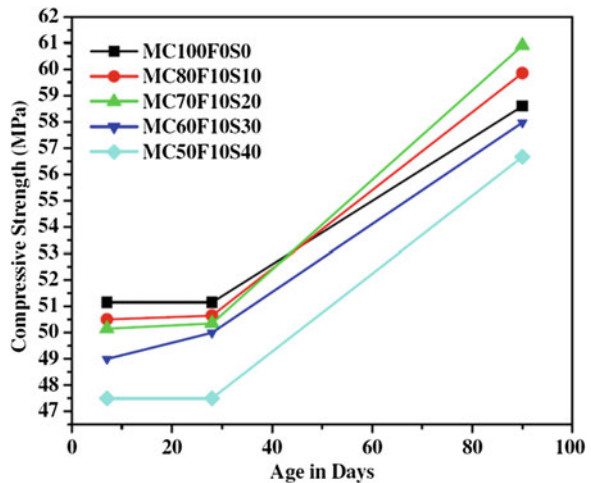
3.2 Determination of Strength Deterioration Factor

The strength deterioration factor (SDF) which is defined as

$$SDF = (1 - \sigma_R/\sigma) \times 100 \qquad (1)$$

where σ_R = compressive strength of cubes after exposed to sea water for a period of 't' days, σ = compressive strength of cubes in normal water curing after 't' days, t = curing period in days.

Fig. 5 SDF (%) versus age in days for FA based concrete
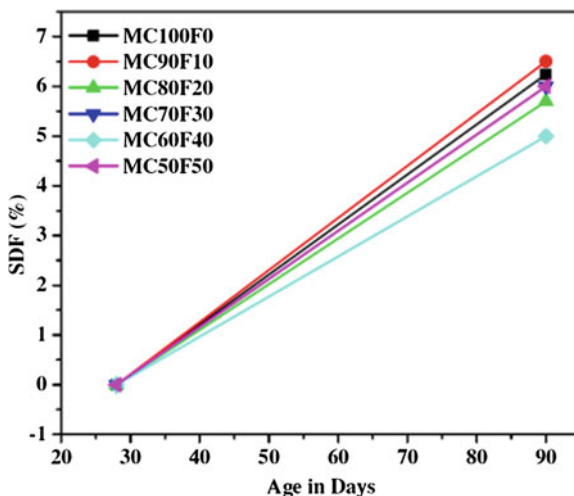
The SDF in percentage versus age in days for FA based concrete sample is presented in Fig. 5. It is observed from Fig. 5, the deterioration factor of concrete mix MC60F40 is less as compared with other concrete mixes.

Figure 6 represents the SDF in percentage versus age in days for 10 % FA and SF based concrete samples. Figure 6 shows that the deterioration factor is low for concrete mix with 10 % FA and up to 20 % replacement of SF with cement. It is found that the blended concrete made with a suitable proportion of FA and SF can reduce the effect of sea water. Since the porosity of blended cement concrete reduces with corresponding hardening of concrete, it is expected that the sea water attack will be less. It is also found that the compressive strength decreases on the

Fig. 6 SDF (%) versus age in days for 10 % FA and SF based concrete
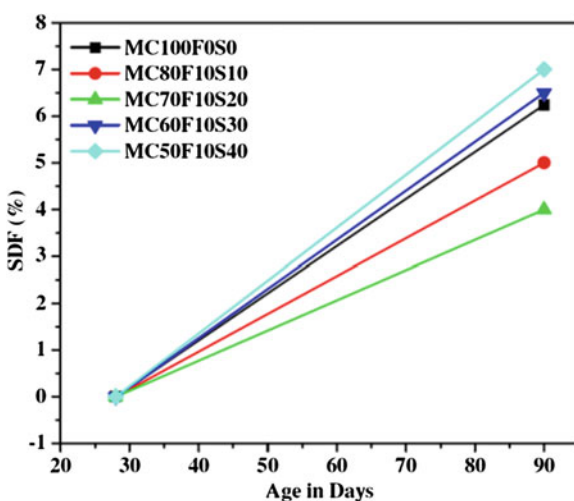
effect of sea water in concrete specimens and this loss increases with age of exposure. The rate of deterioration of concrete in marine environment is dependent on its total porosity and the porosity of blended concrete decreases with time due to the process of hydration of cement.

3.3 Determination of Chloride Content

The chloride content in concrete specimens is determined in form of water soluble chloride and acid soluble chloride as per IS 14959—2001 (Part-1) [14]. The water soluble and acid soluble chloride was determined for samples at 28 days of SWC up to 30 % replacement of FA with cement and combination of 10 % FA with up to 30 % replacement of SF with cement. Figure 7 shows the graph between water soluble chlorides in mg/kg and types of concrete mix.

From Fig. 7, it is observed that MC90F10 and MC60F10S30 are having low water soluble chloride compared to other specimen. Figure 8 shows the graph between acid soluble chloride in mg/kg and types of concrete mix. It is observed from Fig. 8 that the mix MC60F10S30 is having less acid soluble chloride than other specimen. It is found that the addition of silpozz (SF) with 10 % FA may reduce the porosity of the transition zone between cement paste and aggregate.

Fig. 7 Water soluble chloride versus types of concrete mix
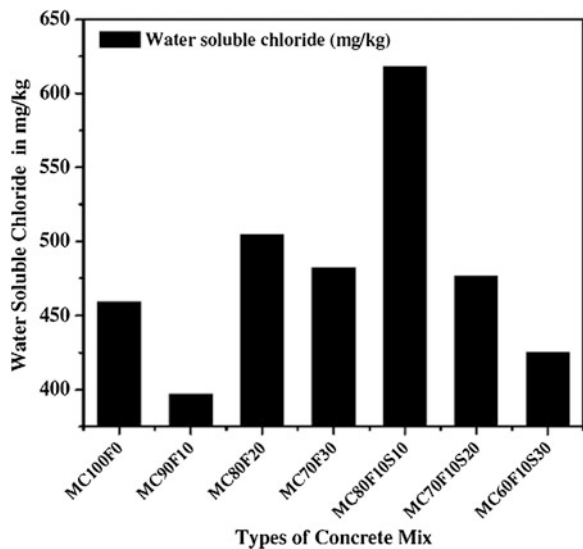
Fig. 8 Acid soluble chloride versus types of concrete mix
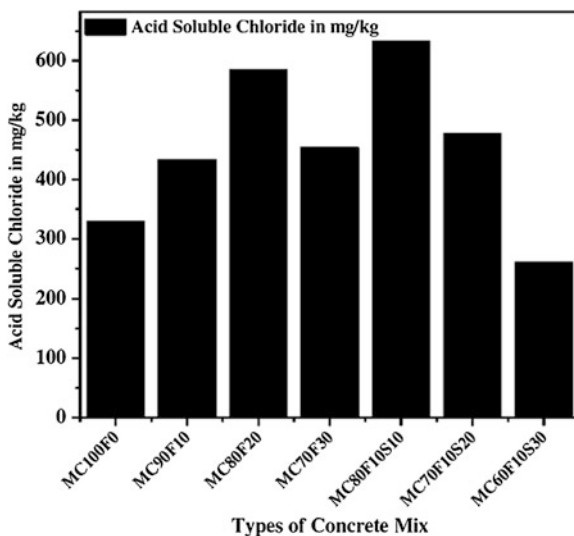
4 Concluding Remarks

It is observed that the deterioration factor decreases when percentage replacement of FA is 10 % and SF replacement is 10 and 20 % for SWC samples in 90 days after 28 days of NWC.

From the study it reveals that the deterioration factor is not significantly changed. But 10 % replacement of FA and up to 20 % SF with cement, the deterioration factor is found to be less than 5 %.

The water soluble chloride and acid soluble chloride in blended cement concrete (MC60F10S30) cured in sea water for 28 days after 28 days of NWC is found less as compared to the control specimen. It is concluded that the concrete made with a suitable proportion of FA and silpozz (SF) can reduce the effect of sea water.

References

1. IS 456-2000, Plain and Reinforces Concrete-Code of Practice (Forth Revision). Bureau of Indian Standards, New Delhi
2. Guerrero A, Goñi S, Macías A (2000) Durability of new fly ash-belite cement mortars in sulfated and chloride medium. Cem Concr Res 30:1231–1238
3. Bouzoubaa N, Zhang MH, Malhotra VM (2000) Laboratory-produced high-volume fly ash blended cements compressive strength and resistance to the chloride-ion penetration of concrete. Cem Concr Res 30:1037–1046

4. Sunil K (2000) Influence of water quality on the strength of plain and blended cement concretes in marine environments. Cem Concr Res 30:345–350
5. Prince W, Gagne R (2001) The effects of types of solutions used in accelerated chloride migration tests for concrete. Cem Concr Res 31:775–780
6. Basheer PAM, Gilleece PRV, Long AE, Mc Carter WJ (2002) Monitoring electrical resistance of concretes containing alternative cementitious materials to assess their resistance to chloride penetration. Cem Concr Compos 24:437–449
7. Meck E, Sirivivatnanon V (2003) Field indicator of chloride penetration depth. Cem Concr Res 33:1113–1117
8. Lay S, Liebl S, Hilbig H, Schießl P (2004) New method to measure the rapid chloride migration coefficient of chloride-contaminated concrete. Cem Concr Res 34:421–427
9. Chindaprasirt P, Rukzon S, Sirivivatnanon V (2008) Resistance to chloride penetration of blended Portland cement mortar containing palm oil fuel ash, rice husk ash and fly ash. Constr Build Mater 22:932–938
10. Andrade C, Prieto M, Tanner P, Tavares F, d'Andrea R (2013) Testing and modelling chloride penetration into concrete. Constr Build Mater 39:9–18
11. IS: 8112:1989, Indian Standard, 43 Grade Ordinary Portland Cement Specification, (First Revision). Bureau of Indian Standards, New Delhi, India
12. IS: 383-1970, Indian Standard Specification for Coarse and Fine aggregates from Natural Sources for Concrete, (Second Revision). Bureau of Indian Standards, New Delhi, India
13. IS: 10262:2009, Concrete Mix Proportioning-Guidelines. Bureau of Indian Standards, New Delhi, India
14. IS: 14959:2001 (part-1), Method of Test determination of water soluble and acid soluble chlorides in mortar and concrete. Bureau of Indian Standards, New Delhi, India

Corrosion Behavior of Reinforced Concrete Exposed to Sodium Chloride Solution and Composite Sodium Chloride-Sodium Sulfate Solution

Bulu Pradhan

Abstract The present paper presents the findings of an experimental work that was undertaken to investigate the effect of aggressive ions such as chloride ions and sulfate ions on rebar corrosion in concrete. In the present work, reinforced concrete specimens were prepared with Portland pozzolana cement and Tempcore TMT steel bar at w/c ratios of 0.45, 0.50 and 0.55. The reinforced concrete specimens were exposed to sodium chloride solutions and composite solutions of sodium chloride and sodium sulfate. Corrosion tests such as half-cell potential measurement and linear polarization resistance technique for corrosion current density measurement were carried out on the specimens after a specified exposure period. From the obtained results of potential values and corrosion current density, behavior of reinforced concrete subjected to chloride and composite chloride-sulfate solutions has been assessed.

Keywords Concrete · Rebar · Chloride ion · Sulfate ion · Potential values · Corrosion current density

1 Introduction

Dense concrete normally exhibits excellent durability properties. However, concrete is not free from degradation problems during its service life as it is exposed to different environmental conditions. Aggressive ions such as chloride ions, sulfate ions etc. enter into concrete and cause various durability problems. Rebar corrosion in concrete structures is a serious problem and is of great concern to civil

B. Pradhan (✉)
Department of Civil Engineering, Indian Institute of Technology Guwahati, Guwahati, India
e-mail: bulu@iitg.ernet.in

infrastructure around the world. The premature failure of reinforced concrete structures due to steel reinforcement corrosion leads to huge repair and maintenance cost.

Steel reinforcement corrosion in concrete is considered as an electrochemical process [1–3]. In this electrochemical process, anodes and cathodes are formed adjacent to each other on the steel bar with concrete pore solution as the electrolyte. The presence of oxygen and moisture is required at the steel-concrete interface for corrosion to proceed. Corrosion products formed during the corrosion process occupy a greater volume than the parent steel and exert swelling pressure to surrounding concrete that results in expansion and cracking of the concrete [4]. The main cause of corrosion is the presences of chloride ions near steel bar. Corrosion initiation takes place when a certain amount of chloride ions has reached near the steel bar and destroys the passive layer which is formed over the steel surface in highly alkaline environment of concrete. This concentration of chloride ions is known as critical or threshold chloride content. Chloride ions can enter the concrete at the time of its preparation and/or enter the hardened concrete [5]. Chloride ions enter fresh concrete through the use of chloride contaminated mixing water, aggregates and chloride bearing admixtures. In the hardened concrete chloride ions enter through the application of deicing salts and from seawater and groundwater.

The ingress of chloride ions as well as sulfate ions takes place into concrete in case of reinforced concrete structures exposed to seawater and groundwater. Seawater and groundwater contain both chloride and sulfate salts. As the penetration of both the aggressive ions takes place, the presence of sulfate ions may affect the chloride induced corrosion of steel reinforcement in concrete. Due to the concomitant presence of both chloride ions and sulfate ions, the chloride biding in concrete may also get affected as both chloride and sulfate ions react with hydrated C_3A. The concentration of free chloride increases as the bound chloride content decreases due to the concomitant presence of both chloride and sulfate ions in concrete as compared to presence of only chloride ions [6].

The durability performance of reinforced concrete against chloride induced corrosion in the presence of sulfate ions can be carried out by determining the corrosion parameters such as potential value and corrosion current density. Potential measurement is a simple technique. In this technique potential value of steel bar is measured with reference to a reference electrode. There are different techniques which are used for determination of corrosion current density (or corrosion rate). These techniques are linear polarization resistance (LPR) measurement, AC impedance spectroscopy technique, gravimetric measurement etc. In this work, effect of chloride ions and combined effect of chloride-sulfate ions on rebar corrosion has been evaluated by exposing the reinforced concrete specimens to chloride solutions and composite chloride and sulfate solutions and determining potential values and corrosion current density.

2 Experimental Program

2.1 Materials

The reinforced concrete slab specimens with a centrally embedded steel bar of diameter 12 mm were prepared from different concrete mixes. Portland pozzolana cement and w/c ratios of 0.45, 0.50 and 0.55 were used in the preparation of the specimens. Locally available sand was used as fine aggregate. Coarse aggregates of size 20 mm maximum size of aggregate (MSA) and 12.5 mm MSA were used in the proportion of 66 and 34 % of the total mass of coarse aggregate respectively. Tap water from laboratory was used as the mixing water. Concrete mixes for different w/c ratios were designed for similar workability with slump value 30–50 mm and water content of 200 kg/m^3 was taken on the basis of trial tests for the desired workability. The mix quantities of cement, sand and coarse aggregate were calculated as per the guidelines of British mix design method [7] with some modifications. The quantities of water, cement, sand and coarse aggregate at different w/c ratios are presented in Table 1.

2.2 Specimen

Reinforced concrete slab specimens of size 320 mm × 320 mm × 52 mm with a centrally embedded steel bar were prepared from PPC and w/c ratios of 0.45, 0.50 and 0.55. Tempcore TMT (thermo-mechanically treated) steel bar of diameter 12 mm was centrally embedded in the slab specimens. The concrete cover to steel bar both at top and bottom was 20 mm. After 24 h of casting, the slab specimens were demoulded and moist cured in a curing tank for 27 days. After completion of moist curing, the slab specimens were removed from the curing tank and kept in the laboratory exposure condition for 14 days before exposure to test solutions. The schematic diagram of the slab specimen is shown in Fig. 1.

Table 1 Quantities of mix ingredients of concrete

w/c ratio	Water content (kg/m^3)	Cement content (kg/m^3)	Sand content (kg/m^3)	Coarse aggregate content (kg/m^3)
0.45	200	444.44	605.69	1,124.86
0.50		400.00	621.25	1,153.75
0.55		363.64	633.98	1,177.39

Fig. 1 Schematic diagram of slab specimen with a centrally embedded steel bar
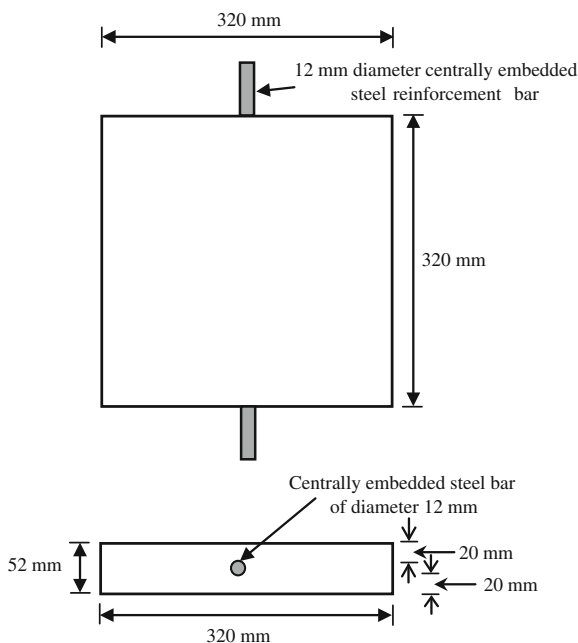
2.3 Chloride and Composite Chloride-Sulfate Solutions

As already stated, after completion of moist curing the slab specimens were kept in laboratory exposure condition for 14 days. After that the specimens were exposed to chloride solutions and composite chloride and sulfate solutions with alternate wetting-drying cycles. The chloride solutions were prepared by dissolving analytical reagent grade sodium chloride (NaCl) of different concentrations (% by mass of water) in the required quantity of water. Similarly the composite solutions were prepared by dissolving different concentrations (% by mass of water) of both sodium chloride and sodium sulfate (Na$_2$SO$_4$) of analytical reagent grade in water. The details of chloride solutions and composite chloride-sulfate solutions are shown in Table 2. During each alternate wetting-drying cycle, the slab specimens prepared from different concrete mixes were immersed in plastic containers containing test solutions for 7 days followed by laboratory drying for next 7 days.

2.4 Corrosion Tests

The corrosion tests such as potential measurement and linear polarization resistance (LPR) measurement were carried out on the slab specimens at the age of 180 days from the day of casting, after exposure to different solutions with alternate wetting-drying cycles using the corrosion monitoring instrument (Make ACM, Gill AC

Table 2 Exposure solutions

S. No.	Concentration of NaCl (NC) (%)	Concentration of Na$_2$SO$_4$ (NS)	Solution concentration
1	1.5	–	1.5 % NC
2	3.5	–	3.5 % NC
3	5	–	5 % NC
4	1.5	2.5 %	1.5 % NC + 2.5 % NS
5	3.5	2.5 %	3.5 % NC + 2.5 % NS
6	5	2.5 %	5 % NC + 2.5 % NS

serial no. 1542). For measurement of half-cell potential, saturated calomel electrode (SCE) was used as the reference electrode. For determining corrosion current density, LPR test with IR compensation was carried out with guard ring arrangement on the slab specimens. As concrete is a high resistive medium, IR drop in the concrete cover is compensated while determining the corrosion current density of the steel bar embedded in concrete. In order to have a proper electrical contact with the specimen, the conducting sponge attached to the guard ring was wetted with soap solution and then the guard ring assembly was placed on the surface of the slab specimen. For determination of corrosion current density by LPR technique, the embedded steel bar (working electrode) in the slab specimen was polarized to ±20 mV from the equilibrium potential at a scan rate of 0.1 mV per second. The polarized surface area of the steel bar is taken as that lying under a circle intersecting the midpoint between the two sensor electrodes [8, 9] present in guard ring assembly. Further it is assumed that only top half surface area of the steel bar is polarized [9, 10]. The corrosion current density of steel bar was determined using the Stern-Geary equation and is given as follows;

$$i_{corr} = \frac{B}{R_p} \tag{1}$$

where

I$_{corr}$ corrosion current density
B   Stern-Geary constant
R$_p$ polarization resistance of steel

The value of B is considered as 26 mV for steel bar in active condition [9].

3 Results and Discussion

As already stated earlier, the potential values of steel bar embedded in slab specimens and subjected to chloride and composite chloride-sulfate solutions were measured with reference to saturated calomel electrode (SCE). The results of

Fig. 2 Potential values (with
respect to SCE) of steel in
concrete subjected to chloride
solutions
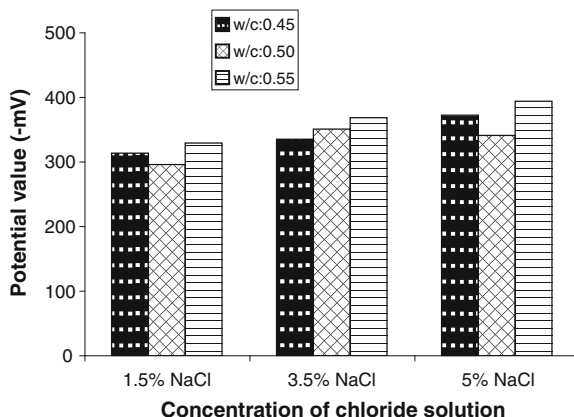
Fig. 3 Potential values (with
respect to SCE) of steel in
concrete subjected to
composite chloride-sulfate
solutions

NC: Sodium Chloride (NaCl) and NS: Sodium Sulfate (Na_2SO_4)
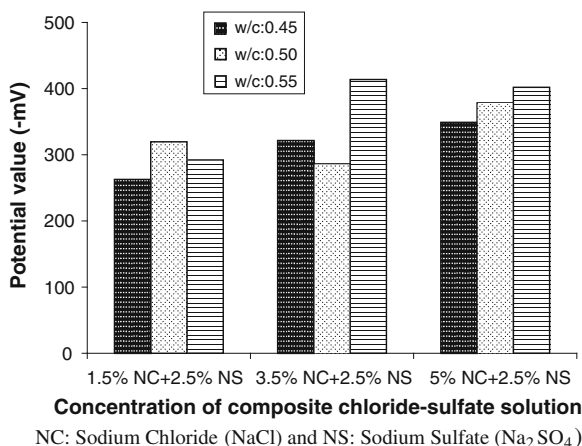
half-cell potential values at different w/c ratios are shown in Figs. 2 and 3 for
specimens exposed to chloride solutions and composite chloride-sulfate solutions,
respectively.

From these figures it is observed that, mostly there is no systematic variation in
half-cell potential values with w/c ratio for both chloride and composite chloride-
sulfate solutions. Further it is noted, that the half-cell potential values of steel bar
were mostly more negative than −270 mV (with respect to SCE)/−350 mV (with
respect to Cu/CuSO$_4$ reference electrode) in both types of exposure solutions and as
per ASTM C876 [11], the obtained potential values correspond to a greater than
90 % probability of steel reinforcement corrosion occurrence. From Fig. 2, it is
observed that the potential values mostly decreased with increase in sodium
chloride concentration. Further it is inferred that, there is no systematic variation in
potential values between chloride solution and composite chloride-sulfate solutions
at different w/c ratios as evident from these figures.

Fig. 4 Corrosion current density values of steel embedded in concrete and exposed to chloride solutions
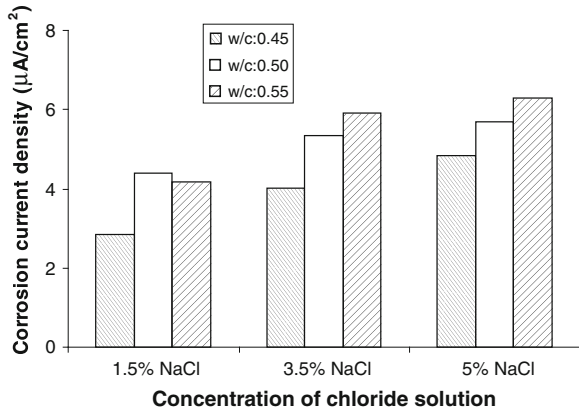
Fig. 5 Corrosion current density values of steel embedded in concrete and exposed to composite chloride-sulfate solutions

NC: Sodium Chloride (NaCl) and NS: Sodium Sulfate (Na_2SO_4)
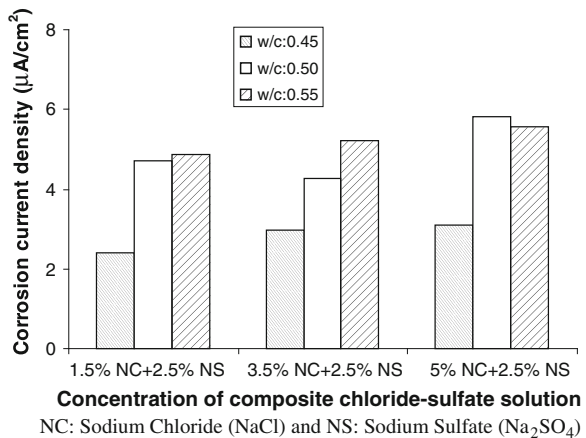
The results of corrosion current density values at different w/c ratios are shown in Figs. 4 and 5 for specimens exposed to chloride solutions and composite chloride-sulfate solutions respectively.

From these figures, it is inferred that the corrosion current density mostly increased with increase in w/c ratio for both chloride and composite chloride-sulfate solutions. The lower corrosion current density in the specimens made with lower w/c ratio may be due to higher resistivity as a result of denser microstructure at lower w/c ratio as compared to that at higher w/c ratio. Further from Fig. 4, it is observed that, there is increase in corrosion current density with increase in concentration of sodium chloride. This is attributed to increase in conductivity of concrete at higher concentration of sodium chloride solution. On comparison of corrosion current density between chloride solutions and composite chloride-sulfate solutions, it is observed that the specimens exposed to composite solutions of sodium chloride and sodium sulfate mostly exhibited lower values of corrosion density as compared to those exposed to only sodium chloride solution.

4 Conclusions

From the results of the experimental investigation, it is observed that the half-cell potential values of steel bar in the concrete specimens exposed to both chloride and composite chloride-sulfate solutions were mostly more negative than −270 mV (with reference to saturated calomel electrode). There is no systematic variation in potential values of steel bar between chloride solution and composite chloride and sulfate solutions. Mostly there is increase in corrosion current density with increase in w/c ratio in both types of exposure solutions. In case of exposure to only chloride solutions, the corrosion current density increased with increase in sodium chloride concentration. The steel reinforcement in concrete specimens exposed to composite chloride-sulfate solutions mostly showed lower corrosion current density than those exposed to only chloride solution.

References

1. Liu T, Weyers RW (1998) Modeling the dynamic corrosion process in chloride contaminated concrete structures. Cem Concr Res 28:365–379
2. Hope BB, Page JA, Ip AKC (1986) Corrosion rates of steel in concrete. Cem Concr Res 16:771–781
3. Elsener B (2002) Macrocell corrosion of steel in concrete—implications for corrosion monitoring. Cem Concr Compos 24:65–72
4. Neville AM, Brooks JJ (2004) Concrete technology. Pearson Education, Delhi
5. Saricimen H, Mohammad M, Quddus A, Shameem M, Barry MS (2002) Effectiveness of concrete inhibitors in retarding rebar corrosion. Cem Concr Compos 24:89–100
6. Dehwah HAF, Maslehuddin M, Austin SA (2002) Long-term effect of sulfate ions and associated cation type on chloride-induced reinforcement corrosion in Portland cement concretes. Cem Concr Compos 24:17–25
7. SP 23: 1982 Handbook on concrete mixes (based on Indian standards). Bureau of Indian Standards, New Delhi
8. Law DW, Millard SG, Bungey JH (2000) Linear polarisation resistance measurements using a potentiostatically controlled guard ring. NDT&E Int 33:15–21
9. Pradhan B, Bhattacharjee B (2009) Performance evaluation of rebar in chloride contaminated concrete by corrosion rate. Constr Build Mater 23:2346–2356
10. Gu GP, Beaudoin JJ, Ramachandran VS (2001) Techniques for corrosion investigation in reinforced concrete. In: Ramachandran VS, Beaudoin JJ (eds) Handbook of analytical techniques in concrete science and technology. Noyes Publications, New Jersey, pp 441–504
11. ASTM C 876-09 (2009) Standard test method for corrosion potentials of uncoated reinforcing steel in concrete. West Conshohocken, PA

Service Life Prediction Model for Reinforced Concrete Structures Due to Chloride Ingress

D.R. Kamde, B. Kondraivendhan and S.N. Desai

Abstract The present paper tries to contribute to quantify the relationship between the mixed factors which directly or indirectly affect the corrosion of reinforcement, with corrosion current and service life. The variables studied were water cement ratio, concrete cover, bar diameter and exposure condition. Effect of percentage of fly ash and silica fume was studied considering general corrosion models to study the effect of corrosion pattern for the same. MATLAB code was developed and using Monte-Carlo simulation technique set of data was gathered to observe the effect of various factors on service life. Multiple regression analysis was implemented to obtain relationship of corrosion current with different factors like concrete cover, bar diameter, water to cement ratio, percentage of loss of reinforcement due to corrosion and time after corrosion initiation.

Keywords Reinforced concrete · Corrosion · Chlorine attach · Service life

1 Introduction

We live in world of concrete structures which involves different structures with different utility and different location, due to demand we have moved to on-shore and even to off-shore structures in recent decades. The number of marine reinforced concrete (RC) structures has been increasing due to the requirement of large infrastructure. For marine concrete structures, chloride-induced reinforcement corrosion is the most common form of structural deterioration, which may eventually result in the damage to the structures in the form of cracking, spalling and delimitation of concrete cover and loss of bond between concrete and reinforcement.

D.R. Kamde (✉)
RK University, Rajkot, Gujrat, India
e-mail: Deepak.kamde@rku.ac.in

B. Kondraivendhan · S.N. Desai
Sardar Vallabhbhai Patel National Institute of Technology (SVNIT), Surat, Gujrat, India

Therefore it is necessary to study the factors affecting the service life. Tuutti [1] proposed a service life model which has been modified in this work.

Service life of RC structures has been divided into three parts, corrosion initiation, corrosion propagation and strength reduction time. Corrosion initiation is the time during which threshold amount of chloride reaches the rebar level and pH value at the surface of rebar reaches the limit to start the corrosion. Corrosion propagation on the other hand is the time period during which corrosion initiates and due to formation of corrosion products radial pressure gets developed and ultimately results into cracking due to increase in radial pressure up to critical value. In this study propagation period has been considered as the time when crack width reaches the threshold limit 0.65 mm, normally it ranges between 0.6 and 0.7 mm. generally it was found that the strength of RC structures does not reduces up to critical limit therefore 'Time to strength reduction' was involved as an additive of the former two periods.

2 Research Significance

It is the objective of this paper to present a methodology that can be used to predict the service life of RC structure particularly exposed to marine environment using different model of corrosion. The methodology will explain the parameters involved in different steps. It was found in literature review that many concepts have been discussed and explained earlier, but present research combine them into one single technique.

3 Methodology

To predict service life with precision one should understand the corrosion process. For example in case of submerged structures corrosion process is very slow due to lack of sufficient oxygen. And in case of splash zone where the structure comes under continuous wet and dry condition goes for higher rate of corrosion. Also corrosion process depends on the location of structures. First chlorine has been assumed to follow Fick's law of second derivative for the transport of chlorine ion from surface to rebar level, once threshold amount of chloride ion has been occupied at surface of rebar level corrosion of reinforcement starts. Since corrosion product has lesser density than steel it occupies more space and impose radial pressure on surrounding concrete cover, which when exceed the tensile strength of concrete, concrete cover cracks, which ultimately leads to failure element.

3.1 Time to Initiation: Transport of Chloride

To study the transport of chloride in concrete Fick's second law of diffusion should be solved

$$\frac{\partial c}{\partial t} = D \frac{\partial^2 c}{\partial x^2}$$

(1)

There are few limitations which are not possible to incorporate in mathematical model such as surrounding environment changes frequently which leads to change in chloride content continuously. Also concrete pores interconnectivity is unpredictable which may not be connected throughout the depth which may stop chloride transport. Excluding all these limitations equation one can be solved using some boundary conditions such as $c(x = 0, t = 0) = c_s$ and $c(x = 0, t = 0) = c_i$, $c(x = 0, t) = \Phi(t)$ results in,

$$c(x,t) = c_i + (c_s - c_i)\left[1 - erf\left(\frac{x}{2\sqrt{D(t) * t}}\right)\right]$$

(2)

where, $c(x, t)$ is the chloride content at depth x and time t, c_s is surface chloride content c_i is initial chloride content, $D(t)$ is diffusion constant x is concrete cover depth t is time of interest, $\Phi(t)$ is any function with variable time and *erf* is error function.

$$erf(y) = \int_0^y e^{-u^2} du$$

(3)

Surface chloride concentration has been assumed as constant with respect to the location of structure. Depending upon chlorine concentration environment has been divided into five categories mild, moderate, severe, very severe and extreme exposure condition. Chlorine content has been assumed varying from 0.1 to 3 % of binder/cement content.

Variable chloride diffusivity: Chloride diffusivity is indirect representation of porosity of concrete, which has been assumed as constant by many researchers. In present study diffusivity has been assumed as the time varying mathematical function.

$$D(t) = D_0 \left(\frac{t_0}{t}\right)^n$$

(4)

where, D_0 is an apparent diffusion coefficient at a reference time ($t_0 = 28$ days) and n is the age factor which depends on the type of binder or water-cement ratio and exposure condition respectively. Value of n was taken as 0.3–0.6 depending upon

exposure condition; 0.6 for splash zone and 0.3 for mild exposure condition. Also the value of D was taken as the fraction of 10^{-12} to 10^{-11} m²/s for less water cement ratio to high water to cement ratio (say from 0.35 to 0.6) [2].

If chloride ion concentration reaches the threshold limit Eq. (2) can be modified as

$$T_{corr} = \frac{x^2}{4D\left[erfc^-\left(c_{th}\big/(c_o + c_i)\right)\right]} \tag{5}$$

where T_{corr} is time to initiation, c_{th}, c_o, c_i is threshold, surface and initial chloride concentration and other D is apparent diffusivity.

3.2 Time to Propagation: Corrosion and Cracking

Corrosion products when fill the minor cracks and pore space available between rebar and concrete cover, extra corrosion products impose the radial pressure in outward direction which results into cracking. A service life prediction formula which directly depends upon the percentage of area loss, in present model prediction model depends on corrosion current which is result of formation of small electrochemical cell formed due to difference in voltage inside pit.

Figure 1 shows the systematic diagram which shows the formation of small electrochemical cell. The surface of corroding steel functions as the composite of anodes and cathodes connected through the body of steel itself. Concrete pore water act as the complex electrolyte. The chemical reactions take place during the process has been shown in the Fig. 1.
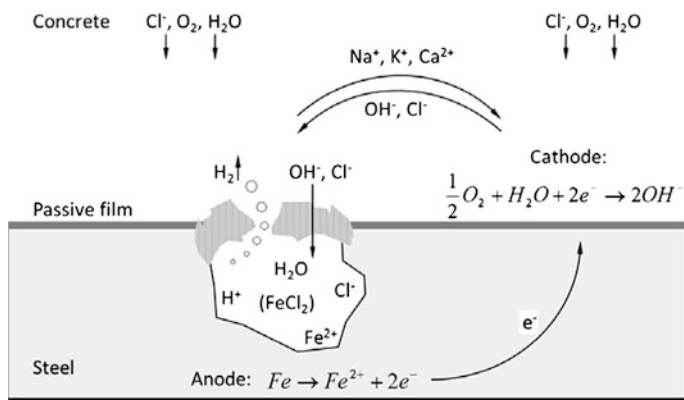
Fig. 1 Schematic representation of chloride induced pitting corrosion

If corrosion current density i_{corr} ($\mu A/cm^2$) is defined as the corrosion current per unit steel surface and the unit length equals 1 cm, considering steel density $\rho_s = 7.85$ g/cm^3 and z = 2.5 (mean value for Fe2+ and Fe3+), the percentage mass loss (ρ) = ($M_{bss} \times 100/M_s$) %, can be rewritten below with Eq. (6)

$$\rho = \frac{400 \times M_{loss}}{\pi \times d^2 \times \rho_s} = \frac{i_{corr}}{26.80 \times d} t \tag{6}$$

M_{loss} is the mass loss of reinforcement due to corrosion, which can be mathematically predicted as,

$$M_{loss} = V_{loss} \times \text{density of steel} = (A_{loss} \times \text{length} (=1\text{unit}) \times \text{density of steel}) \tag{7}$$

$$A_{st} = \frac{n\pi(D_o - r_{corr}(t - T_{corr}))^2}{4} \tag{8}$$

where n is the number of bars experiencing active corrosion D_0 is Initial diameter of bar (in mm), r_{corr} is rate of corrosion (in mm/year), T_{corr} is the time to corrosion initiation (years) and t is the instantaneous time. Values of r_{corr} have been adopted from Ramamrutham [3]. And therefore the modified form of model proposed by Vu et al. [4] to predict the radial pressure [using Eq. (6)]

$$q = \left[\sqrt{1 + \frac{(n-1) \times i_{corr}}{26.80(d + K \times x)} t} - 1 - 2\delta_0/d \right] \times E_{cef} \times \left[\frac{(r_0 + x)^2 + r_0^2}{(r_0 + x)^2 - r_0^2} + v_c \right]^{-1} \tag{9}$$

The radial pressure required to cause entire cracking of concrete cover q_{cr}, can be calculated

$$q_{cr} = \left(0.3 + 0.6 + \frac{x}{d} \right) f_{ct} \tag{10}$$

where f_{ct} is tensile strength of concrete, x and d, are concrete cover and diameter respectively. When q is equal to q_{cr} time elapsed is the time from corrosion initiation to cover first cracking.

Crack width developed due to uniform corrosion considering corrosion current density into account.

$$w = 0.0062 \times \left\{ (59.88 \times i_{corr} \times t) - 42.9 \left(\frac{x}{(w/c)} \right)^{0.54} \right\}^{2/3} + 0.3 \tag{11}$$

Solving Eqs. (7–9),

$$t_p = 0.0167 \times i_{corr}^{-1.1} \times \left[42.9 \left(\frac{x}{(w/c)} \right)^{0.54} + \left(\frac{w_{\lim} - 0.3}{0.0062} \right)^{1.5} \right] \tag{12}$$

where w is crack width, i_{corr} is corrosion current density; t_{p} is the time to propagation. Corrosion current density depends on many factors as concrete cover, bar diameter, percentage loss in area of reinforcement corrosion, water to cement ratio and time after corrosion started. Many researchers have worked on this aspect but no one has tried to include all the variables which directly affect the corrosion. By gathering the data from available research paper, using multiple regression analysis we have proposed a new model to predict the corrosion current at instantaneous time which can be further used to calculate the radial pressure, crack width and time to propagation from Eqs. (9–11) respectively. The proposed model for corrosion current density is shown in Eq. (13)

$$i_{corr} = 0.88 \times e^{\left(\left(\ln(0.974)^x \right) + \left(\ln(0.977)^d \right) + (\ln(21.099)^{w/c}) - (\ln(0.978)^{\%loss}) + \left(\ln(1.002)^{(t - t_{corr})} \right) \right)} \tag{13}$$

$$i_{corr} = 0.837 \times e^{\left(\left(\ln(0.974)^x \right) + \left(\ln(0.998)^d \right) + (\ln(26.81)^{w/c}) - (\ln(0.9377)^{\%loss}) + \left(\ln(1.05)^{(t - t_{corr})} \right) \right)} \tag{14}$$

for (t-tcorr) < 1

3.3 Deterioration Period: Time to Strength Reduction

This period involves the time after critical crack width is achieved till the time when compressive strength of concrete reduces to the minimum acceptable limit or when reinforcement reduces its tensile strength up to the minimum acceptable limit and structure becomes unsafe from stability point of view. It was seen that the steel loses its strength up to minimum acceptable limit much before concrete fails therefore this paper has mainly concentrated upon strength reduction of steel. Du et al. [5] had introduced the equations to understand the strength reduction pattern of steel but in broader view we can consider the reduction in 30 % of cross sectional area of rebar can considered as the end of service life. Equation (12) explains the deterioration period as the time when residual strength becomes less than or equal to minimum acceptable strength.

$$R_s(t_r) = R_a \tag{15}$$

MATLAB code was developed using the same methodology explained above and Monte-Carlo simulation was used to study the variation of initiation time, propagation time, time to strength reduction and service life with respect to concrete cover and bar diameter under different exposure condition for concrete mix with different water to cement ratio.

4 Results and Discussion

As expected initiation time is proportional to concrete cover, as already explained in Eq. (5) time of corrosion is proportional to concrete cover. Structure exposed to low chloride atmosphiric condition will have more service life which signifies that the initiation time is inversely proportional to the chloride content in atmosphere as shown in Fig. 2. Also it was seen that the initiation time does not depend on bar diameter since it is the time for chloride to reach threshold limit.

Propagation time is the time when corrosion starts and crack starts propagating which depends on concrete cover, and bar diameter. Figures 3 and 4 indicate that the propagation period is directly proportional to concrete cover as well as bar diameter. Since it is the time when concrete cover cracks up to 0.65 mm (threshold limit ranges between 0.6 and 0.7 mm), which is dependent of tensile strength of concrete which is directly dependent of water to cement ratio. Figure 5 shows the variation of propagation time with respect to concrete cover for different water to cement ratio which indicate that the radial pressure required to cause threshold

Fig. 2 Variation of initiation time with respect to concrete cover for concrete mix with w/c 0.4 for different exposure condition
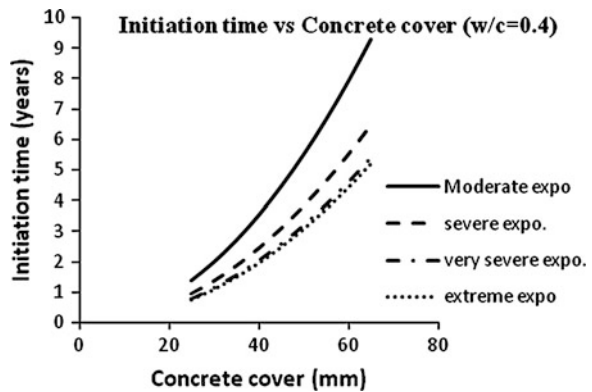
Fig. 3 Variation of propagation time with respect to concrete cover for concrete mix with w/c 0.4 for different exposure condition
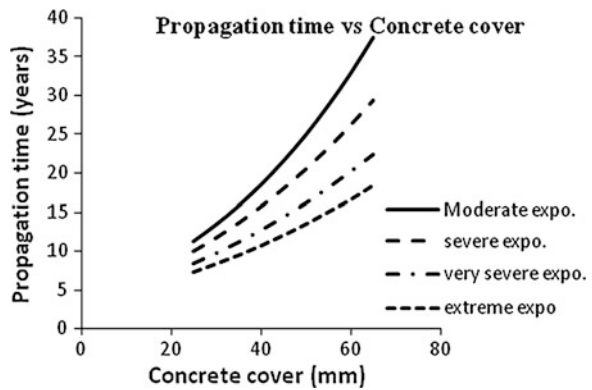
Fig. 4 Variation of propagation time with respect to bar diameter for concrete mix with w/c 0.4 for different exposure condition
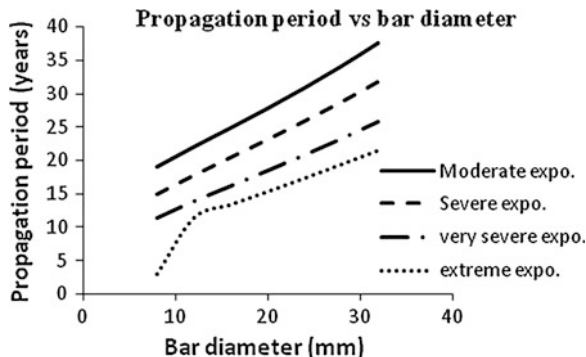
Fig. 5 Variation of radial pressure versus time for the concrete with w/c = 0.4 (CC = 50 mm, Dia = 16 mm)
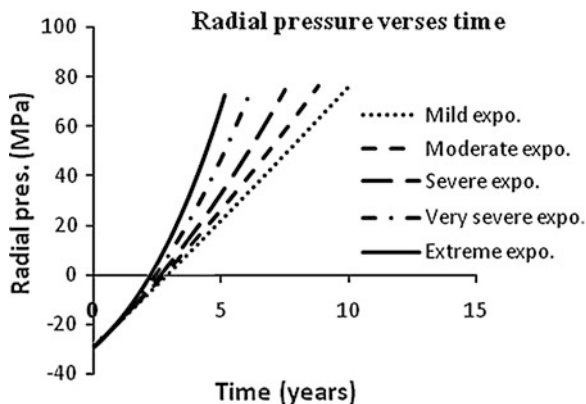
crack is maximum for concrete mix with w/c of 0.4 and minimum for mix with w/c of 0.6.

Figure 5 indicates the stages during propagation time. The negative radial pressure indicates the time when corrosion has not started and so internal pressure is higher than radial pressure which results into negative radial pressure. While the case when internal pressure becomes equal to the radial pressure at that particular instant radial pressure is equal to zero and in later stage when radial pressure exceeds the tensile strength of concrete due to formation of more corrosion products, results in cracking.

The Figure 6 shows that the water binder ratio plays an important role for deciding the service life of RC structures. w/c ratio is direct representation of porosity of concrete which regulates the transport of chloride into the concrete cover as well as corrosion of reinforcement.

As expected concrete cover and bar daimeter plays an important role in prediction of service life of RC structures (Figs. 7 and 8). An increase of 10 mm of concrete cover results into increase of 50 % of service life in case of extreme exposure condition, which can be easily understood using fick's law.

Fig. 6 Variation of service
life versus concrete cover for
extreme exposure condition
with different w/c ratio
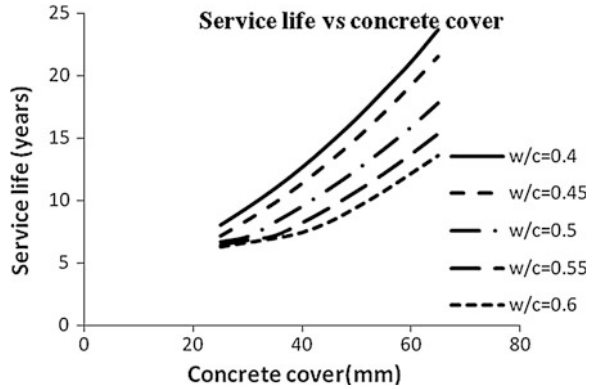
Fig. 7 Variation of service
life with respect to concrete
cover for concrete mix with
w/c 0.4 for different exposure
condition
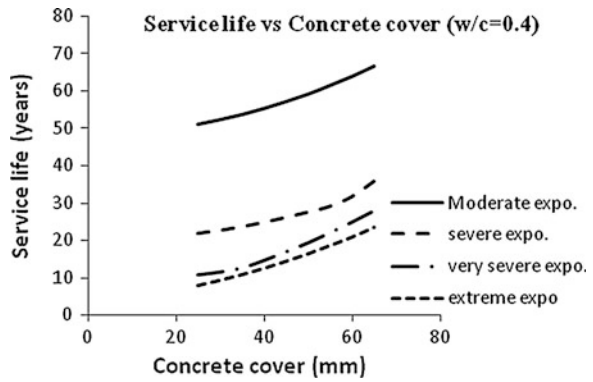
Fig. 8 Variation of service
life with respect to bar
diameter for concrete mix
with w/c 0.4 for different
exposure condition
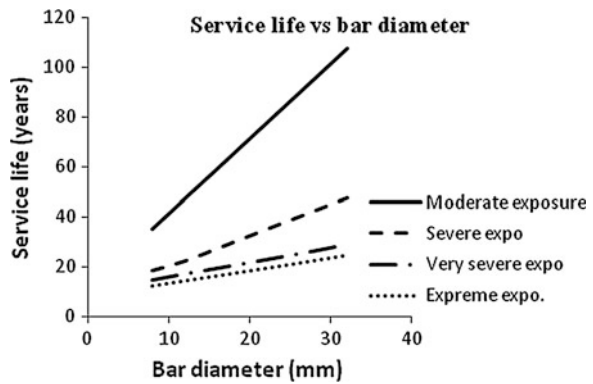
Bar chart shown in Fig. 9 indicates that in case of lower chloride contaminated region more bar diameter gives better results as compared to more concrete cover, which indicates that the in chlorinated environment propagation period is much less

Fig. 9 Bar diagram representing service life for different exposure condition
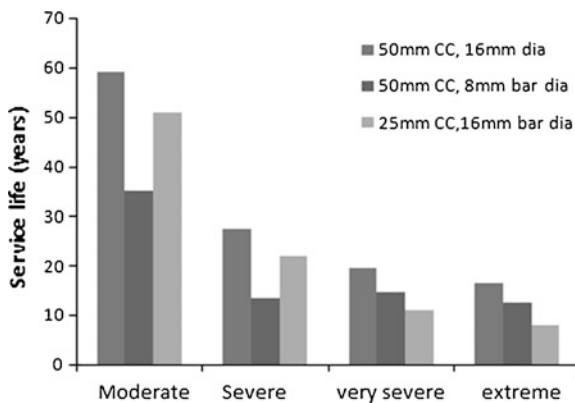
as compared to initiation period due to high rate of corrosion. Since higher concrete cover offers more hindrance for chlorine to reach reinforcement which increases the service life of structure.

Bar chart shown in Fig. 10 states that the replacement of 25 % of fly ash is sufficient in point of view of service life in case of high chlorinated environment; while in case of low chlorinated environment only 20 % is proven to be beneficial in all. Same effect was observed for the case of other w/c ratio but in case of concrete mix with w/c = 0.6 initiation time was observed to be zero which means the corrosion of reinforcement starts very early, which may be because fly ash could not form bond with adhesive material at such high water to cement ratio.
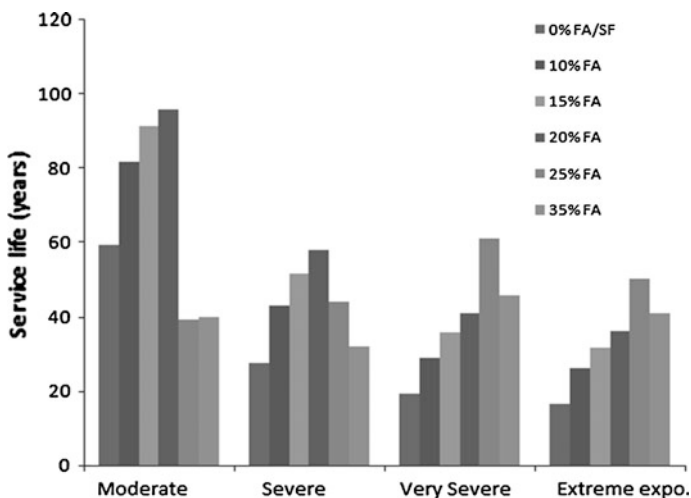
Fig. 10 Bar diagram representing service life for concrete mix of w/c 0.4, with different percentage of silica fume and fly ash under different exposure conditions

5 Conclusion

1. Chloride ingress depends on the porosity of concrete; which is dependent on water to cement ratio. More the w/c ratio more will be the porosity and so rate of transport of chloride will be more.
2. Exposure conditions are directly an indication of the amount of surface chloride concentration. Initiation time also depends on the exposure condition in other words depends on surface chloride concentration. Initiation time is found to be 45, 72 and 75 % less than moderate exposure condition for sever, very severe and extreme exposure condition.
3. Replacement of fly ash up to 25 % (In case of more chlorinated environment) is found to be sufficient to occupy all the voids, further addition of which does not make any difference in diffusivity.
4. Addition of fly ash in case of concrete mix with high w/c ratio 0.6, does not results into increase in initiation time; this might be due to no development in bonds between cement and fly ash.
5. Radial pressure develops more rapidly in case of concrete with water to cement ratio of 0.4 and develops with least rate for the concrete mix with w/c = 0.6.
6. Replacements of 25 % of fly ash increases the increases the Initiation time, propagation time and service life by 75, 25, and 60 % respectively for very severe and extreme exposure condition as compared to case of 0 % fly ash.

References

1. Tuutti K (1982) Service life of structures with regards to corrosion of embedded steel. SP 65–13:223–236
2. Magne M, Helland S, Poulsen E, Vennesland O, Carlsen JE (1996) Service life prediction of existing concrete structures exposed to marine environment. ACI Mater J 93(6):1–7
3. Ramamrutham (2011) Design of steel structure. Chapter 15, Oxford Publication, UK, pp 15.1–15.28
4. Vu K, Mark G, John M (2005) Corrosion induced cracking: experimental data and predictive models. ACI Struct J 102(5):719–726
5. Du YG et al (2004) Residual capacity of corroded reinforcing bar. Mag Concr Res 53 (3):135–147
6. Riding KA, Thomas MD, Folliard KJ (2013) Apparent diffusivity model for concrete containing supplementary cementitious materials. ACI Mater J 110(6):705–713

Bibliography

7. Alonso C, Angrade C, Gonzalez JA (1998) Relation between resistivity and corrosion rate of reinforcements in carbonated mortar made with several cement type. Cem Concr Res 15 (5):687–698
8. Bhattacharjee B (2012) Some issues related to service life of concrete structures. The Indian Concr J pp 23–29

9. Pradhan B (2007) Role of steel and cement type on chloride-induced corrosion in concrete. ACI Mater J 104(6)
10. Alonso C, Angrade C, Rodriguez J, Diez JM (1998) Factors controlling cracking of concrete affected by reinforced corrosion. J Mater Struct 31:435–441
11. Angrade C, Angrade R The use of Electrical resistivity as NDT for the specification of concrete durability
12. IS 5555-1970 Indian standard code of procedure for conducting field studies on atmospheric corrosion of metals. Bureau of Indian Standards, New Delhi
13. IS 45919-1996 Indian standard corrosion of metals and alloys classification of corrosivity of atmosphere. Bureau of Indian Standards, New Delhi

Electrochemical Behaviour of Steel in Contaminated Concrete Powder Solution Extracts

Fouzia Shaheen and Bulu Pradhan

Abstract The main cause of reinforced concrete degradation is the corrosion of reinforcing steel. This paper reports the influence of chloride and sulfate ions on steel reinforcement corrosion. In the present work, concrete specimens were admixed with sodium chloride, sodium sulfate and magnesium sulfate. The concentration of sodium sulfate and magnesium sulfate is fixed at 3 % whereas the concentration of sodium chloride is varied as 3, 5, and 7 %. Tempcore TMT steel, Portland pozzolana cement (PPC) and w/c ratio of 0.5 were used in the present experimental investigation. Concrete powder was obtained by crushing concrete specimens those were admixed with different concentrations of chloride and sulfate ions. The electrochemical behaviour of steel has been evaluated by conducting potentiodynamic polarization study on steel in contaminated concrete powder solution extracts. On the basis of the results obtained, ranges of potential for different zones of corrosion of steel reinforcement in concrete powder solution extracts contaminated with composite chloride and sulfate ions have been obtained.

Keywords Corrosion · Concrete · Steel reinforcement · Chloride ion · Sulfate ion · Potentiodynamic polarization · Zones of corrosion

1 Introduction

Performance of concrete is generally judged by strength and durability properties. Durability of concrete is its resistance to deteriorating agencies to which it may be exposed during its service life, or which inadvertently, may reside inside the concrete itself [1]. The low durability of reinforced concrete structures is of major

F. Shaheen · B. Pradhan (✉)
Department of Civil Engineering, Indian Institute of Technology, Guwahati, Assam, India
e-mail: bulu@iitg.ernet.in

F. Shaheen
e-mail: fouzia@iitg.ernet.in

concern to the construction industry throughout the world. Understanding the concept of concrete durability and the right specification of materials for infrastructure project is significantly important to protect the structures from possible adverse effects of the exposed environment [2]. Deterioration due to reinforcement corrosion and degradation of concrete exposed to sulfate bearing environments are probably the most important durability issues encountered in reinforced concrete [3].

Steel is thermodynamically unstable in the earth's atmosphere and will always tend to revert to the lower energy state such as an oxide or hydroxide by reaction with oxygen and water [4]. In reinforced concrete, steel provides the required tensile strength, whereas concrete essentially takes care of the compressive stresses. Furthermore, concrete provides both physical and chemical protection to the steel reinforcement [5]. The physical protection is provided by its dense structure which retards the ingress of aggressive species, such as oxygen, moisture and chloride ions to the steel-concrete interface. The chemical protection is provided by the high alkalinity of the concrete pore solution that results in the formation of passive layer on the steel surface [6, 7]. However the breakdown of passive film takes place either due to carbonation or due to presence of chloride ions at the rebar level. The breakdown of passive film on steel surface results in corrosion initiation. The corrosion products occupies larger volume as compared to parent metal and this increase in volume results in swelling pressure, that causes cracking and spalling of the concrete [8, 9]. Chloride ions are considered to be the primary cause of rebar corrosion than that due to carbonation. The rebar corrosion in concrete has become a major world-wide problem especially, for structures such as bridges, parking structures, tunnels, off shore structures etc., which are exposed to sea water or de-icing salts. As the reinforcement corrosion in concrete results in huge repair and maintenance cost, these costs nowadays constitute a major component of the current spending on infrastructure [10].

Chlorides can enter the concrete through the use of admixtures, aggregates and/or mixing and curing water. Alternatively the chlorides may also penetrate the hardened concrete from the external environment, such as seawater, soil, and ground water that contain chloride salts [11]. Although cement has natural ability to bind the chloride ions, but not all the chloride ions can be bound. There always exists dissolution equilibrium between bound chloride and free chloride ions in the pore solution of concrete [2, 8]. The free chloride ions are mainly responsible for steel reinforcement corrosion in concrete.

Sulfate ions react with hydrated calcium hydroxide and C_3A to form gypsum and ettringite respectively [7, 9]. During the early stage of exposure the expansive reaction products may fill the pores in the concrete, thereby densifiying the microstructure of concrete and thus increasing its weight and compressive strength. However the long term exposure of concrete to sulfate ions may lead to reduced weight and compressive strength, because of disruption of the hydrated cementitious matrix by the expansive reaction products [12].

In the marine environments and contaminated soil and ground water, chloride and sulfate salts do exist concomitantly. The conjoint presence of these two salts

may cause the deterioration of concrete due to reinforcement corrosion and sulfate attack. The role of sulfate ions, on mechanism of steel reinforcement corrosion in concrete, when chloride and sulfate ions are conjointly present is not clearly known. The present experimental investigation is carried out to study the effect of the conjoint presence of chloride and sulfate ions on the electrochemical behaviour of steel in concrete powder solution extracts. The electrochemical behaviour of steel is studied by obtaining anodic polarization curves. To obtain the polarization curves, potentiodynamic cyclic sweep test has been conducted on bare steel specimens in concrete powder solution extracts. The objective of the present study is to determine the various zones of corrosion namely; semi-immune zone, active zone, passive zone and pitting zone for Tempcore TMT steel reinforcement in concrete powder solution extracts contaminated with chloride and sulfate salts. The concrete powder solution extract has been prepared from the concrete mix made from PPC at w/b ratio of 0.5.

2 Experimental Program

2.1 Materials

Portland pozzolana cement (PPC) was used for preparing of concrete specimens. Water-cement (w/c) ratio used was 0.5. A water content of 195 kg/m^3 used for a slump value of 20–50 mm. Fine aggregate (sand) conforming to grading zone II as per IS: 383-1970 [13], was used in the preparation of specimens. The determined value of specific gravity of sand is 2.61. Coarse aggregate of size 20 mm maximum size aggregate (MSA) and 10 mm (MSA) were used in proportion of 66 and 34 % respectively of the total mass of coarse aggregate. The determined values of specific gravity of 20 mm (MSA) and 10 mm (MSA) are 2.64 and 2.63 respectively. The proportion of cement, fine aggregate, and coarse aggregate at w/c ratio of 0.5 is 1:1.661:2.953 by mass.

2.2 Admixed Chloride and Sulfate Salts

The concrete cubes were admixed with varying concentrations chloride and sulphate ions at the time of preparation. Sodium chloride was used as the source of chloride ions, whereas sodium sulphate and magnesium sulphate were used as the source of sulphate ions. These salts were added in the mixing water as percentage by mass of cement content. The concentrations of different combinations of NaCl and Na_2SO_4 and that of NaCl and $MgSO_4$ are presented in Table 1.

Table 1 Composition of admixed chloride and sulfate salts

Mix designation	Concentration
Mix 1	0 %
Mix 2	3 % NaCl + 3 % Na_2SO_4
Mix 3	5 % NaCl + 3 % Na_2SO_4
Mix 4	7 % NaCl + 3 % Na_2SO_4
Mix 5	3 % NaCl + 3 % $MgSO_4$
Mix 6	5 % NaCl + 3 % $MgSO_4$
Mix 7	7 % NaCl + 3 % $MgSO_4$

2.3 Preparation of Concrete Cubes

Concrete cubes of size 150 mm × 150 mm × 150 mm were prepared from the different mixes admixed with chloride and sulfate salts as shown in Table 1. The specimens were demoulded after 24 h of casting and after that the specimens were moist cured in a curing tank till the age of 28 days.

2.4 Steel Specimen

Tempcore TMT (Thermomechanically Treated) steel bar of diameter 12 mm was used as bare steel specimen. The steel bars were cut to a length of 70 mm, and then they were drilled and threaded at one end. The steel specimens were cleaned with a wire brush to remove any rust present on the surface and coated with epoxy coating leaving 5 mm height at the end opposite to drilled end. The schematic diagram of bare steel specimen is shown in Fig. 1.
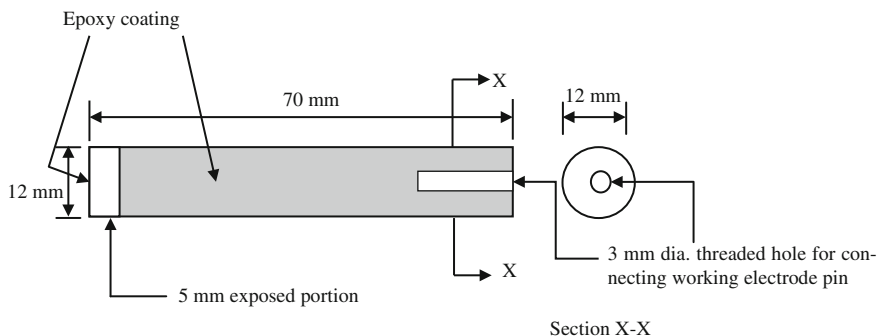
Fig. 1 Schematic diagram of bare steel specimen

Fig. 2 Samples of collected concrete powder
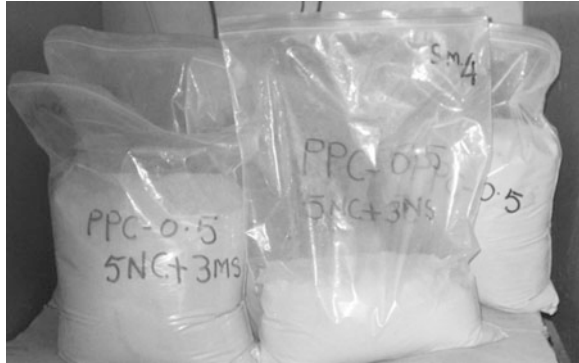
2.5 Concrete Powder Solution Extracts

After completion of moist curing the cube specimens were removed from the curing tank and then kept in the laboratory exposure condition till the period of crushing. The concrete cube were crushed at the age of 56 days from the day of preparation in the compression testing machine followed by further crushing in abrasion testing machine. The collected powder is then sieved through a sieve of square mesh of size 150 μm. Then the sieved powder was stored in air tight plastic containers. A typical photograph of concrete powder samples is shown in Fig. 2.

In order to prepare the concrete powder solution extracts, the stored powder is mixed with distilled water in 1:1 proportion by mass and then stirred for half an hour and then boiled for 15–20 min. After that the solution is allowed to settle and cool to room temperature. Then the solution is filtered through Whatman no. 1 filter paper. The filtered solution extract which is a mixture of cement hydrates, coarse aggregate, fine aggregate and admixed chloride and sulphate ions is used for the electrochemical test on the bare steel specimens.

2.6 Potentiodynamic Cyclic Sweep Test

The electrochemical behaviour of bare steel was evaluated by conducting potentiodynamic cyclic sweep test using corrosion monitoring instrument (make ACM, Gill AC serial no. 1542). The cyclic polarization was carried out in the electrochemical cell with three electrodes such as a working electrode (WE), an auxiliary electrode (AE), and a reference electrode (RE). The bare steel specimen is connected to the working electrode pin of the instrument. The filtered solution extract was poured into the electrochemical cell and potentiodynamic cyclic sweep test was carried out from 0 to 1,500 mV with offset from corrosion potential at a sweep rate of 50 mV/min. Saturated calomel electrode (SCE) was used as a reference electrode for measuring potential of the bare steel specimen. The schematic diagram of electrochemical cell is shown in Fig. 3.
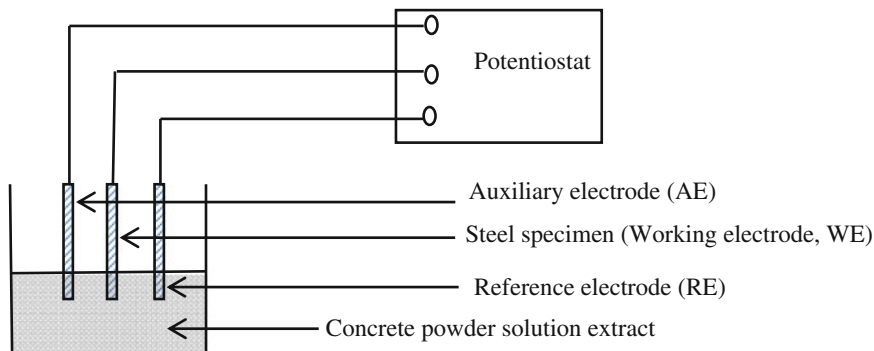
Fig. 3 Electrochemical cell

3 Results and Discussions

3.1 Corrosion Zones for Steel Reinforcement

The anodic polarization curves were obtained from the potentiodynamic cyclic sweep test on bare steel specimens in concrete powder solution extracts. The anodic polarization curve for Tempcore TMT steel specimen in concrete powder solution extracts made from PPC at w/c ratio of 0.5 for the control mix (Mix 1) is shown in Fig. 4.

In Fig. 4, different zones of corrosion namely semi-immune zone, active zone, passive zone and pitting zone are identified. The zone of corrosion below the rest potential is termed as semi-immune zone. In semi-immune zone the steel is
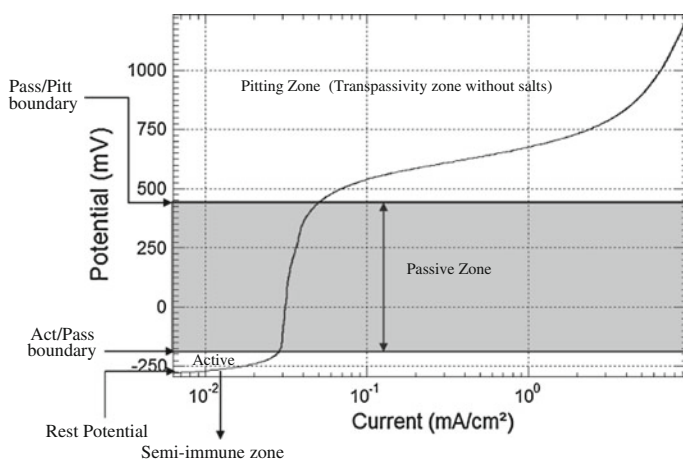
Fig. 4 Anodic polarization curve for Tempcore TMT steel in control mix (Mix 1)

thermodynamically unable to undergo anodic reactions and thus immune to dissolution. The zone above the semi-immune zone is termed as the active zone. In this zone there is significant increase in corrosion current density with small change in potential. The zone above the active zone is known as passive zone and in this zone change in current density is very less whereas there is significant increase in potential. The zone above the passive zone is called as pitting zone. In pitting zone the anodic current density increases significantly leading to localized dissolution of steel reinforcement. The potential values at boundaries of different zones such as, the active-passive zone boundary (Act/Pass) potential and passive-pitting zone boundary (Pass/Pitt) potential are shown in Fig. 4.

3.2 Effect of Conjoint Presence of Chloride and Sulfate Ions on Corrosion Zones

The anodic polarization curves of steel reinforcement in concrete mixes admixed with sodium chloride and sodium sulfate are shown in Figs. 5, 6 and 7, whereas those for concrete mixes admixed with sodium chloride and magnesium sulfate are shown in Figs. 8, 9 and 10.

From Fig. 4, it is observed that the rest potential value is −280.0 mV (in SCE scale), active/passive boundary potential and passive/pitting potential values are −184.17 and +447.77 mV respectively for uncontaminated concrete mix (Mix 1). From Figs. 5, 6 and 7 it is observed that the rest potential values for 3, 5 and 7 % sodium chloride concentration with 3 % sodium sulfate concentration are −316.86, −349.59 and −440.44 mV respectively, whereas the active/passive boundary potential are −245.14, −262.1 and −320.33 mV and the passive/pitting boundary values are +26.08, −23.25 and −189.08 mV respectively.

Fig. 5 Anodic polarization curve for concrete mix admixed with 3 % $NaCl$ + 3 % Na_2SO_4
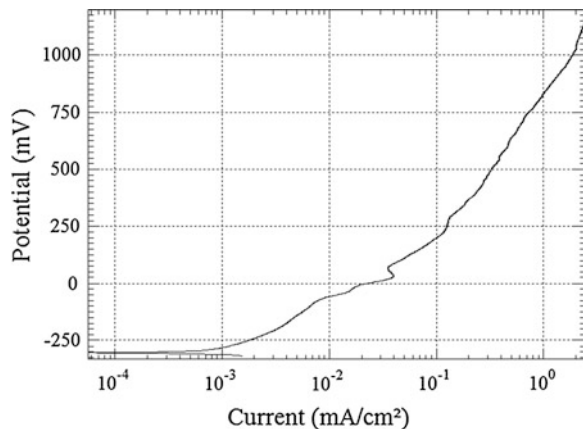
Fig. 6 Anodic polarization curve for concrete mix admixed with 5 % NaCl + 3 % Na$_2$SO$_4$
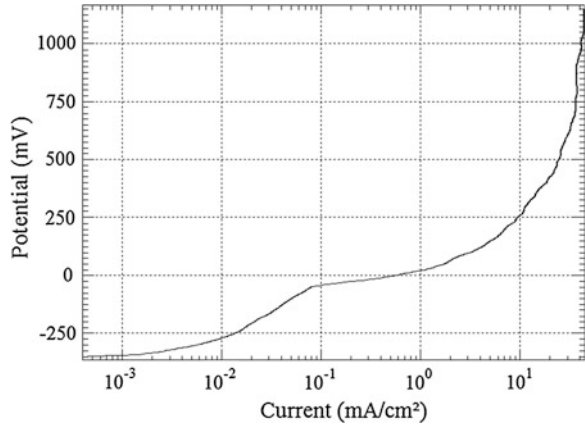
Fig. 7 Anodic polarization curve for concrete mix admixed with 7 % NaCl + 3 % Na$_2$SO$_4$
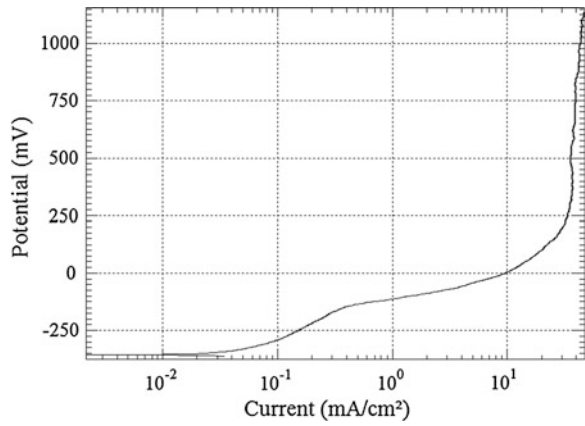
Fig. 8 Anodic polarization curve for concrete mix admixed with 3 % NaCl + 3 % MgSO$_4$
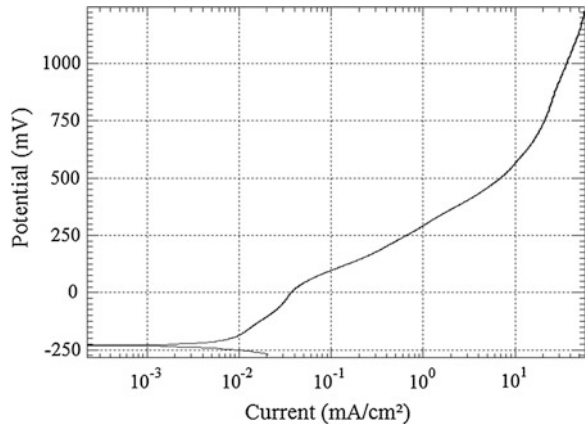
Fig. 9 Anodic polarization curve for concrete mix admixed with 5 % NaCl + 3 % MgSO$_4$
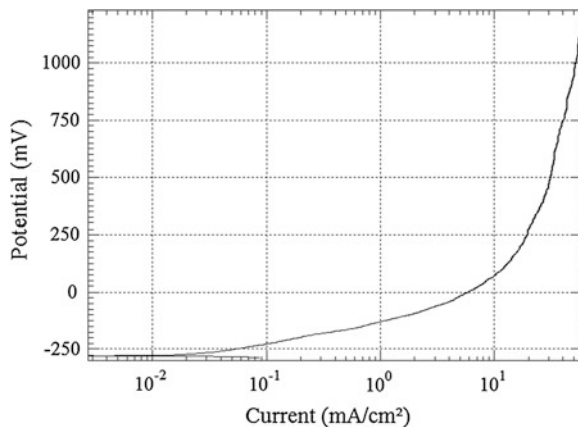
Fig. 10 Anodic polarization curve for concrete mix admixed with 7 % NaCl + 3 % MgSO4
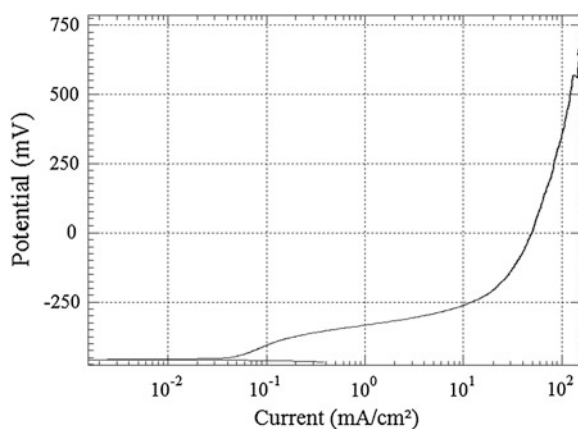
From Figs. 8, 9 and 10 it is observed that the rest potential values for 3, 5 and 7 % sodium chloride concentration with 3 % magnesium sulfate concentration are −319.7, −350.59 and −479.44 mV respectively, while the active/passive boundary potential are −199.47, −257.09 and −393.64 mV respectively. The passive/pitting boundary values are +13.39, −84.05 and −219.72 mV respectively.

From the above results, it is observed that the rest potential decreases with increase in sodium chloride concentration at both 3 % sodium sulfate and 3 % magnesium sulfate. Further it is noted that the rest potential values for 3 % magnesium sulfate are more negative as compared to 3 % sodium sulfate with varying sodium chloride concentrations.

From active/passive boundary potential values and passive pitting boundary potential values, it is observed that the passivity range reduces with increase of sodium chloride concentration, therefore the breakdown potential decreases as the chloride ion concentration increases and the chances of localized corrosion

increases. Further it is noted that the range of passive zone is less in 3 % magnesium sulfate as compared that in 3 % sodium sulfate at various concentrations of sodium chloride.

In control mix (Mix 1) the potential of +447.77 mV represents the beginning of transpassivity zone characterized by oxygen evolution, whereas in chloride and sulfate contaminated concrete much lower pitting potential values were observed. Hence the range of passive zone is higher in control mix and thus there is less chance of localized corrosion.

4 Conclusions

From the results of the potentiodynamic cyclic sweep test conducted on Tempcore TMT steel in concrete powder solution extracts prepared from different concrete mixes made with Portland pozzolana cement and admixed with chloride-sulfate salts, various zones of corrosion are identified. The range of passive zone is more in concrete powder solution extracts contaminated with sodium sulfate as compared with that contaminated with magnesium sulfate. The obtained zones of corrosion, namely semi-immune zone, active zone, passive zone, and pitting zone, of steel provides the information about the behaviour of steel with respect to potential values in concrete powder solution extracts contaminated with both chloride and sulfate ions.

References

1. Mullick AK (2007) Performance of concrete with binary and ternary cement blends. The Indian Concr J 81(1):15–22
2. Saleh A (2008) Chloride induced corrosion and sulfate attack—a literature review on concrete durability. The 3rd international conference-ACF/VCA, Elkem Materials South East Asia, Singapore
3. Khan AR, Zafar NS (2009) Performance of different types of Pakistani cements exposed to aggressive environments. In: 1st international conference on sustainable built environment infrastructures in developing countries ENSET Oran, Algeria
4. Hansson, CM, Poursaee A, Jaffer SJ (2007) Corrosion of reinforcing bars in concrete. R&D serial no. 3013, Portland cement association, Skokie, Illinois, USA
5. Dehwah HAF, Maslehuddin M, Austin SA (2003) Effect of sulphate ions and associated cation type on the pore solution chemistry in chloride-contaminated plain and blended cement. Cem Concr Compos 25:513–525
6. Jarrah NR, Al-Amoudi OSB, Maslehuddind M, Ashiru OA, Al-Mana AI (1995) Electrochemical behaviour of steel in plain and blended cement concretes in sulphate and/ or chloride environments. Constr Build Mater 9:97–103
7. Al-Amoudi OSB (2002) Attack on plain and blended cements exposed to aggressive sulfate environments. Cem Concr Compos 24:305–316
8. Shi X, Xie N, Fortune K, Gong J (2012) Durability of steel reinforced concrete in chloride environments: an overview. Constr Build Mater 30:125–138

9. Neville AM, Brooks JJ (1996) Concrete technology
10. Ismail M (2006) Corrosion rate of ordinary and high performance concrete subjected to chloride attack by AC impedance spectroscopy. Constr Build Mater 20:458–469
11. Dehwah HAF, Maslehuddin M, Austin SA (2002) Long term effect of sulphate ions and associated cation type on chloride-induced reinforcement corrosion in Portland cement concrete. Cem Concr Compos 24:17–25
12. Al-Amoudi OSB (1995) Sulphate attack and reinforcement corrosion in plain and blended cements exposed to Sulphate environments. Constr Build Mater 9:149–158
13. IS 383-1990 (reaffirmed 2002) Specification for coarse and fine aggregate from natural sources for concrete. Bureau of Indian Standard, New Delhi

Part XX
Fiber Reinforced Concrete (FRC)

Parametric Study of Glass Fiber Reinforced Concrete

Shirish Vinayak Deo

Abstract Increasing the durability of structures is necessary for sustainability and low life cycle cost. With passage of time and exposure to various harsh environments, many reinforced concrete (RC) structures begin to degrade. Early degradation of the structures is caused due to the development of minor fissures and cracks in concrete. Early development of cracks starts from the moment the structure is cast due to shrinkage. These micro-cracks propagate further upon loading and give entry to water, CO_2 or other gases up to reinforcement. Small discrete glass fibers when added to concrete reduce the cracking and increase durability. Durability tests generally carried at laboratory don't consider the effect of cracks due to loading on structure on durability of concrete. Present study focuses on understanding the effect of glass fiber and loading on the durability of concrete. To know the effect of loading on structures under service, on the durability of concrete, cubes were loaded to 60 % of the expected ultimate load. This load may open the cracks already existing in the concrete and created more cracks. After loading cubes were subjected to 100 drying and wetting cycles. After drying and wetting cycles, ultrasonic pulse velocity and compressive strength were investigated. About 20 % increase in case of fibre reinforced concrete was reported over control concrete. Tested samples had also shown more than 10 % improvement in the compressive and flexural strength. However the slump has reduced from 20 to 0 mm for fiber reinforced concrete.

Keywords Fiber reinforced concrete · Durability · Cracks

S.V. Deo (✉)
Department of Civil Engineering, National Institute of Technology Raipur (NITRR),
Raipur, Chhattisgarh, India
e-mail: svdeo.ce@nitrr.ac.in

1 Introduction

Concrete is the most common building material in today's world, next to water due to its use in highways, bridges, dams and other heavy structures. Higher durability of concrete over other construction materials is the main reason behind concretes popularity. Initially RCC structures were expected to have 100 years of service life with minor maintenance. However, practically after 30 years concrete requires major maintenance. With passage of time and exposure to various harsh environments, many RC structures begin to deteriorate due to the development of fissures and cracks in almost all the cases. Some causes of deterioration are: alkali silica reaction (ASR), corrosion of the rebar due to chlorides or carbonation, sulphate attack, acid attack, leaching, and freeze and thaw damage. In the recent researches, alternate drying and wetting has been found to play a supporting role in this degradation.

In India and other tropical countries, during the rains, the structure gets exposed to alternate drying wetting cycles causing the volume changes that may also contribute to surface crazing and cracking. Those elements of structures exposed to cyclic wetting and drying (BS 8500-1, XD3) have proven to be the most vulnerable to corrosion damage. With these cracks on the concrete surface, the fluids can easily enter the core and corrode the reinforcement reducing the service life.

Cracks in concrete could be reduced by incorporation of glass fibers in concrete. With its ability to reduce the propagation of the early micro cracks, fibre-reinforced concrete has proved to improve the durability of concrete. In plain concrete and similar brittle materials, structural micro cracks develop even before loading, particularly due to drying shrinkage or other causes of volume changes. When loaded, the micro cracks propagate and open up, and owing to the effect of stress concentration, additional cracks form in the places of minor defects. The addition of small closely spaced and uniformly dispersed fibers to concrete would act as a crack arrestor and would substantially improve its static and dynamic properties.

The aim of the present work is to examine the effects of fibres on properties of fresh and hardened concrete and to evaluate the effect of fibres on improvement of durability of concrete with application of load on concrete and to compare it with non fiber concrete.

2 Experimental Work

Portland slag cement was used. It was tested as per Indian codes and properties are given in Table 1. Natural sand passing through 10 mm sieve was used as a fine aggregate. It was tested as per Indian Standard. Sand was conforming to Zone II. Coarse aggregates passing 40 and 12.5 mm sieves were combined using 60:40 proportion. The combined grading is as given below in Table 2. Anti-crack high dispersion alkali resistant glass fibres were used for the study.

Table 1 Properties of Portland slag cement

Property	Result
Standard consistency	32 %
Initial setting time	160 min
Final setting time	240 min
Fineness by sieving	3.0 %
Soundness	1 mm
Compressive strength	
3 days	28 N/mm^2
7 days	36 N/mm^2
28 days	55 N/mm^2

Table 2 Sieve analysis of all in aggregate

BIS sieve size	Sieves as per ASTM	Sand % passing	Coarse aggregate % passing	Combined grading % passing	Desirable grading IS 383 % passing
40 mm	1^1/$_2$ in.	100	100	100	100
20 mm	^{3}/$_4$ in.	100	91	94.00	95–100
10 mm	3/8 in. (9.5 mm)	100	38	61.60	–
4.75 mm	No. 4 (4.75 mm)	92	5	39.20	30–50
2.36 mm	No. 8 (2.36 mm)	83	0	31.80	–
1.18 mm	No. 16 (1.18 mm)	75	0	28.00	–
600 μ	No. 30 (600 μm)	40	0	17.20	10–35
300 μ	No. 50 (300 μm)	7	0	2.60	–
150 μ	No. 100 (150 μm)	0	0	0.00	

3 Mix Proportions

Two control mixes for water cement ratios 0.45 and 0.5 were designed as per Indian Standard concrete mix design method. For each water cement ratio three alternative cases were studied. C1 and C4 were control mixes without glass fibres. C2 and C5 were concrete mixes with 0.05 % by volume of glass fibre of total volume of concrete. C3 and C4 were mixes with 0.025 % by volume of glass fibre of total volume of concrete. Mix proportions are given in Table 3.

Table 3 Quantities for 1 m³ of compacted concrete and concrete properties

Mix	W/C ratio	Water (kg)	Cement (kg)	Sand (kg)	C. A. (kg)	Slump (mm)	Remark
C1	0.45	184.5	410	700	1,120	30	Control (0.45 w/c)
C2	0.45	184.5	205	688	1,081	20	0.05 % fibre (0.45 w/c)
C3	0.45	176.3	205	716	1,125	25	0.025 % fibre (0.45 w/c)
C4	0.5	184.4	205	664	1,044	50	Control (0.5 w/c)
C5	0.5	176.3	205	585	1,112	30	0.05 % fibre (0.5 w/c)
C6	0.5	180	450	664	1,135	40	0.025 % fibre (0.5 w/c)

C. A. Coarse aggregate

4 Preparation, Casting, Curing and Testing of Specimens

All the cubes and beams were vibrated on vibration table. After casting, all the test specimens were finished with a steel trowel. They were de moulded after 24 h and were put into a water-curing tank at standard temperature 27 ± 2 °C. Total 54, 100 mm cubes, 18, 150 mm cubes and 18, 100 mm beams were casted. Three cubes per day per mix were tested on 28 days. Remaining 36, 100 mm cubes were tested after drying and wetting cycles for durability.

5 Fresh Concrete Properties

Value of slump was found for fresh concrete in each case. The results are presented in Table 3. Workability of FRC was always lower than control concrete.

6 Compressive Strength of Concrete

100 and 150 mm cubes were tested on 28 days age. The results are given in Table 4.

Table 4 Compressive strength of 100 and 150 mm cubes

Mix	Description	28 days compressive strength (N/mm²)	
		100 mm	150 mm
C1	Control (0.45 W/C)	40.3	38.1
C2	0.05 % fibre (0.45 W/C)	38.6	37.0
C3	0.025 % fibre (0.45 W/C)	41.6	40.2
C4	Control (0.5 W/C)	32.3	31.0
C5	0.05 % fibre (0.5 W/C)	34.3	31.9
C6	0.025 % fibre (0.5 W/C)	35.6	33.0

Table 5 Compressive strength of 100 mm beams

Mix	Description	28 days flexural strength (N/mm^2)
C1	Control (0.45 W/C)	2.9
C2	0.05 % fibre (0.45 W/C)	2.9
C3	0.025 % fibre (0.45 W/C)	3.1
C4	Control (0.5 W/C)	2.6
C5	0.05 % fibre (0.5 W/C)	2.7
C6	0.025 % fibre (0.5 W/C)	2.8

7 Flexural Strength of Concrete

100 mm × 100 mm × 500 mm beams were tested on 28 days age. The results are given in Table 5.

8 Drying and Wetting Cycles

Effect of loading on durability of concrete is not very well reported in literatures. Presently available durability testing methods are yet to consider this effect fully. Loading on structure is expected to open up the already existing cracks. These cracks shall adversely affect the durability of concrete under service loads. In the present study, an attempt has been made to simulate the site loading on the concrete cubes before testing them for durability. To achieve site loading in lab, out of the six 100 mm cubes remaining for testing, three cubes were applied a compressive load of 60 % of the average load of the already tested three 100 mm cubes at 28 days. These three cubes along with remaining three cubes without any load application were exposed to hundred drying and wetting cycles.

For the drying cycle cubes were kept in the oven at 100 °C for 24 h. For the wetting cycle cubes were kept in a water tank with water at normal temperature. The 0 % load samples were directly kept in oven at 100 °C for 24 h. However other three cubes were applied a compressive load of 60 % of the average load of the already tested three 100 mm cubes at 28 days and then kept in oven at 100 °C. After completion of 24 h of drying all the cubes were submerged into the curing tank for wetting. All the concrete cubes were exposed to hundred such cycles of drying and wetting. Finally these cubes were tested under compressive load. Results are reported in Table 6.

Table 6 Compressive strength of 150 mm cubes

Mix	Description	Compressive strength (N/mm^2)	
		No load	60 % load
C1	Control (0.45 W/C)	35.0	33.8
C2	0.05 % fibre (0.45 W/C)	34.7	33.6
C3	0.025 % fibre (0.45 W/C)	38.3	35.4
C4	Control (0.5 W/C)	27.6	19.7
C5	0.05 % fibre (0.5 W/C)	30.2	28.5
C6	0.025 % fibre (0.5 W/C)	32.0	30.3

9 Results and Discussion

9.1 Compressive Strength

Compressive strength of 100 and 150 mm cubes at 28 days given in Table 4 reveals that strength of control concrete in both the water cement ratios was lower than 0.025 % fibre reinforced concrete. This may be due to crack arresting ability of glass fibres. However in case of 0.05 % fibres strength of concrete was lower than concrete without fibre. This may be due to up to about 40 % reduction of slump. Reduced slump may have affected uniform dispersion of glass fibres for reducing cracks. Further trials are required for confirmation the present results.

9.2 Flexural Strength

Compressive strength of 100 mm beams at 28 days given in Table 5 reveals that flexural strength of control concrete in both the water cement ratios was less than 0.025 % fibre reinforced concrete. This may be due to crack arresting ability of glass fibres. However in case of 0.05 % fibres flexural strength of concrete was higher than or equal to concrete without fibre. Further trials are required for confirmation of the present results.

9.3 Workability

Workability of fresh concrete was measured with slump and the results are given in Table 4. It is evident from the result that slump decreases with increase in fibre percentage. This may be due to higher surface area of glass fibres. Considering the moderate loss in workability and increase in strength for 0.025 % addition of fibres, may be a better choice over 0.05 % addition of fibres.

Table 7 Percentage increase in compressive strength of 100 mm cubes

Mix	Description	Percentage increase in compressive strength (N/mm^2)	
		No load	60 % load
C1	Control (0.45 W/C)	Control	Control
C2	0.05 % fibre (0.45 W/C)	−0.9	−0.6
C3	0.025 % fibre (0.45 W/C)	9.4	4.7
C4	Control (0.5 W/C)	Control	Control
C5	0.05 % fibre (0.5 W/C)	9.4	44.7
C6	0.025 % fibre (0.5 W/C)	15.9	53.8

9.4 Durability with Drying and Wetting Cycles

Durability in terms of compressive strength after 14 drying and wetting cycles was reported in Table 6. 100 mm cubes were tested with 0 % load and 60 % load of the average load of the already tested three 100 mm cubes at 28 days. Percentage increase in final compressive strength over control concrete is given in Table 7. In all cases except C2 concrete could take more load after hundred drying and wetting cycles over control concrete. These results suggest that durability of concrete under drying and wetting cycles was improved by addition of glass fibres. Results also indicate substantial reduction of compressive strength of concrete without fibre in 60 % loading case. This indicates that opening of cracks after loading could also be checked by addition of glass fibres improving the durability of concrete. Application of 60 % load has accelerated the deterioration of concrete under drying and wetting cycles. This method with verification by further studies could also be used as accelerated durability study.

10 Conclusions

The following conclusions could be drawn from the present investigation.

- The compressive strength of FRC concrete at a small dose of 0.025 % of total volume of concrete was about 10 % higher than the control concrete.
- The flexural strength of FRC concrete at a small dose of 0.025 % of total volume of concrete was about 8 % higher than the control concrete.
- Workability of FRC was lower than the control concrete.
- Durability of concrete measured as failure load after hundred drying and wetting cycle was up to 54 % more than the control concrete.
- Application of 60 % of the average load of the already tested three 100 mm cubes at 28 days along with drying and wetting cycles has reduced failure load

of control concrete by about 30 % and of FRC by about 6 %. This may be due to crack arresting by addition of fibres.

- Application of 60 % of the average load of the already tested three 100 mm cubes at 28 days along with drying and wetting cycles has reduced failure load of control concrete and of FRC due to crack opening. This may be useful to develop an accelerated durability test for concrete.

Finally it could be concluded that durability of concrete could be increased by addition of a small dose of 0.025 %. Application of 60 % of the average load of the already tested three 100 mm cubes at 28 days along with any durability test shall accelerate deterioration and with further study accelerated durability test could be developed.

Bibliography

1. Hong K (1998) Cyclic wetting and drying and its effects on chloride ingress in concrete. University of Toronto
2. Ball H (2003) Durability of naturally aged, GFRC mixes containing forton polymer and SEM analysis of the facture interface. In: Clarke JN, Ferry R (eds) Proceedings of 12th congress of GRCA, GRC 2003, Barcelona, Spain
3. Gambhir ML (1987) Concrete manual: laboratory testing for qualifying control of concrete, 3rd edn. Dhanpat Rai and Sons, New Delhi
4. IS: 456-2000 Code of practice for plain and reinforced concrete. Fourth revision, Bureau of Indian standards, Manak Bhawan, New Delhi
5. Shetty MS (2005) Concrete technology: theory and practice. S. Chand and Company, New Delhi (2005, 23rd revised edition)
6. Neville AM, Brooks JJ (1987) Concrete technology, 2nd edn. Longman Scientific & Technical, Harlow
7. Heiyantuduwa R, Alexander MG (2009) Studies on prediction models for concrete durability. University of Cape Town, Cape Town
8. Dali JS, Tande SN Performance of concrete containing mineral admixtures subjected to high temperature. Executive engineer, Govt. of Maharashtra, Pune, India
9. Paul D (2010), Weathering of hardened concrete causes and suggested remedies
10. Report on the Physical properties and durability of fiber-reinforced concrete—reported by ACI Committee 544
11. Nagesh M Notes on concrete durability. VTU Edusat series 16th program, Civil Engineering. Department, Government Engineering College, Ramanagara
12. Al-Tamimi AK, Al-Samarai M, Elian A, Harries N, Pocock D Guidelines for concrete durability testing in the UAE
13. Rana A (2013) Studies on "Steel fiber reinforced concrete," 2013. Sarvajanik College of Engineering and Technology, Surat, Gujarat, India

An Experimental Approach to Investigate Effects of Curing Regimes on Mechanical Properties and Durability of Different Fibrous Mortars

Damyanti Badagha and C.D. Modhera

Abstract Fibre Reinforced Concrete (FRC), in the recent decades, became a very popular and attractive material in structural engineering because of its good mechanical performance. There were many research performed on concrete but very few on mortar. This paper reports an investigation on different fibrous mortar in two different curing conditions. In this investigation the performance of carbon, glass, polyester and steel fibrous mortars were studied under acidic and alkaline curing regimes. The water–cement ratio of all the mortar mixtures was kept constant. The mortar specimen containing fibre of 0.0, 0.3, 0.4, 0.5, 0.6, 0.8 and 1.0 % by weight of cement were casted and tested. The specimens were subjected to acidic curing in 5 % HCl solution after 28 days of normal curing and direct alkaline curing in 3.5 % NaCl solution in water after demoulding at room temperature of 27 °C and 60 % relative humidity. The compressive strength, impact strength and shear strength were determined. The results indicate that the addition of different fibres in plain mortar results in improvement of strength of mortar. The increased compressive strength of different fibrous mortar was 18.04 % for steel fibre in acidic curing and 19.01 % for polyester fibre in alkaline curing. The increased absorb energy in impact strength of different fibrous mortar were 377.78 % for steel fibre in acidic curing and 192.87 % for carbon fibre in alkaline curing. The increased shear strength of different fibrous mortar was 14.60 % for carbon fibre in acidic curing and 49.49 % for glass fibre in alkaline curing.

Keywords Carbon fibre · Glass fibre · Steel fibre · Polyester fibre · Mortar · Compressive strength · Impact strength · Shear strength · Acidic environment · Alkaline effect

D. Badagha (✉)
Department of Applied Mechanics, SVNIT, Surat 395007, India

C.D. Modhera
Department of Applied Mechanics, Faculty of Technical Education, SVNIT, Surat 395007, India

1 Introduction

Cement-based composites have long been used for civil structures such as highways, bridges and buildings. However, unexpected deterioration of reinforced or pre-stressed concrete structures has led to the improvement of durability of concrete. Traditionally, the constituents of cement-based composites include cementitious material, water, aggregate and/or admixtures. Fibre has been added in cement based composites since 1960s to enhance concrete properties, particularly tensile strength, abrasion resistance and energy absorbing capacity. The presence of fibre would refrain the growth or propagation of internal cracks and helps to transfer load. The specimen with fibre has much higher ductility than the specimen without fibre, for which fibre reinforced composites (FRC), also demonstrates a significant increase in energy absorption or toughness. However, the properties of FRC would be affected by the type, volume fraction and aspect ratio of fibre. Lower fibre volume fraction is usually preferred as far as material cost and workability are concerned [2–8].

It was also reported that the combination of silica fume with steel fibre would effectively enhance the compressive strength, splitting tensile strength, abrasion resistance and impact resistance and be beneficial for fibre dispersion in cement-based composites. Silica fume would increase the bonding between fibre and mortar by strengthening the interfacial zone [9–13]. This study was aimed to evaluate the effect of different fibre on the mechanical properties of cement mortar under different curing condition.

This investigation is aimed at generating information on the overall response of compressive, resistant against impact and shear behaviour of cement mortar reinforced with different fibre percentage of different fibres. 150 specimens were casted for each test. Specimens were cured in acidic water with 5 % of HCl concentration after curing in tap water and alkaline water with 3.5 % of NaCl concentration directly after demoulding. Tests were performed to know the effect of Fibres in acidic and alkaline environment on the plain mortar. Effect of fibre content was demonstrated by the stress–fibre content curves. Results of all tests were studied and depicted in graphical form for the sake of convenient design of steel fibre cement mortar in structural applications.

2 Research Significance

The problem of failure mechanism and bearing capacity of fibre reinforced concrete (FRC) under various loading conditions has been studied quite extensively in the past. In spite of the volume of information available, relatively very little or no research work is reported in the technical literature on the shear strength of thin cementitious composites containing different fibres with varying quantities although it presents considerable versatility towards the development of cementitious composites for structural applications. The purpose of this research is to investigate the

shear behaviour of fibre-reinforced cementitious composites and to identify synergistic effects of quantities, if present.

3 Experimental Program

In order to study the effects of different fibres on the behaviour of cement composites in terms of Shear strength tests was carried out on specimens with and without inclusion of different fibres. For the case of cement composite with fibre, it was reinforced by the variable percentage of fibre content, chosen for this investigation were 0.3, 0.4, 0.5, 0.6, 0.8 and 1.0 % of cement weight whereas the size and shapes of the test cubes was kept constant for all the specimens to investigate the effectiveness of amount of fibres in cement composites. L-Shape specimens were casted for shear strength test. Specimens were cure in acidic and alkaline environment.

4 Materials and Methods of Testing

4.1 Cement

Ordinary Portland cement of 53 grade was used throughout the work. Cement was tested at the beginning and end of each phase of work to ensure no deterioration in quantity of cement during the interim period. The samples of the element were taken in accordance with the requirements of standard IS 3535-1986 and the relevant specification for the type of cement being tested. The representative sample of the cement selected as above was thoroughly mixed before testing. The temperature of the testing room, dry materials and water was maintained at 27 ± 2 °C. The relative humidity of the laboratory was maintained 65 ± 5 %. On balance in use, the permissible variation at a load of 1,000 g was ±1.0 g. Gauging trowel used for entire testing of cement was conforming to IS: 10086-1982 [23]. The following tests were carried out for cement.

Consistency of cement, Initial setting time, Final setting time, Specific gravity, Fineness, Soundness, Compressive strength (Table 1).

4.2 Sand

The fine aggregate as river sand available locally in Surat has been used in this experimental program. The following tests were carried out for fine aggregate: sieve analysis, specific gravity, water absorption, bulk density, silt content. Results for the sieve analysis of sand are shown in Fig. 1 (Table 2).

Table 1 Properties of cement [24–29]

Test for cement	Results
Consistency of cement	28.5 [17]
Initial setting time	115 min (should not less than 30 min as per [18], Cl. 5.2)
Final setting time	220 min (should not more than 600 min as per [18], Cl. 5.3)
Soundness of cement by Le-Chartlier method	2 mm (should not have expansion more than 10 mm as per [16])
Compressive strength	3 days—27.5 N/mm^2 (should not less than 27 N/mm^2 as per [19])
	7 days—37.5 N/mm^2 (should not less than 37 N/mm^2 as [19])
	28 days—57 N/mm^2 (should not less than 53 N/mm^2 as per [19])
Fineness of cement by sieve analysis	3 g retained [29]

Fig. 1 Sieve analysis of sand
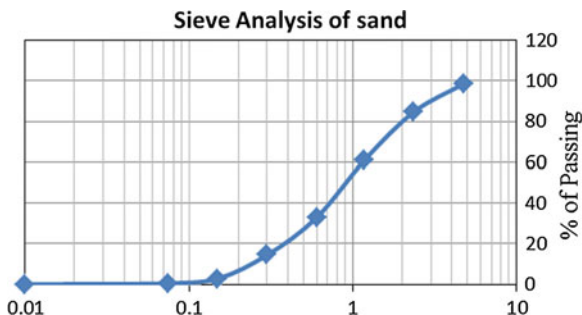
Table 2 Properties of sand [21]

Test for sand	Results
Grading zone	1 (as per IS 383: 1970, Table 4)
Silt content	0.45 %
Water absorption	1.04 %
Specific gravity	2.56
Bulk density	1664.4 kg/m^3
Fineness modulus	3.0485

4.3 Fibres

The different properties of fibres which are used in this experimental work are listed in Table 3. It contains length, diameter, density, tensile strength, elastic modulus, softening point and elongation at breaking for all the fibres which were used in this experimental work.

Table 3 Properties of fibres

Property	Carbon fibre	Glass fibre	Polyester fibre	Steel fibre
Length (mm)	10	25	18	25
Diameter (μm)	7	10	20–40	50
Density	1.8	2.6	1.3–1.6	7.95
Tensile strength (GPa)	4	1.7	4–6	1.1
Elastic modulus	70,000	73,000	>5,000	193
Softening point (°C)	1,000	775	250–265	1,350
Elongation (%)	1.6	4.5	20–60	40

5 Mortar–Fibre Mixture

In this study, ordinary Portland cement and river sand with fineness modulus of 3.05 were used. The water to cement ratio and cement to sand ratio were kept as 0.405 and 0.33 by weight in all the mixes. The details of the Proportion of mortar mix are given in Table 4. The required amount of sand, cement and steel fibre were dry mixed manually on a glass plate in such a way that the procedure involves several passes of scoop through the dry mix to ensure an even distribution of cement and fibre in the mixture. The calculated amount of water to be necessary to obtain a water–cement ratio of 0.405 was added gently to the dry mix and finally, the components were mixed thoroughly. Nearly 3–5 min was required to obtain a homogeneous mortar–fibre mixer.

Table 4 Proportion of mortar mix

Index	Cement (gm)	Sand (gm)	Water (ml)	Carbon fibre (% weight of cement)	Glass fibre (% weight of cement)	Polyester fibre (% weight of cement)	Steel fibre (% weight of cement)
M0	200	600	81	–	–	–	–
M1	200	600	81	0.3	–	–	–
M2	200	600	81	0.4	–	–	–
M3	200	600	81	0.5	–	–	–
M4	200	600	81	0.6	–	–	–
M5	200	600	81	0.8	–	–	–
M6	200	600	81	1.0	–	–	–
M7	200	600	81	–	0.3	–	–
M8	200	600	81	–	0.4	–	–
M9	200	600	81	–	0.5	–	–
M10	200	600	81	–	0.6	–	–
M11	200	600	81	–	0.8	–	–

(continued)

Table 4 (continued)

Index	Cement (gm)	Sand (gm)	Water (ml)	Carbon fibre (% weight of cement)	Glass fibre (% weight of cement)	Polyester fibre (% weight of cement)	Steel fibre (% weight of cement)
M12	200	600	81	–	1.0	–	–
M13	200	600	81	–	–	0.3	–
M14	200	600	81	–	–	0.4	–
M15	200	600	81	–	–	0.5	–
M16	200	600	81	–	–	0.6	–
M17	200	600	81	–	–	0.8	–
M18	200	600	81	–	–	1.0	–
M19	200	600	81	–	–	–	0.3
M20	200	600	81	–	–	–	0.4
M21	200	600	81	–	–	–	0.5
M22	200	600	81	–	–	–	0.6
M23	200	600	81	–	–	–	0.8
M24	200	600	81	–	–	–	1.0

5.1 Casting of Cubes

The test cubes were cast in steel moulds with open tops. Each of the four side-walls and the base of the mould were detachable to facilitate the demoulding process after its initial setting. The specimens were air-dried for 1 day for initial setting and then immersed in water for curing. After different curing period, the specimens were air-dried in room temperature at about 27 °C with relative humidity of about 60 %.

5.2 Compressive Strength Test

The testing machine was calibrated, of sufficient capacity for the tests and capable of applying the load at the rate specified for relevant test code. The permissible error was not greater than ±2 % of the maximum load. The load was applied without shock and increased continuously at a rate of approximately 140 kg/cm^2/mm until the resistance of the specimen to the increasing load breaks down and no greater load can be sustained. Arrangement of specimen for compressive strength is shown in Fig. 2.

Fig. 2 Arrangement of specimen for compressive strength

5.3 Impact Test

Impact tests consist of striking a suitable specimen with a controlled blow and measuring the energy absorbed in bending or breaking the specimen. The energy value indicates the toughness of the material under test. Schrader has proposed test method to determine the impact resistance by drop weight method and also shown that addition of fibre in concrete improve the good amount of impact resistance. According to the current recommendations of ACI Committee 544, the test is to be carried out by dropping a hammer weighing 44.7 N from a height of 457 mm repeatedly on a 63.5 mm-diameter hardened steel ball that is placed on the top of the center of a 150, 63.5 mm cylindrical concrete specimen (disc). The steel ball is free to move vertically within a 63.5 mm cylindrical sleeve. Arrangement of specimen for impact test is shown in Fig. 3.

5.4 Shear Strength (L Shape) Test

JSCE-SF6 suggested direct shear method by using beam of size ($150 \times 150 \times 500$ mm) and load applied through male–female arrangement and failure under double shear. Another method suggested by Bairagi and Modhera [1], arrangement for which is shown in Fig. 4 [1] where all dimensions are in mm. In this method load P is given on upper plate until the crack developed on the failure plane in single shear. The failure load P_2 is considered as half of the total load P. The shear stress in N/mm^2 is calculated by Load P_2 divided my shear area which is 60×150 mm.

Fig. 3 Arrangement of specimen for impact test
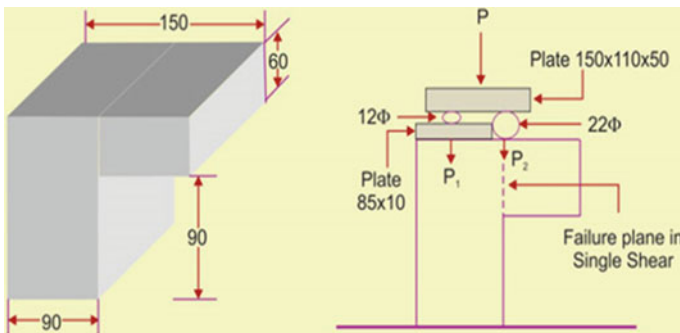
Fig. 4 Arrangement of specimen for shear strength

5.5 Curing

Specimens for various strengths were casted and cured in tap water for 28 days. After that specimens were cured in water with 5 % concentration of HCl for 28 days for acidic environment. Also specimens were casted and directly cured in water with 3.5 % concentration of NaCl to know the effect of fibres in acidic and alkaline environment; shear test was conducted for specimens cured in acidic and alkaline water.

6 Results and Discussion

The results obtained from the experimental investigations are presented in Figs. 5, 6, 7, 8, 9 and 10. The results are discussed in detail in the following paragraphs.
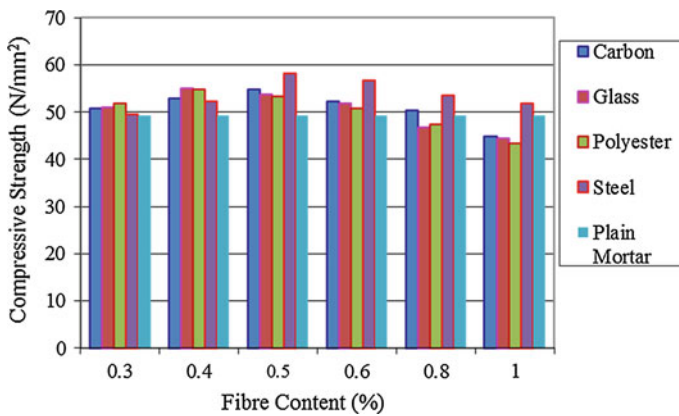
Fig. 5 Compressive strength with various fibre dosages for acidic curing
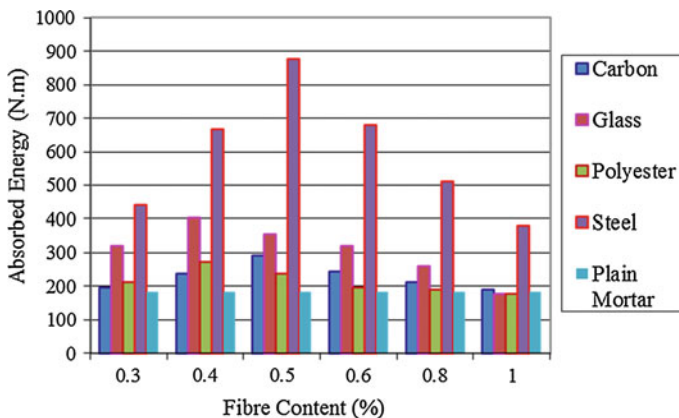
Fig. 6 Impact strength with various fibre dosages for acidic curing
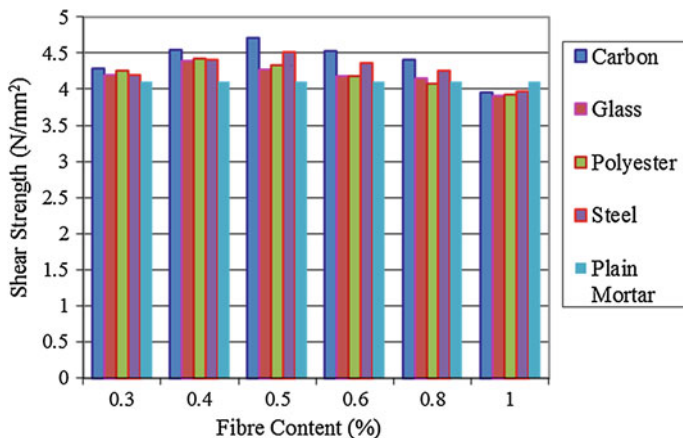
Fig. 7 Shear strength with various fibre dosages for acidic curing
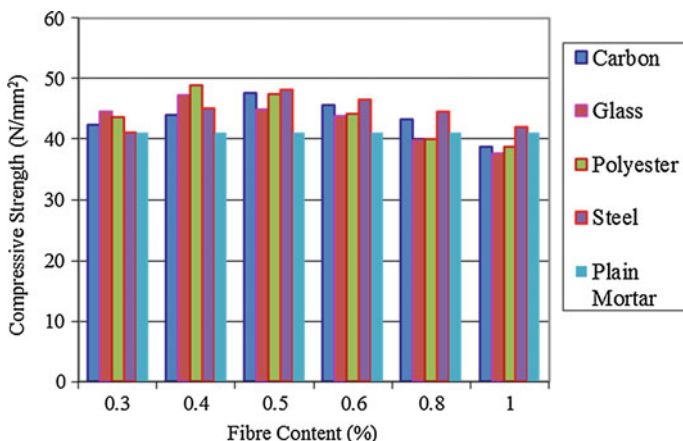
Fig. 8 Compressive strength with various fibre dosages for alkaline curing

In acidic environment, compressive strength of specimens were increased by 10.96, 11.81, 10.98 and 18.04 % for carbon fibre, glass fibre, polyester fibre and steel fibre compare to plain mortar respectively where in alkaline environment with direct NaCl curing, those were increased by 15.92, 16.21, 19.01 and 17.24 % for carbon fibre, glass fibre, polyester fibre and steel fibre compare to plain mortar respectively.

In acidic environment, absorbed energy in impact test were increased by 59.26, 118.52, 48.15 and 377.78 % for carbon fibre, glass fibre, polyester fibre and steel fibre compare to plain mortar respectively where in alkaline environment with direct NaCl curing, those were increased by 192.87, 16.09, 228.55 and 39.29 % for
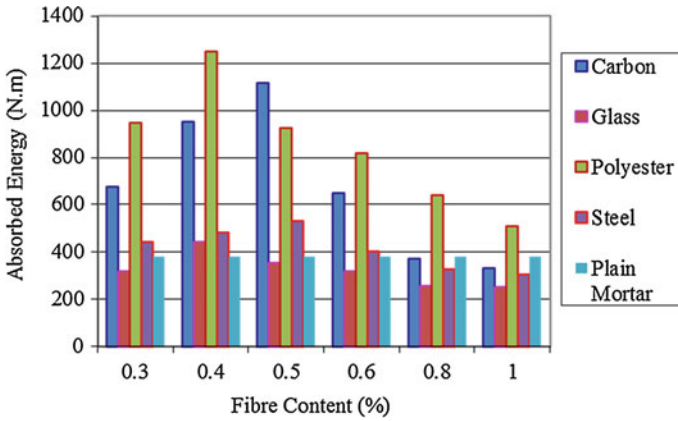
Fig. 9 Impact strength with various fibre dosages for alkaline curing
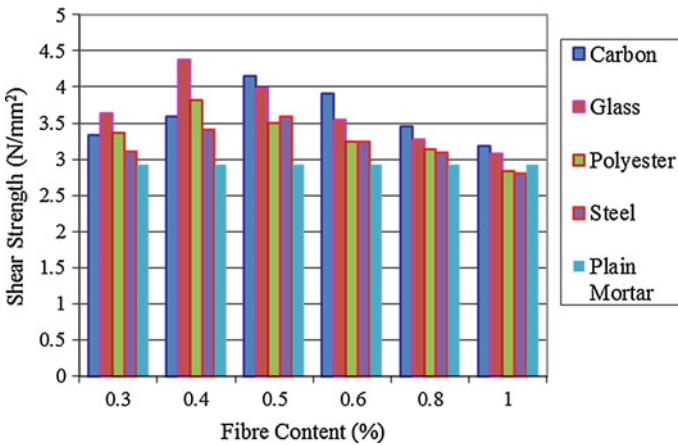
Fig. 10 Shear strength with various fibre dosages for alkaline curing

carbon fibre, glass fibre, polyester fibre and steel fibre compare to plain mortar respectively.

In acidic environment, shear strength of specimens were increased by 14.60, 6.81, 7.54 and 9.73 % for carbon fibre, glass fibre, polyester fibre and steel fibre compare to plain mortar respectively where in alkaline environment with direct NaCl curing, shear strength of specimens were increased by 41.64, 49.49, 30.03 and 22.23 % for carbon fibre, glass fibre, polyester fibre and steel fibre compare to plain mortar respectively.

7 Conclusion

From this investigation we can conclude that addition of fibres in mortar will increase the mechanical properties of mortar. As steel fibre gives better increased strength in acidic environment, it is advisable to use steel fibre in mortar where acid attack is likely to occur. Polyester fibre is advisable to use in sea coastal area as it gives better strength in direct NaCl curing. As addition of fibres improve the strength of mortar so it will be beneficial to use fibres in load bearing structures where mortar is very much important component.

References

1. Bairagi NK, Modhera CD (2001) Shear strength reinforced concrete. ICI 1(4):47–52
2. Chen PW, Chung DDL (1996) Low-drying-shrinkage concrete containing carbon fibres. Compos B Eng 27:269–274
3. Chen PW, Fu X, Chung DDL (1997) Micro structural and mechanical effects of latex, methylcellulose and silica fume on carbon fibre reinforced cement. ACI Mater J 94:147–155
4. Chung DDL (2002) Review: improving cement-based materials by using silica fume. J Mater Sci 37:673–682
5. De Gutierrez RM, Diaz LN, Delvasto S (2005) Effect of pozzolans on the performance of fibre-reinforced mortars. Cem Concr Compos 27:593–598
6. Eren O, Marar K, Celik T (1999) Effects of silica fume and steel fibres on some mechanical properties of high-strength fibre-reinforced concrete. J Test Eval 27:380–387
7. Fu X, Chung DDL (1998) Effects of water–cement ratio, curing age, silica fume, polymer admixtures, steel surface treatments, and corrosion on bond between concrete and steel reinforcing bars. ACI Mater J 95:725–734
8. Gambhir ML (2010) Concrete technology, theory and practice. Tata McGraw Hill Education Private Limited, New Delhi
9. Kesner K, Billington SL (2005) Investigation of infill panels made from engineered cementitious composites for seismic strengthening and retrofit. J Struct Eng 131:1712–1720
10. Li H, Zhang MH, Ou JP (2006) Abrasion resistance of concrete containing nano-particles for pavement. Wear 260:1262–1266
11. Maalej M, Hashida T, Li V (1995) Effect of fibre volume fraction on the off-crack-plane fracture energy in strain hardening engineered cementitious composites. J Am Ceramal Soc 78:3369–3375
12. Naaman AE (2003) Engineered steel fibres with optimal properties for reinforcement of cement composites. J Adv Concr Technol 1:241–252
13. Song PS, Wu JC, Hwang S, Shen BC (2005) Assessment of statistical variations in impact resistance of high-strength concrete and high-strength steel fibre-reinforced concrete. Cem Concr Res 35:393–399
14. IS 35351: 1986 Sampling hydraulic cements
15. IS 10086: 1982 Specification for moulds for use in tests of cement and concrete
16. IS 4031(Part 3): 1988 Methods of physical tests for hydraulic cement: part 3 determination of soundness
17. IS 4031(Part 4): 1988 Methods of physical tests for hydraulic cement: part 4 determination of consistency of standard cement paste
18. IS 4031(Part 5): 1988 Methods of physical tests for hydraulic cement: part 5 determination of initial and final setting times

19. IS 4031(Part 6): 1988 Methods of physical tests for hydraulic cement: part 6 determination of compressive strength of hydraulic cement (other than masonry cement)

Bibliography

20. Abalaka AE, Babalaga AD (2011) Effects of sodium chloride solutions on compressive strength development of concrete containing rice husk ash. ATBU J Environ Technol 4(1)
21. Barhum R, Mechtcherine V (2012) Effect of short, dispersed glass and carbon fibres on the behavior of textile-reinforced concrete under tensile loading. Eng Fract Mech 92:56–71
22. Barluenga G, Hernandez-Olivares F (2007) Cracking control of concretes modified with short AR-glass fibres at early age. Experimental results on standard concrete and SCC. Cem Concr Res 37:1624–1638
23. Chawla KK (2012) Composite materials science and engineering, 2nd edn. Springer, Berlin
24. Huang P, Bao Y, Yao Y (2005) Influence of HCl corrosion on the mechanical properties of concrete. Cem Concr Res 35(3):584–589
25. Hyer MW (2009) Stress analysis of fibre reinforced composite materials. McGraw Hill International edition, New York
26. IS 650: 1991 Specification for standard sand for testing of cement
27. IS 2116: 1980 Specification for sand for masonry mortars
28. IS 12269: 1987 Specification for 53 grade ordinary Portland cement
29. IS 4031(Part 1): 1996 Methods of physical tests for hydraulic cement: part 1 determination of fineness by dry sieving
30. IS 4031(Part 7): 1988 Methods of physical tests for hydraulic cement: part 7 determination of compressive strength of masonry cement

Part XXI
Low-Cost Housing

A Scientific Approach to Bamboo-Concrete House Construction

Ashish Kumar Dash and Supratic Gupta

Abstract Wall is a part of building industry that consumes a lot of construction materials. In past, bamboo weaved wall with or without clay plaster was very common in rural India. This was very comfortable and used renewable resources. Modern construction has not adopted these wall as these wall panels did not have longevity and require regular maintenance. Brick became the most popular material used in wall panel. Since brick consumes a lot of energy and top soil and it is being replaced with fly ash brick, autoclave brick etc. In Assam and north-east India bamboo weaved wall with cement mortar had once become popular. This too did not find way in modern construction. This research is done to establish this as a modern construction material. This paper presents the details of wall joints that were developed to replace the wooden frames in such wall panel.

1 Introduction

Construction industry consumes a lot of non-renewable resources and depleting those natural resources at a fast pace. It is important that we look towards alternate sources and techniques such that material can be conserved for longer period. Bamboo is one material that is a giant woody grass and natural product in use since ancient times. A tree usually takes 30–50 years to mature and when cut for timber, it dies. Unlike trees, bamboo grows from the same mature fibrous root and in fact provides a continuous supply of timber material if it is monitored and harvested

A.K. Dash (✉) · S. Gupta
Civil Engineering Department, Indian Institute of Technology (IIT) Delhi,
New Delhi 110016, India
e-mail: ashishigit59@gmail.com

S. Gupta
e-mail: supratic@yahoo.com

scenically. Bamboo has good compressive stress and fairly good tensile strength while it has lower modulus of elasticity compared to steel and more near to concrete [1, 2]. These properties make it an ideal material to be used as wall panel. Often the bamboo panels are covered with mud for longevity. In fact, this is a very popular practice to have bamboo mesh with mud plaster from almost every part of the world [3, 4]. In last century, the concept of mud plaster was replaced with cement mortar plaster [5, 6]. The second author (S Gupta) had lived in one such house from childhood at Guwahati (Fig. 1g). This type of house was very popular in north east of India and have shown excellent performance. This type of wall panel should have become popular even in multi-storeyed houses but has unfortunately not become popular because of unacceptability of wood as joint and lack of technical experimental data showing its suitability [7]. The authors has taken up extensive testing and attempted to solve the technical problems that can be adopted to make this type of wall panel popular in multi-storied buildings. The paper presents a brief outline of the work and the technical development being done.

2 Material Used in Walls

Wall consumes large amount of construction material (Fig. 1). Traditionally, burnt *clay brick* used to be used as primary building material in walls. Regulatory bodies are restricting the use and production of burnt clay brick and *fly ash brick* made with high volume fly ash and smaller quantity of cement or lime is becoming popular. *Hollow blocks* are also an option. Recently *autoclaved blocks* and *gypsum* boards are also competing to be part of this.

On the other hand, bamboo is being used extensively by the rural people and in resort applications for wall applications. A tradition of using cement mortar on bamboo panel has developed in various parts of the world, including the north-eastern part of India as shown in Fig. 1. This is an extremely nice wall system. However, this type of bamboo wall with cement mortar of making Assam type housing is phasing out as these single story houses are being replaced with multi storied building where mostly brick, hollow blocks, autoclaved bricks are being used and bamboo rarely finds its use as external cladding on them. The following problems were realized:

(a) Assam type house required wooden batons as shown in Fig. 1 and use of wood as a construction material is not acceptable from environmental point of view. Hence, it is important to develop joints that can help this type of panel become acceptable to the modern construction industry.

(b) Possibilities of concealed wiring.

(c) Extensive experimental data scientifically proving the validity of this wall panel, satisfying international standards does not exist and is needed to be documented.
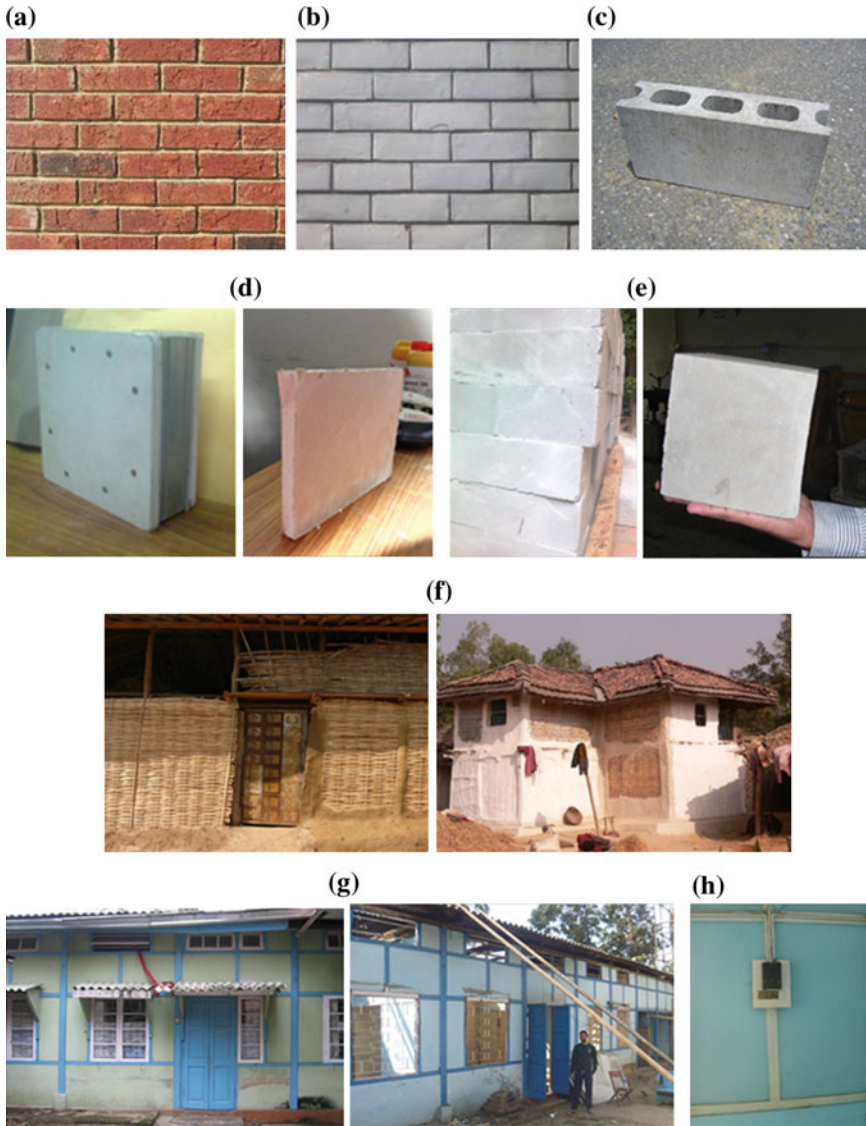
Fig. 1 Bamboo wall panelled house in Assam using wooden frames. **a** Burnt clay brick. **b** Fly ash brick. **c** Hollow block. **d** Gypsum fibre board. **e** Autoclayed concrete block. **f** Ekra wall with and without mud plaster. **g** Bamboo panels joint with wooden frames. **h** Electric wiring on wooden frame

This paper presents a series of pictorial description of various type of joints that were developed in this research to address the above problems with a hope that this type of wall panels can find a place in modern construction also. A model house, as shown in Fig. 2, has built at IIT Delhi.

Fig. 2 Different stages of bamboo concrete house construction at IITD

The house demonstrates the possibilities of three type bamboo walls along with their continuous and corner joint detailing. This house also uses bamboo column developed earlier along with concrete foundations.

The roof RCC slab was casted using M35 concrete. The details of the foundation, column and roof slab are outside the scope of this paper.

3 Making of Bamboo Wall Panel with Bamboo Batons

Assam type house was popular with wooden batons with bamboo mesh in between. It gives a typical look, providing rigidity to the wall. Since wood is not an acceptable alternative, bamboo itself has been used as an alternative. Figure 3 shows the details of how prefabricated walls panel were manufactured. Panels were made with bamboo frames joint to each other with nuts and bolts system (Fig. 3b) and bamboo strips were weaved inside the groove made on frames. The picture clearly shows the possibility of window inside the frame. Figure 3d, e show Grooves on intermediate bamboo frames at right opposite side at 180°, in which strips were inserted maintaining the continuity of the wall.

Fig. 3 Bamboo framed wall panel detailing. **a** Slivering of bamboo strips. **b** Assembly of bamboo frames with nut and bolts. **c** Making of bamboo panel using bamboo frames. **d** Grooves on intermediate bamboo frames. **e** Panel made with window opening and its installation

4 Development of U and W-Framed Bamboo Panel

It was observed that use of bamboo frames may not be a suitable option to carry forward this wall panel technology into modern day construction practices. So a new framing technique was developed to use of this product in a better way. Two types of GI (galvanised Iron) frames were considered i.e. (i) U-channel frame (ii) W-channel frame with having material thickness of 1.22 mm for the making of bamboo wall panels. Two different dimensions of W-Channel were procured shown in Fig. 4. At first panel of dimension 0. 65 m × 0. 65 m were prepared to analyse the practical feasibility of this framing concept (Fig. 4d). The W-panel system is a twin wall system, where bamboo strips were fabricated on both the end grooves of the channel and the mid space of W-channel serves for the purpose of concealed electric wiring passing the cable through it. U framed and W framed bamboo panels were fabricated dimensioning appropriately as per the use on different side of the
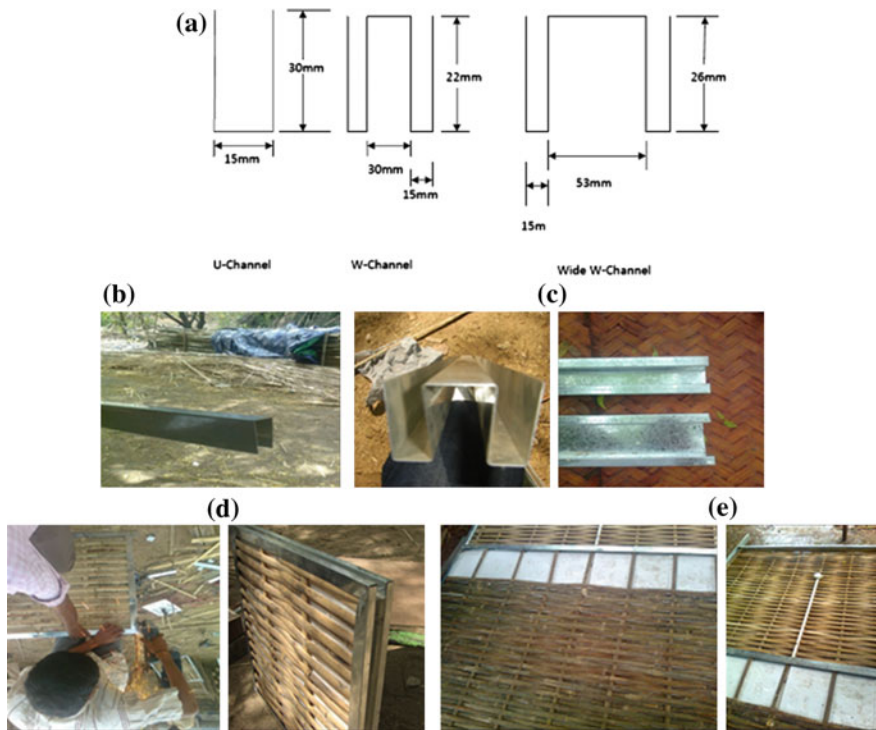
Fig. 4 Making of U and W-framed bamboo panel. **a** Dimensional detailing of U and two types W channeled frame. **b** U-frame. **c** Different mid spaced W-frames. **d** U and W framed bamboo panel of 0.65 m × 0.65 m. **e** Insertion of polystyrene sheet and electric cable through the mid space of W-frame

house, providing openings at different position for the installation of door, window and ventilator fitting. The intermediate inner space of W framed panel was filled with polystyrene sheets (thermocole sheet) shown in Fig. 4e.

5 Construction of Corner Joints

Placing two panels at two different sides of the corner making the wall discontinuous and gap persists at the corner of the adjacent panels. Three methods for the continuity of wall panel at corner point were adopted.

(a) *Bamboo at the Corner*: A bigger size straight bamboo is taken a slits were made right angle to each other as shown in Fig. 5a (i) or b (i). The bamboo weaved strips are inserted in them. This type joint is applicable in straight joint also.

(a)

i) Bamboo I Corner   ii) Bamboo bent by heating   iii) Metalic Corner

(b)

i) Bamboo I Corner   ii) Bamboo bent by heating   iii) Metalic Corner
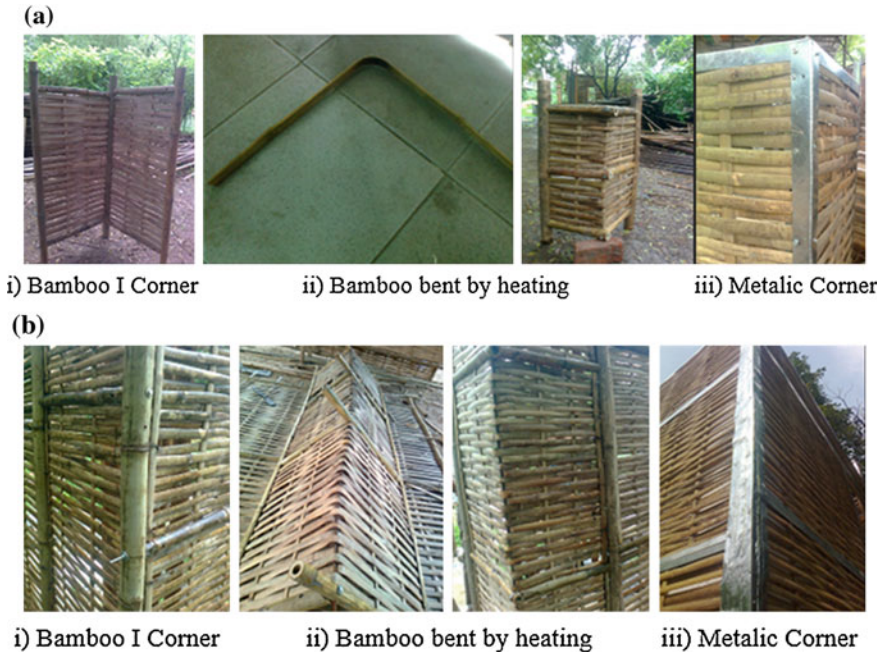
Fig. 5 Detailing of corner joints. **a** Development of modelled corner joints. **b** Different types of corner joints in real structure

(b) *Right Angle bamboo bent by heating* [Fig. 5a (ii) or b (ii)]: Bamboo can be bent to right angle by heating. This bent bamboo strips can be used to create right angle corner of the walls.

(c) *Metallic Joints* [Fig. 5a (iii) or b (iii)]: Both U and W frames have straight edges and can easily be connected.

6 Installation of Wall Panel

The bamboo wall panels were assembled on all the four side of the house using different framing pattern and joint details. The bamboo frames and metal frame panels were joined using screw. To protect the bamboo from degradation, bamboo in the bottom is also inserted in the concrete (Fig. 6a). One may or may not adopt this technology as any way it would be covered by the cement plaster. By putting it inside the plinth concrete, possibly some load will also be transferred through the walls and bamboo columns will be relieved of some loads and these walls will act partially as load bearing walls after plastering.

Fig. 6 Installation of wall panel and completion of bamcrete house at IITD. **a** Fixation of bamboo panel in concrete. **b** Installation of windows and door fittings. **c** Bamboo wall panels before mortar plaster. **d** Insertion of anchorages. **e** Mortar plastering of bomboo panles. **f** Bamboo concrete house

Concealed electrical wiring was done in W framed bamboo panel providing outlets at certain points for the electrical fitting. Doors and window fittings were done after assembling the bamboo panel's frames firmly at the bottom (Fig. 6b). On the bamboo walls anchorages of flat mild steel bars and reinforced bar were inserted for hanging purposes before plastering (Fig. 6d). It is possible to easily insert drilled screws too. Plastering of cement mortar was done on bamboo wall panels and white washing of the house was completed together with flooring (Fig. 6e). This is a clear example of practical viability of bamboo concrete house construction with a hope of its influence in construction practices.

7 Discussion and Conclusion

Plastered bamboo weaved wall or bamcrete wall was popular as wall panel in north eastern part of India. The strength and other properties have been tested and are being compiled and will be published in future publications. The mortar used had high strength. In this paper possibility of different possible joints have been presented presenting construction details of the demonstration house where these joints were utilized has been presented. Three different type of joints have been presented. Corner details were shown. The following were the important salient points:

(a) Bamboo weaved panels can be connected using bamboo joints. U-type and W type metallic connectors can also be used to create single or double layer walls respectively.
(b) Straight or corner joints are easily possible.
(c) Pre-installed nails or post installed nails are possible as the mortars used are high strength mortars.
(d) In W-type metallic connectors, one can put concealed wiring also.
(e) In structural bamboo, thick walled, straight and strong bamboo is required. In the bamboo wall, any type of bamboo can be used.

This type of wall panel has high potential to be used as wall panel among other possibilities like brick, fly ash brick, autoclaved brick, hollow blocks etc. Though clay plastered is also a good option, one may also explore the possibility of unplastered version with paint on it to provide durability.

References

1. Gupta S, Supravin K Study of mechanical properties for application of bamboo as a structural element. Bamboo as a green engineering material in rural housing and agricultural structures for sustainable economic growth, NAIP, component 4, Chapter 5C, pp 99–108
2. Gnanaharan R, Janssen JJA (1994) Bending strength of Guadua bamboo comparison of different testing procedures. Kerala Forest Research Institute and International Development Research Centre, Canada, INBAR, No. 3, New Delhi

3. Vengala J, Jagadeesh HN, Pandey CN (2007) Development of bamboo structure in India. Modern bamboo structures, ICBS, Changsha, China, pp 23–32
4. Janssen JJA (2000) Designing and building with bamboo. International Network for Bamboo and Rattan, vol 20
5. Gupta S, Korde C, Sudhakar P Study of structure using bamboo. Bamboo as a green engineering material in rural housing and agricultural structures for sustainable economic growth, NAIP, component 4, Chapter 5C, pp 22–74
6. Dash AK, Gupta S (2014) Bamboo wall structure: a step towards sustainable construction. Advances in civil and structural engineering—CSE, Institute of Research Engineers and Doctors, pp 11–14
7. Jayanetti DL, Follett PR (2007) Bamboo in construction. Modern bamboo structures, ICBS, Changsha, China, pp 23–32
8. Lopez OH (2003) Bamboo: the gift of gods. ISBN 958-33-4298-X
9. Ghavami K (2003) Eco-construction and infrastructure. RIO 3—world climate and energy event, Rio de Janeiro, Brazil, pp 431–438

A Review of Low Cost Housing Technologies in India

Vishal Puri, Pradipta Chakrabortty and Swapan Majumdar

Abstract One of the three basic needs for mankind's survival is shelter which is not adequate in India as per the estimation reported by the Ministry of Housing and Urban Poverty Alleviation, Government of India. With an annual population growth rate of 1.64 % as compared to world population growth rate of 1.23 % during the last decade there is a great vulnerability to housing needs in the coming decades. This would result in an enormous over dependence on traditional building materials like steel, cement and wood. To reduce this over dependence there is a need to review alternate building materials and formulate guidelines for their application in construction industry. This paper focuses on the recent advancements in energy efficient, eco-friendly low cost building materials like fly ash, earthen materials and natural fibers (bamboo) along with the different problems associated with them. Numerous technologies are available nowadays to build two storey bamboo house, pre-engineered bamboo portal frame buildings, composite bamboo beams and columns, fly ash concrete, fly ash bricks, fly ash blocks, non-erodible mud plaster, terra cotta skin in mud walls, tumbler tiles, and fibrous boards. The recent developments in this area in India by various organizations like Building Materials and Technology Promotion Council (BMTPC), Central Building Research Institute (CBRI), Indian Institute of Technology (Delhi, Roorkee, Madras, Kharagpur) and Indian Plywood Industries Research and Training Institute (IPIRTI) have been discussed along with their potential applications, cost aspects. Numerous problems such as lack of codal guidelines, technology transfer and manufacturing facilities associated with these materials have been discussed. Need of the hour is for their widespread usage and awareness among peoples but the lack of specific guidelines unlike other countries hinder their application.

Keywords Low cost housing · Bamboo · Fly ash · Earthen material · Natural fibres

V. Puri (✉) · P. Chakrabortty · S. Majumdar
Department of Civil and Environmental Engineering, IIT Patna, Patna, India
e-mail: vishal.pce13@iitp.ac.in

1 Introduction

The housing shortage at the beginning of 12th Five Year plan (2012–2017) is estimated at 18.78 million as per the Report of the Technical Group on Urban Housing Shortage, Ministry of Housing and Urban Poverty Alleviation, Government of India [1]. With the annual population growth rate of 1.64 % as compared to world population growth rate of 1.23 % [2] during 2000–2010 there is a great vulnerability to housing needs in the coming decades. However, with the traditional building technologies it is impossible to solve this menace as we cannot solely depend on the traditional construction materials such as concrete, bricks, wood to cover all housing needs, as they are produced from the natural resources. The continuous exploitation and depletion of natural resources is harming the environment. Moreover, different toxic substances such as carbon monoxide, sulfur oxides, nitrogen oxides and suspended particulate matter are invariably emitted to the atmosphere during the manufacturing process of traditional construction materials. Emission of toxic matter further contaminates the air, water, soil, and aquatic life which influence the human health and the standard of living. Thus there is a need for adoption of "Eco-Structures", which are the constructions that are in harmony with the surroundings and does not violate the environment neither through building materials or construction methods [3]. Also with the over exorbitant dependence on the building materials like steel, cement and wood the construction cost is increasing day by day because of high demand, scarcity of raw materials and high price of energy. The use of alternative construction materials has now become a global concern from the standpoint of energy concerns. Thus there arises the need to look out for cheaper yet sustainable low cost housing technologies.

Sustainability is defined as the development that meets the needs of the present without compromising the ability of future generations to meet their own needs [4]. Sustainable development involves the social, environmental and economic accountability often known as triple bottom line [4]. For every sustainable material, the selection and usage depends on its performance which depends on different factors such as [5]:

1. Locally produced and sourced materials
2. Transport costs and environmental impact
3. Thermal efficiency
4. Occupant needs and health considerations
5. Financial viability
6. Recyclability of building materials and the demolished building
7. Waste and pollution generated in the manufacturing process
8. Energy required in the manufacturing process
9. Use of renewable resources
10. Toxic emissions generated by the product
11. Maintenance costs.

Use of natural materials like straw, bamboo, fibers and husk is a very old practice in India. These materials are locally available and have easy workability and also promotes speedy construction. Also different industrial wastes like fly ash, rice husk can be used for construction purposes as they are easily available. This paper focuses on the recent advancements in the various energy efficient, eco-friendly and alternative materials like bamboo, fly ash, earth, natural fibers along with their affordability and problems associated.

2 Low Cost Housing Building Materials

Low cost housing refers to those housing units which are affordable by that section of society whose income is below than median household income. This depends on three key parameters—income level, size of dwelling unit and affordability. Affordability depends on the type of construction materials used and the cost associated with them. Natural materials such as fibers, earth and fly ash are some of the materials which are easily available and have excellent prospects of being used in the construction industry. Figure 1 categorizes the different low cost housing building materials. The following sections focus on the emerging technologies available in India that provide an alternative to traditional construction materials.

2.1 Earthen Material

Oldest building material used for centuries even though with faced difficulties like erosion, water penetration, attack by termites and pests and high maintenance. Figure 2 shows the world's largest mud brick building. However, with recent advancements this technology can be still widely used for enhanced positive results. Central Building Research Institute (CBRI) has developed Non-Erodible mud plaster. This is prepared by mixing bitumen cutback (Bitumen and Kerosene oil mixture) with a specified mud plaster [6]. This is an economical and effective technique that provides protection against water. Also to protect mud-walls from rain and moisture, Centre for Science for Villages, Wardha, India has developed a technique of providing potter made tile lining also termed as Terra Cotta Skin to Mud walls [6]. They have also developed a technique for manufacturing Tumbler tiles which are used for roofing, are light weight and can bear the weight up to 1 T/m^2 with an expected lifespan of 50 years and require no repairs [7]. CBRI has developed a machine to produce C-Bricks which has enhanced properties over the conventional bricks [8]. BMTPC has developed a technique to manufacture red mud polymer door shutters and panel products which are termite, fungus, fire, and weather resistant [9]. They are cheaper than wood, energy efficient, requires less maintenance cost. With such a widespread development in technology the challenge is now to bring it to the masses and use them on a massive scale.
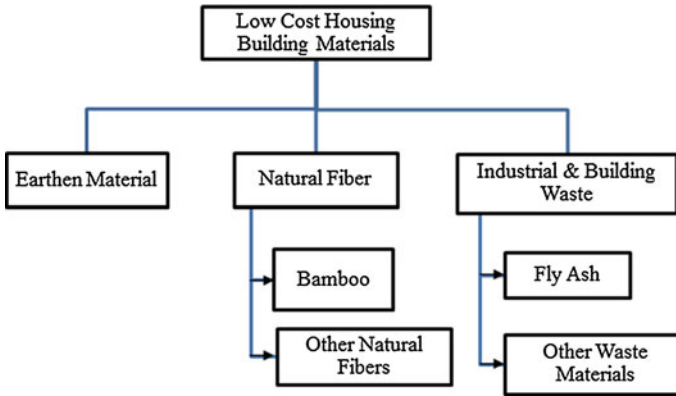
Fig. 1 Different low cost building materials

Fig. 2 The great mosque of Djenné—largest mud brick building in the world, Mali, West Africa

http://lanalog.blogspot.in/

2.2 Natural Fibers

Natural fibers are those which are found from vegetable or animal origin. They are environment friendly, biodegradable, cheap as compared to synthetic fibers and can be used as an excellent substitute to the synthetic fibers.

2.2.1 Bamboo

One of the fastest growing plants in the world with some of its species growing at an incredible rate of 91 cm per day as per Guinness Book of world Records [10] is an excellent low cost substitute to wood. India is the second largest producer of bamboo in the world after china with over 136 species presently cultivated [6]. Figure 3 shows the major bamboo growing areas in India. A specimen bamboo structure is shown in Fig. 4.

Fig. 3 Major bamboo growing areas in India
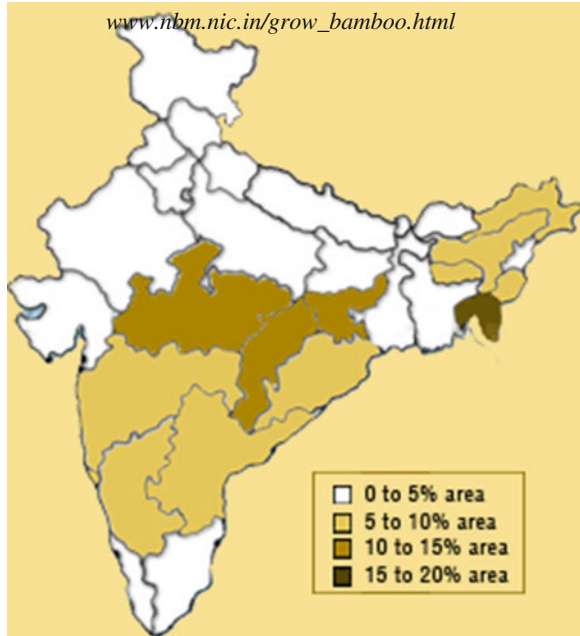
Fig. 4 Bamboo structure

Bamboo has high tensile strength and a very good weight to strength ratio which makes it highly useful against high velocity winds and earthquakes. As compared to materials like steel, plastics, aluminum it requires very less energy for production. Steel requires 50 times more energy than bamboo to produce 1 m^3 material per unit of stress [11]. However being susceptible to termite attack it needs to be treated first either by chemical or non-chemical treatment [3] which increases its life span. In India, the treatment specification for bamboo structures are defined by IS 9096 [12].

The structural design guidelines are stipulated by National Building Code 2005 [13]. With such a widespread availability, affordability and excellent material properties bamboo is an excellent construction material with great future prospects.

Bamboo has various applications in all components of small buildings both structural and nonstructural. Bamboo could be used in foundations, floors, walls, roofs, roof covering, doors and windows [14]. Numerous studies have been carried out to study the engineering characteristics of bamboo. Prospects of bamboo as a replacement of steel in reinforced concrete beams, columns were studied by Ghavami [11]. Fracture behavior of bamboo reinforced concrete members were studied by Terai and Minami [15]. Seismic performance of bamboo structure was studied by Elizabeth and Datta [16] and Sharma [17]. A special type of Glue laminated girder using laminated bamboo veneers were studied by Xiao et al. [18]. A two story house constructed using laminated bamboos were demonstrated by Xiao et al. [19]. Prefabricated bamboo panel houses were demonstrated by Zehui et al. [20].

In India bamboo is used traditionally in many regions. However, its usage is limited to semi load bearing element or as infill material in light frame wood houses.

Indian Plywood Industries Research and Training Institute (IPIRTI) have developed a two story house using bamboo at Bangalore. The house has split bamboo grid and wire mesh plastered with cement mortar for walls with bamboo columns providing support and ceiling was made up of light bamboo mat corrugated sheets. These types of houses are best suitable for earthquake prone areas as the test results showed that these houses resisted seven repetitions of typical zone 5 earthquakes.

Researchers at IIT Delhi have developed pre-engineered bamboo portal frames, bamboo domes, composite bamboo beams, and columns for low cost housing. Considerable research is also being carried out to establish whether the bamboo composites could be used for high rise buildings especially in earthquake prone areas. Research has highlighted that the structures made from bamboo could be replaced to those made by conventional building materials. These structures are several times cheaper, eco-friendly and could be used for sustainable housing development.

Building materials and Technology Promotion Council (BMTPC) in collaboration with different organizations have also developed several products like bamboo mat corrugated sheets, bamboo mat doors, pre-fabricated double walled composite house, bamboo roofing sheets, bamboo laminates. These products have shown good performance in different climates. Table 1 shows a comparison between different properties of bamboo and steel. The R and D efforts for development of these products have established the technical feasibility and are being commercially produced and marketed.

Bamboo which has a great potential as a substitute to steel is available in the market for about Rs. 5,000 per ton as compared to steel bars price of Rs. 40,000–50,000 per ton. In two recent case studies it was observed that about 26 and 23 % of the construction cost could be saved using low cost housing technologies [21].

Table 1 Comparison for different properties of bamboo and steel

S. No.	Property	Bamboo	Steel
1	Density (kg/m^3)	(515–817) for different species in green condition	7,850
		(640–758) for different species in air dry condition [13]	
2	Modulus of elasticity (N/mm^2)	$(0.61–15.01) \times 10^3$ for different species in green condition	2×10^5
		$(3.77–21.41) \times 10^3$ for different species in air dry condition [13]	
3	Grading for structural utilization	As per diameter, taper, straightness, inter nodal length, wall thickness, density and strength, durability and seasoning [13]	As per its yield stress, ultimate tensile stress, elongation
4	Compression strength	(25–100) MPa [14]	Mild steel—compression in column bars: 130 MPa
5	Tensile strength	(100 to 400) MPa [14]	Mild steel—permissible stress in tension
			140 MPa (up to 20 mm dia)
			130 MPa (over 20 mm dia)
6	Bending strength	(70–300) MPa [14]	$0.66 \times$ yield stress
7	Factor of safety (F.O.S)	For safe working stresses of bamboo [13]	1.15—Structural member for limit state of collapse
		4—Extreme fiber stress in beams	
		4.5—Modulus of elasticity	
		3.5—Maximum compressive stress parallel to fibers	

However number of important considerations still limits the use of bamboo as a universally applicable construction material. Durability of bamboo is affected by attack of fungi and insects. Effective joining methods are still being researched. Figure 5 shows the different types of bamboo cuts to make bamboo joints. Bamboo structures don't behave well in fire and cost of treatment is relatively high. Also there is a lack of design guidance and standardization of the design of bamboo structures [14]. Although India has an extensive distribution of bamboo but still raw material supply chain for manufacturing different composites is not adequate. Adhesives used for bamboo products are similar to those used in wood. Thus there arises a need to formulate or improve the formulations of existing adhesives to make them more environment-friendly. Also there is a great need to enhance the scale of manufactured bamboo products along with spreading awareness so as to use it on a mass level.
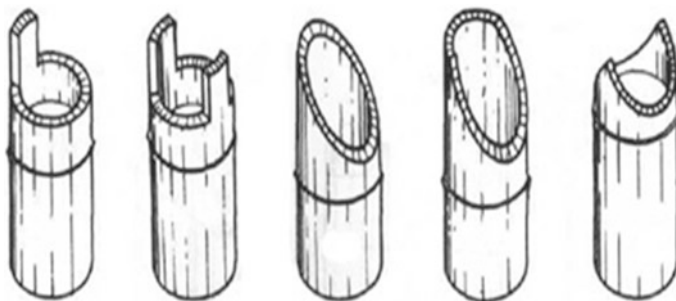
Fig. 5 Different types of bamboo cuts to make bamboo joints

2.2.2 Other Natural Fibers

Considerable research has been carried out on developing artificial fibers like carbon, aramid and glass. However the other natural fiber's such as straw, kenaf, flax, jute, sisal widespread usage is still lacking. Main advantages of natural fibers over synthetic fibers include—biodegradability, energy recovery, lower specific weight which gives higher specific strength and stiffness, renewable resource, low investment, good thermal and acoustic properties, natural working conditions. Figure 6 shows three different fibers—kena, flax and hemp.

Glass fiber reinforced gypsum panels were utilized by IIT Madras researchers [22] to showcase a low cost housing model. The 800 sq. ft house was constructed at a cost of Rs. 10 lakhs. GFRG panels were utilized for entire building system including floors, roofs, staircases which significantly reduced the consumption of reinforced cement concrete.

BMTPC has developed several products like fiber fly ash cement boards, fibrous gypsum plaster boards, coir cement board, straw panels, jute fiber polyester panels in association with different other organizations. Red mud jute fiber polymer composite which is made up of raw materials like red mud, polymers and natural fibers has been developed which is used for door shutters and panels [23]. These materials provided excellent alternative to conventional building materials which are costlier and polluting our environments.

Fig. 6 Different natural fibers

2.3 Industrial and Building Waste

2.3.1 Fly Ash

Presently India generates about 70 % of electricity through thermal power plants which produces fly ash in plenty and with the future production also predominantly on coal; the fly ash disposal seems to be a big concern. India ranks 4th in the world in production fly ash after USSR, USA and China [24]. As per the recent estimates fly ash generation is expected to reach 225 million tons by 2017 [25]. With such huge volume requiring massive land area for disposal along with the presence of heavy metals in it which are not biodegradable. Its safe disposal is also a huge concern as it affects the environment and ground water.

Fly ash is defined as a heterogeneous mixture of amorphous and crystalline phases and is a finely powdered ferro-alumino-silicate material having Al, Ca, Fe, Na and Si as predominant materials. Fly ash is a finely divided powdered material the particles of which are spherical in shape and range in size from 0.5 to 100 µm. Fly ash is broadly classified into two categories as Class C and F as per ASTM C-318 [26]. The properties of both the classes vary based on the type of fuel from which they are produced. Based on the fly ash characteristics it could have various applications.

To study the elemental characteristics of fly ash authors performed elemental analysis using energy dispersive X-ray emission spectroscopy (EDXE) and XRD analysis. Figure 7 shows the FESEM image of fly ash samples obtained from NTPC Kahalgaon, Bihar. Twenty one elements were quantified in the fly ash samples with predominant O, Al and Si.

Fly ash has a great potential for usage in building materials as it possesses pozzolanic properties which are utilized to produce different construction materials like—ready-mix fly ash concrete, clay-fly ash bricks, lime-fly ash bricks, lime-fly ash cellular concrete blocks, Portland pozzolona cement, and fly ash sand lime bricks.

Fig. 7 FESEM image of fly ash samples obtained from NTPC Kahalgaon
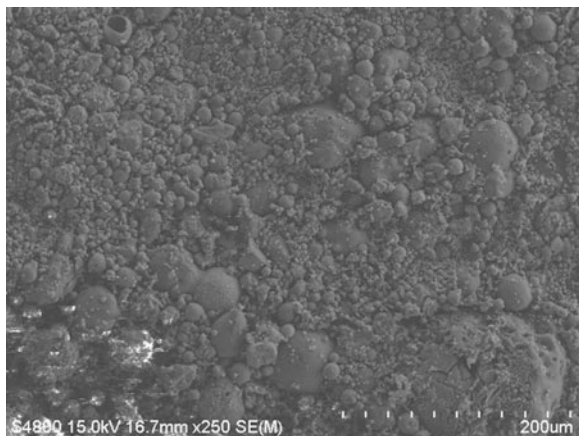
Indian metals and ferro-alloys have showcased a new effective method of fly ash utilisation [27] by producing low-density aggregate (LDA). The low-density aggregate (LDA) are produced using 85 % fly ash along with sand and lime. These low density aggregates can be used as substitute to natural aggregates as they are lightweight, reduces pollution and also the permeable surface of LDA pellets enables better quality concrete as compared to stone chips. Being lightweight these aggregates just add mass to concrete not much weight. Although this technology is widely used abroad but in India recent advances have just started.

BMTPC in collaboration with regional research laboratory, Bhopal have developed a technology to use fly ash based polymer composites [28] as wood substitute which is used in many applications like door shutters, partition walls, flooring tiles, wall paneling.

Materials such as fly ash which could be used as a potential replacement to cement costs just around Rs. (75–500) per million Tons as compared to cement which costs nearly Rs. 330 for a bag of 50 kg. As fly ash is a waste product of thermal power plants it is sold very cheaply especially during monsoons when the demand is very less. Fly ash could be used as part replacement in cement up to 35 % without compromising its strength, durability and economy in construction [29].

With the recent advancements in technology fly ash is now recognized as a valuable substance which is useful for different applications and is categorized as "resource material" instead of "waste material". Even though numerous steps have been taken by Government of India like—updating existing standards IS 3812, IS 456, IS 1489, enhanced policies for effective utilization of fly ash. Ministry of Environment and Forests (MOEF) issued a regulation making it mandatory for both existing and new coal based thermal power plants to utilize 100 % of the fly ash produced within a stipulated timeframe [30]. However, the fly ash utilization rate in construction field is only 38 % [30]. There is a great need to implement the order for utilization of fly ash by developing different above mentioned bi-products in a massive scale.

2.3.2 Other Waste Materials

Different industrial and construction waste materials also have a great potential in low cost housing. Construction waste is basically the unwanted material that is produced incidentally or directly during the construction purposes. They include electrical wiring, metal waste, concrete waste, marble waste. Also in industrial sector, different waste materials are produced such as blast furnace slag, cement kiln dust. These could be utilized for soil stabilization before construction. Waste tyres in the automobile industry could be utilized as aggregates. Glass waste from the glass industry could be utilized in the glass fiber reinforcement. Concrete waste could be utilized for making tiles, earth fill. Since all these materials are waste products they are cheaply available and have a great potential for low cost housing.

3 The Traditional Versus Low Cost House Construction Technologies

Walls: Low cost housing involves cheap materials such as wall panels made from fibers or polymers whereas traditional method involves brick walls.

Roof: In low cost housing it is generally of tiles made from cheap materials whereas traditional building involves R.C.C. slabs.

Beams and columns: In traditional buildings they are generally made from cement concrete whereas in low cost buildings materials such as bamboo, fly ash partially replaced with cement are used.

Plaster: In low cost housing plastering is generally avoided or cheaper conventional materials are used whereas traditional houses involves cement plaster along with high costs exterior paints.

Doors and Windows: The doors and windows of low cost houses are generally formed from fiber boards whereas traditional houses involve high costs wooden doors.

Flooring: It is generally made of terracotta tiles or color oxides in low cost houses whereas traditional houses involve costly marble flooring.

4 Summary

Building houses for low income families poses a great challenge. It involves a great effort to develop new technologies for using different alternate materials in the construction industry. In this study, low cost housing technologies were studied and the potential for the materials to be used as alternative building materials was discussed. Even though different low cost housing technologies have been developed but still there is a shortage of housing. Still we are unable to provide shelter to people from low income sections. There are no proper guidelines formulated for structural aspects of these alternate building materials. Lack of awareness is also there among builders on the applicability and benefits of these materials.

Although fly ash bricks are good alternative to conventional bricks, but still there is a shortage of manufacturers as there is a lack of awareness regarding its benefits and applications. There is no proper network chain for supply of raw materials like fly ash from different thermal plants. Fly ash is a great substitute to cement but still a lot of research is required to be carried out for all products made of cement where fly ash could be replaced such as frames, arches, domes.

Bamboo has been used traditionally in India but only recently a 2 storey house was showcased. That also could not be replicated widely in the market. Bamboo is called as poor man's steel but still its usage is limited in villages with traditional construction practices. Research for its application in composite materials has been

carried out but its market replication on a mass scale is still lacking due to dearth of policies and regulations.

A lot of continuous efforts are required especially from the industry point of view so as to attain the dream of housing for all.

References

1. Report of the technical group on urban housing shortage (TG-12), Ministry of Housing and Urban Poverty Alleviation, 2012–2017
2. Report on provisional population totals—India, census India 2011
3. Nwoke OA, Ugwuishiwu BO (2011) Local bamboo and earth construction potentials for provision of affordable structures in Nigeria. Int J Sustain Constr Eng Technol 2(2)
4. Darwish MM, Agnello MF (2009) Enabling construction engineering students in sustainable thinking: curricular changes to foster sustainability. Seventh LACCEI Latin American and Caribbean conference for engineering and technology (LACCEI 2009), 2–5 June 2009
5. Roux P, Alexander A (2009) Sustainable neighborhood design manual—a non-technical guide. The Sustainability Institute, South Africa. www.sustainabledevelopmentnetwork.com/manuals.php
6. Chowdhury S, Roy S (2013) Prospects of low cost housing in India. Geo-materials 3:60–65
7. Sarkar R (2006) Post earthquake housing construction using low cost building materials. 4th international conference on earthquake engineering, Taiwan, 12–13 Oct 2006
8. Shinde SS, Karankal AB (2013) Affordable housing materials and techniques for urban poor's. Int J Sci Res 1(5)
9. Agrawal SK (2011) Innovative materials and technology, standardisation of design for low cost housing. In: 10th national convention on affordable housing, New Delhi, 8–9 Jan 2011
10. Guinness book of world record (1999). www.guinnessworldrecords.com/records-3000/fastest-growing-plant/
11. Ghavami K (2007) Bamboo: low cost and energy saving construction materials. In: Proceedings of first international conference on modern bamboo structures (ICBS-2007), Changsha, China, 28–30 Oct 2007
12. IS 9096 (2006) Preservation of bamboo for structural purposes—code of practice. Bureau of Indian Standards
13. National Building code of India (2005) SP 7, Bureau of Indian Standards
14. Jayanetti DL, Follett PR (2007) Bamboo in construction. In: Proceedings of first international conference on modern bamboo structures (ICBS-2007), Changsha, China, 28–30 Oct 2007
15. Terai M, Minami K (2011) Fracture behaviour and mechanical properties of bamboo reinforced concrete members. Procedia engineering, 11th international conference on the mechanical behavior of materials (ICM11), vol 10, pp 2967–2972
16. Elizabeth S, Datta AK (2013) On the seismic performance of bamboo structures. Bull Earthquake Eng
17. Sharma B (2010) Seismic performance of bamboo structures. PhD thesis, University of Pittsburgh
18. Xiao Y, Shan B, Chen G, Zhou Q, She LY (2007) Development of a new type Glulam—GluBam. In: Proceedings of first international conference on modern bamboo structures (ICBS-2007), Changsha, China, 28–30 Oct 2007
19. Xiao Y, Chen G, Shan B, She L (2010) Two-by-four house construction using laminated bamboos. 11th world conference on timber engineering (WCTE), Trentino, Italy, 20–24 June 2010

20. Zehui J, Xuhe C, Yan Y (2009) Prefabricated bamboo panel house for disaster relief. Annual 2009 (IAWS) plenary meeting and conference, International Academy of Wood Science, Saint Petersburg–Moscow, 15–21 June 2009
21. Tam VWY (2011) Cost effectiveness of using low cost housing technologies in construction. The twelfth East Asia-Pacific conference on structural engineering and construction, Hong Kong China, 26–28 Jan 2011
22. Department of Civil Engineering—IIT Madras (2013) Affordable rapid mass housing. National symposium on affordable housing, New Delhi, 22 July 2013
23. Department of Forests, Ecology and Environment (2007) Parisara, ENVIS Newsletter—status of environment and related issues. Government of Karnataka, vol 2, no 9
24. Senapati MR (2011) Fly ash from thermal power plants—waste management and overview. Curr Sci 100(12):25
25. Nawaz I (2013) Disposal and utilization of fly ash to protect the environment. Int J Innov Res Sci Eng Technol 2(10)
26. ASTM C618—12a. Standard specification for coal fly ash and raw or calcinated natural pozzolana for use in concrete
27. Indian metals and ferro alloys—Orissa, Press release—June 2014. www.thehindubusinessline.com/news/ststat/industry-body-devises-novel-method-for-fly-ash-disposal/article6089952.ece
28. Alam J, Akhtar MN (2011) Fly ash utilization in different sectors in Indian scenario. Int J Emerg Trends Eng Develop 1(1)
29. IS 1489 (Part 1)—1991 (2000) Portland—pozzolona cement—specification. Bureau of Indian Standards, Amendment No 3
30. Lokeshappa B, Dikshit AK (2011) Disposal and management of fly ash. Int Conf Life Sci Technol 3

Part XXII
Fiber Reinforced Polymer (FRP) in Structures

Bond-Slip Response of FRP Sheets or Plates Bonded to Reinforced Concrete Beam Under Dynamic Loading

Mohammad Makki Abbass, Vasant Matsagar and A.K. Nagpal

Abstract The performance of bond-slip of fiber reinforced polymer (FRP) sheets or plates bonded to reinforced concrete (RC) beam under dynamic loading are studied. Model for composite beam are developed and simulations are carried out by developing finite element (FE) models in ANSYS under static and dynamic loading. Parametric studied are carried out by varying width of the FRP sheets or plates, their thickness, and for compressive strength of concrete. The RC beam subjected to static load is designed according to the ACI 318-11 and ACI 440R-08. Further, the beams are subjected to dynamic loading by applying harmonic excitation. The performance of the composite beam is analyzed in terms of load-slip relationship. The theoretical results are compared with the results reported in the standard literature from experiments conducted.

1 Introduction

Strengthening or retrofitting of existing reinforced concrete (RC) structures to resist dynamic loading, higher design loads, correct strength loss due to deterioration, correct design or construction deficiencies, or increase ductility has traditionally

M.M. Abbass (✉)
College of Engineering, Al-Mustansiriya University, Baghdad, Iraq
e-mail: mohammadmakki2003@yahoo.com

V. Matsagar · A.K. Nagpal
Department of Civil Engineering, Indian Institute of Technology (IIT) Delhi,
Hauz Khas, New Delhi 110016, India
e-mail: matsagar@civil.iitd.ac.in

A.K. Nagpal
e-mail: aknagpal@civil.iitd.ac.in

been accomplished using conventional materials and construction techniques. Externally bonded steel plates, steel or concrete jackets, and external post-tensioning are just some of the many traditional techniques available. Composite materials made of fibers in a polymeric resin, also known as fiber-reinforced polymers (FRP), have emerged as an alternative to traditional materials for repair and rehabilitation [1]. The FRP materials are lightweight, noncorrosive, and exhibit high tensile strength. These materials are readily available in several forms, ranging from factory-made laminates to dry fiber sheets that can be wrapped to conform to the geometry of a structure before adding the polymer resin. The relatively thin profiles of cured FRP systems are often desirable in applications where aesthetics or access is a concern. The polymer composite derives its mechanical characteristics wholly from those of the fiber and the quality of the fiber/matrix interface, therefore the most important properties required of the polymer is its physical and in-service characteristics. High-performance thermosetting resins are required to provide specific properties in highly demanding environments. These matrices must possess high dimensional stability at elevated temperatures and thermal resistance, low water absorption, good chemical resistance, high mechanical strength, excellent stiffness, and high compressive strength. This combination of properties is essential for advanced composites to be utilized in the construction industry, however due to the increase in cross-linking density observed during polymerization, conventional thermosetting matrices are considered to be brittle and this limits the damage tolerance of the composite. Hollaway [2] demonstrated the types of structures which have been developed from the FRP composite material and the most advantageous way to employ composites in civil engineering. The material has extraordinary mechanical and important in-service properties which when combined with other materials are utilized to improve the stiffness/strength, durability, the whole-life cost benefit, and the environmental impact. Seleem et al. [3] investigated numerically mode of failure and flexural behavior of both steel and steel-concrete composite beams strengthened by different lengths of the carbon fiber reinforced polymer (CFRP) plates. Pellegrin and Modena [4] investigated the bond behavior between the FRP and concrete with a critical review of the principal bond-slip models available in the literature and proposed a model calibrated on the basis of experimental diagrams ($\tau - s$), taking into account the influence of the FRP strengthening rigidity. Zhao and Farhad [5] investigated the shear stress distributions on the bonded joints, to quantify the anchorage lengths, and to investigate the influence of the concrete strength and the glue line thickness on the bond strength. The interface between the FRP and concrete plays a critical role in this strengthening method by providing effective stress transfer from the existing structures to externally bonded FRP plates or sheets, and keeping integrity and durability of the composite performance of the FRP concrete structures. De-bonding along the FRP and concrete interface can lead to premature failure of structures [6]. The aim of the analysis presented herein is to determine the response of a system subject to static and dynamic loading (harmonic) forcing functions.

2 Analytical/Numerical Study

Different finite element (FE) models for the same geometry and reinforcement of RC beams were developed, with the FRP sheets (different width and layers), or without the presence of the FRP sheets. These models were analyzed under the static and dynamic loads. The analysis was performed using finite element program ANSYS. Throughout the FE simulation the effect of the FRP on the deflection and load carrying capacity were investigated. The general form of the ordinary differential equation in which the mass, damping, stiffness, and applied force of the system is governed by the expression,

$$[M]\{u''\} + [C]\{u'\} + [K]\{u\} = \{F\} \tag{1}$$

where, $[M]$ = structure mass matrix; $\{u\}$ = nodal displacement vector; $[C]$ = structure damping matrix; $\{u'\}$ = nodal velocity vector; $[K]$ = structure stiffness matrix; $\{u''\}$ = nodal acceleration vector; and $\{F\}$ = time-dependent forcing function.

Damping can be specified by any or all of the following methods: mass damping α; structural damping (constant β_i, material dependent); constant equivalent viscous damping ratio ξ; discrete element damping. In this work, structural damping was included. This allowed models to run with a different damping value, in each layer of the superstructures. Structural damping depends on the natural frequency, such as,

$$\beta_i = \frac{2\zeta_i}{\omega_i} = \frac{\zeta_i}{\pi f_i} \tag{2}$$

where $\omega_i = 2\pi f_i$ and f_i is the frequency of mode i.

Modal analysis is used to determine the natural frequencies and mode shapes of a structure. Free undamped vibrations are assumed in ANSYS.

$$F(t) = \{0\} \text{ and } [C] = [0] \tag{3}$$

A modal analysis then precedes other dynamic analysis. The governing equation then becomes,

$$[M]\{u''\} + [K]\{u\} = \{0\} \tag{4}$$

For a linear system, free vibration will be a harmonic of the form,

$$\{u\} = \{u_o\} \cos \omega t \tag{5}$$

For the non-trivial solution, the determinant should be zero,

$$\big|[K] - \omega^2[M]\big| = \{0\} \tag{6}$$

This is an Eigenvalue problem, whose solutions are the Eigen values and the corresponding Eigenvectors. The Eigen values represent the natural frequencies of the system and the Eigenvectors correspond to mode shapes. Harmonic analysis is used to determine the response of a structure to harmonic sinusoidal varying forces. The function $F(t)$ is a periodic value of known amplitude and frequency. The equation of motion, therefore, can be solved to obtain displacements as function of frequency. The dynamic equilibrium equation therefore now be,

$$[M]\{u''\} + [C]\{u'\} + [K]\{u\} = \{F(t)\} \tag{7}$$

Any sustained cyclic load will produce a sustained cyclic response in a structure which is often called a harmonic response. The harmonic response analysis solves the equation of motion, Eq. (7) for linear structures undergoing steady-state vibrations. All loads and displacements vary sinusoidal with the same known frequency although not necessarily in phase. With the second term of Eq. (7), it is also possible to specify a constant damping ratio regardless of each natural frequency. Damping ratio is defined as the ratio between the actual damping and the critical damping. The specified damping ratio for the harmonic response analysis is internally used to get the stiffness matrix multiplier (β_i), appearing in Eq. (7) which further depends on each imposed exciting frequency.

Three-dimensional non-linear finite element models of reinforced concrete (RC) beam strengthened by the FRP were created using the finite element (FE) package ANSYS for conducting static and dynamic analyses. An eight node solid element (Solid65) was used to model the concrete beams. The element is defined by eight nodes having three degrees of freedom at each node (translation in the nodal directions x, y, and z). This element is similar to Solid45 with the addition of special cracking and crushing capabilities along with the ability of creep, plastic deformation, cracking in three orthogonal directions, and crushing. Solid45 was used for modeling the steel plates and it is defined with eight nodes having three degrees of freedom at each node and eight translations in the nodal directions x, y, and z. Bond between concrete, steel, and FRP sheets was assumed by defining one node for both the Solid65 and Solid45 elements having the same coordinates. The full harmonic structural analyses (load-frequency analysis) were performed to predict the load-deflection behavior of the RC beam strengthened by the FRP sheets. Loads were applied incrementally by means of an equivalent displacement to overcome convergence problems. Concentrated loads were applied at one-third of span from both the ends and the load step increments. In order to model the simply supported beam condition, the vertical (Z) displacement of the bottom of steel tube or plate (at supports) nodes was restrained and also all the rotational degrees of freedom were released to allow rotation. Figure 1 shows the loading and boundary condition assigned to the beam [7].
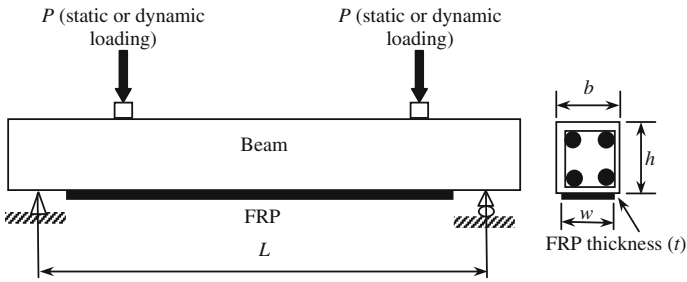
Fig. 1 Reinforced concrete beam with FRP layout

3 Material Properties

The concrete behavior is modeled using multi-linear isotropic hardening relationship and the compressive strength of the concrete (f_c) is taken as the cylinder compressive strength of the concrete as shown in Fig. 2. Poisson's ratio of the concrete was assumed as 0.2, and the modulus of elasticity, E_c was evaluated by ACI-318-11 [1],

$$E_c = 4700\sqrt{f_c} \tag{8}$$

The uniaxial stress–strain relationship of the concrete was constructed by compression. Figure 2 shows the uniaxial stress–strain relationship of the concrete that was used in present study.

Fig. 2 Stress–strain variation of concrete of different grades considered
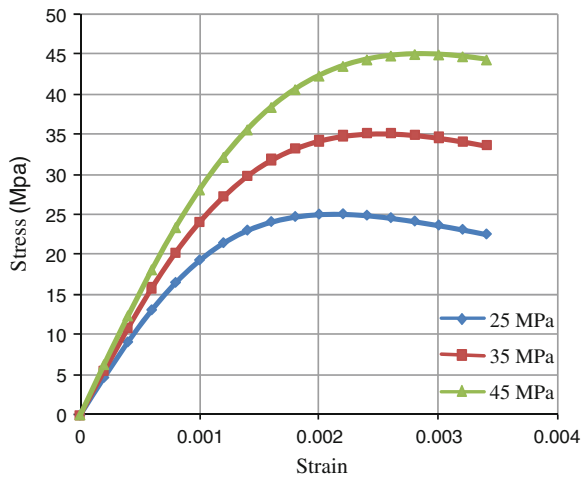
$$f = \frac{E_c \, \varepsilon}{1 + \left[\frac{\varepsilon}{\varepsilon_o}\right]^2}, \varepsilon_o = \frac{2 f'_c}{E_c}, E_c = \frac{f}{\varepsilon} \qquad (9)$$

The isotropic properties such as Young's modulus and Poisson's ratio of the reinforcement (main and secondary) were considered 200 GPa and 0.3, respectively. The non-linear behavior of steel was considered as full plastic. The properties of the FRP composites are same in all the directions, they were considered as an isotropic material. The thickness of single composite layer was 1 mm which is epoxy coated fiber thickness and the unidirectional elastic properties namely Young's modulus and Poisson's ratio were assigned as 240 GPa and 0.22, respectively. For analysis purpose, the density of concrete and steel was assigned as 2,400, 7,850 kg/m^3, respectively. The cylinder compressive strength was taken 25, 35, and 45 MPa for studying the cases. The concrete is modeled using SOLID65 8-node brick element capable of simulating the cracking and crushing of brittle materials. The data of the cylinder compressive strength and split tensile strength based on the tested results have been used for defining the concrete CONCR properties in the ANSYS. For plain concrete of all grades, the shear transfer coefficients in opening (β_t) or closing (β_c) have been assumed to take a value of 0.2 (β_t) and 0.7 (β_c). In the ANSYS model, smeared representation of crack is used for SOLID65. The main reinforcement of 10 mm in diameter and stirrups 8 mm in diameter, reinforcement is modeled as discrete reinforcement using LINK8 elements. Rate independent multi-linear isotropic hardening option with full plastic is used to define the material property of steel rebar. Solid45 elements are used for modeling the steel plates at the supports and loading locations to prevent stress concentration problem and to provide stress distribution over the supports and loading areas. The element is defined with eight nodes having three degrees of freedom at each node—translations in the nodal x, y, and z directions. The FRP is modeled using Shell41 which is a 3-D element having membrane (in-plane) stiffness but no bending (out-of-plane) stiffness. It is intended for shell structures where bending of the elements is of secondary importance. The element has three degrees of freedom at each node: translations in the nodal x, y, and z directions [8]. The FRP used in this study was 60 and 100 mm.

4 Results

The static and dynamic characteristic of loads has a great incidence on the structural behavior of reinforced concrete beam with and without FRP. Previous researches have demonstrated that there is a direct proportion relationship between load and slip. Figures 3 and 4 show the elements modeling for beam dimensions of 100 mm width, 200 mm depth, and 2 m long.

Fig. 3 Finite element modeling showing finite elements and mesh density

Fig. 4 Finite element modeling showing main and stirrups reinforcement with FRP

Before starting the dynamic analysis the static behavior was studied. The results (static), at the end of FRP near the supports the slip increased when the increased and decreased when the compressive strength of concrete increased and the thickness, width of FRP increased see Fig. 5.

The dynamic approach shows that the slip increased at a certain frequency which represents the critical frequency and then the slip decreases subsequently. The load frequency influences the slip distribution. With dynamic loads, slip is amplified when the load frequency is close to the resonance frequencies of the structure. The stiffness of the materials produces increase of the resonance frequencies. The steel reinforcement, compressive strength of concrete FRP thickness and width, as it has a stiffening effect on an increase of the composite beam resonance frequencies. The FRP enhance to increase the tensile strength of concrete so that the slip decreases.

5 Discussion

The design may rely on the partial interaction connection, and, thereby, the slip between the concrete beams and the FRP plates cannot be overlooked. in present study, finite element (FE) models of a reinforced concrete (RC) beam strengthened by FRP, with steel reinforced were developed in order to understand its static and dynamic (harmonic) performance. Static, modal and harmonic analyses were performed and results were extracted. Parameter studies were also carried out, with various width and number of layers of the FRP and compressive strength of concrete. The aim was to study how the slip distributed between FRP plate and reinforced concrete beam, and deflection of the RC beam depend on the dynamic characteristics of the load. Before applying harmonic loading, modal analysis must be run to determine the resonance frequency.

The compressive strength is the capacity of a material or structure to withstand loads tending to reduce size. In a compression test, there is a linear region where the
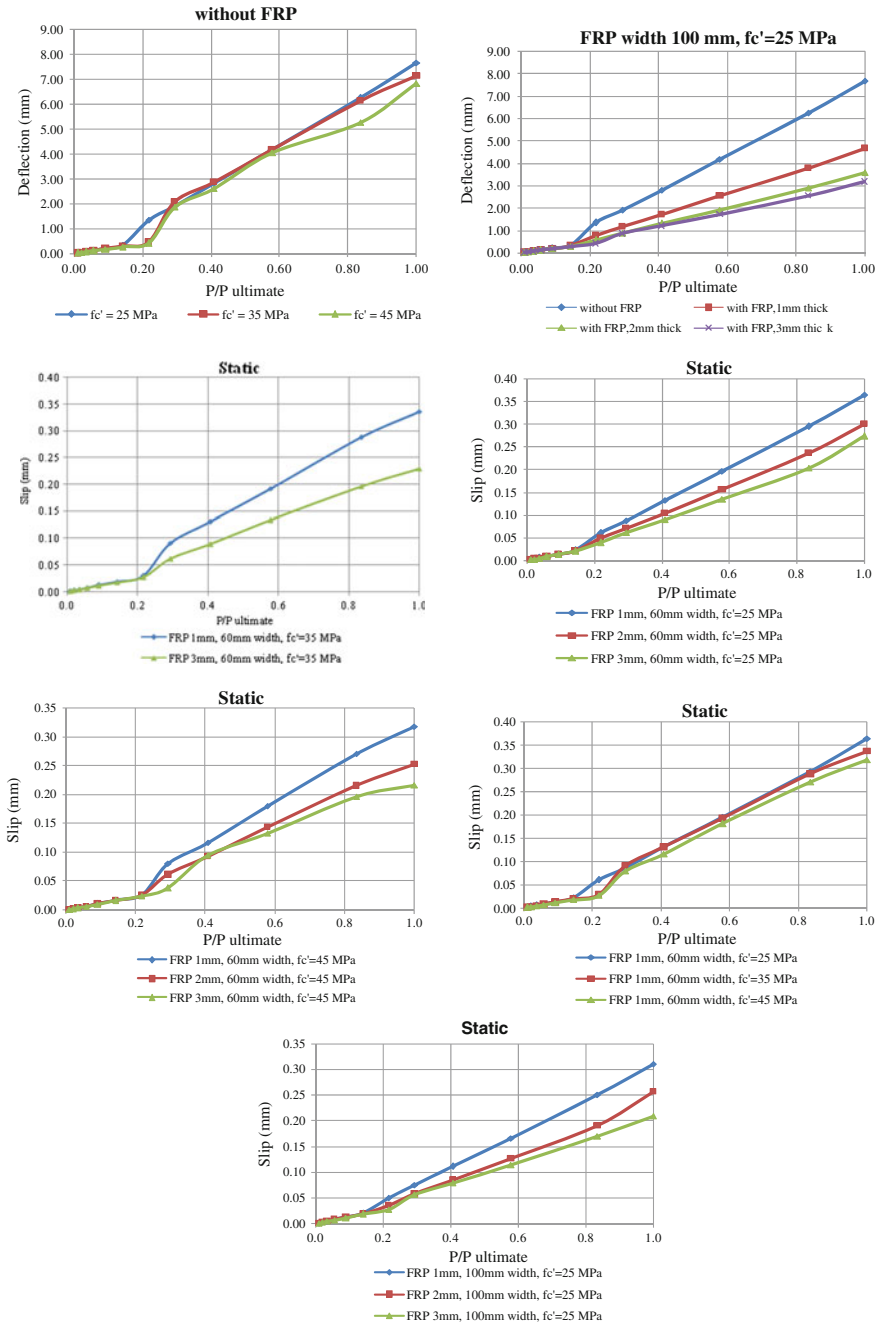
Fig. 5 Slip-load relationships under static load

material follows Hooke's Law. Hence for this region $\sigma = E/\varepsilon$ where this time E refers to the Young's Modulus for compression. In this region, the material deforms elastically and returns to its original length when the stress is removed. This linear region terminates at what is known as the yield point. Above this point the material behaves plastically and will not return to its original length once the load is removed, as shown in Fig. 2. The increase in strength is higher for low strength concrete.

5.1 Static Loading

Figure 5 shows the variation of load-deflection and load-slip of a composite beam under static loading. If the compressive strength of concrete higher, the deflection is lower as compared to that for lower grade of concrete. Maximum deflection for M45 is 6.8 mm, M35 is 6.84 mm and M25 is 7.67 mm, i.e. the deflection reduced by 12 % for M45 and 11 % for M35 as compared with M25, because of the higher compressive strength and increase in the modulus of elasticity or rupture. According to ACI318, BS8110, the stiffness of an un-cracked member increases in proportion to the elastic modulus which varies in proportion to the square root of the cylinder/cube strength. In presence of FRP/plates sheet the deflection is reduced. For concrete of grade M25, deflection observed was 7.67 mm and upon using FRP with 100 mm width the deflections experienced were 4.68, 3.59, and 3.17 mm for 1, 2 and 3 mm thickness of FRP, respectively. Deflection decreased 38, 53, and 58 %, respectively if compared with RC beam without FRP. The effect of FRP/plate sheet thickness on slip values are also shown in Fig. 5. In case of M35, with FRP width 60 mm, slip for 1 mm thick is 0.336 mm and for 3 mm thick is 0.229 mm, reduced about 31 %, owing to stiffer response from FRP. In case of 1 mm thickness by 60 mm width of FRP/plate sheet with M25, M35, and M45 grade of concrete the maximum slip is 0.364, 0.336, and 0.319 mm, respectively. The slip reduced by 8 and 13 % for M35 and M45 as compared with M25, reduced stresses induced at interface so that the strain become less thereby reducing the slippage.

5.2 Dynamic Loading

Figure 6 shows the variation of load-deflection and load-slip of a composite beam under dynamic loading, harmonic in nature. The important investigation made in dynamic analysis is to determine frequency that makes the deflection and slip maximum. In case of FRP having width 60 mm the slip value is 0.0384 mm at frequency 0.02 Hz; for 100 mm the slip value is 0.0151 mm at frequency 0.1 Hz for same compressive strength M25 and same FRP thickness of 1 mm. The magnitude of frequency to make slip becomes maximum depending on the internal stiffness of
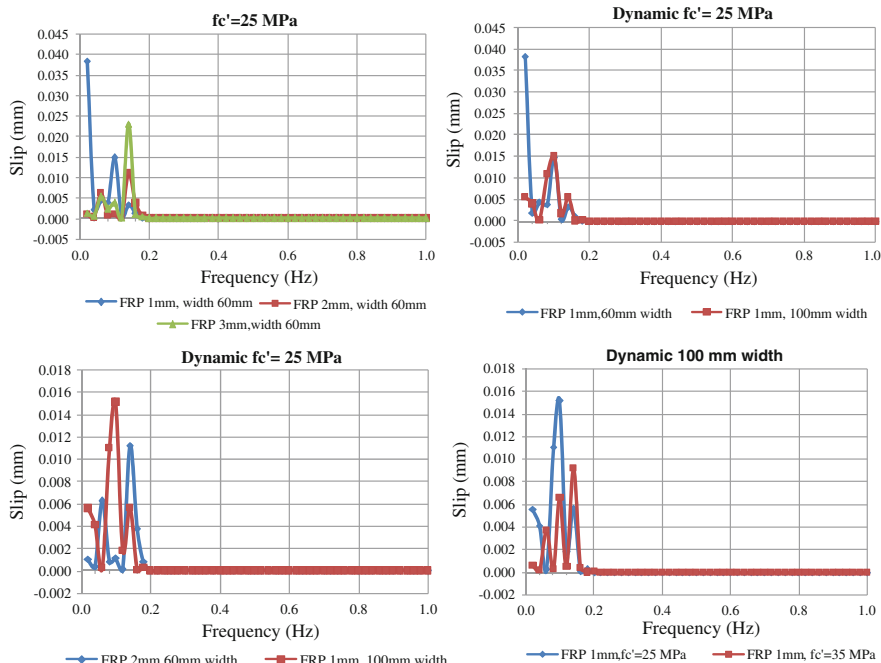
Fig. 6 Slip-load relationships under dynamic load

a body, i.e. geometry of composite beam, modulus of elasticity of materials, and masses. The values of frequency near the value of frequency which make the whole structure to resonate provide maximum deflection and slip. In case of FRP of 60 mm width, with 1, 2, and 3 mm thickness but same grade of concrete M25; the maximum slip values are 0.0384 mm at 0.02 Hz, 0.0112 mm at 0.14 Hz, 0.023 mm at 0.14 Hz, respectively. In case of M25 grade of concrete with 1 mm FRP thickness and 60 mm width leads to 0.02 Hz with slip of 0.0384 mm, however for width of 100 mm, slip of 0.0151 mm at frequency 0.1 Hz occurs.

In dynamic analysis, if the loading increase, the interface between FRP/plate and RC beam experience increased cracks even under moderate or strong dynamic loadings. Under these conditions, the ability of epoxy to dissipate energy depends on its capability to withstand under dynamic loading; therefore, the stiffness and strength of epoxy reduce at all stages owing to crack propagation and formation of cracks in concrete. At present, design codes do not predict the strength of bonding i.e. composite action—partial interaction, under dynamic loading.

The connection between FRP/plate and concrete needs to be properly designed in order to maximize the composite action. Evaluating the connection stiffness is important because the static and dynamic behaviors of the composite structure are strongly influenced by the slip at the FRP/plate-to-beam interface which requires careful consideration in design.

6 Conclusions

From the finite element (FE) based simulations the following major conclusions are arrived at.

1. The deflection of RC beam decreased as the FRP was used and also decreased when the number of layers or FRP width increased because presence of the FRP plate enhances the tensile strength of RC beam under static or dynamic loading.
2. The slip decreased when the compressive strength of concrete increased or the layer thickness of the FRP or width under static or dynamic loading.

References

1. ACI 440.2R-08, Guide for the design and construction of externally bonded FRP systems for strengthening concrete structures. American Concrete Institute, Farmington Hills, Michigan, USA
2. Hollaway LC (2010) A review of the present and future utilization of FRP composites in the civil infrastructure with reference to their important in-service properties. Constr Build Mater 24:2419–2445
3. Seleem MH, Sharaky IA, Sallam HEM (2010) Flexural behavior of steel beams strengthened by carbon fiber reinforced polymer plates—three dimensional finite element simulation. Mater Des 31:1317–1324
4. Pellegrin C, Modena C (2008) Bond-slip relationships between FRP sheets and concrete. Fourth international conference on FRP composites in civil engineering (CICE2008), Zurich, Switzerland
5. Zhao M, Farhad A (2004) Bond properties of FRP fabrics and concrete joints. 13th world conference on earthquake engineering, Vancouver, B.C., Canada, Paper No 35
6. Wang J (2006) De-bonding of FRP-plated reinforced concrete beam, a bond-slip analysis-I theoretical formulation. Int J Solids Struct 43:6649–6664
7. ANSYS User's Manual, vol 4: theory. Swanson Analysis Systems Inc
8. ACI-318-11, American Concrete Institute, building code requirements for structural concrete and commentary. American Concrete Institute, Farmington Hills, Michigan, USA

Assessment of Debonding Load for RC Beam Strengthened with Pre-designed CFRP Strip Mechanism

Mitali R. Patel, Tejendra G. Tank, S.A. Vasanwala and C.D. Modhera

Abstract With passage of time, strengthening techniques have become more and more refined. Carbon fiber reinforced polymer (CFRP) and steel plates have been adopted since years as few of the popular materials for strengthening of structural elements such as beams and columns. A series of studies have been carried out in the past for shear strengthening of reinforced concrete beams using various mechanisms of strengthening, and response of such strengthened structural elements is found to be quite satisfactory as compared to non-strengthened structural elements. De-lamination/debonding is a major issue faced while strengthening any structural member using fiber reinforced polymer (FRP). Debonding occurs at regions of high stress concentration, which are often associated with material discontinuities and with presence of cracks. However, this can be avoided, if strengthening is done after proper understanding and analysis of the problem. Adaptation of proper guideline to overcome debonding plays a vital role in the resolution of debonding problem, however these guidelines are also limited. The increasing use of FRP in structural strengthening although has revoked a need for framing of guidelines in this segment, but eventually fails to address the debonding aspect to a larger extent. Also, the debonding load after strengthening remains unknown. The magnitude of this load, if known, can contribute to a much greater extent as long as FRP strengthening is concerned. This paper aims at highlighting the method for strengthening of reinforced concrete beam in flexure and shear using CFRP strip mechanism and thereby overcoming CFRP debonding problem in order to achieve enhanced performance in flexure and shear along with prevention of strengthened member failure against debonding.

Keywords Strengthening · RC beams · CFRP · Shear · Flexure · De-lamination

M.R. Patel (✉) · T.G. Tank · S.A. Vasanwala · C.D. Modhera
Applied Mechanics Department, Sardar Vallabhbhai National Institute of Technology (SVNIT), Surat, Gujarat, India

Notations

f_{ctm}	Mean value of concrete tensile strength
Γ_{Fd}	Design value of specific fracture energy
I_{cr}	Moment of inertia of cracked section transformed to concrete
L_e	Active bond length of FRP laminate
M_{DL}	Moment due to dead load
M_n	Nominal flexural strength
M_{nf}	Contribution of FRP reinforcement to nominal flexural strength
M_{ns}	Contribution of steel reinforcement to nominal flexural strength
S_f	Spacing between FRP strips
V_f	Nominal shear strength provided by FRP stirrups
$f_{f,s}$	Stress level in FRP caused by a moment within elastic range of member
f_{fdd}	Design debonding strength of FRP
f_{fe}	Effective stress in FRP
$f_{s,s}$	Stress level in steel reinforcement at service loads
f_s	Stress in steel reinforcement
k_G	Corrective factor
k_b	Geometric corrective factor
k_v	Bond dependent coefficient for shear
α_1	Multiplier on f'_c to determine intensity of an equivalent rectangular stress distribution for concrete
β_1	Ratio of depth of equivalent rectangular stress block to depth of neutral axis
$\gamma_{f,d}$	Partial safety factor for FRP
ε_{bi}	Strain level in concrete substrate at the time of FRP installation
ε_c	Strain level in concrete
ε_{cu}	Ultimate axial strain of unconfined concrete
ε_{fd}	Debonding strain of externally bonded FRP reinforcement
ε_{fe}	Effective strain level in FRP reinforcement attained at failure
ε_s	Strain level in steel reinforcement
ψ_f	FRP strength reduction factor
$\varnothing$	Diameter of reinforcement
A_f, A_{fv}	Area of externally bonded FRP
A_s	Area of steel reinforcement
b	Width of beam
b_f	Width of FRP sheet
c	Distance from extreme compressive fiber to neutral axis
C_E	Environmental reduction factor
d, d_{fv}	Effective depth of beam
d_f	Overall depth of beam
E_c	Modulus of elasticity of concrete
E_f	Modulus of elasticity of FRP
E_s	Modulus of elasticity of steel

f^*_{fu}	Ultimate tensile strength of FRP
f'_c, f_{cm}	Specified compressive strength of concrete
FC	Confidence factor
f_{fu}	Design ultimate tensile strength of FRP
f_y	Specified yield strength of steel reinforcement
L	Length of beam
M_s	Moment due to dead load and live load
M_u	Moment after 50 % increase in live load
n	Number of layers of FRP sheet
P_{db}	Debonding load of CFRP strip
P_{max}	Actual load on CFRP strip
s_{sv}	Permissible tensile stress in shear reinforcement
t_f	Thickness of FRP strip
V	Total shear capacity of beam
V_c	Nominal shear strength provided by concrete with steel flexural reinforcement
$V_{f, required}$	Shear force to be resisted by FRP strip
V_s	Nominal shear strength provided by steel stirrups
V_u	Maximum shear force on strengthened beam
ε^*_{fu}	Rapture strain of FRP
ε_{fu}	Design rupture strain of FRP reinforcement
k	Ratio of neutral axis to reinforcement depth measure from extreme compressive fiber
m	Modular ratio
α	Angle between FRP strip and longitudinal axis of beam measured anti-clockwise
ϕ	Strength reduction factor

1 Introduction

It has been observed from the past literature that, there are a number of mechanisms available for strengthening of reinforced concrete (RC) members. Sprayed concrete method is used for heavy structures where increase in structural dimensions is not a major issue. However, it is not a cost effective option; also, time needed for strengthening is more in comparison to other techniques. Opting for steel tendons was also prevalent in past. This was less cumbersome than the sprayed concrete method but it involved the risk of damage caused to the structure due to bending reinforcement being cut off during drilling of holes through the member. Use of externally bonded steel plates with the help of epoxy was also an option available for strengthening. However, this too is not a cost effective alternative. A need is

therefore felt here, for a safe and cost effective recourse for strengthening of RC members. Hence, we switch on to the use of externally bonded carbon fiber reinforced polymer (CFRP) sheets with a view to strengthen the member against shear and flexure. The use of CFRP involves various bonding mechanisms for strengthening such as wrapping, side bonding, U-jacketing and Near Surface Mounting (NSM) techniques. The work carried out in this manuscript explains an effective use of CFRP sheet at soffit of beam to strengthen it against flexure. Side bonding technique to strengthen in shear the same beam using externally bonded CFRP strips is also adopted. In addition, eventually, the beam is checked for a load, which causes the debonding of CFRP sheet/strips in order to achieve safety against debonding failure. The work is divided into three parts, which eventually deal with the strengthening of a pre-designed beam, subjected to revised loading, and providing load at which the strengthened beam will undergo failure.

2 Research Significance

Research carried out in the past, and available in the literature has shown that CFRP is extensively used in strengthening of structural components. However, debonding of CFRP sheet is quite significant in such structural elements. Supposing, if a beam is designed for a particular load, and if after a couple of years it has to take revised and increased load due to revamped occupancy conditions or any such reason, dismantling and re-casting the beam is not a feasible alternative. Hence, retrofitting is a solution, which can be successfully adopted. The debonding of CFRP is mainly due to failure of bond between concrete and CFRP which results in underutilization of material strength. However, CFRP can be utilized more effectively if a well-defined approach is chosen to analyze the problem and carry out strengthening operation. In the current work, efforts have been made to study, highlight and present the improvement in structural response of beams strengthened to take revised loads and moments with the use of externally bonded CFRP strips.

3 Problem Formulation

Work carried out here involves consideration of an arbitrary problem, comprising of a pre-designed simply supported beam having span of 3 m and subjected to two point loads of 60 kN each at a distance of span/3 from supports. The cross-section of the beam is supported and loaded as shown in Figs. 1 and 2. The beam considered is now subjected to a 50 % increase in its live load carrying requirements. The beam is hence inadequate to carry the increased live load. To begin with the solution, the detailed dimensional considerations of the beam are as provided in

Fig. 1 Beam considered
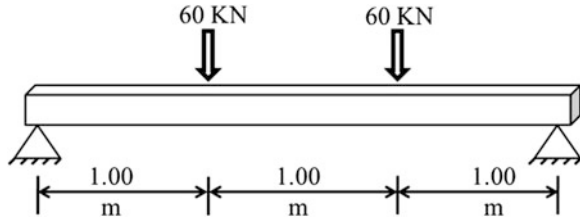
Fig. 2 Section details of original beam
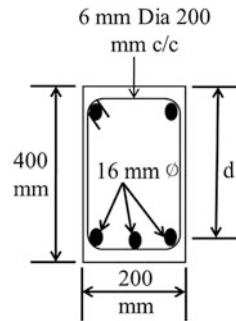
Table 1 Sectional properties of beam

Length of beam (L)	3.00 m
Width of beam (b)	200 mm
Overall depth (d_f)	400 mm
Effective depth (d)	369 mm
Clear cover	25 mm
Tensile reinforcement	3–Ø16 mm
Shear reinforcement (2-legged)	Ø6 mm
Existing and anticipated moments	
Moment carrying capacity of the designed beam (DL + LL) (M_s)	62.25 kN m
Anticipated moment carrying capacity (after 50 % increase in live load) (M_u)	92.25 kN m

Table 1. All necessary material properties and other required data are as mentioned in Table 2.

In order to increase the revised moment carrying capacity, externally bonded CFRP sheet is attached at the soffit of the beam for flexural strengthening. In addition, side bonded technique is adopted to strengthen the beam in shear. Since there are no existing Indian Standard provisions in particular for the strengthening of RC structures using externally bonded FRP systems, provisions from ACI-440.2R-08 are adopted.

Table 2 Material properties

Specified compressive strength of concrete (f'_c)	20 MPa
Modulus of elasticity of steel (E_s)	2×10^5 MPa
Specified yield strength of steel reinforcement (f_y)	415 MPa
Permissible tensile stress in shear reinforcement (σ_{sv})	230 MPa
Ultimate axial strain of unconfined concrete (ε_{cu}) [1]	0.003
Manufacturer's reported CFRP properties [1]	
Modulus of elasticity of CFRP (E_f)	37,000 MPa
Ultimate tensile strength of CFRP (f^*_{fu})	621 MPa
Rapture strain of CFRP (ε^*_{fu})	0.015
Assumed thickness of CFRP strip (t_f)	2.5 mm

4 Flexural Strengthening of Beam [1]

Assuming initially 200 mm wide and 3 m long CFRP ply bonded to the soffit of the beam using the wet lay-up technique. The strengthening process is as per the following sequence.

Step 1 **FRP system design material properties**

$$f_{fu} = \left(C_E \cdot f^*_{fu}\right) = 0.95 \times 621$$
$$= 590 \text{ MPa}$$

$$\varepsilon_{fu} = \left(C_E \cdot \varepsilon^*_{fu}\right) = 0.95 \times 0.015$$
$$= 0.0142$$

Step 2 **Preliminary calculations**

(a) Concrete properties:

$$E_c = 4,700 \sqrt{f'_c} = 4,700 \times \sqrt{20}$$
$$= 21,019 \text{ MPa}$$

(b) Area of reinforcing steel:

$$A_s = 3 \times (\pi/4) \times 16^2 = 603 \text{ mm}^2$$

(c) Area of externally bonded CFRP strip:

$$A_f = n \cdot t_f \cdot b_f = 1 \times 2.5 \times 200$$
$$= 500 \text{ mm}^2$$

Step 3 **Existing state of strain of soffit**

$$\varepsilon_{bi} = \frac{M_{DL}(d_f - kd)}{I_{cr}E_c}$$

where,

$M_{DL} = 2.25\,\text{kN}\,\text{m}$

$E_c = 21,019\,\text{MPa}$

$k = \dfrac{\text{Depth of neutral axis}}{\text{Depth of reinforcement}} = 0.4097$

$$I_{cr} = \frac{bx^3}{3} + mA_{st}(d - x)^2$$

where, value of 'x' can be obtained from,

$\dfrac{bx^2}{2} = mA_{st}(d - x)$

$I_{cr} = 470.93 \times 10^6 \,\text{mm}^4$

$\varepsilon_{bi} = 5.66 \times 10^{-5}$

Step 4 **Design strain of CFRP system**

$$\varepsilon_{fd} = 0.41\sqrt{\frac{f'c}{nE_f t_f}} \leq 0.9\varepsilon_{fu}$$

$$\varepsilon_{fd} = 0.00603 < 0.0128$$

Step 5 **Estimation of the depth of neutral axis**

An initial estimate of the depth of neutral axis 'c' is 0.2 d, however, here the value of 'c' is taken as 0.339 d after a number of trials and iterations. This value of 'c' assumed here, must match with the value of 'c' obtained finally in Step 9.

Here taking,

$c = 0.339\,d = 125.10$ mm

Step 6 **Effective level of strain in CFRP strip**

$$\varepsilon_{fe} = \varepsilon_{cu}\left(\frac{d_f - c}{c}\right) - \varepsilon_{bi} \leq \varepsilon_{fd}$$

$$\varepsilon_{fe} = 0.00654 > 0.00603$$

hence, $\varepsilon_{fe} = \varepsilon_{fd} = 0.00603$

Since, section failure is controlled by CFRP, concrete strain at failure ε_c may be less than 0.003 and is calculated as,

$$\varepsilon_c = \left(\varepsilon_{fe} + \varepsilon_{bi}\right)\left(\frac{c}{d_f - c}\right)$$
$$\varepsilon_c = 0.002769 < 0.003$$

Step 7 **Strain in existing reinforcing steel**

$$\varepsilon_s = \left(\varepsilon_{fe} + \varepsilon_{bi}\right)\left(\frac{d - c}{d_f - c}\right)$$
$$\varepsilon_s = 0.0054$$

Step 8 **Stress level in reinforcing steel and CFRP**

$$f_s = E_s \varepsilon_s \leq f_y$$
$$f_s = 1{,}080\,\text{MPa} > 415\,\text{MPa}$$

hence, adopt $f_s = 415\,\text{MPa}$

$$f_{fe} = E_f \varepsilon_{fe}$$
$$f_{fe} = 223.1\,\text{MPa}$$

Step 9 **Internal force resultants and check for equilibrium (as mentioned in Step 5)**

Force equilibrium is verified by checking the initial estimate of 'c' with following equation.

$$c = \frac{A_s f_s + A_f f_{fe}}{\alpha_1 f'_c \beta_1 b}$$

where,
  b = 200 mm (Fig. 2)
  α_1 [1] and β_1 [2] are stress block factors.
  here, values adopted are $\alpha_1 = \beta_1 = 0.85$
  $c = 125.18\,\text{mm}$

Step 10 **Adjustment of value of 'c' until force equilibrium is satisfied**

Steps 6–9 were repeated several times with values of 'c' ranging from 0.2 to 0.4 until force equilibrium was achieved. The value of 'c' considered was 0.339

d which yielded a value of 125.10 mm, and which matches with the value of $c = 125.18$ mm obtained in Step 9.

Step 11 Flexural strength components

Contribution of steel in flexure can be given by:

$$M_{ns} = A_s f_s \left(d - \frac{\beta_1 c}{2} \right)$$

$$M_{ns} = 79.1 \text{ kN m}$$

Contribution of CFRP in flexure can be given by:

$$M_{nf} = A_f f_{fe} \left(d_f - \frac{\beta_1 c}{2} \right)$$

$$M_{nf} = 38.7 \text{ kN m}$$

Step 12 Design flexural strength of the section

$$M_n = A_s f_s \left(d - \frac{\beta_1 c}{2} \right) + \psi_f A_f f_{fe} \left(d_f - \frac{\beta_1 c}{2} \right)$$

where, $\psi_f = 0.85$ [1]
  $M_n = 112 \text{ kN m}$
  Now,
  $\phi M_n \geq M_u$
where, $\phi = 0.9$ [1]
  $\phi M_n = 101 \text{ kN m} > 92.25$
  The strengthened section is now capable to sustain the revised moment.

Step 13 Check service stresses in reinforcing steel and CFRP

Checking the stress level in the reinforcing steel by following equation must be verified so that it is less than the recommended limit [1].

$$f_{s,s} = \frac{\left[M_s + \varepsilon_{bi} A_f E_f \left(d_f - \frac{kd}{3} \right) \right] (d - kd) E_s}{A_s E_s \left(d - \frac{kd}{3} \right)(d - kd) + A_f E_f \left(d_f - \frac{kd}{3} \right)(d_f - kd)}$$

$f_{s,s} \leq 0.80 f_y$
$f_{s,s} = 273.6 \text{ MPa} \leq 332 \text{ MPa}$
The stress level in reinforcing steel and CFRP is within recommended limit.

Step 14 Creep rapture limit in CFRP at service

Calculating the stress level in CFRP using equation below and verifying that it is less than creep rupture stress limit.

$$f_{f,s} = f_{s,s} \left(\frac{E_f}{E_s} \right) \left(\frac{d_f - kd}{d - kd} \right) - \varepsilon_{bi} E_f$$

$f_{f,s} \leq 0.55 f_{fu}$

$f_{f,s} = 55.72\,\text{MPa} < 324.5\,\text{MPa}$

The stress level in CFRP is within the recommended sustained plus cyclic stress limit.

5 Shear Strengthening of Beam [1]

Since, the live load carrying capacity of the beam has been increased by 50 %, there must be a corresponding increase in shear to be resisted by the beam. Hence, shear strengthening has been carried out as per ACI 440.2R-08.

Step 15   **Shear capacity of the existing non-strengthened beam**

Concrete shear capacity of the existing beam (V_c):

$$V_c = 42.51\,\text{kN}$$

Stirrups shear capacity of the existing beam (V_s):

$$V_s = 24\,\text{kN}$$

Total shear capacity of the existing beam (V):

$$V = V_c + V_s$$
$$= 66.51\,\text{kN} \ > 63\,\text{kN}$$

Maximum shear force on strengthened beam:

$$V_u = M_n/\text{shear span}$$
$$= 101/1$$
$$= 101\,\text{kN}$$

$$V_{f,\text{required}} = V_u - V = 101 - 66.51$$
$$= 34.5\ \text{kN}$$

Step 16   **Effective strain level in CFRP shear strips** (ε_{fe})

$\varepsilon_{fe} = k_v \varepsilon_{fu} \leq 0.004$

(For 'ε_{fu}' refer Step 1 in flexural strengthening)
where,

$$k_v = \frac{k_1 k_2 L_e}{11{,}900\varepsilon_{fu}} \le 0.75$$

where,

$$k_1 = \left(\frac{f'_c}{27}\right)^{2/3} = 0.819$$
$$L_e = \frac{23{,}300}{\left(n t_f E_f\right)^{0.58}} = 30.69 \text{ mm}$$
$$k_2 = \left(\frac{d_{fv} - 2L_e}{d_{fv}}\right) = 0.834$$
$$k_v = 0.124 \le 0.75$$
$$\varepsilon_{fe} = 0.00176 \le 0.004$$

Step 17 Contribution of CFRP strips to shear strength

Area of CFRP $\left(A_{fv}\right)$:

$$A_{fv} = 2n\, t_f b_f$$

where, b_f is 150 mm assumed width, and n is 1.

$$A_{fv} = 750 \ \text{mm}^2$$

Effective stress in CFRP (f_{fe}):

$$f_{fe} = \varepsilon_{fe}\, E_f$$
$$f_{fe} = 65.12 \,\text{MPa}$$

Shear contribution of CFRP $\left(V_f\right)$:

$$V_f = \frac{A_{fv} f_{fe} (\sin \alpha + \cos \alpha) d_{fv}}{S_f}$$

where,
$\alpha = 90°$ (90° orientation of CFRP)
$S_f = 170$ mm (Assumed spacing)
$V_f = 106\,\text{kN}$
Note: Change in orientation renders change in shear contribution of CFRP (Fig. 3).

Step 18 Shear strength of the section

Design shear strength (ϕV_n)

$$\phi V_n = \phi(V_c + V_s + \psi_f V_f)$$

Fig. 3 CFRP orientation versus shear contributions
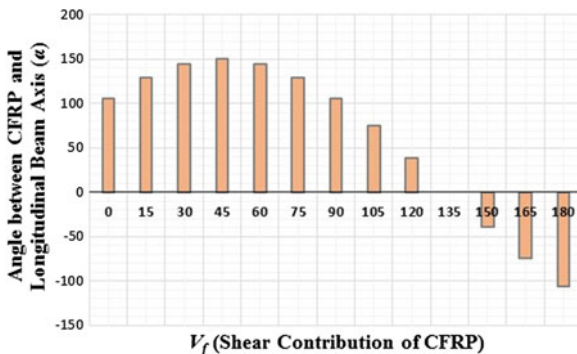
where [2],

$$\psi_f = 0.85 \text{ and } \phi = 0.75$$
$$\phi V_n = 118\,\text{kN} > V_u$$

hence, strengthened section is capable of sustaining the required shear strength (V_u—in Step 1 above).

6 Debonding Load [3]

To overcome the problem of CFRP debonding, mainly two methodologies are practiced:

1. Adopt an appropriate retrofitting mechanism.
2. Find a safe debonding load after which debonding will occur.

The former is mostly based on visual inspection and engineering judgment, for which criteria on paper cannot be laid down. For the later one, since there are no Indian or ACI code provisions for finding safe debonding load, we adopt CNR-DT 200 R1/2013 guidelines for the same. Calculations for debonding load are as per the given sequence below.

Step 1 **Design debonding strength of CFRP strip**

The ultimate design strength (f_{fdd}) is the maximum allowed stress before debonding of the ends and can be calculates as,

$$f_{fdd} = \frac{1}{\gamma_{f,d}} \sqrt{\frac{2E_f \Gamma_{Fd}}{t_f}}$$

where,

$$\gamma_{f,d} = 1.2$$

$$\Gamma_{Fd} = \frac{k_G k_b}{FC} \sqrt{f_{cm} f_{ctm}}$$

where [4],

$$k_G = 0.037$$

$$FC = 1.35$$

$$f_{cm} = 20\text{MPa}$$

$$f_{ctm} = 0.7\sqrt{f_{cm}} = 3.13\,\text{MPa}$$

$$k_b = \sqrt{\frac{2 - b_f/b}{1 + b_f/b}} \geq 1$$

here, if $b_f/b \geq 0.25$, above equation can be adopted. However, if $b_f/b < 0.25$, $k_b = 1.18$.

$$k_b = 0.707 < 1$$

hence taking,

$$k_b = 1$$

$$\Gamma_{Fd} = 0.2168\,\text{MPa}$$

$$f_{fdd} = 66.75\,\text{MPa}$$

Step 2 Debonding load of CFRP strip (P_{db})

$$P_{db} = f_{fdd} \times A_f$$
$$= 33.38\,\text{kN}$$

Step 3 Actual load on CFRP strip (P_{max})

$$P_{max} = f_{f,s} \times A_f$$

($f_{f,s}$ from Step 14 flexural strengthening)

$$P_{max} = 55.72 \times 500$$
$$= 27.86\,\text{kN} < \text{Debonding Load } (P_{db})$$

It is evident from Step 2 and Step 3 above, that the actual load encountered by the CFRP strip is less than the debonding load, which causes the strip to peel off.

7 Observations

From the work carried out here, the following observations are made.

1. The flexural capacity of beam after strengthening the soffit with a CFRP sheet (2.5 × 200 mm), enhances the flexural performance of the beam to a considerable extent.
2. The shear capacity is seen to be increasing by provision of the CFRP strips in the shear span. Although, here 90° orientation is provided for shear strengthening, other orientations can also be tried.

3. The CFRP debonding load found out for the considered formulation is more than the actual shear on the CFRP strips. Hence, the beam shall not undergo any debonding failure before attainment of debonding load of 33.38 kN.

8 Conclusions

1. The strengthening of reinforced concrete (RC) beams using carbon fiber reinforced polymer (CFRP) sheet in flexure, enhances the moment carrying capacity of the beam. The percentage increase in the moment carrying capacity of beam depends on the width and thickness of the CFRP sheet used, also on the number of layers of CFRP strips provided for strengthening.
2. The shear capacity of the strengthened beam by providing 90° orientation shows 16–17 % increase in shear resistance. Other orientations also lead to the increase in shear capacity. The 45° orientation yields the best performance in shear strengthening (Fig. 3).
3. If economy criterion is focused on to, a CFRP strip cross-sectional area rendering a particular shear capacity with 45° orientation, yields 42–43 % more shear capacity achieved by same strip having same cross-sectional area but at 90° orientation (Fig. 3).
4. The CFRP debonding load calculated leads to a conclusion that, the beam shall not undergo any CFRP debonding till the actual shear does not exceed the debonding load.
5. For the considered beam, the debonding load comes out to be approximately 18–20 % more than the actual load on the beam.
6. The beam is strengthened with the CFRP in shear as well as in flexure and checked against debonding of the CFRP. However, for shear strengthening, the strips if provided in the shear span region only will satisfy economy criteria.
7. For flexural strengthening, one has to compulsorily opt for providing the CFRP at the beam soffit, and there are no further mechanisms that can be adopted for flexural strengthening. However, for shear strengthening, provision of side bonded CFRP mechanism or U-wrap technique can be adopted.
8. Although the beam is strengthened in flexure, it will also yield some shear strength to the beam, hence it is always advisable to check the beam in shear, if in case any shear strengthening is required.

References

1. ACI 440 2R (2008) Guide for the design and construction of externally bonded FRP system for strengthening concrete structures. American Concrete Institute (ACI), Committee, 2008, Farmington Hills, Michigan, USA

2. ACI 318 (2005) Building code requirements for structural concrete (ACI 318-05) and commentary (318R-05). American Concrete Institute (ACI), Farmington Hills, Michigan, USA
3. CNR-DT 200 R1 (2013) Guide for the design and construction of externally bonded FRP systems for strengthening existing structures. National Research Council (NRC), May 2014
4. Faella C, Martinelli E, Nigro E, Billota A (2012) The influence of the load condition on the intermediate debonding failure of EBR-FRP strengthened. In: Proceedings of composites in civil engineering (CICE), Rome, Italy

Bibliography

5. Khalifa A, Gold WJ, Nanni A, MI AA (1998) Contribution of externally bonded FRP to shear capacity of RC flexural members. J Compos Constr 2(4)195–202
6. Billota A, Ludovico DM, Nigro E (2009) FRP debonding on concrete member. In: Fiber reinforced plastics for reinforced concrete structures (FRPRCS-9), Sydney, Australia
7. Jummat MZ, Rahman MA, Alam MA, Rahman MM (2011) Premature failure in plate bonded strengthened RC beam with an emphasis on premature shear. Int J Phys Sci 6(2):156–168

Performance Assessment of RC Beams with CFRP and GFRP Sheets

Chennakesavula Venkateswarlu and Chidambarathanu Natarajan

Abstract Concrete is one of the most common building materials and is used for constructing buildings, bridges and other heavy structures. Strengthening structures via external bonding of advanced fibre reinforced polymer (FRP) composites is becoming very popular worldwide during the past few decades, because it provides a more economical and technically superior alternative to the traditional techniques in many situations, as it offers high strength, low weight, corrosion resistance, high fatigue resistance, easy and rapid installation and minimal change in structural geometry. It is important to understand the behaviour of a strengthened structure well and realize what parameters affect the failure mode and load-bearing capacity. The aim of this study is to investigate and improve the understanding of the behaviour of reinforced concrete (RC) beams strengthened with fibre composite. In the present study, a numerical investigation is carried out to study the behaviour of RC beams under static three-point loading. Concrete beam specimens with dimensions of 130 mm width, 200 mm height, and 2,500 mm length were modelled. The beams were strengthened with externally bonded glass fibre reinforced polymer (GFRP) sheets and carbon fibre reinforced polymer (CFRP) sheets. The present study examines the responses of the RC beams with GFRP and CFRP sheets by increasing number of layers using finite element simulation in ABAQUS, in terms of failure modes, enhancement of load carrying capacity, load-deflection behaviour and flexural behaviour.

Keywords Flexural strengthening · GFRP · CFRP · Load-deflection behaviour

Ch. Venkateswarlu (✉) · C. Natarajan
Department of Civil Engineering, National Institute of Technology (NIT), Tiruchirappalli,
Tiruchirappalli, India

1 Introduction

The traditional material used in the strengthening of concrete structures is steel. Because of the drawbacks of steel, such as low corrosion resistance and of handling problems involving excessive size and weight, there is a need for the engineering community to look for alternatives. Due to lightweight, high strength and good fatigue and corrosion properties, fibre-reinforced plastics (FRP) have been intensively used in the repair and strengthening. Though the study of using FRP to strengthen reinforced concrete (RC) structures started around the 1990s, the technology is currently widely used. Research and design guidelines confirm that externally bonded fibre reinforced polymers (FRPs) are efficiently increasing the performance of reinforced concrete. Observations made on beams strengthened with FRP have revealed a loss of ductility due to the linear elasticity of FRP material up to tensile rupture. Although glass fibre reinforced polymers (GFRPs) have a lower elastic modulus and tensile strength than carbon fibres, its high deformability, good impact and break resistance properties turn them into a superior material for strengthening, alone as well as in a combination with carbon fibres. When two different FRP sheets, are used together to strengthen concrete members, high ductility of glass fibre reinforced plastic (GFRP) and high strength of carbon fibre reinforced plastic (CFRP) can compensate each other, and demolish process of concrete members from micro to macro can be stayed. It will improve fracture strains of the hybrid fibre composites greatly. When CFRP and GFRP are combined to strengthen concrete beams, by changing the ratio of volume of CFRP and GFRP the modulus of the strengthening material can be changed within a specific range and consequently the ductility of the strengthened beams can be improved. At the same time, the tensile strength of GFRP in hybrid strengthening is more distributed than is achieved with solely CFRP or GFRP strengthening.

1.1 Flexural Strengthening of Beams

For flexural strengthening, there are many methods such as: section enlargement, steel plate bonding, external post-tensioning method, near-surface mounted (NSM) system and externally bonded (EB) system. While many methods of strengthening structures are available, strengthening structures via external bonding of advanced fibre-reinforced polymer composite (FRP) has become very popular worldwide. During the past decade, their application in this field has been rising due to the well-known advantages of FRP composites over other materials. Consequently, a great quantity of research, both experimental and theoretical, has been conducted on the behaviour of FRP-strengthened reinforced concrete (RC) structures.

1.2 Applications of FRP in Construction

There are three broad divisions into which applications of FRP in civil engineering can be classified: applications for new construction, repair and rehabilitation applications, and architectural applications. The FRPs have been used widely by civil engineers in the design of new construction. Structures such as bridges and columns built completely out of FRP composites have demonstrated exceptional durability and effective resistance to effects of environmental exposure. Pre-stressing tendons, reinforcing bars, grid reinforcement and dowels are all examples of the many diverse applications of FRP in new structures. One of the most common uses for FRP involves the repair and rehabilitation of damaged or dete-riorating structures. Several companies across the world are beginning to wrap damaged bridge piers to prevent collapse and steel-reinforced columns to improve the structural integrity and to prevent buckling of the reinforcement. Architects have also discovered the many applications for which FRP can be used. These include structures such as siding/cladding, roofing, flooring and partitions.

In this investigation, proper constitutive models are introduced to simulate the behaviour of reinforced concrete and FRP. Then the finite element (FE) program ABAQUS is used to perform a failure analysis of rectangular reinforced concrete (RC) beams strengthened by FRP.

2 Material Properties and Constitutive Models

The materials used in the analysis involve steel reinforcing bars, concrete and FRP. Reliable constitutive models applicable to steel reinforcing bars and concrete are available in the ABAQUS material library. Three-dimensional (3D) reinforced concrete elements and layered shell elements are used to simulate the behaviour of CFRP and GFRP strengthened reinforced concrete beams. The 3D solid continuum element (C3D8R) with eight nodes and three degrees of freedom at each node, translations in the nodal x, y, and z directions, is used. CFRP and GFRP composites are modelled with 3D shell elements (S8R) which is an 8-node doubly curved thick shell, conventional stress/displacement shell element. It has six degrees of freedom at each node. A 3D truss element (T3D2) with two nodes and three degrees of freedom at each node, translations in the nodal x, y, and z directions, was used to model discrete steel reinforcement.

The material considered in the analysis is mild steel. The average value of yield stress (σ_y) of the steel is 250 MPa, the Young's modulus (E_s) is 200 GPa and Poisson's ratio (v) is 0.3. The basic properties of concrete specified in IS 456: 2000 are used in this study. A commonly used approach is to relate the multi-dimensional stress and strain conditions to a pair of quantities, namely, the effective stress σ_c and effective strain ε_c, such that results obtained following different loading paths can all be correlated by means of the equivalent uniaxial stress-strain curve. The stress-strain

relationship proposed has been widely adopted as the uniaxial stress-strain curve for concrete used in this study and it has the following form:

$$\sigma_c = \frac{E_c \varepsilon_c}{1 + (R + R_E - 2)\left(\frac{\varepsilon_c}{\varepsilon_o}\right) - (2R - 1)\left(\frac{\varepsilon_c}{\varepsilon_o}\right)^2 + R\left(\frac{\varepsilon_c}{\varepsilon_o}\right)^3}. \tag{1}$$

where,

$$R = \frac{R_E(R_\sigma - 1)}{(R_\varepsilon - 1)^2} - \frac{1}{R_\varepsilon}, R_E = \frac{E_c}{E_o}, E_o = \frac{f_c'}{\varepsilon_o}, R_\sigma = \frac{f_{cm}}{f_{cf}}, R_\varepsilon = \frac{\varepsilon_f}{\varepsilon_o} \tag{2}$$

The typical stress-strain curves for different grades of concrete resulted using Eq. 1 is shown in Fig. 1.

For this study M30 grade concrete is considered for RC beam. The default value of the strain at which the tension stiffening stress reduced to zero is, $\varepsilon^* = 0.003$. The tension stiffening model for reinforced concrete is presented in Fig. 2. In this study, the Poisson's ratio of concrete is assumed to be 0.2.

Fig. 1 Stress-strain curves for different grades of concrete
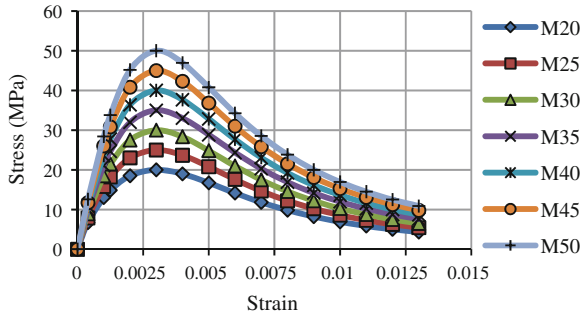
Fig. 2 Tension stiffening model for reinforced concrete
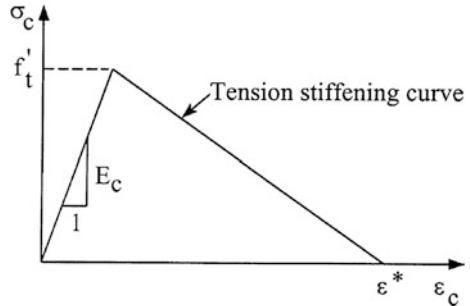
Table 1 Properties of CFRP and GFRP used [1]

Property	CFRP	GFRP
t (thickness of single layer)	1.0 mm	1.0 mm
E_{11}	141.3 GPa	72 GPa
E_{22}	14.5 GPa	9.8 GPa
$G_{12} = G_{13}$	5.86 GPa	4.21 GPa
G_{23}	3.52 GPa	2.48 GPa
$\bar{X}$	2,758 MPa	1,570 MPa
$\bar{X}'$	2,758 MPa	1,570 MPa
$\bar{Y}$	52 MPa	34 MPa
$\bar{Y}'$	206 MPa	148 MPa
S	93 MPa	64 MPa
ν_{12}	0.21	0.18

2.1 Carbon Fiber Reinforced Polymer (CFRP) and Glass Fiber Reinforced Polymer (GFRP)

The properties of CFRP and GFRP [1] used are shown in Table 1.

3 Boundary and Loading Conditions

The reinforced concrete (RC) beams considered for this study are simply supported. For that one end of the beam support is attached with hinge and other end with roller. In hinged support, all the three displacements ($U_1 = U_2 = U_3 = 0$) along x, y, and z directions are arrested. In roller support, two displacements ($U_2 = U_3 = 0$) along y and z directions are arrested and other one ($U_1 \neq 0$) along x direction is free to move along its axis. The modelled beam with both types of boundary conditions is shown in Fig. 3.

In the present study, the beam is analysed under four point loading condition. To simulate the actual point load condition which is applied in laboratory experiments
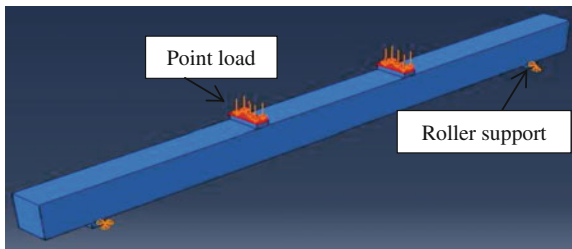
Fig. 3 Beam model with loading and boundary conditions (BCs)

the point load is applied over a small area as pressure of a total constant magnitude equal to magnitude of point load and also a small support block is provided to avoid the stress concentration over few nodes, as shown in Fig. 3.

4 Interactions

Interaction is a tool in ABAQUS which enables the various components of the beam act as a whole assembly. The steel reinforcements are assumed to be embedded fully into the concrete mass, hence "Embedded Region" interaction is given to provide necessary contact between them. The interaction given between reinforcement and concrete is shown in Fig. 4.

The full interaction is assigned to beam surface and CFRP or GFRP by assigning tie constraint as shown in Fig. 5. For creating tie constraint the beam surface should be considered as master surface and the CFRP or GFRP shell surface should be considered as slave surface. The slave surface should have same or finer mesh size than the master surface in ABAQUS so as to avoid numerical error in the analysis. Master surface can penetrate into slave surface (Fig. 6) in the analysis and hence known as master surface.
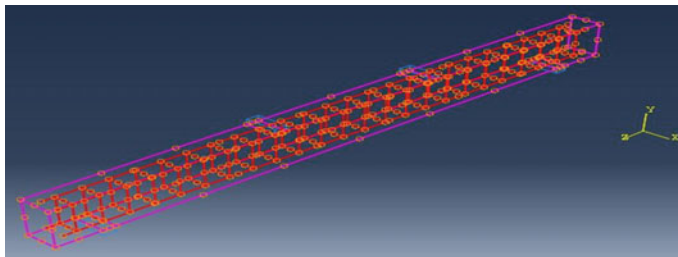
Fig. 4 Interaction between concrete and steel reinforcement
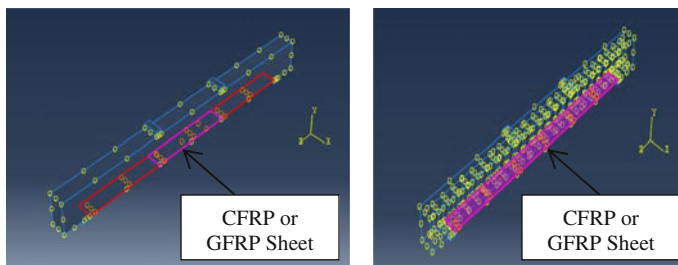
Fig. 5 Interaction between concrete and CFRP or GFRP
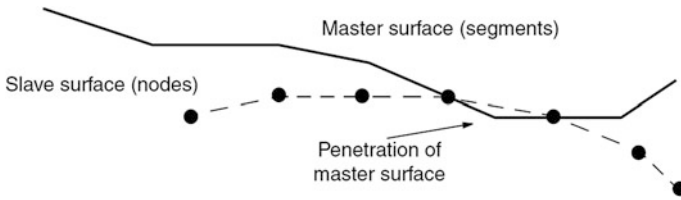
Fig. 6 Master surface and slave surface

5 Results

A total 13 number of combinations are formed with various cases of strengthening with different configurations of CFRP and GFRP strengthening for the RC beam. Results of all these cases and configurations are explained below.

5.1 Beam Designations

CB	Control beam
CF1	RC beam with single layer CFRP sheet under constant moment region (CMR)
CF2	RC beam with two layers CFRP sheet under constant moment region (CMR)
CF3	RC beam with three layers CFRP sheet under constant moment region (CMR)
CF4	RC beam with single layer CFRP sheet up to full length of the beam
CF5	RC beam with two layers CFRP sheet up to full length of the beam
CF6	RC beam with three layers CFRP sheet up to full length of the beam
GF1	RC beam with single layer GFRP sheet under constant moment region (CMR)
GF2	RC beam with two layers GFRP sheet under constant moment region (CMR)
GF3	RC beam with three layers GFRP sheet under constant moment region (CMR)
GF4	RC beam with single layer GFRP sheet up to full length of the beam
GF5	RC beam with two layers GFRP sheet up to full length of the beam
GF6	RC beam with three layers GFRP sheet up to full length of the beam

5.2 Comparison of Control, CFRP, GFRP Beams Results

The load-deflection behaviour of all the beams was recorded. The deflection (middle) of each beam was compared with that of their respective control beam. The deflection behaviour of the beams is as presented in Tables 2, 3, 4, 5, 6 and 7.

Table 2 Load versus deflection for control, single layer CFRP and GFRP sheet beams (middle)

Load (kN)	Deflection (mm)				
	CB	GF1	% of decrease in deflection (CB and GF1)	CF1	% of decrease in deflection (CB and CF1)
5	1.612	1.584	1.74	1.572	2.48
10	3.241	3.183	1.79	3.159	2.53
15	4.979	4.912	1.35	4.857	2.45
20	7.035	6.925	1.56	6.806	3.26
25	9.373	9.205	1.79	8.928	4.75
30	14.292	13.183	7.76	12.839	10.17
35	20.584	18.543	9.92	18.185	11.65
40	27.254	24.418	10.41	22.352	17.99
45		33.846		31.235	

Table 3 Load versus deflection for control, two layer CFRP and GFRP sheet beams (middle)

Load (kN)	Deflection (mm)				
	CB	GF2	% of decrease in deflection (CB and GF2)	CF2	% of decrease in deflection (CB and CF2)
5	1.612	1.608	0.25	1.542	4.34
10	3.241	3.234	0.22	3.097	4.44
15	4.979	4.912	1.35	4.771	4.18
20	7.035	6.994	0.58	6.665	5.26
25	9.373	8.859	5.48	8.732	6.84
30	14.292	12.887	9.83	12.152	14.97
35	20.584	18.215	11.51	17.279	16.06
40	27.254	22.485	17.50	21.235	22.08
45		29.235		27.855	
50		34.758		32.586	

From Fig. 7, it can be observed that the beam with single layer GFRP sheet under CMR is controlling the deflection 0–10.42 %; the beam with single layer CFRP sheet under CMR is controlling the deflection 0–17.99 %. The load carrying capacity of CFRP beam was 12.5 % more than the control beam.

From Fig. 8, it can be observed that the beam with two layers GFRP sheet under CMR is controlling the deflection 0–17.50 %; the beam with two layers CFRP sheet under CMR is controlling the deflection 0–22.08 %. The load carrying capacity of CFRP beam was 25 % more than the control beam.

From Fig. 9, it can be observed that the beam with three layers GFRP sheet under CMR is controlling the deflection 0–25.09 %; the beam with three layers CFRP sheet under CMR is controlling the deflection 0–33.04 %. The load carrying capacity of CFRP beam was 10 % more than the GFRP beam and 37.5 % more than the control beam.

Table 4 Load versus deflection for control, three layer CFRP and GFRP sheet beams (middle)

Load (kN)	Deflection (mm)				
	CB	GF3	% of decrease in deflection (CB and GF3)	CF3	% of decrease in deflection (CB and CF3)
5	1.612	1.586	1.61	1.516	5.96
10	3.241	3.182	1.82	3.045	6.05
15	4.979	4.835	2.89	4.704	5.52
20	7.035	6.884	2.15	6.566	6.67
25	9.373	8.942	4.60	8.589	8.36
30	14.292	12.135	15.09	11.784	17.55
35	20.584	15.236	25.98	13.866	32.64
40	27.254	20.415	25.09	18.248	33.04
45		23.665		21.68	
50		27.348		25.786	
55				32.418	

Table 5 Load versus deflection for control, single layer full CFRP and GFRP sheet beams (middle)

Load (kN)	Deflection (mm)				
	CB	GF4	% of decrease in deflection (CB and GF4)	CF4	% of decrease in deflection (CB and CF4)
5	1.612	1.552	3.72	1.539	4.53
10	3.241	3.116	3.86	3.093	4.57
15	4.979	4.812	3.35	4.727	5.06
20	7.035	6.726	4.39	6.586	6.38
25	9.373	8.926	4.77	8.592	8.33
30	14.292	12.325	13.76	11.932	16.51
35	20.584	17.218	16.35	16.481	19.93
40	27.254	22.886	16.03	21.541	20.96
45		30.689		28.685	
50		34.487		33.965	
55				44.356	

From Fig. 10, it can be observed that the beam with single layer GFRP sheet up to full length of the beam is controlling the deflection 0–16.03 %; the beam with single layer CFRP sheet up to full length of the beam is controlling the deflection 0–20.96 %. The load carrying capacity of CFRP beam was 10 % more than the GFRP beam and 37.5 % more than the control beam.

From Fig. 11, it can be observed that the beam with two layers GFRP sheet up to full length of the beam is controlling the deflection 0–25.84 %; the beam with two layers CFRP sheet up to full length of the beam is controlling the deflection

Table 6 Load and deflection for control, two layer full CFRP and GFRP sheet beams (middle)

Load (kN)	Deflection (mm)				
	CB	GF5	% of decrease in deflection (CB and GF5)	CF5	% of decrease in deflection (CB and CF5)
5	1.612	1.518	5.83	1.492	7.44
10	3.241	3.118	3.80	2.994	7.62
15	4.979	4.834	2.91	4.561	8.40
20	7.035	6.614	5.98	6.301	10.43
25	9.373	8.475	9.58	8.175	12.78
30	14.292	11.102	22.32	10.66	25.41
35	20.584	15.843	23.03	14.349	30.29
40	27.254	20.212	25.84	18.422	32.41
45		26.753		22.753	
50		30.235		29.477	
55		35.418		33.535	
60				36.486	

Table 7 Load versus deflection for control, three layers full CFRP and GFRP sheet beams (middle)

Load (kN)	Deflection (mm)				
	CB	GF6	% of decrease in deflection (CB and GF6)	CF6	% of decrease in deflection (CB and CF6)
5	1.612	1.524	5.46	1.449	10.11
10	3.241	3.016	6.94	2.905	10.37
15	4.979	4.538	8.86	4.417	11.29
20	7.035	6.345	9.81	6.06	13.86
25	9.373	8.215	12.35	7.824	16.53
30	14.292	10.942	23.44	9.82	31.29
35	20.584	13.847	32.73	12.953	37.07
40	27.254	17.659	35.21	16.396	39.84
45		21.774		20.091	
50		25.236		23.92	
55		30.478		29.074	
60		36.332		34.893	
65				41.231	

0–32.41 %. The load carrying capacity of CFRP beam was 9.09 % more than the GFRP beam and 50 % more than the control beam.

From Fig. 12, it can be observed that the beam with three layers GFRP sheet up to full length of the beam is controlling the deflection 0–35.21 %; the beam with three layers CFRP sheet up to full length of the beam is controlling the deflection 0–39.84 %. The load carrying capacity of CFRP beam was 8.33 % more than the GFRP beam and 62.5 % more than the control beam.
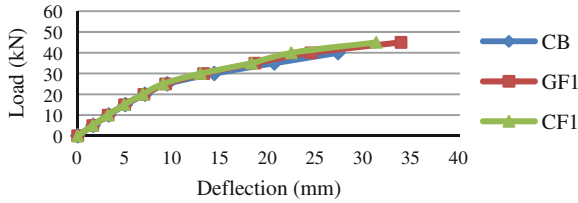
Fig. 7 Load versus deflection for control, single layer CFRP and GFRP sheet beams (*middle*)
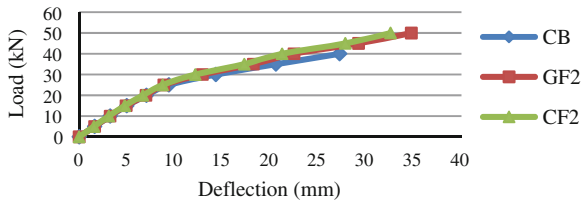
Fig. 8 Load versus deflection for control, two layer CFRP and GFRP sheet beams (*middle*)
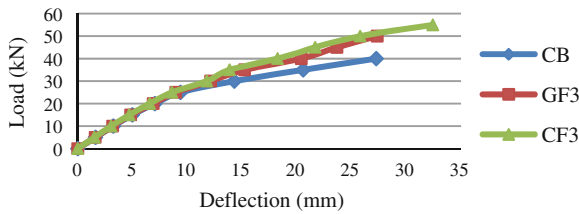
Fig. 9 Load versus deflection for control, three layer CFRP and GFRP sheet beams (*middle*)
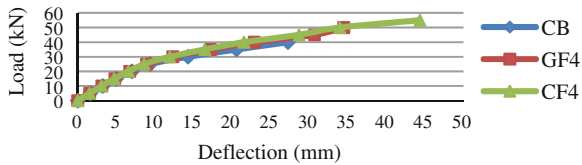
Fig. 10 Load versus deflection for control, single layer full CFRP and GFRP sheet beams (*middle*)
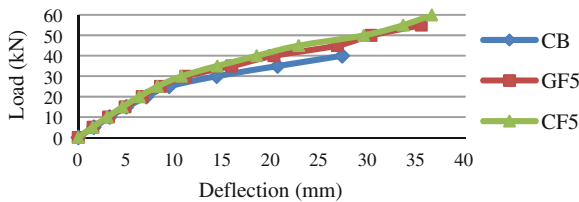
Fig. 11 Load versus deflection for control, two layers full CFRP and GFRP sheet beams (*middle*)
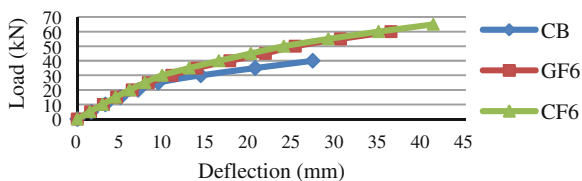
Fig. 12 Load versus deflection for control, three layers full CFRP and GFRP sheet beams (*middle*)

6 Conclusions

Based on the results of finite element analysis (FEA), the following conclusions are derived.

1. In general, it is observed that, the load carrying capacity and the deflection controlling capacity of the RC beam increases with increase of number of layers of GFRP or CFRP sheets.
2. It was observed that the RC beams with CFRP sheets are more effective than that of RC beams with GFRP sheets.
3. The FRP sheets up to full length of the beam are showing improved results than the FRP sheets under constant moment region (CMR).

Comparison of control, CFRP, GFRP beams results; FRP sheet under constant moment region (CMR).

1. It was observed that the beam with single layer GFRP sheet under CMR is controlling the deflection 0–10.42 % and the beam with single layer CFRP sheet under CMR is controlling the deflection 0–17.99 % when compared with the control beam. The load carrying capacity of CFRP and GFRP beam was 12.5 % more than the control beam.
2. Beam with two layers GFRP sheet under CMR is controlling the deflection 0–17.50 % and the beam with two layers CFRP sheet under CMR is controlling the deflection 0–22.08 % when compared with the control beam. The load carrying capacity of CFRP and GFRP beam was 25 % more than the control beam.
3. Beam with three layers GFRP sheet under CMR is controlling the deflection 0–25.09 % and the beam with three layers CFRP sheet under CMR is controlling the deflection 0–33.04 % when compared with the control beam. The load carrying capacity of CFRP beam was 10 % more than the GFRP beam and 37.5 % more than the control beam.

The FRP up to full length of the RC beam.

1. It was observed that the beam with single layer GFRP sheet up to full length of the beam is controlling the deflection 0–16.03 %; the beam with single layer CFRP sheet up to full length of the beam is controlling the deflection 0–20.96 %

when compared with the control beam. The load carrying capacity of CFRP beam was 10 % more than the GFRP beam and 37.5 % more than the control beam.

2. Beam with two layers GFRP sheet up to full length of the beam is controlling the deflection 0–25.84 %; the beam with two layers CFRP sheet up to full length of the beam is controlling the deflection 0–32.41 % when compared with the control beam. The load carrying capacity of CFRP beam was 9.09 % more than the GFRP beam and 50 % more than the control beam.

3. Beam with three layers GFRP sheet up to full length of the beam is controlling the deflection 0–35.21 %; the beam with three layers CFRP sheet up to full length of the beam is controlling the deflection 0–39.84 % when compared with the control beam. The load carrying capacity of CFRP beam was 8.33 % more than the GFRP beam and 62.5 % more than the control beam.

From all the results, finally it was observed that deflection controlling capacity and load carrying capacity of beams with CFRP sheets are more than that of the beams with GFRP sheets.

Reference

1. Hu H-T, Lin F-M, Jan Y-Y (2004) Nonlinear finite element analysis of reinforced concrete beams strengthened by fibber-reinforced plastics. J Compos Struct 63(3):271–281

Bibliography

2. Badawi M, Soudki K (2002) The effect of FRP wraps on the tensile strength of plain and reinforced concrete beams. In: 4th structural specialty conference of the Canadian Society for Civil Engineering, vol 42, 5–8 June 2002
3. Almusallam TH, Al-Salloum YA (2003) Use of glass FRP sheets as external flexure reinforcement in RC beams. Department of Civil Engineering, King Saud University
4. Barros JAO, Fortes AS (2005) Flexural strengthening of concrete beams with CFRP laminates bonded into slits. Cem Concr Compos 27:471–480
5. Esfahania MR, Kianoushb MR, Tajaria AR (2007) Flexural behaviour of reinforced concrete beams strengthened by CFRP sheets. Mater Res 8(3):357–360
6. Abaqus/CAE Version 6.11 (2011) User's manual, Abaqus Inc. Dassault Systèmes, Simulia Corp., Providence, RI, USA
7. Attari N, Amziane S, Chemrouk M (2012) Flexural strengthening of concrete beams using CFRP, GFRP and hybrid FRP sheets. Constr Build Mater 37:746–757
8. Ronagh HR, Eslami A (2013) Flexural retrofitting of RC buildings using GFRP/CFRP—a comparative study. Compos B 46:188–196
9. Sen T, Reddy HNJ (2013) Strengthening of RC beams in flexure using natural jute fibre textile reinforced composite system and its comparative study with CFRP and GFRP strengthening systems. Int J Sustain Built Environ 2:41–55
10. Parikh K, Modhera CD (2012) Application of GFRP on preloaded retrofitted beam for enhancement in flexural strength. Int J Civil Struct Eng 2(4)

11. Pannirselvam N, Nagaradjane V, Chandramouli K (2009) Strength behaviour of fibre reinforced polymer strengthened beam. ARPN J Eng Appl Sci 4(9)
12. Gorji MS (2009) Analysis of FRP strengthened reinforced concrete beams using energy variation method. World Appl Sci J 6(1):105–111
13. Balamuralikrishnan R, Antony Jeyasehar C (2009) Flexural behaviour of RC beams strengthened with carbon fibber reinforced polymer (CFRP). Open Civil Eng J 3:102–109
14. Irwin R, Rahman A (2008) FRP strengthening of concrete structures—design constraints and practical effects on construction detailing. Asian J Civil Eng Build Hous 8(6):677–690
15. Fitzwilliam J (2006) An introduction to FRP composites for construction. Prepared by ISIS Canada
16. IS 456: 2000 Indian standard plain and reinforced concrete—code of practice, 4th revision. Bureau of Indian Standards, New Delhi

Strain Analysis of RC T-beams Strengthened in Shear with Variation of U-wrapped GFRP Sheet and Transverse Steel

K.C. Panda, S.K. Bhattacharyya and S.V. Barai

Abstract The strengthening of concrete structures with fibre reinforced polymer (FRP) composites has existed since last two decade. The most common way to strengthen structures is in bending, shear and retrofitting of columns. FRP offers excellent corrosion resistance to environmental agents as well as the advantages of high stiffness-to-weight ratio and strength-to-weight ratio. This paper presents an experimental investigation on strain analysis of a reinforced concrete (RC) T-beams strengthened in shear with U-wrapped glass fibre reinforced polymer (GFRP) sheet. A total of eighteen (18) full scale simply supported RC T-beams are tested. Nine beams are used as control beam with three different stirrups spacing (transverse steel) without GFRP wrap and rest nine beams are strengthened in shear with one, two, and three layers of GFRP sheet in U-configuration for each type of stirrup spacing. This study focuses on strain analysis of U-wrapped GFRP sheet, transverse steel reinforcement and longitudinal steel reinforcement. It is observed that the strain in the U-wrapped GFRP sheet is higher in the specimens strengthened with one layer of GFRP, as compared to two and three layers in all the series. The stiffness of GFRP sheet is indirectly proportional to the strain.

Keywords Reinforced concrete (RC) · Strengthening · Glass fibre-reinforced polymer (GFRP) · Shear strength · T-beams

K.C. Panda (✉)
Department of Civil Engineering, ITER, SOA University,
Bhubaneswar 751030, Odisha, India

S.K. Bhattacharyya
CSIR-Central Building Research Institute, Roorkee 247667, India

S.V. Barai
Department of Civil Engineering, IIT Kharagpur, Kharagpur 721302, India

1 Introduction

The technique of strengthening RC structures by externally bonded carbon fiber reinforced polymer (CFRP) laminates was started about two decades back and has since attracted researchers around the world. Very few works have been carried out by some researchers on the influence of longitudinal and transverse steel effect on GFRP strengthening. Pellegrino and Modena [1] experimentally investigated on shear behaviour of RC beams with and without the transverse steel reinforcement, and with different amount of FRP shear strengthening bonded to both sides of the beams. Chaallal et al. [2] have studied the effectiveness of large scale girders having low shear span with externally bonded CFRP, varying transverse steel reinforcement and CFRP layers. The authors have studied these variations for deep beams. Bousselham and Chaallal [3] demonstrated the interaction between the transverse steel reinforcement and the externally applied CFRP in gaining shear capacity. Bousselham and Chaallal [4] presented the shear resistance mechanisms involved in RC T-beams strengthened in shear with externally bonded FRP. The local behavior of the FRP and the transverse steel, particular in the failure zones, were thoroughly examined. Panda et al. [5] carried out an experimental investigation on shear behavior of RC T-beams strengthened with U-wrapped GFRP sheets and transverse steel reinforcement in 200 mm stirrup spacing. Panda et al. [6] studied the behavior of RC T-beams strengthened in shear with U-wrapped GFRP sheet. The effectiveness, shear behavior, the cracking pattern, and modes of failure were presented. Panda et al. [7] studied the effect of transverse steel on the performance of RC T-beams strengthened in shear zone with GFRP sheet and demonstrated that GFRP sheet in U-jacket with anchorage is more effective than U-jacket scheme. This paper is an extension work of the paper, Panda et al. [6] and is focuses on the strain analysis of GFRP sheet, transverse steel, and longitudinal steel reinforcement.

2 Experimental Program

2.1 Details of Test Specimen

A total of eighteen (18) RC T-beams having cross-sectional dimensions of 250 mm flange width with 60 mm thickness and 100 mm web width with 200 mm depth are cast at the structural laboratory of Civil Engineering Department, IIT Kharagpur. All the T-beams are 2,500 mm long and designed to fail in shear as per IS: 456-2000. The longitudinal reinforcement used in this study consisted of two (2) Nos. 20 mm diameter Tor steel bars in the bottom and four (4) Nos. 8 mm diameter Tor steel bars in the top of the beam. The transverse reinforcement consisted of 6 mm diameter stirrups. Nine (9) T-beams are tested as control beam and the rest nine beams are tested as strengthened beam. Nine control beams are tested in three

different series. The first series, without stirrups, only the stirrups are provided at the support and loading points i.e. total six number of stirrups 2 Nos. at the support and 1 No. at the loading points are provided to prevent local shear failure. The second series of control specimen, the stirrups are provided @ 300 mm c/c whereas in third series, the spacing of the stirrups is 200 mm c/c. The control specimen details and dimensions are shown in Fig. 1. The other nine (9) T-beams are strengthened in shear with one, two and three layers of U-wrapped GFRP sheet in all the series.

2.2 Materials Used

A concrete mix with ordinary Portland cement (OPC-43 grade) and 12.5 mm downgraded coarse aggregates are used for casting. The mix design is carried out for M30 grade of concrete. The mix design proportions of cement, fine aggregate, and coarse aggregate are (1:0.946:2.03). Fe415 grade steel used for longitudinal steel reinforcement and Fe250 used for transverse steel reinforcement as reinforcement in the experiment. Glass fiber fabric of thickness 0.32 mm is used for strengthening of beams. Epoxy adhesive is used to attach the glass fabric to the beam; the resin used is a 9:1 mixture of Araldite CY-230 and hardener HY-951. The one layer GFRP thickness is 0.36 mm and the mean ultimate tensile strength used 160 MPa and the elastic modulus is 13.18 GPa.

Fig. 1 Reinforcement details of test specimens
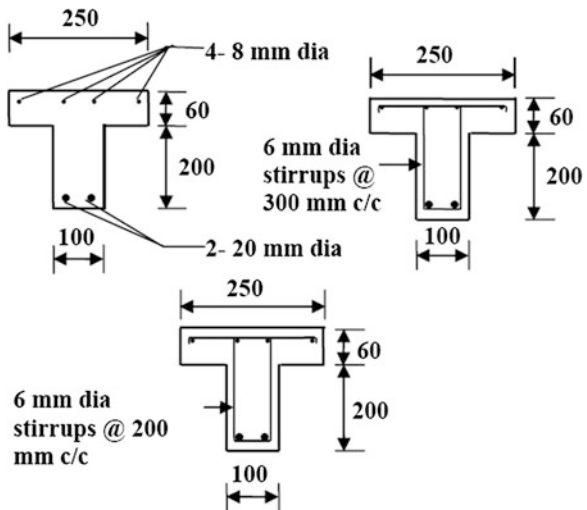
2.3 Experimental Scheme

Beams S0-0L, S300-0L, and S200-0L are not strengthened and served as control beam. S0-0L without stirrups, whereas in S300-0L and S200-0L the stirrups are provided at a spacing of 300 and 200 mm c/c respectively. The strengthened T-beams of S0 series designated as S0-1L-CT-U-90, S0-2L-CT-U-90 and S0-3L-CT-U-90 are strengthened with one, two, and three layers of U-wrapped GFRP sheet respectively on the web. Similarly the strengthened beams of S300 series are designated as S300-1L-CT-U-90, S300-2L-CT-U-90 and S300-3L-CT-U-90 and for S200 series designated as S200-1L-CT-U-90, S200-2L-CT-U-90 and S200-3L-CT-U-90 for one, two, and three layers of GFRP sheet respectively. The main fiber direction is oriented perpendicular to the longitudinal axis of the beam. The details of strengthening scheme with U-wrapped GFRP sheet with one, two and three layers are presented in Fig. 2.

2.4 Instrumentation and Measurements

All specimens are tested under two point loading over the span of 2,500 mm long with shear span to effective depth ratio (a/d) equal to 3.26. The tests are conducted using a 300 T universal testing machine (UTM). Load is applied monotonically to the test beams until failure. Strains, deflections are recorded at every 6 kN load. Figure 3 shows the details of the test setup with location of external strain gauges and dial gauges. Two types of electrical resistance strain gauges are used in the test; gauges BKNIC-10 are used on the surface of the longitudinal steel reinforcement and transverse steel, and gauges BKCT-30 are used on the concrete surface and on the GFRP sheet attached parallel to the orientation of the fiber in the vertical

Fig. 2 Details of strengthening scheme with U-jacketed GFRP
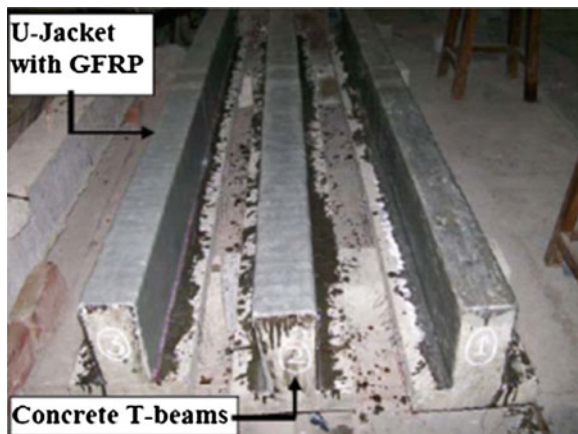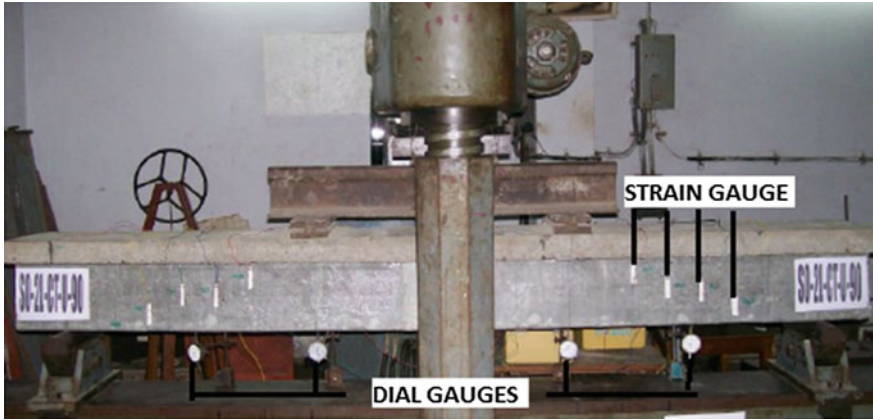
Fig. 3 Test setup with location of external strain gauges and dial gauges
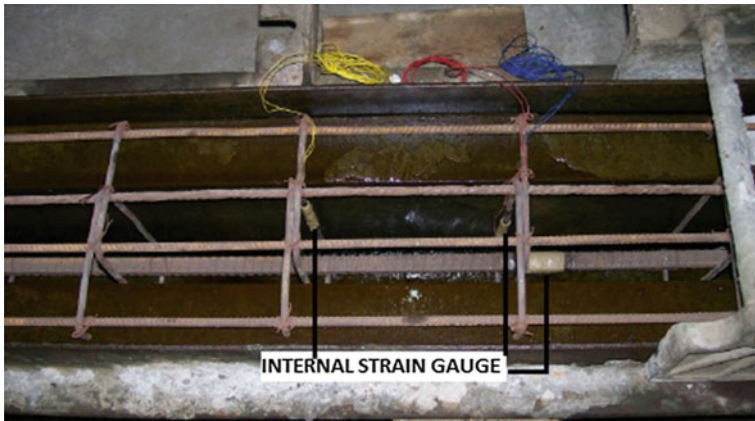
Fig. 4 Internal strain gauges in longitudinal steel and transverse steel

direction. BKNIC-10 is attached on the longitudinal steel and transverse steel to measure deformation during the different stages of loading and to monitor yielding as shown in Fig. 4.

3 Experimental Results and Discussions

The strain measured experimentally in the U-wrapped GFRP sheet, transverse steel reinforcement and longitudinal steel reinforcement is presented with graphical representation.

3.1 Strain in GFRP Sheet

The developed vertical strains in GFRP sheet due to shear force for different layers of GFRP in S0 and S300 series specimens are shown in Figs. 5 and 6. The strain in the GFRP sheet in all the strain gauges did not contribute to the load carrying capacity in the initial stages of loading as observed by Bousselham and Chaallal [3]. It is observed that, in single layer (S0-1L-CT-U-90) specimen, the strain in the strain gauge Sg1 increases slowly up to 55 kN shear force. Thereafter, as shear force increases, the curve suddenly increased and attained the maximum value of 7,747 μstrains at 65 kN shear force. Whereas in two (S0-2L-CT-U-90) and three (S0-3L-CT-U-90) layer specimens, the strain in the GFRP started increasing in all

Fig. 5 Variation of vertical strains in GFRP sheet for series S0
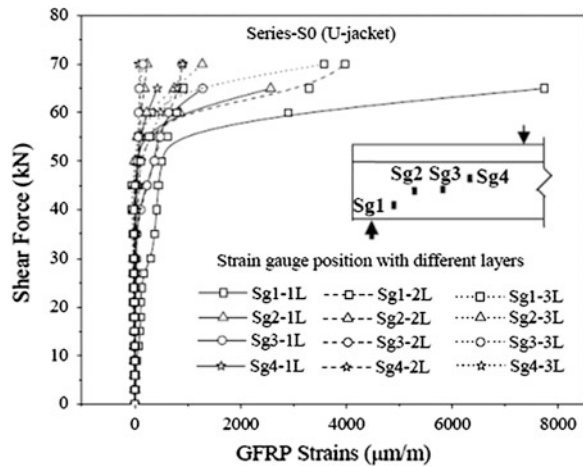
Fig. 6 Variation of vertical strains in GFRP sheet for series S300
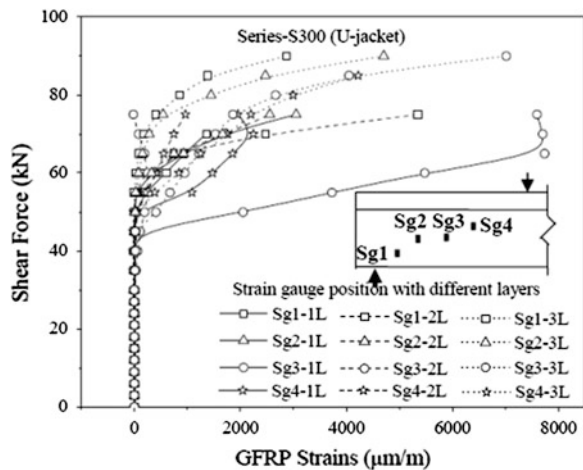
the strain gauges after 35 kN shear force. The maximum strain observed in Sg1 strain gauge is 3,978 and 3,581 µstrains at 70 kN shear force. In series S0, the strain in the GFRP sheet is higher in the specimens strengthened with one layer of GFRP as compared to two and three layers. It is also observed that in all the specimens, the GFRP strain is higher at 150 mm distance from the support.

The same trend is also observed in S300 and S200 series. In S300 series, the strain in the GFRP sheet in all the strain gauges did not contribute to the load carrying capacity up to 45 kN shear force approximately. After 45 kN shear force, the strain started increasing steadily in the single layer (S300-1L-CT-U-90) GFRP sheet and reached the maximum value of 7,739 µstrains at 65 kN shear force in strain gauge Sg3. Whereas in two (S300-2L-CT-U-90) and three (S300-3L-CT-U-90) layers specimens, the strain corresponding to this shear force is very less. Maximum strain observed in two and three layers specimen is 5,348 µstrains, and 7,018 µstrains in Sg1 and Sg3 strain gauges at 75 and 90 kN shear force respectively. In series S300, the strain in the GFRP sheet is higher in the specimens strengthened with one layer of GFRP, as compared to two and three layers. It is also observed that in one and three layers specimen, the GFRP strains are higher at 350 mm distance from the support, whereas in two layers specimen, it is 150 mm distance from the support.

3.2 Strain in Transverse Steel

The curves representing the shear force versus the strains in the transverse steel reinforcement for series S200 and S300 is shown in Figs. 7 and 8.

It is observed that, like GFRP, the transverse steel reinforcement did not contribute to the load carrying capacity in the initial stage of loading as observed by Bousselham and Chaallal [3]. This contribution is more effective after the diagonal

Fig. 7 Variation of strain in transverse steel for S200 series
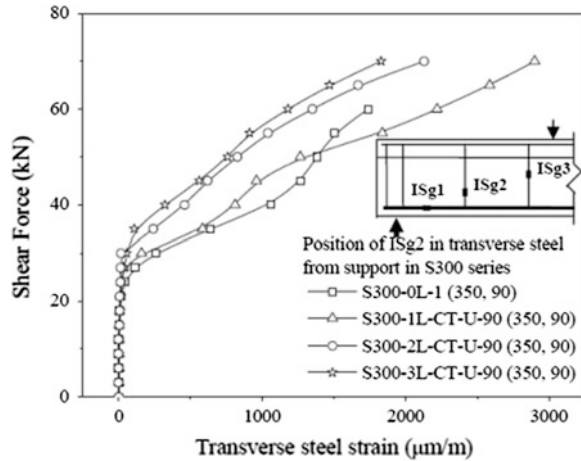
cracking. In the control specimen S200-0L, it occurred at a shear force of approximately 35 kN. Whereas for the strengthened specimens S200-1L-CT-U-90, S200-2L-CT-U-90, and S200-3L-CT-U-90, it occurred at a shear force of approximately 40, 45, and 50 kN respectively. In the series S300, in the control specimen S300-0L, it occurred at a shear force of approximately 24 kN, whereas for the strengthened specimen S300-1L-CT-U-90, S300-2L-CT-U-90, and S300-3L-CT-U-90 it occurred at shear force of approximately 27, 30, and 35 kN respectively. Thereafter, as shear force increases, the strain in the transverse steel get increases. It may be observed that the strain in the transverse steel is less in strengthened beams as compared to the control beam for the same amount of shear force. It is also observed that the strain in the specimens strengthened with three layers of GFRP sheet is less as compared to the specimens strengthened with one layer of GFRP sheet.

It may also be observed that the addition of the GFRP sheet delayed the contribution of transverse steel to the load carrying capacity of the specimens, also as layers concerned, the addition of second and third layer of GFRP sheet resulted in an additional decrease of the strains in the transverse steel, previously observed by Bousselham and Chaallal [3] using CFRP as strengthening material.

3.3 Strain in Longitudinal Steel

The curve representing the shear force versus the strains in the tensile longitudinal steel reinforcement for varying layers of series S0, S300 and S200 is shown in Fig. 9. The strain gauge ISg1 located in tensile longitudinal steel reinforcement at 150 mm distance from the support for the beams of series S0, S200 and S300 respectively. As observed from Fig. 9, the strain near the support point is very small in the initial stages of loading in all the series. As shear force increases, the strain

Fig. 9 Variation of strain in longitudinal steel for varying layers
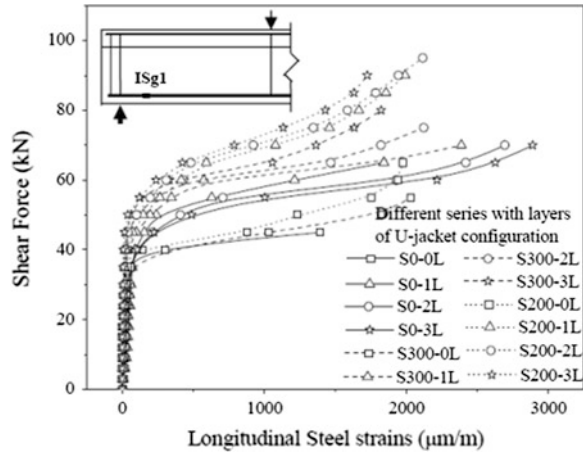
increases linearly up to about 35 kN shear force as the diagonal cracks appear in the concrete. After the appearance of diagonal cracks in the concrete, the longitudinal steel reinforcement resists the further increments of shear force. It may be observed that, the strain in the longitudinal steel, in beams strengthened with GFRP sheet is less as compared with control specimen for the same amount of shear force for all the series.

It is concluded that, the presence of GFRP sheet eased the strains in the longitudinal steel reinforcement at a given shear force; the longitudinal steel seems to be less strained in strengthened specimens as compared with control specimen, previously observed by Bousselham and Chaallal [3] using CFRP as strengthening material. It is also observed that as shear reinforcement increases, the longitudinal steel seems to be less strained for the same amount of shear force. So far as the number of GFRP layers is concerned, the longitudinal steel is less strained in three layered specimen as compared to single layer specimen.

4 Conclusions

The following conclusions may be drawn from this study:

The shear force-GFRP strain curves clearly indicates that, the strain in the U-wrapped GFRP sheet is higher in the specimens strengthened with one layer of GFRP sheet, as compared to two and three layers in all the series. As expected, the stiffness of GFRP sheet is indirectly proportional to the strain.

The strain in transverse steel is more in control specimens, as compared with strengthened beam specimens. This indicates that the addition of GFRP sheet delayed the contribution of transverse steel to the shear carrying capacity of the beam. But, so far as the number of GFRP sheet is concerned, the addition of second

and third layer of GFRP sheets resulted in an additional decrease of strains in the transverse steel.

The strain in longitudinal steel is more in control specimens, as compared with strengthened beam specimens. This indicates that the addition of GFRP sheet helps in reducing the strain in longitudinal steel. But, so far as the number of sheet is concerned, the strain in the longitudinal steel reinforcement is less in strengthened specimen with three layers of GFRP sheet as compared with single layer of GFRP sheet.

References

1. Pellegrino C, Modena C (2002) Fiber reinforced polymer shear strengthening of reinforced concrete beams with transverse steel reinforcement. J Compos Constr 6(2):104–111
2. Chaallal O, Shahawy M, Hassan M (2002) Performance of reinforced concrete T-girders strengthened in shear with carbon fiber-reinforced polymer fabric. ACI Struct J 99(3):335–343
3. Bousselham A, Chaallal O (2006) Effect of transverse steel and shear span of the performance of RC beams strengthened in shear with CFRP. Compos B 37:37–46
4. Bousselham A, Chaallal O (2008) Mechanisms of shear resistance of concrete beams strengthened in shear with externally bonded FRP. J Compos Constr 12(5):499–512
5. Panda KC, Bhattacharyya SK, Barai SV (2010) Shear behaviour of reinforced concrete T-beams with U-bonded glass fibre reinforced plastic sheet. Indian Concr J 84(10):61–71
6. Panda KC, Bhattacharyya SK, Barai SV (2012) Shear behaviour of RC T-beams strengthened with U-wrapped GFRP sheet. Steel Compos Struct Int J 12(2):149–166
7. Panda KC, Bhattacharyya SK, Barai SV (2013) Effect of transverse steel on the performance of RC T-beams strengthened in shear zone with GFRP sheet. Constr Build Mater 41:79–90
8. Indian Standard (2000) Plain and reinforced concrete code of practice IS 456: 2000, India, 100 p

Bibliography

9. ACI Committee 440 (2002) Guide for the design and construction of externally bonded FRP systems for strengthening concrete structures (ACI 440.2R-02). American Concrete Institute, Farmington Hills, Michigan, USA, 45 p

Structural Response of Thin-Walled FRP Laminated Mono-symmetrical I-Beams

S.B. Singh and Himanshu Chawla

Abstract This paper deals with an analytical study on flexural-torsional buckling analysis of thin-walled FRP laminated I-beams with different sizes of flange. A general analytical model is developed based on shear deformable beam theory. The response of I-beam has been investigated for different flange width to thickness, depth to thickness, and length to depth ratios. Furthermore, comparison of critical buckling load is done with and without consideration of shear deformation. The same study is extended to check the response of beam for different types of flexural loading such as point and uniformly distributed transverse loads with different boundary conditions. The results obtained from an analytical model are compared with FEM software ABAQUS for the same geometric configuration and loading on the beam. It is observed that the results obtained from the analytical modeling are in good agreement with that of ABAQUS.

1 Introduction

A thin-walled beam is a very useful and efficient type of structural element. The cross-section of thin-walled beams is made up of thin plates connected to create closed or open cross section of a beam. Thin-walled beams are economical and efficient because their bending stiffness per unit cross sectional area is much higher than that of solid cross sections such as rod or bar. In this way, stiff beams can be achieved with minimum weight. However, it is very prone to buckling in case of

S.B. Singh (✉) · H. Chawla
Civil Engineering Department, BITS, Pilani 333031, India
e-mail: sbsinghbits@gmail.com; sbsingh@pilani.bits-pilani.ac.in

H. Chawla
e-mail: himanshuchawla11@gmail.com

unrestrained beams. If the section is slender and the member bends about the strong axis, then it may fail by flexural-torsional or lateral buckling of beams. For the long span FRP beams, flexural-torsional buckling is more likely to occur than the local buckling.

Researchers have carried out the analytical study on flexural-torsional buckling analysis of FRP beam with different approaches. Mottram [1] investigated the flexural-torsional buckling behavior of pultruded E-glass FRP I-beams experimentally and compared the results obtained by a finite-difference method. Kabir and Sherbourne [2] proposed an analytical solution for the optimal fiber orientation in pulturded laminated channel section beams to resist the lateral buckling. They [2] have checked the effect of fiber orientation in web and flanges on twist angle and observed that buckling load has maximum value for long beams when web fiber angle is directed at ±35°. Pandey et al. [3] presented a theoretical formulation for flexure-torsional buckling of thin-walled composite I-section beams with the purpose of optimizing the fiber orientation, and simplified formulas for several different loading and boundary conditions. Davalos et al. [4] studied the flexural-torsional and lateral-distortional buckling of simply supported FRP I-beams loaded at midspan, both experimentally and analytically. There was good agreement between experimental and analytical results. Loughlan [5] used finite strip method to examine the effect of bend-twist coupling on the shear buckling behavior of laminated composite and demonstrated that thinner laminates are more prone to the effects of bend–twist coupling, is also shown [5] that with increase in laminate thickness, the shear buckling response tends to increase towards that of the orthotropic solution. Lee and Lee [6] have performed the lateral buckling analysis of a composite I-section beam subjected to various types of loading. They have checked the effect of different loading conditions (i.e., by varying locations of applied load and types of load) and the effect of fiber orientation on the critical buckling load and central deflection. The authors [6] observed that deflection increases with increase in fiber orientation angle. Lee and Kim [7] presented an analytical model based on classical lamination theory for calculating the critical buckling load due to axial loading. Numerical results were obtained for axially loaded thin-walled composites considering the effect of fiber angle, anisotropy, and boundary conditions on critical buckling loads and mode shapes. Lee [8] presented a model based on shear deformable beam theory. He analyzed the beam for flexural behavior under vertical load for arbitrary laminate stacking sequence configuration. It is observed that this analytical solution exhibits better results than that of classical beam theory. In his study, he emphasized that there is a potential danger in analysis and design of FRP beams without including shear deformation. Kollar [9], Kollar and Springer [10] presented the governing equations of thin-walled open-section orthotropic composite column including the effect of shear deformation both for in-plane displacements and restrained warping. Kollar [9] has also derived a closed-form solution for the flexural-torsional buckling load of a composite beam and verified the results using ABAQUS. Lee [11] developed an analytical model for open cross-section of laminated beams with symmetric and unsymmetrical laminates. He has obtained a relation between centroid and shear center with fiber angle

of laminated beams. Roberts and Masri [12] described the experimental determination of the flexural and torsional properties of a pultruded profile, based on a full section and coupon tests. Also, they have developed the closed-form solutions for the influence of shear deformation on global flexural, torsional and lateral buckling of pultruded FRP profiles. They have shown that for wide flange I-profiles, prebuckling displacement increases more than 20 %. Based on experimental and theoretical results, they have studied the behavior of pultruded FRP channel section beams under the influence of gradually increasing static loads.

In this paper, a computational approach is used to study the effect of width-to-thickness, depth-to-thickness and length-to-depth ratio on the critical buckling load of mono-symmetric laminated I-beam. Critical buckling load is found out for different loading and boundary conditions. An analytical model is made based on classical beam theory and shear deformation beam theory and results are compared with commercial software ABAQUS.

2 Kinematic Formulation

In this paper, we have presented the buckling analysis of thin walled laminated FRP I-beam. A global Cartesian coordinate system (x, y, z) is taken for representation of beam. The 'x' axis is tangent to the centroidal axis of the beam; 'y' and 'z' directions coincide with the principal axes of the cross-section as shown in Fig. 1. The displacement of the whole member can be divided into three distinct motions, i.e., axial displacement 'u' is in x-direction, horizontal displacement 'v' is in y-direction, vertical displacement 'w' in z-direction and 'φ' is angle of twist.

To study the buckling behavior of beam, simply supported boundary condition is maintained. The beam is restrained against rotation about x and z-axis at ends, but is allowed to rotate about y-axis at the ends. In short, the displacements and torsion at the ends are zero. Therefore the boundary conditions of the I-beam can be defined as

$$u = v = w = \frac{dv}{dx} = \varphi = 0 \quad \text{at x = 0, L} \tag{1}$$

A formal engineering approach is incorporated for deriving the equations of thin-walled FRP beams under flexural loading. Shear deformation has significant effect on FRP beams, so Timoshenko beam theory is considered for analysis. The displacement field of flange plates of I-beam based on the first-order shear deformation beam theory (FSDT) is as follow:

$$u(x, y) = u_o(x, y) + z\phi_x(x, y) \tag{2}$$

$$v(x, y) = v_o(x, y) + z\phi_y(x, y) \tag{3}$$

Fig. 1 Cordinate system of
I-beam and plate
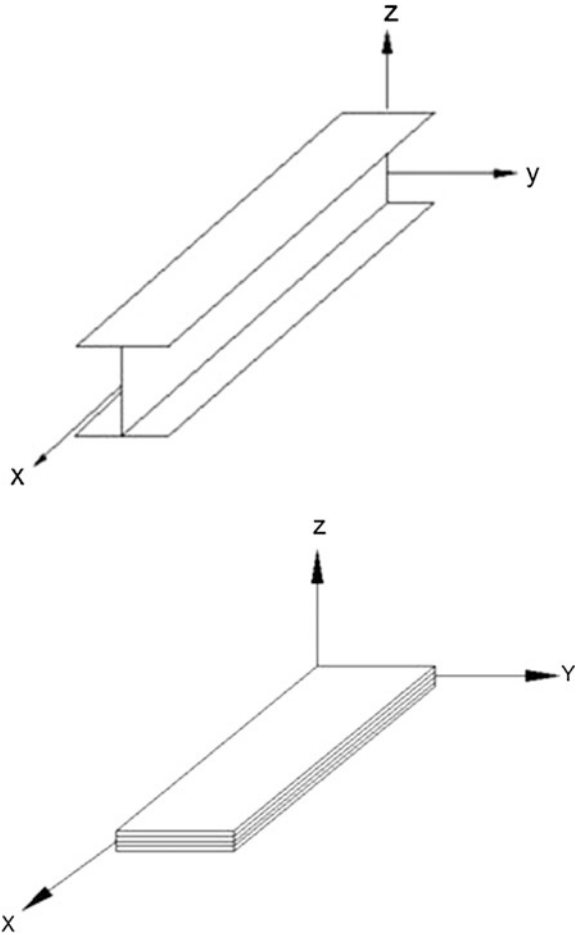
$$w(x, y) = w_o(x, y) \tag{4}$$

In these relations ϕ_x and ϕ_y are rotation about the y and x axis and it is $\dfrac{\partial u}{\partial z}$ and $\dfrac{\partial v}{\partial z}$. Strains associated with displacement of a element in Cartesian coordinate system are

$$\varepsilon_{xx} = \frac{\partial u}{\partial x} + \frac{1}{2}\left(\frac{\partial w}{\partial x}\right)^2 \tag{5}$$

$$\varepsilon_{yy} = \frac{\partial v}{\partial y} + \frac{1}{2}\left(\frac{\partial w}{\partial y}\right)^2 \tag{6}$$

$$\gamma_{xy} = \left(\frac{\partial u}{\partial y} + \frac{\partial v}{\partial x} + \frac{\partial w}{\partial x}\frac{\partial w}{\partial y}\right) \tag{7}$$

The resulting strains obtained after substituting Eqs. (2)–(4) in Eqs. (5)–(7) as follows:

$$\varepsilon_{xx} = \frac{\partial u_o}{\partial x} + \frac{1}{2}\left(\frac{\partial w_o}{\partial x}\right)^2 + z\frac{\partial \phi}{\partial x} \tag{8}$$

$$\varepsilon_{yy} = \frac{\partial v_o}{\partial y} + \frac{1}{2}\left(\frac{\partial w_o}{\partial y}\right)^2 + z\frac{\partial \phi}{\partial y} \tag{9}$$

$$\gamma_{xy} = \left(\frac{\partial u_o}{\partial y} + \frac{\partial v_o}{\partial x} + \frac{\partial w_o}{\partial x}\frac{\partial w_o}{\partial y}\right) + z\left(\frac{\partial \phi_x}{\partial y} + \frac{\partial \phi_y}{\partial x}\right). \tag{10}$$

2.1 Stiffness Matrix for Orthotropic Beam

In this paper, the beam considered is an orthotropic laminated I-beam. A beam is orthotropic, when it is made up of an orthotropic laminate or one of orthotropic axis is aligned towards the axis of beam. The laminate can be of woven or uni-directional fiber with different angle. Thickness of cross-section is considered to be very thin; therefore it is possible to assume plane-stress for obtaining the relation between stress and strain. If the orientation of fibers in flanges and web are same then stiffness matrix of flanges and web are equal. The stiffness of a laminate depends upon no. of ply and material properties of each ply; stiffness of each ply is denoted by [Q],

$$\left\{\begin{array}{c}\sigma_x \\ \sigma_y \\ \sigma_{xy}\end{array}\right\} = \begin{bmatrix}Q_{11} & Q_{12} & Q_{16} \\ Q_{12} & Q_{22} & Q_{26} \\ Q_{16} & Q_{26} & Q_{66}\end{bmatrix}\left\{\begin{array}{c}\varepsilon_x \\ \varepsilon_y \\ \gamma_{xy}\end{array}\right\} \tag{11}$$

Stiffness matrix of angle ply is obtained by transforming the [Q] in particular angle. The stiffness matrix of laminate is shown in Eq. (13),

$$\left\{\begin{array}{c}N_x \\ N_y \\ N_{xy}\end{array}\right\} = \int\limits_{-t/2}^{t/2}\left\{\begin{array}{c}\sigma_x \\ \sigma_y \\ \sigma_{xy}\end{array}\right\}dz \quad \text{and} \quad \left\{\begin{array}{c}M_x \\ M_y \\ M_{xy}\end{array}\right\} = \int\limits_{-t/2}^{t/2}\left\{\begin{array}{c}\sigma_x \\ \sigma_y \\ \sigma_{xy}\end{array}\right\}zdz \tag{12}$$

$$\left\{\frac{N}{M}\right\} = \left[\begin{array}{c|c}A & B \\ \hline B & D\end{array}\right]\left\{\frac{\varepsilon}{k}\right\} \tag{13}$$

where A is the extensional, D is bending and B is the bending-extensional coupling stiffnesses of stiffness matrix of a laminate. ε and k are strain and curvature of

section after deformation. These elements are nothing but the total stiffness due to all ply present in laminates. Similarly, elements of compliance matrix is obtained by taking inverse of stiffness matrix which is used to obtain the strains and curvature. If the laminate has symmetrical layup then B is zero and elements of compliance matrix can be expressed as follow:

$$[a] = [A]^{-1} \quad \text{and} \quad [d] = [D]^{-1} \tag{14}$$

where 'a' and 'd' represent elements of compliance matrix.

3 Analytical Modeling

In this section, bending stiffness of I-beam is derived. The bending stiffness depends upon the cross-section and ply stiffness. Terminology used in this paper to represent the cross-section is shown in Fig. 2.

As shown in Fig. 2, b_1 and b_2 represents the width of top and bottom flange, respectively, 'h' is the height of web, 't' represents the thickness of flange and web, z_c represents the height of centroid from center of bottom flange, and Δ is the height of loading from shear center. The coordinates of centroid is given as

$$z_c = \frac{1}{EA} \left(\frac{b_1 d}{a_{11}} + \frac{hd}{2a_{11}} \right) \tag{15}$$

For unsymmetrical section, position of shear center and centroid is not same. Therefore position of shear center is required to be find out. The distance of shear center from center of bottom flange is given by below equation:

Fig. 2 Typical cross-section of I-beam
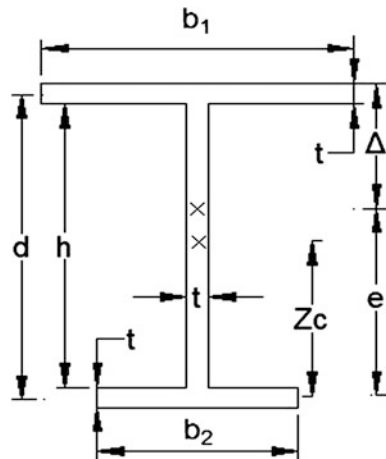
$$e = d \frac{\frac{b_1^3}{a_{11}}}{\frac{b_1^3}{a_{11}} + \frac{b_2^3}{a_{11}}} \tag{16}$$

The axial stiffness of the beam is summation of stiffness of all panels (i.e. web and flanges). Therefore the axial stiffness of beam is given by expression below

$$EA = \frac{b_1 + b_2 + h}{a_{11}} \tag{17}$$

Thin-walled section is very prone to buckling in case of unrestrained beams. If the section is slender and the member bends about the strong axis, then it may fail by flexural-torsional or lateral buckling of beams. This phenomenon is known as lateral-torsional buckling of beams. For the long span FRP beams, lateral-torsional buckling is more likely to occur than the local buckling. Therefore it is very important to find out the buckling load of a beam. The buckling load of I-beam depends on the stiffness of the flanges and web as well as on the boundary conditions of beam. If an axially loaded beam buckles in lateral direction i.e. in x–y plane then critical buckling load in this direction is denote by N_{crz}. The critical buckling load is defined as

$$N_{crz} = \frac{\pi^2 EI_{zz}}{(kL)^2} \quad \text{and} \quad EI_{zz} = \frac{h}{d_{11}} + \frac{b_1^3 + b_2^3}{12a_{11}} \tag{18}$$

On the other hand, if a beam rotates about its centroidal axis, then it is defined as torsional buckling. The torsional buckling load depends on the torsional stiffness and critical warping load and is given by

$$N_{cr\psi} = N_{cr\omega} + \frac{GI_t}{i_\omega^2} \quad \text{and} \quad N_{cr\omega} = \frac{\pi^2 EI_\omega}{i_\omega^2 (kL)^2} \tag{19}$$

where $N_{cr\psi}$ and $N_{cr\omega}$ denotes torsional and warping buckling loads, respectively. GI_t is torsional and EI_ω is warping stiffness, it induces due to restrain provided at the ends of beam. It can be expressed as:

$$GI_t = 4\left(\frac{b_1 + b_2}{d_{33}} + \frac{h}{d_{33}}\right) \quad \text{and} \quad EI_\omega = \frac{\frac{b_1^3}{a_{11}}}{12} ed \tag{20}$$

The polar radius of gyration about the shear center can be expressed in the form as given in Eq. (21).

$$i_w = \sqrt{\frac{EI_{yy} + EI_{zz}}{EA}} \tag{21}$$

The critical buckling moment based on CLPT is expressed by Eq. (22) [13].

$$Q_{cr} = F_1 N_{crz} \left((F_2\Delta + F_3\beta) \pm \sqrt{((F_2\Delta + F_3\beta))^2 + \left(\frac{N_{crw}i_\omega^2}{N_{crz}}\right)} \right) \qquad (22)$$

where F_1, F_2 and F_3 are constant (see Table 1), z_{sc} is distance between shear center and centroid of a cross-section, Δ is the distance between load and centroid of I-beam and β is given below:

$$\beta = J_1 + J_2 - 2z_{sc} \qquad (23)$$

where

$$J_1 = \frac{1}{EI_{yy}} \left(\frac{b_1(d-z_c)^2}{a_{11}} - \frac{b_2 z_c^3}{a_{11}} + \frac{(h_1^4 - h_2^4)}{4a_{11}} \right) \quad \text{and}$$
$$J_2 = \frac{1}{EI_{yy}} \left(\frac{b_1^3(d-z_c)}{12a_{11}} - \frac{b_2^3 z_c}{12a_{11}} \right) \qquad (24)$$

$$EI_{yy} = \frac{b_1(d-z_c)^2}{a_{11}} + \frac{b_2 z_c^2}{a_{11}} + \frac{b_1 + b_2}{d_{11}} + \frac{1}{a_{11}}\frac{(h_1^3 + h_2^3)}{3} \qquad (25)$$

$$h_1 = z_c - t/2 \quad \text{and} \quad h_2 = h - h_1 \qquad (26)$$

where, EI_{yy} is the bending stiffness of the beam in x–z plane.

3.1 Effect of Shear Deformation

In the first-order shear deformation laminated plate theory (FSDT), the Kirchhoff hypothesis is relaxed by considering that the transverse normals do not remain perpendicular to the mid-surface after deformation. Therefore, it is necessary to include the transverse shear strain in the theory. Timoshenko (Reddy, [14]) was the

Loading case	Critical buckling load	F_1	F_2	F_3
Concentrated load	$P_{cr} = \frac{4Q_{cr}}{L}$	1.35	0.55	0.212
Distributed load	$P_{cr} = \frac{8Q_{cr}}{L^2}$	1.13	0.45	0.267

Table 1 Buckling loads and corresponding constants

first to include the effect of rotatory inertia and shear deformation in the beam theory. This theory is now widely referred to as Timoshenko beam theory or the first order shear deformation theory (FSDT).

Based on the above theory the shear compliance matrix elements [15] are presented below:

$$S_{zz} = \frac{a_{33}}{d} + \frac{a_{33}b_1}{12d^2y_1^2} + \frac{1}{12}\frac{a_{33}b_2}{d^2y_2^2} \quad \text{and} \quad S_\omega = \frac{1.2}{d^2}\left(\frac{a_{33}}{b_1} + \frac{a_{33}}{b_2}\right) \tag{27}$$

where

$$y_1 = 1 + \frac{1}{3}\frac{d}{b_1\left(1 + \frac{1}{S_c}\right)} \quad , \quad y_2 = 1 + \frac{1}{3}\frac{d}{b_2(1 + S_c)} \quad \text{and} \quad s_c = (d - e)/d \tag{28}$$

Similarly, critical buckling load considering the effect of shear stiffness is given below:

$$N_{crzs} = \left(\frac{1}{N_{crz}} + \frac{1}{S_{zz}}\right)^{-1} \quad \text{and} \quad N_{cr\omega s} = \left(\frac{1}{N_{cr\omega}} + \frac{i_w^2}{S_\omega}\right)^{-1} \tag{29}$$

The critical buckling load with shear deformation is obtained by substituting Eq. (27) in Eq. (22) and is given by Eq. (30).

$$Q_{cr} = F_1 N_{crzs}\left((F_2\Delta + F_3\beta) \pm \sqrt{((F_2\Delta + F_3\beta))^2 + \left(\frac{N_{crws}i_\omega^2}{N_{crzs}}\right)}\right). \tag{30}$$

4 Finite Element Modeling

To verify the accuracy of the analytical results, the same beam is modeled in ABAQUS 6.10, with shell element S4R. The beam is meshed with fine size 0.005 of length of member. The concentrated load is applied at the mid-span of the top flange. The boundary conditions are applied at the end of the centroidal axis of the beam. At the ends, beam is not allowed to rotate about centroidal axis as well as its ends translation along y and z-axis is restrained. Deformation of fixed supported FRP laminated beam under flexural loading is shown in Fig. 3. Concentrated load is applied on the all nodes of mid-span of top flange. While uniformly distributed load is applied on the all central node of width along the length of beam. If L/h ratio of beam is less than 7 or width of top flange is high then beam fails by local buckling or torsion. The results obtained from ABAQUS are presented in in the following sections. Comparison of FEM results with analytical results shows a good agreement until local buckling is prevented.
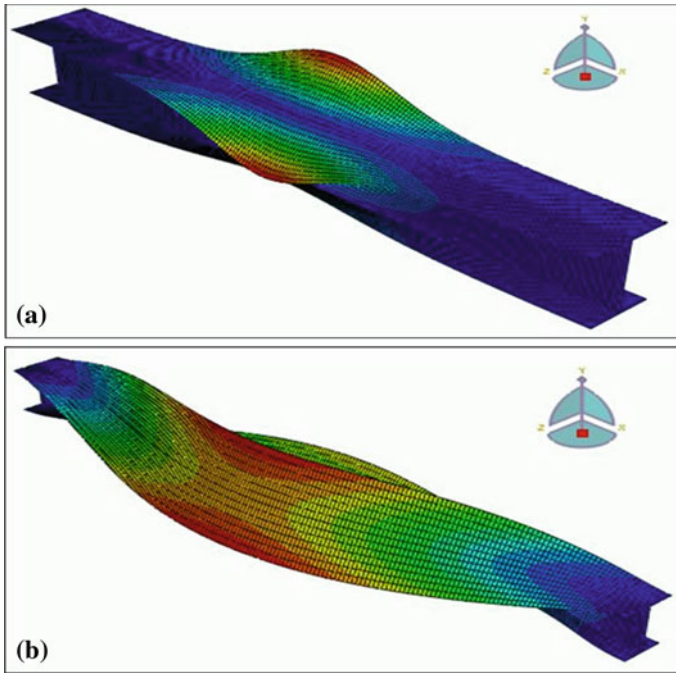
Fig. 3 Deformation of the fixed supported I-beam under concentrated load. **a** Local buckling of flanges, low L/h, **b** lateral-torsional buckling, high L/h

Table 2 Mechanical properties of a laminate (GPa)

E_1	E_2	E_3	v_{12}	G_{12}	G_{13}	G_{23}
75	14	14	0.3	8.5	8.5	2.5

5 Numerical Evaluation

In this section, the torsional-buckling strength of thin walled FRP I-beam has been presented. On the basis of the analytical procedure presented in the previous sections, a computer program is written in MATLAB R2013. The critical buckling load is computed for concentrated load (at mid-span) and uniformly distributed load applied on the top flange of FRP I-beam. The mechanical properties of beam are summarized in Table 2. The standard dimension taken for whole analysis is shown in Fig. 4. The stacking sequence in flanges and web is taken (0/90/0/0/0/0/90/0). The orientation of fiber in this beam fully resembles a pultruded beam. Laminated FRP I-beam is analyzed for variation of width of flanges, depth of web and length of beam separately. The response of beam is checked by varying one dimension of beam and keeping other constant. In this way critical buckling load is computed for different width-to-thickness ratio, depth-to-thickness ratio and length-to-depth ratio.

Fig. 4 Cross-section of I-beam
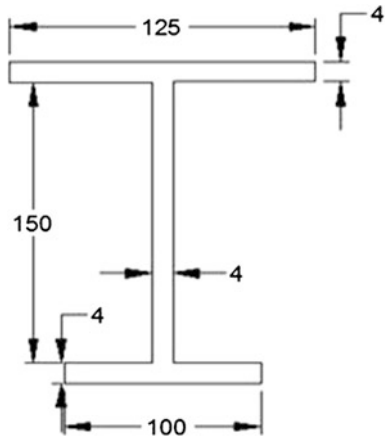
The same beam is also modeled in FEM software ABAQUS 6.10. The comparison of results obtained from classical lamination beam theory (CLPT), first order beam theory (FSDT) and ABAQUS results are presented in the following section.

6 Result and Discussion

6.1 Effect of Width-to-Thickness Ratio (b_1/t)

In this section, critical buckling load of FRP laminated I-beam is measured for different width-to-thickness ratio (b_1/t) of top flange. The material properties are taken same for whole analysis and the width is varied from 100 to 175 mm. The results of critical buckling load of FRP I-beam subjected to concentrated and uniformly distributed load is presented in Tables 3 and 4. It is observed that results obtained from both theories and FEM software shows increase in critical buckling load with increase in b/t ratio of beam. Critical buckling load has good agreement of results between both theories but little difference in results obtained from ABA-QUS, which is due to consideration of local buckling of web (or flanges). The effect of local buckling is higher for high b_1/t, so there is difference of results obtained from theories and FEM software.

6.2 Effect of Height-to-Thickness Ratio (h/t)

The critical buckling load is calculated for varied height of web with constant thickness of beam. The height of beam is varied from 100 to 175 mm with constant thickness of beam. It is observed that as expected critical buckling load increases

Table 3 Critical buckling load of FRP I-beam subjected to concentrated load at mid-span

b_1/t	Simply supported			Fixed support			Cantilever		
	ABAQUS	CLPT	FSDT	ABAQUS	CLPT	FSDT	ABAQUS	CLPT	FSDT
25	59	62	60	166	141	130	17	31	31
31	90	105	102	255	383	335	20	34	34
38	127	161	155	210	319	291	27	51	50
44	133	232	221	260	430	391	47	71	70

Table 4 Critical buckling load of FRP I-beam subjected to uniformly distributed load

b_1/t	Simply supported			Fixed support			Cantilever		
	ABAQUS	CLPT	FSDT	ABAQUS	CLPT	FSDT	ABAQUS	CLPT	FSDT
25	128	75	73	155	165	153	59	39	39
31	100	129	125	479	472	413	32	42	41
38	138	200	192	577	747	636	39	62	61
44	151	291	276	540	1,098	901	46	193	185

Table 5 Critical buckling load of FRP I-beam subjected to concentrated load at mid-span

h/t	Simply supported			Fixed support			Cantilever		
	ABAQUS	CLPT	FSDT	ABAQUS	CLPT	FSDT	ABAQUS	CLPT	FSDT
25	71	75	73	247	252	222	23	28	28
31	81	90	87	270	317	277	24	31	31
38	110	105	102	255	383	335	37	34	34
44	147	121	117	240	450	393	40	38	38

Table 6 Critical buckling load of FRP I-beam subjected to uniformly distributed load

h/t	Simply supported			Fixed support			Cantilever		
	ABAQUS	CLPT	FSDT	ABAQUS	CLPT	FSDT	ABAQUS	CLPT	FSDT
25	82	91	91	140	312	273	10	33	33
31	91	110	110	466	391	342	31	37	37
38	86	129	129	407	472	413	32	42	41
44	146	149	149	585	556	485	48	46	46

with increase in h/t ratio (Tables 5 and 6). The results obtained from ABAQUS are in good comparison for low h/t ratio, but for high, there is significant difference of results from analytical due to local buckling of web.

Table 7 Critical buckling load of FRP I-beam subjected to concentrated load at mid-span

L/h	Simply supported			Fixed support			Cantilever		
	ABAQUS	CLPT	FSDT	ABAQUS	CLPT	FSDT	ABAQUS	CLPT	FSDT
7	174	331	307	281	737	608	48	96	95
8	127	175	167	269	380	335	34	54	54
10	110	89	87	255	382	335	17	35	34
12	65	69	67	228	244	221	19	24	24

Table 8 Critical buckling load of FRP I-beam subjected to uniformly distributed load

L/h	Simply supported			Fixed support			Cantilever		
	ABAQUS	CLPT	FSDT	ABAQUS	CLPT	FSDT	ABAQUS	CLPT	FSDT
7	155	612	567	660	1,300	1,077	79	105	110
8	130	258	246	601	970	801	48	55	57
10	86	128	125	407	472	413	32	42	41
12	74	72	71	368	258	233	23	43	42

6.3 Effect of Length-to-Depth Ratio (L/h)

In order to investigate the effect of critical buckling load on different span length, length of beam is varied with constant cross-section. The length of I-beam is varied from 1 to 1.75 m. The results are generated for different boundary conditions, along with including the effect of different loading and it is presented in Tables 7 and 8. Throughout the whole study, buckling load decreases with increase in L/h ratio. It is also observed that for relatively short beams (i.e. L/h = 7), results of both theories shows significant difference of results due to shear deformation and results of FEM software is lesser than results from both theories. Local buckling is dominant in low L/h but has less effect for high L/h ratio.

7 Conclusions

The Lateral-torsional buckling analysis for mono-symmetric FRP I-beam is studied with different loading and boundary conditions. The critical buckling load is derived based on classical lamination plate theory and first order shear deformation beam theory. For verification of results, beam is also modeled in FEM software ABAQUS. A parametric study is performed on the effect of width-to-thickness ratio, depth-to-thickness ratio, and length-to-depth ratio with different loading conditions and supports.

Based on the study conducted, following conclusions can be made:

1. Analytical model with consideration of shear deformation has significant effect on the critical buckling load of laminated I-beam

2. Beams with wide flanges are more prone to local buckling under the loading, which decreases the overall strength of beam
3. For short beams, FSDT and CLPT overestimate the value of critical buckling load because it does not consider the local buckling effect
4. The analytical model is capable of predicting the lateral-torsional buckling load of a mono-symmetric beam when local buckling is prevented.

References

1. Mottram JT (1992) Lateral-torsional buckling of a pultruded I-beam. Composites 32:81–92
2. Kabir MJ, Sherbourne AN (1998) Optimal fiber orientation in lateral stability of laminated channel section beams. Compos Part B: Eng 29:81–87
3. Pandey MD, Kabir MZ, Sherbourne AN (1995) Flexural-torsional stability of thin-walled composite I-section beams. Compos Eng 5:321–342
4. Davalos JF, Qiao PZ, Salim HA (1997) Flexure-torsional buckling of pultruded fiber reinforced plastic composite I-beams: experimental and analytical evaluations. Compos Struct 38(1–4):241–250
5. Loughlan J (1999) The influence of bend-twist coupling on the shear buckling response of thin laminated composite plates. Thin-Walled Struct 34:97–114
6. Lee J, Lee S (2004) Flexural-torsional behavior of thin-walled composite beams. Thin-walled Struct 42:1293–1305
7. Lee J, Kim SE (2001) Flexural-torsional buckling of thin-walled I-section composites. Comput Struct 79:987–995
8. Lee J (2005) Flexural analysis of thin-walled composite beams using shear-deformable beam theory. Compos Struct 70:212–222
9. Kollar LP (2001) Flexural-torsional buckling of open section composite columns with shear deformation. Int J Solids Struct 38:7525–7541
10. Kollar LP, Springer GS (2003) Mechanics of composite materials. Cambridge University Press, Cambridge, pp 296–300
11. Lee J (2001) Center of gravity and shear center of thin-walled open-section composite beams. Compos Struct 52:255–260
12. Roberts TM, Masri HM (2003) Section properties and buckling behavior of pultruded FRP profiles. J Reinf Plast Compos 22:1305–1317
13. Allen HG, Bulson PS (1980) Background to buckling. McGraw-Hill, New York, p 492
14. Reddy JN (2003) Mechanics of composite materials. CRC Press, Boca Raton
15. Sapkas A, Kollar LP (2002) Lateral-torsional buckling of composite beams. Int J Solids Struct 39:2939–2963

Bibliography

16. Jones RM (1975) Mechanics of composite materials. McGraw-Hill, New York, pp 37–45

Performance of the FRPC Rehabilitated RC Beam-Column Joints Subjected to Cyclic Loading

Abhijit Mukherjee and Kamal Kant Jain

Abstract This paper discusses both experimental and analytical investigations for evaluation of the performance of the fiber reinforced polymer composites (FRPC) rehabilitated reinforced concrete (RC) beam-column joints subjected to cyclic loading. For experimental investigations, two types of beam-column joint specimens, with ductile and brittle reinforcement detailing are cast and investigated in this study. The joint specimens are subjected to the cyclic displacements of increasing amplitude until failure. Post failure, the joint specimens are rehabilitated using the FRPC. The rehabbed joint specimens are then subjected to the similar regime of cyclic displacements until failure. Salient details of the procedures for preparation and investigation of both control and rehabbed joint specimens are discussed in this paper. Performances of joint specimens are recorded in the form of the load-displacement plots. Comparisons between performances of control and rehabbed joint specimens highlight the efficiency of the discussed rehabilitation scheme in enhancement of strength, ductility, and deformability of the RC beam-column joints. In analytical investigations, the load-displacement relationships for both control and rehabbed joints are modeled in the form of the multi-scale models which consider stiffness degradation under cyclic loading. Accordingly, this paper also reports brief discussion on the stepwise development of the analytical models for performance of the materials; the cross-section; and that of the joints. Good agreement between experimentally observed and analytically modeled load-displacement relations facilitates validation of the analytical models, which then provides useful means for field applications of the FRPC in rehabilitation of RC beam-column joints.

Keywords Reinforced concrete · Fiber reinforced polymer composites (FRPC) · Beam-column joints · Cyclic loading · Rehabilitation

A. Mukherjee (✉) · K.K. Jain
Department of Civil Engineering, Curtin University, Bentley, Perth, WA 6102, Australia
e-mail: abhijit.mukherjee@curtin.edu.au

K.K. Jain
e-mail: kamal.jain@curtin.edu.au

1 Introduction

Hundreds of thousands of successful reinforced concrete (RC) frame structures are annually constructed worldwide, there are large numbers of them that deteriorate, or become unsafe due to changes in loading, changes in use, or changes in configuration. Occurrence of natural calamities also renders a large number of structures unusable. Failure of structures at the beam-column joints has been identified as one of the prominent causes of deficiency in RC frame structures subjected to cyclic loads. Existing literature highlights that joint failures under cyclic loads are typically caused due to lack of adequate reinforcements and their improper detailing at the joints. Strategies of joint rehabilitation have therefore drawn wide attention. Objective of the work reported in this paper is to demonstrate a rehabilitation strategy for damaged beam-column joints of representative size. Application of the fiber reinforced polymer composites (FRPC) has been considered for rehabilitation of the RC beam-column joints subjected to cyclic loads. Comprehensive discussions about associated experimental and analytical investigations have been reported respectively by Rai [1] and Jain [2]. Salient details that facilitated development of the mentioned rehabilitation strategy are discussed henceforth.

2 Experimental Investigations

Experimental investigations for assessment of the performance of FRPC rehabilitated RC beam-column joints subjected to cyclic loading were sub-divided in four stages: specimen preparation, damage infliction, rehabilitation, and tests on the rehabilitated specimens. Each of these stages are discussed henceforth.

2.1 Specimen Preparation

Schematic configuration and dimensions of the two types of the beam-column joints are shown in Fig. 1. All the specimens had identical dimensions. They had the same longitudinal reinforcements in the beams and columns. However, the spacing and the position of stirrups differed in the two sets. One set had closely spaced stirrups (75 mm, D-type) to provide adequate confinement and shear capacity. The stirrups were also provided in the columns of the core joint region. In the other set of specimens the spacing of stirrups was relatively sparse (150 mm, B-type) that would lead to brittle failure. In this case, there are no stirrups in the core joint region. The reinforcement cages were prepared taking care of the precise position of the longitudinal bars and stirrups. They were placed in steel molds and a cover of 20 mm was maintained by means of spacers. The specimens were demolded after 72 h and kept in the curing tank for 28 days. The surface dried specimens were used in testing i.e. for damage infliction.
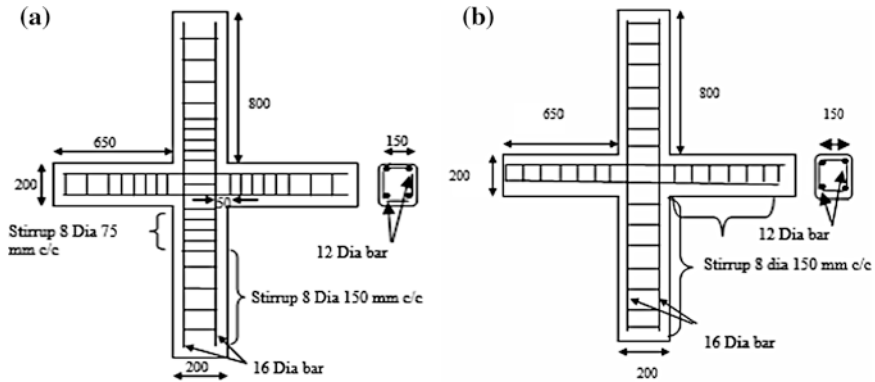
Fig. 1 Details of the test specimens: configurations and dimensions. **a** D-Type. **b** B-Type

2.2 Damage Infliction

The experimental setup for damage infliction is shown in Fig. 2. The specimen was fixed at the ends of columns and the columns were subjected to a constant axial load by means of hydraulic jacks. The magnitude of load was monitored through a load cell. The columns were loaded with 10 % of their axial capacity.

To inflict damage the joints were subjected through a predetermined displacement regime. The displacement was applied by attaching a dynamic load actuator of 500 kN capacity. The initial displacement amplitude was 2 mm and it was incremented with a step of 2 mm in each epoch until 40 mm displacement was reached (as shown in Fig. 3), thereafter steps of 5 mm were adopted until failure. Three identical displacement cycles consisted of one epoch of displacement. The accuracy of the displacement measurement was ±0.01 mm. The frequency of load was maintained at 1 cycle in 4 min.

Several displacements and strains were recorded during the experiment. The displacements were recorded by means of linear variable displacement transducers
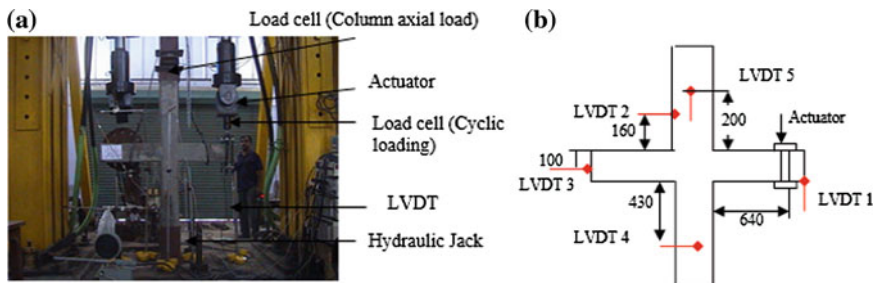
Fig. 2 Experimental setup and instrumentation for damage infliction. **a** Experimental setup. **b** Instrumentation

Fig. 3 Displacement cycles
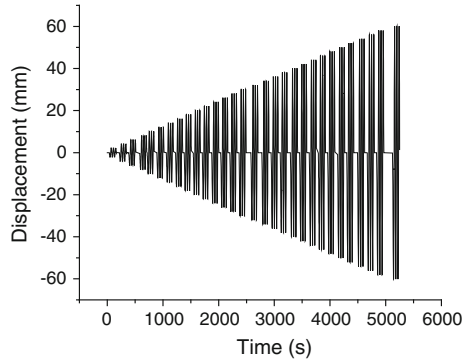
(LVDT) of travel ±150 mm. LVDT1 measured the tip displacement of the loaded beam. LVDT2 and LVDT4 measured the horizontal deformation of the centers of the columns. From these readings we can estimate the rotation of the column at the joint. LVDT3 measured the horizontal displacement of the center of the joint. If all the loads are applied vertically and the ends are restrained properly there should not be any displacement of the center in the horizontal direction. There was no appreciable displacement recorded by LVDT3. LVDT5 was placed perpendicular to the plane of the joint. This was done to ensure absence of any out-of-plane displacement of the specimen at the time of loading. The strains were measured at the critical locations. The responses were recorded online using a data acquisition system. However, the strain gages were affected at the onset of damage in the specimen. Therefore, only limited results could be recorded by the strain gages.

The cracks on the surface of the specimens were marked at the completion of each load cycle and they were traced on a grid paper. Widths and paths of the cracks were noted after each cycle. Developed crack patterns are presented in Sect. 4 of this manuscript. Failed specimens were then rehabilitated using the CFRP composites, details of the rehabilitation scheme are discussed henceforth.

2.3 Rehabilitation

For rehabilitation, damaged sections of the specimens were rebuilt using fresh concrete, an epoxy mortar and a low viscosity grout. The damaged specimens were rebuilt using the following steps:

1. Loose concrete was removed and the surfaces were cleaned of dirt.
2. Areas where almost whole section had severe spalling were rebuilt with fresh concrete. Formwork was placed in the affected region and free flowing concrete was poured.
3. Areas where there were large cracks but the concrete did not spall totally; epoxy mortar (one part epoxy with 5 parts quartz sand) was used to replace the lost concrete.

4. Cracks of less than 1 mm width were filled with an epoxy resin of viscosity 100 cps by pressure grouting.
5. Concrete surface was smoothened by removing sharp protrusions (where the FRP is to be overlaid). Thixotropic epoxy filler was used in filling small dents.
6. The corners were rounded off to a minimum radius of 15 mm and then the surfaces were dusted using dry cloth and then cleaned with acetone.

No additional steel reinforcement was provided to compensate for the yielded and ruptured reinforcement. The FRP composite was used in two forms—composite plates (CP laminates) and composite sheets (CS wraps). Lack of confinement and shear capacity of the joints were compensated by the CS wraps on both beams and columns (extended onto the joints). Precured unidirectional carbon fiber composite plates of 50 mm width that have one surface roughened for adhesive bonding with concrete was used as CP. It was used on both faces of the beam to compensate for the lost longitudinal reinforcement. On the other hand, the CS was used as transverse reinforcement at the time of rehabilitation by wrapping them around the beams and column sections.

The wraps need to be flexible and therefore are used in uncured form. The FRP was applied in the following steps (Fig. 4):

1. CP attachment on beam: The CP had been used on the top and bottom surfaces of the beams as tensile reinforcements. To anchor the CP at the joint, an incision of 5 mm thickness and 60 mm width was made in the column at the beam column interface. The groove was filled up with the adhesive and the CP was inserted into the groove. The epoxy was allowed to cure to obtain an end anchor.
2. CS attachment: The CS was used for the rest of the rehabilitation. The CS was adhesively bonded to the faces of the column and the beam, with fiber direction along the axis of the elements.
3. Wrapping beam and column with CS: Then beam and the column were wrapped with transverse CS to provide additional confinement.
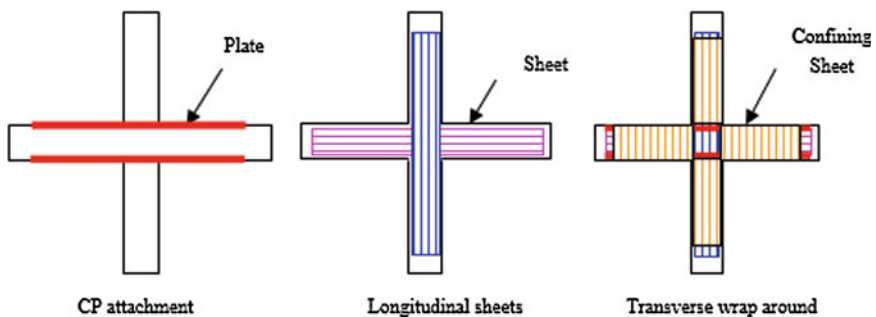
Fig. 4 Sequence of FRP application for rehabilitation

2.4 Tests on the Rehabilitated Specimens

The experimental setup and procedure described in Sect. 2.2 was followed for testing of the rehabbed joint specimens under cyclic loads. The load-deflection characteristics of the joints were observed. Performances of the both control and rehabilitated joint specimens are discussed in Sect. 4.1.

3 Analytical Investigations

Analytical investigations facilitated development of the description models for the performance (load-displacement characteristic) of both control and rehabilitated beam-column joints. Development of the descriptive analytical models was sub-divided in: (1) Material models; (2) Cross-section model; and (3) Structural model. Each of these models are discussed henceforth.

3.1 Material Models

Constitutive stress-strain relations of the materials i.e. concrete, steel reinforcements and CFRP wraps and strips are very important in context of the load-displacement characteristic of the RC beam-column joints under cyclic loads. Therefore, material model are defined as follows:

3.1.1 Concrete

In context of this study, constitutive relation of concrete must consider the effect of confinement provided by steel and composites. Therefore, theoretical model to quantify confinement of concrete in bending compression reported by Mukherjee et al. [3] was adopted in this work. Accordingly, the confinement factor (C_f) is defined as a function of the relative stiffness of the confining material and the concrete core radius:

$$C_f = \left(\frac{E_f t_f + E_s t_s}{E_0 r} \right)^{0.5} \tag{1}$$

where, E_f = Modulus of elasticity of fiber; E_s = Modulus of elasticity of steel; E_0 = Initial modulus of elasticity of concrete; t_f = Thickness of the FRP wrap; t_s = Effective thickness of confining steel reinforcement; and r = Effective radius of concrete core.

The stress-strain relation depends on the effective confinement, because limiting strain (ε_{lim}) is defined as:

$$\varepsilon_{\text{lim}} = 0.002 \times \left(1 + 5C_f\right) \tag{2}$$

The stress-strain relation is defined as:

$$\sigma_c = E_c\varepsilon = \left[\left(1 - \frac{\varepsilon}{\varepsilon_{\text{lim}}}\right)E_0 + \frac{\varepsilon f_{ck}}{\varepsilon_{\text{lim}}^2}\right]\varepsilon \tag{3}$$

where, E_c = Secant modulus of concrete; f_{ck} = Characteristic strength of concrete.

3.1.2 Reinforcement Steel

The steel bars for both longitudinal and transverse reinforcement was tested for tensile capacity and had a yield stress of 500 MPa. Steel bars were extracted after infliction of damage from locations where gages had indicated strains beyond the yield point and were then tested on the universal testing machine. Typical stress-strain relationships for both fresh and yielded steel are presented in Fig. 5. Analytically, these relationships are modeled separately for: (1) pre-yield; (2) yield zone; and (3) post-yield responses.

3.1.3 FRP

The FRP wraps and strips were tested for their strength properties as per American Society for Testing and Materials (ASTM) standard test procedure. The FRPs exhibit linear elastic stress-strain relationship. Detailed properties are presented in Table 1.

Fig. 5 Stress-strain relation for fresh and yielded steel
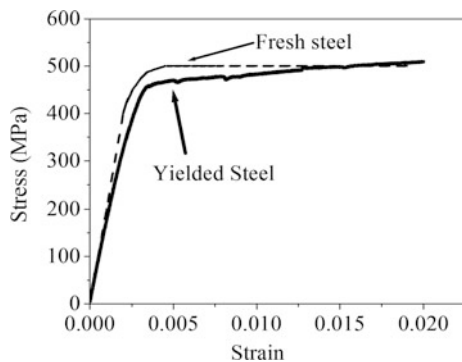
Table 1 Properties of fiber reinforced polymer composites (FRPC)

Material	Thickness (mm)	Tensile strength (GPa)	Tensile modulus (GPa)	Ultimate strain
Carbon wrap	0.23	3.79	230	0.017
Carbon plate	1.4	2.79	155.1	0.018

3.2 Cross-Sectional Model

Material constitutive models were then used for the development of the cross-sectional model in the form of $M-\phi$ relationship. Following assumptions were made for development of the $M-\phi$ relation:

1. Euler-Bernoulli hypothesis, i.e. plane sections before bending remain plane after bending;
2. Effect of concrete in tension is neglected;
3. Perfect bonding between all materials, i.e. no bar slippage occurs;
4. Displacements are small; and
5. Properties of steel in tension and compression are identical.

For a given curvature, the magnitude of the strains in concrete (ε_c), compression steel (ε_{sc}), tension steel (ε_{st}), compression FRP (ε_{cf}), and tension FRP (ε_{tf}) are determined from the strain compatibility relations.

Depth of neutral axis (X_u, from top of compression surface) for a given curvature is obtained by imposing the condition of equilibrium over the section. Compression force (C) and tension force (T) are obtained as follows:

$$C = \sigma_{sc}A_{sc} + b\int_0^{X_u} \sigma_c dx + \sigma_{fc}A_{fc} \qquad (4)$$

$$T = \sigma_{st}A_{st} + \sigma_{tf}A_{tf} \qquad (5)$$

where, σ_{sc}, σ_{fc}, and σ_c are stresses respectively in compression steel, compression laminate, and concrete in compression; and A_{sc} and A_{fc} represent cross-sectional areas of compression steel and compression FRP respectively. σ_{st}, σ_{tf}, are stresses respectively in tension steel and tension laminate; and A_{st} and A_{ft} represent the cross-sectional area of tension steel and tension FRP, respectively.

After obtaining the depth of neutral axis, forces in concrete, FRP and steel are determined using material constitutive relationships. The moments of these forces about the neutral axis is obtained by the multiplication of forces and the corresponding lever arms. Resisting moment (M) is then obtained by imposing moment equilibrium on the section. This procedure is adopted to obtain the $M-\varphi$ relationship for the reinforced concrete sections. Equations 4 and 5 are initially solved iteratively with a small value of φ and corresponding M. Subsequently, φ is

increased with small steps (i.e. $\Delta\varphi$ in the range of 10^{-7} rad/m), till maximum allowable strain in concrete is reached. The gradient of the $M-\varphi$ relation gives us the elastic tangent EI that includes all the section properties.

3.3 Structural Model

The results of the cross-section model (Moment and EI values) have been used in the structural model. Total displacement of the beam tip in a joint, due to a static load consists (is sum) of the displacements from flexural and shear deformations of the beam, axial deformations of the column, and deformations due to the rotation of the column. In this context, following additional assumption are made for development of the structural model:

1. Displacements are small, i.e. no geometric nonlinearity;
2. Displacement due to column axial deformation is negligible;
3. Bond slip manifests through additional reduction in EI;
4. Joint deformation manifests through additional reduction in GA; and
5. Both EI and GA reduce exponentially in the damaged zone.

Incremental loads corresponding to the incremental displacements (as used in experimental investigations) are obtained using an iterative method. Mathematically:

$$\Delta P_i = [k_i]\,\Delta\delta_i \tag{6}$$

where, ΔP_i = Increment load for ith cycle; $\Delta\delta_i$ = Incremental displacement for ith cycle; and $[k_i]$ = Stiffness matrix for ith cycle. Total load and displacement at the beam tip, after ith cycle are computed respectively as; $P_i = P_{i-1} + \Delta P_i$ and $\delta_i = \delta_{i-1} + \Delta\delta_i$.

A cohesive damage model was developed to obtain the stiffness matrix $[k_i]$ and hence to define the load-displacement relation. Detailed derivation of the $[k_i]$ has been published by the authors [4], and following relation has been obtained:

$$\Delta P_i = \frac{\Delta\delta_i}{\left[f(L_d, EI_y, EI, \Delta P) + \frac{(L-L_d)^3}{3EI_y} + \frac{1}{K_{s_i}} + \frac{L_2 L^2}{12EI_y} \right]} \tag{7}$$

where, L = Length of beam; L_d = Length of plastic hinge in beam; L_2 = Length of column; EI_y = Flexural rigidity (elastic); EI = Flexural rigidity at joint-beam interface; K_{si} = Shear Stiffness of beam for ith step.

Cohesive damage model for static loads has then been extended for cyclic loading by multiplying a softening factor (R_i). This factor considers energy dissipation and loss of stiffness in previous load cycles, i.e. effect of load-displacement

history. Henceforth, the load displacement relation for concrete beam-column joints subjected to cyclic loads is defined as:

$$\Delta P_i = R_i * [k_i] * \Delta \delta_i \tag{8}$$

A semi-analytical expression has been developed for R_i. The softening factor depends on parameters such as load-displacement history, number of load cycles completed, displacement increments and confinement.

$$R_i = \exp\left\{-C_m * N_c * \left(1 + C_h^2\right)\right\} \tag{9}$$

where, R_i = Softening factor; C_m = Empirical fragmentation factor; N_c = Number of completed displacement cycles; C_h = Displacement history factor = $d/(d_h + \Delta d)$. Here, Δd = Incremental displacement in the cycle; d = Total displacement in the present cycle; and d_h = Peak displacement in history.

Equation 8 provides analytical tool for estimation of the load-displacement characteristic of the beam-column joint. Analytical results for both control and rehabilitated joints are discussed in Sect. 4.2.

4 Performances of the Control and Rehabilitated Joints

Performance of the control and rehabilitated joints are discussed henceforth with particular focus on load-displacement characteristic. Results obtained from both experimental and analytical investigations are discussed.

4.1 Experimental Results

4.1.1 Control Joint Specimens

The hysteresis of the ductile and the brittle joints for 10 % column compression is presented in Fig. 6.

It is clear from the hysteretic loops that although the peak load in both the specimens was comparable, D-type specimens show gradual decrease in stiffness, while B-type specimens show sudden decrease in stiffness after reaching the peak value. To compare the performance of the two specimen types, the envelopes of the two load-displacement graphs are plotted in Fig. 7. The ductile and the brittle specimens behave quite similarly until the yield. Post-yield, while the brittle specimen degrades rapidly the ductile specimen retains a large proportion of its strength leading to a graceful failure.

To understand the improved post-yield behavior the history of appearance of cracks in the two specimens is studied (Fig. 8).
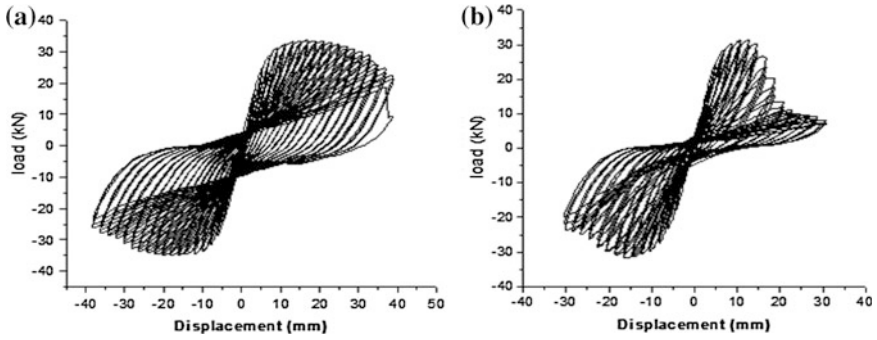
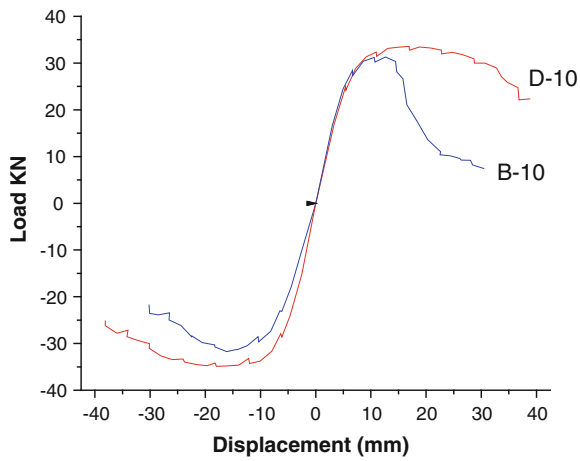**Fig. 6** Load-displacement curves for ductile and brittle specimens. **a** D-10. **b** B-10

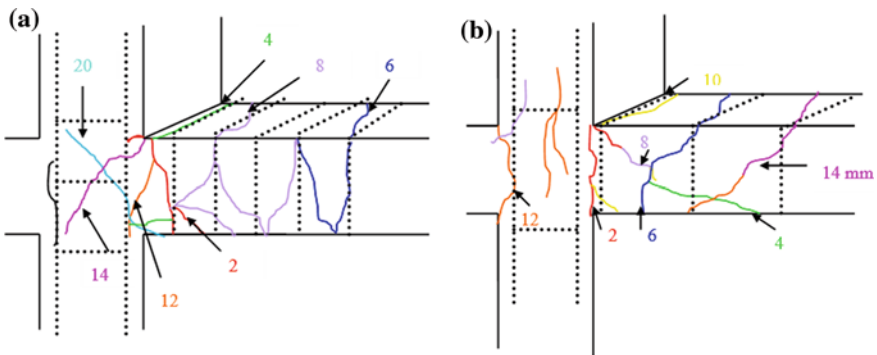**Fig. 7** Envelope curves for D and B type specimens

Fig. 8 Damage history of D and B type specimens. **a** D-type. **b** B-type

In Fig. 8, the position of reinforcements is marked in dotted lines. The first link in the beam in the D-type specimens was at 50 mm from the column longitudinal reinforcement and at 75 mm spacing thereafter. In B-type specimens, the first link was at the face of the column and the spacing was 150 mm. Another notable difference is that, in the D-type joint there is one column link at the center of the joint while it is absent in the B-type joint. In Fig. 8, the locations of the links serve as reference lines for mapping the cracks. The differently colored solid lines indicate the paths of the cracks and the associated number indicates the level of tip displacement at which the crack appeared. It may be noted that the first crack appeared at the face of the column at 2 mm tip displacement in both samples. This is the tension crack in concrete. Therefore, at this displacement level the concrete under tension transferred the entire force on to the tensile reinforcement. Thereafter, the main difference in the two specimens was the number and inclination of the cracks. The cracks were mainly confined in the compartments formed by the successive links. In the D-type samples the shear cracks formed at 45°. However, they got deflected along the reinforcement after reaching the links. There was little bridging of the cracks by the links. The links, in all probability, wouldn't have yielded at that time. As a result, the length and density of cracks were much higher in D-type specimens. The crack deflection mechanism renders toughness to the joint. Understandably, the dissipation of energy in the D-type specimens would be higher. In the B-type specimens the angle of cracks was approximately 45°. Due to the absence of shear links in the path of the crack it split the space between the two links diagonally. This demonstrates the paramount importance of spacing of stirrups in the joint behavior.

The initial cracking was restricted in the arm of the beam outside the joint area. At 12 mm tip deflection the cracks started developing inside the joint area. Therefore, only the post-yield behavior was influenced by the joint cracks. There was a major difference between the D-type and B-type specimens in the cracking inside the joint area. In D-type specimens, the cracks developed diagonally indicating shear deformation in the joint. In B-type specimens, on the other hand, vertical tension cracks started developing both at the center of the joint and at the distant face of the column. This indicates reduction in bond between the reinforcement and concrete. The presence of the central link in the D-type column made a major difference at this phase. The central link ensured a negligible strain along itself and therefore, it impeded tension cracks. The loss of bond in the B-type specimens resulted in rapid stiffness degradation. This is borne out by the remarkably narrower waistline of the hysteresis plot of the B-type specimen (Fig. 6b). The pinching of the hysteresis graph is a testimony of bond slip in the joint.

Ability of the structure to survive during an earthquake depends to a large extent on its capability to dissipate the input energy. An estimate of the hysteretic damping can be found by the area enclosed in the load-displacement hysteresis loops. It may be noted that a wider loop (i.e. a large difference in ordinates in the ascending and the descending paths) would signify higher hysteretic damping. Cumulative energy dissipated was calculated by summing up the energy dissipated in consecutive loops throughout the test. The energy dissipation curves for D-type and B-type specimens are shown in Fig. 9. Stepped nature of the curves is due to the repetition

Fig. 9 Energy dissipation curves for ductile and brittle specimens
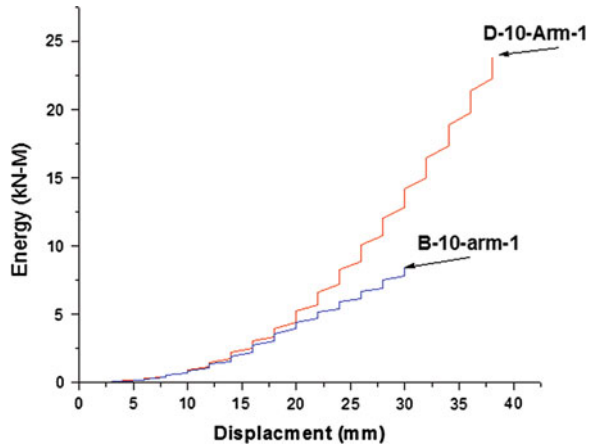
of the same displacement level three times in each load epoch. It indicates that the incremental damage, and therefore energy dissipation of energy, takes place in the first cycle of the epoch. There is no significant energy dissipation in the following cycles of the same epoch. The D-type joint exhibits much higher dissipation of energy than the B-type joint.

4.1.2 Rehabilitated Joint Specimens

The damage process in the case of rehabbed specimens was less visual due to the CS wrap on the potential damage zone. The wrapped specimens did not show any damage until an advanced stage of deformation. A crack across the depth of the beam at the face of the column had appeared and increased in width along with the increase in the deformation. A small quantity of fine cement powder escaped from the crack at each epoch of deformation. After the termination of the loading the CS wraps were removed and condition of the concrete was examined for damages.

The load-deflection hysteresis plots for rehabilitated specimens have been presented in Fig. 10. These graphs may be compared with the plots in Fig. 6 to evaluate the performance of the rehabbed joints.

Although it is clear from the hysteresis plots that both the peak load and the peak deformation have increased in the rehabbed specimens it is difficult to compare the plots. To maintain clarity we shall compare the envelope graphs that are derived from the hysteresis plots.

4.1.3 Control Versus Rehabbed

The envelope graphs of the control and rehabbed specimens have been presented in Fig. 11. It is clear that both the ductile and brittle specimens had gained in strength
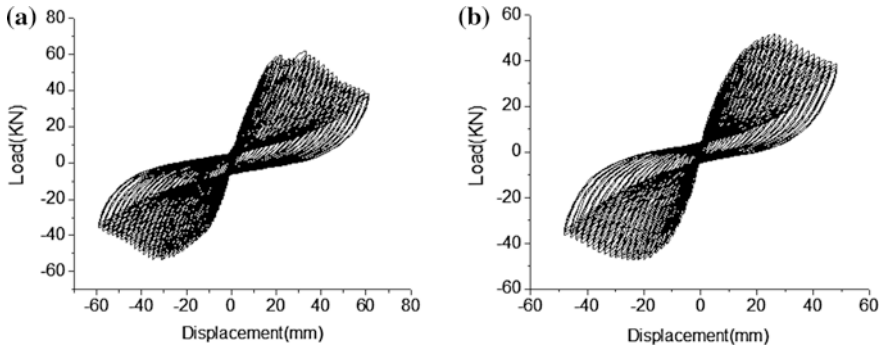
Fig. 10 Load-displacement hysteresis plots for rehabilitated specimens. **a** D-T-0. **b** B-T-0

Fig. 11 Envelope curve for control and rehabbed specimens
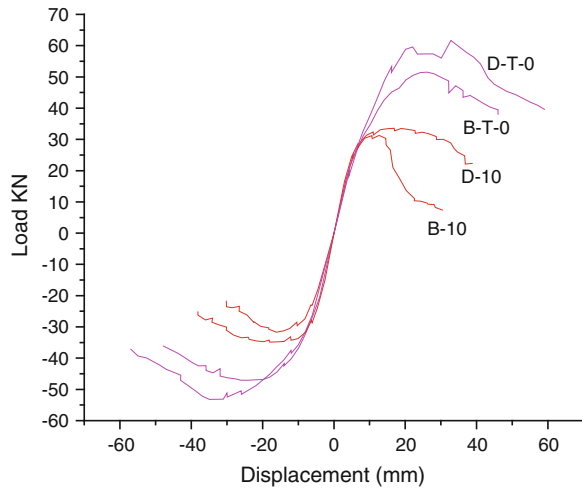
and ductility through the rehabilitation. The rapid loss of stiffness in the brittle specimens could be avoided totally. The rehabbed brittle specimen had much higher peak load and deformation than the control ductile specimen. There is improvement in both yield and peak loads and final displacements in rehabbed specimens. This demonstrates that deficient joints can be effectively rehabbed by the proposed technique.

The energy dissipation graphs for the control and rehabbed specimens, both brittle and ductile, have been presented in Fig. 12. The energy dissipation of the rehabbed specimens is far higher than that in the control specimens. The rehabbed brittle specimens had higher energy dissipation than even the control ductile specimens. Hence, it can be concluded that the proposed rehabilitation technique can remedy all the deficiencies in the brittle specimens.

Fig. 12 Energy dissipation curves for control and rehabbed specimens
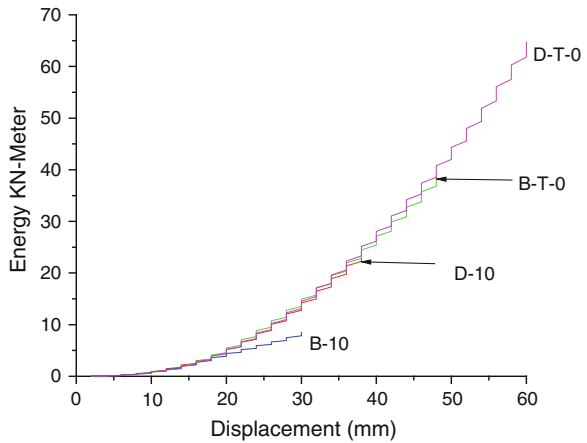
4.1.4 Failure Modes

Unlike the control specimens, the progression of damage in the rehabilitated specimens was not visible, except occasional discoloration of the adhesive, due to the CS wrapping on the specimens. The wrapping was cut open after the tests to observe the failure mode (Fig. 13).

The shear cracks that occurred in the control specimens were absent in the rehabbed ones. The spalling and subsequent formation of hinge did not occur in the rehabbed specimens. Hence, it can be concluded that the wrapping was able to avoid both modes of brittle failures- shear and loss of confinement; the two most common occurrences in the structures that suffer an earthquake. The damage in the rehabbed specimens was due to wide cracks at the column faces. Clearly, this is a bending failure and therefore, the rehabbed joints exhibited ductility and higher energy dissipation.

Fig. 13 Damages in the rehabilitated specimens
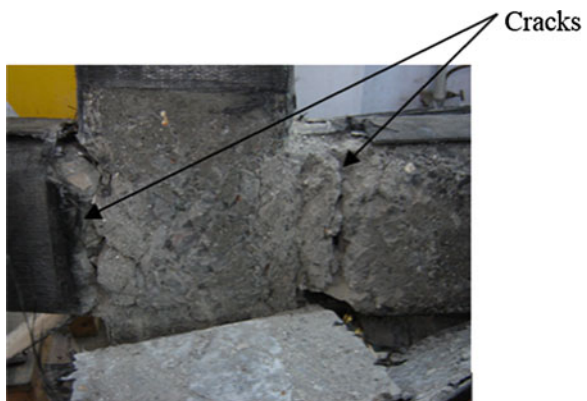
4.2 Analytical Results

Analytical investigation described progressive development of the material, cross-section, and structural models. Analytical results obtained in form of the cyclic load displacement curves for both control and rehabilitated specimens are presented in Fig. 14a–d, along with the experimental results. To maintain clarity, comparisons are made between envelope graphs that are derived from the hysteresis plots. Figure 15a–d present the corresponding envelop curves.

In Figs. 14 and 15, the solid line plots represent the experimental results, while dotted lines represent obtained analytical results.

From Figs. 14 and 15, it can be observed that the agreement between analytical and experimental results is very good.

Figure 15a shows asymmetry in the experimental results in the positive and negative zones for control brittle specimens. This happened due to premature cracking and spalling of concrete in the positive zone, fracture of one of the longitudinal reinforcing bars was eventually observed. Clearly, the brittle specimen can behave in somewhat unpredictable manner. It is inferred that analytical model provides reasonably good prediction for all other parts of the experimental curve, but the unloading of post reinforcement fracture of the brittle specimen is not captured.
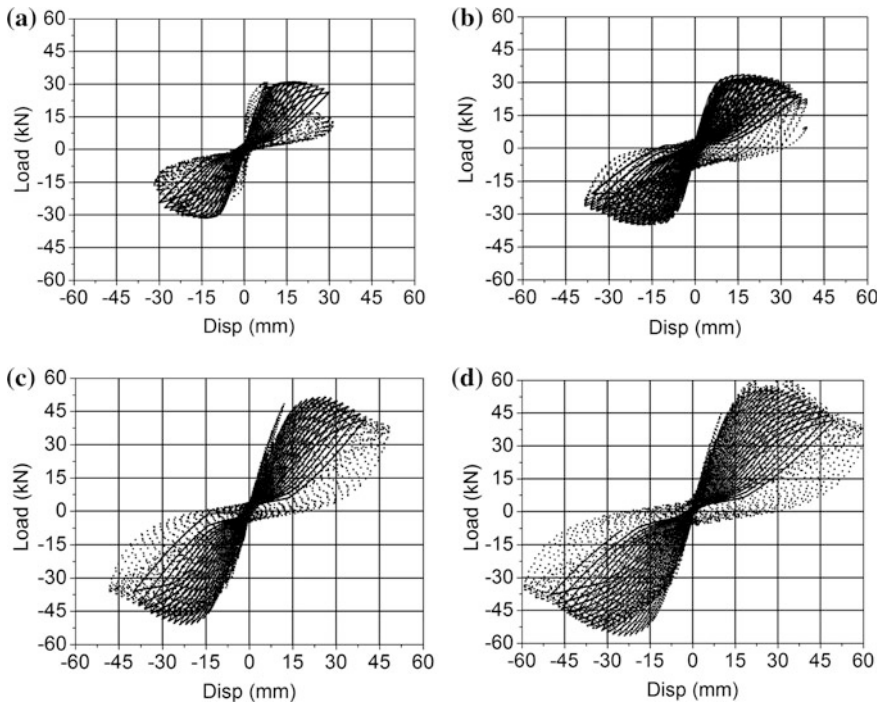
Fig. 14 Cyclic load-displacement plots for control and rehabilitated specimens. **a** Control brittle (B-10). **b** Control ductile (D-10). **c** Rehabilitated brittle (B-10). **d** Rehabilitated ductile (D-T-0)
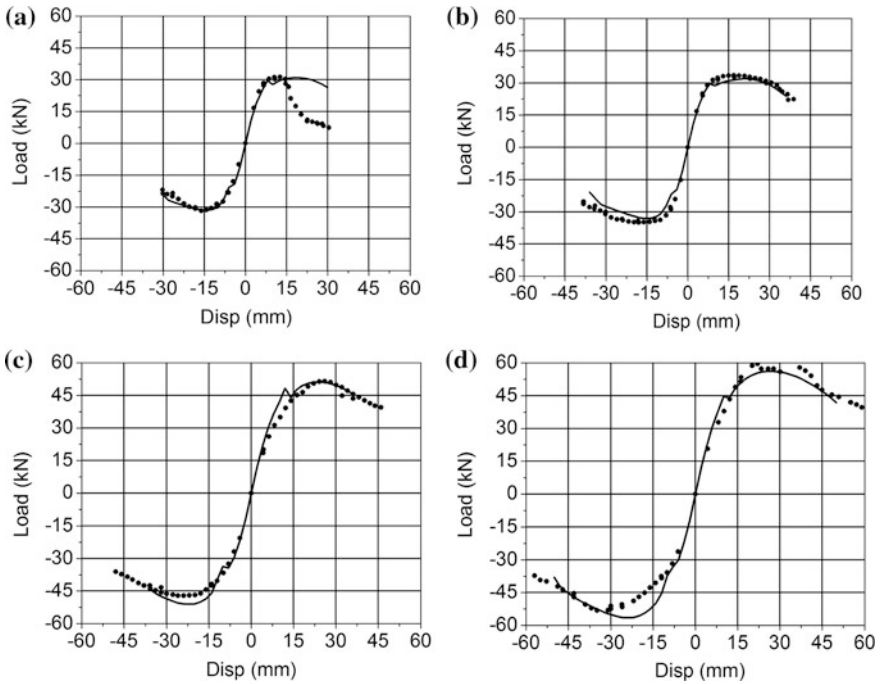
Fig. 15 Envelop load-displacement curves. **a** Control brittle (B-10). **b** Control ductile (D-10). **c** Rehabilitated brittle (B-10). **d** Rehabilitated ductile (D-T-0)

Comparison between envelope curves for control and rehabilitated brittle specimens (Fig. 15a, c) demonstrates that brittle joints can be effectively rehabilitated by the FRP. The unpredictable behavior of the brittle joint can also be controlled through the FRP wrapping. Both the peak load and ultimate displacement have increased significantly through the rehabilitation. Figure 15b, d show that the ductile joints can also be very effectively rehabilitated by the presented technique. The peak load and peak displacement both increased considerably through application of the FPR composites. Thus, the efficacy of the proposed system for both brittle and ductile joints is established.

Figure 14 highlights that the hysteresis plots predicted by the analytical model are slightly lower than that experimentally observed. Thus, the model is conservative and it can be used for design of both control and rehabilitated reinforcement concrete joints.

5 Conclusions

This paper describes the performance of RC joints, both control and rehabilitated, under cyclic loading. Salient details of the experimental and analytical investigations have been reported. Parameters for design of the rehabilitated joints with the

FRP composites have been investigated and obtained results have been reported. From the reported results the following conclusions have been drawn:

1. The beam-column joints with closely spaced shear links (ductile) have superior post-yield behavior than the joints with sparse links (brittle) due to better confinement of concrete and crack deflection mechanism. The longer and denser shear cracks in the ductile joints lead to higher energy dissipation.
2. The loss of capacity in strength and energy dissipation in the damaged ductile specimens is much higher than that in the damaged brittle specimens. This is due to more pronounced bond slip in the damaged ductile specimens than the control ones.
3. The links in the core area of ductile joints prevent bond slip and therefore, increases the hysteretic damping. The pattern of cracking in the core area of the joints is different for the ductile and the brittle joints.
4. The lack of confinement and shear capacity of the joints lead to brittle failure. The carbon fiber sheets wrapped around the members dramatically improves the ductility and energy absorption of the joint.
5. The FRP rehabilitation is effective in improving both strength and ductility of the RC joints. In the present experiments, the ultimate load went up by 100 % and ultimate displacement by 50 %.
6. Analytical results agree with the experimental observations that rehabilitation using the FRP composites improves load carrying capacity of the RC beam-column joints significantly. Ductile behavior of the system also shows considerable improvement as depicted by higher post-yield load carrying capacity.
7. Discussed analytical model, that considers both cohesive damage and softening due to cyclic loads and energy dissipation, is able to capture the softening behavior of joints in the post-yield zone.

Conclusively, the reported investigations can be used beneficially for design of the structural rehabilitation with targeted performance parameters such as initial stiffness, yield point, ultimate deformation and ultimate load.

References

1. Rai GL (2007) Short-term and long-term performance of externally prestressed RC beams and joints. Ph.D. thesis, Department of Civil Engineering, Indian Institute of Technology (IIT) Bombay
2. Jain KK (2007) Modeling of FRC rehabilitated reinforced concrete joints under cyclic loads. Dual degree thesis, Department of Civil Engineering, Indian Institute of Technology (IIT) Bombay
3. Mukherjee A, Bagadi SP, Rai GL (2009) Semi-analytical modeling of concrete beams rehabilitated with externally prestressed composites. J Compos Constr, ASCE 13(2):74–81
4. Mukherjee A, Jain KK (2013) A semi-analytical model of cyclic behavior of reinforced concrete joints rehabilitated with FRP. Adv Struct Eng 16(12):2019–2034

Is GFRP Rebar a Potential Replacement for Steel Reinforcement in Concrete Structures?

P. Gandhi, D.M. Pukazhendhi, S. Vishnuvardhan, M. Saravanan and G. Raghava

Abstract The use of Glass Fibre Reinforced Plastic (GFRP) rebars as a potential replacement for steel reinforcement has raised quite a bit of controversy among the professionals and engineers engaged in the construction industry. Divergent views have been opined by the professionals for its usage in civil engineering structures. Even though, the GFRP rebar has some advantages with regard to corrosion, its usage in the construction industry is still a big question mark due to its low modulus of elasticity and serviceability aspects towards construction of structural elements. In this background, experimental investigations have been taken up at the CSIR—Structural Engineering Research Centre, Chennai to study the static and fatigue behavior of concrete beams reinforced with GFRP and Thermo Mechanically Treated (TMT) bars. Concrete beams with GFRP bars of dimensions 100 mm × 200 mm × 1500 mm have been subjected to static monotonic loading to study the flexural behaviour and companion concrete beams of same dimensions with TMT bars have also been investigated. The investigations have revealed that the concrete beams with GFRP bars resulted in unacceptable deflections and crack widths, with regard to serviceability, compared to the companion beams with TMT bars of same amount of area of reinforcement. The fatigue studies conducted on concrete beams, at four different load ranges, with GFRP bars were also not encouraging. This paper presents the details of experimental investigations and the results.

Keywords Flexural behavior · GFRP bar · Life cycle cost · Reinforced concrete · TMT bar

P. Gandhi (✉) · D.M. Pukazhendhi · S. Vishnuvardhan · M. Saravanan · G. Raghava
CSIR-Structural Engineering Research Centre (SERC), Council of Scientific and Industrial Research, CSIR Campus, Taramani, Chennai 600113, India
e-mail: pgandhi@serc.res.in

1 Introduction

Fibre-reinforced plastic rebars are currently entering the market as a replacement for steel reinforcement in concrete structures. There are many existing methods available for preventing, delaying or repairing the deterioration of concrete structures due to corrosion of reinforcing steel. However, these methods are costly and their long time effectiveness is not assured. A better and a more innovative solution to the corrosion problem in structures is to eliminate one of the contributing ingredients (i.e.) steel. This can be achieved by replacing the steel bars with fibre reinforced polymer bars. The civil engineering community's progress towards comfort with FRP rebar is very slow, but it has not discouraged the pursuit of new approaches to its manufacture that could make the composite rebar a much more attractive alternative to steel. Although the initial cost of composite rebar is generally higher than standard steel rebar, however when considered on a Life Cycle Cost (LCC) basis, it can be quite economical for structures that typically require frequent repair and maintenance provided serviceability criteria is satisfied. For all these reasons and more, composite rebar has slowly begun to gain share in the civil engineering market. If the composite rebar can add a price advantage and serviceability requirements to its other benefits, then it will stand a much better chance of being specified in higher volume. It is a challenge and an opportunity for the whole composites industry. Hence, investigations on GFRP bars are being carried out across the globe as a substitute for steel reinforcement. However, their extensive use in reinforced concrete structural engineering has been very limited, due to lack of research data and design specifications [1–8].

In this background, experimental investigations have been take up at the CSIR—Structural Engineering Research Centre, Chennai to study the static behaviour of concrete beams reinforced with GFRP and TMT bars and fatigue behaviour of concrete beams reinforced with GFRP bars. Concrete beams with GFRP bars of dimensions 100 mm × 200 mm × 1500 mm were subjected to static monotonic loading to study the flexural behaviour and companion concrete beams of same dimensions with TMT bars were also investigated. Fatigue studies were also carried out on concrete beams reinforced with GFRP bars of the same dimensions. The static and fatigue experiments were carried out using a ±100 kN servo hydraulic actuator. During the static and fatigue studies the various data obtained include the load, displacement, strains in the reinforcement bars and on the concrete surface, crack widths, deflections at critical locations and the rotation of the beams. This paper investigates the flexural behaviour of concrete beams reinforced with both GFRP and TMT rebars under static monotonic loading. The experimental investigations also include fatigue studies on concrete beams with GFRP bars at four different load ranges.

2 Details of the Experimental Investigations

2.1 Test Specimens

The size of the beams used for both static and fatigue studies is 100 mm × 200 mm × 1500 mm. Totally fifteen numbers of beam specimens have been used for the experimental investigations. Out of the fifteen concrete beams, three concrete beams were reinforced with two numbers of 10 mm diameter TMT bars as main reinforcement and hanger bars, twelve concrete beams were reinforced with two numbers of 10 mm diameter GFRP bars as main reinforcement and hanger bars. Conventional steel stirrups of 8 mm diameter TMT bars were used at a spacing of 125 mm centre to centre on the shear span. Bottom and top concrete cover of 25 mm was maintained for all the beams. A view of longitudinal section and cross section of a typical beam specimen is shown in Figs. 1 and 2.
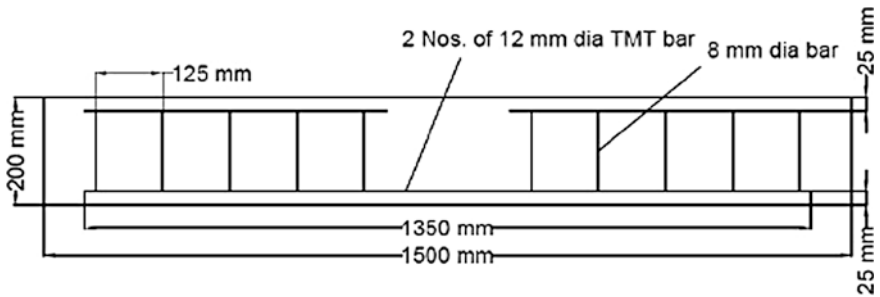
Fig. 1 A view of longitudinal cross section of the beam

Fig. 2 A view of cross section of the beam
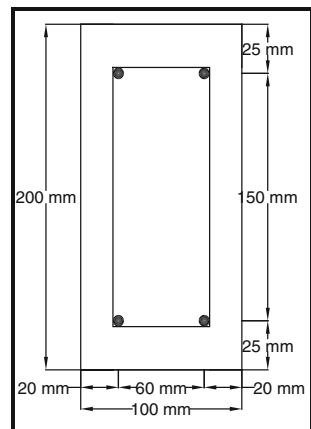
2.2 Material Properties

2.2.1 Concrete

All the test specimens were cast using a design concrete mix with a target 28-days concrete compressive strength of 30 MPa. The type of cement used was 53 grade Ordinary Portland Cement (OPC). The mix proportion designed as per ACI 211-4R-08 was 1:2.68:3.76 with water cement ratio of 0.55 [9]. All the beams were cast and kept in a curing tank for 28 days. The average compressive strength, split tensile strength and flexural strength after 28 days were 39.6, 3.7 and 5.2 MPa [10].

2.2.2 Reinforcement

Two types of reinforcing bars were used in this study: sand-coated GFRP rods and Fe 500 grade TMT bars. The GFRP bars made of continuous E-glass fibers are manufactured by pultrusion process. A view of the GFRP reinforcement grills is shown in Fig. 3. Table 1 summarizes the mechanical properties of the materials used in the experimental studies.

2.3 Loading Arrangement

The beams of 1,500 mm length were simply supported with an effective span of 1,350 mm. Two point loads were applied at a distance of 225 mm from the centre of the beams to get pure bending at the middle third portion of the beams. The loading arrangement is shown in Fig. 4. A distribution beam was fixed to the bottom end of

Fig. 3 A view of GFRP reinforcement grills

Table 1 Mechanical properties of the GFRP and TMT reinforcing bars used in the study

Bar type	Bar diameter (mm)	Bar area (mm^2)	Modulus of elasticity (GPa)	Ultimate tensile strength (MPa)
Fe 500 Gr. TMT	10	78.5	190	670
GFRP	10	78.5	44	641
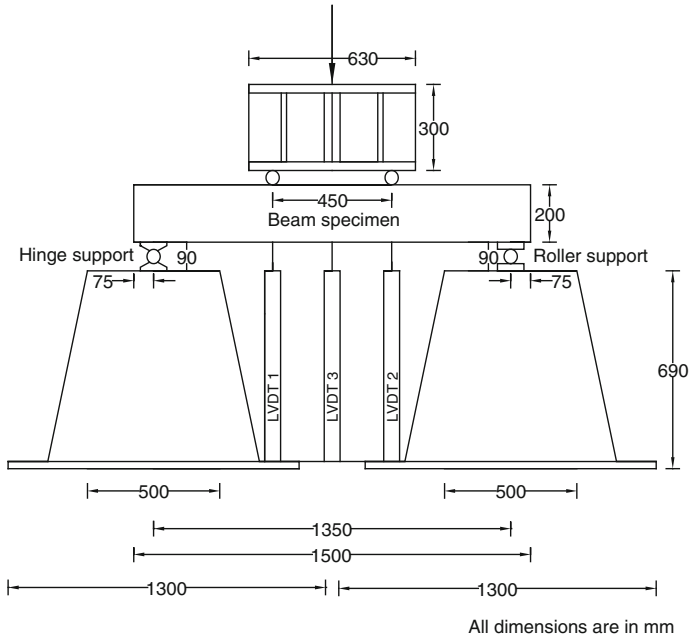
Fig. 4 Schematic view of loading arrangement

the actuator for application of two point loads on the concrete beam specimens. The concrete beams were simply supported on heavy duty steel pedastals which in turn were anchored to the strong floor of the laboratory.

2.4 Experimental Set-up

The beams were simply supported with an effective span of 1,350 mm. To measure deflection of the beams during testing, Linear Variable Differential Transformers (LVDT) were placed one at the centre of the beams and two numbers at middle third points of the effective span of the beams. For all the concrete beams, three strain gauges were fixed on the surface of concrete beams in tension zone and one strain gauge in compression zone of gauge length 60 mm to measure the variation of strain during static/fatigue loading. The rate of loading was 0.02 mm/s. Figure 5 shows a view of the experimental test set up used for static/fatigue tests.

Fig. 5 Experimental test set up for static/fatigue tests

3 Test Results and Observations

3.1 General Observations

Three numbers of concrete beams reinforced with GFRP bars and three numbers of concrete beams reinforced with TMT bars were subjected to static monotonic loading to study their flexural behavior. Cracks were initiated on the tension face of the beams and propagated towards the compression face with the increase in load. The concrete beams reinforced with GFRP bars failed suddenly due to snapping of the GFRP bars whereas the concrete beams reinforced with TMT bars failed gradually by crushing of concrete in the compression zone. The various data obtained during the static monotonic tests on three beams reinforced with GFRP bars and three beams with TMT bars are given in Table 2.

Table 2 Results of static monotonic tests

Beam designation	Crack initiation load (kN)	Ultimate load (kN)	Bending moment (kN-m)	Deflection (mm)	Tensile strain (micro strain)[a]
GFRP-1S	12.1	63.5	14.3	21.3	12,974
GFRP-2S	12.0	59.3	13.3	21.2	16,391
GFRP-3S	10.1	55.0	12.4	19.6	19,643
TMT-1S	22.0	72.1	16.2	18.3	31,026
TMT-2S	18.0	58.3	13.3	25.5	31,667
TMT-3S	20.0	57.1	12.8	14.4	25,442

No. 1, 2 and 3 denotes the beam designation number

S denotes static test

[a] in the reinforcing bar

3.2 Behaviour of Concrete Beams Under Static Flexural Loading

The performance of the GFRP and TMT reinforced concrete beams were analyzed using various parameters like deflection, strain variation in the reinforcement as well as on the concrete surface, etc. The deflection at mid span of the beams at ultimate load is given in Table 2. Figure 6 shows load versus deflection curves during the static monotonic loading for concrete beams reinforced with GFRP and TMT bars. The load carrying capacity of the beams along with the corresponding bending moment are also given in Table 2. The average value of crack initiation load for the beams reinforced with GFRP and TMT bars was 11.4 and 20 kN respectively. As can be seen from the table, the average value of ultimate load for beams reinforced with GFRP and TMT bars was 59.2 and 62.5 kN respectively.

3.2.1 Deflection Profile of Beam Specimens

As can be seen from Fig. 6, the average deflection of the concrete beams reinforced with GFRP bars at a load of 55 kN (minimum failure load among the three beams tested in static monotonic loading) was 18.2 mm and the average deflection for concrete beams reinforced with TMT bars at the same load (55 kN) was 8.7 mm. An increase in average deflection of more than 100 % was observed at the same load level.

3.3 Behavior of Concrete Beams Under Fatigue Loading

Fatigue studies were carried out on nine numbers of concrete beams reinforced with GFRP rebars to evaluate their fatigue strength. As mentioned in Sect. 2.2, two numbers of 10 mm diameter GFRP rebars were provided as main reinforcement and

Fig. 6 Load versus deflection curves at mid span during static loading
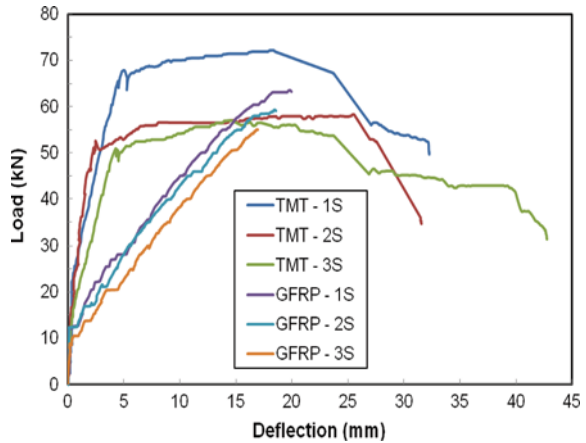
hanger reinforcement in all the nine beams. Conventional steel stirrups of 8 mm diameter TMT bars were used for all the nine beams. The beams were made with a target 28 days concrete compressive strength of 30 MPa. Fatigue investigations were carried out on nine numbers of concrete beams under four different load ranges with a load ratio (ratio of minimum load to maximum load) of 0.1. The fatigue tests were conducted under four point bending with inner and outer spans of 450 and 1,350 mm respectively. The frequency of loading was 1–2 Hz. Fatigue load was applied on the beam specimens using a ±100 kN capacity servo hydraulic actuator. Figure 7 shows fatigue test set-up for concrete beams reinforced with GFRP bars. The details of fatigue tests are given in Table 3. During the fatigue studies, the various response measurements obtained include the maximum and minimum cyclic loads, deflection of the beams at three locations, strain measurements in the reinforcement bars (embedded in concrete) and on the surface of beams, crack width measurements using a video microscope and the load— deflection hysteresis at regular intervals of fatigue cycles.

The load ranges were fixed in such way that the maximum cyclic load corresponded to 40, 50, 60 and 70 % of the average ultimate static load capacity of the three GFRP beams. The minimum cyclic load was 10 % of the maximum cyclic load. Two specimens were tested in each load range except in 50 % load range in which three specimens were tested. The corresponding load range values were 21.6, 27.0, 32.0 and 37.8 kN. The number of cycles endured in each load range is given in Table 4. The average number of cycles completed before the failure of the specimens was 293, 1,286, 3,224 and 5,708 cycles respectively. The maximum crack width observed was 2.9, 3.5, 4.1 and 2.9 mm for the load ranges 37.8, 32.0, 27.0 and 21.6 kN respectively.

As can be seen from Table 4, the number of cycles endured in each load range was consistent i.e., as the load range increases the number of cycles decreased. The repeatability of the fatigue test results are also good, except in load range corresponds to 40 % where in some deviation is observed. The total number of fatigue

Fig. 7 Fatigue test set-up for concrete beams reinforced with GFRP bars

Table 3 Details of fatigue tests

S. No.	Specimen ID	Load (kN)		Load range (kN) $(P_{max} - P_{min})$	As a % of ultimate static load	Frequency (Hz)
		Maximum (P_{max})	Minimum (P_{min})			
1.	GFRP-1F	42.0	4.2	37.8	70	0.5
2.	GFRP-2F	42.0	4.2	37.8	70	0.5
3.	GFRP-3F	30.0	3.0	27.0	50	0.5
4.	GFRP-4F	35.5	3.5	32.0	60	0.5
5.	GFRP-5F	35.5	3.5	32.0	60	0.5
6.	GFRP-6F	30.0	3.0	27.0	50	0.5
7.	GFRP-7F	30.0	3.0	27.0	50	0.5
8.	GFRP-8F	24.0	2.4	21.6	40	1.0
9.	GFRP-9F	24.0	2.4	21.6	40	1.0

Load ratio = minimum load/maximum load = 0.1 for all the beam specimens

Table 4 Results of the tested beams under fatigue loading

Specimen ID	Load (kN)		Number of cycles till failure of the specimen	Maximum crack width (mm)	Maximum strain in the bar (micro strain)	Maximum compressive strain (surface) (micro strain)
	P_{max}	P_{min}				
GFRP-1F	42.0	4.2	239	3.9	11,331	246
GFRP-2F	42.0	4.2	347	1.9	11,653	230
GFRP-3F	30.0	3.0	2,982	1.3	7,354	208
GFRP-4F	35.5	3.5	1,281	4.3	8,916	487
GFRP-5F	35.5	3.5	1,292	2.6	7,473	220
GFRP-6F	30.0	3.0	4,978	2.9	6,446	169
GFRP-7F	30.0	3.0	1,713	2.5	6,949	958
GFRP-8F	24.0	2.4	5,823	2.9	5,503	209
GFRP-9F	24.0	2.4	5,593	3.0	8,488	714

cycles endured was so less at various load ranges tested, rising a big question mark on the usage of these bars in structures subjected to fatigue.

Figure 8 shows a view of concrete beam reinforced with GFRP bars after failure. Figure 9 shows load versus load-line displacement curves at various cycles of loading for a typical concrete beam with GFRP bars. Figure 10 shows number of cycles versus crack width curves obtained during the fatigue tests. Figure 11 shows
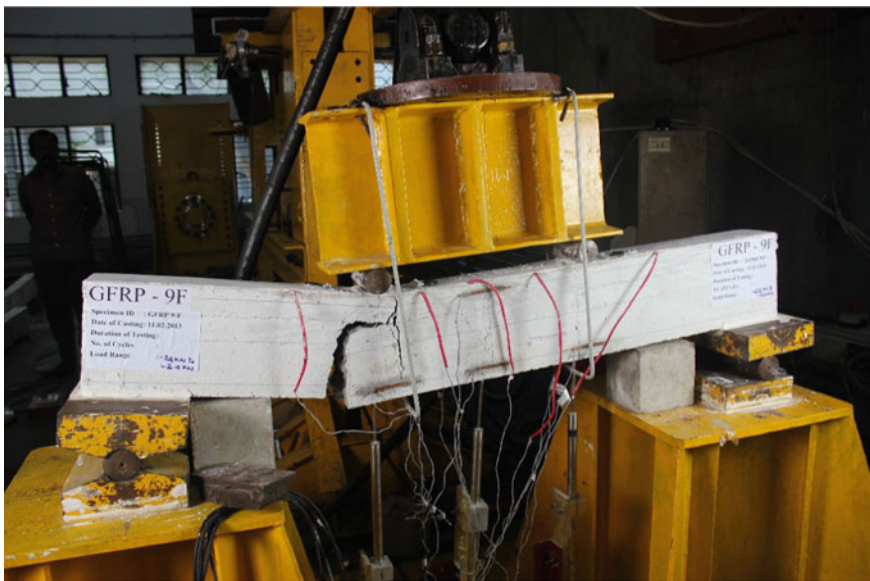
Fig. 8 A view of concrete beam reinforced with GFRP bars after failure
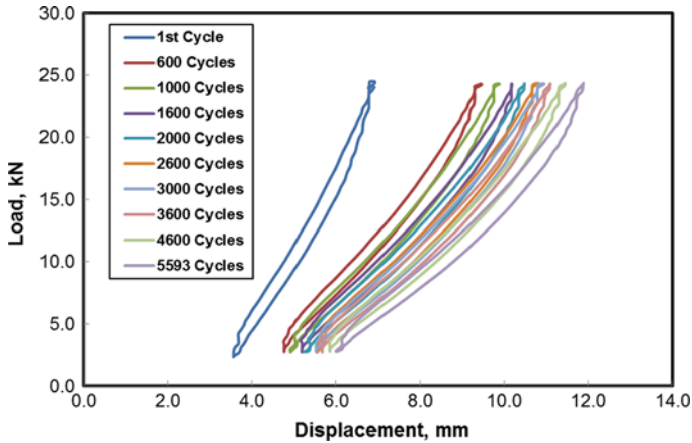
Fig. 9 Load versus displacement curves for a typical concrete beam (GFRP-9F) reinforced with GFRP bars obtained during fatigue test

the number of cycles versus tensile strain in tensile reinforcement curves obtained during the fatigue tests. During fatigue tests, very few cracks were observed in GFRP beams and the beams were failed suddenly with snapping of rebars in all the four load ranges. Based on fatigue life evaluation of nine concrete beams reinforced with GFRP bars tested at four different load ranges, a best fit fatigue life curve has been obtained. Figure 12 shows the best fit fatigue life curve for concrete beams reinforced with GFRP bars.
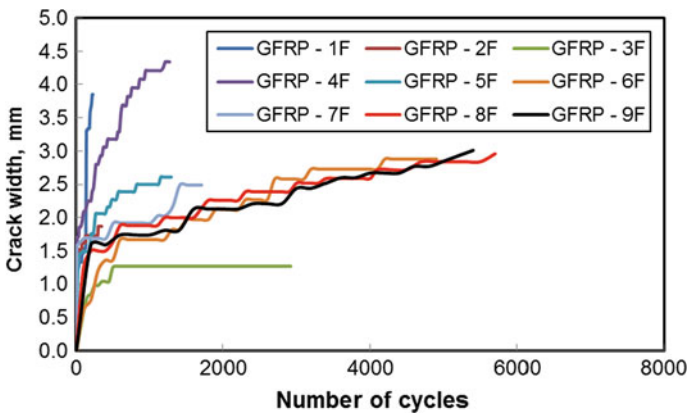
Fig. 10 Number of cycles versus crack width curves
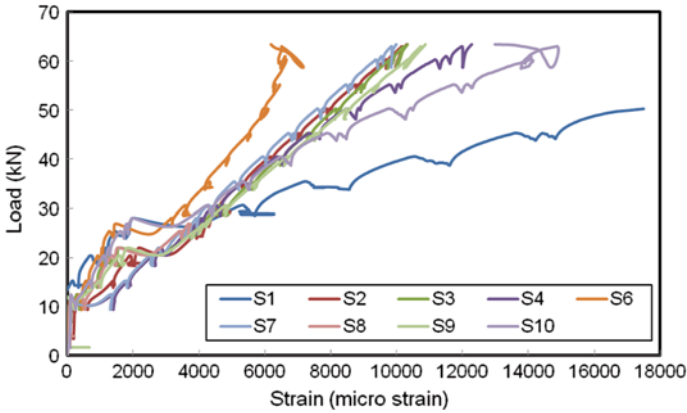
Fig. 11 Number of cycles versus tensile strain in tensile reinforcement

Fig. 12 Load range versus number of cycles curve
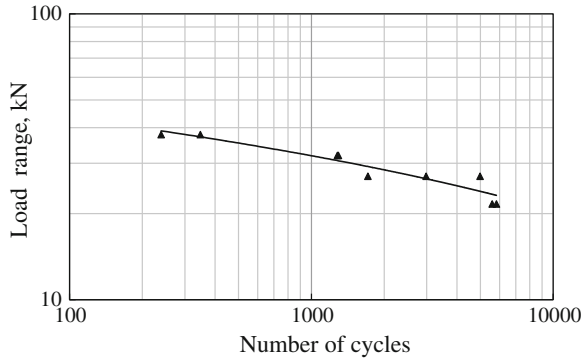
4 Conclusions

Experimental investigations were carried out on concrete beams reinforced with GFRP and TMT bars. All the investigations were carried out under four point bending. In order to study the static behavior of concrete beams reinforced with GFRP and TMT bars, static monotonic tests were carried out on three numbers of concrete beams in each category with same amount of area of reinforcement. Fatigue investigations were carried out on concrete beams reinforced with GFRP bars under four different load ranges (70, 60, 50 and 40 % of static ultimate load capacity) with load ratio of 0.1. Based on the investigations carried out, the following conclusions are made.

The crack initiation load was found to be early in beams with GFRP reinforcement when compared to beams with conventional TMT reinforcement. The

average values of crack initiation loads for beams with GFRP and TMT reinforcement were 11.4 and 20.0 kN respectively.

The average values of ultimate load carrying capacity for beams with GFRP and TMT reinforcement were 59.2 kN and 62.5 kN respectively. A reduction of 5.2 % in ultimate load carrying capacity was found in beams with GFRP reinforcement when compared with the conventional beams with TMT reinforcement. The average deflection of the concrete beams reinforced with GFRP bars at a load of 55 kN (minimum failure load among the three beams tested in static monotonic loading) was 18.2 mm. Whereas, the average deflection for concrete beams reinforced with TMT bars at the same load (55 kN) was 8.7 mm, an increase in average deflection of more than 100 %.

Based on the results of fatigue studies carried out on nine numbers of concrete beams reinforced with GFRP bars under four different load ranges, load range versus number of cycles curve was obtained. Even at the lowest load range of 21.6 kN (40 % of static ultimate load capacity of three GFRP beams), the number of cycles to failure was very less. Hence, use of these bars in structures subjected to fatigue loading seems to be undesirable.

In the light of the present investigations, the usage of GFRP bars as reinforcement in structures subjected to fatigue loads seems to be undesirable unless the beams reinforced with GFRP bars are modified for matching serviceability condition of beams reinforced with TMT bars. Currently, the usage of the GFRP bars is limited only to a few structures, due to its limitation of serviceability criteria and further research is in progress across the globe on the acceptability of GFRP bars in the construction industry.

References

1. ACI Committee 440, 440.1R-06 (2006) Guide for the design and construction of structural concrete reinforced with FRP bars. American Concrete Institute, USA
2. Benmokrane B, Chaallal O, Masmoudi R (1995) Glass fibre reinforced plastic (GFRP) rebars for concrete structures. Constr Build Mater 9:353–364
3. Biswarup S, Phanindra K, Job T, Nanjunda RKS, Ananth R (2007) Strength and serviceability performance of beams reinforced with GFRP bars in flexure. Constr Build Mater 21:1709–1719
4. Barris C, Torres L, Turon A, Baena M, Catalan A (2009) An experimental study of the flexural behaviour of GFRP RC beams and comparison with prediction models. Compos Struct 91:286–295

5. Challal O, Benmokrane B (1996) Fiber reinforced plastic rebars for concrete applications. Compos Part B 27:245–252
6. Pukazhendhi DM, Gandhi P, Vishnuvardhan S, Saravanan M, Raghava G (2013) Static and fatigue behaviour of concrete beams reinforced with GFRP bars. Report No. R&D 03-MLP 14941-RR-10, CSIR-Structural Engineering Research Centre, Chennai
7. Hamed A (1998) Flexural behaviour of concrete beams reinforced with GFRP bars. Cem Concr Compos 20:1–11
8. Valter C, Marco AP, Carlo P (2010) Fatigue behaviour of concrete bridge deck slabs reinforced with GFRP bars. Compos Part B 41:560–567
9. ACI 211.4R-08 (2008) Guide for selecting proportions for high-strength concrete using portland cement and other cementitious materials. American Concrete Institute, USA
10. IS: 516 (1959) Methods of test for strength of concrete. Bureau of Indian Standards, New Delhi, India

Flexural Behaviour of Damaged RC Beams Strengthened with Ultra High Performance Concrete

Prabhat Ranjan Prem, A. Ramachandra Murthy, G. Ramesh, B.H. Bharatkumar and Nagesh R. Iyer

Abstract This paper presents the details of flexural behaviour of damaged RC beams strengthened with Ultra High Performance Concrete (UHPC) overlay. Details of UHPC including mechanical properties are described in detail. Control RC beams of size 100 × 200 × 1,500 mm with M30 grade of concrete are tested up to failure. Damage is introduced by preloading the RC beams up to 80 and 90 % of the failure load of control RC beam. UHPC overlay is added on the tension face of the beam with epoxy and tests are conducted for flexural behaviour. It is observed that there is significant increase in load carrying capacity and ductility in the case of preloaded RC beams strengthened with UHPC overlay.

Keywords Flexural behaviour · Retrofitting · Strengthening · UHPC

1 Introduction

Existing concrete structures may, for a variety of reasons, be found to perform unsatisfactorily. This could manifest itself by poor performance under service loading, in the form of excessive deflections and cracking, or there could be inadequate ultimate strength. Additionally, revisions in structural design and loading codes may render many structures previously thought to be satisfactory, noncompliant with current provisions. In the present economic climate, rehabilitation of damaged concrete structures to meet the more stringent limits on serviceability and ultimate strength of the current codes, and strengthening of existing concrete structures to

P.R. Prem (✉)
Academy of Scientific and Innovative Research,
CSIR Campus, Taramani, Chennai 600113, India
e-mail: prabhat@serc.res.in

P.R. Prem · A. Ramachandra Murthy · G. Ramesh · B.H. Bharatkumar · N.R. Iyer
CSIR—Structural Engineering Research Centre,
CSIR Campus, Taramani, Chennai 600113, India

carry higher permissible loads, seem to be a more attractive alternative to demolishing and rebuilding [1]. Various repair procedures are resin injection, stitching, bonding of external reinforcement, routing and sealing, drilling and plugging, chemical grouting, flexible sealing and portland cement grouting [2]. The techniques used for carrying out repair of damaged structures vary from one structure to the other, depending on the type of distress. Depending on the location and environmental conditions, suitable materials should be chosen for retrofitting, from the point of view of long term performance of the structures after repair. Retrofitting schemes are based on the cost and availability of the materials. The different methodologies include patch repair, jacketing technique using concrete or steel, fibre reinforced polymer (FRP) wrapping, attaching steel plates externally to flexural members by epoxy bonding or bolting, fibre shotcreting and external prestressing. The technical details of the different schemes vary from building to building and severity of the existing level of damage.

Patch repair is done for spalled concrete by applying mortar or concrete by hand, recasting, using sprayed concrete, or by using ferro-cement with mortar or concrete [3]. Reinforced concrete jacketing is a traditional method for seismic upgrading of damaged or poorly detailed reinforced concrete construction [4]. Steel plate jacketing are successful in creating strong column-weak beam mechanisms used to improve the flexural performance of the beam but suffer from considerable loss of floor space and disruption to building occupancy. External plate bonding is a method of strengthening which involves adhering additional reinforcement to the external faces of a structural member [5]. Different types of FRP materials have been considered for repair and retrofit of concrete and masonry structures which is well established with design guidelines in the form of ACI 440-02 and European fib bulletin 14. From the literature studies, it is observed that the problems generally encountered in such repair works include removal of unsound concrete, preparation of concrete bonding surfaces, cleaning and/or replacement of reinforcing steel, surface inspection, and, finally, the selection of right repair materials, depending on the severity of the existing damage and exposure conditions.

A premature debonding failure is the major problem for the patch repair. The use of steel jacketing does not increase the weight of the structure significantly and saves construction time when compared with reinforced concrete jacket. The steel elements can be pre-fabricated, and are more rapidly installed and less disruptive to building occupants than other, but the drawback includes corrosion. Plate-bonding technique has many practical advantages but ultimate failure of a reinforced concrete (RC) beam strengthened for flexure occurs in a brittle manner due to sudden debonding of the plate from the concrete. FRP materials have the benefits of high strength to weight ratio, corrosion resistance, can be adhesively bonded, and have a stiffness comparable to that of steel. Despite its advantages over other methods, the FRP strengthening, technique is not entirely problem-free. It has been reported in the literature that organic resins used to bind and impregnate the fibres are flammable and their behaviour degrade at temperatures close to the glass transition temperature ranging from 60 to 82 °C. The high cost of resins and release of toxic fumes during application pose potential hazards for the manual worker. The non-applicability on wet surfaces or at low temperatures, lack of vapour permeability,

incompatibility of resins and substrate materials and recycling or disposal of excess organic resin from a rehabilitation application are other important drawbacks for application of FRP [6, 7].

Recently, use of Ultra-High Performance Concrete (UHPC) overlay to retrofit reinforced concrete (RC) members has gained a lot of attention to strengthen the flexural members, in terms of load carrying capacity, stiffness and ductility. The main purpose of an overlay is to extend the service life of the structure and increase the structural performance and durability of a wearing surface. The superior ductility and durability characteristics of engineered cementitious composites (ECC) suggest that they could be used as an attractive alternative to conventional concrete overlay materials [8].

UHPC is a novel cementitious material consisting of dense, high strength matrix containing large number of evenly embedded steel fibres and it has exceptional mechanical properties and transport characteristics including very high tensile strength, strain hardening, ductility combined with very low permeability making it ideal for the production of thin structural members as well as for the rehabilitation and modification of existing structures. Ultra high performance is achieved by optimizing the microstructure of the composites by appropriate selection of materials and adopting special process technology such as, self-compacting, extrusion, spray/concreting as well as modification of micromechanical properties [9]. Non-destructive tests results show that this concrete displays excellent repair and retrofit potentials on compressive and flexure strengthening and high bond strength, dynamic modulus and bond durability as compared with other concretes [10–12].

UHPC has been used in the construction industry for more than two decades, applications are still limited to a few market sectors. This is mainly due to the lack of standard guidelines for design procedures. To facilitate the design process, technical guidelines for UHPC are being developed [13, 14]. The use of UHPC overlay is one of the viable options for excellent performance of repaired structure in terms of strength and durability. With lot of bridges and highways being constructed all around the globe using UHPC and its global, growing application for repair purpose, there is need to study the performance and behaviour of UHPC using Indian materials.

2 Present Study

The present research is focussed towards the development of a novel retrofitting system using the addition of a thin overlay of Ultra High performance Concrete (UHPC) to reinforced concrete (RC) members of M30 grade as a new technique to enhance the performance of the existing members in terms of load carrying capacity, stiffness and ductility. In this work mixing, casting, preparation of UHPC is explained with methodology for retrofitting damaged beams.

2.1 Ultra High Performance Concrete

The mix design of UHPC is based on the reference mixes available in the literature and various trials done at the laboratory. It is observed that silica fume/cement ratio and quartz powder/cement is 0.25 and 0.40 respectively. The cost-effective optimal dosage of steel fibres is equivalent to a ratio of 2 % by volume, or about 155 kg/m^3. Sand is used here as a filler and superplasticizer is added in the mix to provide workability in the mix. The mix design of UHPC for the present study is shown in Table 1 [15].

2.1.1 Materials Properties

(i)   Ordinary Portland cement—The cement of grade 53 conforming to IS 12269:1987 was used. According to IS 4031 the tested 28-days mortar compressive strength is 58 MPa. The specific gravity is 3.15; the initial and final setting times are 110 and 260 min. The normal consistency being 28 % and the particle size range lies between 31 and 7.5 μm.

(ii) Silica Fume—The silica fume used in the experiment conforms to ASTM C1240-97b. The specific gravity being 2.25, percentage passing through 45 μm sieve in wet sieve analysis is 92 % and the particle size range lies between 5.3 and 1.8 μm.

(iii) Quartz Powder—The specific gravity being 2.59, percentage passing through 45 μm sieve in wet sieve analysis is 75 % and the particle size range lies between 5.3 and 1.3 μm.

(iv) Sand—The sand used for the experimental studies are: Grade I—coarse (particle size range—0.6–2.36 mm) and Grade III—fine (particle size range—0.075–0.15 mm).

(v)   Super Plasticizer (SP)—Poly-Acrylic-Ester based type SP was used.

(vi) Steel Fibres—The tensile strength of steel fibres is 2,000 MPa.

The chemical composition of cement and silica fume is given in Table 2.

Table 1 Mix design of UHPC and normal concrete (M30)

Materials (kg/m^3)	C	SF	QP	FA	CA	SP	W	SF	w/c
UHPC	788	197	315	866.8		14.77	173	155	0.22
M30	393			888	923				0.50

C cement, *SF* silica fume, *Q* quartz powder, *FA* sand, *W* water, *SP* super plasticizers, *SF* steel fibers

Table 2 Chemical composition of cement and silica fume

Oxides	SiO_2	Al_2O_3	Fe_2O_3	CaO	MgO	Na_2O	K_2O	TiO_2	Mn_2O_3	SO_3	Lime	Chlorides	LOI
OPC	20.49	5.91	4.07	62.90	1.13	0.20	0.47	0.20	0.08	1.87	0.45	0.012	2.29
SF	94.73	–	–	–	–	0.51	–	–	–	0.2	–	0.07	1.5

2.1.2 Mixing

A Planetary mixer machine (300 kg capacity) is used to cast UHPC. The advantage of the mixer is its ability, to rotate the mixing drum and the blades simultaneously at the same time and hence provide uniform blending of the materials. The mixing was done at three speed levels low, medium and high each for 10 min. At slow level, dry binder powder was poured in the pan and mixed. Around 30 % of the water and super plasticizer was added at medium speed. 50 % of the water and SP were added to inhibit homogeneity in the mix at high speed. The steel fibres were added to the mix manually through the open split available at the top of the drum. Finally, remaining 20 % of the SP and water are added and drum is rotated at very high speed for 10 min.

2.1.3 Curing Cycles

Total 36 cubes of 100 mm × 100 mm × 100 mm is cast and divided into three equal parts for studying the effect of moist, steam and heat curing on UHPC. For standard moist curing, the samples are kept in water after demoulding for curing till the date of testing, i.e. after 3, 7, 14 and 28 days. In case of steam curing, the samples after demoulding are subjected to a curing temperature of 100 °C and a relative humidity of 95 % for 18 h in a steam curing chamber. The delay period is 2 h and the rise in temperature is 20–30 °C per hour, which takes around 4 h to reach the peak temperature. The treatment duration is 18 h and the samples taken out from curing chamber are allowed to attain thermal equilibrium with the atmosphere, which takes another 4 h and then kept in water till the date of testing. An ultra-thermal cyclic chamber model is used for heat curing, in which the temperature range varies up to +300 ± 1 °C. The rate of rise in temperature is 2 °C/min. The samples before being subjected to hot air curing, are kept in water and then exposed to 200 °C for the duration of 48 h from the 3rd day, after which they are allowed to attain thermal equilibrium with the atmosphere and then kept in water till the date of testing.

2.2 Reinforced Beams

The under-reinforced RC beams were designed (as per IS 456-2000) to fail in flexure. Typical mechanical properties for the plain concrete are: compressive strength = 30 MPa (in accordance with IS: 516-1959) and split cylinder strength = 3 MPa (in accordance with IS 5816:1999). Total number of 15 RC beams were cast having overall dimension of 100 mm wide, 200 mm depth and 1,500 mm length. The characteristic strength of the steel (f_y) is 415 N/mm^2. Two numbers of 12 and 8 mm diameters of steel rod was used as tensile and compression reinforcement respectively. 6 mm diameter of steel rod was used as stirrups at 125 mm c/c distance to avoid the shear failure. Same reinforcement detailing is maintained

for all the beams. The beams after casting were removed from their moulds after 1 day and water cured at ambient temperature (20 °C) for a minimum of 28 days.

2.3 Preparation of Damaged Beams

Out of 15 RC beams three RC beams were tested till failure to find the ultimate load. The remaining 6 beams each, was subjected to 90 and 80 % of ultimate load of RC beam to induce flexural cracks and distress in the beams.

2.4 Adhesive Bonding of UHPC Overlay and Damaged Beams

As proposed twelve number of damaged beams (100 × 200 × 1,500 mm) is retrofit with UHPC overlay (100 × 20 × 1,500 mm) with epoxy. To improve the bond between the retrofit strips and the damaged beams, all contacting surfaces were cleaned of any debris and roughened using an angle grinder. In addition, a grid of diagonal grooves (2–3 mm deep at a spacing of 20 mm) was cut into the faces of the beams to increase the contact area. The strips were bonded to the prepared surfaces of the damaged beams with a thixotropic epoxy. The main reasons for the selection of such an adhesive for retrofitting were the high bond and mechanical properties of the epoxy adhesive. Moreover, the epoxy can be easily used in the field, applied to vertical as well as horizontal surfaces, and in wet conditions. The two parts of the adhesive were thoroughly mixed and applied to the tension side of the damaged beam with a serrated trowel to a uniform thickness of 3 mm. The strip was then placed on the adhesive and evenly pressed. To ensure good adhesion, pressure was applied by placing masonry bricks along the strip during the hardening of the adhesive for 24 h [1].

2.5 Testing

For studying the effect of curing on UHPC, total 36 cubes (70 mm) cured under different curing regimes are tested at different ages for its compressive strength. Compression test is carried out under water saturated surface dry condition, after 3, 7, 14 and 28 days according to ASTM C109. The test is performed in a 3,000 kN capacity compression testing machine with the load applied at the rate 0.2 kN/s. The maximum load is recorded after the specimens fail to resist any more loads and from the average reading of three cubes.

Fig. 1 Test set up

All the control beams and retrofitted beams were tested under four-point loading. The supports for the beam consisted of wide steel plates resting on free rollers, allowing the support conditions to be idealized as simply-supported. The centre to-centre span between supports was 1,200 mm. Hydraulic jack was placed at the centre of the beam so that the load will be transmitted to the beam as two point loads. The loading set up of the test beams are shown in the Fig. 1. The load was applied under a displacement rate of 0.5 mm/min by a 500 kN servo-controlled hydraulic actuator attached to a rigid frame. The tested beams are instrumented with three transducers placed at mid span and loading point. The required data were recorded by the data logger when the beam was loaded. Acoustic and Vibration tests were also conducted on the beam, the results of which will be reported in future publications.

3 Results and Discussions

1. Thermal regime is highly significant for curing UHPC in order to activate silica fume and quartz powder, if not the materials will act only as filler materials and not as binders. The chemical reaction of binders develops simultaneously in an interdependent way, resulting in a solid skeleton progressive formation and rearrangement of hydration products, which are responsible for strength development.

2. The results of the compressive strength of UHPC specimens are given in Table 3. The samples thermally cured after 2 days of hot air curing and then continued with water curing shows the highest strength results at all ages. At the age of 7 days, steam curing and hot air curing provides better results of 120 and 160 MPa respectively, when compared with moist curing. The results vary widely among both the techniques, and the highest strength is achieved with hot air curing. The results at the age of 14 and 28 days reveal that, there is no much

Table 3 Compressive strength of cubes cured by MC, SC and HC

Age at testing (days)	Compressive strength (MPa)		
	Moist curing (MC)	Steam curing (SC)	Hot air curing (HC)
3	53	53	53
7	64	120	160
14	111	128	185
28	144	142	196

difference between moist curing and steam curing. This is because with steam curing, only high early age strength is achieved and the later age strength is always same as that of standard curing.

3. The details of the tested beam with retrofitting parameters are given in Table 4, and the results obtained from the experiments are presented in Table 5. Out of the 15 beams, 3 beams (control beam—B1) are tested to failure. During the testing of the B1 beams, it is noticed that first visible hairline crack occurs at the load of 27 kN at the tension face (near the mid-span) having a deflection of 1 mm. As the load increases, cracks propagates in different regions of the beam. The beams continues to carry load with constant stiffness till the load of 68 kN

Table 4 Details of the tested beams

S. No		Tested (X1) (beam dimension 100 mm × 200 mm × 1,500 mm)	Curing of retrofitted UHPC overlay (Y1) 100 mm × 20 mm × 1,500 mm	Final composite beam (X1 + Y1)
1	B1	Failure (P1—ultimate load)	–	
2	B2	90 % of P1	Heat curing (HC)	100 mm × 220 mm × 1,500 mm
3	B3	80 % of P1	HC	
4	B4	90 % of P1	Steam curing (SC)	
5	B5	80 % of P1	SC	
6	B6	90 % of P1	Normal curing (NC)	
7	B7	80 % of P1	NC	

Table 5 Results of the tested beams

S. No.	Beam type	Ultimate load (P_{ult}) (kN)	Increase in failure load (kN)
1	B1	76.27	–
2	B2	95.97	25.8
3	B3	99.82	30.8
4	B4	83.29	9.2
5	B5	84.34	10.5
6	B6	90	18
7	B7	91	19.3

Increase in failure load = {Retrofitted beam (P_{ult}) − Control beam (P_{ult})}/Control beam (P_{ult}) × 100

when a local drop is observed in load-displacement response having a corresponding deflection of 2.8 mm. At this position the yielding of the steel bar has started. One of the existing cracks in the middle of the beam started opening while the other cracks progressively closed. This behaviour is observed till the peak ultimate load of 76 kN (P1). The load carrying capacity increased because of the strain hardening behaviour of steel. This stable condition continued until the mid-span deflection reached around deflection 15–16 mm, at which the loading was stopped and unloading started, followed by concrete crushing in the compression. The beam exhibited a very ductile failure and can be regarded as a classical flexural failure. The testing was continued till a deflection of 30 mm for all the beams.

4. Based on the tested control beams, 6 RC beams are preloaded till 90 % of the ultimate load (P1) and 6 beams till 80 % of P1. The 12 distressed beams are divided in six sub classes B2–B7, two beams are tested for each group.

5. Due to induced distress in the beams (B2–B7), many cracks are visible in the beam. During the testing of the beams, it was observed that these cracks start growing first during the testing of beam. After continued testing, a flexural crack that was situated nearly in the middle of the beam penetrated to the retrofit strip and started to open. The bridging action of steel fibres to transfer tensile force from one face of the crack to the other was quite clear. Then, a few unusual cracks with different directions appeared in the middle third of the beam, but the beam carried more load at a reduced stiffness than before. Finally, the maximum load carrying capacity of beams are reached, where after, due to yielding of the rebar, the beam exhibited plastic behaviour. Although, all beams exhibited a very ductile failure, in some beams there were some signs of the influence of shear stress such as local drops in the load displacement curve and also cracking with different angles in the middle third of the beam.
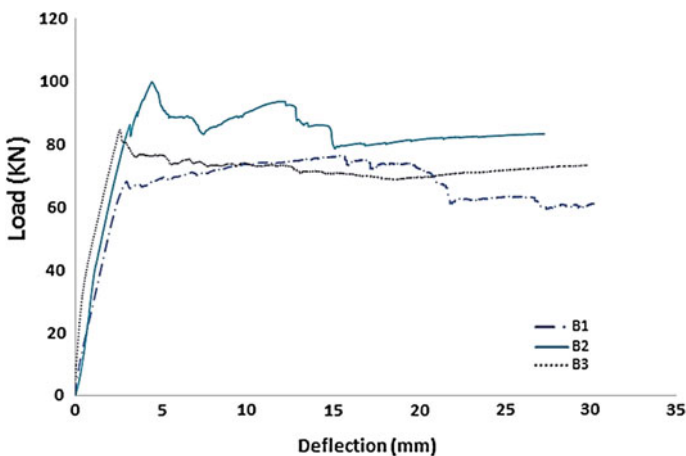
Fig. 2 Load—deflection plot of tested beams B1–B3

6. The addition of a retrofit strip on the tension face, not only improves the failure load but it can also decrease the crack opening and the deflection. The addition of a retrofit strip on the tension face, not only improves the failure load but it can also decrease the crack opening and the deflection. Figures 2, 3 and 4 show the load deflection of retrofitted beam with UHPC overlay cured with heat, steam and normal curing. The retrofitted beam failed as a composite and no delamination was observed between prefabricated UHPC overlay and RC beam (Fig. 5).
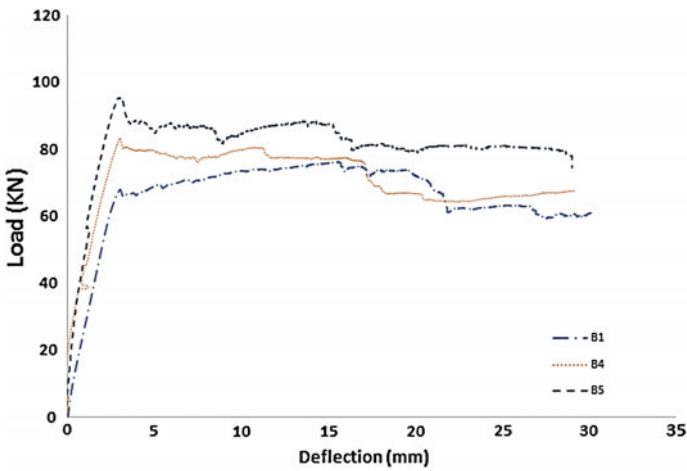
Fig. 3 Load—deflection plot of tested beams B1, B4 and B5
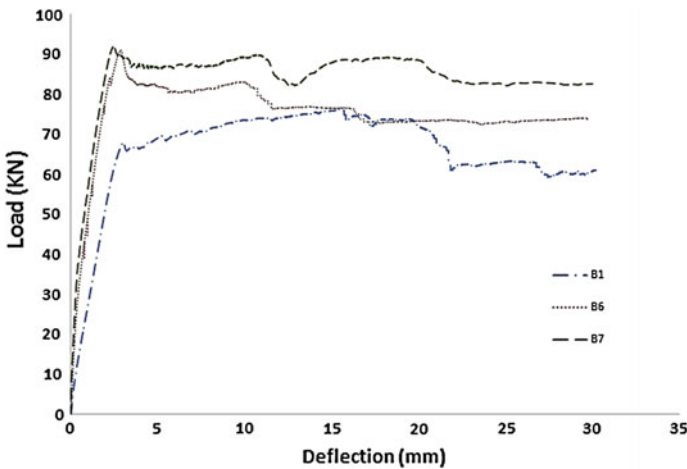
Fig. 4 Load—deflection plot of tested beams B1, B6 and B7

Fig. 5 Retrofitted beams till failure
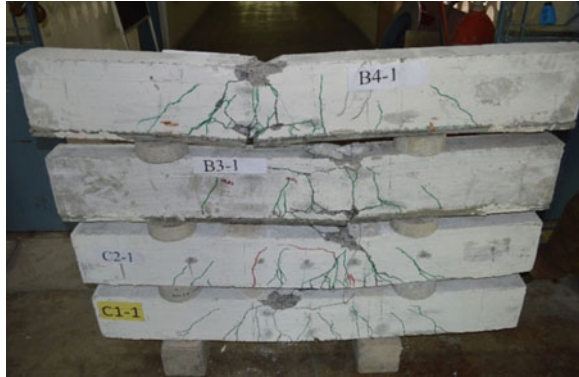
4 Conclusions

1. The best curing technique for UHPC is found to be the hot air curing method, which gives highest compressive strength of 196 MPa at 28 days. With steam curing only high early age strength is attained, while the 28 days strength is lesser than that of moist curing. Hence, steam curing can be adopted instead of moist curing, only if high early age strength is required. Furthermore, increase in strength can be achieved by controlled increase in temperature and the treatment duration.
2. The retrofit studies results obtained from the present study are encouraging and depict good bond between NSC and UHPC. The method for retrofitting damaged beam is discussed. From the study, it was observed that the heat treated overlays of UHPC can enhance the strength of damaged beam up to 30 %. The application of epoxy and surface preparation is very critical for proper bonding between the overlay and damaged beam.
3. From the tests it was concluded that reinforced concrete beams can be successfully retrofitted with UHPC using adhesive bonding of precast material. Studies are being conducted to generalize the method for retrofitting flexural members using UHPC overlay which will be communicated in future publications.

References

1. Alaee FJ, Karihaloo BL (2003) Retrofitting of reinforced concrete beams with CARDIFRC. J Compos Constr 7(3):174–186
2. American Concrete Institute (ACI) Committee 224 (1984) Causes, evaluation, and repair of cracks in concrete structures. ACI J Proc 81(3)

3. Jumaat MZ, Kabir MH, Obaydullah M (2006) A review of the repair of reinforced concrete beams. J Appl Sci Res 2(6):317–326
4. Thermou GE, Pantazopoulou SJ, Elnashai AS (2007) Flexural behavior of brittle RC members rehabilitated with concrete jacketing. J Struct Eng 133(10):1373–1384
5. Mukhopadhyaya P, Swamy N (2001) Interface shear stress: a new design criterion for plate debonding. J Compos Constr 5(1):35–43
6. Hollaway LC, Leeming MB (1999) Strengthening of reinforced concrete structures: using externally-bonded FRP composites in structural and civil engineering. CRC Press, Florida
7. American Concrete Institute (ACI) Committee 440 (2008) Guide for the design and construction of externally bonded FRP systems for strengthening concrete structures. ACI, Michigan
8. Sahmaran M, Yücel HE, Yildirim G, Al-Emam M, Lachemi M (2014) Investigation of bond between concrete substrate and ECC overlays. J Mater Civil Eng 26(1):167–174
9. Richard P, Cheyrezy M (1995) Composition of reactive powder concretes. Cem Concr Res 25(7):1501–1511
10. Harris DK, Sarkar J, Ahlborn TM (2011) Interface bond characterization of ultra-high performance concrete overlays. In: Transportation research board 90th annual meeting, Washington, DC
11. Tayeh BA, Abu Bakar BH, Megat Johari MA, Voo YL (2012) Mechanical and permeability properties of the interface between normal concrete substrate and ultra high performance fiber concrete overlay. Constr Build Mater 36:538–548
12. Brühwiler E (2012) Rehabilitation and strengthening of concrete structures using ultra-high performance fibre reinforced concrete. In: International conference on concrete repair, rehabilitation and retrofitting, Cape Town
13. AFGC (Association Francaise de Genie Civil) Interim Recommendations (2002) Ultra-high performance, fiber-reinforced concretes. AFGC Publication, France
14. Uchida Y, Niwa J, Tanaka Y, Katagiri M, Fischer G, Li V (2006) Recommendations for design and construction of ultra high strength fibre reinforced concrete structures. In: Concrete Committee of Japan Society of Civil Engineers (JSCE), pp 343–351
15. Prem PR, Bharatkumar BH, Iyer NR (2013) Influence of curing regimes on compressive strength of ultra high performance concrete. Sadhana 38(6):1421–1431

Concrete Jacketing of Deficient Exterior Beam Column Joints with One Way Spiral Ties

K.R. Bindhu, Mohana and S. Sivakumar

Abstract Post-earthquake examination of the structures designed for gravity loads showed that one of the weakest links in the lateral load-resisting system is the beam-column joints, especially exterior ones because of a sudden geometric discontinuity and also they are not confined by beams from all the sides. Seismic retrofitting of reinforced concrete structures is aimed at strengthening its structures, in general, and components, in particular, to achieve more and consistent strength ductility and energy dissipation. Experimental investigation is carried out on non ductile beam column joint sub assemblage specimens keeping a scale ratio of 3. The two group of specimens designated as control specimens and retrofitted specimens. The specimens were prepared using M 25 grade concrete with average 8 mm sized coarse aggregate and manufactured sand. The seismic loading simulation was arranged through reverse cyclic loading using hydraulic jacks. The control specimens clearly showed poor performance under cyclic loading. The behaviour was characterized by the diagonal cracks at joint region leading to plastic hinge formation. The upgraded specimens using concrete jacket were exhibited well performance than the deficient joint sub assemblage. The performance improvement of upgraded specimens was characterized by 26.20 % higher displacement ductility, 40 % higher ultimate load carrying capacity and 127.10 % higher energy dissipation capacity than control specimens. The ultimate failure in case of retrofitted specimens occurred on beam at jacket interface, which contributes to most acceptable failure modes i.e., strong column weak beam. The proposed technique of providing one way spiral ties was useful in reducing the reinforcement congestion in thin wall concrete jacketing around joint. The experimental results revealed that the concrete jacketing around the beam column joint sub assemblage is effective in inducing the seismic requirements in the external beam column joints.

Keywords Beam column joints · Concrete jacketing · Earthquake · Spiral ties

K.R. Bindhu (✉) · Mohana · S. Sivakumar
Department of Civil Engineering, College of Engineering, Thiruvananthapuram
695 016, Kerala, India
e-mail: bindhukr@yahoo.co.in

1 Introduction

In recent years, devastating earthquakes worldwide confirmed the deficiencies of building structures. The experience gained from field observations and back analysis led to improvement of knowledge and the evolution of seismic codes. The observation of the damage caused by strong earthquakes has highlighted the typical collapse mechanisms affecting the Reinforced Concrete (RC) buildings designed for gravity loads only, such as formation of plastic hinges on columns driving to soft storey, shear failure in beams, bar slip and shear failure of beam column joints. The capacity design approach provided in modern seismic codes aims at avoiding brittle collapse mechanism both in the structural members and in the structure as a whole. In order to obtain local and global ductility, a series of structural details are required in the seismic design and it is generally absent or inadequate in the existing RC buildings. Among many factors influencing the structural performance of RC buildings, an important role is carried by the ultimate capacity of the beam column joints.

Energy dissipation takes place mainly through the inelastic behaviour of the structural system since the structure must be damaged to dissipate energy. If seismic energy is dissipated at locations, which make the structure unable to satisfy the equilibrium of forces, collapse is inevitable. For avoiding any collapse in column or in joint, a commonly termed "strong column-weak beam" concept is generally followed over "strong beam-weak column" [1–3]. Strengthening of RC beam-column joints has received much attention during the past two decades. Seismic retrofitting of reinforced concrete structures is aimed at strengthening structures, in general, and components, in particular, to achieve more and consistent strength, ductility and energy dissipation. Numerous research have been carried out on different retrofit techniques including the use of concrete jackets, bolted steel plates and FRP sheets for the structural upgrading, especially in columns and beam-column joints of the moment-resisting frames [4, 5]. The purpose of the rehabilitation is to prevent columns or joints from a brittle shear failure and shift the failure towards a beam flexural hinging mechanism, which is a more ductile behaviour. Among these retrofit techniques, the RC jacketing is widely used. This is because concrete jacketing is more consistent with as-built RC structures than the other retrofit materials such as steel or FRP jacketing and the deficient beam-column joints can be easily repaired as well.

The scope of this study is the experimental investigation to evaluate the improvement of seismic capacity of external beam column joints using a nonconventional concrete jacketing arrangement under reverse cyclic loading. In conventional jacket reinforcement detailing [6], the joint region is free from lateral or diagonal collars, whereas in proposed jacket detailing, collars are provided diagonally around the joint and the ties in column region was replaced by rectangular spirals. The results from the concrete jacketed specimens are compared with the results of non ductile control specimens, in terms of ultimate load carrying capacity, hysteretic response, ductility and energy dissipation.

2 Experimental Programme of Exterior Beam Column Joints

2.1 Specimen Characteristics

A six storeyed reinforced concrete building located in seismic zone-III is considered for the present study. The cross sectional dimensions of beams and columns are considered as 300 mm × 420 mm. M 25 grade concrete and Fe415 grade steel were considered in the design. The beam and columns were designed as per IS 456:2000 [7] and SP 16:1980 [8]. The beam-column sub assemblage selected from the structure is scaled to 1/3rd of the actual size. The specimens were classified into three groups with two numbers in each group. The Type 1 specimens (CS) were cast with transverse reinforcement detailing as per IS 456:1978 and SP 16: 1980 representing non ductile control specimen (Fig. 1). Total four numbers of control specimens were cast. Out of the four control specimens, two control specimens were used for retrofitting after 28 days of curing and designated as NCSR. Concrete jacket of 30 mm thick was provided as per the guidelines given in reference [6]. One way spiral ties were provided in the jacket as shown in the Fig. 2. The Type 3 specimens (NCSSTR) represents monolithically strengthened by concrete jacket wherein the beam column joint sub assemblage was cast along with 30 mm concrete jacket. The study also evaluates the effect of bond between the older and new concrete interface of the joint region. Ties with 135° hooks were provided around the joint region as shown in the Fig. 2. High yield strength bars were used as longitudinal reinforcement and ties. The column was rectangular in shape with dimensions 100 mm × 140 mm and the beam with dimensions 100 mm × 140 mm with an effective cover of 15 mm in all specimens. 30 mm concrete jacket over a

Fig. 1 Dimension and reinforcement details of control specimens
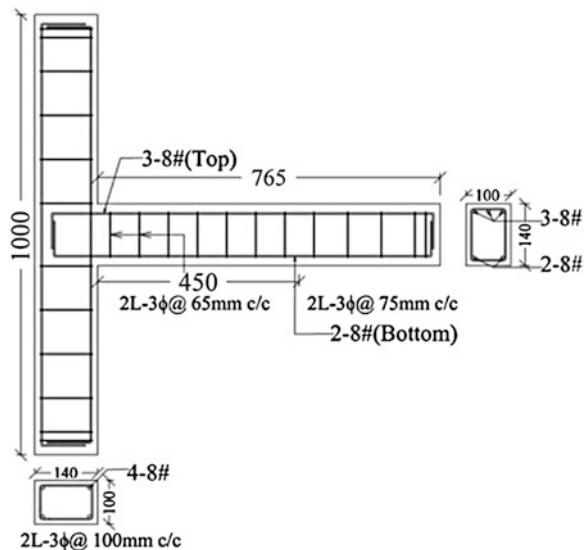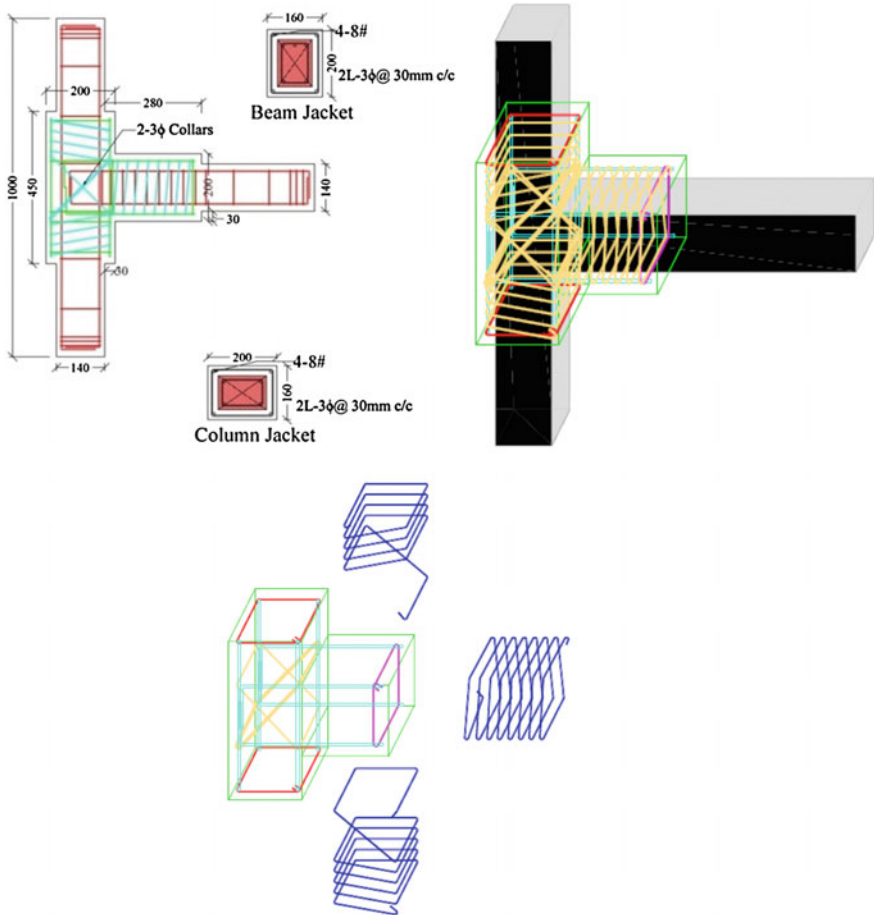
Fig. 2 Dimension and reinforcement details of non-conventionally spiral retrofitted specimens

length of 450 mm on column and 250 mm on beam is provided. The dimensions and reinforcement details of the joint and test specimens are shown in Figs. 1 and 2.

2.2 Preparation of Specimen

The specimens were cast using Portland Pozzolona Cement (fly ash based) conforming to IS 1489:1991 (Part 1) [9]. Manufactured sand (M-sand) confirming to zone II as per IS 383:1970 [10] was used as fine aggregate. Crushed granite stone of maximum size not exceeding 8 mm was used as coarse aggregate. The mix design was carried out as per IS 10262:2009 [11]. The mix proportion was 1: 1.569: 2.769 by weight and the water-cement ratio was kept as 0.40 as shown in Table 1. The

Table 1 Quantities of materials per cubic meter of M 25 grade concrete

S No.	Materials	Quantity in (kg/m^3)	Proportion
1	Cement	410.00	1
2	Fine aggregate	643.25	1.569
3	Coarse aggregate	1135.35	2.769
4	Water	164.00	0.40

28-day average compressive strength from 150 mm cube test was 34.15 N/mm^2. The yield stress of reinforcement was 432 N/mm^2. All the specimens were cast in horizontal position inside a steel mould as shown in Figs. 3 and 4. Two control specimens were cleaned, sharp edges were chipped off and surface is roughened by hacking as surface preparation on old concrete to receive new concrete for proper

Fig. 3 Casting of control (CS) and retrofitted (NCSR) specimens

Fig. 4 Casting of monolithically strengthened specimens (NCSSTR)

bonding as shown in Fig. 3. Reinforcement cage was placed around the joint region. The entire assembly was positioned inside steel mould for concreting. Retrofitted and monolithically jacketed specimens were cast simultaneously with the same mix for better comparison. Specimens were demoulded after 24 h and then cured in curing tank for 28 days.

3 Test Setup and Loading

The test setup is shown in Fig. 5. The column was mounted vertically with the hinged supports at both upper and lower ends, which are tightly fastened to the testing frame by 2 MS clamps using bolts. Cyclic loading was applied by two 196.20 kN hydraulic jacks, one kept fixed to top of the loading frame and the other to the bottom of the loading frame. Reverse cyclic load was applied at 75 mm from the free end of the beam portion of the assemblage. The test was load-controlled and the specimen was subjected to an increasing cyclic load up to failure. The load increment chosen was 1.962 kN. The specimen was first loaded up to 1.962 kN and unloaded and then reloaded on the reverse direction up to 1.962 kN. The subsequent cycles were also loaded in a similar way. Figure 6 shows the loading sequence of the test assemblages. To record loads precisely, load cell with least count 0.981 kN was used. The specimens were instrumented with Linear Variable Differential Transformer (LVDT) having least count 0.1 mm to measure the deflection at the loading point. MS plates were provided at the point of loading to avoid local crushing of concrete. Computer base data acquisition system was used for capturing data.

Fig. 5 Test setup

Fig. 6 Loading cycles
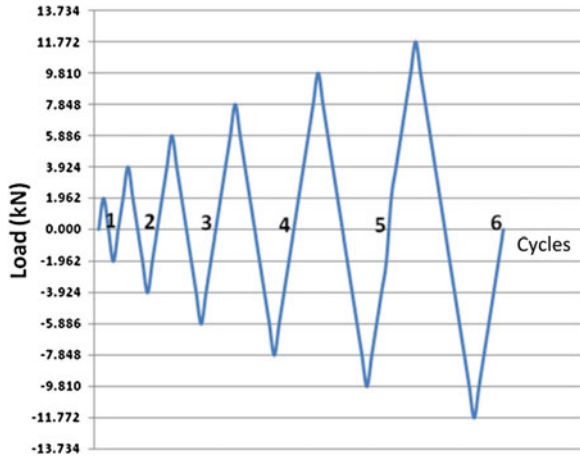
4 Results and Discussion

The test results are presented in the form of load-deformation hysteretic curves, energy dissipation curves, ductility charts and load-deformation envelope curves. The observations during the test are briefly described here.

4.1 Cracking Patterns and Failure Modes

Figures 7, 8, 9 and 10 shows the crack patterns and failure modes of the tested specimens. The failure of control specimens were characterized by the formation of cracks near the joint. As the load increases the cracks were observed in the joint

Fig. 7 Crack formation in joint region of control specimen

Fig. 8 Failure pattern of control specimen

Fig. 9 Failure pattern of retrofitted specimen

region for upward and downward directions of loading. The diagonal cracks were widened with the increase in load leading to hinge formation in the joint region. The concrete wedge mechanism was observed i.e., concrete at rear side of column got detached in a wedge shape. The retrofitted and monolithically jacketed specimens performed better in terms of ultimate load carrying capacity, energy dissipation and ductility. In monolithically jacketed specimens, the cracks occurred in the beam at the interface of jacket which shows a shifting of plastic hinge formation beyond the joint region.

Fig. 10 Crack pattern in monolithically strengthened specimen

The cracking patterns in the retrofitted specimens were similar when compared to that of the control specimen. Improvement in performance was also observed for the retrofitted specimens. The first crack itself occurred in the beam at 6th cycle, which was at 4th cycle in joint region for the control specimen. The cracking started at jacket face on beam and cracks got widened further as the load increases. At the ultimate load, the failure occurred in the beam and also minor cracks were noticed in the jacket as shown in Fig. 10. Thus, it is evident that the concrete jacketing around joint region is capable of transferring the failure to the beam, thus exhibits an appreciable seismic behaviour through plastic hinge formation in the beam.

4.2 Ultimate Load Carrying Capacity

From the experimental results, it is observed that the yield and ultimate load carrying capacity of retrofitted specimens are higher than that of control specimens as shown in Table 2.

Table 2 Ultimate load carrying capacity of test specimens

Specimen	Average yield load (kN)	Average ultimate load (kN)
CS	8.00	10.00
NCSR	10.99	13.73
NCSSTR	15.70	19.62

4.3 Energy Dissipation

As a measure of the dissipated energy of the specimens, the area under the load displacement curves for all cycles were computed and called as energy that could be dissipated by the specimens before the specimen lost its stability. Figures 11, 12 and 13 represents the hysteresis loop for all the specimens. The cumulative values of full energy dissipation for the tested specimens are shown in Table 3. It is evident that
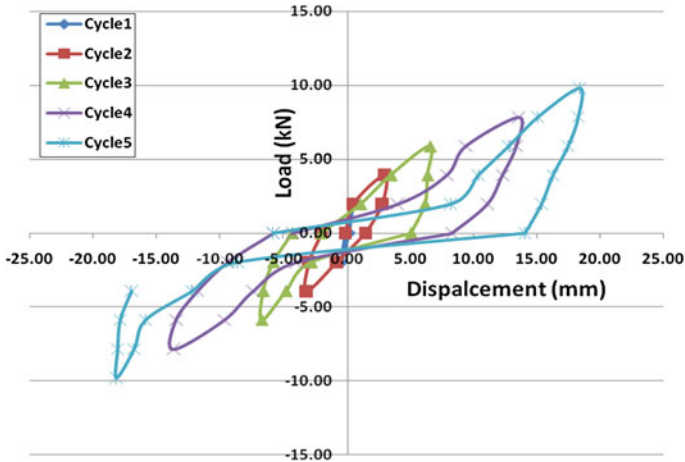
Fig. 11 Hysteresis curves for control specimens (CS)
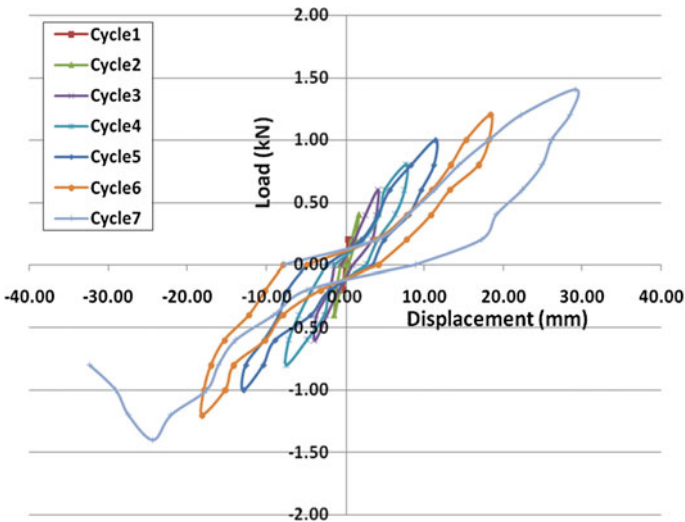
Fig. 12 Hysteresis curves for retrofitted specimen (NCSR)
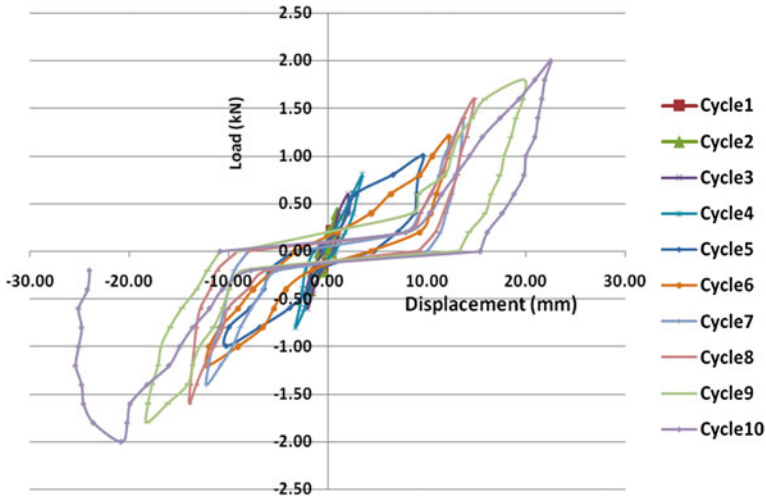
Fig. 13 Hysteresis curves for monolithic jacketed specimen (NCSSTR)

Table 3 Displacement ductility and energy dissipation of test specimens

Specimen	Average yield displacement (mm)	Average ultimate displacement (mm)	Average displacement ductility	Energy dissipation (kN mm)
CS	13.65	18.30	1.34	108.66
NCSR	15.81	26.75	1.69	246.36
NCSSTR	14.35	21.65	1.51	254.28

the energy dissipation for the specimen retrofitted with concrete jacket and monolithically jacketed specimens are much larger than the control specimens.

4.4 Displacement Ductility

The ratio between the maximum and yield displacement is defined as displacement ductility [12, 13]. The load displacement envelope (Fig. 14) is used to define the displacement ductility for each specimen and is tabulated in Table 3. The displacement ductility values for control specimen are less and resulted poor seismic performance. This is due to the lack of confining reinforcement in the joint region. The upgraded specimens showed better seismic performance in terms of displacement ductility, which is due to the increased concrete section and additional reinforcement around joint region.

Fig. 14 Load deflection envelopes
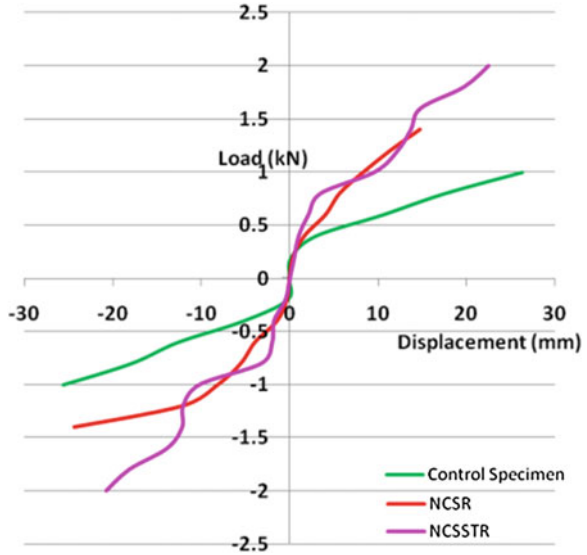
5 Conclusion

Based on the experimental results in the present study the following conclusions can be drawn.

1. In the non ductile beam column joints the diagonal cracks were developed in the joint region leading to global failure of the structure. The performance of beam column joints is well improved by providing concrete jacket around the joint region. From the present experimental results it was observed that there is 40 and 100 % increase in ultimate load carrying capacity, 127 and 134.01 % increase in energy dissipation, 26 and 14 % increase in displacement ductility for retrofitted and monolithically strengthened specimens respectively over deficient non ductile specimens.
2. The concrete jacket provided is capable of altering the failure mode i.e. plastic hinge formation at a distance of twice the depth of the beam (280 mm) along the beam from the column face in lieu of shear failure in the joint region.
3. The performance of beam column joint retrofitted by concrete jacket can be further improved by ensuring an effective bonding between the old and new concrete interfaces.

References

1. Alcocer SM, Jirsa JO (1993) Strength of reinforced concrete frame connections rehabilitated by jacketing. ACI Struct J 90(3):249–261
2. Tsonos AG, Tegos IG, Penelis GG (1992) Seismic resistance of type-2 exterior beam-column joints reinforced with inclined bars. ACI Struct J 89(1):3–12
3. Shannag MJ, Alhassan MA (2005) Seismic upgrade of interior beam-column subassemblages with high-performance fiber_reinforced concrete jackets. ACI Struct J 102(1):131–138
4. Engindeniz M, Kahn FL, Zureick A-H (2005) Repair and strengthening of reinforced concrete beam-column joints: state of the art. ACI Struct J 102(2):1–14
5. Pampanin S, Christopoulos C, Priestley MJN (2003) Performance-based seismic response of frame structures including residual deformations. Part II: multi-degree of freedom systems. J Earthq Eng 7(1):119–147
6. Arya AS, Agarwal A (2009) Indian standard seismic evaluation and strengthening of reinforced concrete buildings-guidelines, prepared under GOI-UNDP. Disaster risk management programme, India, pp 17–41
7. IS: 456 (2000) Indian standard code of practice for plain and reinforced concrete, Bureau of Indian Standards, New Delhi
8. SP 16 (1980) Design Aids for Reinforced Concrete to IS: 456 (1978), Bureau of Indian Standards, New Delhi
9. IS: 1489 (Part-1) (1991) Indian standard code for Portland-pozzolona cement specification, Part-1 Fly Ash Based, Bureau of Indian Standards, New Delhi
10. IS: 383 (1970) Indian standard code for specification for coarse aggregate and fine aggregates from natural sources for concrete. Bureau of Indian Standards, New Delhi
11. IS: 10262 (2009) Indian standard code of practice for mix proportioning-guidelines. Bureau of Indian Standards, New Delhi
12. Bindhu KR, Jaya KP, Manicka SVK (2008) Seismic resistance of exterior beam-column joints with non-conventional confinement reinforcement detailing. Struct Eng Mech 30(6):733–761
13. Calvi GM, Magenes G, Pampanin S (2002) Relevance of beam-column joint damage and collapse in RC frame assessment. J Earthq Eng 6(1):75–100

Part XXIII
Concrete Filled Steel Tubes/Structures

Experimental Investigation on Uniaxial Compressive Behaviour of Square Concrete Filled Steel Tubular Columns

N. Umamaheswari and S. Arul Jayachandran

Abstract This paper presents a brief review of previous research work done on uniaxial compressive behavior of concrete filled steel tubular (CFT) columns and the results of experimental study conducted on twenty four number of cold-formed steel square sections filled with conventional concretes of grade M30 and M60 tested under uniaxial compression. The effect of length to breadth (L/B) ratio of square steel tubes and concrete core strength of CFTs on axial compressive strength and behavior of CFT columns was studied. The experimental strength values were compared with predictions using Eurocode 4-1994, ACI 1999, AS 3600-1994, AISC-LRFD-1999, AISC 2005, GJB 4142-2000 and BS 5400-1979 and from equation suggested by previous researcher. The effect of breadth to thickness (B/t) ratio, % steel area contribution and constraining factor on axial compressive strength was also examined. The results showed that the axial compressive strength of CFTs increases due to confinement effect of concrete core on steel tubes and the estimation of axial compressive strength using all methods is conservative. A modified equation is also suggested.

Keywords Concrete-filled tubes · Cold-formed steel · Axial compression · Concrete confinement · Local buckling · Overall buckling

Abbreviations

MN	Mega newton
D	Diameter of steel tube
t	Thickness of steel tube
L	Length of column
A_s	Area of steel tube
A_c	Area of concrete core
L.B	Local buckling

N. Umamaheswari (✉)
SRM University, Kattankulathur, Kancheepuram District, Tamilnadu, India

S. Arul Jayachandran
Indian Institute of Technology (IIT) Madras, Chennai, Tamilnadu, India

P_{exp}	Experimental axial strength
P_{ec4}	Axial strength as per EC 4-1994
P_{lrfd}	Axial strength as per AISC-LRFD-1999
P_{aisc}	Axial strength as per AISC-2005
P_{gjb}	Axial strength as per GJB 4142-2000
P_{bs}	Axial strength as per BS 5400-1979
O.B	Overall buckling
$P_{aci/as}$	Axial strength as per ACI 318-1999/AS 3600-1994
P_{muh}	Axial strength as per Muhammad's equation

1 Introduction

Concrete filled steel tubular (CFT) columns exhibit the beneficial qualities of steel and concrete, such as high tensile strength, ductility, high compressive strength and stiffness, Shams and Saadeghvaziri [1]. The confinement effect of steel tubes on concrete core in CFT columns enhances the material properties of concrete by developing composite action and the inward buckling of steel tube is prevented by concrete thus increasing the strength and stability of CFT columns, Liu et al. [2]. The load corresponding to failure of CFTs will be considerably larger than the sum of steel and concrete failure loads. According to Shanmugam and Lakshmi [3], the level of increase in the failure load of CFTs caused by the confining effect of the steel tube on concrete core is influenced by factors such as cross-sectional shape, length to diameter/width ratio, diameter/width to thickness ratio or thickness of steel tube, eccentricity of loading, concrete core strength and steel strength. Furlong [4] found that there was no enhancement due to confinement based on investigations done on 13 specimens with diameter to thickness ratio ranging from 29 to 98. Gardner and Jacobson [5] noted an increased strain level for the steel tube without local buckling due to concrete confinement upon investigation on 22 columns of diameter to thickness ratio ranging from 30 to 40. Knowles and Park [6, 7] noted increase in axial capacity occurs only for circular cross-sections, that too for short CFTs. They tested 21 circular and 7 square columns with D/t as 15, 22 and 59 and L/D ratio ranging from 2 to 21. The confinement offered by steel tubes was found to be less from the series of tests conducted by O'Shea and Bridge [8] on the behavior of circular thin walled steel tubes of diameter to thickness ratio greater than 55 filled with high strength concrete in the range of 110–120 N/mm^2. Schneider [9] investigated fourteen short CFT columns to examine the influence of steel tube shape and tube thickness on the axial compressive strength of CFT columns. The D/t values ranged from 17 to 50, L/D from 4 to 5. The results suggested that circular tubes offer substantial post-yield strength and stiffness, which was not available in most square or rectangular cross-sections. Brauns [10] found that effect of confinement exists at higher stress levels only. Han [11] tested 24 rectangular CFT

columns to analyze the influence of constraining factor and tube width ratio on the behavior of CFT columns and to compare the accuracy of the predictions by using various international codes and standards. The results indicate that the constraining factor and the tube width ratio have significant influence on both the compressive load capacity and the ductility of the steel tube. Lam and Williams [12] tested 18 short square CFT columns to check the effect of concrete shrinkage on the axial strength of CFT columns. The B/t ratio ranged from 10 to 25 and concrete cube strength 30–100 N/mm^2. The results showed that concrete shrinkage has an effect on the axial compressive strength. Tao et al. [13] mentioned that the confinement is less in square or rectangular CFTs compared to circular sections due to the effect of local buckling of steel tube walls.

From the earlier research, it can be concluded that composite action is less exhibited in slender columns whereas in short columns, improved axial strength occurs due to composite action and confinement offered by steel tube on concrete core. Also it was found that composite action is less pronounced due to plate bending in non-circular sections. However an attempt has been made in this paper to evaluate the effect of confinement in square CFTs.

In the present investigation, the effect of length to breadth ratio and concrete core strength on axial compressive strength and behavior of square concrete filled steel tubular short columns was studied. The results were compared with the predicted values obtained using eight methods. The enhancement in axial compressive strength, effect of constraining factor was also studied.

2 Methods and Materials

Experimental program
Twenty four cold-formed steel square column specimens of varying length to breadth ratio (L/B = 2–12) and breadth to thickness ratio (B/t = 43–45) have been tested under uniaxial compression till failure in a Compression Testing Machine of 3 MN capacity. The grade of concrete-infill used was M30 and M60. The unconfined compressive strength values are 28 and 52 N/mm^2. The Steel Yield strength and Modulus of Elasticity are 255 and 200,000 N/mm^2. The experimental set-up is shown in Fig. 1. The limit of breadth to thickness ratio (B/t) of square sections suggested in Eurocode 4-1994, ACI 318-1999, AISC-LRFD-1999, AISC 2005 [14–17], has been followed to avoid premature local buckling of CFTs. The cut steel tube specimens were cast in upright position, membrane cured and tested for uniaxial compressive strength. The peak load, axial compressive load versus axial strain behavior and failure modes of CFT column specimens were observed. The properties of square CFT columns are shown in Table 1.

Fig. 1 Experimental set-up

Table 1 Properties of square CFT columns

| S.No.	Column type	Properties of columns					
		L/B	B/t	A_s mm^2	A_c mm^2	% A_s/A_g	f_c N/mm^2
1	Square CFT-Set-I	1.99	43.59	225.31	2,282	8.9	28
2		4.01	44.76	219.56	2,293	8.7	28
3		6.00	45.16	217.65	2,295	8.7	28
4		7.99	45.14	217.56	2,293	8.7	28
5		9.99	44.36	221.48	2,292	8.8	28
6		11.96	44.76	219.56	2,293	8.7	28
7		2.01	44.77	219.61	2,294	8.7	52
8		4.01	45.15	217.60	2,294	8.7	52
9		6.01	45.15	217.60	2,294	8.7	52
10		7.99	45.16	217.65	2,295	8.7	52
11		9.98	45.15	217.60	2,294	8.8	52
12		11.98	44.36	221.48	2,292	8.9	52
13	Square CFT-Set-II	1.99	43.59	225.31	2,282	8.9	29
14		4.01	44.76	219.56	2,293	8.7	29
15		6.00	45.16	217.65	2,295	8.7	29
16		7.99	45.14	217.56	2,293	8.7	29
17		9.99	44.36	221.48	2,292	8.8	29
18		11.96	44.76	219.56	2,293	8.7	29
19		2.01	44.77	219.61	2,294	8.7	51
20		4.01	45.15	217.60	2,294	8.7	51
21		6.01	45.15	217.60	2,294	8.7	51
22		7.99	45.16	217.65	2,295	8.7	51
23		9.98	45.15	217.60	2,294	8.8	51
24		11.98	44.36	221.48	2,292	8.9	51

2.1 Prediction of Axial Compressive Strength of Square CFT Columns

The axial compressive strength values of square CFTs were estimated by using international codes and design method suggested by Muhammad et al. [18].The equations and methods are available in literature.

The first set of predicted values of axial compressive strength of CFTs was obtained by adding the steel and concrete contribution of loads as specified in Eurocode 4-1994 [14]. The second set was obtained from ACI 318-1999 [15] (AS 3600-1994 [19] also uses the same formula) provisions for square CFTs. According to this code, a factor of 0.85 was included to concrete contribution to obtain axial compressive strength of CFTs. The third set was obtained from AISC-LRFD-1999 [17] provisions for square CFTs. A modified radius of gyration, elastic modulus and non-dimensional slenderness were calculated to obtain cross-sectional capacity. The fourth set was obtained from AISC-2005 [16] provisions (which include confinement effect) for square CFTs. Effective stiffness was calculated. The fifth set was obtained from GJB 4142-2000 [20] provisions which involve calculation of constraining factor which is considered to be a measure of confinement effect of concrete. The sixth set was obtained from BS 5400-1979 [21] provisions for square CFTs, which includes a factor of 0.675 to concrete contribution to obtain axial compressive strength of CFTs. The seventh set was obtained by using the method suggested by Muhammad et al. [18]. In this method, a coefficient of 1.1 was included to concrete contribution to account for concrete confinement. Based on the analysis of experimental results, a modified equation of ACI 318-1999 [15] was suggested by authors. The eighth set of estimated values of axial compressive strength of CFTs was obtained by the proposed method suggested by authors, which includes confinement effect. A factor of 1.2 was included to concrete contribution to obtain axial compressive strength of CFTs. Hence modified equation is given by, Axial compressive strength of square CFT = Steel Contribution ($A_s f_y$) + 1.2 * Concrete Contribution ($A_c f_c$).

Five test results of Schneider [9] and ten test results of Lam and Williams [12] were also used along with twenty four current results for comparison purposes. These tests are selected because of relatively smaller slenderness of specimens to ensure that they would act as short columns and to cover a wide range of parameters. The tested specimens of Schneider [9] have width to thickness ratio ranging from 16 to 40 with constant slenderness 4.8. The tube width is 126 mm with wall thickness ranging from 3 to 7 mm. The steel yield strength ranges from 312 to 357 N/mm^2 while compressive strength of concrete ranges from 23 to 30 N/mm^2. The tested specimens of Lam and Williams (2008) have width to thickness ratio ranging from 10 to 24 with constant slenderness 3. The tube width is 100 mm with wall thickness ranging from 4.1 to 9.6 mm. The steel yield strength ranges from 289 to 400 N/mm^2 while compressive strength of concrete ranges from 24 to 79 N/mm^2.

Fig. 2 Variation of
experimental axial strength
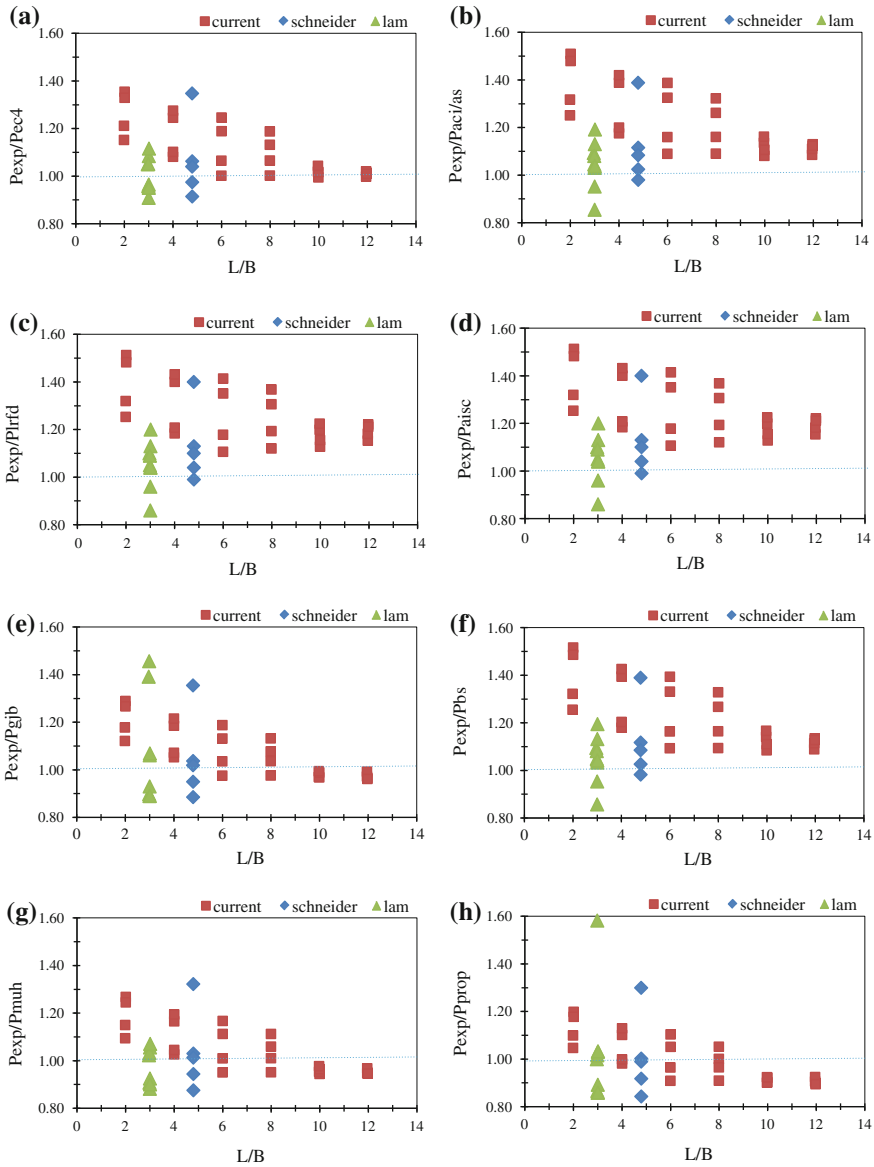w. r. to length to breadth ratio
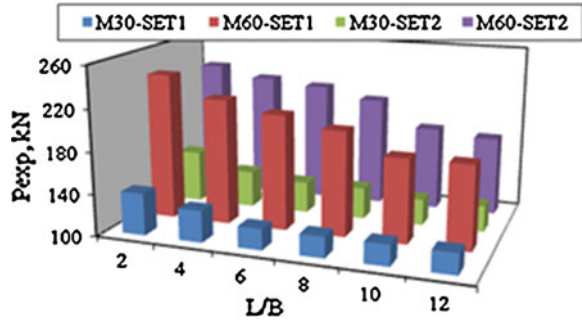
3 Results and Discussion

3.1 Experimental Axial Compressive Strength of CFTs

The variation of experimental axial compressive strength with respect to length to breadth ratio for M30 and M60 grade CFTs is shown in Fig. 2. The axial compressive strength of CFT columns was found to be decreasing by 14–25 % with increase in length to breadth ratio from 2 to 12 whereas as expected, it was increasing up to 70 % with increase in concrete core strength, for the same gross-sectional area.

3.2 Comparison of Experimental Axial Compressive Strength with Strength Predicted According to Provisions of Eurocode 4-1994, ACI 318-1999/AS 3600-1994, AISC-LRFD 1999, AISC 2005, GJB 4142-2000 [14–20] and as Per Suggested Design Equations

The variation of normalized axial compressive strength calculated based on predictions using various methods, with respect to length to breadth ratio for square CFTs (based on 24 current tests and 15 tests conducted earlier (by Schneider [9] and Lam and Williams[12]) is shown in Fig. 3a–h. The values predicted using Eurocode 4-1994 [14] and GJB 4142-2000 [20] are closer to test values for L/B ranging from 10 to 12.

The variation of normalized axial compressive strength calculated based on predictions using various methods, with respect to breadth to thickness ratio for square CFTs (based on 24 current tests and 15 tests conducted earlier (by Schneider [9] and Lam and Williams [12]) is shown in Fig. 4a–h. The values predicted using Eurocode 4-1994 [14] and GJB 4142-2000 [20] are closer to test values for B/t ranging from 20 to 30.

Fig. 3 Variation of normalised axial compressive strength **a** (P_{exp}/P_{ec4}), **b** ($P_{exp}/P_{aci/as}$), **c** (P_{exp}/P_{lrfd}), **d** (P_{exp}/P_{aisc}), **e** (P_{exp}/P_{gjb}), **f** (P_{exp}/P_{bs}), **g** (P_{exp}/P_{muh}), **h** (P_{exp}/P_{prop}) w. r. to length to breadth ratio
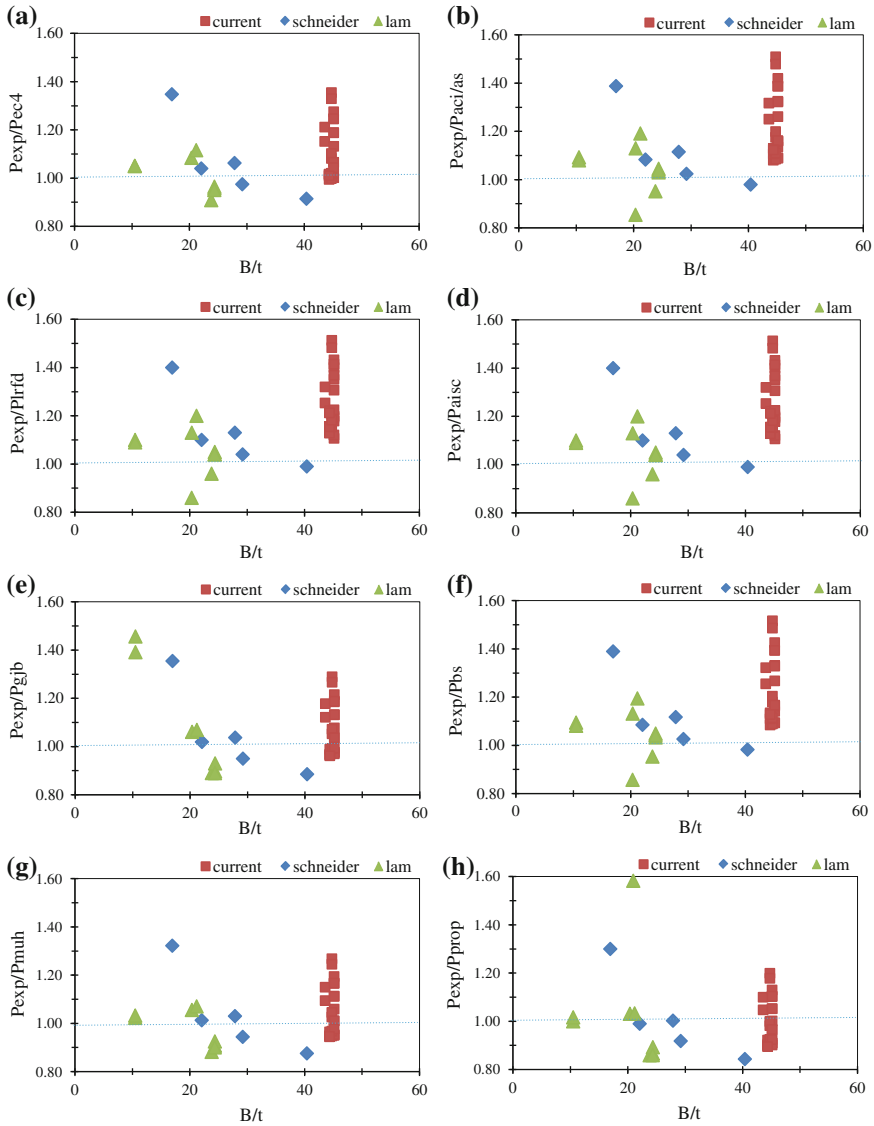
The variation of normalized axial compressive strength calculated based on predictions using various methods, with respect to % steel area contribution for square CFTs (based on 24 current tests and 15 tests conducted earlier (by Schneider

Fig. 4 Variation of normalised axial compressive strength **a** (P_{exp}/P_{ec4}), **b** ($P_{exp}/P_{aci/as}$), **c** (P_{exp}/P_{lrfd}), **d** (P_{exp}/P_{aisc}), **e** (P_{exp}/P_{gjb}), **f** (P_{exp}/P_{bs}), **g** (P_{exp}/P_{muh}), **h** (P_{exp}/P_{prop}) w. r. to breadth to thickness ratio

[9] and Lam and Williams [12]) is shown in Fig. 5a–h. The values predicted using Eurocode 4-1994 [14] and GJB 4142-2000 [20] are closer to test values for % A_s/A_g ranging from 14 to 18.
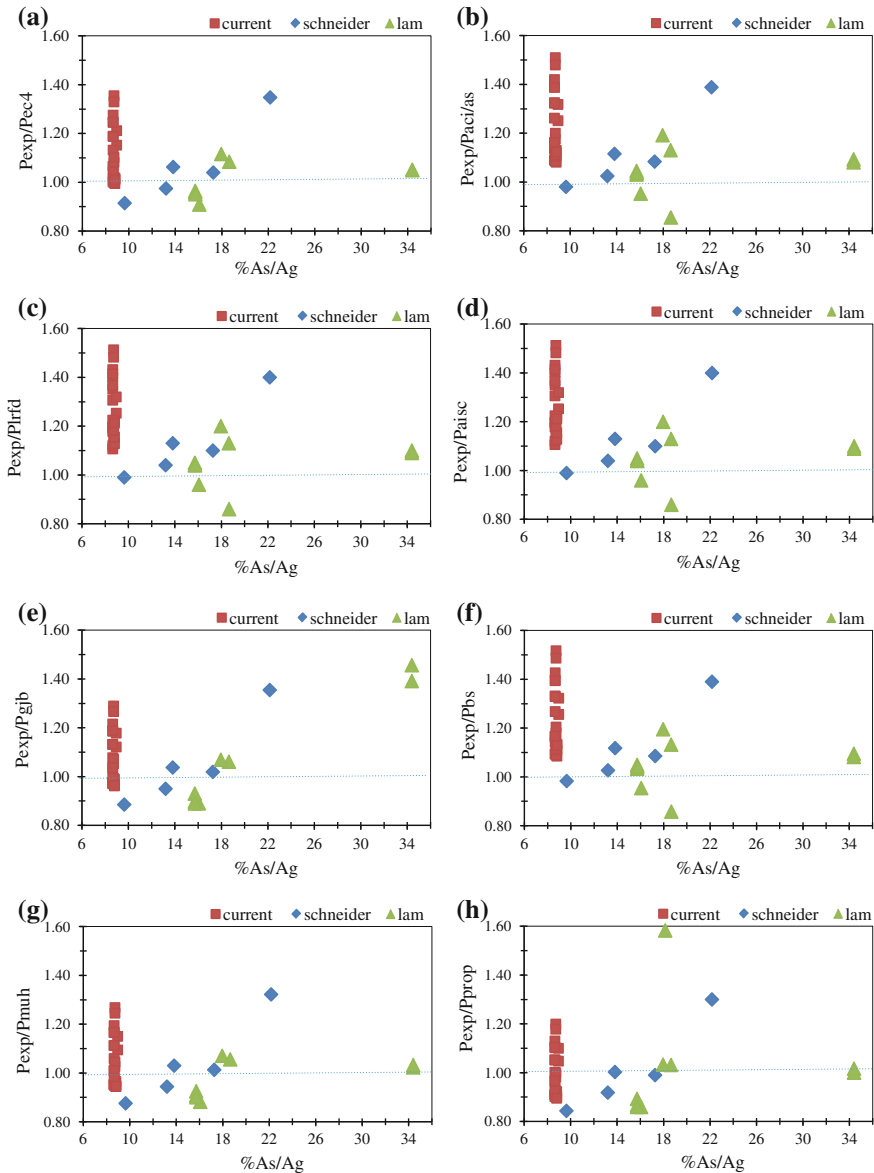
Fig. 5 Variation of normalised axial compressive strength **a** (P_{exp}/P_{ec4}), **b** ($P_{exp}/P_{aci/as}$), **c** (P_{exp}/P_{lrfd}), **d** (P_{exp}/P_{aisc}), **e** (P_{exp}/P_{gjb}), **f** (P_{exp}/P_{bs}), **g** (P_{exp}/P_{muh}), **h** (P_{exp}/P_{prop}) w. r. to % steel contribution

The variation of normalized axial compressive strength calculated based on predictions using various methods, with respect to unconfined compressive strength of concrete core for square CFTs (based on 24 current tests and 15 tests conducted earlier (by Schneider [9] and Lam and Williams [12]) is shown in Fig. 6a–h. The
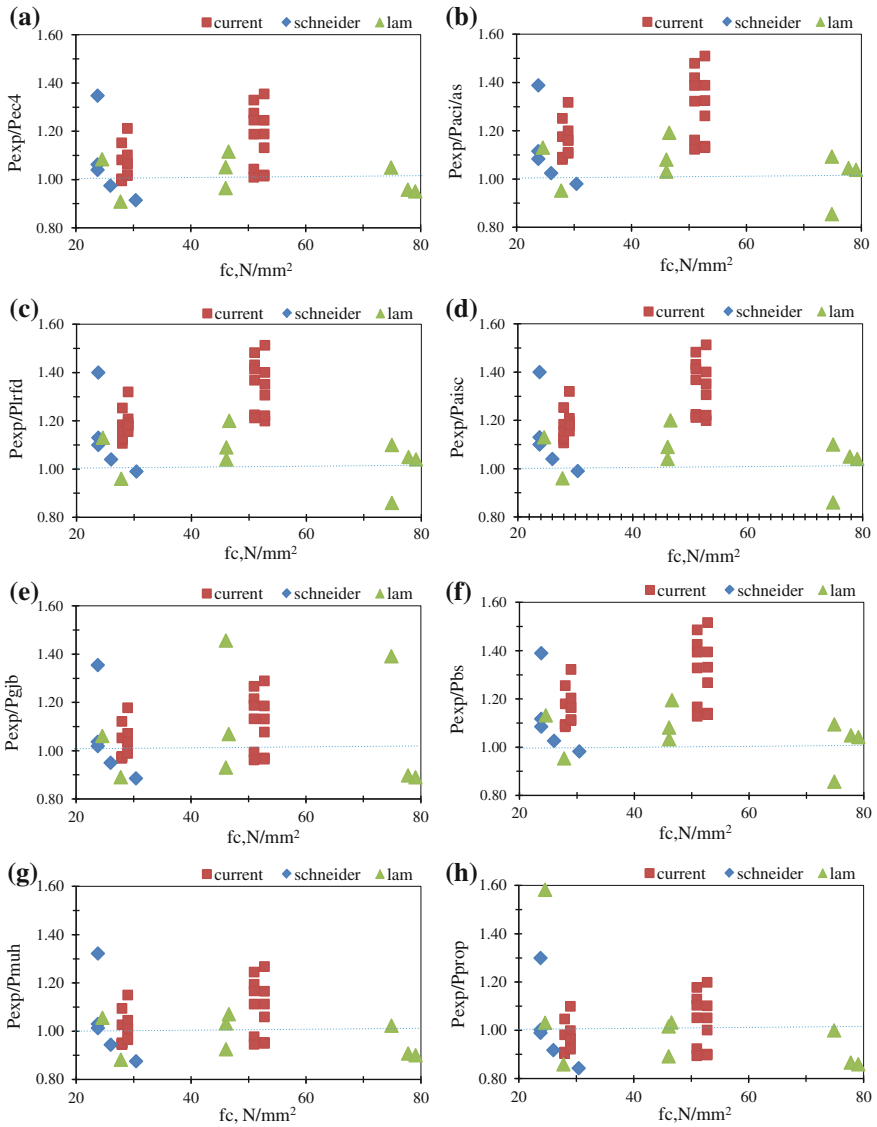
Fig. 6 Variation of normalised axial compressive strength **a** (P_{exp}/P_{ec4}), **b** ($P_{exp}/P_{aci/as}$), **c** (P_{exp}/P_{lrfd}), **d** (P_{exp}/P_{aisc}), **e** (P_{exp}/P_{gjb}), **f** (P_{exp}/P_{bs}), **g** (P_{exp}/P_{muh}), **h** (P_{exp}/P_{prop}) w. r. to unconfined compressive strength

values predicted using Eurocode 4-1994 [14] are closer to test values for greater concrete core strengths.

The mean and standard deviation of experimental to predicted values based on provisions of Eurocode 4-1994, ACI 318-1999/AS 3600-1994, AISC-LRFD-1999, GJB 4142-2000 and BS 5400-1979 [14–17, 19–21] are 1.09 and 0.16, 1.18 and

0.17, 1.19 and 0.17, 1.19 and 0.17, 1.08 and 0.18 and 1.19 and 0.17 respectively. The mean and standard deviation of experimental to predicted values based on design equations proposed by Muhammad et al. [18] are 1.04 and 0.15 respectively. Based on the analysis of 39 test results with the available international design standards, it is found that Eurocode 4-1994 [14] and GJB 4142-2000 [20] provides predictions closer to experimental values. The design equations proposed by Muhammad et al. [18] includes confinement effect but it shows that it is underestimated. It is apparent that there is little confinement existing in square sections also. The modified equation proposed by author yields results in good agreement with test results. The mean and standard deviation of experimental to predicted values based on design equations proposed by author are 0.99 and 0.15 respectively.

3.3 Effect of Concrete Confinement in Square CFTs

The effect of concrete confinement was analyzed with the variation of Strength Index, SI (ratio of experimental axial compressive strength to cross-sectional capacity, as per [11] with respect to constraining factor, ξ (ratio of steel to concrete contribution) and is shown in Fig. 7. The SI values were found to be increasing with increase in ξ.

3.4 Axial Compressive Load Versus Axial Strain Behavior

The axial compressive load versus axial strain behavior of square CFT columns with M30 and M60 grade concrete infill is shown in Fig. 8a, b respectively. Obviously all square CFT columns exhibited non-linear behavior and it was difficult to locate the yield values. There was no significant difference in behavior with respect to concrete core strength under consideration, except for load carrying

Fig. 7 Variation of strength index, SI w. r. to constraining factor, ξ
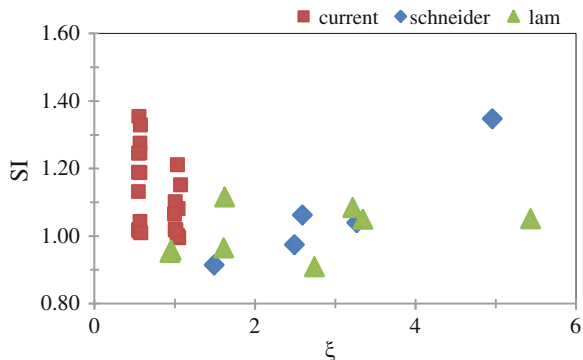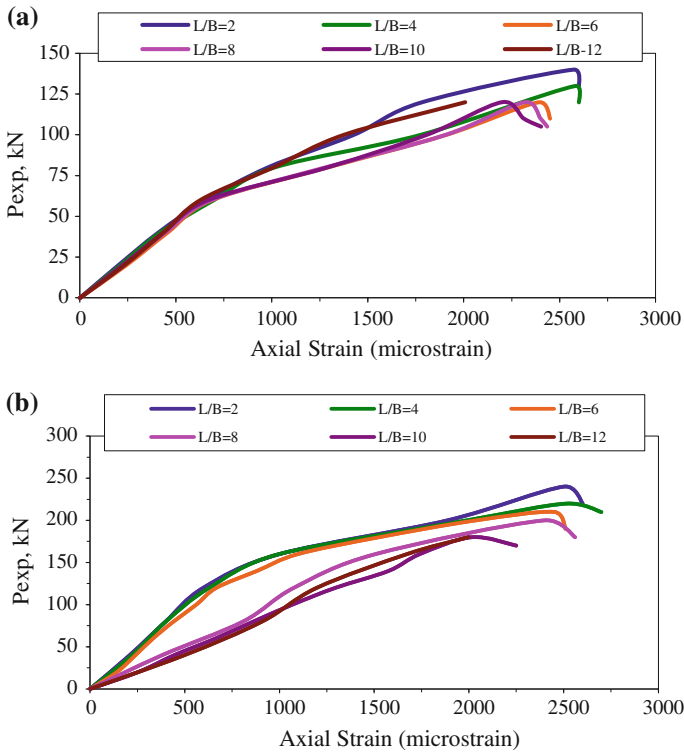
Fig. 8 Variation of experimental axial strength w. r. to axial strain **a** M30 concrete infill. **b** M60 concrete infill

capacity. The maximum axial strain occurred for square CFT columns of least L/B ratio (2–4). The ductility factor was calculated based on the method proposed by Usami and Ge [22], as the ratio of strain corresponding to ultimate load to the strain at yield. Since the yield point could not be defined clearly on the axial compressive load versus axial strain curve, the yield strain has been taken as 0.2 %, as suggested by Schneider [9]. The decrease in ductility observed with increase in L/B ratio from 2 to 12 was 18–20 %.

3.5 Failure Modes

CFT columns failed by local buckling as well as overall buckling as shown in Fig. 9. CFT columns of L/B ≥ 8 failed due to overall buckling. It was observed that local buckling of steel tube was delayed due to concrete filling in CFT column specimens. In CFT columns, concrete inside the tube prevents inward buckling mode of failure of the steel tube and steel tube in turn provides effective lateral confinement to the

Fig. 9 Failure modes of CFT columns

Local Buckling   Overall Buckling

concrete inside the tube. CFT columns of L/B < 8, exhibited bulging of steel tubes near top for most of the specimens and at centre for few specimens. Similar behavior was observed by Schneider [9] and Muhammad et al. [18].

4 Conclusions

Twenty four cold-formed steel square column specimens of varying length to breadth ratio and breadth to thickness ratio have been tested under axial compression till failure and tested strength values were compared with the axial compressive strength values predicted by using various international codes and standards and design methods suggested by previous author. A modified equation was also proposed. Fifteen test results which are available in literature were also considered for validation purposes. The conclusions arrived within the scope of these tests are as follows,

- The axial compressive strength of square CFT columns was found to be decreasing by 14–25 % with increase in length to breadth ratio whereas it was increasing up to 70 % with increase in concrete core strength, for the same gross-sectional area.
- The predicted values of axial compressive strength from international codes and design methods under consideration were found to be conservative for all CFTs under consideration. Of all the methods investigated, Eurocode 4-1994 [14] and GJB 4142-2000 [20] values are closer to test values. The modified equation proposed by author yields results in good agreement with test results. The mean and standard deviation of experimental to predicted values are 0.99 and 0.15 respectively.

- The Strength Index values were found to be increasing with increase in Constraining factor, ξ.
- All square CFT columns exhibited non-linear behavior, the maximum axial strain occurred for columns of least L/B ratio (2–4). The decrease in ductility observed with increase in L/B ratio was 18–20 %.
- CFT columns failed by local buckling as well as overall buckling. CFT columns of L/B ≥ 8 failed due to overall buckling. CFT columns of L/B < 8, exhibited bulging of steel tubes near top for most of the specimens and at centre for few specimens.

References

1. Shams M, Saadeghvaziri MA (1997) State of the art of concrete-filled steel tubular columns. ACI Struct J 94(5):558–571
2. Liu D, Gho WM, Yuan J (2003) Ultimate capacity of high strength rectangular concrete filled steel hollow section stub columns. J Constr Steel Res 59:1499–1515
3. Shanmugam NE, Lakshmi (2001) State of the art report on steel concrete composite columns. J Constr Steel Res 57(1):1041–1080
4. Furlong RW (1967) Strength of steel-encased concrete beam-columns. J Struct Eng, ASCE 93 (5):113–124
5. Gardner J, Jacobson R (1967) Structural behavior of concrete-filled steel tubes. ACI 64 (7):404–413
6. Knowles RB, Park R (1969) Strength of concrete filled steel tubular columns. J Struct Eng, ASCE 105(12):2565–2587
7. Knowles RB, Park R (1970) Axial load design for concrete filled steel tubes. J Struct Eng, ASCE 96(10):2125–2153
8. O'Shea MD, Bridge RQ (2000) Design of circular thin-walled concrete filled steel tubes. J Struct Eng, ASCE 126(11):1295–1303
9. Schneider SP (1998) Axially loaded concrete-filled steel tubes. J Struct Eng, ASCE 124 (10):1125–1138
10. Brauns J (1999) Analysis of stress state in concrete-filled steel columns. J Const Steel Res 49 (2):189–196
11. Han LH (2002) Tests on stub columns of concrete-filled RHS sections. J Constr Steel Res 58:353–372
12. Lam D, Williams CA (2004) Experimental study on concrete-filled square hollow sections. Steel Compos Struct 4(2):95–112
13. Tao Z, Han LH, Zhao XL (1998) Behaviour of square concrete filled steel tubes subjected to axial compression. In: Proceedings of the fifth international conference on structural engineering for young experts, Shenyang, P.R. China, pp 61–67
14. EC 4: 1994, Eurocode 4: design of composite steel and concrete structures, European Committee for Standardization, Brussels, Belgium
15. ACI 318: 1999, Building code requirements for structural concrete and commentary, American Concrete Institute, Farmington Hills, Mich
16. AISC: 2005, Load and resistance factor design specification for structural steel building, American Institute of Steel Construction, Chicago

17. AISC-LRFD: 1999, Load and resistance factor design specification for structural steel building, American Institute of Steel Construction, Chicago
18. Muhammad NB, FAN J, NIE J (2006) Strength of concrete filled steel tubular columns. ISSN 1007-0214, 11(6):657–666
19. AS 3600: 1994, Australian standards for reinforced concrete structures, Standards Australia, Sydney
20. GJB 4142: 2000, Technical specifications for early-strength model composite structures, Peking, 2001
21. BS 5400: 1979 Steel, concrete and composite bridges, Part 5, Code of practice for design of composite bridges, London
22. Usami T, Ge HB (1994) Ductility of concrete-filled steel box columns under cyclic loading. J Struct Eng, ASCE 120(7):2021–2040

Comparative Study on Response of Boiler Supporting Structure Designed Using Structural Steel I-Columns and Concrete Filled Square Steel Tubular Columns

T. Harikrishna and Kaliyamoorthy Baskar

Abstract Boiler supporting structure is one of the most important structures employed in any power plant project. A typical boiler supporting structure will be of 100 m height subject to a concentrated load in the range of 15,000–20,000 tons hung from the top. The distributed loads attached to the rest of the portion (i.e. from 0 to 100 m) are comparatively less and therefore, this type of structure is typically like an inverted pendulum with huge mass attached at the top. These kinds of structures are highly sensitive to lateral and dynamic loads. In the present day Indian scenario, the boiler supporting structures are designed using huge Plus columns made with two major I-sections in the order of 1.0–1.2 m web depth with a typical web and flange thicknesses in the order of 16–63 mm. As a typical once through supercritical boiler supporting structure consists of around 25–45 columns of such mega size, such structures becomes more expensive in terms of money and fabrication time. In view of optimizing the structural steel usage and to develop an efficient structural system, a theoretical attempt is made in this study through design of such structures using concrete filled square steel tubular column. Typical boiler structure is modeled using structural analysis program and analyzed for various conditions such as various seismic zones, wind zones, different load combinations and various section sizes. The story drift of the structure is estimated at various levels and compared with that of structure made using Plus I-column. Typical cost comparison also made to study the effectiveness of the project. This paper describes the complete analytical procedure along with results and conclusions.

Keywords Boiler supporting structure · Concrete filled square steel tubular column · Plus-I column · Wind · Seismic · Power plant

T. Harikrishna (✉)
Fossil Boiler Division, Bharat Heavy Electricals Limited (BHEL), Trichy 620014, India
e-mail: harikrish@bheltry.co.in

K. Baskar
Department of Civil Engineering, National Institute of Technology (NIT),
Trichy 620015, India
e-mail: kbaskar@nitt.edu

1 Introduction

In a thermal power plant, Boiler supporting structure forms 25 % of the total weight of a steam generator i.e., in the range of 12,000–15,000 MT and the columns forms 25 % of the weight of boiler supporting structure i.e., in the range of 3,000–3,750 MT. Boiler supporting structure transmits the entire pressure parts and non-pressure parts load to the foundation through a structural system network consisting of column, beams, bracings and ceiling structure. In the boiler supporting structure, columns are subjected to heavy axial compressive loads in the range of 300–3,500 MT and at present these are designed using Plus-I columns.

Composite columns are a combination of concrete and steel columns combining the advantages of both types of columns. The concrete filling not only leads to a bearing capacity which is much higher than that of steel columns but it also promotes the resistance against fire. Concrete Filled Square Steel Tubular (CFST) column sections have many excellent structural properties, such as high compressive strength, high cyclic strength, large ductility and large energy absorption capacity. The stiffness of the CFST column is greatly enhanced because the steel, which has a much greater modulus of elasticity than the concrete, is situated farthest from the centroid, where it makes the greatest contribution to the moment of inertia. Increased stiffness, leading to reduced slenderness and increased buckling resistance. The steel tube of a CFST column confines the encased concrete that in return constraints local buckling of steel tube. Therefore, it is most advantageous to use CFSTs for the columns subjected to the large compressive loading. The steel tube prohibits excessive concrete spalling and CFST column add significant stiffness to a frame compared to traditional steel frame construction. The steel of the CFST section is well plasticized under bending because it is located most outside the section. The concrete is held by the steel profile and cannot split away even if the ultimate concrete strength is reached. As far as the ductility and the rotation capacity are concerned, concrete filled steel hollow section columns show the best behavior compared to other types of composite columns. Braced frames are an ideal use for CFST column because of their high compressive strength and stiffness.

In the present study, the Boiler structure is analyzed designed and estimate is done for two different cases. In these two cases, only the column sections are changed i.e. Case I with Plus-I columns, Case II with Concrete Filled Square Steel Tubular (CFST) columns (refer Fig. 1). For modeling and analysis of boiler supporting structure, STAAD-Pro software is used. Design of columns is carried out using excel programming and from obtained result, cost comparison is made between Plus-I columns and CFST columns. In both the cases, limit state method of design is adopted. Design of Plus-I columns is carried out as per Indian code, IS-800:2007 [1] and design of CFST columns is carried out as per Euro code-4 [2], which incorporates latest research on composite construction. Comparative study includes story drift of the boiler structure and cost comparison of columns and it also includes the axial force and displacement comparison of Plus-I column with

Fig. 1 Typical column sections used
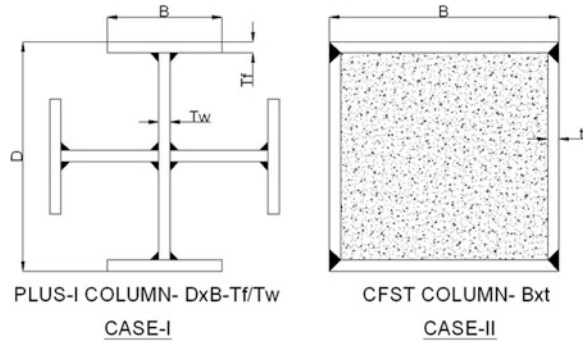
CFST column. From the results it is found that boiler structure with CFST columns is economical than Plus-I columns in terms of cost.

2 Literature Review

A brief review of the research carried out in recent years related to behavior of concrete filled steel tubular columns is presented here.

- Under axial load and uni-axial bending, experimental behavior of pin ended normal strength square concrete filled steel tube columns was investigated by Bridge [3], Matsui et al. [4] and Chung et al. [5]. Test results indicated that the ultimate axial strengths of CFST beam-columns increased with increasing the steel tube thickness. Increasing the loading eccentricity ratio/slenderness ratio reduced the ultimate axial strengths of CFST beam-columns.
- Mursi and Uy [6] studied the experimental behavior of bi-axially loaded CFST short and slender beam-columns which were constructed from high strength structural steel tubes with yield strength of 690 MPa. Their study indicated that the concrete core delayed the local buckling of thin steel walls. Local buckling occurred at the maximum load and steel plates buckled outward on all faces of a slender column. Test results indicated that the ultimate axial strength of hollow steel short beam-columns under axial load and biaxial bending was significantly increased by the infill concrete which delayed the local buckling of the steel plates in compression.
- Hu et al. [7] proposed proper material constitutive models for concrete-filled tube (CFT) columns and verified the nonlinear finite element program ABA-QUS against experimental data. For Square CFT columns, the tubes do not provide large confining effects to the concrete, especially, when the width-to-thickness ratio is large (>30). Both the lateral confining pressure and the material degradation parameter decrease with an increase in width to thickness ratio (D/t or B/t).

- Ellobody et al. [8] presented an accurate nonlinear finite element model for the analysis of normal and high strength concrete-filled square and RHS compact steel tube columns. The columns strengths, load-axial shortening curves and deformed shapes of the columns have been predicted using the finite element model and generally compared well with the experimental results. They have reported that the design strengths calculated using the European Code are accurate, except for the concrete-filled RHS compact steel tube columns having the overall depth of the steel tube-to-plate thickness ratio of 40 and the design strengths calculated using the ACI/AS are conservative.

- Guo et al. [9] carried out experimental and numerical study (ABAQUS) on bare steel and concrete-filled tubes to investigate the occurrence of local buckling and how different depth-to-thickness ratios affect the response of the steel component. Study suggests that for depth-to-thickness ratios >50, (i) effects of local buckling needs to be considered in the design (ii) significant reserve in capacity in the post-local buckling range which evidently increases the bearing capacity (iii) the initial deformation decreases the buckling capacity (iv) the residual stress also decreases the bearing capacity.

3 Load Details and Structural Data

A Once Through Super Critical (OTSC) boiler supporting structure which is situated in earthquake zone-II as per Indian standard IS: 1893 (part 1)-2002 [10] and wind speed 47 m/s as per IS: 875 (Part 3)-1987 [11] is considered for this comparative study. The plan dimension and height of structure is 53.35 m × 82.80 m and 90.50 m (refer Figs. 2 and 3). Also, Fig. 2 represents Boiler structural plan at 0.00 m and Fig. 3 represents 3D Boiler structural model in Staad.pro. The study is carried out on the same structural plan for both the cases. The basic loading for both the cases are kept same. Structure is designed for permanent loads, imposed loads, lateral buckling and action due to wind/seismic forces. The most unfavorable combinations of the above mentioned force actions had considered as required by IS: 875 (Part 5)—1987 [12].

3.1 Dead Loads

The dead loads like boiler weight including water filled water walls, economizer water filled bank tubes, 300 mm ash build-up in pent house with ash density of 1,300 kg/m^3, equipment weight, structure own weight, other loads like ash water piping, supply ash and instrument air piping, service water piping etc., cantilever loads of not less than 500 kg/m at a distance of 1,200 mm from the external face of
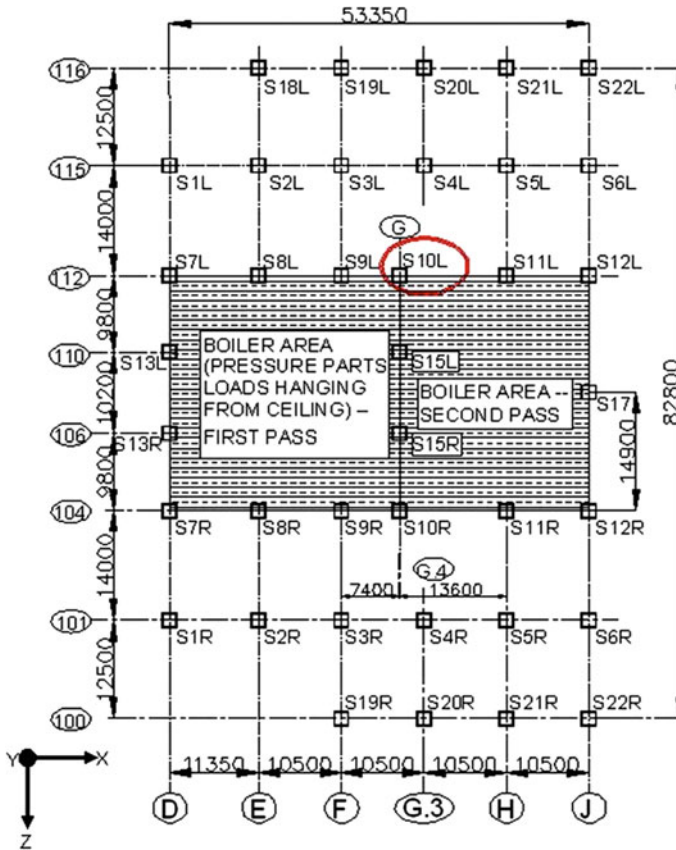
Fig. 2 Boiler structural plan at 0.00 m

the column on both sides of the boilers for supporting cable trays, pipe load and contingent load (including scaffolding). Dead loads are calculated as per IS: 875 (Part 1)-1987 [13].

3.2 Live Loads

As per IS: 875 (Part 2)-1987 [14], Imposed floor loads available for the power stations.

- 500 kg m^2 on the grating or the chequered plate of walkways and stairs.
- 1,000 kg per m^2 on the grating or the chequered plate of operating floors.
- 75 kg per m^2 on roof covering.

Fig. 3 3D boiler structural model in staad.pro
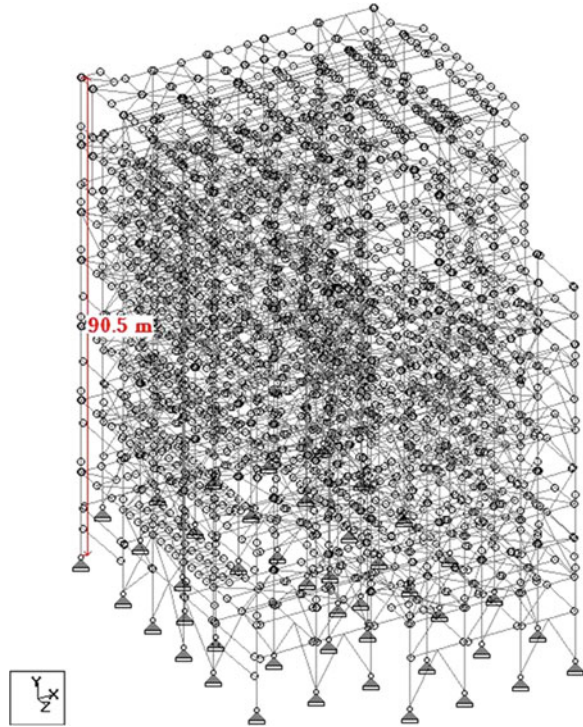
- Side cladding loads
- Interconnection platform loads at various levels.

Considering that the platform live loads never reach their maximum values at the same time on all the points of the structure concerned, these live loads are reduced according to IS:875 (Part 2)-1987 [14].

3.3 Wind Loads

Dynamic wind analysis using Gust Factor or Gust Effectiveness Factor method is carried out as per IS: 875 (Part 3)-1987 [11].

3.4 Seismic Loads

Dynamic analysis of the structure is done as per Response Spectrum Method for Jaipur region (Zone-II), Medium soil. The basic value determination of the seismic action is carried out according IS: 1893 (part 1)-2002 [10].

3.5 Loads and Load Combinations

- Type of Loads

  - DL: Dead Load including self weight
  - LL: Live Load
  - WL: Wind Load (in both directions)
  - SL: Seismic Load (corresponding to DL + 50 % LL)
  - TL: Secondary loads like Climatic temperature effect. (± 25 °C)

- Load Combinations

  - DL + LL
  - DL + LL ± WL/SL
  - DL + LL + TL ± WL/SL
  - 0.75 DL ± WL/SL

At ceiling level 90.00 M, 'I' shape Plate Girders of size 3,800 × 1,000-115/50 to a length of 30.5 m are resting between the two columns in the boiler area (refer Fig. 4). Welded 'I' beams are connected between Girders and in turn between Welded 'I' beams, rolled beams (] [, I I) are connected from where all the pressure parts loads in the range of 16,000 MT are hanged in the boiler area.
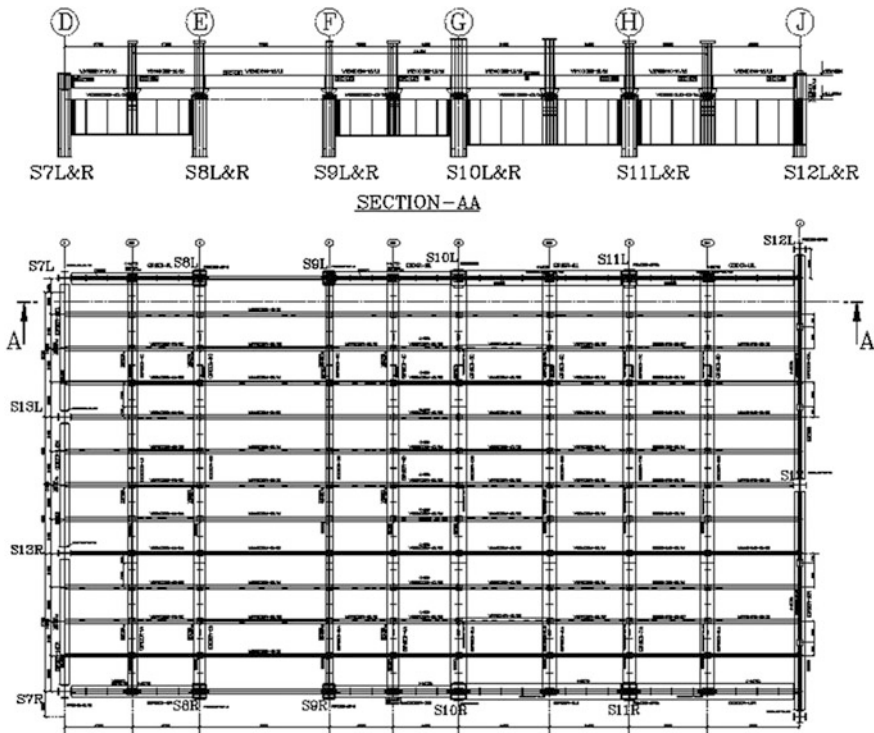

Fig. 4 Boiler structural plan at 90.00 m (ceiling level)

Table 1 Structural data of boiler supporting structure

1. Plan dimension	53.350 × 82.800 m
2. Total height of structure	90.5 m
3. Main brace levels—7 levels	15.00, 28.70, 42.80, 55.40, 64.60, 77.20, 90.00 m
4. Erection joints of column—6 Nos.	16.50, 30.20, 44.30, 56.90, 66.10, 78.70 m
5. Beam profiles	Rolled Beams : I-125, I-150, I-200, I-250, I-300, I-400, I-450, I-500 and I-600
	Welded Plate formed "I" Beams
6. Vertical bracing profiles	Welded Plate formed Box "[]" sections
7. Horizontal bracing profiles	Double angles (back to back connected)
	Star angles (diagonally connected)
8. Grade of steel	Indian Standard IS: 2062 E250 (Fe410 W)
9. Plate thickness used for structural profiles	8, 10, 12, 16, 20, 25, 32, 36, 40, 50, 56, 63 mm
10. Class of sections considered	Plastic/compact sections
11. Grade of concrete for CFST columns	M30

3.6 Structural Data

Structural data of boiler supporting structure are briefed in Table 1.

4 Design Methodology

- The column bases and the erection joints of columns are assumed as pinned. Hence, no bending moment is acting at column base for any of the column.
- All the beam-column joints and the joints of vertical and horizontal bracings are assumed as pinned. Accordingly, all end moments are released.
- The boiler columns are considered to have lateral support at Main Brace Levels only. Main Brace Levels are acts as Horizontal diaphragm, where all the columns are tied with horizontal beams and horizontal bracings in plan, at that level.
- For the effective cost comparison of boiler columns, the utility ratio is maintained same while designing steel plus-I columns and CFST columns.
- Eurocode-4 [2] provides two methods for calculation of the resistance of composite columns. The first is a general method which takes explicit account of imperfections, the influence of deflections on the equilibrium (second order theory) and the loss of stiffness if parts of the section become plastic (partially plastic regions). The second is a simplified design method which makes use of the European buckling curves for the influence of instability and on cross-section interaction curves determining the resistance of a section. This method is limited in application to composite column of doubly symmetrical and uniform cross-section over the member length. This method is used in this work.

Table 2 Material properties for typical column sections

Material property	Steel plus-I column sections	CFST column sections
Elastic modulus (E)	2.05×10^5 N/mm^2	0.6175×10^5 N/mm^2
Poisson's ratio (u)	0.3	0.22
Density	78.50 kN/m^3	35 kN/m^3
Thermal coefficient of expansion (α)	1.2×10^{-5} °C	1.0×10^{-5} °C
Damping	2 %	3.5 %

- The effective flexural stiffness (EI)$_{eff}$ of a cross section of a composite column according to Eurocode-4 is given as

  - (EI)$_{eff}$ = $E_a I_a$ + $K_e E_{cm} I_c$
  - I_a, I_c—Second moments of area of the structural steel section and the uncracked concrete section
  - E_a, E_{cm}—Stiffness moduli of the structural steel and secant modulus of concrete
  - K_e—correction factor that should be taken as 0.6

- Width to thickness ratio of steel plate for CFST column sections are maintained equal/less than 30 (i.e. B/t · 30), to have a large confining effect to the concrete.
- Material properties for analysis of boiler structure for typical column sections are considered as per Table 2.

5 Results

Linear static analyses of boiler supporting structure are carried out for two different cases i.e. Case-1 with steel plus-I columns and Case-2 with CFST columns and comparison is made; the following results are drawn from the study.

Comparison of maximum lateral drift of boiler structure along Z-axis is done at Main Brace Levels. The Fig. 5 shows the maximum lateral drift of the boiler structure along Z-axis is reduced by 40, 34, 35, 36, 36, 35 and 34 % respectively at seven MBLs from bottom to top, by replacing the Steel plus-I columns with CFST columns.

Comparison of maximum lateral drift of boiler structure along X-axis is done at Main Brace Levels. The Fig. 6 shows the maximum lateral drift of the boiler structure along X-axis is reduced by 37, 36, 39, 39, 39, 37 and 36 % respectively at seven MBLs from bottom to top, by replacing the Steel plus-I columns with CFST columns.

From Fig. 7, Total steel weight of boiler columns using plus-I columns is 3,704.80 MT. Total steel weight and concrete weight of boiler columns are 2,799.79 MT and 3,380 MT respectively, using CFST columns. Hence, there is a

Fig. 5 Comparison of maximum lateral drift of structure along Z-axis (load case considered: wind load along Z-axis)
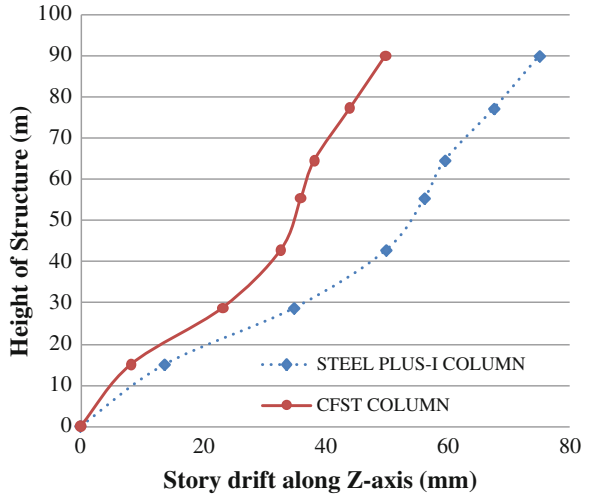
Fig. 6 Comparison of maximum lateral drift of structure along X-axis (load case considered: wind load along X-axis)
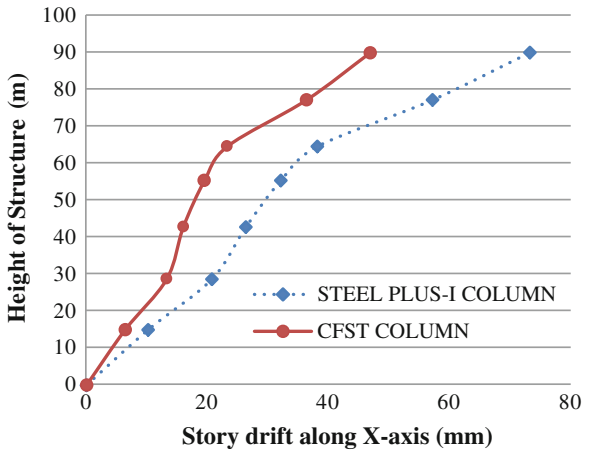
saving of 905 MT of structural steel and an addition of 3,379.25 MT of M30 concrete.

Comparison of axial force in S10L column is done for seven column pieces from bottom to top. From the Fig. 8 it is noticed that maximum axial force in S10L column is increased by 9, 7, 7, 7, 4, 2 and 1 % from first piece to seventh piece of the column, by replacing steel plus-I columns with CFST columns in a boiler structure. S10L column is chosen for comparison, since it is the heavily loaded column in the boiler structure.
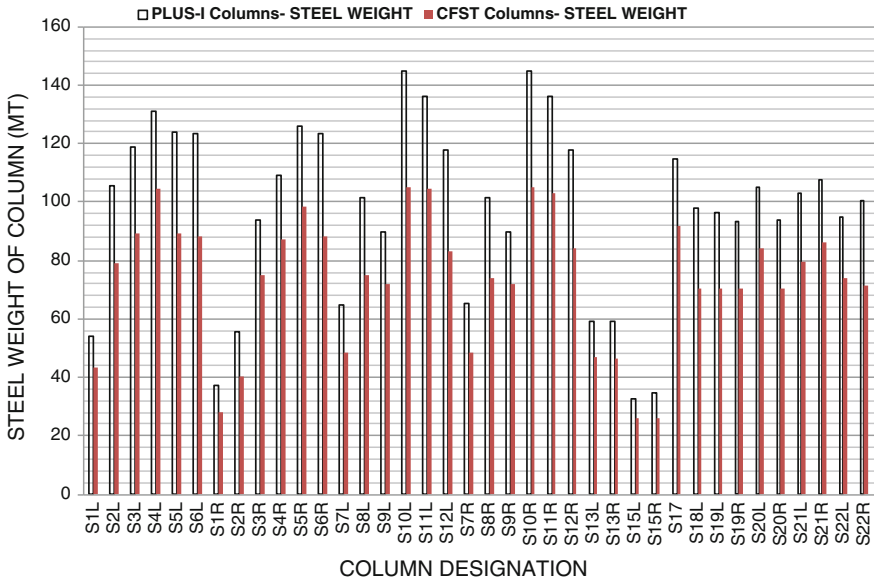
Fig. 7 Comparison of total steel weight for columns

Fig. 8 Comparison of axial force for column (s10L)
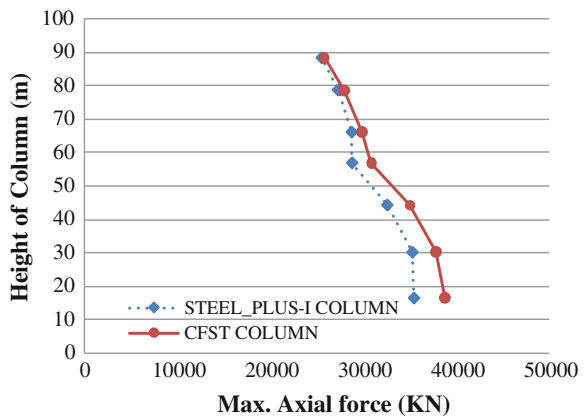
Comparison of maximum displacement in S10L column is done at six erection joints and at top of column. From the Fig. 9 it is noticed that displacement in S10L column is reduced by 41, 36, 35, 37, 35, 33 and 37 % from first erection joint to top of the column, by replacing steel plus-I columns with CFST columns in a boiler structure.

Fig. 9 Comparison of maximum displacement in s10L column
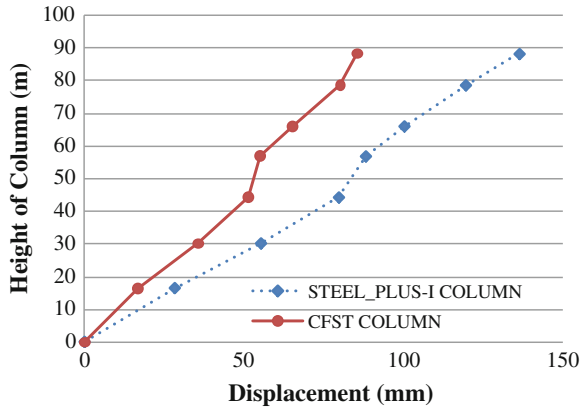
Table 3 Comparison of cost of boiler columns

	Total steel weight (MT)	Material + fabrication cost Per MT (Rs)	Total concrete volume in m^3	Rate of M30 concrete per m^3 (Rs)	Total cost of columns (Rs)
Steel plus-I columns	3,704.80	INR 77,500.00	–	–	INR 287,122,000.00
CFST columns	2,799.79	INR 77,500.00	1,351.69	INR 5,500.00	INR 224,418,020.00
				Savings	INR 62,703,980.00

5.1 Comparison of Cost of Boiler Columns

From Table 3, by replacing CFST columns with steel plus-I columns in a boiler structure, there is a saving of 905 MT of structural steel and an addition of 1,351.69 m^3 of M30 concrete. Hence, there is a net savings of 62.70 millions of Indian rupees. In the cost estimation of boiler columns, erection cost is not included.

6 Conclusions

Analysis and design of boiler supporting structure is done for two different cases i.e., one with steel plus-I columns and the other with CFST columns and comparison is made between them and from that results, conclusions can be drawn out are as follows:-

- The structure with CFST columns shows a reduction in storey drift up to 40 % compared to that of Plus-I columns.
- Structural steel weight reduction of 905MT is achieved by replacing plus-I columns with CFST columns. But, there is an addition of 1351.69 Cubic meter of M30 concrete that is used in CFST columns.
- 1–9 % increase in axial force is noticed in S10L column when CFST column is employed.
- Maximum displacement in S10L column is reduced by an average of 36 % with CFST column than with plus-I column.
- In the cost estimation of boiler columns, erection cost is not included. As compared to steel plus-I columns there is a net saving of 62.70 million (INR) is noticed when CFST columns are employed for the structure considered.
- Present work shows that the use of CFST columns in boiler structures provides considerable cost saving in addition to its better structural performance.

References

1. IS 800 (2007) Code of practice for general construction in steel. Bureau of Indian Standard, New Delhi
2. Code and Commentary on Eurocode 4 (2004) Design of composite steel and concrete structures—part 1-1: general rules and rules for buildings
3. Bridge RQ (1976) Concrete filled steel tubular columns. School of Civil Engineering, The University of Sydney, Sydney, Australia, Research report No. R283
4. Matsui C, Tsuda K, Ishibashi Y (1995) Slender concrete filled steel tubular columns under combined compression and bending. In: Proceedings of the 4th Pacific structural steel conference, Singapore, Pergamon, vol 3(10), pp 29–36
5. Chung J, Tsuda K, Matsui C (1999) High-strength concrete filled square tube columns subjected to axial loading. In: 7th East Asia-Pacific conference on structural engineering and construction, Kochi, Japan, vol 2, pp 955–960
6. Mursi M, Uy B (2006) Behaviour and design of fabricated high strength steel columns subjected to biaxial bending part I: experiments. Adv Steel Constr 2(4):286–313
7. Hu HT, Huang CS, Wu MH, Wu YM (2003) Nonlinear analysis of axially loaded concrete-filled tube columns with confinement effect. J Struct Eng 129(10):1287–1430
8. Ellobody E, Young B, Lam D (2006) Behaviour of normal and high strength concrete filled compact steel tube circular stub columns. J Constr Steel Res 62(7):706–715
9. Guo L, Zhang S, Kim WJ, Ranzi G (2007) Behaviour of square hollow steel tubes and steel tubes filled with concrete. Thin-Walled Struct 45(2007):961–973
10. IS 1893-Part 1 (2002) Criteria for earthquake resistant design of structures. Bureau of Indian Standards (BIS), New Delhi
11. IS 875-Part 3 (1987) Code of practice for wind loads. Bureau of Indian Standards (BIS), New Delhi
12. IS 875-Part 5 (1987) Code of practice for special loads and combinations. Bureau of Indian Standards (BIS), New Delhi
13. IS 875-Part 1 (1987) Code of practice for design loads (other than earthquake)for buildings and structures, Dead loads. Bureau of Indian standards (BIS), New Delhi
14. IS 875-Part 2 (1987) Code of practice for live loads. Bureau of Indian Standards (BIS), New Delhi

Effect of Concrete Strength on Bending Capacity of Square and Rectangular CFST Elements

P.K. Gupta and S.K. Katariya

Abstract Present study deals with concrete filled square and rectangular steel tube structural elements subjected to bending. The square section (176.77 mm × 176.77 mm) and rectangular section (125 mm × 250 mm) are selected in such a way to have equal concrete and steel sectional area. Steel tubes having ultimate strength 400, 480 and 560 MPa are filled with concrete having cylinder compressive strength 30, 50, 70 and 100 MPa. Behaviour of specimens was studied by fiber element analysis computer code developed in Oracle database. The efficiency and accuracy of the developed computer code are demonstrated through comparisons between computer code results and experimental results. It was found that increment in concrete strength from 30 to 50 MPa, 70 and 100 MPa resulted to increase in the moment capacity of CFST beams by 4, 7 and 11 % for square section and 5, 10 and 15 % for rectangular section, respectively. The moment capacity of CFST beams increases by 17–18 % and 34–36 % when steel tube strength was increased by 20 and 40 %, respectively.

Keywords Concrete-filled steel tubes · Bending capacity · Ductility and moment-curvature

1 Introduction

Steel-concrete composite construction is widely used in the construction of high-rise buildings and bridges. The composite construction ideally combines the advantages of both steel and concrete to achieve high capacity, high stiffness, speed

P.K. Gupta · S.K. Katariya (✉)
Department of Civil Engineering, Indian Institute of Technology,
Roorkee, Roorkee 247667, Uttarakhand, India
e-mail: skkatariya.gbpuat@gmail.com

P.K. Gupta
e-mail: pkgupfce@iitr.ernet.in

of construction, and economy [1]. Furlong [2] tested one CFST beam with diameter to thickness ratio of 32. It was found that the flexural strength of the hollow steel tube alone was about 49 % lower than that of the same steel tube filled with concrete having 3.14–4.18 kips per square inch compressive strength. Tomii and Sakino [3] performed tests on eight CFST beam-column specimens with width to thickness ratio range from 23.5 to 45 for a strength study. Prion and Boehme [4] tested four circular CFST beams with diameter to thickness ratio of 89.4 and filled with concrete having cylinder strength 73 MPa. It was found that beam specimens failed in a ductile manner. Gupta et al. [5] studied the behaviour of circular CFST columns under axial load till failure. They concluded that load carrying capacity of such columns can be maximized by choosing correct value of D/t ratio of steel tube.

Experimental methods have been basic means of researching the behaviour of CFST, while numerical modelling methods become increasingly important because they can simulate cases that are difficult to be completed by experiments [6]. Calculation methods for flexural capacity of CFST beam have been proposed by a few researchers [3, 7, 8]. Liang presented theory and algorithms of a performance-based analysis technique for the nonlinear analysis of thin-walled concrete-filled steel tubular beam-columns with local buckling effects [9]. Gupta and Katariya [10] studied effect of size of square section on bending capacity of CFST beams. They used fiber element analysis model and concluded that bending capacity of CFST beams increases in incremental order due to more utilization of steel area in bigger sections. In present study, a parametric study has been conducted using fiber element analysis code developed in Oracle database to investigate the effects of steel tube cross-sectional area on the flexural capacity of CFST beams.

2 Computer Code and Its Validation

Fiber element analysis technique is used to develop a computer code and written in Oracle-10g form 6i database. The efficiency and accuracy of the developed computer code are demonstrated through comparisons between computer code results and corresponding experimental results. Details of the computer code can be found elsewhere [11].

The composite beam section was divided into number of parts known as fibers as shown in Fig. 1b. With the help of value of curvature as an input, strain in each element was calculated. The stress-strain relationships for materials like steel and concrete were used to calculate the stress in each fiber corresponding to strain values. Force in each fiber was calculated using sectional area of fiber and stress developed in it due to curvature. Neutral axis depth was determined by iteration method. Finally bending moment for any given value of curvature was calculated.
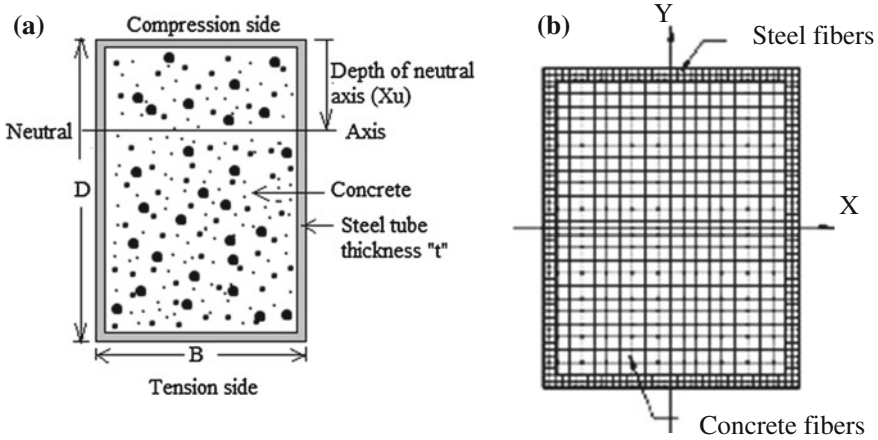
Fig. 1 **a** Typical sectional view of CFST beam. **b** Discretization of section for fiber element analysis

3 Stress-Strain Behaviour of Steel and Concrete

Stress-strain relationships for steel and concrete were incorporated in the computer code. The stress-strain relationship used for cold formed steel both in tension as compression is shown in Fig. 2. The stress-strain behavior is characterized by a rounded stress-strain curve from A to B. The rounded part of the stress-strain curve is represented as

$$\sigma_s = f_{sy}\left(\frac{e_{sy} - 0.9e_{sy}}{e_{st} - 0.9e_{sy}}\right)^{1/45} \left(\text{for } 0.9e_{sy} < e_s < 0.9e_{st}\right) \tag{1}$$

Fig. 2 Stress-strain relationships for structural steels [12]
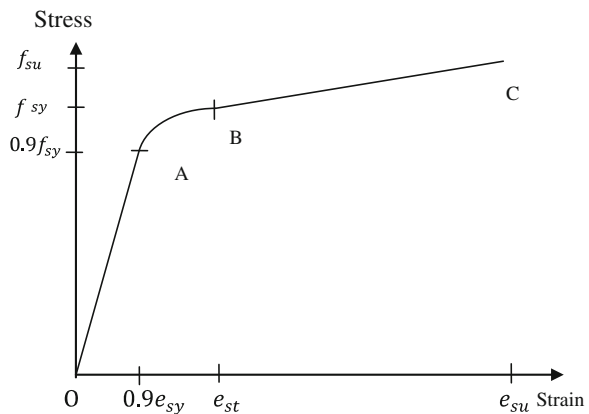
where σ_s is the stress in a steel fiber, e_s is the strain in the steel fiber, f_{sy} is the yield strength of steel, e_{sy} is the yield strain of steel. The value of strain in steel at strain hardening (e_{st}) is taken as 0.005. The ultimate strain e_{su} is taken as 0.1 [12].

Yield strain (e_{sy}) is calculated from the modulus of elasticity (E_s) and yield strength of steel (f_{sy}) [8].

Modulus of elasticity of concrete (E_c) is calculated by ACI [13].

$$E_c = 3{,}320 \sqrt{f'_{cc}} + 6{,}900 \text{ MPa} \qquad (2)$$

where f'_{cc} is compressive cylinder strength of concrete in MPa.

The stress-strain relationship for confined concrete is shown in Fig. 3. This curve is divided into four parts in compression side like OA, AB, BC and CD and two parts in tension side OS and SQ. The concrete stress from O to A can be calculated from the equation suggested by Mander et al. [14]

$$\sigma_c = \frac{f'_{cc}\lambda(\varepsilon_{cc}/\varepsilon'_{cc})}{\lambda - 1 + (\varepsilon_{cc}/\varepsilon'_{cc})^\lambda} \qquad (3)$$

where

|	
σ_c	longitudinal compressive stress in concrete at any part of compression
ε_{cc}	longitudinal compressive strain in concrete at any part of compression
f'_{cc}	compressive cylinder strength of concrete in MPa
ε'_{cc}	strain in concrete corresponding to stress f'_{cc}
λ is a parameter	$E_c/(E_c - (f'_{cc}/\varepsilon'_{cc}))$
ε_{to}	tensile strain in concrete at cracking
ε_{tu}	ultimate tensile strain in concrete
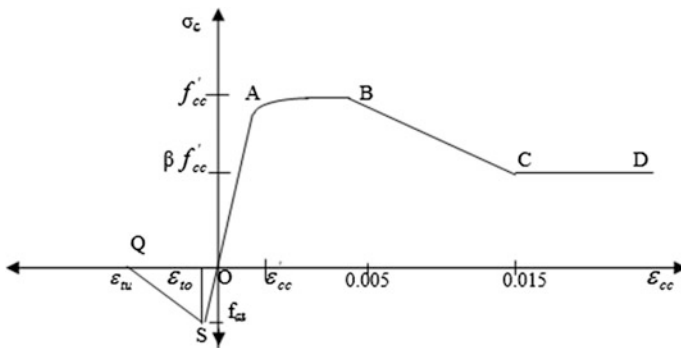
Fig. 3 Stress-strain curve for concrete in concrete filled steel tube [12]

The strain ε'_{cc} at peak is taken as 0.002 for concrete compressive strength below 28 MPa and 0.003 for concrete strength above 82 MPa. For concrete strength between 28 and 82 MPa, the strain is calculated as a linear function of concrete strength [8].

The stress in the confined concrete stress-strain curve part AB, BC and CD is calculated as below:

$$\sigma_c = f'_{cc} \quad \text{for} \quad \varepsilon'_{cc} < \varepsilon_{cc} \leq 0.005$$
$$\sigma_c = \beta f'_{cc} + 100\,(0.015 - \varepsilon_{cc})\,(f'_{cc} - \beta f'_{cc}) \quad \text{for} \quad 0.005 < \varepsilon_{cc} \leq 0.015 \qquad (4)$$
$$\sigma_c = \beta f'_{cc} \quad \text{for} \quad \varepsilon_{cc} > 0.015$$

The value of β depends upon the D/t ratio, as proposed by Liang [9] based on the experimental results presented by Tomii and Sakino [3]

$$\beta = 1.0 \quad \text{if} \quad D/t < 24$$
$$\beta = 1.5 - (D/48t) \quad \text{if} \quad 24 < D/t \leq 48 \qquad (5)$$
$$\beta = 0.5 \quad \text{if} \quad D/t > 48$$

where t is the wall thickness of steel section and D is the larger side of the section.

For concrete in tension zone, tensile strength of concrete (f_{ct}) corresponding to strain ε_{to}. ε_{to} is taken as $0.6\,\sqrt{f'_{cc}}$. The concrete tensile stress is proportional to tensile strain of concrete up to its cracking. After cracking, the strain in concrete is inversely proportional to stress in concrete. The ultimate strain is taken as 10 times of the strain at cracking ($\varepsilon_{tu} = 10\varepsilon_{to}$) [8].

Two specimens are used to validate the written code and fiber element analysis technique. The details of the specimens are presented in Table 1.

Figures 4 and 5 show variation of load with deflection for specimen RB4-2 and SP04. It is clear from these figures that the computed capacity and actual capacity of beam specimens are comparable.

Table 1 Details of specimens used for validation

Specimen	B × D (mm)	t (mm)	f'_{cc} (MPa)	f_{sy} (MPa)	f_{su} (MPa)	E_s (MPa)	Reference
RB4-2	120 × 120	5.86	32.00	321.10	377.76	20,0000	Han [7]
SP04	120 × 150	1.58	64.18	260.00	320.00	205000	Lab result

Fig. 4 Moment-deflection curve for specimen RB4-2
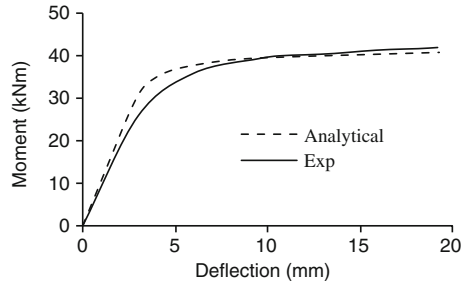
Fig. 5 Moment-deflection curve for specimen SP04

4 Parametric Study

To find out the results of similar cases through experimental work, it is costly as well as time consuming. In such type of problems, to find the effect of change or variation in any parameter of the specimen it is batter to use computer code after its validation. Computer code is best suitable tool for a parametric study.
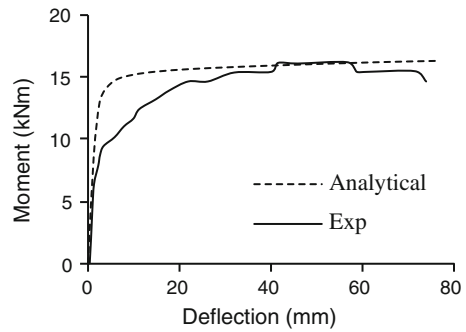
4.1 Beam Specimens

Typical sectional view of CFST beam is shown in Fig. 1a. Two different shapes of sections are taken. The rectangular section has width 125 mm and depth 250 mm. Other section has square shape size of 176.77 mm. The square section is derived from rectangular section to keep equal cross-sectional area of 125×250 mm^2. Three different strengths of steel are taken in the study. The yield strength of steel tubes were 325, 390 and 455 MPa and ultimate tensile strength were 400, 480 and 560 MPa respectively. The modulus of elasticity was considered as 205 GPa for each type of steel. The concrete having cylinder compressive strength 30, 50, 70 and 100 MPa were used to fill the tubes. The failure of CFST beams was tracked from tension as well as compression side. Steel on tension side was considered as

fractured when strain reached to a value of 0.1 while concrete on compression side was considered as crushed when strain reached to a value of 0.015. Local buckling failure of CFST beams on compression side is ignored and not considered as failure. The dimensions of all sections are given in Table 2.

5 Results

The following paragraphs summaries the salient findings of the parametric study. The results are covered in different structural aspects of the beam section.

5.1 Failure of Section

The CFST beams having square section filled with concrete having cylinder strength 100 MPa are failed as under reinforced. All rectangular section beams failed due to failure of concrete in compression side except specimen R-400 filled with concrete having cylinder strength 100 MPa. The tubes filled with concrete having cylinder strength 30, 50, and 70 MPa behaved as over reinforced section except specimen S-400 filled with concrete having cylinder strength 70 MPa. From Table 2 it is clear that specimen S-400 and S-560 filled with concrete having cylinder strength 70 and 100 MPa respectively are close to balanced section.

5.2 Concrete Utilization

The position of neutral axis was found nearer to compression side when steel tube was filled with higher grade of concrete. So utilized concrete area reduced at failure level. This behavior also found in other cases also as clear from Fig. 6. It can be concluded that as the grade of concrete increases the utilization of concrete area decreases.

5.3 Neutral Axis

From Fig. 7 it is clear that as the moment value increases the position of neutral axis shifts towards compression side.

Table 2 Details of simulated CFST beams

Specimen	B (mm)	D (mm)	t (mm)	f_sy (MPa)	f_su (MPa)	f'_cc (MPa)	Xu/D	A_cc/A_c (%)	Failure at collapse of beam				B. M. (kN-m)	B.M. ratio (concrete strength-wise)	B.M. ratio (steel strength-wise)	Moment ratio (M_Recti/M_squ)
									Steel in tension		Concrete in comp.					
									Str-ain	Str-ess (MPa)	Strain	Stress (MPa)				
S-400	176.77	176.77	2.1242	325	400	30	0.272	26.61	0.1	400	0.03402	15	42.47	1.000	1.000	1.000
	176.77	176.77	2.1242	325	400	50	0.198	19.12	0.1	400	0.02179	25	44.41	1.046	1.000	1.000
	176.77	176.77	2.1242	325	400	70	0.151	14.22	0.1	400	0.01496	35.15	45.83	1.079	1.000	1.000
	176.77	176.77	2.1242	325	400	100	0.109	9.98	0.1	400	0.00958	77.11	47.18	1.111	1.000	1.000
R-400	125.00	250.00	2.0000	325	400	30	0.298	29.48	0.1	400	0.03961	15	55.05	1.000	1.000	1.296
	125.00	250.00	2.0000	325	400	50	0.226	22.14	0.1	400	0.02664	25	58.44	1.062	1.000	1.316
	125.00	250.00	2.0000	325	400	70	0.178	17.32	0.1	400	0.01929	35	60.95	1.107	1.000	1.330
	125.00	250.00	2.0000	325	400	100	0.132	12.55	0.1	400	0.01282	60.90	63.75	1.1580	1.000	1.351
S-480	176.77	176.77	2.1242	390	480	30	0.297	29.17	0.1	480	0.03882	15	50.24	1.0000	1.183	1.000
	176.77	176.77	2.1242	390	480	50	0.225	21.78	0.1	480	0.02586	25	52.42	1.0430	1.180	1.000
	176.77	176.77	2.1242	390	480	70	0.177	16.85	0.1	480	0.01851	35	54.06	1.0760	1.178	1.000
	176.77	176.77	2.1242	390	480	100	0.129	11.98	0.1	480	0.01205	64.72	55.89	1.1120	1.185	1.000
R-480	125.00	250.00	2.0000	390	480	30	0.324	32.06	0.1	480	0.04464	15	64.81	1.0000	1.177	1.291
	125.00	250.00	2.0000	390	480	50	0.253	24.90	0.1	480	0.03118	25	68.59	1.0580	1.1737	1.308
	125.00	250.00	2.0000	390	480	70	0.205	20.01	0.1	480	0.02324	35	71.47	1.1030	1.1726	1.323
	125.00	250.00	2.0000	390	480	100	0.156	15.07	0.1	480	0.01613	50	74.71	1.1530	1.1719	1.337
S-560	176.77	176.77	2.1242	455	560	30	0.320	31.52	0.1	560	0.04348	15	57.95	1.0000	1.3645	1.000
	176.77	176.77	2.1242	455	560	50	0.248	24.19	0.1	560	0.02983	25	60.33	1.0410	1.3585	1.000
	176.77	176.77	2.1242	455	560	70	0.199	19.20	0.1	560	0.02196	35	62.15	1.0730	1.3561	1.000
	176.77	176.77	2.1242	455	560	100	0.150	14.17	0.1	560	0.01487	50.67	64.25	1.1090	1.3618	1.000
R-560	125.00	250.00	2.0000	455	560	30	0.344	34.18	0.1	560	0.04946	15	74.48	1.0000	1.3530	1.286
	125.00	250.00	2.0000	455	560	50	0.276	27.28	0.1	560	0.03526	25	78.52	1.0540	1.3436	1.302
	125.00	250.00	2.0000	455	560	70	0.229	22.41	0.1	560	0.02678	35	81.70	1.0970	1.3404	1.316
	125.00	250.00	2.0000	455	560	100	0.179	17.39	0.1	560	0.01935	50	85.41	1.1470	1.3398	1.330

Where A_s is net sectional area of steel and A_g is gross sectional area of composite section. A_{cc} and A_c are the concrete area in compression and total area of concrete in CFST beam section respectively. Where A_s is net sectional area of steel and A_g is gross sectional area of composite section. A_{cc} and A_c are the concrete area in compression and total area of concrete in CFST beam section respectively. M_x shall be M_x of beam section filled with 30 MPa strength concrete when BM ratio is calculated as per concrete strength, M_o shall be M_x of S-400 and R-400 section when BM ratio is calculated as per steel strength and M_o shall be M_x of square section when BM ratio is calculated as sectional shape

Fig. 6 Concrete utilization versus cylinder strength of concrete

Fig. 7 Moment ratio versus neutral axis depth ratio (X_u/D)

5.4 Influence of Concrete Compressive Strength

As compressive strength of infilled concrete increases the moment capacity also increases. This increase in moment capacity is not in the same ratio in which infilled compressive strength of concrete increases. Figure 8 shows the moment increment

Fig. 8 Moment ratio versus cylinder strength of concrete

of CFST beams with respect to concrete strength. Figures 12 and 13 show the value of maximum strain and stress respectively in outer most compression fiber of concrete at failure of CFST beams. From Fig. 13 it is clear that beam section behaves as under reinforced section. Moreover, Table 2 indicates that the specimens S-400 and S-560 are filled with concrete having cylinder strength 70 and 100 MPa respectively are close to balanced section.

5.5 Influence of Steel Strength

When the ultimate strength of steel is increased by 20 and 40 %, the moment capacity of CFST beams increases approximately 18 and 36 % for square section and 17 and 34 % for rectangular section respectively. Figures 9 and 10 depict the moment increment with respect to increment in steel strength of CFST beams. Figure 10 shows that moment increment in square section is slightly higher in comparison to rectangular section. Figure 11 shows the ratio between the moment capacities of the beam having rectangle cross section and circular cross section.
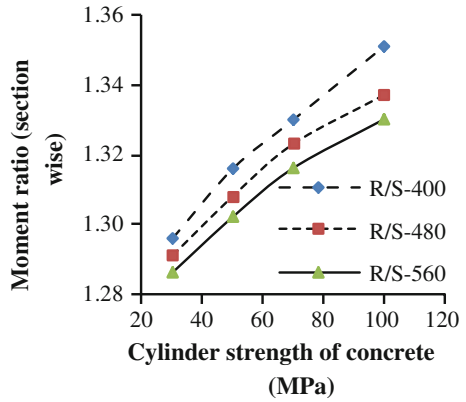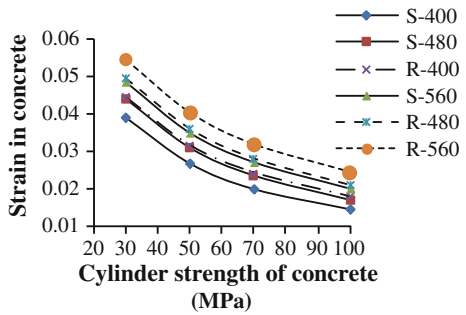

Fig. 9 Moment ratio versus ultimate strength of steel
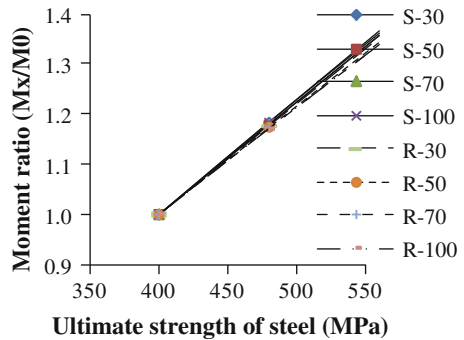
Fig. 10 Comparison of moment ratio of CFST beams having rectangular and square section
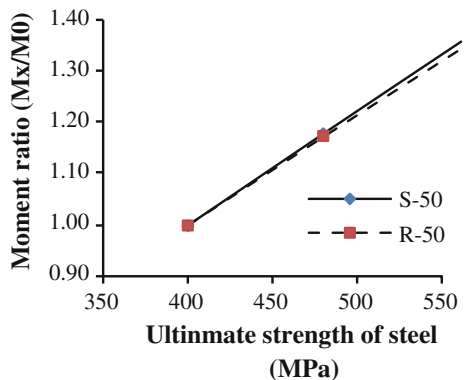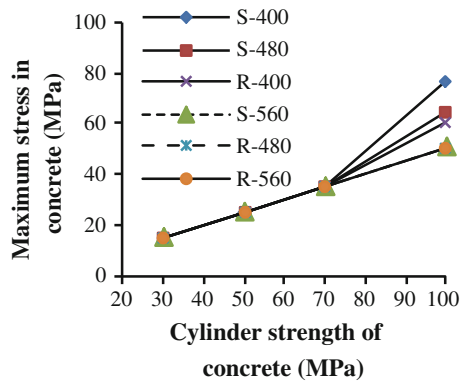
Fig. 11 Sectional rectangular to square moment ratio of CFST beams

Fig. 12 Strain in concrete in compression versus compressive strength of concrete

Fig. 13 Maximum stress in concrete in compression versus compressive strength of concrete

5.6 Influence of Shape of the Section

The flexural capacity of rectangular CFSTs beams is higher compared to square section composite beams using same materials in similar quantity. Moment capacity of rectangular section in comparison of square section increases by 29.60–35.10 %, 29.10–33.70 % and 28.60–33 % when steel have ultimate strength 400, 480 and 560 MPa, respectively. Figure 13 clears that the moment capacity of rectangular CFST beams increases at reducing rate with increment in strength of steel.

6 Conclusions

A total of twenty four CFST beams of equal concrete and steel area have been simulated to study the effects of shape of section, compressive strength of concrete and strength of steel on the flexural capacity of beams. A fiber element analysis computer code is prepared in Oracle database to perform the study. It can be concluded that the choice of material strength significantly affects the behavior of CFST beams. Some conclusions are listed below.

1. The increment in concrete strength from 30 to 50 MPa, 70 and 100 MPa, the moment capacity of CFST beams increases by 4–11 % for square section and 5–15 % for rectangular section.
2. The moment capacity of CFST beams increases by 17–18 % and 34–36 % when steel tube strength is increased by 20 and 40 %, respectively.
3. Moment capacity of rectangular section increases at reducing rate compared to square section when high strength steel tubes are used.

References

1. Verma AH, Ricles JM, Sause R, Lu LW (2001) Seismic behaviour and modeling of high-strength composite concrete-filled steel tube (CFT) beam-columns. J Constr Steel Res 58:725–758
2. Furlong R (1967) Strength of steel-encased concrete beam-columns. J Struct Div 93 (ST5):113–124
3. Tomii M, Sakino K (1979) Elasto-plastic behaviour of concrete filled square steel tubular beam-columns. Architectural Institute of Japan, p 280
4. Prion HG, Boehme J (1994) Beam-column behaviour of steel tubes filled with high strength concrete. Can J Civil Eng 21:207–218
5. Gupta PK, Sarda MS, Kumar MS (2007) Experimental and computational study of concrete filled steel tubular columns under axial loads. J Constr Steel Res 63:182–193
6. Lu H, Han LH, Zhao XL (2009) Analytical behaviour of circular concrete-filled thin-walled steel tubes subjected to bending. Thin-Walled Struct 47:346–358
7. Han LH (2004) Flexural behaviour of concrete-filled steel tubes. J Constr Steel Res 60:313–337

8. Laing QQ (2008) Nonlinear analysis of short concrete-filled steel tubular beam-columns under axial load and biaxial bending. J Constr Steel Res 64:295–304
9. Liang QQ (2009) Performance-based analysis of concrete-filled steel tubular beam-columns, part-II: verification and applications. J Constr Steel Res 65:351–362
10. Gupta PK, Katariya SK (2014) Effect of cross-section on flexural capacity of square concrete-filled steel tube (CFST) beams. Int J Appl Eng Res 9(7):783–789. ISSSN 0973-4562
11. Gupta PK, Katariya SK (2013) A study on concrete filled rectangular steel tubes subjected to bending. In: The 5th Asia and Pacific young researchers and graduates symposium on current challenges in structural engineering, Jaipur, India, pp 309–319
12. Liang QQ (2009) Performance-based analysis of concrete-filled steel tubular beam-columns, part-I: theory and algorithms. J Constr Steel Res 65(2):363–372
13. ACI-318 (2002) Building code requirements for reinforced concrete. Detroit (MI) ACI
14. Mander JB, Priestly M, Park R (1991) Theoretical stress-strain model for confined concrete. J Struct Eng 117(3):657–666

Effect of Tension Stiffening on Torsional Behaviour of Square RC Columns

T. Ghosh Mondal and S. Suriya Prakash

Abstract Codes specify high factory of safety in design to prevent brittle torsional failure of reinforced concrete (RC) columns. This necessitates accurate prediction of the torsional behavior for efficient design of these members. However, very few analytical models are available to predict the response of RC members under torsional load condition. Softened truss model (STM) developed in the University of Houston is one of them, which is widely used for this purpose. The present study shows that STM prediction is not sufficiently accurate particularly in the post cracking region when compared to test results. It also aims at developing an improved analytical model for RC square members under torsional load conditions. Since concrete is weak in tension, its contribution to torsional capacity of RC members was neglected in the original STM. The present investigation revealed that, disregard to tensile strength of concrete is the main reason behind the discrepancies in the STM predictions. The original STM has been extended in this study to include the effect of tension stiffening (TS) to get an improved prediction of torsional behaviour of RC members. Three different tension stiffening models have been considered in this paper. The efficiencies of the models were calibrated through comparison with test data on local and global behaviours. The exponential tension stiffening model is found to give more accurate predictions.

Keywords RC columns · Softened truss model · Tension stiffening · Torsional behaviour

1 Introduction

Torsional loadings can significantly affect the flow of internal forces and deformation capacity of RC columns. This in turn can influence the performance of vital components of bridges and consequently impact the daily operation of the transportation

T.G. Mondal · S.S. Prakash (✉)
Indian Institute of Technology Hyderabad, Hyderabad, India
e-mail: suriyap@iith.ac.in

2131

system. Moreover, presence of torsional loading increases the possibility of brittle shear dominated failure, which may result in fatal catastrophe. However, a review of previously published studies indicates that the torsional behaviour of reinforced concrete members has not been studied in as much depth as the behaviour under flexure and shear in spite of its frequent occurrence in bridge columns under earthquake loading. So, the present study focuses on the development of improved analytical models for RC square columns subjected to torsion with or without axial compression. Very few investigations in the past have explored the predictions of STM on behaviour of RC columns members. The present investigation tries to fill in the knowledge gap in this important research area. The existing STM is extended to include the effect of tension stiffening to get better prediction of the behaviour of square RC columns under torsion. The experimental results obtained from two square columns (TP-92) tested in University of Tokyo [1] and University of Missouri [2] are used for validation of the developed model.

2 Tension Stiffening Effect

The tension stiffening effect represents the capacity of the intact concrete between cracks to continue to carry tensile stresses and offer stiffness. This phenomena becomes important in depicting the behaviour of RC members particularly in the post-cracking region. Therefore, a realistic model, which takes into account, the tension stiffening effect is necessary to be formulated. This effect is usually treated by assuming the average concrete tensile stress over relatively long gauge length in the direction perpendicular to the adjacent parallel cracks, whereas additional stress is carried by the reinforcement. Under pure tensile loading, soon-after the first cracking, the steel carries the entire force at the crack and the stress in the concrete becomes zero at the cracked locations. In the adjacent region to the crack, there exists a length of partial bond break-down, which has been called the transfer length, where the steel and concrete stresses vary considerably due to the released stress in concrete (Fig. 1). If the axial tensile load is increased to the level that causes the first crack, new primary cracks will form and this mechanism continues to take place until the final crack configuration is attained. In the context, it should be noted that the average tensile stress is decreased due to simultaneous tensile stress relief over the transfer length after cracking. The tension stiffening effect is decreased due to the tensile stress relief after cracking. Incorporation of tension stiffening is expected to increase the load resistance and reduced deformation and it is validated with experimental data on RC columns.
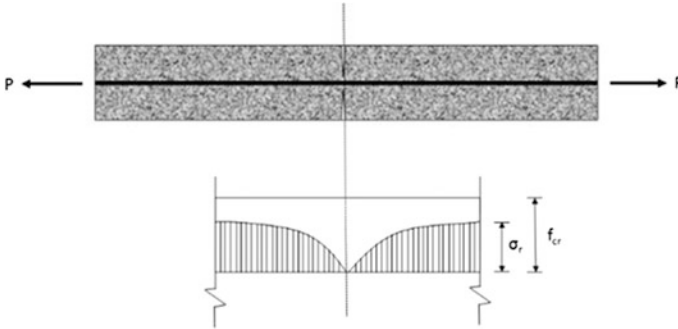
Fig. 1 Distribution of concrete stress after cracking (adapted from Koon and Hoon [11])

3 Tension Stiffened Softened Truss Model

3.1 Background

This section describes the development of the existing Softened Truss Model (STM) [3] including the effect of concrete tension stiffening (TS) for improved predictions. The inclusion of tension stiffening in the model is important because it allows an improved prediction of the service-level twist. A stress-strain relationship for concrete in tension was taken from literature [4]. The proposed TS-STM adopts the equilibrium and compatibility equations developed for an RC panel under a membrane stress field. The torsional moment and thickness of shear flow are given by Bredt's [5] thin-tube theory. TS-STM model has not validated well for columns under combined axial compression and torsion. The scope of present study includes validation of TS STM model with test data of RC square columns under torsion combined with and without axial compression.

3.2 Thickness of Shear Flow Zone

An important issue in extending the behavior of the membrane elements to a 3D member under pure torsion and combined loading is in the accurate estimation of the thickness of shear flow zone, td. When an RC member twists, the walls are warped causing flexural stresses in the concrete struts. Thus, there is a compatibility relationship between twisting and curvature. In the original STM, the shear flow zone is assumed to extend into the member up to the neutral axis. The concrete inside the neutral axis is acting in tension and considered ineffective. Such a member is assumed to be fully cracked, with the concrete and reinforcement acting as a truss. Although research has shown this to be an effective way to model a fully cracked RC member [3], it does not reflect the behaviour of an uncracked member.

But in the present study, the developed formulations are valid for uncracked elements as well. Since the pre-cracking torsional behaviour of RC members under torsion is known to be linear, therefore one can plot the variation of torque with twist before cracking from the cracking torsional moment and cracking twist values calculated from the expressions given by Collins and Mitchell [6]. The expression for t_{d0} is given by Eq. (1) (ACI 318 2008) [7] and represents the effective thickness of a thin tube at cracking. In Eq. (1), p_c is the perimeter of the section and A_p is the area of concrete bounded by p_c.

$$t_{d0} = \frac{3}{4} \frac{A_{cp}}{p_c}$$

(1)

The thickness of shear flow zone increases after a cracking according to the increase in torsional moment till the peak point.

3.3 Shear Element in Shear Flow Zone

Figure 2 shows stress conditions in reinforced concrete membrane element subjected to in-plane stress, which made a foundation of basic governing equations for shear. The directions of the longitudinal and transverse steel bars are designated as the l and t axes, respectively, constituting the l–t coordinate system. Accordingly, the normal stresses are σ_l and σ_t and τ_{lt} the shear stress is After the development of
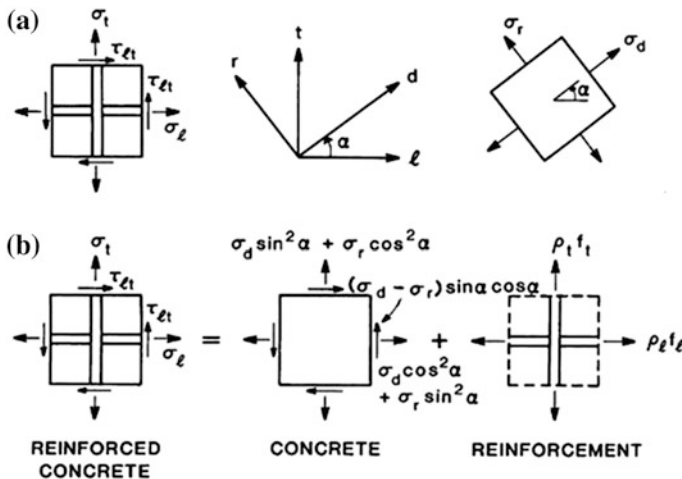

Fig. 2 RC membrane element subjected to in-plane stresses (adapted from [12]). a Definitions of stress and coordinate system. b Superposition of concrete stresses and steel stresses

diagonal cracks, the concrete struts are subjected to compression and the steel bars act as tension links, thus forming a truss action. The compression struts are oriented in the d-axis, which is inclined at an angle α to the longitudinal steel bars. This direction is also assumed to be the direction of the principal compressive stress and strain. Taking the direction perpendicular to the d-axis as the r-axis, we have a d-r coordinate system in the direction of the principal stresses and strains. The normal principal stresses in the d and r directions are σ_d and σ_r respectively.

3.4 Governing Equations in TS-STM

3.4.1 Equilibrium Equations

The two dimensional equilibrium equations relate the average internal stresses developed in the concrete (σ_d and σ_r) and in the reinforcement (f_l and f_t) to the average applied stresses (σ_l, σ_t and τ_{lt}) with respect to the angle of inclination of d-axis to the l-axis, α. The torsional moment induced by internal shear stress can be expressed as Eq. (6).

$$\sigma_l = \sigma_d \cos^2 \alpha + \sigma_r \sin^2 \alpha + \rho_l f_l \tag{2}$$

$$\sigma_t = \sigma_d \sin^2 \alpha + \sigma_r \cos^2 \alpha + \rho_t f_t \tag{3}$$

$$\tau_{lt} = (-\sigma_d + \sigma_r) \sin \alpha \cos \alpha \tag{4}$$

$$\rho_l = \frac{A_l}{p_o t_d} \tag{5a}$$

$$\rho_t = \frac{A_t}{s t_d} \tag{5b}$$

$$T = \tau_{lt}(2A_0 t_d) \tag{6}$$

where A_l, A_t are total cross-sectional areas of longitudinal and transverse mild steels and p_0, t_d are perimeter of the shear flow zone and the width of the shear flow zone respectively.

3.4.2 Compatibility Equations

The two dimensional compatibility equations relate the average strains in different co-ordinate systems namely (ε_l, ε_t and γ_{lt}) in the l–t co-ordinate system to the d–r principal axes (ε_d and ε_r). The compatibility equations are alone, not sufficient to solve the torsion problem. Infact additional equations that relate, the out of plane

warping effects are necessary. The curvature of the concrete struts (ψ) can be related by geometry to the angle of twist (θ), angle of inclination (α), the thickness of shear flow zone (t_d) and the outer face strain of the concrete strut (ε_{ds}) as shown below.

$$\varepsilon_l = \varepsilon_d \cos^2 \alpha + \varepsilon_r \sin^2 \alpha \tag{7}$$

$$\varepsilon_t = \varepsilon_d \sin^2 \alpha + \varepsilon_r \cos^2 \alpha \tag{8}$$

$$\frac{\gamma_{lt}}{2} = (-\varepsilon_d + \varepsilon_r) \sin \alpha \cos \alpha \tag{9}$$

$$\theta = (p_o/2A_o)\gamma_{lt} \tag{10}$$

$$\psi = \theta \sin 2\alpha \tag{11}$$

$$t_d = \varepsilon_{ds}/\psi \tag{12}$$

$$\varepsilon_d = \varepsilon_{ds}/2 \tag{13}$$

3.4.3 Constitutive Laws

Concrete Struts:

$$\sigma_d = k_1 \zeta f_c' \tag{14}$$

$$k_1 = \frac{\varepsilon_{ds}}{\zeta \varepsilon_o}\left(1 - \frac{\varepsilon_{ds}}{3\zeta \varepsilon_o}\right) \quad \text{for } \frac{\varepsilon_{ds}}{\zeta \varepsilon_o} \leq 1 \tag{15a}$$

$$k_1 = \left[1 - \frac{\zeta^2}{(2-\zeta)^2}\right]\left(1 - \frac{\zeta \varepsilon_o}{3\varepsilon_{ds}}\right) + \frac{\zeta^2}{(2-\zeta)^2}\frac{\varepsilon_{ds}}{\zeta \varepsilon_o}\left(1 - \frac{\varepsilon_{ds}}{3\zeta \varepsilon_o}\right) \quad \text{for } \frac{\varepsilon_{ds}}{\zeta \varepsilon_o} > 1 \tag{15b}$$

$$\zeta = 0.9/\sqrt{(1 + 600\,\varepsilon_r)} \tag{16}$$

Concrete Stress Strain Curves under Tension:
Models of tension stiffening are typically linear before cracking as shown in Eq. (17).

$$\sigma_r = E_s \varepsilon_r \tag{17}$$

After cracking, the tensile stress decreases rapidly with further increase in tensile strain. Previous equations for the descending branch were developed by Vecchio and Collins [8], Belarbi and Hsu [9] and Stevens et al. [10], which were empirical

Table 1 Constants for σ_r

TS model	C	ε_{cr0}	λ_t
Linear	0.500	0.00450	–
Parabolic	0.500	0.00700	–
Exponential	0.500	–	350

Note ε_o was assumed to be −0.002 [8]

expressions developed using data from shear panels and do not closely model the data from tests on RC specimen under torsion [4]. So, a modified set of equations, comprising a linear, a parabolic and an exponential relationship, proposed by Greene [4] based on regression analysis of torsional test data are used in this study and are shown by Eqs. (18a)–(18c) respectively. The term β_r is a function of ε_r and is given by Eq. (20). The λ_t term in Eq. (18c) is a constant that controls the rate at which the function decays. The term ε_{cr0} in Eq. (20) is the strain at which the tensile stress intersects the strain axis. Also, the parabolic function is tangent to the stress axis at ε_{cr0}. The selected values of the constants are summarised in Table 1.

$$\sigma_r = f_{cr}(1 - \beta_r) \tag{18a}$$

$$\sigma_r = f_{cr}(1 - 2\beta_r + \beta_r^2) \tag{18b}$$

$$\sigma_r = f_{cr}e^{-\lambda_t(\varepsilon_r - \varepsilon_{cr})} \tag{18c}$$

$$f_{cr} = C\frac{A_g}{A_{cp}}\sqrt{f_c'} \tag{19}$$

$$\beta_r = \frac{\varepsilon_r - \varepsilon_{cr}}{\varepsilon_{cr0} - \varepsilon_{cr}} \tag{20}$$

where ε_{cr} and f_{cr} are cracking strain and cracking stress respectively.

Stress-strain relationship in mild steel:
In compression:

$$f_l = E_s\varepsilon_l; \quad \varepsilon_l < \varepsilon_{ly} \tag{21a}$$

$$f_l = f_{ly}; \quad \varepsilon_l \geq \varepsilon_{ly} \tag{21b}$$

$$f_t = E_s\varepsilon_t; \quad \varepsilon_t < \varepsilon_{ty} \tag{22a}$$

$$f_t = f_{ty}; \quad \varepsilon_t \geq \varepsilon_{ty} \tag{22b}$$

In tension:
Young's modulus of steel, E_s was assumed to be 200 GPa (ACI 318, 2008) [7]. The yield strain of steel (ε_{ly} and ε_{ty}) was calculated dividing yield strength by E_s.

A_o and p_o have been expressed as functions of t_d as follows:

$$A_o = A_c - \frac{p_c t_d}{2} + t_d^2 \tag{23}$$

$$p_o = p_c - 4t_d \tag{24}$$

The expressions for ε_1 and ε_t are given as:

$$\varepsilon_l = \varepsilon_r + \frac{\varepsilon_r - \varepsilon_d}{\sigma_r - \sigma_d}(\sigma_l - \sigma_r - \rho_l f_l) \tag{25}$$

$$\varepsilon_t = \varepsilon_r + \frac{\varepsilon_r - \varepsilon_d}{\sigma_r - \sigma_d}(\sigma_t - \sigma_r - \rho_t f_t) \tag{26}$$

The above equations can be solved simultaneously with the stress-strain relationships for mild steel. The experimental ε_r value can be calculated from the following equation.

$$\varepsilon_r = \varepsilon_l + \varepsilon_t - \varepsilon_d \tag{27}$$

The α can be calculated from the equation:

$$\tan^2 \alpha = \frac{\varepsilon_l - \varepsilon_d}{\varepsilon_t - \varepsilon_d} \tag{28}$$

The Young's modulus (E_c) and shear modulus (G) of concrete are given by:

$$E_c = 5000\sqrt{f_{ck}}\,\text{MPa} \tag{29}$$

where
f_{ck} Compressive strength of concrete in MPa.

$$G = E_c/(1 + 2\gamma) \tag{30}$$

γ Poission's ratio.
Note: γ value was chosen to be equal to 0.5.
The parameters at cracking are provided in Table 2.

Table 2 Parameter to evaluate cracking torque and twist

Parameter	Expression
t_{cr}	$3/4\ A_c/p_c$
GK	$G\frac{4A_o^2}{p_o}t$
T_{cr}	$\frac{A_c^2}{p_c}f_{cr}\sqrt{1 + \frac{f_{pc}}{f_{cr}}}$
θ_{cr}	T_{cr}/GK

GK is the torsional stiffness. t_{cr}, T_{cr} and θ_{cr} are the depth of shear flow zone, values of torque and twist at cracking respectively. A_c is the area enclosed by the outer perimeter of the concrete cross-section and p_c is the outside perimeter of concrete cross-section. f_{pc} is applied axial stress in the member.

4 Solution Procedure

1. Select a value of ε_d.
2. Assume a value of ε_r.
3. Assume a value of t_d.
4. Calculate ζ, k_1, σ_d, A_o and p_o from the corresponding Eqs. (16), (15a), (14), (23) and (24). Before cracking, calculate σ_r using Eq. (17). After cracking, use the tension stiffening model to calculate σ_r using Eqs. (18a)–(18c), respectively.
5. Calculate ε_l using Eq. (25).
6. Calculate ε_t using Eq. (26).
7. Calculate ε_r from Eq. (27). If the difference between the assumed and calculated value of ε_r is not within a tolerable limit, then repeat Steps 2–6 until the convergence is achieved by assuming different values of t_d and ε_r.
8. Calculate α, τ_{lt}, T, γ_{lt} and θ using Eqs. (28), (4), (6), (9) and (10), respectively corresponding to one value of ε_d.
9. Repeat the process for different values of ε_d.

## 5 Experimental Corroboration of Proposed Model

The TS-STM was validated by comparing the predicted response to the response obtained from specimens TP-92 tested in the University of Tokyo and one specimen tested in the University of Missouri. Separate predictions were made using the linear, parabolic, and exponential models for tension stiffening. The cracking and ultimate torque and twist values obtained from the analytical and experimental results, on comparison, yielded an appreciable correlation. The observed error was due to material imperfections or the discrepancy in loading steps. The details of the test specimens are summarised in Table 3 and the reinforcement detailing are shown in Fig. 3.

6 Overall Torsional Response

The torque—twist behaviour of the three columns predicted by TS-STM are shown in Fig. 4 and compared with the experimental results. It is evident that the response predicted by the three tension stiffening models used in this study are identical until

Table 3 Specimen details

Specimen ID	TP-92	Missouri
Section shape	Square	Square
Section dimension (m × m)	0.4 × 0.4	0.56 × 0.56
Clear cover (mm)	27.5	38
Column height (m)	1.75	3.35
Cylinder strength of concrete (MPa)	28.4	34.6
Longitudinal reinforcement yield strength (MPa)	354	512
Transverse reinforcement yield strength (MPa)	328	454
Axial force (kN)	160	0
Young's modulus of steel (MPa)	200,000	200,000
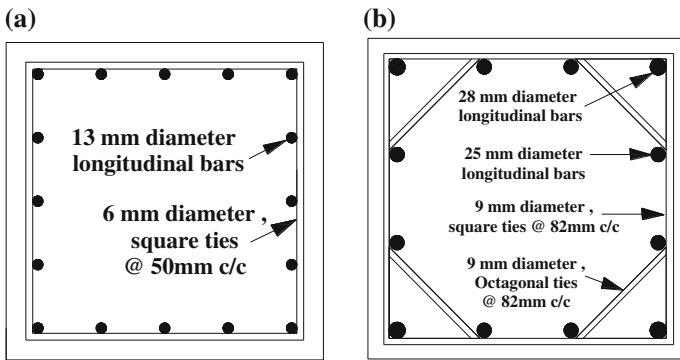
Fig. 3 Reinforcement detailing of the test specimens. **a** TP-92. **b** Missouri specimen
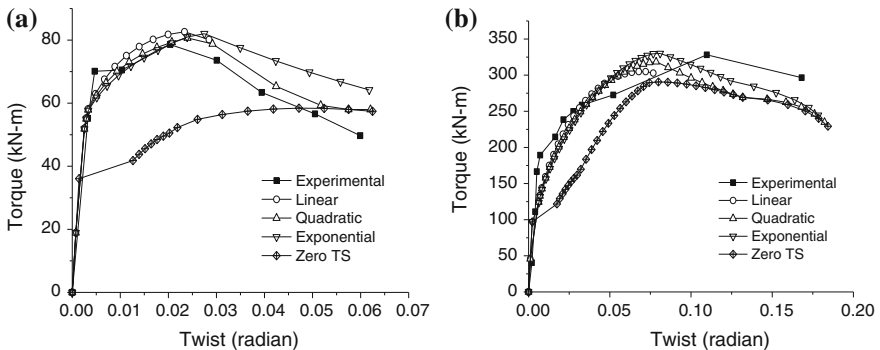
Fig. 4 Comparison of efficiency of different TS model in predicting torque—twist behavior. **a** Test specimen TP-92. **b** Test specimen-Missouri

near the peak torque, which is near the end of any significant tension stiffening model. For large principal tensile strains, the average tensile stresses predicted by the models are markedly different and therefore, the predicted behaviours are no longer identical. Though the magnitude of difference is small because the effect of tension stiffening is small near the peak. The behaviours predicted by all the three models are close to the experimentally measured behaviour and therefore any of the three models can be used to obtain equally valid predicted response. But the torque —twist behaviour predicted by the original STM is initially very stiff up to cracking, followed by a reduced stiffness up to the peak torque, which contrasts sharply with the behaviour predicted by TS-STM. The STM overestimate the deformation in post cracking region. It is worth mentioning that the model neglects dowel action and assumes perfect bond between the concrete and reinforcement and is a scope for further work. The peak torque predicted by TS-STM is larger than the peak torque predicted by STM due to the effect of tension stiffening.

7 Peak Response

A comparison of the predicted and experimental values of ultimate torque and twist is demonstrated in Table 4. It can be observed that the linear and the parabolic tension stiffening model, on an average, predicts the ultimate torque value exactly while the exponential model overestimates the same by 2.67 %. On the other hand, the linear and the parabolic models underestimate the ultimate twist values by 7.67 and 2.67 % respectively whereas the exponential model predicts the same accurately. So it is evident that all the three tension stiffening models predict the behaviour reasonably well and the predictions are close to experimental response.

Table 4 Ultimate torque and twist

TP-92	Experimental	Linear model	Parabolic model	Exponential model	Zero TS
T_u(kN-m)	78.59	82.62	80.70	82.01	57.46
θ_u(rad)	0.020	0.023	0.024	0.027	0.037
$T_{u,calc}/T_{u,test}$	NA	1.05	1.03	1.04	0.73
$\theta_{u,calc}/\theta_{u,test}$	NA	1.15	1.2	1.35	1.79
Missouri	Experimental	Linear model	Parabolic model	Exponential model	Zero TS
T_u(kN-m)	328.09	304.92	318.49	330.04	290.59
θ_u(rad)	0.110	0.072	0.079	0.081	0.080
$T_{u,calc}/T_{u,test}$	NA	0.93	0.97	1.01	0.89
$\theta_{u,calc}/\theta_{u,test}$	NA	0.65	0.72	0.74	0.73
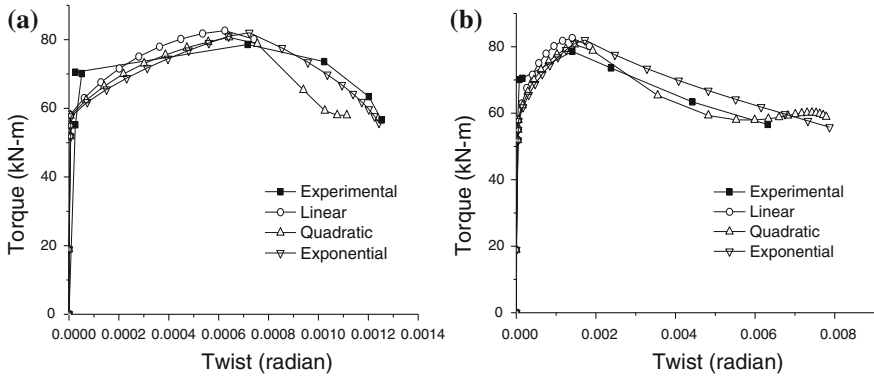
Fig. 5 Comparison of efficiency of different TS model in predicting average strain in reinforcements. **a** Longitudinal reinforcement. **b** Transverse reinforcement

8 Strains in Longitudinal and Transverse Reinforcements

Figure 5 shows the variation in strain in the longitudinal and the transverse reinforcements with applied torque for test specimen TP-92. The prediction of all the three tension stiffening models closely follow the experimental measurements up to the peak torque. The behaviour shows an initial steep slope as torque increases without significant increase in stress in the reinforcements. This is due to the shear flow in concrete resisting most of the applied torque (before the development of tensile cracks concrete is less stiff compared to steel and so attracts more load). The response is effectively linear before cracking and subsequently it flattens out. The strain in both kinds of reinforcement is tensile bringing about an apparent truss action. It can be inferred from the figure that the exponential model represents the variation in strain in the longitudinal reinforcements with applied torque more efficiently than the remaining two models whereas the same in the transverse reinforcements can be best represented by the parabolic model.

9 Concluding Remarks

The proposed model includes the effect of concrete tension stiffening to provide a continuous prediction of torsional behaviour both before and after cracking. In this model, the alignment of cracks rotate to remain normal to the principal tensile stress and the contribution of concrete in shear is neglected. The model has been validated by comparing the predicted and experimental behaviour of square columns tested under torsion with or without axial compression.

The following conclusions can be derived based on the comparison of predictions of TS-STM and experimental data:

1. Validation of analytical predictions with experimental data shows that tension stiffening has a significant influence in the torque-twist response of an RC member under pure torsion and combined torsion and axial compression.
2. The torque-twist behaviour and reinforcement strains predicted by the TS-STM was compared to test results and showed a close comparison.
3. The exponential model for concrete behaviour in tension produced better predictions compared to other tension stiffening models considered in the study.

References

1. Tirasit P, Kawashima K (2008) Effect of nonlinear seismic torsion on the performance of skewed bridge piers. J Earthq Eng 12(6):980–998
2. Prakash S, Li Q, Belarbi A (2012) Behaviour of circular and square reinforced concrete bridge columns under combined loading including torsion. ACI Struct J 109(3):317–328
3. Hsu TTC, Mo YL (1985) Softening of concrete in torsional members—theory and tests. J Am Concr Inst Proc 82(3):290–303
4. Greene GG (2006) Behaviour of reinforced concrete girders under cyclic torsion and torsion combined with shear: experimental investigation and analytical models. Ph.D. thesis, Department of Civil, Architectural, and Environmental Engineering, University of Missouri at Rolla, Rolla
5. Bredt R (1896) Kritische Bemerkungen zur Drehungselastizitat. Zeitschrift des Vereines Deutscher Ingenieure 40(28):785–790, and 40(29):813–817
6. Collins MP, Mitchell D (1991) Prestressed concrete structures. Response Publications, Canada
7. ACI 318-08 (2008) Building Code Requirements for Reinforced Concrete and Commentary. American Concrete Institute, Detroit, MI, USA
8. Vecchio FJ, Collins M (1986) The modified compression-field theory for reinforced concrete elements subjected to shear. ACI Struct J 83(2):219–231
9. Belarbi A, Hsu TTC (1994) Constitutive laws of concrete in tension and reinforcing bars stiffened by concrete. ACI Struct J 91(4):465–474
10. Stevens NJ, Uzumeri SM, Collins MP (1987) Analytical modelling of reinforced concrete subjected to monotonic and reversed loadings. Department of Civil Engineering, University of Toronto, Canada
11. Koon CC, Hoon CS (1996) Tension stiffening model for planar reinforced concrete members. Comput Struct 59:179–190
12. Hsu TTC (1988) Softened truss model theory for shear and torsion. ACI Struct J 85 (6):624–635

Bibliography

13. Greene GG, Belarbi A (2009) Model for RC members under torsion, bending, and shear. J Eng Mech ASCE 135(9):961–969
14. Hsu TTC (1984) Torsion of reinforced concrete. Library of Congress Cataloging, Van-nonstrand Reinhold Company Inc., New York, USA
15. Belarbi A, Prakash SS, You YM (2008) Effect of spiral reinforcement on flexural-shear-torsional seismic behavior of reinforced concrete circular bridge columns. Struct Eng Mech J 33(2):1190–1205
16. Fang IK, Shiau JK (2004) Torsion behaviour of normal and high strength concrete beams. ACI Struct J 101(3):304–312
17. Gopalratnam VS, Shah SP (1985) Softening response of plain concrete in direct tension. ACI J Proc 82(3):310–323
18. Hsu TTC (1991) Nonlinear analysis of concrete torsional members. ACI Struct J 88 (6):674–682
19. Hsu TTC (1993) Unified theory of reinforced concrete. Library of Congress Cataloging, C.R. C. Press, Boca Raton
20. Han L-H, Yao G-H, Tao Z (2007) Performance of concrete-filled thin-walled steel tubes under pure torsion. Thin-Walled Struct 45(1):24–36
21. Prakash S (2009) Seismic behavior of RC circular columns under combined loading including torsion. Department of Civil Engineering, Missouri University of Science and Technology, Missouri, USA
22. Rao TDG, Rama SD (2005) Analytical model for the torsional response of steel fiber reinforced concrete members under pure torsion. Cem Concr Compos 27(4):493–501
23. Peng X-N, Wong Y-L (2011) Behaviour of reinforced concrete walls subjected to monotonic pure torsion-an experimental study. Eng Struct 33(9):2495–2508
24. Lee J-Y, Kim S-W (2010) Torsional strength of RC beams considering tension stiffening effect. J Struct Eng ASCE 136(11):1367–1378

Part XXIV
Concrete Structures

Estimation of Fundamental Natural Period of RC Frame Buildings with Structural Walls

Pratik Raj and Kaustubh Dasgupta

Abstract The natural vibration characteristics of a structure play a significant role in estimation of seismic behaviour of a structure. The principal natural vibration characteristic, namely the natural period of vibration, is experimentally estimated by either carrying out ambient vibration studies or from the observed seismic behaviour of the building. The design guidelines of different countries also provide some estimate of the natural period by prescribing empirical expressions. Reinforced Concrete (RC) frame buildings with structural walls are commonly prescribed for highrise buildings in regions of strong earthquake shaking. Currently, the Indian Earthquake Code IS:1893 (Part 1): 2002 does not prescribe any expression for estimation of natural period of an RC frame building with structural wall. The present study is intended to prescribe such an expression based on parametric studies of structural walls in RC frame buildings. In the current study, a symmetrical plan RC frame building is modeled in the computer program SAP2000. The beams and columns have been modeled as frame elements and the slabs and shear walls have been modeled as shell elements. The building is assumed to be founded on rocky stratum with the restraint of all translational and rotational degrees of freedom of the nodes at the bottom of the columns. The investigations were carried out varying three parameters of the structural wall, namely (a) height, (b) modulus of elasticity of concrete, and (c) thickness. Modal analysis was carried out for each building model for obtaining the fundamental natural period of vibration. Based on the regression analysis of the results of parametric studies, an expression is proposed for obtaining the fundamental period of vibration of RC frame buildings with structural walls.

P. Raj
L&T Construction, Mumbai, India
e-mail: pratikrajiitgw@gmail.com

K. Dasgupta (✉)
Department of Civil Engineering, Indian Institute of Technology
(IIT) Guwahati, Guwahati, India
e-mail: kaustubh.dasgupta@gmail.com

2147

1 Introduction

Structural walls, commonly known as shear walls, are important components of earthquake resistant RC frame buildings that contribute significantly to the strength and stiffness of the overall structure and decreasing the lateral sway in the direction of the seismic forces so as to reduce the damage significantly. The fundamental time period of a building with structural walls, is expected to primarily depend on the vibration characteristics of the walls. For obtaining the natural period of the building, the natural periods of the constituent walls need to be suitably combined. The combination criteria used till date by different researchers is based on methodologies in which the wall is assumed not to behave as a continuous system. These approximations render the natural period, obtained from the combination criteria, deviate from its realistic values. Thus, a new combination criterion needs to be developed which would be able to predict the value of the overall natural time period of the building with higher accuracy.

2 Past Research

Goel and Chopra [5] proposed an equation and derived considering flexure and shear deformations of a uniform cantilever. Though the formulation produced a better fit to the period data considered, a significant inconsistency can be observed when some shear walls do not extend to the top of the building. Moreover, the method of combination of time periods of more than one shear walls is based on Dunkerley's method which is a method applicable to lumped mass systems only. Wallace and Moehle [12] studied the fundamental period of a uniform cantilever of rectangular cross section, supporting regularly distributed floor loads, considering only flexural deformations. Based on a theoretical analysis with assumed values of floor weight, modulus of elasticity of concrete, and storey height, expressions were suggested for computing the fundamental period of un-cracked and cracked reinforced concrete shear wall (RCSW) buildings.

Lee et al. [7] derived a theoretical model following the similar procedure as that of Goel and Chopra [5], to predict the fundamental period of a uniform cantilever, considering both flexural and shear deformations; assuming the thickness of all walls to be identical. Morales [9] recognized that the fundamental period of a uniform flexural cantilever is dependent on the ratio of the height to the second moment of area. It was also suggested that the second moment of area, I of RCSW buildings, in either principle direction, could be approximated as the summation of

the second moments of area of individual walls, in the same direction. Pan et al. [10] carried out a parametric study with respect to height or number of storeys for the empirical calculation of natural time period of high rise buildings in the city of Singapore with the help of data collected from 116 instrumented buildings based on micro tremors measurements. Different classes of results were obtained for soft-soil sites and firm soil sites with the former having 40 % longer vibration periods. Ghrib and Mamedov [3] investigated the evaluation of the fundamental period of shear wall buildings considering the flexibility of the base. Both experimental and analytical approaches were used to assess the effect of the base flexibility on the fundamental period buildings with shear walls. In total, twenty buildings built on different types of soil are tested under ambient vibration. The stiffness of the base is represented by translational and rotational discrete springs. The rigidities of these springs are evaluated from the elastic uniform compression of the soil mass and the size of the foundation. Gilles and McClure [4] used ambient motions recorded in 27 RCSW buildings in Montreal to evaluate the effectiveness of various empirical models to predict the fundamental time period of RCSW buildings compared to periods measured in actual buildings under ambient loading conditions.

3 Codal Equations for Natural Period

Seismic codes of different countries prescribe empirical expressions for fundamental natural periods of RC shear wall buildings, with parameters based on extensive regression analyses (Table 1). On comparing the codal estimates of natural periods with the actual measured values of the natural periods [5], it is

Table 1 Codal equations for RC wall-frame buildings

Sl. no.	Formula	Reference	Unit for dimension
1	$T = 0.02h^{0.75}$	ASCE 7 (2005), NEHRP (2000), Eurocode 8 (2004)	ft
2	$T = 0.05h^{0.75}$	GBJ-11-95 (1995), Taiwan (1997)	ft
3	$T = 0.06h^{0.75}$	NZSEE (2006)	m
4	$T = 0.05 \frac{h}{\sqrt{d}}$	SEAOC (1996), ATC-3-06 (1978)	ft
5	$T = 0.08 \frac{h}{\sqrt{d}} \sqrt{\frac{h}{h+d}}$	Jordon (1990)	m
6	$T = 0.03048 \frac{h^{0.75}}{\sqrt{A}}$	NSCP (1992)	ft
7	$T = 0.0743 \frac{h^{0.75}}{\sqrt{A}}$	Korea (2000), Turkey (2000)	m
8	$T = 0.075 \frac{h^{0.75}}{\sqrt{A_c}}$	Eurocode 8 (2004)	m

where

$$A = A_c = \sum A_i \left[0.2 + \left(\frac{l_{wi}}{h} \right)^2 \right], \quad \frac{l_{wi}}{h} \le 0.9$$

observed that for majority of buildings, the codal values tend to overestimate the natural period. This may lead to underestimate the design values of spectral acceleration, and consequently, the lateral force on the building.

4 Sensitivity Analysis

To account for the deficiencies in the codal equations, preliminary analyses of different models are carried out using the computer program *SAP2000* [2]. Seven parameters are observed to affect the fundamental time period of the building in any direction of vibration, namely (a) height of the building, (b) height of the shear walls, (c) material properties of concrete used for shear walls, (d) length of shear wall in the direction under consideration, (e) thickness of the shear wall, (f) location of shear wall in the building plan and (g) material properties of concrete used in the frame elements linking the shear walls (Table 2).

The cross-sections of beam and column are considered as 350 mm × 450 mm and 350 mm × 350 mm respectively. The thickness of floor slab is considered as 100 mm. Unless specified, the grade of concrete is taken as M25. The floor slabs and walls are modeled using 4-noded shell elements with six degrees of freedom at each node. The beams and columns are modeled as 2-noded frame elements with six degrees of freedom at each node. All the beam-column joints are considered as rigid joints. Each storey height has been kept as 3 m except for the foundation which is 2 m. The building is assumed to be founded on rocky stratum, thus the translational and rotational degrees of freedom at the bottom nodes are restrained.

The results (Table 2) clearly indicate that the height of the building is an important parameter and significantly affects the fundamental time period of the building. With increase in height of building, the increase in mass influences the natural period significantly. Also, the influence of combined lateral stiffness of RC wall and frame elements, leads to an inconsistent trend in variation of natural periods.

Table 2 Results of sensitivity analyses

Height of the building H_b (m)	11	14	17	20
Time period (s)	0.10496	0.14164	0.19164	0.24993
Height of the shear wall H_s (m)	11	14	17	20
Time period (s)	0.24993	0.22929	0.22751	0.23389
Grade of concrete for shear wall	M15	M20	M25	M30
Time period (s)	0.19332	0.19044	0.18824	0.18645
Grade of concrete for frame elements	M15	M20	M25	M30
Time period (s)	0.22339	0.21108	0.20196	0.19479
Total length of shear wall (m)	3	6	9	12
Time period (s)	0.22393	0.17731	0.15359	0.13916
Thickness of shear wall (mm)	100	150	200	250
Time period (s)	0.18824	0.18680	0.18680	0.18735

Table 3 Inconsistency in fundamental natural period of walls

Sl. no.	Location of shear wall	Length of wall (m)	Fundamental natural period (s)
1	●●●●●●●●●●●	6	0.18673
2	●●●●●●●●●●●	6	0.15704
3	●●●●●●●●●●●	12	0.13916
4	●●●●●●●●●●●	12	0.09656

The increase in the modulus of elasticity results in the increase in the wall stiffness and thereby, reduces the fundamental natural period. In the current study, the RC walls are not modeled in consecutive bays as this will lead to a single continuous shear wall. As expected, a decrease in fundamental time period with increase in the total length of the shear wall. Similar to the height parameter, variation in thickness of wall leads to an inconsistent variation in natural period. The influence of location of wall along the frame on the natural period is not significant except the end bay location. The results for that case have not been shown here for brevity.

The interference of several parameters in the estimation of natural period of wall-frame buildings, leads to difficulty in identification of salient parameters to be incorporated in a unified expression. This is further reinforced with the observed variation in natural periods of the buildings with change in the length and location of wall (Table 3).

5 Combination Criteria of Fundamental Time Periods

In the past studies on natural vibration, the significant contribution of RC wall in the lateral stiffness of a frame-wall building has led to prescription of natural period expressions based on wall characteristics only. Also, in a multi-storied building, the RC wall is assumed to behave like a vertical cantilever with continuous distribution of mass. Thus, based on the continuous distributed mass system, the individual natural period of the shear wall is prescribed which is applied for the entire building. However, the contribution of frame system may also become significant particularly, when two or more walls are present in the same bay. Thus, combination criteria need to be established for prescription of the overall natural period of the building.

In the study by Goel and Chopra [5], Dunkerley's method has been used to combine the natural periods of the individual RC walls. In the method, the combined natural period T of a system is given as,

$$T^2 = T_1^2 + T_2^2 \tag{1}$$

where, T_1 and T_2 are the two natural periods of the similar mode of vibration of the component systems. This method tends to give reasonably good results for well

separated values of T_1 and T_2. Although this method is applicable strictly for lumped mass systems, the criterion has been considered for combining continuous systems like RC walls. This may lead to significant deviation from the actual natural time periods.

5.1 Coplanar RC Walls

In order to propose the combined natural period for a system of 2 coplanar RC walls linked by a frame (Fig. 1a), repeated modal analyses are carried out in *SAP2000* to find out the resultant natural period. The salient parameters affecting the natural period of the RC wall, namely (a) height (H), (b) modulus of elasticity of concrete (E_c) and (c) thickness of shear wall (t), are varied (Table 4). The cross-sections of the beams and columns were kept the same as in the preliminary study. The bay length and typical storey height are considered as 3 m. The depth of the foundation was considered as 2 m for all the models. The parameter E_c was obtained from the grade of concrete as per the expression prescribed in IS:456-2000. The shear walls are modeled as thin shell elements.

A total of 27 models were thus generated for a single RC wall, and this led to a total of 729 data points after modal analysis of each model. The variation of the observed combined fundamental period of the system (T_{comb}) with the natural period of the individual walls, can be expressed as

$$T^2_{comb} = T_1^x T_2^y \tag{2}$$

(a)   **(b)**
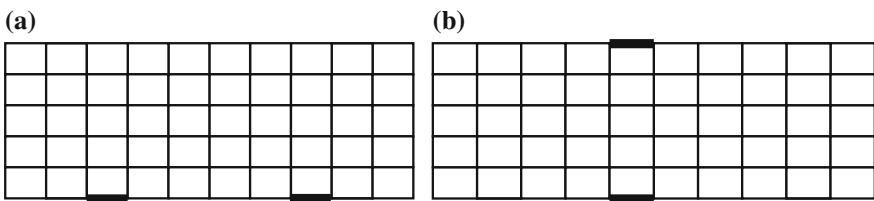
Fig. 1 Building plan with **a** two coplanar and **b** two non-coplanar RC walls

Table 4 Variation of parameters for an individual wall	Height of shear wall (m)	Grade of concrete	Thickness of shear wall (mm)
	11	M20	100
	14	M25	150
	17	M30	200

where, x and y are weightage indices for the walls. Considering the logarithm of both sides in Eq. (2), unconstrained linear regression analysis is carried out to obtain the coefficients x and y, using dataset of 729 points by least square fit method [8]. The values of x and y are the same as the properties of both the shear walls are varied to the same extent. The final expression is,

$$T_{comb} = (T_1 T_2)^{0.56}. \tag{3}$$

5.2 Non-coplanar RC Walls

In case of non-coplanar RC walls, it is observed that the different locations of walls along the individual frames do not influence the overall natural period significantly. Similar regression analysis on parametric variations for the chosen configuration (Fig. 1b), gives the following expression,

$$T_{comb} = (T_1 T_2)^{0.296}. \tag{4}$$

The Dunkerley's method, as per Eq. (1), tends to give the following expression through regression analysis:

$$T_{comb} = (T_1 T_2)^{0.707}. \tag{5}$$

The same equation is applied to both coplanar as well as non-coplanar configurations. It is observed that the Eq. (5) will not give reasonably accurate estimates of the natural period.

5.3 Combined Coplanar and Non-coplanar Walls

For the natural period of a symmetric building plan with combination of two coplanar and two non-coplanar walls (Fig. 2), the building height, storey height and foundation depth are considered as 17, 3 and 2 m respectively. In Fig. 2, (1) and (2) constitute a set of coplanar walls, along with (3) and (4).

For prismatic uniform cantilever members, the fundamental natural period in flexural and shear modes of vibration are prescribed as [1, 6, 11],

$$T_F = \frac{2\pi}{3.516} \sqrt{\frac{m}{EI}} H^2, \quad \text{and} \tag{6}$$

$$T_F = 4 \sqrt{\frac{m}{kGA}} H \tag{7}$$
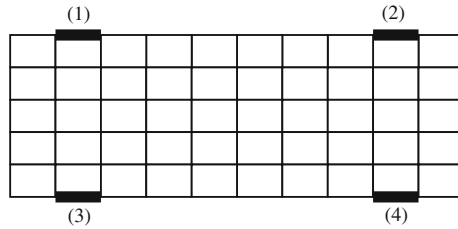
Fig. 2 Building plan with combination of two coplanar and two non-coplanar RC walls

where, m is the mass per unit height, E modulus of elasticity, G shear modulus, I section moment of inertia, A area of cross-section and k shape factor for non-uniform distribution of shear stresses (taken as 5/6 for rectangular sections). Combination of these two periods by *Dunkerley's method* gives the resultant natural period very close to T_F value, possibly due to the absence of shear mode of deformation. Thus, Eq. (6) is considered as the natural period of cantilever RC wall. For coplanar sets of walls (1)–(2) and (3)–(4) (Fig. 2), the combined natural periods are given as,

$$T_{12} = \left[\left(\frac{2\pi}{3.516} \right)^2 \frac{m}{(E_1 I_1 E_2 I_2)^{0.5}} (H_1 H_2)^2 \right]^{0.56}, \text{ and} \tag{8}$$

$$T_{34} = \left[\left(\frac{2\pi}{3.516} \right)^2 \frac{m}{(E_3 I_3 E_4 I_4)^{0.5}} (H_3 H_4)^2 \right]^{0.56}. \tag{9}$$

Combining T_{12} and T_{34} as non-coplanar sets of walls, the natural period is,

$$T = \left[\left(\frac{2\pi}{3.516} \right)^4 \frac{m^2}{(E_1 E_2 E_3 E_4)^{0.5} (I_1 I_2 I_3 I_4)^{0.5}} (H_1 H_2 H_3 H_4)^2 \right]^{0.16576}. \tag{10}$$

Equation (10) may also be simplified as,

$$T = \left[\frac{(104 m \sum H_i)^{0.33}}{(\sum E_i I_i)^{0.083}} \right]. \tag{11}$$

6 Conclusions

The following salient conclusions are drawn from the study:

(a) The geometry and material properties of structural walls influence significantly the lateral stiffness of an RC frame building with shear walls.

(b) The proposed expression for natural periods, combining the planar and non-coplanar walls, is based on variation of three parameters. More parametric values can be included to possibly improve the expression.

The combination criteria developed for two shear walls in coplanar or non-coplanar configurations can be extended to any number of shear walls. The results of the work need to be further validated using data from the experiments or the measured time period of instrumented buildings having similar plan configurations.

References

1. Chopra AK (2007) Dynamics of structures, 3rd edn. Pearson Education, New Delhi, India
2. CSI (2011) Structural analysis program SAP2000 V14.0. Computers and Structures Inc., Berkeley, USA
3. Ghrib F, Mamedov H (2004) Period formulas of shear wall buildings with flexible bases. Earthquake Eng Struct Dynam 33(3):295–314
4. Gilles D, McClure G (2012) Measured natural periods of concrete shear wall buildings: insights for the design of Canadian buildings. Can J Civ Eng 39:867–877
5. Goel RK, Chopra AK (1998) Period formulas for concrete shear wall buildings. J Struct Eng ASCE 124(4):426–433
6. Jacobsen LS, Ayre RS (1958) Engineering vibrations: with applications to structures and machinery. McGraw-Hill, New York
7. Lee L, Chang K, Chun Y (2000) Experimental formula for the fundamental period of RC buildings with shear-wall dominant systems. Struct Des Tall Buildings 9:295–307
8. MATLAB R2012a (2012) Numerical computing environment and fourth generation programming language. MathWorks, Natick, Massachusetts
9. Morales MD, (2000) Fundamental period of vibration for reinforced concrete buildings. Master of Science thesis, Department of Civil Engineering, University of Ottawa, Ottawa, Ontario, Canada
10. Pan T, Goh KS, Megawati K (2014) Empirical relationships between natural vibration period and height of buildings in Singapore. Earthq Eng Struct Dynam 43(3):449–465
11. Timoshenko S, Young DH, Weaver W (1974) Vibration problems in engineering. Wiley, New York
12. Wallace JW, Moehle JP (1992) Ductility and detailing requirements of bearing wall buildings. J Struct Eng ASCE 118(6):1625–1644

Enhancement of Lateral Capacity of Damaged Non-ductile RC Frame Using Combined-Yielding Metallic Damper

Romanbabu M. Oinam and Dipti Ranjan Sahoo

Abstract Non-ductile reinforced concrete (RC) frames are vulnerable to severe damages or complete collapse under seismic excitations. Several such deficient RC frames are prevalent in the moderate-to-high seismic regions of India. In order to improve their seismic performances, suitable strengthening schemes should be adopted. The use of passive energy dissipation devices in the seismic strengthening technique is considered as an efficient and cost-effective solution. In this study, a reduced-scale single-bay single-storey damaged RC frame specimen was retrofitted with the combined-yielding metallic dampers (CMD). In addition, the damaged beam and columns were strengthened using steel elements. The retrofitted frame was experimentally investigated under a constant gravity load and gradually-increased reversed-cyclic loading. The test specimen was tested up to 6.0 % drift level. The RC frame exhibited better hysteretic response with mild pinching. Unlike other metallic devices, CMD was capable of dissipating hysteretic energy through the flexure and shear yielding of metallic plates. The main parameters investigated are lateral strength, ductility and hysteretic response Test results showed that the proposed strengthening technique significantly enhanced the lateral strength and ductility.

Keywords Non-ductile · Ductile detailing · Steel caging · Retrofitting · Lateral strength

R.M. Oinam (✉) · D.R. Sahoo
Department of Civil Engineering, Indian Institute of Technology Delhi, New Delhi, India
e-mail: romaniitd@gmail.com

D.R. Sahoo
e-mail: drsahoo@civil.iitd.ac.in

1 Introduction

Prior to the development of seismic codes in India, several concrete buildings have been constructed as per gravity load requirements. The main deficiencies in the earlier designs were insufficient shear reinforcement in joints, lack of splicing, less confinement on plastic regions, insufficient development length etc. [1]. Many countries have used different strengthening techniques to enhance the overall capacity of all the existing non-earthquake resistant buildings which were impossible to replace. The strengthening techniques used can be divided into two categories (a) local and (b) global. If the strengthening is done at the structural system level then it is called global strengthening and strengthening done at member level is called local strengthening. The techniques used for local level include, steel jacketing [2–5], concrete jacketing [6], steel caging [7, 8] and composite jacketing [9] and the ones in global level include, RC shear wall [10, 11], Steel plate shear wall [12], Steel brace [13, 14], and dampers [15]. In certain cases, the desired seismic performance of a RC structure may not be achieved by a single strengthening technique or, sometimes strengthening using a single configuration may be costly and labor-intensive. In such cases, both the strengthening techniques, i.e., local and global modifications can be used to avoid underperformance of structure and economy loss [16]. In this study, combined metallic yielding damper (CMD) and steel caging are used together as a strengthening strategy. Steel caging will enhance lateral confinement of column and CMD will enhance flexural and shear capacity of the frame globally [16]. This study explores the effectiveness of CMD in enhancing the seismic performance of a damaged non-ductile RC frame.

2 Strengthening Technique

2.1 Steel Caging

Commonly steel caging has been in use for RC columns and bridge piers as a local strengthening technique. Particularly, steel cage are used on columns because of its free accessibility and easiness in wrapping [17, 18]. This method is much simpler than other types of strengthening techniques. In steel caging, angle sections at four corners of the columns are provided and they are tied together using steel batten plates. The main objective of steel caging is to provide passive lateral confinement on the strengthened member due to Poisson's effect [2]. In steel cage, battens (horizontal member) take high tensile stresses, this happens due to internal crack propagation during axial compressive load application, and vertical steel angles provide uniform confinement along the height. And near the battens, there is no concrete confinement due to absence of confinement pressure.
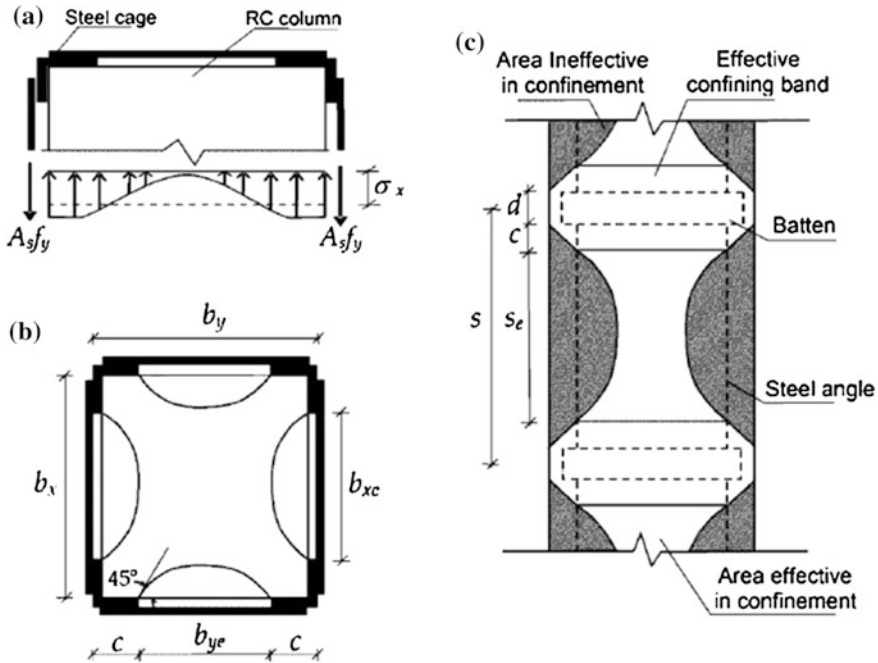
Fig. 1 Confinement of RC column due to steel caging: **a** half-body equilibrium at battened portion of steel cage; **b** effective confinement in plan; and **c** effective confinement in elevation [2]

Figure 1 shows clearly the arrangement of batten plates and angles as used for retrofitting a column. Same pattern has been followed for the present study.

2.2 Combined Metallic Yielding Damper (CMD)

Generally, global strengthening technique enhances capacity of the structure globally in terms of lateral strength, stiffness and ductility. There are many types of global strengthening techniques and CMD is one of them.

CMD is a device, which dissipates the seismic energy through plastic hinge mechanism. It has both flexural and shear yielding characteristic under slow cyclic load [15]. It consists of two triangular shape flexural plates and one rectangular shape shear plate. Flexural plates and shear plates were kept transversely and longitudinally respectively in the loading directions. In between flexural and shear plates a gap was kept for the yielding the flexural plate and this system was bounded by two base plates [15]. Figure 2 shows the details of various components of CMD.

Fig. 2 Combined metallic
yielding damper (CMD)
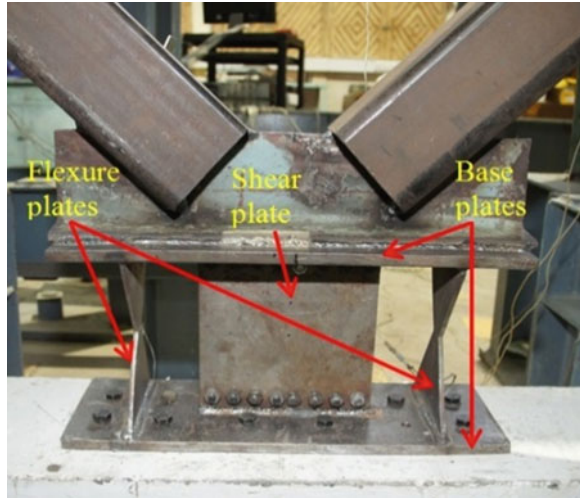
3 Experimental Program

3.1 Description of RC Bare Frame

A single-storey single-bay reinforced concrete (RC) frame representing an interior
bay of a prototype framed structure was considered as the test frame in this study
and was casted. All the dimensions and percentage of reinforcement of test frame
was simulated using 0.4 scale factor. The overall width and height of test frame was
taken as 3,200 and 2,100 mm respectively. The cross sectional dimension of beam
was taken as 160 × 130 mm, whereas both the columns dimension was
160 × 160 mm. To include the on slab effect on the test frame, a monolithic slab of
50 mm thick and 500 mm wide was casted over the beam [1]. Figure 3 shows the
details of the geometric properties of the test frame. In representing the existing
non-earthquake resistant building, ductile detailing was not considered. The frame
was tested under cyclic load up to 3.5 % lateral drift with constant gravity load [1].
This damaged frame was retrofitted using steel caging and CMD device and the
same test was repeated up to 6.0 % drift.

3.2 Description of Retrofitted Frame

The damaged RC bare frame was retrofitted using steel caging technique along with
CMD device. Four numbers of Indian standard rolled angles of ISA
50 × 50 × 6 mm was used to fabricate the steel cage with intermediate battens
provided at the rate of 330 mm center to center. Here mild steel plate of 50 × 5 mm

Fig. 3 Detailing of test frame

was used as battens. At the beam column junction, steel collar was provided on column and steel cage was extended up to the end of the column. Indian standard rolled angles of ISA 60 × 60 × 8 mm angles were provided at the junction of slab and beam, and was extended from the actuator face up to ¾th of beam span to transfer the actuator load uniformly on to the test frame.

Combined metallic yielding damper (CMD) was installed at foundation level and it was supported by two bracing systems. Two Indian square hollow section of 113.5 × 113.5 × 5.4 mm was used as brace and were connected to steel collar at the top of the column. For the CMD, 150 mm wide, 200 mm height and 6 mm thick mild steel plate was used as flexural plate; while 200 mm width, 200 mm height and 3.2 mm thick mild steel plate was used as shear plate. The flexural plate was welded on to the base plate, which was 12 mm thick at both sides. Compared to shear plate and flexural plate, shear plate was thinner than flexural plate so this size was not suitable for welding connection. Hence, 12 mm thick shear tabs were provided at both sides of the base plate using welding connection. Shear tabs and shear plate were connected using 8 numbers of 8 mm diameter high strength bolts. The bottom base plate was fixed as rigid a connection with foundation, while the upper base plate was connected to a supporting brace, allowing it to move longitudinally along the loading direction. The detail of retrofitting technique adopted in this study is as shown in Fig. 4. All dimensions of various components of CMD used in this study is as per Table 1.

Fig. 4 Retrofitting technique adopted in this study

Table 1 Dimensions of various components of CMD

Flexural plates	Shear plates	Base plates	All dimensions are in millimeters
150 × 200 × 6	200 × 200 × 3.2	500 × 160 × 12	

3.3 Test Set-up

Lateral cyclic load was applied at beam level with the help of servo hydraulic actuator (250 kN capacity of 125 mm stroke) for up to 3.5 % lateral drift on RC frame and 6.0 % drift on retrofitted RC frame. Displacement history was referred from ACI Committee 374.1-05 [19] in addition with constant gravity loads. The gravity load was applied above the slab by putting concrete cubes.

A detail of displacement history is as shown in Fig. 5. Both the frames were fixed on strong floor with the help of Indian hot rolled I-Sections and high strength bolts. Rigid steel frames were connected to the test frame as side support with the help of rollers. Main application of side support was to transfer the actuator load on frame in-plane. Due to this side support there is no free energy losses.

Fig. 5 Displacement history
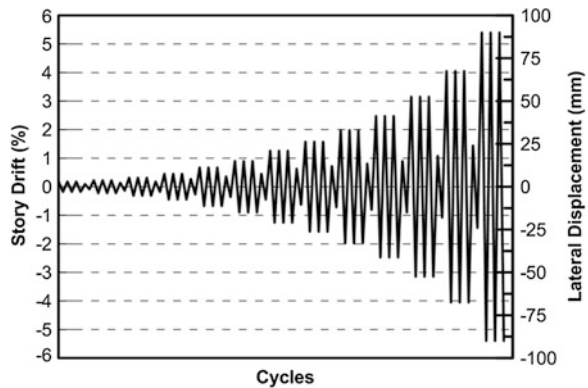
4 Result and Discussion

In this study, the following parameters were investigated from the specimens, (i) overall behaviors, (ii) hysteretic response, (iii) energy dissipation. Brief explanations of these parameters are given in the following sections.

4.1 Overall Behavior

Initially there was no visible damage on both the specimens for smaller drift. Under these small drift, both the specimens showed elastic nature. At 1.0 % drift, few micro cracks were noticed on the cover concrete of RC bare frame. These micro cracks became major cracks on column concrete, when displacement amplitude was increased to 1.4 % lateral drift. At 2.75 % drift, a single major crack (horizontal) was noticed on column face, which corresponded to ultimate load capacity of the frame in push direction. At 3.5 % drift, crushing of concrete was observed at column base near the foundation. After this observation, the test was stopped and further higher drift level was not applied. From the overall observation of RC bare frames performance it showed that the plastic hinge was formed on both columns of top and bottom [1]. In case of retrofit frame, some micro cracks were noticed on the beam and on column face at 1.0 % drift level. And in this drift level, CMD was behaving elastically. At 1.4 % drift, the shear plate was buckled (out of plane) on CMD and this was corresponding to the ultimate load carrying capacity (130.0 and 135.5 kN in tension and in compression respectively). The steel cage was left with no deformation for this drift. When displacement amplitude was increased to 1.75 % drift, shear plate started tearing up from top right end, meanwhile shear cracks were observed at column bottom. Many minor cracks were noticed at beam column joints. At 2.2 % drift, shear plate started tearing from top left end and micro cracks were noticed on foundation. Shear plate tore fully and got separated from upper the base plate at 2.75 % drift. Major cracks on foundation were noticed at 3.5 % drift. At 4.5 % drift, the joint between damper and foundation became loose and concrete spalling was observed. At the first cycle of 6.0 % drift, the welding connection between brace and steel collar failed and the test was stopped thereafter. The performance of the retrofitted frame was excellent as compared to undamaged bare RC frame. In RC bare frame, pinching effect was observed tremendously while it was comparatively less in retrofitted frame. In general, concrete structure has a tendency for pinching effect, due to this behavior RCC structures dissipates its non-recoverable energy. Due to CMD device, pinching action was reduced in retrofit frame as compared to RC frame. Details of hysteretic behavior of retrofit frame are as shown in Fig. 7b. Installation of CMD on test frame and buckle deformed shape of CMD is shown clearly in Fig. 6.

Fig. 6 Deformed shapes of CMD at the end of the test
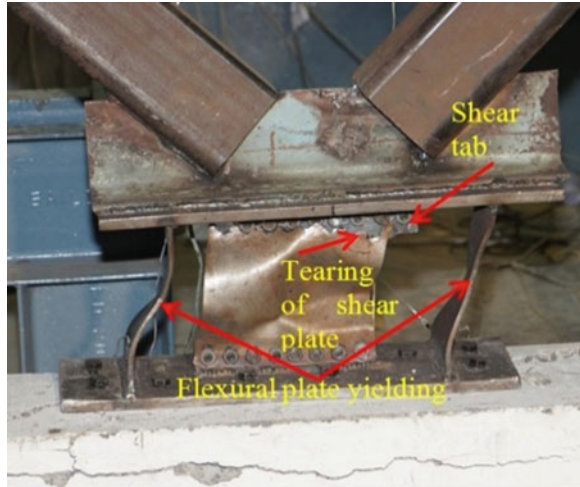
4.2 Hysteretic Response

Lateral load versus displacement (Hysteresis) response of RC bare frame and retrofit frame is shown in Fig. 7. Both the frames have same yield value of 0.5 % (7.5 mm). At 2.75 % drift, RC bare frame showed ultimate load carrying capacity in push direction. However, in the last cycle (3.5 % drift) the load carrying capacity of RC bare frame was symmetrical in push and pull directions. And the values were noted as 56.7 and −57.0 kN in push and pull direction. At the end of loading, there was not much difference between the load carrying capacity of last cycle and its previous cycle. Hence, there was less load degradation in hysteresis. The load resisted by retrofit frame was 130.0 and 135.5 kN in tension and in compression respectively at 1.4 % lateral drift. At this drift shear plate was buckled up and
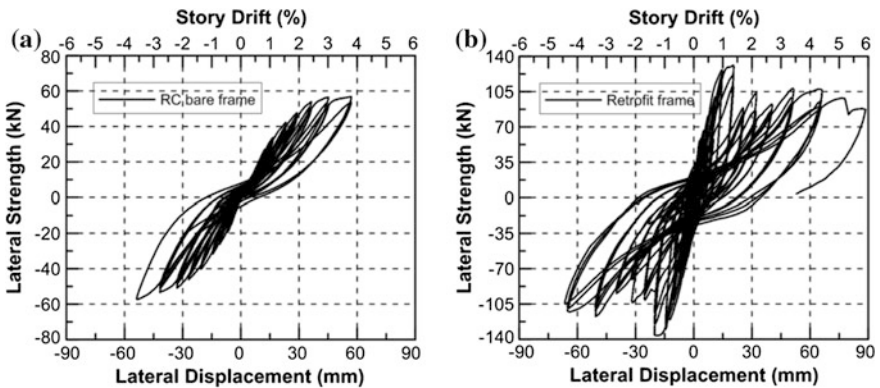
Fig. 7 Hysteretic behavior of **a** RC frame and **b** retrofit frame
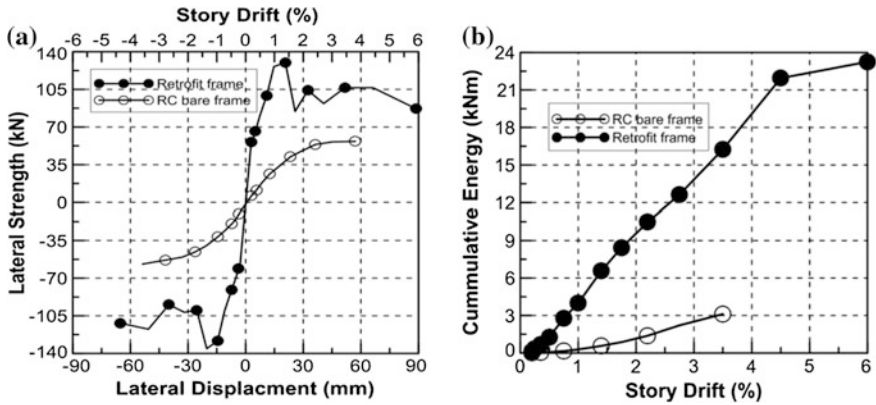
Fig. 8 Comparisons of **a** backbone curve and **b** energy dissipation of RC frame and retrofit frame

suddenly load resisting capacity was reduced. Up to certain extend of 1.4 % drift; retrofit frame was dominated by shear behavior and later by flexural behavior. During the last cycle, the frame carried a load of 87.2 kN on push direction.

Figure 8a shows backbone comparison of RC bare frame and retrofit frame. From this comparison, it can be observed that both the curves have symmetrical nature in push and pull directions. In case of RC bare frame, the curve is smooth and bi-linear. While retrofit frame behaved in a trilinear form. Maximum load carrying capacity of RC bare frame was 56.63 and 56.87 kN in tension and compression respectively at 3.5 % lateral drift, while retrofit frame showed 130.0 and 135.5 kN in tension and in compression respectively at 1.4 % lateral drift. This showed that retrofit frame has higher load carrying capacity than the RC bare frame. As compared to RC bare frame, retrofit frame has 56.44 and 58.03 % improved performances in tension and in compression respectively. It can also be seen that retrofit frame and RC bare frame can resist the displacement up to 6.0 and 3.5 % drift respectively. From the backbone comparison it can also be observed that RC bare frame showed very low stiffness while retrofit frame showed very high stiffness.

4.3 Energy Dissipation

Area under the hysteresis loop is known as energy dissipation for that particular specimen. Figure 8b shows the comparison of cumulative energy dissipation for the test frames. Here cumulative energy of test frames were calculated for each drift. A big difference in dissipates energy was observed from the beginning. Particularly at drift level of 3.5 %, RC bare frame dissipated energy at an amount 3.46 kNm while retrofit frame dissipation amounted to 16.3 kNm. It shows that retrofit frame has higher capacity of load resistance because of high energy dissipation in

nonlinear range. Retrofit frame has 78.8 % higher energy dissipation than RC bare frame at a particular range of 3.5 % drift. At end of the retrofit frame test, total amount of energy dissipated was 23.3 kNm.

5 Conclusions

Overall performances of retrofit frame were much better than the RC bare frame because of lateral confinement of column and the contribution of CMD in terms of shear and flexural yield. Excess load on the structure was released through this yield mechanism as energy dissipated from it. Additionally, there was less pinching effect on retrofit frame than RC bare frame. This dissipated energy improved the overall behavior of the structure. Hence, it can be concluded that the proposed retrofitting technique (combination of local and global strengthening technique) has achieved its target performance and the energy dissipating device (CMD) yields perfectly and adds to the target performance. In future, it can also be used in many other local and global retrofitting techniques and with proper arrangement; it can lead to the most feasible system in terms of performance and cost.

References

1. Oinam RM, Sahoo DR, Sindhu R (2014) Cyclic response of non-ductile RC frame with steel fibers at beam-column joints and plastic hinge regions. J Earthq Eng 18(6):908–928
2. Nagaprasad P, Sahoo DR, Rai DC (2009) Seismic strengthening of RC columns using external steel cage. Earthq Eng Struct Dyn 38:1563–1586
3. Sakino K, Sun Y (2000) Steel jacketing for improvement of column strength and ductility. In: 12th world conference earthquake engineering, vol 1985
4. Cuevas OMG, Correa JJG, Gonzalez BG, Diaz FAF (2000) Shear strength of concrete columns with steel jackets. In: 12th world conference earthquake engineering
5. Aboutaha R, Engelhardt M, Jirsa J, Kreger M (1999) Rehabilitation of shear critical concrete columns by use of rectangular steel jackets. Am Concr Inst Struct J 96(1)
6. Vandoros KG, Dritsos SE (2008) Concrete jacket construction detail effectiveness when strengthening RC columns. Constr Build Mater 22(3):264–276
7. Campione G (2013) RC columns strengthened with steel angles and battens: experimental results and design procedure. Pract Period Struct Des Constr © ASCE 18:1–11
8. Sahoo DR, Rai DC (2007) Built-up battened columns under lateral cyclic loading. Thin-Walled Struct 45(5):552–562
9. Xiao Y, Wu H, Martin GR (1999) Prefabricated composite jacketing of RC columns for enhanced shear strength. J Struct Eng ASCE 125:255–264
10. Erdem I, Akyuz U, Ersoy U, Ozcebe G (2006) An experimental study on two different strengthening techniques for RC frames. Eng Struct 28(13):1843–1851
11. Esmaili O, Epackachi S, Samadzad M, Mirghaderi SR (2008) Study of structural RC shear wall system in a 56-story RC tall building. In: The 14th world conference earthquake engineering
12. Zhao Q, Astaneh-asl A (2010) Experimental and analytical studies of a steel plate shear wall system. In: Structures congress 2008

13. Jain AK (1986) Seismic response of RC frames with steel braces. J Struct Eng ASCE I (10):2138–2148
14. Viswanath K, Prakash K, Desai A (2010) Seismic analysis of steel braced reinforced concrete frames. Int J Civ Struct Eng 1(1): 114–122
15. Taraithia SS, Sahoo DR, Madan A (2013) Experimental study of combined yielding metallic passive devices for enhanced energy dissipation of structures. In: The Pacific structural steel conference, pp 8–11, Oct 2013
16. Sahoo DR, Rai DC (2009) A novel technique of seismic strengthening of nonductile RC frame using steel caging and aluminum shear yielding damper. Earthq Spectra 25(2):415–437
17. Aboutaha RS, Engelhardt MD, Jirsa JO, Kreger ME (1996) Retrofit of concrete columns with inadequate lap splices by the use of rectangular steel jackets. Earthq Spectra 124:693–714
18. Li Y, Hwang J, Chen S, Hsieh Y (2005) A study of reinforced concrete bridge columns retrofitted by steel jackets. J Chin Inst Eng 28(2):319–328
19. ACI, Committee, and 374.1-05 (2006) Acceptance criteria for moment frames based on structural testing and commentary—an ACI standard. American Concrete Institute, Farmington Hills, Michigan

Comparative Modelling of Infilled Frames: A Descriptive Review and Analysis

Shujaat Hussain Buch and Dilawar Mohammad Bhat

Abstract Infilled Frames are most common today. However, the general analysis is performed only for frame action without considering effect of infills. The reason is that the behavior and action of infill frame is more complicated than bare frames. Moreover, the structural and material parameters also vary greatly in infilled frames. Infill is made of different materials, usually brick, block and stone masonry while as frame is usually made of steel and reinforced concrete. A review of various modelling techniques is done which are descriptive, defining various experimental and mathematical techniques of infill frame modelling. The various mathematical macro-models and micro-models for infill frames are compared with the experimental models for their behavioral action. This comparison is done on bay frames which are studied for strength, stiffness, cracking pattern and mode of failure under in-plane and vertical loads. The feasibility study of each model is performed for single bay space frame. A deterministic flow-chart is finally generated which describes the modelling and analysis methodologies and reports the effective modelling and analysis technique.

Keywords Behavior · Frame · Infill · Modelling · Stiffness · Strength

1 Introduction

Frames are an assembly of beams and columns and are subjected to flexural and shear forces. The beam-column junction is semi-flexible subjected to combination of flexural, shear and torsion forces. Infilled frames have a different behavior.

S.H. Buch (✉)
Civil Engineering Department, Islamic University of Science and Technology,
Awantipora, Jammu and Kashmir, India
e-mail: shujaatbuch@yahoo.com

D.M. Bhat
Engineering Wing, Sarva Shiksha Abhiyan, Srinagar, Jammu and Kashmir, India
e-mail: dilawar.bhat@gmail.com

2169

This behavior depends on the structural interaction of the frame and the infill and on the relative strength and stiffness of infill and frame. Besides, other material properties of infill and frame are also accounted for in this complex behavior.

1.1 Behavior of Infilled Frame (IF)

IF is with or without a gap between infill and frame. A shear connector may connect the infill with frame. A beam band may also stiffen the frame. The opening with or without an opening frame may be present within the infill. Infills are hardly, believed to have no structural action to vertical structural loads. Lateral forces are both in-plane and out-of-plane. Out-of-plane loads have little action on overall structure though it may have a local effect on an individual infill.

In-plane lateral load on IF leads to a complex behavior of the structure. It increases the mass of structure. Besides, it is widely believed to increase strength, stiffness and energy dissipation while as it decreases the time-period. The modes of failure of infill are: (1) Corner crushing at beam-column junction for strong infills; (2) Diagonal crushing for strong infills; (3) Diagonal compression cracking for weak infills; (4) Sliding shear failure for weak infills in shear. The modes of frame failure in IF are: (1) Column flexure; (2) Column shear.

1.2 Modelling of Infilled Frame (IF)

A realistic structure has unknown variables. The material and structural variables are: (1) Material of infill and frame; (2) Frame joint connections; (3) Aspect and area of infill; (4) Location and size of openings; (5) Number of bays and stories; (6) Space and 2-D frame; (7) Masonry bondage; (8) Interface between infill and frame; (9) Opening frames (material and patterns); (10) Beam/Lintel band.

Mathematical and experimental models are all finite expressions of the realistic models. The basic idea of idealized modelling is to make analysis simpler from the complex derivations, considering control parameters and other discrete variables. Experimental tests give discrete results, depending on scale of models. Moreover, loading is applied hysterically, in cyclic patterns or as a dynamic load. Analytical modelling has been broadly resolved into macro-models or micro-models, where infill is considered as single phase and multi-phase respectively. This classification is based on Lourenco's idealization of masonry as either: (1) Homogenous-isotropic continuum; (2) Expanded units, mortar and mortar joints as lumped interface; (3) Masonry unit and mortar are modeled separately with interface elements [29].

2 Modelling History

Masonry infill has been in use since 200 years. There has been an extensive research on experimental, numerical, empirical and finite element based techniques. The analysis techniques implemented are finite element, finite difference, plastic methods and Airy's stress functions. However, experimental investigation is needed to determine some of the parameters.

2.1 Development of Macro-model Struts

An experimental tests on 3-story, 3-bay infilled steel frame was conducted by Polyakov [36] and came to a conclusion that a diagonal braced system is developed where stresses are transmitted through compression zone of infill-frame interface. Infill separation is observed, which is a result of greater deformations on compression than tension diagonals. Based on this infill property, Holmes [25] performed experimental tests on 1-bay IF and developed an analytical model based on semi-empirical equations. First macro-model determined is an equivalent strut of width 1/3rd of diagonal length of infill panel. However, forces in frames and infill are determined separately and super-imposed for determining failure strength of overall IF. This was not based on relative stiffness of frame and infill.

Experimental tests on small 1:20 scale models by Smith [39] on IF determines lateral loads causing cracking and failure, while length of contact between infill panel and frame is also determined. A macro-model equivalent strut is also developed. Stiffer frames have longer contact length and wider effective width. Contact length also depends on panel aspect ratio while as strut width ratio varies from 0.10 to 0.25. Aspect ratio parameters are studied through experimental tests [8]. They observe that increase in aspect ratio of frame increased its strength while as infill brick size had little effect on overall failure strength of IF. Besides, for IF the change in column area and reinforcement area also had little effect on overall strength and rigidity. Infill reduces flexural frame forces and increases axial column forces [21]. Through experimental tests on infill, it is observed that wall cracks first while as frames without infill fail in flexure [46]. Final failure occurs in extension hinges or pure shear failure in tension column with low amount of reinforcement and high amount of reinforcement respectively. It is observed from experimental tests on steel frames with infills that initial gaps in infill are undesirable as it leads to decrease in stiffness [37].

Contact length parameter 'λ' is developed for IF by Smith and Carter [40]. He observes that in stiff frames, diagonal cracking occurred first while as in flexible frames, crushing occurred without cracking. Change in number of stories in determining 'λ' is not considered. The change in equivalent width of strut with cracking is not reported by Smith.

$$\lambda = h \sqrt[4]{\frac{E_w t_w \ \sin(2\theta)}{4EIh_w}} \tag{1}$$

$$\theta = \tan^{-1}(h_w/L_w) \tag{2}$$

h = height of frame, h_w = height of infill, E_w = Modulus of infill, t_w = thickness of infill, E = Modulus of frame, I = moment of frame, L_w = Length of infill.

Infill modeled as equivalent strut can be used to determine the strain in stress analysis of IF and to determine the lateral stiffness [40]. Lateral strength is considered to be based on weakest modes of failure which is based on tests. Experimental tests on IF for many number of bays, stories, reinforcement amount, vertical loads on columns and wall openings were performed [22]. Failure modes are studied and shearing crack for infill and frame is based on segmental cracking of infill and frame. A knee-braced frame braced by these segments of cracked infill is modeled and studied. Further, cracking loads were determined which vary between the upper and lower limit. A mathematical representation given for upper limit is cantilever beam and lower limit of cracking is frame without infill. But final overall failure of the structural system is not accounted for. First crack modelling is determined from experimental tests on concrete IF from stress fields. Approximate superposition method is determined from experimental tests on linear elastic principles; where contact pressures, spaces, shear and axial deformation, infill wall acts as a shear wall and is formulated into a matrix [41]. Mathematical model for interface slips and axial deformation is carried further by the experimental tests on mortar infilled steel frames for lateral loads. Dynamic behavior of masonry IF is further studied under cyclic loads by Zarnic and Tomazevic [47]. They study the drift patterns for IF and compare them with bare frames. It is also seen from experimental tests on masonry infill that infill increases strength of rigid steel frame while as bond beams leads to cracking load being reached before ultimate load [14].

It is seen from comparison of experimental and analytical models that the infill fits perfectly within the boundary frame forming a narrow compression mathematical strut [31]. Both stiffness and strength are determined from this equivalent strut of width equal to 0.16 $\lambda_h^{-0.3}$. Though the width of the strut is not based on loading stage and cracking, this strut was modified by him in 1974 by further experimentation to a width equal to 0.175 $\lambda_h^{-0.4}$, where 'λ_h' is contact length parameter. It is confirmed that initial lateral load leads to boundary cracking and then with further loading the infill behaves as a diagonal strut with width depending on the contact length. Contact length in turn depends on relative stiffness of column and infill and on the stress-strain relation of infill [27]. This is on basis of experimental tests that the behavior of infill-frame is studied. An analytical model developed is a beam analogy and a diagonal strut which gives stiffness and is not accurate for determining strength. Simplified macro-models are further compared with the experimental tests using for IF 1/3rd scale models [26]. Increase in lateral strength, lateral stiffness and energy dissipation occurs with addition of IF. Analytic model is used to determine the energy dissipation capacity of the IF.

An equivalent strut is also determined based on analytic investigation at failure of infill [7]. A simple representation for this equivalent strut for cracked sections at failure, with width 'w' is given with respect to diagonal length 'd' as:

$$w/d = 0.20 \sin\theta \sqrt{\frac{E_c A_c}{G_w A_w}} \tag{3}$$

G_w = Shear Modulus of infill, A_w = Area of infill, A_c = Area of concrete frame, E_c = Modulus of concrete frame.

Further, the equivalent width for change in contact length and aspect ratio for a particular diagonal infill angle between 25° and 50° with horizontal, where 'λ_h', the contact length is as obtained by Smith; is determined by Liauw and Kwan [28]:

$$w/d = \frac{0.95 \sin(2\theta)}{\lambda_h} \tag{4}$$

The effect of cyclic loading on strength deterioration is also studied [17]. The equivalent strut is modeled accordingly. Infill is not connected to frame initially, thereafter on further loading, the boundary conditions are unilateral. A diagonal strut with higher limit value of equivalent width equal to 1/4th of diagonal length is determined from analyzing IF [35]. This is based on earlier works and their interpretation of analytical equations, whereby, stiffer structure with lesser strength degradation is proposed. An equivalent strut of width equal to 1/8th of diagonal length is determined from experimental tests on ½ scale models with clay/concrete infills [3]. Initial cracking cause's stiffness to decrease while as stiffness is found to be proportional to masonry compressive strength. Strong infills in strong frames have excellent load resistance and energy dissipation capacity, while as weak framed strong infills develop a shear failure in column [33]. This is obtained from experimental tests on weak and strong IF of masonry in RC. Strong frames fail by diagonal cracking showing ductile behavior while as weak frames fail by diagonal cracking and hinging in windward column [1, 2]. This is obtained from experimental tests on ½ scale models for strong and weak frames.

2.2 Development of Modified Macro-model Struts

Two equivalent strut models for both before and after cracking are proposed on basis of the finite element analysis [15]. It depends on the relative change in modulus of infill and frame and on the aspect of the frame.

For un-cracked panel

$$w/d = 0.085 + \left(\frac{0.748}{\lambda_h}\right) \quad \text{if} \quad \lambda_h \leq 7.85 \tag{5}$$

$$w/d = 0.130 + 0.393/\lambda_h \quad \text{if} \quad \lambda_h > 7.85 \tag{6}$$

For cracked panel

$$w/d = 0.010 + \frac{0.707}{\lambda_h} \quad \text{if} \quad \lambda_h \leq 7.85 \tag{7}$$

$$w/d = 0.040 + \frac{0.47}{\lambda_h} \quad \text{if} \quad \lambda_h > 7.85 \tag{8}$$

An equivalent strut with 'w' given below is also proposed [14]:

$$w = a_c \cos\theta + a_b \sin\theta \tag{9}$$

$a_c = \pi/1.5\,\lambda_h$ = effective contact length of infill and column
$a_b = \pi/1.5\,\lambda_t$ = effective contact length of infill and beam

$$\lambda_h = \sqrt[4]{\frac{E_w H_{in}\,\sin(2\theta)}{4E_c I_c t_w}} \tag{10}$$

$$\lambda_t = \sqrt[4]{\frac{E_w L_{in}\,\sin(2\theta)}{4E_b I_b t_w}} \tag{11}$$

where, terms have usual meaning.

The equivalent strut of Smith and Carter is considered with limitation of contact length to 20 % of infill height for stiff columns and cracked moment of inertia of beams and columns is taken as ½ of the gross moment of inertia. A piecewise linear equivalent diagonal strut is also proposed through experimental investigation of clay infilled steel frames [23]. The area of strut is given by:

$$A = wt = \frac{\pi t_w}{C\lambda\,\cos\theta} \tag{12}$$

'C' being a constant which depends on in-plane drift displacement, the value changing with loading.

A modified equivalent strut for hysteretic behavior using Bouc-Wen model resembles stiffness and strength degradation as well as pinching in infill [16]. However, column behavior is assumed to be elastic. Static analysis using fundamental period and response spectrum is carried out. Another macro-model for masonry IF is a four-noded panel element connected to the frame at beam-column. Compressive and shear behavior of masonry panel is studied using two parallel struts and shear spring in each direction [13]. It is feasible for lateral stiffness and strength of the infill. Panel has limitations of not suggesting actual bending moment and shear forces in frame.

Yet another model has a homogenous continuum RC frame model, while characteristics of infill strut and non-linear material properties are obtained from

inverse analysis, along with statistical hypothesis tests to have proper hypothesis and accuracy [44]. Many parameters are studied and geometric and material non-linearity is considered in further finite element analysis. Others use a reduction factor for the effective width of the diagonal strut over that of the solid RC IF to calculate its initial lateral stiffness for a central window [34]. Stiffness of IF is based on size and location of opening. Finite element models are compared with width of struts by Smith and Carter [40], Mainstone [31], Pauley and Priestly [35], Liauw and Kwan [28] and Holmes [25]. A further reduction factor for diagonal struts of IF takes into account the presence of openings in infill. This reduction factor is the ratio of the effective width of diagonal strut representing wall with opening over that of solid RC infill [5, 6]. Comparison of single and multi-strut models is done with finite element models and compared with experimental value. A macro-model which is a discrete physical model is developed where infill is analytically modeled as plate with finite number of degrees of freedom (DOF). An infill lumped spring-mass system producing deformations and stresses is also developed [21].

2.3 Development of Multi-strut Macro-models

A multi-strut model with diagonal and vertical struts is initially developed [45]. For initial condition, two pin-ended diagonal struts in two different directions are used. Vertical struts represent vertical stiffeners. Natural frequencies and modes of vibration are determined by this mathematical model. However, contact length and location of strut are not known. IF can be modeled as five parallel struts in each direction [43]. They study the frame behavior and the effect of contact length on the bending moment distribution in frame.

Further a six-strut compression IF, three struts in each direction is also used to model the IF [11]. The two off-diagonal struts are placed at critical locations specified by parameter 'α' as defined by Liauw and Kwan [28]. This location specifies plastic hinge location. Moreover, the hysteretic behavior of this model is defined by this strut which has an advantage of taking into account strength and stiffness degradation controllable by six definitive parameters from experimental data. Multi-strut analytical models for IF with openings has a plastic hinges formed at mid-span of beams leading to more strong and more ductile IF as is the requirement for an earthquake resistant structure [24].

Further, a two diagonal compressive strut is dependent on the infill aspect ratio, shear stresses at infill-frame interface and relative beam and column strengths [38]. They perform in-elastic iteration of equivalent strut of IF, considering elastic-plastic behavior and limited ductility of the infill. Lack of infill-to-frame fit and shrinkage of infill and imperfections are included in the analysis. One, two and three strut infill frames with finite element models are studied for stiffness and behavior of surrounding frames [12]. Stiffness changes with separation of struts and two and three strut models show lower stiffness values. The frame bending moment values

are better for 3-strut models while as single strut underestimates it and double strut gives larger values.

Although some experimental tests on IF with openings is conducted for change in opening location, where stiffness and strength is seen to decrease with an opening in an infill [32]. Multiple strut models for IF with openings are included by FEMA-356 (2000) [9]. It is based on the model of Thiruvengadam. Another six-strut model for concrete masonry infilled steel frame is compared with experimental models [19]. A masonry infill wall is considered orthotropic and to have a simpler non-linear model. One diagonal and two off-diagonal struts are used in each direction. Besides, three-strut models for concrete masonry infilled steel frame are also used [20].

2.4 Development of Micro-models

A Finite element analysis model is used for IF to be depicted as equivalent struts with width determined separately for IF with and without opening [18]. This model is compared with that of Smith and Main-stone. Equivalent strut width is determined as:

$$w/d = \gamma \, \sin(2\theta) \tag{13}$$

$$\gamma = 0.32 \left(\frac{h^4 E_w t_w}{m E_c I_c h_w} \right) \sqrt{\sin(2\theta)} \tag{14}$$

$$m = 6(1 + \left(\frac{6 E_b I_b h}{\pi E_c I_c L} \right) \tag{15}$$

where, terms have usual meaning.

Further, finite element analysis of IF is compared with experimental results and subsequent comparison of analytical model with new finite element model gives failure modes, failure loads and initial stiffness. Interface model is determined from the experimental results on mortar joints. A failure criterion is determined from Von-Mises criteria for plane stress condition for un-cracked masonry and smeared crack model. These models are made for flexible and stiff frames. Cracking in tension and plasticity in compression of infill is modeled by smeared crack and plasticity model respectively. A new finite element method for analysis of IF is used, where; infill/frame contact length and contact stresses are estimated as integral part of the solution [4]. Successive contact points from deformed meshes are determined. Work on openings is done and studied for stiffness.

Another non-linear finite element model for masonry infilled RC frame is calibrated [42]. The modelling combines the smeared and discrete crack approaches to see failure modes of infill, fracture of mortar joints and RC shear failure. Comparing with the experimental data, it is good to predict strength and failure, besides doing

sensitivity analysis of various modelling parameters. Work of Lotfi in 1992, Lourenco in 1996 and Attard et al. in 2007 for masonry model has been incorporated in discretization of infill.

Elasto-plastic model of Saneinejad and Hobb's for IF for static and quasi-static cyclic loading is a hysteresis model which uses slip pinching and degrading properties of stiffness and strength [30]. Full scale frame models are subject to monotonic loading and an artificial joint describing both discontinuous and continuous behavior of masonry is used [10]. Stress distribution and structural behavior of framed wall show that masonry is highly influenced by failure of mortar. Partially filled masonry induces short column effect while as completely filled wall increases stiffness of structure and adjacent column fails in uniform cracks. DDA (discrete deformation analysis) model is used where infilled frame is modeled as a block and frame as triangular element, reinforcement as bolt.

3 Comparison of Modeling Techniques

Some work on comparison of models has been done. Experiments on frames with and without infill are compared and it is observed that stronger frames are stiffer than weak ones [2]. In this study, a 2-D Al-Chaar's experimental model is compared with various analytical macro-models and micro-models for sensitivity analysis. Al-Chaar's model is given in Fig. 1. And the validation and sensitivity analysis for linear and non-linear behavior is performed. The sensitivity of the various modelling techniques for a solid infilled 2-D Al-Chaar frame is illustrated (Table 1). The infill crack load and frame peak load for a 2D single bay is depicted best by Smith's Strut. Higher end values for axial infill stresses are depicted by

Fig. 1 Al-Chaar's experimental model
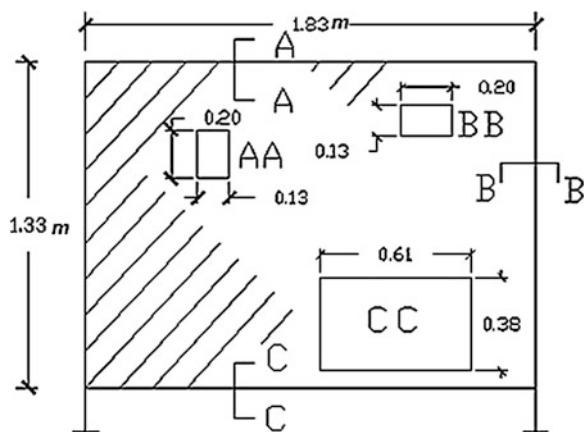
Table 1 Comparison of various modeling techniques for Al-Chaar's experimental model

Model type	Equivalent width (m) (contact length-m)	Infill crack load (kN)	Frame peak load (kN)	Frame bending moment (kNm)	Frame max. shear force (kN)	Infill max. axial stresses (KN/m^2)	Peak load variation (% age)
Al-Chaar's experimental model	–	75.6	84.1	–	–	–	–
Holmes strut	0.75 (none)	57.13	76.39	1.3	1.8	1148.7	−9.16
Smith strut	0.45 (0.12)	58.97	78.20	13.0	18.9	11011.3	−7.02
Mainstone strut	0.45 (0.12)	48.27	78.01	13.1	18.6	11030.6	−7.24
Tassios strut	0.22 (none)	40.23	40.4	4.0	5.6	3527.1	−51.96
Decanini and Fantin strut	0.37 (none)	44.48	65.31	2.5	3.6	2216.7	−22.34
Dawe and Seah strut	0.59 (none)	51.97	61.79	1.8	2.6	1554.9	−26.53
Pauley and Priestley strut	0.57 (none)	51.01	59.07	1.7	2.4	1489.8	−29.76
Durrani and Luo strut	0.39 (none)	45.41	70.28	2.3	3.3	2077.1	−16.43
Angel strut	0.28 (none)	41.65	50.14	3.2	4.5	2815.1	−40.38
Crisafulli 2-strut	Both 0.22 (none)	47.33	52.40	1.9	2.6	1794.7	−37.69
Crisafulli 3-strut	Central strut 0.22, Off-strut 0.11	49.28	52.19	4.0	5.7	3640.4	−37.94

Fig. 2 Stiffness variation of 3-D frame models
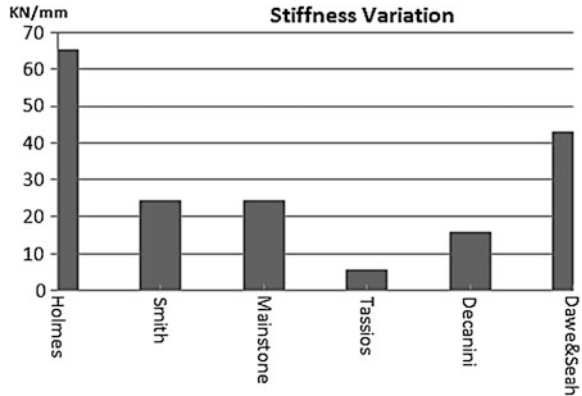
Mainstone's Strut. Perfect moment resisting frame is depicted by Pauley and Priestley. Both Smith's Strut and Mainstone's strut depict better moment resisting capacity and shear action of frame, with the result a higher peak load.

3.1 Feasibility for Different Modeling for 3-D Frames

A space 3D 1-Bay 1-Story infill frame of dimensions about 'x' and 'y' axis same as Al-Chaar's model as depicted in Fig. 1 is modeled by different infill modeling methods. Feasibility study for 3-D Frames is performed as depicted in Fig. 2.

On comparison with experimental models, stiffness for 1-Bay 1-story Infill frames obtained is more accurate for Mainstone and Smith Models and less for Holmes and Tassios.

3.2 Feasibility for Different Modeling for Infill Openings

Al-Chaar's 2-D model with openings of area 30 % of the total infill area are modeled. The modeling is done by different methods. The initial lateral stiffness at 15 % of the peak load is compared for the finite element model and different macro-models. This is done by decreasing the equivalent width (w) of the infill struts and comparing the initial lateral stiffness with the finite element model of Mehrabi and Shing. The feasibility of such reduction factors for different models is given in Fig. 3.

It is observed that the Infill opening can be effectively depicted by Smith, Mainstone and Crisafulli 3-Strut model. Holmes model can be used in other
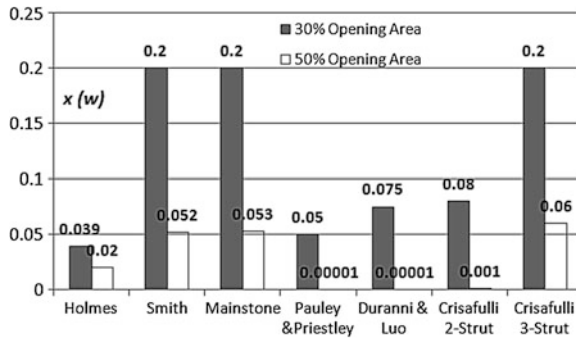
Fig. 3 Feasibility of equivalent width-reduction factor for different models compared for 30 and 50 % opening areas

Fig. 4 Peak load variation for Al-Chaar's model with change in modeling

cases. It is important to realize that the multi-strut models give better description of the behavior of infill with openings. Moreover, a 3-Strut model is better illustrative of the behavior of the openings in infill than a 2-Strut model. Pauley and Priestley strut model, Duranni and Luo model are not valid for openings at 50 % area of the infill. Failure patterns are studied at peak infill and frame loads for openings modeled by different techniques. The range of peak load variation is up-to ±6.7 % to maximum 7.2 % when modeled as different struts. This is shown in Fig. 4.
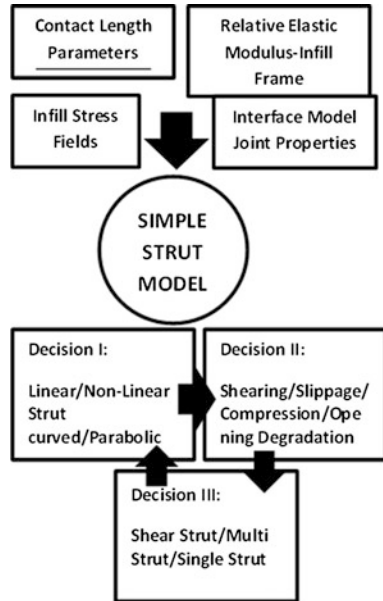
4 Conclusion and Discussion

Mathematical modelling is based on experimental values for interface action, joint behavior, infill stress fields and frame-infill action. Once these parameters are put into a mathematical equation, the mathematical modelling becomes more descriptive and more complicated. The plate/shell mesh models, with descriptive interface models or discrete or smeared crack have been generally used to form a complex mathematical model. The simplest mathematical model for infill that has been agreed for last sixty years has been an equivalent strut. Another question is the modelling of openings that change strut action drastically and if the opening is at corner, the compressive strut may not be formed at all, with a plain shearing action. Shear strut has been introduced to give effect to shearing behavior of infill. The story and bay effect has been patterned in infill modelling. The reduction factor has been used for strut model to take into account the effect of opening.

Thereby, the following scheme of reasoning can be followed in future modelling and analysis:

1. Experimental testing needs to resolve the slippage action of infill from frame based on the drift of the frame. Besides, it needs to study the effect of patterns of bonding of masonry infill on IF. The effect of opening frames or stiffeners needs to be studied. Besides, the shrinkage effects need to be studied effectively.
2. The complex mathematical modelling techniques need further detailing as discrete models for non-linear cases. The infill masonry mortar joints need to be

resolved not only for stiffening action but also for bonding, strengthening, dilatation and shear. The interface behavior is based on infill-frame shear slippage apart from axial stresses. The effect of openings on stress distribution and of opening stiffeners on change in such distributions needs a thorough study.

3. The simple strut analogy can be followed for all basic analysis on account of its simplicity. However, it needs to be considered separately for compression axial stresses and for horizontal shearing. The frame is to be modeled accurately as knee braced column and strutted beam and column. The effect of openings needs to be incorporated for IF to have a proper evaluation. A reduction factor based strut for IF with openings is not generally valid as it oversimplifies the behavior; rather a simple shear model for infills with openings is more conclusive, subject to openings above a particular size and openings at corners. While a reduction factor based strut is valid for openings below a particular size and openings at center, but with a shear strut model also being incorporated. The effect of openings on contact length also needs to be broadly elaborated. All other parameters need an elaboration and further research. The decision review process that can be adopted is given in Fig. 5. It is important to realize the properties of the strut for macro-model for infill based on scheme developed for comparing and validating a trial method. Various results obtained are to be reprocessed by analytical and experimental results.

References

1. Al-Chaar G (1997) Non-ductile behavior of reinforced concrete frames with masonry infill panels subjected to in-plane loading. PhD thesis, University of Illinois at Chicago
2. Al-Chaar G, Sweeney S (2002) Behavior of masonry infilled non-ductile reinforced concrete frames. J Struct Eng 128(8):1055–1063
3. Angel R, Abrams DP, Shapiro D, Uzarski J, Webster M (1994) Behavior of reinforced concrete frames with masonry infills. Structural research series report, University of Illinois, p 589
4. Asteris PG (2003) Lateral stiffness of brick masonry infilled plane frames. J Struct Eng 129 (8):1071–1079
5. Asteris PG, Kakaletsis DJ, Chrysostomou CZ, Smyrou EE (2011) Failure modes of infilled frames. Electr J Struct Eng 11(1):11–20
6. Asteris PG, Giannopoulos IP, Chrysostomou CZ (2012) Modeling of infilled frames with openings. Open Constr Build Technol J 6:81–90
7. Bazan E, Meli R (1980) Seismic analysis of structures with masonry walls. In: Proceedings of 7th world conference on earthquake engineering, IAEE, Tokyo, Oct 1980
8. Benjamin JR, Williams HA (1958) The behavior of one story shear walls. J Struct Div ASCE ST-4:1723–30
9. Chaker AA, Sherifati A (1999) Influence of masonry infill panels on the vibration and stiffness characteristics of RC frame buildings. Earthq Eng Struct Dyn 28(9):1061–1065

10. Chiou YJ, Tzeng JC, Liou YW (1999) Experimental and analytical study of masonry infilled frames. J Struct Eng 125(10):1109–1117
11. Chrysostomou CZ (1991) Effects of degrading infill walls on the nonlinear seismic response of two-dimensional steel frames. Ph.D. thesis, Cornell University, New York
12. Crisafulli FG (1997) Seismic behavior of reinforced concrete structures with masonry infills. Ph.D. thesis, University of Canterbury, New Zealand
13. Crisafulli FG, Carr AJ (2007) Proposed macro-model for the analysis of infilled frame structures. Bull NZ Soc Earthq Eng 40(2):69–77
14. Dawe JL, Seah CK (1989) Behaviour of masonry infilled steel frames. Can J Civ Eng 16:865–876
15. Decanini LD, Fantin GE (1987) Modelossimplificados de la mamposteríaincluida en porticos Características de rigidez y Resistencia lateral en astadolímite. Jornadas Argentinas de Ingeniería Estructural, Argentina 2:817–836
16. Degefa M (2005) Response of masonry infilled RC frame under horizontal Seismic force. Ph. D thesis, Addis Ababa University
17. Doudoumis IN Mitsopoulou EN (1986) Non-linear analysis of multi-story infilled frames for unilateral contact conditions. In: Proceedings of 8th European conference on earthquake engineering, Istanbul, Turkey, April 1986
18. Durrani AJ, Luo YH (1994) Seismic retrofit of flat-slab buildings with masonry infills. In: Proceedings of NCEER workshop on seismic response in masonry infills, NCEER, Buffalo, NY, 3–4 Jan 1994
19. El-Dakhakhni WW (2000) Non-linear finite element modeling of concrete masonry-infilled steel frame. M.S. thesis, Drexel University, Philadelphia
20. El-Dakhakhni WW, Elgaaly M, Hamid AA (2003) Three-strut model for concrete masonry-infilled frames. J Struct Eng 129(2):177–185
21. Fedorkiw JP, Sozen MA (1968) A lumped-parameter model to simulate the response of reinforced concrete frames with filler walls. University of Illinios, Urbana. http://www.hdl.handle.net/2142/14775. Accessed 07 Jan 2010
22. Fiorato AE, Sozen MA, Gamble WL (1970) An investigation of the interaction of reinforced concrete frames with masonry filler Walls. University of Illinios, Urbana. http://www.hdl.handle.net/2142/14303. Accessed 25 Nov 2009
23. Flanagan RD, Bennett RM (1999) In-plane behavior of structural clay tile infilled frames. J Struct Eng 125(6):590–599
24. Hamburger RO, Chakradeo AS (1993) Methodology for seismic-capacity evaluation of steel-frame buildings with infill unreinforced masonry. In: Proceedings of national earthquake conference, Central US earthquake consortium, Memphis, 1–2 May 1993
25. Holmes M (1961) Steel frames with brickwork and concrete infilling. ICE Proc 19:473–478
26. Klinger RE, Bertero VV (1978) Earthquake resistance of infilled frames. J Struct Eng ASCE 104(6):973–989
27. Leuchars JM, Scrivener JC (1976) Masonry infill panels subjected to cyclic in-plane loading. Bull NZ Nat Soc Earthq Eng 9(2):122–131
28. Liauw TC, Kwan KH (1984) Non-linear behavior of non-integral infilled frames. J Comput Struct 18(3):551–560
29. Lourenco PB, Pina-Henriques JL (2006) Masonry micro-modelling, a continuum approach in compression. J Comput Struct 84:1977–1989
30. Madan A, Reinhorn AM, Mander JB, Valles RE (1997) Modeling of masonry infill panels for structural analysis. J Struct Eng 123(10):1295–1302
31. Mainstone RJ (1971) On the stiffness and strengths of infilled frames. ICE Proc IV:57–90
32. Mallick DV, Garg RP (1971) Effect of openings on the lateral stiffness on infilled frames. Struct Build 49:193–209
33. Mehrabi AB, Shing PB, Schuller M, Noland J (1997) Experimental evaluation of masonry infilled RC frames. J Struct Eng 122(3):228–237
34. Mondal G, Jain SK (2008) Lateral stiffness of masonry infilled reinforced concrete (RC) frames with central opening. Earthq Spectra 24(3):701–723

35. Paulay T, Priestley MJN (1992) Seismic design of reinforced concrete and masonry buildings. Masonry structures. Wiley, New York
36. Polyakov SV (1956) Masonry in framed buildings. (J Gosudarstvennoe izdatel'stvo Literatury postroitel'stvui arkhitekture) In: Cairns GL, 1963. National Lending Library for Science and Technology, Boston, 1956
37. Riddington JR (1984) The influence of initial gaps on infilled frame behavior. ICE Proc 17 (3):295–310
38. Saneinejad A, Hobbs B (1995) Inelastic design of infilled frames. J Struct Eng 121(4):634–650
39. Smith BS (1962) Behavior of square infilled frames. J Struct Div ASCE ST-1: 381–403
40. Smith BS, Carter C (1969) A method of analysis for infilled frames. ICE Proc 44(1):31–48
41. Smolira M (1973) Analysis of infilled shear walls. ICE Proc 55(4):895–912
42. Stavridis A, Shing PB (2010) Finite element modeling of non-linear behavior of masonry infilled RC frames. J Struct Eng 136(3):285–296
43. Syrmakezis CA Vratsanou VY (1986) Influence of infill walls to RC frames response. In: Proceedings of 8th European conference on earthquake engineering, Istanbul, Turkey, 22–25 Sept 1986
44. Taher SEF, Afefy HME (2008) Role of masonry infill in Seismic resistance of RC structures. Arab J Sci Eng 33(2B):291
45. Thiruvengadam V (1985) On the natural frequencies of infilled frames. Earthq Eng Struct Dyn 13:401–419
46. Yorulmaz M Sozen MA (1968) Behavior of single-story reinforced concrete frames with filler walls. University of Illinios, Urbana. http://www.hdl.handle.net/2142/14253. Accessed 17 Nov 2009
47. Zarnic R Tomazevic M (1984) The behavior of masonry infilled reinforced concrete frames subjected to cyclic lateral loading. In: Proceedings of 8th world conference on earthquake engineering, San Francisco, USA, 21–28 July 1984

Bibliography

48. Ghosh AK, Made AM (2002) Finite element analysis of infilled frames. J Struct Eng 128 (7):881–889
49. Mc Bridge RT, Yong TC, Dawe JL, Valsangkar AJ (1984) Behavior of masonry infilled steel frames subjected to racking. In: Proceedings of CSCE annual conference, Halifax, NS, Canada, 20–25 May 1984
50. Pinto A, Verzeletti G, Molina J, Varum H, Pinho R, Coelho E (2002) Pseudo-dynamic tests on non-seismic resisting RC frames (bare and selective retrofit frames). Joint Research Centre, Ispra

Pushover Analysis of Symmetric and Asymmetric Reinforced Concrete Buildings

V.K. Sehgal and Ankush Mehta

Abstract It has been observed that conventional elastic design methods don't give realistic basis to control seismic performance of structures in severe earthquakes. Inelastic time-history methods are very powerful but computationally, being very expensive and complex, are not feasible for most of the practical applications. The pushover method of analysis, being a nonlinear static method, considers inelastic response characteristics and it can be used to estimate the dynamic demands imposed on the structures during seismic excitation. In reinforced concrete buildings, irregularities are introduced to meet various functional requirements and architectural demands. These irregularities add an additional effect of torsion or sudden change in stiffness which affects the demands of the structure. In the present paper, 3 storey and 6 storey symmetric buildings have been analyzed using pushover analysis. The plan of the same buildings is modified and plan asymmetry is created by introducing eccentricities of magnitudes varying from 5 to 20 % about both the principal axes. Various vertical irregularities of soft storey and extreme soft storey are also introduced by increasing the height of the ground storey. All the above models have been analyzed using pushover method. The capacity curve and performance point are obtained for all the models. Based on analytical results, comparisons between symmetric, plan asymmetric and vertically asymmetric buildings have been drawn. SAP 2000 has been used to carry out the pushover analysis. It has been observed that beyond elastic range, developed base shear increases with increase in plan asymmetry and decreases with increase in vertical asymmetry. Same trend is followed for ultimate base shear. Also, the performance point lies in elastic range and it is relatively on left side for 3 storey buildings when compared with 6 storey buildings, indicating 3 storey building to be safer.

Keywords Pushover analysis · Target displacement · Asymmetric building · Irregularities · Capacity curve · Demand curve · Performance objectives · Plastic hinge · SAP 2000

V.K. Sehgal (✉) · A. Mehta
NIT Kurukshetra, Kurukshetra, India
e-mail: vksehgalnitk@rediffmail.com

1 Introduction

Engineers concerned with the development of seismic design procedure understand that the conventional elastic design methods do not give realistic basis to control seismic performance of the structures in severe earthquakes. Inelastic time-history methods are very powerful but computationally very expensive and complex, are not feasible for most of the practical applications. The pushover method of analysis, being a nonlinear static method, considers inelastic response characteristics and can be used to estimate the dynamic demands imposed on the structures during seismic excitation.

In reinforced concrete buildings, irregularities are introduced to meet various functional requirements and architectural demands. These irregularities add an additional effect of torsion or sudden change in stiffness which affects the demands of the structure. The structures having asymmetry in plan or elevation are more susceptible to damage due to the earthquake loading. Various asymmetric buildings have shown excessive damage in past due to strong earthquake motions. Buildings having asymmetry in plan are subjected to torsion effects which are due to the non-coincidence of centre of mass and centre of stiffness. The distance between these two is the eccentricity which may be unidirectional or bidirectional. Torsion leads to non-uniform distribution of floor displacements and uneven demands on the lateral resisting elements at different locations of the building.

Now a days, in reinforced concrete buildings, ground storey is kept open for the purpose of parking etc. or the height of ground storey is kept more in comparison with the storeys above. This type of construction introduces sever irregularity in the vertical plane due to sudden change in stiffness between the ground storey and upper storeys. This type of stiffness irregularity is characterized as soft storey or extreme soft storey depending on the magnitude of the stiffness of bottom storey with respect to upper storeys. In such buildings the ductility demand during the earthquake gets concentrated in the lower storey (soft storey or extreme soft storey) and the upper storeys tend to remain elastic. Collapse of the buildings has also occurred due to this type of stiffness irregularity.

Krawinkler and Seneviratna [1] carried out pushover analysis on a two-dimensional steel frame model. It was shown that for a structure vibrating in fundamental mode, the pushover analysis provides satisfactory results and for the structures vibrating in higher modes, the pushover analysis may give inaccurate results. Moghadam and Tso [2] used elastic spectrum analysis of the building to obtain the target displacement and load distributions for pushover analysis. They found that it is sufficient to find the target displacements of the planes of interest for 2-D pushover analyses. Chandler and Mendis [3] presented a case study for reinforced concrete moment resisting frames having low, medium and high ductility capacity using Elcentro NS earthquake ground motion as the seismic input. The authors concluded that the displacement based approach predicts accurately the overall displacement demands for the frames. Chintanapakdee and Chopra [4] determined the median and dispersion values of the ratio of story drift demands by modal

pushover analysis and nonlinear response history analysis to measure the bias and dispersion of pushover estimates. They concluded that the bias in the pushover procedure does not increase in spite of irregularity in stiffness, strength, or stiffness and strength provided the irregularity is in the middle or upper story and the pushover procedure identifies stories with largest drift demands and estimates them to a sufficient degree of accuracy. Barros and Almeida [5] proposed the static pushover analysis and utilized a load pattern proportional to the fundamental mode of vibration of the structure. They found the results very accurate for the structures which respond in the fundamental mode. For higher modes of vibration this load pattern loses its accuracy. To minimize this problem, they proposed a new multi-mode load pattern based on the relative participation of each mode of vibration in the elastic response and applied the proposed load pattern to the analyses of symmetric frames as well as to stiffness asymmetric and mass asymmetric irregular building frames. The authors found pushover methodology to be faster and easier than nonlinear dynamic ones. Dinh and Ichinose [6] carried out pushover analysis of the structure using inverted triangular forces to evaluate the most probable mechanism during earthquakes and satisfactorily predicted the mean and standard deviation of story drifts of the structures. Mouzzoun et al. [7] performed the pushover analysis using SAP 2000 to assess the seismic performance of a five storey reinforced concrete building and detected the locations of the plastic hinges. The performance point was found at immediate occupancy under moderate levels of shaking and at the same time plastic hinges occurred and the structure remained stable.

In the present study, 3 storey and 6 storey reinforced concrete building frames-symmetric in plan as well as in vertical plane are considered. The plan of the same buildings is modified and asymmetry is created by introducing eccentricities of magnitudes varying from 5 to 20 % about both the principal axes. Various vertical irregularities of soft storey and extreme soft storey are also introduced by increasing the height of the ground storey. Pushover analysis of all the models has been done using SAP 2000 14 version. The buildings are designed for the gravity and seismic loadings as per IS 456: 2000 [8] and IS 1893: 2002 [9]. In the analysis, the building is subjected to monotonically increasing pattern of lateral loads until the maximum displacement at the roof level equal to 4 % of the building height is reached or the structure becomes unstable.

2 Pushover Analysis of Building

In nonlinear static pushover procedure, a building is subjected to monotonically increasing lateral loading having a predefined vertical distribution. The building is displaced at the control node at roof level till it achieves target displacement or till the building collapses. The sequence of cracking, formation of plastic hinges and failure of structural components throughout the procedure are observed. The curve representing the variation of base shear with the displacement at the control node is

plotted. This curve is known as pushover curve or the capacity curve. The capacity curve is the basis of estimation of target displacement. The seismic demands (storey drifts, storey forces, and component deformation) for the selected earthquake are calculated at the target displacement level. The seismic demand is then compared with the corresponding structural capacity to know what performance the structure will exhibit. By correlating the capacity curve to the seismic demand generated by any specific earthquake or ground shaking intensity, a point is found on the capacity curve that estimates the maximum displacement of the building caused by the specific earthquake. This defines the performance point. The location of the performance point indicates whether the performance objective is met or not. The performance point is found by using Capacity Spectrum Procedure. For a particular capacity curve, the performance point obtained on the left indicates a safer design in comparison with the design in which the performance point is obtained on the right.

In Capacity Spectrum Method, also known as Acceleration-Displacement Response Spectra method (ADRS), both capacity curve and demand curve are represented in response spectral variables. Performance point is represented by the point which the capacity curve intersects the reduced demand. At performance point, both capacity and demand are equal. The Acceleration Displacement Response Spectrum (ADRS) i.e. demand spectrum, is obtained by plotting S_a versus S_d.

Where,

$$S_d = \left(\frac{T_1^2}{4\pi^2}\right) z \left(\frac{S_a}{g}\right) \tag{1}$$

$$S_a = \frac{\left(V/W\right) g}{\alpha} \tag{2}$$

and

$$S_d = \frac{\Delta_{roof}}{PF_{R,1}} \tag{3}$$

where, α and $PF_{R,1}$ are the modal mass coefficient and modal participation factor, respectively for the first mode.

The various performance levels given by FEMA 273 and 274 are (i) Operational level, (ii) Immediate occupancy, (iii) Life safety, (iv) Collapse prevention (Fig. 1).

In order to satisfy the life-safety requirement, the roof displacement should be less than 1.2 % of height for ordinary frames and 2 % for special moment-resisting frames. Life-safety requirement can be considered as corresponding to the design basis earthquake.

Fig. 1 Force-deformation indicating various performance levels [11]
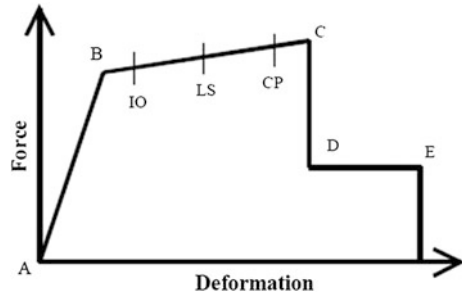
3 Building Models

The pushover analysis is performed by the application of monotonically increasing load patterns in any particular direction until a target displacement is reached. This pushover loading is accompanied with the gravity loading. To perform pushover analysis, hinges are assigned to the beams and columns.

In the symmetric buildings, plan asymmetry is created by introducing eccentricity of various magnitude (5, 10, 15 and 20 %) about both the principal axes. The symmetric buildings considered are of 3-storey and 6-storey. The plan dimensions of both the building types is same. All the buildings are fixed at the base.

In this way a total of fourteen models are prepared out of which two are symmetric, eight are plan asymmetric, two are soft storey and two are extreme soft storey models.

General Dimensions of the Buildings: In general, the plan of the building is divided into 4 panels as shown in the Fig. 2.

In the symmetric frame, all the panels are of size 5 m × 5 m. With the introduction of eccentricity, the dimensions of various panels varies. The height of each storey in symmetric and asymmetric buildings is kept as 4 m. For soft storey, the height of ground storey is kept as 4.6 m. For extreme soft storey, the height of ground storey is kept as 5 m (Fig. 2).

Material Properties: In all the models M 25 concrete and Fe 415 grade of reinforced steel bar is used. The elastic properties of the materials are taken as per IS 456: 2000 [8]. The short-term modulus of elasticity (E_c) of concrete is taken as:

$$E_C = 5000\sqrt{f_{ck}} \text{ MPa}$$

where f_{ck} is the characteristic compressive strength of concrete cube in MPa at 28-days (25 MPa in this case). For the steel rebar, yield stress (f_y) is 415 MPa and modulus of elasticity (E_s) of steel is 200,000 MPa.
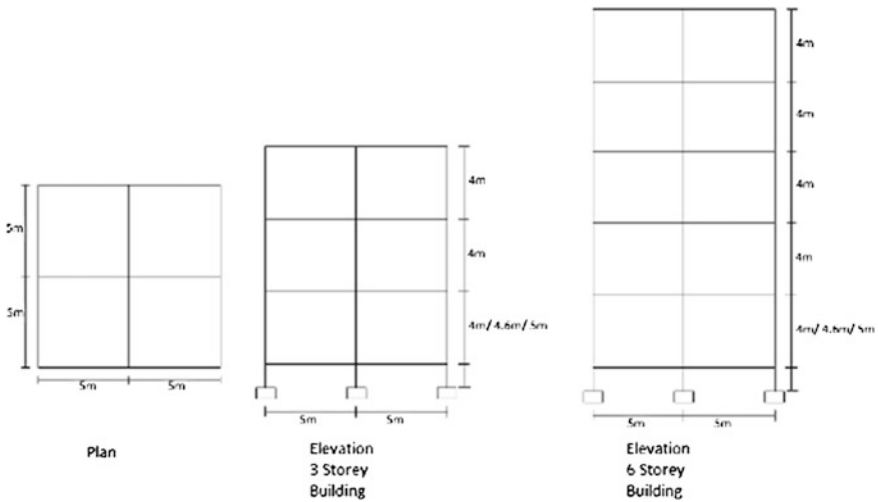
Fig. 2 Plan and elevation of building frames

Frame Sections: The sectional properties of various elements of the frames are taken as (i) Beam Size: 300 mm × 450 mm, (ii) Column size: 350 mm × 350 mm, (iii) Slab thickness: 125 mm, (iv) Brick masonry thickness: 230 mm.

Other parameters for which the building is analysed are: (i) Zone: IV (IS 1893:2002 [9]), (ii) Depth of foundation: 1.2 m, (iii) Soil Type: II, (iv) Damping Ratio: 0.05, (v) Target Displacement at the roof at coordinate (0, 0, H): 4 % of building height, Where H is the height of building.

Loads: The various loads acting on the building are considered as per IS 875 [10] and IS 1893:2002. The following load are considered to act on the building: (i) Dead load of wall (20.00 kN/m), (ii) Dead load of slab (3.125 kN/m^2), (iii) Dead load of floor finishing (1.00 kN/m^2), (iv) Dead load of roof treatment (1.50 kN/m^2), (v) Live Load on each floor (3.00 kN/m^2), (vi) Live load on roof slabs (1.50 kN/m^2), (vii) EQX, (viii) EQY. Limit State design of building models is carried out using 13 factored load combinations of DL, LL and EQ loads.

Modelling of Flexural Plastic Hinges: In the present study, a point-plasticity approach is considered for modelling nonlinearity behaviour, in which the plastic hinge is assumed to be concentrated at both ends of the beams and columns.

The flexural hinges in beams are modelled with uncoupled moment (M3) hinges whereas for columns the flexural hinges are modelled with coupled P-M2-M3 properties that include the interaction of axial force and bi-axial bending moments at the hinge locations.

4 Results and Discussions

The pushover analysis has been carried out on all the fourteen models discussed above. The capacity curves (which show variation of base shear with the displacement at the control node) for three storey and six storey symmetric and asymmetric buildings are shown in Figs. 3 and 4 respectively. Also, the performance point (which is the intersection of the capacity spectrum and demand spectrum) is determined for all the frames. From the curves, so obtained from the pushover analysis, the results are interpreted and are discussed in the following sections.

Fig. 3 Base shear versus displacement for 3 storey symmetric and asymmetric frames (plan and vertical)
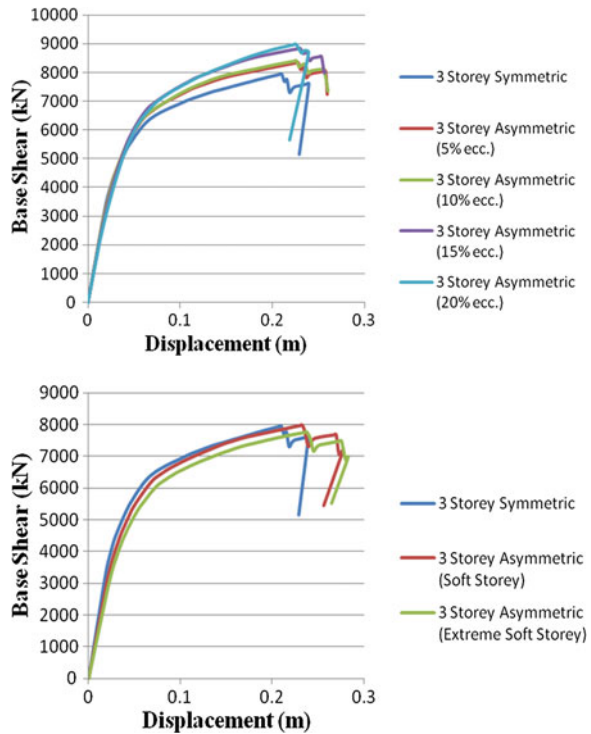
Fig. 4 Base shear versus displacement for 6 storey symmetric and asymmetric frames (plan and vertical)
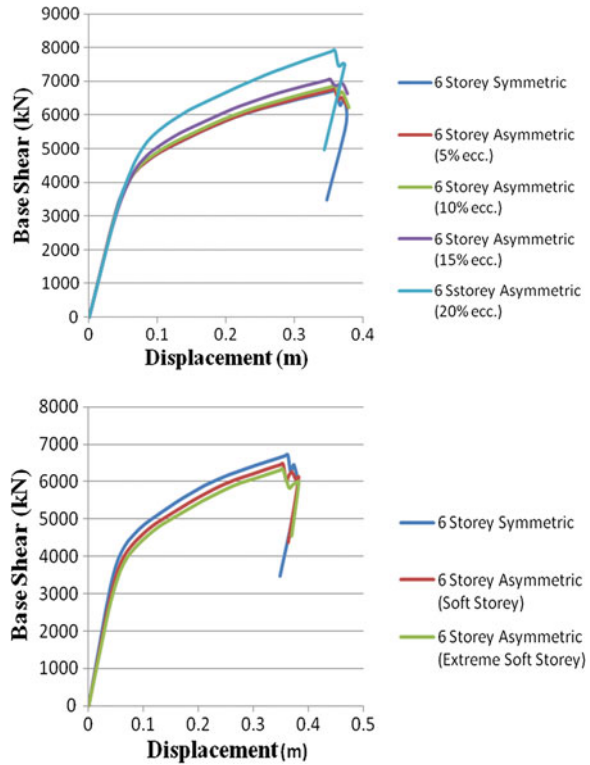
5 Comparison of Base Shear Versus Displacement Curves (Capacity Curves)

1. 3 Storey Buildings
2. 6 Storey Buildings.

6 Comparison of Ultimate Base Shear, Performance Point and Maximum Displacement for Various Buildings

The ultimate base shear for symmetric, plan asymmetric and vertically asymmetric three storey and six storey building frames is shown in Table 1. The spectral displacement and spectral acceleration at performance point in symmetric and asymmetric frames are shown in Table 2 and the maximum displacement for symmetric and asymmetric frames is shown in Table 3.

Symmetric, Plan Asymmetric and Vertically Asymmetric Buildings.

Table 1 Ultimate base shear for symmetric and asymmetric frames

Building specimen	Ultimate base shear (kN)	Building specimen	Ultimate base shear (kN)
3 storey symmetric	7958.99	6 storey symmetric	6,447.874
Plan asymmetric			
3 storey asymmetric (5 % ecc.)	8353.545	6 storey asymmetric (5 % ecc.)	6,778.725
3 storey asymmetric (10 % ecc.)	8409.671	6 storey asymmetric (10 % ecc.)	6,877.597
3 storey asymmetric (15 % ecc.)	8838.362	6 storey asymmetric (15 % ecc.)	7,055.245
3 storey asymmetric (20 % ecc.)	8993.993	6 storey asymmetric (20 % ecc.)	7,540.472
Vertically asymmetric			
3 Storey asymmetric (soft storey)	7675.348	6 storey asymmetric (soft storey)	6,468.117
3 Storey asymmetric (extreme soft storey)	7484.704	6 storey asymmetric (extreme soft storey)	6,323.727

Table 2 Spectral displacement and spectral acceleration at performance point in symmetric and asymmetric frames

Building specimen	Spectral displacement (m)	Spectral acceleration (m/s2)	Building specimen	Spectral displacement (m)	Spectral acceleration (m/s^2)
3 storey symmetric	0.017	0.901	6 storey symmetric	0.051	0.474
Plan asymmetric					
3 storey (5 % ecc.)	0.018	0.871	6 storey (5 % ecc.)	0.051	0.475
3 storey (10 % ecc.)	0.018	0.862	6 storey (10 % ecc.)	0.051	0.480
3 storey (15 % ecc.)	0.019	0.852	6 storey (15 % ecc.)	0.052	0.488
3 storey (20 % ecc.)	0.019	0.843	6 storey (20 % ecc.)	0.052	0.524
Vertically asymmetric					
3 storey (soft storey)	0.022	0.876	6 storey (soft storey)	0.054	0.445
3 storey (extreme soft storey)	0.025	0.863	6 storey (extreme soft storey)	0.057	0.426

Table 3 Maximum displacement for symmetric and asymmetric frames

Building specimen	Maximum lateral displacement (mm)	Building specimen	Maximum lateral displacement (mm)
3 storey symmetric	239.455	6 storey symmetric	376.502
Plan asymmetric			
3 storey (5 % ecc.)	258.968	6 storey (5 % ecc.)	379.561
3 storey (10 % ecc.)	260.308	6 storey (10 % ecc.)	380.02
3 storey (15 % ecc.)	256.465	6 storey (15 % ecc.)	377.461
3 storey (20 % ecc.)	239.016	6 storey (20 % ecc.)	373.967
Vertically asymmetric			
3 storey (soft storey)	277.474	6 storey (soft storey)	382.432
3 storey (extreme soft storey)	282.704	6 storey (extreme soft storey)	383.00

7 Discussion on the Results

From the graphs obtained from the pushover analysis, various results obtained are:

1. All 3 storey and 6 storey buildings, symmetrical and asymmetric in plan (i.e. eccentric buildings) follow almost same force-deformation relationship in the elastic range.

   The lateral displacement at the elastic point in 3 storey building is 0.040055 m (0.3034 % of the building height) and the corresponding base shear is 5233.017 kN.

   For 6 storey buildings, the lateral displacement value at the elastic point is 0.053742 m (0.213 % of the building height) and the corresponding base shear is 3984.609 kN.

2. In the initial stage of elastic range, for symmetric, soft storey and extreme soft storey buildings, the capacity curve is almost same and it deviates from that of the symmetric frame in the later stage in case of vertical asymmetric frames.

   In 3 storey as well as in 6 storey frames, base shear value corresponding to elastic point is at relatively larger lateral displacement for soft storey and extreme soft storey frames.

   In 3 storey frames, for soft storey, lateral displacement at the elastic point is 0.0459 m (0.333 % of the building height) and for extreme soft storey its value is 0.05207 m (0.367 % of the building height).

   In 6 storey frames, the lateral displacement at the elastic point in case of soft storey is 0.0639 m (0.248 % of the building height) and in case of extreme soft storey its value is 0.07144 m (0.273 % of the building height).

3. Beyond elastic limit, the curves deviate from each other and the base shear developed for a particular lateral displacement is maximum in frames with 20 % eccentricity (about both the axis) in 3 storey as well as 6 storey frames. The values of

developed base shear reduce with decrease in the magnitude of eccentricity with least value for the symmetric frame. In vertically asymmetric buildings, the base shear developed for a particular lateral displacement is maximum for symmetric frame, the value being lesser in soft storey and least in extreme soft storey.

4. The lateral displacement corresponding to the performance point in 3 storey symmetric and plan asymmetric buildings varies from 0.167 to 0.181 % of the building height whereas in 6 storey symmetric and plan asymmetric buildings, its value varies from 0.254 to 0.258 % of the building height. It implies that performance point lies on left in 3 storey buildings when compared with the performance point in 6 storey buildings indicating 3 storey buildings to be safer than 6 storey buildings.

5. The lateral displacement corresponding to the performance point in 3 storey symmetric building is 0.167 % of the building height, the value being 0.196 and 0.211 % of building height for soft storey and extreme soft storey respectively. The lateral displacement values in case of 6 storey symmetric building at performance point is 0.254 % of the building height, the values being 0.26 and 0.263 % for soft storey and extreme soft storey respectively.

   The maximum displacement increases with increase in vertical asymmetry, the value being maximum for extreme soft storey.

6. The performance points for all the buildings lie in the elastic range AB, the 3 storey buildings being on the left side of the 6 storey buildings.

8 Conclusions

Based on the results of pushover analysis, following conclusions are drawn:

1. In the elastic range, all the symmetric and asymmetric buildings follow almost same force-deformation relationship, the deformation being more for 3 storey buildings than that of 6 storey building at elastic point, when expressed in terms of building height.

2. In case of vertically asymmetric buildings, the capacity curve is almost same for symmetric, soft storey and extreme soft storey in the initial stage of elastic range and it deviates from that of symmetric frame in the latter stage.

3. The base shear developed beyond elastic limit is minimum for symmetric frames, the value increases with increase in eccentricity.

4. Beyond elastic limit, base shear developed is minimum in extreme soft storey, the value being more for soft storey and maximum in case of symmetric frames.

5. The performance point in 3 storey buildings lie on left when compared with the performance point of 6 storey buildings which indicates 3 storey buildings to be safer than 6 storey buildings.

6. In case of vertically asymmetric frames, the performance point lies on the right when compared with symmetric frames, which indicates symmetric frame to be more safe and extreme soft storey to be least safe.
7. The performance points for all the buildings lie in the elastic range AB, for 3 storey buildings being on the left of the 6 storey buildings.
8. The magnitude of ultimate base shear developed increases with increase in plan asymmetry and decreases with increase in vertical asymmetry.

References

1. Krawinkler H, Seneviratna GDPK (1998) Pros and cons analysis of seismic evaluation. Eng Struct 20(4–6):452–464
2. Moghadam AS, Tso WK (2000) Pushover analysis for asymmetric and set back multistory buildings. In: 12WCEE
3. Chandler AM, Mendis PA (2000) Performance of reinforced concrete frames using force and displacement based seismic assessment methods. Eng Struct 22(4):352–363
4. Chintanapakdee C, Chopra AK (2004) Seismic response of vertically irregular frames: response history and modal pushover analyses. J Struct Eng 130(8):1177–1185
5. Barros RC, Almeida R (2005) Pushover analysis of asymmetric three dimensional building frames. J Civil Eng Manag 11(1):3–12
6. Dinh TV, Ichinose T (2005) Probabilistic estimation of Seismic sorey drifts in reinforced concrete buildings. J Struct Eng 131(3):416–427
7. Mouzzoun M, Moustachi O, Taleb A, Jalal S (2013) Seismic performance assessment of reinforced concrete buildings using pushover analysis. IOSR J Mech Civil Eng 5(1):44–49
8. IS 456: 2000 Plain and reinforced concrete-code of practise
9. IS 1893: 2002 Indian standard code of criteria for earthquake resistant design of structures Part 1 (fifth revision). Bureau of Indian Standards, New Delhi, India
10. IS 875: 1987 Code of practice for design loads (other than earthquake) for buildings and structures
11. Kadid A, Boumrkik A (2008) pushover analysis of reinforced concrete frame structures. Asian J Civil Eng 09(1):75–83

Challenges Posed by Tall Buildings to Indian Codes

Ashok K. Jain

Abstract What should be the criteria for limiting height of a building in a given location in the country? Who should specify that limit? Height limitations can be imposed by the local authorities based on the availability of services or heritage considerations, or by the codes based on technical considerations. It is the earthquake loading code that specifies different types of structural systems appropriate under different seismic zones and for various heights. But Indian Standard (IS):1893 does not restrict the height of any building except prohibiting ordinary shear wall frames in seismic zones IV and V. The American Society for Civil Engineers (ASCE) 7 code specifies seismic design category based on its risk category and the severity of the design earthquake ground motion at the site under consideration and restricts certain types of structural systems and their heights. In India, there appears to be no rules or restrictions for developing the plan or a structural system for a tall building. Plans with numerous reentrant corners and offsets are being used. Flat slabs are also being used with and without shear walls. Normal weight bricks are being extensively used for walls without any anchorage. Besides, IS:13920 specifies same level of detailing for ductility for all buildings irrespective of the seismic zone and type of building. There are no guidelines for employing energy dissipating devices and base isolation. It is concluded that there is a need to update the code provisions in IS:456, IS:875, IS:1893 and IS:13920 on an urgent basis.

Keywords Tall buildings · Earthquake · Structural system · Irregularity · Height · Code · Ductility

A.K. Jain (✉)
Indian Institute of Technology (IIT) Roorkee, Roorkee, Uttarakhand 247 667, India
e-mail: ashokjain_iitr@yahoo.co.in

1 Introduction

What should be the criteria for limiting height of a building in a given location in the country? Who should specify that limit? The answer to these questions lies in the selection of the structural system, nature of geotechnical strata, and magnitude of various loads. In other words, level of risk to life and property. Height limitations can be imposed by the local authorities based on the availability of services or heritage considerations, or by the codes based on technical considerations. Among the various loads acting on a tall building, the wind loads and earthquake loads are the most critical. It is very rare that a building has collapsed under the wind loads. It is the earthquake loading code that specifies different types of structural systems appropriate under different seismic zones and for various heights.

A few tall buildings in the range of 75–100 m have been built in Mumbai during the past few decades. However, during the past one decade more buildings in the range of 40–75 m range have come up in various parts of the country including Bangalore, Hyderabad, Chennai, Kolkata, and the national capital region (NCR) of Delhi. Among all these regions, the NCR region appears to be more critical because of seismic zone IV, while others were in seismic zone II or III. In the first two seismic zones II and III, a properly designed moment resistant frame building or a shear wall frame building would be sufficient. They do not pose a great risk to life and property. However, a tall building in seismic zones IV and V would certainly require more precautions. Nevertheless, it appears that the code committee perhaps did not apply its mind seriously towards the essential provisions for taller buildings greater than about 60 m. Recently, Jain [15] published a paper on the state of codes on structural engineering in India highlighting various issues.

The 381 m Empire State Building in New York was built in 1931 and remains even today its most iconic buildings. In those days there were no codes and not even calculators. This and many other tall buildings were built in various parts of United States of America (USA) based on the experience and judgment of engineers. Federal Emergency Management Authority (FEMA), USA is engaged in developing state of the art codal provisions through extensive research grants and very detailed publications to mitigate the aftermath of various disasters including earthquake. In addition, Council on Tall Buildings, Chicago is an international association of professionals working in the analysis and design of tall buildings. It also publishes reports and guides to supplement the code provisions for designing better tall buildings [3]. The purpose of this paper is to highlight the challenges posed by tall buildings to Indian Codes.

2 Current Provisions in IS:1893

There is no clause in IS:1893 Part 1 [11] code that explicitly limits height of any building in any seismic zone. Clause 7.8.1 does specify when a dynamic analysis must be carried out in a given seismic zone depending upon the height and

Table 1 Structural system and height limits

Structural system	Seismic zone II and III	Seismic zone IV and V
Load bearing masonry wall building	No limit	No limit
Ordinary moment resisting (M-R) frame	No limit	No limit
Ordinary shear wall frame	No limit	Not permitted
Special M-R Frame	No limit	No limit
Special shear wall frame	No limit	No limit
Concentric steel braced frame	No limit	No limit
Eccentric steel braced frame	No limit	No limit
Dual frame	No limit	No limit

Note The M-R frame or dual frame can be in concrete or steel

irregularity of a building. Moreover, Clause 6.4.2 does specify response reduction factor (R) for a given structural system depending upon the perceived seismic damage performance of the structure, characterized by ductile or brittle mode of collapse. Although there are doubts if this factor R does justice with its objective or is it just a calibration factor for the seismic forces between the earlier edition of the code and the current edition [17].

Clause 7.1 of IS:1893-Part 1 states: to perform well in an earthquake, a building should possess four main attributes, namely simple and regular configuration, and adequate lateral strength, stiffness and ductility. Buildings having simple regular geometry and uniformly distributed mass and stiffness in plan as well as in elevation, suffer much less damage than buildings with irregular configurations.

However, the Code puts no restriction on the height of a building having any irregularity in any seismic zone. Clause 7.2 of IS:1893-Part 1 (Table 7) requires as shown in Table 1.

The "Structural System" is the key term in tall buildings. Apparently, it is a very wide qualitative term and some of the architects and designers may not be fully aware of its full meaning and implications. Moreover, there are very few major earthquakes that have shaken the urban cities except the 2001 Bhuj Earthquake. Therefore, it appears that many designers are not convinced about the level of seismicity and risk especially in zones IV and V. It is well known that loss of rationale will lead to loss of compliance. It is pertinent to note that even the proposed draft code on IS:1893 [12] does not address any of these issues so far.

3 Current Provisions in IS:875 Part 3

IS:875-Part 3 [10] specifies wind pressures at different heights through wind profiles. However, it is silent about the structural system, modern intricacies in the building plan and elevation and their effect on the wind pressure distribution. Neither has it given any patch loading nor change in pressure distribution due to change in vertical offsets in elevations. If the structure is to be located close to

another structure, that is, at least twice as high as the average height of its neighboring structures, then it could be exposed (dependent on the properties of the structure) to increased wind velocities for certain wind directions. Such cases should be taken into account. The Eurocode 1-Part 1.4 [5] and other international codes deal with these aspects in more detail.

4 ASCE 7

Let us examine ASCE 7 code of America [1] which is a very comprehensive code on the estimation of various loads for buildings. Chapter 12 talks about seismic design requirements for building structures, seismic design category based on its risk category and the severity of the design earthquake ground motion at the site under consideration. Chapter 13 deals with seismic design requirements for non-structural components. Factors that affect seismic risk of a structure include (i) the intensity of ground shaking and other earthquake effects the structure is likely to experience and (ii) the structure's use including consideration of the number of people who would be affected by the structure's failure and the need to use the structure for its intended purpose after an earthquake. They have mapped the entire America in six site classes A–F depending upon the type of soil and its engineering properties. They have also developed Risk-Targeted Maximum Considered Earthquake (MCE_R) Spectral Response Acceleration Parameters for short periods (S_{MS}) and at 1 s (S_{M1}), adjusted for site class effects. This requires massive fine mapping of the entire country with respect to geotechnical and seismological perspectives.

India lacks such an exhaustive study even for seismic zoning of the country. It needs massive instrumentation stretching the entire country over a period of several decades to get some meaningful seismic data. Instead, it follows a simplistic approach. The seismic force can be computed based on the soil investigation at a given location. The country was divided in seven seismic zones in 1962 and reduced to five zones in 1970. Since 2002, they have been regrouped in only four seismic zones. The earthquake force can be determined on any building—short or tall in any part of the country. For an important structure at a given site, detailed seismic and geotechnical investigations are expected to be undertaken.

4.1 Seismic Design Category (FEMA P749)

Each structure is assigned a seismic design category based on the risk category I, II, III or IV and spectral response acceleration parameters for short periods (S_{MS}) and at 1 s (S_{M1}) [8]. There is no such classification in the Indian Codes yet. The Provisions make use of seismic design category (SDC) concept to categorize structures according to the seismic risk they could pose. There are six SDCs ranging from A to F with structures posing minimal seismic risk assigned to SDC A and

structures posing the highest seismic risk assigned to SDC F. As a structure's potential seismic risk as represented by the SDC increases, the *Provisions* require progressively more rigorous seismic design and construction as a means of attempting to ensure that all buildings provide an acceptable risk to the public. Thus, as the SDC for a structure increases, so do the strength and detailing requirements and the cost of providing seismic resistance.

4.2 The Structural System

ASCE 7 [1] requires that the structural system used shall be in accordance with the structural system limitations and the limits on structural height, contained in Table 12.2-1. The appropriate response modification coefficient, R, over strength factor, and the deflection amplification factor indicated in Table 12.2-1 shall be used in determining the base shear, element design forces, and design story drift. This is indeed a very exhaustive table for all possible structural systems for each seismic design category A–F, for various heights running in five A4 pages. Clause 12.3.3 of ASCE 7 specifies that buildings having certain horizontal and vertical irregularities cannot be built in any seismic zone. Similarly, buildings having extreme weak stories cannot exceed 9 m in height. It is interesting to look at a few systems that are common to IS:1893-part 1 as shown in Table 2.

It can be seen in Table 2 that the frames listed under S. no. 2 and 3 can be built in any seismic zone without any limit on the height. The same is the provision in the Indian Code as seen in Table 1. However, the catch lies in the understanding of the term "structural system". In USA, most of the taller buildings have virtually symmetric rectangular plan on the East coast as well as West coast. In contrast, the NCR region has many 40–60 m buildings having plans with horizontal irregularity

Table 2 Structural systems and height limitations [1]

S. no.	Structural system	Structural system and height limitations in SDC, m				
		B	C	D	E	F
1	Bearing wall system/building frame system					
	Special reinforced concrete shear walls	NL	NL	50	50	50
	Eccentrically braced steel frame	NL	NL	50	50	50
2	M-R frame systems					
	Special moment frames (steel or concrete)	NL	NL	NL	NL	NL
3	Dual frames with special M-R frames (25 %)					
	Special shear wall frames	NL	NL	NL	NL	NL
	Steel eccentrically braced frames	NL	NL	NL	NL	NL
	Steel special concentrically braced frames	NL	NL	NL	NL	NL

NL no limit

re-entrant corners (Figs. 1 and 2) some of these buildings can be easily classified as irregular and will be prohibited as per ASCE 7.

ASCE 7 further requires that value of the response modification coefficient, R, used for design in the direction under consideration shall not be greater than the least value of R for any of the systems utilized in that direction. Similarly, ASCE 7 specifies combination rule for frames having different R values in the vertical direction. There is no such clarity in IS:1893-part 1.

5 Characteristics of Typical Buildings in the NCR Region—30 to 60 M Height Range

The following observations can be made in a large number of buildings in the NCR region (Figs. 1 and 2):

1. Use of very large number of small size shear walls of varying cross-sections
2. Changing the alignment of beams and columns along a grid line laterally by about 30–100 cm
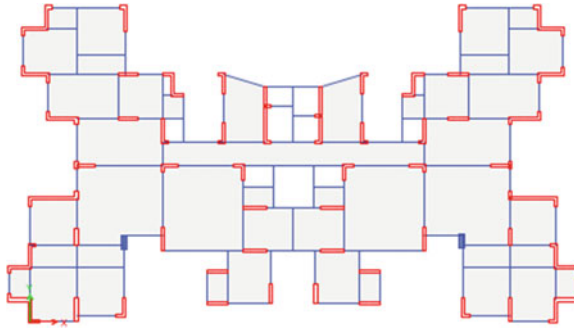
Fig. 1 Plan of a 25 storey building (typical)
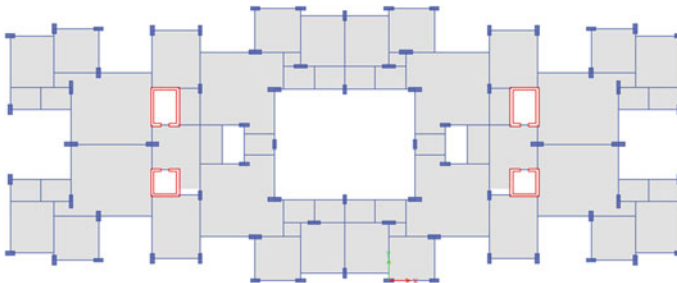
Fig. 2 Plan of a 20 storey building (typical)

3. Use of a large number of re-entrant corners leading to horizontal irregularity
4. Use of flat slabs in seismic zones IV and V without proper slab-column joint detailing
5. Use of normal weight brick walls both as internal partition walls and external walls.

In order to understand the implications of item 1 of these features, Dehuri [4] carried out pushover analysis on a 20-storey MRF building and a 25-storey shear wall building shown in Figs. 1 and 2. ETABS 13 software was used to carry out the static non-linear analysis. Moment hinges were introduced in beams, while moment and axial force hinges were introduced in columns. The shear walls were modeled using layered element. The pushover analysis was carried out in accordance with FEMA 440 [7]. It was concluded that although the shear wall building had a higher target displacement (55 cm) but many beams behaved like coupled beams. It was difficult to design them for shear unless their depth was increased considerably to be able to provide diagonal reinforcement. The behaviour of the MRF frame was quite satisfactory in terms of ductility demand and plastification. The latter should be preferred over the former.

(a) Use of large number of shear walls by definition in IS:13920

As far as the author's understanding goes, a tall building should have fewer shear walls but of considerable length, say 6–12 m each. There should be at least two walls in each direction preferably located on the periphery. However, in accordance with IS:13920, any column whose width to depth ratio lies beyond 0.4 is classified as a shear wall. Thus, the designers are coming up with structural systems having a very large number of so called shear walls in each direction scattered all over the plan. These walls are of varying cross-sections—I, L, C, Z or any other. Such walls pose another challenge—how to design these unsymmetric cross-sections under bi-axial bending at collapse? Some designers model such shear walls as membrane area elements and try to avoid bi-axial bending. Moreover, such an arrangement also gives rise to large number of small span beams connected to "shear walls" at each end subjected to very high shear. Some of these beams may be classified as coupled beams and need to be detailed accordingly. Certainly such an arrangement of shear walls would neither be desirable nor acceptable in a higher seismic zone. The detailing of reinforcement in coupling beams in IS:13920 needs revision to be in line with ACI 318.

(b) Changing the alignment of beams and columns along a grid line

By changing the alignment of beams and columns along a grid line laterally by about 30–100 cm, there are many beams that have to be supported on cross beams. These beam junctions may be very close to a column or away from a column. How these junctions and beam segments will behave at collapse is any body's guess. These beams do introduce torsion in the cross-beams. Many designers introduce torsion release in the computer model, but it is not certain

if these joints are appropriately detailed. Even so, their non-linear behaviour is difficult to conceive.

(c) Use of a large number of re-entrant corners leading to horizontal irregularity
This practice is quite rampant for the sake of architectural aesthetics. It is difficult to envisage the post-inelastic ductile behaviour of such buildings. As stated earlier, a building having horizontal irregularity is prohibited in SDC E and F in USA. However, the current Indian provision only requires it to be analyzed using the modal analysis.

(d) Use of flat slabs in seismic zones IV and V
There is no restriction on the height of such systems in seismic zones IV and V even while providing shear walls to carry the lateral forces. The only condition is that this system should be able to displace laterally along with the shear wall system and must account for P-delta effects. Moreover, IS:13920 [13] does not give any provision on slab-column joint detailing under seismic conditions. As per the ASCE 7 classification, in high seismic zones, its height will be restricted to 50 m but not in India. Clause 21.13 of ACI 318 [2] gives provisions for members not designated as part of the seismic-force-resisting system and covers slab-column systems. For two-way slabs without beams, slab-column connections must meet the requirements of Clause 11.11 and 21.13.6 of ACI 318. Even the flat slab-column joint detailing in IS:456 [9] dates back to 1976 since no changes were made in this part in its 2000 edition. It is again pertinent to note that the draft IS:13920 [14] also does not cover the detailing of joints of flat slab systems in seismic zones.

(e) Use of normal weight brick walls
These are the most dangerous elements in a tall building. There is absolutely no restriction on their use. These walls are neither anchored nor is it possible to anchor them. Therefore, in the event of a seismic activity, there is a strong possibility that they may topple and fall outside the building perimeter. The resulting causality on the ground would be unimaginable. Currently, hollow blocks and Autoclaved Aerated Concrete (AAC) blocks having a density of about 600 kg/m^3 are easily available in India and must be used. However, this would require change of mindset of the Indian users before such elements can become acceptable.

6 Detailing for Ductility

At present, IS:13920 code prescribes the same level of detailing for ductility in any building in any seismic zone. It is highly unfair. The detailing must conform to the level of risk. The Eurocode 8 [6] specifies three classes of ductility detailing—ductility class L, class M and class H. There is a need to introduce this concept in the Indian code also. The proposed format is shown in Table 3 based on experience and judgment. Table 4 shows the level of horizontal design acceleration in two

Table 3 Proposed format for different ductility level requirements in buildings

Seismic zone	Ductility class L	Ductility class M	Ductility class H
II and III	H ≤ 40 m	H > 40 m	NA
IV	H ≤ 25 m	25 m < H ≤ 60 m	H > 60 m
V	NA	0 < H ≤ 40 m	H > 40 m

Table 4 Design horizontal spectral accelerations

Seismic zone	Soil type	Period, 0.1 s (%)	Period, 4 s (%)
II	Soft	2.5	0.42
	Hard	2.5	0.25
V	Soft	9	1.5
	Hard	9	0.9

Importance factor $I = 1.0$, response reduction factor $R = 5.0$, damping = 5 %

seismic zones II and V for buildings at the two ends of period range: 0.1 and 4 s, located on soft or hard soil. It shows that the acceleration varies from 0.25 to 9 % for $R = 5$. In taller buildings, the design acceleration may be less, but the seismic weight is very high, therefore, the base shear will also be high. The different classes of ductility can be related to building heights for acceptable structural systems in different seismic zones. The next step will be to develop detailing for different ductility classes for beams, columns and walls as available in Eurocode 8-part 1 [6]. This proposal is a first step towards igniting a debate on this issue. Such a classification will help save precious national resources. After all, it is well known that loss of rationale will lead to loss of compliance.

7 Energy Dissipating Devices and Base Isolation

Use of active and passive energy dissipation is an emerging technology that enhances building performance by reducing the demands through addition of damping devices and stiffening elements. There are quite a large number of buildings that have been built in Japan and California using this concept. However, most codes are silent about their design perhaps because it involves use of non-linear analysis which is fairly complicated and is difficult to codify at present. Therefore, the design of such buildings is left to the experts who can demonstrate the safety of such devices either experimentally or theoretically or both. In the foreword to the IS:1893-2002 code, it states that: only standard devices having detailed experimental data on the performance should be used. The designer must demonstrate by detailed analyses that these devices provide sufficient protection to the buildings and equipment as envisaged in this standard. Performance of locally

assembled isolation and energy absorbing devices should be evaluated experimentally before they are used in practice. Design of buildings and equipment using such device should be reviewed by the competent authority. Base isolation systems are found useful for short period structures, say less than 0.7 s including soil-structure interaction. There is a need to include detailed specifications on these aspects in the Code [16].

8 Conclusions

Taller buildings are coming up fast in various parts of the country. In the absence of proper provisions, it is probable that a few unsafe building plans may get approved and built. There is an urgent need to revise IS:1893—Part 1, IS:456, IS:875 and IS:13920 codes to address the following issues:

Revision of IS:1893-Part 1

1. Limit the use of certain frames having horizontal as well as vertical irregularity in high seismic zones
2. Limit the height of certain types of frames in high seismic zones
3. To restrict the use of flat slab (slab-column system) in high seismic zones
4. To provide seismic requirements for nonstructural components
5. To provide combination rules for response reduction factor R in horizontal and vertical directions
6. To include requirements for energy dissipation devices and base isolation

Revision of IS:456

1. To provide joint detailing of slab-column junctions in flat slab construction

Revision of IS:875

1. Wind loading on tall buildings

Revision of IS:13920

1. To provide different levels of detailing for ductility in buildings in different seismic zone—DCL, DCM and DCH in beams, columns and walls
2. To provide joint detailing of slab-column junctions in flat slab construction and lastly, to introduce an overriding clause that all buildings more than certain height, say 60 m, must be validated using the nonlinear analysis to verify the functionality of the structural system. Under certain circumstances wind tunnel test may be desirable. There should also be some pre-qualifications of the architects, structural designers and proof consultants who can undertake the design of such tall buildings.

References

1. ASCE 7 (2010) Minimum design loads for buildings and other structures. ASCE/SEI/7-10, Reston, VA
2. ACI 318 (2008) Building code requirements for structural concrete (ACI 318M-08) and commentary, Detroit, MI
3. CTBUH (2010) Recommendations for the seismic design of high-rise buildings. Council on tall buildings and Urban Habitat, Chicago, IL
4. Dehuri M (2014) Staged construction and temperature analysis of multistoreyed buildings. M. Tech. thesis, Indian Institute of Technology Roorkee, Roorkee
5. Eurocode 1 (2005) Basis of design and actions on structures, part 1.4. Action on structures—wind actions. European committee for standardization, Brussels
6. Eurocode 8 (2004) Design of structures for earthquake resistance—part 1: general rules, seismic actions and rules for buildings. European committee for Standardization, Brussels
7. FEMA 440 (2005) Improvement of nonlinear static seismic analysis procedures, Washington, DC
8. FEMA P749 (2009) NEHRP recommended seismic provisions for new buildings and other structures, Washington, DC
9. IS:456 (2000) Plain and reinforced concrete—code of practice, Bureau of Indian Standards, New Delhi
10. IS:875-Part 3 (1987) Code of practice for design loads (other than earthquake) for buildings and structures—wind loads, Bureau of Indian Standards, New Delhi
11. IS:1893-Part 1 (2002) Criteria for earthquake resistant design of structures, part 1 general provisions and buildings, Bureau of Indian Standards, New Delhi
12. IS:1893-Part 1 (draft 2006) Criteria for earthquake resistant design of structures, part 1 general provisions and buildings, Bureau of Indian Standards, New Delhi
13. IS:13920 (1993) Ductile detailing of reinforced concrete structures subjected to seismic forces, Bureau of Indian Standards, New Delhi, India
14. IS:13920 (draft 2013) Ductile detailing of reinforced concrete structures subjected to seismic forces, Bureau of Indian Standards, New Delhi, India
15. Jain AK (2014) The state of codes on structural engineering in India. Bridge Struct Eng 44 (1):1–7
16. Jain AK (2014) Code of practice on earthquake resistant structures—past, present and future, contributory. In: Wason et al (eds) Earthquake engineering—future directions. Elsevier, London (under publication)
17. Prakash V, Pore SM, Jain AK (2006) The role of reduction factor and importance factor in fifth revision of IS:1893. In: Proceedings of 13th symposium on earthquake engineering, IIT Roorkee, 18–20 Dec 2006, pp 964–977

Influence of Openings on the Structural Response of Shear Wall

G. Muthukumar and Manoj Kumar

Abstract Shear wall has been conferred as a major lateral load resisting element in a building structure in any seismic prone zone. It is essential to determine the behavior of shear wall in the pre-elastic and post-elastic stage. Shear walls may also be provided with openings due to the functional requirement of the building. The size and location of opening may play a significant role in the response of the shear wall. Nonlinear finite element analysis has been performed using degenerated shell element with assumed strain approach to predict the displacement response of reinforced concrete shear wall with and without openings, subjected to monotonic as well as dynamic loading conditions. Material non-linearity has been considered using plasticity approach. A five parameter Willam-Warnke failure criterion is considered to define the yielding/crushing of the concrete with tensile cut-off. The ductility ratio has been calculated for different opening cases with various locations of openings in the shear wall. The shear wall with central opening resulted in less displacement in comparison to other shear walls. It is recommended that openings should not be located too close to the boundary, as evident from the poor performance of such shear walls during severe shaking.

Keywords Shear wall · Plasticity · Nonlinear · Openings · Seismic · Earthquake

1 Introduction

The reinforced concrete tall buildings are subjected to lateral loads due to wind and earthquake. In order to resist these lateral loads, shear walls are provided in the framed structure as a lateral load resisting element [24, 12, 13]. The shear wall

G. Muthukumar (✉) · M. Kumar
Department of Civil Engineering, Birla Institute of Technology and Science (BITS),
Pilani, India
e-mail: muthug@pilani.bits-pilani.ac.in

M. Kumar
e-mail: manojkr@pilani.bits-pilani.ac.in

should possess sufficient strength and stiffness under any loading conditions. The importance of shear wall in mitigating the damage to reinforced concrete structures is well documented in the literature [7, 13]. The shear walls are generally classified on the basis of aspect ratio (height/width ratio). The shear walls with aspect ratio between 1 and 3 are generally considered to be of squat type and shear walls with aspect ratio greater than 3 are considered to be of slender type. In general, the structural response of shear wall depends strongly on the type of loading, aspect ratio of shear wall, size and location of the openings in the shear wall. The Squat shear walls generally fail in shear mode whereas the slender shear walls fail in a flexural mode. The presence of opening in the shear wall makes the performance of shear wall slightly vulnerable under severe loading conditions. The structural analysis of the shear wall with opening becomes complex due to the stress concentration near the openings [21]. Various experimental investigations have been performed on shear walls with and without openings subjected to severe dynamic earthquake loading conditions. Neuenhofer [21], in his study on shear wall with opening, has observed that for the same opening area, the reduction in stiffness for squat and slender shear walls are 50 and 20 % respectively [21]. Thus, the aspect ratio becomes critical for squat shear walls. Few analytical studies have been made on the response of shear wall with openings [18, 21, 26, 27, 28]. Rosman [26] developed a approximate linear elastic approach using laminar analysis, based on different assumptions to analyze the shear wall with one row and two rows of openings. Schwaighofer and Microys [27] used this approach to analyze the shear wall with three rows of openings and observed that the Rosman's theory predicts the behavior of shear wall with three rows of openings also with sufficient accuracy. Though reasonable studies have been made on the response analysis of shear wall with openings, very few literatures exist on the influence of opening locations on the structural response of shear wall [15, 30]. Hence, it is essential to study the influence of opening location on the structural response of RC shear wall. The present study analyses the static and dynamic response of RC shear wall with different opening locations for squat shear wall with boundary elements [6]. Moreover, it was found that the use of conventional methods for the analysis of shear wall with openings resulted in remarkably poor results especially for the squat shear walls where the mode of failure is predominantly shear. It was also shown in literature that the hand calculation either underestimates/overestimates the response in predicting the response of shear wall with openings [21]. The finite element analysis has been the most versatile and successfully employed method of analysis in the past to accurately predict the structural behavior of reinforced concrete shear wall in linear as well as non-linear range under any severe loading conditions. With the advent in computing facilities, finite element method has gained an enormous popularity among the structural engineering community, especially in the non-linear dynamic analysis. The nonlinearity of the structure may be due to geometry or due to material. Since shear wall is a huge structure, the deformation of the shear wall has been assumed to be in control and hence the geometric non-linearity has not been considered. The next section describes the formulation of degenerated shell element formulation.

2 Degenerated Shell Element Formulation

The displacement based finite element method has been considered to be the most popular choice because of its simplicity and ease with which the computations can be performed. The use of shell element to model moderately thick structures like shear wall is well documented in the literature [17]. In this section, the underlying basic ideas in the formulation of the degenerated curved shell element are described. Two assumptions are made in the formulation of the curved shell element which is degenerated from three-dimensional solid. First, it is assumed that, even for thick shells, the normal to the middle surface of the element remains straight after deformation. Secondly, the strain energy corresponding to stresses perpendicular to the middle surface is disregarded, i.e. the stress component normal to the shell mid-surface is constrained to be zero. Five degrees of freedom are specified at each nodal point, corresponding to its three translations and two rotations of the normal at each node. The independent definition of the translational and rotational degrees of freedom permits the transverse shear deformation to be taken into account during the formulation of the element stiffness, since rotations are not necessarily normal to the slope of the mid-surface.

Coordinate Systems

The geometry of the shell can be represented by the coordinates and normal vectors of its middle surface as Fig. 1. The geometry of the degenerated shell element and kinematics of deformation are described by using four different coordinate systems, i.e. global, natural, local, and nodal coordinate systems. The global coordinate system (x, y, z) is used to define the shell geometry. The shape functions are expressed in natural curvilinear coordinates (ξ, η, ζ). In order to easily deal with the thin shell assumption of zero normal stress in the z-direction, the strain components are defined in terms of local coordinate set of axes (x′, y′, z′). At each node of shell element, the nodal coordinate set ($\overline{V}_{1k}, \overline{V}_{2k}, \overline{V}_{3k}$) with unit vectors is defined. The four coordinate sets employed in the present formulation are now described.

Global coordinate set (x, y, z)

This is a Cartesian coordinate system, freely chosen, in relation to which the geometry of the structure is defined in space. Nodal coordinates and displacements,

Fig. 1 Geometry of 9-noded degenerated shell element
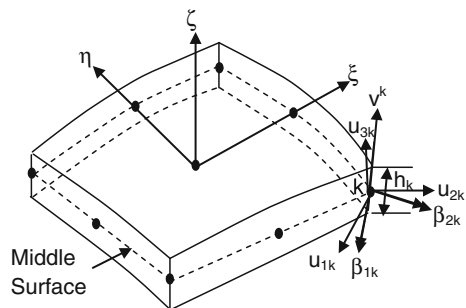
as well as the global stiffness matrix and applied force vector are referred to this system. The displacements corresponding to x, y, z directions are u, v, w respectively.

Nodal coordinate Set ($\overline{\mathbf{V}}_{1k}, \overline{\mathbf{V}}_{2k}, \overline{\mathbf{V}}_{3k}$)

A nodal coordinate system is defined at each nodal point with origin at the reference surface (mid-surface). The vector V_{3k} is constructed from the nodal coordinates at top and bottom surfaces at node k and is expressed as

$$
\left\{ \begin{array}{c} V_{3k}^{x} \\ V_{3k}^{y} \\ V_{3k}^{z} \end{array} \right\} = \left\{ \begin{array}{c} x_{3k}^{top} - x_{3k}^{bot} \\ y_{3k}^{top} - y_{3k}^{bot} \\ z_{3k}^{top} - z_{3k}^{bot} \end{array} \right\}
\tag{1}
$$

$\mathbf{V}_{3k}$ defines the direction of the normal at any node 'k', which is not necessarily perpendicular to the mid surface. The major advantage of the definition of $\mathbf{V}_{3k}$ with normal not necessary to be perpendicular to mid surface is that, there are no gaps or overlaps along element boundaries.

The vector $\mathbf{V}_{1k}$ is constructed perpendicular to $\mathbf{V}_{3k}$ and parallel to the global xz plane. Hence

$$
\mathbf{V}_{1k}^{x} = \mathbf{V}_{3k}^{z}, \mathbf{V}_{1k}^{y} = 0.0, \mathbf{V}_{1k}^{z} = -\mathbf{V}_{3k}^{x}
\tag{2}
$$

Alternatively, if the vector $\mathbf{V}_{3k}$ is in the y-direction ($\mathbf{V}_{3k}^{x} = \mathbf{V}_{3k}^{y} = 0.0$), the following expressions are assumed. $\mathbf{V}_{1k}^{x} = -\mathbf{V}_{3k}^{y}, \mathbf{V}_{1k}^{y} = \mathbf{V}_{1k}^{z} = 0.0$ (x−direction). The superscripts refer to the vector components in the global coordinate system.

The vector $\mathbf{V}_{2k}$ is constructed perpendicular to the plane defined by $\mathbf{V}_{1k}$ and $\mathbf{V}_{3k}$.

Hence $\mathbf{V}_{2k} = \mathbf{V}_{1k} \times \mathbf{V}_{3k}$. The unit vectors in the directions of $\mathbf{V}_{1k}, \mathbf{V}_{2k}, \mathbf{V}_{3k}$ are represented by $\overline{\mathbf{V}}_{1k}, \overline{\mathbf{V}}_{2k}, \overline{\mathbf{V}}_{3k}$ respectively. The vectors $\overline{\mathbf{V}}_{1k}, \overline{\mathbf{V}}_{2k}$ define the rotations (β_{2k} and β_{1k} respectively) of the corresponding normal.

Curvilinear coordinate set (ε, η, ζ)

In this system, ξ, η are the two curvilinear coordinates in the middle plane of the shell element and ζ is a linear coordinate in the thickness direction. It is assumed that ξ, η, ζ vary between −1 and +1 on the respective faces of the elements. The relations between the curvilinear coordinates and the global coordinates are given in Eq. 3. It should also be noted that the ζ direction is only approximately perpendicular to the shell-surface, since ζ is defined as a function of $\overline{\mathbf{V}}_{3k}$.

Local coordinate set (x′, y′, z′)

This is the Cartesian coordinate system defined at the sampling points wherein stresses and strains are to be calculated. The direction z′ is taken perpendicular to the surface ξ = constant, being obtained by the cross product of the ξ and η directions. The direction x′ can be taken tangent to the ξ direction at the sampling point. The direction y′ is defined by the cross product of the z′ and x′ directions.

$$z' = \begin{bmatrix} \frac{\partial x}{\partial \xi} \\ \frac{\partial y}{\partial \xi} \\ \frac{\partial z}{\partial \xi} \end{bmatrix} \times \begin{bmatrix} \frac{\partial x}{\partial \eta} \\ \frac{\partial y}{\partial \eta} \\ \frac{\partial z}{\partial \eta} \end{bmatrix} ; \; x' = \begin{bmatrix} \frac{\partial x}{\partial \xi} \\ \frac{\partial y}{\partial \xi} \\ \frac{\partial z}{\partial \xi} \end{bmatrix} ; \; y' = z' \times x' \tag{3}$$

Element Geometry

The global coordinates of pairs of points on the top and bottom surface at each node are usually input to define the element geometry. Alternatively, the mid-surface nodal coordinates and the corresponding directional thickness can be furnished. In the iso-parametric formulation, the coordinates of a point within an element are obtained by interpolating the nodal coordinates through the element shape functions and are expressed as

$$\begin{Bmatrix} x \\ y \\ z \end{Bmatrix} = \underbrace{\sum_{k=1}^{9} N_k(\xi, \eta) \begin{Bmatrix} x_k^{mid} \\ y_k^{mid} \\ z_k^{mid} \end{Bmatrix}}_{mid-surface\ only} + \underbrace{\sum_{k=1}^{9} N_k(\xi, \eta) \frac{\zeta h_k}{2} \begin{Bmatrix} V_{3k}^x \\ V_{3k}^y \\ V_{3k}^z \end{Bmatrix}}_{effect\ of\ shell\ thickness} \tag{4}$$

where x_k^{mid}, y_k^{mid}, z_k^{mid} are the coordinates of the shell mid-surface and h_k is the shell thickness at node k. In the above expression $N_k(\xi, \eta)$ are the element shape functions at the point considered within the element (ξ, η) and ζ tells the position of the point in the thickness direction. The unit vector in the directions of V_{3k} is represented by $\overline{V}_{3k}$. The element shape functions are calculated in the natural coordinate system as

$$N_1 = \tfrac{1}{4}\xi(1+\xi)\eta(1+\eta); \qquad N_2 = \tfrac{1}{2}(1+\xi)(1-\xi)\eta(1+\eta); \qquad N_3 = -\tfrac{1}{4}(1-\xi)\eta(1+\eta);$$

$$N_4 = -\tfrac{1}{2}\xi(1-\xi)(1+\eta)(1-\eta); \quad N_5 = \tfrac{1}{4}(1-\xi)\eta(1-\eta); \qquad N_6 = -\tfrac{1}{2}(1+\xi)(1-\xi)\eta(1-\eta);$$

$$N_7 = -\tfrac{1}{4}\xi(1+\xi)\eta(1-\eta); \qquad N_8 = \tfrac{1}{2}\xi(1+\xi)(1+\eta)(1-\eta); \quad N_9 = (1+\xi)(1-\xi)(1+\eta)(1-\eta) \tag{5}$$

Based on the two assumptions of the degeneration process previously described, the element displacement field can then be expressed by the five degrees of freedom at each node. The global displacements are determined from mid surface nodal displacements u_k^{mid}, v_k^{mid} and w_k^{mid} and the relative displacements are caused by the two rotations of the normal as

$$\begin{Bmatrix} u \\ v \\ w \end{Bmatrix} = \sum_{k=1}^{n} N_k \begin{Bmatrix} u_k^{mid} \\ v_k^{mid} \\ w_k^{mid} \end{Bmatrix} + \sum_{k=1}^{n} N_k \zeta \frac{h_k}{2} \begin{bmatrix} v_{1k}^x & -v_{2k}^x \\ v_{1k}^y & -v_{2k}^y \\ v_{1k}^z & -v_{2k}^z \end{bmatrix} \begin{bmatrix} \beta_{1k} \\ \beta_{2k} \end{bmatrix} \tag{6}$$

where β_{1k} and β_{2k} are the rotations of the normals which results in the relative displacements and V_{1k} and V_{2k} are the unit vectors defined at each node and n is the number of nodes. At any point on the mid-surface of the nodes, an orthogonal set of

local coordinates $\overline{V}_{1k}, \overline{V}_{2k}$ and $\overline{V}_{3k}$ is constructed. $\overline{V}_{1k}$ and $\overline{V}_{2k}$ are constructed in the following manner. $\overline{V}_{1k} = \bar{i} \times \overline{V}_{3k}$; $V_{1k} = V_{1i} \times V_{3k}$. The vectors $\overline{V}_{1k}, \overline{V}_{2k}$ and $\overline{V}_{3k}$ are mutually perpendicular.

2.1 Strain Displacement Relationship

The Mindlin and Reissner type assumptions are used to derive the strain components defined in terms of the local coordinate system of axes $x' - y' - z'$ where z' is perpendicular to the material surface layer. For the small deformations and neglecting the strain energy associated with stresses perpendicular to the local $x' - y'$ surface, the strain components may be written as

$$\varepsilon = \left\{ \begin{array}{c} \varepsilon'_f \\ \varepsilon'_s \end{array} \right\} = \left\{ \begin{array}{c} \varepsilon_{x'} \\ \varepsilon_{y'} \\ \gamma_{x'y'} \\ \gamma_{x'z'} \\ \gamma_{y'z'} \end{array} \right\} = \left\{ \begin{array}{c} \frac{\partial u'}{\partial x'} \\ \frac{\partial v'}{\partial y'} \\ \frac{\partial u'}{\partial y'} + \frac{\partial u'}{\partial x'} \\ \frac{\partial u'}{\partial z'} + \frac{\partial w'}{\partial x'} \\ \frac{\partial v'}{\partial z'} + \frac{\partial w'}{\partial y'} \end{array} \right\} \tag{7}$$

In the above equation, ε'_f and ε'_s are the in-plane and transverse shear strains respectively and u', v', w' are the displacement components in the local system $x'\,y'\,z'$. Assuming the shell mid-surface tangential to $x' - y'$, the in-plane shear strains ε'_f can further be divided into membrane strains ε'_m and bending strains ε'_b as

$$\varepsilon'_f = \varepsilon'_m + \varepsilon'_b \tag{8}$$

where

$$\varepsilon'_m = \begin{bmatrix} \partial u'/\partial x' \\ \partial v'/\partial y' \\ \partial u'/\partial y' + \partial v'/\partial x' \end{bmatrix} \text{ and } \varepsilon'_b = \begin{bmatrix} z'\partial \theta_{x'}/\partial x' \\ z'\partial \theta_{y'}/\partial y' \\ z'\left(\partial \theta_{x'}/\partial y'\right) + \left(\partial \theta_{y'}/\partial x'\right) \end{bmatrix} \tag{9}$$

The transformation matrix [T] is used to convert the strains in local coordinate system into strains in global coordinate system as

$$\begin{bmatrix} \frac{\partial u'}{\partial x'} & \frac{\partial v'}{\partial x'} & \frac{\partial w'}{\partial x'} \\ \frac{\partial u'}{\partial y'} & \frac{\partial v'}{\partial y'} & \frac{\partial w'}{\partial y'} \\ \frac{\partial u'}{\partial z'} & \frac{\partial v'}{\partial z'} & \frac{\partial w'}{\partial z'} \end{bmatrix} = [\mathbf{T}]^T \begin{bmatrix} \frac{\partial u}{\partial x} & \frac{\partial v}{\partial x} & \frac{\partial w}{\partial x} \\ \frac{\partial u}{\partial y} & \frac{\partial v}{\partial y} & \frac{\partial w}{\partial y} \\ \frac{\partial u}{\partial z} & \frac{\partial v}{\partial z} & \frac{\partial w}{\partial z} \end{bmatrix} [\mathbf{T}] \tag{10}$$

where, transformation matrix [T] is given by

$$\mathbf{T} = \begin{bmatrix} \partial x/\partial x' & \partial x/\partial y' & \partial x/\partial z' \\ \partial y/\partial y' & \partial y/\partial y' & \partial y/\partial z' \\ \partial z/\partial z' & \partial z/\partial y' & \partial z/\partial z' \end{bmatrix} \tag{11}$$

The derivatives of displacements with respect to Cartesian coordinate system into derivatives of displacements with respect to natural coordinate system are transformed as,

$$\begin{bmatrix} \frac{\partial u}{\partial x} & \frac{\partial v}{\partial x} & \frac{\partial w}{\partial x} \\ \frac{\partial u}{\partial y} & \frac{\partial v}{\partial y} & \frac{\partial w}{\partial y} \\ \frac{\partial u}{\partial z} & \frac{\partial v}{\partial z} & \frac{\partial w}{\partial z} \end{bmatrix} = \mathbf{J}^{-1} \begin{bmatrix} \frac{\partial u}{\partial \xi} & \frac{\partial v}{\partial \xi} & \frac{\partial w}{\partial \xi} \\ \frac{\partial u}{\partial \eta} & \frac{\partial v}{\partial \eta} & \frac{\partial w}{\partial \eta} \\ \frac{\partial u}{\partial \zeta} & \frac{\partial v}{\partial \zeta} & \frac{\partial w}{\partial \zeta} \end{bmatrix} \tag{12}$$

where, [J] is the Jacobean matrix defined as

$$\mathbf{J} = \begin{bmatrix} \frac{\partial x}{\partial \xi} & \frac{\partial y}{\partial \xi} & \frac{\partial z}{\partial \xi} \\ \frac{\partial x}{\partial \eta} & \frac{\partial y}{\partial \eta} & \frac{\partial z}{\partial \eta} \\ \frac{\partial x}{\partial} & \frac{\partial y}{\partial \zeta} & \frac{\partial z}{\partial \zeta} \end{bmatrix} \tag{13}$$

The strain-displacement matrix [$\mathbf{B}$] relates the strain components and the nodal variables as

$$\boldsymbol{\varepsilon} = \mathbf{B}\boldsymbol{\delta} \tag{14}$$

where

$$\{\delta\} = \{u \ v \ w \ \beta_1 \beta_2\}^T \tag{15}$$

The layered element formulation [29] allows the integration through the element thickness, which are divided into several concrete and steel layers. Each layer is assumed to have one integration point at its mid surface. The steel layers are used to model the in-plane reinforcement only. The strain-displacement matrix $\mathbf{B}$ and the material stiffness matrix $\mathbf{D}$ are evaluated at the midpoint of each layer, and for all integration points in the plane of the layer. The element stiffness matrix K_e defined using numerical integration as follows:

$$\mathbf{K}^e = \iiint \mathbf{B}^T \mathbf{D} \mathbf{B} \, dV \tag{16}$$

where the integration is made over the volume of the element.

In the Euclidean space, the volume element is given by the product of the differentials of the Cartesian coordinates and is expressed as $dV = dx \, dy \, dz$. Using

numerical integration, the volume integration is converted into area integration using Jacobean and is expressed as

$$K^e = \iint \mathbf{B}^T \mathbf{DB} |\mathbf{J}| d\zeta \, dA \tag{17}$$

Similarly, the internal force vector is expressed as $\{f^e\}$ as

$$f^e = \iint \mathbf{B}^T \boldsymbol{\sigma} |\mathbf{J}| d\zeta \, dA \tag{18}$$

The element stiffness matrix relates the force vector with the displacement vector as

$$\{f\} = [K]\{\delta\} \tag{19}$$

where

$$\int dA = |\boldsymbol{J}| \int\limits_{-1}^{+1} \int\limits_{-1}^{+1} d\xi \, d\eta \ \text{(Integration on layer mid-surface)} \tag{20}$$

Once the displacements are determined, the strains and stresses are calculated using strain-displacement matrix and material constitutive matrix respectively. The formulation of degenerated shell element is completely described in Huang [9].

2.2 Assumed Strain Approach

Nevertheless, the general shell theory based on the classical approach has been found to be complex in the finite element formulation. On the other hand, the degenerated shell element [1, 11] derived from the three-dimensional element, has been quite successful in modeling moderately thick structures because of their simplicity and circumvents the use of classical shell theory. The degenerated shell element is based on assumption that the normal to the mid surface remain straight but not necessarily normal to the mid surface after deformation. Also, the stresses normal to the mid surface are considered to be negligible. However, when the thickness of element reduces, degenerated shell element has suffered from shear locking and membrane locking when subjected to full numerical integration. The shear locking and membrane locking are the parasitic shear stresses and membrane stresses present in the finite element solution. In order to alleviate locking problems, the reduced integration technique has been suggested and adopted by many authors [23, 33]. However, the use of reduced integration resulted in spurious mechanisms or zero energy modes in some cases. The reduced integration ignores the high

Fig. 2 Sampling point locations for assumed shear/membrane strains
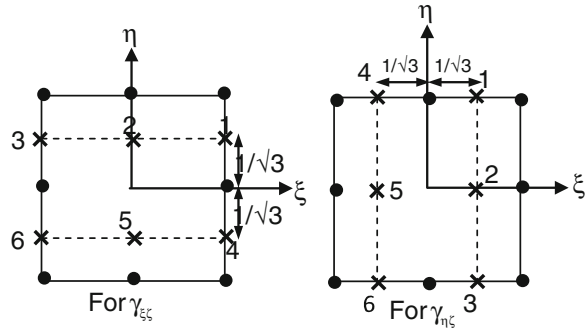
ranked terms in interpolated shear strain by numerical integration, thus introducing the chance of development of spurious or zero energy modes in the element. The selective integration, wherein different integration orders are used to integrate the bending, shear and membrane terms of stiffness matrix, avoids the locking in most of the cases.

The assumed strain approach has been successfully adopted by many researchers [2, 10] as an alternative to avoid locking. In the assumed strain based degenerated shell elements, the transverse shear strain and membrane strains are interpolated from the assumed sampling points obtained from the compatibility requirement between flexural and shear strain fields respectively. The layered element formulation [29] allows the integration through the element thickness, which are divided into several concrete and steel layers. Each layer is assumed to have one integration point at its mid surface. The steel layers are used to model the in-plane reinforcement only. The assumed transverse shear strain fields, interpolated at the six appropriately located sampling points, as shown in Fig. 2. The assumed transverse shear strain fields, interpolated at the six appropriately located sampling points, as shown in Fig. 2, are

$$
\left.\begin{aligned}
\bar{\gamma}_{\xi\zeta} &= \sum_{i=1}^{3} \sum_{j=1}^{2} P_i(\eta) \cdot Q_j(\xi)\, \gamma_{\xi\zeta}^{ij} \\
\bar{\gamma}_{\eta\zeta} &= \sum_{i=1}^{3} \sum_{j=1}^{2} P_i(\xi) \cdot Q_j(\eta)\, \gamma_{\eta\zeta}^{ij}
\end{aligned}\right\}
\tag{21}
$$

In the above equation, $\gamma_{\xi\zeta}^{ij}$ and $\gamma_{\eta\zeta}^{ij}$ are the shear strains obtained from Lagrangian shape functions. The interpolating functions $P_i(z)$ and $Q_j(z)$ are

$$
\left.\begin{aligned}
P_1(z) &= \tfrac{z}{2}(z+1),\ P_2(z) = 1 - z^2,\ P_3(z) = \tfrac{z}{2}(z-1) \\
Q_1(z) &= \tfrac{1}{2}\left(1 + \sqrt{3}z\right),\ Q_2(z) = \tfrac{1}{2}\left(1 - \sqrt{3}z\right)
\end{aligned}\right\}
\tag{22}
$$

Hence, it can be observed that $\bar{\gamma}_{\xi\zeta}$ is linear in ξ direction and quadratic in η direction, while $\bar{\gamma}_{\eta\zeta}$ is linear in η direction and quadratic in ξ direction. The

polynomial terms for curvature of nine node Lagrangian element, κ_ξ and κ_η are the same as the assumed shear strain, as given by

$$\left.\begin{aligned}
\kappa_\xi &= \tfrac{\partial\theta_\xi}{\partial\xi}\left(1,\xi,\eta,\xi\eta,\xi^2,\xi^2\eta,\eta^2,\xi\eta^2,\xi^2\eta^2\right)\\
\kappa_\xi &= \kappa_\xi\left(1,\xi,\eta,\xi\eta,\eta^2,\xi\eta^2\right)
\end{aligned}\right\}
\tag{23}$$

$$\left.\begin{aligned}
\kappa_\eta &= \tfrac{\partial\theta_\eta}{\partial\eta}\left(1,\xi,\eta,\xi\eta,\xi^2,\xi^2\eta,\eta^2,\xi\eta^2,\xi^2\eta^2\right)\\
\kappa_\eta &= \left(1,\xi,\eta,\xi\eta,\xi^2,\xi^2\eta^2\right)
\end{aligned}\right\}
\tag{24}$$

$$\left.\begin{aligned}
\bar{\gamma}_{\xi\zeta} &= \bar{\gamma}_{\xi\zeta}(\kappa_\xi) = \bar{\gamma}_{\xi\zeta}\left(1,\xi,\eta,\xi\eta,\eta^2,\xi\eta^2\right)\\
\bar{\gamma}_{\eta\zeta} &= \bar{\gamma}_{\eta\zeta}(\kappa_\eta) = \bar{\gamma}_{\eta\zeta}\left(1,\xi,\eta,\xi\eta,\eta^2,\xi\eta^2\right)
\end{aligned}\right\}
\tag{25}$$

The original shear strain obtained from the Lagrange shape functions $\gamma_{\xi\zeta}$ and $\gamma_{\eta\zeta}$ are

$$\left.\begin{aligned}
\gamma_{\xi\zeta} &= \theta_\xi + \tfrac{\partial w}{\partial\xi} = \gamma_{\xi\zeta}\left(1,\xi,\eta,\xi\eta,\xi^2,\xi^2\eta,\eta^2,\xi\eta^2,\xi^2\eta^2\right)\\
\gamma_{\eta\zeta} &= \theta_\eta + \tfrac{\partial w}{\partial\eta} = \gamma_{\eta\zeta}\left(1,\xi,\eta,\xi\eta,\xi^2,\xi^2\eta,\eta^2,\xi\eta^2,\xi^2\eta^2\right)
\end{aligned}\right\}
\tag{26}$$

The total potential energy expression has the form

$$\bar{\pi} = \pi + \int \lambda^{13}\left(\bar{\gamma}_{\xi\zeta} - \gamma_{\xi\zeta}\right)\mathrm{dv} + \int \lambda^{23}\left(\bar{\gamma}_{\eta\zeta} - \gamma_{\eta\zeta}\right)\mathrm{dv}
\tag{27}$$

In the above equation, λ^{13} and λ^{23} are Lagrangian multipliers and are independent functions. The terms $\gamma_{\xi\zeta}$ and $\gamma_{\eta\zeta}$ are the transverse shear strains evaluated from the displacement field. The assumed shear strain fields are chosen as

$$\bar{\gamma}_{\xi\zeta} = \sum_{i=1}^{n} R_i(\xi,\eta)\gamma_{\xi\zeta}^i; \quad \bar{\gamma}_{\eta\zeta} = \sum_{i=1}^{n} S_i(\xi,\eta)\gamma_{\eta\zeta}^i
\tag{28}$$

The Lagrangian multipliers are taken as

$$\left.\begin{aligned}
\lambda^{13} &= \sum_{i=1}^{n} \lambda_i^{13}\delta\left(\tilde{\xi}_i - \xi\right)\delta(\tilde{\eta}_i - \eta)\\
\lambda^{23} &= \sum_{i=1}^{n} \lambda_i^{23}\delta\left(\bar{\xi}_i - \xi\right)\delta(\bar{\eta}_i - \eta)
\end{aligned}\right\}
\tag{29}$$

By substituting, the following equation can be obtained.
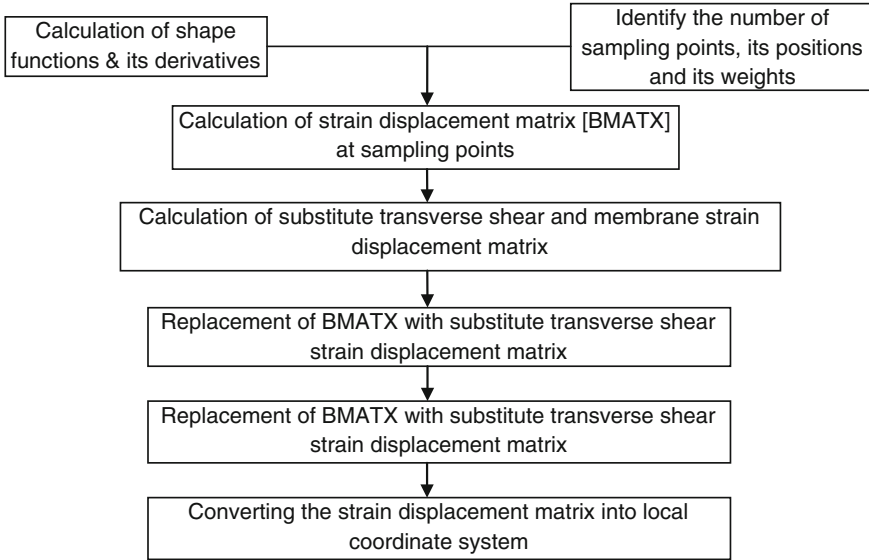
Fig. 3 Determination of strain displacement matrix using the assumed strain approach

$$\left.\begin{array}{l} \bar{\gamma}_{\xi\zeta}\left(\tilde{\xi}_i, \tilde{\eta}_i\right) = \gamma_{\xi\zeta}\left(\tilde{\xi}_i, \tilde{\eta}_i\right) \\ \bar{\gamma}_{\eta\zeta}\left(\bar{\xi}_i, \bar{\eta}_i\right) = \gamma_{\eta\zeta}\left(\bar{\xi}_i, \bar{\eta}_i\right) \end{array}\right\} \tag{30}$$

In the above equation, θ_ξ and θ_η are the rotating normal and w is the transverse displacement of the element. It can be clearly seen that the original shear strain and assumed shear strain are not compatible and hence the shear locking exist for very thin shell cases. The appropriately chosen polynomial terms and sampling points ensure the elimination of risk of spurious zero energy modes. The assumed strain can be considered a special case of integration scheme wherein, for function $\bar{\gamma}_{\xi\zeta}$ full integration is employed in η direction and reduced integration is employed in ξ direction. On the other hand, for function, $\bar{\gamma}_{\eta\zeta}$ reduced integration is employed in η direction and full integration is employed in ξ direction. The membrane and shear strains are interpolated from identical sampling points even though the membrane strains are expressed in orthogonal curvilinear coordinate system and transverse shear strains are expressed in natural coordinate system. The flow chart explaining the formulation of strain displacement matrix using assumed strain approach is shown in Fig. 3.

3 Material Modeling

The modeling of material play may a crucial role in achieving the correct response. The presence of nonlinearity may add another dimension of complexity to it. The nonlinearities in the structure may accurately be estimated and incorporated in the solution algorithm. The accuracy of the solution algorithm depends strongly on the prediction of second order effects that cause nonlinearities, such as tension stiffening, compression softening, and stress transfer nonlinearities around cracks. These nonlinearities are usually incorporated in the constitutive modeling of the reinforced concrete. In order to incorporate geometric nonlinearity, the second order terms of strains are to be included. In this study, only material non-linearity has been considered. The subsequent sections describe the modeling of concrete in compression and tension, modeling of steel.

3.1 Concrete Modeling in Tension

The presence of crack in concrete has much influence on the response of nonlinear behavior of reinforced concrete structures. The crack in the concrete is assumed to occur when the tensile stress exceeds the tensile strength. The cracking of concrete results in the loss of continuity in the load transfer and hence the stresses in both concrete as well as steel reinforcement differ significantly. Hence the analysis of concrete fracture has been very important in order to predict the response of structure precisely. The numerical simulation of concrete fracture can be represented either by discrete crack, proposed by Ngo and Scordelis [20] or by smeared crack, proposed by Rashid [25]. The objective of discrete crack is to simulate the initiation and propagation of dominant cracks present in the structure. In the case of discrete crack approach, nodes are disassociated due to the presence of cracks and therefore the structure requires frequent renumbering of nodes, which may render in the huge computational cost. Nevertheless, when the structure's behavior has been dominated by only few dominant cracks, the discrete modeling of cracking seems the only choice. On the other hand, the smeared crack approach smears out the cracks over the continuum, and captures the deterioration process through the constitutive relationship and reduces the computational cost and time drastically.

Crack modeling has gone through several stages due to the advancement in technology and computing facilities. Earlier research work indicates that the formation of crack results in the complete reduction in stresses in the perpendicular direction, thus neglecting the phenomenon called tension stiffening. With the rapid increase in extensive experimental investigations as well as computing facilities, many finite element codes have been developed for the nonlinear finite element analysis, which incorporates the tension stiffening effect. The first tension stiffening model using degraded concrete modulus was proposed by Scanlon and Murray and subsequently many analytical models have been developed such as Lin and
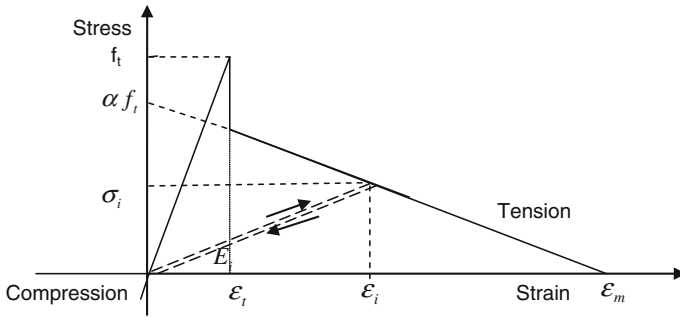
Fig. 4 Tension stiffening effect of cracked concrete

Scordelis model, Vebo and Ghali model, Gilbert and Warner model [16, 19]. The cracks are always assumed to be formed in the direction perpendicular to the direction of the maximum principal stress. These directions may not necessarily remain the same throughout the analysis and loading and hence the modeling of orientation of crack plays a significant role on the response of structure. Still, due to simplicity, many investigations have been performed using fixed crack approach, wherein the direction of principal strain axes may remain fixed throughout the analysis. In this study also, the direction of crack has been considered to be fixed throughout the duration of the analysis. However, the modeling of aggregate interlock has not been taken very seriously. The constant shear retention factor or the simple function has been employed to model the shear transfer across the cracks. Apart from the initiation of crack, the propagation of crack also plays a crucial role on the response of structure. The prediction of crack propagation is a very difficult phenomenon due to scarcity and confliction of test results. Nevertheless, the propagation of cracks plays a crucial role on the response of nonlinear analysis of RC structures. The plain concrete exhibits softening behavior and reinforced concrete exhibits stiffening behavior due to the presence of active reinforcing steel. A gradual release of the concrete stress is adopted in this present study as shown in Fig. 4 [22]. The reduction in the stress is given by the following expression:

$$E_i = \alpha f_t' \left(1 - \frac{\varepsilon_i}{\varepsilon_m} \right) \frac{1}{\varepsilon_i}; \ \varepsilon_t \leq \varepsilon_i \leq \varepsilon_m \tag{31}$$

In the above equation, α and ε_m are the tension stiffening parameters. ε_m is the maximum value reached by the tensile strain at the point considered. ε_i is the current tensile strain in material direction i. The coefficient depends on the percentage of steel in the section. In the present study, the value of α and ε_m are taken as 0.5 and 0.0020 respectively. It has also been reported that the influence of the tension stiffening constants on the response of the structures are generally small and hence

the constant value is justified in the analysis [22]. Generally, the cracked concrete can transfer shear forces through dowel action and aggregate interlock. The magnitude of shear moduli has been considerably affected because of extensive cracking in different directions. Thus, the reduced shear moduli can be put to incorporate the aggregate interlock and dowel action. In the plain concrete, aggregate interlock is the major shear transfer mechanism and for reinforced concrete, dowel action is the major shear transfer mechanism, with reinforcement ratio being the critical variable.

In order to incorporate the aggregate interlock and dowel action, the appropriate value of cracked shear modulus has been considered in the material modeling of concrete.

Cracked in one direction

The stress-strain relationship for cracked concrete where cracking is assumed to take place in only one direction (NSTAT = 2) is given as

$$
\begin{bmatrix} \sigma_1 \\ \sigma_2 \\ \tau_{12} \\ \tau_{13} \\ \tau_{23} \end{bmatrix} = \begin{bmatrix} 0 & 0 & 0 & 0 & 0 \\ 0 & E & 0 & 0 & 0 \\ 0 & 0 & G_{12}^c & 0 & 0 \\ 0 & 0 & 0 & G_{13}^c & 0 \\ 0 & 0 & 0 & 0 & 5G/6 \end{bmatrix} \begin{bmatrix} \varepsilon_1 \\ \varepsilon_2 \\ \gamma_{12} \\ \gamma_{13} \\ \gamma_{23} \end{bmatrix}
\quad
\begin{aligned}
& G_{12}^c = 0.25 \times G\left(1 - \frac{1}{0.004}\right) \\
& G_{12}^c = 0 \quad if \ \varepsilon_1 \geq 0.004 \\
& G_{13}^c = G_{12}^c; \quad G_{23} = \frac{5G}{6}
\end{aligned}
$$

$$(32)$$

Crack in two directions

The stress-strain relationship for cracked concrete where cracking is assumed to take place in both directions (NSTAT = 3) is given as

$$
\begin{bmatrix} \sigma_1 \\ \sigma_2 \\ \tau_{12} \\ \tau_{13} \\ \tau_{23} \end{bmatrix} = \begin{bmatrix} 0 & 0 & 0 & 0 & 0 \\ 0 & 0 & 0 & 0 & 0 \\ 0 & 0 & G_{12}^c/2 & 0 & 0 \\ 0 & 0 & 0 & G_{13}^c & 0 \\ 0 & 0 & 0 & 0 & G_{23}^c \end{bmatrix} \begin{bmatrix} \varepsilon_1 \\ \varepsilon_2 \\ \gamma_{12} \\ \gamma_{13} \\ \gamma_{23} \end{bmatrix}
$$

$$(33)$$

$$
\begin{aligned}
& G_{13}^c = 0.25 \times G\left(1 - \frac{\varepsilon_1}{0.004}\right); \quad G_{13}^c = 0 \quad if \ \varepsilon_1 \geq 0.004 \\
& G_{23}^c = 0.25 \times G\left(1 - \frac{\varepsilon_2}{0.004}\right); \quad G_{13}^c = 0.25 \times G\left(1 - \frac{\varepsilon_1}{0.004}\right); \\
& G_{13}^c = 0 \ if \ \varepsilon_1 \geq 0.004 \\
& G_{23}^c = 0.25 \times G\left(1 - \frac{\varepsilon_2}{0.004}\right); \quad G_{13}^c = 0.25 \times G\left(1 - \frac{\varepsilon_1}{0.004}\right) \\
& G_{12}^c = 0.5 \times G_{13}^c \quad if \ G_{23}^c < G_{13}^c;
\end{aligned}
$$

It has also been mentioned by Hinton and Owen [8] that the tensile strength of concrete is a relatively small and unreliable quantity which is not highly influential to the response of structures. In the above stress-strain relationship, the cracked shear modulus (G^c) is assumed to be a function of the current tensile strain. In the above equation, G is the un-cracked concrete shear modulus. If the crack closes, the un-cracked shear modulus G is assumed in the corresponding direction. Even after

the formation of initial cracks, the structure can often deform further without further collapse. In addition to the formation of new cracks, there may be a possibility of crack closing and opening of the existing cracks. If the normal strain across the existing crack becomes greater than that just prior to crack formation, the crack is said to have opened again; otherwise it is assumed to be closed. Nevertheless, if all cracks are closed, then the material is assumed to have gained the status equivalent to that of non-cracked concrete with linear elastic behavior.

3.2 Concrete Modeling in Compression

The theory of plasticity has been used in the compression modeling of the concrete. The failure surface or bounding surface has been defined to demarcate plastic behavior from the elastic behavior. Failure surface is the important component in the concrete plasticity. Sometimes, the failure surface can be referred to as yield surface or loading surface. The material behaves in the elastic fashion as long as the stress lies below the failure surface. Several failure models have been developed and reported in the literature [3]. Nevertheless, the five parameter failure model proposed by Willam and Warnke [31] seems to possess all inherent properties of the failure surface. The failure surface is constructed using two meridians namely, compression meridian and tension meridian. The two meridians are pictorially depicted in a meridian plane and cross section of the failure surface is represented in the deviatoric plane.

The variations of the average shear stresses τ_{mt} and τ_{mc} along tensile ($\theta = 0°$) and compressive ($\theta = 60°$) meridians, as shown in Fig. 5, are approximated by second-order parabolic expressions in terms of the average normal stresses σ_m, as follows:

$$
\begin{aligned}
\frac{\tau_{mt}}{f_c'} = \frac{\rho_t}{\sqrt{5}f_c'} = a_0 + a_1\left(\frac{\sigma_m}{f_c'}\right) + a_2\left(\frac{\sigma_m}{f_c'}\right)^2 \quad \theta = 0° \\
\frac{\tau_{mc}}{f_c'} = \frac{\rho_c}{\sqrt{5}f_c'} = b_0 + b_1\left(\frac{\sigma_m}{f_c'}\right) + b_2\left(\frac{\sigma_m}{f_c'}\right)^2 \quad \theta = 60°
\end{aligned}
\tag{34}
$$

(i) Meridian Plane   (ii) Deviatoric Plane
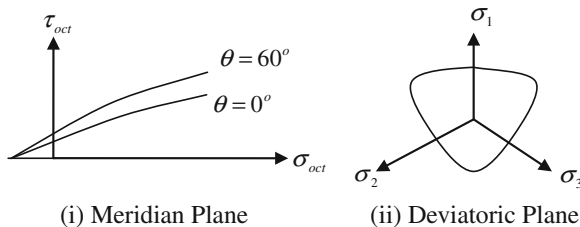
Fig. 5 Willam Warnke Failure Model

These two meridians must intersect the hydrostatic axis at the same point $\sigma_m/f_c' = \bar{\xi}_0$ (corresponding to hydrostatic tension), the number of parameters need to be determined is reduced to five. The five parameters (a_0 or b_0, a_1, a_2, b_1, b_2) are to be determined from a set of experimental data, with which the failure surface can be constructed using second-order parabolic expressions. The failure surface is expressed as

$$f(\sigma_m, \tau_m, \theta) = \sqrt{5}\frac{\tau_m}{\rho(\sigma_m, \theta)} - 1 = 0 \tag{35}$$

$$\rho(\theta) = \frac{2\rho_c\left(\rho_c^2 - \rho_t^2\right)\cos\theta + \rho_c(2\rho_t - \rho_c)\left[4\left(\rho_c^2 - \rho_t^2\right)\cos^2\theta + 5\rho_t^2 - 4\rho_t\rho_c\right]^{1/2}}{4\left(\rho_c^2 - \rho_t^2\right)\cos^2\theta + (\rho_c - 2\rho_t)^2} \tag{36}$$

The formulation of Willam-Warnke five parameter material model is described in Chen [3]. Once the yield surface is reached, any further increase in the loading results in the plastic flow. The magnitude and direction of the plastic strain increment is defined using flow rule, which is described in the next section.

3.2.1 Flow Rule

In this method, associated flow rule is employed because of the lack of experimental evidence in non-associated flow rule. The plastic strain increment expressed in terms of current stress increment is given as

$$d\varepsilon_{ij}^p = d\lambda\frac{\partial f(\sigma)}{\partial\sigma_{ij}} \tag{37}$$

$d\lambda$ determines the magnitude of the plastic strain increment. The gradient $\partial f(\sigma)/\partial\sigma_{ij}$ defines the direction of plastic strain increment to be perpendicular to the yield surface; $f(\sigma)$ is the loading condition or the loading surfaces.

3.2.2 Hardening Rule

The relationship between loading surfaces (or effective stress) and the plastic work (accumulated plastic strain) is represented by a hardening rule The "Madrid parabola" is used to define the hardening rule. The isotropic hardening is adopted in the present study, as shown in Fig. 6.

$$\sigma = E_0\varepsilon - \frac{1}{2}\frac{E_0}{\varepsilon_0}\varepsilon^2 \tag{38}$$
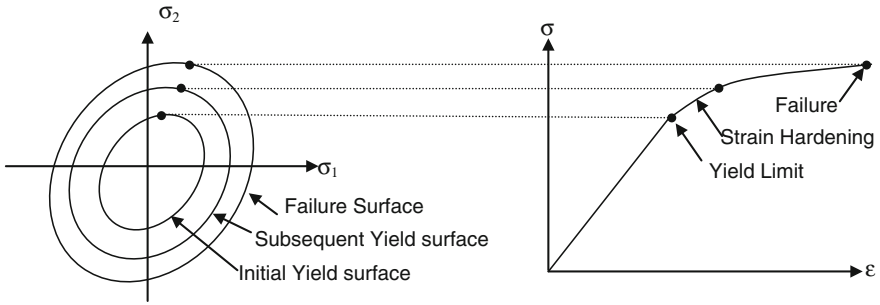
Fig. 6 Isotropic hardening with expanding yield surfaces and the corresponding uni-axial stress-strain curve

In the above equation, E_0 is the initial elasticity modulus, ε is the total strain and ε_0 is the total strain at peak stress f'_c. The total strain can be divided into elastic and plastic components as

$$\varepsilon = \varepsilon_e + \varepsilon_p \tag{39}$$

$$\{\dot{\sigma}\} = [D^e](\{\dot{\varepsilon}\} - \{\dot{\varepsilon}^p\}) \tag{40}$$

$$\{\dot{\varepsilon}^p\} = \dot{\lambda}\{a\}; \ \{a\} = \left\{\frac{\partial F}{\partial \sigma}\right\} \tag{41}$$

In the above equation, F is the yield function and $\dot{\lambda}$ is the consistency parameter, defines the magnitude of the plastic flow. The loading, unloading conditions (Kuhn-Tucker conditions) can be stated as

$$\dot{\lambda} \geq 0; \quad F \leq 0; \quad \dot{\lambda}F = 0 \tag{42}$$

The first of these Khun-Tucker conditions indicates that the consistency parameter is non-negative; the second condition implies that the stress states must lie on or within the yield surface. The third condition ensures that the stresses lie on the yield surface during the plastic loading.

$$\{a\}^T\{\dot{\sigma}\} = 0; \ \{a\}^T[D^e](\{\dot{\varepsilon}\} - \{\dot{\varepsilon}_p\}) = 0; \ \{a\}^T[D^e]\left(\{\dot{\varepsilon}\} - \dot{\lambda}\{a\}\right) = 0$$
$$\dot{\lambda} = \frac{\{a\}^T[D^e]\{\dot{\varepsilon}\}}{\{a\}^T[D^e]\{a\}} \tag{43}$$

The elasto-plastic constitutive matrix is given by the following expression

Fig. 7 Stress-strain curve of
steel
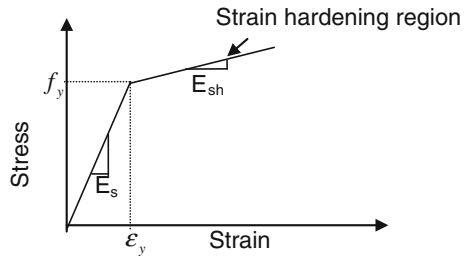
$$\left[D_{ep}\right] = [D] - \frac{[D]\{a\}\{a\}^T[D]}{H + \{a\}^T[D]\{a\}} \tag{44}$$

In the above equation, a = flow vector, defined by the stress gradient of the yield
function; D = constitutive matrix in elastic range. The second term in the above
equation represents the effect of degradation of material during the plastic loading.

3.3 Modeling of Reinforcement in Tension and Compression

Reinforcing bars in structural concrete are generally assumed one-dimensional
elements without transverse shear stiffness or flexural rigidity. The reinforcing bar
can generally be treated as either discrete or smeared. The major advantage of
discrete representation of reinforcing bar is existence of one-to-one correspondence
between the real structure and model. In the smeared reinforcement, the average
stress-strain relationship is calculated for an element area and incorporated directly
as part of the overall concrete element stiffness matrix. In the present investigation,
the smeared layered approach is adopted. The bi-linear stress strain curve with
linear elastic and strain hardening region is adopted in this study as shown in Fig. 7.
Sometimes, the tri-linear idealization has also been adopted as the stress-strain
curve in tension. Typically, the hardening strain modulus is assumed to be 1 % of
initial elasticity modulus. The position and thickness of steel layers are to be defined
in the program along with the elasticity modulus and hardening modulus. The
direction of steel (horizontal or vertical) can be set up by defining the angle with
respect to local x-axis. There can only be two states of stress for the reinforcing bar,
namely, elastic and linear strain hardening.

4 Dynamic Analysis of RC Shear Wall

The dynamic analysis of structure can be performed by three ways namely (i)
Equivalent lateral force method (ii) Response Spectrum method (iii) Time History
Method. The equivalent lateral force method determines the equivalent dynamic

effect in the static manner. The response spectrum method aims in determining the maximum response quantity of the structure. For tall and irregular buildings, dynamic analysis by Response Spectrum Method seems to be a popular choice among designers. The time history analysis of the structure has been successfully used to analyze the structure especially of huge importance. Even though, time history analysis consumes time, it is the only method capable of giving results closer to the actual one especially in the non-linear regime. In the dynamic analysis, the loads are applied over a period of time and the response is obtained at different time intervals. The equation of dynamic equilibrium at any time 't' is given by Eq. (1)

$$[M]\left[\ddot{U}^t\right] + [C]\left[\dot{U}^t\right] + [K]\left[U^t\right] = [R^t] \tag{45}$$

In the above equation, M, C and K are the mass, damping and stiffness matrices respectively. The mass matrix can be formulated either by using consistent mass approach or by using lumped mass approach. Since damping cannot be precisely determined analytically, the damping can be considered proportional to mass or stiffness or both depending on the type of the problem. The direct time integration [2] of the equation of motion can be performed using explicit (central difference scheme) and implicit (Houbolt method, Newmark Beta method and Wilson Theta method, etc.,) time integration. In the explicit time integration, the formation of complete stiffness matrix of the structure is not required and hence saves the lot of computer time and money in storing and saving those data. Moreover, in the case of all explicit time integration schemes, the iterations are not required as the equilibrium at time $t + \Delta t$ depends on the equilibrium at time t. Nevertheless, the major drawback of explicit time integration is that the time step (Δt) used for calculation of response has to be smaller than the critical time step (Δt_{cr}) to ensure the stable solution.

$$\Delta t \leq \Delta t_{cr} = \frac{T_n}{\pi} = \frac{2}{\omega} \tag{46}$$

On the other hand, implicit time integration requires the iterations to be carried out within the time step as the solution at time $t + \Delta t$ involves the equilibrium equation at $t + \Delta t$. The Newmark β method converges to various implicit and explicit schemes as shown in Table 1 for different values of Beta, called the stability parameter. In this study, for $\beta = 0.25$, the Newmark β method converges to the constant acceleration implicit method, known as trapezoidal rule. The trapezoidal rule is unconditionally stable and hence allows larger time step to be used in the calculation of response. Nevertheless, the time step can be made smaller from the accuracy point of view. The formulation of implicit Newmark Beta method (Trapezoidal rule) is mentioned in Table 1 [2].

Table 1 Step by step Newmark β method of time integration

Step	Step description	Equations
1	Set the iteration counter	$i = 0$
2	Begin the predictor phase	$d_{n+1}^{[i]} = d'_{n+1} + \Delta t v_{n+1} + \Delta t^2 (1 - 2\beta) a_n / 2$
		$V_{n+1}^{[i]} = v'_{n+1} = v_n + \Delta t (1 - \gamma) a_n$
		$a_{n+1} = \frac{d_{n+1}^{[i]} - d'_{n+1}}{\Delta t^2 \beta} = 0$
3	Evaluation of residual forces	$\psi^{[i]} = f_{n+1} - M a_{n+1}^{[i]} - p(d_{n+1}^{[i]}, v_{n+1}^{[i]})$
4	Evaluation of effective stiffness matrix and solving the equation	$K^* = \frac{M}{\Delta t^2 \beta} + \frac{\gamma C_T}{\Delta t \beta} + K_T \left(d_{n+1}^{[i]} \right)$
		$K^* \Delta d^{[i]} = \psi^{[i]}$
5	Begin the corrector phase	$d_{n+1}^{[i+1]} = d_{n+1}^{[i]} + \Delta d^{[i]}$
		$v_{n+1}^{[i+1]} = v_{n+1} + \Delta t \gamma \, a_{n+1}^{[i+1]}$
		$a_{n+1}^{[i+1]} = \frac{d_{n+1}^{[i+1]} - d'_{n+1}}{\Delta t^2 \beta}$
6	Setting up the initial values for next step once the convergence is achieved	$d_{n+1} = d_{n+1}^{[i+1]}; \ v_{n+1} = v_{n+1}^{[i+1]}; \ a_{n+1} = a_{n+1}^{[i+1]}$

4.1 Formulation of Mass Matrix

In any dynamic analysis, the formulation of mass matrix is very important in capturing the correct response of a structure. The masses can be assumed to be distributed over the entire finite element mesh or can be assumed to be lumped at nodes. The former is known as consistent mass matrix and later is known as lumped mass matrix. The mass matrix is said to be consistent if uses the same shape functions (N_i) as used for the determination of stiffness matrix. The consistent mass matrix contains off-diagonal terms. Nevertheless, the consistent mass matrix is computationally expensive. The consistent element mass matrix is given by

$$[M_e] = \int_V \rho [N_i][N_i]^T dV \qquad (47)$$

For linear or translational motion, resistance of object to a change of state in motion is measured in terms of mass and given by Newton's law as follows

$$F = ma \qquad (48)$$

On the other hand, when a rigid body is rotated, the resistance of object to a change of state in a rotator motion given by rotational inertia measured in terms of moment of inertia. The influence of rotary inertia in the case of thick plates is established in the literature [10]

$$T = \sum_{i=1}^{N} \frac{1}{2} m_i v_i^2 = \sum_{i=1}^{N} \frac{1}{2} m_i (\omega r_i)^2 = \frac{1}{2} \omega^2 \left[\sum m_i r_i^2 \right]; \ I = \sum_{i=1}^{N} m_i r_i^2; \ T = \frac{1}{2} I \omega^2$$

$$(49)$$

where in the above expression of kinetic energy, I is the moment of inertia and ω is the angular velocity; The above equation can be comparable in linear terms by replacing the moment of inertia by mass and angular velocity by linear velocity. The Newton's law of rotational motion is given by

$$\tau = I \alpha \tag{50}$$

where α is the angular acceleration. The lumped mass matrix is purely diagonal and hence computationally cheaper than the consistent mass matrix. Nevertheless, the diagonalization of the mass matrix from the full mass matrix results in the loss of information and accuracy [9]. There are many ways to lump the mass matrices as described in the literature. Nodal quadrature, row sum and special lumping are the three lumping procedures available to generate the lumped mass matrices. It has found that all three methods of lumping lead to the same mass matrix for nine-node rectangular elements. One of the most efficient means of lumping is to distribute the element mass in proportion to the diagonal terms of consistent mass matrix (Archer and Whalen 2005) and also discarding the off-diagonal elements. This way of lumping has been successfully used in many finite element codes in practice. The advantage of above special lumping scheme is that the assurance of positive definiteness of mass matrix. Lumped mass matrix is preferred if not mandatory, over consistent mass matrix in the case of explicit time integration. The use of lumped mass matrix is mostly employed in lower order elements. For higher order elements, the use of lumped mass matrix may not be an appropriate option. The linear inertia or translational inertia is given by the following expression

$$m_{ii} = w_i \int \rho dV \tag{50}$$

The rotational inertia is given by the following expression

$$I_{ii} = w_i \int_{V_e} \rho z'^2 dV = W_i I'; \ I' = \int_{V_e} \rho z'^2 dV \tag{51}$$

where W_i is the multiplier and ρ is the mass density and z' is the position of the layer with respect to the axis of rotation. The multiplier is represented by a following expression.

$$W_i = \frac{\int\limits_{V_e} \rho[N_i][N_i]^T dV}{\sum_{K=1}^{n} \int\limits_{V_e} \rho[N_k][N_k]^T dV} \tag{52}$$

4.2 Formulation of Damping Matrix

Mass and stiffness matrices can be represented systematically by overall geometry and material characteristics. However, damping can only be represented in a phenomenological manner and thus making the dynamic analysis of structures in a state of uncertainty. Nevertheless, several investigations have been done in making the representation of damping in a simplistic yet logical manner [32]. There is no single universally accepted methodology for representing damping because of the nature of the state variables which control damping. Rayleigh dissipation function assumes that the dissipation of energy takes place and can be idealized as the function of velocity. Damping matrix can be formulated analogous to mass and stiffness matrices [4]. When Rayleigh Damping is used, the resultant damping matrix is of same size as stiffness matrix. It is also important to note that the damping matrix should be formulated from damping ratio and not from the member sizes. Rayleigh damping is being used conveniently because of its versatility in segregating each modes independently. The amount of damping can be set appropriately by setting the values of alpha and beta relevantly depending on the requirement of including higher modes. Sometimes, the additional concentrated damping is also incorporated at selected degrees of freedom in addition to Rayleigh damping. Since damping is a function of velocity, if there is no motion, there will be no damping. It has been mentioned that visco-elastic dampers are being employed in structures to mitigate dynamic effects. Usually, viscous damping is assumed because closed form solution can be easily available. Very little information is available about variation of damping of linear and non-linear systems. However, the effect of damping is generally less than the inertial and stiffness effects in most of the practical situations. Therefore, it is reasonable to account for damping by a simplified approximation. The representation of damping through viscous damping coefficient has been in use due to simplicity and accuracy. The damping force is assumed to be proportional to velocity and the constant of proportionality being the viscous damping coefficient. Whenever the system vibrates in a fluid, viscous damping is said to occur. The damping forces are proportional to velocity of the medium and is represented as

$$F = c\dot{u} \tag{53}$$

$$[C] = [M] \sum_{k=0}^{k=p-1} \left(a_k [M]^{-1} [K] \right)^k \tag{54}$$

In the above equation, k = 2 yields

$$[C] = \alpha [M] + \beta [K] \tag{55}$$

$$\zeta_i = \frac{\alpha}{2\omega_i} + \frac{\beta \omega_i}{2} \tag{56}$$

From the above equation, it is essential to note that if beta parameter is zero, the higher modes of the structure will be assigned very little damping. When the parameter alpha is zero, the higher modes will be heavily damped as the damping ratio is directly proportional to frequency [5]. Thus, the choice of damping is problem dependent. Hence, it is inevitable to perform modal analysis to determine the different frequencies for different modes. It is also to be noted that the damping is controlled by only two parameters. Thus, in the Cauchy series, one may include as many terms as possible depending upon the computational efficiency. The use of proportional damping is implemented in most of the finite element codes. In the equation of motion, the coupling of terms usually occurs which are reflected in the mass and stiffness matrices. Inertia coupling is present when the mass matrix is non-diagonal and static coupling is present when the stiffness matrix is non-diagonal. The coupling of the modes usually can be avoided easily in the case of un-damped free vibration. The same is not true for damped vibration. Hence in order to represent the equation of motion in uncoupled form, it is suggested to have a damping matrix proportional to uncoupled mass and stiffness matrices. Thus, Rayleigh's proportional damping has the specific advantage that the equation of motion can be uncoupled when it is proportional to mass and stiffness matrices. Thus, it is proposed to use Rayleigh damping in this study.

4.3 Nonlinear Solution

The numerical procedure for nonlinear analysis employs the iterative procedure to satisfy the equilibrium at the end of the load step. Once the convergence of the solution is achieved, the algorithm proceeds to the next step. It is always desirable to keep the load step very small especially after the onset of nonlinear behavior. The stiffness matrix is updated at the beginning of each load step. The convergence is said to be achieved if the out of balance forces, calculated as under, is less than the specified tolerance.

$$\psi_i^n = f^n - p_i^n = f^n - \int_V B^T \sigma_i^n dV < Tolerance \ (0.0025) \tag{57}$$

5 Influence of Openings on the Static Displacement Response of Shear Wall

The reinforced concrete shear wall tested by Lefas et al. [14], shown in Fig. 8, has been considered for the present analysis. The shear wall specimen consists of shear wall panel, top beam and bottom beam. The wall panel is 650 mm wide × 1300 mm high × 65 mm thick. The height to width ratio of wall panel is two, thus resulting in squat type. While the upper beam provides anchorage for vertical reinforcement, and lower beam provides the base for wall panel. In this study, the entire structure is divided into 156 elements [100 elements in wall panel + 28 elements each for top and bottom beam] using 9-noded degenerated shell element with 5 degrees of freedom per node. The element size of wall panel is 65 mm × 130 mm mesh size. The lateral load is increased incrementally at the middle of top slab and the displacement response is obtained accordingly.

The bottom beam has been constrained in all degrees of freedom. The discretized finite element model is shown in Fig. 9. The concrete characteristic compressive strength (f_{ck}) is taken as 42.8 Mpa. The elasticity modulus of concrete is calculated as $5{,}000\sqrt{f_{ck}}$, where f_{ck} is the characteristic compressive strength of concrete. The Poisson's ratio is taken as 0.17. The tensile strength is assumed to be $0.33\sqrt{f_c'}$. The hardening modulus for both concrete and steel is assumed to be 1/10th of initial elasticity modulus. The yield stresses (for both reinforcing steel zone-I and zone II)
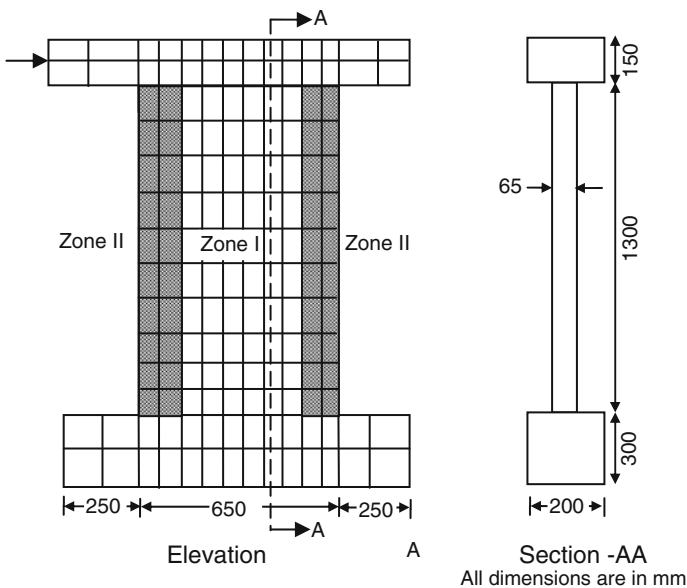
Fig. 8 Geometry of solid RC shear wall
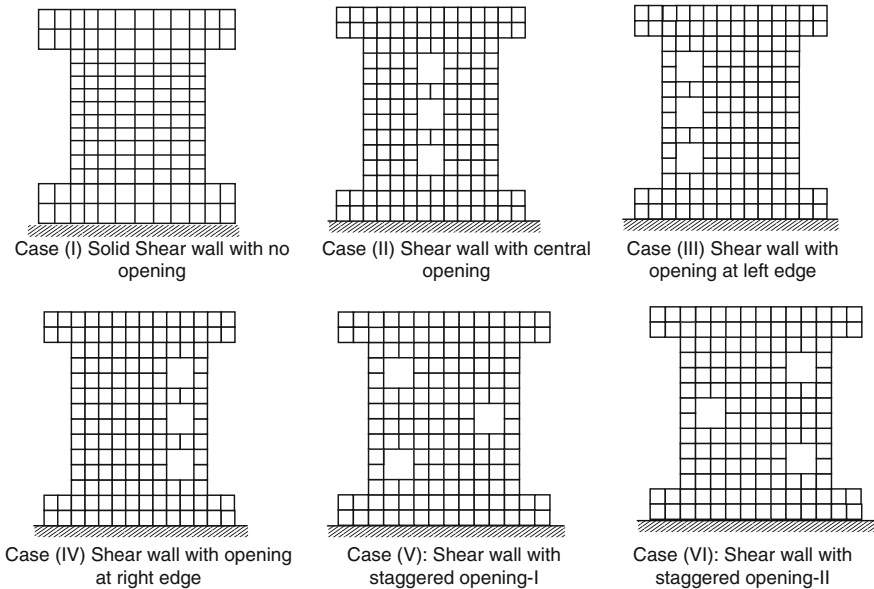
Fig. 9 Shear wall with different opening locations

in the x- and y-direction are 520 and 470 MPa respectively. The percentages of reinforcement of steel in x-direction and y-direction are 0.8 and 2.1 in zone I and 1.2 and 3.3 in zone II. The vertical reinforcement is provided in two layers and horizontal reinforcement is concentrated in single layer. The reinforcement is considered to be smeared inside the element. The maximum crushing strain is assumed to be 0.0035. The maximum number of iterations is restricted to 50 and tolerance limit is kept as 0.025. The tension stiffening constants α_{ts} and ε_{ts} are taken as 0.6 and 0.0020 respectively. In order to determine the influence of opening locations on the structural response of shear wall, the shear wall is pierced with openings at different locations as mentioned in Fig. 9. The response of the shear wall with openings is compared with solid shear wall case (i). The opening size has been kept constant at 12 % for all cases.

The load-displacement response has been plotted for all opening locations as shown in Fig. 10. It is observed that the solid shear wall undergoes maximum displacement and possesses higher collapse load in comparison to shear wall with openings. The collapse load and collapse displacement has been found to be the least in the case of shear wall with right opening.

Table 2 shows the ductility ratio and strength ratio of shear wall with various opening locations. The strength ratio has been found to be maximum in the case of solid shear wall and least in the case of shear wall with right opening. It was observed that the shear wall with staggered opening-I opening resulted in the maximum ductility with the displacement ductility ratio (Table 2) of 17.14 and

Fig. 10 Load-displacement
response for shear wall panel
with various opening
locations
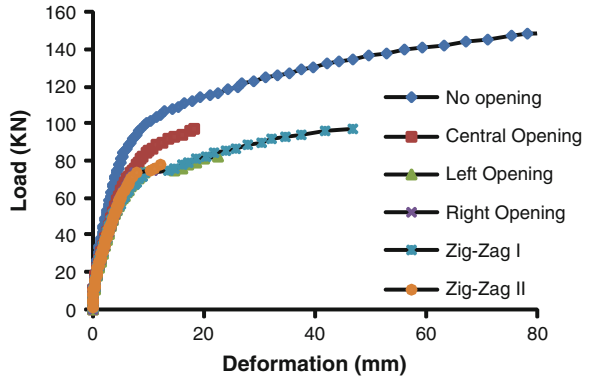
Table 2 Ductility ratio and strength ratios of shear wall with various opening locations

| Case | Opening locations | No. of yielded elements | Load (kN) at | | Displacement (mm) at | | Ductility ratio $\mu = \delta_u/\delta_y$ | Strength ratio $r = P_u/P_y$ |
			Yield (P_y)	Collapse (P_u)	Yield (δ_y)	Collapse (δ_u)		
I	No opening	63	51.0	148.50	3.66	78.28	21.39	2.91
II	Central opening	100	36.0	97.50	2.14	18.31	8.56	2.71
III	Left opening	30	36.0	82.50	2.38	22.58	9.49	2.29
IV	Right opening	25	39.0	76.50	2.68	11.48	4.28	1.96
V	Staggered opening-I	41	40.5	97.50	2.73	46.79	17.14	2.40
VI	Staggered opening-II	25	39.0	78.00	2.56	12.14	4.74	2.00

maximum collapse displacement of 46.79 mm. This is partly because the stiffness
degradation is progressive enough to ensure the ductile failure and inculcates the
coherency of the shear wall for longer time.

The ductility has been found to be the least when the openings in shear wall are
located in the compression zone (right opening and staggered opening-II). The
collapse load has also been found to be less for right opening and thus inheriting the
brittle failure. Moreover, number of yielded elements (Fig. 11) at the collapse load
for shear wall with right and staggered opening II is only 25 % in comparison to
central opening, where the number is 100 %. This reflects upon the fact that the
ductile fracture dominates in the case of shear wall with central opening and shear
failure occurs in the case of right opening. Moreover, in the case of shear wall with
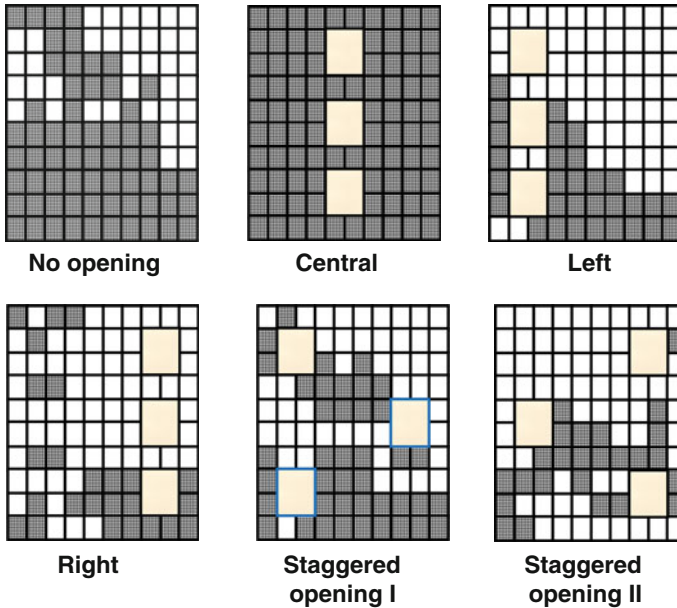
Fig. 11 Yield pattern of shear wall panel with various opening locations

right opening, around 60 % of total yielded elements have been concentrated on the compression zone, near the bottom most opening, thus prompting for the local failure even at the smaller load. Some zones are very unaffected and hence such opening locations inhibits undesirable mode. The response of shear wall with no opening and central opening resulted in the maximum number of yielded elements, 63 and 100 % respectively and thus possessing better ductility than the shear wall with right side openings.

1. It is desirable to avoid opening at the compression side so as to have better structural performance.
2. Staggered opening-I has been found to yield maximum displacement ductility ratio and hence is preferred over other opening locations.
3. Though central opening may not have resulted in huge ductility, it has been observed from the yield pattern that the stiffness degradation is very much progressive and hence is preferred from the ductile failure point of view.
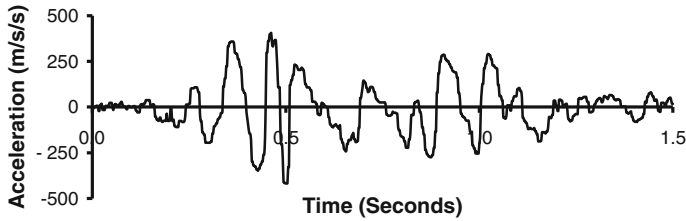
Fig. 12 Input ground acceleration (applied at the base of the structure)

6 Influence of Openings on the Dynamic Displacement Response of Shear Wall

The displacement at failure for the present study has been considered when the structure is subjected to severe cracking and yielding, explicitly resulting in larger number of iterations for a time step. In order to determine the influence of opening location on the dynamic response of RC shear wall panel, the shear wall has been subjected to dynamic ground acceleration, as shown in Fig. 12. Only four opening locations were considered as the determining the response of left and right openings separately is immaterial. The ground acceleration values have been escalated in order to create a significant and recognizable effect on the structural response. The total duration of the ground motion has been taken as 1.5 s. The analysis has been carried out with the time step of 0.015 s and damping has not been considered. The displacement time histories of shear wall with different opening locations have been presented in Fig. 13. The maximum displacement and time at which the maximum displacement occurred have also been reported in Table 3.

The shear walls with different opening locations were also analyzed for dynamic loading conditions and it was observed that the openings located centrally resulted in the better ductile performance with least displacement than other opening locations, and surprisingly, even better than the solid shear wall. The shear wall with left opening has been found to be severely shaken especially towards the end of the time history, indicating its vulnerability under dynamic loading conditions. The shear wall with staggered opening has been considered to possess better dynamic characteristics with uniform displacement throughout the time history response.
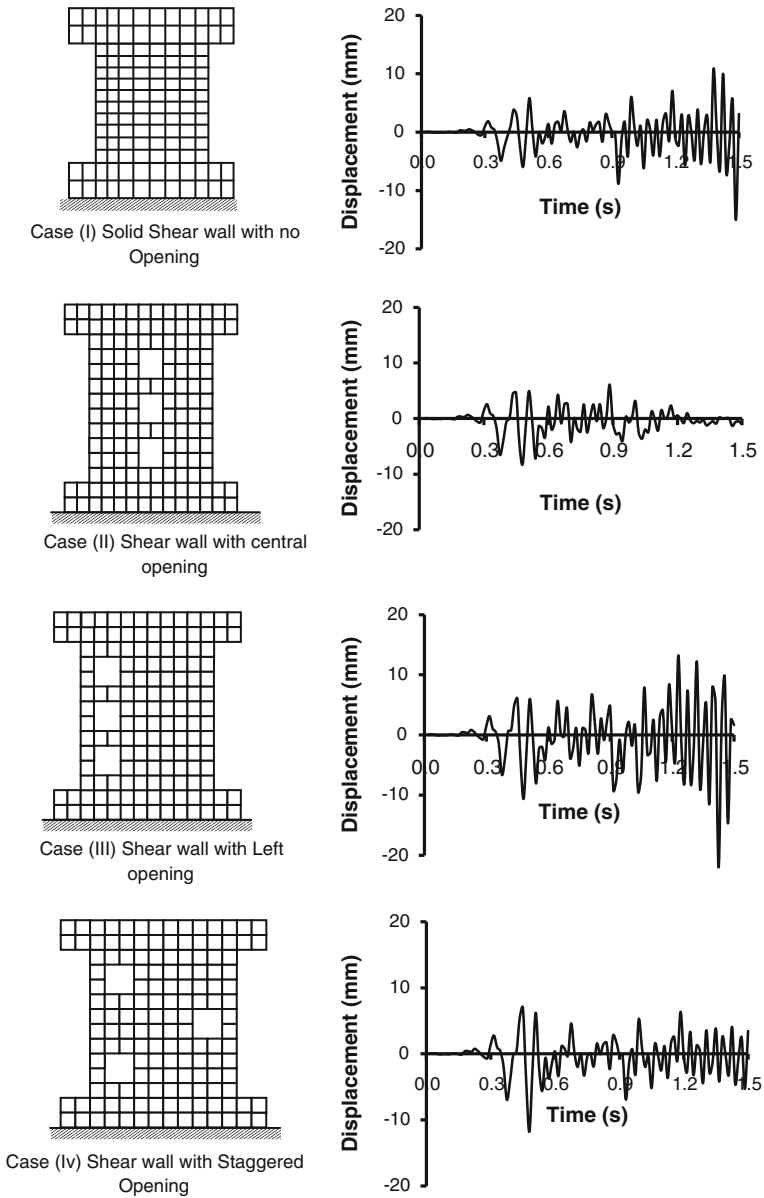
Fig. 13 Displacement time history response of barbell shaped shear wall with multiple opening locations

Table 3 Maximum displacement and time of flanged shear wall with multiple opening locations

Case no.	Opening locations	Maximum displacement (mm)	Time of maximum displacement (s)
1	No opening	15.02	1.49
2	Central opening	8.279	0.480
3	Left opening	22.03	1.43
4	Staggered opening	11.78	0.48

7 Conclusions

On the basis of above discussion, it has been concluded that the openings should not be located at the extreme edges of the shear wall, which inevitably spoils the benefit of boundary elements, especially under severe shaking. It is desirable that the openings be located centrally as far as possible, to result in the best performance both under static and dynamic loading conditions.

References

1. Ahmad S, Irons BM, Zienkiewicz OC (1970) Analysis of thick and thin shell structures by curved finite elements. Int J Numer Methods Eng 2(3):419–451
2. Bathe KJ (2006) Finite element procedures. Prentice Hall of India Private Limited, New Delhi
3. Chen WF (1982) Plasticity in reinforced concrete. McGraw Hill, New York
4. Chopra A (2006) Dynamics of structures: theory and application to earthquake engineering, 3rd edn. Prentice-Hall, Englewood Cliffs
5. Clough RW, Penzien J (2003) Dynamics of structures. McGraw-Hill Book Co, New York
6. IS-13920 (1993) Ductile detailing of reinforced concrete structures subjected to seismic forces. Bureau of Indian Standards, New Delhi
7. Fintel M (1977) Performance of buildings with shear walls in earthquakes of the last thirty years. PCI J 95(2):62–71
8. Hinton E, Owen DRJ (1984) Finite element software for plates and shells. Pineridge Press, UK
9. Huang HC (1987) Implementation of assumed strain shell elements. Comput Struct 25 (1):147–155
10. Huang HC (1989). Static and dynamic analyses of plates and shells: theory, software and applications. Springer, Berlin
11. Kant T, Kumar S, Singh UP (1994) Shell dynamics with three-dimensional degenerate finite elements. Comput Struct 50(1):135–146
12. Kim HS, Lee DG (2003) Analysis of shear wall with openings using super elements. Eng Struct 25:981–991
13. Kuang JS, Ho YB (2008) Seismic behavior and ductility of squat reinforced concrete shear walls with non-seismic detailing. ACI Struct J 105(2):225–231
14. Lefas ID, Kotsovos MD, Ambraseys NN (1990) Behavior of reinforced concrete structural walls: strength, deformation characteristics, and failure mechanism. ACI Struct J 87(1):23–31
15. Lee DJ (2008) Experimental and theoretical study of normal and high strength concrete wall panels with openings. PhD Thesis, Griffith University, Australia

16. Lin CS, Scordelis AC (1975) Nonlinear analysis of RC shells of general form. ASCE J Struct Div 101(3):523–538
17. Liu Y, Teng S (2008) Nonlinear analysis of reinforced concrete slabs using non-layered shell element. ASCE J Struct Eng 134(7):1092–1100
18. MacLeod IA (1970) Shear wall-frame interaction. Portland Cement Association, p 17
19. Nayal R, Rasheed HA (2006) Tension stiffening model for concrete beams reinforced with steel and FRP Bars. ASCE J Mater Civil Eng 18(6):831–841
20. Ngo D, Scordelis AC (1967) Finite element analysis of reinforced concrete beams. ACI J 64 (3):152–163
21. Neuenhofer A (2006) Lateral stiffness of shear walls with openings. ASCE J Struct Eng 132 (11):1846–1851
22. Owen DRG, Hinton E (1980) Finite elements in plasticity, theory and practice. Pineridge Press Limited, UK
23. Paswey SF, Clough RW (1971) Improved numerical integration of thick shell finite elements. Int J Numer Meth Eng 3(4):575–586
24. Rahimian A (2011) Lateral stiffness of concrete shear walls for tall buildings. ACI Struct J 108 (6):755–765
25. Rashid YR (1968) Analysis of pre-stressed concrete pressure vessels. Nucl Eng Redesign 7 (4):334–344
26. Rosman R (1964) Approximate analysis of shear walls subject to lateral loads. Proc ACI J 61 (6):717–732
27. Schwaighofer J, Microys HF (1969) Analysis of shear walls using standard computer programmes. ACI J Proc 66:1005–1007
28. Taylor CP, Cote PA, Wallace JW (1998) Design of slender reinforced concrete walls with openings. ACI Struct J 95(4):420–433
29. Teng S, Liu Y, Soh CK (2005) Flexural analysis of reinforced concrete slabs using degenerated shell element with assumed strain and 3-D concrete model. ACI Struct J 102 (4):515–525
30. Tomii M, Miyata S (1961) Study on shearing resistance of quake resisting walls having various openings. Trans the Archit Inst Jpn, p 67
31. Willam K, Warnke E (1975) Constitutive model for triaxial behavior of concrete. In: Proceedings of the international association for bridge and structural engineering, vol 19, Switzerland, pp 1–30
32. Zareian F, Medina RA (2010) A practical method for proper modeling of structural damping in inelastic plane structural systems. Comput Struct 88(1–2):45–53
33. Zienkiewicz OC, Taylor RL, Too JM (1971) Reduced integration technique in general analysis of plates and shells. Int J Numer Methods Eng 3(2):275–290

Ductility of Concrete Members Partially Prestressed with Unbonded and External Tendons

R. Manisekar

Abstract Partial prestressing is basically a prestressed concrete approach in which prestressed reinforcement or prestressed and non prestressed reinforcement is used such that tension and cracking in concrete is allowed under service loads. Although there were studies on ductility in partial prestressing available in literature, it is necessary to take up further studies on ductility by applying different types of experiment data for better understanding. Curvature ductility is chosen for the present study and the same is evaluated using the data published in literature. Curvature ductility μ is defined as the ratio of curvature at ultimate ϕ_u to that of yield ϕ_y. Totally the data of 45 specimens were used for the study. Shape of the specimens consists of rectangular section and T-beam section. There is a strong opinion among researchers and practicing engineers that compressive reinforcing steel would enormously improve the ductility of concrete members. In view of this, data of specimens with and without compressive reinforcement was also studied. Parametric studies by taking into account of different parameters on ductility namely, reinforcement index, yield curvature, deflection curvature, M_{ult}/M_{yld} and Partial Prestressing Ratio (*PPR*) in partially prestressed concrete members of unbonded post tensioning tendons have been carried out. There are many criteria reported in literature regarding curvature at yield. However, criteria namely: (i) yielding of reinforcing steel; (ii) 0.75 M_n, where M_n corresponds to 0.003 strain; and (iii) intersection point of two lines of moment-curvature curve have been studied. It is observed that Reinforcement index is the influencing parameter in evaluating ductility for partially prestressed concrete beams with unbonded and external tendons. Partial Prestressing Ratio (*PPR*) is not an influencing parameter for evaluating ductility. There is a proportional decrease in M_{ult}/M_{yld} and a proportional increase in the yield moment and ultimate moment according to the ascending order of reinforcement index. Curvature ductility is linearly proportional to the deflection ductility, if the reinforcement index is in ascending order. Curvature ductility is the better index for evaluating ductility of unbonded partially prestressed concrete members rather than displacement ductility.

R. Manisekar (✉)
CSIR-Structural Engineering Research Centre (SERC), Chennai 600113, India
e-mail: rmanisekar17@yahoo.co.in

1 Introduction

Partial prestressing is basically a prestressed concrete approach in which contribution of prestressed reinforcement or prestressed and non-prestressed reinforcement is used such that tension and cracking in concrete is allowed under service loads. However serviceability and strength requirements are satisfied.

Partial prestressing is achieved using both bonded and unbonded prestressing steel. Although there were studies on ductility in partial prestressing available in literature, it is necessary to take up further studies on ductility by applying different types of experiment data for better understanding. The paper deals with influence of different parameters on ductility in partially prestressed concrete members of unbonded post tensioning tendons namely, reinforcement index, yield curvature, deflection curvature, M_{ult}/M_{yld} and partial prestressing ratio (*PPR*) and concludes.

2 Literature Review

Au and Du [2] conducted review on partially prestressed concrete members of bonded and unbonded tendons subjected to static and fatigue loading. Ductility usually refers to the ability of a material, section, structural element, or structural system to sustain inelastic deformation prior to collapse, without substantial decrease in the load-carrying capacity. Apart from giving warning before failure, ductility is also important for seismic design and moment redistribution in continuous members. The member ductility is usually in the form of a dimensionless ductility factor, which is the ratio of one type of deformation at failure to the same type of deformation at yield. The deformation can be the curvature of a critical section, the rotation over a plastic hinging region, or the displacement of a member. The curvature ductility factor is often adopted to evaluate the ductility behaviour of prestressed concrete (PC) members. In modelling the nonlinear response of bonded partially prestressed concrte (PPC) sections, Cohn and Bartlett [6] related the yield curvature to the yielding of prestressed tensile steel. Naaman [9] defined the yield curvature as that corresponding to the intersection of two lines on the moment-curvature plot of a section as shown in Fig. 1. Different definitions are also available for the maximum curvature. One of these is to take the maximum curvature as that corresponding to the concrete compression strain of 0.003, as in the ACI 318 [1].

The other is to take the maximum curvature as that corresponding to the maximum resisting moment. Park [10] adopted the definition of yield and maximum curvatures, as shown in Fig. 2.

Fig. 1 Yield curvature ϕ_y and ultimate curvature ϕ_u [9]
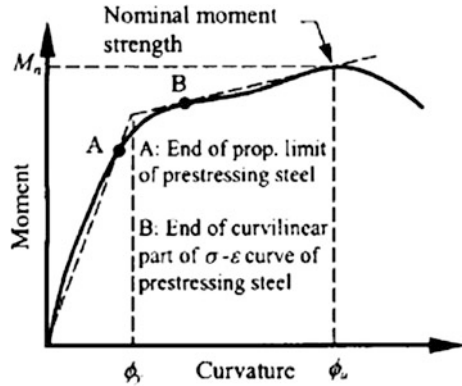
Fig. 2 Yield curvature ϕ_y and ultimate curvature ϕ_u [10]
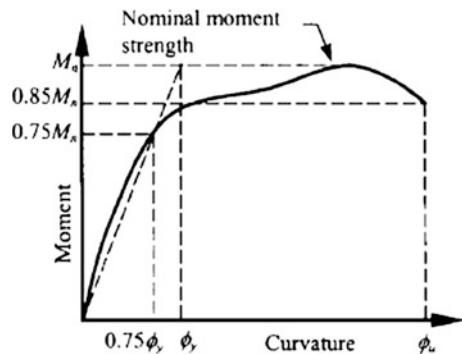
This definition of the curvature ductility factor can be applied to all kinds of structures and is relatively easy to determine either analytically or experimentally. Having taken into account the ability of the member to deform beyond the peak load, it is regarded as a much better measure of ductility than most other definitions. Naaman [9] analysed the ductility of bonded PPC flexural members, and found the reinforcement index to be an excellent independent variable to describe flexural ductility. There is no consistent trend of the effect of PPR on ductility and such effect can be assumed to vanish with high concrete compressive strength.

They concluded that the concept of partial prestressing was developed about half a century ago. Over the years, partial prestressing has been gradually accepted by engineers to the extent that it is now a normal way to design PC structures. This is true for bonded PPC as well as unbonded PPC members. The behaviour of bonded PPC members has been extensively studied, while the research of UPPC members has mainly been focused on the prediction of flexural resistance that is closely related to the ultimate tendon stress at flexural failure. As a result, formulae of different sophistication have been suggested for the purpose. However, experimental and analytical studies of serviceability limit state and ductility of UPPC members are comparatively limited. Investigations of time dependent effects of

UPPC members are also very few. Although external prestressing is an effective technique for strengthening concrete flexural members, the strength acquired with external prestressing is accompanied by a reduction in ductility of flexural failure. It is necessary to study the suitable range of the amount of prestressing tendons to ensure the necessary ductility.

3 Parametric Studies

Ductility is the capacity of a structural member to sustain inelastic deformation prior to collapse so that the structure could give warning to the users before collapse. In general, ductility is expressed as the ratio of curvature at ultimate to that at yield as follows:

$$\mu = \frac{\phi_u}{\phi_y} \tag{1}$$

where ϕ_u is the curvature at ultimate; and ϕ_y is the curvature at yield.

It is clear that the curvature at ultimate is associated with ultimate load corresponding to 0.003 extreme compressive fiber strain. It is applicable to reinforced, prestressed and partially prestressed concrete members. In RC members, the curvature at yield corresponds to yielding in the reinforcing steel. In partially prestressed concrete members, yielding of the reinforcing steel occurs prior to that of the prestressing steel. Therefore, curvature at yield of partially prestressed concrete members and their application in evaluating ductility is an important phenomenon. Cohn and Bartlett [6] suggested that the yield curvature corresponds to the curvature at yielding of reinforcing steel. Thompson and Park [12] defined that yield curvature corresponds to the curvature at the section assuming linear elastic behavior up to the theoretical strength of the section in the first load application. Park and Folconer [11] suggested that the curvature calculated at moment M_n assuming the member had a constant flexural rigidity equal to that computed at 0.75 M_n, where, M_n is the nominal moment of resistance corresponds to 0.003 extreme compressive fiber strains. Naaman [9] defined the yield curvature as the curvature corresponding to the intersection of two lines. The first line corresponds to the linear portion of the moment-curvature curve while the second line corresponds to the final portion of the curve.

Although there are many suggestions regarding yield curvature reported in literature, the following criteria were selected and used in the parametric study. Curvature corresponds to

1. Curvature at yielding of reinforcing steel [6]

$$\phi_y = \frac{M_y}{E_c I_{tr}} \tag{2}$$

$$I_{tr} = \left(\frac{M_{cr}}{M}\right)^3 I + \left(1 - \left(\frac{M_{cr}}{M}\right)^3\right) I_{cr} \tag{3}$$

$$I_{cr} = \frac{bd_n^3}{3} + m \cdot A_{st}(d - d_n)^2 \tag{4}$$

where
I is the moment of inertia of gross cross section
M_y is the moment corresponds to yielding of reinforcing steel
Φ_y is the curvature corresponds to yielding of reinforcing steel
d_n is the depth of neutral axis

2. 0.75 M_n, where M_n corresponds to 0.003 strain [11]
   Curvature at yield corresponds to 0.75 M_n

$$\phi_y = \frac{M_{0.75M_n}}{E_c I_{tr}} \tag{5}$$

3. Intersection point of two lines of moment-curvature [suggested by Naaman [9])
   Curvature at yield corresponds to Moment–Curvature curve

$$\phi_y = \phi_{graphical} \tag{6}$$

Curvature at ultimate

$$\phi_u = \frac{M_u}{E_c I_{tr}} \tag{7}$$

$$I_{tr} = \left(\frac{M_{cr}}{M}\right)^3 I + \left(1 - \left(\frac{M_{cr}}{M}\right)^3\right) I_{cr} \tag{8}$$

$$I_{cr} = \frac{bd_n^3}{3} + m \cdot A_{st}(d - d_n)^2 \tag{9}$$

Ductility

$$\mu = \frac{\phi_u}{\phi_y} \qquad (10)$$

3.1 Discussion

3.1.1 Influence of PPR and Reinforcement Index on Parameters of Ductility

In partially prestressed concrete members, both non-prestressed steel and pre-stressed steel are being used. The flexural behaviour and yielding of a partial prestressed concrete member is depending on the combined effect of non- pre-stressed and prestressing steel. In this view, combined reinforcement index have been in use for studying the flexural behaviour of partial prestressed concrete members. Partial prestressing ratio (*PPR*) are also being used to account the combined effect of prestressing and non-prestressing steel. Therefore, influence of these two parameters on the yielding stage is studied first. They are given as follow:

Partial prestressing ratio:

$$PPR = \frac{A_p f_{pe}}{A_{p.} f_{pe} + A_s f_y} \qquad (11)$$

Combined reinforcement index:

$$\omega = \frac{A_p f_{ps}}{b d_p f_c'} + \frac{d_s}{d_p} \left(\frac{A_s f_y}{b d_s f_c'} - \frac{A_s' f_y'}{b d_s f_c'} \right) \qquad (12)$$

where

A_p Area of prestressing tendons
f_{pe} Effective prestress
f_y yield stress of reinforcing steel
f_c' compressive strength of concrete
A_s Area of tensile reinforcement
A_s' Area of compressive reinforcement
d_s depth of tensile steel
d_p depth of prestressing tendons

Experiment data of Du and Tao [7], Chakrabarti et al. [5], Campbell and Chouinard [4], Au et al. [3], Harajli and Naaman [8] have been used for parametric study. Totally 45 specimens were used. Shape of the specimens consists of

rectangular section and T-beam section. There is a strong opinion among researchers and practicing engineers that compressive reinforcing steel would enormously improve the ductility of concrete members. In view of this, data of specimens with and without compressive reinforcement was also decided to study. Accordingly, the specimens of Du and Tao [7] and Chakrabarti et al. [5] do not contain compressive reinforcement while others contain compressive reinforcement.

Researchers have been using reinforcement index and PPR as index for evaluating flexural behaviour and ductility of partially prestressed concrete unbonded beams. To examine this, PPR is compared with moment at yield, moment at ultimate and the ratio M_{ult}/M_{yld}. As the ductility is measured between yield stage and ultimate stage the ratio M_{ult}/M_{yld} is also used. In the comparison, PPR is arranged in an ascending order to observe a trend in the graph. The comparisons using data of Harajli and Naaman [8] are shown in Figs. 3 and 4. It can be observed that a trend is observed from the comparison of PPR to M_{ult}/M_{yld}. However, in the comparison of PPR to M_{yld} and M_{ult}, a constant trend is not obtained. When the PPR increases

Fig. 3 Comparison of PPR to M_{ult}/M_{yld} using data of Harajli and Naaman
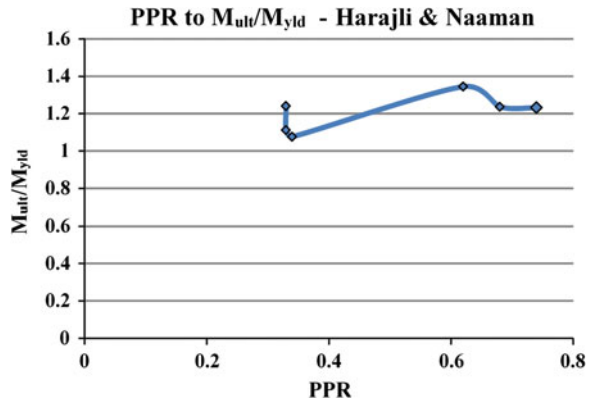
Fig. 4 Comparison of PPR with M_{yld} and M_{ult} using data of Harajli and Naaman
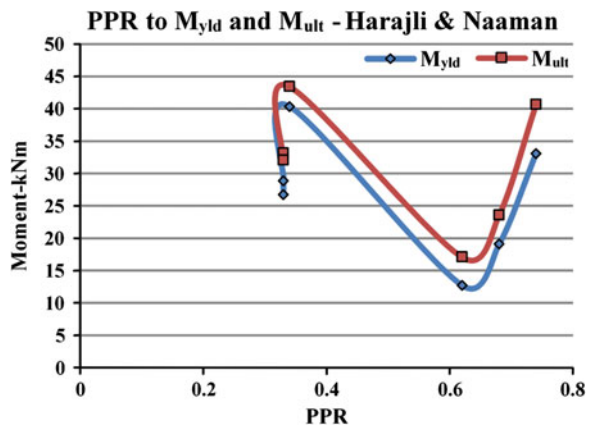
Fig. 5 Comparison of *PPR* with M_{ult}/M_{yld} using data of Au et al.
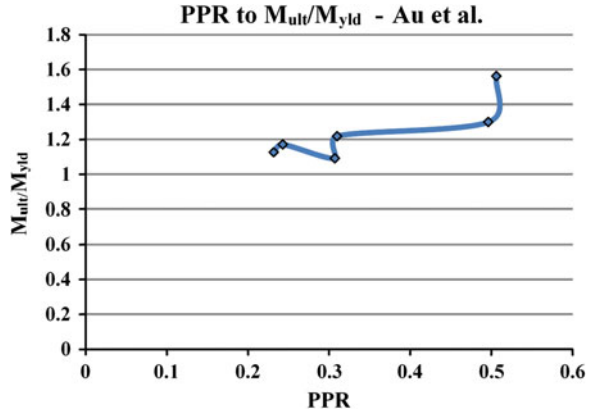
Fig. 6 Comparison of *PPR* with M_{yld} and M_{ult} using data of Au et al.
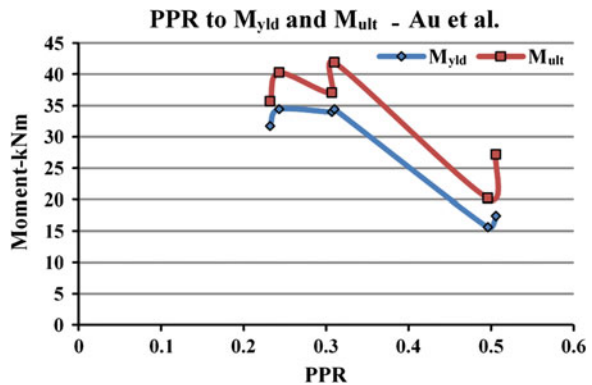
there are mixed response both increase and decrease are obtained. The cross section shape of the Harajli and Naaman is rectangular. Therefore, shape of T-beam using data of Au et al. are also compared in Figs. 5 and 6 respectively for *PPR* to M_{ult}/M_{yld} and *PPR* to M_{yld} and M_{ult}. In both the comparisons using different data, it can be observed that the *PPR* could not give a constant trend.

In the next case, the reinforcement index was taken and the same comparisons have been made, which are shown in Figs. 7 and 8 respectively for the data of Harajli and Naaman, and Figs. 9 and 10 respectively for the data of Au et al. It can be observed that reinforcement index has given an acceptable trend and therefore it could be decided that in the ascending order of reinforcement index there is a proportional decrease in M_{ult}/M_{yld} and a proportional increase in the yield moment and ultimate moment. Accordingly, the same comparisons of reinforcement index with parameters have been made for other data sets are done.

Comparison of reinforcement index with M_{ult}/M_{yld} and M_{yld} and M_{ult} using data of Campbell and Chouinard [4] are shown in Figs. 11 and 12 respectively. It can be observed that in the ascending order of reinforcement index there is a proportional

Fig. 7 Comparison of Reinforcement index with M_{ult}/M_{yld} using data of Harajli and Naaman
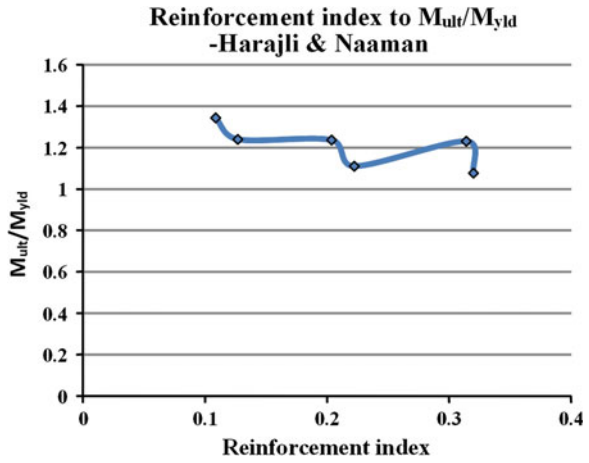
Fig. 8 Comparison of Reinforcement index with M_{yld} and M_{ult} using data of Harajli and Naaman
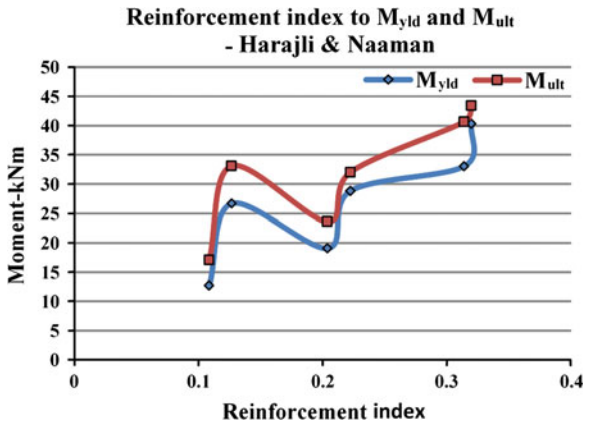
Fig. 9 Comparison of Reinforcement index with M_{ult}/M_{yld} using data of Au et al.
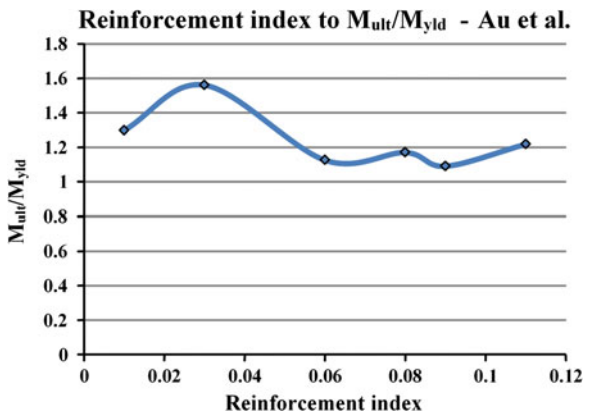
Fig. 10 Comparison of reinforcement index with M_{yld} and M_{ult} using data of Au et al.
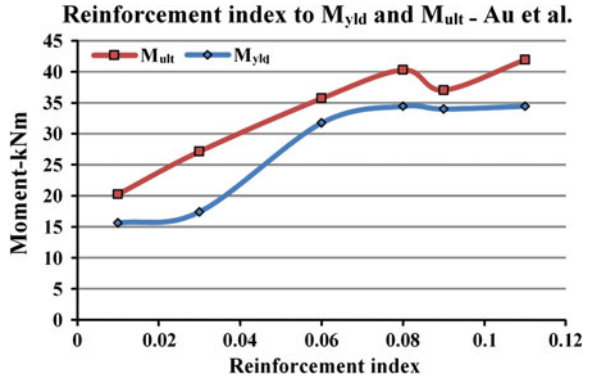
Reinforcement index to M_{yld} and M_{ult} - Au et al.

Fig. 11 Comparison of reinforcement index with M_{ult}/M_{yld} using data of Campbell and Chouinard
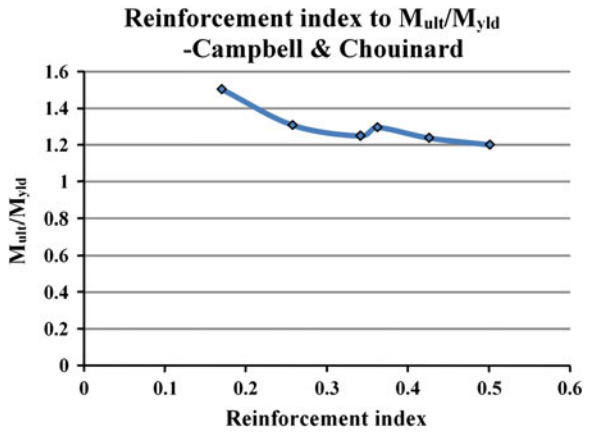
Reinforcement index to M_{ult}/M_{yld} -Campbell & Chouinard

Fig. 12 Comparison of reinforcement index with M_{yld} and M_{ult} using data of Campbell and Chouinard

Reinforcement index to Myld and Mult -Campbell & Chouinard
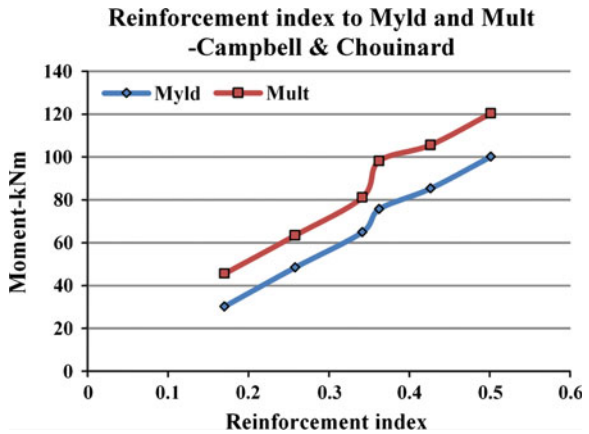
decrease in M_{ult}/M_{yld} and a proportional increase in the yield moment and ultimate moment.

The same comparison of reinforcement index using data of Du and Tao [7] is done and they are shown in Figs. 13 and 14 respectively for M_{ult}/M_{yld} and M_{yld} and M_{ult}. Here also, the same trend, which captured in the figures using data of Harajli and Naaman [8], Au et al. [3] and Campbell and Chouinard [4] is obtained.

Comparison of reinforcement index with M_{ult}/M_{yld} and M_{yld} and M_{ult} using data of Chakrabarti et al. [5] are shown in Figs. 15 and 16 respectively. Because the data included T-beams and rectangular sections there is some non uniform trend. Therefore, it can be ignored. Considering all the illustrations, it can be concluded that the reinforcement index is an influencing parameter for parameters associating with ductility namely, M_{yld}, M_{ult}, M_{ult}/M_{yld}. Moreover, a proportional decrease in

Fig. 13 Comparison of reinforcement index with M_{ult}/M_{yld} using data of Du and Tao
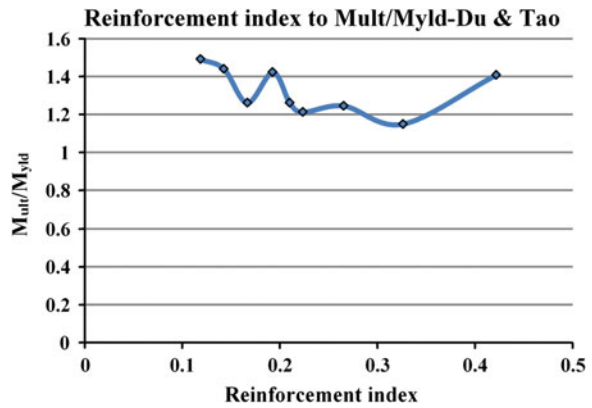
Fig. 14 Comparison of reinforcement index with M_{yld} and M_{ult} using data of Du and Tao
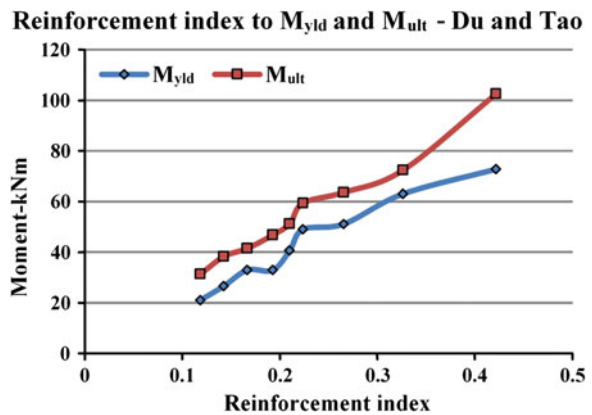
Fig. 15 Comparison of reinforcement index with M_{ult}/M_{yld} using data of Chakrabarti et al.
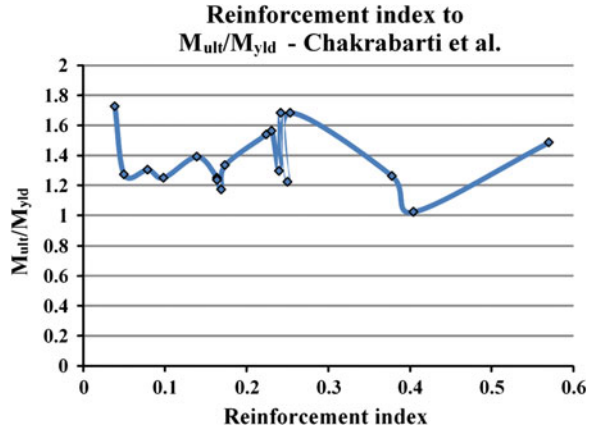
Fig. 16 Comparison of reinforcement index with M_{yld} and M_{ult} using data of Chakrabarti et al.
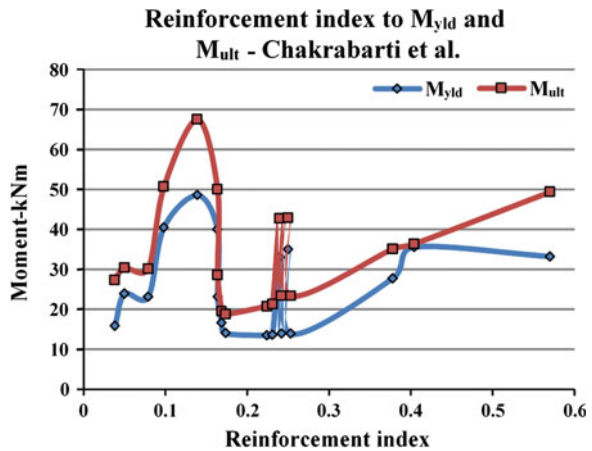
M_{ult}/M_{yld} and a proportional increase in the yield moment and ultimate moment are obtained according to ascending order of reinforcement index. On this basis, it is intended to continue discussion on ductility in the following section.

3.1.2 Ductility

Curvature ductility is chosen for the discussion and the same is evaluated using all the data set i.e. $\mu = \frac{\phi_u}{\phi_y}$, where, ϕ_u is the curvature at ultimate and ϕ_y is the curvature at yield. Curvature at yield corresponds to yielding of non-prestressing steel. Thomson and Park [12] suggested that Curvature ductility index is 3 times more than the displacement ductility index and the curvature ductility is more accurate than that of displacement. Therefore, curvature ductility is chosen and used for the

Fig. 17 Comparison of
reinforcement index with
Curvature ductility using data
of Harajli and Naaman
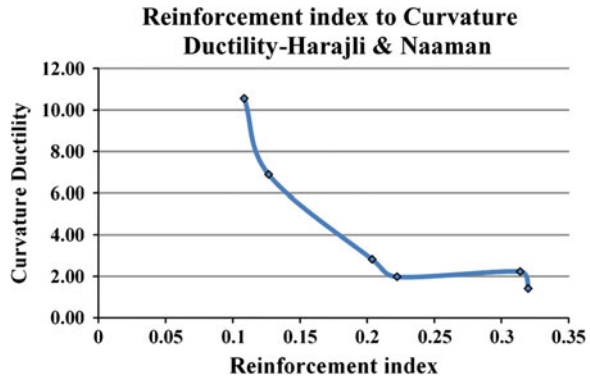
study. Comparison of reinforcement index with ductility is done using data of
Harajli and Naaman [8] and the same is shown in Fig. 17. It is observed that the
trend of the Fig. 17 followed the same trend of Fig. 7, which compared rein-
forcement index to M_{ult}/M_{yld}. It is true that the ductility falls in the state of
behaviour from yielding of non-prestressed steel to the ultimate corresponds to
0.003 strain or concrete crushing. This phenomenon reflects in Figs. 7 and 17.

Similarly the comparison of reinforcement index with curvature ductility using
other data set was made and they are shown in Figs. 18, 19, 20 and 21 for Au et al.
[3], Campbell and Chouinard [4], Du and Tao [7] and Chakrabarti et al. [5]
respectively. They follow the same trend of their comparison pertaining to rein-
forcement index with M_{ult}/M_{yld}, which showed in previous section. It is observed
that the Fig. 18 made using data of Au et al. [3] followed the same trend of Fig. 9.
Figure 19 made using data of Campbell and Chouinard [4] followed the same trend
of Fig. 11. Similarly, Fig. 20 using data of Du and Tao [7] and Fig. 21 using data of
Chakrabarti et al. [5] followed the trend of Figs. 13 and 15 respectively.

Fig. 18 Comparison of
reinforcement index with
curvature ductility using data
of Au et al.
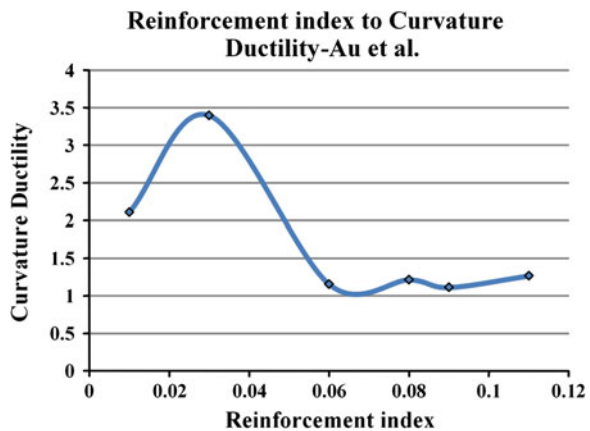
Fig. 19 Comparison of
reinforcement index with
curvature ductility using data
of Campbell and Chouinard
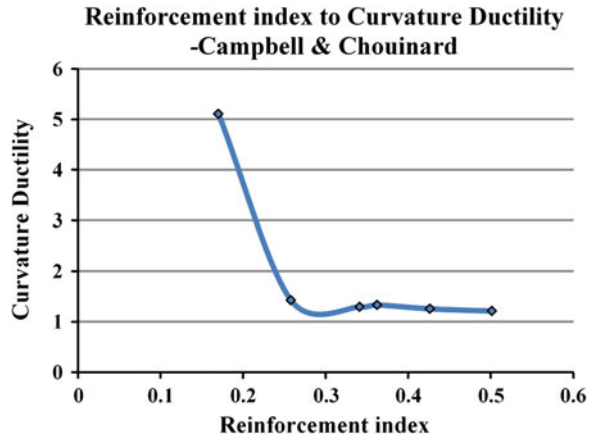
Fig. 20 Comparison of
reinforcement index with
curvature ductility using data
of Du and Tao
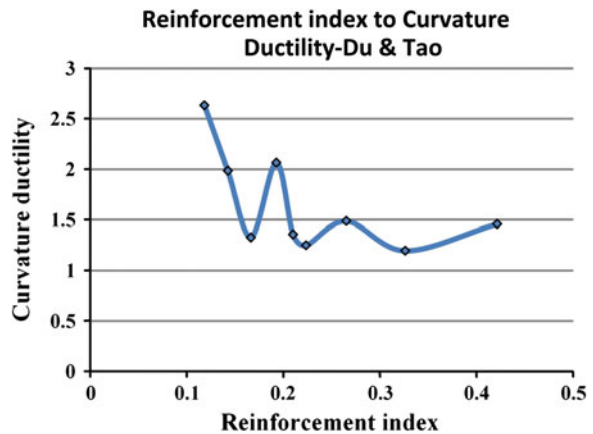
3.1.3 Curvature Ductility and Deflection Ductility

It is intend to study the deflection ductility too since the deformation at yield and
the deformation at ultimate defines the phenomenon for ductility. Therefore, the
deflection ductility, which is defined as the ratio of deflection at ultimate to that at
yield, is compared with the curvature ductility which is discussed in the previous
section. Both the ductility's have been arranged according to the ascending order of
reinforcement index. Accordingly, the comparison between curvature ductility and
deflection ductility is made. The comparison using data of Harajli and Naaman [8]
is shown in Fig. 22 and the comparison using data of Au et al. [3] are shown in
Fig. 23 respectively. It is observed from Figs. 22 and 23 that the curvature ductility
is linearly proportional to the deflection ductility. It is further to state that the
parameters M_{ult}/M_{yld}, curvature ductility and deflection ductility give uniform trend

Fig. 21 Comparison of reinforcement index with curvature ductility using data of Chakrabarti et al.
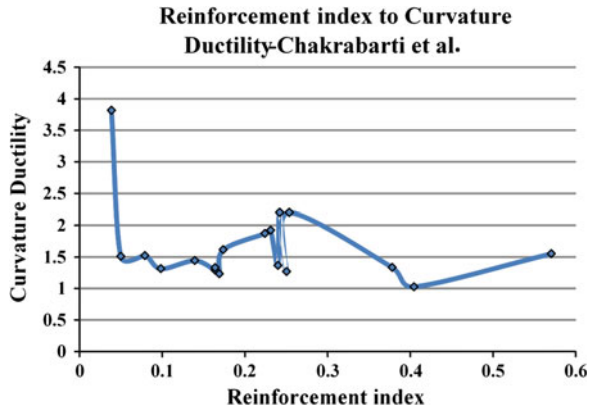
Fig. 22 Comparison of curvature ductility with deflection ductility using data of Harajli and Naaman
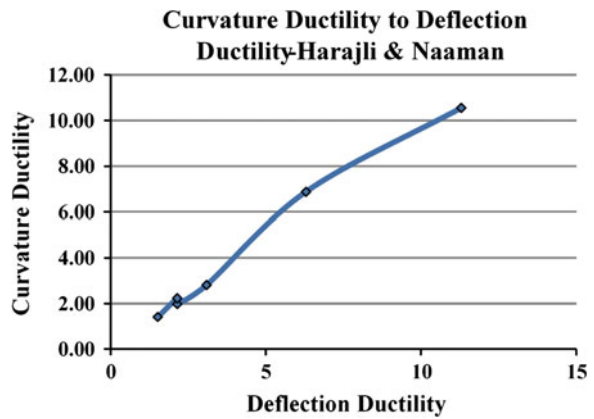
Fig. 23 Comparison of curvature ductility with deflection ductility using data of Au et al.
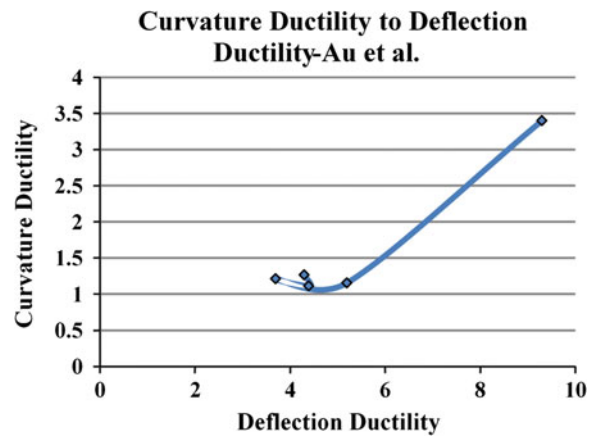
in the illustrations, if the reinforcement index is in an ascending order. Secondly, increase in reinforcement index could delay the moment at yield and ultimate and hence improving in the ductility.

4 Conclusions

1. Reinforcement index is the influencing parameter in evaluating ductility for partially prestressed concrete beams with unbonded and external tendons.
2. Partial prestressing ratio (*PPR*) is not an influencing parameter for evaluating ductility.
3. There is a proportional decrease in M_{ult}/M_{yld} and a proportional increase in the yield moment and ultimate moment according to the ascending order of reinforcement index.
4. Curvature ductility is linearly proportional to the deflection ductility, if the reinforcement index is in ascending order.
5. Curvature ductility is the better index for evaluating ductility of unbonded partially prestressed concrete members rather than displacement ductility.
6. As for as curvature ductility-reinforcement index relation is concerned, the curve for data of members contain compressive reinforcement is distinct from that do not contain compressive reinforcement.

References

1. ACI Committee 318 (2002) Building code requirements for reinforced concrete (ACI 318-02). American Concrete Institute, Detroit
2. Au FTK, Du JS (2004) Partially prestressed concrete. Prog Struct Eng Mater 6:127–135
3. Au FTK, Su RKL, Tso K, Chan KHE (2008) Behaviour of partially prestressed beams with external tendons. Mag Concr Res 60(6):455–467
4. Campbell TI, Chouinard KL (1991) Influence of non-prestressed reinforcement on the strength of unbonded partially prestressed concrete members. ACI Struct J 88(5):546–551
5. Chakrabarti PR, Whang TP, Brown W, Arsad KM, Amezeua E (1994) Unbonded post-tensioning tendons and partially prestressed beams. ACI Struct J 91(5):616–625
6. Cohn MZ, Bartlett M (1982) Nonlinear flexural response of partially prestressed concrete sections. J Struct Div ASCE 108(ST12):2747–2765
7. Du G, Tao X (1985) Ultimate stress of unbonded tendons in partially prestressed concrete beams. PCI J 30(6):72–91
8. Harajli MH, Naaman AE (1984) Deformation and cracking of partially prestressed concrete beams under static and fatigue loading. Report No UNMEE 84R1, University of Michigan, Ann Arbor, Michigon, pp 1–178

9. Naaman AE (1985) Partially prestressed concrete: review and recommendations. PCI J 30 (5):31–71
10. Park R (1988) Ductility evaluation from laboratory and analytical testing. In: Proceedings of the 9th world conference on earthquake engineering, vol VIII, Tokyo-Kyoto, pp 605–616
11. Park R, Folconer TJ (1983) Ductility of prestressed concrete piles subjected to simulated seismic loading. PCI J 28:112–117
12. Thompson KJ, Park R (1980) Ductility of prestressed and partially prestressed concrete beam sections. PCI J 25(2):46–70

A Full Scale Fire Test on a Pre Damaged RC Framed Structure

Asif H. Shah, Umesh K. Sharma, Pradeep Bhargava, G.R. Reddy, Tarvinder Singh and Hitesh Lakhani

Abstract A full scale Reinforced concrete (RC) frame assemblage was constructed and induced a predefined level of damage by subjecting the frame to simulated seismic loads and then was tested against a designed 1 h compartment fire. The RC frame was instrumented with a number of sensors which recorded strains, displacements and temperatures during the test. This paper provides a report on a full scale RC frame subjected to post earthquake fire. The frame could withstand the fire without collapse however the residual capacity of the frame was reduced to 65 % of the original. Important observations have been made about the development of the temperatures and displacements in various elements during the test.

Keywords Fire load · Post earthquake fire · High performance concrete · Residual strength · Spalling

A.H. Shah (✉) · U.K. Sharma · P. Bhargava
Department of Civil Engineering, Indian Institute of Technology, Roorkee,
Roorkee 247667, India
e-mail: shahaasifhussain@gmail.com

U.K. Sharma
e-mail: umuksh@rediffmail.com

P. Bhargava
e-mail: bhpdpfce@iitr.ernet.in

G.R. Reddy · T. Singh · H. Lakhani
Reactor Safety Division, Bhabha Atomic Research Centre,
Trombay, Mumbai 400094, India
e-mail: tarvindersinghs@gmail.com

H. Lakhani
e-mail: hiteshrssred@barc.gov.in

1 Introduction

Fire remains one of the serious potential risks to which the buildings and structures can be exposed to. Famous for its ubiquitous influence, concrete is most widely used material in the construction arena thereby making the research on fire resistance more and more important. Concrete structure design must take into account the risk of temperature increase. Heating can be caused by the fires for example in tunnels, high rise buildings or by accidental situations in nuclear power plants. Concrete behavior at high temperature is very complex and influences the global behavior of structure during heating [1]. The overall behavior of Reinforced concrete structures, during the time it is exposed to fire and even after, is still a hot issue in Civil Engineering. As far as the behavior during fire is concerned, the human safety and the structural resistance of the structures are two important associated interests involved while as the behavior of the structure after fire is related to the residual bearing capacity of the structure. Research into the effect of fire on concrete and concrete structures has been conducted since at least 1922 [2] mainly with respect to the building structures. The main focus of the study was the understanding the behavior of the concrete as a material under elevated temperature conditions and at the residual conditions. Also studied was the structural safety and integrity of the buildings during the course of fire and also the residual strength [3]. With time the research on concrete vis-à-vis the exposure to elevated temperature has gained much importance and with the development of high performance concrete (HPC) for use in buildings, bridges, tunnels etc. and also the use of performance-based analysis and design of structures, the studies on fire performance of concrete has evolved into an important research area ever since then. The behavior of concrete exposed to elevated temperatures is also known to be quite complex as the concrete when subjected to heat doesn't respond just in terms of physical changes such as the expansion but undergoes a series of chemical changes which in itself is a complex phenomenon owing to the non uniform nature of the concrete as a material. Each component of concrete i.e. the cement, aggregate and the moisture manifest their reactions in altogether different ways rendering the behavior of concrete at elevated temperature complex. The complex nature of the concrete at elevated temperature can be attributed to three different material factors which include physicochemical changes in the cement paste; physicochemical changes in the aggregate; thermal incompatibility between the aggregate and the cement paste which in turn are influenced by a number of factors which include but not limited to temperature level; heating rate; applied loading; moisture loss etc. [3]. Another important aspect of the concrete exposed to elevated temperature which makes the behavior complex to understand is the spalling. Spalling is regarded as one of the most poorly understood processes in the reaction of concrete to high temperatures. It is the ejection of the chunks of the concrete from the surface of a concrete element exposed to elevated temperatures. Depending on a number of factors, spalling leads to the decrease in the cross sectional area of a concrete member thereby drastically reducing its load carrying capacity. Significant research on the

containment of spalling has also been carried out [4–6], which suggest use of fibers like steel fibers and polypropylene fibers to help stop spalling. However till date spalling continues to remain a phenomenon with no accepted theory to explain its mechanism and the effect of the associated factors [7].

Another very important aspect of the research on the concrete structures exposed to elevated temperatures is the study of impact of fires on the structures damaged by earthquakes. Over the past centuries fire has emerged as an integral part of emergency response strategies which are focused on life safety as well as the infrastructure safety of any nation. However, no current regulations consider the fire and earthquake hazard in a sequential manner [8]. The occurrence of fires in many past earthquakes, which led to widespread devastations and resulted in a damage greater in extent and magnitude than the original earthquake, has made it necessary to consider the effect of seismic and fire loading on the structures not on a separate basis but in a sequential manner. The threat posed by fire following earthquake has been highlighted by a number overseas earthquakes, notably San Francisco (1906), Northridge, Los Angeles USA (1994), and Kobe, Japan (1995). Even though the strategy of taking both the extreme loads together in a sequential manner sometimes may not be desirable and feasible, but in highly important structures where economics and technology are no barriers, it will be sensible to provide such resistance.

Testing of concrete structures at elevated temperatures can be accomplished in a number of ways depending upon the factors and situations being simulated and the affect of the dependencies to be studied. Tests vary from being conducted on simple cubes [6], cylinders, small scale columns [9], full scale columns [10], beams and slabs [11], each studying the different parameters. Structural fire testing is undergoing rejuvenation with full scale tests being performed on various structural systems. The conventional, and widely used, method for fire testing, where in single structural elements are subjected to a standard fire test [12] and the thereby obtaining a fire resistance rating which is mainly in the form of a time to failure, has of late been noticed to have a number of drawbacks [13] though the method is still widely used.

Full scale tests are being performed to establish the global behavior of the structures under any condition though the fire tests on full scale concrete structures are very uncommon and very few tests have been carried on complete structural systems. Vecchio and Sato [14] reported the results from extensive testing on three large-scale reinforced concrete portal frame models to combinations of thermal and mechanical loads under different test conditions and the results indicated that the thermal loads can result in significant stressing of a structure and can lead to concentrated damage in local regions. Full scale test on a reinforced concrete frame conducted at Cardington, UK [15] provided an insight into the structural behavior of a heated concrete structure. Although this test suffered from instrumentation failure prior to its end rendering the dataset incomplete, a number of observations were derived from these tests. This test showed that the spalling of the floor slab was extensive and exposed the bottom steel reinforcement. In the first of its kind, Sharma et al. [16] tested a damaged reinforced concrete frame in fire. A Reinforced Concrete (RC) frame assemblage was first subjected to simulated earthquake

loading which was followed by subjecting the damaged frame to a compartment fire. Massive spalling in different elements of the assemblage was observed. Even though the strength of the frame was reduced after the fire, the frame assemblage escaped the complete structural failure. The test provided a massive data in terms of temperatures, strains, displacements as recorded for the beams, columns and the roof slab.

The present paper discuses a full scale fire test on a pre-damaged RC frame sub assemblage. A detailed description of the test setup, the test methodology and some of the key findings of the test will be presented in the paper. It is hoped that the test provides an understanding into the global behavior of the RC framed structures in fire and also the data provides for the benchmarking of the various computer models.

2 Experimental Programme

2.1 Test Frame

In order to evaluate the behavior of a Reinforced Concrete (RC) frame in post earthquake fire, a full scale RC frame assemblage was constructed before subjecting to predetermined earthquake damage and then exposing it to a compartment fire of one hour duration. The structure subjected to the tests was a symmetric RC frame assemblage which was a part of a three storey framed structure (G + 3) with 4 bays in East-West direction and 3 bays in North-South direction. The G + 3 structure was modelled and designed out of which the frame sub assemblage was constructed, as it was not feasible to construct the complete G + 3 structure due to the paucity of space and the economics associated, and tested first against the simulated seismic loading and then the fire loading. The plan and the elevation of the structure are shown in Fig. 1.

The hatched area in the figure represents the actual constructed RC frame sub assemblage. The test frame consisted of four columns (300 mm × 300 mm), four plinth beams (230 mm × 230 mm), four roof beams (230 mm × 230 mm) and a roof slab (120 mm thick). All the elements of the test frame were cast monolithically and the column fixity at the base was provided by the termination of all the four columns into a 900 mm thick RC raft foundation of plan size 6,900 mm × 8,700 mm. The RC frame was designed as per the guidelines of Indian standard code of practice IS 456: 2000 [17] without providing the ductile detailing. However, the minimum shear reinforcement was provided as per the recommendations as prescribed by [17]. An M30 concrete was designed, and utilized for the construction of the RC frames. The aggregates used were locally available crushed stone aggregates of nominal size of 20 mm and 12.5 mm. The steel reinforcement consisted of different diameter bars in different elements of the RC frame with each diameter bar having 500 MPa yield strength.
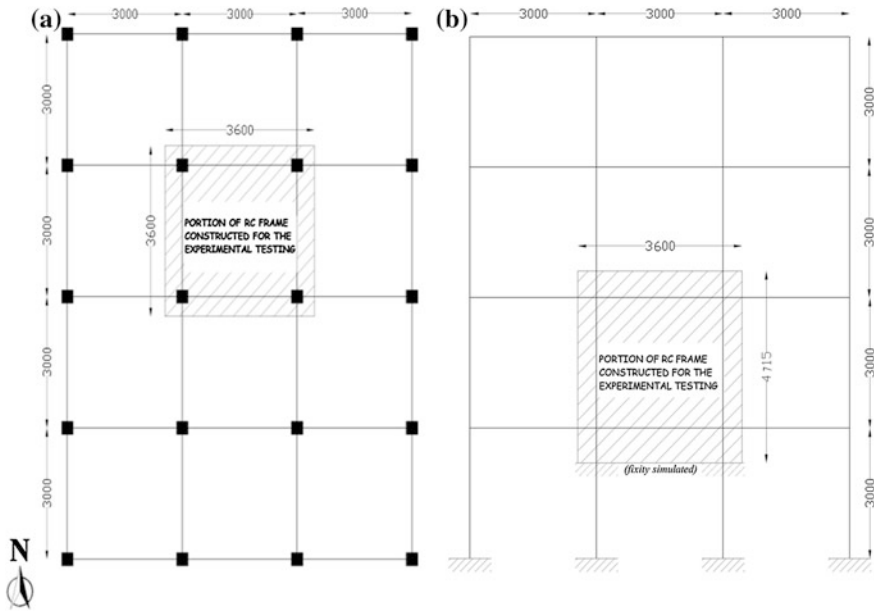
Fig. 1 G + 3 RC frame structure **a** in plan, **b** in elevation

2.2 Test Setup and Procedure

The gravity loads applied on the frame were based on the Indian standards for general loading, IS: 875 (Part-1 and Part-2): 1987 [18] and the Indian seismic design code, IS 1893 (Part-1): 2002 [19]. The dead load and the imposed load applied were 1 and 2 kN/m² respectively. The design loads applied for earthquake forces was however 0.5 kN/m² (25 % of 2 kN/m²) as per the guidelines of IS 1893 (Part-1): 2002 [19]. In order to simulate gravity loads of the upper floors of the G + 3 structure on the columns of the test frame a self equilibrating loading arrangement was developed as shown in the Fig. 2. The vertical loading from the top stories was simulated by applying the calculated equivalent load using 4 hydraulic jacks positioned centrally on each column. These jacks were made to rest on a specially designed ball bearing assembly in order to keep the verticality. Verticality of the jacks was maintained during the simulated seismic load so that the actual simulation of the applied top loads is achieved. The live load on the slab of the test frame was calculated and simulated by putting the equivalent load using the sand bags placed uniformly throughout the area of the slab. Similarly the wall load on the top beams coming from the walls of the immediate top floor was calculated and simulated by putting the sand bags along the four top beams. The sand bags were put in four layers and their stability during the load tests was ensured by putting a steel mesh all around the sand bags. Figure 3 shows the actual test arrangement before the test phase one (pre-damage).
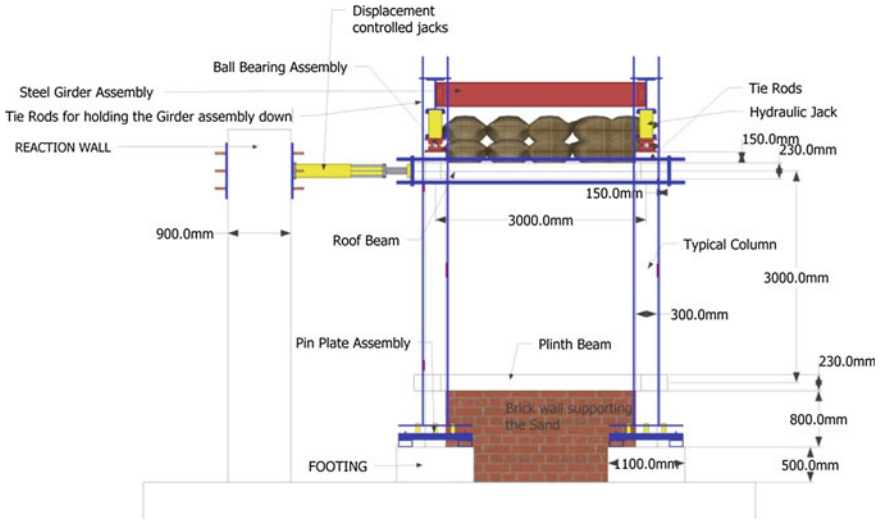
Fig. 2 A schematic diagram of the test arrangement (elevation)

Fig. 3 Test arrangement for the seismic loading as seen from the top

A three phase test procedure was adopted and followed in testing RC frame, which consisted of subjecting the frame to a simulated cyclic lateral load in a quasi-static fashion followed by a 1 h compartment fire and after which the frame was subjected to a residual load test. The simulated cyclic lateral load was applied onto the RC frame using two double acting hydraulic actuators acting in tandem with each other against a strong reaction wall.

On the outset the RC frame sub assemblage was subjected to a predefined seismic damage by subjecting the test setup to a simulated cyclic lateral load in a quasi-static manner with the help of two displacement controlled double acting hydraulic actuators which acted in tandem with each other against a strong reaction wall. The jacks are having a capacity of producing the displacement of 300 mm in either direction. The initial seismic damage was achieved by inducing a pre-planned lateral displacement through applying lateral cyclic load corresponding to the collapse prevention structural performance level (S-5) of FEMA 356: 2000 [20]. The damage level was ensured by subjecting the RC frames to a maximum roof level lateral displacement of 150 mm corresponding to a roof drift ratio of 4 % as given in [20].

Following the simulated lateral seismic load test, the RC frames were subjected to a full scale fire test wherein a designed compartment fire was developed using kerosene as the fire load. The fire load was kept same in both the frames with the peak burning rate of 0.117 kg/m^2/s corresponding to a peak fuel flow rate of 1.43×10^{-4} m^3/s which was maintained using a fixed head. This was done in order to attain a gas temperature of about 1,000 °C within 5 min after ignition to simulate a realistic compartment fire [16]. Ventilation to the fire compartment was ensured by providing a window of 1 m × 3 m along one of the faces of the RC frame. Figures 4 and 5 show the compartmentalization of the test frame before being subjected to the fire test. Following the fire test the fire panels were removed and the RC frame was again tested under simulated lateral seismic load for measuring the residual lateral load capacities of the frame.

2.3 Instrumentation

Data recorded for the structural aspects consisted of temperatures within the roof slab, columns, beams, and the compartment; strains on the rebars embedded in all the structural elements of the RC frame; deflections of the roof slab at different points both vertical as well as horizontal. The temperature measurement was taken by means of thermocouples embedded in concrete at a number of points and at different levels. The temperature build up inside the concrete of various structural elements of the RC frame was recorded using 0.5 mm dia K-type thermocouples embedded along the depth and width of the elements. To record the buildup of the gas temperature inside the frame compartment thermocouple trees were placed at five different plan locations, each at the four corners and one near the centre. A total

Fig. 4 Top view of the test arrangement with compartmentalization

Fig. 5 View of the test frame before the fire test with ventilation window

of 312 thermocouples, which included 287 K- type and 25 MI type thermocouples, were utilized for the measurement of the temperatures.

The strains were recorded by pasting strain gauges on the steel rebars at different locations in the RC frames. Electrical resistance-type surface mounted strain gauges were mounted on rebars at three sections in plinth beams, columns and top beams. Similarly steel rebars at four key locations in plan of the roof slab were instrumented with strain gauges.

Extensive instrumentation using linearly varying displacement transducers (LVDT's) of different ranges and stroke lengths was done in order to measure displacements of the different structural elements during all the test phases. Unique identifications (ID) were given to each of the sensors to enable programming of the channels of data acquisition systems.

3 Results of Tests and Discussions

3.1 Results of Seismic Loading

Figure 6 shows the (a) load history and (b) the displacement history of the test frame. The displacements were imparted the to the RC test frame using the displacement controlled jacks and after achieving the planed target displacement in each cycle, the load was maintained and the distress mapping was carried out by marking the crack development, crack growth and the crack widths on the different elements of the test frame. The frame was subjected to a total of 15 push pull displacement cycles and targeted for 150 mm displacement. A load of 320 kN was measured at the lateral displacement of 150 mm. At the end of the simulated seismic loading the frame was subjected to a push of 160 mm and left to take its own position and a plastic residual displacement of 41 mm was registered upon unloading. After the seismic loading a detailed distress mapping was carried in all the structural elements of the RC test frame assemblage. It was observed that the beams, (plinth as well as the roof) B2, B4, B6 and B8 (for location of different structural components of the frame refer to Fig. 7), perpendicular to the loading were not damaged as expected. However, the
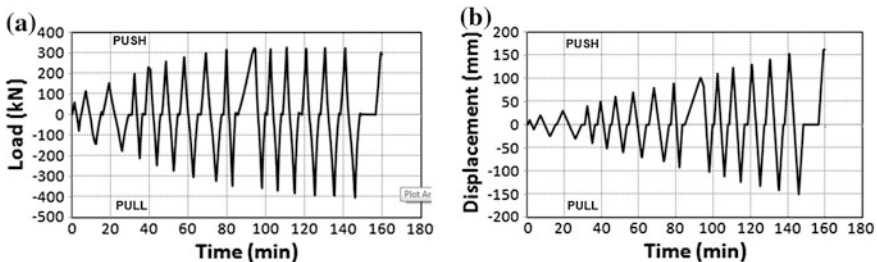
Fig. 6 **a** Load history and the **b** displacement history of the test frame

Fig. 7 Position of different structural elements of the frame

Fig. 8 Hinge formation at beam column joint

columns, slab and the beams parallel to the seismic loading direction were observed to have undergone extensive damage in terms of cracks and the concrete cover spalling. The roof beam B5 near column C1 had undergone extensive spalling with a spall volume of 230 mm × 60 mm × 16 mm being registered resulting in the exposure of the underlying reinforcing rebars as shown in Fig. 8.

A crack with a width of 6–7.5 mm was measured on the top of the slab, as shown in Fig. 9, which originated as a shear crack in the beam B5 near column C2 and protruded into the slab depth, running through the slab extensions and on the top of the slab traversing through the slab top along the edge of the beam B6. This crack

Fig. 9 A 6 mm wide crack measured on slab

converged with the shear crack originated from the beam B7. Figure 10 shows the strains developed on the reinforcing bars in different elements of the test frame as measured by the strain gauges. The damage as mapped by the visual inspection after the seismic load test is the manifestation of the large strains. During the loading a large number of shear cracks were formed in different elements of the frame which indicates a buildup of large vertical strains. From compatibility, the large vertical strain produce a large increase of strain in steel bars, which has been captured by the strain gauges on the steel rebars as shown in Fig. 10.

3.2 Results of Fire Test

Figure 11 depicts the compartment time-temperature history at one of the key locations of the RC frame. The temperature history shows an 18 h log with a complete heating and cooling cycle. The maximum temperature recorded during the course of fire was 1,369 °C in RC frame. Spalling was observed in all the structural elements with massive spalling in the slab. During the course of fire it was seen that the slab started to spall within 4 min of the fire with intense bullet shot sound like noise heard at 5 min. The spalling was intense at 6 min which corresponded to a slab temperature of 300 °C. Post fire inspection of the structure revealed the damage in various structural elements. As seen in Fig. 12 slab spalled extensively, attributed to high temperature gradients across the slab cross section (refer Fig. 13), with most of the cover concrete lost exposing the reinforcement. Sintering of aggregate was also seen in most of the slab area. A maximum temperature of 845 °C was recorded in the slab section near column 1 of the RC frame. Temperature profiles were captured at a number of key locations in beams, columns and slabs. Figure 14a–c depict the temperature profiles as generated in C1 top section, B3 Mid section and B8 Mid section. The temperature profiles by the curves are the representative of the thermocouples installed at different depths at a number of sections in each structural member. Each section in case of columns and top beams consisted of five
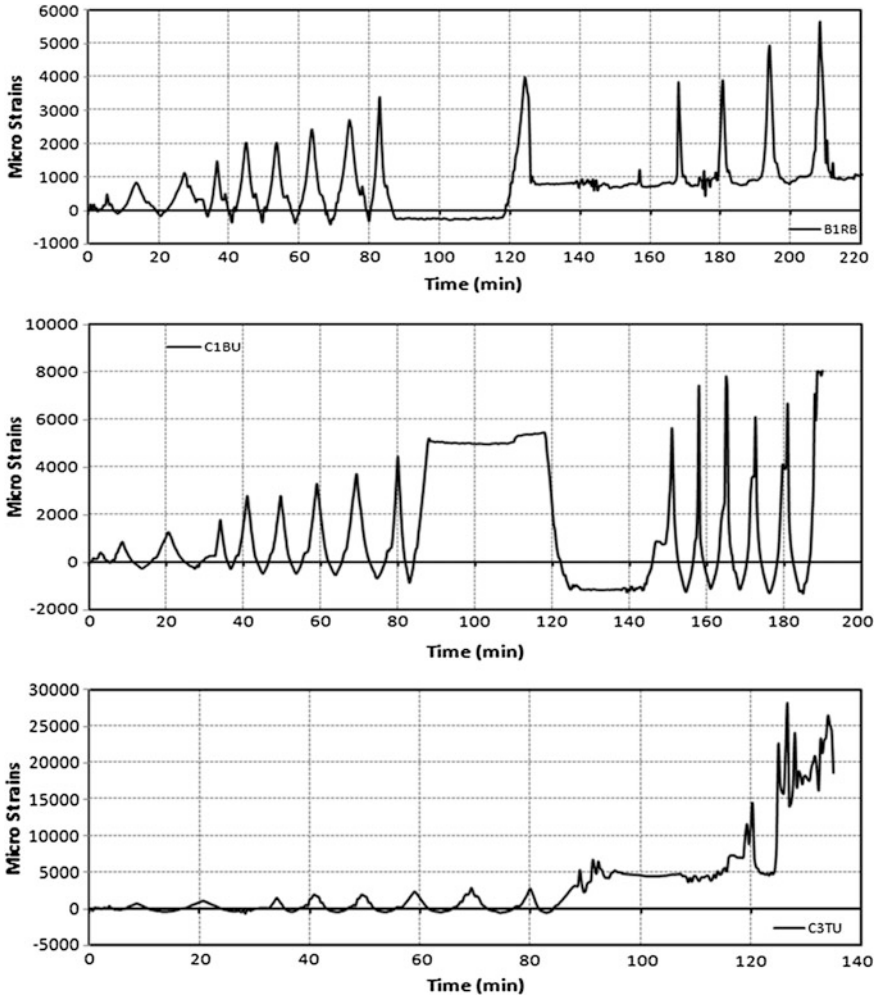
Fig. 10 Strains measured in different structural elements of the test frame during the seismic loading

Fig. 11 Temperature profile inside the compartment
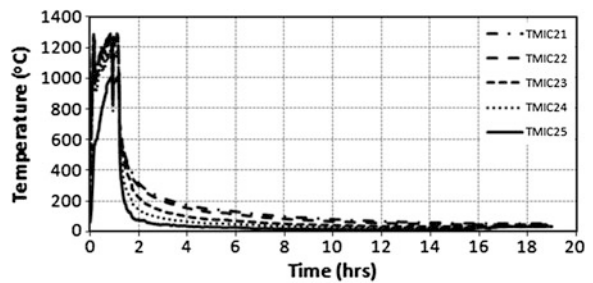
Fig. 12 Post fire view of the slab

Fig. 13 Temperature gradients of the slab near column C1
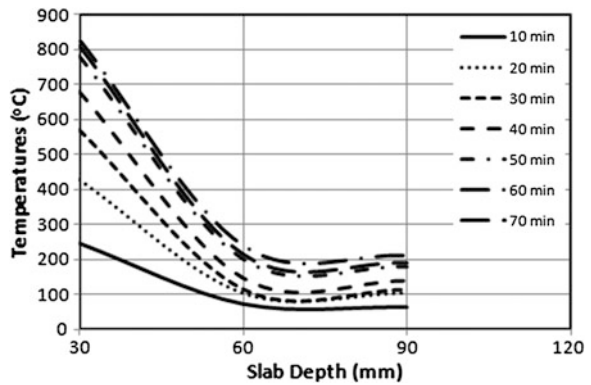
thermocouples with three thermocouples along the depth of the cross section and two along the width of the cross section. While as in case of the plinth beams three thermocouples were placed along the cross sectional depth. A temperature of about 1,200 °C was measured in beam B3 at midsection of the beam. In case of the beam B8 a temperature of about 980 °C was recorded while as a temperature of 410 °C was recorded in column C1 at the top section.

After the fire test the frame was again tested for the lateral loads to estimate the residual strength and it was measured to be 65 % of the actual capacity.
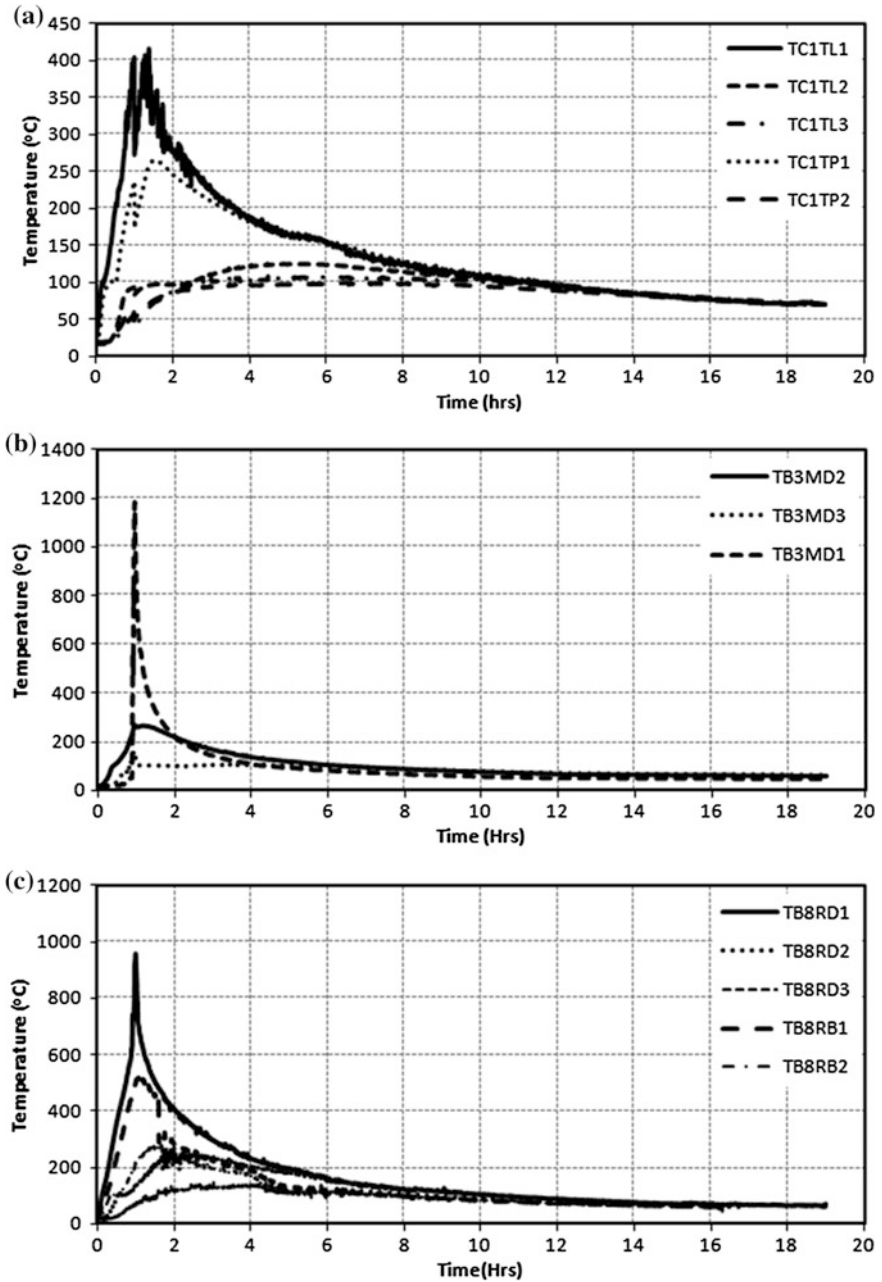
Fig. 14 Temperature–time curves for **a** typical column (*at end*); **b** plinth beam (*near centre*); **c** roof beam (*near joints*)

4 Conclusions

A report on a full scale fire test on a damaged RC frame has been presented. A novel test setup has been developed and tested which gives an understanding of the global behavior of a concrete structure in post earthquake fire. The higher levels of initial damage cause more number of wide cracks which leads to development of higher temperatures in the structural elements of the frame. A huge data base of the data in terms of temperatures, strains, displacements has been extracted from the test which will help in benchmarking of both computer and analytical models of structural behavior, heat transfer and material behavior.

References

1. Mindeguia J-C, Pimienta P, Noumowé A, Kanema M (2010) Temperature, pore pressure and mass variation of concrete subjected to high temperature—experimental and numerical discussion on spalling risk. Cem Concr Res 40(3):477–487
2. Lea F, Stradling R (1922) The resistance to fire of concrete and reinforced concrete. Engineering 114(4):341–344
3. Gabriel AK (2000) Effect of fire on concrete and concrete structures. Prog Struct Mat Eng 2 (4):429–447
4. Kalifa P, Menneteau F-D, Quenard D (2000) Spalling and pore pressure in HPC at high temperatures. Cem Concr Res 30(12):1915–1927
5. Phan LT (2008) Pore pressure and explosive spalling in concrete. Mater Struct 41 (10):1623–1632
6. Shah AH, Sharma UK, Danie ABR, Bhargava P (2013) Spalling behavior of nano SiO_2 high strength concrete at elevated temperatures. In: MATEC web of conferences, EDP Sciences, vol 6, p 01009
7. Jansson R (2013) Fire spalling of concrete-a historical overview. In: MATEC web of conferences, EDP Sciences, vol 6, p 01001
8. Usmani AS (2008) Research priorities for maintaining structural resistance after seismic damage. In: Proceedings of the 14th world conference on earthquake engineering, Beijing, China
9. Rahim A, Sharma UK, Murugesan K, Arora P (2013) Effect of load on thermal spalling of reinforced concrete containing various mineral admixtures. In: MATEC web of conferences, EDP Sciences, vol 6, p 01006
10. Kodur VKR, Raut NK, Mao XY, Khaliq W (2013) Simplified approach for evaluating residual strength of fire-exposed reinforced concrete columns. Mater Struct 46(12):2059–2075
11. Fellinger J and Joost W (2005) Shear and anchorage behaviour of fire exposed hollow core slabs. Heron 50(4):279–302
12. ISO (International Organisation for Standardization) (1975) ISO 834: fire resistance tests. elements of building construction. Switzerland, Geneva
13. Drysdale D (1998) An introduction to fire dynamics, 2nd edn. Wiley, Chichester
14. Vecchio FJ, Sato JA (1990) Thermal gradient effects in reinforced concrete frame structures. ACI Struct J 87(3):262–275

15. Bailey C (2002) Holistic behaviour of concrete buildings in fire. Proc Inst Civil Eng Struct Build 152(3):199–212
16. Sharma UK et al (2012) Full-scale testing of a damaged reinforced concrete frame in fire. Proc Inst Civil Eng Struct Build 165(SB7):335–346
17. IS 456 (2000) Indian standard code of practice: plain and reinforced concrete (fourth revision). Bureau of Indian Standards, New Delhi
18. IS 875-Part 1 (1987) Code of practice for design loads (other than earthquake) for buildings and structures-part 1: dead loads—unit weights of building material and stored materials (incorporating IS: 1911–1967). Bureau of Indian Standards, New Delhi
19. IS 1893-Part 1 (2002) Criteria for earthquake resistant design of structures: part 1 General provisions and buildings (reaffirmed 2007). Bureau of Indian Standards, New Delhi
20. FEMA-356 (2000) Pre-standard and commentary for the Seismic rehabilitation of buildings. Federal Emergency Management Agency, Washington, DC

Effect of Temperature Load on Flat Slab Design in Thermal Analysis

Sanjay P. Shirke, H.S. Chore and P.A. Dode

Abstract Long structures without any expansion joint has become a necessity in view of demanding architecture and present industrial trend in construction industry. Increasing demand for large commercial spaces, office buildings, IT parks, Multi-level parking structures and there serviceability aspects have put forward a situation where it has become necessary to review the provisions in Indian codes of practice. As per Indian Standard code, IS-456:2000, buildings longer than 45 m shall be analyzed for the thermal stresses and appropriate measures shall be taken during fixing the structural system. However, IS codes are silent in terms of process to follow in such kind of designs as well as on load factors to be considered in design combination of temperature load with gravity loads. To worsen the situation, there are no guidelines available with design engineers to arrive at design temperature value that should be considered in working out thermal stresses. This paper mainly focuses on systematic methodology to be adopted in analysis and design of flat slab structures in presence of temperature loads.

Keywords Temperature load · Thermal analysis · Long structures · Elimination of expansion joint

1 Introduction

As a standard practice based on IS code, expansion joints are usually provided every after 45 m length in case of long buildings. These expansion joints affects the execution of work, construction sequence, façade design (in case of dry

S.P. Shirke (✉) · H.S. Chore · P.A. Dode
Department of Civil Engineering, Datta Meghe College of Engineering, Maharashtra, India
e-mail: shirkesp@gmail.com

H.S. Chore
e-mail: hschore@rediffmail.com

P.A. Dode
e-mail: padode@rediffmail.com

cladding/ACP cladding) and also act as a source of leakage in monsoon during life span of buildings. Temperature variation induces stresses in a structure, if the structure is restrained. These stresses vary with the magnitude of the temperature change; large temperature variation can result in substantial stresses that must be accounted for in design, while low temperature changes may result in negligible stresses. Elongation caused by temperature variation can simply be worked out by using relation:

$$\Delta L \ = \alpha \times L \times \Delta t$$

where

ΔL   Elongation due to temperature variation
α   Co-efficient of thermal expansion of concrete (9.9E-06 considered here)
L   Length of building
Δt   Design temperature change

Design temperature change considered in this study is two third of the difference between the extreme values of the normal daily maximum and minimum temperatures i.e. 2/3(40–25) (as per Martin and Acosta 1970). Martin and Acosta arbitrarily chose the two-third factor to account for the fact that the temperature at which the building is completed would statistically not be at the maximum or minimum daily temperature, but somewhere between the two. Values of maximum and minimum temperature can be referred from meteorological department of the city. As a case study, data for Hyderabad city was referred to arrive at the value of design temperature change. Basically, buildings can be divided into three separate categories:

• Cladded buildings with controlled temperature like, commercial offices, shopping malls, etc.
• Cladded buildings without temperature control like residential buildings, Industrial estates, schools, colleges, etc.
• Un-cladded buildings like stadiums, sport complexes, multi-level car parks, etc.

Different effect can be seen in the structural design of buildings coming under above categories due to variation in seasonal as well as day and night time temperature variation. As the thermal stresses goes on increasing with respect to the length of building, a study has been carried out to understand the effect of these increased stresses on overall reinforcement consumption in flat slabs. Flat slabs are analyzed for temperature loads in addition to gravity as well as lateral loads and results are tabulated to access the behaviour of slab under ambient temperature condition.

Table 1 Building features

1.	Type of structure	Multi-storey pin jointed frame
2.	Earthquake zone	III
	Response reduction factor	5
	Importance factor	1
3.	Layout	As shown in Figs. 1, 2 and 3
4.	Number of stories	8 (G + 7)
5.	Ground storey height	3.0 m
6.	Floor-to-floor height	3.0 m
7.	External walls	1.2 m high, 200 thick parapets
8.	Internal walls	200 mm thick concrete block walls
9.	Live load	2.5 kN/m^2
10.	Materials	M 40 and Fe 500
11.	Seismic analysis	Equivalent static method
12.	Design philosophy	Limit state method conforming to IS 456:2000 + IS 13920:1993
13.	Size of exterior column	900 × 1500 mm
14.	Size of interior column	900 × 900 mm
15.	Thickness of shear wall	300, 450, 525, 600 as per design requirements
16.	Size of beams	300 × 750 mm
17.	Flat slab thickness	250 mm/300 mm
18.	Drop panel thickness	500 mm

2 Building Description

Un-cladded multilevel car park (MLCP) buildings fixed at base are considered in this report to study the effect of temperature variation. Three multilevel car park buildings are analyzed here in order to study the effect of temperature load with respect to length of building viz. 80, 160 and 240 m as referred in Table 1.

3 Analytical Simulations and Design

Structural analysis carried out using CSI software Etabs 9.7. Buildings having variable floor plates are selected for this study.

1. Columns and beams modeled as line elements
2. Shear wall and flat slabs modeled as finite shell elements
3. Temperature load assigned to the floor plate/slabs.

All the three structures are initially analyzed in ETABS to include the effect of lateral forces. As structural framing consists of RCC flat slab with shear walls and columns without any peripheral beams, floor slabs are acting as in plane diaphragm distributing the effect of lateral forces. After analyzing the structure in ETABS, floor slabs were exported to SAFE using f2k files of selected floors.

Computer aided design and analysis software 'SAFE' was used for flat slab analysis and design. Finite element approach was adopted for the analysis of the flat slab. Variation in temperature 'Δt' was assigned as 10 °C to top and bottom surface of flat slab assuming linear stress across the thickness of slab. Reinforcement design was carried out using strip method averaging out the results within column and middle strips. Based on analysis and design results, various graphs are plotted to discuss the effect of temperature variation with respect to the length of building. Following load combinations were used for designing the building against thermal variation:

1.2 Dead Load + 1.2 Live Load + 1.2 Temperature Load
1.5 Dead Load + 1.5 Temperature Load

Fig. 1 MODEL I (80 m long MLCP building)
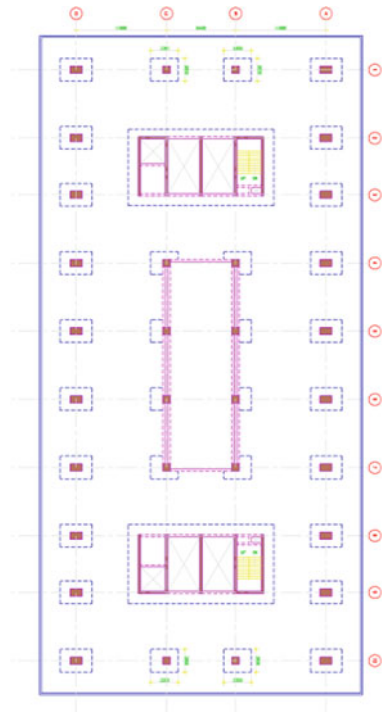
Fig. 2 MODEL II (160 m
long building)
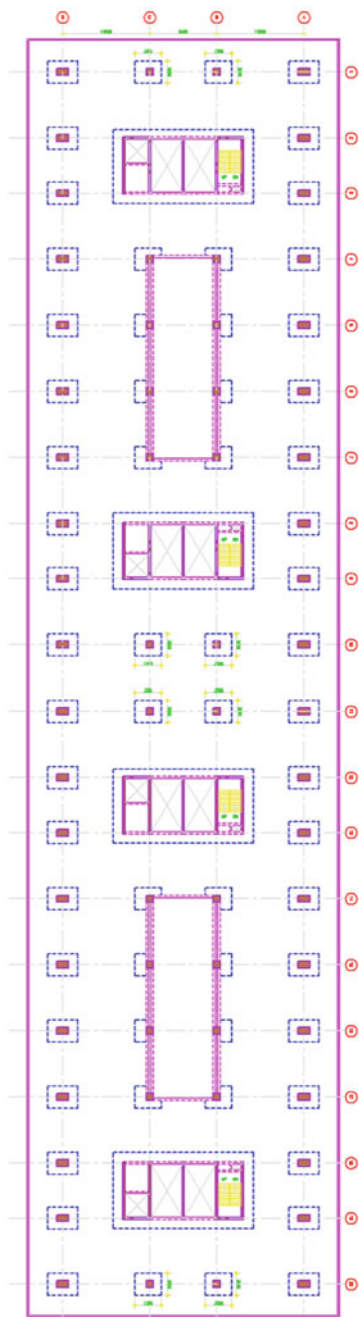
Fig. 3 MODEL III (240 m
long MLCP building)
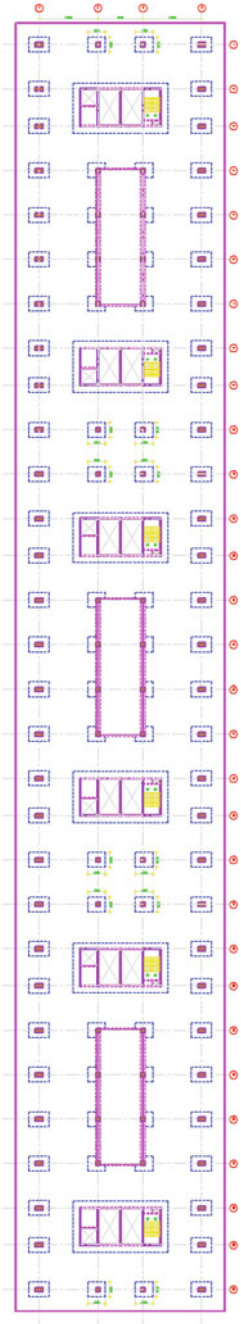
Fig. 4 Expansion of slab across the floors
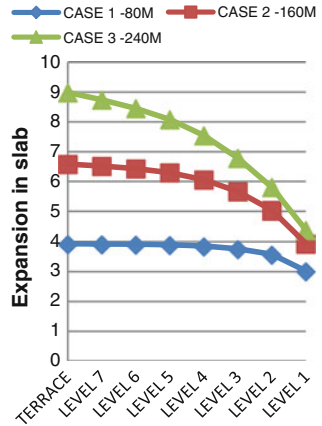
4 Results and Discussion

4.1 Point Displacement

Figure 4 represents the graphical representation of increase in length of building at every floor on each side along its length from this graph, it is clear that higher the length of building more will be the expansion.

4.2 Axial Tensile Stress Versus Modulus of Rupture

Figure 5 represents the maximum axial tensile stress in a typical flat slab middle strip at Terrace floor level due to temperature load. Stresses along length of building are calculated using the strip forces from SAFE analysis. It clearly indicates that the

Fig. 5 Maximum tensile stress in flat slab due to temperature load
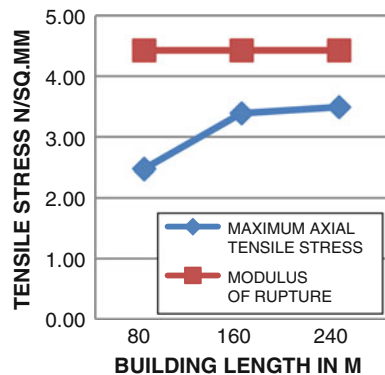
Fig. 6 Percentage of increase in flat slab reinforcement due to temperature load
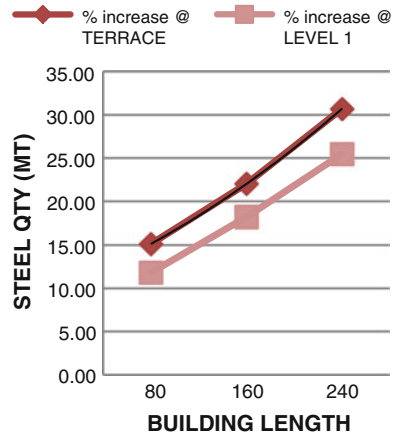
stress level keep increasing with the length of the building. Structural designer has to keep a tab on this value as it should not exceed beyond modulus of rupture given by equation, modulus of rupture = $0.75 * \sqrt{(f_{ck})}$.

Material grades specifically concrete shall be decided based on the maximum tensile stress to be experienced by flat slab. Although the grade of concrete plays important role in reinforcement calculations, limiting conditions of modulus of rupture shall not be overlooked.

4.3 Increase in Steel Consumption

Figure 6 represents the increase in reinforcement consumption in flat slab at two different levels. Level 1 was selected representing normal loading conditions of typical parking floor, i.e. 100 mm thick floor finish + services + live load of 2.5 kPa. To study the similar effect, terrace floor was also considered having additional imposed load due to waterproofing. In both the case, it was observed that reinforcement consumption goes on increasing with increase in length of building. It was observed to be 15 % for 80 m long building whereas more than 30 % for 240 m long building.

5 Conclusions

The behaviors of multistoried car park building exposed from all sides without any cladding, with and without temperature loads for various lengths have been studied in present paper. Structural quantities like linear expansion and increased axial stresses indicates that there are always chances of exceeding rupture modulus

causing splitting of concrete under an effect of temperature load. In buildings analyzed without considering temperature load may not require top reinforcement mesh in middle strip as the design is governed by sagging moment predominantly. However, in case of temperature loads, it becomes mandatory to provide top reinforcement mesh to cater for tensile stresses on extreme top surface even in middle strips. This results increase in reinforcement content in flat slab.

It is concluded that the large floor plates without any expansion joint can be adopted with marginal increase in reinforcement content ranging from 15 to 30 % over and above regular flat slab reinforcement. This additional cost of the extra reinforcement can easily be justified in view of high initial and maintenance cost of expansion joints. Along with flat slab, other structural elements like shear walls, columns and beams can be reviewed for the overall effect of temperature load.

Bibliography

1. Lewerenz AC (1907) Notes on expansion and contraction of concrete. Eng News 57 (19):512–514
2. Merrill WS (1943) Prevention and control of cracking in reinforced concrete buildings. Eng News-Rec 131:91–93
3. Bilig K (1960) Expansion joints in structural concrete. Macmillan, London
4. Reynolds CE (1960) Reinforced concrete designer's handbook, 6th edn. Concrete Publications, London
5. Mann OC (1970) Expansion-contraction joint locations in concrete structures. In: Proceedings of symposium on designing for the effect of creep, shrinkage, and temperature in concrete structures, SP-27
6. National Academy of Sciences (1974) Expansion joints in buildings. Technical report no. 65, National Academy of Sciences, Washington DC
7. Hirst MJS (1984) Thermal loading of concrete roofs. J Struct Eng ASCE 110(8):1847–1860
8. Maria AP (1998) Thermal analysis of reinforced concrete shells. J Struct Eng ASCE 124 (1):105–108
9. Paul M, Robert K, Cornell CA (1980) Design temperature for structural elements. J Struct Div ASCE 106(4):877–895
10. BS 8110 (1985) Structural use of concrete. British Standard Institute, London, UK
11. Pfeiffer MJ, Darwin D (1987) Joint design for reinforced concrete buildings. SM Report no. 20, University of Kansas Center For Research, Lawrence, KS
12. Bazant ZP, Maurice FK (1996) Concrete at high temperature: material properties and mathematical models. Longman Group Limited, Harlow
13. Bill F, Trivedi N (2007) Temperature and shrinkage study for 300 m long building. Technical report prepared for M/s. Tishman Speyer Inc., Hyderabad, India
14. Portland Cement Association (1992) Joint design for concrete highways and street pavements. Portland Cement Association, Skokie
15. IS 456 (2000) Indian standard code of practice for plain and reinforced concrete. Bureau of Indian Standard, New Delhi, India
16. ACI Committee 224.3r-95 (2005) Joints in concrete construction. American Concrete Institute, Farmington Hills, MI, USA

17. ACI Committee 318 (2008) Building code requirements for structural concrete and commentary. American Concrete Institute, Farmington Hills, MI, USA
18. IS 3414 (2010) Indian standard code of practice for design and installation of joints in buildings. Bureau of Indian Standard, New Delhi, India
19. Jack HE, F ASCE F, Charles MT (1985) Length—thermal stress relations for composite bridges. J Struct Eng, ASCE 111(4):788–804

Behaviour of Two Way Reinforced Concrete Slab at Elevated Temperature

N. Raveendra Babu, M.K. Haridharan and C. Natarajan

Abstract The reinforced concrete slabs have experienced significant levels of stressing and cracking as a result of restrained thermal deformations. However, for evaluating the thermal strains in the slab, temperature distribution of the slab is required. Temperature distribution of the reinforced concrete slab varies from point to point. The temperature of unexposed concrete slab also rises due to the adjacent slab which is exposed to fire, even though concrete is having significant resistance for the propagation of fire. In this study, temperature distribution over the surface of concrete slab is obtained using finite element computer program (ABAQUS). Two different cases are considered to estimate the heat propagation through slab. In the first case, slab is subjected to fire at its center region. In the second case, slab is subjected to fire at outer region means along the walls. Modelling is carried out to predict the temperature distribution and thermal strains of concrete slab. The other parameters considered for this study are varying thickness of slab (100 and 200 mm) and exposed temperature (100, 200, 300 and 400 °C). The duration of exposure considered for the study is 4 h.

Keywords ABAQUS · Concrete slab · Fire region · Thermal strains · Transient analysis

1 Introduction

The behaviour of reinforced concrete slabs under fire has been studied by many researchers and still taking place. It is well known that when the temperature is increased in the slab, its resistance decreases. This is because when concrete is exposed to heat, chemical and physical changes occur such as loss of moisture, dehydration of cement paste and decomposition of the aggregate. Such changes lead to high pore pressures caused by the water evaporation thus leading to internal

N.R. Babu (✉) · M.K. Haridharan · C. Natarajan
National Institute of Technology, Thiruchirappalli, India

micro cracks and spalling in concrete. The increase in the temperature also affects the reinforcement, resulting in decreased yield strength. The behaviour of concrete slabs under fire was found to be very sensitive to the stiffness and ends restrain condition. The fire resistance of restrained slabs is generally higher than those for unrestrained slabs because of compressive restraint which decreases the slab's thermal expansion.

The finite element method was considered in the current research to study the behaviour of reinforced concrete two way slabs subjected to fire. There are generally three modes of heat transfer namely conduction, convection and radiation. For concrete members, the convection is usually ignored when calculating the exposed surface temperature because convection is responsible for less than 10 % of the heat transfer at the exposed surface of the concrete members [1]. On the other hand, convection is usually accounted for when calculating the unexposed surface temperature. The internal heat transfer through concrete members is typically calculated by conduction only [2, 3].

2　Material Properties

In order to assess the adequacy of coupled thermal displacement analysis to determine the temperature distribution and behaviour of reinforced concrete structures at elevated temperatures, a thorough investigation of the material models available also required. In a fully developed fire, the thermal and mechanical properties of concrete and steel such as thermal conductivity, specific heat, high thermal expansion and modulus of elasticity vary with the effect of temperature.

The temperature dependent mechanical and thermal properties of concrete and reinforcement which are essential were derived from Eurocode 2 Part 1-2 (2004) [4, 5]. Some of these properties of concrete and steel are shown in Figs. 1 and 2 respectively.

2.1　Finite Element Type and Mesh

Finite element package ABAQUS [6] was used to model a slab of size 3 m × 3 m and thickness 100 mm. The 8-node (C3D8RT) elements were used for coupled temperature-displacement analysis.

2.2　Model Validation

For validating the existing numerical model, experimental test result of Cooke (2001) is considered [7]. The comparison of analysis results with experimental results is shown in Fig. 3.
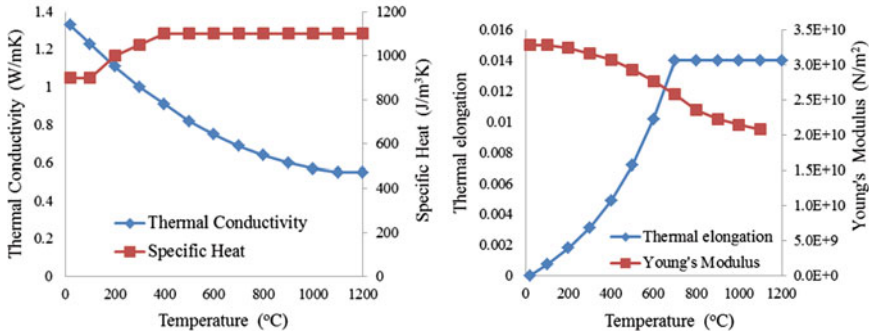
Fig. 1 Thermal and mechanical properties of concrete as represented in Eurocode
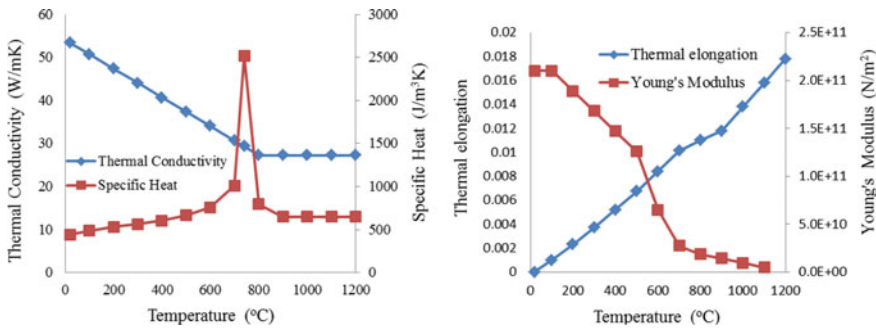
Fig. 2 Thermal and mechanical properties of steel as represented in Eurocode

Fig. 3 Comparison of
150 mm BRE slab with
ABAQUS model, mid-span
deflection with time
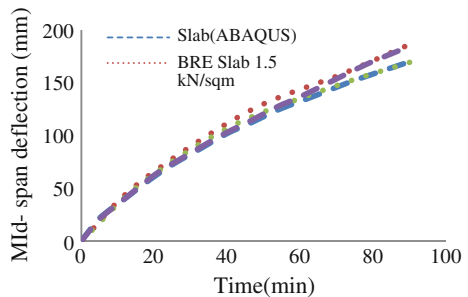
3 Result and Discussion

3.1 Transient Heat Transfer Analysis—Parametric Study

In this study, a two way slab of size 3 × 3 m was considered and the thicknesses of the slab were 100 and 200 mm. We considered the side faces of the slab are insulated as the slab was continuous along all sides. The bottom surface was

exposed to the temperature and the top surface of the slab was subjected to air convection. To estimate the heat propagation from fire region to surrounding unexposed surface of slab, two different critical cases (Case-1 and Case-2) of exposure of fire were considered.

Case (1): **Fire at center region of slab.**

From the entire floor area of the slab, only the center portion of the slab of size 1.5 m × 1.5 m was subjected to fire as shown in Fig. 4.

Case (2): **Fire at outer region of slab.**

When the fire was spreading along the walls due to the wall finishes, only the slab of 0.3 m strip from the walls was subjected to fire as shown in Fig. 5. To compare the propagation of heat from exposed region to un-exposed surface, two different node paths (Path-1 and Path-2) were considered. The first path (Path-1) was moving away from the edge of exposed surface to edge of the concrete slab. But, the second path (Path-2) was moving away from corner of exposed surface to corner of slab. In the reinforced concrete slab, the coefficient of thermal expansion of reinforcement and concrete were almost same. But the thermal conductivity varies.

Case (1): **Fire at center region of slab**

The temperature distribution was found out for two different thickness of the slab (100 and 200 mm). In the first case, the temperature propagation along considered paths was found on three different layers namely on the exposed surface (bottom), on the unexposed surface (top) and an intermediate layer at half of the depth of the slab (middle).

Fig. 4 Fire region for case (1)
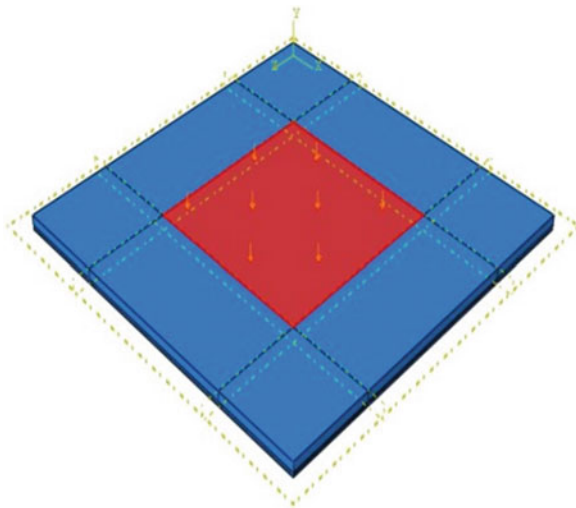
Fig. 5 Fire region for
case (2)
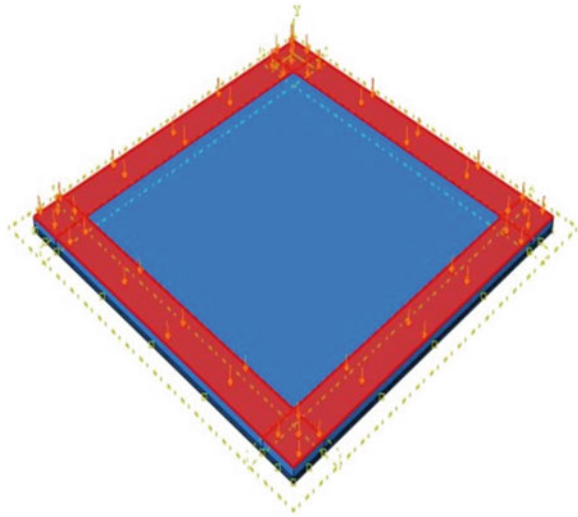
3.1.1 Slab of Thickness 100 mm

Along path-1 The above Fig. 6 illustrates the propagation of fire through the unexposed region with the distance from exposed region for the case (1) of exposure type and along the considered path-1. The distribution was found by varying the exposure temperatures from 100 to 400 °C for the slab thickness of 100 mm and the results of each exposure were compared. From the observation of these values, we can say that on the exposed surface (bottom), initially temperature decreases suddenly at higher exposed temperatures. Later the propagation was limited and gradually decreased at all exposed temperatures. When comparing the distributions in all three layers, the distribution pattern was similar in all layers except exposed surface. The propagation of fire was extended up to 300 mm distance from exposed region to unexposed region in both different paths. At certain places slabs were subjected to temperature exceeding the integrity criteria given in most of the codes for exposed temperature of 300 and 400 °C.

Along path-2 Similarly along path-1, the propagation of fire from exposed region for the case (1) exposure along path-2 was shown in Fig. 7 in three different layers as mentioned above. The comparison of these results points out that the sudden drastic decreases in temperature were more along path-2 than the path-1.but there was no such region as equal temperature in path-1.

3.1.2 Slab of Thickness 200 mm

Along path-1 To consider the variation in the propagation of fire due to the thickness of slab, a slab of thickness 200 mm was modelled as previous one. The
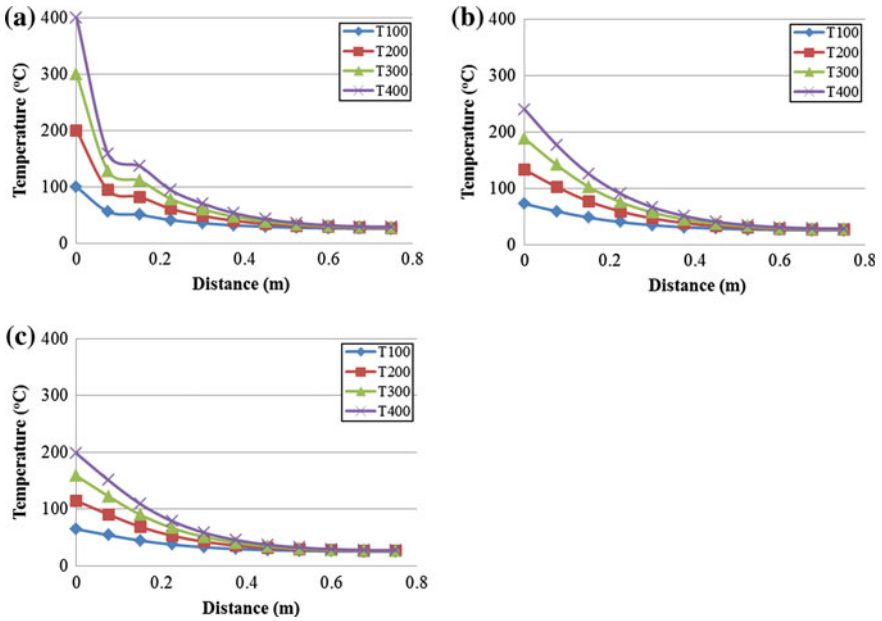
Fig. 6 Temperature distribution of 100 mm thick slab along path-1 for case (1) **a** bottom, **b** middle, **c** top
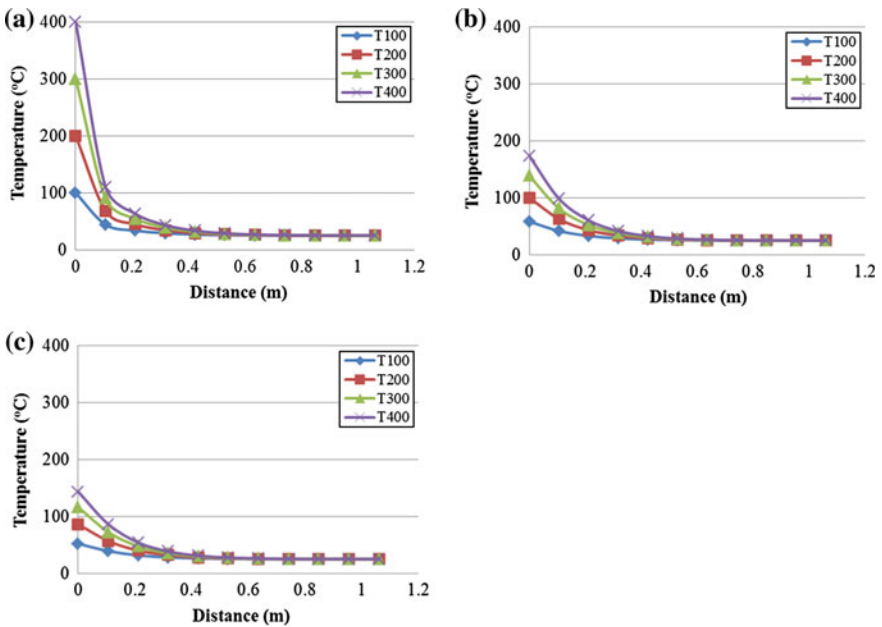
Fig. 7 Temperature distribution of 100 mm thick slab along path-2 for case (1) **a** bottom, **b** middle, **c** top

distribution was found along the two different paths in three different layers as mentioned above and compared these results with 100 mm thick slab. In this case, the intermediate layer (middle) lies at 100 mm from the exposed surface. But for previous slab, it was at 50 mm from exposed surface. From the comparison of these results with 100 mm thick slab, there is no variation in propagation on exposed surface. Whereas on the other layers, we observed similar type of distribution, but the temperature values are smaller than that in the 100 mm thick slab.

Along path-2 Similarly, the propagation of fire for the 200 mm depth slab was same as that of 100 mm slab. The distribution pattern was same in considered two different paths with irrespective of depth of slab. Suppose, if we consider a layer at same distance from the exposed surface for two different thick slabs, the temperature values were more for the 100 mm thick slab because, the unexposed surface was there to allow the convection of heat to atmosphere by air convection.

Case (2): **Fire at outer region of slab**

The temperature distribution was found out for two different thickness of the slab (100 mm and 200 mm) for the case (2) type of exposure. The temperature propagation along two considered paths was found on three different layers namely on the exposed surface (bottom), on the unexposed surface (top) and an intermediate layer at half of the depth of the slab (middle) as case (1) type of exposure.

3.1.3 Slab of Thickness 100 mm

Along path-1 The above Fig. 8 illustrates the propagation of fire through the unexposed region with the distance from exposed region for the case (2) of exposure type and along the considered path-1. The distribution was found by varying the exposure temperatures from 100 °C to 400 °C for the slab thickness of 100 mm and the results of each exposure were compared. From the observation of these values, we can say that on the exposed surface (bottom), initially temperature decreases suddenly at higher exposed temperatures than case (1) type of exposure. Later the propagation was limited and gradually decrease at all exposed temperatures. When comparing the distributions in all three layers, the distribution pattern was similar in all layers except exposed surface. The propagation of fire was extended up to 300 mm distance from exposed region to unexposed region in both different paths. Similarly as in case 1 of along path 1, here also 100 mm slab exceed the integrity criteria specified in various codes [4, 5, 8, 9].

Along path-2 Similarly as path-1, the propagation of fire along path-2 from exposed region for the case (2) type of exposure are shown in Fig. 9 for three different layers as mentioned above. The comparison of these results points out that the sudden drastic decreases in temperature were more along path-2 than the path-1. but there was no such region as equal temperature in path-1. In case (2) type of exposure, near to exposed surface temperatures are more than case (1) type of
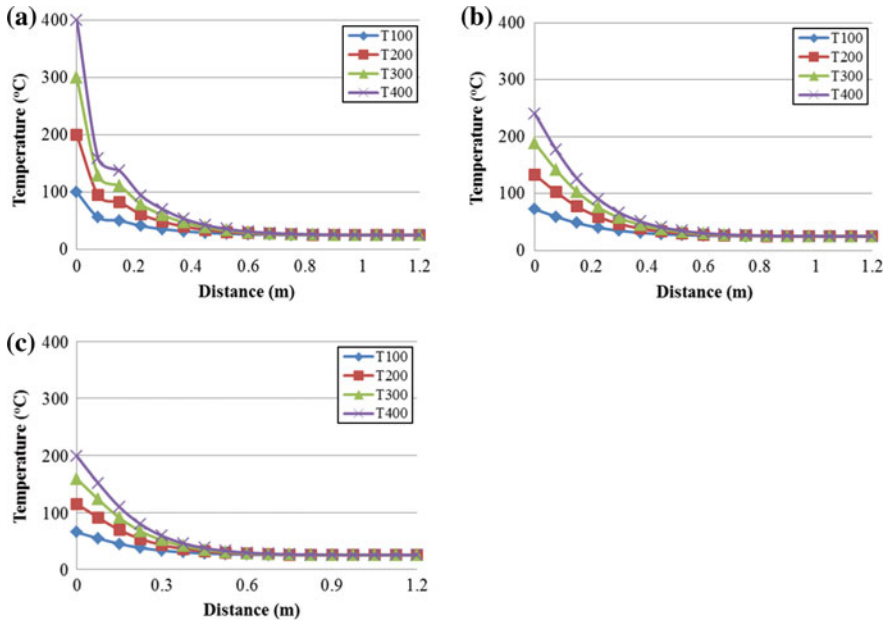
Fig. 8 Temperature distribution of 100 mm thick slab along path-1 for case (2) **a** bottom. **b** middle. **c** top
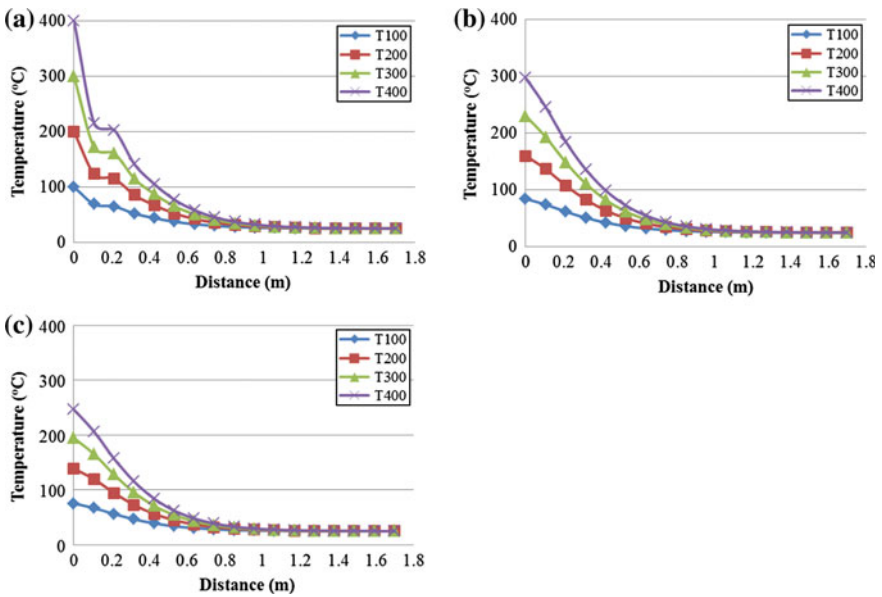
Fig. 9 Temperature distribution of 100 mm thick slab along path-2 for case (2) **a** bottom. **b** middle. **c** top

exposure. The propagation of fire was extended up to 300 mm distance from exposed region to unexposed region in both different paths as well as two different cases of exposure. The 100 mm slab exceed the integrity criteria specified in various codes for case2 along path2.

3.1.4 Slab of Thickness 200 mm

Along path-1 To consider the variation in propagation due to the thickness of slab, slab of thickness 200 mm was modeled as the previous case. The distribution was found along the three different paths in three different layers as mentioned above. From the comparison of these results with 100 mm thick slab, there is no variation in propagation on exposed surface whereas on the other two layers, we observed similar type of distribution.

Along path-2 Similarly, the propagation of fire for the 200 mm depth slab was same as that of 100 mm slab. The distribution pattern was same in considered two different paths with irrespective of depth of slab. Suppose, if we consider a layer at same distance from the exposed surface for two different thick slabs, the temperature values were more for the 100 mm thick slab because, the unexposed surface was allowed for convection of heat to atmosphere by air convection.

3.2 Thermal Strains

Whenever a reinforced concrete slab subjected to fire, the temperature of the slab rises. The temperature variation of slab induces thermal strains depending upon temperature. These thermal strains are maximum when slab was exposed to higher temperature. The induced thermal strains can be estimated by coupled temperature-displacement analysis in ABAQUS.

3.2.1 Slab of Thickness 100 mm

Similar to that of heat propagation, thermal strains are also estimated in the slab of depth 100 mm for two different cases of temperature exposures of 400 °C. These thermal strains were compared in three different layers (L1, L2, and L3) along two different paths (P1, P2) as shown in Fig. 10.

Figure 10 shows the comparison of thermal strains in three different layers for the case (1) exposure type and along two different paths individually from the center of slab to outer edge. The first constant region of strain represents the exposed surface in both the paths. It shows that the thermal strains were maximum at the exposed surface. When compared to path-1, the thermal strains near to the exposed surface are high along path-2. And these strains gradually decrease to minimum within the region of 300 mm distance.

Fig. 10 Thermal strains for 100 mm thick slab of case (1) exposure
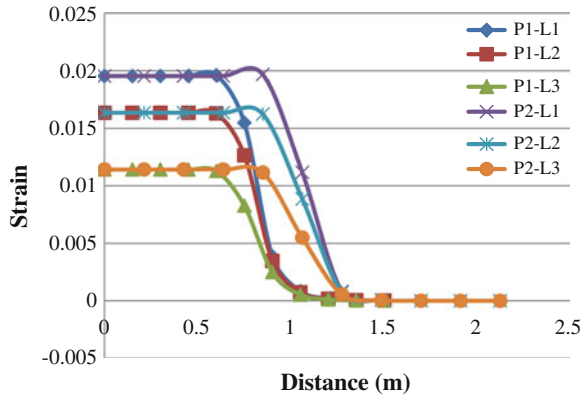
Fig. 11 Thermal strains for 100 mm thick slab of case (2) exposure
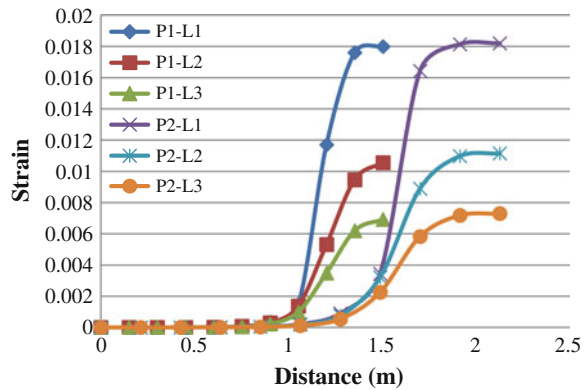
Figure 11 shows thermal strain comparison in three different layers for case (2) type of exposure along two different paths individually. Here, initially there is no strain in the unexposed region. These thermal strains gradually increases and reaches maximum. When compared to path-1, path-2 takes more distance to reach the maximum strains. When comparing the case (1) and case (2) exposures for 100 mm thick slab, there is more variation of strains along layer-3 than other layers in case (1). But, there is more variation along layer-2 and layer-3 than other layer in case (2).

3.2.2 Slab of Thickness 200 mm

Similarly, thermal strains also estimated in the slab of depths 200 mm for two different cases of exposures of 400 °C. These thermal strains were compared in different layers (L1, L2, and L3) along two different paths (P1, P2) as shown in Fig. 12.

Figure 12 shows the comparison of thermal strains in three different layers for the case (1) exposure type and along two different paths individually from the

Fig. 12 Thermal strains for 200 mm thick slab of case (1) exposure
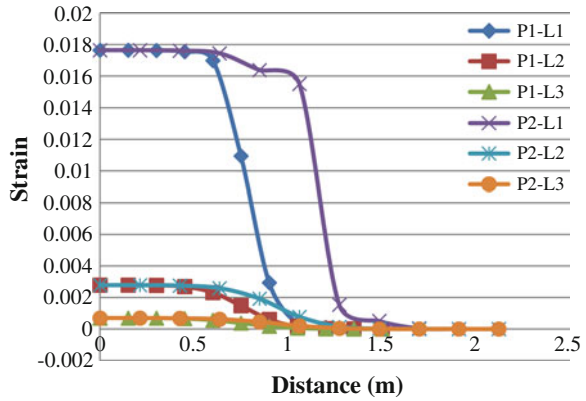
Fig. 13 Thermal strains for 200 mm thick slab of case (2) exposure
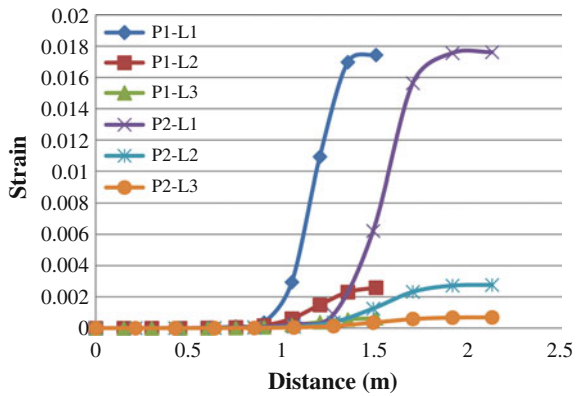
center of slab to outer edge. The first constant region of strain represents the exposed surface in both the paths. In the exposed region, there is more thermal strain in exposed surface than other two layers. It shows that the thermal strains were maximum at the exposed surface. When compared to path-1, the thermal strains near to exposed surface are high along path-2. And these strains gradually decrease to minimum within the region of 300 mm distance.

Similarly, the above Fig. 13 is the thermal strain comparisons for the slab of thickness 200 mm for two different cases of exposure along two different paths. From these graphs, the maximum strain in all layers for two different paths was same. From the comparison thermal strains for two different thick slabs, it was observed that the induced thermal strains are very less in unexposed layer and intermediate layer as compared to exposed layer due to less temperature variation. On the unexposed layer very minor amount of thermal strains are observed than other layers.

4 Conclusions

In this study behaviour of concrete slabs subjected to temperatures starting from 100 to 400 °C were studied for 4 h of duration using a FEM model in ABAQUS. Concrete slab thickness has been taken for studying the variation of temperature profiles. Two different thicknesses have been modeled using ABAQUS. In this study two different cases of exposures were considered to estimate the propagation of fire along two different paths. From the above parametric studies the major conclusions drawn out are as follows:

- It is observed that on the bottom surface (exposed) heat propagation was high as compared to other layers.
- On the other two layers (middle and top) has same pattern of distribution. but the temperature was found to be less when compared to the bottom surface.
- On the exposed surface, initially a sudden decrease of temperature was observed. Whereas on the other two conditions gradual decrease of temperature was observed.
- By the comparison of propagations for two different exposure conditions, we can say that the propagation of fire was limited up to 300 mm distance from exposed surface.
- The propagation of fire on any intermediate layer was same, but its magnitude differs from the exposed surface for both 100 and 200 mm thick slabs.
- The 100 mm thick slab for exposure of 300 and 400 °C found to exceed the integrity limit of most of the codes of unexposed surface
- The thermal strains induced were maximum near to the exposure and gradually decreases to minimum within the region of small distance.
- When the thickness of slab was high, the thermal strains induced in intermediate layers were very low as compared to in the exposed surface.

References

1. Bailey C (2002) Holistic behavior of concrete buildings in fire. Struct Build 152(3):199–212
2. Bailey CG, Toh WS (2007) Small-scale concrete slab tests at ambient and elevated temperatures. Eng Struct 29:2775–2791
3. Bailey CG, Toh WS (2007) Behaviour of concrete floor slabs at ambient and elevated temperatures. Fire Saf J 42:425–436
4. British Standard Institute (2004) The European standards. Design of concrete structures, part 1.1 general rules and rules for buildings. British Standard Institute, London. ENV 1992-1-1
5. British Standard Institute (2002) 1-The European standards. Design of the steel structures, part 1.1 general rules and rules for buildings. British Standard Institute, London. ENV 1993-1-1
6. ABAQUS 6.11 General purpose finite element analysis software Documentation
7. Cooke GME (2001) Behaviour of precast concrete floor slabs exposed to standardized fires. Fire Saf J 34:459–475
8. ISO (1975) Fire resistance tests. Elements of building construction, ISO 834, International Organization for Standardization, Geneva
9. ASTM Standards (1988) Standard test methods for fire tests of building construction and materials, in annual book of ASTM standards. 04, Designation: E 119-88, ASTM, pp 922–942

Bibliography

10. Arioz Omer (2007) Effects of elevated temperatures on properties of concrete. Fire Saf J 42 (2007):516–522
11. Terro MJ (1998) Numerical modelling of the behaviour of concrete structures in fire. ACI Struct J 95(2):183–193
12. Bailey CG, Ellobody E (2009) Whole-building behaviour of bonded post-tensioned concrete floor plates exposed to fire. Eng Struct 31:1800–1810
13. Luccioni BM, Figueroa MI, Danesi RF (2003) Thermo-mechanic model for concrete exposed to elevated temperatures. Eng Struct 25(2003):729–742
14. Allam SM, Rabeai HMF, Allam AG (2013) Behavior of one-way reinforced concrete slabs subjected to fire. Alexandria Eng J 52:749–761
15. Sangluaia C, Haridharan MK, Natarajan C (2012) Behaviour of reinforced concrete slab subjected to fire. Int J Comput Eng Res 3(1):195–206
16. Raveendra Babu N, Haridharan MK, Natarajan C [2013] Temperature distribution in concrete slab exposed to elevated temperature. Int J Eng Sci Invention, ISSN: 2319-6726
17. Kodur VKR, Baolin Yu, Dwaikat MMS (2013) A simplified approach for predicting temperature in reinforced concrete members exposed to standard fire. Fire Saf J 56 (2013):39–51
18. Moss PJ, Dhakal RP, Wang G, Buchanan AH (2008) The fire behaviour of multi-bay, two-way reinforced concrete slabs. Eng Struct 30:3566–3573
19. Bailey Colin G, Toh Wee Siang (2007) Small-scale concrete slab tests at ambient and elevated temperatures. Eng Struct 29(2007):2775–2791
20. Breccolotti M, Materazzi AL, Venanzi I (2006) Fire performance of HPLWC hollow core slabs. In: Proceedings of the SiF'06, the 4th international workshop for structures in fire, University of Averio, Portugal, May 2006, pp 587–598
21. Malhotra HL (1956) The effect of temperature on the compressive strength of concrete. Magine of Concr Res 8(23):85–94
22. Zoldners NG (1960) Effect of high temperature on concrete incorporating different aggregates. In: American Society of Testing Materials, 60/1960, 63rd annual meeting of the society 1960, pp 1087–1108
23. Gille M, Usmani A, Rotter M (2002) Bending and membrane action in concrete. In: Proceedings of the SiF'02, the 2nd international workshop for structures in fire, Christchurch, New Zealand, March 2002, pp 95–114
24. Cameron NJK, Usmani A (2002) Analytical solutions for floor slab in fire. In: Proceedings of the SiF'02, the 2nd international workshop for structures in fire, Christchurch, New Zealand, March 2002, pp 115–125
25. Bamonte P, Fernandez Ruiz M, Muttani A (2012) Punching shear strength of concrete at elevated temperature. In: Proceedings of the SiF'12, the 7th international workshop for structures in fire, Zurich, Switzerland, June 2012, pp 689–698
26. Rotter JM, Sanad AM, Usmani AS, Gillie M (1999) Structural performance of redundant structures under local fires. In: Distribution in concrete slab, Edinburgh, pp 165–181
27. Schiender U (1988) Concrete at high temperature—a general review. Fire Saf J 13:55–68
28. Huang Z, Burgess I, Plank R, Bailey CG (2006) Behaviour of reinforced concrete structures in fire In: Proceedings of the SiF'06, the 4th international workshop for structures in fire, University of Averio, Portugal, May 2006, pp 561–572
29. BS 476: Part 20: 1987 (1987) Fire tests on building materials and structures, method for determination of the fire resistance of elements of construction (general principles), British Standards Institution, London
30. BS 476: Part 21: 1987 (1987) Fire tests on building materials and structures, Method for determination of the fire resistance of load bearing elements of construction, British Standards Institution, London, UK (1987)

31. BS 476: Part 22: 1987 (1987) Fire tests on building materials and structures, Method for determination of the fire resistance of non-load bearing elements of construction, British Standards Institution, London, UK
32. Eurocode 2 (2004) Design of concrete structures-part 1.1: General rules—rules for buildings, Commission of the European communities, Brussels, Belgium
33. Eurocode 2 (2004) Design of concrete structures-part 1.2: General rules—structural fire design, Commission of the European communities, Brussels, Belgium
34. ISO Fire resistance tests (1975) Elements of building construction, ISO 834, International Organization for Standardization, Geneva
35. SP-24 Explanatory Handbook on Indian Standard Code of Practice for Plain and Reinforced Concrete, IS-456-1978, Bureau of Indian Standards

Experimental Investigations on Behaviour of Shear Deficient Reinforced Concrete Beams Under Monotonic and Fatigue Loading

Nawal Kishor Banjara, K. Ramanjaneyulu, Saptarshi Sasmal and V. Srinivas

Abstract In the present study, investigations were carried out on reinforced concrete (RC) beams under monotonic and fatigue loading. Experimental study consists of the evaluation of the response of RC beam without and with the shear deficiency. Both types of specimens were tested under monotonic loading using four point bending set up. Under monotonic loading shear deficient RC rectangular beams clearly depicted the shear failure pattern and confirmed the expected response. Further, shear deficient RC beams were investigated under fatigue loading and three different load ranges were adopted. Using the results obtained from the study, fatigue characterisation of shear deficient reinforced concrete beams is carried out and the influence of load range during fatigue load is studied. It is found that fatigue remaining life of the RC component significantly depends on the applied load range. It is also observed from the present study that the responses of the structures change considerably under the fatigue loading than that under monotonic loads. So, any interpretation of structural behaviour parameters of RC structures from responses obtained from static loading would lead to erroneous design. The study would help in understanding the fatigue behaviour of RC structural components in various stress range which is very common in bridges.

Keywords Experimental study · Monotonic loading · Fatigue loading · Stress range · Structural behavior

N.K. Banjara (✉) · K. Ramanjaneyulu
Academy of Scientific and Innovative Research, CSIR Campus,
Taramani, Chennai 600 113, India

N.K. Banjara · K. Ramanjaneyulu · S. Sasmal · V. Srinivas
CSIR-Structural Engineering Research Centre, CSIR Campus,
Taramani, Chennai 600 113, India

1 Introduction

In recent years, there has been growing awareness about the problems associated with existing old bridges, most of which have deteriorated or may not be adequate to meet the current demand. Fatigue loading due to the traffic with various types, arrangements, speeds and loads is one such loading, bridges are subjected. Concrete is often used in structures which are subjected to cyclic loads. Bridges over highways and railways suffer cyclic loads from vehicles which cause the structures to fail, but the failure of these structures and their components due to fatigue loads are far early than their original strength. Structural failure refers to the loss of structural integrity, which is the loss of the load-carrying capacity of a component or member within a structure, or of the structure itself. When a material is stressed to its strength limit, structural failure is initiated, leading to excessive deformations and fracture. It should be taken care that, a localized failure do not cause immediate or more importantly progressive collapse of the entire structure for any well designed system. Basic information about the fatigue behaviour of concrete specimens is represented by S-N curve which provided the number of cycles to failure versus stress amplitude. The number of cycles to failure is estimated when stress amplitude reaches the ultimate stress of concrete. When the stress amplitude is small compared to the ultimate stress, the number of cycles to failure is very high, and many days are required to carry out such a fatigue test. Fatigue in concrete was recognized rather late, in comparison to steel.

Concrete is a non-homogenous material and its fatigue resistance is influenced by many different factors e.g. moisture content, cement/water ratio and load effects such as load frequency and maximum load level. When the micro-cracks propagate, the fatigue process starts, which is a progressive process. At the beginning of the loading the propagation of the micro-cracks is rather slow. As loading continues, the micro-cracks will proceed further and lead to macro-cracks. The macro-cracks determine the remaining fatigue life caused by stress. During the fatigue life of reinforced concrete structures under flexure, the contribution of concrete in tension between cracks is degraded; therefore tensile stresses are mainly supported by reinforcing steel and compression by concrete in the greatest length of the element. Because of that, it is important to understand the fatigue of concrete in compression and its influence in the response of the whole reinforced section. A structure can be deficient in shear, flexure or torsion, depending on the geometry and loading conditions to which it is subjected. Depending on the type of loading and other conditions to which it is subjected, the deterioration of the structural member will get affected by several factors. In several occasions, existing reinforced concrete beams have been found to be deficient in shear. Shear deficiencies occur because of several reasons such as insufficient shear reinforcement or reduction in steel area due to corrosion, increased service load, and defects. Maintenance and upgrading of existing structures plays a major role in extending the service life of any kind of structures. Apart from structural deterioration due to aging, errors made during

design and construction phase, new and increased load demands and new design standards, all contribute to the deficient behavior of structures.

Wang and Zhang [1] investigated the practical application of composite materials for retrofitting, by studying the behaviour of FRP plated RC bridge girders under cyclic loading. The response of plated beams subjected to cyclic and fatigue loading, to service and ultimate loads was observed. Strengthening was done using CFRP plates for flexure and GFRP U strips for shear in order to increase the service load-carrying capacity, ensuring controlled failure at ultimate limit state. Yi et al. [2] investigated the performance of RC beams with corroded reinforcement under fatigue loading. Results shown that an increase in the corrosion degree of steel reinforcement decreased the fatigue life of the beams and caused them to collapse in a brittle failure mode. Static and accelerated fatigue testing performance of nine reinforced concrete beams strengthened with different number and configuration of CFRP sheets was studied both experimental and analytical by Al-Rousan and Issa [3]. The beams were tested for the different stress ranges. The stress ranges shown a significant effect on the permanent deflection at mid-span. Cyclic fatigue loading produced a time-dependent redistribution of the stresses that lead to a sudden drop in concrete stresses and a mild increase in steel and CFRP sheet stresses as fatigue life was exhausted. A study was carried out by Suresh et al. [4], on fatigue strength of high performance cement concretes subjected to flexural loading. Static flexural strength tests were conducted to determine the static failure loads on prism specimen. From the experimental studies carried out, the number of load repetitions to failure on the concretes under study was determined for three stress ratios. From the data obtained S-N curves were developed using linear regression models considering log normal distribution. Dong et al. [5] carried out a study on the shear fatigue behaviour of RC beams made with the normal concrete strengthened with FRP (CFRP or GFRP) sheets and investigated the effectiveness of FRP sheets on the fatigue behaviour and their contributions to the ultimate strength of ordinary RC beams. Sang-Wook et al. [6], investigated the shear performance of an RC beam strengthened in shear with externally bonded carbon fiber-reinforced Polymer (CFRP) strips, subjected to a cyclic loading for 2 million cycle's at 1 Hz. The stress level in the stirrups caused by the cyclic loading used in this study was higher than those typically used in fatigue studies, which could have caused the yielding of some stirrups from the beginning of cyclic loading. The flexural cracking behaviour of plain concrete subjected to monotonic loading and cyclic loading was studied by Hamad et al. [7]. Four point bending tests on simply supported un-notched prisms were conducted. Cracking process was monitored using a digital image correlation system. Flexure fatigue behaviour of self-compacting rubberized concrete with and without steel fibres were studied by Ganesan et al. [8]. The variables included in this study were different values of fine aggregate by shredded rubber (15 and 20 %) and volume fraction of steel fibres (0.5 and 0.75 %). A total of 60 prism specimens were tested under fatigue loading considering maximum stress levels ranging from 90 to 60 % of the static strength. The number of cycles to failure of specimen was noted as fatigue life N. The tests were terminated as and when the failure of the

specimen occurred or number of cycles exceeded 2 million. Fatigue performance of reinforced concrete (RC) T-beams strengthened in shear with Carbon Fiber Reinforced Polymer (CFRP) composite was carried out by Farghal [9]. Experiments were conducted on RC beams with and without CFRP sheets bonded on their web surfaces and subjected to static and cycling loading. The obtained results showed that the strengthened beams could survive 1 million cycles of cyclic loading (=50 % of maximum static load) with no apparent signs of damage (pre-mature failure) demonstrating the effectiveness of CFRP strengthening system on extending the fatigue life of structures.

From the in-depth review of the existing knowledge and progress in shear and flexural deficient structures, it is found that many research works have been reported on behaviour of shear deficient or strengthened structures under monotonic loading and flexural deficient structure under fatigue loading, but investigations on the behaviour of shear deficient reinforced concrete structure under fatigue loading are very scanty. So, toward this, an experimental study has been carried out to understand the behaviour mechanism of shear deficient beams subjected to both monotonic and fatigue loading.

2 Experimental Study

The RC beams were divided into four types, a control beam and with various degrees of shear deficiency (such as 20, 40 and 60 % deficient) with stirrups spacing of 275, 375, 500 and 750 mm c/c respectively. The beams are of 150 mm width, 200 mm depth and 1,800 mm length with adequate longitudinal reinforcement against flexure. The effective span of the beam was limited to 1,500 mm. Concrete mix was designed for the characteristic compressive strength of 30 MPa. The constituents of the mix were ordinary Portland cement, natural sand and gravels with 10 and 20 mm aggregate. Cement, water, fine aggregate and coarse aggregate was mixed in the ratio 1:0.5:2.25:2.35. For all the RC beams, three numbers of 12 mm diameter bars were provided on the tension face, two numbers of 8 mm diameter bars were used as hanger bars on the compression face and for shear reinforcement as shown in Fig. 1. A concrete cover of 25 mm was used.

2.1 Instrumentation Details

Prior to the casting, electrical resistance strain gages of 5 mm size were affixed on both flexural and shear reinforcements. On the cast specimen, 60 mm gauge length electrical resistance strain gauges were pasted on the concrete surface in order to measure concrete strains during loading. The beam deflection was measured using Linear Variable Displacement Transducer (LVDT). Three LVDT's were used at
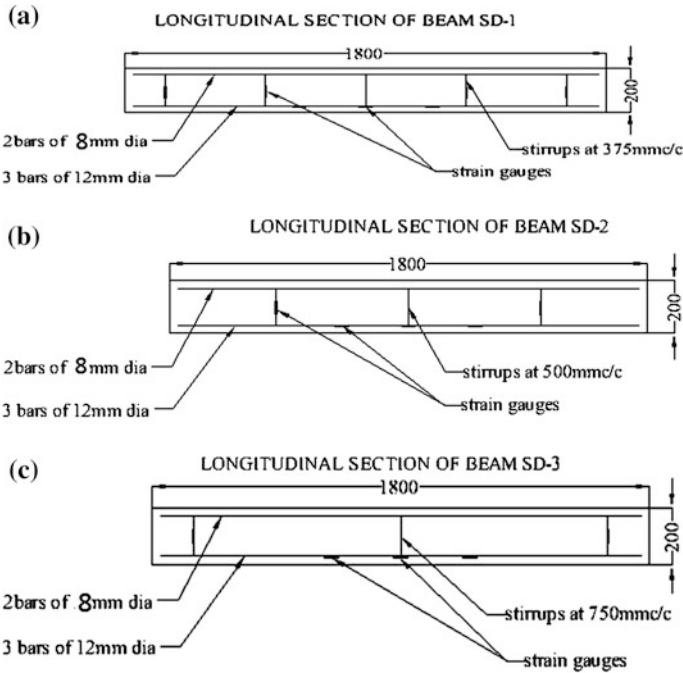
Fig. 1 Cross-section and reinforcement arrangements in beams with varying shear deficiencies **a** SD-1, **b** SD-2 and **c** SD-3

mid span, one-thirds and two-thirds of the span. Specimens were white washed and grids were marked on two sides of surface of beam. The size of grids is 50 mm × 50 mm to get the crack location during loading.

3 Investigations Under Monotonic Loading

Initially, tests were conducted on simply supported RC beams under monotonic loading up to failure to investigate the deflections, strains on the steel rebar, stirrups, and concrete, crack behaviour as well as shear capacity. The beams were loaded with the rate of loading 0.2 mm/min up to failure. The test setup is shown in Fig. 2. Failure of beams occurred by formation of shear cracks from the support towards the loading point and mild crushing of concrete at the compression face of the beam.

Under monotonic loading, the beams initially developed vertical flexure cracks from the tension side. This leads to the initiation of development of flexural cracks and a reduction in the flexural stiffness of the beam. With increase in load, new

Fig. 2 Loading test setup
of RC beams
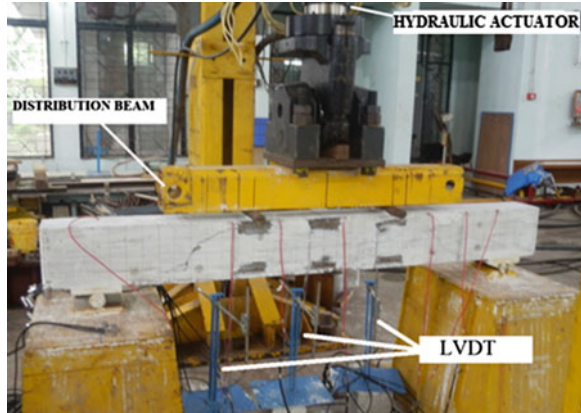
cracks were found to develop, while existing cracks propagated vertically towards
the compression zone. First crack load, ultimate load and deflection of the beams
are given in Table 1. Shear cracks were observed near the supports at loads
approximately 40 % of the maximum load for all deficient beams and at 60 % of
maximum load for the control beam. The diagonal shear cracks propagated from the
supports towards the loading point, until the beam failed. Shear deficient beams
which were tested showed a typical shear failure, with the sudden formation of
major diagonal tension crack, which extended from supports towards the loading
points as shown in Fig. 3. Load versus deflection plots for all the beams are shown
in Fig. 4. It was observed that in the control beam yielding of longitudinal bars
occurred and but in the shear deficient beams, beams failed before yielding of
longitudinal bars due to failure of concrete. At failure of control beam, strain in
longitudinal bar was found to be around 3,000 microstrain and in concrete it was
around 4,000 microstrain. But in shear deficient RC beams, strain in longitudinal
bar was found to be below 2,000 microstrain and in the concrete it was found to be
more than 4,500 microstrain.

Table 1 First crack load, ultimate load, deflection and failure mode

Type of beam	First crack load (kN)	Ultimate load (kN)	Deflection (mm)	Failure mode
Control	18.344	97.62	12.95	Shear/flexural
SD1	12.68	83.86	4.90	Shear failure
SD2	12.20	77.63	4.43	Shear failure
SD3	9.04	64.15	4.04	Shear failure
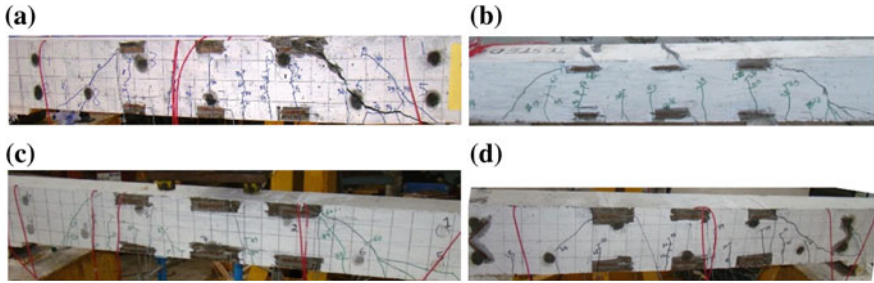
Fig. 3 Failure patterns of tested beams. **a** Control beam, **b** SD1, **c** SD2, **d** SD3

Fig. 4 Load versus deflection plot for all type of beams
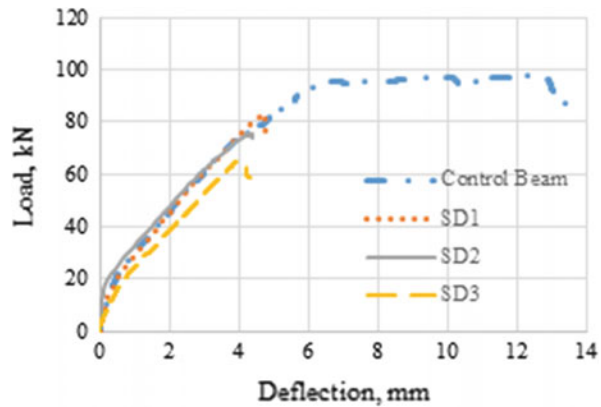
4 Investigations Under Fatigue Loading

From the study carried out under monotonic loading, the load carrying capacity and failure mode of the beams were assessed. Using load carrying capacity of the shear deficient beams, range of load under fatigue loading was fixed. Shear deficient beams (such as 20 % of shear deficiency, stirrups spacing 375 mm c/c) were tested under fatigue loading with three different load ranges i.e., maximum load of 65, 75 and 85 % of ultimate load (P_u) and minimum load of 20 % of ultimate load (P_u). Instrumentation used during static testing, was also used under the fatigue loading. Due to fatigue loading, sudden degradation on the displacement in the beam occurred for higher range as compared to lower range of loading. Under the fatigue load, it was found that due to loading range and level of deficiency, considerable variation in the fatigue life (N) of the specimen were found. RC beam with shear deficiency was tested for load range of 20–65 % of ultimate load under fatigue loading as shown in Fig. 5a, b. Beams withstood the load up to 1 million (10^6) cycles and not failed after million cycles also, under 65 % of ultimate load. So, after 1 million cycles test was stopped and tested under monotonic loading as shown in
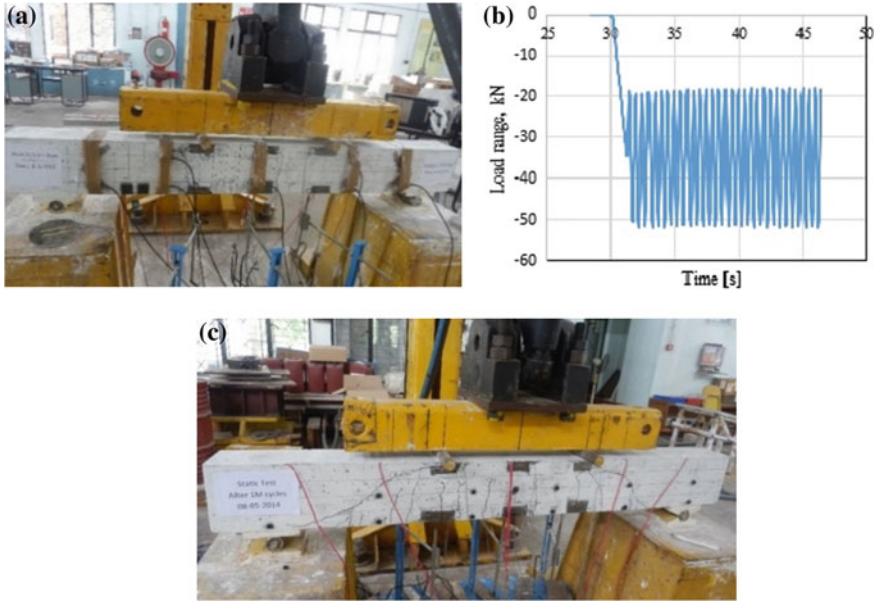
Fig. 5 Testing of shear deficient beam under fatigue loading. **a** Under fatigue loading. **b** Loading range. **c** Static test after 1 million cycles

Fig. 6 Testing of shear deficient beam under monotonic loading before and after 1 million cycles
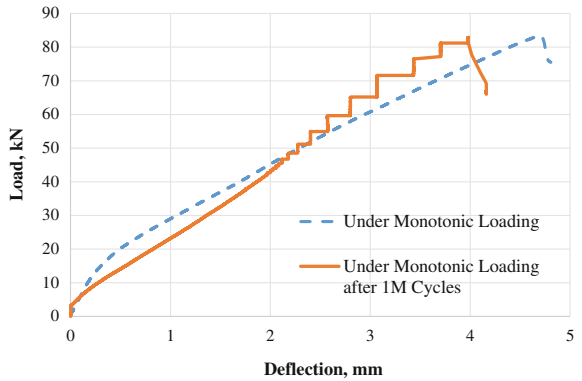
Fig. 5c. Load deflection curve of tested beam under monotonic loading before and after 1 million of cycles were shown in Fig. 6. It was observed that after 1 million cycles there were not much changes occurred in the load carrying capacity of the beam. RC beams failed very early with very less number of cycles when subjected higher loading range such as 85 % of ultimate load.

5 Conclusions

Control and shear deficient beams tested under monotonic load failed under shear/flexural and shear mode. It is found that in RC structures shear failure occurs sudden or brittle kind of failure under monotonic loading. Shear deficient beams are failed before yielding of reinforcement bars. Fatigue characterisation of the deficient reinforced concrete beams is carried out and the influence of range of fatigue load is also brought out. It is found that under fatigue loading, life of the RC component reduces based on the degree of shear deficiency and applied load range. It is found that under the fatigue loading, RC beams can sustain more number of cycles of lower range of loading and vice versa for higher range. It is also observed from the present study that the responses of the structures change considerably under the fatigue loading than that under static or monotonic loads. The experimental studies would help in designing effective retrofitting schemes for shear deficient structural components subjected to fatigue loading.

References

1. Wang J, Zhang C (2008) Nonlinear fracture mechanics of flexural-shear crack induced debonding of FRP strengthened concrete beams. Int J Solids Struct 45(10):2916–2936
2. Yi W-J, Kunnath SK, Sun X-D, Shi C-J, Tang F-J (2010) Fatigue behavior of reinforced concrete beams with corroded steel reinforcement. ACI Struct J 107(5):526–533
3. Al-Rousan R, Issa M (2011) Fatigue performance of reinforced concrete beams strengthened with CFRP sheets. Constr Build Mater 25:3520–3529
4. Suresh KKS, Kamalakara GK, Sagar K, Amarnath MS (2012) Fatigue analysis of high performance cement concrete for pavements using the probabilistic approach. Int J Emerg Technol Adv Eng 2(11):640–644
5. Dong JF, Wang QY, Guan ZW (2012) Structural behavior of RC beams externally strengthened with FRP sheets under fatigue and monotonic loading. Eng Struct 41:24–33
6. Sang-Wook B, Michael M, Amir M, Abdeldjelil B (2013) Behavior of RC T-beams strengthened in shear with CFRP under cyclic loading. J Bridge Eng (ASCE) 18(2):99–109
7. Hamad WI, Owen JS, Hussein MFM (2013) An efficient approach of modelling the flexural cracking behaviour of un-notched plain concrete prisms subject to monotonic and cyclic loading. Eng Struct 51:36–50
8. Ganesan N, Bharati Raj J, Shashikala AP (2013) Flexural fatigue behavior of self-compacting rubberized concrete. Constr Build Mater 44:7–14
9. Farghal OA (2014) Fatigue behavior of RC T-beams strengthened in shear with CFRP sheets. Ain Shams Eng J. http://dx.doi.org/10.1016/j.asej.2014.03.007. Available online 21 April 2014

Reverse Cyclic Tests on High Performance Cement Concrete Shear Walls with Barbells

N. Ganesan, P.V. Indira and P. Seena

Abstract Behaviour of reinforced conventional concrete (CC) and reinforced high performance cement concrete (HPC) squat and slender shear walls with barbells are investigated. The aspect ratios selected for the shear walls were 1 and 2.75. The specimens were subjected to quasi-static lateral reverse cyclic loading until failure. The grade of concrete used was M60. The mix proportion of conventional concrete (CC) was obtained as per ACI 211.4. In order to obtain a mix proportion for high performance concrete (HPC), the guidelines given by Aitcin which is a modified version of ACI 211.1 was used. The values of longitudinal and transverse reinforcement ratio used in the walls were 0.57 and 0.18 %, respectively for squat shear walls and 0.47 and 0.63 %, respectively for slender shear walls. The observed failure mode in squat shear wall was by shear and in slender shear wall, it was by flexure. The performance based parameters such as strength, stiffness degradation, energy dissipation capacity and ductility were obtained and the results are presented.

Keywords Barbells · High performance concrete · Reverse cyclic load · Stiffness degradation · Squat shear wall · Slender shear wall · Web reinforcement ratio

1 Introduction

The use of high performance cement concrete (HPC) in the construction of earthquake-resistant structures, long-span bridges, off-shore structures, nuclear power plants, and other mega-structures generally result in the reduction in size and hence

N. Ganesan (✉) · P.V. Indira · P. Seena
Department of Civil Engineering, National Institute of Technology Calicut, Kozhikode, India
e-mail: ganesan@nitc.ac.in

P.V. Indira
e-mail: indira@nitc.ac.in

P. Seena
e-mail: seenajiju17@gmail.com

leads to lighter and cost-effective structures. This brand of concrete has enhanced compressive strength, stiffness and durability. Other characteristics include almost no paste-aggregate transition zone, higher modulus of elasticity, very low permeability, exceptional abrasion resistance, outstanding resistance to freeze-thaw cycles, very low creep and high flexural strength [5].

Shear walls are commonly used to resist the actions imposed on buildings due to earthquake ground motions. Shear walls can be classified based on their overall height-to-length ratio known as the aspect ratio. Walls with an aspect ratio greater than two are usually referred to as slender shear walls that exhibit flexural behaviour. Slender shear walls are quite common in tall buildings. Squat shear walls are defined as walls with an aspect ratio smaller than or equal to one. The mode of deformation in this type of wall is dominated by shear. The main application of squat shear walls are in residential buildings, parking structures, industrial buildings, nuclear power plants, and also in highway overpasses and bridge abutments. The types of failures observed in squat shear walls, subjected to lateral loading are diagonal tension failure, diagonal compression failure (or web crushing and/or splitting failure), and sliding shear failure at the base of the wall. Most commonly used shear walls are symmetrical sections like rectangular and barbell shaped. Flanged shear walls are asymmetrical wall sections that are also often used. When a shear wall is provided monolithically between two columns a barbell shape results and which increases the strength and behaviour of the wall significantly [17] (Wallace et al. 2012).

Review of literature indicates that numerous studies were conducted in the past to study the strength and behaviour of normal concrete slender shear walls [8, 13, 15–18, 20, 21]. The major aim of these studies had been to investigate the influence of various parameters such as aspect ratio of wall, shape, axial load ratio, shear stress demand, horizontal and vertical reinforcement ratio, and compressive strength of concrete on the behaviour of shear walls. Even though several studies on reinforced concrete (RC) shear walls have been done in the past, only limited information is available on the strength and behaviour of reinforced high performance concrete (HPC) shear wall. Hence, an experimental investigation was undertaken to evaluate the strength and behaviour of HPC squat and slender shear walls with barbells and compare the same with reinforced conventional concrete (CC) shear walls with barbells under reverse cyclic loading.

2 Experimental Programme

The experimental programme consisted of casting and testing of four shear walls with barbells made up of CC (CCW) and HPC (HPCW) under quasi-static lateral reversed cyclic loading. Out of these, two specimens were squat shear walls and the remaining two were slender shear walls.

2.1 Materials

The materials consist of (i) ordinary Portland cement (OPC) of 53 grade conforming to IS 12269-1987 (reaffirmed 2004) [12] (ii) fine aggregate conforming to grading zone III of IS 383-1970 (reaffirmed 2002) [11] and having a specific gravity of 2.52, and (iii) coarse aggregate of 12.5 mm maximum size and having specific gravity of 2.80. The supplementary cementitious materials used were fly-ash and silica fume. Fly-ash was obtained from Mettur Thermal Power Plant, Tamil Nadu that conforms to ASTM C 618-2003 [7] and silica fume from ELKEM India (P) Ltd., Navi Mumbai conforms to ASTM C 1240-2005 [6]. Super-plasticizer (Conplast430) was used as a chemical admixture. The reinforcing steel consisted of high yield strength deformed bars (HYSD) of Fe 415 grade.

The longitudinal and transverse reinforcement for squat shear walls consist of 6 and 4 mm diameter HYSD bars, respectively in the form of rectangular grid and placed in two layers. In the case of slender, shear walls both reinforcement consist of 8 mm diameter HYSD bars in the form of rectangular grid and placed in two layers. Because of the large overturning effects caused by horizontal earthquake forces, edges of the shear wall experience high compressive and tensile stresses. To avoid this, special boundary elements were provided at the edges. The main longitudinal reinforcement, provided in the boundary region of squat shear wall was 1.13 % of the area of cross-section of the boundary element and provided over a width of 100 mm at the boundary of the element on each side. In slender shear wall the longitudinal reinforcement, provided in the boundary region was 1.19 % of the area of cross-section of the boundary element and provided over a width of 130 mm at the boundary of the element on each side. The nominal dimension of the specimens, together with the details of reinforcement is shown in Fig. 1.

2.2 Details of Mix Proportioning

The HPC used in this study was proportioned to attain a compressive strength of 60 MPa. Mix design was done based on the guidelines given in ACI 211.1 [1] modified by Aitcin [4]. The mixes were obtained by replacing 20 % of cement mass by fly-ash and 8 % cement mass by silica fume. The water-binder (w/b) ratio considered was 0.29. The same mix proportions were maintained for all the mixes. Conventional concrete was designed for a characteristic compressive strength of M60 grade as per ACI 211.4 [2]. The HPC mix proportion for M60 concrete is given in Table 1.
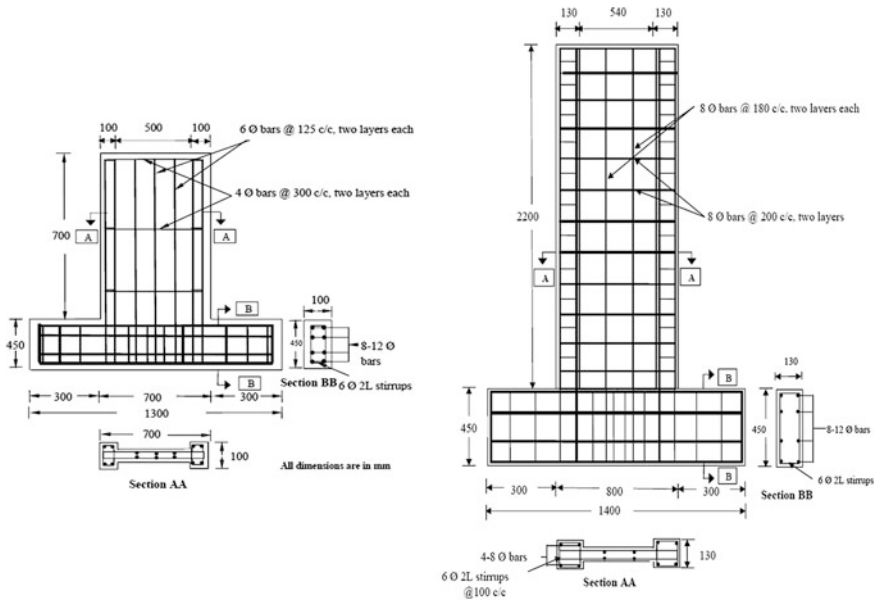
Fig. 1 Geometry and reinforcement details of shear wall specimens

Table 1 HPC mix proportions (kg/m^3)

Cement	Fly-ash	Silica fume	Sand	Coarse aggregate	Water	Super-plasticizer
405	110	45	600	1,041	156	11.6

2.3 Test Specimen

The experimental work consists of casting and testing of two squat shear walls with an aspect ratio of one and two slender shear walls with an aspect ratio of 2.75. The walls had a barbell-type cross-section with thin webs and heavily confined boundary elements. The overall dimensions of squat and slender shear walls were 700 mm × 700 mm × 60 mm and 2,200 mm × 800 mm × 80 mm, respectively. The dimensions of the barbells provided for squat and slender shear walls were 100 mm × 100 mm and 130 mm × 130 mm, respectively. To provide fixity at the bottom, a base block was constructed monolithically with the shear walls. The specimens were designed and detailed according to the seismic provisions of ACI 318-2008 [3]. The details of the specimens are summarised in Table 2.

Table 2 Details of specimens

Specimen designation	Type of shear wall	Aspect ratio of shear wall (*H/L*)	Longitudinal reinforcement ratio in web ρ_l (%)	Transverse reinforcement ratio in web ρ_t (%)
CCBW1	Squat	1	0.57	0.18
HPCBW2		1	0.57	0.18
CCBW3	Slender	2.75	0.47	0.63
HPCBW4		2.75	0.47	0.63

2.4 Casting of Specimens

For the construction of wall specimens, a specially designed plywood mould was used. The mould was fabricated in such a way that it could be easily dismantled and assembled for repetitive use and also the wall and its base block can be cast monolithically. The specimens were cast horizontally on a level floor in the Structural Engineering Laboratory. Required numbers of bolt holes of 50 mm diameter were also provided in the base block of the wall corresponding to the position of holes in foundation block. Figure 2 shows the reinforcement cage placed in the mould for squat and slender shear walls.
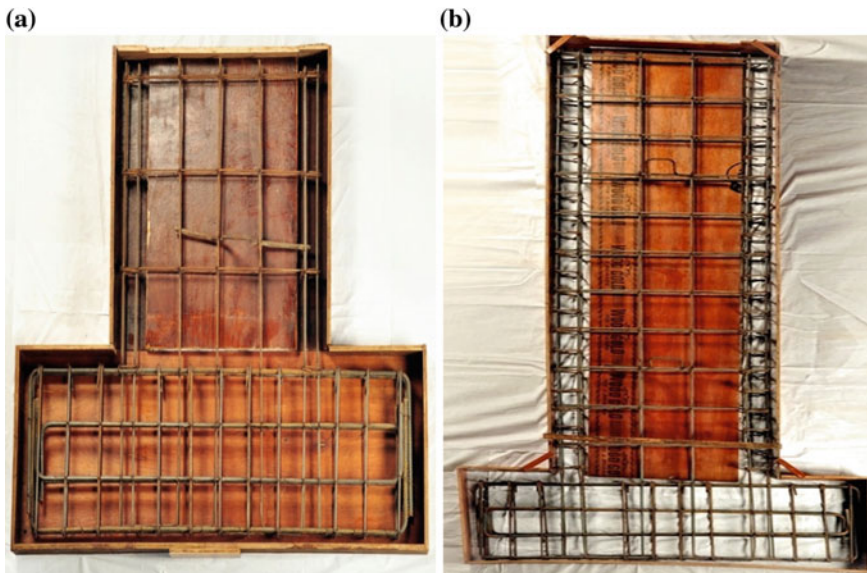
Fig. 2 Reinforcement cage in mould. **a** Squat shear wall. **b** Slender shear wall

3 Test Set up and Instrumentation

Double-acting hydraulic jacks of capacities 250 and 100 kN were used for applying lateral reverse cyclic loads for squat and slender shear walls, respectively. Linear variable displacement transducer (LVDT) having 300 mm travel and a least count of 0.01 mm was used for monitoring the in-plane horizontal displacement at the top of the wall. A data acquisition system was used for measuring the displacements continuously. A load cell of 250 and 100 kN capacities were used to measure the applied load accurately. Load cell readings were measured from a load indicator. The application of push and pull cyclic loading was done on the specimen using an arrangement consisting of mild steel rods with 25 mm diameter, threaded on both ends and connected to mild steel channels and fixed to the hydraulic jacks through load cells for the forward and reverse application of loads. The specimen was inserted into the foundation block and connected through the holes on the web portion of the foundation using 50 mm diameter mild steel rods. Figure 3 shows the photograph of the test set up.

3.1 Testing of Wall Specimens

The walls were subjected to quasi-static lateral reversed cyclic loading until failure. The squat and slender shear walls were incrementally loaded with hydraulic jacks having capacity of 250 and 100 kN, respectively. One cycle of loading consisted of
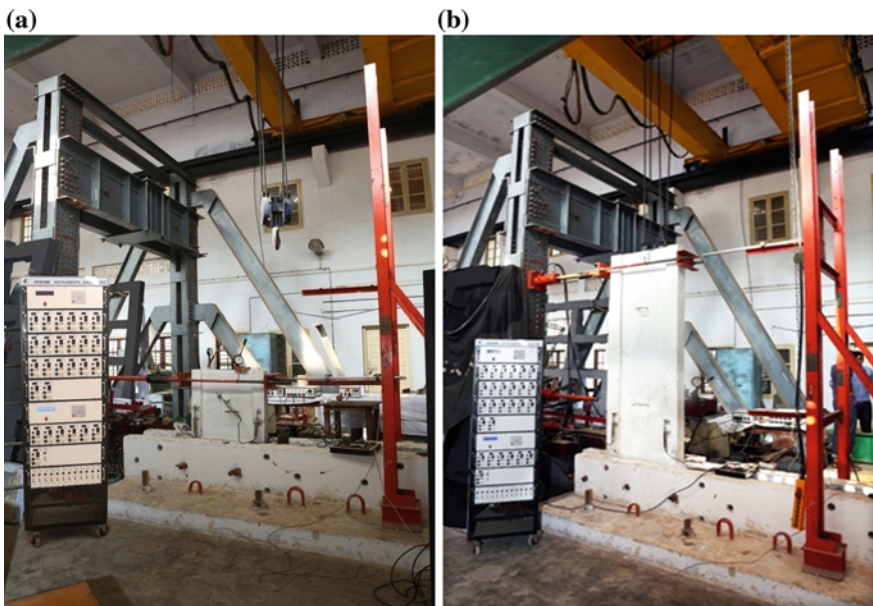
Fig. 3 Photograph of the test setup. **a** Squat shear wall. **b** Slender shear wall
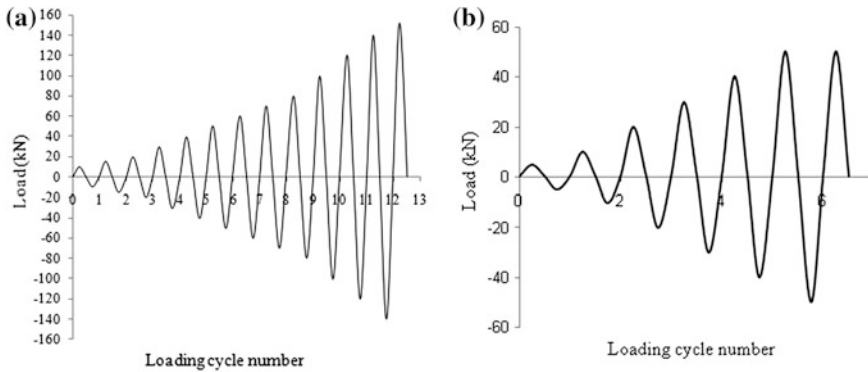
Fig. 4 Loading history. **a** Squat shear wall. **b** Slender shear wall

both forward and reverse cycles and after each cycle, the amplitude of loading was increased. This process was continued until lateral failure occurred. The loading history for the specimens consist series of stepwise increasing loading cycles as shown in Fig. 4.

4 Results and Discussions

4.1 Cracking Process and Failure Mode

Both walls exhibited a hysteretic behaviour and the observed failures in squat and slender shear walls were by flexure and shear, respectively. The HPC shear walls shows a dense pattern of cracks than CC shear walls. For all the specimens cracks initially appeared near the bottom of the walls. For squat shear walls as the horizontal load reaches 60 % of its maximum load significant inclined cracks initiated from the boundary element and it penetrated deeply into the web. At the failure, a major crack formed between the interface of wall foundation and web. The CCBW1 squat shear wall failed during 12th cycle at a load of 145 kN and HPCBW2 squat shear wall also failed in 12th cycle at a load of 152 kN. In slender shear walls, when the horizontal load reaches 47 % of its maximum load, horizontal cracks initiated from the boundary element of wall and after that it propagates to the wall web. Further loading caused new flexural cracks developed in the bottom one third of the wall. The CCBW3 slender shear wall failed during 6th cycle at a load of 53.5 kN and HPCBW4 slender shear wall also failed in 6th cycle at a load of 55 kN. Details of test results are given in Table 3. It may be noted from Table 3 that the first crack load of HPCBW squat shear wall is 1.14 times higher than the CCBW squat shear wall. The first crack load HPCBW slender shear wall is 1.12 times higher than the CCBW slender shear wall. Figure 5 shows the photograph of tested specimens.

Table 3 Experimental results

Specimen	Type of shear wall	First crack load (kN)	Ultimate load (kN)	Displacement corresponding to ultimate load (mm)	Type of failure
CCBW1	Squat	37.20	145.00	24.86	Shear
HPCBW2		42.50	152.00	26.86	
CCBW3	Slender	15.30	53.50	51.90	Flexure
HPCBW4		17.10	55.00	52.10	
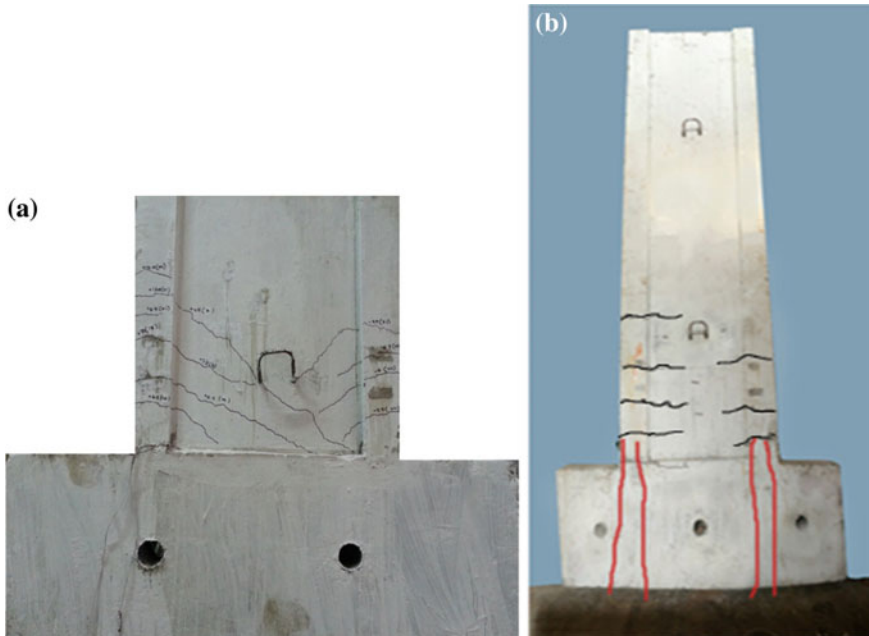
Fig. 5 Crack patterns of shear walls. **a** Squat shear wall. **b** Slender shear wall

4.2 Load Deformation Behaviour

A load-displacement hysteresis loop is an important plot that must be generated to assess the structural seismic performance. Structures are expected to enter into elasto-plastic range during strong earthquakes and the hysteresis loops can provide a good understanding for the analysis of seismic elastoplastic response. The load-displacement hysteresis curves for the specimens are shown in Fig. 6. The load-displacement curves are linear up to the formation of first crack. After cracking, slope of the hysteresis curves (secant stiffness) degrades with increase of displacement. The HPCBW specimens exhibited less amount of deflection than CCBW specimen for the same level of loading in the initial cycles, which indicates the increase in stiffness.
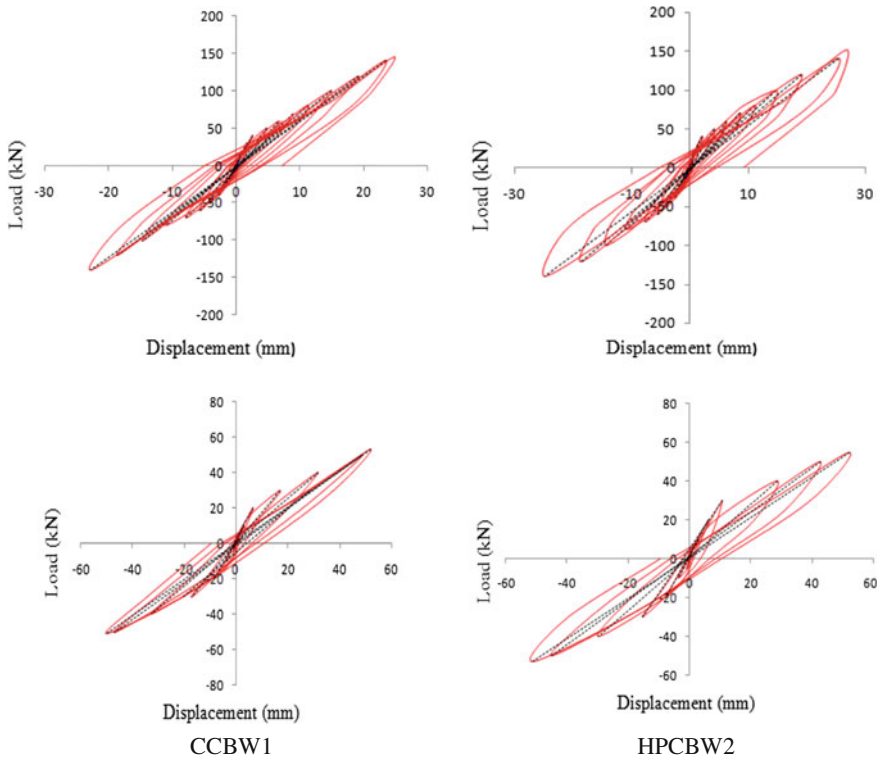
Fig. 6 Load-displacement hysteresis of CCBW and HPCBW shear walls

4.3 Stiffness Degradation

The lateral stiffness of the shear wall specimens were calculated from the base shear required for causing unit deflection at the top of the wall [9, 10]. The stiffness in a particular cycle was calculated from the slope of the line joining peak values of the base shear in each half cycle. Figure 7 shows the comparison of stiffness degradation for CCBW and HPCBW shear wall specimens. From the plots it may be noted that the initial stiffness of HPCBW shear wall is higher than the CCBW shear wall.

4.4 Energy Dissipation Capacity

In seismic design, inelastic ductile behaviour is associated with energy dissipation upon load reversal, which is an essential mechanism to survive strong earthquakes. The energy dissipation capacity of a member under the load is equal to the work
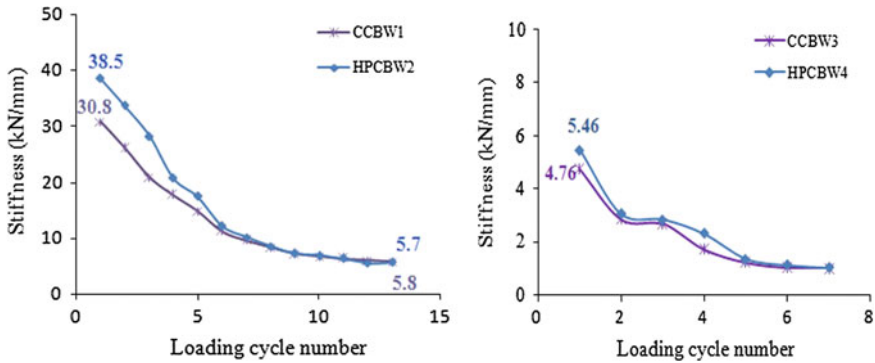
Fig. 7 Comparison of stiffness degradation of shear walls
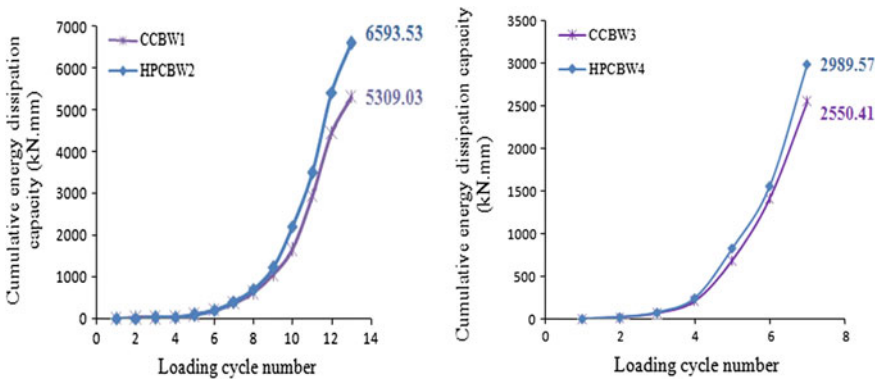
Fig. 8 Comparison of cumulative energy dissipation capacity of shear walls

done in straining or deforming the structure up to the limit of useful deflection, that is, numerically equal to the area under the load-deflection curve [14, 22]. The energy dissipation capacity during various load cycles was calculated from the sum of the area under the hysteretic loops. Figure 8 shows the cumulative energy dissipation capacity with loading cycle number of the specimens. The cumulative energy dissipation capacity of the shear walls HPCBW2 and HPCBW4 are 24.19 and 17.21 % higher than that of CCBW1 and CCBW3 shear walls.

4.5 Plastic Hinge Length

Due to the low inclination of the inelastic branch of the stress–strain diagram of the steel reinforcement that is used in reinforced concrete (RC) structures and due to the high capacity for inelastic elongation that this material exhibits, plastic hinges are

formed at the ends of the structural elements. To determine the plastic hinge length (L_p) formed during experiments, dense instrumentation is required [19]. However, this length can be estimated by the calculation of curvature ductilities and corresponding displacement ductilities. Plastic hinge length is calculated according to the equations proposed by respective researchers as listed below.

1. Paulay and Priestley (1992):

$$L_p = 0.08h_w + 0.022d_b f_y \tag{1}$$

   where h_w and f_y are the wall height and yield strength of reinforcement.

2. Panagiotakos and Fardis (2001):

$$L_p = 0.12h_w + 0.014d_b f_y \tag{2}$$

   where d_b is the diameter of reinforcement.

3. Sawyer (1964):

$$L_P = \alpha D + \beta h_w \tag{3}$$

   where $\alpha = 0.25$.

(a) The displacement ductility is calculated by the equivalent plastic hinge length equation proposed by Priestley and Park (1987):

$$\mu_\Delta = 1 + 3(\mu_\emptyset - 1)\frac{L_P}{h_w}\left(1 - 0.5\frac{L_P}{h_w}\right) \tag{4}$$

   where μ_Δ and $\mu_\emptyset$ are the displacement and curvature ductility.

(b) The curvature ductility ($\mu_\emptyset$) is expressed as:

$$\mu_\emptyset = \frac{\emptyset_u}{\emptyset_y} \tag{5}$$

   where $\emptyset_u$ and $\emptyset_y$ are ultimate and yield curvatures.

The displacement ductility thus obtained is compared with the experimentally measured displacement ductility (resulting from load—deflection plot). Table 4 shows the calculated and measured displacement ductilities of slender shear walls with barbells.

Table 4 Calculated and measured displacement ductilities of slender shear walls with barbells

Specimen	Φy (m^{-1})	Φu (m^{-1})	L_p (m) Computed using equations			Displacement ductility obtained from Eq. 4 μ_Δ			Displacement ductility obtained from experiment μ_Δ
			Eq. 1	Eq. 2	Eq. 3	(1)	(2)	(3)	
CCBW3	0.0032	0.038	0.243	0.299	0.159	4.56	5.31	3.38	3.48
HPCBW4	0.0032	0.049				5.68	6.68	4.13	4.39

From Table 4, it may be noted that the empirical Eqs. (1) and (2) overestimates the experimental values. However, equation by Sawyer (1964) i.e. Eq. (3) approximately matches with the experimental values.

5 Conclusions

This investigation leads to the following conclusions.

1. The first crack load of HPCBW2 and HPCBW4 shear walls are 1.14 and 1.12 times higher than the CCBW1 and CCBW3 shear walls.
2. The squat shear walls exhibited shear mode of failure in the final stages of loading and slender shear walls exhibited flexure mode of failure.
3. The HPCBW shear walls exhibit less stiffness degradation compared to CCBW shear walls. The initial stiffness of HPCBW2 and HPCBW4 shear walls are higher than the CCBW1 and CCBW3 shear walls by 25 and 14.7 %, respectively.
4. The cumulative energy dissipation capacity of the shear walls, HPCBW2 and HPCBW4 are higher than that of CCBW1 and CCBW3 shear walls by 24.19 and 17.21 %, respectively.
5. The plastic hinge length empirical equation by Sawyer (1964) approximately matches with the experimental values.
6. From the experimental results, it is shown that the HPC shear walls with edge boundary elements have superior deformation behaviour, stiffness and energy dissipation capacity compared to CC shear walls.

References

1. ACI 211.1-1991 (reapproved 2009) Standard practice for selecting proportions for normal, heavyweight, and mass concrete. American Concrete Institute, Farmington Hill, Michigan
2. ACI 211.4R-2008 Guide for selecting proportions for high-strength concrete with portland cement and fly-ash. American Concrete Institute, Detroit, Michigan
3. ACI 318-2008 Building code requirements for reinforced concrete. American Concrete Institute, Farmington Hill, Michigan
4. Aitcin PC (1998) High performance concrete. E & FN Spon, London
5. Aitcin PC (1995) Developments in the application of high-performance concretes. Constr Build Mater 9(1):13–17
6. ASTM C 1240-2005 Standard specification for silica fume used in cementitious mixtures. American Society for Testing and Materials
7. ASTM C 618-2003 Standard test method for coal fly-ash and raw or calcined natural pozzolana for use in concrete. American Society for Testing and Materials
8. Dazio A, Beyer K, Bachmann H (2009) Quasi-static cyclic tests and plastic hinge analysis of RC structural walls. Eng Struct 31:1556–1571

9. Devi GN, Subramanian K, Santhakumar AR (2011) Experimental investigations on reinforced concrete lateral load resisting systems under lateral loads. Int J Exp Tech 59–73. doi:10.1111/j.1747-1567.2010.00634.x
10. Ganesan N, Indira PV, Shyju PT (2010) Effect of ferrocement wrapping system on strength and behaviour of RC frames under reversed lateral cyclic loading. Int J Exp Tech 1–5. doi:10.1111/j.1747-1567.2010.00617.x
11. IS 383-1970 (reaffirmed 2002) Specification for coarse and fine aggregates from natural sources for concrete. Bureau of Indian Standards (BIS), New Delhi
12. IS 12269-1987 (reaffirmed 2004) Specification for 53 grade ordinary Portland cement. Bureau of Indian Standards (BIS), New Delhi
13. Julian C, Sergio MA (2013) Shear strength of reinforced concrete walls for seismic design of low-rise housing. ACI Struct J 110(3):415–423
14. Kuang JS, Ho YB (2008) Seismic behaviour and ductility of squat reinforced concrete shear walls with non-seismic detailing. ACI Struct J 105(2):225–231
15. Lefas ID, Kotsovos MD, Ambraseys NN (1990) Behaviour of reinforced concrete structural walls: strength, deformation characteristics and failure mechanism. ACI Struct J 87(1):23–31
16. Lowes LN, Lehman DL, Birely AC, Kuchma DA, Marley KP, Hart CR (2012) Earthquake response of slender planar concrete walls with modern detailing. Eng Struct 43:31–47
17. Oesterle RG, Aristizabal-Ochoa JD, Shiu KN, Corley WG (1984) Web crushing of reinforced concrete structural walls. ACI J 81(22):231–241
18. Paulay T, Priestley MJN, Synge AJ (1982) Ductility in earthquake resisting squat shearwalls. ACI J 79(26):257–269
19. Salonikios TN (2007) Analytical prediction of the inelastic response of RC walls with low aspect ratio. J Struct Eng ASCE 844–854
20. Sittipunt C, Wood SL (1995) Influence of web reinforcement on the cyclic response of structural walls. ACI Struct J 92(6):1–12
21. Tasnimi AA (2000) Strength and deformation of mid-rise shear walls under load reversal. Eng Struct 22(4):311–322
22. Yun-Do Y, Chang-Sik C, Li-Hyung L (2004) Earthquake performance of high-strength concrete structural walls with boundary elements. In: International proceedings of 13th world conference on earthquake engineering

Investigation of Shear Behaviour of Vertical Joints Between Precast Concrete Wall Panels

Aparup Biswal, A. Meher Prasad and Amlan K. Sengupta

Abstract An experimental program is undertaken to study the behaviour of vertical joints between precast wall panels. The parameters such as type of transverse reinforcement in the joint, amount and distribution of joint reinforcements, shape of the joint and strength of the joint grout are considered in this experimental program. The test setup, specimens, instrumentation are reported in this paper. The results of a typical test are presented.

1 Introduction

Precast concrete wall panels are being used in multi-storeyed building construction due to numerous advantages offered by them. Precast concrete structure has high quality control, which is achieved at the manufacturing plants, and it provides faster construction at site. However, the structural integrity of a building depends on the joints between the wall panels. Based on location, the joints are broadly of two types, horizontal joints and vertical joints. A horizontal joint can be at the floor levels or in-between the floor levels. A vertical joint can be between two in-plane panels or perpendicular panels. When a building is subjected to lateral forces, the magnitude of force resisted by a wall depends on the rigidity of the wall. The rigidity depends on the behaviour of the two types of joints. A horizontal joint has to transfer both shear and vertical forces. A vertical joint has to resist the shear force resulting from the lateral forces, as well as any differential settlement in the foundation. To ensure the integrity of the structure, the joints have to be designed

A. Biswal (✉) · A. Meher Prasad · A.K. Sengupta
Department of Civil Engineering, Indian Institute of Technology (IIT) Madras,
Chennai, India
e-mail: tim.aparup@gmail.com

and constructed properly. The present study is restricted to the behaviour of the vertical joints under in-plane shear.

A vertical joint between two panels consists of U-bars or commercially available loops placed at regular intervals, and cement-sand grout cast in the intermediate space between the panels. If the joint deformability is negligible, a wall system can be considered to emulate monolithic behaviour. The wall system is then treated as a homogeneous vertical cantilever. However, if the deformability of the joint is significant, then the wall system is treated as a group of parallel cantilevers. In reality, the behaviour of a wall system is expected to be somewhere in between. To accurately predict the behaviour, it is necessary to characterize the deformability of the joint.

2 Research Significance

An experimental program is undertaken to study the behaviour of vertical joints between precast concrete panels under in-plane shear. Various parameters affecting the strength and deformability of the joints are investigated. Specifically, the influence of transverse reinforcements in the joint is studied. A model for the in-plane shear behaviour of a joint will be developed. This can be used in the analysis of wall-type buildings.

3 Literature Review

A number of experimental programmes were carried out by various researchers to study the behaviour of vertical joints. The following parameters were considered in the earlier works.

  I. Amount and distribution of transverse reinforcement
 II. Compressive strength of joint concrete
III. Type of joint surface (plane, shear key/castellated etc.)
IV. Shape and dimension of shear keys, if present

The study carried out by Cholewicki [4] revealed two different working phases of the behaviour of a joint. In Phase-I, the joint carry load till the first crack appears along any one interface of the joint. In Phase-II, the transverse reinforcement transfers the full shear force for a plane joint. So the cross-sectional area of reinforcement, arrangement of reinforcement and anchorage length play a deciding role in the shear friction. But for a shear key type of joint, the load transferred by the mechanical action of the keys is significant.

The role of the shear deformability and the mechanism of failure in shear key type of joints were studied by Chakrabarti et al. [2], by performing an experimental programme on 23 specimens. They considered the parameters mentioned above as

well as the factors like shrinkage and water-cement ratio of the joint concrete, bond and surface finish of the interface. They concluded that, the presence of transverse reinforcement improves the ductility of the joint, and the shear deformability was greatly influenced by the above factors. To study the effects of the geometry of the shear keys and the transverse reinforcement on the vertical shear strength of joint, Chatveera and Nimityongskul [3] conducted a series of experiments. They considered the variation in height of the keys, keeping the depth and sloping angle of the keys constant. In their specimens, the strength of the panel concrete was more than that of the joint concrete. They revealed that for large size of shear keys, failure is due to crushing of concrete at the sloping faces, but for smaller size of keys the joint concrete gets sheared off at their bases. Also, they found that due to the presence of transverse reinforcement, diagonal tension cracks were formed in the joint region after crushing or shearing of the concrete in shear keys.

The behaviour of vertical plane joints subjected to different types of loading i.e. shear, bending, shear-bending and shear-compression were studied by Abdul-Wahab and Sarsam [1]. They tested 18 specimens with parameters such as the width of the joint opening (referred to as joint width) and shape of the joint reinforcement [straight bar or loop (U-bar)]. They concluded that, the ultimate shear strength and displacement of plane joints are directly affected by the joint width and amount of transverse reinforcement. They found that 50 % increase in the joint width causes 44 % reduction in ultimate shear strength, and 50 % increase in the spacing of transverse reinforcement causes 50 % reduction in ultimate shear strength of plane joint.

4 Experimental Programme

An experimental program is conducted to study the shear behaviour of vertical joints. The parameters considered in this study are the type, amount and spacing of joint reinforcement. The values of the parameters and strength of the cement-sand grout were so chosen that they represent the values mostly adopted in practice. The details of the experimental programme are described as follows.

4.1 Test Setup

The test setups used by the various researchers were mainly of two types, that is single shear type and double shear type. In the single shear type, two panels are joined to form a specimen. Among the two panels, one panel is supported and the other is subjected to a vertical load. This type of setup requires an extra support in the supported panel to counter-balance the moment generated due to the hanging panel. In double shear type, three panels are used and two joints are formed. Among the three panels, two panels are supported and the middle one is subjected to a

Fig. 1 Test setup
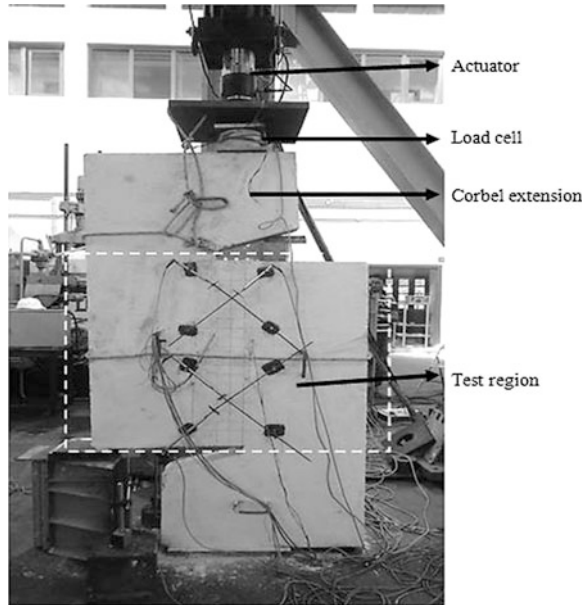
vertical load. This type of test produces strut action of the concrete, which affects the uniformity of shear stress in the joints.

The test setup used in the present study is of single shear type. To avoid extra supports, each panel consists of a corbel extension. The corbel is provided to allow the applied vertical load to pass through the center of the grouted region. This avoided additional stresses at the interface due to any moment. The dimension of a panel was selected so that the height of the test region was 1 m. The corbel was adequately reinforced to avoid any crack or crushing of concrete leading to failure. Two specimens were tested till the writing of this paper. The first specimen was tested under load control by using a 50T hydraulic jack attached to a reaction frame. When the first crack occurred at one of the interfaces of joint, a sudden movement in the top panel was observed. Due to the sudden movement, the vertical LVDT malfunctioned. Thus, the reading of slip terminated at cracking. To overcome the above problem, displacement control test was performed for the second specimen by using a 50T actuator for loading. A load cell was provided to record the load from the actuator. Figure 1 shows the test setup.

4.2 Specimens

A specimen consists of two panels, the details of which are shown in Fig. 2. Each panel is reinforced with 8 mm diameter bars in two layers. The corbel is reinforced with 20 mm diameter main bars and 10 mm diameter links. Deformed bars of 8 mm

Fig. 2 Geometric details of a specimen (all dimensions are in mm)
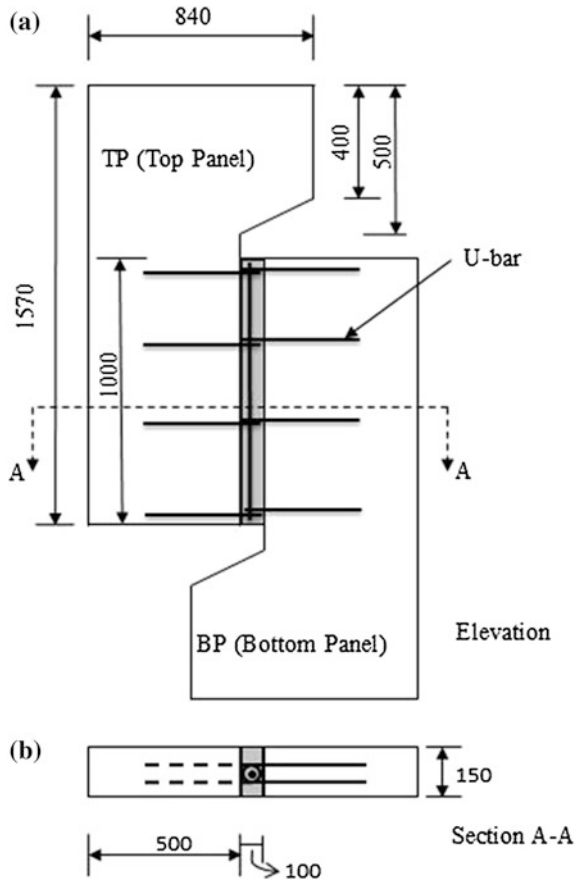
diameter and yield strength of 415 MPa were used as U-bars in the joint. A vertical holder bar of 12 mm diameter was provided in between the overlap of the U-bars from adjacent panels. Figure 3 shows the image of mould and reinforcement. Concrete mix proportion of 3.16:1.89:1 (Coarse aggregate:Sand:Cement) and water-cement ratio of 0.45 with super plasticizer of 0.2 % (to the weight of cement) was used in casting of the panels. The cube compressive strengths of concrete for Specimens 1 and 2 were 52 and 56 MPa, respectively. Proprietary grout of cube compressive strength 42 MPa was used in the joint region. The grout was prepared from a cement-sand and admixture premix with addition of water, during casting of the joint.

First, the panels were cast in a horizontal position and then cured adequately using gunny sacks. After the curing, the interior face of a panel was hacked to generate proper bond with the grout. The grout was cast in a vertical position of the panels to avoid tilting after casting and to simulate the site condition. Two pieces of plywood were placed at front and rear sides of the joint as formwork. The top panel was propped and laterally supported during casting of the joint.
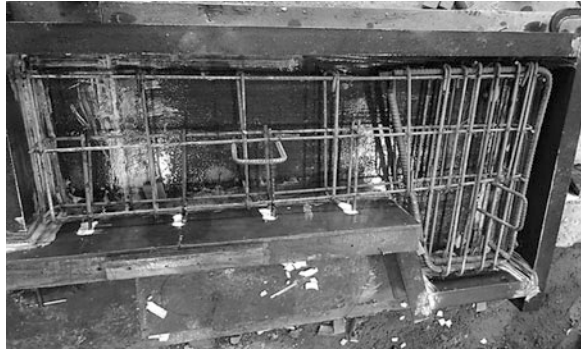
4.3 Instrumentation

Total nine linear variable differential transducers (LVDTs) and eight numbers of strain gauges were used in the testing of a specimen. Three pairs of diagonal LVDTs (D1–D6) were used for measuring the shear deformation of the joint. Three vertical LVDTs (V1–V3) were used to measure the vertical slip of the top panel. Figure 4 shows the location of LVDTs. Strain gauges (TP1–TP4 and BP1–BP4) were provided in the intermediate U-bars to observe the deformation due to dowel action. Each U-bar has two strain gauges located at the interface of the panel and joint region. Figure 5 shows the location of strain gauges.
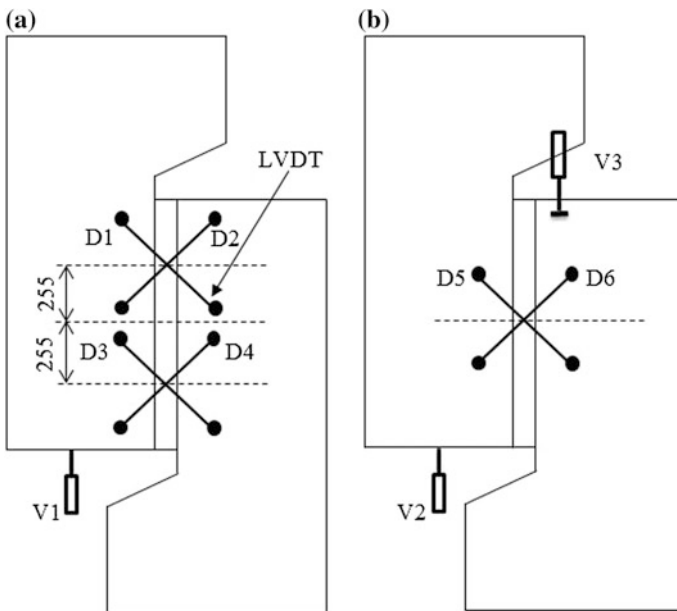
Fig. 4 Location of LVDTs in a specimen. **a** Front face. **b** Rear face

Fig. 5 Location of strain gauges used in a specimen
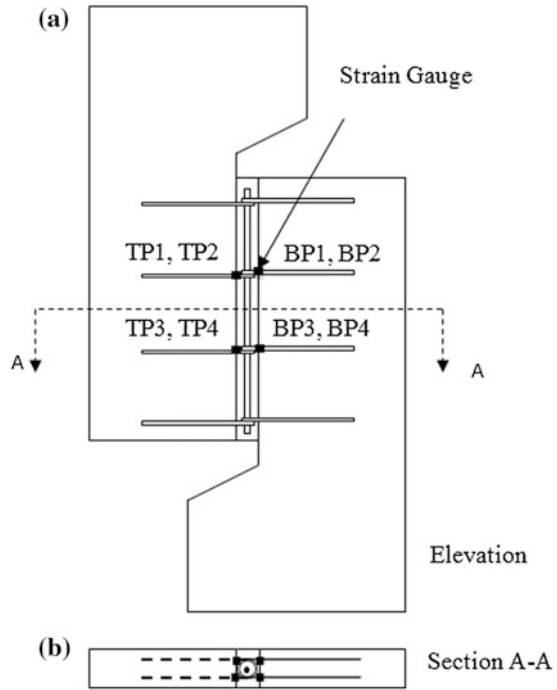
5 Preliminary Test Results

As mentioned earlier that Specimen 2 was tested under displacement controlled loading. Here, the results of Specimen 2 are presented. The first crack was observed in the interface of the top panel. Later another crack was observed in the interface of the bottom panel also. Figure 6 shows the crack pattern observed in Specimen 2. Representative load versus deformation curves from the LVDTs and strain gauges are shown in Figs. 7, 8 and 9. After the first crack, a sudden drop in load was observed till the transverse reinforcement (U-bars) started carrying the load (Fig. 7). The deformation recorded in the diagonal LVDT (D5) is positive (tensile) and in D6 is negative (compressive) (Fig. 8). This is because of the slip at the interface, and not due to shear deformation of the joint grout. From the strain curve of TP1, it is concluded that the U-bars at the interface of the top panel underwent deformation due to dowel action, as the crack was initiated in that interface. But the bars at the interface of the bottom panel showed no dowel action (Fig. 9).

Fig. 6 Crack pattern after
failure of Specimen 2
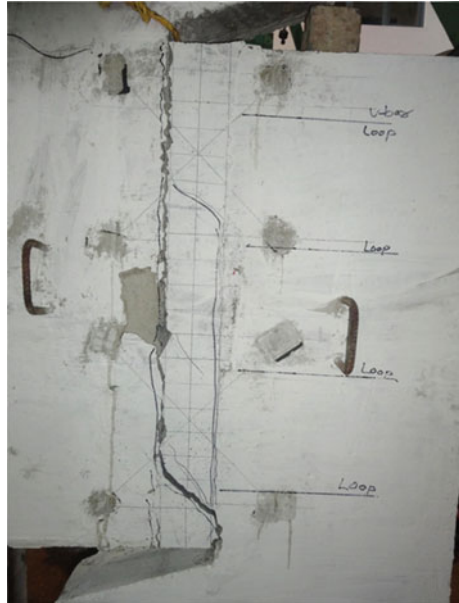
Fig. 7 Load versus slip curve
for a vertical LVDT (V2)
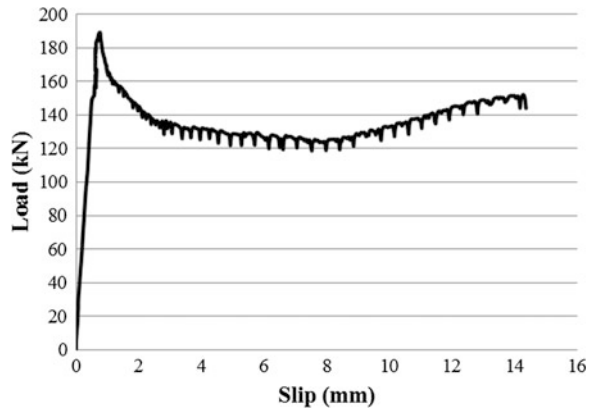
6 Summary

A vertical joint between precast wall panels can lead a wall system to behave as a
homogeneous vertical cantilever or a group of parallel cantilevers. To predict the
behaviour of wall systems accurately, it is necessary to characterize the behaviour
of vertical joints. The study carried out by various researchers revealed that
parameters like amount and distribution of transverse reinforcement, compressive
strength of joint concrete, type of joint surface, etc. affect the behaviour of vertical
joints.

Fig. 8 Load versus deformation curves for a pair of diagonal LVDTs. a Load versus deformation curves of diagonal LVDT (D5). b Load versus deformation curves of diagonal LVDT (D6)

(a)

(b)
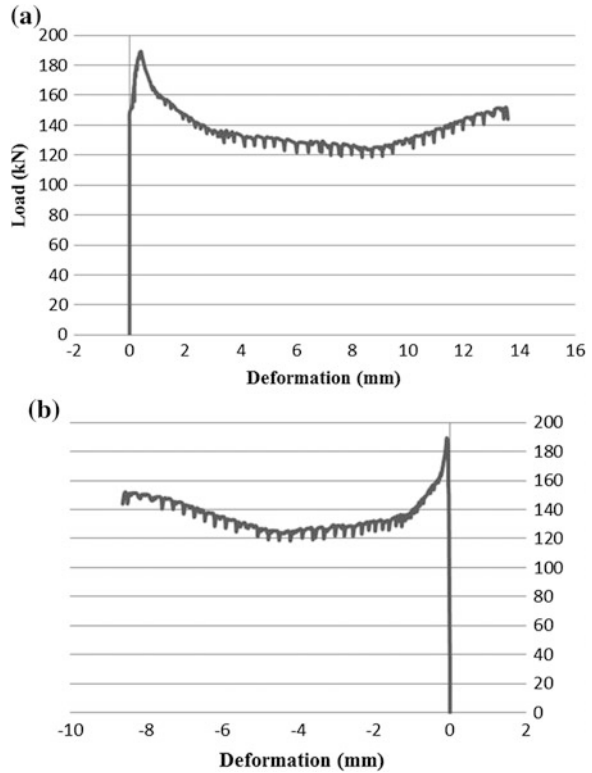
Fig. 9 Load versus strain curves for strain gauges
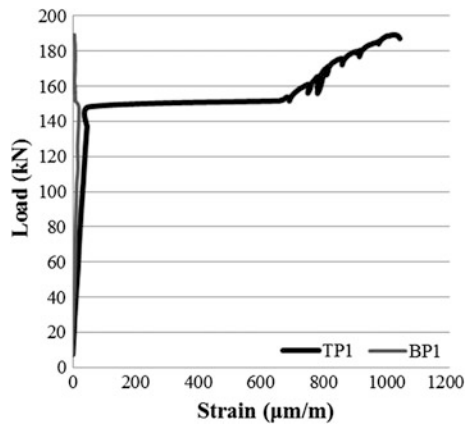
To study the behaviour of vertical joints, an experimental programme is undertaken incorporating parameters like type, amount and spacing of joint reinforcement. Each specimen consists of two panels. The panels are provided with corbel extension to allow the vertical load axis to pass through the center of the joint

region. The setup used in the testing of specimens was of single shear type and the provision of the corbel extension allowed avoiding extra support and additional stresses at the interfaces due to any moment.

Two specimens were tested, one under load control and the other under displacement control. The displacement controlled test allowed obtaining the post-crack behaviour of the joint. It was observed that the transverse reinforcement in the joint had a direct effect on the strength and deformability behaviour of a vertical joint. Further tests will be undertaken to observe the behaviour of transverse reinforcement more clearly.

References

1. Abdul-Wahab HMS, Sarsam SYH (1988) Strength of vertical plane joints between large, precast concrete panels. Struct Engineer 66(14):211–215
2. Chakrabarti SC, Nayak GC, Paul DK (1979) Characteristics of deformable vertical joints in prefabricated shear wall assembly. Indian Concr J 51(11):306–311
3. Chatveera B, Nimityongskul P (1994) Vertical shear strength of joints in prefabricated load bearing walls. J Natl Res Council Thailand 26(1):11–36
4. Cholewicki A (1971) Load bearing capacity and deformability of vertical joints in structural walls of large panel buildings. Build Sci J 6(4):163–184

Experimental Evaluation of Performance of Dry Precast Beam Column Connection

Chintan B. Naik, Digesh D. Joshi and Paresh V. Patel

Abstract Precast concrete construction is being adopted worldwide including India during recent past. In precast concrete construction all the components of structures are produced in controlled environment and it is being transported to the site. At site such individual components are connected appropriately. This leads to many advantages like minimizing cast in place concrete, reduced amount of waste, less requirement of formwork, scaffolding and skilled labors, massive production with better quality, faster construction etc. But connections are the most critical elements of any precast structure, because in past major collapse of precast structure was taken place because of connection failure. In this study, behavior of two different exterior reduced scaled dry precast beam column was studied and its performance is compared with their monolithic counterpart. Precast connections are constructed by using cleat angles stiffened with single stiffener and double stiffeners for connections between beam and column. Performance of specimen is evaluated on the basis of ultimate load carrying capacity, maximum deflection. The deflection is measured along the length of the beam. From the results, it is observed that precast connections are capable to produce ductile behavior but load carrying capacity is lesser than that of the monolithic connection.

Keywords Precast construction · Dry beam column connection · Cleat angles · Stiffeners · RC corbel

C.B. Naik · D.D. Joshi (✉) · P.V. Patel
Civil Engineering Department, Institute of Technology,
Nirma University, Ahmedabad 382481, Gujarat, India
e-mail: digesh.joshi@nirmauni.ac.in

C.B. Naik
e-mail: 12MCLC15@nirmauni.ac.in

P.V. Patel
e-mail: paresh.patel@nirmauni.ac.in

1 Introduction

Now days, there is increasing trend towards construction of buildings using precast concrete. In precast concrete construction all the components of structures are produced in controlled environment and it is being transported to the site. At site such individual components are connected appropriately. This leads to faster construction, reduced formwork and scaffolding, less requirement of skilled labors, massive production with reduced amount of construction waste, better quality and better surface finishing as compared to normal reinforced concrete construction. Because of such advantages the precast concrete construction is being adopted world-wide including India. In precast concrete construction, connections are the most critical elements of the structure, because in past major collapse of precast building was taken place because of connection failure. Therefore it is very important to study the performance of connection between beam and column under a progressive collapse scenario.

The precast beam and column are connected either by mechanical means or by embedding reinforcements in preformed ducts which will subsequently filled by grouting. Accordingly the precast beam column junctions are known as dry and wet connections. Many researchers have studied behavior of various types of precast beam column connections. Parastesh et al. [1] developed new ductile moment resisting precast beam column connections. They have tested six full scale interior and exterior precast beam column connections under cyclic loading and compared their performance with monolithic connections. Seismic response of four full scale precast beam column connections subjected to cyclic loading was studied by Xue and Yang [2] through experiments. Beam column connection includes exterior connection, interior connection, T connection and knee connections. Performance was evaluated in terms of stiffness degradation, energy dissipation capacity, displacement ductility and failure mode.

Shariatmadar and Beydokhti [3, 4] tested three full scale precast beam to column connections by considering different detailing i.e. straight spliced, U-shaped spliced and U-shape spliced with steel plates within connection zone which was part of 5-storey frame under reverse cyclic loading and compared its performance with monolithic connections. Choi et al. [5] proposed design of precast beam column connections using steel connectors constructed by bolting steel tubes and steel plates fixed within precast components was suggested based on the results of cyclic load tests performed on five half scale interior precast beam column assemblies. Maya et al. [6] recommended new beam column connection for precast construction using Ultra High Performance Fibre Reinforced Concrete (UHPFRC) to achieve shorter splice length. They have tested four interior precast beam column assemblies subjected to cyclic loading.

Performance of reduced scaled and full scaled dry and wet precast exterior beam column connections were evaluated by conducting experiments under reversed cyclic loading [7–12]. Different means for precast beam column connections were adopted such as connection using dowel bar, dowel bar with cleat angles, cleat

angles with single stiffener and double stiffener, tie rod and steel plates, use of cast in place concrete in beam and column, composite connection with welding, bolted connections etc. Performance of precast connections were measured on the basis of strength, hysteretic behavior, energy dissipation capacity, ductility and stiffness degradation and the same was compared with monolithic beam column connection.

Design handbooks are also available in which examples of different beam column connections are described [13, 14]. These handbooks gives design dimensions, capacity of different type of precast elements.

In this study behavior of two different exterior reduced scaled dry precast beam column connections is studied by performing the experiments and performance is compared with monolithic connection. Total of two precast connections and one monolithic connections are constructed, which is part of 6-storey building. Each specimen includes separate RC column with corbel and RC beam extending from the face of the column. Response is measured in terms of ultimate load carrying capacity and deflection along the span of the beams under the application of monotonic vertical load near the free end of the beam. Load is applied with the help of hydraulic jack having capacity of 250 kN. From the study, it is observed that precast dry connections are more ductile but load resisting capacity is less as compared to monolithic connections.

2 Connections Detailing

The 6-storey symmetrical building with rectangular plan is considered for the study. The building has 4 bays in longitudinal direction and 3 bays in transverse direction with 4 m c/c spacing in each direction. Overall plan dimensions of the building are 16 m × 12 m. A typical floor height of building is 3.2 m with height at bottom storey equal to 3.5 m. The typical floor plan and elevation of the building is shown in Fig. 1.

Reduced scaled specimens from exterior junction at first storey is casted and tested under application of static loads. The cross-sectional dimensions of both precast and monolithic concrete specimens are 135 mm × 135 mm for column and 100 mm × 135 mm for beam. The cantilever length of the beam is 500 mm and height of the column is 1,100 mm. Cover of 20 mm is provided for both monolithic and precast beam and column specimens. Design and detailing of specimens having monolithic and precast connections is carried out by following the design provisions of relevant Indian Standards [15–17]. M25 grade of concrete and Fe415 grade of steel is used for casting of all specimens.

In monolithic test specimen, the longitudinal reinforcement of the beam consisted of four-8 mm diameter bars with one bar at each corner of the beam. At beam ends one bar of 8 mm diameter is provided at top as an extra reinforcement. The shear reinforcement consisted of 8 mm diameter two legged stirrups spaced at 70 mm c/c with spacing of stirrups reduced to 50 mm c/c at beam ends. The column reinforcement arrangement consisted of four-12 mm diameter longitudinal bars and

Fig. 1 Typical floor plan and elevation of the building
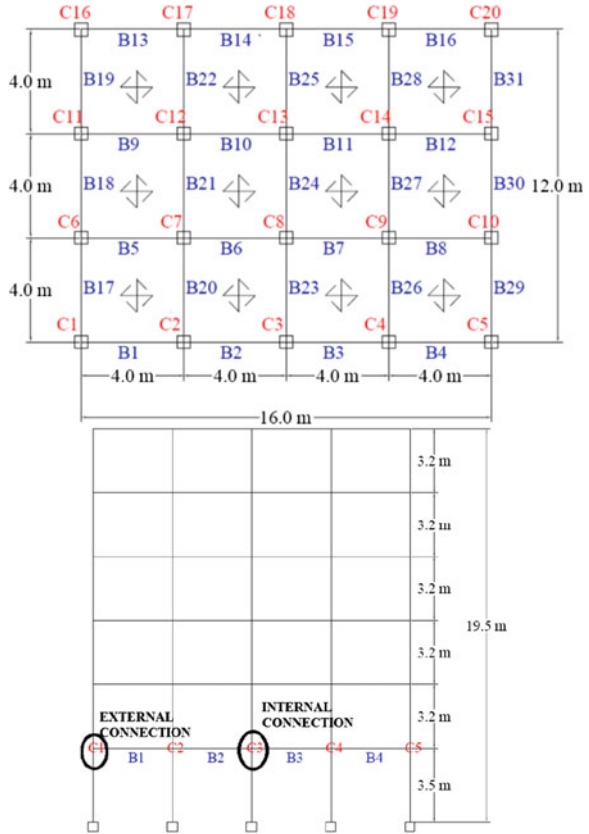
8 mm diameter stirrups provided at spacing of 75 mm c/c. At beam column junction and at column ends spacing of stirrups reduced to 50 mm c/c to avoid concrete crushing at top and bottom of column.

Reinforcement detailing of precast test specimens is similar to that of monolithic test specimen. In precast specimen, column with corbel and beam are casted separately by keeping two holes in both beam and column to pass the bolts used for connection. Precast beam is supported on the corbel in a manner such that two-12 mm diameter bolts projecting from corbel passed through holes provided in beam. Later on, beam and column is connected by means of cleat angles having dimension equal to 100 mm × 100 mm × 8 mm. For connecting cleat angles with both beam and column, 12 mm diameter bolts are used. Cleat angles are also stiffened by providing single stiffener of 8 mm thickness and two stiffeners of 6 mm thickness as shown in Fig. 2. Stiffeners are connected to cleat angle by means of 6 mm fillet weld. Photograph of precast dry beam column connections adopted in the study is shown in Fig. 3.
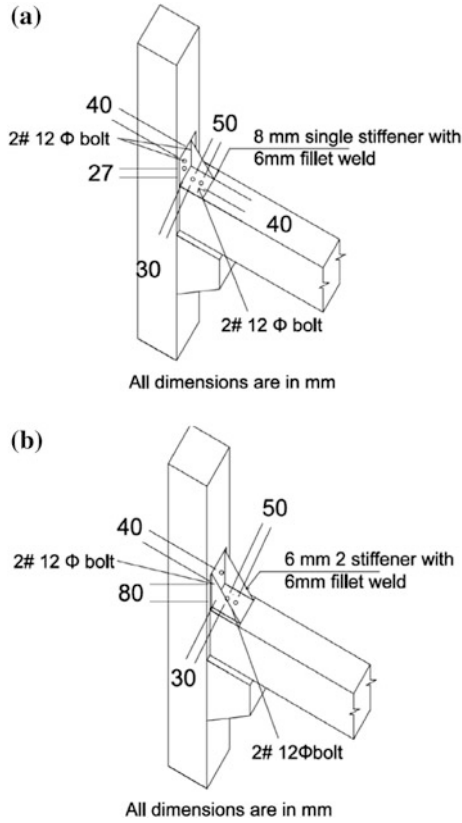
Fig. 2 Detailing of dry precast beam column connections **a** single stiffener and **b** double stiffener

Fig. 3 Dry precast beam column connection **a** single stiffener and **b** double stiffener

3 Test Set-up and Instrumentation

Schematic diagram of test set-up is shown in Fig. 4. End column is restrained vertically by providing reactive force through hydraulic jack at bottom of it and at top it is connected with the steel plate. The gap between hydraulic jack and top of the specimen is filled with spacer plates. The monotonic vertical load is applied near the free end of the beam with the help of hydraulic jack of capacity 250 kN till the complete failure of specimen takes place. The response of specimen is observed in terms of load resisting capacity and vertical deflection. The arrangement of instrumentation system consists of three dial gauges to measure vertical deflections at three different location along the length of beam as shown in Fig. 5.

4 Results and Discussion

To study the behavior of beam column connections, two different dry precast connections and one monolithic connection are tested. Different connection detailing i.e. cleat angle with single and double stiffener, is adopted to construct
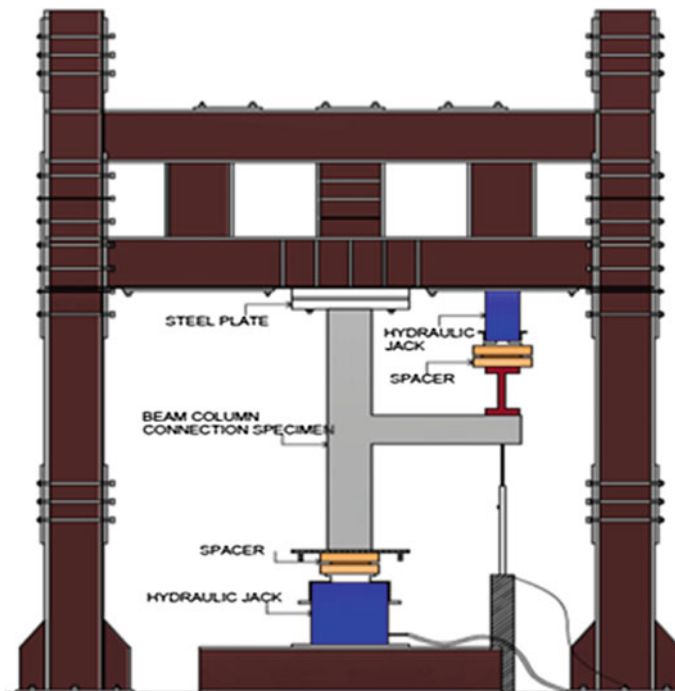
Fig. 4 Schematic diagram of test set-up

Fig. 5 Schematic layout of instrumentation—location of dial gauges
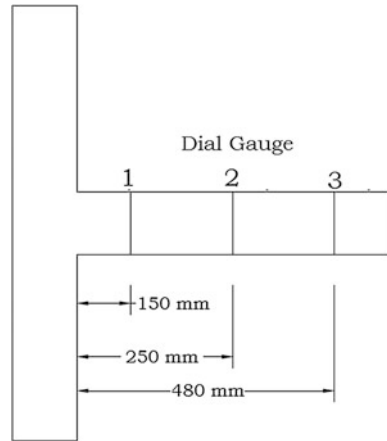
precast connections. To accommodate the specimen in available testing facility, reduced scaled specimens are constructed. Each specimen contains beam extending from face of the column in one direction in a plane. Behavior of connections is observed by applying load near the free end of the beam with the help of hydraulic jack of capacity 250 kN. Result in terms of vertical deflection along the length of beam and ultimate load carrying capacity are measured. Deflections at three different locations are measured with the help of dial gauges as shown in Fig. 5. Deflection measured along the length of beam for monolithic and precast specimens is presented in Fig. 6. The graph of load versus deflection measured near the free end of the beam, for all the three specimens is shown in Fig. 7.

The deflected shape of beam at various loads gives indication about the fixity of connection. The change in curve pattern revealed that, connection gradually losses fixity as load is increased. For monolithic specimen, first crack is developed at the load of 14 kN at beam column junction which propagates further on application of further load. Cracks are also observed on the face of the column at the load of 16 kN. The specimen is completely failed at the load of 26 kN with deflection equals to 10.79 mm. For precast connection with single stiffener, cracks are initiated at the load of 8 kN and specimen completely failed at the load of 14 kN with maximum deflection equals to 12.25 mm. No cracks are developed in column for this specimen. Specimen is failed at the location of bolts used for connecting beam and corbel. Similar type of behavior is observed for precast connection with double stiffener. The maximum deflection for precast connection with double stiffener is 13.05 mm at load carrying capacity of 14 kN. Comparison of maximum load carrying capacity and deflection corresponding to maximum load value is presented in Table 1.

Monolithic specimen is able to resist 26 kN with corresponding deflection equals to 10.79 mm. For the same specimen, deflection of 3.4 mm is observed at the load of 14 kN, which is 260.29 and 283.82 % less as compared to precast connection with single stiffener and double stiffener, respectively.
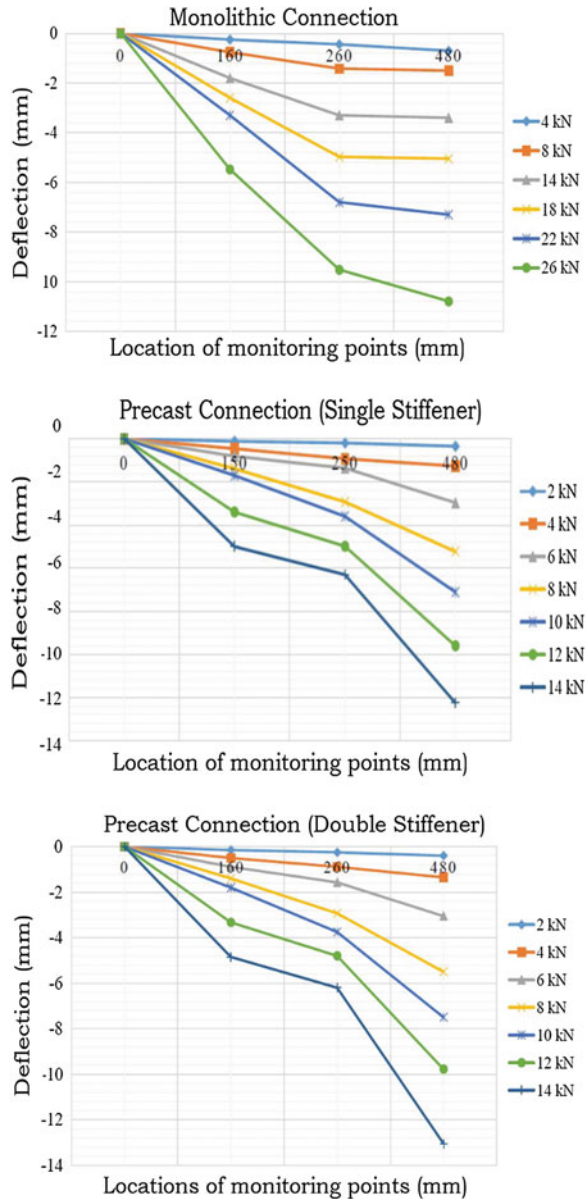
In this study, response of specimen is measured in terms of deflection along the
length under the effect of monotonic load only. In addition to load versus deflection
relationship, this study can be extended by measuring parameters like hysteresis
loops, energy dissipation capacity, strength and stiffness degradation, strain

Fig. 7 Load versus deflection curve

Load v/s Deflection Curve
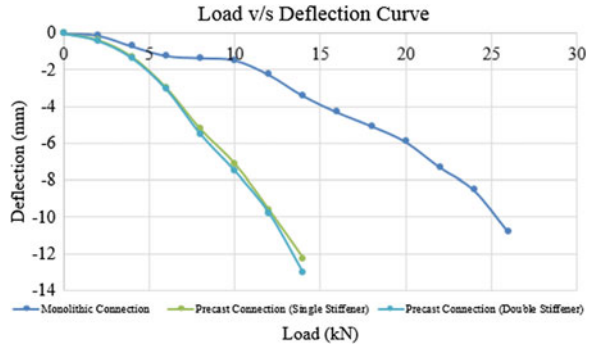
Table 1 Comparison of maximum load and corresponding deflection

Specimen type	Maximum load (kN)	Percentage of increase in load	Deflection corresponding to maximum load (mm)
Monolithic connection	26	–	10.79
Precast connection (single stiffener)	14	−46.15	12.25
Precast connection (double stiffener)	14	−46.15	13.05

measurement in reinforcement etc. when beam column connection is subjected to cyclic loading, to predict the more realistic and accurate behavior of precast beam column connection.

5 Conclusion

Based on experimental study carried out, to investigate the behavior of dry precast beam column connections, following conclusion are drawn.

- From the comparison of maximum load, it has been seen that load carrying capacity of precast connections with single stiffener and double stiffener is 46.15 % less as compared to monolithic connection.
- Deflection of precast connection with single stiffener and double stiffener is 260.29 and 283.82 % more respectively, as compared to monolithic connection. This indicates more flexibility of precast connections as compared to monolithic connection.
- Crushing of concrete at column ends is not observed due to closer stirrups spacing at the column ends.
- From the results of current study, it is observed that precast connections can be used in low seismic regions. However to use precast connections in high seismic regions, a ductile connection should be developed with more load resisting capacity.

References

1. Parastesh H, Hajirasouliha I, Ramezani R (2014) A new ductile moment-resisting connection for precast concrete frames in seismic regions: an experimental investigation. Eng Struct 70:144–157
2. Xue W, Yang X (2010) Seismic tests of precast concrete, moment resisting frames and connections. PCI J 55:102–121
3. Shariatmadar H, Beydokhti EZ (2014) An investigations of seismic response of precast concrete beam to column connections: experimental study. Asian J Civil Eng 15:41–59
4. Shariatmadar H, Beydokhti EZ (2011) Experimental investigation of precast concrete beam to column connections subjected to reversed cyclic loads. In: Proceedings of the 6th international conference on seismology and earth engineering, Tehran, Iran, 16–18 May 2011, pp 1–9
5. Choi HK, Choi YC, Choi CS (2013) Development and testing of precast concrete beam-to-column connections. Eng Struct 56:1820–1835
6. Maya LF, Zanuy C, Albajar L, Lopez C, Portabella J (2013) Experimental assessment of connections for precast concrete frames using ultra high performance fibre reinforced concrete. Constr Build Mat 48:173–186
7. Vidjeapriya R, Jaya KP (2012) Experimental investigation of precast concrete beam-column wet connection under cyclic loading. In: Proceedings of the structural engineering convention (SEC), Surat, Gujarat, India, 19–21 Dec 2012, pp 287–292
8. Vidjeapriya R, Jaya KP (2013) Experimental study on two simple mechanical precast beam-column connections under reverse cyclic loading. J Perform Constr Facil 27:402–414
9. Vidjeapriya R, Jaya KP (2014) Behaviour of precast beam-column mechanical connections under cyclic loading. Asian J Civil Eng (Build Hous) 13:233–245
10. Rahman A et al (2006) Hybrid beam-to-column connections for precast concrete frames. In: Proceedings of the 6th Asia-Pacific structural engineering construction conference, Kuala Lumpur, Malaysia, 5–6 Sept 2006, pp A281–A290
11. Ertas O, Ozden S, Ozturan T (2006) Ductile connections in precast concrete moment resisting frames. PCI J 5:2–12
12. Joshi MK, Murty CVR, Jaisingh MP (2005) Cyclic behaviour of precast RC connections. Indian Concr J 79:43–50
13. Elliot KS (2002) Precast concrete structures. Butterworth-Heinemann Publications, Great Britain
14. Precast/Prestressed Concrete Institute (2010) PCI design handbook: precast and prestressed concrete, 7th edn. Precast/Prestressed Concrete Institute, Chicago
15. Bureau of Indian Standards IS: 456-2000 Indian standard code of practice for plain and reinforced concrete. Bureau of Indian Standards, New Delhi
16. Bureau of Indian Standards IS: 1893-2002 Criteria for earthquake resistant design of structures. Bureau of Indian Standards, New Delhi
17. Bureau of Indian Standards IS: 13920-2003 Ductile detailing of reinforced concrete structures subjected to seismic forces-code of practice. Bureau of Indian Standards, New Delhi

Behaviour of Precast Beam-Column Stiffened Short Dowel Connections Under Cyclic Loading

R. Vidjeapriya, N. Mahamood ul Hasan and K.P. Jaya

Abstract An experimental investigation was conducted on two types of dry precast concrete connections subjected to reverse cyclic loading. Three one-third scale exterior beam-column assemblies representing a portion of a frame subjected to reverse cyclic loading were tested, including one monolithic specimen and two precast specimens. Displacement controlled loading system was adopted. A data acquisition system (DEWE-43) was used to record the load and displacement signals. The performance of the three connections with respect to strength, load displacement relationship, ductility and energy dissipation was studied. Test data showed that the monolithic specimen was found to perform better when compared to the precast specimens in terms of strength. All the three connections exhibited ductile behaviour and satisfactory energy dissipation capacity.

Keywords Beam-column connection · Dry connection · Precast concrete · Reverse cyclic loading · Short dowel · Stiffeners

1 Introduction

Precast concrete framed construction is well established as one of the principal construction methods worldwide. Precast concrete construction have been getting popular and being widely applied in construction sector today. The rapid growth of the building industry together with increasing demand for quality buildings necessitates the construction industry to continuously seek for improvement, leading to industrialization in this industry. In precast concrete construction, economy is achieved through lesser construction time and amount of labor. Structural systems based on precast concrete elements have been shown to be safe, durable, reliable and cost-effective. Structural concrete members fabricated

R. Vidjeapriya · N. Mahamood ul Hasan · K.P. Jaya (✉)
Department of Civil Engineering, Anna University, Chennai 600025, India
e-mail: kpjaya@nayan.co.in

in a plant under controlled factory conditions are typically of higher quality than cast-in-place concrete. Connections are one of the most essential parts in prefabricated structures. The performance of a precast structure in the seismic risk regions depends on the behavior of the connections, which depends on the proper selection and design of connections. The most common criterion for the design of precast concrete lateral force resisting systems is the emulation of monolithic reinforced concrete construction. The other type is the use of the unique properties of the precast concrete elements interconnected either by dry or wet connections. In this paper, an attempt has been made to develop two types of dry precast connections.

2 Literature Review

Saqan [5] investigated on the behavior of ductile connection between precast beam column elements. Four Beam Column sub-assemblages were tested to characterize the overall behavior of different connection details. Each connection was designed to incorporate one of three behavioral concepts in the connection element, tension/compression yielding, substantial energy dissipation and nonlinear elastic response. It was concluded that it is possible to design and construct beam column connections, where beam and column are joined with ductile connecting elements, to withstand severe inelastic deformations resulting from earthquake forces. Alcocer et al. [1] conducted experiments on two full scale beam-column precast concrete joints under uni-directional and bi-directional loading that simulated earthquake type loadings. The most relevant feature of the connection is that conventional mild steel reinforcing bars or prestressing strands, rather than welding or special bolts, were used to achieve beam continuity. Specimen design followed the strong-column–weak-beam concept. Beam reinforcement was purposely designed and detailed to develop hinges at the joint faces and to impose large inelastic shear force demands into the joint. As expected, the joint controlled the specimen failure. In general, the performance of both beams-to-column connections was satisfactory. Joint strength was 80 % of that expected for monolithic reinforced concrete construction. Specimen behavior was ductile due to hoop yielding and bar pullout, while strength was nearly constant up to drifts of 3.5 %. Rahman et al. [4] investigated the moment of resistance and the behavior of simple beam-to-column connections in precast concrete frames. The experimental test comprised a total of four specimens, which were limited to simple beam-to-column connections in precast concrete frames. The behavior of load displacement relationships, moment-rotation relationships and types of failure in connections were also investigated. It was concluded that simple connection with single dowel and grouted beam-to-column connection provides very minimum moment resistance and hence the connection can be best modelled as pinned. Therefore, in the case of analysis of global frame, the stiffness of such connection is negligible and can be ignored. The single dowel grouted connection can be employed in precast concrete construction in order to maintain the frame stability, the stiffness of the global frame is provided

by other lateral stability systems such as bracing, core or shear wall. Shariatmadar and Beydokhti [6] tested two types of precast and one type of monolithic full scale beam-column connections under reversed cyclic loads. Both of the precast concrete connections tested were cast in place, but with different connection details, namely straight spliced and U-shaped. The results showed that the specimen in which the top and bottom reinforcement are continued by lap splicing exhibited a good behavior very similar and close to those of control monolithic specimen and pre-formed very good based on seismic demand. The behavior of specimen that used U-shaped rebar in its connection was not satisfactory in comparison with other specimens. Some shear deteriorations observed in both the connections. It was concluded that the precast connections could be adopted in precast moment resisting frames with moderate ductility located in high seismic zones.

3 Analysis and Detailing

A three storey reinforced concrete building was considered for analysis. A typical exterior beam, column joint is considered for this study. The monolithic reinforced concrete test specimen was designed according to IS: 456-2000 [2] and detailed according to IS: 13920-1993 [3]. Two numbers of 10 mm diameter bars were provided as tension reinforcement and two numbers of 10 mm diameter bars were provided as compression reinforcement. The shear reinforcement consisted of 3 mm diameter two legged stirrups spaced at 60 mm. For a distance of 100 mm from the column face the spacing of the lateral ties were decreased to 25 mm. The column reinforcement arrangement also consisted of four 10 mm diameter. Along the column height excluding the joint region, the lateral ties were spaced at 50 mm. At the joint region, the spacing of the lateral ties was reduced to 25 mm. The precast specimens were detailed as the monolithic specimen. The corbel reinforcement consisted of two 10 mm diameter bars. Three numbers of 3 mm diameter bars and two numbers of 3 mm diameter bars were provided as were provided as horizontal and vertical stirrups in the corbel.

4 Connections

4.1 Monolithic Specimen (MO)

The monolithic specimen is designed and detailed according to IS: 456-2000 and IS: 13920-1993, respectively.

Fig. 1 Schematic sketch of
monolithic and precast
specimen. **a** Monolithic
specimen. **b** Precast specimen
with short dowel
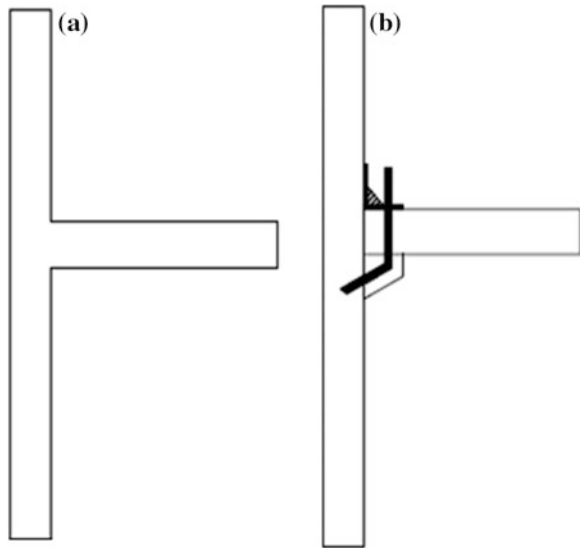
4.2 Short Dowel with Single Stiffener (SD-SS)

In this connection, the precast column is connected to the beam using a short dowel
bar and cleat angle with single stiffener.

4.3 Short Dowel with Double Stiffener (SD-DS)

In this connection, the precast column is connected to the beam using a short dowel
bar and cleat angle with double stiffener. Figure 1a, b show the schematic repre-
sentation of the monolithic and precast specimen respectively.

5 Test Setup and Loading Program

The experiments were carried out on a loading frame of 2,000 kN capacity.
A hydraulic jack was fixed to the loading frame for the application of the axial load
along the axis of the column. Two hydraulic jacks were used to apply the reverse
cyclic loading. Displacement controlled loading system was adopted. The speci-
mens were tested in an upright position with column in vertical and beam in
horizontal position. The column was hinged at floor and was laterally restrained at
the top. The schematic representation of the experimental test setup is shown in
Fig. 2. Loading program is tabulated in Table 1. Figure 3 shows the photograph of
the experimental setup.

Fig. 2 Experimental set up
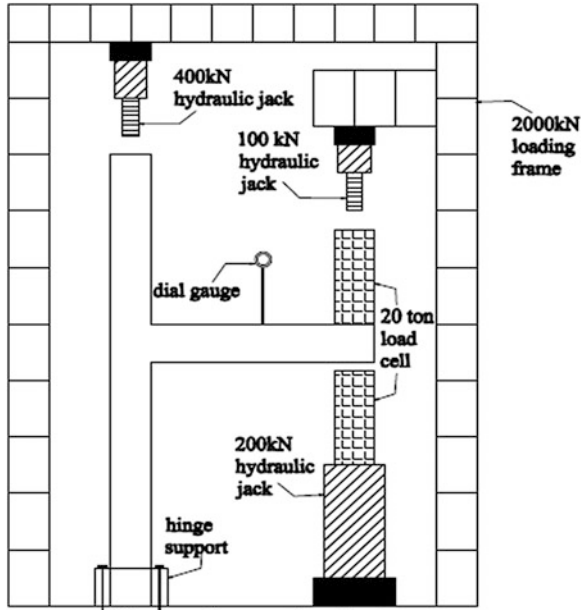
Table 1 Loading program

Increment	Displacement (mm)		Increment
	Start	End	
1	1	10	1
2	10	20	2
3	20	30	2

Fig. 3 Photograph of monolithic specimen

6 Data Acquisition System

The purpose of any data acquisition system is to gather useful measurement data for characterization, monitoring, or control. The applied load in the hydraulic jack was measured by connecting the load cell to the data acquisition system. The corresponding displacement for the applied load was measured by connecting the LVDT to the system. The hysteresis curve for the applied load and corresponding displacement was obtained from the data acquisition system using the DEWE Soft 7.0 software.

7 Results and Discussions

7.1 Strength

The specimens were subjected to reverse cyclic loading. The experimental results of the precast specimens were compared with those of the monolithic connection. The ultimate load carrying capacity of the specimen MO was found to be 10.83 and 12.09 kN in positive and negative directions respectively, whereas for the specimen SD-DS, the ultimate load carrying capacity was found to be 7.78 and 7.17 kN in positive and negative directions and 9.63 and 9.36 kN respectively which was very much lesser than the monolithic specimen MO. From the results, it is observed that the load carrying capacity of specimen SD-DS was 11.08 and 22.58 % lesser than the monolithic specimen in the positive and negative direction, respectively. Out of the two precast specimens, the specimen SD-DS performed better than the other specimen. While comparing with the precast specimens, the monolithic specimen performed better in resisting the load. Figure 4 shows comparison of strength of all specimens.

Fig. 4 Comparision of strength of all specimens. **a** Yield load. **b** Ultimate load

7.2 Hysteretic Load-Displacement Relationship

Figure 5 shows the load-displacement hysteresis of all the specimens. It is observed that the specimen MO exhibited stable and large hysteresis loops which are an indication of good energy dissipation. Less pinching was also observed. Out of the two precast specimens, specimen SD-SS exhibited stable load displacement hysteresis with less pinching.

7.3 Crack Pattern

All the specimens were subjected to reverse cyclic loading. For the specimen MO, the flexural crack initiated at the beam-column junction at 3 mm displacement cycle (5.99 kN) and propagated further. The flexural cracks in beams were initiated at 5 mm displacement cycle (7.79 kN) and were developed away from the beam-column junction. Shear cracks first occurred at the beam-column junction at 8 mm displacement cycle (9.03 kN) and cracks further propagated at 14 mm (10.64 kN), 18 mm (10.74 kN), 24 mm (8.89 kN), 28 mm (6.83 kN), 30 mm (6.11 kN)
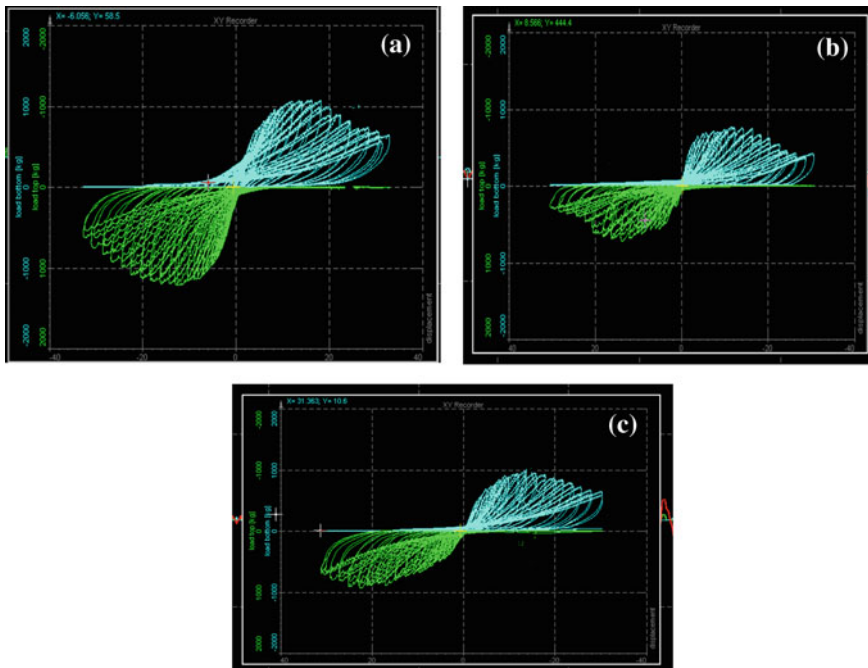
Fig. 5 Hysteresis load-displacement curves. **a** Specimen MO. **b** Specimen SD-SS. **c** Specimen SD-DS

Fig. 6 Crack pattern of all specimens. **a** Specimen MO. **b** Specimen SD-SS. **c** Specimen SD-DS

displacement cycles. Shear cracks should be occurred in column at 8 mm (9.03 kN). For the specimen SD-SS, the first flexural crack initiated on the beam where the bolt has been fixed at 2 mm displacement cycle (2.64 kN). Further cracks will propagate. For the specimen SD-DS, flexural cracks occurred at 5 mm (5.50 kN), 9 mm (6.24 kN), and 14 mm (7.19 kN) displacement cycles. All the cracks in the beam and corbel occurred at the position of dowel. No cracks were observed in the column and corbel region. The crack pattern of all the specimens is shown in Fig. 6.

7.4 Moment Rotation Relationship

It is seen that under beam self-weight, the beam end rotated easily. The axis of rotation was observed at the interface between dowel bar. After rotation due to beam self weight, the connection rotated further under incremental applied loads. Based on the LVDT readings at column face, no column rotation was observed. Hence, in this case, the connection rotation is equal to the beam end rotation. From Table 2, it was observed that the moment carrying capacity of monolithic specimen has performed well while compared with precast specimens. The moment carrying capacity of the specimen MO was 10.88 and 25 % more than that of the specimen SD-DS (Fig. 7).

Table 2 Comparison of maximum moment carrying capacity

Specimen	Moment (kN m)	
	Positive	Negative
MO	5.88	6.75
SD-SS	3.95	4.21
SD-DS	5.24	5.06
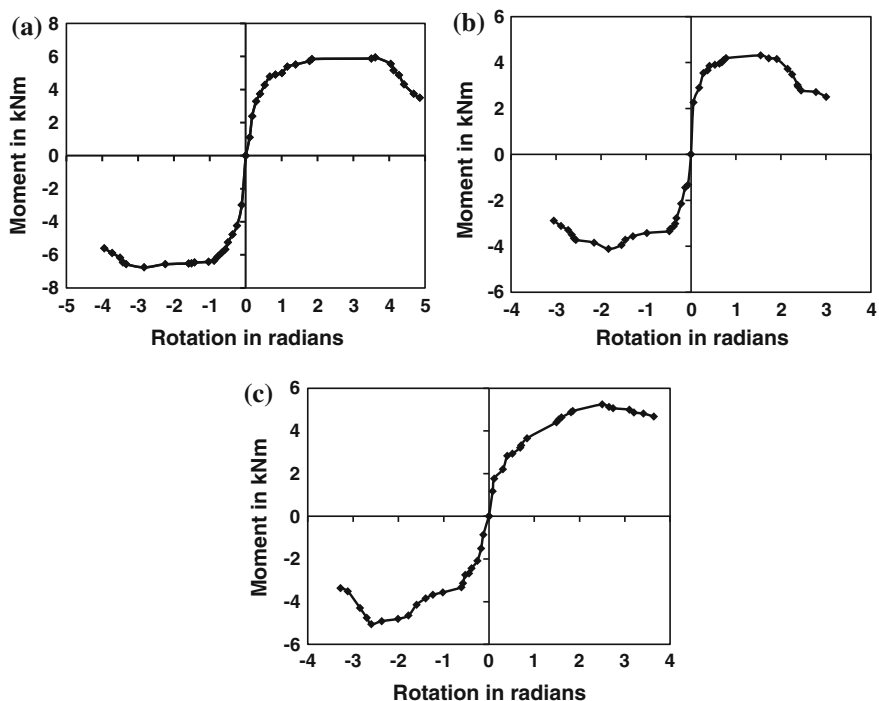
Fig. 7 Moment rotation curves for all specimens. **a** Specimen MO. **b** Specimen SD-SS. **c** Specimen SD-DS

7.5 Ductility

From Table 3, it is observed that specimen SD-DS has performed well and has the maximum average displacement ductility factor out of the two precast specimens. The specimen SD-SS has the least average displacement ductility factor.

Table 3 Displacement ductility factor

Specimen	Displacement ductility factor		Average displacement ductility factor
	Positive	Negative	
MO	5.2	5.52	5.36
SD-SS	4.9	4.5	4.56
SD-DS	5.4	4.06	4.73

Specimen MO
= 1075 kN-mm

Specimen SD-SS
= 510 kN-mm

Specimen DS-DS
= 845 kN-mm
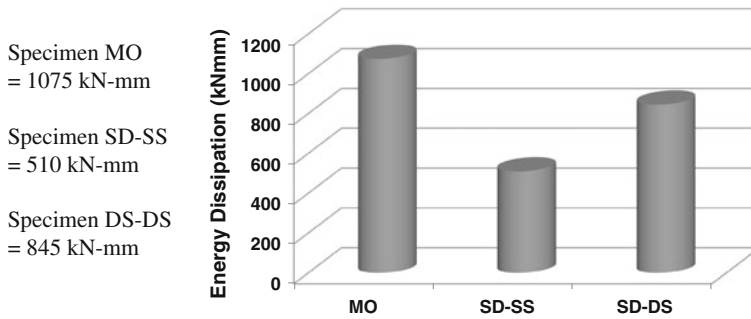
Fig. 8 Energy dissipation of all the specimens

7.6 Energy Dissipation

The area under the load displacement curve gives the energy dissipation of the specimen. To resist seismic forces the energy dissipation capacity of the connections should be good. In this study, the energy dissipated by the specimen SD-DS is greater when compared to specimen SD-SS. The energy dissipated by SD-DS is 21 % less than specimen MO, 66 % greater than short specimen SD-SS. Out of the two precast connections the short dowel with double stiffener connection performed well in terms of energy dissipation. Figure 8 shows the energy dissipation of all the specimens.

8 Conclusions

Following conclusions are drawn from the results of the experiments:

(i) The ultimate load carrying capacities of short dowel with double stiffener (SD-DS) was 11.08 and 22.58 % lesser than the monolithic specimen (MO) in the positive and negative direction, respectively. The specimen resisted more load in the positive direction due to the presence of the double stiffeners.

(ii) It was observed that short dowel with double stiffener (SD-DS) has the maximum average displacement ductility factor of 4.73 out of the two precast specimens. The ductility of short dowel with double stiffener (SD-DS) was 11.75 % lesser than monolithic specimen (MO) and 37.28 % greater than short dowel with single stiffener (SD-SS). The specimen short dowel with single stiffener (SD-SS) has the least average displacement ductility factor.

(iii) The energy dissipated by the specimen short dowel with double stiffener (SD-DS) was 21 % lesser than monolithic specimen MO, 66 % greater than specimen short dowel with single stiffener (SD-SS). Of the two precast

connections, short dowel with double stiffener (SD-DS) performed well in terms of energy dissipation.

(iv) In conclusion, short dowel with double stiffener (SD-DS) has satisfactory performance when compared to monolithic connection in terms of ductility and energy dissipation.

(v) The precast connection using short dowel with double stiffener (SD-DS) can be used in moment resisting frames in low seismic risk regions.

References

1. Alcocer SM, Carranza R, Perez-Navarrete D, Martinez R (2002) Seismic tests of beam-to-column connections in a precast concrete frame. PCI J 47(3):70–89
2. Indian Standard IS: 456-2000 Code of practice for plain and reinforced concrete. Bureau of Indian Standards, New Delhi
3. Indian Standard IS: 13920-1993 Code of practice for ductile detailing of reinforced concrete structures subjected to seismic forces. Bureau of Indian Standards, New Delhi
4. Rahman ABA, Leong DCP, Saim AA Osman MH (2006) Hybrid beam-to-column connections for precast concrete frames. In: Proceedings of the 6th Asia-Pacific structural engineering and construction conference, Kuala Lumpur, Malaysia, pp 281–290
5. Saqan EI (1995) Evaluation of ductile beam column connections for use in seismic resistant precast frames. PhD thesis, University of Texas, Austin
6. Shariatmadar H, Beydokhti EZ (2011) Experimental investigation of precast concrete beam to column connections subjected to reversed cyclic loads. In: 6th international conference on seismology and earthquake engineering, Tehran, Iran, pp 1–9

Stability of Highly Damped Concrete Beam-Columns

Mamta R. Sharma, Arbind K. Singh and Gurmail S. Benipal

Abstract In an earlier paper, authors have investigated the static and dynamic stability of cracked concrete flanged conservative beam-columns. The cantilever column with a lumped mass at its free end is subjected to an axial compressive force and a lateral force. Two critical values each of the axial and lateral loads are defined. Loss of static stability is predicted to occur by excessive displacements or brittle buckling while dynamic instability called divergence is shown to occur by vanishing natural frequency. In this paper, the dynamic stability of highly damped concrete beams-columns is investigated. Two measures—damping ratio and damping coefficient—of structural damping have been employed. Critical loads and displacements are not affected by level of structural damping. Application of inadmissible set of loads results in dynamic instability by divergence at all levels of damping. In particular cases, higher damping has been predicted to destabilize even these conservative structures. Effects of initial conditions and higher damping on the inelastic stability, passive stability control and creep buckling of concrete beam-columns have been delineated. Theoretical significance and practical relevance of the paper are also discussed.

Keywords Concrete beam-columns · Dynamic stability · Divergence · Damping measures · Stability control · Creep buckling

M.R. Sharma (✉) · G.S. Benipal
Department of Civil Engineering, Indian Institute of Technology (IIT) Delhi,
New Delhi, India
e-mail: mamta.kitu@gmail.com

A.K. Singh
Department of Civil Engineering, Indian Institute of Technology (IIT) Guwahati,
Guwahati, India

1 Introduction

Linear structural members subjected to axial compressive forces and undergoing finite lateral displacements are called beam-columns. Conventional beam-columns are physically linear elastic mechanical systems. Their lateral stiffness decreases with increase in compressive force but is independent of the lateral displacement. Their lateral stiffness as well as natural frequency vanishes asymptotically as the critical axial load is reached [2, 3]. Classical theory of beam-columns is valid only for uncracked beam-columns. The behavior of concrete beam-columns is rendered more complex due to cracking of concrete, yielding of reinforcement, crushing of concrete, etc. Even under service loads, concrete structures are cracked at discrete locations. The extent and pattern of cracking depend upon the load history. Available experimental investigations deal with their nonlinear inelastic quasi-static behavior till failure [6]. Reinforced concrete columns are also observed to fail by an instability resembling creep buckling [12]. A new method premised on the average stress strain approach has been proposed for creep analysis of uncracked reinforced concrete elements [1].

Recently, authors have studied the static and dynamic stability of fully cracked flanged concrete beam-columns. The relevant two-part paper titled Elastic Stability of Concrete Beam-Columns has been communicated to International Journal of Structural Stability and Dynamics in July 2012. In this paper, closing and reopening of these existing flexural cracks has been shown to render these structures physically nonlinear elastic. Two values each of the critical axial and lateral loads are identified. Failure can occur by brittle-buckling mode at quite small lateral displacements. These structures can have two equilibrium states corresponding to the same set of specified axial and lateral loads. The axial load-lateral load space is partitioned into statically stable and unstable regions. It has also been established that while the first equilibrium state stable is dynamically stable, the second one is not. Loss of dynamic stability by divergence occurs as and when the natural frequency vanishes. The phase-plane of initial conditions is partitioned into dynamically stable and unstable regions. Like other nonlinear dynamical systems, concrete beam-columns are shown to exhibit regular and irregular subharmonic resonances. For some particular cases, the irregular subharmonic resonance peaks can exceed the fundamental and regular subharmonic peaks [8, 9]. Also, recently, the dynamic instabilities of concrete beam-columns like flutter under follower loads and parametric resonance under pulsating loads have been investigated by the authors [10, 11].

In the above investigation, the damping ratio has been assigned a value (0.03) characteristic of concrete structures under service loads. However, situations can arise when the effect of higher damping on structural behavior becomes significant. Concrete structures subjected to ultimate loads are known to exhibit nonlinear elastoplastic behavior. Their dynamic analysis is simplified by modeling them as linear elastic structures with higher equivalent viscous damping. Various available models of equivalent viscous damping are premised on the expectation that the assumed highly damped linear elastic structures simulate closely the real nonlinear

inelastic structures. Typical values of equivalent viscous damping ratio lie in the range 0.2–0.4 [5].

Similarly, one of the popular passive vibration control techniques involves the use of supplemental viscous dampers or hysteretic dampers at some locations in the structures. Typical damping ratio of such controlled structures is about 0.2 [7, 13]. Obviously, dynamic stability can also be controlled by higher damping. At this point, one important distinction between the inherent structural damping and damping introduced by viscous dampers needs to be appreciated. As per the dominant paradigm in structural engineering, the single degree of freedom (SDOF) structures are characterized by their damping ratios, not by their damping coefficients [4]. Their damping coefficients depend upon their damping ratio, stiffness and mass. In contrast, the damping characteristics of the viscous dampers are independent of such dynamic parameters of the controlled structures. Thus, there is a case for characterizing the structures with viscous dampers by their damping coefficients in preference to their damping ratios. As argued later, such a distinction between these measures of structural damping becomes particularly important for physically nonlinear structures.

The classical linear theory of vibrations as well as the theory of nonlinear dynamical systems as Duffing and van der Pol oscillators is based upon the Kelvin-Voigt rheological model. The same model is used for modeling the creep of viscoelastic solids. Also, overdamped SDOF structures exhibit creep-like non-oscillatory response under sustained loading. Thus, it seems quite promising to explore the phenomenon of 'creep buckling' of overdamped concrete beam-columns under sustained axial and lateral loads.

Obviously, there is a need to conduct dynamic and stability analysis of highly damped conservative cracked concrete beam-columns under service loads. In view of this, the objective of the present paper is to investigate the effect of higher damping on the dynamic stability of cracked concrete beam-columns. Here, both the measures of damping—damping ratio and damping coefficient—have been employed to assign different levels of damping. The predicted dynamic response is discussed for its theoretical significance and possible engineering importance.

2 Normally Damped Concrete Beam-Columns

Consider a vertical flanged concrete cantilever, as shown in Fig. 1, undergoing finite lateral displacements 'w' under axial load P and lateral load Q. This massless beam-column carries a lumped mass M at its free end.

The equation of motion is for this SDOF structure is stated as follows:

$$M\ddot{w} + C\dot{w} + Kw = F(t) \tag{1}$$

(a)

(b)
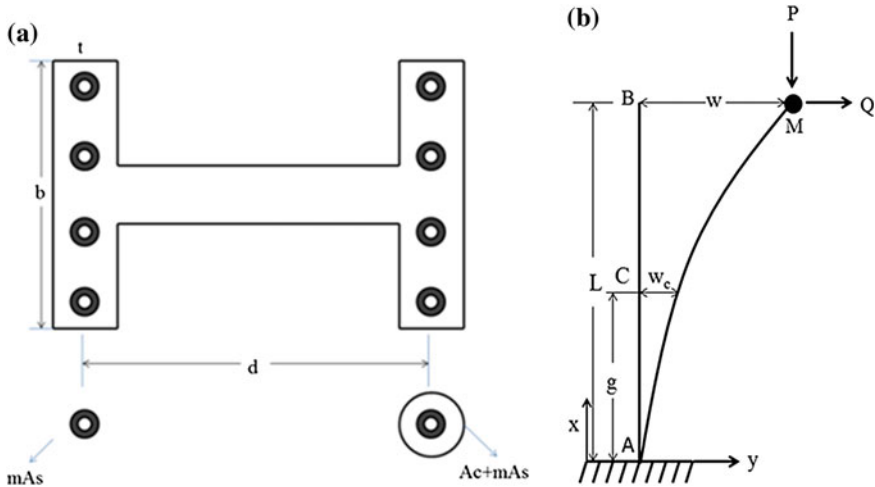
Fig. 1 Flanged concrete beam-column. **a** Cross-section details. **b** Loading details

The expression for the lateral stiffness K of the expressions for the completely uncracked structure is obtained as

$$K = \frac{k_1 P}{\tan k_1 L - k_1 L} \tag{2}$$

When the structure is partly cracked, the expression for K is derived by the authors as

$$K = \frac{Q}{w} = \frac{k_2 P Z_1}{\left(\frac{1-B}{\sqrt{B}}\right) \tan k_1 (L - g) + Z_2 - k_2 L Z_1} \tag{3}$$

Here, subscripts 1 and 2 refer to the uncracked and cracked sections. The symbols I and r denote the section moment of inertia and the distance of the centroid from the compression face respectively. Here, $k_1 = \sqrt{\frac{P}{EI_1}}$ $k_2 = \sqrt{\frac{P}{EI_2}}$ and $I_2 = BI_1$. The length of g of the cracked segment depends upon the loads P and Q as per the following relation:

$$Q = \frac{P k_1 r_1 Z_1}{\tan k_1 (L - g)} \tag{4}$$

$$Z_1 = \cos k_2 g - \sqrt{B} \sin k_2 g \tan k_1 (l - g)$$

$$Z_2 = \sin k_2 g + \sqrt{B} \cos k_2 g \tan k_1 (l - g)$$
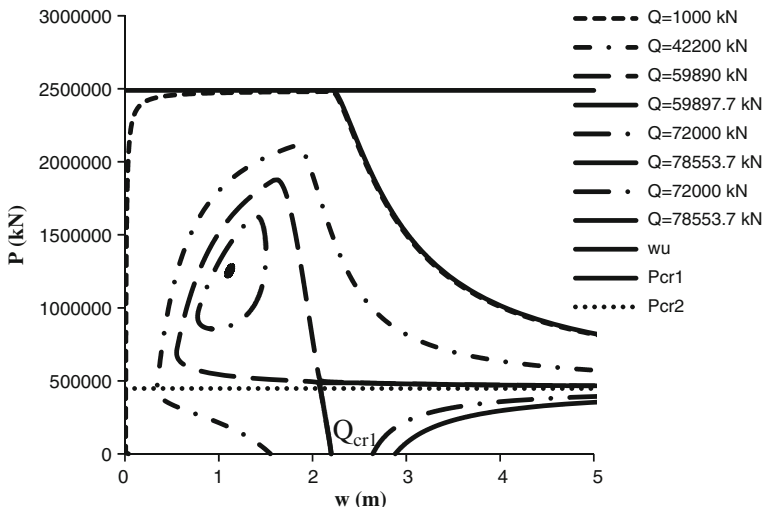
Fig. 2 Static stability

Lateral stiffness K vanishes as lateral displacement of the partly cracked beam-columns reaches a limiting value w_u given by

$$w_u = a + r_2 \sec k_2 g \tag{5}$$

Static and dynamic stability of such cracked concrete beam-columns is investigated by the authors in details. Here, for ready reference, certain characteristic aspects of their static stability are presented in Fig. 2 in the form of a P–w curves for different constant values of Q. This study pertains to concrete beam-columns with following specific details:

Length: 20 m, Flange width: 4.45 m, Flange thickness: 0.330 m, Depth of section: 4.45 m.

Concrete grade M25	$M = 450 \times 1{,}000 \, \text{kg}$
$p = 0.01$	$E_c = 25{,}000 \, \text{N/mm}^2$
$A_1 = 3.2595 \times 10^6 \, \text{mm}^2$	$A_2 = 1.791 \times 10^6 \, \text{mm}^2$
$I_1 = 1.6167 \times 10^{13} \, \text{mm}^4$	$B = 0.18006$

The two critical values each for the axial and lateral loads turn out to be as follows:

$P_{cr1} = 2.4885 \times 10^6 \, \text{kN}$	$P_{cr2} = BP_{cr1} = 4.4808 \times 10^5 \, \text{kN}$
$Q_{cr1} = 59{,}897.65 \, \text{kN}$	$Q_{cr2} = 78{,}553.7 \, \text{kN}$

For the partly cracked concrete beam-column, the lateral stiffness is known to depend upon both the axial load and the lateral load (or equivalently on lateral displacement). As the axial load reaches either of the two critical loads, P_{cr1} and P_{cr2}, the stiffness vanishes. Such also is the case, when, for $P_{cr2} < P < P_{cr1}$, the lateral displacement reaches a value w_u. Decrease in stiffness also implies the corresponding decrease in the damping coefficient, even though the damping ratio remains invariant. However, when the damping coefficient is adopted as the preferred measure of damping, its value remains invariant. In such a case, the decrease in stiffness results in an increase in the damping ratio. For sufficiently low values of stiffness the system behaves as an overdamped system.

For $Q < Q_{cr1}$, the lateral displacement first decreases with increase in axial load before it starts increasing with further increase in axial load. The $P - w$ curve shows a maximum axial load P_{max} and a post-peak response. In contrast, where $Q_{cr1} < Q < Q_{cr2}$, the lateral displacement asymptotically reaches infinitely high values as axial load reaches P_{cr2}. In addition, another segment of $P - w$ curve lying between P_{min} and P_{max} is predicted in the form of a closed loop for $P_{cr2} < P < P_{cr1}$. In both the cases, two equilibrium lateral displacements are admissible for some specific sets of axial and lateral loads. For $P_{cr2} < P < P_{cr1}$, the lateral stiffness vanishes as a certain value w_u of lateral displacement is reached.

The system executes vibrations under sustained axial force. The magnitude of the elastic internal resistive force Q varies with the lateral displacement w. Thus, the lateral stiffness depends upon the lateral displacement for this physically nonlinear structure. The instantaneous value of the damping coefficient C is conventionally determined from the instantaneous stiffness K and the constant value of the damping ratio ξ as $2\xi\sqrt{KM}$. Dynamic stability of the concrete beam columns under specified axial load P and lateral load, $F(t) = q_0$ is explored by introducing perturbations in the form of chosen initial lateral displacement and velocity. When the damping ratio is chosen as damping measure, it is assigned different values in this study. When the damping coefficient is the chosen damping measure, its values are estimated as $2\xi_0\sqrt{K_0M}$. Here, K_0 is the conventional lateral stiffness $\frac{3EI_1}{L^3}$ of the uncracked beam-column undergoing only small displacements. For the purpose of comparison, ξ_0 is assigned the same values as ξ above. In both of these cases, the effect of damping on the frequency domain response, $F(t) = q_0 + p_0 \sin \omega t$ is also investigated.

3 Highly Damped Concrete Beam-Columns

Figure 3 shows the structural behavior under constant lateral force (72,000 kN) and for different magnitudes of the axial force held constant. For this case, the lateral force Q lies within the range $Q_{cr1} - Q_{cr2}$. The admissible ranges of magnitudes of the axial force are $0 - P_{cr2}$ and $P_{min} - P_{max}$ ($0.34P_{cr1} - 0.65P_{cr1}$). Thus, the axial force falls within these ranges, e.g., at $0.1P_{cr1}$ and $0.45P_{cr1}$, respectively, the underdamped ($\xi = 0.2$) system is expected to execute oscillations with the amplitude asymptotically reaching the corresponding first (stable) equilibrium displacements

($w_1 = 3.081$ m and $w_1 = 0.857$ m). The beam-columns cannot support axial forces outside these admissible ranges. Thus, for axial forces equal to $P_{cr2} < 0.3P_{cr1} < P_{min}$ and $P_{max} < 0.7P_{cr1} < P_{cr1}$, the lateral displacements are expected to increase exponentially to their respective limiting displacements ($w_u = 5.7506$ m and $w_u = 2.7716$ m). Such indeed happens to be the case except for the axial load at $0.45P_{cr1}$. Even though this value of axial load happens to be in the admissible range, dynamically unstable behavior is predicted. This anomaly will be explained later in the text after discussing Fig. 7. The displacement waveform shown in Fig. 3a and the corresponding phase plots shown in Fig. 3b depict such predicted
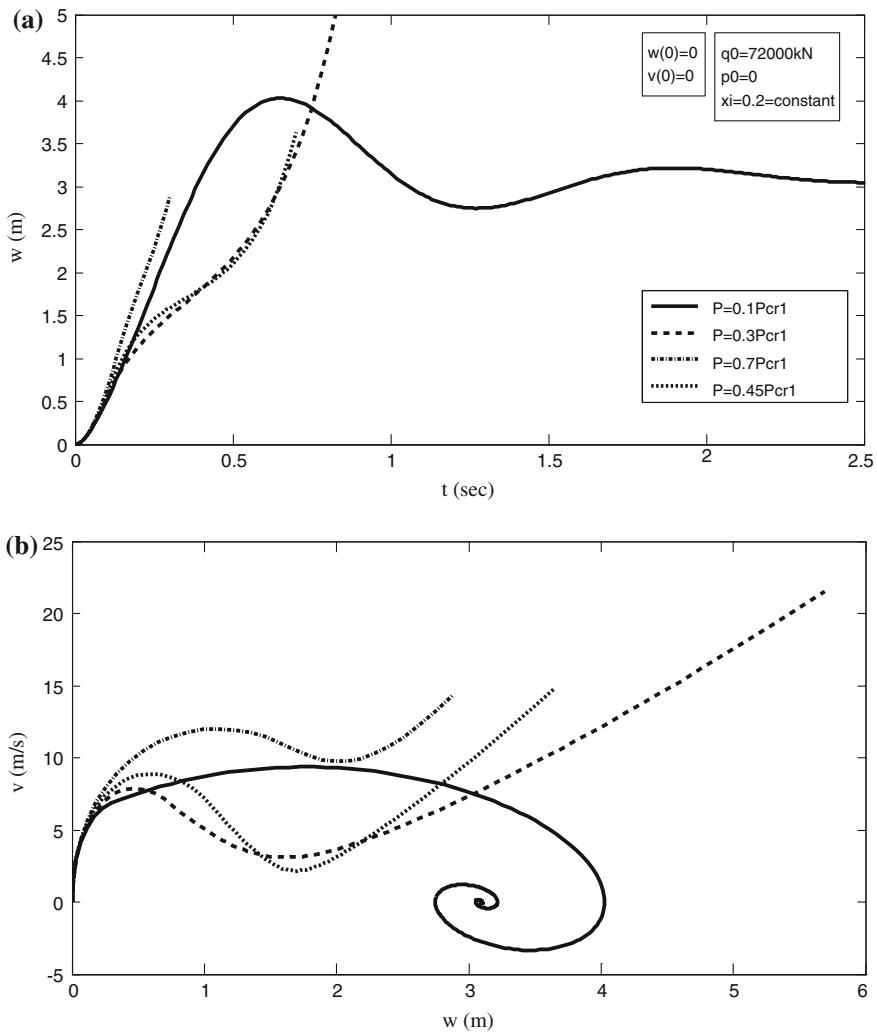
Fig. 3 Dynamic response for constant damping ratio. a Displacement waveforms. b Phase plots

behavior. Asymptotically vanishing velocity implies dynamically stable behavior while simultaneously increasing displacements and velocities imply loss of dynamic stability by divergence.

The above predictions pertain to the structure characterized by damping ratio measure or ξ-measure of damping. The corresponding predictions about the dynamic stability using C-measure of damping ($\xi_0 = 0.2$) are presented below. Displacement waveforms for different axial compressive forces and the corresponding phase plots are shown in Fig. 4a, c, respectively.

The predicted response is similar to the ξ-measure response. Dynamically stable system under constant axial and lateral forces gravitates towards stable first equilibrium displacement, w_1. In contrast, dynamically unstable system exhibit divergent response. Figure 4b depicts the temporal variation of the instantaneous damping ratio, ξ. For such systems, instantaneous damping ratio depends upon the instantaneous lateral stiffness which depends upon the lateral displacement. There is little variation in damping ratio for dynamically stable systems. In contrast, dynamically unstable systems are predicted to register substantial increase in damping ratio. Specifically, the system is rendered overdamped when the displacements approach w_u and the lateral stiffness vanishes.

The above discussion pertains to initially vertical beam-columns at rest. The effect of initial displacement and velocity on dynamic stability of concrete beam-columns under constant axial and lateral forces is presented in Fig. 5. The phase-plane of initial conditions is partitioned into an inner dynamically stable region and an outer unstable region.

As can be observed from Fig. 5a, b respectively, the system behavior for ξ-measure and C-measure is similar. In all the cases pertaining to ξ or ξ_0 values of 0.03, 0.2 and 2, the system with lateral displacement w_2 is destabilized by an infinitesimally small perturbing velocity. Also, positive or negative initial displacements cannot exceed lateral displacement, w_u. More importantly, generally, highly damped beam-columns can be stabilized by sufficiently high structural damping. However, such is not always the case. Beam-columns with initial displacements in the range w_2–w_u exhibit unexpected counter-intuitive effect of damping on their dynamic stability. As shown in Fig. 6, an increase in damping can result in destabilizing the motion of the vibrating beam-columns.

Beam-columns with lower constant damping ratio ($\xi = 0.03$) exhibit dynamically stable response while systems with higher damping ratio ($\xi = 0.2, 2$) can be observed from Fig. 6a to exhibit unstable response. Similarly, as shown in Fig. 6b, the stable motion of beam-column with lower constant damping coefficient ($\xi_0 = 0.03$) is destabilized when damping coefficient is increased ($\xi = 0.2, 2$).

Demarcation between the dynamically stable and unstable regions is predicted to depend upon the adopted measure of structural damping. This effect is shown in Fig. 7 for a particular level of damping ($\xi = \xi_0 = 0.2$). As can be observed, a beam-column with certain initial conditions characterized to be dynamically unstable for one measure turns out be dynamically unstable for the other and vice versa. For example, for certain initial conditions $w(0) = -2$ m and $v(0) = 0$, the system predicted to be stable for C-measure is unstable $v(0) = 0$, the system
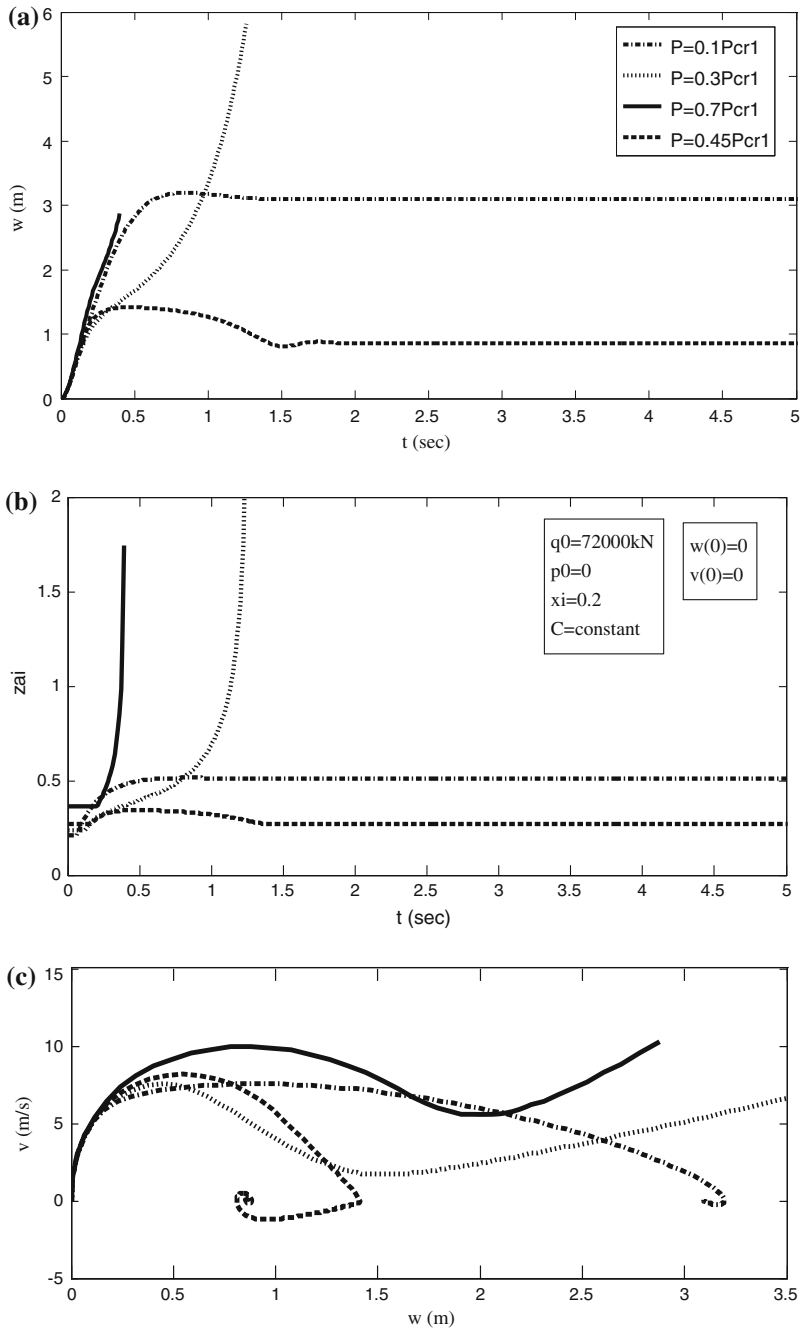
Fig. 4 Dynamic response for constant damping coefficient. **a** Displacement waveforms. **b** Instantaneous damping ratio. **c** Phase plot
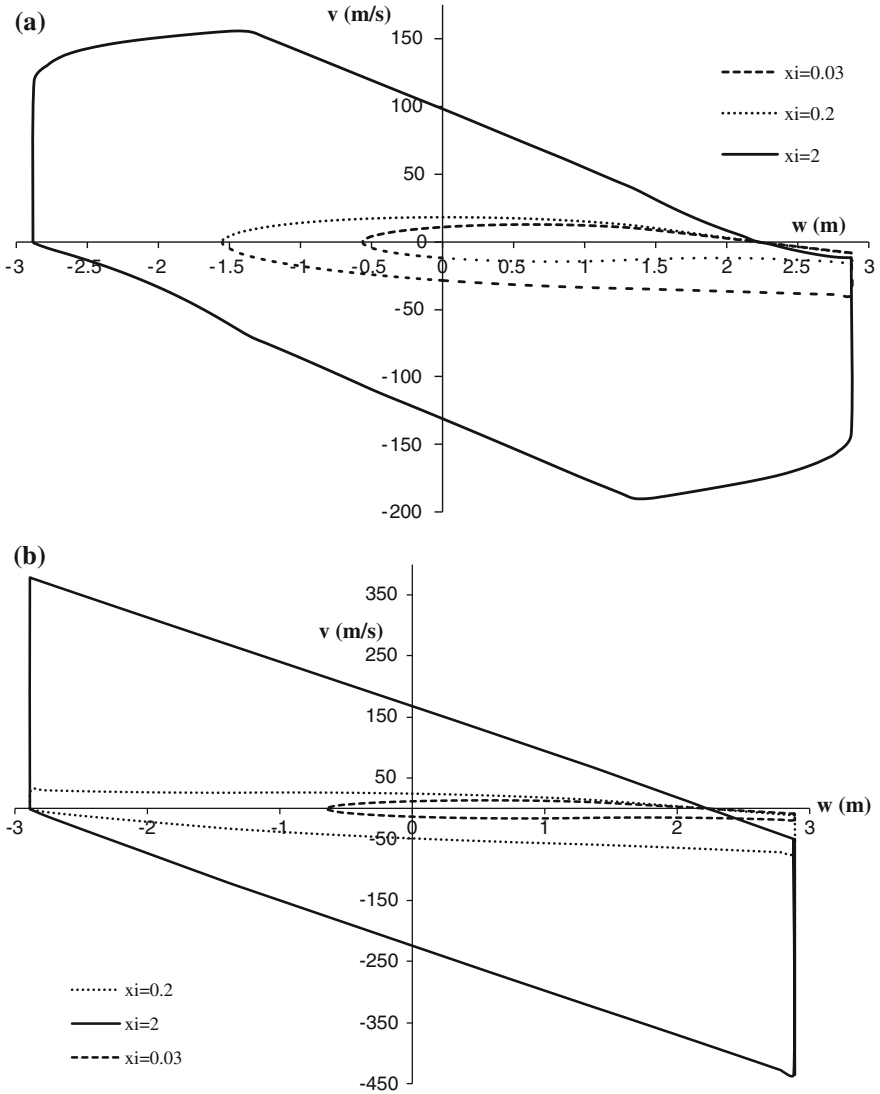
Fig. 5 Stable and unstable regions in phase-plane. **a** Constant damping ratio ($P = 0.65P_{cr1}$, $q_0 = 0.015P_{cr1}, p_0 = 0$). **b** Constant damping coefficient ($P = 0.65P_{cr1}, q_0 = 0.015P_{cr1}, p_0 = 0$)

predicted to be stable for C-measure is unstable as per predictions based upon ξ-measure.

As promised above, the anomaly involving unstable behavior for admissible sustained forces ($P = 0.45P_{cr1}$ and $q_0 = 72{,}000\,\text{kN}$) shown in Fig. 3 is explained here. Both Figs. 3 and 4 are based on computations assuming vanishing initial conditions: $w(0) = 0$ and $v(0) = 0$. It so happens that, for the above set of applied
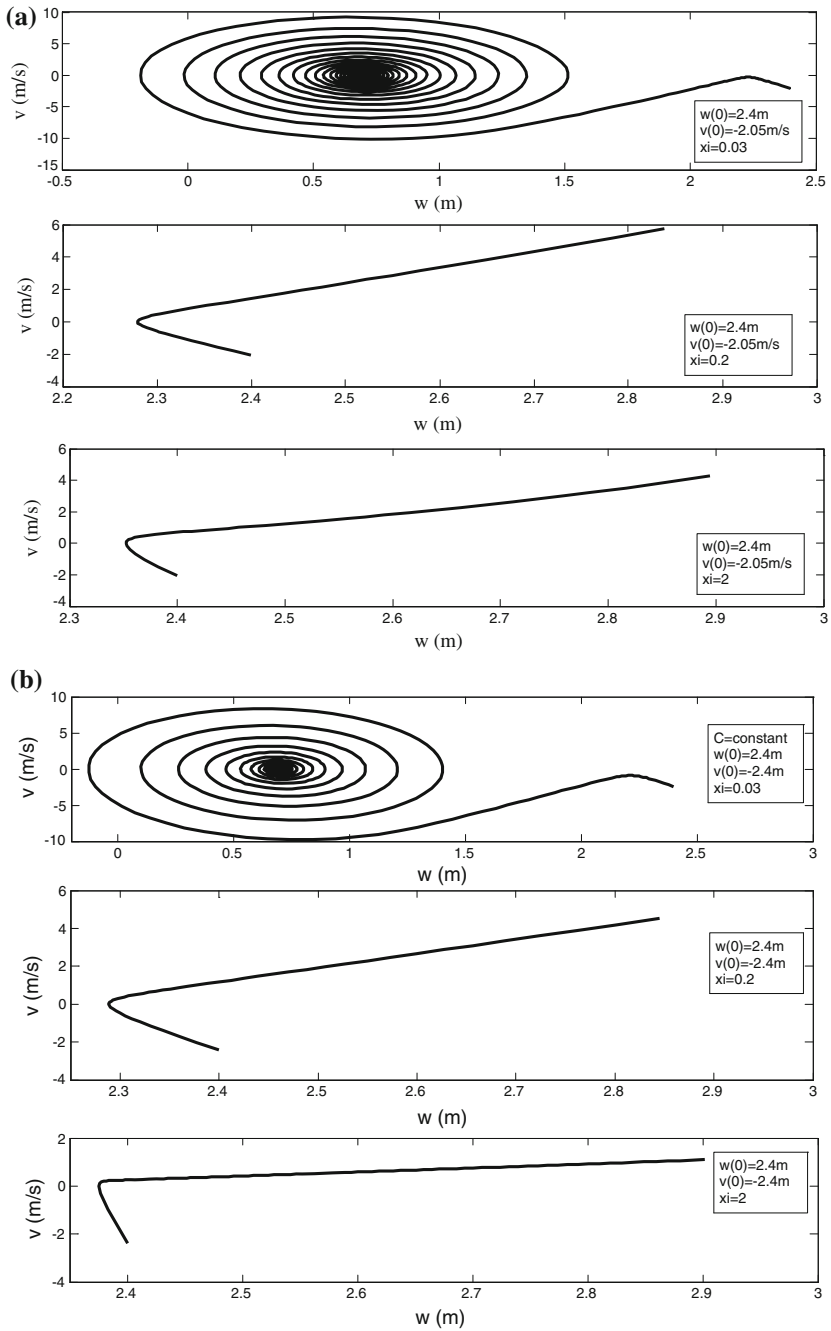
Fig. 6 Effect of damping in dynamic stability ($P = 0.65P_{cr1}, q_0 = 0.015P_{cr1}, p_0 = 0$). **a** Constant damping ratios. **b** Constant damping coefficients
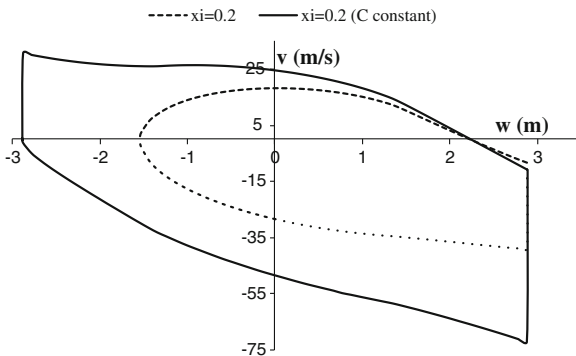
Fig. 7 Effect of damping measure on stability ($P = 0.65P_{cr1}, q_0 = 0.015P_{cr1}, p_0 = 0$)

forces, the system turns out to be dynamically unstable for chosen initial conditions in the phase-plane representation. It has been verified that, for $w(0) > 0.537$ m, the system is dynamically stable. In this latter case, the asymptotic displacement converges to the first stable equilibrium displacement ($w_1 = 0.857$ m).

The effect of level of structural damping upon the typical frequency domain response of the concrete beam-columns is depicted in Fig. 8 for both the measures of damping. Here, the frequency ratio is the ratio of the forcing frequency to the natural frequency defined for the small deformation lateral stiffness K_0 of the uncracked beam-column. The horizontal portion of the curves imply dynamical instability with the peak displacement amplitude exceeding limiting value w_u. With increase in level of damping, ξ in Fig. 8a and ξ_0 in Fig. 8b, such unstable regions get shorter and shift to lower frequency ratios. Thus, generally, higher damping stabilizes the vibrating beam-columns. It can be observed that, at higher frequency ratio exceeding about 0.5, the system with constant damping ratio ($\xi = 0.2$) is predicted to exhibit considerably higher peak displacement amplitudes than those with constant damping coefficient ($\xi_0 = 0.2$).

An attempt is also made to obtain creep-like response for the concrete beam-columns under constant axial and lateral forces. The aim is sought to be achieved by assigning very high value (50) to both ξ and ξ_0 respectively for ξ-measure and C-measure of damping. As shown in Fig. 9, the lateral force remaining constant at 72,000 kN, for the concrete beam-columns under an axial force of $0.649P_{cr1}$ is dynamically stable. In contrast, under higher axial force of $0.649P_{cr1}$, the same system exhibits dynamically unstable behavior.

Here, dynamical instability by divergence can be interpreted to imply creep-buckling by divergence. Such creep-buckling under sustained load occurs at about 645 s and at about 616 s concrete beam-columns with constant damping ratio and constant damping coefficient respectively. The critical axial load $0.65P_{cr1}$, for lateral load of 72,000 kN equals the maximum load for this lateral load in range
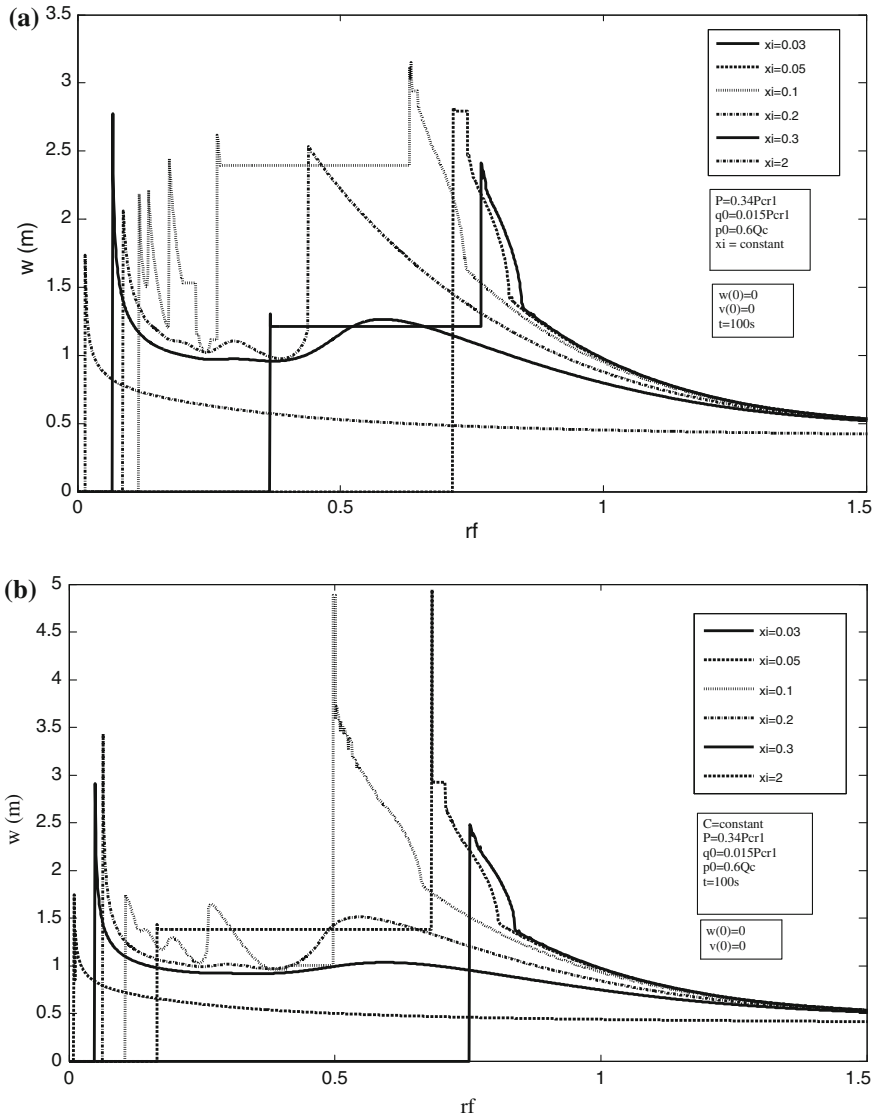
Fig. 8 Effect of damping on frequency domain response. **a** Constant damping ratio. **b** Constant damping coefficient

$Q_{cr1} - Q_{cr2}$. The minimum value of 0.34 P_{cr1} for the same lateral load also plays the role of critical load for dynamic instability. However, in this later case axial load in the range $P_{cr2} - 0.34P_{cr1}$ implies creep buckling by divergence.
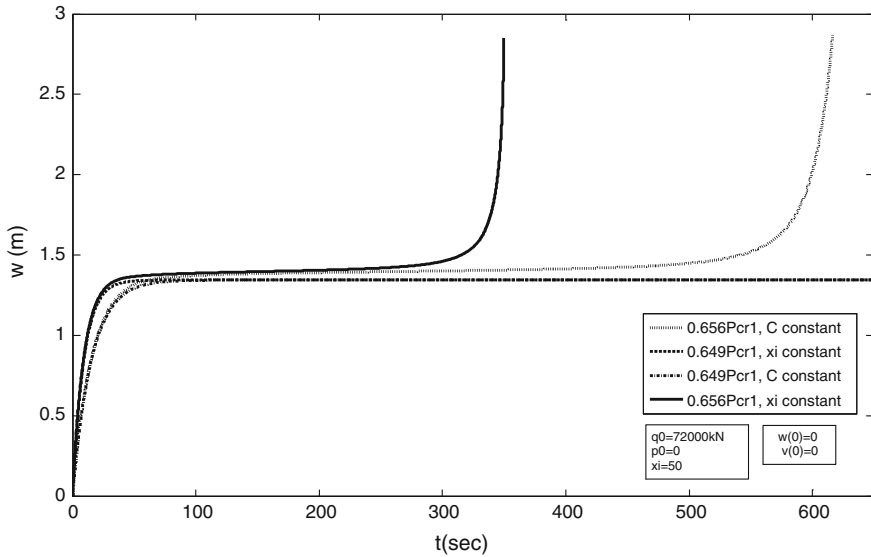
Fig. 9 Creep buckling

4 Discussion

Safety of concrete structures is affected by cracking of concrete, debonding and yielding of reinforcement, inelastic behavior and failure of both concrete and steel, etc. Codal design recommendations aim to incorporate the effect of all these factors. Currently, the research in concrete structural engineering is design-oriented and so prefers an empirical-computational methodology. However, rational methodology has historically been followed in the development of the structural theory. Theories of limited scope restricted by underlying assumptions or hypotheses are constructed. Examples include statical theory of physically linear elastic structures, theory of classically damped lumped mass linear structures, theory of elastic stability, etc. Following this rational methodology, the static and dynamic stability of fully cracked flanged concrete beam-columns in the form of a cantilever has been investigated by the authors earlier. In this paper, the effect of chosen measures and levels of damping on the dynamic stability of concrete beam-columns has been studied. Despite the limited scope of the problem, some new conclusions have been deduced.

In the classical theory of stability, the same critical values of conservative loads apply to both static as well as dynamic stability. Such also happens to be the case for these physically nonlinear conservative cracked concrete beam-columns as well. The same critical values of the axial and lateral loads are predicted to determine the vulnerability of concrete beam columns to creep-buckling. Also, the critical values of the axial and lateral loads are independent of the level as well as the measure of

structural damping adopted. However, statically stable structures can be rendered dynamically unstable for certain choices of initial conditions.

When the initial displacement $w(0)$ happens to be less than w_2, the second static equilibrium displacement, higher damping stabilizes the motion. However, for $w_2 < w(0) < w_u$, higher damping has been predicted to destabilize the vibrating structure. This is so because highly damped structures demand higher negative velocity to decrease the amplitude below w_2 when velocity vanishes. If this condition is not satisfied, the structure is rendered dynamically unstable. These conclusions hold for both for measures of the structural damping. Also, when $w(0) < w_2$, C-measure based computations can predict dynamic stability for the structures predicted to be unstable by ξ-based computations. Opposite is the case, when $w_2 < w(0) < w_u$.

As per the dominant paradigm in seismic analysis [4], elastic analysis predicts higher vibration amplitudes than the nonlinear (elastoplastic or hysteretic) analysis. In fact, the effect of structural ductility is incorporated in terms of a response reduction factor. Since higher damping also results in smaller vibration amplitudes, the nonlinear dynamic behavior is sought to be simulated by assigning higher equivalent viscous damping ($\xi = 0.2$) in the linear analysis. It has been predicted in this paper, that, in some cases, higher damping can destabilize the structure. This can be interpreted to imply that ductility may render the structures dynamically unstable. Similarly, the use of passive viscous or hysteretic dampers ($\xi_0 = 0.2$) may not be effective in controlling dynamic instability. Instead, in some cases, it may destabilize the motion of an underdamped ($\xi_0 = 0.03$) dynamically stable structure. Overdamped concrete beam-columns with sufficiently high level of damping are predicted to exhibit 'creep buckling'. Such is the case when the structure is subjected to statically inadmissible values of constant axial and lateral loads.

Conventionally, concrete structures are analyzed by estimating their stiffness based on the flexural rigidity of the gross (uncracked unreinforced) section. In contrast, in this paper, the flanged concrete beam-columns are assumed to be cracked in tension at all sections. Or equivalently, concrete has been assumed to be a no-tension solid. However, real concrete structural members are cracked in tension at discrete locations up to different depths. Obviously, the present theory has to be extended to simulate the dynamic stability of real concrete structures.

5 Conclusions

In this paper, the dynamic stability of highly damped flanged fully cracked conservative concrete beam-columns is investigated. Damping ratios and damping coefficients have been adopted as measures of structural damping. As per the dominant paradigm in structural dynamics, higher levels of damping are expected to control vibration amplitudes and hence dynamic instability. However, counter-intuitively, the higher equivalent viscous damping simulating the hysteretic ductile beam-columns is predicted here to destabilize their motion in some cases. Provision

of viscous or hysteretic dampers intended for passive control is instead shown to render some controlled structures dynamically unstable. Also, overdamped concrete beam-columns under sustained axial and lateral loads are shown to exhibit dynamic behavior resembling 'creep buckling'. Finally, rational methodology adopted here has been demonstrated to predict some genuinely new aspects of dynamic stability of concrete beam-columns.

References

1. Balevicius R (2010) An average stress strain approach to creep analysis of RC uncracked elements. Mech Time-Depend Mater 14:69–89
2. Bazant ZP, Cedolin L (2010) Stability of structures: elastic, inelastic, fracture and damage theories. Word Scientific Pub. Co., Singapore
3. Chajes A (1974) Principles of elastic stability. Prentice Hall, Englewood Cliffs
4. Datta TK (2010) Seismic analysis of structures. Wiley (Asia), Singapore
5. Dwairi H, Kowalski M (2004) Investigation of Jacobsen's equivalent viscous damping approach as applied to displacement-based seismic design. In: 13th world conference on earthquake engineering, Vancouver, BC, Canada, 1–6 Aug, Paper No 228
6. Hoyer TG, Hansen LZ (2002) Stability of concrete columns. PhD theses, Technical University of Denmark, Lyngby
7. Occhiuzzi A (2009) Additional viscous dampers for civil structures: analysis of design methods based on effective evaluation of modal damping ratios. Eng Struct 31:1093–1101
8. Sharma MR, Singh AK, Benipal GS (2012) Elastic stability of concrete beam-columns, part I: static stability. Communicated to International Journal of Structural Stability and Dynamics (IJSSD), July 2012
9. Sharma MR, Singh AK, Benipal GS (2012) Elastic stability of concrete beam-columns, part II: dynamic stability. Communicated to International Journal of Structural Stability and Dynamics (IJSSD), July 2012
10. Sharma MR, Singh AK, Benipal GS (2014) Stability of concrete beam-columns under follower forces. Latin Am J Solids Struct (LAJSS) 11(5):790–809
11. Sharma MR, Singh AK, Benipal GS (2014) Parametric resonance of concrete beam-columns under pulsating axial force. Latin Am J Solids Struct (LAJSS) 11(6):925–945
12. Simbirkin V, Balevicius R (2004) Long-term strength and deformational analysis of reinforced concrete columns. J Civil Eng Manage X(1):67–75
13. Zhou Y, Lu X, Weng D, Zhang R (2012) A practical design method for reinforced concrete structures with viscous dampers. Eng Struct 39:187–198

Part XXV
Steel Structures

Ductility Demand on Reduced-Length Buckling Restrained Braces in Braced Frames

Muhamed Safeer Pandikkadavath and Dipti Ranjan Sahoo

Abstract Concentrically braced frames (CBFs) experience strength and stiffness degradation due to the compression buckling of conventional braces in the event of seismic loading. This effectively reduces the ductility potential of conventional buckling-type braces (BTBs). On the other hand, the inhibition of global buckling instability of buckling-restrained braces (BRBs) results in nearly symmetric load displacement response with enhanced energy absorption ability and excellent low-cycle fatigue capacity in the non-elastic regions. The reduced axial stiffness and the preferred moment-released end connections of BRBs in buckling-restrained braced frames (BRBFs) sequels in an increased drift demand requirements as compared to the CBFs with BTBs. A hybrid brace with a combination of elastic BTB and yielding RLBRB for a smaller length in line can limit the drift response while maintaining the superior hysteretic behavior as that of the BRB. For such hybrid braces during the seismic action, RLBRB component can undergo balanced inelastic cyclic displacement response while the longer elastic BTB can provide the desired stiffness to reduce the drift response. However the ductility demand requirement in the RLBRB segment of the composite brace will be increased in proportion with the decrease in yield length of RLBRB in comparison with the full length yielding brace. The present study is focused on the ductility demand requirement in a low-rise 3-story building frame fitted with the proposed hybrid braces in all story levels. The study frame is designed considering design parameters similar to conventional BRBFs. Inverted-V (chevron) arrangement of braces were considered for the study frame in which the yielding length of the brace is considered to be one-third of the distance between the work points. The seismic performance of the hybrid braced frame is analyzed for design base earthquake (DBE) hazard level. The maximum inter story drift response, residual drift response, maximum ductility demand in RLBRB of the hybrid brace and the

M.S. Pandikkadavath · D.R. Sahoo (✉)
Department of Civil Engineering, Indian Institute of Technology Delhi,
New Delhi, India
e-mail: drsahoo@civil.iitd.ac.in

M.S. Pandikkadavath
e-mail: msafeerpk@gmail.com

distribution of brace ductility demand over the height of the frame were studied. The results are compared with the response of a low rise conventional BRBF designed with the same parameters.

Keywords Braced frames · Buckling · Ductility · Performance based design

1 Introduction

Concentrically braced frames (CBFs) are efficient lateral load resisting systems. The CBFs are widely used in buildings located in seismically active zones. The compression buckling of conventional buckling type braces (BTBs) leads to a loss in strength and stiffness in conventional CBFs in the event of severe earthquakes. This in turn reduces the energy absorption potential of conventional CBFs. Braces which were prevented from compression buckling can retain both stable stiffness and energy dissipation abilities. Buckling restrained braces (BRBs) are braces that can yield both in tension and compression. The BRBs show steady and nearly symmetrical hysteretic response without strength and stiffness deterioration. The frames with BRBs were termed buckling restrained braced frames (BRBFs). BRBFs are comparatively new types of CBFs which possess superior energy absorption capabilities compared to conventional CBFs in the post yield response scenario [7, 8].

BRBs consist of a central metallic yielding core (mostly made of steel), a buckling restraining concrete/mortar filled hollow steel section (HSS) and a de-bonding agent between the central yielding core and buckling restraining concrete/mortar. The de-bonding agent minimizes the shear interaction between the central core and the confining concrete. Figure 1a shows the cross sectional details of a typical BRB. The de-bonding agent facilitates the free expansion and contraction of the central core to achieve an improved ductility capacity in the BRBs. The central metallic/steel core of BRBs consists of a restrained yielding segment, a pair of restrained non yielding transition zones and unrestrained end connection zones on both ends as shown in Fig. 1b. The cross sectional area design of BRBs is governed by tension yielding as opposed to the compression buckling criteria in the case of
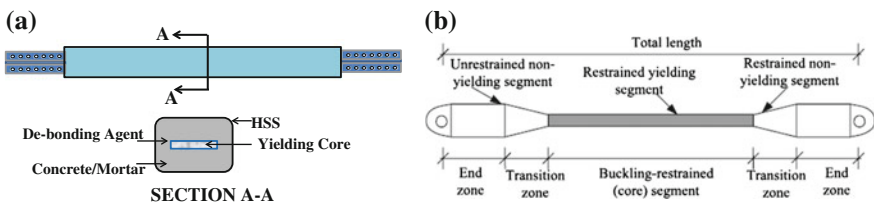
Fig. 1 **a** Schematic representation of a typical BRB and it's cross sectional details. **b** Central metallic core of a BRB

BTBs. This is possible due to the global buckling prevention and the resulting compression yielding capability of the BRBs. This effectively provides a smaller design cross sectional area to the BRBs compared to BTBs. Along with reduced cross sectional area of BRBs, the favored moment released beam-column joints lend a lower lateral stiffness to BRBFs. Past numerical and experimental investigations concluded that the reduced lateral stiffness of BRBFs results in an increased drift demand especially in the case of residual drift ratio (RDR) [2, 4].

The magnitude of RDR directly accounts for the extent of damage experienced by the frame system due to the dynamic ground shock. Any increase in axial brace stiffness and thereby the lateral stiffness of the braced frame can reduce the drift demands. Thus it can check the amount of damage and can make retrofitting/ reusability of the structure economical. A composite brace having a reduced buckling restrained yielding length brace and an elastic component in series for the remaining major length can increase the axial stiffness of the braces. The connection between reduced yielding length buckling restrained brace segment and the elastic section should be continuous without any secondary effects. During the inelastic action the reduced length BRB (RLBRB) can undergo balanced cyclic yielding and the elastic segment in series can provide the enhanced axial stiffness. A frame braced with such a composite brace having RLBRB for a minor length and an elastic BTB for major length in series can increase the lateral strength and thereby limit the drift demands to a desirable level. In this study the braced frame with the proposed composite brace (instead of BRBs) was termed as hybrid braced frame (HBF). Prior studies concluded that framed systems with the proposed braces (HBF) can reduce the drift requirement compared to BRBFs [6].

Apart from the drift limits, ductility capacities of the BRBs in BRBFs should be adequate to meet the maximum and cumulative ductility demands in the expected range of seismic action. Conventional BRBs have sufficient ductility capacities to meet the expected range of plastic deformations [5]. Most of the BRBs possess 60–70 % work point to work point length as yielding segment. Any reduction the yielding length (similar to RLBRB) will increase the ductility demand in the BRBs. This was due to the concentration of entire plastic demand in a smaller yielding length of reduced yielding length of BRBs compared to the longer yielding length of conventional BRBs. For the reduced proportion, yielding length of RLBRBs, the ductility demand hike should be quantified to develop a robust design procedure for HBFs. To quantify the ductility demand, the present study considered a yielding length of 30 % of work point to work point for RLBRBs. A proportionate length was assigned for non-yielding zones of RLBRB (7.5 % length each on both ends). The remaining length was allocated for elastic BTB with 7.5 % length of work point length for rigid ends on either ends. Figure 2a represent the proposed composite brace and Fig. 2b shows the HBF with composite brace.

For the above mentioned case a three story HBF and a three story BRBF were designed. The objectives of the present study were (i) to verify the increase in lateral strength of the HBF compared to BRBF through push over analysis, (ii) to verify the drift reduction in the HBF with respect to BRBF through non-linear time history analysis and (iii) to quantify the ductility demand increase in RLBRBs of
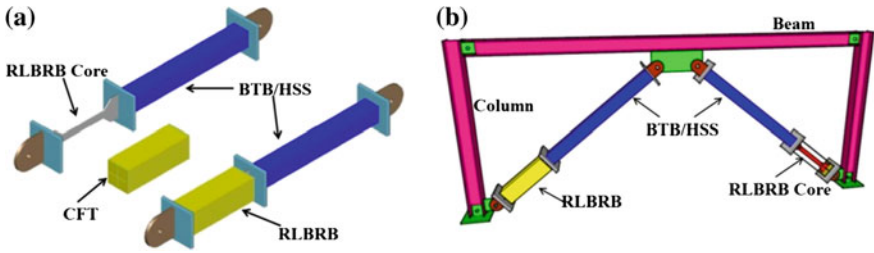
Fig. 2 **a** Composite brace having RLBRB and BTB in series. **b** HBF frame with composite brace

hybrid braces in the HBF in comparison with the BRBs in the BRBF. For the non-linear time history analysis of BRBF and HBF, twenty ground motions were considered which represent deign base earthquakes (DBE) [10]. The simulations were carried out and the results were analyzed.

2 Study Frame

A 3-story steel building having center to center plan dimensions of 54.84 m (6 bays at 9.14 m distance) by 36.56 m (four bays at 9.14 m distance) and a total height of 11.88 m as (three stories at 3.96 m height) shown in Fig. 3a was considered. For each principal loading direction two bays of BRBFs (symmetrically on both sides) were placed to resist lateral loads. All other interior beam column assemblies were kept as gravity load resisting frames. The braced frame with BRBs is termed BRBF and the frame with composite brace (RLBRB and BTB in series) was termed HBF. For the present study one braced frame along the longer plan dimension was taken and designed as per current recommendations of ASCE/SEI7-10 [1]. The total seismic weights on the first, second and third floors were 9,892, 11,875 and 11,875 kN respectively. A response reduction factor (R) of 8 was considered for both BRBF and HBF. The base of the column was assumed as fixed and the beam-column as well as brace end joints were assumed as moment free
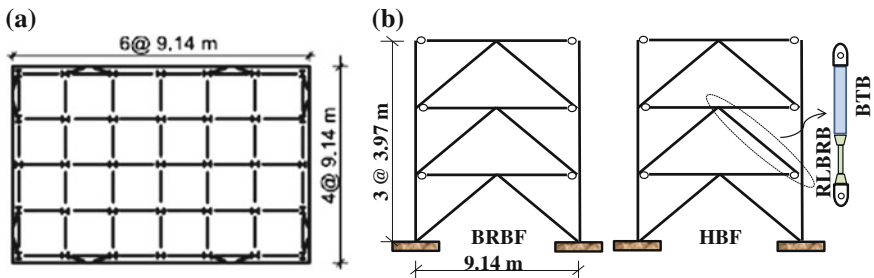
Fig. 3 **a** Plan of 3 story steel building. **b** Schematic plot of BRBF and HBF

Table 1 Member details of BRBF and HBF

Story	Frame	Beam	Column	Brace details	
				BTB/HSS	BRB (mm^2)
1st floor	BRBF	W 14 × 82	W 14 × 82	–	1,508
2nd floor		W 14 × 82	W 14 × 82	–	2,714
3rd floor		W 14 × 68	W 14 × 82	–	3,316
1st floor	HBF	W 14 × 82	W 14 × 82	HSS 12 × 12 × 1/2	1,658
2nd floor		W 14 × 82	W 14 × 82	HSS 12 × 12 × 1/2	2,985
3rd floor		W 14 × 68	W 14 × 82	HSS 10 × 10 × 1/2	3,647

connections. Chevron (inverted-V) configuration for the braces was chosen. For the design of BRBs a material over strength (R_y) of 1.3, tension strength adjustment factor (ω) of 1.4 and compression strength adjustment factor (β) of 1.1 was taken [9]. The yield strength of the braces was taken as 248 MPa. For the BTB the yield strength was 317 MPa and for all other members the material yield value was 345 MPa.

For the composite brace of HBF, top two third length was assigned for elastic BTB segment. The BTB segment was over sized to act elastically during the seismic loading. The RLBRB cross section was taken as 1.1 times the corresponding BRB area. This hike in cross sectional area was to account for the reduction in the yielding length of RLBRB. The increased cross sectional area of RLBRBs can provide better stiffness and reduce the excessive plastic demand in the RLBRBs. The connection between the BTB part and the RLBRB part in the HBF brace was assumed to be continuous without any lag effect. The intention of the composite brace in HBF was to allow RLBRBs to yield cyclically on demand, simultaneously letting BTBs to act as reinforcement to the system stiffness. Figure 3b shows the schematic representation of BRBF an HBF and Table 1, shows the cross section details of BRBF and HBF.

3 Analytical Modeling

In order to carry out the nonlinear analysis, analytical models of BRBF and HBF were created in SAP 2000 [3]. The beam column connections and brace end connections were taken as pinned joints. The column bases of the frames were fixed at the base and were continuous till the top floor. Panel zones were not modeled (assuming it has sufficient rigidity) and center to center frame dimensions were used for dimension. Bi-linear moment plastic hinges at the central regions of each beam were assigned. For the columns, flexural and axial-moment interaction plastic hinges at both ends were ascribed. For the BRBs of BRBF a yield length of 70 % of work point to work point length were assigned. The remaining 15 % on either side

were considered for rigid transition and end connection zones. The composite brace of the HBF had 30 % work point to work point length of total brace at bottom as RLBRB yielding length and 40 % length (top) was assigned for conventional BTB brace segment. For both RLBRB and BTB 7.5 % of work point to work point length on either side was assigned as rigid zone.

For BRBs and RLBRBs bilinear plastic force-deformation behaviors with yielding in both tension and compression was considered. The behavior of plastic yielding was characterized by a post yield stiffness of 2 % with kinematic strain hardening as shown on Fig. 4a. The plastic hinge was assigned at the center of the BRBs and RLBRBs. Figure 4b shows typical hysteretic behavior of bilinear plastic hinge response of BRBs/RLBRBs from the analysis. For the BTB segment of HBF (∼top two third length) a bilinear tension force-displacement behavior without strain hardening and having post compression buckling strength ratio as 0.3 was taken. This back-bone is as shown in Fig. 4a. The plastic hinges for BTB segments were allocated at 0.25, 0.5 and 0.75 lengths of the BTBs to monitor the probable hinge mechanism on the elastic section of the composite brace in case of yielding. The elastic BTB segment was selected on a slightly higher side to act elastically.

To take account of P-Δ effect of the frame system a gravity column with pinned base end at a distance of one bay from the braced frame was considered. The gravity column was connected with the frame using a pinned end rigid link at all floor levels, so that the link transfers only axial loads. The gravity column had moment release at each floor level to get the maximum drift and ductility demands on the frames. The moment release at each joint of the gravity column will offer least resistance to the frame to resist lateral loads. Twenty SAC ground motions (LA01 to LA20) which represents the design basis earthquake (DBE) were chosen for the dynamic analysis.
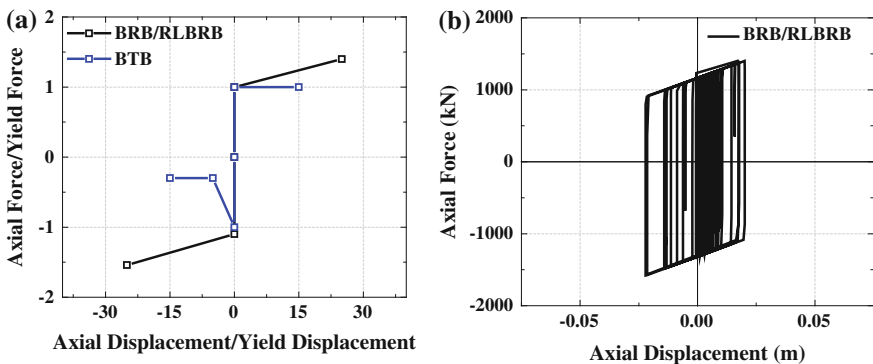
Fig. 4 **a** Plastic deformation nature of BRB/RLBRB and BTB. **b** Typical BRB/RLBRB analysis hysteresis

4 Analysis Results

The BRBF and HBF were modeled in SAP 2000 [3] software. The nonlinear static and dynamic analyses were carried out successively. The lateral load capacity, inter-story drift ratio, residual drift ratio and maximum brace ductility response under DBE hazard level are discussed in the following sections.

4.1 Push-Over Analysis

The lateral strength of the BRBF and HBF were obtained from the non-linear static analysis (Push-over analysis) and plotted in-terms of base shear and roof drift. The roof drift was taken as the ratio of top floor (roof) lateral displacement to the total height of the frame structure. The initial lateral stiffness and yield base shear of the HBF system was higher than the BRBF. The increased axial area and improved axial stiffness of the composite brace directed the HBF to such a refined response. The lateral yield forces were 1,628 and 1,790 kN respectively for BRBF and HBF. The column hinging was observed at around 1.5 % lateral drift for both BRBF and HBF. However the base shear at the point of column hinging for HBF (2,442 kN) was greater than that of BRBF (2,059 kN). The yielding of all the braces occurred at 2.6 % drift level in the HBF. The same (yielding of all braces) was observed in BRBF at a later stage (∼3.75 % of lateral drift) owing to possession of a longer brace yield length for conventional BRBs. At 5 % roof drift level all the braces of HBFs reached the ultimate strength. The BRBF showed a lateral capacity of 2,901 kN at 5 % roof drift level. While the HBF exhibited an enhanced base shear capacity of 3,356 kN for a similar level of lateral roof displacement. Figure 5a shows the comparison of base shear versus roof drift and Fig. 5b shows the plastic hinge mechanism at the end of 5 % roof drift.
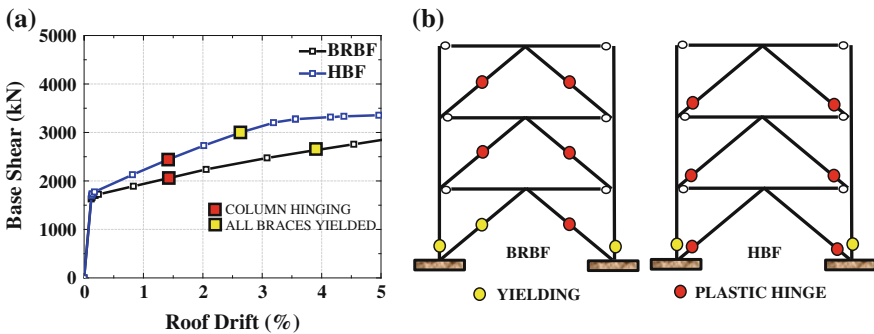
Fig. 5 **a** Base shear versus roof drift comparison of BRBF and HBF. **b** Yield mechanism at 5 % roof drift

4.2 Inter-story Drift Ratio

The maximum ratio of relative lateral displacement between any consecutive floors to the corresponding story height is termed the maximum inters story drift ratio (ISDR). ISDR gives the realistic lateral displacement demand on different floor levels over the height of the frame structure. The dynamic analysis to get the maximum ISDR for the DBE level ground motions were carried out and presented for both BRBF and HBF. From the ISDR responses for different earthquakes (DBE), quantities such as average ISDR, standard deviation and their combinations were estimated. Figure 6a shows the maximum ISDR over the story height of
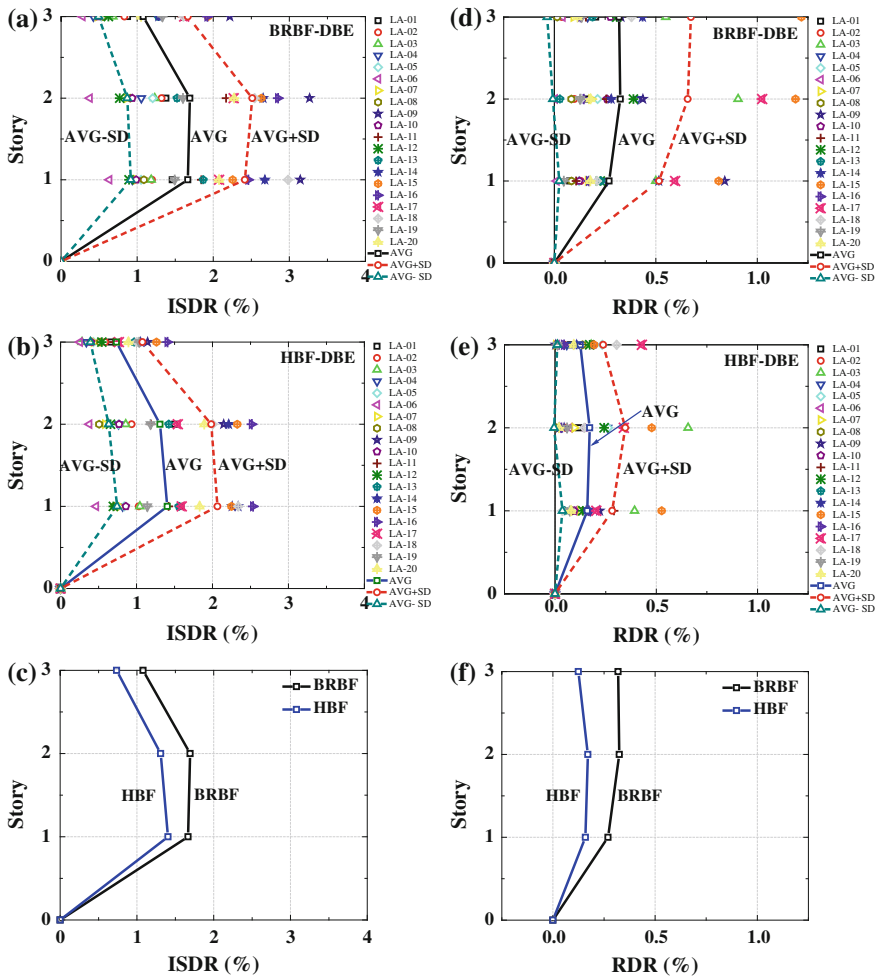
Fig. 6 **a** ISDR response of BRBF, **b** HBF, **c** comparison of ISDR response of BRBF and HBF, **d** RDR response of BRBF, **e** HBF and **f** comparison of RDR of BRBF and HBF

BRBF. The average of maximum ISDR observed at the second story was 1.69 %. The lowest maximum ISDR (average) was obtained at third story, which was numerically equal to 1.08 %. The first story had an average maximum ISDR of 1.67 %. The standard deviations of ISDR were 0.75, 0.82 and 0.57 respectively for first, second and third story of the BRBF.

The average maximum ISDR was noted at first story of HBF and it was equal to 1.40 %. The value was $\sim$16.2 % less than corresponding ISDR of BRBF. At second story and third story level the ISDRs were 1.31 and 0.74 % respectively. This result displayed a reduction in ISDR of 22.5 and 31.5 % for second and third story respectively in HBF compared to the BRBF. The standard deviation of ISDR values were 0.66, 0.68 and 0.34 % for first, second and third story respectively. Figure 6b shows the plot of average maximum ISDR of HBF over the frame height for DBE hazard level. Figure 6c depicts the comparison of average maximum ISDR of BRBF and HBF for the considered level of seismicity.

4.3 Residual Drift Ratio

The residual drift ratio (RDR) was considered as the drift response after the end of ground shaking analysis. RDR portrays the extent of damage suffered by the frame system due to the exposure to earthquakes. One of the central objectives of this investigation is to reduce the RDR of the braced frame system by implementing the proposed composite brace. The RDR distribution over the stories for the analyzed earthquakes were extracted and plotted. Figure 6d gives the average maximum RDR for BRBF. The maximum value was pointed at second story as 0.33 % with a standard deviation of 0.34 %. First story endured a RDR of 0.27 % with standard deviation of 0.25 %. The third story had RDR of 0.31 % (variation of 0.35 %).

The RDR for HBF is shown in the Fig. 6e. The HBF showed average maximum RDR of 0.16, 0.17 and 0.12 % for first, second and third floor respectively. The corresponding variations in mean maximum RDR values were 0.12, 0.18 and 0.12 % in the increasing sequence of story number. In all the story level HBF had lesser RDR compared to BRBF. The percentage difference of average maximum RDR of HBF and BRBF was about 48.5 % in the second story. The maximum percentage difference was about 61.30 % in first story and the least was about 40.7 % in the first story.

4.4 Brace Ductility

Ductility is defined as the ratio of maximum in-elastic displacement to the corresponding yield displacement. The brace ductility gives the maximum axial in-elastic extension/compression demand in the braces. The ductility capacities of braces should be adequate to meet the lateral drift and damage limits of braced frame

systems in the event of seismic loading. For the present study the maximum brace ductility of BRBF and HBF on DBE level earthquake was considered.

For the two braces on each floor the absolute maximum among the tension elongation and compression shortening was taken as the maximum brace ductility for each earthquake. The brace ductility distributions among the story height along with its standard deviation combinations were plotted for both frames.

Figure 7a shows the variation of brace ductility over the height of the BRBF. An average maximum ductility of 7.09 was observed for the second story with a
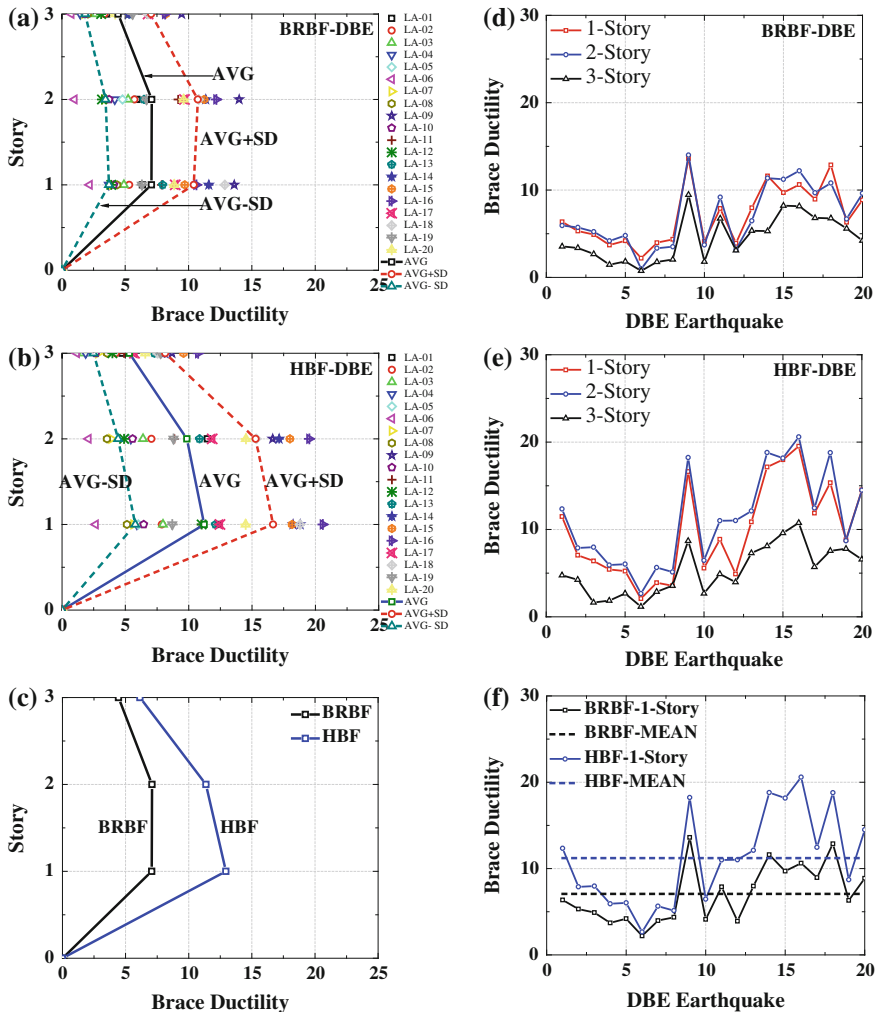
Fig. 7 **a** Brace ductility demand over the height of BRBF, **b** HBF, **c** comparison of brace ductility demand of BRBF and HBF, **d** brace ductility demand of BRBF over the height for DBE earthquake, **e** for HBF and **f** comparison of first story brace ductility demand of BRBF and HBF DBE earthquake

standard deviation of 3.65. The first story showed an average ductility of 7.07 and the top story exhibited a value of 4.45. The standard deviations observed for first and third stories were 3.35 and 2.60 respectively. The HBF showed an average maximum ductility of 11.22 at first story with a deviation of 7.38. This value was 1.59 times the corresponding average maximum brace ductility of BRBF. Second story braces of HBF showed a ductility value of 9.86 (deviation of 6.97) and third story showed ductility of 5.32 (deviation of 3.70). This indicates 1.39 and 1.20 times hike in ductility demand in the second and third story respectively in HBF to that of BRBF. Figure 7b shows the brace ductility of HBF on the floor level and Fig. 7c shows the comparison of the same with the BRBF.

The maximum brace ductility value distribution for different DBE ground excitation was presented. For BRBF story maximum ductility for all levels were observed for LA09. The values were 13.61, 13.94 and 9.46 respectively for first, second and third floor braces respectively. Figure 7d shows the plot of DBE versus brace ductility for all the floors for BRBF and Fig. 7e gives the same for HBF. The maximum ductility for HBF for all the floors was observed for LA16. First, second and third floor exhibited ductility's of 10.75, 19.52 and 20.60 respectively. As a comparison the behavior of first floor braces of BRBF and HBF were compared in Fig. 7f. For these cases, average ductility for BRBF was 7.07 and for HBF, it was 11.22. This shows an increase of demand 1.59 times in HBF than in the BRBF for first floor.

5 Conclusions

A 3 story BRBF with conventional BRB brace and a 3 story HBF with composite brace was modeled and analyzed for both non-linear static and dynamic analysis. The HBF was successful in reducing both ISDR and RDR under DBE level when compared to BRBF. The brace ductility demands in BRBF and HBF was inspected and compared. Table 2 shows the summary of analytical study results and from that, following conclusions were drawn.

- The HBF was more successful in reducing both ISDR and RDR than the BRBF. The average maximum ISDR at second story of HBF (1.31 %) was lesser by 22.5 % than that of BRBF (1.69 %).

Table 2 Comparison of ISDR, RDR and brace ductility's of BRBF and HBF

Story	BRBF			HBF			Difference		
	1	2	3	1	2	3	1	2	3
ISDR (%)	1.67	1.69	1.08	1.40	1.31	0.74	16.2	22.5	31.5
RDR (%)	0.27	0.33	0.31	0.16	0.17	0.12	40.7	48.5	61.3
Ductility	7.07	7.09	4.45	11.22	9.86	5.32	1.59	1.39	1.20

- The HBF had an average maximum RDR at second story of 0.17 %, which was 46.48 % less than the corresponding RDR of BRBF (0.33 %).
- The average maximum first floor brace ductility for BRBF (for DBE) was 7.07 and for HBF it was 11.22. HBF first story brace ductility demand was 1.58 greater than BRBF.

References

1. ASCE/SEI 7-10 (2010) Minimum design loads for buildings and other structures. American Society of Civil Engineers, Reston
2. Chao S-H, Karki NB, Sahoo DR (2013) Seismic behavior of steel buildings with hybrid braced frames. ASCE J Struct Eng 139(6):1019–1032
3. CSI (2009) CSI analysis reference manual for SAP 2000. Computers and Structures, Inc., Berkeley
4. Fahnestock LA, Ricles JM, Sause R (2007) Experimental evaluation of a large-scale buckling-restrained braced frame. ASCE J Struct Eng 133(9):1205–1214
5. Merritt S, Uang CM, Benzoni G (2003) Subassemblage testing of star seismic buckling-restrained braces. Report No. TR-2003/04, University of California, San Diego, CA
6. Pandikkadavath MS, Sahoo DR (2013) Seismic performance of steel frame structures with hybrid concentrically brace systems. In: Proceedings of international conference on rehabilitation and restoration of structures, IIT Madras, Chennai
7. Sabelli R (2000) Research on improving the design and analysis of earthquake resistant steel braced frames. FEMA/EERI report
8. Sabelli R, Mahin SA, Chang C (2003) Seismic demands on steel braced frame buildings with buckling-restrained braces. Eng Struct 25(5):655–666
9. Sahoo DR, Chao S-H (2010) Performance-based plastic design method for buckling-restrained braced frames. Eng Struct 32(9):2950–2958
10. Somerville PG, Smith M, Punyamurthula S, Sun J (1997) Development of ground motion time histories for phase 2 of the FEMA/SAC steel project. Report No. SAC/BD-97/04, SAC Joint Venture, Sacramento, CA

Stress Concentration Factor in Tubular to a Girder Flange Joint: A Numerical and Experimental Study

Dikshant Singh Saini and Samit Ray-Chaudhuri

Abstract Tubular to a girder-flange joints are widely used in various applications. For fatigue design of such joints, stress concentration factors (SCFs) are required. The stress concentration, especially in the welded joints of these structures, is a complex phenomenon. Usually, at the locations of high stress, cracks initiate and grow leading to a fatigue failure. For evaluation of SCF, in current practice, the 'hot spot stress' method is used. In this study, at first, a finite element (FE) analysis has been performed to predict the location of hot spot stresses in a fillet welded tubular to girder-flange joints under in-plane bending. The FE results show that the stresses are very high on the brace near the weld-toe and gradually decrease in the direction away from the weld. The SCFs and strain concentration factors (SNCFs) are then determined at the weld toe using linear extrapolation method. Further, a full scale tubular to a girder-flange joint was fabricated and tested in Structural Engineering Laboratory at IIT Kanpur. A monotonic loading scheme was used for applying in-plane bending through a displacement control scheme. Apart from the measurement of actuator load and displacement data, strains were measured at several locations through micro strain gauges. Based on the strain data, SNCF was calculated at various stages of loading. Although the trend of SNCF calculated from the experiments is found to be in reasonable agreement with the numerically obtained trend, the experimental results are, in general, found to be higher than those obtained from the FE analysis. This anomaly may be due to the placement of strain gauges. Further research is needed to confirm the findings.

Keywords Displacement control scheme · Finite element analysis · Hot spot stress method · Stress concentration factors

D.S. Saini (✉) · S. Ray-Chaudhuri
Department of Civil Engineering, IIT Kanpur, Kanpur 208016, Uttar Pradesh, India
e-mail: dikshant@iitk.ac.in

S. Ray-Chaudhuri
e-mail: samitrc@iitk.ac.in

1 Introduction

Tubular to a girder-flange T-joint are made up of circular hollow section (CHS) braces and girder chords. These are used in variety of structures such as trusses and offshore structures. Especially in offshore structures, there joints are quite common in the deck of fixed or floating type (water depth >300 m) offshore platforms. During the service life, these structures are subjected to fatigue damage attributable to several loads such as wind, waves and ice loads. Usually, fatigue damage initiates near the weld toe in the highly stressed region. Therefore, it is of foremost importance to determine stress distribution for the proper fatigue design of these joints.

The hot-spot stress method, also known as geometric stress method, is currently being used in practice for fatigue design of these joints. The governing parameter in this approach is the hot-spot strain (HSSN) range ($\Delta\varepsilon_{HS}$) or the hot-spot stress (HSS) range ($\Delta\sigma_{HS}$). They are determined by considering all the stress raising effect due to structural discontinuity except the stress concentration due to weld profile. Therefore, extrapolation procedures are adopted in the specified region to obtain the hot-spot stress. The location from which the strains are extrapolated depends on the dimensions of the joint. The boundaries for the extrapolated region are given in CIDECT Design Guide No. 8 [1].

At present, the literature related to stress concentration in tubular to a girder-flange T-joint is minimal. In this paper, detailed finite element (FE) models were developed in ABAQUS CAE [2]. A full-scale specimen were then fabricated and tested in Structural Engineering Laboratory at IIT Kanpur to verify the FE model. The FE results and the experimental results are then compared to study if the stress/strain concentration phenomenon near the brace-chord intersection is captured well.

2 SNCF and SCF

The ratio of hot-spot strain to the nominal strain is defined as the Strain Concentration Factor (SNCF). If stress is used instead of strain, it is known as Stress Concentration Factor (SCF). Thus,

$$SNCF = \frac{\varepsilon_{HS}}{\varepsilon_{nom}} \quad SCF = \frac{\sigma_{HS}}{\sigma_{nom}} \tag{1}$$

The ratio of SCF to SNCF is known as the S/N ratio. The nominal stress or strain is calculated using beam theory as follows:

$$\sigma_{nom} = \frac{My}{I} \quad \varepsilon_{nom} = \frac{My}{EI} \tag{2}$$
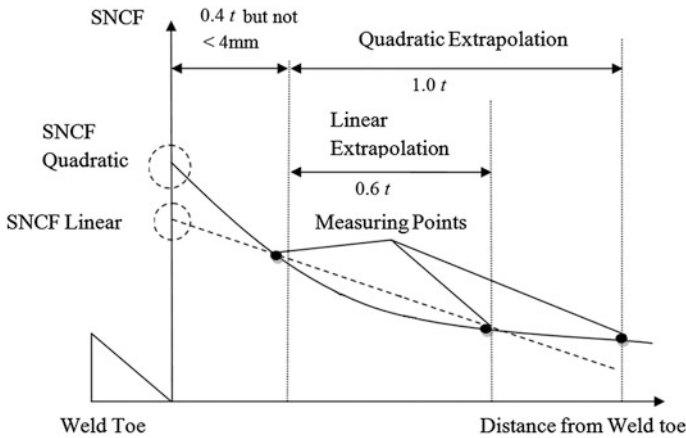
Fig. 1 Methods of extrapolation to the weld toe (CIDECT Design Guide No. 8 [1])

where, M = maximum moment at the weld-toe; I = moment of area at the weld-toe; y = distance of the extreme fiber of the brace member from the neutral axis. In order to evaluate SCF and SNCF, two extrapolation methods: (i) linear and (ii) quadratic are popular (CIDECT Design Guide No. 8 [1]). These are shown in Fig. 1, where t is wall thickness.

3 Finite Element Model

The finite element analysis of tubular to a girder-flange T-joint was carried out using well known finite element software ABAQUS CAE [2]. Three-dimensional ten-node tetrahedral element with modified formulation (C3D10M) was used in this study. This is because this element is affected minimally from shear and volumetric locking, and is more suitable in high stress gradient areas. This elements also offers free meshing technique, which was required in the modeling due to complexities involved in geometry of tubular to a girder-flange T-joint. Mesh convergence study was carried out in order to achieve an optimum mesh size in terms of computation time and accuracy. For obtaining a more accurate model, smaller elements were used in the region of high stress gradient, i.e., near the weld toe, whereas coarser elements were used away from the weld toe to save computation time. From this study, two elements were found to be reasonable for the thickness of the brace and chord members.

In this study, Young's modulus (E) and Poisson's ratio (v) were taken as 2×10^5 N/mm^2 and 0.3, respectively, for the girder and circular hollow section. The welding material is assumed to have the same material properties as that of the structural sections. Similar assumption was made in earlier studies [3, 4]. In this work, the weld was modeled as a ring of solid elements having triangular

Table 1 Geometric properties of chord and brace

Chord		Brace	
Sectional area (a)	5,626 mm^2	Outside diameter (d_o)	88.9 mm
Depth of section (D)	300 mm	Thickness (t_o)	4.8 mm
Width of flange (b_f)	140 mm	Sectional area (A)	1,270 mm^2
Thickness of flange (t_f)	12.4 mm	Length (l)	840
Thickness of web (t_w)	7.5 mm		
Length (L)	1,000		

cross-section, wherein, the weld size was modeled in accordance with the specifications given in CIDECT Design Guide No. 3 [5]. The throat thickness 't_a' was taken as 1.1 t. The geometrical properties are given in Table 1.

Coupling constraints with kinematic coupling were used to apply load at the center of brace to prevent unwanted moments in brace ends. Displacement control loading scheme was adopted in the load displacement analysis. Only half of the non-tubular joint was modeled by taking advantage of the plane of symmetry in loading and boundary conditions and cutting the section along this plane. The nodes at the symmetrical plane were not allowed to move perpendicular to that plane and were restrained against rotation in the other directions. The two chord ends were fixed against all degrees of freedom.

Further, load displacement analysis was also carried out. For non-linear analysis, the experimentally obtained stress-strain curves of the materials were used in the finite element modeling. However, weld properties were assumed to be elastic for non-linear analysis as the strength of weld is much higher than the strength of material used for structural sections.

The SCF and SNCF were found to be 2.269 and 2.01, respectively. Figure 2 shows the variation of SCF versus SNCF around the weld toe with maximum SCF at 0° and 180° angles. The SCF and SNCF values at 90° can not be defined as the nominal bending stress at the neutral axis is zero. However, a crude value of 0 was

Fig. 2 The variation of SCF and SNCF with angle around the under in-plane bending
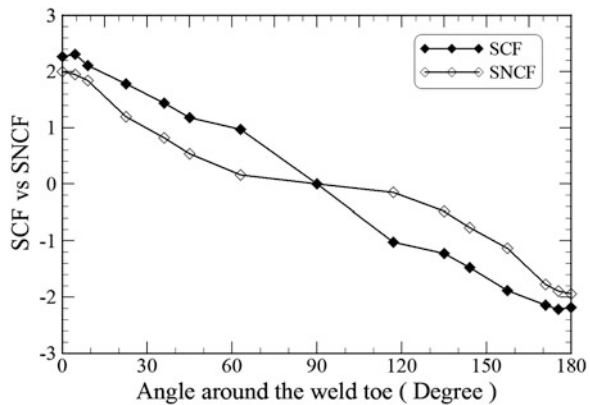
Fig. 3 Stress distribution in the chord under in-plane bending
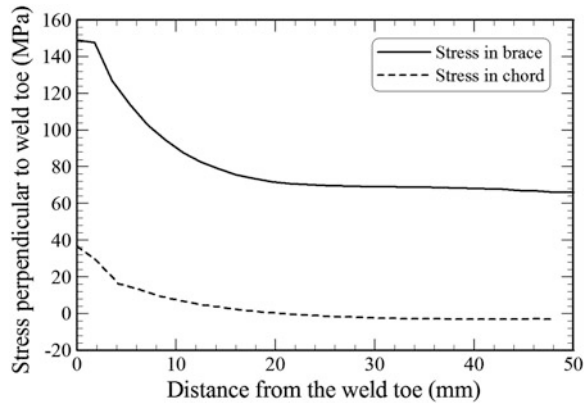
taken for 90° angle. The SCF/SNCF was found varying from 0° to 180° angle around the weld toe. From this figure, the S/N ratio (ratio of SCF and SNCF) for this model was found to be same for 0° to 180° angles. Hence, these locations are defined as the hot-spot location. Figure 3 shows the stress distribution in the chord of the joint. The maximum stress in chord was about 25 % of the maximum stress in the brace. Hence, it can be inferred that the failure will eventually occur in the brace under in-plane bending. In this study, SCF was calculated only for the brace member.

4 Experimental Investigation

An experimental study was carried out to determine SCFs for welded tubular to a girder-flange T-joint. A full scale joint specimen was fabricated from a circular hollow section (CHS) and an I-section as brace and chord members, respectively. The mechanical properties of the steel coupons of CHS and Girder/I-sections were evaluated from a series of tensile coupon tests.

4.1 Specimen

A full-scale specimen was designed and fabricated. Full-scale specimen was preferred as the reduced scale model tends to have oversized weld, which causes stiffening around the joint intersection. Figure 5 shows a schematic diagram of the T-joint with the dimensional and geometrical properties. In this study, ISMB300 I-section/Girder was taken as the chord and a circular hollow section of diameter 88.9 mm and thickness 4.8 mm as the brace. The dimensions of the joint were taken same as that in the Finite Element model.
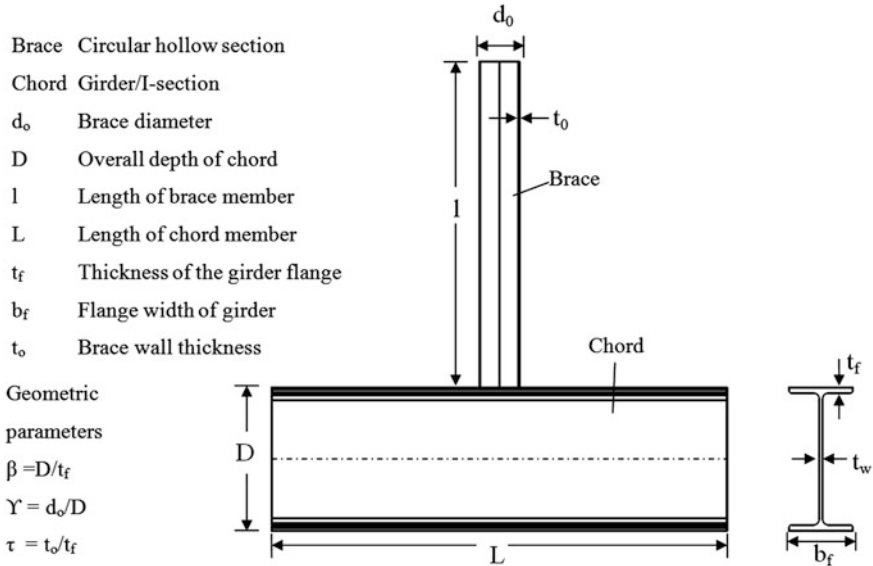
Fig. 4 Definition of geometric parameters of tubular to a girder-flange T-joint

Based on Table 1, the geometric parameters as defined in Fig. 4 are $\beta = 0.296$, $\gamma = 24.194$, $\tau = 0.387$. The specimen was fabricated with brace member aligned at right angle to the continuous chord member. The weld connection between the CHS section and girder was achieved using fillet weld as per the specifications proposed by Packer et al. [5]. The welding was done in three layers. The other end of the CHS section was welded to a 25 mm thick plate, which was then connected to an another plate of dimensions 330 mm × 330 mm × 25 mm through weld. This plate was connected to the actuator. Two plates were required to make a perfect T-junction in order to cause pure bending in the in-plane direction only. It was ensured that the junction was rigid enough to cause any deformation in itself. The web of the chord was connected to the supports through a bolted web-angle connection, which was designed to carry a reaction of 250 kN due to factored loads. The length of the brace member was considered from the connected chord surface to the end support (Fig. 5).

4.2 Strain-Gauge Locations

Sixteen micro strain gauges were used for experiment. TML (http://www.tml.jp/) strain gauges model no. FLK-2-17 having gauge length of 2 mm were used. Strain gauges were placed back to back in such a way that they can record values at a distance of 4 and 8 mm from the weld toe. Figures 7 and 8 show details of strain gauges used to measure strain gradient at hot-spots and nominal strain in the brace,
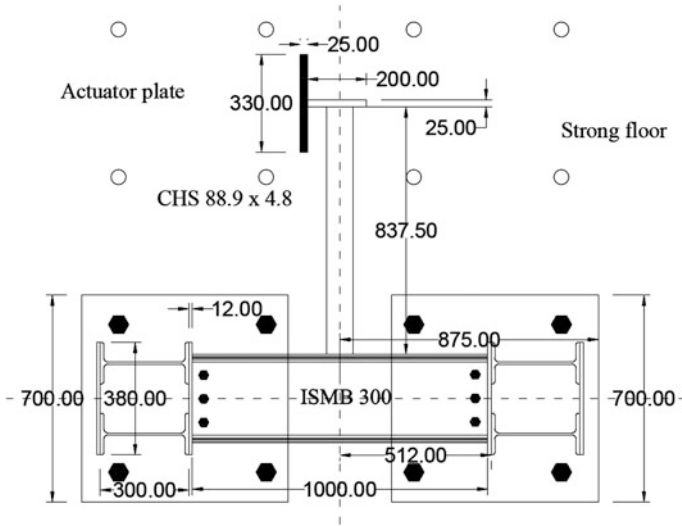
Fig. 5 Schematic diagram experimental setup of tubular to a girder-flange T-joint

respectively. In aforementioned figures, the SGB strain gauges were placed on the brace and SGC strain gauges were placed on the chord. Figure 6 shows the locations of the strain measurement in brace and relative orientation of strain gauges placed on the brace. Strains were measured along three lines i.e., 0°, 15° and 345° on the compression side and along a 180° line on the tension side as shown in Figs. 7 and 8. Strain gauges placed on the brace member to measure the nominal strain shown in Fig. 8a. These strain gauges were placed at a distance of 300 mm from the weld toe on both the sides of the brace i.e., at 0° and 180°. Two strain gauges were placed in chord at 0° and 180° near the weld toe.
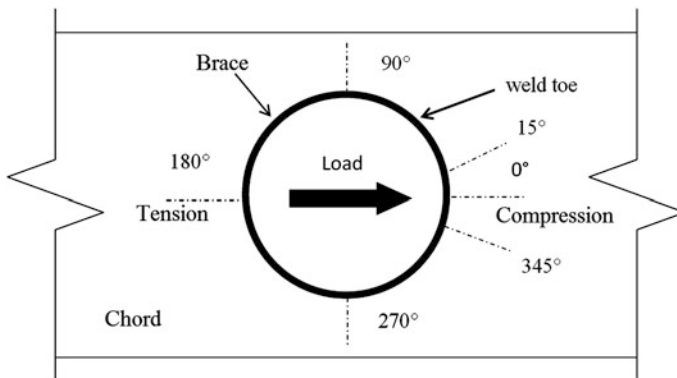
Fig. 6 Specimen plan showing different angle lines
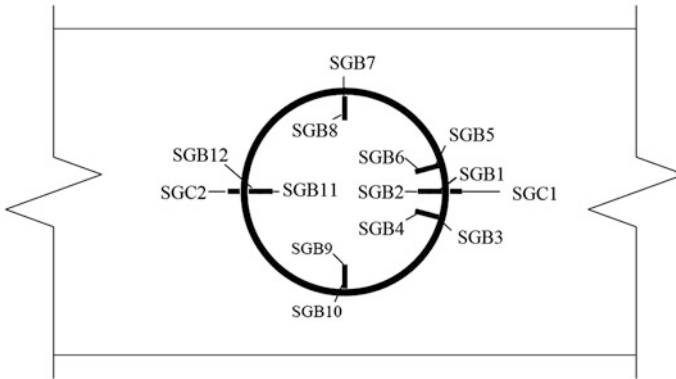
Fig. 7 Distribution of strain gauges on brace and chord members

Fig. 8 Distribution of strain gauges on brace to measure nominal strain
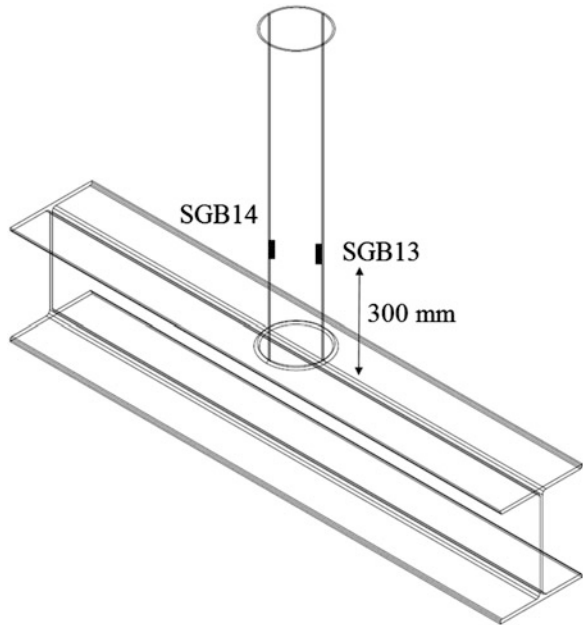
4.3 Loading Scheme

A 500 kN servo hydraulic actuator was used to apply load to cause in-plane bending in the joint. The specimen was subjected to a prior (low level) loading and unloading in order to remove the effect of residual stresses in strain measurements that may have occurred due to fabrication flaws of the joints. The actuator had a stroke length of ±125 mm from its mean position. A monotonic test was conducted

to determine SNCF in a number of steps. Displacement control loading scheme was used for the monotonic test. Initially, a rate of loading of 0.2 mm/min was employed for session duration of 3 min. After the specimen reached non-linear zone, the rate of loading was increased to 0.4 mm/min and then to 1 mm/min. The strain gauge data were recorded continuously by System 5000, a PC based data acquisition system.

5 Results and Discussion

Load displacement curves obtained from experiment and findings from the finite element results, respectively were compared to verify the finite element model. Comparison of relationship between load (kN) versus displacement (mm) for in-plane bending load obtained from experiment and FE results is shown in Fig. 9. A maximum load of 14.75 kN was observed from the experiment as compared to 16.9 kN of FE results. The load displacement curve obtained from experiment matches well with the FE results, with a slight deviation in the post yield part. Thus, deviation between the results of FE and the experiment can be attributed with the fact that the plastic material properties of the weld were not incorporated in the FE model. Figure 10 shows the stress distribution along a path perpendicular to the weld-toe. The figure clearly shows that the FE results matches with the experimental results. It is clear from this figure that outside the area of stress concentration, FE analysis solution perfectly matches with an analytical solution. In these figures, the stress/strain distribution is drawn for compression side i.e., 0° angle. However, similar results with slightly lower values were obtained on the tension side (180°).

Figures 11 and 12 show the SNCF values calculated from the extrapolated strain on tension and compression sides of the joint. The SNCF values were calculated using Eq. 1 on both tension and compression sides. The SNCF values on the

Fig. 9 Load versus deformation curve under in-plane bending
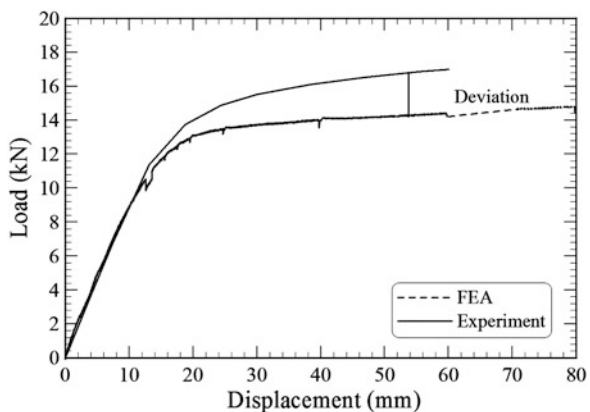
Fig. 10 Comparison of strain distribution in the brace member under in-plane bending
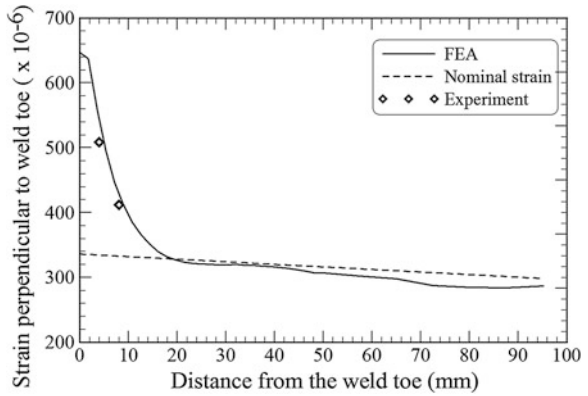
Fig. 11 Comparison of experimental and numerical SNCF on compression side
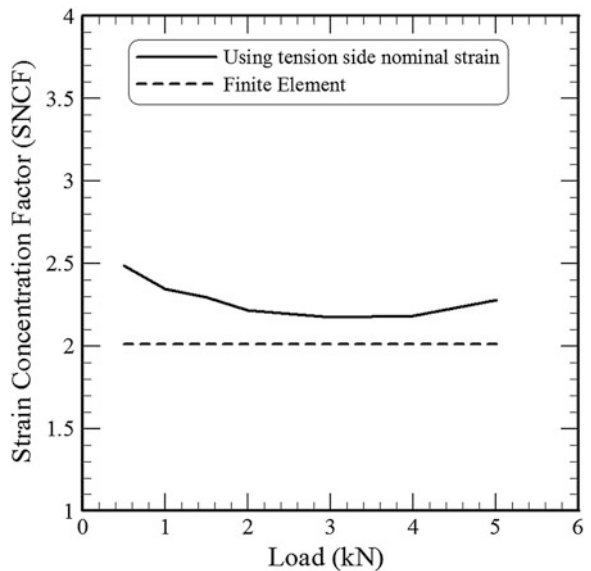
compression side matches well with FE results. The SNCF values on the tension side (180°) calculated from the experimental nominal strains were found to deviate largely from the SNCF values calculated from the theoretical nominal strain. However, the extrapolated strains on both tension and compression sides were found to be same. This anomaly may be due to the faulty calibration of the strain gauge SGB14 which is evident from Fig. 13. The comparison of nominal strain measured on the tension side and the nominal strain obtained from analytical formula did not have a 45° slope. Therefore, SNCF on tension side were also calculated using nominal strain on compression side. The results show significant reduction in the difference between experiment and FE results (see Fig. 12).

Fig. 12 Comparison of SNCF on tension side
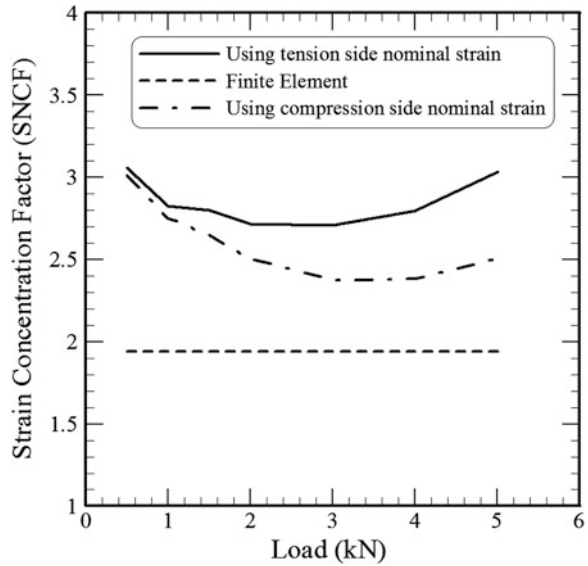
Fig. 13 Comparison of nominal strain measured on tension and compression sides
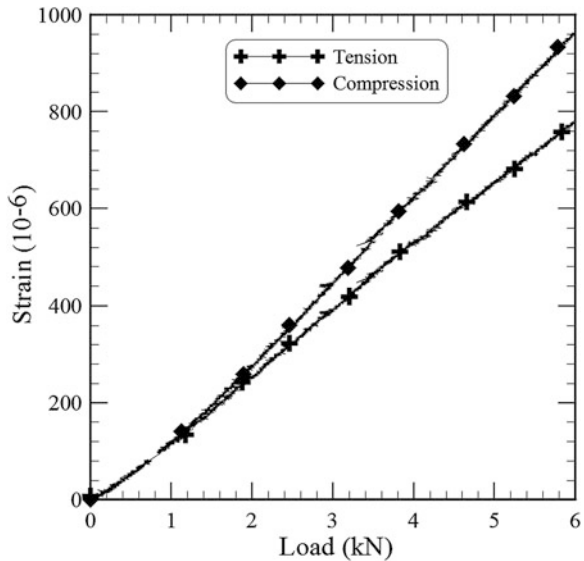
The SCF/SNCF values obtained from the experimental results were found to be higher than the FE results. This is due to sensitivity of hot-spot stress to location of extrapolation points. Since, the length of strain gauges is 4 mm with a gauge length of 2 mm; the strain could not be measured at the desired (recommended) places. This seems to be the major source of error. The weld geometry was also non-uniform

around the circumference in the test specimen. Further experiments are thus needed with better strain measuring instruments to accurately predict the value of SNCF and SCF.

6 Conclusions

An experimental study to evaluate SCF/SNCF was conducted on full-scale tubular to a girder-flange T-joint under in-plane bending. Strain gauges were used at weld toes to determine strain concentration factor. Three-dimensional finite element (FE) models were developed in ABAQUS CAE [2] using tetrahedral elements. Apart from the strain/stress evaluation, Load displacement analysis was also carried to compare with the experimental results. The FE models were found to capture the strain/stress distribution phenomena at the brace-chord intersection. From the experimental investigation, the trend of load-displacement curve obtained was found to match well with the finite element analysis results with a slight deviation in the post-yield part. The following key conclusions can be drawn from this study:

1. For the chosen specimen, the SNCF is found to be in the range of 2–2.25 under in-plane bending when the linear extrapolation used.
2. Using linear extrapolation, the S/N ratio at the hot-spot location is found to be 1.13 under in-plane bending.
3. The hot-spot location under in-plane bending are found to be at 0° and 180° angles (as shown in Fig. 6).

References

1. Zhao XL, Herion S, Packer JA, Puthli R, Sedlacek G, Wardenier J, Weynand K, van Wingerde AM, Yeomans N (2000) Design guide for circular and rectangular hollow section joints under fatigue loading. Verlag TÜV Rheinland, Köln
2. ABAQUS CAE (2012) Analysis user's manual, Version 6.12. ABAQUS, Inc
3. Kršćanski S, Turkalj G (2012) FEM stress concentration for fillet welded CHS-plate T-joint. Eng Rev 32(3):147–155
4. Tong L, Zheng H, Mashiri F, Zhao X (2013) Stress-concentration factors in circular hollow section and square hollow section T-connections: experiments, finite-element analysis, and formulas. J Struct Eng, ASCE 139(11):1866–1881
5. Packer JA, Zhao XL, Wardenier J, Van Der Vegte GJ, Kurobane Y (2009) Design guide for rectangular hollow section (CHS) joints under predominantly static loading. Verlag TÜV Rheinland, Köln

Studies on Fatigue Life of Typical Welded and Bolted Steel Structural Connections

G. Raghava, S. Vishnuvardhan, M. Saravanan and P. Gandhi

Abstract This paper presents the results of fatigue tests conducted on typical welded and bolted connections made of IS 2062: 2011 steel and conforming to selected Constructional Details categorised in IS 800: 2007. The connection types include: longitudinal and transverse butt welded connections, fillet welded cruciform connections with load-carrying and non-load-carrying welds, and bolted (double cover butt type) connections. The tests were carried out at various values of maximum stress which were decided as a percentage of the yield strength of the base material. The *S–N* data obtained were compared with the characteristic *S–N* curves recommended in IS 800: 2007. In the case of transverse butt welded joints, all specimens which were tested at a maximum stress value equal to 65 % of the yield strength of the material and above, and one out of the two specimens tested at a maximum stress value equal to 60 % of the yield strength of the material failed to satisfy the codal provisions. Two out of the three cruciform joints with load-carrying welds tested at a maximum stress value equal to 80 % of the yield strength of the material failed to satisfy the codal provisions. Bolted specimens which were tested at a maximum stress value equal to 60 % of the yield strength of the material and above failed to satisfy the codal provisions.

Keywords Bolted connections · Fatigue life · Steel structures · Structural connections · *S–N* curves · Welded connections

G. Raghava (✉) · S. Vishnuvardhan · M. Saravanan · P. Gandhi
Fatigue and Fracture Laboratory, CSIR—Structural Engineering Research Centre (SERC),
CSIR Campus, Taramani, Chennai 600113, India
e-mail: raghavag@serc.res.in; raghavag@yahoo.com

S. Vishnuvardhan
e-mail: svvardhan@serc.res.in

M. Saravanan
e-mail: sardirajm@serc.res.in

P. Gandhi
e-mail: pgandhi@serc.res.in

1 Introduction

Fracture due to fatigue and consequent failure is very common in steel structures. Such failures occur predominantly at component connections. "Connections" refer to those locations in a structure where elements are joined to accommodate changes in geometry and/or fabrication or service requirements. Fatigue cracking in bridges, ships, offshore structures, pressure vessels, and buildings occurs, almost without exception, at the welded or bolted connections and attachments. Classification method or S–N curve approach is the basic method for fatigue strength evaluation of structural connections recommended in most of the current fatigue design specifications. The design rules are based on a statistical analysis of data obtained from fatigue tests, to produce the best-fit mean S–N curve by the method of least squares. IS 800: 2007, "General construction in steel—code of practice" [1] also includes a section on 'fatigue' where S–N curves have been given for different non-welded and welded Constructional Details. The S–N curves adopted in IS 800: 2007 [1] are similar to those given in EN 1993-1-9: 2005, "Eurocode 3: Design of steel structures—fatigue" [2], for different Constructional Details. In this background, it was felt necessary to check, at least in selected cases, whether the steel structural connections fabricated in Indian conditions and made of structural steel available in open market in India, conforming to IS 2062: 2011 [3], "Hot rolled medium and high tensile structural steel—specification", would satisfy the IS codal provisions in terms of fatigue life, i.e., number of cycles to failure. The steel used in the present studies was procured from open market in Chennai. Fabrication of the connections was carried out by a fabricator who is considered 'reasonably good' and is regularly carrying out fabrication jobs related to structural engineering applications.

Kainumaa and Kimb [4] examined the fatigue behavior of load-carrying cruciform fillet welded joints made with mild steel plates of different thicknesses. The fatigue strength was also analyzed using linear elastic fracture mechanics on 34 parametric models simulating welded joints with different plate thicknesses. From the experimental and analytical results, the effects of the thickness ratio of the main plates and the change in cross plate thickness on fatigue strength were evaluated. The fatigue life of butt welded joint specimens under oblique loading was experimentally investigated by Jen et al. [5]. Five types of specimens with different oblique butt welding angles were used for the fatigue tests and subjected to fixed-directional loading to study the effect of oblique loading on fatigue strength of butt welded structures. Based on the local stresses obtained from finite element analysis, fatigue life of the specimens were evaluated using multiaxial fatigue prediction models.

Lee et al. [6] carried out studies on the effect of weld geometry on the fatigue life of non-load carrying fillet welded cruciform joints. The weld geometry of the cruciform specimens was varied, and fatigue tests were carried out on various weld geometry configurations. The configurations included weld flank angle, weld toe radius and weld throat thickness. Based on the experimental results, correlation between the weld geometry and the fatigue life of non-load carrying fillet welded cruciform joints was studied. Minguez and Vogwell [7] studied the effect of torque tightening on the

fatigue strength of bolts by experimenting on single and double lap bolted joints. The effect of pre-tensioning the bolts and plate thickness on the fatigue life of the bolted joints was also studied. Chakherlou et al. [8] carried out fatigue life and crack growth investigations on torque tightened bolted joints by comparing experimental results with numerical models. The effect of torque tightening on the fatigue life of bolted joints was studied. The fatigue life improvement due to clamping force is due to the compressive stresses developed during clamping.

In the present studies, fatigue life of transverse and longitudinal butt welded connections, fillet welded cruciform connections with load-carrying and non-load-carrying welds, and bolted (double cover butt type) connections conforming to selected Constructional Details categorized in IS 800: 2007 [1] is evaluated.

2 Material Properties

The steel used in the present studies is regular structural steel used in India, conforming to IS 2062: 2011 [3]. Chemical analysis and tension tests were carried out on samples of the steel to evaluate chemical composition and mechanical properties. The chemical analysis was carried out at the Chennai unit of the CSIR—National Metallurgical Laboratory. Table 1 shows the chemical composition of the steel and the specified values of various constituents as per IS 2062: 2011 [3]. Mechanical properties of the material were determined by carrying out tension tests as per ASTM E 8 M-2004 [9]. Three specimens were tested using a ±250 kN capacity Universal Testing Machine. An extensometer of 50 mm gauge length was used to measure the elongation during testing. Table 2 shows the mechanical properties of the steel,

Table 1 Chemical composition of the steel

Constituent	Welded specimens (%)	Bolted specimens (%)	Specified (%, max.) (IS 2062: 2011)
Carbon	0.130	0.164	0.200
Manganese	1.100	1.063	1.500
Sulphur	0.038	0.002	0.045
Phosphorous	0.034	0.013	0.045
Silicon	0.030	0.147	0.450

Table 2 Mechanical properties of the steel

Properties	Welded specimens	Bolted specimens	Specified (min) (IS 2062: 2011)
Yield strength, σ_y (MPa)	306	306	300
Ultimate strength, σ_u (MPa)	468	455	440
Modulus of elasticity, E (GPa)	200	190	–
Elongation (%)	31.50	25.65	22

average values based on the three tests, and the specified values as per IS 2062: 2011 [3]. The average yield strength and ultimate tensile strength of the material were found to be 306 and 462 MPa, respectively. The Young's Modulus and % elongation of the material were 195 GPa and 28.58 respectively. The steel used in the present studies satisfies the requirements of Grade E 300 of IS 2062: 2011.

3 Experimental Studies

S–N testing and crack growth testing are two different approaches for fatigue life evaluation. In S–N testing, fatigue life of a specimen, a component, or a structure is determined under given conditions of stress and environment. In crack growth testing, material parameters are obtained, characterizing fatigue crack growth as a material property in the given environment. In the present studies, fatigue life evaluation of welded and bolted connections made of IS 2062: 2011 [3] steel, using S–N testing approach, have been carried out.

3.1 Specimen Details

Fatigue life of four different types of welded connections and one type of bolted connections made of IS 2062: 2011 [3] steel and conforming to selected Constructional Details categorized in IS 800: 2007 [1] was evaluated. The connection types include: (a) longitudinal butt weld conforming to Constructional Detail 12 (Detail Category 83), (b) transverse butt weld conforming to Constructional Detail 19 (Detail Category 66), (c) cruciform joint with load-carrying welds conforming to Constructional Detail 26 (Detail Category 52), (d) non-load carrying longitudinal fillet weld conforming to Constructional Detail 32 (Detail Category 52) and (e) bolted connections conforming to Constructional Detail 4 (Detail Category 103). Constructional Detail is the number given to each connection type categorized in IS 800: 2007 [1]. Detail Category is the designation given to a particular Constructional Detail to indicate the S–N curve to be used in fatigue life assessment.

Figures 1, 2, 3, 4 and 5 show the details of the test specimens. In the case of welded specimens, the joints were formed by Manual Metal Arc (MMA) welding conforming to Indian Standard Code of practice IS 9595: 2003 [10]. ASTM E 466-1996 [11] was followed in fabricating the longitudinal butt welded specimens. The overall size of the specimens was 500 mm × 90 mm × 16 mm and width at the test section was 50 mm. The size of the transverse butt welded specimens was 500 mm × 36 mm × 20 mm. Welding was carried out with weld run-off tabs, which were subsequently removed and ends ground flush in the direction of stress. In the case of cruciform joints with load-carrying welds, size of the main plate including weld was 500 mm × 50 mm × 16 mm and size of the intermediate plate was 300 mm × 50 mm × 16 mm. The overall size of the non-load carrying longitudinal
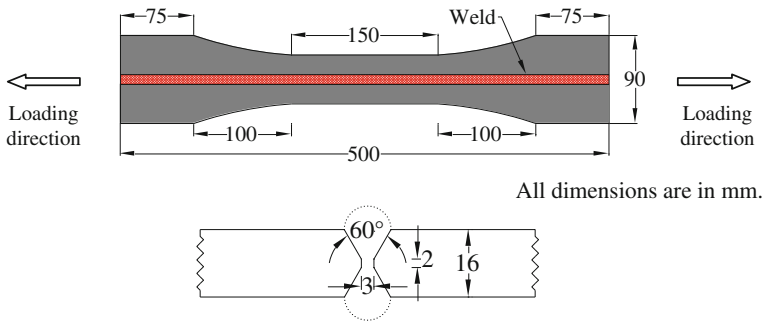
Fig. 1 Longitudinal butt welded joint
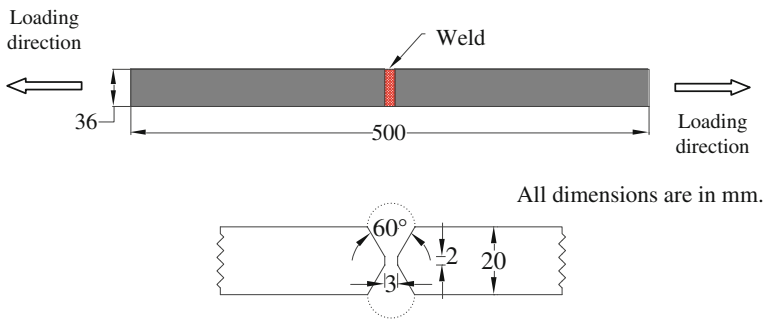
Fig. 2 Transverse butt welded joint

fillet welded specimens was 500 mm × 50 mm × 16 mm and size of the lateral attachment was 100 mm × 50 mm × 16 mm. The overall size of the bolted connections was 500 mm × 75 mm × 16 mm. The specimens were designed such a way that the strength of the connection was equal to the strength of the plate. The connection consisted of eight numbers of 12 mm diameter bolts (8.8 Grade). The ultimate tensile strength of the bolts was 800 MPa and the bolts were tightened with a torque of 100 Nm. In many of the day-to-day structural fabrications, no post-fabrication non-destructive testing (NDT) is carried out. The objective of the present studies was to evaluate such connections for fatigue life. Hence, no NDT has been carried out on the connections after welding/fabrication.

3.2 Test Details

Depending on availability of the equipment, the fatigue tests were carried out using either a ±250 kN capacity or a ±500 kN capacity fatigue rated Universal Testing Machine. The stress ratio for all the specimens was maintained at 0.1. The tests were carried out at various values of maximum stress, which were decided as a
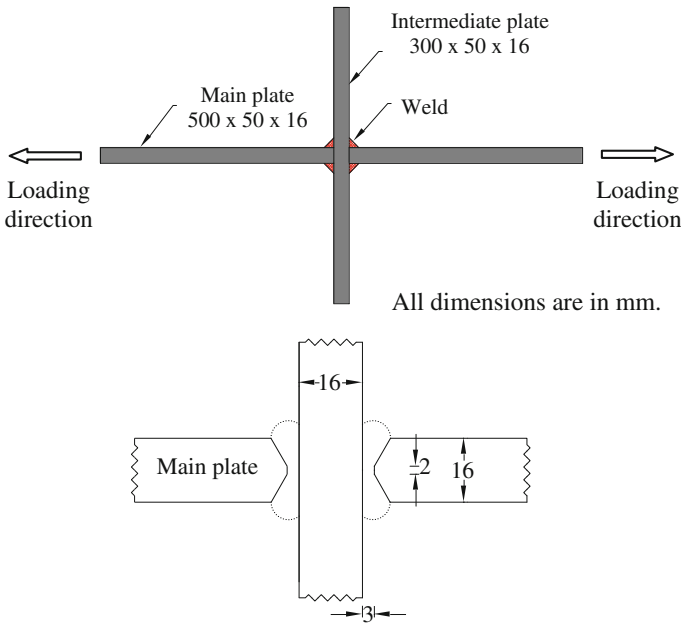
Fig. 3 Cruciform joint with load-carrying welds
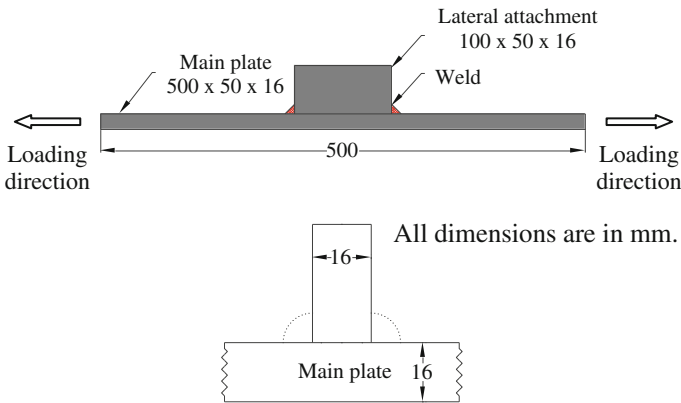
Fig. 4 Non-load carrying longitudinal fillet welded joint

percentage of the yield strength of the material. Totally 36 specimens, eight speci-
mens in each welded category and four bolted specimens, were tested for fatigue life
evaluation. Tests on longitudinal butt welded specimens were carried out at three
different values of maximum stress, i.e., 65, 75 and 85 %, of the yield strength of the
material. Three specimens were tested at a maximum stress value of 200 MPa (stress
range = 180 MPa), two at 230 MPa (stress range = 207 MPa) and three at 260 MPa
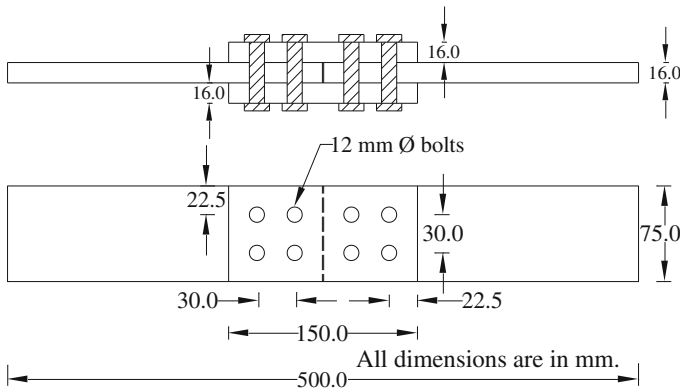
Fig. 5 Bolted connection

(stress range = 234 MPa). Two transverse butt welded specimens each were tested at maximum stress values of 230, 200, 184 MPa (stress range = 166 MPa) and 153 MPa (stress range = 138 MPa). These values correspond to 75, 65, 60 and 50 % of the yield strength of the material, respectively. Similarly, details of the number of specimens, maximum and minimum stresses and stress range for all the types of connections studied are given in Table 3. The test frequency for all the cases ranged from 5 to 15 Hz; in inert environment, the test frequency does not affect fatigue test results. Figure 6a shows close-up view of cruciform joint with load-carrying welds during fatigue test. Figure 6b shows fatigue test on a bolted connection. Figure 6c shows close-up of the connection after failure.

4 Results and Discussion

Table 3 gives fatigue test results for all the connections studied till date by the authors [12, 13]. Table 3 also gives fatigue life predicted as per IS 800: 2007 [1] for the corresponding Constructional Details. All the specimens except one bolted connection were tested till failure, which was defined as total separation or fracture of the specimens into two parts. The specimens failed in the next section. Fatigue test on one bolted connection which was tested at a maximum stress value equal to 50 % of the yield strength of the material (stress range = 138 MPa) was stopped at 3,038,327 cycles (run out test). All the longitudinal butt welded specimens tested endured more number of cycles than provided for in the codal provisions. The specimens failed in the test section transverse to the weld. On careful examination of the fractured surface of the specimens, it was observed that in every case a crack had initiated from a point/defect in the weld, propagated almost symmetrically in both the directions, along the width of the specimen, leading to final fracture.

Two transverse butt welded specimens which were tested at a stress range of 138 MPa (maximum stress = 153 MPa, i.e., 50 % of f_y) and one specimen which

Table 3 Fatigue test results of welded and bolted connections

Specimen ID	Maximum stress (MPa)	Minimum stress (MPa)	Stress range (MPa)	Number of cycles		Codal provisions passed or not passed
				To failure	As per IS: 800	
Longitudinal butt welded connections						
CD12-16-5	260 (0.85 f_y)	26	234	1,292,775	223,129	✓
CD12-16-6				870,586		✓
CD12-16-8				680,586		✓
CD12-16-3	230 (0.75 f_y)	23	207	1,074,109	322,324	✓
CD12-16-4				816,229		✓
CD12-16-1	200 (0.65 f_y)	20	180	1,203,711	490,215	✓
CD12-16-2				2,059,952		✓
CD12-16-7				2,508,971		✓
Transverse butt welded connections						
CD19-20-1	230 (0.75 f_y)	23	207	83,849	162,066	✗
CD19-20-2				104,389		✗
CD19-20-3	200 (0.65 f_y)	20	180	121,863	246,481	✗
CD19-20-4				67,227		✗
CD19-20-5	184 (0.60 f_y)	18	166	309,554	314,251	✗
CD19-20-6				442,941		✓
CD19-20-7	153 (0.50 f_y)	15	138	1,092,428	546,971	✓
CD19-20-8				1,389,531		✓
Cruciform joints with load-carrying welds						
CD26-16-2	245 (0.80 f_y)	25	220	146,731	66,025	✓
CD26-16-6				55,203		✗
CD26-16-7				63,614		✗

Table 3 (continued)

Specimen ID	Maximum stress (MPa)	Minimum stress (MPa)	Stress range (MPa)	Number of cycles		Codal provisions passed or not passed
				To failure	As per IS: 800	
CD26-16-3	214 (0.70 f_y)	21	193	185,505	97,793	✓
CD26-16-5				158,006		✓
CD26-16-4	184 (0.60 f_y)	18	166	357,684	153,693	✓
CD26-16-8				458,313		✓
CD26-16-1	153 (0.50 f_y)	15	138	937,992	267,511	✓
Non-load carrying longitudinal fillet welded connections						
CD32-16-8	245 (0.80 f_y)	25	220	214,472	66,025	✓
CD32-16-6	230 (0.75 f_y)	23	207	263,373	79,262	✓
CD32-16-7				190,119		✓
CD32-16-1	200 (0.65 f_y)	20	180	338,604	120,548	✓
CD32-16-2				303,279		✓
CD32-16-4	168 (0.55 f_y)	17	151	607,618	204,196	✓
CD32-16-5				693,340		✓
CD32-16-3	153 (0.50 f_y)	15	138	977,283	267,511	✓
Bolted connections						
CD04-16-1	245 (0.80 f_y)	25	220	33,983	513,113	×
CD04-16-3	214 (0.70 f_y)	21	193	80,913	759,993	×
CD04-16-2	184 (0.60 f_y)	18	166	617,112	1,194,420	×
CD04-16-4	153 (0.50 f_y)	15	138	3,038,327[a]	2,078,951	✓

[a] Run out; ✓ passed; × not passed

(a) **(b)** **(c)**
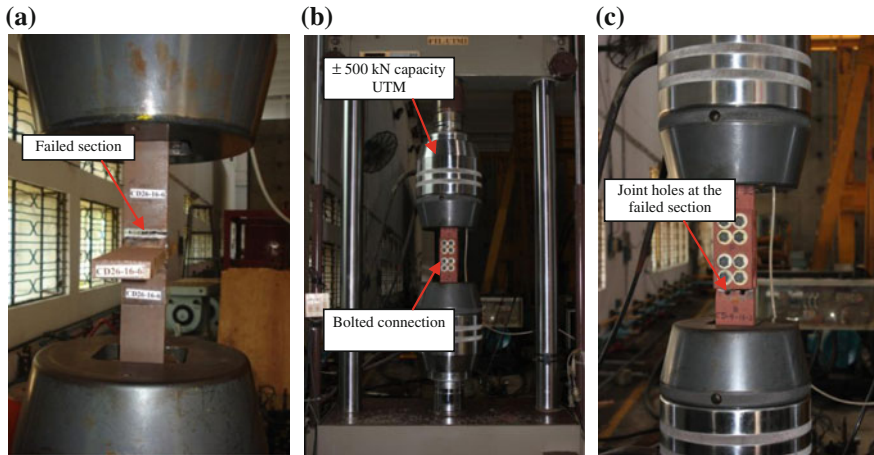
Fig. 6 **a** Close-up view of a cruciform joint with load-carrying welds during fatigue test; **b** test set-up for fatigue test on a bolted connection; **c** close-up view of the bolted connection after failure

was tested at a stress range of 166 MPa (maximum stress = 184 MPa, i.e., 60 % of f_y) have satisfied the requirements of IS 800: 2007 [1] provisions. All specimens which were tested at a maximum stress value equal to 65 % of the yield strength of the material (stress range = 180 MPa) and above, failed to satisfy the codal provisions. The specimens failed much earlier and in the weld region. One out of the two specimens tested at a maximum stress value equal to 60 % of the yield strength of the material (stress range = 166 MPa) also failed to satisfy the codal provisions. All the specimens failed adjacent to the weld.

Two out of the three cruciform joints with load-carrying welds tested at a maximum stress value of 80 % of the yield strength of the material (stress range = 220 MPa) failed to satisfy the codal provisions. The third cruciform specimen tested in this category and the remaining specimens tested at lower stress ranges, i.e., 138, 166 and 193 MPa, endured more number of cycles than provided for in IS 800: 2007 [1]. The specimens failed at one of the load-carrying welds. All the non-load carrying welded specimens endured more number of cycles than provided for in the codal provisions. The specimens failed adjacent to the welded attachment, perpendicular to the weld. Bolted specimens which were tested at a maximum stress value equal to 60 % of the yield strength of the material (stress range = 166 MPa) and above failed to satisfy the codal provisions. All the three specimens failed in the net section. The specimen which was tested at a maximum stress value equal to 50 % of the yield strength of the material (stress range = 138 MPa) sustained 3,038,327 cycles without failure; the same satisfied the codal provisions and endured more number of cycles than provided for in the IS 800: 2007 [1].

5 Conclusions

Fatigue life evaluation of longitudinal and transverse butt welded connections, fillet welded cruciform connections with load-carrying and non-load-carrying welds, and bolted connections conforming to Constructional Details 12, 19, 26, 32 and 4 of IS 800: 2007 [1] was carried out. The studies were carried out at different values of maximum stress, which were decided as a percentage of the yield strength of the material. The stress ratio was 0.1 for all the tests. All the longitudinal butt welded specimens and non-load carrying longitudinal fillet welded specimens endured more number of cycles than provided for in the codal provisions. In the case of transverse butt welded joints, all specimens which were tested at a maximum stress value equal to 65 % of the yield strength of the material (stress range = 180 MPa) and above, and one out of the two specimens tested at a maximum stress value equal to 60 % of the yield strength of the material (stress range = 166 MPa) failed to satisfy the codal provisions. Two out of the three cruciform joints with load-carrying welds tested at a maximum stress value equal to 80 % of the yield strength of the material (stress range = 220 MPa) failed to satisfy the codal provisions. Bolted specimens which were tested at a maximum stress value equal to 60 % of the yield strength of the material (stress range = 166 MPa) and above failed to satisfy the codal provisions.

Based on the experimental fatigue studies on totally 36 connections carried out till date, coming under four different types of welded connections and one type of bolted connections, it is observed that 10 specimens failed to satisfy the codal provisions in terms of fatigue life. For all the failed specimens, the maximum stress was equal to or more than 60 % of the yield strength of the material. The experimental studies will be continued. A few more selected connection types will be studied.

References

1. IS 800: 2007 Code of practice for general construction in steel. Bureau of Indian Standards, New Delhi, India
2. EN 1993-1-9: 2005 Eurocode 3: design of steel structures—fatigue. European Committee for Standardisation, Brussels, Belgium
3. IS 2062: 2011 Hot rolled medium and high tensile structural steel—specification. Bureau of Indian Standards, New Delhi, India

4. Kainumaa S, Kimb I-T (2005) Fatigue strength evaluation of load-carrying cruciform fillet-welded joints made with mild steel plates of different thickness. Int J Fatigue 27:810–816
5. Jen Y-M, Chang L-Y, Fang C-F (2008) Assessing the fatigue life of butt-welded joints under oblique loading by using local approaches. Int J Fatigue 30:603–613
6. Lee C-H, Chang K-H, Jang G-C, Lee C-Y (2009) Effect of weld geometry on the fatigue life of non-load-carrying fillet welded cruciform joints. Eng Fail Anal 16:849–855
7. Minguez JM, Vogwell J (2006) Effect of torque tightening on the fatigue strength of bolted joints. Eng Fail Anal 13:1410–1421
8. Chakerlou TN, Mirzajanzadeh M, Vogwell J, Abazadeh B (2011) Investigation of the fatigue life and crack growth in torque tightened bolted joints. Aerosp Sci Technol 15:304–313
9. ASTM E 8 M-2004 Standard test methods for tension testing of metallic materials (Metric). ASTM International, Pennsylvania
10. IS 9595: 1996 Metal arc welding of carbon and carbon manganese steels—recommendations. Bureau of Indian Standards, New Delhi, India
11. ASTM E 466-1996 Standard practice for conducting force controlled constant amplitude axial fatigue tests of metallic materials. ASTM International, Pennsylvania
12. Vishnuvardhan S, Raghava G, Gandhi P, Saravanan M, Pukazhendhi DM (2011) Studies on fatigue life evaluation of IS 2062 steel structural connections. Civil Eng Div, J Inst Engineers (India) 92:49–55
13. Vishnuvardhan S, Raghava G, Gandhi P (2012) Studies on fatigue life evaluation of welded steel structural connections. In: Proceedings of 8th structural engineering convention, Surat, 19–21 Dec 2012, pp 707–712

Effect of Gap on Strength of Fillet Weld Loaded in Out-of-Plane Bending

Pathipaka Sachin and A.Y. Vyavahare

Abstract When fillet weld loaded in the out-of-plane eccentricity there will be contact between the plates. The strength of fillet weld depends on weld yielding and bearing between the connected plates. But, the contact between plates is not considered in the present Indian standard code (IS 800, General construction in steel—code of practice. Bureau of Indian Standards, New Delhi, 2007), Euro code (EC 3, Eurocode 3: design of steel structures—part 1–8: design of joints. European Committee for Standardization, Brussels, 1993) and Australian Code (AS 4100, Steel structures. Standards Australia, Homebush, 1998). For this, a finite element analysis (FEA) of weld was made for a plate thickness and varying weld sizes with no gap between plates. The study was limited to elastic state of weld and a significant difference was observed in elastic state between codes and FEA for the bending stresses that are developed due to loading. The comparison was also carried out between stress distribution in weld for the case of gap between plates and no gap between plates. Analysis was carried out for different loading pattern i.e., combinations of moment, shear and axial force.

Keywords Fillet weld · Finite element analysis · Out-of-plane bending · Steel structures · Von Mises yield criterion

1 Introduction

Eccentrically loaded fillet weld connections are often unavoidable in the construction of steel structures. There are two types of eccentrically loaded fillet weld. They are in-plane and out-of-plane eccentricity. The main difference between them is in in-plane eccentricity the weld is free to deform along its length and the stress distribution is not effected by bearing between plates (refer Fig. 1). Whereas, in the

P. Sachin (✉) · A.Y. Vyavahare
Department of Applied Mechanics, VNIT, Nagpur 440010, India
e-mail: sachin.pathipaka@gmail.com
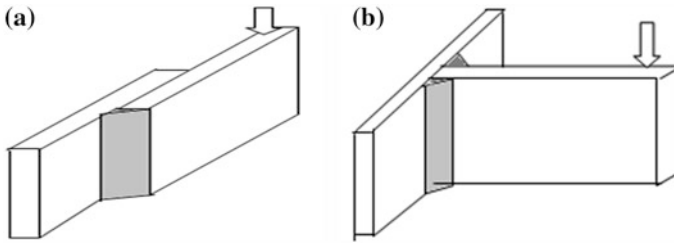
Fig. 1 Eccentrically loaded welded connections. **a** In plane eccentricity. **b** Out-of-plane eccentricity

out-of-plane eccentricity weld is not free to deform in the compression region and the stress distribution is effected by bearing between plates. This is elaborated by Dawe and Kulak [5], Gomez et al. [7] and Kanvinde et al. [9]. AISC-360 [2] uses instantaneous centre of rotation to calculate the stresses that are developed in the weld for in-plane and out-of-plane eccentricity, and do not consider the difference between them. Moreover, in the fabrication of out-of-plane eccentricity a minute gap is provided plates for the cooling and contracting of weld material.

Gomez et al. [7] have performed experiments on the fillet weld with contact between plates for the effect of root notch on the strength of weld. Kanvinde et al. [9] have taken experimental results from Dawe and Kulak [5], Beaulieu and Picard [4] and Gomez et al. [7] and finite element analysis (FEA) was carried out using ABAQUS. They have proposed model for calculation of strength of weld considering contact between plates.

Herein, a study has been carried out on the fillet weld loaded for different loading patterns in out-of-plane eccentricity to know the effect of gap on the strength of fillet weld joint, and to compare the FEA results with three types of design codes.

2 Finite Element Analysis

ANSYS, version 12, has been used for the FE Analysis. The material properties of weld and steel material are taken as same (Table 1). The residual stresses that are developed due to welding is assumed to be small and neglected in the analysis.

An ANSYS first-order solid hexahedral element (SOLID185, 8 nodes, 3 translation DOF's per node) is used for all parts of model. The geometrical discontinuity is simulated with surface-to-surface contact elements (TARGET170 and CONTA174). The contact surface is created where the hanging plate meets the supporting plate by using contact wizard command in ANSYS. The finite element (FE) model consists of about 40,000–44,000 nodes. The weld is discretized into small elements as this is the main part that has studied and the element size maintained is 1 mm and aspect ratio of 2. The parameters that are studied are listed

Table 1 Material properties of steel and weld

Property	Value
Young's modulus (E)	200,000 N/mm^2
Poison's ratio (μ)	0.3
Yield stress (f_y)	250 N/mm^2
Yield strain (ε_y)	0.00125
Ultimate stress (f_u)	410 N/mm^2
Ultimate strain (ε_u)	0.2

Table 2 Geometric variables in the parametric study

Variables	Selected values (mm)
Weld size (w)	6, 8, 12
Eccentricity (e)	170, 160
Thickness of plate (t)	32

in Table 2. The geometry, boundary conditions and the loading pattern of FE model is shown in Fig. 2.

An isotropic type material is chosen with multilinear stress-strain law and isotropic hardening rule. The well suited for steel elements von Mises yield criterion is adopted. The welding is also modeled as the solid volume to know the variation of stresses in weld due to loading. The effect of the welding is established by merging the common nodes for the weld and the plates. For this the meshing is made such that the when the model is assembled the nodes of the plate and the weld should overlap on each other. By merging the nodes it creates a restrained condition between the weld and the plate.
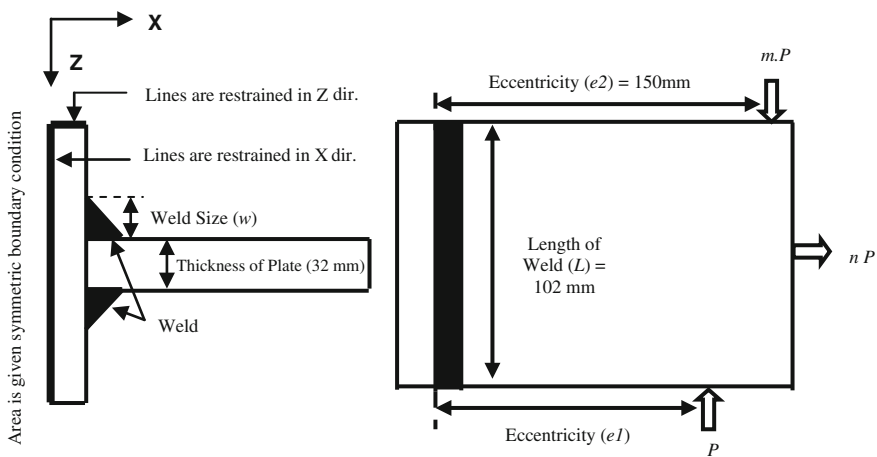
Fig. 2 Geometry, boundary conditions and loading of case bending and axial tension

The finite element analysis of 0.5 mm (W8T32L1G5), 1 mm (W8T32L1G10) and 1.5 mm (W8T32L1G15) gap were analyzed along with no gap between plates to know the effect of gap on the strength of fillet weld. The models with no gap between plates subjected to different loading patterns are analyzed and the results compared with Indian code [8], Australian code [3] and Euro code [6].

3 Results and Comparison with Design Codes

A comparison of stress distribution is made between with and without contact between plates for the variation of stress developed in weld at the cross section where weld and supporting plate are in contact for a particular load (Fig. 3a). From the study it has been observed that the stresses developed in the weld for contact is about 50 % of the bending stresses that are developed in the weld for no contact between plates. It has also been observed that the gap between plates does not affect the bending stress value. From the separation of plates versus load (P–δ) graph it is observed that the yield load for contact is about double the yield load for no contact between plates but there is no much difference when compared for gap between

Fig. 3 Comparison of results of contact and no contact between plates. **a** Stress distribution in weld. **b** Separation between plates
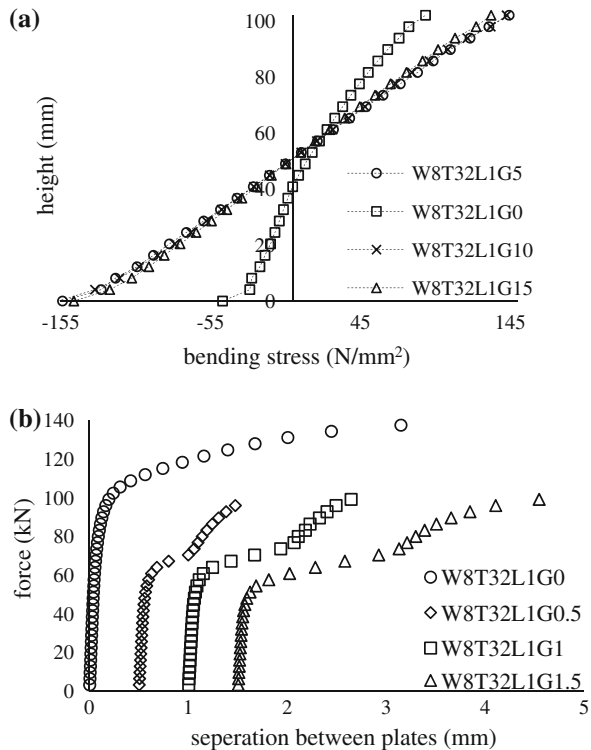
Fig. 4 Comparison of yield load of weld for contact and no contact between plates
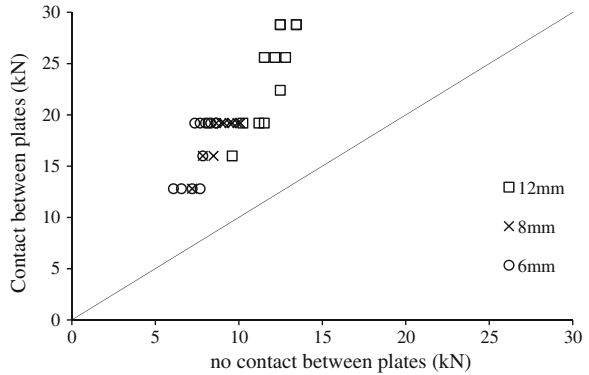
plates (Fig. 3b). It has been observed that the contact between plates is going to take place only after the yielding of weld material has occurred. May be this may be reason the cross section taken in design codes is the throat area of the weld.

For the comparison between contact and no contact yield load the gap taken is 1 mm as the gap doesn't affect much on the yield load. Figure 4 shows the comparison between yield load for contact and no contact between plates. Table 3 shows the % reduction of yield load reduced due to gap between plates.

Table 3 Percentage difference of reduction in yield load of no contact with contact between plates

Model	% reduction	Model	% reduction
W12T32L120	44.29	W8T32L132	53.33
W12T32L121	41.67	W8T32L133	55.00
W12T32L122	46.67	W8T32L140	47.50
W12T32L123	40.00	W8T32L141	47.50
W12T32L130	50.00	W8T32L142	50.00
W12T32L131	52.50	W8T32L143	52.50
W12T32L132	55.00	W6T32L120	51.00
W12T32L133	40.00	W6T32L121	43.75
W12T32L140	53.33	W6T32L122	48.75
W12T32L141	53.33	W6T32L123	52.50
W12T32L142	56.67	W6T32L130	56.67
W12T32L143	56.67	W6T32L131	58.33
W8T32L120	50.83	W6T32L132	40.00
W8T32L121	47.00	W6T32L133	61.67
W8T32L122	51.00	W6T32L140	55.00
W8T32L123	43.75	W6T32L141	53.35
W8T32L130	48.33	W6T32L142	48.55
W8T32L131	50.00	W6T32L143	49.84

Note W6 weld size is 6 mm; *T32* thickness of plate is 32 mm; *L115* loading pattern 1: m:n

Table 4 Percentage difference of design codes with FEA

Model	IS 800-2007	EC 3-1993	AS 4100-1998
W12T32L120	8.94	65.33	15.32
W12T32L121	14.40	72.05	22.42
W12T32L122	6.80	61.10	12.29
W12T32L123	16.01	78.59	24.44
W12T32L130	1.92	53.55	7.14
W12T32L131	3.14	45.94	1.80
W12T32L132	8.02	39.06	3.05
W12T32L133	15.04	77.08	23.40
W8T32L120	17.00	28.59	10.31
W8T32L121	6.67	40.46	2.06
W8T32L122	16.45	28.88	10.18
W8T32L123	0.79	48.83	3.70
W8T32L130	38.54	36.46	4.76
W8T32L131	16.00	29.72	9.52
W8T32L132	21.52	23.57	13.82
W8T32L133	21.46	17.98	17.74
W6T32L120	30.00	15.73	19.28
W6T32L121	14.11	31.68	8.19
W6T32L122	24.27	20.83	15.78
W6T32L123	34.40	11.62	22.22
W6T32L130	47.10	38.27	28.57
W6T32L131	54.66	2.71	32.14
W6T32L132	8.16	39.06	3.05
W6T32L133	4.82	42.65	1.22
W6T32L140	30.63	4.52	27.06
W6T32L141	32.97	1.48	29.59
W6T32L142	35.16	2.42	31.94
W6T32L143	37.22	5.56	34.14

Note W6 weld size is 6 mm; *T32* thickness of plate is 32 mm; *L115* loading pattern 1: m:n

The comparison of contact between plates is made for the Yield load of weld with FEA results and three Design codes. As the clauses that are stated in the Design codes are based on stress criteria the equations are rearranged to determine the Yield load for a given weld size and eccentricity. In this comparison the factor of safety that were adopted in the codes are not taken into consideration. Table 4 shows the percentage difference of Codes with FEA and Fig. 5 shows comparison of yield Load from FEA with IS 800 [8], EC 3 [6] and AS 4100 [3].
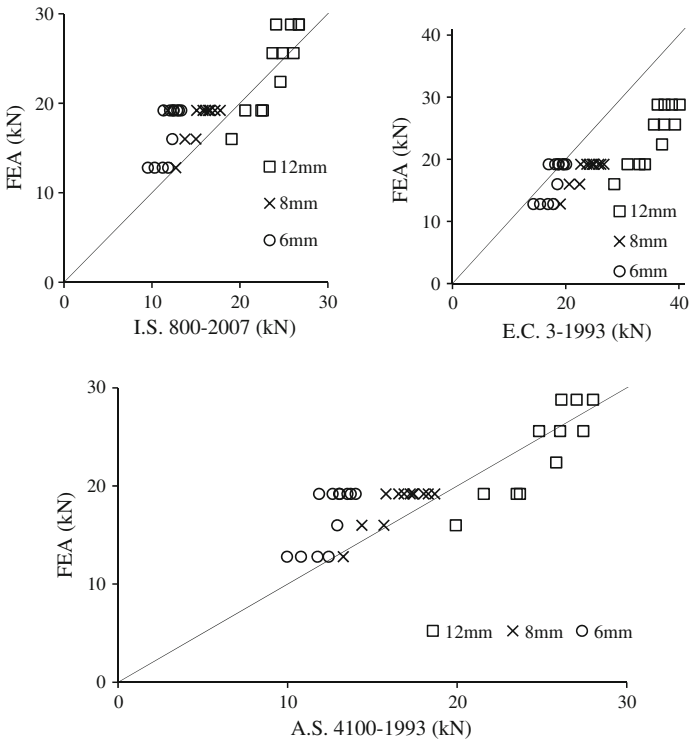
Fig. 5 Comparison of FEA with design codes

4 Summary and Conclusions

Finite element analysis of fillet weld loaded in out-of-plane is made with contact and no contact between plates. It was observed from the study that there is no much difference in the yield load for 0.5 m and 1 mm and 1.5 mm gap. There is a reduction of 50 % in the yield load due to the presence of gap between plates and contact between plates has taken place only after the yielding of the weld material. Yield load is compared between FEA and design codes and at an average of 20.22, 34.42 and 15.54 % difference is observed for IS 800 [8], EC 3 [6] and AS 4100 [3] respectively with FEA. Due to the correlation factor used in EC 3 [6], it over estimates the strength of the fillet weld connection. In the IS 800 [8] and AS 4100 [3] codes are conservative for smaller weld sizes, and no regular pattern was followed for large weld size.

References

1. ANSYS User's manual, version 12, Houston USA. Swanson Analysis System Inc., India
2. AISC-360 (2010) Specification for structural steel building. American Institute of Steel Construction, Chicago
3. AS 4100 (1998) Steel structures. Standards Australia, Homebush, Australia
4. Beaulieu D, Picard A (1985) Résultats d'essais sur des assemblages soudés excentriques en flexion. Can J Civ Eng 12(3):494–506
5. Dawe JL, Kulak GL (1972) Welded connections under combined shear and moment. J Struct Div, ASCE 100(4):727–741
6. EC 3 (1993) Eurocode 3: design of steel structures—part 1–8: design of joints. European Committee for Standardization, Brussels, Belgium
7. Gomez IR, Kanvinde AM, Kwan YK, Grondin GY (2008) Strength and ductility of fillet welds subjected to out of plane bending. American Institute of Steel Construction, Chicago
8. IS 800 (2007) General construction in steel—code of practice. Bureau of Indian Standards, New Delhi, India
9. Kanvinde AM, Liu J, Fu X, Cooke RJ (2013) Fillet weld groups loaded with out-of-plane eccentricity: simulations and new model for strength characterization. J Struct Div, ASCE 139 (3):305–319

Strength Comparison of Fixed Ended Square, Flat Oval and Circular Stub LDSS Columns

Khwairakpam Sachidananda and Konjengbam Darunkumar Singh

Abstract Structural behaviors of fixed supported Lean Duplex Stainless Steel (LDSS) hollow stub columns of flat oval, circular and square cross-sections are presented on the basis of 54 models using finite element (FE) analyses. In order to assess the relative performance of various cross-sections, the material consumption has been made equal (i.e. equal perimeter). It is observed that for thinner sections ($t \leq 10$ mm), the influence of local imperfection on decreasing ultimate load (P_u) is in the order square > flat oval > circular cross sections. For $t < 10$ mm an increase in P_u is seen in the order square < flat oval < circular cross sections, with no significant change in P_u for higher thicknesses. With increase in cross-sectional perimeter of ~ 24 % from ~ 828 mm, the percentage change in P_u of thin section ($t = 3$ mm), are $\sim +20, -20, -2.5$ % for circular, square and flat oval (l/r i.e., ratio of flat length to curvature radius = 1 to 2; $r = 100$ mm), while for thicker sections ($t = 25$ mm) it is $\sim +23$ % for all sections. The deformation corresponding to P_u, showed relatively similar values for thin section as compared to thicker sections ($t \geq 15$ mm) wherein the square section showed greater deformation capacity whereas both circular and flat oval section showed similar values.

Keywords Finite element analysis · Flat-oval · Square · Circle · LDSS · Stub

1 Introduction

In the early days, carbon steel dominates the construction industry because of its early existence and well developed design rules, long experience and low cost etc. But due to problems of low corrosion resistance and lower strength, various types of stainless steel have been produced to incorporate advantages of high corrosion resistance, high strength, smooth and uniform surface, aesthetic appearance etc.

K. Sachidananda (✉) · K.D. Singh
Indian Institute of Technology (IIT) Guwahati, Guwahati, India
e-mail: khwairakpam@iitg.ernet.in

Among stainless steel, traditionally austenitic stainless steel (ASS) variety with nickel content of ~ 8–11 % has been used mainly for the construction industry. The increasing price in nickel content led to the introduction of a new material called Lean duplex stainless steel (LDSS) stainless steel such as grade EN 1.4162 with much lower nickel content of ~ 1.5 % and having higher strength than that of ferritic and austenitic stainless steels [1, 2]. The higher strength of LDSS material can help in reducing section sizes thereby providing higher strength to weight ratio. Stainless steel comes in different shapes e.g. open and closed sections, however in comparison to open sections, closed sections are more popular due to higher strength carrying capacity. Closed/hollow stainless steel sections can take a variety of geometric shapes such as circle, square, oval, ellipse, rectangle etc. In the literature, studies have been reported for square [3, 4], oval [5, 6] and circular [7] hollow sections, but to the best of authors' knowledge, a systematic comparison in ultimate load of square, flat oval and circular stub columns subjected to pure axial compression considering the same material consumption has not been reported, particularly for LDSS. Hence, in this paper, an attempt has been made to compare load carrying capacities of LDSS square, flat oval and circular stub columns under pure axial compression.

2 Finite Element Modelling

The finite element software, ABAQUS version 6.9 EF1 has been used to find the comparative strength (i.e. strength and deformation) of flat oval, square and circle hollow section column subjected to axial compression considering the same perimeter of sections i.e. 828, 1,028 mm and thickness (t) maintaining same height of 900 mm. The cross sections considered for the analysis are shown in Fig. 1. The modelling approach followed similar pattern reported by Theofanous and Gardner [4] and Patton and Singh [1].

In the FE modeling, the column ends were fixed against all degrees of freedom except the vertical displacement at the loaded end.

Four-noded doubly curved shell (S4R) elements with reduced integration have been used to discretize the models as they can accurately model square [1], circle [7] and oval [5] hollow sections. The flat and corner portion material are assumed to
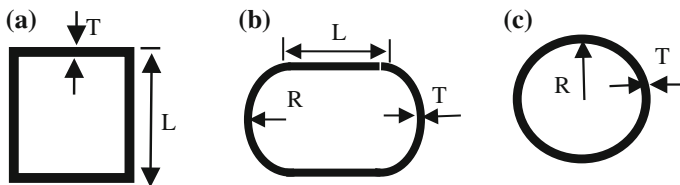
Fig. 1 Cross-sections **a** square, **b** flat-oval, **c** circle, considered

be same. Typical mesh size is of 11.5 mm × 11.5 mm dimensions with an aspect ratio of 1 has been taken after mesh convergence. The plates composing the tubular column are not totally perfect for various reasons such as denting or undulation during transportation or manufacturing. These imperfection in steels are provided in modelling as imperfection as to simulate the behaviour of real members. The local imperfection amplitude has been taken as 1 % of plate thickness.

The FE model have been validated with the experimental square LDSS 80 × 80 × 4-SC2 [4] as in Fig. 4 and the validated geometric details of square LDSS column 80 × 80 × 4-SC2 is given in Table 1. The material properties of LDSS suggested by Gardner and Ministro [8] i.e. a modified version of original Ramberg-Osgood 1943 has been used in deriving the stress-strain curve as in Fig. 2. Typical FE mesh and boundary conditions of LDSS-Square hollow column are shown in Fig. 3. Poisson's ratio is taken as 0.3. The residual stress is neglected as it gives negligible effect on ultimate load [11]. The material properties in stress-strain curve has been converted into true stress (σ_{true}) and true strain $\left(\varepsilon_{true}^{pl}\right)$ using the following Eqs. 1 and 2.

$$\sigma_{true} = \sigma_{nom}(1 + \varepsilon_{nom}) \tag{1}$$

$$\varepsilon^{pl}_{\ true} = \ln(1 + \varepsilon_{nom}) - \frac{\sigma_{true}}{E_o} \tag{2}$$

where σ_{nom} and ε_{nom} are engineering stress and strain respectively.

Table 1 Stub column dimensions [4]

Specimen	L (mm)	B (mm)	H (mm)	t (mm)	r_i (mm)
80 × 80 × 4-SC2	332.2	80	80	3.81	3.6

Fig. 2 Experimental stress-strain curve of LDSS material Grade EN 1.4162 [4]
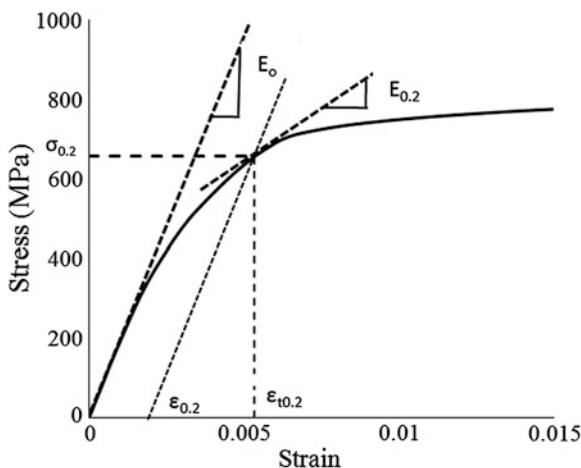
Fig. 3 Typical **a** FE mesh and **b** boundary conditions of LDSS-square hollow column
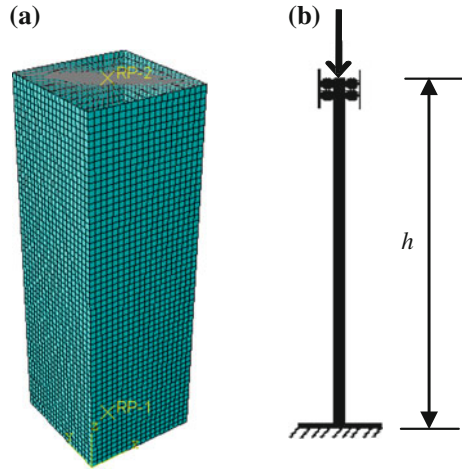
Fig. 4 Variation of P (load) versus δ (axial displacement) for stub column (SHC-$80 \times 80 \times 4$-SC2)
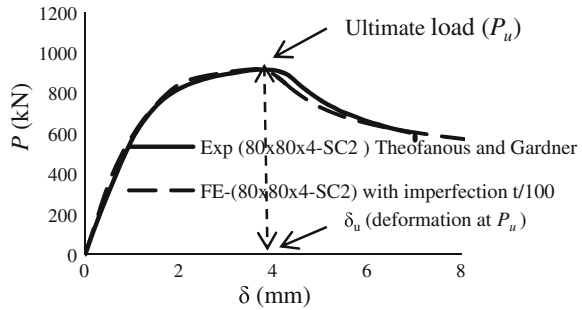
3 Parametric Study of Square, Flat Oval and Circle Hollow Column

A total of 54 FE models of square, flat oval and circle hollow columns have been studied by taking equal perimeters ($L_P = 828$ and $1,028$ mm). The thicknesses have been varied from $t = 3$ to 25 mm. The nomenclatures of the specimens follow the patterns L207T10, L100R100T10, R131.85T10, where L denotes side length of square and flat length of flat oval section, R denotes the radius of curvature of curve section in flat oval and the radius of circle, T denote the thickness of section i.e. number following the letter indicate their respective values.

4 Results and Discussion

The three sections i.e. square, flat oval and circle have been provided with equal local imperfection amplitude of $t/100$ and their reduced ultimate load (P_u) in comparison to perfect models have been plotted in Fig. 5. It is shown that the effect of imperfection on the % difference in P_u from perfect model capacity for different sections goes in the order of square > flat oval > circle for thin sections, $t \leq 10$ mm while for thick section $t > 10$ mm there is no effect of local imperfection as the whole section comes into effect. The reason for having more effect of imperfection on square and flat oval may be due to reduced stiffness offered by the flat parts, thereby subjecting to local buckling than curve section. Even though the same quantity of material has been used for different sections, the P_u differs for different section. Figure 6 shows P_u versus cross-section shapes i.e. (SQ for square, OL for flat-oval, CR for circle), showing that for $t < 10$ mm an increase in P_u is seen in the order square < flat oval < circular cross section but for higher thickness $t > 10$ mm there is no significant changes in P_u for all sections considered. For thinner section the curve faces has more stiffness than flat ones while for thick section, curve face
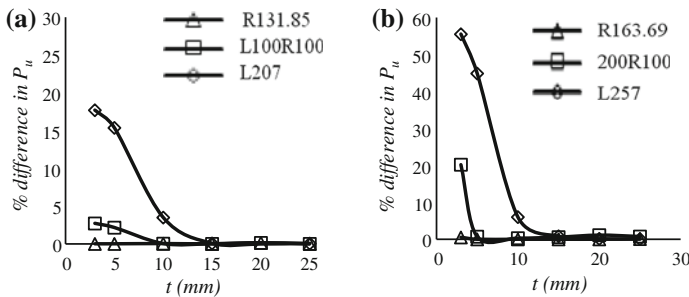
Fig. 5 % difference in P_u models with and without imperfection versus t (mm). **a** Perimeter 828 mm (oval, $l/r = 1$). **b** Perimeter 1,028 mm (oval, $l/r = 2$)
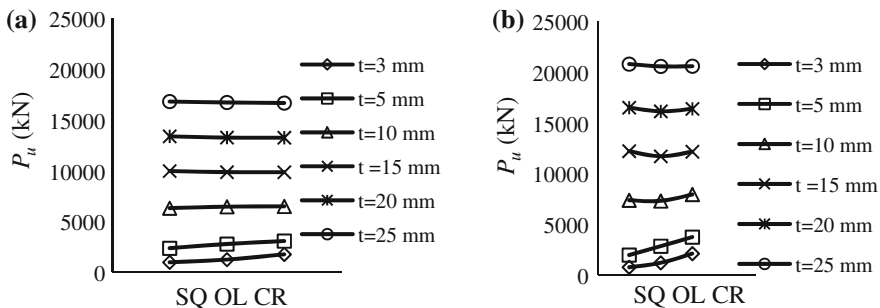
Fig. 6 P_u versus cross-sections of square (*SQ*), flat oval (*OL*) and circle (*CR*). **a** Perimeter 828 mm (oval $l/r = 1$). **b** Perimeter 1,028 mm (oval $l/r = 2$)

(a)

(b)
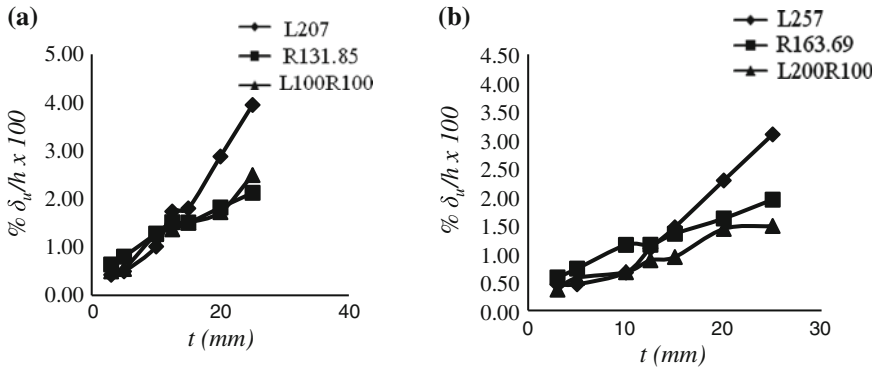
Fig. 7 % $\delta_u/h \times 100$ versus t of square (*SQ*), circle (*CR*) and flat oval (*OL*). **a** Perimeter 828 mm ($l/r = 1$). **b** Perimeter 1,028 mm ($l/r = 2$)

Table 2 Percentage increase in ultimate load (P_u) with increase in perimeter

Increasing perimeter from 828 to 1,028 mm		% increase in P_u
R131.85T3 to	R163.69T3	20.64
L207T3 to	L257T3	−20.26
L100R100T3 to	L200R100T3	−2.69
R131.85T25 to	R163.69T25	23.50
L207T25 to	L257T25	23.61
L100R100T25 to	L200R100T25	22.97

and flat faces almost have equal stiffness as whole section becomes effective. Figure 7 shows the deformation capacity showing similar deformation values for $t \leq 15$ mm as compared to $t > 15$ mm wherein the square section showed greater deformation capacity whereas circular and flat oval section showed similar values. The deformation is indirectly related to its stiffness and square has less stiffness than circle and flat oval. Table 2, shows that the increase in cross-sectional perimeter by ~ 24 % from ~ 828 mm, for thin section ($t = 3$), changes the percentage P_u by $\sim$ +20, −20, −2.5 %; for circular, square and flat oval (l/r i.e., flat length by curvature radius = 1 to 2; $r = 100$ mm) cross-sections respectively, however, in the case of thicker sections ($t = 25$ mm) the percentage increase in P_u is computed to be $\sim$ +23 % for all sections.

5 Conclusion

Based on the parametric studies of the finite element analyses of fixed ended LDSS stud columns of square, flat oval and circle under pure axial compression, the following conclusions are drawn:

1. Circular section has more load carrying capacity in comparison to square and oval sections.
2. Comparing strength of circle, flat oval and square hollow sections under the same material consumption, P_u increase in the order circle > flat oval > square for thin section ($t < 10$ mm) but for higher thickness ($t \geq 10$ mm) strength remains same for all sections.
3. The deformation capacity of square, flat oval and circle shows similar values for $t \leq 15$ mm but for higher thickness $t > 15$ mm, square has higher deformation capacity than flat oval and circle, while flat oval and circle shows almost same value.
4. Increase in cross-sectional perimeter of ~ 24 % from ~ 828 mm, for thin section ($t = 3$), changes the percentage P_u by $\sim +20, -20, -2.5$ %; for circular, square and flat oval (l/r i.e., flat length by curvature radius = 1 to 2; $r = 100$ mm) cross-sections respectively, however, in the case of thicker sections ($t = 25$ mm) the percentage change in P_u is computed to be $\sim +23$ % for all the sections.

6 Scope for Future Research

It is expected that the current findings will be useful in deciding the type of sections to be chosen for a particular application. The current study can be extended for slender columns, with or without eccentric loadings.

References

1. Patton L, Singh KD (2012) Numerical modeling of lean duplex stainless steel hollow columns of square, L−, T−, and ±shaped cross sections under pure axial compression. Thin-Walled Struct 53:1–8
2. EN 10088-4 (2009) Stainless steels part 4. Technical delivery conditions for sheet/plate and strip of corrosion resisting steels for general purposes
3. Liu Y, Young B (2003) Buckling of stainless steel square hollow section compression members. J Constr Steel Res 59:165–177
4. Theofanous M, Gardner L (2009) Testing and numerical modelling of lean duplex stainless steel hollow section columns. Eng Struct 31(12):3047–3058
5. Zhu J, Young B (2012) Design of cold-formed steel oval hollow section columns. J Constr Steel Res 71:26–37
6. Zhu J, Young B (2011) Cold-formed-steel oval hollow sections under axial compression. J Struct Eng 137(7):719–727
7. Ellobody E, Young B (2007) Investigation of cold-formed stainless steel non slender circular hollow section columns. Steel Compos Struct 7(4):321–337
8. Gardner L, Ministro A (2004) Testing and numerical modelling of structural steel oval hollow sections. 04-002-ST, Department of civil and environmental engineering, Imperial college, London
9. ABAQUS (2009) Version 6.9-EF1. Hibbitt, Karlsson and Sorensen, Inc., USA
10. Ramberg W, Osgood WR (1943) Description of stress-strain curves by three parameters. Technical note No. 902. National advisory committee for aeronautics, Washington, DC
11. Ellobody E, Young B (2005) Structural performance of cold formed high strength stainless steel columns. J Constr Steel Res 61:1631–1649

Part XXVI
Masonry Structures

Non-linear Behavior of Weak Brick-Strong Mortar Masonry in Compression

Syed H. Basha and Hemant B. Kaushik

Abstract Non-linear (stress-strain) properties of masonry form a pre-requisite in carrying out the non-linear analysis of structures. A detailed study on the non-linear behavior of strong burnt clay brick masonry was carried out by Kaushik et al. (J Mater Civ Eng 19:728–739, 2007), whereas non-linear stress-strain characteristics for weak brick-strong mortar was not available. To evaluate the same, fly ash bricks whose compressive strength was lesser than the strength of mortar were selected. Prisms with three different grades of mortar: strong (cement:sand 1:3), intermediate (1:4) and weak (1:6) were constructed to evaluate the non-linear behavior of weak brick-strong mortar, and to assess the influence of strength of mortar on masonry prisms. Specimens were instrumented with strain measuring instruments and tested under monotonic compressive loading using servo controlled hydraulic actuator. Stress-strain curves for weak brick-strong mortar masonry were plotted and the results were compared with strong brick-weak mortar masonry (Kaushik et al. J Mater Civ Eng 19:728–739, 2007). From the results, it was observed that strength of weak brick-strong mortar masonry was lower when compared to strong brick-weak mortar masonry, but the failure strain observed in case of weak brick-strong mortar masonry was significantly higher when compared to strong brick-weak mortar masonry.

Keywords Fly ash brick · Burnt clay brick · Strong mortar · Stress-strain

1 Introduction

Masonry is the oldest building material used in building construction and it forms the major building stock around the world including India. A number of different masonry materials ranging from burnt clay bricks, concrete bricks, and now-a-days fly ash bricks are used in the construction. Most of the times masonry is constructed

S.H. Basha (✉) · H.B. Kaushik
Department of Civil Engineering, Indian Institute of Technology Guwahati, Guwahati, India
e-mail: humayunbashasyed@gmail.com

using locally available materials and due to this reason, their behavior in terms of strength and elastic modulus with respect to mortar varies from region to region. During the last three decades a lot of research was dedicated to evaluate the non-linear behavior of clay brick masonry [4, 9, 11–13]. It was observed that the strength and stiffness of brunt clay bricks was found to be higher than mortar joints. Due to the variability in material characteristics it was observed in the past studies [8, 10, 14] that the strength of the bricks was found to be significantly lesser than the strength of the mortar. But the non-linear stress-strain characteristics of the weak brick-strong mortar have not been evaluated in detail till date. In order to evaluate the same, fly ash bricks whose strength was found to be lesser than the strength of mortar joints was employed in the current study to evaluate non-linear characteristics of weak brick-strong mortar masonry. Later on, non-linear stress-strain characteristics of strong brick-weak mortar masonry evaluated in the previous study [11] was compared with the weak brick-strong mortar masonry.

2 Evaluation of Non-linear Behavior of Fly Ash Bricks and Mortar Units

Masonry is an assemblage of brick and mortar units, and to understand the non-linear behavior of masonry under compression, the properties of its constituents need to be first evaluated individually. Non-linear stress-strain characteristics of fly ash brick units and three different grades of 50 mm mortar cubes were determined using the uniaxial monotonic compressive (displacement controlled) loading using servo controlled hydraulic actuator of 250 kN capacity with a stroke length of ±125 mm. Brick units, and mortar cubes specimens were instrumented with epsilon contact and laser non-contact extensometer to record the deformations during the tests. Contact extensometer was connected to the test specimen, whereas non-contact extensometer uses a high speed laser scanner to measure the deformations. As the thickness of the fly ash brick unit was 75 mm and that of mortar cubes was 50 mm, the gauge length of both contact and non-contact extensometers was adjusted to 25 mm. Applied loads and deformations at various locations were recorded using a computer based data acquisition system. The average stress-strain curves of fly ash brick units, mortar cubes were plotted by double averaging method [11]. The modulus of elasticity was calculated as the slope of the secant connecting 5–33 % of the maximum compressive strength of the specimens.

Compressive strength of fly ash bricks is determined in accordance with ASTM C67-13 [2] and IS 3495 [6]. Fly ash brick units were tested by placing the specimen under the loading surface between two plywood sheets. Brick units was found to be behaving linearly up to about half of the ultimate failure load after which the behavior found to be highly non-linear and is shown in Fig. 1. Average compressive strength of fly ash bricks found to be about 5.7 MPa. After reaching the maximum
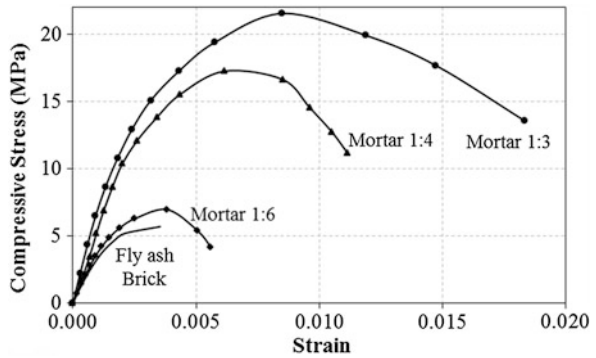
load carrying capacity bricks were crushed. The average failure strain was found to be about 0.0035.

The compressive strength of mortar cubes was determined on 50 mm cubes in accordance with ASTM C109/C109M-13 [3] and IS 2250 [7]. In the current study, three different grades of mortar were used (cement:sand); 1:3 (strong), 1:4 (intermediate) and 1:6 (weak). Water-cement ratio was maintained in the range of 0.6–0.7 to obtain a workable mix. The average stress-strain curve for each mortar grade was plotted and is shown in Fig. 1. The average compressive strength of strong mortar units was about 21.6 MPa, whereas, it was about 17.3 and 6.9 MPa for intermediate and weak mortar units, respectively. From Fig. 1, it can be observed that the 1:3 (strong) mortar grade observed higher load carrying capacity compared to intermediate (1:4) and weak (1:6) mortar grade. At the same time, it was observed that the drop down in lateral load capacity in case of strong mortar was gradual when compared to intermediate and weak mortar units.

From Fig. 1, it was observed that the strength of fly ash bricks (5.7 MPa) was lesser than the strength of mortar (21.6–6.9 MPa). It was also observed that the stiffness of the fly ash brick units was lesser than three grades of mortar. The average modulus of elasticity of fly ash brick units was about 3,878 MPa, whereas, it was about 7,591 MPa for strong mortar, 7,403 and 4,361 MPa for intermediate and weak mortars, respectively.

3 Evaluation of Non-linear Behavior of Fly Ash Brick Masonry Prisms

The stress strain characteristics of fly ash brick masonry was determined by testing masonry prisms using servo controlled hydraulic actuator in accordance with ASTM C1314-12 [1] and IS 1905 [5]. Masonry prisms were constructed using three different grades of mortar 1:3 (strong), 1:4 (intermediate) and 1:6 (weak). Size of the fly ash brick was about 230 × 110 × 75 mm, and the thickness of mortar joint

Fig. 2 Comparison of non-linear stress-strain curves of fly ash brick masonry prisms
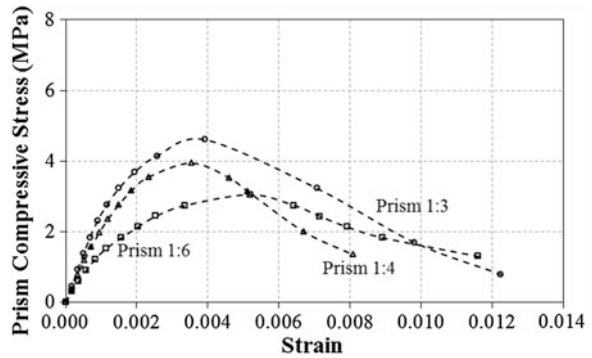
varied from 10 to 12 mm, and the average height of the fly ash masonry prism was about 420 mm. Similar type of contact and non-contact extensometers with a gauge length of 200 mm with a displacement capacity of ±12 mm were used to measure the strain under compressive loading. The rate of loading was in accordance with ASTM C1314-12 [1] and IS 1905 [5] standards.

The stress strain characteristic of masonry prisms with different grades of mortar was plotted using double averaging method and is shown in Fig. 2. The average maximum compressive strength of fly ash brick masonry prisms found to be 4.6 MPa (strong), 3.9 MPa (intermediate), and 3.1 MPa (weak), across three different grades of mortar. Stress-strain curves were found to be behaving linearly up to about one third of their maximum strength followed by the nonlinear behavior. From Fig. 2, it can be observed that the strain corresponding to lateral capacity was found to be approximately same for masonry prisms with strong and intermediate mortar whereas, it was found to be slightly higher for masonry prisms with weak mortar. From the non-linear stress strain curves, it was observed that initial stiffness of strong and intermediate mortar grade masonry prisms found to be same whereas, weak mortar masonry prisms observed slightly lesser initial stiffness.

4 Comparison of Non-linear Behavior of Fly Ash (Weak) and Burnt Clay (Strong) Brick Masonry

In the previous study, Kaushik et al. [11] tested burnt clay brick masonry prisms using three different grades of mortar (cement:lime:sand by volume), i.e., 1:0:3 (strong), 1:0.5:4.5 (intermediate), and 1:0:6 (weak). The average compressive strength of burnt clay bricks was found to be about 21 MPa, whereas the strength of strong, intermediate, and weak mortar units was about 20.6, 15.2 and 3.1 MPa, respectively. The stress-strain characteristics of burnt clay brick masonry was obtained by testing five brick high masonry prisms under monotonic compressive loading using servo controlled hydraulic actuator.

Fig. 3 Comparison of non-linear stress-strain *curves* of fly ash brick and burnt clay masonry prisms
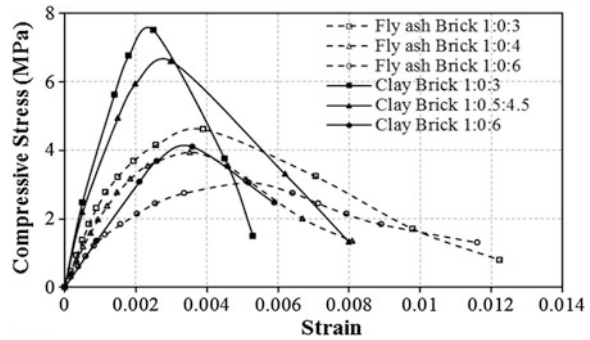
Compressive stress-strain curves of burnt clay bricks for three grades of mortar were plotted using double-averaging method and are shown in Fig. 3. It was reported that brunt clay brick masonry prisms observed linear behavior till one third of their lateral load capacity, later on the behavior found to be highly non-linear. The average compressive strength of burnt clay brick prisms was found to be 7.5, 6.6 and 4.1 MPa, for strong, intermediate and weak burnt clay brick prims, respectively, whereas it varied from 4.6 to 3.1 MPa in case of fly ash brick masonry. It is observed that burnt clay brick prisms with strong mortar grade observed higher initial stiffness followed by intermediate and weak mortar grade masonry prisms. Due to high initial stiffness observed in strong mortar burnt clay masonry prisms, highest compressive strength was reported. The drop-down in capacity was rapid owing to its higher strength when compared to its counterparts.

The initial stiffness of fly ash brick prisms found to be lesser than their corresponding burnt clay brick masonry prisms even though the strength of mortar remained almost same in both type of masonry prisms. The reason may be due to the low strength (weak) fly ash bricks when compared to the high strength mortar joints. The strain corresponding to maximum compressive strength in case of burnt clay brick masonry prisms was comparatively lesser than the strain observed in fly ash brick masonry prisms (Fig. 3). It was observed that drop-down in strength in case of brunt clay brick masonry prisms was very rapid when compared to fly ash brick masonry prisms and it may be due to their higher stiffness which attracted more forces leading to early failure compared to fly ash brick masonry prisms. Burnt clay brick masonry prisms observed significantly higher compressive strength when compared to fly ash brick masonry prisms highlighting the influence of stronger bricks.

The increase in strength from weak to strong mortar units was about 3.1 times (current study) and 6.6 times [11], whereas, the increase in strength from weak to strong mortar grade masonry prisms was about 1.5 and 1.8 times in the current and previous studies [11], respectively. The increase in masonry prism strength was nominal for different grades of mortar for same type of masonry even though the increase in strength of mortar was many folds (Fig. 4). From the results, it can be inferred that for an increase of 3.6 times brick strength, normalised prism strength with respect to mortar strength has been increased by about 1.7, 1.9 and 2.9 times
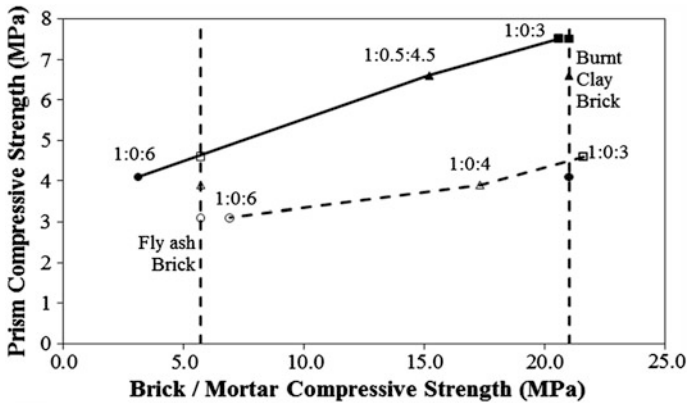
Fig. 4 Influence of brick and mortar compressive strength on masonry prism strength

for strong, intermediate, and weak mortar grades, respectively. The increase in normalised prism strength with respect to fly ash brick strength was about 1.5 times for an increase of 3.1 times mortar strength. Similarly, the increase in normalised prism strength with respect to burnt clay brick strength was about 1.8 times mortar strength. Therefore, it can be inferred that masonry prism strength increases with increase in mortar and brick strength. But the increase in masonry prism strength was nominal with increase in mortar strength, whereas, prism strength increases significantly with increase in brick strength.

5 Conclusions

In the current study, non-linear stress-strain characteristics of weak brick-strong mortar were evaluated in accordance with relevant standards. It was observed that the strength of brick was found to be lesser than the strength of mortar. Fly ash (weak) brick masonry prism strength was found to be lesser than the strength of both fly ash bricks and mortar units. From the stress-strain characteristics of fly ash brick prisms, it was observed that the strength and stiffness of strong mortar masonry prisms was comparatively higher than the masonry prisms with intermediate and weak mortar. Later on, stress-strain curves of weak brick (fly ash)-strong mortar prisms were compared with strong brick (burnt clay)-weak mortar prisms. From the comparison, it was inferred that the strength of weak brick-strong mortar masonry was lower when compared to strong brick-weak mortar masonry. It was also observed that the weak brick-strong mortar masonry was less stiff when compared to strong brick masonry, but the failure strain observed in case of weak brick-strong mortar masonry was significantly higher. From the results, it was also observed that strength of masonry depends primarily on the strength of brick rather than strength of mortar.

References

1. ASTM (2012) Standard test method for compressive strength of masonry prisms. Masonry test methods and specifications for the building industry, ASTM C1314-12, ASTM International, USA
2. ASTM (2013) Standard test methods for sampling and testing brick and structural clay tile. Masonry test methods and specifications for the building industry, ASTM-C67-13, ASTM International, USA
3. ASTM (2013) Standard test method for compressive strength of hydraulic cement mortars using 2-in or 50-mm cube specimens. Masonry test methods and specifications for the building industry, ASTM C109/C109M-13, ASTM International, USA
4. Atkinson RH, Noland JL (1983) A proposed failure theory for brick masonry in compression. In: Proceedings of 3rd Canadian masonry symposium, Edmonton, Alta, Canada, pp 5.1–5.17
5. Bureau Indian Standards (BIS) (1987) Indian standard code of practice for structural use of unreinforced masonry, IS 1905, 2nd revision, New Delhi, India
6. Bureau of Indian Standards (BIS) (1992) Indian standard methods of test of burnt clay building bricks—part 1: determination of compressive strength, IS 3495, 3rd revision, New Delhi, India
7. Bureau of Indian Standards (BIS) (1995) Indian standard code of practice for preparation and use of masonry mortars, IS 2250, 5th revision, New Delhi, India
8. Christy CF, Tensing D, Shanthi RM (2013) Experimental study on compressive strength and elastic modulus of clay and fly ash brick masonry. J Civil Eng Constr Technol 4(4):134–141
9. Drysdale RG, Hamid AA, Baker LR (1994) Masonry structures: behavior and design. Prentice-Hall, Englewood Cliffs
10. Gumaste KS, Nanjunda Rao KS, Venkatarama Reddy BV, Jagadish KS (2007) Strength and elasticity of brick masonry prisms and wallets under compression. Mater Struct 40:241–253
11. Kaushik HB, Rai DC, Jain SK (2007) Stress-strain characteristics of clay brick masonry under uniaxial compression. J Mater Civ Eng 19(9):728–739
12. McNary WS, Abrams DP (1985) Mechanics of masonry in compression. J Struct Eng 111 (4):857–870
13. Sarangapani G, Venkatarama Reddy BV, Jagadish KS (2005) Brick-mortar bond and masonry compressive strength. J Mater Civ Eng 17(2):229–237
14. Turgut P (2012) Manufacturing of building bricks without Portland cement. J Clean Prod 37:361–367

Performance of Hollow Concrete Block Masonry Under Lateral Loads

Shujaat Hussain Buch and Dilawar Mohammad Bhat

Abstract Hollow concrete block masonry is widely in use. In this study hollow blocks are tested for their compressive strength. The overall lateral strength of masonry walls made of hollow concrete blocks is compared with the lateral strength of the fire-brick kilned masonry wall. Different models with and without reinforcement, with and without sand infill and with different types of mortar, are compared for stiffness. The cracking patterns are studied.

Keywords Blocks · Finite-element · Hollow · Masonry · Stiffness · Strength

1 Introduction

Masonry walls are an important feature of all types of load bearing or non-load bearing buildings. The reason of their widespread use is the ease of availability of materials, economy, easy and skilled labor and construction. Traditional clay brick masonry walls have been replaced with fire-kilned bricks and in Kashmir region lately by hollow and solid concrete blocks. Hollow concrete blocks have been used in many parts of India for last few decades. The present study is an experimental investigation and comparison of behavior of reinforced and un-reinforced hollow concrete blocks, and of fire-kilned bricks in clay and mortar. The bricks and blocks are all locally manufactured in Kashmir valley. The compression behavior is determined by three methods. In first method, ACI 530 1992, BSI 1992, Euro-code 6 and IS 1905-1987, Koksal et al. [10], gave masonry strength based on unit block

S.H. Buch (✉)
Civil Engineering Department, Islamic University of Science and Technology,
Awantipora, Jammu and Kashmir, India
e-mail: shujaatbuch@yahoo.com

D.M. Bhat
Engineering Wing, Sarva Shiksha Abhiyan, Jammu, Jammu and Kashmir, India
e-mail: dilawar.bhat@gmail.com

strength and the type of mortar. Second method is based on prism testing given by ASTM E447 1992 [7]. Prisms have height to thickness ratio of 2–5 in stack bond. Third method is given by British masonry code BS 5628-1978 which proposes testing procedures using wall prototypes of 1.2 m (3.936 ft.) to 1.8 m (5.90 ft.) length × 2.4 m (7.87 ft.) to 2.7 m (8.86 ft.) height, with a minimum cross-sectional area of 0.125 m^2 (1.35 ft.^{2}). In-plane lateral load testing is performed on wall specimens of varied aspect ratios to determine the lateral behavior.

2 Research Significance

Hollow concrete block masonry has been in use in many regions of India but in Kashmir region, this is a new entrant in the market. Lot of research has been conducted on hollow concrete block masonry earlier. In this study, not only has the traditional brick masonry been compared with the hollow concrete block masonry but the effect of addition of sand filler, and reinforcement to hollow block wall in terms of stiffness and strength has also been compared, to know their feasibility.

3 Behavior and Failure Mechanisms of Masonry

Masonry is a non-homogenous, in-elastic and anisotropic material. The mechanics of masonry is a combination of mechanics of mortar and masonry units. Tri-axial compression exists in mortar and bilateral tension along with axial compression exists in bricks for strong bricks in weak mortar [11]. The failure occurs on vertical split cracking of prisms [2]. Compression tests on soft bricks in strong mortar have shown that tri-axial compression exists in bricks, which is coupled with axial compression with lateral tension in mortar [11]. Prism strength is just three-tenths of the brick compressive strength, although both are linearly related [3]. The compressive behavior of masonry walls is non-linear [13] whereas, three main behaviors exist: brittle, ductile and bi-linear [2]. The relationship between the masonry compressive strength (f_m) and brick (f_{bm}) and mortar compressive strengths (f_{mm}) is $f_m = k\, f_{bm}^{\alpha} f_{mm}^{\beta}$, $\alpha = 0.7$, $\beta = 0.3$, 'k' depends on brick/block unit properties and their arrangement as per Euro-code 6 [5]. The linear portion of masonry compression stress-strain curve gives chord modulus of elasticity as $E_m = k f_m$, where 'k' is 0.05 to 0.33 [6]. The value of secant modulus of elasticity is 0.25 f_m [8]. Modified "Kent-Park Model" gives a compression pattern with parabolic rising curve, linear falling branch and final horizontal plateau at 20 % of the masonry compressive strength [18]. Modified Ritter curves for compressive stress-strain diagram of masonry give better understanding [13]. The failure of hollow block masonry occurs by mortar crushing and transverse block splitting [4].

Masonry under in-plane loads exhibits a complex shear behavior and a simple flexural action [16]. The complex shear behavior is a result of bed-joint splitting

which is a result of the varying load combination, wall geometry and properties of materials. Besides, shear coupled with diagonal tensile stresses due to lateral in-plane forces leads to a complex state of normal and shear stresses along any bed joint [1]. The masonry failure in shear depends on combination of applied loads, wall geometry, properties of materials [9] and on masonry bond pattern [22]. Under in-plane loads, the masonry has brittle failure [21]. Bed joint reinforcement gives ductility and allows masonry to carry stresses even after cracking [19]. Vertical reinforcement increases flexural capacity of wall [20]. Vertical reinforcement without horizontal bed reinforcement is three times less effective in resisting shear [17]. The shear resistance is in itself the combination of distribution of horizontal and vertical bars [12].

4 Experimental Program

Initially, the unit compressive strengths of fire-kilned bricks, hollow unit blocks and of mortar are individually tested and then compared with existing brick, block and mortar values. Next, the wall base models of dimensions 1,200 mm (46.8 in.) (H) × 1,000 mm (39 in.) (W) × 190 mm (7.4 in.) (T) are modeled in hollow concrete blocks and fire-kilned clay bricks in clay and cement mortar. Horizontal and vertical reinforcements are also used as ties and groove fillers. Besides, sand is also used as filler for the walls. The specifications of different models are given in Table 1.

Table 1 Model parameters

Model	Masonry type	Properties of elements	Compressive strengths (N/mm^2)
I	Brick in mud mortar	Brick size (228 mm × 100 mm × 100 mm)	f_b = 11.30
II	Brick in cement mortar	Mortar (10 mm) with 1:4 cement mortar	f_{cb} = 3.50
III	Hollow block in cement mortar	Block size; hollow with web thickness of 32 mm (390 mm × 190 mm × 190 mm)	
IV	Hollow block sand filled in cement mortar	Bed block (rich cement mortar of 1:3)	f_m = 16.0
V	Hollow block reinforced in cement mortar	Horizontal reinforcement (2–12 mm dia.) after 2 block-layers and vertical reinforcement (1–12 mm dia.)-Fe415 at wall corners	

f_b Compressive strength of brick
f_{cb} Compressive strength of concrete block
f_m Compressive strength of mortar
Note 1 mm = 0.039 in., 1 N/mm^2 = 20,885.4 lb/ft.^{2}

Fig. 1 Test set-up
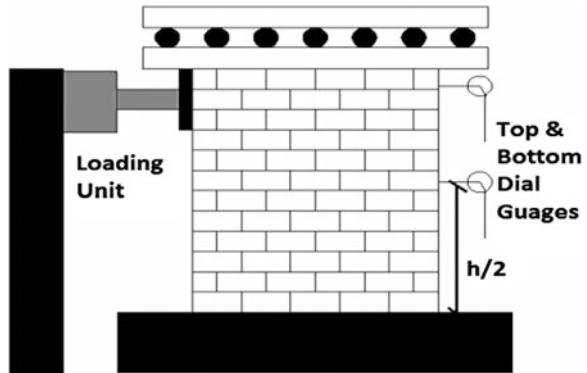
The wall models are base fixed with rigid diaphragm by rich mortar. The wall models are loaded monotonically in lateral in-plane direction by a hydraulic jack of capacity 1,000 kN (224,700 lb) as in Fig. 1.

4.1 Material Parameters

(a) Fire-kilned bricks—size 228 mm × 100 mm × 100 mm; compressive strength 11.3 N/mm^2.

(b) Hollow concrete block—Full size 390 mm × 190 mm × 190 mm, thickness 32 mm, and two and four compartments; compressive strength of 2.80–3.50 N/mm^2 (Fig. 2).

(c) Mud mortar—made of sticky thatched mud; compressive strength 2.3 N/mm^2.

(d) Cement mortar—rich mix (1:4).

(e) Sand—fine river sand as filler and mortar binder.

(f) Reinforcement—12 mm diameter bars of Fe-415.
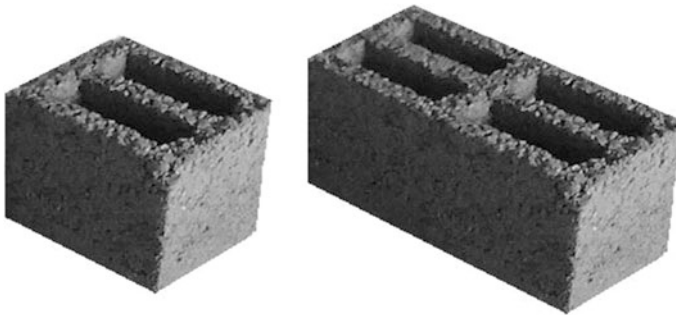
Fig. 2 Hollow concrete blocks
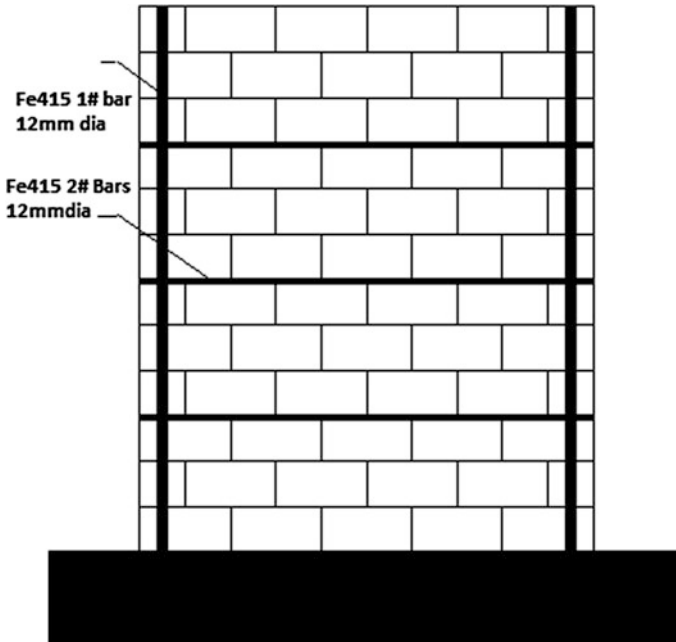
Fig. 3 Reinforcement location in model V

4.2 Modelling Parameters

(a) In Models I and II, the bricks are laid as alternate header and stretcher courses.
(b) In Models III, IV and V, hollow blocks are laid as all stretcher courses.
(c) In Model IV, sand is filled within the hollow spaces in blocks.
(d) In Model V, steel reinforcement bars are given as described in Fig. 3.

4.3 Test Results

It is seen in the present study that hollow concrete blocks fail in compression at lower unit strength than that of fire-kilned bricks. This is validated from the compressive strengths of each unit as detailed in (Table 2).

From the lateral load tests on the walls, for models I–V, the base-shear-deflection graphs are determined as given in Fig. 4. Further, the cracking patterns for different models are studied. The cracking pattern for fire-kilned brick masonry in clay mortar is an exact diagonal flexural failure as a toothed joint failure. Mid-deflection cracking occurs first corresponding to 0.563 % drift while as complete failure occurs corresponding to 0.813 % drift at 31 kN (6,965.7 lb) lateral load.

Cracking pattern for fire-kilned brick masonry in cement mortar is also a diagonal flexural toothed failure. Cracking initiates with corner crushing (as the

Table 2 Unit compressive strengths of bricks/blocks, mortar and masonry prism

Unit	Present study (N/mm^2)	Naraine and Sinha (N/mm^2)	Ganesan and Ramamurthy (N/mm^2)	Sarangapani et al. (N/mm^2)	Mohammad et al. (N/mm^2)
Fire-kilned brick	11.30	13.10	–	3.17–10.67	–
Hollow concrete block	2.80–3.50	–	6.74–19.75	–	18.2–27.0
Cement mortar	16.0	6.10	4.27–21.20	4.11–10.57	2.9–19.9
Masonry prism	6.40	5.40	–	2.15–5.24	7.54–11.7

Note Conversion of 1 N/mm^2 = 20,885.4 lb/ft.^{2}
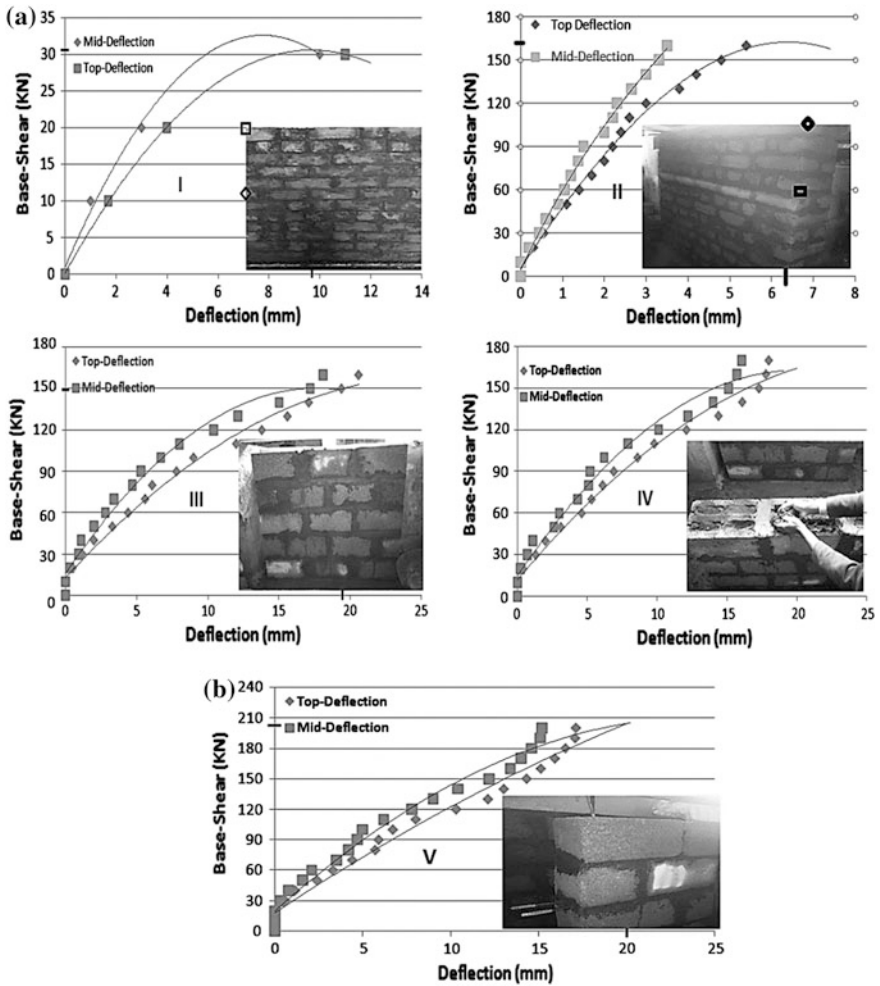
Fig. 4 **a** Load-deflection *curves* for different models (from Table 2). **b** Load-deflection *curves* for different models (from Table 2)

aspect ratio, that is width to height ratio of the wall specimen in this set-up is less than 1.0), corresponding to a lateral drift of 0.525 % at a lateral load of 162 kN (36,401.4 lb). Hollow concrete block masonry in cement mortar is a mid-shear failure. The bed joint cracks corresponding to 1.458 % lateral drift and slips further corresponding to 1.583 % lateral drift at a lateral load of 149.5 kN (33,592.6 lb).

Hollow concrete block filled with sand cracks along multiple bed joints as shear failure is coupled with flexural failure. This happens corresponding to 1.542 % lateral drift and failure occurs corresponding to 162 kN (36,401.4 lb) lateral load. Hollow concrete block with steel reinforcement fails in bed joint shear slippage coupled with vertical joint pier slippage in zones of no reinforcement. The failure is uniform at a lateral drift of 1.67 % corresponding to a lateral load of 202 kN (45,389.4 lb).

A comparative behavior of load strength to deflection curves is given in Fig. 5.

The cracking patterns for the masonry walls are illustrated in Fig. 7. Hollow concrete blocks commercialized in Kashmir region (lying in earthquake prone zone) show appreciable stiffness decrease by 54 %. This is depicted in Fig. 6. The
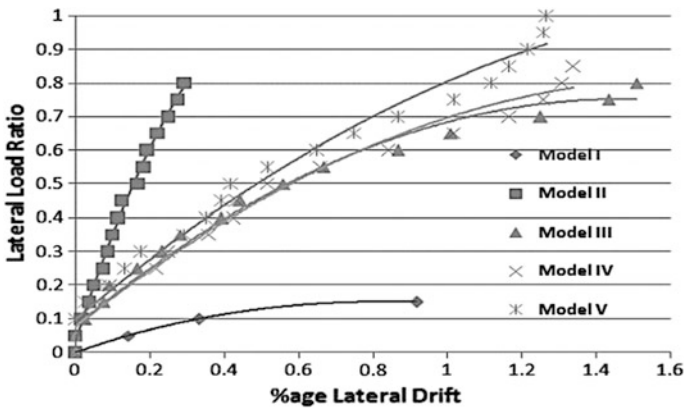
Fig. 5 Comparative load-deflection *curves* of different models (from Table 2)

Fig. 6 Lateral stiffness of different models
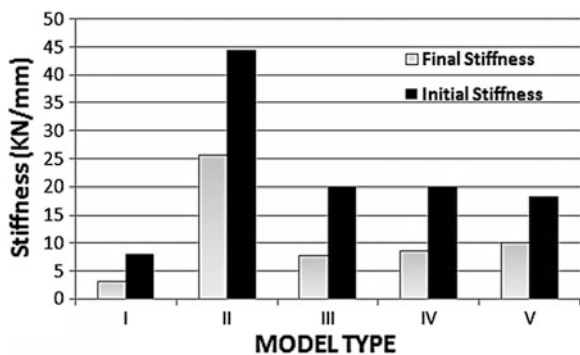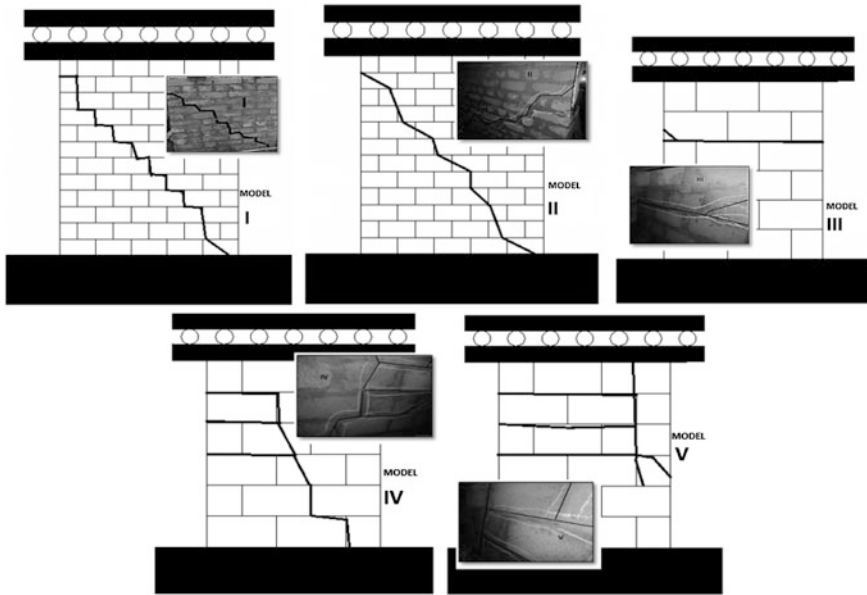
Fig. 7 Cracking patterns of different models (from Table 2)

stiffness degradation for hollow concrete blocks is 65 % compared to 41 % for fire-kilned brick masonry. Sand filled hollow concrete masonry shows slightly lesser stiffness degradation (60 % approx.). Reinforced hollow concrete blocks have lower stiffness degradation of up to 44 %. This is on account of improved stiffness at cracking and uniform shearing and greater ductility offered by tensioning of reinforced bars.

4.4 Comparison with Other Works

The present work is compared with studies on in-plane lateral load behavior of hollow block masonry. The comparison is explained in (Table 3).

Table 3 Comparison of stiffness values for masonry models

Model	Final stiffness (kN/mm) (present study)	Final stiffness (kN/mm) V.G. Haach et al.	Final stiffness (kN/mm)
II	44.0	–	22.0
V	10	7.27–21.41 (for different reinforcing patterns)	

5 Modeling the Behavior of Hollow Concrete Block Masonry

Traditionally, the masonry is modelled as a micro-model discrete element [14]. Finite element modelling is mostly used in modeling their behavior [15]. The hollow concrete blocks and brick masonry are both modelled as shell finite elements and as plate finite elements. With addition of reinforcement, the hollow concrete blocks behave rigidly showing more stiffness and more uniform cracking at failure while as with addition of sand, the hollow concrete blocks show more strength and higher initial lateral stiffness. The modelling is done in computer software SAP 2000 (Structure Analysis Programmer). The elastic analysis is performed by either drawing a secant in the load-deflection envelope from initial point and ultimate point or by drawing an initial tangent. In the former case, the point of intersection of elastic curves (where the non-linear curve is bisected) is selected as loading point for elastic analysis. In the later, the point of maximum tangential intersection of the tangent curve and non-linear curve is selected as point of loading.

6 Conclusion

The hollow concrete block masonry is more ductile (by 55 %) than brick masonry and when used with reinforcement, it is stronger (by 25 %) than brick masonry. Besides, reinforced hollow concrete masonry is even more ductile (by 61 %) than traditional bricks. Reinforced hollow blocks show comparable stiffness degradation (44 %) on loading as do bricks (41 %). Sand filled hollow concrete blocks (162 kN/ 36,401 lb) show comparable strength with traditional bricks (162 kN/36,401 lb) although making the masonry stiffer.

References

1. Atkinson RH, Amadei BP, Saeb S, Sture S (1989) Response of masonry bed joints in direct shear. J Struct Eng 115:2276–2296
2. Atkinson RH, Noland JL (1983) A proposed failure theory for brick masonry in compression. In: Proceedings 3rd Canadian masonry symposium, Edmonton, Alta, Canada
3. Bennett RM, Boyd KA, Flanagan RD (1997) Compressive properties of structural clay tile prisms. J Struct Eng 123:920–926
4. Cheema TS, Klingner RE (1986) Compressive strength of masonry prisms. Am Concr Inst J 83:88–97
5. Deodhar SV (2000) Strength of brick masonry prisms in compression. J Inst Engineers (India) 81:133–137
6. Drysdale RG, Hamid AA, Baker RL (1999) Masonry structures: behavior and design, 2nd edn. The Masonry Society, Boulder, Colorado, USA

7. Drysdale RG, Hamid AA, Baker RL (1994) Masonry structures-behavior and design, 1st edn. Princeton-Hall, Englewood Cliffs
8. Gumaste KS, Nanjunda-Rao KS, Venkatarama-Reddy BV, Jagadish KS (2006) Strength and elasticity of brick masonry prisms and wallettes under compression. Mater Struct 40:241–253
9. Haach VG, Vasconcelos G, Laurenco PB (2010) Experimental analysis of reinforced concrete block masonry walls subjected to in-plane cyclic loading. J Struct Eng 136:452–462
10. Koksal HO, Karakov C, Yildrim H (2005) Compression behavior and failure mechanisms of concrete masonry prisms. J Mater Civ Eng 17:107–115
11. Kaushik HB, Rai DC, Jain SK (2007) Stress-Strain characteristics of clay brick masonry under uniaxial compression. J Mater Civ Eng 19:728–739
12. Khattab MM, Drysdale RG (1993) The effect of reinforcement on the shear response of grouted concrete masonry. TMS J 12:38–44
13. Knutson HH (1993) Stress-strain relationship for masonry. Masonry Int 17:31–33
14. Lemos JV (1997) Discrete element modeling of the seismic behavior of stone masonry arches. In: 4th international symposium on computer methods in structural masonry, London
15. Lotfi H, Shing PB (1994) Interface model applied to fracture of masonry structures. J Struct Eng 120:63–80
16. Mahmoud ADS, Hamid AA, El-Mags SA (1995) Lateral response of unreinforced solid masonry shear walls: an experimental study. In: Proceedings 7th Canadian masonry symposium, McMaster University, Hamilton, Ontario
17. Priestley MJN, Bridgeman DO (1974) Seismic resistance of brick masonry walls. New Zealand Natl Soc Earthq Eng Bull 7:167–187
18. Priestley MJN, Elder DM (1983) Stress-strain curves for unconfined and confined concrete masonry. Am Concr Inst J 80:192–201
19. Schultz AE, Hutchinson RS, Cheok GC (1998) Seismic performance of masonry walls with bed-joint reinforcement. In: Proceedings structural engineers world congress. Elsevier, San Francisco
20. Shing PB, Noland JL, Klamerus E, Spaeh H (1989) Inelastic behavior of concrete masonry shear walls. J Struct Eng 115:2204–2225
21. Tomazevic M (1999) Earthquake resistant design of masonry buildings. Imperial College Press, London
22. Vasconcelos G (2005) Experimental investigations on the mechanics of stone masonry: characterization of granites and behavior of ancient masonry shear walls. PhD thesis, University of Minho, Portugal

Feasibility of Using Compressed Earth Block as Partition Wall

Md. Kamruzzaman Shohug, Md. Jahangir Alam and Arif Ahmed

Abstract In a reinforced concrete (RC) frame structure building, partition wall has very low compressive stress. To replace traditional fired brick, environment friendly Compressed Earth Block (CEB) may be used as partition wall. This study investigated the feasibility of using CEB as interior and exterior partition wall. Soil samples were collected from 8 traditional brick fields and their index properties and percentage of sand were determined for selecting suitable soil for making CEB. After that, standard proctor test was performed for the selected soil sample to know the optimum moisture content under which maximum compaction can be achieved which will ensure the maximum strength also. A mould with a dimension 241 mm × 114 mm × 203 mm was made for making CEB and 36 bricks were made using compression testing machine. Compressive strength test was performed after 7 and 28 days maturation of brick whereas absorption capacity was determined for 24 h submergence under water for different condition i.e. normal CEB, CEB with slurry coating, plaster coating. From this study it is concluded that CEB is feasible for using as interior wall but not as external wall in flood prone areas. Cement slurry and plaster coating could not reduce absorption capacity of CEB. Cement plaster coating has very little use in case of reducing absorption capacity of CEB. Soil composition used for making fired brick in Bangladesh is not suitable for making CEB because of very low percentage of sand. There is always a certain range of moisture content for which CEB gains its maximum compression and results maximum compressive strength.

Keywords Compressed earth block · Partition wall · Compressive strength · Absorption capacity

Md.K. Shohug (✉) · Md.J. Alam · A. Ahmed
Department of Civil Engineering, Bangladesh University of Engineering and Technology, Dhaka 1000, Bangladesh
e-mail: kamruzzamanshohagh@gmail.com

1 Introduction

Compressed earth block is an ideal candidate for sustainable construction material because it needs less energy, contribute fewer CO_2 emissions and help to promote the local economy and local labor. Compressed Earth Block is a type of manufactured construction material formed in a mechanical press that forms a compressed block out of an appropriate mix of fairly dry inorganic soil, non-expansive clay, aggregate, and sometimes a small amount of cement. Usually, 21 MPa compressive stress is applied and the original soil volume is reduced to about half in making CEB.

Now a day, 50 % of the population in developing countries, including majority of the rural population and at least 20 % of the urban and suburban population, live in earthen dwellings [1]. At present, 6,000 traditional brick fields are emitting 8.75 million tons carbon annually [2]. According to the UNDP, Bangladesh uses about 23 tons of coal to produce 100,000 bricks [3]. Figure 1 shows the effect of air pollution of Dhaka caused by brick manufacture [4].

The problem inherent with fired brick can be solved to a great extent by soil block named Compressed Earth Block (CEB) which has been developed and became popular in many parts of the world for its low cost construction, eco friendliness, and efficiency and for being available locally and cheaply. Again, the wall made by CEB resists better to external forces than walls built from all others block-mortar associations [5].

The problems inherent with CEB construction are cracks of wall due to shrinkage of soil, wash ability of wall and foundation due to heavy shower and prolonged stagnant water of heavy flood. In this research work, attempt has been made to investigate the performance of compressed earth block (CEB) as a partition wall in a reinforced concrete (RC) frame structure building.
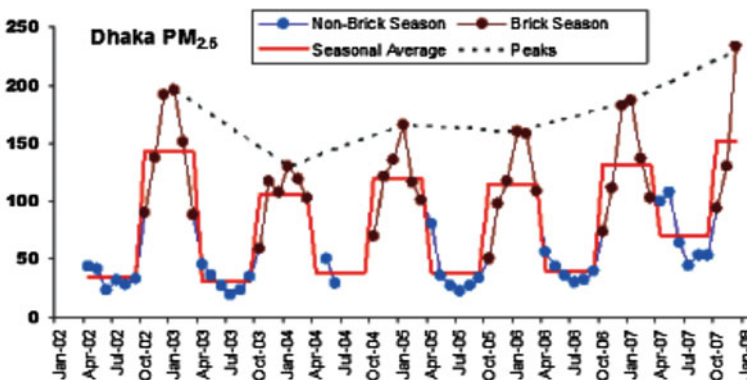
Fig. 1 Air pollution of Dhaka caused by brick manufacture [4]

2 Experimental Program

Suitable soil composition ensures good quality brick. However, the curve shown in Fig. 2 gives an approximate indication of the types of soil which are recommended for the manufacture of compressed earth blocks. As can be seen, the proportions of each type of material can vary considerably depending on the qualities of each, which differ quite widely, particularly for clays. Knowing the proportions of each (gravel, sand, silt and clay), shown on a particle size distribution curve, is an important indicator but is rarely enough for soil selection purposes [6].

Normally the suitable ranges are: clays = 8–30 %, silts = 10–25 %, gravel = 0–40 %, sands = 25–80 %, clay plasticity index = up to 25–30 would be acceptable, mixed soil plasticity index = 12–15.

2.1 Index Property Test

The soils used for making the blocks were evaluated first by performing some tests for the purpose of classifying and identifying the types of soils. The tests performed were as follows: Atterberg Limits Tests, Wet sieving and Compaction Test. Eight samples were used for this study. All the samples were collected from the brick fields of different location of Gazipur district under Dhaka Division of Bangladesh. The samples were collected from the soil that is used for making fired brick. Results of index property tests are listed in Table 1.

From index property result, very low percentage of sand is observed in traditional brick field. But for CEB, this percentage should be higher comparing to the soil that is used in our traditional brick field because low percentage of sand allows the brick to shrink. So, percentage of sand was the main criteria behind selecting the soil sample. SIC brick was selected for our study which has high percentage of sand (7.5 %) within our collected soil sample.

Fig. 2 Suitable ranges for CEB
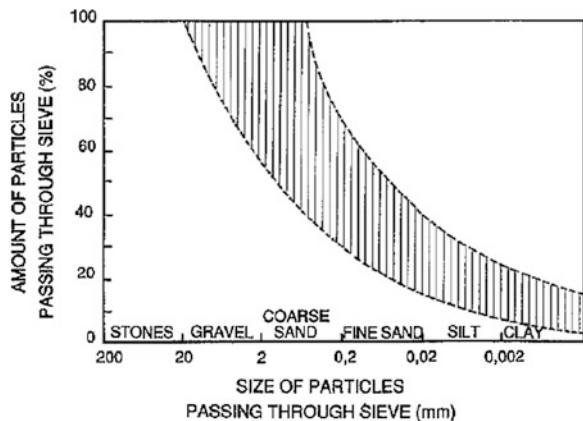
Table 1 Index properties of soil sample

Brick name	LL	PL	PI	Soil symbol	Soil name	Sand fraction (%)
AUTO	58	30	28	CH	Fat clay	1.4
DSSS	33	19	14	CL	Lean clay	1.5
AUL	49	19	30	CL	Lean clay	0.2
MAB	40	21	19	CL	Lean clay	4.5
RTB	31	25	6	ML	Silt	4.7
MSB	41	18	23	CL	Lean clay	0.4
ABC	37	29	7	ML	Silt	0.2
SIC	43	22	21	CL	Lean clay	7.5

Optimum moisture content is important because it shows the amount of water needed for maximum compaction of soil under mechanical press. It is difficult to calculate beforehand the precise volume of water which will be needed to reach the optimum moisture content for compaction, as this will depend on the natural moisture content of the various materials (soil, sand, etc.) which varies greatly. In our study, standard proctor test was done to find out the optimum moisture content. Figure 3 shows the result of the standard proctor test performed and Optimum moisture content of our selected soil sample was found to be 20 %. Maximum dry density was 16.7 kN/m^3.

2.2 Brick Preparation

Soil preparation operation plays a crucial part in the ultimate quality of the CEB. These operations can sometimes make it possible to use soils which are unusable in their natural state, because they can include modifying the grain size distribution.

Fig. 3 Graph of standard proctor test
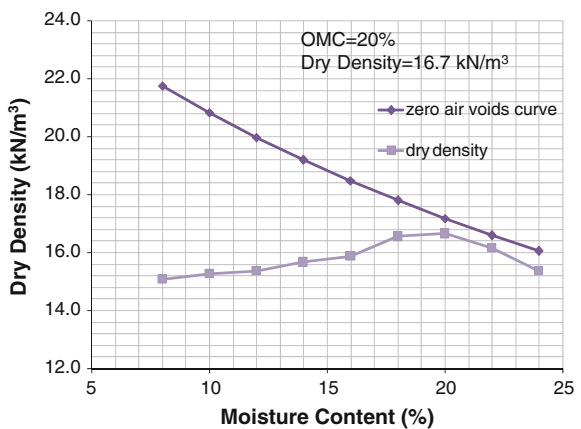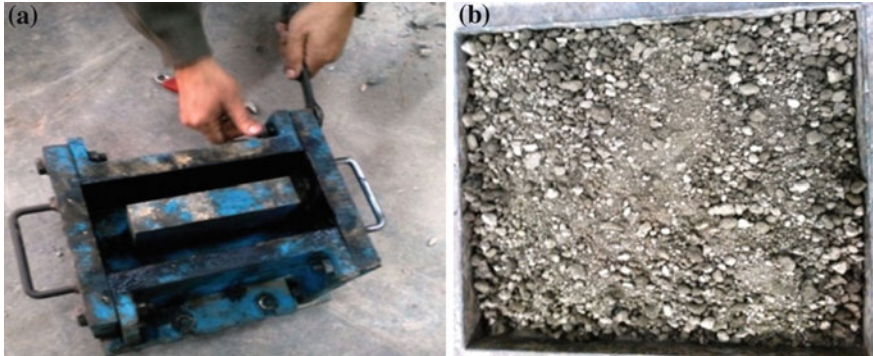
Fig. 4 Photograph of **a** mould and tightening of bolts, **b** prepared soil sample

Initially, the soil was pulverized by wooden hammer. After pulverization, the soil which passes the #4 sieve was used to make CEB. In general, this is mainly done to remove the particles which are too coarse. The difference between the optimum moisture content and moisture content of existing soil was determined and is thoroughly mixed into the soil. Figure 4b is the photograph of prepared soil sample for CEB. Then, prepared soil sample was poured into the mould. This mould was specially prepared for this study having a dimension of 241 mm × 114 mm × 203 mm. The bolts of the mould were properly tightened and the surfaces of the mould were well greased (as shown in Fig. 4a). As the press is fitted with a lid, it must be correctly positioned and soil must not get trapped in the edge between the mould and the lid as this can cause the lid to be displaced or the compression system to jam. Using compression testing machine, the soil was compressed and the volume was reduced to half. After removing the brick from the mould, the CEB was kept drying on a place that is not humid and protected from direct sun and wind. A photograph showing drying of CEB is given in Fig. 5.

Fig. 5 Drying of compressed earth block (*CEB*)

2.3 Compressive Strength Test

There is no specification in Bangladesh National Building Code for CEB. According to the New Mexico Compressed Earth building code, CEB shall be tested on flat position. The length of the test unit must be a minimum of twice the width. The surface must be smooth. The test shall be subjected to a uniform compressive load that is gradually increased at a rate of 3.45 MPa/min until failure occurs. A true platen should be used in the testing machine, along with swivel head to accommodate nonparallel bearing surfaces.

However, in our experiment the actual brick was halved and the length of the test unit was almost equal to the width. The surface was smooth. Compression testing machine was used for mechanical press instead of CEB machine and photograph of mechanical press is given in Fig. 6. The compressive strength test was subjected to a uniform compressive load that is gradually increased at a rate of 0.95 MPa/min until load started to decrease.

2.4 Treatment by Slurry Coating

Cement slurry coating was provided on CEB after completion of 28 days maturation period. Ratio of cement and water in cement slurry ratio was 1:2 and 1:3 and the mixing was done on weight basis (shown in Fig. 7). Then the bricks were kept on drying again and subjected to absorption capacity test and compressive strength test after 7 and 28 days.

Fig. 6 Photograph of mechanical press by compression testing machine
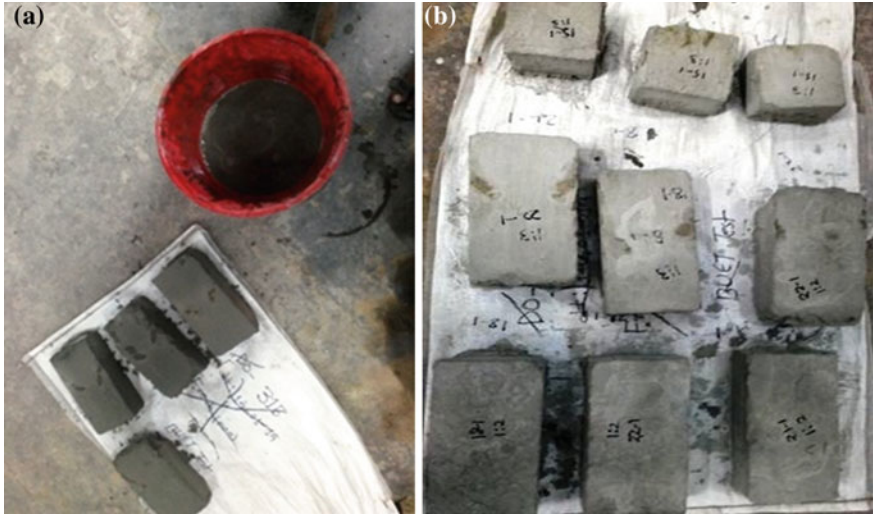
Fig. 7 Photographs of **a** preparation of slurry, **b** after treatment by cement slurry

2.5 Treatment by Plaster Coating

Some of the CEBs were provided with plaster coating for reducing absorption capacity. Ratio of cement and sand was 1:2 in plastering and the thickness of plastering was 12 mm. The mixing was done in volume basis. Photograph of mixing and plastering of CEB is shown in Fig. 8. Figure 9b is the photograph of plastered CEB kept for drying. Water was added so that mortar was suitable for plastering.
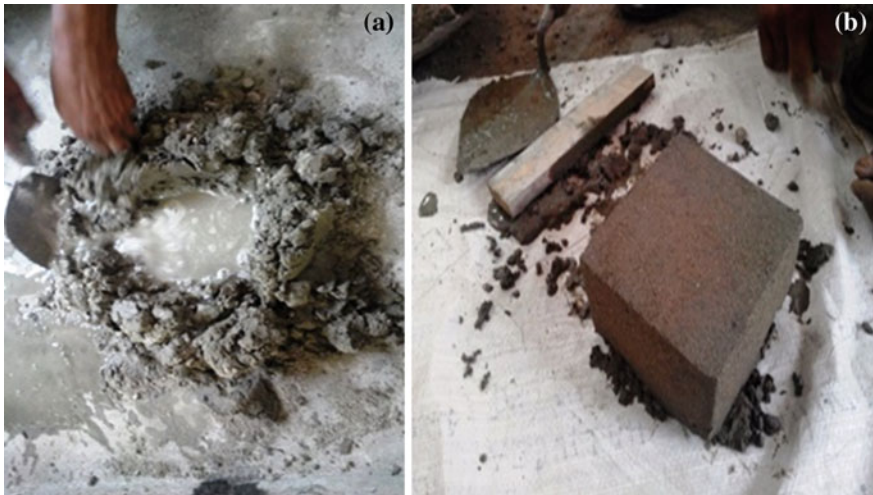
Fig. 8 Photographs of **a** mixing, **b** after plastering
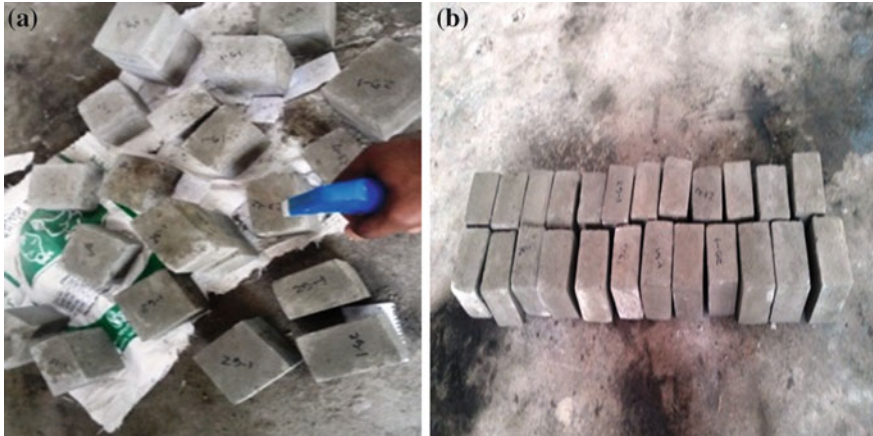
Fig. 9 Photograph of **a** spraying on CEB, **b** plastered on CEB

For proper curing of plastered CEB, regular watering was provided. Importantly, it is not feasible to provide water in traditional way for CEB because this will make the soil soft underneath the plaster layer. So, spraying was a better option for watering (shown in Fig. 9a). The plastered brick was kept on drying again and subjected to absorption test and compressive strength test after 7 and 28 days.

Table 2 Summary of test schedule

Test		Condition	Parameters investigated
Index property test	Liquid limit	Soil sample passing #200 sieve	Liquid limit and plasticity index
	Plastic limit	Soil sample passing #200 sieve	Plastic limit and plasticity index
	Wet sieving	Soil sample retain on #200 sieve	Percentage of sand on certain soil sample
Moisture density relationship test	Standard proctor test	Soil sample from SIC brick field	Optimum moisture content
Compressive strength test	Normal CEB	Sun dried brick	Compressive strength test after 7 and 28 days
	CEB with cement slurry layer	Cement slurry ratio 1:2 and 1:3 (cement:water)	Compressive strength test after 7 and 28 days
	CEB with plaster layer	Plaster ratio 1:2 (cement: sand)	Compressive strength test after 7, 21 and 28 days
Absorption capacity test	Normal CEB	Sun dried brick	Absorption capacity
	CEB with cement slurry layer	Cement slurry ratio 1:2 and 1:3 (cement:sand)	Absorption capacity
	CEB with plaster layer	Plaster ratio 1:2 (cement: sand)	Absorption capacity

2.6 Test Plan

A summary of the test schedule is given in Table 2. This table describes the composition of material used in preparing the respective specimens and the intended parameters to investigate from the tests.

3 Result and Discussion

3.1 Effect of Moisture Content on Applied Load During Mechanical Press and Compressive Strength of CEB

One of the most unique things about making CEB is the moisture content. When a block machine compresses a block, it reduces the volume by about 50 % by mechanically aligning the moist particles, removing the air pockets and sticking the clay to sand. If too much water is in the mix, there will be more air spaces between the particles when the brick dries. If the moisture content is too high the soil may swell and the pressure of the compacting machine will be dissipated by the water trapped between particles. If, on the other hand, the moisture content is too low, the particles will be insufficiently lubricated and it will not be possible to compact the soil to its minimum volume.

So there is always an optimum range for which the brick will gain optimum strength. A similar phenomenon was observed in our experiments which are shown in Figs. 10 and 11. Different moisture content was used for different bricks.

In Fig. 10, we can observe that maximum strength is achieved at a moisture content of 20 % which was our determined optimum moisture content also. Again, after certain value of moisture content, applied load during mechanical press decreased with increasing amount of moisture content as the compaction energy dissipated by the water trapped between particles. In this graph, applied load during mechanical press was highest at moisture content of 12 % and beyond this level

Fig. 10 Effect of moisture content on applied load during mechanical press and compressive strength of CEB at 7 days
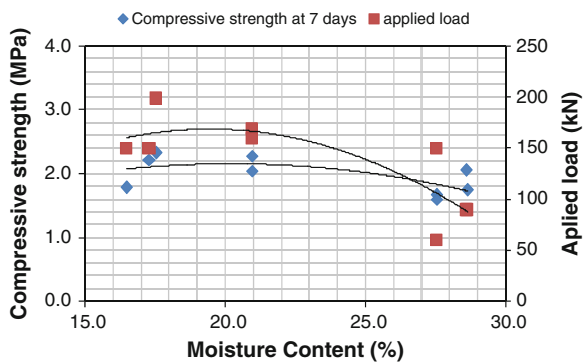
Fig. 11 Effect of moisture content on applied load during mechanical press and compressive strength of CEB at 28 days
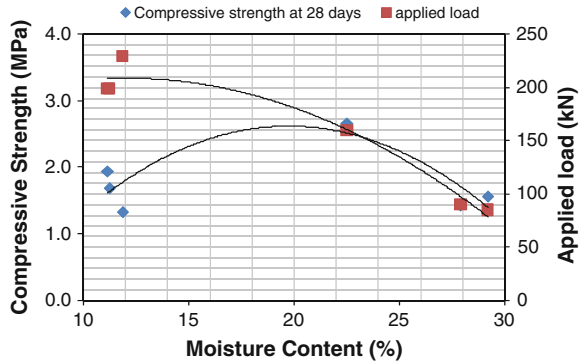
applied load started to decrease. From point of view, we can see that moisture content near to optimum moisture content will give high strength of CEB.

In Fig. 11, we can observe similar behavior as Fig. 10. Here, moisture content for maximum applied load during mechanical press and high strength of block is almost same and it is very close to our determined optimum moisture content. Again, in Fig. 11, applied load is decreasing at a moisture content that is less or greater than the optimum level. Lower moisture content less than the optimum value has made the soil insufficiently lubricated which caused lower value of applied load and compaction energy dissipated by the water trapped between particles in case of higher moisture content and results lower applied load during mechanical press.

3.2 Result of Compressive Strength

According to New Mexico Compressed Earth Block building code, cured units shall have a minimum compressive strength of 2.1 MPa when tested. The compressed earth block shall be tested in the flat position. Loading rate is 3.45 MPa/min. The compressive strength is defined as P/A, where P = load and A = area of compression surface. In our study, compressive strength was satisfactory in all condition i.e. normal CEB, CEB with cement slurry coating with a ratio of 1:2 and 1:3 and plaster coating. Strength comparisons under these conditions are shown in a column chart in Fig. 12. In Fig. 13, compressive strength of 7 days matured plastered CEB has very low compressive strength.

Water that was provided for curing purpose has leached into the soil underneath the plaster layer and made the soil soft. As a result, very much lower value of strength was observed after 7 days strength test but the bricks regained its strength with time and satisfactory strength was found after 28 days.

Fig. 12 Column chart showing comparison between CEB under different condition
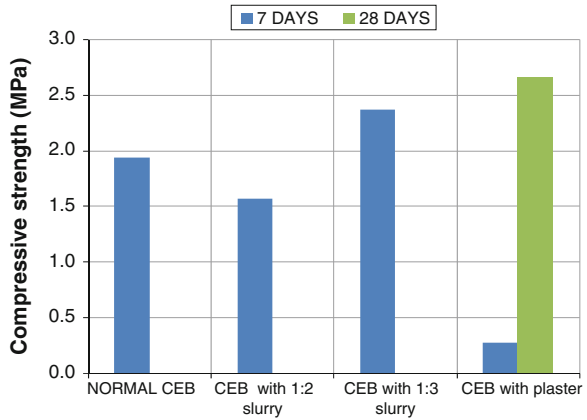
Fig. 13 Relation between compressive strength and maturation period
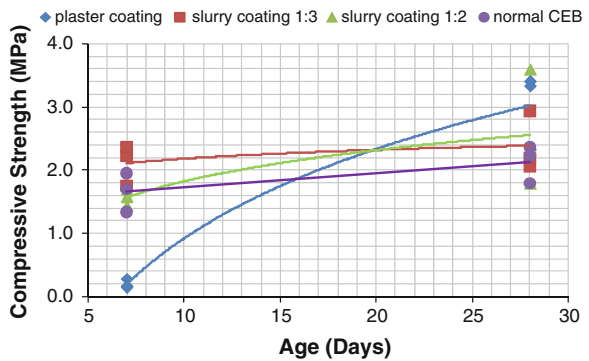
3.3 Result of Absorption Test

Results of absorption test were almost same for different conditions and they are summarized in Table 3. Photographs of CEB with slurry coating and plastered CEB after 24 h submergence under water is given Fig. 14.

Table 3 Results of absorption test

Condition	Result
Normal CEB	Washed away after 24 h submergence
CEB with cement slurry coating (1:3 ratio)	Washed away after 24 h submergence
CEB with cement slurry coating (1:2 ratio)	Washed away after 24 h submergence
CEB with cement plaster coating	Very little amount of soil washed away after 24 h submergence
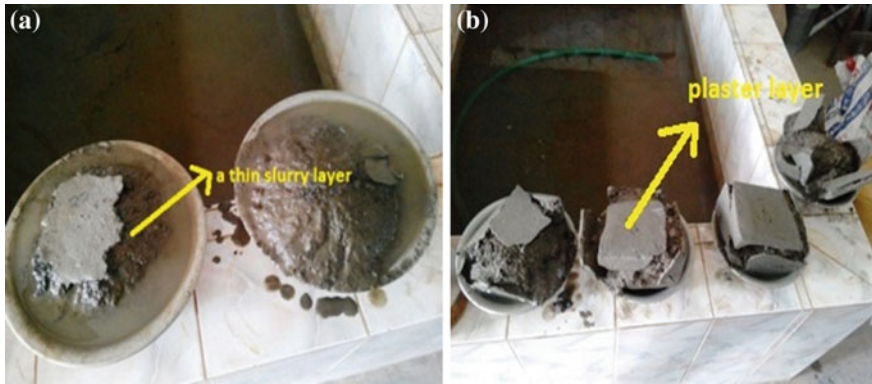
Fig. 14 Photograph of **a** CEB with cement slurry after 24 h submergence, **b** CEB with plaster coating after 24 h submergence

4 Conclusions

CEB can effectively reduce the cost of reinforced concrete frame structure building. It can be a good alternative of traditional brick for its low cost and environment friendliness. In this study following conclusions were drawn from the experimental results.

- CEB is feasible for using as interior wall but not as external wall in flood prone areas. Places which are not flood prone, CEB can be used there for both interior and exterior wall.
- Cement slurry coating could not reduce absorption capacity of CEB.
- Cement plaster coating has no use in case of reducing absorption capacity of CEB.
- Soil composition used in traditional brick fields in Bangladesh is not suitable for making CEB because of having very low percentage of sand.
- There is always a certain range of moisture content for which CEB gains its maximum compression and results maximum compressive strength. The range of moisture content should be around optimum moisture content of the soil.

References

1. Houben H, Guillaud H (2005) Earth construction: a comprehensive guide. ITDG Publishing, London
2. The Daily Ittefaq (2009) Deal to reduce carbon omission from Brickfield. Retrieved from http://www.carbonoffsetsdaily.com/newschannels/asia/deal-to-reduce-carbon-omission-from-brickfield-11219.htm
3. UPI (2010) Bangladesh adopts green brick making. Retrieved from http://www.upi.com/Business_News/EnergyResources/2010/04/06/Bangladeshadopts-green-brick-making/UPI-69981270565548/

4. Guttikunda S (2009) Impact analysis of brick kilns on the air quality in Dhaka, Bangladesh. SIM working paper series 21-2009. Retrieved from http://www.indiaenvironmentportal.org.in/files/Dhaka-AQ-Brick%20Kilns.pdf
5. Ntamack GE, Fokou CK, Beda T, D'Ouazzane SC (2012) Simulation of the walls dynamic behaviour by the modelling of the block-mortar set. Int J Sci Technol 2(11)
6. Rigassi V (1985) Compressed earth blocks: manual of production, vol I. Manual of production. A publication of the Deutsches Zentrum für Entwicklungstechnologien—GATE. In: Deutsche Gesellschaft für Technische Zusammenarbeit (GTZ) GmbH in coordination with BASIN—1985

Structural Behavior of Rectangular Cement-Stabilized Rammed Earth Column Under Compression

Deb Dulal Tripura and Konjengbam Darunkumar Singh

Abstract The paper presents a novel experimental investigation, comprising material tests and column tests, focusing on the effect of concentric axial loading and slenderness on the capacity reduction factors of cement stabilized rammed earth (CSRE) columns of rectangular (R) cross sections. The study also attempted to calculate the ultimate compressive strength of columns using the tangent modulus theory. The experimental results compare quite favorably with published codal provisions. There is a reduction in strength as the slenderness ratio (effective height to thickness ratio) increases from about 2 to 10. At higher slenderness ratios, there was a close agreement between the experimental value and value predicted by tangent modulus theory on ultimate strength.

Keywords Stabilized soil · Rammed earth · Compressive strength · Prism · wallette · Column

1 Introduction

Rammed earth is a construction technique and in the recent past it has gain much popularity as a sustainable building technology in various parts of the world. In this technique, the temporary formwork is filled with a 10–12 cm moist earth (stabilized or unstabilized) layer followed by ramming and then a new 10–12 cm layers are added and rammed in progressive layers. The formwork is removed and placed at a higher level until the desired height is reached. Soil, sand, gravel and stabilizers (cement, lime etc.) are the major constituents for both stabilized and unstabilized rammed earth construction. A significant number of magnificent rammed earth buildings are to be found in southern India, particularly in Bangalore.

D.D. Tripura (✉) · K.D. Singh
Department of Civil Engineering, Indian Institute of Technology Guwahati, Guwahati, India
e-mail: debdulaltripura@gmail.com

K.D. Singh
e-mail: k_darun@yahoo.com

Due to limited structural design regulations for earth buildings, rules developed for masonry construction are generally followed. At present, the most well known structural design standard for earth building has been developed in New Zealand [1–3], India [4], Australia [5], the United States [6] and Zimbabwe [7]. Over the past 50–60 years, structural design guidance for simple earth buildings has also been published in various parts of the world, some of them are Australia [8], the United States [9], Germany [10] and the United Kingdom [11].

Apart from the aforementioned standards and guidelines, some extensive study has also been carried out on structural behavior of rammed earth columns and walls. Maniatidis and Walker [12] studied the structural capacity of unstabilized rammed earth columns of square cross section focusing on the effect of load eccentricity and slenderness, determined the capacity reduction factors in combined axial compression, and bending. The study states that the variation between theoretical and experimental results of column failure load for high load eccentricities is attributed to suppressed cracking, ignored in the simple analysis, due to the inherent material tensile strength and confinement. There was a significant variation in material performance between small-scale 100 mm diameter cylinders and full-scale prisms and columns using the same material. The reduction in compressive strength and stiffness of the full-scale specimens is attributed to variation in material grading inclusion of aggregates greater than 20 mm, subsequent crushing of the higher aggregate content during compaction, and variation in compactive effort. The study also presented that the load carrying capacity of the axially loaded columns increases with increasing slenderness ratio, which is a contradictory result. Reddy and Kumar [13] investigated the strength and structural behavior of story-high CSRE walls under compression, assessed its ultimate crushing strength considering slenderness effects, and reported that the CSRE wall strength decreases steadily as the slenderness ratio increases and there is a close agreement between the experimental value and the value predicted by tangent modulus theory for the height-to-thickness ratio of 19.74.

From the detailed literature review it is observed that there is still a lacking in systematic studies on structural behavior of rammed earth columns and walls. Hence, there is a need to study the strength and behavior of columns and walls for better understanding of structural behavior and design principles.

2 Objectives and Scope

The primary aim of the study is to investigate the validity of using masonry design rules for the design of CSRE columns. The paper presents a novel experimental investigation, comprising material tests, prism and wallette, and column tests, focusing on the effect of concentric axial loading and slenderness on the capacity reduction factors using rectangular columns of varying slenderness ratios.

3 Experimental Programs

3.1 Material

Table 1 outlines the properties of soil used. The properties of soil were determined as per Indian Standards: IS: 2720 Part 4 [14], IS: 2720 Part 5 [15] and IS: 2720 Part 7 [16]. Properties of the selected soil comply with general published recommendations for rammed earth construction. Ordinary Portland cement of 43-grade conforming to IS: 8112 [17] was used in the experimental investigations.

3.2 Equipments for Production of Test Specimen

For production of 150 mm square prisms and 150 mm × 230 mm rectangular wallettes, each of 300 mm heights and the corresponding rectangular columns of heights 900–1,500 mm, the following equipments were used:

(a) A mild steel rammer weighing 5.6 kg with a solid handle of 25 mm diameter and 1,020 mm length attached with a 95 mm × 95 mm mild steel ramming face was used for compaction.
(b) A wooden mold of 150 mm square section (inner dimension) with 1,500 mm height having 20 mm wall thickness was fabricated and fastened with nuts and bolts and further provided with a wooden base plate for fixing the mold in position.
(c) A 0.5 mm thick wall mild steel collar of 97 mm × 97 mm cross section having 300 mm height was used to facilitate the location of the rammer in the mold whenever required.

Table 1 Properties of soil used

Soil property	Percentage value
Grain size distribution	
Sand	79 %
Silt	13 %
Clay	8 %
Atterberg limits	
Liquid limit	31.7 %
Plastic limit	22.9 %
Plasticity index	8.8 %
Compaction characteristics	
(a) Soil	
Optimum moisture content	19 %
Maximum dry density (g/cc)	1.7
(b) Soil with 10 % cement	
Optimum moisture content	19.1 %
Maximum dry density (g/cc)	1.71

Compaction throughout the test program was carried out with the help of a compaction machine capable of compacting with a free fall of rammer height of 300 mm approximately.

3.3 Casting of Prism, Wallette and Column

Prior to production of test specimens the soil sample was sun-dried, ground and pass through 4.75 mm sieve. The soil was then dry mixed with 10 % cement (by mass of dry soil) before mixing with water. Optimum moisture content (OMC) was occasionally determined by Rapid Moisture Meter during the entire production run. The inner walls of the mold were covered with either thin polythene or sellotape to avoid adhesion of test specimen with the mold walls. The wetted mix was then poured into a mold and compacted with a rammer height of fall 300 mm into layers of 100–120 mm thick followed by making of 10–20 mm deep frog/dent on every compacted layer to enhance proper bonding between the successive layers. This process was continued until the desire height was achieved. To achieve the required density, compaction energy equivalent to standard Proctor value was adopted throughout the production run. The compaction energy or effort was determined using the formula given in ASTM: D698-12 [6] as follows:

$$E_c = \frac{\left(\begin{array}{c} No.\,of \\ layers \end{array}\right)\left(\begin{array}{c} No.\,of\,blows \\ /layer \end{array}\right)\left(\begin{array}{c} Weight\,of \\ rammer,\,\mathrm{kg} \end{array}\right)(Height\,of\,drop,\,\mathrm{cm})}{Volume\,of\,mould,\,\mathrm{cm}^3} \tag{1}$$

where, E_c = Compaction energy, kg cm/cm^3. Within 30–40 min after casting, the wooden formwork was removed and the test specimens were kept in air for 24 h prior to wet curing. After 28 days of curing under wet burlap/gunny cloths, the test specimens were dried in air inside the laboratory for 3–4 weeks prior to testing. At least three representative samples from three different locations of the failed specimen were collected immediately in a beaker to determine the moisture content at the time of testing.

3.4 Testing of Prism, Wallette and Column

Five specimens each of wallette and prism were used to determine the compressive strength and stress-strain behavior. A load controlled Universal Testing Machine of 400 kN capacity was used for testing and the load was applied at a uniform rate of 2.5 kN/min up to failure. The columns tests were comprised of three samples of three specimens, each 230 mm wide by 150 mm thick, with approximate heights of 900 mm (denoted R900), 1,200 mm (R1200), and 1,500 mm (R1500). The columns were placed in position as shown in Figs. 1 and 2. The vertical load was applied

using 500 kN capacity hydraulic jack and measured using a 250 kN load cell at the rate of 2.5 kN/min until failure. Lateral movement of each column was recorded using three digital dial gauges, one at the top, one in the middle, and one at the bottom of each column. Furthermore, digital dial gauge was attached on top of each column, to monitor the vertical movement under incremental increasing load. All the tests were monitored and recorded both manually and automatically through a digital data acquisition system at a load interval of 10 kN. As collapse was difficult to predict, some instrumentation was removed as a precaution before the ultimate load was reached.

Fig. 1 Column test setup
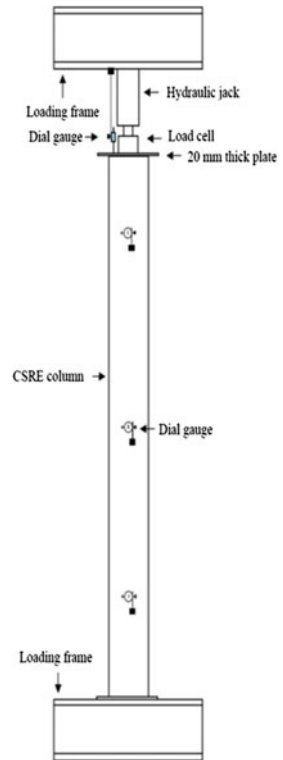
Fig. 2 Testing of column

4 Results and Discussions

4.1 Strength and Failure Pattern of Wallette

Test results of wallettes are summarized in Table 2. Wallettes failed by vertical cracking followed by shearing of the material along the full height of each specimen. Mostly failure originated from cracks propagating from mid-height of the specimens towards the top and bottom edges. Figure 3 shows the failure pattern of wallette.

4.2 Deflections and Failure Patterns of Columns

Lateral deflections of the columns occurred at various stages of loading, but this effect was not visible by eye. Maximum lateral deflections of columns were in the

Table 2 Summary of test results

Physical properties	Specimen details			
	Wallette	R900	R1200	R1500
Average compressive strength (MPa)	3.23	3.03	2.83	2.64
Standard deviation (MPa)	0.19	0.02	0.02	0.04
Average moisture content at test (%)	4.67	4.59	7.59	7.07
Standard deviation (%)	0.32	0.91	0.64	0.09
Height to thickness ratio (h/d)	2	6	8	10
Slenderness ratio (l/r)	4.5	13.5	18.1	22.6
Tangent modulus at a stress level of ultimate strength (MPa)	457	503	514	528
$\sigma_{critical}$ (MPa)[a]	97.7	11.5	6.6	4.3

[a] Critical buckling stress based on tangent modulus theory

Fig. 3 Failure of CSRE wallette

range of 2.5–3.5 mm for R1500, 1.5–2 mm for R1200 and 0.4–0.8 mm for R900 respectively (Fig. 4). These profiles were typical of the column responses up to the last available measurement, prior to removal of the measuring instruments.

The failures of R1500 columns were initiated by development of vertical cracking at about 350–500 mm distance from top toward mid-height followed by crushing failure. The crushing failure occurred at about 300–400 mm height from bottom and failed at the point nearer to maximum lateral deflections in some of the column. In R1200 columns shear crack developed at about 450 mm from top towards mid height followed by splitting at the load of about 70–80 kN, but in case of R900 columns splitting occurred at about 580 mm from the top towards mid
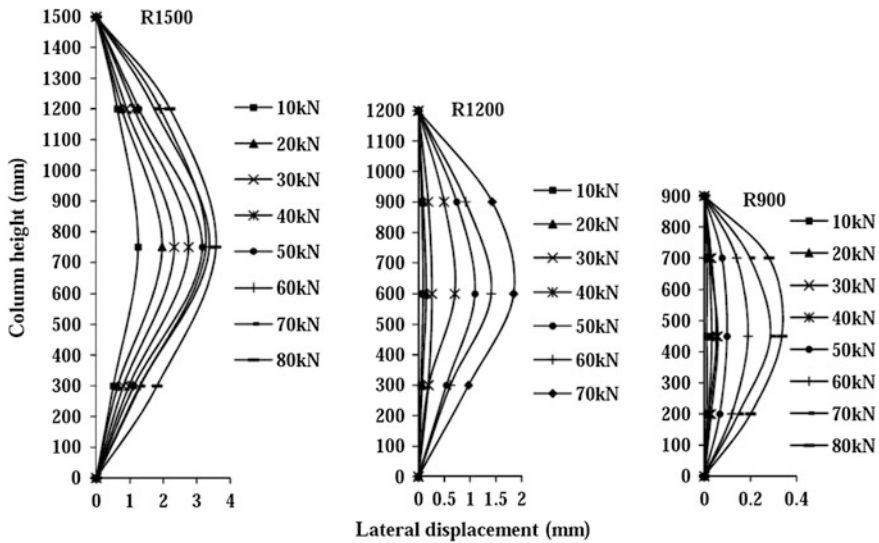
Fig. 4 Lateral deflections along the height of the column at various stages of loading

height in some of the columns at the load of about 80–85 kN. The columns did not show visible buckling and most of the columns failed by crushing once the material failure occurred. The crushing failures noticed in the column resemble the failure pattern of wallettes. Failure of columns occurred mostly at the joint of compacted layers, which is attributed to poor bond between the layers. Furthermore, the deflection patterns of columns were dominated by slenderness ratios, i.e., greater the slenderness ratio of column greater is the deflection.

4.3 Compressive Strength and Design of Column

Present study deals with three slenderness ratios (i.e., effective height to thickness ratios) of 6, 8 and 10 with zero eccentricity were investigated (Table 2). The maximum average compressive strength measuring 3.03 MPa was obtained for R900 (i.e., least slender), followed by 2.83 and 2.64 MPa for R1200 and R1500 columns respectively. As the slenderness ratio of the columns was increased from 6 to 10, the compressive strength declined by about 7–15 %.

It was observed that the ultimate load carrying capacity decreases with the increasing slenderness ratio. The stress reduction factor for a slenderness ratio of 8 and 10 are found to be 0.93 and 0.87 respectively. These values were determined by dividing the compressive strength of each column and the compressive strength of column having slenderness ratio 6. The strength of wallette is about 0.2–1.2 times greater than rectangular columns. The ultimate strength of the CSRE columns was also determined using tangent modulus theory as discussed by Bleich [18], Sahlin

[19] and Reddy and Kumar [13]. The buckling strength may be theoretically computed using the following formula:

$$\sigma_{cr} = \frac{P_{cr}}{A} = \frac{\pi^2 E}{(l/r)^2} \tag{2}$$

where, P_{cr} = buckling load (N); A = cross-sectional area of the wall (mm^2); E = tangent modulus at failure (N/mm^2); l/r = slenderness ratio; l = effective height of the column (mm); r = radius of gyration = $\sqrt{(I/A)}$ (mm); and I = moment of inertia (mm^4). Reddy and Kumar [13] stated that cube or cylinder strength may not be ideal to arrive at characteristic compressive strength for stabilized rammed earth. A square prism with a height to thickness ratio in the range of 2–6 may be an ideal candidate for determining the characteristic compressive strength of stabilized rammed earth. Hence, in order to attempt a semi-theoretical prediction based on elastic analysis, E was determined from the stress-strain curve of prism (Fig. 5) corresponding to ultimate strength. The tangent modulus and stress values corresponding to each column are outlined in Table 2.

The effect of slenderness ratio on the compressive strength of column is shown in Fig. 6. The experimental value and the value predicted by tangent modulus theory tend to converge with each other as the slenderness ratio increases beyond 12. The difference between experimental and theoretical values for lower

Fig. 5 Stress-strain relationship for the CSRE prism
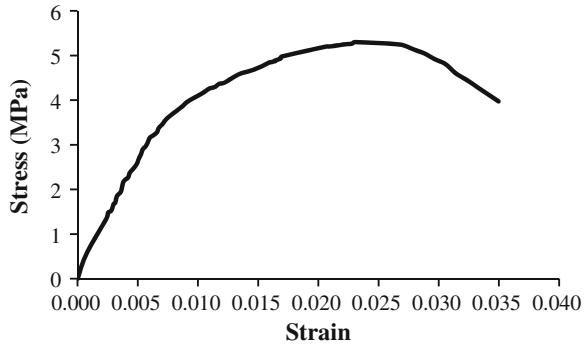
Fig. 6 Effect of slenderness ratio on compressive strength of column
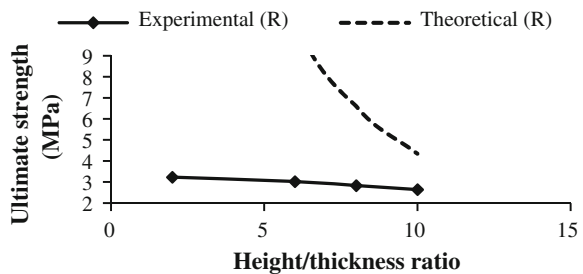
Table 3 Comparison of experimental and published capacity reduction factors

Column series	R900	R1200	R1500
Slenderness ratio	6	8	10
	Stress reduction factors		
Experimental	1	0.93	0.87
NZS: 4297-1998	1	0.94	0.88
IS: 1905-2002	1	0.95	0.89
SA: 2000	1	0.94	0.88
BS: 5628-1 [20]	1	1	0.97
Maniatidis and Walker [12]	1	1.41	1.24

slenderness ratio values can be attributed to the brittle nature of failure and the absence of buckling in short columns.

4.4 Comparison of Experimental and Published Results

The experimental capacity reduction factors under concentric loading derived from the experimental analysis are compared with published values for structural masonry as shown in Table 3. Stress reduction factor from the literature, which are based on reduction factors for masonry, are slightly different from the actual value obtained from the present investigation. Hence, it is important to consider the actual values of the CSRE columns while designing the rammed earth structural members.

5 Summary and Conclusions

From the results of rectangular column tests the following conclusions have been made:

(a) The stress reduction factors of rectangular columns compare quite favorably with published codal provisions. The minor difference between experimental and published results may be attributed to material properties i.e., rammed earth is a monolithic material and hence its behavior under compressive loads is different from that of masonry.
(b) The reduction in compressive strength and stiffness of columns is affected by the variation in slenderness ratio i.e., greater the slenderness ratio lesser is the strength.
(c) Due to limited study it is not possible to propose the use of stress reduction factors for designing of columns, until further research is carried out.

6 Scope for Further Research

There is a need for further investigations on CSRE columns in order to derive stress reduction factors useful for the design calculations. The important works need to be carried out are as follows:

(a) Stress reduction factors for higher slenderness ratio and eccentricities.
(b) Behavior of stabilized rammed-earth columns under lateral dynamic loads.
(c) Behavior of shear reinforced CSRE columns under static and dynamic loads.

References

1. NZS: 4297 (1998) Engineering design of earth buildings. New Zealand Standard, Wellington
2. NZS: 4298 (1998) Materials and workmanship for earth buildings. Standards New Zealand, Wellington
3. NZS: 4299 (1998) Earth buildings not requiring specific design. New Zealand Standard, Wellington
4. IS: 13827 (1998) Improving earthquake resistance of earthen buildings—guidelines. Bureau of Indian Standards, New Delhi
5. Standard Australia (2002) Australian earth building handbook. Australia, Sydney
6. ASTM: E2392/E2392M-10 (2010) Standard guide for design of earthen wall building systems. West Conshohocken, PA
7. SAZS: 724 (2001) Rammed earth structures. Standards Association of Zimbabwe, Zimbabwe
8. Middleton GF (1987) Earth wall construction, 4th edn. CSIRO Division of Building, Construction and Engineering, North Ryde [Revised by Schneider, L. M. (1992)]
9. Tibbets JM (2001) Emphasis on rammed earth—the rational. Interaméricas Adobe Builder 9:4–33
10. Minke G (2000) Earth construction handbook. The building material earth in modern architecture. WIT Press, Southampton
11. Walker P, Keable R, Martin J, Maniatidis V (2005) Rammed earth design and construction guidelines. BRE Press, Bracknell
12. Maniatidis V, Walker P (2008) Structural capacity of rammed earth in compression. J Mater Civ Eng 20(3):230–238
13. Reddy BVV, Kumar PP (2011) Structural behavior of story-high cement-stabilized rammed earth wall under compression. J Mater Civ Eng 23(3):240–247
14. IS: 2720 (1995) Specification for methods of test for soils-grain size analysis. Part IV. Bureau of Indian Standards, New Delhi
15. IS: 2720 (1995) Determination of liquid and plastic limit. Part V. Bureau of Indian Standards, New Delhi
16. IS: 2720 (2002) Determination of water content–dry density relation using light compaction. Part VII. Bureau of Indian Standards, New Delhi
17. IS: 8112 (1989) Specification for 43 grade ordinary Portland cement. Bureau of Indian Standards, New Delhi
18. Bleich F (1952) Buckling strength of metal structures. McGraw-Hill, New York
19. Sahlin S (1971) Structural masonry. Prentice Hall, Upper Saddle River
20. BS: 5628 (1992) Structural use of unreinforced masonry. Part I. British Standard

Interaction Study on Interlocking Masonry Wall Under Simultaneous In-Plane and Out-of-Plane Loading

M. Sudhakar, M.P. Raj and C. Natarajan

Abstract A masonry wall subjected to earthquake global acceleration field is subjected to both in-plane and out-of-plane loads. The interaction between these two types of forces in the geopolymer-based interlocking block mortarless wall is presented based on experimental results. The test results show that there is a considerable amount of interaction between in-plane and out-of-plane capacity of interlocking block walls.

Keywords Inter locking system · In-plane loads · Out-of-Plane loads · Capacity interaction · Geopolymer

1 Introduction

An interlocking block masonry wall undergoing earthquake global acceleration field is subjected to both in-plane and out-of-plane loads. The former results from the storey shear force under horizontal loading and the latter is either due to out-of-plane inertia force caused by the considerable mass of the block wall or out-of-plane action of a flexible floor on the wall [1].

The construction industry acknowledges the strong need to accelerate the masonry construction process, as the traditional method is labour intensive, and hence slower, due to the presence of a large number of mortar joints. The number of mortar joints can be reduced by increasing the size of masonry units. This can be done by replacing brick by blocks. The need for further acceleration of the construction led to the elimination of bedding mortar by the use of interlocking masonry system [2]. Interlocking block masonry system is not uniform in India. In this study Hydraform interlocking block units are used.

Cement production contributes to 7 % to the global carbon dioxide emission [3]. The need to reduce the global anthropogenic carbon dioxide encourages the

M. Sudhakar (✉) · M.P. Raj · C. Natarajan
National Institute of Technology (NIT), Tiruchirappalli, India
e-mail: sudhakar5566@gmail.com

researches to search for sustainable building materials. Geopolymer is an excellent alternative to cement.

The constituents of geopolymer binder are geopolymeric source materials (fly ash, metakaolin, rice husk ash etc.) and Alkaline activated liquids. The fly ash, bottom ash and GGBS were mixed in dry pan mixer. Alkaline liquid was prepared by mixing sodium hydroxide, sodium silicate using water. The primary course of reaction is dissolution, condensation, polymerization and growth. This leads to the formation of 3D structure similar to Zeolite and Feldspathoids [4]. This makes it completely different from C-S-H gel that is formed in Ordinary Portland Cement.

Lee [3] introduced homogenization technique to investigate the elastic-brittle behaviour of masonry panels subjected incremental lateral loading. The constitutive model is incorporated in a three dimensional finite element code. It has been verified and validated with experimental data on the response of a set of laterally loaded masonry panels.

Anand and Ramamurthy [2] studied the salient features of interlocking block masonry. Testing wall panels under axial compression, eccentric compression and flexural loading parallel and perpendicular to bed joints were carried out on dry stacked specimens. He found out that flexural capacity of interlocking block masonry normal to the bed joint is higher than that of parallel to the bed joint.

Jaafar et al. [5] developed a correlation between the individual blocks, prism, and basic wall panel for load bearing interlocking hollow mortarless blocks. Interlocking mechanism, crack pattern and failure mechanism of the interlocking masonry specimens are discussed in their work.

Mojsilovic [6] studied the strength of the masonry subjected to in-plane loading. He used the method of the theory of plasticity. He gave an extension to an existing failure criterion for in-plane loaded masonry without tensile strength. He proposed a simplified variation of uni-axial masonry strength as a function of the angle of inclination of the principal compressive stress relative to the head joints deviation and derived and proposed for practical applications.

Bansal [7] studied the strength characteristics of interlocking masonry. He conducted both field and laboratory experimental investigation. Results are compared with IS-1905-1987.

Najafgholipour et al. [8] studied the in-plane and out-of-plane capacity interaction in brick masonry wall. They proposed a conservative formula on the in-plane/out-of-plane interaction in brick walls. The test results are used to validate the representing numerical models of wall panels.

2 Materials Used

2.1 Fly Ash

Fly ash also known as fuel ash, is the residue formed after the combustion of materials like coal which are fine in size and are collected using electrostatic precipitators from flue gas. SiO_2, Al_2O_3, Fe_2O_3 and occasionally CaO are the main chemical components present in fly ashes.

2.2 GGBS

GGBS is the acronym for ground granulated blast furnace slag. Quenching of molten slag from blast furnace produces a glassy granular product, which is then grounded to obtain GGBS. It consists mainly of silicate and aluminate impurities from the ore.

2.3 Bottom Ash

Bottom ash is the ash remaining in the furnace/incinerator after coal is burned. It is the ash that remains after fly ash escapes up the chimney or attack. Bottom ash is hence coarser.

2.4 Alkaline Liquid

Alkaline liquid works as an activating medium for the reaction. This constituent of the geopolymer is the most costly and energy intensive. A solution of 6 M NaOH and silicate was used as activating agent in this study.

The mix design adopted in this study is derived from the previous literature [2] and is used for preparing blocks of dimensions 230 mm × 230 mm × 115 mm. The particular design adopted for testing is Hydra form block system.

3 Experimental Investigation and Results

In total, 11 wall panels of size 690 mm × 460 mm were constructed for finding the in-plane/out-of-plane interaction capacity. Three panels were tested for each in-plane, out-of-plane loading, while the other 5 panels were tested for simultaneous

in-plane/out-of-plane load. A reaction frame consisting of two wedges was designed for the application of in-plane load. For finding the interaction capacity, first a seating load of 50 kN was applied to give proper interlocking of the wall specimen. Load was applied till failure and ultimate in-plane capacity were found out.

In practice there are three out-of-plane bending conditions, two way bending, bending parallel to the bed joints and bending perpendicular to the bed joints [8]. Here, bending parallel to the bed joint was considered. The wall was allowed to bend only in the other direction. Using LVDTs lateral deflection was measured.

The wall panels were subjected to in-plane and out-of-plane loads were applied simultaneously. Different combination of out-of-plane load was applied, and for every combination of out-of-plane load ultimate in-plane load was found out. In total, five load combinations were tested, corresponding to out-of-plane loads of 10, 25, 50, 75, and 90 % of the ultimate flexural strength of the panel.

3.1 In-Plane Capacity of GPC Block Walls

Literature suggests that the most relevant in-plane shear failure mode is characterized by a diagonal crack generally perpendicular to the maximum tensile stress developed in the wall panel due to applied loads.

In-plane load was applied using the set-up given in Fig. 1. The mode of failure of all the three wall panels was characterized by sudden diagonal crack and the coefficient of variation in the ultimate strength was very small (8 %), indicating the performance and proper load transfer in the interlocking system. Table 1 gives the in-plane capacity of 3 wall panels tested.

Crack pattern is shown in the Fig. 2. Cracking in the direction of the applied load was observed, which was a diagonal crack in the thickness direction. Due to proper interlocking, cracks were propagated along the interlocking region, which shows the efficiency of the interlocking system.

Fig. 1 Set up for diagonal compression test

Table 1 Ultimate in-plane load

S. No.	Applied in-plane load (kN)
1	250
2	270
3	260

Fig. 2 Crack pattern due to diagonal compression test

3.2 Out-of-Plane Capacity of GPC Block Walls

Due to the experimental limitations in applying a complex non-uniformly distributed load, out-of-plane load for the experiments was considered to be a horizontally applied central point load.

Lateral load was applied using the arrangement shown in Fig. 3. Wall panel was constructed and held in position against the lateral load by two "I" sections as shown. Using plates and rods "I" sections are connected. Two sides of the wall are restrained to get bending parallel to the bed joints. Plywood panels were used to get a uniform load distribution as shown in the Fig. 4. Load was applied at the center of the specimen for out-of-plane testing. Incremental static lateral loading was applied at the rate of 2 kN per 5 min. The ultimate out-of-plane load capacities are presented in Table 2.

Average out-of-plane capacity was found to be 87 kN. Considerable lateral deflection was observed till the collapse of the specimen. This is due to proper interlocking between the individual block units. Using LVDTs lateral deflection was measured. Maximum deflection of 8 mm was obtained in the LVDT. Crack pattern in the specimen is shown in the Fig. 5.

Fig. 3 Out-of-plane testing on GPC wall

Fig. 4 Closer view of out-of-plane test set up

Table 2 Ultimate out-of-plane load capacity

S. No.	Ultimate out-of-plane load (kN)
1	90
2	85
3	87

Fig. 5 Crack pattern due to out-of-plane load

Fig. 6 Average lateral load-deflection curve
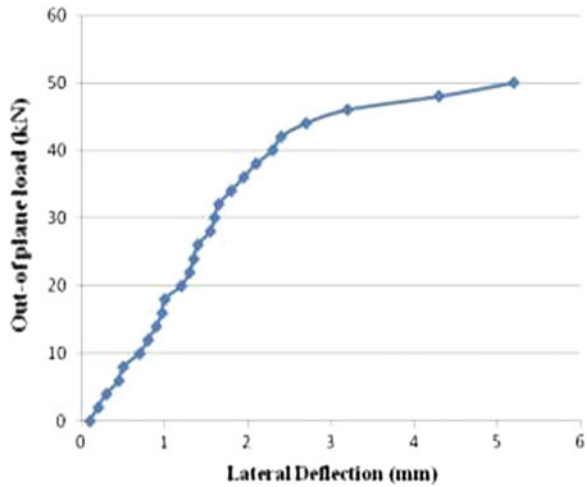
Figure 6 gives the average lateral load-deflection curve. Lateral deflection was found to be increasing up to a load level in which first crack was formed. After the formation of first crack, the middle block where load was applied was coming out due to the failure of interlocking system. It was observed that proper alignment of the blocks would increase the strength of the interlocking system.

3.3 Interaction Study on Capacity of GPC Block Wall

Load was applied as shown in the Fig. 7. As expected, the in-plane shear capacity of the panel decreases with an out-of-plane load increase.

Table 3 gives the in-plane capacity of the wall panels when out-of-plane load is applied. The failure mechanism of the wall panels under combined in-plane and out-of-plane loads is a combination of the in-plane diagonal shear and the out-of-plane bending failures discussed previously. The crack pattern of the panels subjected to low levels of out-of-plane loads follows a diagonal shape. With the increasing out-of-plane load, bending cracks accompany the diagonal shear cracks at failure.

The reduction in the in-plane shear strength of brick wall panels with the out-of-plane load is more profound when the out-of-plane load is closer to the out-of-plane capacity of the panel. To gain better insight into the in-plane shear and out-of-plane bending capacity interaction, the test results are plotted, in the normalized form, in Fig. 8. It is clear that, there is similarity between the experimental results and the theoretical interaction circle.

Fig. 7 Simultaneous in-plane/out-of-plane testing

Table 3 In-plane/out-of-plane capacity interaction

S. No.	Applied out-of-plane load (kN)	Ultimate in-plane load (kN)
1	8.7 (10 % of ultimate load)	252
2	21 (25 % of ultimate load)	247
3	43 (50 % of ultimate load)	208
4	65 (75 % of ultimate load)	140
5	78 (90 % of ultimate load)	59.8

Fig. 8 Normalized
interaction curve
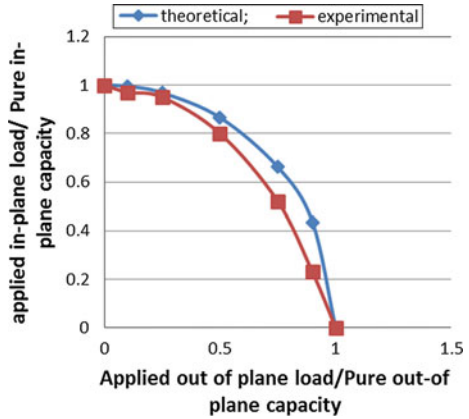
4 Conclusions

The major conclusions of the present study are as follows.

i. Noticeable interaction exists between the in-plane shear and out-of-plane bending capacities of interlocking block walls.

ii. The interaction is particularly strong when one of the load types is near the wall's corresponding ultimate capacity in any of the loading directions. It is therefore recommended that this capacity interaction is to be taken into consideration when designing, assessing vulnerability or retrofitting masonry buildings.

iii. Experimental work indicates that the test results are highly influenced by the proper interlocking of the individual block units. This indicates that the elimination of bedding mortar requires stringent dimensional tolerance for the blocks to ensure uniform load transfer between layers.

iv. Erection of interlocking wall requires less time compared to mortar masonry construction. Hence, mortarless construction technology can be adopted for accelerating the construction work. Also, skilled masons are not required in the interlocking masonry construction.

References

1. Lee JS, Pande GN, Middleton J, Kralj B (1996) Numerical modelling of block masonry subjected to lateral loading. Comput Struct 61:735–745
2. Anand KB, Ramamurthy K (2000) Development and performance evaluation of interlocking block masonry. J Archit Eng 6:45–51
3. Mathew BJ, Sudhakar M, Natarajan C (2013) Development of coal ash-GGBS based geopolymer bricks. Eur Int J Sci Technol 2:133–139

4. Purdon AO (1940) The action of alkalis on blast furnace slag. J Soc Chem Ind Trans Commun 59:191–202
5. Jaafar MS, Thanoon WA, Najm AMS, Abdulkadir MR, Ali AAA (2006) Strength correlation between individual block, prism and basic wall panel for load bearing interlocking hollow block masonry. Constr Build Mater 20:492–498
6. Mojsilovic N (2011) Strength of masonry subjected to in-plane loading: a contribution. Int J Solids Struct 48:865–873
7. Bansal D (2011) Masonry from stabilized earth blocks-sustainable and structurally viable option. Int J Earth Sci Eng 4:772–779
8. Najafgholipour MA, Maheri MR, Loorenco PB (2013) Capacity interaction in brick masonry under simultaneous in-plane and out-of plane loads. Constr Build Mater 38:619–626

Part XXVII
Bridge Structures

Effect of Overweight Trucks on Fatigue Damage of a Bridge

Vasvi Aggarwal and Lakshmy Parameswaran

Abstract Overweight trucks affect the fatigue life of a highway bridge. The stress range increases substantially if trucks are overloaded. Despite of existing regulation of permissible limits of Gross Vehicle Weight (GVW), overloading of trucks is widespread in India. Fatigue is a great concern to bridge engineers especially with the use of high strength steel and concrete for the construction of bridges. In this paper, the effect of overloading on fatigue damage of a highway bridge is studied. The aim of this study is to observe the relationship between prevalent truck overloading and fatigue damage accumulation. The fatigue damage accumulation is calculated for the steel longitudinal girder of a four span continuous steel-concrete composite girder bridge of length 119 m subjected to cyclic loading due to actually weighed overloaded trucks and trucks loaded with permissible GVW as specified in IRC guidelines. From the fatigue damage analysis it is found that the increase in truck weight of 50 % would lead to an increase in fatigue damage accumulation of 80 % in the steel longitudinal girder of road bridges. The relationship between fatigue damage accumulation and overload factor is non-linear. The findings of the study will be useful for fatigue design of bridges especially which are on port connectivity or near to mines and heavy industrial area, where overloading of trucks is prevalent.

Keywords Overloading · Fatigue damage accumulation · Permissible load limits

V. Aggarwal (✉) · L. Parameswaran
Bridges and Structures Division, Council for Scientific and Industrial Research–Central Road Research Institute (CSIR–CRRI), Mathura Road, New Delhi 110025, India
e-mail: vasvi.aggarwal@gmail.com

V. Aggarwal · L. Parameswaran
Academy of Scientific and Innovative Research, CSIR, New Delhi, India

1 Introduction

Road bridges in India are generally designed for load effects due to live loads specified in IRC 6, such as Class AA, Class 70R, Class A or combination of these loads depending on the carriage way width of the bridge. However, the liberalization and globalization of Indian economy has brought unprecedented industrial, trade and commercial developments in our country during the last one decade which in turn has led to many fold increase in road traffic in terms of volume and axle load. The Motor Vehicles Act and Regulations 1988, specifies the revised limit of axle loads, Gross Vehicle Weight (GVW) and new limits on the dimensions of the actual vehicles. However, with the increasing cost of petrol and diesel, the truck operators have a tendency to carry excess weight above the legal limits, and this has been verified by the number of axle load surveys conducted on national highway (NH), state highway (SH) and major district roads (MDR) by Council for scientific and industrial research–Central road research institute (CSIR–CRRI) during the last four decades.

There has been a persistent upward trend all over the world, in permissible vehicle and axle weights, which is the combined result of improvements in vehicle and tyre technology and of the urge of transporters to achieve higher payloads in order to reduce the unit cost of transportation.

The two popular methods to collect the Gross Vehicle Weight (GVW) of trucks plying on the road are Stationary Weigh Scales (SWS) and Weigh-in-Motion (WIM) system. Conventional SWS measurements have several draw backs, such as driver's awareness and traffic congestion during peak hours. On the other hand, the use of WIM system can result in more accurate truck loading, because it can overcome the inherent shortcomings with the use of SWS.

Weigh-in-motion studies conducted in USA indicated a considerable variation in truckload effects on bridges [1]. The occurrence of illegally overloaded vehicles makes these uncertainties especially worrisome. Therefore, in order to refine the uncertainties regarding loads and resistance, there is a need to gather information about the actual traffic effects [2]. By monitoring heavy trucks, the uncertainties regarding loads plying over the roads and bridges can be quantified. Traffic and axle load surveys can provide information regarding traffic volume, truckloads, load on multi-lanes and extreme loads which can be effectively used to control the truckload effects and can provide a basis for a much more efficient operation of highway facilities.

Bridges are critical elements in a road network for the safe and efficient movement of people and freight. Over loaded truck traffic affects the service life of the bridge superstructure. Damages typically occur in the main superstructure elements like bridge deck, girders, diaphragms, joints and bearings. With the rapid growth of highway transportation, the increasing frequency of the over loaded trucks even leads to fatigue damage. Therefore, as with increase in truck loads the damage on highway infrastructure increases and additional funds are required for maintenance and repair, rehabilitation of these bridges.

In this paper an attempt has been made to understand the trend in safe legal limits of axle loads and maximum GVW legally permitted on roads in India and other countries. Subsequently, the axle load data collected using WIM on NH-7 near Bangalore has been analyzed to understand the prevalent over loading in truck traffic. Also, fatigue damage estimation of a longitudinal girder of a four span continuous steel concrete bridge is presented for this observed actual truck traffic plying during a day.

2 Background

The GVW for commercial vehicles are specified by the vehicle manufactures keeping in view vehicle dynamics of operation and design. As a result certain limits for axle loads are stipulated by the government/competent authorities and are referred as 'Safe Axle Load Limits'. However, it is found through axle load surveys that the actual loads carried by trucks seldom follow these specified limits, and always tend to be on higher side. This practice of carrying loads in excess of legally defined loads by a vehicle is known as 'Overloading'.

Every country has specified legal axle load limits and maximum permissible gross load and Fig. 1 shows these specified in some of the countries.

It can be seen from Fig. 1 that the maximum permissible gross load is specified in South Africa, i.e., 56 tons while the maximum permissible gross load for India is 80 % of this load. The minimum permissible gross load is specified in USA, i.e., 36 tons. The maximum load specified for single axle in India, i.e. 10.2 tons is 97 % of the maximum value of single axle load specified for UK which is 10.5 tons
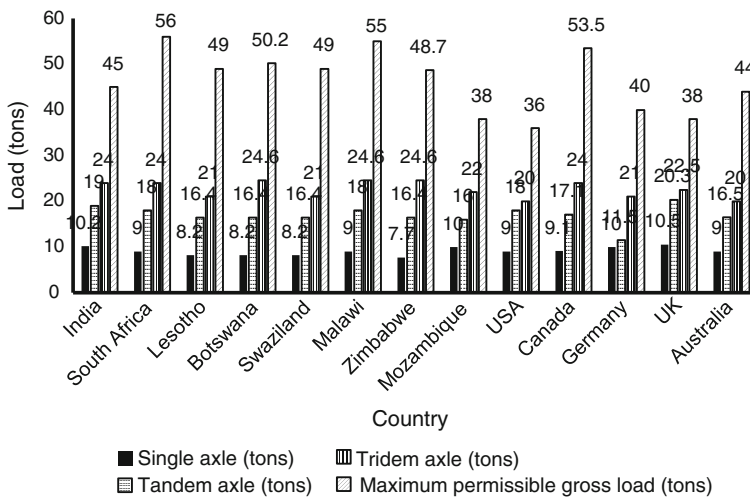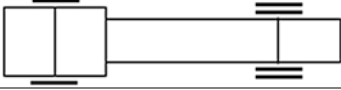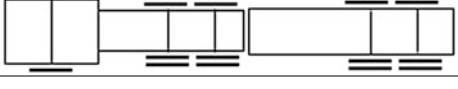
Fig. 1 Legal axle load limits in India and other countries

Table 1 Maximum permissible load for different types of trucks in India

Vehicle axle configuration	Vehicle type	Legal load limits (tons)
	Trucks—2 axle	16.2
	Truck—3 axle-semi trailer	25
	Truck—4 axle-trailer	35.2
	Truck—5 axle (both rear tandem)	45

However, the maximum load specified for tandem axle in India is 93 % of the maximum tandem axle load specified in UK. The maximum tandem axle load specified in India is 98 % of the maximum value specified in three countries, viz, Botswana, Malawi and Zimbabwe which is 24.6 tons.

In India IRC: SP: 37 [3] gives guidelines for evaluation of load carrying capacity of existing bridges based on working stress approach as the design of bridges are performed using allowable stress method. The maximum permissible load limits for different types of trucks or Heavy Commercial Vehicles (HCV) specified in IRC: SP: 37 [3] are given in Table 1.

3 Analysis of Truck Load Data Collected on National Highway (NH) 7

The main purpose of this study is to understand and study the extent of overloading and its effect on road bridges which further requires analysis truck axle load data. For the study purpose, the WIM (piezoelectric sensor type) system was installed on NH 7 at many locations by the CSIR. The WIM equipment in the test section consists of two sets of piezoelectric sensors (S1, S2) and (S3, S4) and two inductance loop detectors L1 and L2 in both the lanes. The installation of WIM system is shown in Fig. 2.

The loop detector installed on each lane at 4 m apart recognizes the presence of a heavy vehicle and then both the piezoelectric sensors weigh each wheel and the average is reported by the WIM system, which also counts the number of axles per vehicle.
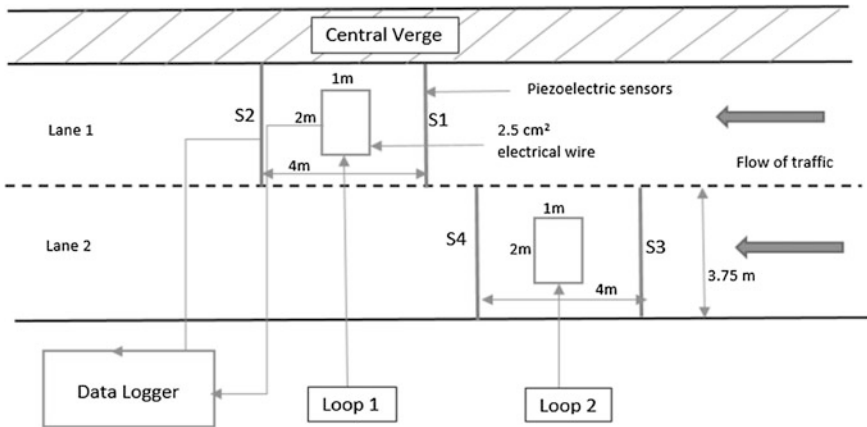
Fig. 2 Installation of WIM system

The truck load data considered for the study was collected on NH 7 during April 2013 near Bangalore and it consisted of 149 trucks collected during the period of 24 h. The average percentage of truck in overall traffic was 20 %. The truck load data collected using WIM was analyzed to estimate percentage distribution of truck by number of axles as shown in Fig. 3.

From Fig. 3 it can be seen that the 33 and 49 % of HCV consists of two and three axle trucks respectively. Also, it is to be noted that the trucks with more than three axles are less prevalent at the location of survey on this NH.

To study the extent of overloading, the percentage of number of trucks overloaded was studied and presented in Table 2 and it can also be seen that on an average 74 % trucks were overloaded.

Along with the high frequency of heavy trucks, over loading of trucks beyond permissible gross vehicle weight affects the bridge performance significantly. Therefore the overload factor was estimated and presented in Table 3.

Fig. 3 Truck percentage distributions by number of axles
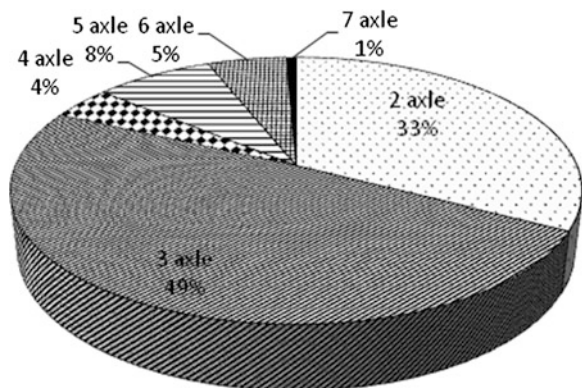
Table 2 Percent overloading in trucks studied on NH 7

Number of axle	Total number of trucks weighed	Number of overloaded trucks out of total trucks	Percentage of over-loaded trucks (%)
2	49	33	67
3	74	59	80
4	6	6	100
5	12	6	50
6	8	6	75
		Average percentage of over-loaded trucks	74

Table 3 Overload factor in trucks studied on NH 7

Number of axle	Safe GVW specified in IRC: SP: 37 [3]	Maximum GVW of trucks plying on NH 7	Overload factor
2	16.2	21.33	1.32
3	25	34.68	1.39
4	35.2	44.50	1.26
5	45.4	50.94	1.12
6	50.4	73.95	1.47
		Average overload factor	1.3

Thus the overload factor for trucks above safe GVW specified in IRC: SP: 37 [3] varies from 1.12 to 1.47. The average overload factor of GVW was found to be 1.3 times above the stipulated vehicle weight limit. Thus it is evident that overloading is prevalent in India and its effect on bridge needs to be studied.

4 Estimation of Fatigue Damage Accumulation

To study the effect of overloading on fatigue damage accumulation, a four span continuous steel-concrete bridge superstructure (21.25 m + 26 m + 42.25 m + 29.5 m) as shown in Figs. 4 and 5 was analyzed.
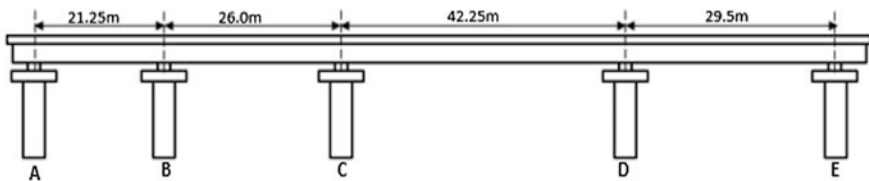
Fig. 4 Span arrangement of four span steel-concrete composite bridge
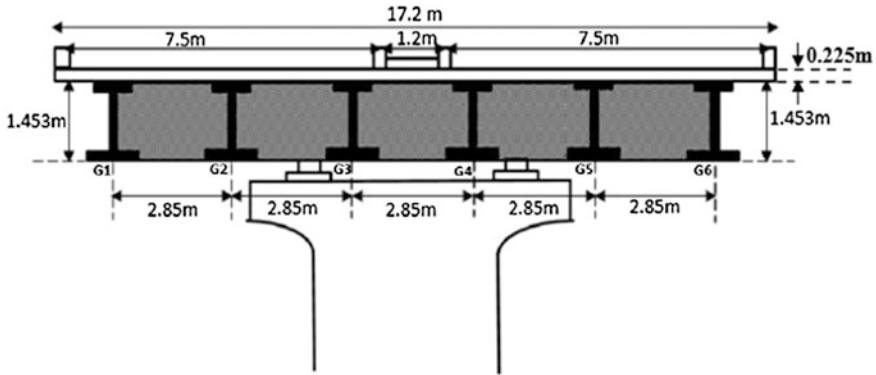
Fig. 5 Typical cross section of superstructure

The superstructure is supported on two POT/PTFE bearings spaced at 4 m apart. The grade of concrete used for deck slab is M40. The Fe 500 grade of reinforcement steel is used for the design of deck slab. The grades of structural steel used for steel plate girders and cross bracing are E350 and E250 respectively.

The road bridge considered was a two lane divided highway and the fatigue damage is calculated for the steel girder G2 (Fig. 5) at the centre of the bottom flange of third span CD (Fig. 4).

There are different approaches to analyze the fatigue damage of a bridge such as stress range concept, linear elastic fracture mechanics approach, continuum damage approach and advanced reliability approach. However, the stress range concept is widely used because of its simplicity and ease of application.

In this study, the methodology adopted to carry out fatigue damage analysis for road bridges is as follows: (1) Mathematical modeling of bridge superstructure, details shown in Figs. 4 and 5 is carried out. (2) Truck with permissible load limits and actual trucks plying on roads was applied as moving loads and stress history is generated. (3) Rainflow cycle counting method was used to decompose the stress history. (4) Stress histogram is prepared from decomposed stress history. (5) The fatigue damage accumulation was calculated using Miner's rule [4] which is given by Eq. 1.

$$D = \sum_i \frac{n_i}{N_i} \tag{1}$$

where, n_i = number of cycles applied at stress range S_i, N_i = total number of cycles to design limit/failure at stress range S_i. When D is greater than unity fatigue limit has been exceeded.

The fatigue damage is calculated due to the actually weighed 149 trucks including two axle, three axle, four axle, five axle and six axle trucks sampled using WIM and for the trucks with safe GVW as specified in IRC: SP: 37 [3] as shown in Table 1.

Table 4 Effect of overloading above permissible GVW of trucks on fatigue damage

Overload factor	Fatigue damage accumulation due to overloaded truck	Percent increase in fatigue damage accumulation (%)
1.05	7.0×10^{-7}	41
1.1	8.1×10^{-7}	49
1.15	9.2×10^{-7}	55
1.2	1.0×10^{-6}	60
1.25	1.2×10^{-6}	65
1.3	1.3×10^{-6}	69
1.35	1.48×10^{-6}	72
1.4	1.7×10^{-6}	75
1.45	1.83×10^{-6}	78
1.5	2.03×10^{-6}	80

The fatigue damage accumulation during a day produced by actually plying truck traffic with a composition as shown in Table 2 is 8.6×10^{-7}. The fatigue damage accumulation by replacing weight of all the overloaded trucks with safe load limits as specified in Table 3 is 4.1×10^{-7}. Thus it is seen that the overloading has increased the fatigue damage accumulation by 53 %.

A parametric study was also carried out to see the effect of overloading on fatigue damage accumulation produced by trucks beyond permissible load limit, by varying the overload factor from 1.05 to 1.5. The fatigue damage accumulation for overloaded truck is calculated by multiplying GVW with overload factors assumed for study and then generating corresponding stresses and calculating fatigue damage accumulation. Further, after multiplying each truck with overload factor the increase in fatigue damage was observed and is presented in Table 4.

From Table 4, it is seen that an increase in truck weight of 50 % would lead to an increase in fatigue damage accumulation of 80 % in the steel longitudinal girder of the road bridge included in the study.

By using the data presented in Table 4, relationship is developed between overload factor and percent increase in fatigue damage and is presented in Fig. 6.

Thus it is clear from this study that overloading of HCV exponentially increases the fatigue damage of the bridges.

Fig. 6 Relationship between overload factor and percent increase in fatigue damage
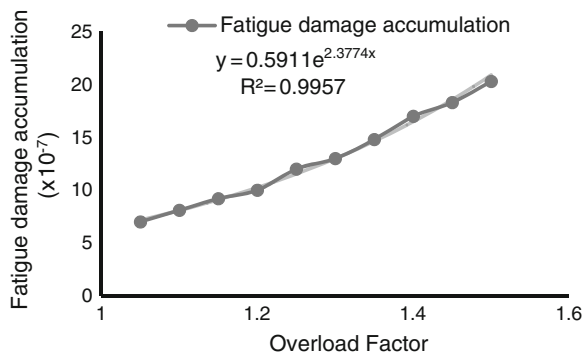
5 Conclusions

This study has highlighted the effect of overweight vehicles on the load effects produced on road bridges. Based on the study, the following conclusions are drawn.

1. Significant violation of permissible limit of gross vehicle weight of trucks involving overweight commercial vehicles is observed, 80 % of the observed three axle trucks were overloaded. The three axle trucks are more prevalent on NH 7.
2. The frequency and degree of overloading of HCV is very significant. The overload factors for two axle trucks, three axle trucks, four axle trucks, five axle trucks and six axle trucks is estimated as 1.32, 1.39, 1.26, 1.12 and 1.47, respectively.
3. The overloading enhances the fatigue damage produced by actually weighed trucks plying on NH 7 by 53 % in comparison to that by the trucks carrying permissible GVW.
4. An increase in truck weight of 50 % for all trucks in the observed traffic composition lead to an increase in fatigue damage accumulation of 80 % at the mid span of steel longitudinal girder of the bridge.
5. The relationship between overload factor and fatigue damage accumulation is exponential.
6. Monitoring of HCV using WIM system would be a right step towards enforcement of legal axle load limits on a road network.

References

1. Nowak AS, Nassif H, De Frain L (1994) Effect of truck loads on bridges. J Transp Eng ASCE 119(6):853–867
2. AASHTO (1994) LRFD bridge design specifications. American Association of State Highway and Transportation Official, Washington, D.C
3. IRC: SP: 37 (2010) Guidelines for evaluation of load carrying capacity of bridges. Indian Road Congress, New Delhi
4. Miner MA (1945) Cumulative damage in fatigue. J Appl Mech, Trans ASME 12(3):A159

Bending of FRP Bridge Deck Under the Combined Effect of Thermal and Vehicle Load

Bibekananda Mandal and Chaitali Ray

Abstract Fibre reinforced plastics (FRP) composite materials have been introduced in bridge engineering as it offers easy installation, lightweight and corrosion resistance. In the present investigation, FRP bridge deck has been modeled using the ANSYS 14.0 software package. A finite element computer code has also been developed for the analysis of the bridge deck. The deck has been formulated as a laminated composite plate stiffened with closely spaced laminated stiffeners having box configuration. The first order shear deformation theory has been applied. The box stiffener induces a considerable amount of torsional rigidity due to its closed attachment with the plate. Therefore, the torsional rigidity of the stiffener has been calculated by considering the stiffener cross section as a hollow box configuration. The bridge deck model has been developed as one plate at top and another plate at bottom with vertical blade stiffeners placed between the horizontal plates using ANSYS 14.0. The temperature gradient between the top and the bottom surfaces of the FRP bridge deck is developed due to low thermal conductivity of FRP materials and hollow section which gives rise to a very high thermal stress. The thermal load on the deck has been considered to be varying linearly through the depth of the deck. The combined effect of vehicle load and temperature gradient through the thickness on the bending behaviour of the FRP deck has been studied in the present analysis. The present formulation has been validated by comparing the obtained results with those available in the published literature.

Keywords ANSYS · FRP · Isoparametric · Thermal load · Vehicle load

B. Mandal (✉)
Department of Civil Engineering, Indian Institute of Technology Roorkee,
Roorkee 247667, Uttarakhand, India
e-mail: bibekdce@iitr.ac.in

C. Ray
Department of Civil Engineering, Bengal Engineering and Science University,
Shibpur, Howrah 711103, India
e-mail: chaitali@civil.becs.ac.in

1 Introduction

The combination of high specific strength and stiffness of laminated composites enables designers to develop innovative designs at lower weight and thickness. Composites have also attractive properties like better weather resistance, low thermal conductivity, low coefficient of thermal expansion, ability to be moulded into various shapes. The composite structures have already been established in ship and aerospace structures. Composite materials are gaining acceptance from civil engineers in the past few decades. FRP decks are appropriate in today's infrastructure market having a critical requirement for light weight to meet the design and operational objectives like benefits of corrosion resistance and longer life cycle.

The analysis and design of a FRP bridge deck is very much complex compared to the bridges with conventional constructional material. Researchers from many institutes and organizations are actively involved to understand the behavior of laminated composite structures under different loading conditions. Thangaratnam et al. [13] carried out thermal bending analysis of unstiffened laminated plates under thermal loading considering temperature gradient across the thickness of the laminates. They also considered material degradation of composite laminates due to the increment of temperature. Huang and Tauchert [6] investigated thermally-induced large-deflection behavior of laminates, including flat plates and cylindrical and doubly-curved panels. The finite element technique based on the first-order shear deformation theory was employed to predict the shell response. Fares et al. [3] studied the effect of the geometric non-linearity on the thermal response of the laminate, using a refined equivalent single-layer thermal model of geometrically nonlinear composite laminates. Laosiriphong et al. [8] carried out theoretical and experimental investigations of a GFRP bridge deck under temperature gradient. The temperature gradient through the depth of deck was assumed to be linear. However, the temperature gradient is nonlinear in hollow decks; nonlinear modeling was not used because of complexities in modeling.

Hayes et al. [5] experimentally measured the deflections and longitudinal strains of a composite bridge deck system assembled from glass/polyester pultruded components. For proper mechanical analysis of bridge deck, analysis under patch loading at different critical locations is required. Qiao et al. [9] presented the bending analysis under patch load on FRP bridge deck. Keller and Schollmayer [7] investigated the bi-directional plate bending behavior of a pultruded GFRP bridge deck system with orthotropic material and system properties by means of two full-scale experiments and numerical modeling. Wan et al. [14] studied the structural behavior of a bridge which had a GFRP composite deck on steel girders and conducted parametric studies to investigate the effects of diaphragms, girder stiffness, girder spacing and composite action on the characteristics of the system. Alagusundaramoorthy et al. [1] evaluated the force-deformation responses of FRP composite bridge deck panels under truck wheel load.

Research works available on the analysis of FRP bridge deck under combined effect of thermal and vehicle load [2, 12] are very limited in number. The combined

effect of thermal and vehicle load has been studied in this present investigation. Finite element package ANSYS have been used for the analysis purpose.

2 Finite Element Formulation

In this present study, a FRP bridge deck has been modeled using the ANSYS and a finite element computer code has also been developed for the thermo-mechanical analysis of the bridge deck.

2.1 Finite Element Formulation Using ANSYS

The finite element formulation of the FRP bridge deck has been carried out using the FE software package ANSYS 14.0. *SHELL281* element with six degrees of freedom per node (viz. translations in the x, y, and z axes, and rotations about the x, y, and z axes) as shown in Fig. 1 has been chosen for the present formulation. The finite element model of the bridge deck has been developed as one plate at top and another plate at bottom with vertical blade stiffeners placed between the horizontal plates as shown in Fig. 2.

2.2 Present Finite Element Formulation

The finite element formulation of FRP bridge deck has been carried out using two types of elements. The plate has been modeled as an eight node isoparametric plate bending element with five degrees of freedom per node viz. translations (u, v, w) and rotations (θ_x and θ_y). The first order shear deformation theory has been applied. The

Fig. 1 Description of the two dimensional shell element *SHELL281* element used for modeling the bridge deck
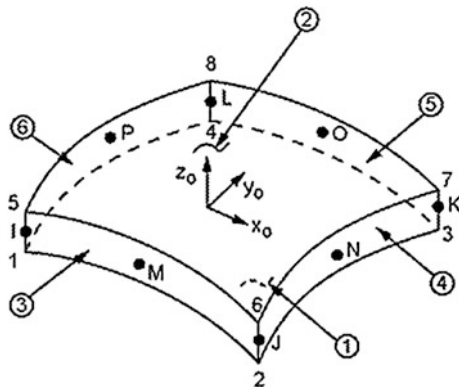
Fig. 2 Finite element model
of the FRP deck panel
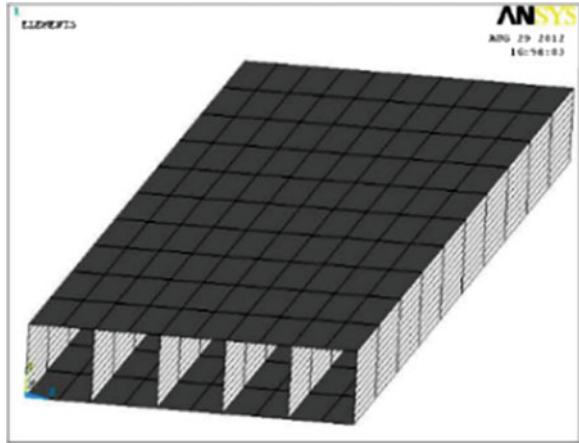
stiffeners have been modeled as three node beam elements with same number of
degrees of freedom per node as in the plate element.

2.2.1 Formulation of Plate Element

The displacements at any point within the plate element can be expressed in terms
of the nodal displacements as:

$$\{ u \quad v \quad w \quad \theta_x \quad \theta_y \}^T = \sum_{r=1}^{8} [N_r][I_5]\{ u_r \quad v_r \quad w_r \quad \theta_{xr} \quad \theta_{yr} \}^T \qquad (1)$$

The formulation of the plate element and the procedure of the linear static
analysis follows the standard finite element formulation and obtained in Ray and
Satsangi [10].

2.2.2 Formulation of Stiffener Element

The stiffener cross section has been considered as a box section with equal top and
bottom width of the section. The stiffness matrix of three node beam element is
calculated as (description available in Ray and Satsangi [10]):

$$[K_h] = \int_{x'} [T]^T[\Lambda]^T[B_h]^T[D_h][B_h][\Lambda][T]dx' \qquad (2)$$

2.2.3 Torsional Rigidity of the Hat Stiffener

The hat stiffener induces a considerable amount of torsional rigidity (J_h) due to its closed attachment with the plate. To compute the torsional rigidity of the hat stiffener accurately, the hat stiffener is considered as a hollow section. J_h has been calculated as: (J_h of the section with outer profile of the hat stiffener—J_h of the inner profile of the hat stiffener). The formula for calculating J_h of a general elliptical section [11] is given by:

$$J = \frac{A_h^4}{4\pi^2 I_{p'}}$$

(3)

where A_h is the area and $I_{p'}$ is the polar moment of inertia of the section.

3 Numerical Results

A number of FRP deck panels have been analyzed in the present investigation under thermal as well as transverse static loading.

3.1 Analysis of a Cross-Ply Laminate Subjected to a Linear Temperature Gradient Across the Thickness

A simply supported symmetric cross-ply laminate (0°/90°/90°/0°) of size 100 mm × 100 mm and thickness 1 mm made of Boron/Epoxy subjected to a linear thermal gradient (0–300 °F) across the thickness with uniform temperature over the surface has been analysed here, case (i) considering constant material properties with respect to temperature and case (ii) considering the effect of variation of material properties with varying temperature. Material properties used for this analysis has been taken from Hahn and Pagano [4]. For case (i), material properties at 80.6 °F (27 °C) and for case (ii), material properties at temperature 0, 80.6, 150, 200 and 300 °F (−17.778, 27, 65.556, 93.333 and 148.89 °C) have been considered. The laminate has been modeled using 20 node layered SOLID186. A 12 × 12 mesh division has been generated. The central (maximum) deflection of the laminate obtained in the present formulation along with the comparison with Thangaratnam et al. [13] has been presented in Table 1.

Table 1 Central deflection of composite plates with symmetric cross ply laminate

	Using constant material property	Using temperature dependent material property
Thangaratnam et al. [13]	1.308	1.346
Present ANSYS	1.319	1.349
Present FEM	1.290	1.355

3.2 Analysis of a FRP Bridge Deck Under Patch Loading

A 5′ × 9′ × 8″ (1,524 mm × 2,743.2 mm × 203.2 mm) FRP bridge deck consisting of 4″ × 8″ × 1/4″ (101.6 mm × 203.2 mm × 6.35 mm) FRP box sections as shown in Fig. 3 has been analysed under patch loading.

Total load applied on the deck is considered to be 1 kips i.e. 4.4463 kN through a plate of dimension 20″ × 10″ (508 mm × 254 mm) placed at the center of the deck. The material properties for this analysis have been taken from Qiao et al. [9]. Two edges of the deck are simply supported and other two edges are free. The results in terms of maximum deflection obtained by using ANSYSand present FE formulation have been presented in Table 2. The comparison shows a very good agreement.
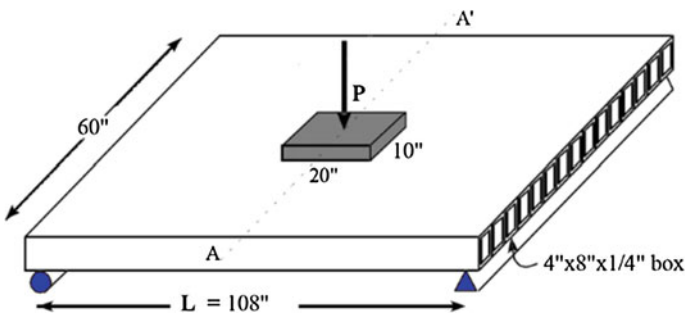
Fig. 3 Bridge deck geometry showing the location and dimensions of the patch load

Table 2 Maximum deflection (in/kips) of the FRP deck from the finite element analysis

Qiao et al. [9]		Present results	
FEM	Experiment	ANSYS	Present FEM
0.0164 (0.418 mm)	0.0204 (0.517 mm)	0.0185 (0.470 mm)	0.0190 (0.483 mm)

3.3 Analysis of a FRP Deck Panel Subjected to a Linear Temperature Gradient and Vehicle Load

A 4,000 mm × 1,000 mm × 250 mm FRP bridge deck panel as depicted in Fig. 4 consisting of E-Glass/Epoxy symmetric cross-ply laminate of thickness 25 mm has been studied here. The deck panel cross section consists of two plates, one at top and another at bottom with vertical blade stiffeners between two plates spaced 200 mm c/ c. E-Glass/Epoxy material has been used for the whole deck panel considering linear orthotropic material properties. Material properties of E-Glass/Epoxy have been taken as $E_1 = 41 \times 10^3$ MPa, $E_2 = E_3 = 12 \times 10^3$ MPa, $v_{12} = v_{13} = 0.28$, $v_{23} = 0.5$, $G_{12} = G_{13} = 5.5 \times 10^3$ MPa, $G_{23} = 3.5 \times 10^3$ MPa, $\alpha_1 = 7.1 \times 10^{-6}/°C$, $\alpha_2 = 20 \times 10^{-6}/$ °C. Symmetric cross-ply lamination scheme (0°/90°/90°/0°) has been considered for all the deck plates. The shorter edges of the deck are simply supported and the other two edges are free. Eight node shell element *SHELL281* has been used for the finite element modeling of the bridge deck panel.

A linear temperature gradient of 100 °F across the depth with temperature variation 0–100 °F has been considered for the thermal analysis. Three type of temperature distributions have been considered: case (i) A constant temperature on top surface only, case (ii) A linear temperature gradient of 100 °F across depth, 0 °F at bottom and 100 °F at top surface and case (iii) A linear temperature gradient of 100 °F across depth, minimum at top and maximum at bottom.

For the vehicle load, in accordance with IRC: 6-2000, class 'B' wheeled vehicle of axle load 6.8 t has been chosen for the analysis. The ground contact area of the wheels considered as 200 mm × 400 mm at centre to centre distance 1.8 m. The analysis has been carried out considering two load positions: case (1) Vehicle load placed symmetrically at centre of deck panel and case (2) Vehicle load at the edge of deck panel as shown in Fig. 4. Uniformly distributed load of (6.8 × 1,000 × 9.8067)/ (2 × 200 × 400) N/mm² = 0.4168 N/mm² has been applied on the ground contact area of the wheels.
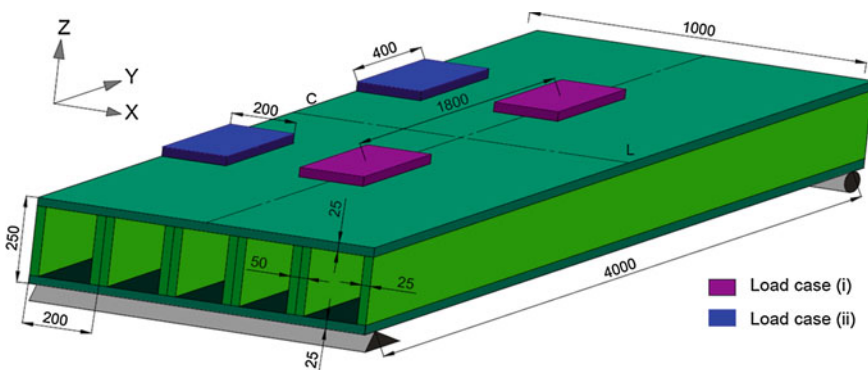
Fig. 4 FRP bridge deck panel geometry with vehicle load positions

Table 3 Maximum deflections due to temperature increment of the FRP bridge deck

Type of loading	Maximum deflections (in mm)	
	Present ANSYS	Present FEM
Case (i) a constant temperature (100 °F) on top surface only	3.836	3.663
Case (ii) a linear temperature gradient across the depth, 0 °F at bottom and 100 °F at top surface	5.173	5.093
Case (iii) a linear temperature gradient across the depth, 0 °F at top and 100 °F at bottom surface	−5.099	−5.086

Table 4 Maximum deflections (in mm) of the E-Glass/Epoxy FRP bridge deck due to vehicle loads

Type of loading	Maximum deflection (mm)	
	Present ANSYS	Present FEM
Case (1) vehicle load placed symmetrically at center of the deck panel	−2.993	−2.965
Case (2) vehicle load placed at the edge of the deck panel	−4.105	3.591

100 mm × 100 mm mesh size has been considered for the analysis. The maximum deflections from thermal analysis of the bridge deck panel for different load cases have been shown in Table 3. Table 4 represents the maximum deflections of the bridge deck panel due to vehicle load for different load cases.

Here, the negative deflections stand for downward deflection of the deck and the positive deflections stands for upward deflection of the bridge deck panel. The deflected shapes of the deck panel due to thermal load and due to vehicle load have been shown in Figs. 5 and 6 respectively.
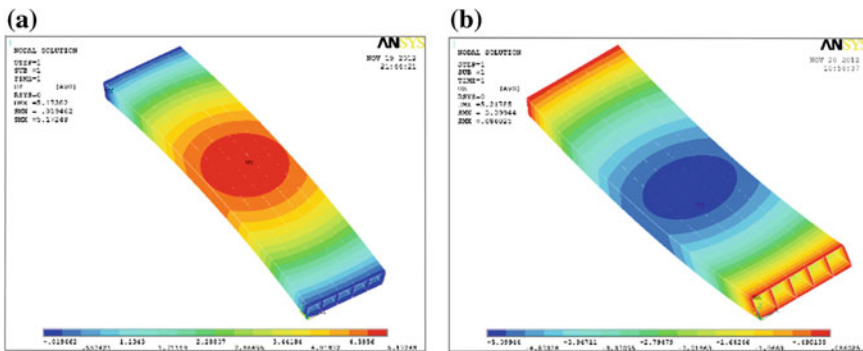
Fig. 5 Deflected shape of the FRP bridge deck panel subjected to only thermal load for **a** Case (i) and (ii), **b** Case (iii)
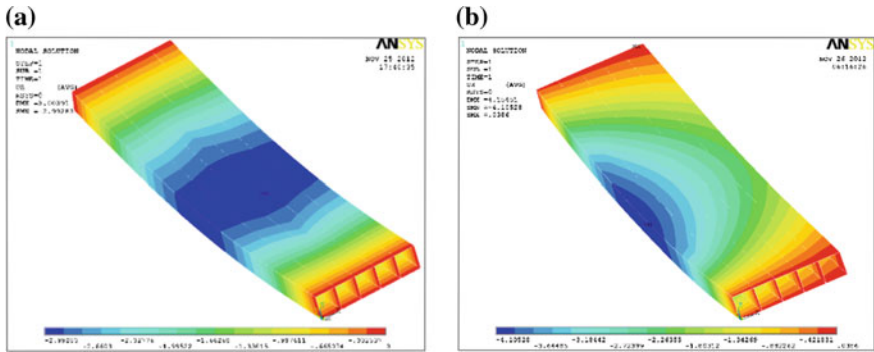
Fig. 6 Deflected shape of the FRP bridge deck panel subjected to only vehicle load for **a** case (i), **b** case (ii)

The maximum deflections from the combined effect of thermal load with vehicle load have been analyzed. Table 5 represents the maximum deflections of the bridge deck panel due to different thermal load cases along with case (1) vehicle load. The maximum deflections of the bridge deck panel due to different thermal load cases along with case (2) vehicle load have been presented in Table 6.

Deflection contours of the bridge deck panel due to temperature gradient combined with vehicle loads have been shown in Figs. 7 and 8.

Table 5 Maximum deflections (in mm) of the E-Glass/Epoxy FRP bridge deck panel due to different thermal load cases along with case (1) vehicle load

Type of loading	Maximum deflections (in mm)
A constant temperature (100 °F) on top surface only with case (1) vehicle load	0.844
A linear temperature gradient 0 °F at bottom and 100 °F at top surface with case (1) vehicle load	2.180
A linear temperature gradient 0 °F at top and 100 °F at bottom surface with case (1) vehicle load	−8.092

Table 6 Maximum deflections (in mm) of the E-Glass/Epoxy FRP bridge deck panel due to different thermal load cases along with case (2) vehicle load

Type of loading	Maximum deflections (in mm)
A constant temperature (100 °F) on top surface only with case (2) vehicle load	1.562
A linear temperature gradient 0 °F at bottom and 100 °C at top surface with case (2) vehicle load	2.917
A linear temperature gradient 0 °F at top and 100 °F at bottom surface with case (2) vehicle load	−8.902
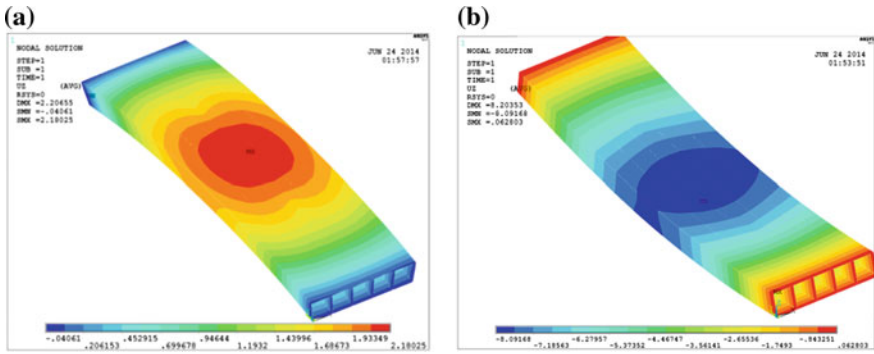
Fig. 7 Deflection contour of the bridge deck panel due to: case (1) vehicle load combined with **a** linear temperature gradient 0 °F at *top* and 100 °F at *bottom* surface, **a** linear temperature gradient 0 °F at *bottom* and 100 °F at *top* surface
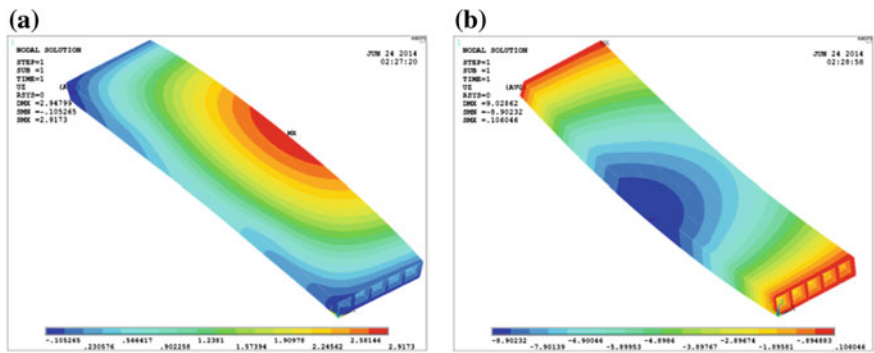
Fig. 8 Deflection contour of the bridge deck panel due to: case (2) vehicle load combined with **a** linear temperature gradient 0 °F at *top* and 100 °F at *bottom* surface, **a** linear temperature gradient 0 °F at *bottom* and 100 °F at *top* surface

4 Conclusions

The maximum deflection of FRPbridge deck has been calculated for different cases considering transverse patch load as well as thermal load. The most critical situation has been found due to most eccentrically placed patch load combination with a temperature gradient maximum at deck bottom. The combination of thermal and mechanical load produces less bending of the deck for a temperature gradient having maximum temperature at top surface of the deck. The temperature gradient between top and bottom surfaces of the deck occurs due to low thermal conductivity of fibre reinforced laminated composites. The present study reveals that effect of temperature gradient in the structural behaviour of FRP bridge deck is significant.

References

1. Alagusundaramoorthy P, Harik IE, Choo CC (2006) Structural behavior of FRP composite bridge deck panels. J Bridge Eng 11:384–393
2. Alnahhal WI, Chiewanichakorn M, Aref AJ, Alampalli S (2006) Temporal thermal behavior and damage simulations of FRP deck. J Bridge Eng 11:452–464
3. Fares ME, Zenkour AM, El-Marghany MK (2000) Non-linear thermal effects on the bending response of cross-ply laminated plates using refined first-order theory. Compos Struct 49:257–267
4. Hahn HT, Pagano NJ (1975) Curing stresses in composite laminates. J Compos Mater 9:91–106
5. Hayes MD, Ohanehi D, Lesko JJ, Cousins TE (2000) Performance of tube and plate fiberglass composite bridge deck. J Compos Constr 4:48–55
6. Huang NN, Tauchert TR (1991) Large deflections of laminated cylindrical and doubly-curved panels under thermal loading. Comput Struct 41:303–312
7. Keller T, Schollmayer M (2004) Plate bending behavior of a pultruded GFRP bridge deck system. Compos Struct 64:285–295
8. Laosiriphong K, Gangarao HVS, Prachasaree W, Shekar V (2006) Theoretical and experimental analysis of GFRP bridge deck under temperature gradient. J Bridge Eng 11:507–512
9. Qiao P, Davalos JF, Brown B (2000) A systematic analysis and design approach for single-span FRP deck/stringer bridges. Compos Part B Eng 31:593–609
10. Ray C, Satsangi SK (1996) Finite element analysis of laminated hat stiffened plates. J Reinf Plast Compos 15:1174–1193
11. Roark RK, Young WC (1975) Formulas for stress and strain, 5th edn. McGraw Hill, New York
12. Song W, Ma ZJ, Asce F (2011) Behavior of honeycomb FRP sandwich structure under combined effects of service load and low temperatures. J Compos Constr 400:985–991
13. Thangaratnam RK, Palaninathan R, Ramachandran J (1988) Thermal stress analysis of laminated composite plates and shells. Comput Struct 30:1403–1411
14. Wan B, Rizos DC, Petrou MF, Harries KA (2005) Computer simulations and parametric studies of GFRP bridge deck systems. Compos Struct 69:103–115

Low Cycle Fatigue Effects in Integral Bridge Steel H-Piles Under Earthquake Induced Strain Reversals

M. Dicleli and S. Erhan

Abstract Under the effect of medium and large intensity ground motions, the seismically-induced lateral cyclic displacements and ensuing bending strains in steel H-piles of integral bridges (IBs) could be considerable. As a result, the piles may experience cyclic plastic deformations following a major earthquake. This may result in the reduction of their service life due to low-cycle fatigue effects. Accordingly, low cycle fatigue in integral bridge piles is investigated under seismic effects in this study. For this purpose, an IB with two spans are considered. Three dimensional nonlinear structural models of this IB including dynamic soil-bridge interaction effects are built. Then, time history analyses of the IB models are conducted using a set of ground motions with various intensities representing small, medium and large intensity earthquakes. In the analyses, the effect of various properties such as soil stiffness, pile size and orientation are considered. The magnitude of cyclic displacements of steel H-piles are then determined from the analyses results. In addition, using the existing data from experimental tests of steel H-piles, a fatigue damage model is formulated. This fatigue damage model is used together with the cyclic displacement obtained from seismic analyses to determine the remaining service life of IBs under cyclic displacement due to thermal effects. The fatigue analyses results reveal that earthquakes with large intensity may reduce the service life of the piles with non-compact sections.

M. Dicleli (✉)
Department of Engineering Sciences, Middle East Technical University, Ankara, Turkey
e-mail: mdicleli@metu.edu.tr

S. Erhan
Department of Civil Engineering, University of Bahrain, Isa Town, Turkey

1 Introduction

An integral bridges is one in which the continuous superstructure, the abutments and the single row of flexible piles supporting the abutments are built monolithically to form a rigid frame structure. The most common types of piles used at the abutments are steel H-piles. Under the effect of medium and large intensity ground motions, the seismically-induced lateral cyclic displacements in steel H-piles of integral bridges (IBs) could be considerable. As a result, the piles may experience cyclic plastic deformations following a major earthquake. This may result in the reduction of their service life due to low-cycle fatigue effects. Accordingly, low cycle fatigue in integral bridge piles is investigated under seismic effects in this study. For this purpose, IBs with two spans are considered. Three dimensional (3-D) nonlinear structural models of these IBs including dynamic soil-bridge interaction effects are built. Then, the time history analyses of the IB models are conducted using a set of ground motions with various intensities representing small, medium and large intensity earthquakes. In the analyses, the effect of various properties such as soil stiffness, pile size is considered. The magnitude of cyclic displacements of steel H-piles are then determined from the analyses results. Then, a fatigue damage model is used together with the cyclic displacement obtained from seismic analyses to determine the remaining service life of IB piles.

2 Properties of Integral Bridge

Two spans IB are considered to investigate the low cycle fatigue in integral bridge piles under seismic effects. The total length of the bridge is 82 m and the width is 16 m. The bridge has two spans with the lengths of 41 m. The bridge has slab-on-prestressed concrete girder deck. There are seven AASHTO type VI girders supporting a 225 mm thick reinforced concrete slab and are spaced at 2,380 mm. A 75 mm thick asphalt pavement is provided on the deck surface. The bridge pier is composed of three reinforced concrete columns supporting a cap beam.

3 Parameters Considered in this Study

A parametric study is conducted to investigate the effects of the pile size and foundation soil properties on the low cycle fatigue of steel H-piles commonly used in the construction of IBs. Accordingly, two different pile sizes, HP 310 × 174 mm and HP 250 × 85 mm are assumed in the parametric study. Furthermore, the pilesare assumed to be made of ASTM A36 steel, commonly used as steel H-piles. Orientation of the piles for bending about their strong axes is assumed. The foundation soil is assumed to be sand. Two different sand stiffness values (medium and dense) are also included in the study.

4 Structural Model of Integral Bridge

The bridge superstructure is modelled using 3-D beam elements. The superstructure is divided into a number of segments and its mass (23.36 tons/m) is lumped at each nodal point connecting the segments. The in-plane translational stiffness of the deck is relatively much higher than that of the other members of the bridge. Accordingly, at the abutment and pier locations, the bridge deck is modelled as a transverse rigid bar of length equal to the center-to-center distance between the two exterior girders supporting the deck slab. The transverse rigid bar is used to simulate the interaction between the axial deformation of the columns and torsional rotation of the bridge deck as well as the interaction between the in-plane rotations of the deck and displacements of the bearings.

The cap beam and the columns are modelled as 3-D beam elements. The parts of the beam elements within the joint connecting the cap beam to the columns are modelled as rigid elements. The tributary masses of the cap beam and the columns are lumped at the joints connecting them. The reinforced concrete piles are modelled using 3-D beam elements as well. The nonlinear structural behavior of the columns and piles is modelled using link elements with Takeda's hysteretic model.

The steel H-piles are modelled as 3-D beam elements and nonlinear link elements are used to represent interaction between the piles and the surrounding soil. The lateral soil resistance deflection (p-y) relationship for sand is defined at any specific depth H, by the following equation [2].

$$P = A \cdot P_u \cdot \tanh\left[\frac{k \cdot H}{A \cdot P_u} \cdot y\right] \qquad (1)$$

where; A is a factor to account for cyclic or static loading condition and assumed as 0.9 for cyclic loading, P_u is ultimate bearing capacity of foundation soil at the depth H, (kN/m) and k is initial subgrade reaction modulus (kN/m^3) and may be obtained as a function of angle of inertial friction (φ) from a table given in API design code [2]. To simulate radiation damping, dashpots are placed at the nodal points along the pile. The radiation damping coefficient (c) for these dashpots is obtained from the following equation [1].

$$c = A_a \cdot \rho \cdot Vs \qquad (2)$$

where, A_a is the tributary area between the nodal points along the pile, ρ is mass density of the soil and V_s is the shear wave velocity.

Nonlinear link elements are used to simulate abutment-backfill interaction in the structural model. The force deformation relationship of these link elements is obtained using hyperbolic p-y curves proposed by Duncan and Mokwa [4] for nonlinear abutment backfill modelling under seismic loadings as follows;

$$P = \frac{y}{\frac{1}{K_{\max}} + R_f \frac{y}{P_{ult}}} \tag{3}$$

where, P is the passive resistance of backfill, P_{ult} is the ultimate passive resistance, y is the backfill deformation, $K_{\max}$ is the initial slope of the load-deformation curve and R_f is defined as follows;

$$R_f = 1 - \frac{P_{ult}}{K_{\max} \cdot y_{\max}} \tag{4}$$

Duncan and Mokwa [4] have used a value of $R_f = 0.85$ for hyperbolic load-deflection curves. Accordingly, in this study, a value of $R_f = 0.85$ for hyperbolic load-deflection curves will be used. Hysteretic behaviour of the backfill soil is also considered and a similar approach proposed by Cole and Rollins [3] is used to simulate this hysteretic behaviour. The radiation damping effects for the abutment-backfill system are simulated in the structural model using dashpots. The potential formation of a gap behind the abutment due to the inelastic cyclic movements is also considered in the analyses.

5 Moment Curvature Relationships of H-Piles

As the relative rotation or displacement capacity of a steel member is proportional to its curvature capacity, the moment curvature relationships of steel H-piles subjected to different levels of axial loads are obtained. The obtained moment-curvature relationships are then used as envelope curves to define the nonlinear hysteretic behaviour of steel H-piles under cyclic loading. The obtained moment-curvature relationships under zero axial loads for HP sections considered in this study are illustrated in Fig. 1.
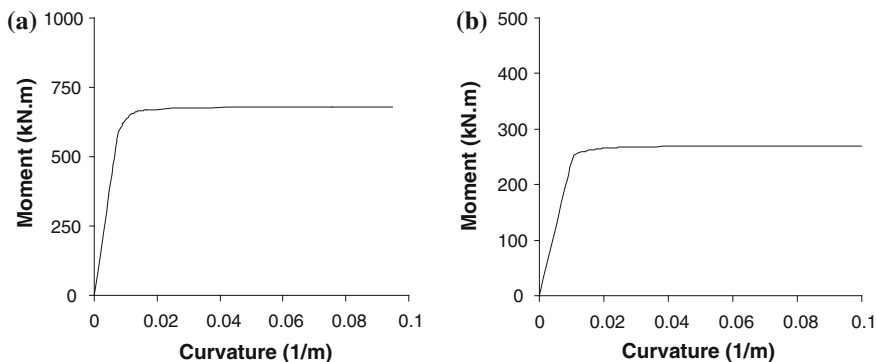
Fig. 1 Moment curvature relationship for **a** HP310 × 174, **b** HP250 × 85 sections

6 Strain-Based Low Cycle Fatigue

Low-cycle fatigue failure of structural components is caused by cyclic loads or displacements of relatively larger magnitude that may produce significant amounts of plastic strains in the structural component. Generally, the number of displacement cycles that leads to failure of a component is determined as a function of the plastic strains in the localized region of the component being analysed. This is referred to as strain-based approach to fatigue life estimate of structural components. This approach is appropriate for determining the fatigue life of steel H-piles supporting the abutments as it considers the seismically-induced large plastic deformations that may occur in localized regions of the piles where fatigue cracks may begin.

Koh and Stephens [5] proposed an equation to calculate the number of constant amplitude strain cycles to failure for steel sections under low cycle fatigue. This equation is based on the total strain amplitude, ε_a, and expressed as follows:

$$\varepsilon_a = M(2N_f)^m \tag{5}$$

where, $M = 0.0795$, $m = -0.448$ for steel H-pile sections and N_f is the number of cycles to failure. The above equation is used for the estimation of the maximum strain amplitude steel H-piles can sustain before their failure takes place due to low-cycle fatigue effects under seismically induced cyclic loadings. For a bridge to serve its intended purpose, it must sustain the effect of seismically-induced cyclic displacements during a seismic event. The seismically-induced strains in steel H-piles are assumed to have variable amplitudes. Therefore, Eq. (5), which is derived for constant amplitude cycles, cannot be used directly alone to obtain the number of cycles to failure to estimate the consumed life of the pile due to low cycle fatigue effects under seismic loading. Accordingly, Miner's rule [6] may be used in combination with Eq. (5) to obtain the consumed life of the pile due to low cycle fatigue. Miner [6] defined the cumulative fatigue damage induced in a structural member by load or displacement cycles of different amplitudes as:

$$\sum_i^n \frac{n_i}{N_i} \leq 1 \tag{6}$$

where, n_i is the cycles associated with the ith loading (or displacement) case and N_i is the number of cycles to failure for the same case. The above equation states that if a load or displacement is applied n_i times (e.g. the number of strain cycles of a certain amplitude under seismic loading), only a fraction, n_i/N_i of the fatigue life has been consumed. The fatigue failure is then assumed to take place when n_i/N_i ratios of the cycles with different amplitudes add up to 1.

7 Analyses of the Bridge Models

A total of four IB models are built considering two different pile sizes and soil stiffness. Then, thermal analyses of these IBs are conducted. The analyses results revealed that the steel H-piles remain within the elastic limits under thermal induced displacements due to the small length of the IBs. Consequently, low cycle fatigue effects under thermal loading are not expected for this particular bridge. Hence, these effects are not considered together with seismic effects for low cycle fatigue life estimates of the IBs considered in this study. Then, the nonlinear time history analyses of the IB models are conducted using two earthquake ground motions; 1971 San Fernando (SF) and 1994 Northridge (NR). The nonlinear time history analyses are repeated for peak ground accelerations of 0.2, 0.5, 0.8 and 1.0 g for each selected earthquake. This led to a total of 32 different analyses cases. The analyses results are presented in the following sections.

8 Analyses Results

The hysteric (cyclic) moment-rotation relationships of the steel H-piles are obtained from the nonlinear time history analyses results (Fig. 2). Then, a Matlab program is developed to calculate the amplitude of positive (ε_{ap}) and negative (ε_{an}) strain cycles using the moment rotation relationships obtained from nonlinear time history analyses. Then the strain amplitudes (ε_a) are calculated as follows;

$$\varepsilon_a = \frac{\left|\varepsilon_{pa}\right| + \left|\varepsilon_{na}\right|}{2} \tag{7}$$

Next, the number of displacement cycles (N_f) that leads to failure of a steel H-pile is determined using the method purposed by Koh and Stephens [5] given earlier. Furthermore, cumulative fatigue damage index for the H-piles are obtained using Miner's rule [6]. The number of cycles and cumulative fatigue damage index
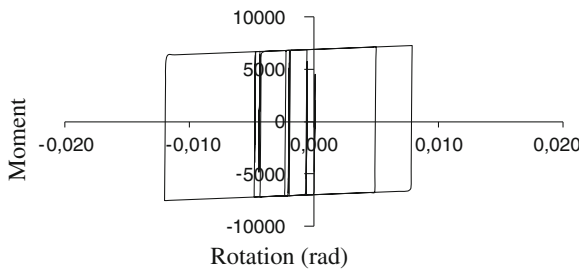
Fig. 2 A typical hysteric (cyclic) moment-rotation relationships of the steel H-piles obtained from time history analysis (San Fernando Earthquake A_p = 0.8 g)

Table 1 Number of cycles and fatigue damage indices for different pile sizes

Pile size	Earthquake	A_p = 0.5 g		A_p = 0.8 g		A_p = 1.0 g	
		Number of cycle	$\sum_i^n \frac{n_i}{N_i}$	Number of cycle	$\sum_i^n \frac{n_i}{N_i}$	Number of cycle	$\sum_i^n \frac{n_i}{N_i}$
HP310 × 174	San Fernando	42	0.0008	46	0.0010	48	0.0014
HP310 × 174	Northridge	52	0.0009	62	0.0013	66	0.0017
HP250 × 85	San Fernando	46	0.0018	49	0.0021	53	0.0035
HP250 × 85	Northridge	58	0.0030	61	0.0037	65	0.0040

Table 2 Number of cycles and fatigue damage indices for different soil stiffness

Soil stiffness	Earthquake	A_p = 0.5 g		A_p = 0.8 g		A_p = 1.0 g	
		Number of cycle	$\sum_i^n \frac{n_i}{N_i}$	Number of cycle	$\sum_i^n \frac{n_i}{N_i}$	Number of cycle	$\sum_i^n \frac{n_i}{N_i}$
Medium	San Fernando	42	0.0008	46	0.0010	48	0.0014
Medium	Northridge	52	0.0009	62	0.0013	66	0.0017
Dense	San Fernando	57	0.0009	61	0.0012	64	0.0015
Dense	Northridge	79	0.0018	81	0.0024	86	0.0025

for the H-piles of IBs are tabulated in Table 1 for different pile sizes and Table 2 for different soil stiffness values. The analyses results are presented for peak ground accelerations of 0.5, 0.8 and 1 g. In the case of peak ground acceleration of 0.2 g, a hysteretic (cyclic) behaviour is not observed due to the elastic behaviour of the H-piles under this small level of peak ground acceleration. In the following subsection, the effect of various pile sizes and soil stiffness on the low cycle fatigue damage of steel H-piles of IBs is further studied.

9 Effect of Pile Sizes and Soil Stiffness

The results presented in Table 1 clearly reveal that as the size of the pile increases, cumulative fatigue damage index decreases. This obviously results from the greater bending capacity of larger piles that produces smaller inelastic displacements and hence strains. The stiffness of the foundation soil is observed to have a remarkable effect on the cumulative fatigue damage index of steel H-piles in IBs under seismic loading. As the soil stiffness increases, cumulative fatigue damage index of steel H-piles increases, as observed from Table 2. This study is also reveal that the cumulative fatigue damage in the steel H-piles induced by seismic loadings are negligible. As mentioned earlier, the fatigue failure is assumed to take place when the cumulative of n_i/N_i ratios of the cycles with different amplitudes add up to 1 according to Miner's rule. However, the cumulative fatigue damage indices

calculated from Miner's rule [6] ranges between 0.0008 and 0.0040 as observed from Tables 1 and 2. Even in the earthquakes with larger peak ground accelerations (1.0 g), the cumulative fatigue damage indices are too smaller than 1. This obviously indicates that the low cycle damages during the earthquakes do not have considerable effects on the service life of small and medium span IBs.

10 Conclusions

In this paper, a parametric study is conducted on the low cycle fatigue in IB piles under seismic effects. This parametric study reveals that soil stiffness and pile sizes have significant effects on the cumulative fatigue damage indices which are used to assess fatigue failure and service life of structures. However, it is found that the cumulative fatigue damage indices calculated for steel H-piles of IBs due to seismic loading is negligible. In the design of small and medium span IBs, these low cycle fatigue effects is not needed to be considered.

References

1. Anandarajah A, Zhang J, Ealy C (2005) Calibration of dynamic analysis methods from field test data. Soil Dyn Earthq Eng 25(7–10):763–772
2. API (American Petroleum Institute) (2000) Recommended practice and planning, designing, and constructing fixed offshore platforms. Washington, DC
3. Cole RT, Rollins KM (2006) Passive earth pressure mobilization during cyclic loading. J Geotech Geoenvironmental Eng 132(9):1154–1164
4. Duncan MJ, Mokwa RL (2001) Passive earth pressure: theories and tests. J Geotech Geoenvironmental Eng 127(3):248–257
5. Koh SK, Stephens RI (1991) Mean stress effects on low cycle fatigue for a high strength steel. Fatigue Fract Eng Mater Struct 14(4):413–428
6. Miner MA (1945) Cumulative damage in fatigue. ASME J Appl Mech 12159–164

Part XXVIII
Reliability and Fragility

Confidence Bounds on Failure Probability Using MHDMR

A.S. Balu and B.N. Rao

Abstract The structural reliability analysis in presence of mixed uncertain variables demands more computation as the entire configuration of fuzzy variables needs to be explored. Moreover the existence of multiple design points plays an important role in the accuracy of results as the optimization algorithms may converge to a local design point by neglecting the main contribution from the global design point. Therefore, in this paper a novel uncertain analysis method for estimating the failure probability bounds of structural systems involving multiple design points in presence of mixed uncertain variables is presented. The proposed method involves weight function to identify multiple design points, multicut-high dimensional model representation technique for the limit state function approximation, transformation technique to obtain the contribution of the fuzzy variables to the convolution integral and fast Fourier transform for solving the convolution integral. In the proposed method, efforts are required in evaluating conditional responses at a selected input determined by sample points, as compared to full scale simulation methods. Therefore, the proposed technique estimates the failure probability accurately with significantly less computational effort compared to the direct Monte Carlo simulation. The methodology developed is applicable for structural reliability analysis involving any number of fuzzy and random variables with any kind of distribution. The accuracy and efficiency of the proposed method is demonstrated through two examples.

Keywords Failure probability · Structural reliability analysis · Random variables · Confidence bounds · Multicut-high dimensional model representation technique

A.S. Balu (✉)
Department of Civil Engineering, National Institute of Technology (NIT) Karnataka, Mangalore, India
e-mail: asbalu@nitk.ac.in

B.N. Rao
Structural Engineering Division, Indian Institute of Technology (IIT) Madras, Chennai, India
e-mail: bnrao@iitm.ac.in

1 Introduction

Reliability analysis taking into account the uncertainties involved in a structural system plays an important role in the analysis and design of structures. Due to the complexity of structural systems the information about the functioning of various structural components has different sources and the failure of systems is usually governed by various uncertainties, all of which are to be taken into consideration for reliability estimation. Uncertainties present in a structural system can be classified as aleatory uncertainty and epistemic uncertainty. Aleatory uncertainty information can be obtained as a result of statistical experiments and has a probabilistic or random character. Epistemic uncertainty information can be obtained by the estimation of the experts and in most cases has an interval or fuzzy character. When aleatory uncertainty is only present in a structural system, then the reliability estimation involves determination of the probability that a structural response exceeds a threshold limit, defined by a limit state/performance function influenced by several random parameters. Structural reliability can be computed adopting probabilistic method involving the evaluation of multidimensional integral [1, 2]. In first- or second-order reliability method (FORM/SORM), the limit state functions need to be specified explicitly. Alternatively the simulation-based methods such as Monte Carlo techniques requires more computational effort for simulating the actual limit state function repeated times. The response surface concept was adopted to get separable and closed form expression of the implicit limit state function in order to use fast Fourier transform (FFT) to estimate the failure probability [3]. The High Dimensional Model Representation (HDMR) concepts were applied for the approximation of limit state function at the MPP and FFT technique to evaluate the convolution integral for estimation of failure probability [4]. In this method, efforts are required in evaluating conditional responses at a selected input determined by sample points, as compared to full scale simulation methods.

In addition, the main contribution to the reliability integral comes from the neighbourhood of design points. When multiple design points exist, available optimization algorithms may converge to a local design point and thus erroneously neglect the main contribution to the value of the reliability integral from the global design point(s). Moreover, even if a global design point is obtained, there are cases for which the contribution from other local or global design points may be significant [5]. In that case, multipoint FORM/SORM is required for improving the reliability analysis [6]. In the presence of only epistemic uncertainty in a structural system, possibilistic approaches to evaluate the minimum and maximum values of the response are available [7]. All the reliability models discussed above are based on only one kind of uncertain information; either random variables or fuzzy input, but do not accommodate a combination of both types of variables. However, in reality, for some engineering problems in which some uncertain parameters are random variables, others are interval or fuzzy variables, using one kind of reliability model cannot obtain the best results. To determine the bounds of reliability of a structural system involving both random and interval or fuzzy variables, every

configuration of the interval variables needs to be explored. Hence, the computational effort involved in estimating the bounds of the failure probability increases tremendously in the presence of multiple design points and mixed uncertain variables. This paper explores the potential of coupled Multicut-HDMR (MHDMR)-FFT technique in evaluating the reliability of a structural system with multiple design points, for which some uncertainties can be quantified using fuzzy membership functions while some are random in nature. Comparisons of numerical results have been made with direct MCS method to evaluate the accuracy and computational efficiency of the present method.

2 Multi-cut High Dimensional Model Representation

High Dimensional Model Representation (HDMR) is a general set of quantitative model assessment and analysis tools for capturing the high-dimensional relationships between sets of input and output model [4, 8]. Let the N dimensional vector $\mathbf{x} = \{x_1, x_2, \ldots, x_N\}$ represent the input variables of the model under consideration, and the response function as $g(\mathbf{x})$. Since the influence of the input variables on the response function can be independent and/or cooperative, HDMR expresses the response $g(\mathbf{x})$ as a hierarchical correlated function expansion in terms of the input variables. The expansion functions are determined by evaluating the input-output responses of the system relative to the defined reference point $\mathbf{c}$ along associated lines, surfaces, subvolumes, etc. in the input variable space. The first-order approximation of $g(\mathbf{x})$ is as follows:

$$\tilde{g}(\mathbf{x}) = \sum_{i=1}^{N} g(c_1, \ldots, c_{i-1}, x_i, c_{i+1}, \ldots, c_N) - (N-1)g(\mathbf{c}) \qquad (1)$$

The notion of 0th, 1st, etc. in HDMR expansion should not be confused with the terminology used either in the Taylor series or in the conventional least-squares based regression model. It can be shown that, the first order component function $g_i(x_i)$ is the sum of all the Taylor series terms which contain and only contain variable x_i. Hence first-order HDMR approximations should not be viewed as first-order Taylor series expansions nor do they limit the nonlinearity of $g(\mathbf{x})$.

The main limitation of truncated cut-HDMR expansion is that depending on the order chosen sometimes it is unable to accurately approximate $g(\mathbf{x})$, when multiple design points exist on the limit state function or when the problem domain is large. In this section, a new technique based on MHDMR is presented for approximation of the original implicit limit state function, when multiple design points exist. The basic principles of cut-HDMR may be extended to more general cases. MHDMR is one extension where several cut-HDMR expansions at different reference points are constructed, and the original implicit limit state function $g(\mathbf{x})$ is approximately represented not by one, but by all cut-HDMR expansions. In the present work,

weight function is adopted for identification of multiple reference points closer to the limit surface. Let $\mathbf{d}^1, \mathbf{d}^2, \ldots, \mathbf{d}^{m_d}$ be the m_d identified reference points closer to the limit state function based on the weight function. The original implicit limit state function $g(\mathbf{x})$ is approximately represented by blending all locally constructed m_d individual cut-HDMR expansions as follows:

$$g(\mathbf{x}) \cong \sum_{k=1}^{m_d} \lambda_k(\mathbf{x}) \left[g_0^k + \sum_{i=1}^{N} g_i^k(x_i) + \cdots + g_{12\cdots N}^k \quad (x_1, x_2, \ldots, x_N) \right] \qquad (2)$$

The coefficients $\lambda_k(\mathbf{x})$ determine the contribution of each locally approximated function to the global function. The properties of the coefficients $\lambda_k(\mathbf{x})$ imply that the contribution of all other cut-HDMR expansions vanish except one when x is located on any cut line, plane, or higher dimensional ($\leq$l) sub-volumes through that reference point, and then the MHDMR expansion reduces to single point cut-HDMR expansion. As mentioned above, the lth order cut-HDMR approximation does not have error when x is located on these sub-volumes. When m_d cut-HDMR expansions are used to construct a MHDMR expansion, the error free region in input x space is m_d times that for a single reference point cut-HDMR expansion, hence the accuracy will be improved. Therefore, first-order MHDMR approximations of the original implicit limit state function with m_d reference points can be expressed as

$$\tilde{g}(\mathbf{x}) \cong \sum_{k=1}^{m_d} \lambda_k(\mathbf{x}) \left[\sum_{i=1}^{N} g^k\big(d_1^k, \ldots, d_{i-1}^k, x_i, d_{i+1}^k, \ldots, d_N^k\big) - (N-1)g^k\big(\mathbf{d}^k\big) \right]. \qquad (3)$$

3 Weight Function for Identification of Multiple Reference Points

The most important part of MHDMR approximation of the original implicit limit state function is identification of multiple reference points closer to the limit state function. The proposed weight function is similar to that used by Kaymaz and McMahon [9] for weighted regression analysis. Among the limit state function responses at all sample points, the most likelihood point is selected based on closeness to zero value, which indicates that particular sample point is close to the limit state function. In this study two types of procedures are adopted for identification of reference points closer to the limit state function, namely: (1) first-order method, and (2) second-order method. The procedure for identification of reference points closer to the limit state function using first-order method proceeds as follows: (a) $n(=3, 5, 7 \text{ or } 9)$ equally spaced sample points $\mu_i - (n-1)\sigma_i/2$, $\mu_i - (n-3)\sigma_i/2$, ..., μ_i, ..., $\mu_i + (n-3)\sigma_i/2$, $\mu_i + (n-1)\sigma_i/2$ are deployed along each of the random variable axis x_i with mean μ_i and standard deviation σ_i, through an

initial reference point. Initial reference point is taken as mean value of the random variables; (b) The limit state function is evaluated at each sample point; (c) Using the limit state function responses at all sample points, the weight corresponding to each sample point is evaluated using the following weight function,

$$w' = \exp\left(-\frac{g(c_1, \ldots, c_{i-1}, x_i, c_{i+1}, \ldots, c_N) - g(\mathbf{x})|_{\min}}{|g(\mathbf{x})|_{\min}|}\right). \tag{4}$$

Sample points $\mathbf{d}^1, \mathbf{d}^2, \ldots, \mathbf{d}^{m_d}$ with maximum weight are selected as reference points closer to the limit state function, for construction of m_d individual cut-HDMR approximations of the original implicit limit state function locally. In this study, two types of sampling schemes, namely FF and SF are adopted.

4 Estimation of Failure Probability in Presence of Mixed Uncertain Variables

Let the N-dimensional input variables vector $\mathbf{x} = \{x_1, x_2, \ldots, x_N\}$, which comprises of r number of random variables and f number of fuzzy variables be divided as, $\mathbf{x} = \{x_1, x_2, \ldots, x_r, x_{r+1}, x_{r+2}, \ldots, x_{r+f}\}$ where the subvectors $\{x_1, x_2, \ldots, x_r\}$ and $\{x_{r+1}, x_{r+2}, \ldots, x_{r+f}\}$ respectively group the random variables and the fuzzy variables, with $N = r + f$. Then the first-order approximation of $\tilde{g}(\mathbf{x})$ can be divided into three parts, the first part with only the random variables, the second part with only the fuzzy variables and the third part is a constant which is the output response of the system evaluated at the reference point c, as follows

$$\tilde{g}(\mathbf{x}) = \sum_{i=1}^{r} g(x_i, \mathbf{c}^i) + \sum_{i=r+1}^{N} g(x_i, \mathbf{c}^i) - (N-1)g(\mathbf{c}) \tag{5}$$

The joint membership function of the fuzzy variables part is obtained using suitable transformation of the variables $\{x_{r+1}, x_{r+2}, \ldots, x_N\}$ and interval arithmetic algorithm. Using the bounds of the fuzzy variables part at each α-cut along with the constant part and the random variables part, the joint density functions are obtained by performing the convolution using FFT in the rotated Gaussian space at the MPP, which upon integration yields the bounds of the failure probability. The steps involved in the proposed method for failure probability estimation as follows:

(i) If $\mathbf{u} = \{u_1, u_2, \ldots, u_r\}^T \in \Re^r$ is the standard Gaussian variable, let $\mathbf{u}^{k*} = \{u_1^{k*}, u_2^{k*}, \ldots, u_r^{k*}\}^T$ be the MPP or design point, determined by a standard nonlinear constrained optimization. The MPP has a distance β_{HL} which is commonly referred to as the Hasofer–Lind reliability index. Note that in the rotated Gaussian space the MPP is $\mathbf{v}^* = \{0, 0, \ldots, \beta_{HL}\}^T$. The transformed

limit state function $g(\mathbf{v})$ therefore maps the random variables along with the values of the constant part and the fuzzy variables part at each α-cut, into rotated Gaussian space V. First-order HDMR approximation of $g(\mathbf{v})$ in rotated Gaussian space V with $\mathbf{v}^{k^*} = \{v_1^{k^*}, v_2^{k^*}, \ldots, v_r^{k^*}\}^T$ as reference point can be represented as follows:

$$\tilde{g}^k(\mathbf{v}) \equiv \sum_{i=1}^{r} g^k\left(v_1^{k^*}, \ldots, v_{i-1}^{k^*}, v_i, v_{i+1}^{k^*}, \ldots, v_r^{k^*}\right) - (r-1)g(\mathbf{v}^{k^*}) \qquad (6)$$

(ii) In addition to the MPP as the chosen reference point, the accuracy of first-order HDMR approximation may depend on the orientation of the first $r-1$ axes. In the present work, the orientation is defined by the matrix. The terms $g^k\left(v_1^{k^*}, \ldots, v_{i-1}^{k^*}, v_i, v_{i+1}^{k^*}, \ldots, v_r^{k^*}\right)$ are the individual component functions and are independent of each other. Equation (6) can be rewritten as,

$$\tilde{g}^k(\mathbf{v}) = a^k + \sum_{i=1}^{r} g^k\left(v_i, \mathbf{v}^{k^{*i}}\right) \qquad (7)$$

(iii) New intermediate variables are defined as

$$y_i^k = g^k\left(v_i, \mathbf{v}^{k^{*i}}\right) \qquad (8)$$

(iv) The purpose of these new variables is to transform the approximate function into the following form

$$\tilde{g}^k(\mathbf{v}) = a^k + y_1^k + y_2^k + \cdots + y_r^k \qquad (9)$$

(v) Due to rotational transformation in v-space, component functions y_i^k are expected to be linear or weakly nonlinear function of random variables v_i.

(vi) The global approximation is formed by blending of locally constructed individual first-order HDMR approximations in the rotated Gaussian space at different identified reference points using the coefficients λ_k

$$\tilde{g}(\mathbf{v}) = \sum_{k=1}^{m_d} \lambda_k \tilde{g}^k(\mathbf{v}) \qquad (10)$$

(vii) Since v_i follows standard Gaussian distribution, marginal density of the intermediate variables y_i can be easily obtained by transformation.

(viii) Now the approximation is a linear combination of the intermediate variable. Therefore, the joint density of $\tilde{g}(\mathbf{v})$, which is the convolution of the marginal density of the intervening variables can be expressed as follows:

$$p_{\tilde{G}}(\tilde{g}) = p_{Y_1}(y_1) * p_{Y_2}(y_2) * \cdots * p_{Y_r}(y_r) \tag{11}$$

(ix) Applying FFT and inverse FFT on both side joint density of $\tilde{g}(\mathbf{v})$ is obtained.

(x) The probability of failure is given by the following equation

$$P_F = \int_{-\infty}^{0} p_{\tilde{G}}(\tilde{g}) d\tilde{g}. \tag{12}$$

(xi) The membership function of failure probability can be obtained by repeating the above procedure at all confidence levels of the fuzzy variables part.

5 Numerical Examples

5.1 Four Dimensional Quadratic Function

This example considers a hypothetical limit state function of the following form:

$$\begin{aligned}
g(\mathbf{x}) = {} & -x_1^2 - x_2^2 - x_3^2 - x_4^2 + 9x_1 + 11x_2 + 11x_3 + 11x_4 \\
& - x_5^2 - 4.6x_5 + x_6^2 + 4.7x_6 + 11
\end{aligned} \tag{13}$$

where x_1, x_2, x_3, x_4 are assumed to be normal variables with mean value as 5.0 and standard deviation value as 0.4, and x_5, x_6 are assumed to be fuzzy variables with triangular membership function having the triplet [4.96, 5.0, 5.04]. Figure 1 shows

Fig. 1 Membership function of failure probability
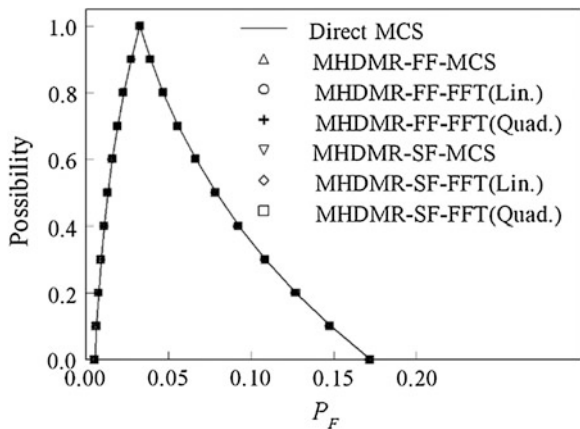
the estimated membership function of the failure probability P_F by the proposed methods, as well as by using direct MCS. The failure probability estimated by the proposed MHDMR approximation with FF sampling scheme requires significantly less computational effort than direct MCS for the same accuracy.

5.2 80-Bar 3D-Truss Structure

A 3D-truss, shown in Fig. 2, is considered in this example to examine the accuracy and efficiency of the proposed method for the membership function of failure probability estimation. The loads at various levels are considered to be random while the cross-sectional areas of the angle sections at various levels are assumed to be fuzzy. The maximum horizontal displacement at the top of the tower is considered to be the failure criterion, as given below.

Fig. 2 80-bar 3D-truss structure
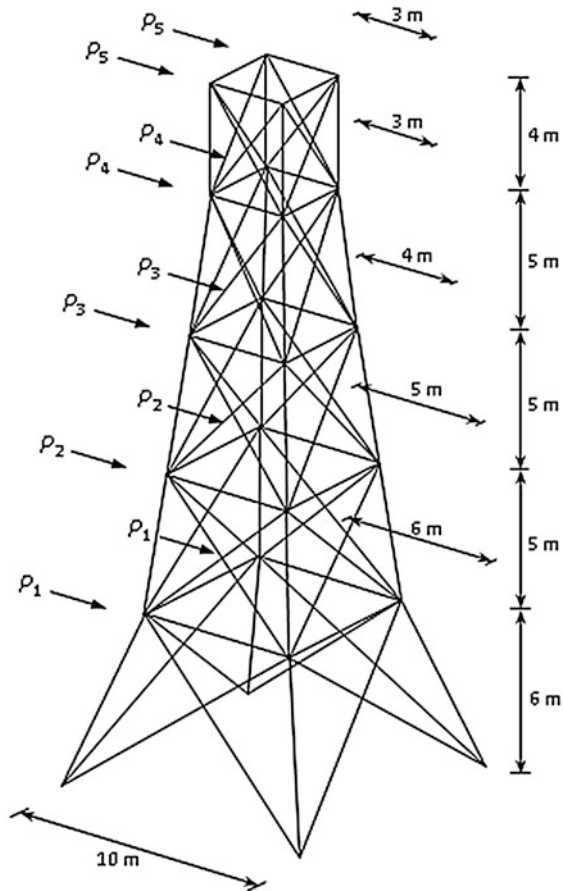
Fig. 3 Membership function of failure probability
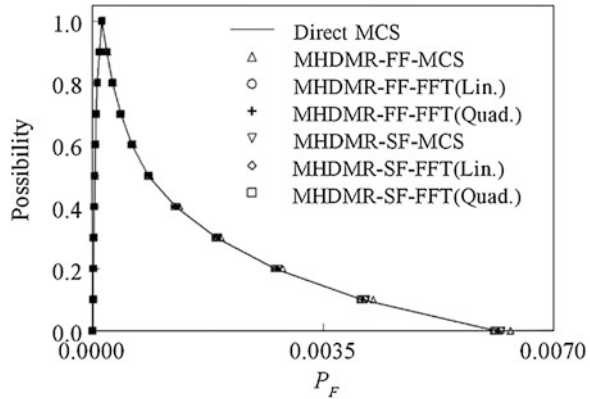
$$g(\mathbf{x}) = \Delta_{\text{lim}} - \Delta(\mathbf{x}) \tag{14}$$

The limiting deflection Δ_{lim} is assumed to be 0.15 m. The limit state function is approximated using first-order HDMR by deploying $n = 5$ sample points along each of the variable axis and taking respectively the mean values and nominal values of the random and fuzzy variables as initial reference point. The two reference points closer to the function producing maximum weights, 1.0 and 0.977 are identified. After identification of two reference points, local first-order HDMR approximations are constructed at the reference points. The bounds of the failure probability are obtained both by performing the convolution using FFT in conjunction with linear and quadratic approximations and MCS on the global approximation. Figure 3 shows the membership function of the failure probability P_F estimated both by performing the convolution using FFT, and MCS on the global approximation, as well as that obtained using direct MCS. In addition, effects of SF sampling scheme and the number of sample points on the estimated membership function of the failure probability P_F are studied.

6 Summary and Conclusion

This paper presented a novel uncertain analysis method for estimating the membership function of the reliability of structural systems involving multiple design points in the presence of mixed uncertain variables. The method involves MHDMR technique for the limit state function approximation, transformation technique to obtain the contribution of the fuzzy variables to the convolution integral and fast Fourier transform for solving the convolution integral at all confidence levels of the fuzzy variables. Weight function is adopted for identification of multiple reference points closer to the limit surface. Using the bounds of the fuzzy variables part at each confidence level along with the constant part and the random variables part,

the joint density functions are obtained by (i) identifying the reference points closer to the limit state function and (ii) blending of locally constructed individual first-order HDMR approximations in the rotated Gaussian space at different identified reference points to form global approximation, and (iii) performing the convolution using FFT, which upon integration yields the bounds of the failure probability. As an alternative the bounds of the failure probability are estimated by performing MCS on the global approximation in the original space, obtained by blending of locally constructed individual first-order HDMR approximations of the original limit state function at different identified reference points. The results of the numerical examples indicate that the proposed method provides accurate and computationally efficient estimates of the membership function of the failure probability. The results obtained from the proposed method are compared with those obtained by direct MCS. The numerical results show that the present method is efficient for structural reliability estimation involving any number of fuzzy and random variables with any kind of distribution.

References

1. Breitung K (1984) Asymptotic approximations for multinormal integrals. ASCE J Eng Mech 110(3):357–366
2. Rackwitz R (2001) Reliability analysis—a review and some perspectives. Struct Saf 23(4):365–395
3. Sakamoto J, Mori Y, Sekioka T (1997) Probability analysis method using fast Fourier transform and its application. Struct Saf 19(1):21–36
4. Rao BN, Chowdhury R (2008) Probabilistic analysis using high dimensional model representation and fast Fourier transform. Int J Comput Methods Eng Sci Mech 9(6):342–357
5. Au SK, Papadimitriou C, Beck JL (1999) Reliability of uncertain dynamical systems with multiple design points. Struct Saf 21:113–133
6. Der Kiureghian A, Dakessian T (1998) Multiple design points in first and second order reliability. Struct Saf 20(1):37–49
7. Penmetsa RC, Grandhi RV (2003) Uncertainty propagation using possibility theory and function approximations. Mech Based Des Struct Mach 81(15):1567–1582
8. Rabitz H, Alis OF, Shorter J, Shim K (1999) Efficient input-output model representations. Comput Phys Commun 117(1–2):11–20
9. Kaymaz I, McMahon CA (2005) A response surface method based on weighted regression for structural reliability analysis. Probab Eng Mech 20(1):11–17

Stochastic Simulation Based Reliability Analysis with Multiple Performance Objective Functions

Sahil Bansal and Sai Hung Cheung

Abstract In this paper, a stochastic simulation approach is proposed to estimate small failure probabilities of multiple limit states. The proposed approach allows for the simultaneous consideration of multiple performance functions and the corresponding thresholds. The approach modifies the stochastic subset simulation algorithm that can efficiently compute small failure probabilities. The proposed approach is robust with respect to the dimension of the failure probability integral, model complexity and nonlinearity. The effectiveness and efficiency of the proposed method are illustrated by a numerical example involving a structural dynamic system subjected to future earthquake excitations modeled as a stochastic process and the results are compared to those obtained using crude Monte Carlo simulation.

Keywords Monte Carlo simulation · Reliability · Stochastic process · Subset simulation

1 Introduction

Reliability of a dynamic system is concerned with the probability that the system will not reach some specific 'failure' states subjected to stochastic excitations. It involves calculating the reliability, or its complement the failure probability P_F, which requires the evaluation of a multi-dimensional integral of the form

$$P_F = \int_F p(\boldsymbol{\theta})d\boldsymbol{\theta} \tag{1}$$

S. Bansal (✉) · S.H. Cheung
Department of Civil and Environmental Engineering, Nanyang Technological University, Singapore, Singapore
e-mail: sbansal@ntu.edu.sg

where $\boldsymbol{\theta} \subset R^{n_\theta}$ is the parameter vector containing all the uncertain quantities of interest quantified by a joint probability distribution function (PDF) $p(\boldsymbol{\theta})$ and $F = \{\boldsymbol{\theta} : g(\boldsymbol{\theta}) > 0\}$ is the failure region with $g(\boldsymbol{\theta})$ as the performance function that separates the safe domain $g(\boldsymbol{\theta}) \leq 0$ and the failure domain $g(\boldsymbol{\theta}) > 0$. One example of a performance function is

$$g(\boldsymbol{\theta}) = u(\boldsymbol{\theta}) - c \tag{2}$$

where $u(\boldsymbol{\theta})$ is the response quantity of the model specified by $\boldsymbol{\theta}$ and c is a threshold value. A reliability analysis with this performance function estimates the 'failure' probability that $u(\boldsymbol{\theta})$ exceeds c. For complex dynamic system problems involving high stochastic dimension, reliability analysis by state-of-the-art stochastic simulation based techniques has proved to be very efficient and reliable, especially for estimating small failure probabilities [1]. However, all these techniques focus on obtaining failure probabilities as a function of a single threshold, i.e., they assume a single performance function. For a problem with multiple performance function, which involves estimation of failure probabilities corresponding to multiple limit states, the aforementioned techniques will require repetitive application that can be very inefficient. Hsu and Ching [2] proposed a Parallel Subset Simulation to estimate small failure probabilities of multiple limit states with only a single subset simulation analysis by introducing a 'principal variable' which is correlated with all performance functions.

In this paper, a stochastic simulation approach is proposed to estimate the small failure probabilities of multiple limit states. The approach adopts and modifies the Subset Simulation [3] algorithm. Conditional samples are generated using samples belonging to a failure domain defined by a particular combination of thresholds. The proposed approach is robust with respect to the dimension of the failure probability integral, model complexity and nonlinearity and efficient in computing small failure probabilities. The effectiveness and efficiency of the proposed approach are demonstrated using a numerical example.

2 Subset Simulation

Subset Simulation is proposed by Au and Beck [3] to compute small failure probabilities for general high-dimensional reliability problems. It is a very efficient algorithm based on Markov chain Monte Carlo (MCMC) simulation. The basic idea of the Subset Simulation algorithm is to consider a sequence of m failure events $F_1 \supset F_2 \supset \cdots \supset F_m = F$ (one being the subset of another) converting a rare-event problem into a problem with a sequence of more frequent events that are conditioned on failing successively increasing threshold levels. This enables the computation of the failure probability as a product of conditional probabilities

$\{P(F_{i+1}|F_i) : i = 0, 1, \ldots, m\}$, where $P(F_1|F_0) = P(F_1)$ and the target failure probability is given by the last element in the sequence

$$P_F = P(F_m) = \left[\prod_{i=1}^{m-1} P(F_{i+1}|F_i) \right] P(F_1). \tag{3}$$

$P(F_1)$ is estimated by simulating samples by Monte Carlo Simulation (MCS)

$$P(F_1) \approx \frac{1}{N} \sum_{k=1}^{N} I_{F_1}\left(\boldsymbol{\theta}^{(k)} \right) \tag{4}$$

where $\{\boldsymbol{\theta}^{(k)} : k = 1, \ldots, N\}$ are independently and identically distributed (i.i.d) samples according to the PDF $p(\boldsymbol{\theta})$; $I_F = 1$ if $\boldsymbol{\theta} \in F_1$ and $I_F = 0$ otherwise. Similarly, $P(F_{i+1}|F_i)$ is estimated using samples distributed according to the conditional PDF $p(\boldsymbol{\theta}|F_i)$

$$P(F_{i+1}|F_i) \approx \frac{1}{N} \sum_{k=1}^{N} I_{F_{i+1}}\left(\boldsymbol{\theta}^{(k)} \right). \tag{5}$$

Samples satisfying the conditional PDF $p(\boldsymbol{\theta}|F_i)$ are generated by a Markov Chain Monte Carlo simulation technique based on the modified Metropolis–Hastings approach [3] using samples distributed according to $p(\boldsymbol{\theta}|F_i)$ obtained from the previous simulation level as seeds. The output of subset simulation analysis is the exceedance probability as a function of a single threshold variable. The intermediate thresholds for the conditional levels are chosen "adaptively" so that the conditional probabilities are approximately equal to some specified value p_0.

3 Proposed Approach

In the proposed approach where N_p performance functions are considered

$$
\begin{aligned}
g^1(\boldsymbol{\theta}) &= u^1(\boldsymbol{\theta}) - c^1 \\
&\vdots \\
g^j(\boldsymbol{\theta}) &= u^j(\boldsymbol{\theta}) - c^j \\
&\vdots \\
g^{N_p}(\boldsymbol{\theta}) &= u^{N_p}(\boldsymbol{\theta}) - c^{N_p}
\end{aligned} \tag{6}
$$

$u^j(\boldsymbol{\theta})$ is the jth response quantity of the model specified by $\boldsymbol{\theta}$ and c^j is the corresponding threshold value. Using samples $\left\{ \boldsymbol{\theta}^{(k)} : k = 1, \ldots, N \right\}$ distributed

according to the PDF $p(\boldsymbol{\theta})$, failure probabilities corresponding to different performance functions can be estimated using

$$P(F_1^j) \approx \frac{1}{N} \sum_{k=1}^{N} I_{F_1^j}\left(\boldsymbol{\theta}^{(k)}\right) \qquad (7)$$

where $I_{F_1^j}$ is an indicator function corresponding to F_1^j failure domain. All response quantities for model with parameters $\boldsymbol{\theta} = \boldsymbol{\theta}^{(k)}$ can be calculated using a single analysis. However, using Eq. (7) will be computationally expensive especially when dealing with small failure probability as the number of samples N required to achieve a given c.o.v is inversely proportional to the failure probability. The proposed procedure for a reliability analysis with multiple performance functions, which involves evaluating failure probability as a function of multiple thresholds, uses the same "sequence of failure events" idea as in Subset Simulation. However, the way in which the intermediate failure domains are selected and samples are propagated between successive failure domains is modified. The Subset Simulation algorithm is adapted to compute the updated robust failure probability as follows

$$P(F^j) = P(F^j|X_{m-1})\left[\prod_{i=1}^{m-1} P(X_m)\right] \qquad (8)$$

where the intermediate failure domain X_i is selected such that

$$X_i = \bigcup_j F_i^j \qquad (9)$$

and where for $j = 1\dots, N_P$

$$P\left(F_{i+1}^j|F_i^j\right) = p_0. \qquad (10)$$

There will be Np_i $\boldsymbol{\theta}$ samples distributed according to $p(\boldsymbol{\theta}|X_i)$. Using these samples as seeds, additional $N(1 - p_i)$ $\boldsymbol{\theta}$ samples which are also distributed according to $p(\boldsymbol{\theta}|X_i)$ are generated by MCMC simulation method based on the modified Metropolis–Hastings method as in the original Subset Simulation. These samples $\{\boldsymbol{\theta}^{(k)} : k = 1, \dots, N\}$ distributed according to the $p(\boldsymbol{\theta}|X_i)$ can be used to estimate the failure probabilities $P(F^j|X_i)$ as follows

$$P(F^j|X_i) \approx \frac{1}{N} \sum_{k=1}^{N} I_{F^j}\left(\boldsymbol{\theta}^{(k)}\right). \qquad (11)$$

4 Illustrative Example

The example used in the study is a hotel structure located in Van Nuys. This building is a seven story reinforced concrete structure that was severely damaged during the 1994 Northridge Earthquake. For illustration, failure is defined as an event where any inter-story drift ratio (*IDR*) or floor acceleration (*FA*) exceeds specific threshold at any discrete time instant during the total duration.

A discrete-time white noise sequence **Z** corresponding to duration of input ground motion $T = 50$ s and a sampling interval $\Delta t = 0.02$ s is considered. For each run using the proposed approach $N = 1,000$ samples or dynamic analysis are used and it is assumed that $p_0 = 0.1$. One-dimensional chain adaptive symmetric uniform distribution is adopted as a proposal for each addictive excitation random variable.

The following results are obtained by simultaneously considering *IDR* and *FA* thresholds. Therefore, the total number of samples required to estimate the failure probabilities equal to 10^{-4} is 3,700. Figures 1 and 2 shows the sample mean of exceedance probability estimates from 60 independent simulation runs and exceedance probability estimates from MCS computed using 100,000 independent samples for *IDR* and *FA* thresholds. It can be seen that the results using the proposed method and MCS agree well except for very small exceedance probabilities where the error in MCS is significant. To investigate the variability of the exceedance probability estimators, the sample c.o.v of the exceedance probability estimates over 60 independent simulation runs is computed and is shown in Figs. 3 and 4. It can be observed, as expected, the c.o.v grows approximately in a linear

Fig. 1 Sample mean of exceedance probability estimates from 60 independent simulation runs and exceedance probability estimates from MCS as a function of maximum interstory drift ratio
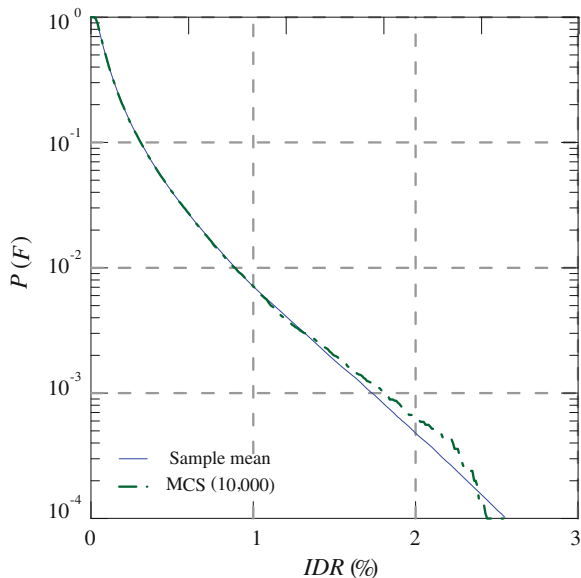
Fig. 2 Sample mean of exceedance probability estimates from 60 independent simulation runs and exceedance probability estimates from MCS as a function of maximum floor acceleration
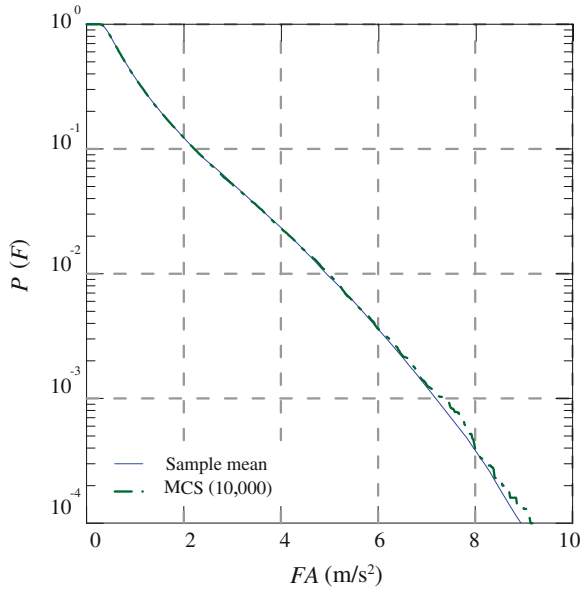
Fig. 3 Sample c.o.v of exceedance probability estimates from 60 independent simulation runs (IDR)
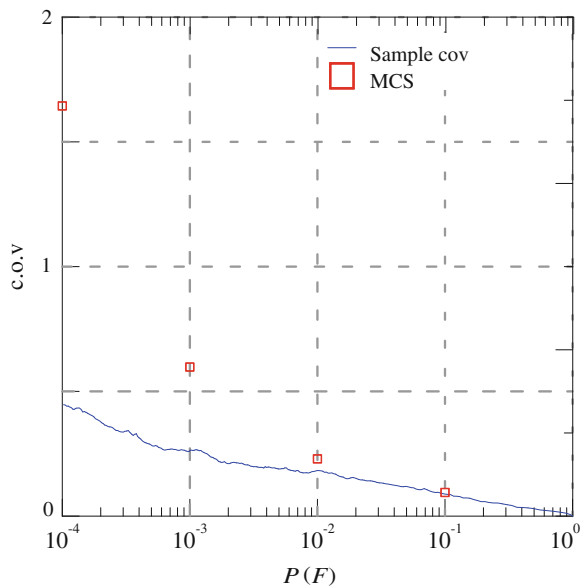
fashion with the logarithm of decreasing exceedance probabilities, which is smaller than the c.o.v for MCS that grows exponentially with decreasing failure probabilities for the same number of samples used.

Fig. 4 Sample c.o.v of exceedance probability estimates from 60 independent simulation runs (FA)
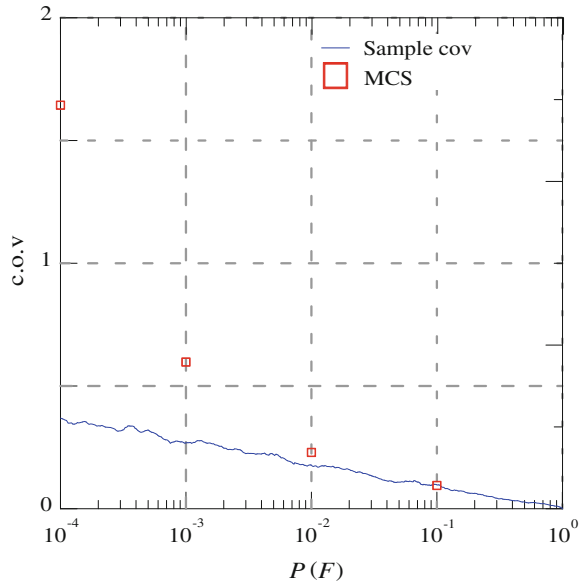
Although the formulation has been presented for the general case of multiple performance objectives, the graphical representation of failure probabilities in more than two dimensions becomes difficult.

5 Conclusion

A new stochastic simulation based approach is proposed for the estimation of failure probabilities of a dynamic system with multiple limit states as a function of thresholds. The proposed approach allows for the simultaneous consideration of multiple performance functions and the corresponding thresholds. An example is presented to show the application of the proposed approach. More discussion and results showing the merits of the proposed approach compared with crude Monte Carlo can be found in the journal version of this paper.

References

1. Schuëller G, Pradlwarter H (2007) Benchmark study on reliability estimation in higher dimensions of structural systems–an overview. Struct Saf 29(3):167–182
2. Hsu WC, Ching J (2010) Evaluating small failure probabilities of multiple limit states by parallel subset simulation. Probab Eng Mech 25(3):291–304
3. Au S, Beck JL (2001) Estimation of small failure probabilities in high dimensions by subset simulation. Probab Eng Mech 16(4):263–277

Accident Modelling and Risk Assessment of Oil and Gas Industries

Srinivasan Chandrasekaran and A. Kiran

Abstract Oil and gas industries around the world are subjected to more threats and accidents as they are handling highly hazardous materials. Downstream sector faces many challenges as their safety is primarily governed by the societal consequences. Detailed mathematical analysis and accident modelling of such scenarios, as applied to oil and gas industries are scarce in the literature. Quantified risk assessment is therefore mandatory for all petrochemical industries to restrict risk within the permissible limits. It is therefore important to develop tools to manage risk efficiently. The present study describes the consequence and risk analysis of the selected accident scenarios for a liquid petroleum gas (LPG) filling station. Consequence analysis will give the hazard distances for dispersion and thermal radiations for leakages, jet fires and fireballs. Risk analysis will give the individual and societal risk due to the selected accident cases of the plant. The study is carried out using the software DNV Phast Risk. Various consequence scenarios that may arise from the plant such as dispersion, jet fires, and fireball are studied and the risk are determined in terms of the quantified hazard distances.

Keywords Risk assessment · Accident modelling · LPG · Jet fire · Fireball

1 Introduction

The demand for the usage of petrochemicals is increasing day by day. This has led to increase in the production of petrochemicals and also complexities in the design. The complexities and continuous change in design led to change in the risk involved in

S. Chandrasekaran (✉) · A. Kiran
Department of Ocean Engineering, Indian Institute of Technology (IIT) Madras,
Chennai 600036, India
e-mail: drsekaran@iitm.ac.in

A. Kiran
e-mail: kiranarjun95@yahoo.com

the oil and gas plants also. So, it is important to have a continuous monitoring of risk associated and its impact to the society as well as to the existing plant. Risk assessment is an important and most commonly acceptable tool for assessing risk and it can be done quantitatively as well as qualitatively. In the present study, the consequence analysis and risk assessment of liquid petroleum gas (LPG) filling station is carried out quantitatively using the DNV Phast Risk software.

Risk assessment is mandatory for all process industries considering the societal impact it is having. This paper mainly focuses on the consequences and risk involved for some of the accident cases of LPG filling station. The main hazards due to LPG include leakages from the pressurized vessels or pipelines leading to rapid vaporization and loss of containments. The consequence depends upon the magnitude of release and type of scenario [1]. Some of the accidents occurred in the LPG filling station include jet fire [2], pool fire [3], fireball and Boiling Liquid Expanding Vapour Explosion (BLEVE) [4]. In the present study, accident cases are pseudo created for the analysis to enable the objective of the study and also to estimate the respective consequences. Some of the accident models are studied, and the consequence analysis in terms of quantified hazard distances and risk for the selected failure cases are discussed in details.

2 Methodology

LPG filling station consists of five numbers of open storage bullets, each having a capacity of 150 t. The LPG contained in the storage vessels are pumped to LPG cylinder filling station. The storage bullets are filled by means of road tankers of 18 t capacity. There are twelve bays in the plant for the road tankers in which the storage bullets can be filled. The layout of the LPG filling station is shown in Fig. 1. From the plant layout, the hazard locations are identified, by categorizing the area such as storage bullets, road tankers, pump station and cylinder filling station. For the current study, the different failure cases from the storage bullets are studied and discussed.

The failure cases selected for the analysis are given in Table 1. The outlet pipeline from the storage bullet to the pump house is of diameter 150 mm. Failure of full bore rupture of this pipeline and 20 % cross-sectional area of the pipeline are considered for the dispersion and thermal radiation due to jet fire analysis. The failure of pipeline may be due to corrosion, safety valve failure, gasket failure etc. Another failure considered is catastrophic failure of storage bullets that may be due to development of cracks due to external heating source, corrosion, safety valve failure etc. The catastrophic failure of single storage bullet may lead to failure of nearby storage bullets in the dyke also, thereby causing a huge explosion or fireball. The consequence analysis is done for the atmospheric conditions taken for the year 2012. For the ease of the analysis, the seasons are grouped according to the stable atmospheric conditions.
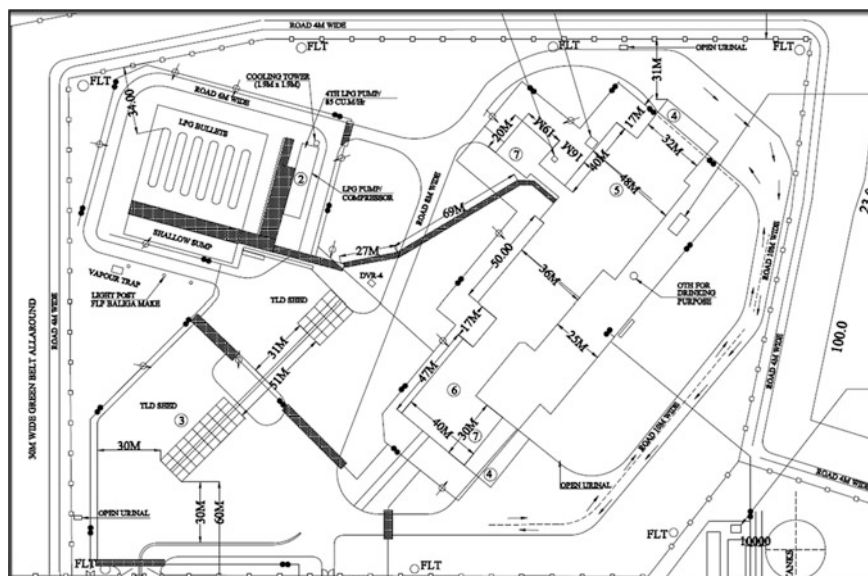
Fig. 1 Layout of LPG filling plant

Table 1 Failure cases

S. No.	Failure cases	Consequences
1	Full bore failure of 150 mm outlet line of bullet	Dispersion, jet fire
2	20 % CSA failure of 150 mm outlet line of bullet	Dispersion, jet fire
3	Catastrophic failure of single bullet	Dispersion, fireball, BLEVE
4	Domino effect of failure of bullets	Dispersion, fireball, BLEVE

3 Input

The fuel properties are given according to the storage conditions at the plant. The LPG is pressurized in the storage bullets in the range of 6–9 bar pressure. Weather conditions considered for the analysis are given in Table 2. It is selected by taking the average value of 3 months for the year 2012 weather data.

For the analysis of full bore failure of 150 mm outlet line from the storage bullet, 1,160 kg mass is considered, which is released over a duration of 60 s. For 20 % of the cross-sectional area failure, 954 kg mass is considered to be released in 180 s. Alternatively, for a catastrophic failure and domino effect of storage bullets, the vessel is considered to be failed instantaneously and the whole mass stored in bullet is considered to be involved in the analysis.

Table 2 Weather data [6]

Month	Stability class	Wind speed (m/s)	Relative humidity	Atm. Temp. (°C)
January–March	B/C	2.5	0.77	26.77
April–June	C	4.5	0.7	32
July–September	B	3.3	0.74	30
October–December	E	2.2	0.82	27.4

For calculating risk, probability of failure of the selected failure cases are taken from the OGP risk assessment data directory [5]. The population data, which is assumed to be present in the plant during operation is taken based on the inspection of the plant.

4 Physics

Greater hazard is posed by the accidental release of flammable materials from the pressurized vessels or pipelines as liquids or vapors. The importance of understanding dispersion in the present study is to find the lower flammability limit. Lower flammability limit (LFL) is the region in which, below a concentration, the fuel will not get ignited even if there is an ignition source. The LFL for LPG is found to be 17,000 ppm. If the ignition of discharging material happen within the LFL region, jet fire will be produced. Jet fires dissipate thermal radiation which will damage the nearby equipment. Most of the jet fire accident cases occurred in the past have led to some other accident cases. If the pressurized vessel fails catastrophically, a vapor cloud will be formed. If this vapor cloud is ignited, fireball will be formed which are generally short lived flames.

5 Consequences

The major types of accidents occurring in the LPG plants are leakages due to various effects. This leakage if not properly monitored is leading to major accidents like fires and explosions. Some of the major fire cases occurring in the LPG plants are jet fires, pool fires and fireball. Some of the explosions cases include boiling liquid expanding vapour explosion and unconfined vapour cloud explosion. The dispersion effects are important to know the flammability limits of the fuel. If the fuel is dispersed and the ignition source is within the flammable region, then the chances of getting fires or explosions are very high. In this paper, the consequences due to dispersion, jet fires, and fireballs are studied considering the failure of pressurized storage bullets. The effect of thermal radiation is given in Table 3.

Table 3 Effect of thermal radiation [3]

Incident thermal radiation intensity (kW/m^2)	Types of damage
37.5	Sufficient to cause damage to process equipment
12.5	Minimum energy required for piloted ignition of wood, melting of plastic tubing etc.
4.5	1st degree burn
1.6	Will cause no discomfort to long exposure
0.7	Equivalent to solar radiation

6 Risk

Risk is the measure of magnitude of damage along with its probability of occurrence. Mathematically, risk is the product of probability of failure of occurrence of an event and its consequence. Risk can be expressed in terms of individual risk and societal risk. Individual risk is viewed as the risk of someone at a specific location being a fatality in a given period. It is expressed on per-year basis. Societal risk is the probability of number of victims per year. The societal risk is plotted as FN curve which gives the relationship between frequency (F) of occurrence of events and number (N) of fatalities per year.

7 Results and Discussion

7.1 Full Bore Rupture of Outlet Line of Bullet

Due to full bore failure of outlet pipeline from the storage bullet, consequence analyses have been carried out for dispersion and jet fire. Due to dispersion, the LFL hazard distances are found for different seasonal changes and is given in Table 4. It can be seen that, the dispersing fuel will get ignited up to a distance of 67 m away from the release source.

If this dispersing fluid gets ignited, it may cause jet fire. Due to jet fire, the hazard distances for thermal radiation is given in Table 5. It can be seen that 37.5 kW/m^2 thermal load will reach a maximum distance of 54 m. The hazard distance is slightly higher in April to June due to the lower relative humidity which

Table 4 LFL distance for full bore rupture of outlet line from storage bullet

S. No.	Weather condition	LFL distance (m)
1	January–March	66
2	April–June	67
3	July–September	67
4	October–December	67

Table 5 Radiation effects due to jet fire

S. No.	Thermal load (kW/m²)	Distance (m)			
		January–March	April–June	July–September	October–December
1	4	89	88	89	89
2	12.5	66	69	67	66
3	37.5	51	54	52	50

Fig. 2 Radiation versus distance downwind for jet fire due to full bore failure
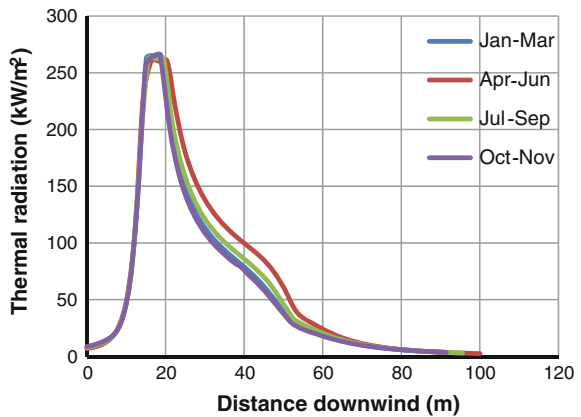
will reduce the transmissivity. The variation of hazard distance to thermal radiation is given in Fig. 2. The lower hazard distance is during the season having higher humidity, which is from October to December.

7.2 20 % CSA Failure of the Outlet Line of the Bullet

The spillage of LPG for 20 % CSA failure is considered for 3 min. The 3 min spillage will cause a hazard distance due to dispersion of maximum of 24 m. During October to December the hazard distance is 24 m which is maximum compared to other seasons. The lower flammability limit distance (LFL) is given in Table 6.

Table 6 LFL distance for 20 % of CSA failure of outlet line from storage bullet

S. No.	Weather condition	LFL distance (m)
1	January–March	23
2	April–June	21
3	July–September	21
4	October–December	24

Table 7 Radiation effects due to jet fire

S. No.	Thermal load (kW/m^2)	Distance (m)			
		January–March	April–June	July–September	October–December
1	4	42	42	42	42
2	12.5	33	34	33	32
3	37.5	26	28	27	25

Fig. 3 Radiation versus distance downwind for jet fire for 20 % CSA failure
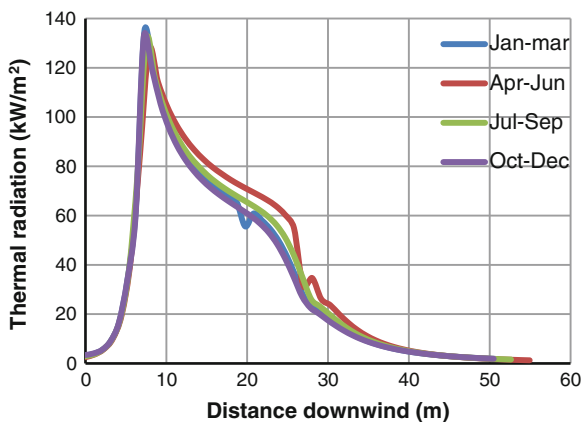
The thermal radiation effects due to jet fire caused due to ignition of dispersing fuel is given Table 7. For the year considered for the analysis, thermal hazard distance of 28 m can be expected for the intensity of 37.5 kW/m^2 thermal load. The variation of thermal radiation for distance downwind for different months is shown in Fig. 3. From the graph, it can be seen that the hazard distance is more during the period from April to June.

7.3 Catastrophic Failure of Single Bullet

The catastrophic failure of single bullet will cause dispersion effects which is non-toxic but if ignited will cause fireball or explosion. The hazard distance due to dispersion is given in Table 8. It can be seen that for catastrophic failure, the hazard distance is expected to be a maximum of 157 m during April to June. During catastrophic failure, the bullet will fail suddenly thereby the liquid will form a pool and then vaporize at atmospheric pressure. As there will be liquid LPG droplets also in the atmosphere and the velocity of wind is higher during April to June, the hazard distance is more.

Table 8 LFL distance for catastrophic failure of storage bullet

S. No.	Weather condition	LFL distance (m)
1	January–March	111
2	April–June	157
3	July–September	125
4	October–December	121

Table 9 Radiation effects due to fireball

S. No.	Thermal load (kW/m^2)	Distance (m)			
		January–March	April–June	July–September	October–December
1	4	742	728	732	734
2	12.5	371	362	364	366
3	37.5	NR	NR	NR	NR

The thermal radiation due to fireball caused by the catastrophic failure of bullet is given in Table 9. It can be seen that, hazard distance of 371 m will be there for catastrophic failure of storage bullet. The fireball duration is for 18.29 s which is for a smaller duration. Therefore, thermal load of 37.5 kW/m^2 is not reached.

7.4 Domino Effect

Domino effect of bullet is caused due to failure of adjacent bullet yielding to series of bullet failure either due to explosion or fireball. The thermal radiation caused due to failures of series of three bullets is given in Table 10. It can be seen that the maximum hazard distance a fireball can cause due to domino effect is 1,404 m during January to March for a thermal load of 4 kW/m^2.

Table 10 Radiation effects due to fireball

S. No.	Thermal load (kW/m^2)	Distance (m)			
		January–March	April–June	July–September	October–December
1	4	1,404	1,372	1,381	1,388
2	12.5	730	712	717	721
3	37.5	112	67	82	92

7.5 Risk

Risk can be represented as individual risk and societal risk. Individual risk will give the units of incident rate over a period of time. For the selected scenarios considered for the consequence analysis, the risk analysis is also done for the same. The individual risk is expressed as risk contour, which is given in Fig. 4. It can be seen that the maximum individual risk contour is 1 E-8 (10^{-8}) per average year which is plotted in blue color. The societal risk will give the total effect of accidents to the society. It is generally expressed as FN curve which will give the frequency (F) of fatalities occurring per average year to the number (N) of fatalities. The societal risk for the accident cases considered for the consequence analysis is shown in the Fig. 5. Since the frequency of selected accident cases is very low and the population
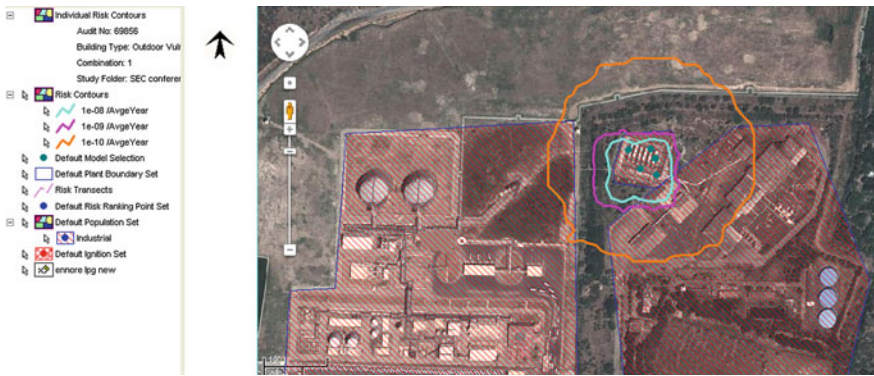
Fig. 4 Risk contour for individual risk
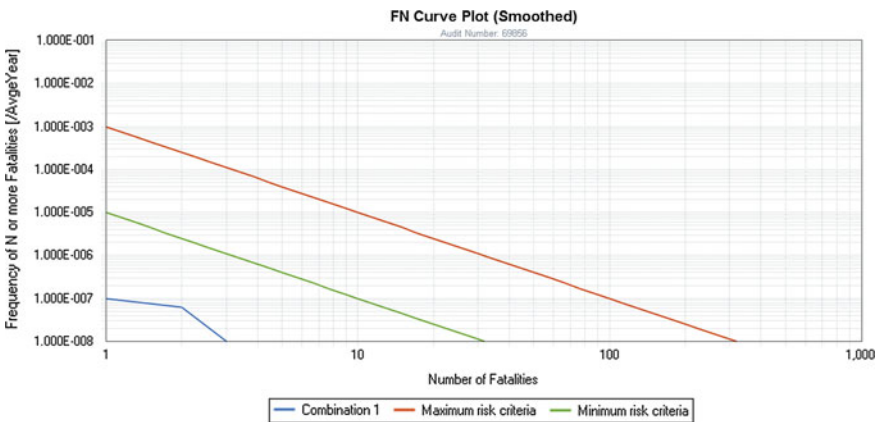
Fig. 5 FN curve for societal risk

nearby the hazard spot is very less, the plant is within the acceptance criteria. From Fig. 5, the red line is the maximum acceptance criteria, green line is the minimum acceptance criteria and the blue line is plant's societal risk which is within the permissible limits as established by Oil Safety Directorate.

8 Conclusions

The consequence and risk analysis of the selected accident cases for the liquid petroleum gas (LPG) plant is carried out for different possible accident scenarios. For the dispersion effects, it is found that the lower flammability region is 157 m due to catastrophic failure of the storage bullet. This can be reduced by constructing mounded bullets in which the dispersing LPG will be confined to the plant area. The jet fires are caused due to ignition of dispersing fuel within lower flammability region. In the present study, maximum of 54 m hazard distance is computed for thermal load of 37.5 kW/m^2. So, the critical equipments can be constructed or kept away from this range in order to avoid series of accidents. Fireballs are generally short lived flames, having large area of impact. Since fireballs are generally due to catastrophic failure of pressurized vessels, the consequence can be reduced by confining the vapor cloud to a smaller space. For mounded bullets, the dispersing fuel will be confined to space and the fireball caused due to that will be reduced depending upon the strength of construction. The risk assessment done for the selected failure cases, even though they are within the permissible limits, it can be further reduced. The risk and consequences have to be recalculated for these recommendations, which may be taken up as a future scope of the study. This present study can be used as a guidelines for the accident cases considered, which are presented in terms of quantified hazard distances.

References

1. Rasbash DJ (1979) Review of explosion and fire hazard of liquefied petroleum gas. Fire Saf J 2:223–236
2. Gomez-Mares M, Zarate L, Casal J (2008) Jet fires and the domino effect. Fire Saf J 43:583–588
3. McGrattan KB, Baum HR, Hamins A (2000) Thermal radiation from large pool fires. NISTIR 6546
4. Qian Xi Z, Dong L (2013) Thermal radiation and impact assessment of the LNG BLEVE fireball. Procedia Eng 52:602–606
5. OGP (2010) OGP risk assessment data directory: report no. 434-1. Process release frequencies, Mar 2010
6. http://weatherspark.com/#!dashboard;q=Chennai

Bibliography

7. Colls J, Tiwary A (2010) Air pollution: measurement, modelling and mitigation, 3rd edn. Taylor and Francis e library. ISBN 0-203-87196-0
8. Shallcross DC (2013) Using concept map to assess learning of safety case studies—the piper alpha disaster. Educ Chem Eng 8:e1–e11
9. Si H, Ji H, Zeng X (2012) Quantitative risk assessment model of hazardous chemicals leakage and application. Saf Sci 50:1452–1461
10. Van Hardeveld RM, Groeneveld MJ, Lehman JY, Bull DC (2001) Investigation of air separation unit explosion. J Loss Prev Process Ind 14:167–180
11. https://maps.google.com
12. Vinnem JE (2007) Offshore risk assessment: principles, modelling and applications of QRA, 2nd edn. Springer, London. ISBN 13:9781846287169
13. Sutherland VJ, Cooper CL (1991) Stress and accidents in the offshore oil and gas industry. Gulf Publishing Company, Houston. ISBN 0-87201-802-4
14. DNV Phast Risk, Det Norske Veritas (2005) User manual—version 6.7

Review of Evaluation of Uncertainty in Soil Property Estimates from Geotechnical Investigation

Ranjan Kumar and Kapilesh Bhargava

Abstract Geotechnical investigations are carried out for important projects in nuclear industries. Investigations involve estimation of soil properties by various laboratory and in situ tests. Estimation of accurate geotechnical parameters is needed in design process. The uncertainties involved in soil property estimates have necessitated reliability analysis in addition to conventional analysis. Unavailability of a large set of sample data and mathematical sophistication for carrying out uncertainty analysis are areas of concern. Reliability based design is done considering individual sources of uncertainties. Quantitative analysis of uncertainty is carried out. Standard deviations (SD) of various parameters need to be evaluated based on the data. There is degree of uncertainties in the calculation of parameters. Varying degree of uncertainties has been observed for different parameters. For some parameters, it is low and for some, it is high which need to be considered in reliability analysis. When sufficient data is available, SD is calculated directly from data. When sufficient data is not available, published value of Values of Coefficient of Variation (COV) is used which when multiplied with mean value gives standard deviation. This paper presents review of evaluation of uncertainties in soil property estimates.

R. Kumar (✉)
Civil Engineering Division, Bhabha Atomic Research Centre (BARC),
Mumbai 400085, India
e-mail: ranjancv42@gmail.com

K. Bhargava
Nuclear Recycle Board, Bhabha Atomic Research Centre (BARC),
Anushaktinagar, Mumbai 400094, India
e-mail: kapil_66@barc.gov.in

1 Introduction

Geotechnical investigations involve estimation of soil properties by various laboratory and in situ tests. There are uncertainties involved in soil property estimates which are caused by inherent variability, measurement error and transformation uncertainty [1]. Inherent variability involves modification of soil properties due to geological processes. Measurement error is caused by methodology, equipment and limited data points. Transformation uncertainty is caused when measured soil data are transformed to design soil properties. Aim should be to evaluate the uncertainties and minimize them. The uncertainties in soil property estimates have necessitated reliability analysis in addition to conventional analysis. As far as possible, uncertainties should be avoided and if those are unavoidable, then those should be eliminated and if elimination is not possible, those should be adapted in planning, design and usage of foundation throughout its life. Unavailability of a large set of sample data and mathematical sophistication for carrying out uncertainty analysis are areas of concern.

In deterministic based design, it is ensured that throughout the structure, the induced stresses are less than the allowable stresses when it is subjected to the 'working' or service applied load. This approach simplifies the problem by considering the uncertain parameters to be deterministic. Uncertainties are accounted by using factor of safety which is based on past experience and empirical formulae. This method does not give idea on how the different parameters influence the safety. Reliability based design is done considering individual sources of uncertainties. Quantitative analysis of uncertainty is carried out. Sometimes, due to unavailability of large set of data and mathematical sophistication, it is difficult to carry out reliability based design.

Standard deviations of various parameters need to be evaluated based on the data. There is degree of uncertainties in the calculation of parameters. Varying degree of uncertainties has been observed for different parameters. For some parameters, it is low and for some, it is high which need to be considered in reliability analysis. This paper presents review of evaluation of uncertainties in soil property estimates.

2 Uncertainty in Soil Properties from Geotechnical Investigation

There are two sources of uncertainties in a system namely non-cognitive (quantitative) and cognitive (qualitative). Non-cognitive (quantitative) source gives three types of variability namely inherent variability, statistical variability and modeling variability. Inherent variability is involved in all physical observations. Even repeated measurements of the same physical quantity do not give the same value. This happens because of complex formation of soil/rock, test procedure, instruments, observers etc. This type of uncertainty may be minimized by collecting large number

of samples. Many a times, limited resources are available to collect large number of samples which causes statistical variability. Actual behavior in many cases is different from predictions. Many idealizations in foundation design parameters are used to simplify the problem like treating soil as homogeneous and isotropic media. Bearing capacity theories are based on the approximate representation of soil behavior. Finite element method or finite difference method for foundation analysis is also approximate representation of system behavior in which computational prediction and actual behavior do not match exactly. All these kinds of idealizations and approximations cause modeling uncertainty. Cognitive (qualitative) sources are structural performance, quality, skill of workers, other human factors etc.

Sources of uncertainties from geotechnical investigation are inherent spatial soil variability, presence of geologic anomaly, modeling uncertainly, testing and measurement errors and human errors. The flow chart of source of uncertainty in geotechnical property evaluation is shown in Fig. 1 [1].

Inherent soil variability in soil is caused primarily from the natural geological processes that produced and continually modify the soil mass in natural state. There is a natural variability of soil. Variability in soil properties is caused by errors in field/laboratory testing, statistical errors due to limited sampling. Errors in field testing may arise due to location of drilled holes, number of drilled holes and method of testing. Errors in laboratory testing may arise due to equipment, instrumentation, collection of disturbed/undisturbed samples, simulating field conditions. Errors are also caused by using simplified transformation models e.g. Mohr circles, bearing capacity, settlement etc. Soil parameters are estimated based on data or results of in situ and laboratory tests. Duncan [2] described four methods to estimate standard deviation of soil parameters. When sufficient data is available, SD is calculated directly from data. When sufficient data is not available, published value of COV is used which when multiplied with mean value gives standard deviation. Published values are rough guide only since conditions of sampling and
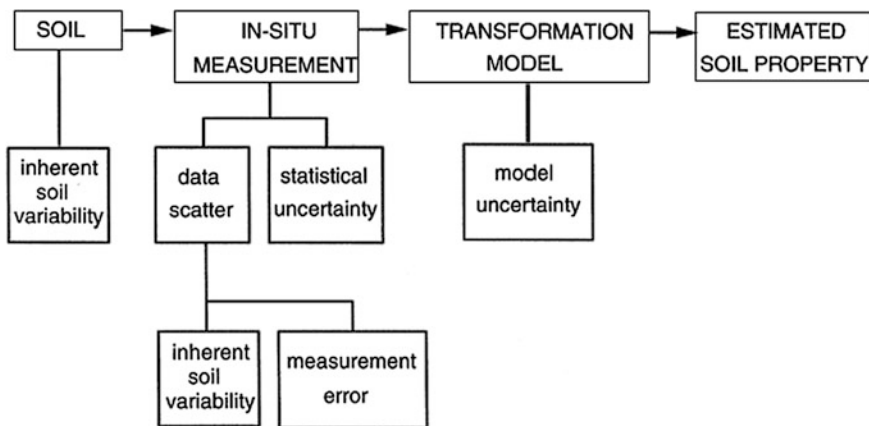
Fig. 1 Source of uncertainty in geotechnical property evaluation [1]

Table 1 Values of coefficient of variation (COV) for geotechnical properties and in situ tests (modified after Duncan [2])

Property or in situ test result	Coefficient of variation COV (%)	Associated mean value	Source
Unit weight (γ)	3–7	7.1	Harr [4], Kulhawy [1]
Buoyant unit weight (γ_b)	0–10	–	Lacasse and Nadim [5], Duncan [2]
Effective stress friction angle (φ')	2–13	12.6	Harr [4], Kulhawy [1]
Undrained shear strength	13–40	32	Harr [4], Kulhawy [1], Lacasse and Nadim [5], Duncan [2]
Compression index (C_c)	10–37	–	Harr [4], Kulhawy [1], Duncan [2]
Preconsolidation pressure	10–35	–	Harr [4], Lacasse and Nadim [5], Duncan [2]
Coefficient of permeability of saturated clay (k)	68–90	–	Harr [4], Duncan [2]
Coefficient of permeability of partly saturated clay (k)	130–240	–	Harr [4], Benson et al. [6]
Coefficient of consolidation (c_v)	33–68	–	Duncan [2]
Standard penetration test blow count (N)	15–45	–	Harr [4], Kulhawy [1]
Electric cone penetration test (q_c)	5–15	–	Kulhawy [1]
Mechanical cone penetration test (q_c)	15–37	–	Harr [4], Kulhawy [1]

testing are not specified. Judgment should be used in applying values of COV from published values. Some of the published values are given in Table 1 (modified after Duncan [2]). When limited data is available or when no data is available, three sigma rule is used. When some parameters e.g. pre-consolidation pressure, undrained shear strength vary with depth, graphical three sigma rule is used. COV of inherent soil variability, scale of fluctuation and COV of geotechnical measurement errors have been evaluated by Phoon and Kulhawy [3].

3 Reliability Based Design in Geotechnical Engineering

Deterministic design does not have high reliability. To take care of uncertainties in soil parameters, reliability analysis has been used in geotechnical engineering in the past. Various sources of uncertainties can be quantified using reliability based design. Different uncertainties are identified and reliability indices are evaluated to ensure the margin of safety based on probability theory. Reliability indices are quantitative measures of accepted performance. There are various measures of risk

Fig. 2 Guidelines for reliability index (β) and corresponding probability of failure (p_f) [8]
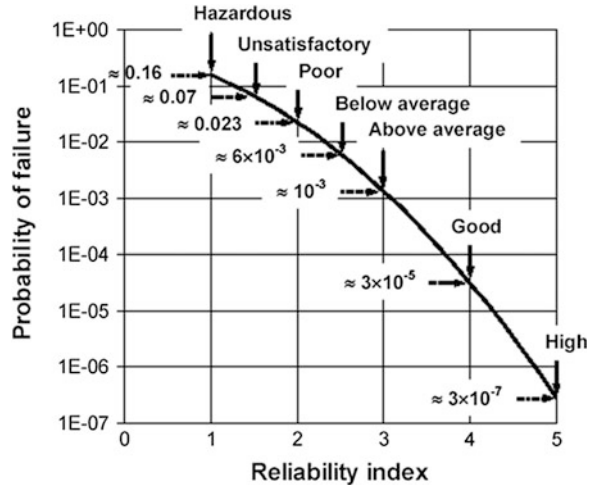
assessment e.g. factor of safety. Reliability index is computed by various methods [7]. In geotechnical engineering, guidelines on target probability of failure and reliability index are given by USACE [8] as shown in Fig. 2. Good performance of the system requires minimum reliability index value of 4.

Reliability analysis has been carried out for stability and settlement problems and their usefulness have been elaborated by Duncan [2]. Uncertainties in soil parameters have been attributed to data scatter and systematic error by Christian et al. [9]. Reliability based design optimization techniques were used for design of reinforced concrete retaining walls considering uncertainties in soil, concrete, steel by Babu and Basha [10]. Uncertainty has been reduced by prediction from empirical correlations by Zhang et al. [11]. Linear correlations were used and by using regional data and site specific observations, variability was reduced. Scale of fluctuation of a stiff clay was evaluated experimentally by performing random theory analysis on cone penetration test data obtained from two sites by Jaksa et al. [12].

4 Summary and Conclusions

Estimation of accurate geotechnical parameters is needed in design process. A review of evaluation of uncertainties in soil property estimates has been carried out. A sensitivity analysis is required to be carried out to find which of the parameter's uncertainty has the greatest effect on the response of the structure. This analysis would help in determining which parameter must be measured more precisely to get the accurate results. Reliability analysis considers uncertainties in the parameters involved in the calculations. There is a need to simplify the procedure of reliability analysis particularly in geotechnical engineering.

References

1. Kulhawy FH (1992) On evaluation of static soil properties. In: Seed RB, Boulanger RW (eds) Instability and performance of slopes and embankments II (GSP 31). American Society of Civil Engineers, New York, pp 95–115
2. Duncan JM (2000) Factors of safety and reliability in geotechnical engineering. J Geotech Geoenvironmental Eng 126(4):307–316
3. Phoon KK, Kulhawy FH (1999) Characterization of geotechnical variability. Can Geotech J 36:612–624
4. Harr M (1984) Reliability-based design in civil engineering. 20th Henry M. Shaw Lecture, Department of Civil Engineering, North Carolina State University, Raleigh, NC
5. Lacasse S, Nadim, F (1997) Uncertainties in characterizing soil properties. Publ. No. 201, Norwegian Geotechnical Institute, Oslo, Norway, 49–75
6. Benson CH, Daniel DE, Boutwell GP (1999) Field performance of compacted clay liners. J Geotech Geoenvironmental Eng, ASCE, 125(5):390–403
7. Haldar A, Mahadevan S (2000) Probability, reliability, and statistical methods in engineering design. Wiley, NY
8. USACE (1997) Risk-based analysis in geotechnical engineering for support of planning studies, engineering and design. US Army Corps of Engineers, Department of Army, Washington, DC
9. Christian JT, Ladd CC, Baecher GB (1994) Reliability applied to slope stability analysis. J Geotech Eng 120(12):2180–2207
10. Babu GLS, Basha BM (2008) Optimum design of cantilever retaining walls using target reliability approach. Int J Geomech 8(4):240–252
11. Zhang L, Tang WH, Zhang L, Zheng J (2004) Reducing uncertainty of prediction from empirical correlations. J Geotech Geoenvironmental Eng 130(5):526–534
12. Jaksa MB, Kaggwa WS, Brooker PI (2004) Experimental evaluation of the scale of fluctuation of a stiff clay. In: 9th Australia New Zealand conference on geomechanics, Auckland

Comparison of Damage Index and Fragility Curve of RC Structure Using Different Indian Standard Codes

Tathagata Roy and Pankaj Agarwal

Abstract In today's world, there is much talk about seismic vulnerability, its features and the necessity of study. The main problem that is faced in today's world is knowledge about proper quantification of damage. The response is obtained after the ground motion has been imparted on the structure. Despite of making significant progress in the field of seismic design codes for dynamic analysis, there is a lack of progress in the quantification of damage. The damage criterion should include large displacements as well as the effect of repeated cyclic loading. An energy-based damage model is used to assess the damage index for the structure taking into account the effect of repeated cycles. The present study has been done to carry out the vulnerability analysis of a four-storey reinforced concrete (RC) moment resisting frame by modified Park and Ang damage model which is then compared by different Indian standard code for earthquake resistant design. A new damage scale has been proposed for each of the analysis against an individual code. Each of the fragility parameter has been individually calculated in carrying out this analysis. Fragility curve is plotted by calculating the uncertainty and the median values.

Keywords Damage index · Fragility · Median · Pushover · Vulnerability

1 Introduction and Background

Seismic vulnerability is practically defined as "the proneness of some category of elements at risk to undergo adverse effects inflicted by potential earthquakes", i.e. the degree of damage to the structure or of a region when the ground motion has been imparted on the structure. Vulnerability is always directly related to risk definition. Every structure is vulnerable to some extent on application of external loading. The main problem that is faced in India is that there has been a significant contribution in the development of various design codes for dynamic analysis, but

T. Roy (✉) · P. Agarwal
Indian Institute of Technology (IIT) Roorkee, Roorkee 247667, Uttarakhand, India
e-mail: roy.tatz@gmail.com

no proper method of quantification of damage. For the developing countries like India, the present code does not meet any requirements against the structural safety for an existing building that is very well exposed to the damage. There has been an urgent concern regarding the structural restoration of the existing building class, which comprises of important structures like historical buildings, lifeline structures, etc. Thus, the earthquake engineers are constantly focusing on the aspects of developing probabilistic risk models or the vulnerability models. Major earthquakes over the last couple of decades show that seismic risk is the only natural risk that affects the socio-economic prospect of the society. So, only rough estimates can be made regarding the damage. Thus, the effect on any existing building must be carried out to check the sustainability of the structure. In urban areas of high seismicity, the probability of collapse is very high, needing the concept of retrofit to a large extent. One of the major parameter by which the seismic risk can be described is on the fragility of the structural component. When the process of information is processed about fragility, the main component that needs to be considered is the uncertainty due to calculation method. Fragility curve is very essential to structural engineers, reliable specialists, and hospital and highway network. It is also used for post-earthquake damage assessment, evaluation and improvement of seismic performance of structural and non-structural systems.

Extensive studies were carried by Park and Ang [5], Powell and Allahabadi [4], DiPasquale et al. [1], and Ghobarah et al. [2] for evaluating the damage index of the reinforced concrete (RC) structure. They laid the contribution for the development of damage index in today's world for assessing the vulnerability of the structure.

The damage model that is used to quantify the damage is the Park and Ang [5] damage model. The damage model is used for expressing the potential damage of RC structure as a function of maximum deformation and dissipated energy that is given in Eq. (1). The study in this paper consists of development of vulnerability curve of a 4-storey RC moment resisting frame model without infill. The damage index is computed by using modified Park and Ang damage model (1992) by performing the non-linear response history analysis. Due to the impetus laid on the vulnerability assessment, the energy-based model is of best use to find out the damage index of the structure. The modified Park and Ang damage model is given as below,

$$I_D = \frac{d_m - d_y}{d_u - d_y} + \beta_e \frac{\int dE}{F_y d_u} \qquad (1)$$

where d_m = maximum displacement obtained from non-linear response history analysis, d_u = ultimate displacement obtained from the pushover analysis, d_y = yield displacement, dE = incremental energy obtained from the time history analysis, β_e = parameter representing the cyclic loading-strength degradation factor, taken as 0.1.

2 Structure Model and Dynamic Properties

The analytical model that is used is 4-storey RC moment resisting frame. The building has a rectangular plan of 12 m × 16 m; 3 bays of 4 m each are present in the X-direction while in Y-direction it has 4 bays of 4 m each. The height of each floor is 3 m as shown in Fig. 1. The damage index is used to quantify the damage caused in beams and columns or due to the local collapses that occur in the structure. Space frame model is used. The characteristic compressive strength that is used in design is M25 and that for steel it is Fe415. Dynamic analysis of the structure is determined by free vibration. Seismic zone V and type II soil is used for calculating the demand.

Dynamic analysis of the structure is determined by free vibration. The first three frequencies obtained are 1.412, 4.831, and 9.556 Hz that is obtained in X-direction. The response is mainly governed by first mode that contributes about 82 %. Table 1 corresponds to the base shear obtained from the analysis by different Indian standard codes.
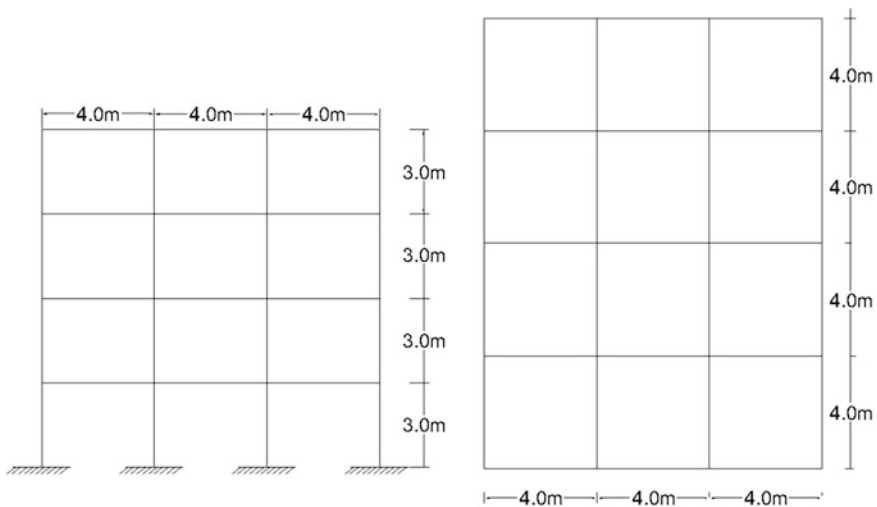
Fig. 1 Building plan and elevation

Table 1 Structural damage state definition	IS code	Base shear (kN)
	IS-1893 (Part I):2002	392
	IS-1893:1984	359
	IS-1893:1970	300

Table 2 Characteristics of the ground motion

Event	Station	PGA (g)	Mechanism	Magnitude	V_s30 (m/s)
Bigbear 1992	North Shore	0.043	Strike-slip	6.46	338.5
Imperial Valley 1979	El Centro E10	0.176	Strike-slip	6.53	202.8
Kobe 1995	Kakogawa	0.058	Strike-slip	6.9	312.0
Landers 1992	Mission Creek Fault	0.122	Strike-slip	7.28	345.4
Northridge 1994	Arleta	0.237	Reverse	6.69	297.7

3 Ground Motion Selection

In the inelastic analysis of the structure, there is great variation of response with a slight change in ground motion. Ground motion plays a great role in assessing the response due to the non-linear analysis of the structure. Large set of ground motion can be used for the analysis. For realistic results, the ground motions are scaled with respect to the design spectrum for which the structure is modeled. In this paper, Indian standard code for earthquake resistant design is used. Zone V type II soil is taken. For comparison and to assess the ductility and damage index, IS-1893 (Part I):2002, IS-1893:1984 and IS-1893:1970 has been used. Five earthquakes are considered in this example model to perform the time history analysis. The dynamic characteristics are mentioned in Table 2. The analyses are carried out for the example building using accelerograms scaled to 0.108g, 0.216g, 0.324g, 0.432g, 0.54g (g denotes gravitational acceleration).

4 Assessment from the Pushover Analysis

A building capacity curve is known as pushover curve, which is a non-linear static approach. It is plotted between building's lateral load resistance component and the roof displacement. It is derived from a plot of static-equivalent base shear versus building displacement. Non-linear hinges are assigned to each beam and column for the observation of failure criteria and to assess the damage states observed after damage. It is basically a displacement-based approach. Thus, the capacity curves obtained for the building under 3 different seismic conditions and codes analyzed in SAP2000 v14.2 are plotted. From these plots, the yield and ultimate values of the response can be found out. Table 3 shows the result of the bilinear plot for different Indian standard codes.

Table 3 Bilinear result of pushover analysis

IS code	Base shear (kN)		Roof displacement (m)	
	Yield	Ultimate	Yield	Ultimate
IS-1893 (Part I):2002	855.875	855.875	0.03649	0.34298
IS-1893:1984	749.945	778.866	0.03196	0.28720
IS-1893:1970	690.4733	702.6597	0.02888	0.22130

5 Assessment from Time-History Method

Time history analysis or the modal analysis is used to determine the response of the structure due to the induced earthquake motion. The non-linear response history analysis is performed for the five earthquakes that are scaled up to visualize the structural response due to these scaled earthquake motions. The non-linear response, i.e. the hysteresis curve is of utmost importance, which is the plot between force and roof displacement. As the maximum displacement occurs in the top storey, so the response of the top storey is plotted. The parameters that are taken into account are: maximum displacement (m), roof drift (%) and inter-storey drift (%). The building is subjected to spectrum scaled ground motion of different peak ground acceleration (PGA). The response of the building is shown in Table 4 that is computed by SAP2000 v14.2. The mean results are tabulated as below. The plots among different responses are given in Fig. 2.

6 Damage States

In this paper, the main focus is on development of fragility curve that would consider the damage states obtained from quantification of the damage of the structure. Thus, the indices or basically the limits of the damage state, i.e. slight, moderate, extensive and collapse are required to set. There is no damage below

Table 4 Plot of responses obtained from time-history analysis

PGA (g)		0.108	0.216	0.324	0.432	0.54
Max. roof displacement (m)	IS-1893:2002	0.02952	0.05280	0.09672	0.11796	0.20976
	IS-1893:1984	0.02712	0.05208	0.08616	0.13284	0.22308
	IS-1893:1970	0.02628	0.04836	0.09572	0.13776	0.20064
Inter-storey drift (%)	IS-1893:2002	0.29	0.52	0.77	1.36	2.96
	IS-1893:1984	0.30	0.56	1.33	1.87	2.86
	IS-1893:1970	0.33	0.66	1.74	2.24	3.27
Damage index	IS-1893:2002	0	0.070	0.201	0.400	0.862
	IS-1893:1984	0.009	0.116	0.280	0.459	0.996
	IS-1893:1970	0.036	0.188	0.466	0.694	1.008
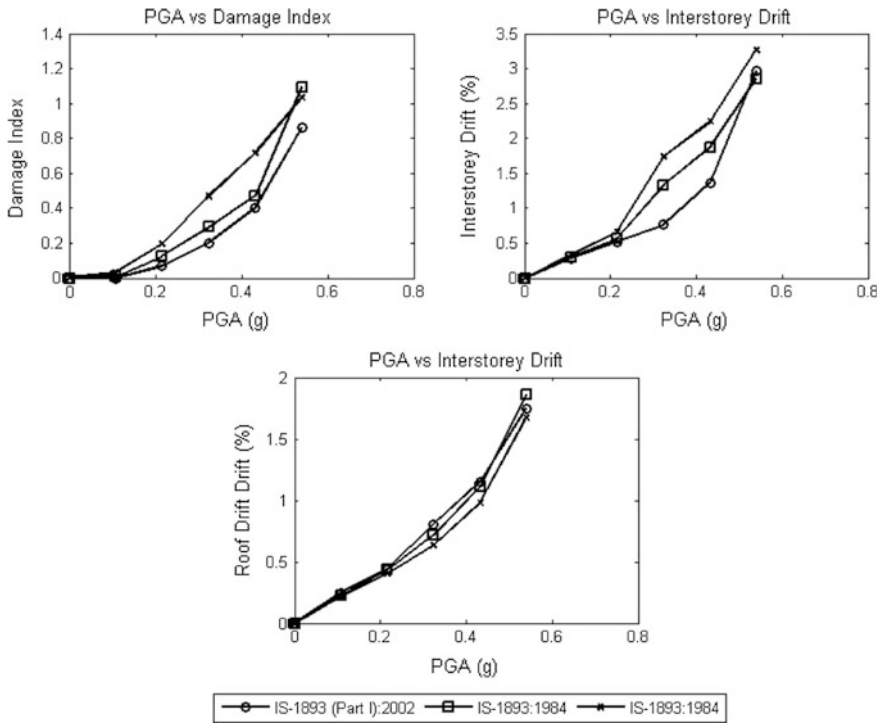
Fig. 2 Building plan and elevation

Table 5 Damage states showing limits

Damage states		Slight	Moderate	Extensive	Collapse
Peak ground acceleration (g)	IS-1893:2002	0.17	0.3	0.44	0.5
	IS-1893:1984	0.10	0.19	0.32	0.46
	IS-1893:1970	0.10	0.16	0.28	0.38
Damage index	IS-1893:2002	0.06	0.18	0.44	0.7
	IS-1893:1984	0.03	0.1	0.3	0.7
	IS-1893:1970	0.04	0.16	0.38	0.6
Inter-storey drift (%)	IS-1893:2002	0.4	0.7	1.5	2.5
	IS-1893:1984	0.3	0.5	1.4	2.2
	IS-1893:1970	0.3	0.5	1.3	2

slight damage. Based on the analytical approach and the damage observed in the structure due to the formation of plastic hinges, the Damage states are set in accordance to the response obtained for the structure. Table 5 plots the damage states, i.e. slight, moderate, extensive and collapse are set for the different seismic conditions provided by Indian standard codes shown in the table.

7 Assessment of Fragility Parameters

Fragility curve is defined as the probability of reaching or exceeding different damage states of a given peak building response. The conditional probability of being in, or exceeding, a particular damage state, ds, given the spectral displacement, S_d, is defined by the function:

$$P[ds|S_d] = \phi\left[\frac{1}{\beta_{ds}}\ln\left(\frac{S_d}{\overline{S_{d,ds}}}\right)\right] \tag{2}$$

where $\overline{S_{d,ds}}$ is the median value of spectral displacement at which the building reaches the threshold of damage state, ds; β_{ds} is the standard deviation of the natural logarithm of spectral displacement for damage state, ds; ϕ is the standard normal cumulative distribution function. So, the main two parameters involved in the fragility curve are $\overline{S_{d,ds}}$ which is the median value of spectral displacement at which the building reaches the threshold of damage state, ds and β_{ds} which is the standard deviation of the natural logarithm of spectral displacement for damage state, ds.

The total variability of each structural damage state, $\beta_{s,ds}$ is modeled by the combination of three contributors to structural damage variability, β_c, β_d and β_m.

$$\beta_{s,ds} = \sqrt{\beta_c^2 + \beta_d^2 + \beta_m^2} \tag{3}$$

where $\beta_{s,ds}$ is the lognormal standard deviation that describes the total variability for structural damage state, ds; β_c is the lognormal standard deviation parameter that describes the variability of the capacity curve; β_d is the lognormal standard deviation parameter that describes the variability of the demand spectrum; and β_m is the lognormal standard deviation parameter that describes the uncertainty in the estimate of the median value of the threshold of structural damage state, ds.

1. **Calculation of variability in capacity curve**

From the non-linear pushover analysis, the main part of concern is the plastic state that after the yield has significant contribution in the energy. The plastic state up to the ultimate position is divided into a number of regions depending upon the damage occurred in the structure. The different occupancy levels denoted are the immediate occupancy, life safety and the collapse prevention. Therefore, we have considered the different damage states as stated earlier to be divided as per the occupancy levels.

Yield to immediate occupancy (IO) = slight damage state, immediate occupancy to life safety = moderate damage state, life safety to collapse prevention = extensive damage state, beyond collapse prevention = collapse damage state. In calculating the variability of the capacity curve, the properties of the building are changed such that it affects the capacity of the structure. Therefore, by changing the material property there will always be a variation in the capacity curve. Thus, the material
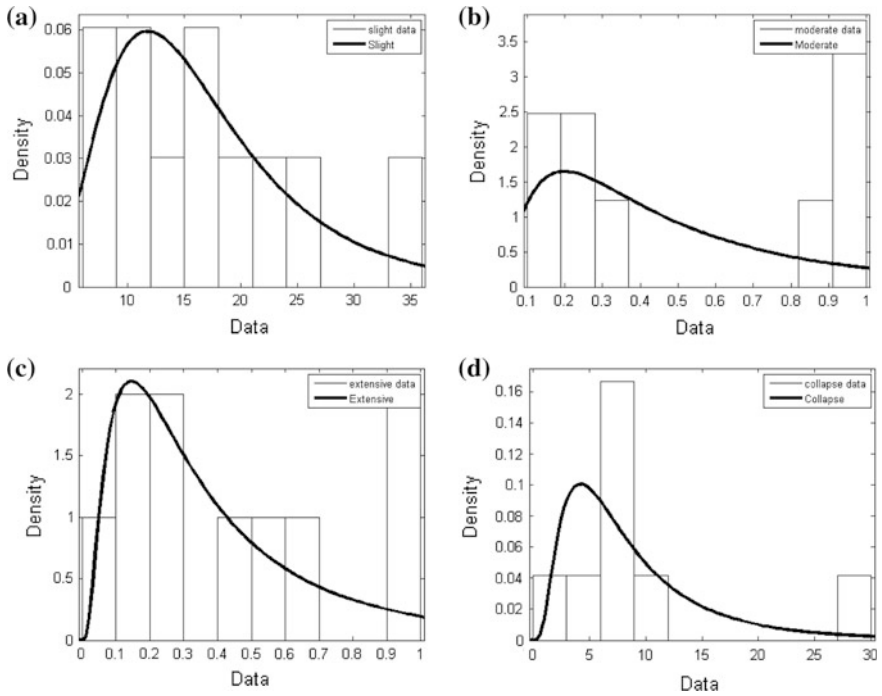
Fig. 3 Uncertainty in the capacity *curve* showing variation in slight, moderate, extensive and collapse damage state

properties, i.e. the grade of concrete and steel are changed. Here, ten models are taken without changing the other parameters except the grade of material. In this work, M20 Fe415, M30 Fe415, M25 Fe500 etc. is assigned to each model building and the pushover analysis is done to find out the capacity curve for each building due to the change in material property. The variation in the capacity curve will give the value of β_c. The variation is then coded in MATLAB program and the value is found out by simulation. Figure 3a–d show the variation in capacity curve for slight, moderate, extensive and collapse damage states, respectively. Table 6 gives the results for the variation in capacity for the different Indian standard codes.

Table 6 Variability of the capacity curve

IS code	$\beta_{c,s|ds}$	$\beta_{c,m|ds}$	$\beta_{c,e|ds}$	$\beta_{c,c|ds}$
IS-1893(Part I):2002	0.502	0.851	0.883	0.722
IS-1893:1984	0.440	0.731	0.554	0.610
IS-1893:1970	0.441	0.424	0.438	0.481

Table 7 Damage state variability of the model structure

IS code	Total variability			
	$\beta_{s,s|ds}$	$\beta_{s,m|ds}$	$\beta_{s,e|ds}$	$\beta_{s,c|ds}$
IS-1893:2002	0.669	0.959	0.989	0.847
IS-1893:1984	0.623	0.854	0.709	0.753
IS-1893:1970	0.624	0.613	0.622	0.653

2. **Calculation of variability in demand**

For 5 % damping, about 50 major earthquakes from all over the world are taken which consist of major Indian earthquakes. Response spectrum is found out for every earthquake and their variation is computed with the help of MATLAB. The variability of the demand curve, $\beta_{dem} = 0.387$. The variability in median is taken as 0.4 for this model type of building [3]. Thus, the total variability is given by (3). Table 7 refers to the damage state variability of the example building.

3. **Calculation of the median**

The inter-storey drift found out for each of the damage state is discussed above. Median values of structural component fragility are based on building drift ratios that describe the threshold of damage states. Damage-state drift ratios are converted to spectral displacement by,

$$\overline{S_{d,sds}} = \delta_{R,sds} \cdot \alpha_2 \cdot h \tag{4}$$

where $\overline{S_{d,ds}}$ is the median value of spectral displacement, in inches, of structural components for damage state, ds; $\delta_{R,sds}$ is the drift ratio at the threshold of structural damage state, ds; α_2 is the fraction of the building (roof) height at the location of push-over mode displacement, which is equal to 0.75; h is the typical roof height, in meter, of the model building type of interest. The median values calculated for different damage states are shown in Table 8.

Table 8 Calculation of Median

IS code	Inter-storey drift at threshold damage state (%)				Median value (m)			
	Slight	Moderate	Extensive	Collapse	Slight	Moderate	Extensive	Collapse
IS-1893:2002	0.4	0.7	1.5	2.5	0.036	0.063	0.135	0.225
IS-1893:1984	0.3	0.5	1.4	2.2	0.027	0.045	0.126	0.198
IS-1893:1970	0.3	0.5	1.3	2.0	0.027	0.045	0.117	0.180
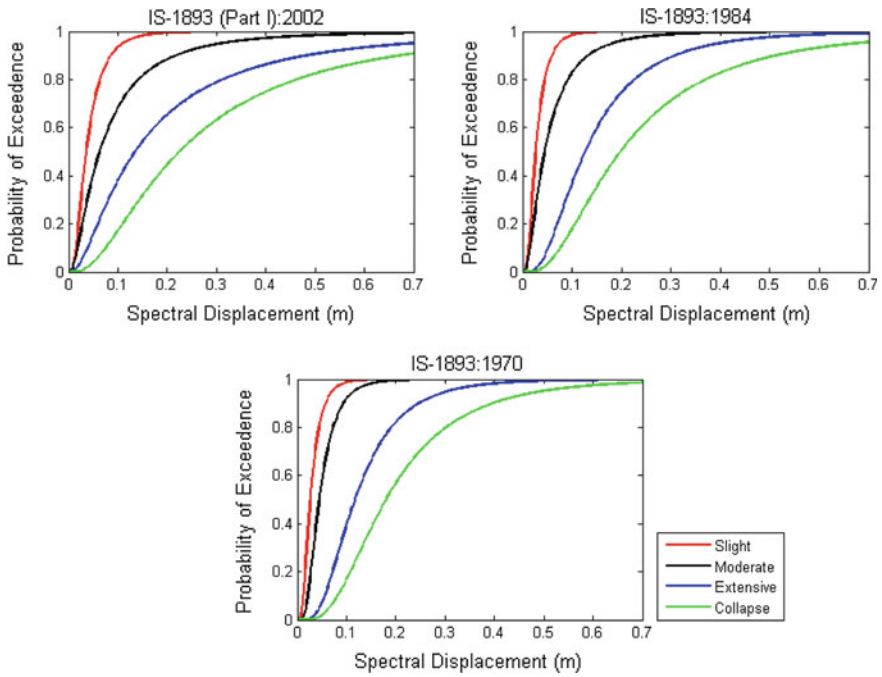
Fig. 4 Cumulative probability of being or exceeding the damage state and spectral displacement

8 Results

The fragility curve distributes among slight, moderate, extensive and collapse damage state. The probabilities of a building reaching or exceeding the various damage levels at a given response level sum to 100 %. From the fragility analysis, the spectral displacement at different damage states is compared against the Indian standard codes. Figure 4 plots the graph between cumulative probability of being or exceeding the damage state and spectral displacement for IS-1893:2002, IS-1893:1984 and IS-1893:1970 and Table 9 shows comparison of probability of exceedance at different damage states.

Table 9 Comparison of probability of exceedance (%) at different damage states

Damage states	IS-1893 (Part 1):2002			IS-1893:1984			IS-1893:1970		
	100 mm	300 mm	500 mm	100 mm	300 mm	500 mm	100 mm	300 mm	500 mm
Slight	90	99	100	98	100	100	99	100	100
Moderate	67	93	98	83	98	100	92	100	100
Extensive	39	77	89	39	87	98	40	94	98
Collapse	17	62	80	18	70	90	18	79	94

9 Conclusions

A new damage scale has been developed based on the response parameters obtained from non-linear time history analysis and damage index. The base shear is compared. The following conclusions are arrived at from the study.

1. Design by recent code or high code ensures proper ductility as the capacity is maximum by this code. More the ductility more is the energy dissipation before collapse.
2. In case of damage obtained by pushover analysis, the damage for IS-1893:1970 is maximum for a fixed value of roof displacement compared to IS-1893:1984 and IS-1893:2002, in which the damage obtained by IS-1893:2002 has the least value.
3. Conventionally, it lightens up that the inter-storey drift would increase as capacity goes on reducing, but for PGA 0.54g the inter-storey drift obtained by IS-1893:2002 is more than that obtained by IS-1893:1984.
4. Due to high ductility obtained by the most recent code, the pattern would follow that the maximum roof displacement will occur for IS-1893:2002, but at 0.54g PGA the maximum roof displacement for IS-1893:1984 comes out to be higher than IS-1893:2002.
5. The variability of the capacity curve for slight to collapse decreases from high to low codes. This is in par with the HAZUS MR4 earthquake model.
6. From the fragility curve, it is clearly observed that the values for slight to collapse increases with change from high to low codes. This is due to the fact that the ductility is of primary concern for energy dissipation.

The further scope of study would be to assess the vulnerability for different type of soil conditions and for different type of building stocks.

References

1. DiPasquale E, Ju J-W, Askar A, Cakmak AS (1990) Relation between global damage indices and local stiffness degradation. ASCE J Struct Eng 116(5):1440–1456
2. Ghobarah A, Abou-Elfath H, Biddah A (1999) Response-based damage assessment of structures. Earthq Eng Struct Dynam 28(1):79–104
3. HAZUS (1999) Earthquake loss estimation methodology. HAZUS99 service release 2 (SR2) technical manual, Federal Emergency Management Agency (FEMA), Washington
4. Powell GH, Allahabadi R (1988) Seismic damage prediction by deterministic methods: concept and procedure. Earthquake Eng Struct Dynam 16(5):719–734
5. Park Y-J, Ang AHS (1985) Mechanistic seismic damage model for reinforced concrete. ASCE J Struct Eng 111:722–739
6. Haselton CB (2012) Selecting and scaling earthquake ground motion for performing response history analyses. In: 15th world conference on earthquake engineering, Lisboa
7. Kunnath SK, Reinhorn AM, Lobo RF (1992) IDARC version 3.0: a program for the inelastic damage analysis of reinforced concrete structures. National Center for Earthquake Engineering and Research, Report # NCEER-92-0022. Buffalo, NY, USA, SUNY

8. Mihai M A (2013) Theoretical review of the damage indices used to model the dynamic nonlinear behavior of reinforced concrete structures, pp 109–119
9. Sanagle K, Patil S, Thakur S (2012) Evaluation of damage index of high rise building using non-linear static seismic analysis. Int J Emerg Technol Adv Eng 2(10):595–600
10. Vimala A, Kumar RP (2012) Displacement based damage estimation of RC bare frame subjected to earthquake loads: a case study on 4 storey building. In: 15th world conference on earthquake engineering, Lisboa

Part XXIX
Non-Destructive Test (NDT) and Damage Detection

Evaluation of Efficiency of Non-destructive Testing Methods for Determining the Strength of Concrete Damaged by Fire

J.S. Kalyana Rama and B.S. Grewal

Abstract An engineering assessment was performed on concrete cubes casted from M25 concrete for checking the efficiency of non-destructive testing methods namely Schmidt's rebound hammer test and Ultra Sonic Pulse Velocity test. The study was aimed at checking the viability of these above named non-destructive tests. Firstly, in the case of undamaged concrete structures and later on in the case of concrete structures damaged by fire, and then to compare the results to find out the efficiency of non-destructive testing methods. It is assumed that in the case of an undamaged structure the concrete is a homogenous mixture with equal strength at all depths. Hence, the non-destructive tests even if they are able to measure the surface strength like in case of the rebound hammer test may give a pretty accurate value when compared to the compressive tests performed in the laboratory. In the case of a structure, which has been damaged by fire, the concrete may no longer be homogenous at all depths and there might be considerable changes in its internal structure. Hence, this study is an attempt to carry out non-destructive tests on such concrete samples, which have been damaged by fire and then find out the viability and accuracy of the results when compared to the compressive tests performed in the laboratory.

Keywords Non-destructive testing · Rebound hammer test · Ultrasonic pulse velocity

1 Introduction

One of the advantages of concrete over other building materials is its inherent fire-resistive properties; however, concrete structures must still be designed for fire effects. Structural components still must be able to withstand dead and live loads

J.S. Kalyana Rama (✉) · B.S. Grewal
Birla Institute of Technology and Science (BITS),
Hyderabad Campus, Hyderabad, India
e-mail: jskr.publications@gmail.com

Fig. 1 Effect of fire on the resistance of a simply supported reinforced concrete slab (*Source* ASTM E119)
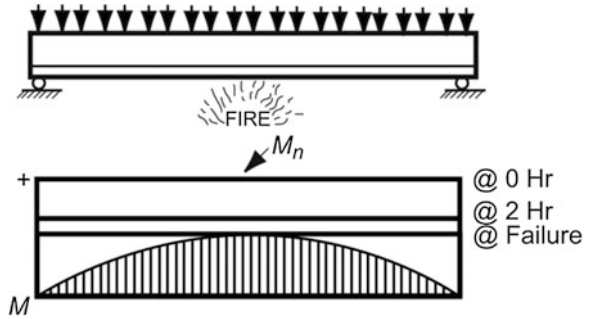
without collapse even though the rise in temperature causes a decrease in the strength and modulus of elasticity for concrete and steel reinforcement. In addition, fully developed fires cause expansion of structural components and the resulting stresses and strains must be resisted. In the design of structures, building code requirements for fire resistance are sometimes overlooked and this may lead to costly mistakes. It is not uncommon, to find that a concrete slab floor system may require a smaller thickness to satisfy strength requirements than the thickness required by a building code for a 2-h fire resistance.

For sound and safe design, fire considerations must, be part of the preliminary design stage. Determining the fire rating for a structure member, can vary in complicity from extracting the relevant rating using a simple table to a fairly complex and elaborate analysis. In the United States, structural design for fire safety is based on prescriptive approach. Attempts are being made to develop performance based design approach for structural design for fire. State and municipal building codes throughout the country regulate the fire resistance of the various elements and assemblies comprising a building structure.

Figure 1 shows the effect of fire on the resistance of a simply supported reinforced concrete slab. If the bottom side of the slab is subjected to fire, the strength of the concrete and the reinforcing steel will decrease as the temperature increase. However, it can take up to 3 h for the heat to penetrate through the concrete cover to the steel reinforcement. As the strength of the steel reinforcement decreases, the moment capacity of the slab decreases. When the moment capacity of the slab is reduced to the magnitude of the moment caused by the applied load, flexural collapse will occur. It is important to point out that duration of fire until the reinforcing steel reaches the critical strength depends on the protection to the reinforcement provided by the concrete cover.

1.1 ASTM E119 Standard Fire Test

The fire-resistive properties of building components and structural assemblies are determined by fire test methods. The most widely used and nationally accepted test

Fig. 2 Time temperature
curve (*Source* ASTM E119)
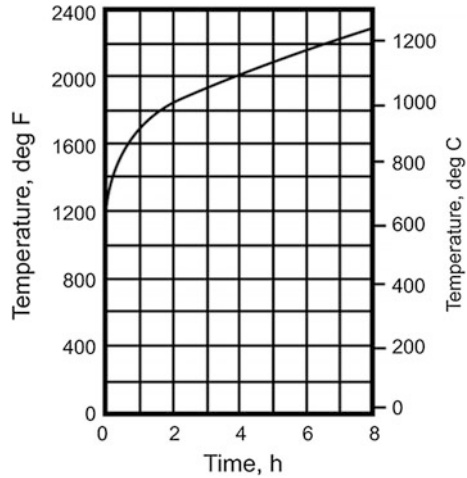
procedure is that developed by the American Society of Testing and Materials
(ASTM). It is designated as ASTM E119, Standard Methods of Fire Tests of
Building Construction and Materials. A standard fire test is conducted by placing a
full size assembly in a test furnace. Floor and roof specimens are exposed to a
controlled fire from beneath, beams are exposed from the bottom and sides, walls
from one side, and columns are exposed to fire from all sides. The temperature is
raised in the furnace over a given period of time in accordance with ASTM E 119
standard time-temperature curve shown in Fig. 2. This specified time-temperature
relationship provides for a furnace temperature of 540 °C at 5 min from the
beginning of the test, 700 °C at 10 min, 930 °C at 1 h, 1,010 °C at 2 h, and 1,100 °C
at 4 h.

1.2 Review of Work Done

To properly maintain the civil infrastructures, engineers required new methods of
inspection. Better inspection techniques are needed for deteriorating infrastructure
Rens et al. [1]. Now in the present century NDT has become more sophisticated, as it
has developed from a hammer to Impact Echo and Impulse response Lim and Cao
[2]. Shaw and Xu [3] have recognized the importance of being able to test in situ, and
this trend is increasing as compared to traditional random sampling of concrete for
material analysis. NDT methods may be categorized as: penetration tests, rebound
tests, pull out tests, dynamic tests, and radioactive methods. According to McCann
and Forde [4], five major factors that need to be considered in NDT survey are:
required depth of penetration, required vertical and lateral resolution, contrast in
physical properties between target and its surrounding, signal to noise ratio for the
physical properties between the target and its surroundings, and historical

information concerning the methods used in the construction of the structure. Breysse et al. [5] described the various aims of NDT methods such as to detect the condition of RC structures, rank the structures according to present condition, and compare the different Sanayei et al. [6] performed static truck load test on a newly constructed bridge, to capture the response of bridge when a truck traveled across it. Amini and Tehrani [7] designed experimentally four sets of exposure conditions, weight and compressive strength of the samples had been measured before and after the freeze thaw cycles, and the results were analyzed. Loizos and Papavasiliou [8] performed a comprehensive monitoring and data analysis research study by using Falling Weight deflectometer (FWD) for in situ evaluation of recycled pavements. Proverbio and Venturi [9] evaluated the reliability of rebound hammer test and UPV test on concrete of different composition and strength. Rens et al. [10] explained application of NDE methods for bridge inspection. Malavar et al. [11] used pull off tests to evaluate effects of temperature, moisture, and chloride content on CFRP adhesion. Pascale et al. [12] carried out an experimental program involving both destructive and nondestructive methods applied to different concrete mixtures, with cube strength varying from 30 to 150 MPa, to define a relation between strength and parameters. Almir and Protasio [13] used NDT methods to determine the compressive strength of concrete. Rens and Kim [14] inspected a steel bridge using several NDT methods. Bhadauria and Gupta [15] presented case study of deteriorated water tanks situated in the semitropical region of India. Amleh and Mirza [16] performed concrete cover test using NDT. Sharma and Mukherje [17] used ultrasonic guided waves for monitoring progression of rebar corrosion in chloride and oxide environment. Terzic and Pavlovic [18] applied NDT methods that is Image Pro Plus (IPP) and Ultrasonic Pulse Velocity (UPV), on the corundum and bauxite-based refractory concretes. Shah and Hirose [19] presented an experimental investigation of the concrete applying nonlinear ultrasonic testing technique. Ervin et al. [20] created an ultrasonic sensing network to assess reinforcement deterioration. Lee et al. [21] used UPV methods for determining setting time of concrete especially high-performance concrete (HPC). Shah et al. [22] described laboratory-based NDE techniques based on measurements of mechanical waves that propagate in the concrete. Methods for non-destructive testing of concrete such as rebound hammer testand ultrasonic pulse velocity test are also described in related Indian standards [23, 24]. The present study focuses on the assessing the behavior of a concrete specimen damaged by fire using Non-Destructive Testing tools rebound hammer and pulse velocity.

2 Preparation of Test Specimen

For the purpose of this work, twelve samples of concrete of grade M30 were prepared. The design mix of the concrete is given in Table 1. Each sample was a cube of size 150 mm × 150 mm.

Table 1 Design Mix for M30 concrete

Material	Quantity (kg/m^3)
Cement	380
Aggregate 20 mm	924
Aggregate 10 mm	359
Fine aggregate	711
Water	160
Admixture	1.90

2.1 Heating of Test Specimen

Cube sample number 1, 2 and 3 were tested in an undamaged condition for their compressive strength, whereas cube sample number 4, 5 and 6 were heated up to a temperature of 250 °C, cube sample number 7, 8 and 9 were heated up to a temperature of 500 °C and cube sample number 10, 11 and 12 were heated up to a temperature of 1,100 °C before carrying out the requisite tests. The heating of the cubes was carried out as per ASTM E 119 [25] instructions at a rate of increase of temperature given in Table 2. Details of the concrete specimens are presented in Table 3.

Table 2 Rate of heat application toe the test specimen with respect to time

Time (min)	Temp (°C)
5	540
10	700
60	930
120	1,010
240	1,100

Table 3 Details of concrete specimen prepared

Sample no.	Weight (kg)	Density (kg/m^3)	Test condition
1	8.30	2,459.26	Undamaged
2	8.36	2,477.04	Undamaged
3	8.18	2,423.70	Undamaged
4	8.21	2,432.59	Heated at 250 °C
5	8.28	2,453.33	Heated at 250 °C
6	8.15	2,414.81	Heated at 250 °C
7	8.09	2,397.04	Heated at 500 °C
8	8.23	2,438.52	Heated at 500 °C
9	8.17	2,420.74	Heated at 500 °C
10	8.12	2,405.93	Heated at 1,100 °C
11	8.32	2,465.19	Heated at 1,100 °C
12	8.29	2,456.30	Heated at 1,100 °C

3 Results and Discussion

All these cubes were initially tested for their strength using Non Destructive tests, namely Schmidt's rebound hammer test and Ultrasonic Pulse Velocity Test before being subjected to testing under compression testing machine for checking the actual value of the compressive strength of the cube. Figures 3, 4, 5 and 6 present the details about the rebound numbers obtained for the cubes to be tested.

Fig. 3 Rebound numbers achieved for undamaged cubes
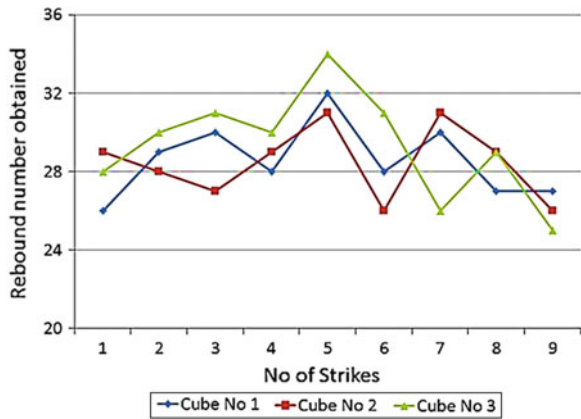
Fig. 4 Rebound numbers achieved for cubes damaged at 250 °C
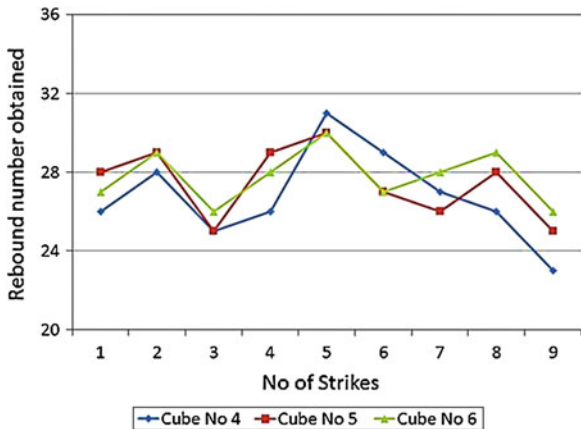
Fig. 5 Rebound numbers achieved for cubes damaged at 500 °C
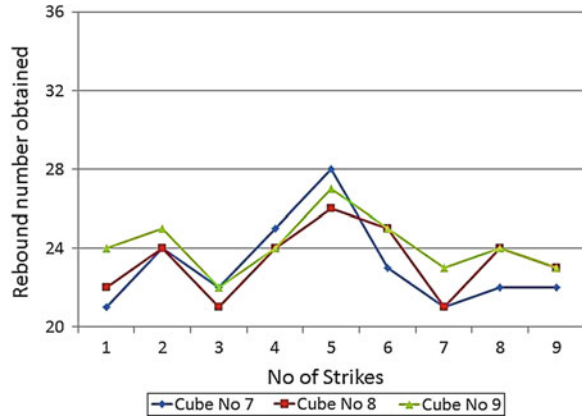
Fig. 6 Rebound numbers achieved for cubes damaged at 1,100 °C
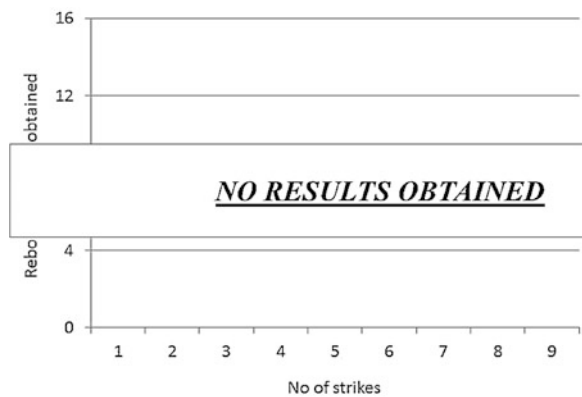
3.1 Performance of Ultrasonic Pulse Velocity

After carrying out the rebound hammer test, the concrete specimens were subjected to Ultrasonic Pulse Velocity test, which is used to find out the quality of the concrete. The results obtained from this test are given in Table 4.

3.2 Performance of Compressive Machine Test

Once, the Non Destructive tests are completed the concrete cubes are to be subjected to compressive tests using Compression testing machine, the results of which are given in Table 5.

Table 4 Test results obtained using ultrasonic pulse velocity test

Sample no.	Heated at (°C)	Distance between transducers (mm)	Time (μs)	Speed (kmph)	Quality of concrete
1	–	150	36.2	4.143	Good
2	–	150	37.5	4.002	Good
3	–	150	37.9	3.957	Good
4	250	150	41.1	3.649	Good
5	250	150	42.1	3.563	Good
6	250	150	40.4	3.708	Good
7	500	150	47.9	3.128	Doubtful
8	500	150	49.6	3.021	Doubtful
9	500	150	50.5	2.968	Doubtful
10	1,100	150	808	0.185	Very poor
11	1,100	150	874	0.171	Very poor
12	1,100	150	786	0.191	Very poor

Table 5 Compressive strength achieved using compression testing machine

Sample no.	Heated at (°C)	Comp. strength (N/mm^2)
1	–	38.8
2	–	39.6
3	–	39.4
4	250	36.0
5	250	35.1
6	250	35.6
7	500	28.9
8	500	28.4
9	500	30.7
10	1,100	6.2
11	1,100	6.0
12	1,100	6.3

3.3 Analysis of Data

Comparing the compressive strength obtained using Compressive Machine Test and the Non Destructive test, it is found that the variation between the two results is more in case of undamaged samples but as the concrete specimen are subjected to increasing temperatures this variation continuously decreases. But at a temperature of 1,100 °C the rebound hammer is not able to give any reading whereas the compressive machine indicates strength of 6 N/mm^2. This is although of no significance where the required strength of a structural element is concerned. Detailed test results are compared in Table 6.

Table 6 Comparative results for rebound hammer test and compression testing machine

Sample no.	Heated at (°C)	Average rebound number	Compressive strength (N/mm^2)		Ratio actual/RHT	Average ratio
			RHT	Actual		
1	–	28.2	23.3	38.8	1.66	1.62
2	–	28.4	23.6	39.6	1.63	
3	–	29.3	25.0	39.4	1.58	
4	250	26.7	22.7	36.0	1.58	1.54
5	250	27.4	23.2	35.1	1.51	
6	250	27.6	23.4	35.6	1.52	
7	500	23.3	19.8	28.9	1.46	1.48
8	500	23.1	19.6	28.4	1.45	
9	500	24.1	20.5	30.7	1.49	
10	1,100	–	–	6.2	–	–
11	1,100	–	–	6.0	–	
12	1,100	–	–	6.3	–	

Table 7 Reduction in strength of concrete with increase in temperature

Concrete specimen	Compression testing machine reading (N/mm^2)	% decrease in strength
Undamaged	39.3	0
Heated up to 250 °C	35.6	9.4
Heated up to 500 °C	29.3	25.4
Heated up to 1,100 °C	6.2	84.2

In addition when the data is studied to check the decrease in strength of concrete with increase in temperature, it is found that the decrease in strength up to 250 °C is about 10 %, which further falls to 25 % at temperature of 500 °C. After the temperature crosses 500 °C, the decrease in strength is observed to be sharper and by the time the temperature reaches a value of 1,100 °C, the reduction in strength is almost 85 %. The reduction in strength is given in Table 7 and also shown in graphical form in Fig. 7.

Checking for the accuracy of the Schmidt's rebound hammer testas compared to the compression machine testing, from Table 8 it was found that the accuracy of results given for undamaged cubes by rebound hammer test were having an accuracy of 62 % when compared to results obtained by compression machine testing. When the same tests were performed for cubes heated up to 250 °C, the accuracy increased to 65 % and it further increased to 69 % when the tests were conducted for cubes heated at 500 °C. No data could be derived for cubes heated at

Fig. 7 Reduction in compressive strength of concrete with increase in temperature
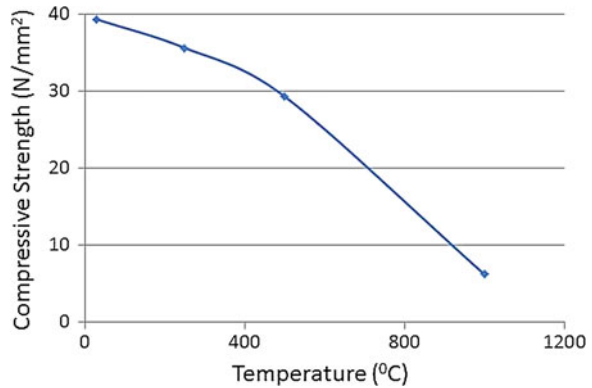
Table 8 Comparative results for rebound hammer test and compression testing machine

Concrete specimen	RHT (N/mm^2)	CTM (N/mm^2)	% accuracy of RHT
Undamaged	24.0	39.3	61
Heated up to 250 °C	23.1	35.6	64
Heated up to 500 °C	19.9	29.3	68
Heated up to 1,100 °C	–	6.2	–

1,100 °C as the rebound hammer test failed to give any reading for concrete specimens heated at that temperature.

4 Conclusions

In conclusion it can be said that concrete although doesn't melt under high temperatures but it may go out of shape slightly and there is a significant reduction in strength and also appearance of cracks when subjected to higher temperatures. Therefore, any building or structure which has been damaged by fire should certainly be checked for its strength to ensure whether it is fit for occupancy and usage after the accident or not. In case of severe fires where temperatures are high, the damage will be to a much higher extent as compared to a fire of small scale as the relation between loss of strength of concrete and increase in temperature is not linear as shown in Table 7 and Fig. 7.

It has been observed that the accuracy achieved using Schmidt's rebound hammer testimproved as the damage caused to the concrete by high temperatures in fire increased as shown in Table 8. The tests carried out using Ultrasonic Pulse Wave Equipment further confirmed the extent of damage to the concrete and were in agreement to the readings achieved using the hammer test.

References

1. Rens KL, Wipf TJ, Klaiber FW (1997) Review of nondestructive evaluation techniques of civil infrastructure. J Perform Constructed Facil 11(4):152–160
2. Lim MK, Cao H (2013) Combining multiple NDT methods to improve testing effectiveness. Constr Build Mater 38:1310–1315
3. Shaw P, Xu A (1998) Assessment of the deterioration of concrete in NPP—causes, effects and investigation methods. NDT.Net, vol 3(2)
4. McCann DM, Forde MC (2001) Review of NDT methods in the assessment of concrete and masonry structures. NDT E Int 34(2):71–84
5. Breysse D, Klysz G, D'erobert X, Sirieix C, Lataste JF (2008) How to combine several non-destructive techniques for a better assessment of concrete structures. Cem Concr Res 38(6):783–793
6. Sanayei M, Phelps JE, Sipple JD, Bell ES, Brenner BR (2012) Instrumentation, nondestructive testing, and finite element model updating for bridge evaluation using strain measurements. J Bridge Eng 17(1):130–138
7. Amini B, Tehrani SS (2011) Combined effects of saltwater and water flow on deterioration of concrete under freeze-thaw cycles. J Cold Reg Eng 25(4):146–161
8. Loizos A, Papavasiliou V (2006) Evaluation of foamed asphalt cold in-place pavement recycling using nondestructive techniques. J Transp Eng 132(12):970–978
9. Proverbio E, Venturi V (2005) Reliability of nondestructive tests for onsite concrete strength assessment. In: 10th DBMC, Lyon, France
10. Rens KL, Nogueira CL, Transue DJ (2005) Bridge management and nondestructive evaluation. J Perform Constructed Facil 19(1):3–16
11. Malavar LJ, Joshi NR, Novinson T (2003) Environmental effects on the short term bond of carbon fibre reinforced (CRPF) composites. J Compos Constr 7(1):58–63
12. Pascale G, Leo AD, Bonora V (2003) Nondestructive assessment of the actual compressive strength of high-strength concrete. J Mater Civ Eng 15(5):452–459
13. Almir PF, Protasio FC (2000) Application of NDT to concrete strength estimation. NDT.Net, vol 5(2), pp 1–6
14. Rens KL, Kim T (2007) Inspection of Quebec street bridge in Denver, Colardo: destructive and nondestructive testing. J Perform Constructed Facil 21(3):215–224
15. Bhadauria SS, Gupta DMC (2007) In situ performance testing of deteriorating water tanks for durability assessment. J Perform Constructed Facil 21(3):234–239
16. Amleh L, Mirza MS (2004) Corrosion response of a decommissioned deteriorated bridge deck. J Perform Constructed Facil 18(4):185–194
17. Sharma S, Mukherje A (2011) Monitoring corrosion in oxide and chloride environments using ultrasonic guided waves. J Mater Civ Eng 23(2):207–211
18. Terzic AM, Pavlovic LM (2010) Application of results of non-destructive testing methods in the investigation of microstructure of refractory concretes. J Mater Civ Eng 22(9):853–857
19. Shah AA, Hirose S (2010) Nonlinear ultrasonic investigation of concrete damaged under uniaxial compression step loading. J Mater Civ Eng 22(5):476–483
20. Ervin BL, Kuchama DA, Bernhard JT, Reis H (2009) Monitoring corrosion of rebar embedded in mortar using high frequency guided ultrasonic waves. J Eng Mech 135(1):9–18
21. Lee HK, Lee KM, Kim YH, Bae DB (2004) Ultrasonic in-situ monitoring of setting process of high performance concrete. Cem Concr Res 34(4):631–640
22. Shah SP, Popovics JS, Subramaniam KV, Aldea CM (2000) New directions in concrete health monitoring technology. J Eng Mech 126(7):754–760

23. IS 13311 Part 1 (1992) Non-destructive testing of concrete—methods of test—ultrasonic pulse velocity test. Bureau of Indian Standard, New Delhi
24. IS 13311 Part 2 (1992) Non-destructive testing of concrete—methods of test—rebound hammer. Bureau of Indian Standard, New Delhi
25. ASTM E 119 (2010) Standard methods of fire tests of building construction and materials. ASTM International, Pennsylvania

Damage Detection in Structural Elements Through Wave Propagation Using Weighted RMS

**T. Jothi Saravanan, Karthick Hari, N. Prasad Rao
and N. Gopalakrishnan**

Abstract The paper presents an application of wave propagation for damage detection in an aluminum plate. The experimental investigation was conducted on an aluminum plate by generating the wave with Lead Zirconate Titanate (PZT) patches by function generator. Normal responses are measured with the Scanning Laser Doppler Vibrometer (SLDV). Eleven sine cycles modulated by hanning window with frequency of 5 kHz have been used as an excitation signal. Recorded signals were analyzed using the signal processing techniques developed for damage detection. The time signals recorded during measurement have been utilized to calculate the values of root mean square (RMS) response. It has turned out that the values of RMS differed significantly in damaged areas from the values calculated for the healthy ones. It is thus become possible to identify precisely the locations of damage over the entire measured surface. The magnitude of propagating wave decreases with travelled distance from the excitation point. This effect produces larger values of RMS near the excitation. To equalize RMS function in whole area time samples are multiplied by a weighting factor called weighted RMS function. The obtained results are presented in the form of scatter plots and numerical contour maps. It may be concluded that the proposed approach enables damage localization in a relatively fast and precise manner.

Keywords Structural health monitoring · Damage detection · Wave propagation · Scanning laser doppler vibrometer · Weighted RMS

T. Jothi Saravanan (✉) · N. Prasad Rao · N. Gopalakrishnan
Academy of Scientific and Innovative Research (AcSIR), Chennai, India
e-mail: tjs.saravanan@gmail.com

K. Hari
Birla Institute of Technology & Science, Pilani, Pilani, India

T. Jothi Saravanan · N. Prasad Rao · N. Gopalakrishnan
CSIR-Structural Engineering Research Centre, Chennai, India

1 Introduction

Damage is defined as an adverse change in the material and geometric properties of a structural system, including changes in system connectivity, which in turn affect the system's performance. Structural Health Monitoring (SHM) is the process of damage detection and the health characterization strategy for engineering structures. Wave propagation based automatic structural health monitoring techniques and the warning-alert systems are some techniques widely adopted in aerospace and nuclear industry. These techniques are however, not in a matured state of development for civil engineering structures and are still evolving. Hence research in this area is of paramount importance [1, 2].

SHM technologies have emerged, for the last 10–15 years, creating an exciting new field within various branches of engineering. Academic conferences and scientific journals have been established during this time that specifically focuses on SHM. These technologies are currently becoming increasingly common [3, 4]. Structural damage detection with smart material can be performed using several methods: (a) wave propagation, (b) frequency response transfer function, or (c) electromechanical (E/M) impedance. Wave propagation in structural elements has been studied over considerable period of time. Although mathematical frameworks are well developed wave propagation problems in real scale engineering structures is an open area of research [5]. The Lamb wave based damage detection techniques using structurally integrated smart material for SHM is still in its formative years [6].

Lamb waves are most complicated guided plate waves. Lamb waves are of two basic varieties, symmetric mode and anti-symmetric mode. Both Lamb wave types are quite dispersive [7]. The velocity of these waves depends on the product of frequency of excitation and thickness of the plate [3, 8]. Lamb waves are guided waves traveling along thin plates, whereas Rayleigh waves are guided waves constraint to the surface. Love waves are guided wave traveling in layered materials, whereas Stoneley waves are guided waves constrained to the material interface [2].

The other papers in this field are described subsequently and by no-means the list is exhaustive. Similar results of experimental measurements in aluminum plates by LSDV for damage detection purposes by Lamb waves were presented in [9, 10], where the surface around the damage was carefully scanned.

The application of a one dimensional (1D) version of LSDV reported in [11] for measurements of Lamb waves in an aluminum plate. This work highlights the effectiveness of LSDV in separation of the in-plane S0 and the out-of-plane A0 Lamb wave modes that can be utilized for damage detection purposes. The application of Lamb waves for damage detection in composite plates was successfully demonstrated in [12], confirming that this approach can be used for delamination detection and localization as well as the assessment of delamination size. The application of two different integral-based indices for damage quantification is described in [13], these being the integral mean value (IMV) and the root mean

square (RMS). The paper [14] presents the method of damage identification in an aluminum plate with riveted stiffeners.

In this paper, a methodology for damage identification in an aluminum plate is presented. In the present work the damage is simulated by adding an additional mass to the plate surface at a specified location. For the purpose of damage detection wave propagation phenomenon is used. Elastic waves have been generated with PZT patches and the normal responses are measured with LSDV. It is envisioned that the proposed special signal processing techniques can be used for analyzing the recorded signals for damage detection. The measured signals have been recalculated for every measurement point by application of RMS and the energy distribution has been analyzed.

2 Experimental Set Up

The experiment was conducted on an aluminum plate of 0.94 × 0.135 × 0.004 m dimensions. Figure 1a shows the test specimen and the schematic picture of analyzed specimen. It also shows the localization of measurement points defined for LSDV and the location of excitation. Figure 1b shows the grid points generated by the LSDV and also explains the scatter plot using MATLAB. Damage has been simulated by attaching a small additional mass of 25 g fixed on the plate surface [square metal]. During the experiment the specimen has been isolated from the influence of external vibration source.

All measurements were recorded using a PSV-500 Laser Scanning Doppler Vibrometer (LSDV). The vibrometer consist of optics (scanning head), electronics (front end), and control (Data Management system). The scanning head consist of interferometer, the scanning mirrors to deflect the laser beam and a video camera to
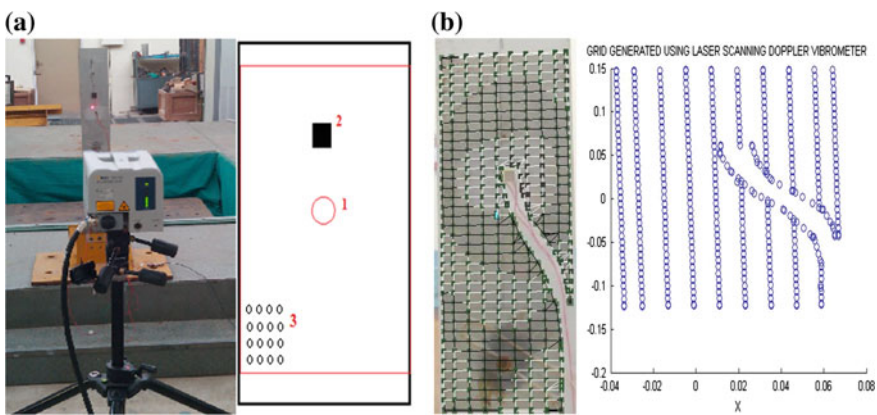
Fig. 1 **a** Schematic view of measured specimen (*1* excitation point; *2* additional mass; *3* some measurement points); **b** plate with grid points and scatter grid plot
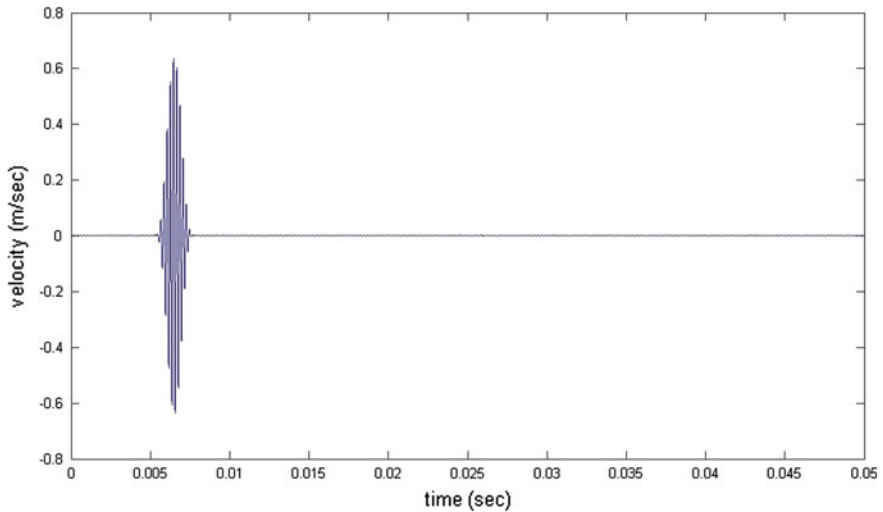
Fig. 2 Excitation signal of frequency of 5 kHz

visualize the measurement object. The light source of instrument is a helium-neon laser with wavelength of 633 nm. This is a multi-mode laser, in which there can be typically two longitudinal modes [Laser Class-II].

The excitation applied is a burst signal followed by a zero padding signal. Generated wave packages for measurements are composed of eleven sine cycles modulated by hanning window with a center frequency of 5 kHz which have been used as an excitation signal (Fig. 2). The excitation is given using Lead Zirconate Titanate (PZT) patches [PI Ceramic 151] by the internal function generator. The sampling frequency was set up at 50 kHz and 2,500 time samples were registered during each measurement. In order to ensure the fading out of previously generated elastic waves, a time interval of 50 ms was kept between each burst of input excitation.

3 Results and Discussions

In order to obtain a picture of the propagating wave the velocities are measured at every measurement point in the direction perpendicular to the plate surface. The signal has been quantified to 2,500 samples and every measurement has been repeated ten times and the average value has been calculated in order to increase the signal-to-noise ratio. For more accurate damages pattern recognition, the root mean square (RMS) based damage detection method is proposed. Owing to the fact that the additional mass introduces discontinuity, propagating waves are reflected and the damage became a source of new reflecting waves. This phenomenon is used for

damage detection. The measured signals have been recalculated for every measurement points according to the following relation:

$$RMS = \sqrt{\frac{\sum_{i=1}^{N} f_i^2}{N}} \qquad (1)$$

where f_i^2 is a squared 'i' sample vibration magnitude and 'N' is the number of registered samples (2,500 in this case). While propagating the wave reflects from the damage and this fact leads to changes of the energy distribution. These subtle changes can also be associated with changes in the RMS values and therefore can be used for damage detection and localization purposes. Therefore calculating the signal energy for every points may give accurate information about the damages. However, relatively large values of RMS function usually dominate the areas near the excitation points and as a result; almost the whole range of scale values is associated with this small area. In order to overcome this problem it is proposed to use a logarithmic scale for the values of the RMS function calculated. Figures 3 and 4 presents the RMS and logarithmic RMS damage maps for the aluminum plate
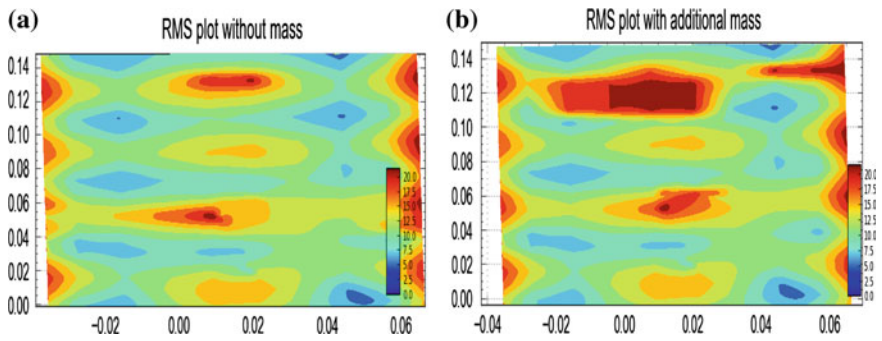
Fig. 3 RMS map for 5 kHz excitation frequency: **a** without mass, **b** with mass
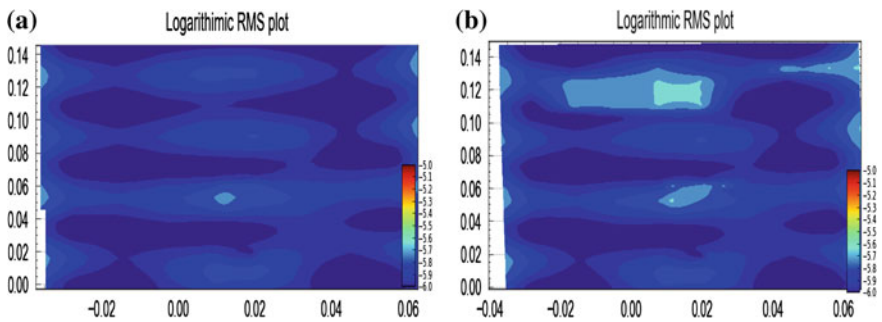
Fig. 4 Log (RMS) map for 5 kHz excitation frequency: **a** without mass, **b** with mass

under investigation calculated based on all 2,500 time samples, i.e., covering the total time span of 50 ms. For better visibility, the energy distribution in logarithmic scale is presented.

From the illustration, plate with additional mass can be compared with the reference map. As it may be concluded from the presented graphs, the place of damage is barely identified.

Weighted RMS: The magnitude of the propagating wave from the excitation point decreases with travelled distances. In order to equalize and smoothen the distribution of the RMS function in the whole surface area under investigation, the registered time samples were multiplied by a weighting factor, called Weighted RMS. The measured signals have been recalculated for every measurement point according to the following relation,

$$W^k\_RMS = \sqrt{\frac{\sum_{i=1}^{N}(f_i^2 \cdot i^k)}{N}} \qquad (2)$$

where W^k_RMS is proposed weighted RMS function and 'k' is a power of the weight factor. Comparison of W^k_RMS and log (W^k_RMS) calculated using 2,500 time samples for different 'k' values are shown in Figs. 5 and 6. It is worth to notice that the higher 'k' factor influences on the RMS function directly. Generally it is observed that the resolution of RMS damage maps can be easily and effectively increased by the use of different values of the weighting factor.

From the experimental measurements by LSV, the results obtained confirm that better resolution corresponds to higher values of the weighting factor W^k, i.e., for
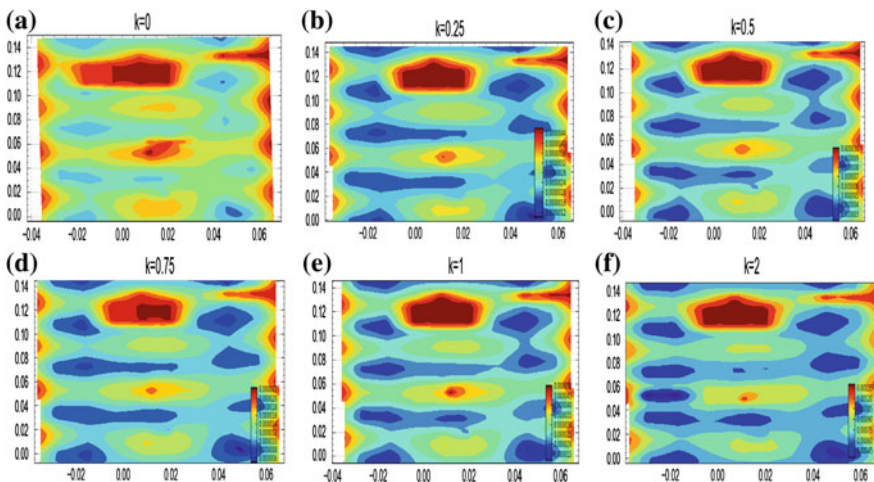
Fig. 5 W^k_RMS function for aluminum plate with mass
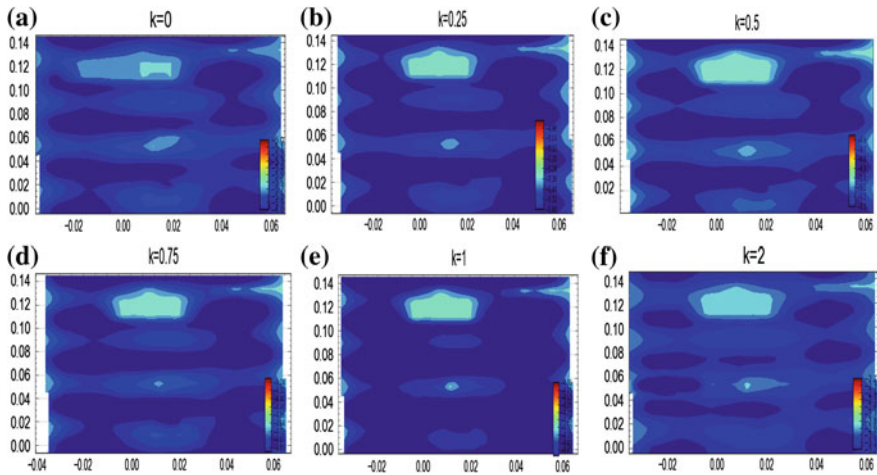
Fig. 6 Log (W^k_RMS) function for aluminum plate with mass

linear $k = 1$ or square $k = 2$ weighted RMS damage maps. However, attention must be given to minimize the influence of the boundary reflected waves. But in case of logarithmic RMS damage maps the influence of the weighting factor W^k is much less prominent and relatively good resolution of the maps can be obtained, even for the unweighted case, i.e., when the weighting factor $W^k = 1$, as clearly seen from the Fig. 6.

4 Conclusion

The paper presents an experimental method of localizing damage in a plate-like structure using low-frequency elastic waves by a new scanning technique based on a complete non-contact laser scanning vibrometery system (LSDV) using a signal processing technique on measured signal for damage visualization and diagnosis. A series of scanning experiments had been performed in order to obtain features related to damage. The method is based on changes in energy distribution of the propagating wave obtained by calculating RMS values at every measured point. It is envisioned that the proposed approach shall be appropriate for precise damage visualization. Since the introduced damage is in the form of additional mass which replicate as structural discontinuity, impedance around the attached mass element changes and so does the energy of propagating and reflecting waves and as a consequence, damage becomes a source of new waves. These effects are clearly registered on the resulting RMS numerical maps. The weight process offers improved localization and detection of damage from the excitation point as well as the structural boundaries. Also, logarithmic values of RMS function allow easier

and effective damage recognition. Also, the present study has to be extended in the area of signal processing and for actual damage detection within more complex structures. In summary, the method shows great potential for rapid damage localization of structural elements and further work is in progress in this direction for other large structures.

References

 1. Dawson B (1976) Vibration condition monitoring techniques for rotating machinery. The shock and vibration digest, vol 8(12). Springer, London, p 3
 2. Giurgiutiu V (2008) Structural health monitoring with piezoelectric wafer active sensors. Elsevier, London
 3. Inman DJ, Farrar CR, Lopes V Jr, Steffen V Jr (2005) Damage prognosis for aerospace, civil and mechanical systems. Wiley, West Sussex
 4. Structural Health Monitoring (2011) Proceedings of the 8th international workshop on structural health monitoring 2011, Stanford
 5. Rucka M (2010) Experimental and numerical studies of guided wave damage detection in bars with structural discontinuities. Arch Appl Mech 80:1371–1390
 6. Doyle JF (1997) Wave propagation in structures: spectral analysis using fast discrete Fourier transforms, 2nd edn. Springer, New York
 7. Staszewski WJ, Boller C, Tomlinson GR (2004) Health monitoring of aerospace structures. Wiley, West Sussex
 8. Radzienski M, Dolinski L, Krawczuk M, Zak A, Ostachowicz W (2011) Application of RMS for damage detection by guided elastic waves. J Phys Conf Ser 305:012085
 9. Staszewski WJ, Lee BC, Mallet L, Scarpa F (2004) Structural health monitoring using scanning laser vibrometry: I. Lamb wave sensing. Smart Mater Struct 13:251–260
10. Mallet L, Lee BC, Staszewski WJ, Scarpa F (2004) Structural health monitoring using scanning laser vibrometry: II. Lamb waves for damage detection. Smart Mater Struct 13:261–269
11. Leong WH, Staszewski WJ, Lee BC, Scarpa F (2005) Structural health monitoring using scanning laser vibrometry: III. Lamb waves for fatigue crack detection. Smart Mater Struct 14:1387–1395
12. Radzienski M, Ostachowicz W (2011) Experimental studies of structure inspection. In: Structural health monitoring. Trans Tech Publications, Stanford, pp 2245–2251
13. Zak A, Radzienski M, Krawczuk M, Ostachowicz W (2012) Damage detection strategies based on propagation of guided elastic waves. Smart Mater Struct 21:18
14. Radzieńskib M, Dolińskia L, Krawczuka M, Palacza M (2013) Damage localization in a stiffened plate structure using a propagating wave. Mech Syst Signal Process 39(1–2):388–395

The Health Monitoring Prescription by Novel Method

P.V. Ramana, Surendra Nath Arigela and M.K. Srimali

Abstract This paper presents, knowledge of the way in which cracks are propagated within the material is a key aspects of understanding. The paper mainly focused on full-field measurement method such as digital image correlation (DIC) is increasingly used in the field of experimental mechanics for non-destructive evaluation system. The study is based on displacement error assessment from synthetic speckle images. The use of an image analysis procedure to capture the crack initiation and propagation process is described, which utilizes digital images of the concrete structure while undergoing the cracking process. It introduce concepts from the very basics and lead to advanced modeling (analytical or numerical), practical aspects (including software or hardware issues). The formed cracks are visible at relatively small crack openings, allowing a thorough investigation and analysis of the cracking process in concrete structure. The resulting displacement information reveals the average motion present from the center of each of the small sub images used in the analysis, relative to the original position. It uses image processing to go from several images of material, and to then calculate the deformation at any point in the field, and to then find crack propagation and strain values. The results obtained with this method have shown that it is possible to monitor relatively small displacements on the specimen surface independently of the scale of the representative area of interest. These results show a great application potential of the DIC technique for various situations such as inspecting shrinkage-induced cracks in fresh concrete, masonry and reinforced concrete structures, and safety of bridges.

P.V. Ramana (✉) · M.K. Srimali
NMDCC, Department of Civil Engineering, Malaviya National Institute of Technology (MNIT), Jaipur, India
e-mail: pvr4567@gmail.com

S.N. Arigela
Sangam University, Bhilwara, India

1 Introduction

The digital image correlation (DIC) technique have been increasing in popularity, especially in micro and nano-scale mechanical testing applications due to its relative ease of implementation and use. It refers to a class of non-contacting methods that acquire images of an object in digital form and perform image analysis to extract sensor-plane motions that can be converted into full-field measurements on the corresponding object [1]. The digital image correlation technique developed in 1980s for measuring the object deformation. This technique is capable of correlating the digital images of an object before and after deformation and further determining the displacement and strain field and crack variation of an object based on the corresponding position on the image. Advances in computer technology and digital cameras have been the enabling technologies for this method and while DIC can be and has been extended to almost any imaging technology. Therefore, the digital image correlation technique is developed to identify the strain and crack propagation. This technique is non-destructive for inspecting the whole displacement and crack field. This is a digital method that employs tracking and image registration techniques for accurate 2D and 3D measurements of changes in images and motion of speckle patterns on a specimen surface before and after deformation of the body. Today, DIC is an important method for characterizing the mechanical response of homogeneous and heterogeneous materials undergoing nominally planar deformation, with commercial grade software available to simplify the image analysis component of the measurement process. It takes advantage of the fact that applied stresses change both the thickness and digital properties of materials, to determine displacements and crack propagation in concrete structures. Cracks induced by external excitation on a material that has defects may generate the stress concentration phenomenon. In this regard, one of important tool is digital camera. Camera with CCD array (small photo sensitive cells and high pixel count) records intensity of light falling on a pixel [2]. Array in high resolution camera is rectangular with thousand or more pixels per line and a thousand or more lines per image. (3×3 pixel) signal from CCD array is digitized and gives a reading of the light intensity for each pixel. Intensity readings are shown as 0 from dark pixels and 100 for light pixel (Grey Scale) see in Fig. 1. Storage of image into pixel and combination of pixel is called convolution. Sensor is an array (rows and columns) of light-sensitive semi-conductors called pixels. Each pixel emits electrons when hit by photons. Number of electrons is proportional to the number of photons (amount of light) [2].

Each pixel is stored as a byte of memory. Byte values range 0–255 (256 scales of gray) see in Fig. 2. Digital Image Correlation (DIC) is a full-field image analysis method, based on grey value digital images that can determine the contour and the displacements of an object under load in three dimensions. Due to rapid new developments in high resolution digital cameras for static as well as dynamic applications, and computer technology, the applications for this measurement method has broadened and DIC techniques have proven to be a flexible and useful
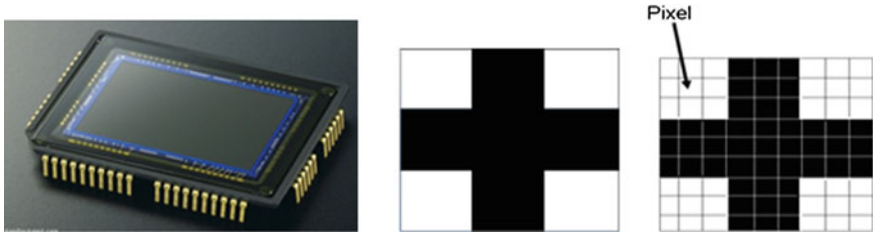
Fig. 1 CCD image sensor (charge coupled device)

Fig. 2 Gray scale images

tool for deformation analysis. For example a 640×480 gray scale image requires over 307,200 bytes (over 300 kB) of storage. Image is stored in the computer as a matrix of gray-scale values. It can divide the matrix into subsets and calculates the displacements of all subsets. Differentiate the displacement data to calculate the crack propagation in structure. The mechanical properties of concrete are very closely related to the formation of cracks [3].

2 Experimental Set up and Procedure

Figure 3 shows that the test setup for DIC, which includes an image grabbing equipment focused lights and computer system. A digital camera (effective megapixels) was used to get digital images from RC test specimen surfaces. Camera with CCD array has (small photosensitive cells and high pixel count) records intensity of

Fig. 3 Setup for DIC
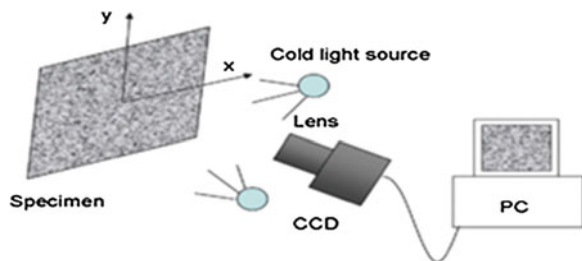
light falling on a pixel. Array in high resolution camera is rectangular with thousand or more pixels per line and a thousand or more lines per image. Before experiment, specimens were prepared by applying a fine spray paint pattern to the surface and generated the speckle random pattern necessary for the image correlation. The images of the specimens were captured continuously at various instances during loading and unloading regimes up to complete failure. The images have been taken for all the cycles using a digital camera and a remote control to avoid any vibration and also to keep the distance between camera lens and the specimen unchanged. The testing procedure developed for the present work consisted of applying a load to a single-edge notched specimen. In particular, for cyclic tests, one key aspect is related to the estimation of crack opening and closure levels when studying the propagation conditions. The latter ones could be determined by analyzing crack opening displacements measured by DIC. In the following, another will be followed to determine the crack position. When the propagation path is not straight, edge detection procedures can also be used to determine the shape of the crack or even the correlation residuals themselves when a global approach to DIC is used. Damage mechanisms could be analyzed in a quantitative manner when using the measured displacement fields as shown in Figs. 4, 5 and 6 [4].
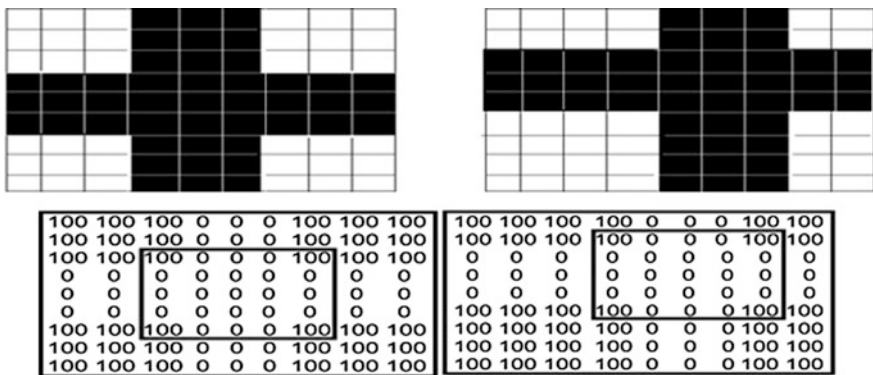
Fig. 4 The reference image to deformed image

Fig. 5 Initial at zero displacement
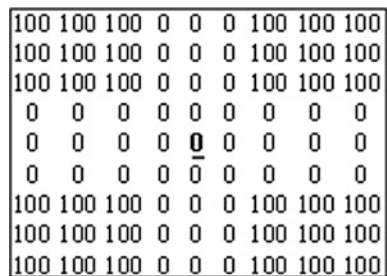
Fig. 6 Displacement at
$C(5,5,-2,-2)$

100	100	100	100	0	0	0	100	100
100	100	100	100	0	0	0	100	100
0	0	0	0	0	0	0	0	0
0	0	0	0	0	0	0	0	0
0	0	**0**	**0**	**0**	0	0	0	0
100	100	**100**	100	0	0	0	100	100
100	100	**100**	100	0	0	0	100	100
100	100	100	100	0	0	0	100	100
100	100	100	100	0	0	0	100	100

Above represents the initial and final position of pixels before and after apply the loads. It compares reference image to deformed image. It is very simple in concept. Digital camera takes picture of surface of the specimen Image is downloaded from camera to a frame grabbing circuit card. Analog signal from CCD array are then digitized. The data is stored for subsequent processing. Surface of specimen is sprayed with target pattern. This is photographed before and after specimen is deformed. Digital image of specimen contains intensity measurements at each pixel location on CCD (charge couple device-sensor) array before and after. Using target features and their location, displacement field is generated. Accuracy up to 0.02 pixels has been achieved. It tracks the gray value pattern of subsets and calculates the displacement and cracks of all subsets.

$$I(x,y) = A + Bfx + Cfy + Dfxfy$$

where fx and fy are the fractional part of x and y

$$A = I(ix, iy)$$
$$B = I(ix + 1, iy) - A$$
$$C = I(ix, iy + 1) - A$$
$$D = I(ix + 1, iy + 1) - (A + B + C)$$

where ix and iy are the integer part of x and y

$$C(x, y, u, v) = \sum_{i,j=-n/2}^{n/2} (I(x+i, y+j) - I^*(x+u+i, y+v+j))^2$$

At the center pixel,

$$C(5, 5, -2, -2) = 0$$

$$C(5, 5, -2, -2) = \sum_{i,j=-2}^{2} (I(5+i, 5+j) - I^*(5-2+i, 5-2+j))^2$$

$$(100 - 0)^2 + (0 - 0)^2 + (0 - 0)^2 + (0 - 0)^2 + (100 - 0)^2$$
$$+ (0 - 100)^2 + (0 - 100)^2 + (0 - 100)^2 + (0 - 100)^2 + (0 - 0)^2$$
$$+ (0 - 100)^2 + (0 - 100)^2 + (0 - 100)^2 + (0 - 100)^2 + (0 - 0)^2$$
$$+ (0 - 100)^2 + (0 - 100)^2 + (0 - 100)^2 + (0 - 100)^2 + (0 - 0)^2$$
$$+ (100 - 100)^2 + (0 - 100)^2 + (0 - 100)^2 + (0 - 100)^2 + (100 - 0)^2 = 18{,}000$$

3 Problem Statements and Results

There are two types of different section solved by using DIC.

Problem 1: In this problem, one has taken the reinforced concrete beam providing notch at below middle portion. Application shown below describe the behavior on simply supported concrete beam is exposed to a concentrated load in the middle of the span, as shown in Fig. 7. The beam transverse section is rectangular and it has a notch in center span lower side. The properties of reinforced concrete beam mentioned below and these properties are same for another two problems.

Young's modulus (E) = 5,000 $\sqrt{fck}$, f_{ck} = 25 N/mm^2, and Poisson's ratio (ϑ) is 0.15.

DIC test were performed on the different concrete beam specimens. This step-by-step equilibration with gradually increasing of relative load helped to get cracks in the different type of beams. Images of specimen surface showing cracks in above Fig. 8. An optical technique (DIC technique) has been used to measure the 3D and 2D surface displacements and strain in reinforced concrete along with the written mathematical program Matlab$^{®}$. For digital image correlation the speckle pattern was made properly on the specimen surface. Some selective images were taken during the test and processed with the mathematical tool Matlab$^{®}$ program. Out of the images taken during loading and unloading, few images were selected for DIC analysis. A square grid pattern of 20 pixels in x-direction and 20 pixels in y-direction has been considered for correlation.
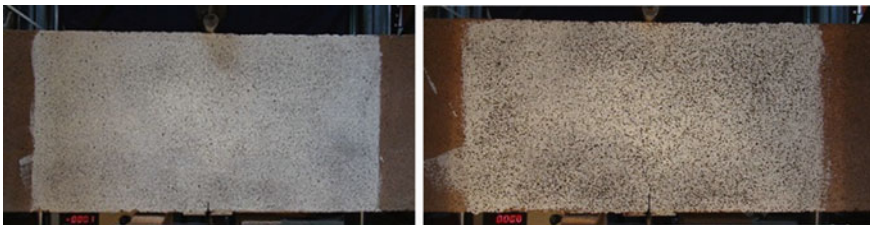
Fig. 7 Speckle pattern marked beam without any load and with maximum load
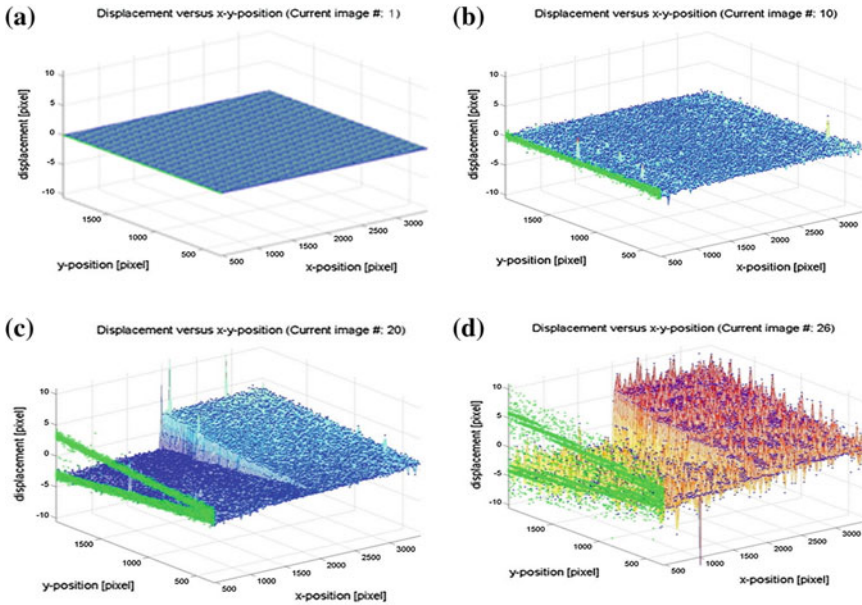
Fig. 8 3D surface displacement diagrams at different load. **a** Image 1. **b** Image 10. **c** Image 20. **d** Image 26

Discussions of Results: In Fig. 7 the concrete beam having notch at below middle portion images of specimen surface having notch showing cracks. Out of the images taken during loading and unloading, few images which are image 1, image 10, image 20, image 26 were selected for analysis. A square grid pattern of 20 pixels in x-direction and 20 pixels in y-direction has been considered for correlation. Figure 8 shows 3D surface displacement plots at different stages of loading. The propagation of the crack with the increase in loading can be seen from Fig. 8. The downward displacement obtained from DIC is compared with the mid span displacement. Also here from Fig. 9 shows strain graph plots between two points at different stages of loading.

In Fig. 9, the strain value is below 5 mm and it is increasing to corresponding load see Fig. 9 by below 8 mm. At ultimate load strain was increased to above 10 mm by seeing this Fig. 10. One can observe that how strain values increasing from one place to another place. Finally, the x-direction strain in concrete versus position has been plotted corresponding to the load to see the variation of strain in reinforced concrete in a cyclic loading. In the same plot it is observed that after 8 cycles the strain in reinforced concrete becomes positive. The variation of strain in reinforced concrete was increases with the increase in loading as shown in Fig. 9.
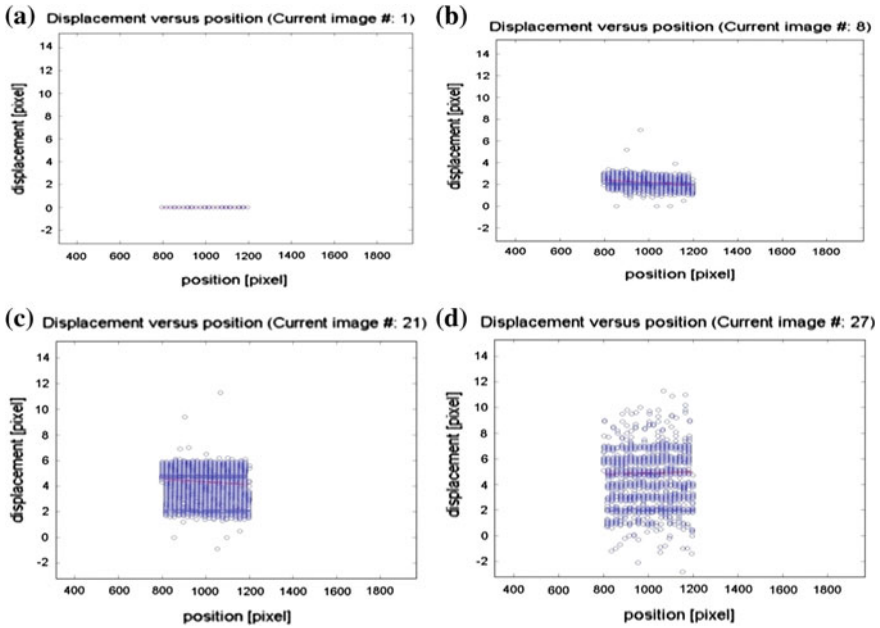
Fig. 9 Strain diagram between 2 points at different load. **a** Image 1. **b** Image 2. **c** Image 21. **d** Image 27
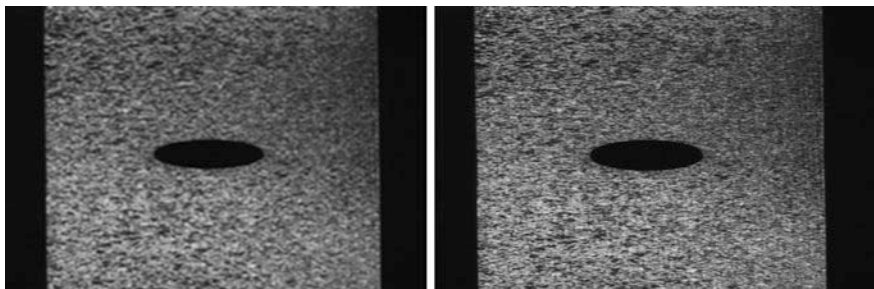
Fig. 10 Beam having hole in middle without and with loading

Problem 2: In this problem, one has taken the reinforced concrete beam providing hole at middle portion along the length of beam. A square grid pattern of 20 pixels in x-direction and 20 pixels in y-direction has been considered for correlation. Figure 11 shows 3D surface displacement plots at different stages of loading. The propagation of the crack with the increase in loading can be seen from Fig. 11. The downward displacement obtained from DIC is compared with the mid span displacement.
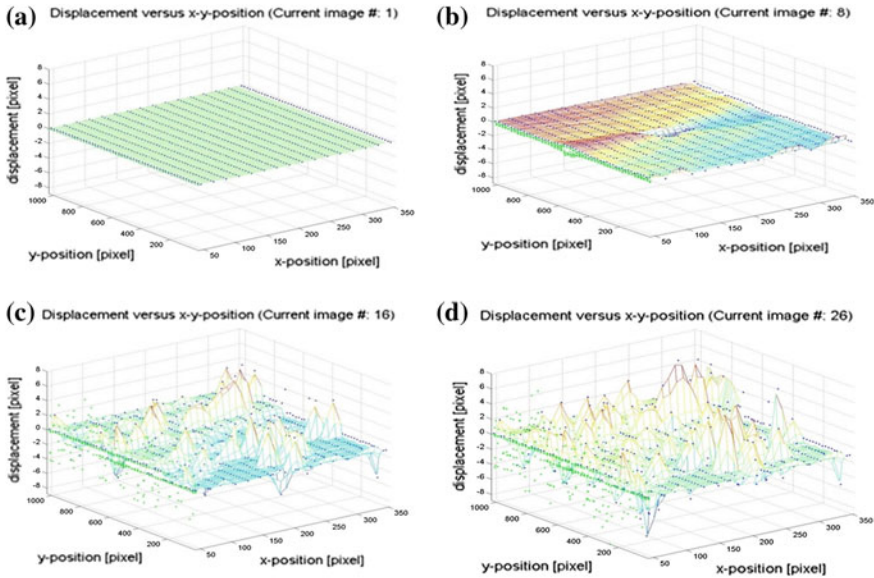
Fig. 11 3D surface displacements diagram for different loading. **a** Image 1. **b** Image 8. **c** Image 16. **d** Image 26

Discussions of Results: In Fig. 11 the concrete beam having hole at middle portion Images of specimen surface having hole showing cracks. Out of the images taken during loading and unloading, few images which are image 1, image 6, image 16, image 26 were selected for analysis. A square grid pattern of 20 pixels in x-direction and 20 pixels in y-direction has been considered for correlation.

Figure 11 shows 3D surface displacement plots at different stages of loading. The propagation of the crack with the increase in loading can be seen from Fig. 11 shows the deflection less than 2 mm and in Fig. 11c it is increased to 5 mm by corresponding incremental of load. At an ultimate cracks were developed more and the deflections are above 6 mm. The downward displacement obtained from DIC is compared with the mid span displacement. The variation of strain in concrete measured using DIC technique increases with the increase in loading. The strains in concrete measured by DIC technique is used to assess the damage in concrete beams. In below also mentioned strain diagrams for different images. In Fig. 12 shows the true strain verses the number of images. In this graph the curve is parabolic from starting image to ninth image. Then it suddenly raise strain value up to 7E−3 at the image 10, then it straight line up to last image. Finally, the x-direction strain in concrete versus image number has been plotted corresponding to the load to see the variation of strain in concrete in a cyclic loading (Fig. 13). In the same plot it is observed that after 8 cycles the strain in concrete becomes positive.
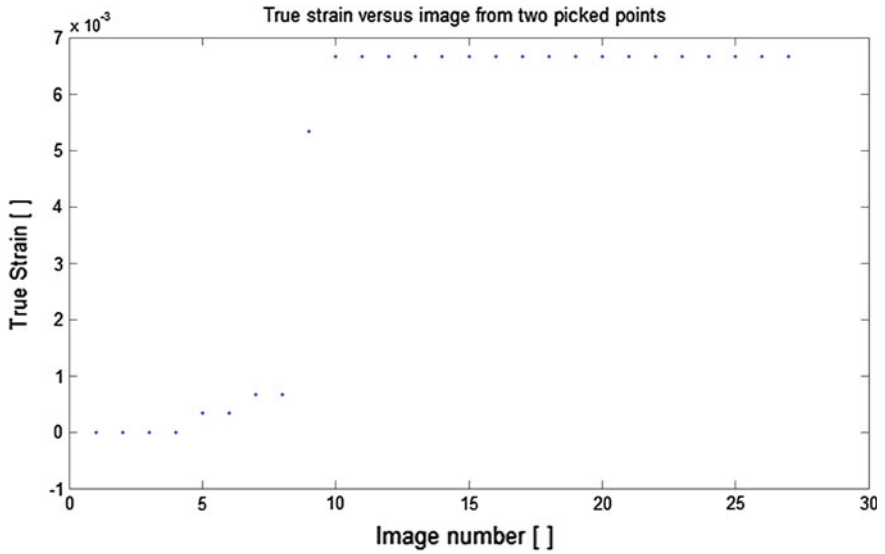
Fig. 12 Strain verses number of images
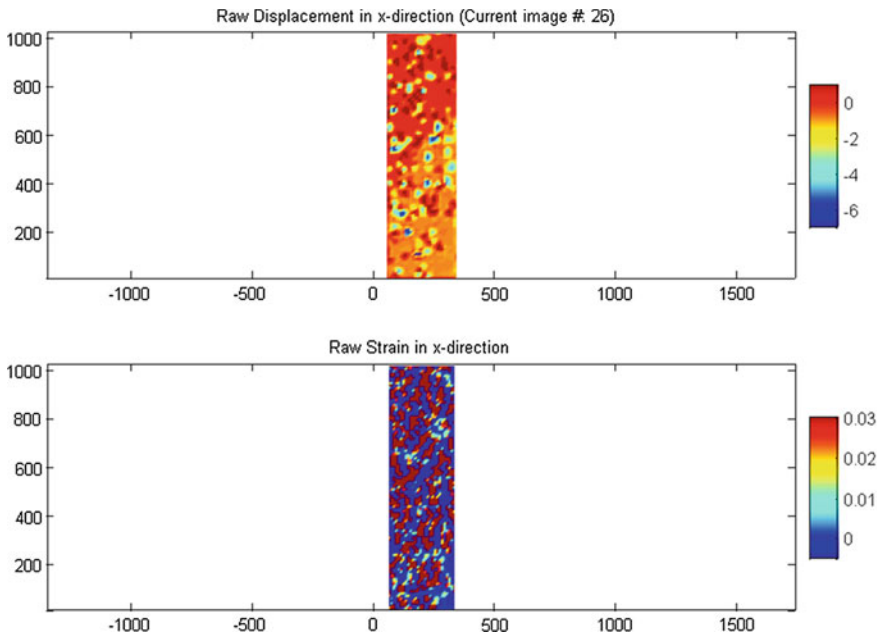
Fig. 13 Displacement and strain in x-direction at ultimate load image

4 Conclusions

In this work, the resolution and application of the digital image correlation techniques are demonstrated. The results show that the how crack propagating from one place to another place during applying loads. Using our self-developed method, one can calculate the stresses, strains and also crack variation in concrete structures and the deformation evolutions can be visualized by means of the digital-image-correlation technique. The identification of crack development in structures forms an important study for investigating the earthquake resistance capability of the masonry structures. DIC is a non-contact method for measuring whole field displacement. Method involves interpolation to smooth gray scale levels and then applies coefficient to map the parameters to find strains and crack growth in structure. Mathematics involved is challenging, but if computer code is available, mapping process becomes automatic. The analysis of concrete structures is carried out. The surface of the sample is marked with black and white paints. The image before applied the load is registered by a digital camera. Then the sample is compressed to the crack propagating. The images at strains are also registered by the digital camera. Then the analysis of the strain and crack with the help of developed software is carried out. This work provided a multi-scale investigation into crack propagation including displacement, strain accumulation, crack path, and their relation to microstructure. The conclusions present from the grain level DIC measurements of deflections, strain, stress and crack propagation and their relation to microstructure. A DIC technique has been used to measure the 3D and 2D surface displacements and strain in reinforced concrete along with the written mathematical program Matlab$^{\circledR}$. For digital image correlation the speckle pattern was made properly on the specimen surface. In future, the crack propagation study at multiple dimensions of different reinforced concrete beams can be carried out using this technique.

References

1. Zou Y, Tong L, Steven GP (1999) Vibration-based model-dependent damage (delamination) identification and health monitoring for composite structures—a review. J Sound Vib 230 (2):357–378
2. Ramana PV, Arigela SN et al (2014) The application of DIC and AE methods. Int Rev Appl Eng Res 4(5):445–454
3. Ramana PV, Arigela SN (2014) The computational efforts in digital correlation image techniques. In: NCETET-2014, national conference on emerging trends in engineering and technology, pp 14–18
4. Ramana PV, Arigela SN (2013) The health monitoring prescription by DIC and AE method. In: ICATET-2013, international conference on 'advance trends in engineering and technology', pp 304–310

Bibliography

5. Mal A, Ricci F, Banerjee S, Shih F (2005) A conceptual structural health monitoring system based on vibration and wave propagation. Struct Health Monit 4:283–293
6. Banerjee S, Ricci F, Monaco E, Mal A (2009) A wave propagation and vibration-based approach for damage identification in structural components. J Sound Vib 322:167–183
7. Abdel-Qader I, Abudayyeh O, Kelly ME (2003) Analysis of edge-detection techniques for crack identification in bridges. J Comput Civil Eng 17(4):255–263
8. Aktan AE, Ciloglu SK, Grimmelsman KA, Pan Q, Catbas FN (2005) Opportunities and challenges in health monitoring of constructed systems by modal analysis. In: The 1st international conference on experimental vibration analysis for civil engineering structures, Bordeaux, France
9. Park S, Yun CB, Inman DJ (2008) Structural health monitoring using electro-mechanical impedance sensors. Fatigue Fract Eng Mater Struct 31:714–724
10. Farrar C, Worden K (2007) An introduction to structural health monitoring. Philos Trans R Soc A 365:303–315
11. Worden K, Farrar C, Manson G, Park G (2007) The fundamental axioms of structural health monitoring. Proc R Soc A 463:1639–1664
12. Muravin G (2000) Inspection, diagnostics and monitoring of construction materials and structures by the acoustic emission method. Minerva Press, London, p 480
13. Ostachowicz WM, Krawczuk M (1990) Vibration analysis of a cracked beam. Comput Struct 36(2):245–250
14. Ramana PV, Arigela SN (2013) A novel analysis for super structures. YRGS-2013, current challenges in structural engineering, MNIT Jaipur, pp 220–227

Structural Damage Identification Using Modal Strain Energy Method

V.B. Dawari, P.P. Kamble and G.R. Vesmawala

Abstract Civil Engineering structures are prone to deterioration and damage during their service life period. Structural health monitoring is gaining high importance in conjunction with damage assessment and safety evaluation of structures. Vibration based damage identification techniques are global methods that are able to assess the condition of the entire structure at once. In this paper, the damage detection potential of two damage indices based on modal strain energy are evaluated for beam structures under different damage scenarios with respect to locations, severities and single and multiple damages. The appropriate finite element models of beam structures are developed and analysed for first five flexural modes using commercial software ANSYS. The algorithms available in the literature use flexural mode shapes for calculation of damage indices. In the present study, normalized mode shapes as well as normalized curvature mode shapes are used for computation of damage indices. The numerical results demonstrate that the indices could successfully detect and locate the damages in the beam models. In addition, there is improvement in the performance of damage indices in terms of reduction in presence of false alarms.

Keywords Damage detection algorithm · Modal strain energy · Finite element analysis

1 Introduction

Nondestructive evaluation (NDE) is one of the powerful tool which helps in assessing the structural condition of structures. These techniques provide valuable information about the condition of a structure at given locations. Vibration based

V.B. Dawari (✉) · P.P. Kamble
Department of Civil Engineering, College of Engineering, Pune 411005, India
e-mail: vbd.civil@coep.ac.in

G.R. Vesmawala
Department of Applied Mechanics, S. V. National Institute of Technology,
Surat 395007, India

damage identification techniques are global methods that are able to assess the condition of the entire structure at once. These methods are based on the fact that damage in a structure alters dynamic characteristics of the structure. The change is characterized by changes in the Eigen parameters that are natural frequency, damping values and the mode shapes associated with each natural frequency. In recent years, significant research and development has been carried out on the use of these methods, in particular modal methods for structural damage detection [1].

There are many damage indices presented in the literature based on different vibration parameters such as frequencies, mode shapes, damping values, mode shape derivatives, flexibility values, and strain energy values [2–6]. Among these damage indices, the strain energy based damage indices have high stability in detecting and localizing the damage as presented by Alvandi and Cremona [7].

Stubbs et al. [3, 4] developed the damage index based on modal strain energy change and applied it to localize the damage in a steel bridge. Further, Cornwell et al. [8] extended this method to plate structure. Park et al. [9] developed another form of strain energy based damage index to localize the damage in 3D truss bridge using numerical and experimental models. They observed that false indications of damage may occur at or near nodal points with the damage index. To minimize such false alarms, many researchers adopted improvements to the strain energy method [9–12].

In this paper, the study is conducted to investigate the capabilities and limitations of different damage detection algorithms based on modal strain energy changes for locating and evaluating damages. The damage index adopted from the literature uses flexural mode shapes for calculation of modal strain energy. In this paper damage index calculations are updated so as to use normalise displacement and curvature mode shapes. The updated damage index is evaluated for damaged steel beam structures under different damage scenarios with respect to locations, severities and single and multiple damages. First five flexural modes are analysed by modal analysis of appropriate finite element models of beam structures using commercial software ANSYS to derive the damage indices.

2 Damage Detection Algorithms

For a particular mode shape, $\phi_j(x)$, the energy associated with that mode shape of a general Euler–Bernoulli beam, is given by

$$U_i = \frac{1}{2} \int_0^l EI \left(\frac{d^2 \phi_i}{dx^2} \right)^2 dx \tag{1}$$

If the beam is subdivided into N_d, divisions, then the fractional strain energy F_{ij} energy associated with each sub-region j from a_j to a_{j+1} due to the ith mode is given by

$$F_{ij} = \frac{U_{ij}}{U_i} = \frac{\frac{1}{2}(EI)_j \int_{a_j}^{a_{j+1}} \left(\frac{d^2\phi_i}{dx^2}\right)^2 dx}{U_i} \tag{2}$$

Similar quantities can be defined for the damaged structure, in which a superscript asterisk is used to denote the damaged state.

$$F_{ij}^* = \frac{\frac{1}{2}(EI)_j^* \int_{a_j}^{a_{j+1}} \left(\frac{d^2\phi_i^*}{dx^2}\right)^2 dx}{U_i^*} \tag{3}$$

The damage index proposed by Cornwell et al. [8] normally indicated false alarms at or near the node points of modes. Park et al. [9] therefore modified the expression as shown as Eq. (4).

$$(\beta_{ij})_1 = \frac{(k)_j}{(k)_j^*} = \frac{\frac{F_{ij}^*+1}{F_{ij}+1} + 1}{2} \tag{4}$$

When several modes m are used, expression takes the form of damage index

$$(\beta_{ij})_1 = \frac{\frac{\left(\sum_{i=1}^{m} F_{ij}^*\right)+1}{\left(\sum_{i=1}^{m} F_{ij}\right)+1} + 1}{2} \tag{5}$$

Li et al. [10] and Shih et al. [11] proposed a new damage index. The peak values of the damage index above the datum level 1 indicate the damage locations. To overcome this limitation (i.e., the division by zero difficulty) caused in β_1, an approximation is made such that the axis of reference for the modal sensitivities is shifted by a value of 1.0. Adding unity to both the numerator and the denominator.

$$(\beta_{ij})_2 = \frac{k_j}{k_j^*} = \frac{\left(\int_j \left[\phi_i''^*(x)\right]^2 dx + \int_0^L \left[\phi_i''^*(x)\right]^2 dx+\right) * \int_0^L \left[\phi_i''(x)\right]^2 dx}{\left(\int_j \left[\phi_i''(x)\right]^2 dx + \int_0^L \left[\phi_i''(x)\right]^2 dx+\right) * \int_0^L \left[\phi_i''^*(x)\right]^2 dx} \tag{6}$$
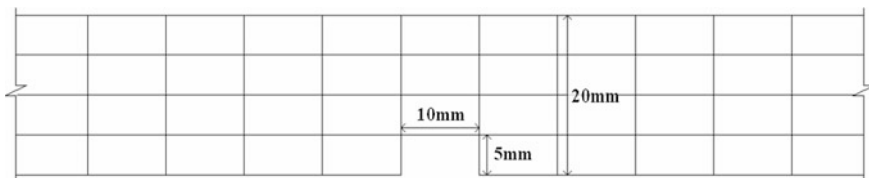
Fig. 1 Flaw size 'A' simulated in FEM

To account all available m number of modes, the damage index is given as

$$(\beta_j)_2 = \frac{\sum_{i=1}^{m} Num_{ij}}{\sum_{i=1}^{m} Denom_{ij}} \tag{7}$$

A judgement based thresh-hold value is selected and used to determine which of the j elements are possibly damaged.

Transforming the damage indicator values into the standard normal space, normalized damage index Zj can be obtained:

$$Z_j = \frac{B_j - \mu_{\beta j}}{\alpha_{\beta j}} \tag{8}$$

where $\mu_{\beta j}$ = mean of βj values for all j elements and $\alpha_{\beta j}$ = standard deviation of β_j for all j elements.

These damage indices could successfully predict single damage localisation but could not locate multiple damages. The indices depend on the summation of the combination of mode shape curvatures. Though mode shape vectors have been normalized, mode shape curvatures are not normalized. Values of mode shape curvature are dependent on the shapes of each individual mode shape. The summation of non-normalized mode shape curvatures may distort the damage index in favour of higher modes, which can result in false damage identifications. To reduce the problem of false alarms, an attempt is made to update these algorithms by using mass normalized mode shapes and normalized mode shape curvatures. In this work value of Z is considered to be 3 for damage.

3 Numerical Studies

Finite element simulation of three beam structures are used in the present study: Simply supported beam with span of 2.8 m; Two span continuous beam with each span length of 2.8 m and; Three span continuous beam with each span length of 2.8 m. The finite element beam models have isotropic material properties of steel whose modulus of elasticity and density are 200 GPa and 7,850 kg/m^3, respectively with cross section dimensions of 40 mm width and 20 mm depth. The beams are modeled with 560 number of 8 nodes brick elements (Solid185) of size 5 mm along the length with ANSYS v13. To simulate damage, the beam is cut to cause flaws on the tension face of the beam. Two different sizes of flaws are induced: Flaw size "A" is with length 10 mm, width 40 mm and depth 5 mm and flaw size "B" is with length 20 mm, width 40 mm and depth 5 mm. The flaws simulated in FEM are shown in Fig. 1. Seven damages cases investigated are detailed out in Table 1.

First five flexural modes of beam structures are extracted for intact and damaged beams from the FE analysis. The preliminary finite element model validation is

Table 1 Damage cases considered in the present study

Damage case	Span (of length (L) 2.8 m each)	Description of the damage
D1	Single	Damage 'B' at L/2
D2	Single	Damage 'B' at L/4 and L/2
D3	Single	Damage 'B' at L/4 from each side
D4	Two	Damage 'A' at L/4 of first span and B at 3L/4 of second span
D5	Two	Damage 'A' at L/4 and L/2 of first span, 'B' at L/2 of second span
D6	Three	Damage 'A' at L/2 of first span and B at L/2 of third span
D7	Three	Damage 'B' at L/2 of second span and 'A' at L/2 and 3L/4 of third span

Table 2 Validation of FE model for single span simply supported beam

State	Frequency mode	Present study	Experiment (Hz) Shih et al. [11]	FEM (Hz) Shih et al. [11]
Undamaged	Mode 1	05.86	5.94	5.84
	Mode 2	23.42	24.38	23.33
Damaged at mid-span	Mode 1	05.79	5.63	5.65
	Mode 2	23.42	23.13	23.33

carried out based on the experiment results presented by Shih et al. [11] as shown in Table 2. Two updated damaged indices are initially evaluated using the combined effect of first five normalized flexural mode shapes and curvature mode shapes. Then normalized updated indices are calculated from them as Z_1^* and Z_2^*. The normalised updated damage indices are plotted against the length of the beam.

4 Results and Discussions

The five mode shapes and their corresponding mode shape curvatures obtained from the results of FE analysis are used for calculating the updated modal strain energy based damage indices on beams. The plot of updated damage indices along the beam for damage cases are shown in Figs. 2, 3, 4, 5, 6, 7 and 8. The location of damaged elements is indicated through the spikes with magnitudes greater than 2 for single spans and 3 for multiple spans. Multiple numbers of peaks as in Figs. 5, 6, 7 and 8 clearly indicate the multiple damages in the beam. Both updated damage indices are able to correctly locate the damage in beams in all damage cases. For the beams with multiple spans, it is observed that, all damage indices show false alarms additional to the location of damages near to the support in terms of additional spikes (Figs. 6 and 8).
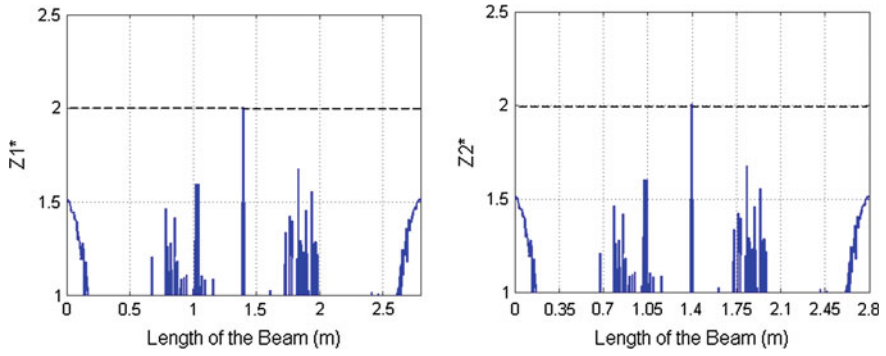
Fig. 2 Damage case: D1
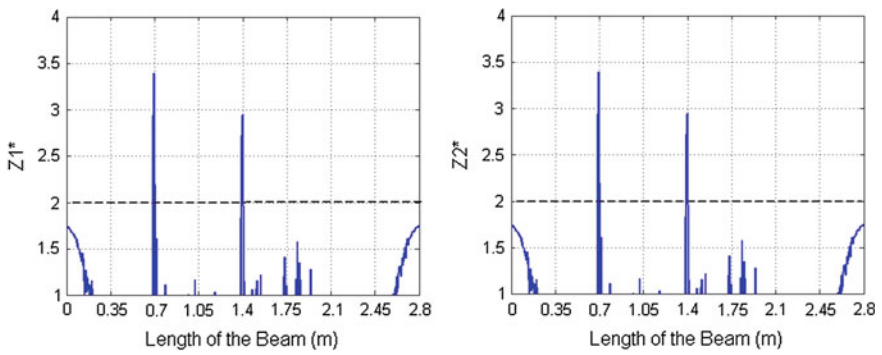
Fig. 3 Damage case: D2
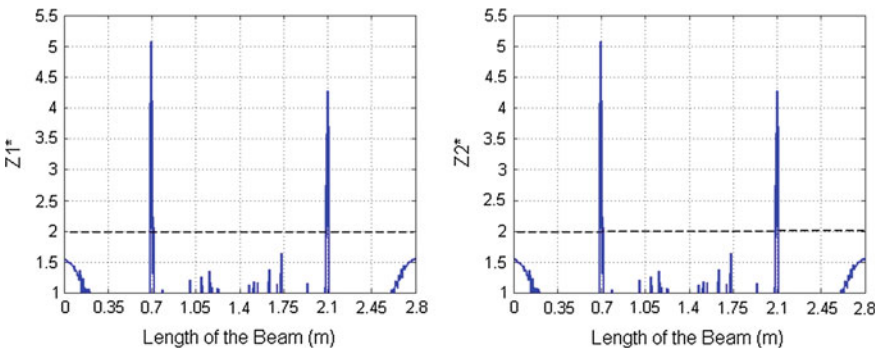
Fig. 4 Damage case: D3
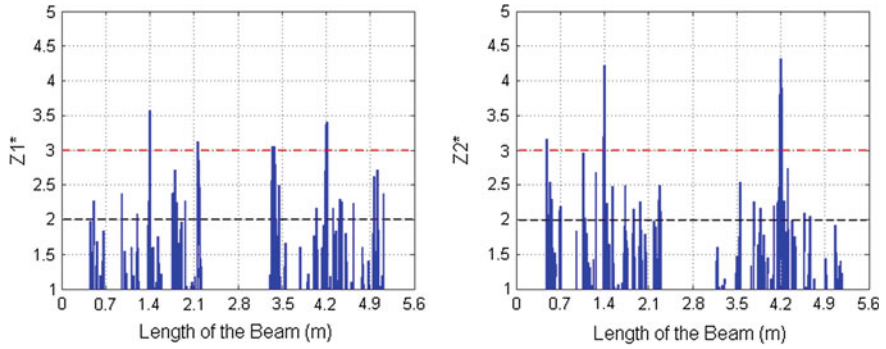
Fig. 5 Damage case: D4
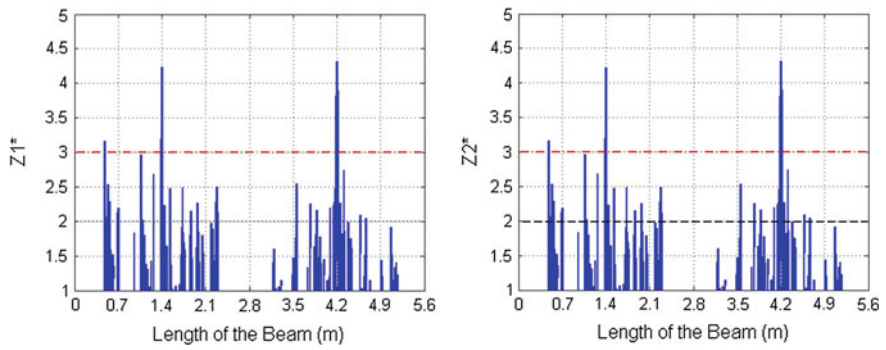
Fig. 6 Damage case: D5
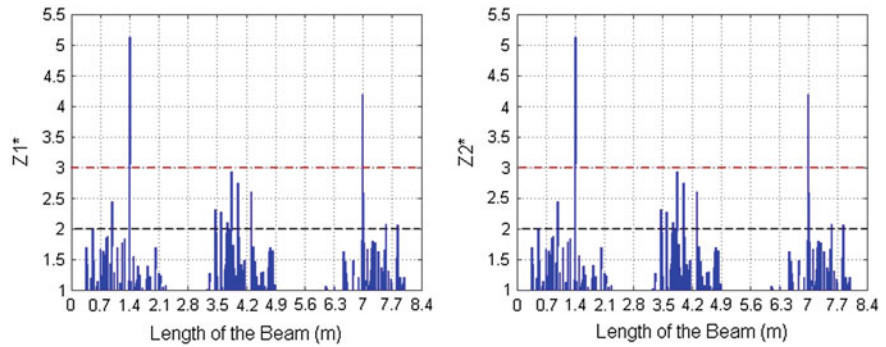
Fig. 7 Damage case: D6
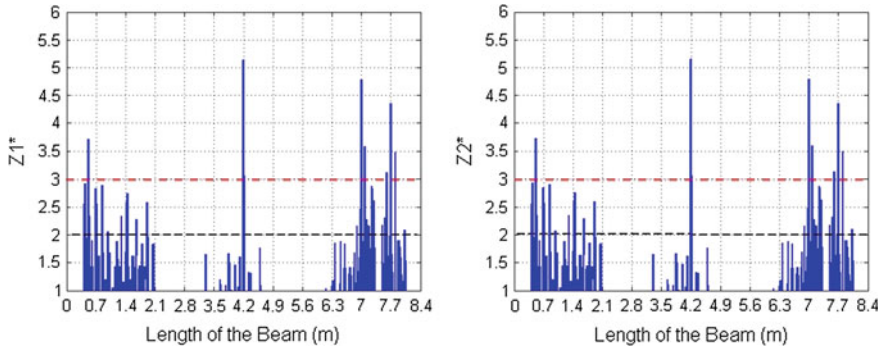
Fig. 8 Damage case: D7

5 Conclusions

A damage localisation method using modal strain energy changes is presented in this paper. Finite element analyses of the healthy and damaged steel beam models for different damage scenarios are carried out to extract first five flexural mode shapes. Two updated damage indices based on modal strain energy method, are evaluated using combined mode shapes. The peak values of each damage index indicate possible damage locations. Numerical results demonstrate that the damage indices successfully locate the single and multiple damage cases in single span beam. For beams with multiple spans and multiple damages, the damage indices located the damage with a few additional false alarms. The damage localisation method using updated damage indices perform better as compared to the original method in terms of giving less false alarms for damage localisation.

References

1. Doebling SW, Farrar CR, Prime MB (1998) A summary review of vibration-based damage identification methods. Shock Vib Dig 30:91–105
2. Pandey AK, Biswas M, Samman MM (1991) Damage detection from changes in curvature mode shapes. J Sound Vib 145(2):321–332
3. Stubbs N, Kim JT, Farrar CR (1995) Field verification of a non-destructive damage localization and severity estimation algorithm. In: Proceedings of 13th international modal analysis conference 1995, pp 210–218
4. Stubbs N, Park S, Sikorsky C, Choi S (2000) A global non-destructive damage assessment methodology for civil engineering structures. Int J Syst Sci 31(11):1361–1373
5. Chang PC, Flatau A, Liu SC (2003) Review paper: health monitoring of civil infrastructure. Struct Health Monit 2(3):257–267
6. Wang L, Chan THT (2009) Review of vibration based damage detection and condition assessment of bridge structures using structural health monitoring. In: The second infrastructure theme postgraduate conference, Queensland University of Technology, March 2009

7. Alvandi A, Cremona C (2005) Assessment of vibration-based damage identification techniques. J Sound Vib 292:179–202
8. Cornwell P, Doebling SW, Farrar CR (1999) Application of the strain energy damage detection method to plate-like structures. J Sound Vib 224(2):359–374
9. Park S, Kim YB, Stubbs N (2002) Nondestructive damage detection in large structures via vibration monitoring. Electron J Struct Eng 2:59–75
10. Li J, Choi FC, Samali B, Crews K (2007) Damage localization and severity evaluation of a beam-like timber structure based on modal strain energy and flexibility approaches. J Building Appraisal 2(4):323–334
11. Shih HW, Thambiratnam DP, Chan THT (2009) Vibration based structural damage detection in flexural members using multi-criteria approach. J Sound Vib 323:645–661

Bibliography

12. Wahalathantri BL, Thambiratnam DP, Chan THT, Fawzia S (2010) An improved modal strain energy method for damage assessment. In: Proceedings of the tenth international conference on computational structures technology. Univeridad Politecnica de Valencia, Spain

New Paradigms in Piezoelectric Energy Harvesting from Civil-Structures

Naveet Kaur and Suresh Bhalla

Abstract In this paper, the recent advances in the field of energy harvesting from piezoelectric transducers have been presented. The energy harvesting from the piezoelectric material using the d_{33} mode has been done enormously in the literature. However, in this paper the energy harvesting feasibility using the d_{31} mode, which has been recently explored, is discussed. The proposed study in this paper provides a proof-of-concept experimental demonstration of achieving energy harvesting from the PZT patch (a) surface bonded on steel beam and (b) embedded concrete vibration sensor (CVS) in reinforced concrete (RC) beam. The CVS has been specifically designed for RC structures. This packaged sensor (CVS) can withstand the harsh conditions encountered during construction due to its unique packaging characteristics. The laboratory experiments for voltage generation by the PZT patches (a) surface bonded on steel beam and (b) embedded CVS in RC beam have been demonstrated. In both cases, a real life sized simply supported beam has been considered as the host structure. The experimental results have been compared with the proposed analytical model. While the experiments provide a proof-of-concept feasibility of employing the d_{31} mode, it is also concluded that the shear lag effect must be taken into consideration in the electro-mechanical coupling model.

Keywords Energy harvesting · Piezoelectric device · Sensor

N. Kaur (✉) · S. Bhalla
Department of Civil Engineering, Indian Institute of Technology (IIT) Delhi,
Hauz Khas, New Delhi 110016, India
e-mail: naveet.kaur1985@gmail.com

S. Bhalla
e-mail: sbhalla@civil.iitd.ac.in

1 Introduction

Energy harvesting from piezo sensors have attracted numerous researchers since last two decades due to development of less power consuming electronic systems [1–4]. Energy can be harnessed from two different modes namely, d_{33} mode and d_{31} mode of vibrations of piezo sensors. In d_{33} mode, the dynamic force application and the voltage generation are in direction 3 (polarization, out of plane) of the piezo patch. In d_{31} mode, on the other hand, the dynamic force is applied in direction 1 (along length, in plane) and the voltage is measured across direction 3. The piezoelectric coefficient of the d_{31} mode is much less than d_{33} mode, hence the latter mode has been frequently used for energy harvesting from piezo sensors in literature. However, for civil structures d_{31} mode is more natural way of excitation [5–7], hence, in the present work, d_{31} mode of vibration experienced by thin piezo (PZT) patches has been utilized for energy harvesting. The energy harvesting capabilities of the PZT patches in the real life sized steel and reinforced concrete (RC) beam has been investigated. The main objective of this paper is to explore the possibility of energy harvesting from PZT patches bonded to a steel and RC beam operating in the d_{31}-mode. The results presented in this paper are based on the detailed experimentation and analytical modelling covered in the recent publications [8, 9] of the authors.

2 Laboratory Experimentation

Experiments were carried out in the laboratory environment to measure the voltage generated by a surface bonded PZT patch when the host structure undergoes vibrations. A real life sized simply supported (a) steel I section beam and (b) RC beam have been considered to demonstrate the energy harvesting potential of PZT patches operating d_{31} mode. The properties of the beam are listed in Table 1. The complete experimental set-up for the steel beam and RC beam is as shown in Fig. 1a, b respectively. A commercially available PZT patch of $10 \times 10 \times 0.3$ mm size conforming to grade PIC 151 [10] was surface bonded on steel beam [8] and embedded in RC beam {in the form of concrete vibration sensor (CVS, [9])}using

Table 1 Properties of host structure

Property	Steel beam	RC beam
Length, L (m)	3.2	4
Cross section	Flange: 0.070 m × 0.006 m Web: 0.133 m × 0.004 m	0.210 m × 0.160 m
Flexural rigidity modulus, EI (N m^2)	1.01×10^6	3.9×10^6
Characteristic strength of concrete, f_{ck}	–	40
Characteristic strength of reinforcement, f_y	–	415
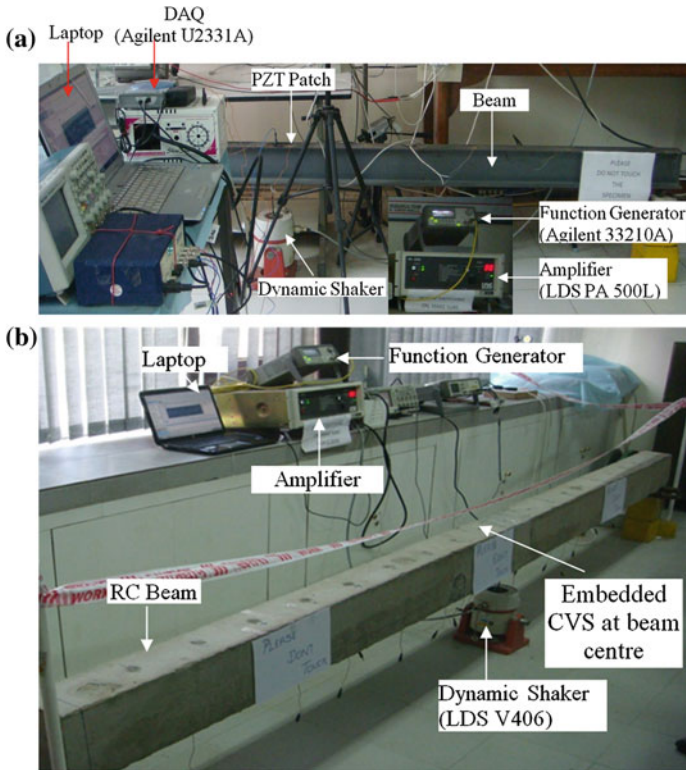
Fig. 1 Complete experimental setup for voltage measurement for **a** surface bonded PZT on steel beam and **b** embedded CVS in RC beam

two part araldite epoxy adhesive at the centre of the beam. The beam was excited using LDS V406 series portable dynamic shaker. A function generator (Agilent 33210A) was employed to generate an electrical signal, which was amplified by a power amplifier (LDS PA500L) and transmitted to the shaker, which converted it into mechanical force the oscilloscope has been used to measure the voltage generated by the PZT patch.

3 Results and Discussions

A coupled electro-mechanical model analytical model has been developed for estimation of the voltage generated by the PZT patch (a) surface bonded [8] and (b) embedded [9] inside the simply supported beam at its centre considering the effect of adhesive layer. The shear lag effect, which occurs due to presence of bond layer deforming in shear mode between the PZT patch and the host structure, was found to

be the main contributor to the voltage loss [8]. The relation between the voltage V_p^S generated by the PZT patch considering the shear lag effect can be expressed as, [8]

$$V_p^S = \in K_p K_b S_q^* \tag{1}$$

This equation was employed for estimation of the PZT output voltage. The symbols used in above equation hold different meanings for surface bonded and embedded CVS as explained in [8, 9]. The variation of voltage generated by (a) surface bonded on steel beam and (b) embedded CVS in RC beam is shown in Fig. 2.

Shear lag effect was incorporated for varying thickness of adhesive bond layer (note that h is the thickness of the PZT patch in Fig. 2). It can be observed that with increase in bond layer thickness, the predicted theoretical voltage significantly reduces. The actual thickness of bond layer was measured to be 0.015 mm (=0.5h) for the surface bonded PZT patch and 3 mm (10h) for the embedded CVS, experimentally. It can be concluded from this analysis that effect of shear lag must be taken into account in the electro-mechanical coupling model. In embedded CVS, in addition to the shear lag effect, other factors are also possibly contributing. Investigations are underway to unearth these factors. The reader may refer to the related publications [8, 9] for modelling details. Typical values of power achieved by this configuration were measured to be 0.270 μW for surface bonded case and 0.017 μW for CVS in the lab environment.

Fig. 2 Comparison of experimental and theoretical voltage incorporating the effect of shear loss for PZT patches **a** surface bonded on steel beam and **b** embedded CVS in RC beam (*h* thickness of PZT patch)
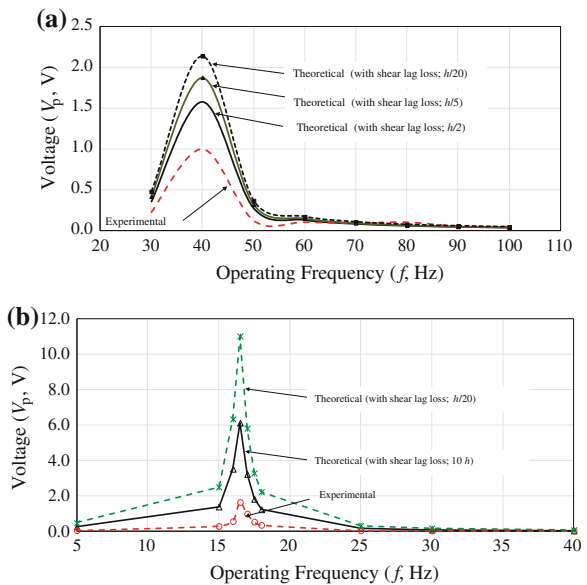
4 Conclusions

The recent advances in the field of energy harvesting from piezoelectric sensors in civil structures achieved at Smart Structures and Dynamics Laboratory [11] have been reported. The laboratory experiments for voltage generation by the PZT patches (a) surface bonded on steel beam and (b) embedded CVS in RC beam have been demonstrated. A real life sized simply supported beam has been considered as the host structure for both the cases. The experimental results have been compared with the proposed analytical model. The study established the feasibility of employing the d_{31} mode for energy harvesting. Typically, power in the microwatt range is achievable from the PZT patches in real-life structures [8, 9]. It is also concluded that the shear lag effect must be taken into consideration in the electro-mechanical coupling model.

References

1. Priya S (2007) Advances in energy harvesting using low profile piezoelectric transducers. J Electroceram 19:165–182
2. Roundy S, Wright PK (2004) A piezoelectric vibration based generator for wireless electronics. Smart Mater Struct 13:1131–1142
3. Sodano H, Inman DJ, Park G (2004) A review of power harvesting from vibration using piezoelectric materials. Shock Vib Dig 36:197–205
4. Starner T (1996) Human-powered wearable computing. IBM Syst J 35:18–628
5. Shanker R, Bhalla S, Gupta A (2011) Dual use of PZT patches as sensors in global dynamic and local EMI techniques for structural health monitoring. J Intell Mater Syst Struct 22 (16):1841–1856
6. Park G, Farrar CR, Todd MD, Hodgkiss W, Rosing T (2007) Energy harvesting for structural health monitoring sensor networks. Report by Los Alamos, National Laboratory
7. Mateu L, Moll F (2005) Review of energy harvesting techniques and applications for microelectronics. Proc SPIE 5837:359–373
8. Kaur N, Bhalla S (2014) Feasibility of energy harvesting from thin piezo sensor patches via axial strain actuation mode. J Civ Struct Health Monit 4:1–15
9. Kaur N, Bhalla S (2014) Combined energy harvesting and structural health monitoring potential of embedded piezo concrete vibration sensors. J Energy Eng Am Soc Civ Eng (ASCE). http://dx.doi.org/10.1061/(ASCE)EY.1943-7897.0000224 (in press)
10. Ceramic PI (2013) Product information catalogue. Lindenstrabe, Germany. http://www.piceramic.de
11. SSDL (2013) Smart structures and dynamic laboratory. Department of Civil Engineering, IIT Delhi. http://ssdl.iitd.ac.in/

Experimental Strain Sensitivity Investigations on Embedded PZT Patches in Varying Orientations

Prateek Negi, Naveet Kaur, Suresh Bhalla and Tanusree Chakraborty

Abstract Piezoelectric ceramic (PZT) patches are well established as dynamic strain sensors. Thin Lead Zirconate Titanate (PZT) patches have been used as strain sensors in the present study in various configurations. The property of PZT to generate voltage on application of strain also works conversely, i.e. they also develop strains on applying a voltage across their ends. It is well known that thin PZT patches, operating in d_{31}-mode i.e. response is measured across the poling direction (dir-3) and strain is applied along longitudinal direction (dir-1) serves best for strain sensing, whereas d_{33}-mode, i.e. both response and application of strain are measured across the poling direction is best for energy harvesting. In this study, PZT patches were tested for their responses while embedded in host structure in three different configurations i.e. horizontal (0°), vertical (90°) and inclined (45°) after embedding in a prototype RC beam, $150 \times 210 \times 2,000$ mm in size. The results show that the 90° configuration is the best and 45° configuration is worst from strain sensing point of view.

Keywords Energy harvesting · D_{33}-mode · D_{31}-mode · PZT patch · Structural health monitoring

P. Negi (✉) · N. Kaur · S. Bhalla · T. Chakraborty
Department of Civil Engineering, Indian Institute of Technology Delhi,
Hauz Khas, New Delhi 110016, India
e-mail: negidynamic@gmail.com

N. Kaur
e-mail: naveet.kaur1985@gmail.com

S. Bhalla
e-mail: sbhalla@civil.iitd.ac.in

T. Chakraborty
e-mail: tanusree@civil.iitd.ac.in

1 Introduction

We all know that each and every structure is designed for a specific lifetime, which can vary from a few years to a century. Between this lifespan, the structure faces a continuous deterioration due to many factors. As the occurrence of many of these factors is unpredictable in nature, so is the deterioration of the structure's strength. This is why many of the structures fail quite early before their estimated life span. This has drawn attention of numerous structural engineers towards using modern sensor technology for making structures, smart enough to warn the concerned authorities before their failure. Structural health monitoring (SHM) is a new engineering discipline, which deals with the continuous monitoring of the structures for incipient to severe damages. Sensors like accelerometers, strain gauges and piezo-based Lead Zirconate Titanate (PZT) patches, are used to monitor the health of the structures.

Among all these, piezo based sensors are becoming popular due many of their advantages over other sensors. Piezo materials, respond by generating a voltage against the application of mechanical strains produced in them due to mechanical vibrations. Also, they can develop mechanical strains and can vibrate mechanically on the applying voltage signals across them. The piezos can vibrate in two modes i.e. d_{31}, which is regarded good for SHM, in which voltage response is measured in thickness and force is applied in the direction of the length and d_{33}, where both response and force are measured across the thickness. The second mode d_{33} is used in energy harvesting. This dual effect has been studied and used by numerous researchers.

For one-dimensional (1D) interaction, the constitutive relations for piezoelectric patches are as follows [1]:

$$D_3 = \overline{\varepsilon_{33}^T} E_3 + d_{31} T_1 \tag{1}$$

$$S_1 = \frac{T_1}{\overline{Y^E}} + d_{31} E_3 \tag{2}$$

where, D_3 is the electric displacement over the PZT patch, $\overline{\varepsilon_{33}^T} = \varepsilon_{33}^T (1 - \delta j)$ is the complex electric permittivity (in direction "3") at constant stress, E_3 is the electric field applied across the direction 3, d_{31} is the piezoelectric strain coefficient and T_1 the axial stress in the direction "1". S_1 is the strain in the direction "1", $\overline{Y^E} = Y^E (1 + \eta j)$ is the complex young's modulus of elasticity of the PZT patch at constant electric field, η and δ denote the mechanical loss factor and the dielectric loss factor of the PZT material, respectively.

Also, when PZT is used as a sensor only, we can derive from the Eq. (1) [2]

$$V = \left(\frac{d_{31} h \overline{Y^E}}{\overline{\varepsilon_{33}^T}} \right) S_1 = K_p S_1 \tag{3}$$

where, V is the potential difference generated across the terminals of the PZT patch of thickness h. This output voltage can be measured using any commercial oscilloscope or digital multi-meter. It is supposed that the PZT develops the same amount of strain which is developed on the host structure in case of a perfect bond condition. However, in actuality, there is a very thin layer of epoxy adhesive between the PZT and the host structure which creates a shear lag in the strain transferred [3, 4]:

$$\frac{S_p}{S_b} = \left(1 - \frac{\cosh \Gamma x}{\cosh \Gamma l}\right) \tag{4}$$

where, S_p and S_b are strains developed in the patch and the surface of the host structure, respectively, and Γ is shear lag parameter, given by:

$$\Gamma^2 = \left(\frac{G_s}{Y_p t_s t_p} + \frac{3 G_s w_p}{Y_b w_b t_b t_p}\right) \tag{5}$$

where, G_s is the shear modulus of the bond layer, Y_p the Young's modulus of the PZT patch, Y_b the Young's modulus of the structure (beam), w_p the width of the patch, w_b the width of the beam, t_p the thickness of the patch and t_b the depth of the beam.

2 Experimental Details

A simply supported reinforced concrete (RC) beam of the properties as listed in Table 1 was casted and cured for 28 days with all the nine sensors embedded in them. The PZT patches were cast in three positions i.e. 0°, 45°, 90° with horizontal. PZT patches used for the present study were of size $10 \times 10 \times 0.3$ mm and confirmed to the grade PIC151, having properties as listed in Table 2. They were bonded with two part araldite epoxy on their respected positions [5]. All the experiments for measuring voltages by the embedded PZT patches were performed in the laboratory environment at Smart Structure and Dynamics Lab (SSDL), Indian Institute of Technology Delhi. To compare these positions PZT patches were fixed in three positions of 0.25 L, 0.50 L and 0.75 L in the beam, where L is the length of the beam as shown in the Fig. 2. Three PZT patches in three different positions as

Table 1 Properties of RC beam

Properties of RC beam	Value
Length (L)	2.0 m
Cross section	210×150 mm
Flexural rigidity (EI)	3.9×10^6 N m^2
Mass per unit length (m)	84 kg/m
Characteristic strength of concrete (f_{ck})	35 N/mm^2

Table 2 Properties of host structure [5]

Properties of PZT—PIC151	Value
PZT Size	10×10 mm
Thickness (h)	0.3 mm
Density (ρ)	7,800 kg/m^3
Piezoelectric strain coefficient (d_{31})	-2.100×10^{-10} m/V
Young's modulus (Y_E)	6.667×10^{-10} N/m^2
Piezoelectric strain coefficient (d_{33})	5.000×10^{-10} m/V
Electric permittivity (ε_{33}^T)	2.124×10^{-8} F/m
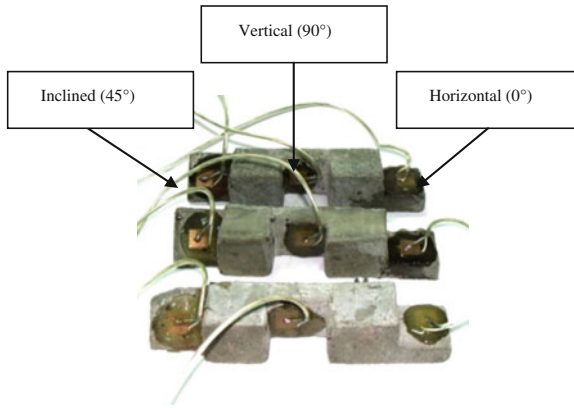
Fig. 1 Mortar castings for fixing PZT's in their positions in precision with each other

discussed above were bonded to small mortar pieces, as shown in Fig. 1, so as to ensure accuracy in their relative positions. They were fixed on the top of the steel cage and were flushed while concreting with the top surface, so as to ensure the maximum distance from the neutral axis.
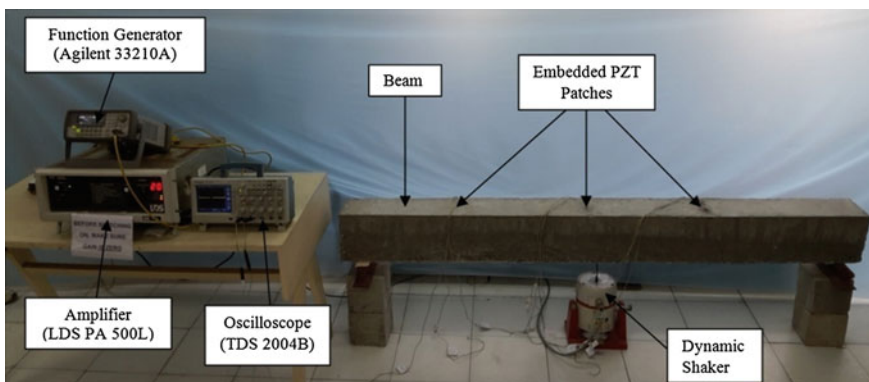
Fig. 2 Complete experimental setup for excitation of beam and voltage measurement from the embedded piezo sensors

A contact type portable dynamic shaker of series LDSV406 was used to excite the beam. Sine wave signals were given to shaker from a function generator (Agilent 33210A). Signals were amplified through a power amplifier (LDS PA500L). Frequency range for excitation was selected from 30 to 100 Hz with a step interval of 10 Hz with excitation amplitude of 10 V. The range was selected due to the prior estimation of experimental natural frequency of the beam, which was 60 Hz. TDS 2004B (Tektronix) oscilloscope was used as a data logger for measuring voltages against PZTs.

3 Results and Discussions

Figure 3 compares the voltage responses of the PZT patches in three typical configurations at two locations in the beam. From these plots, it is observed that the sensitivity of inclined (45°) PZT patches was worst. The sensitivity of 90° configuration is highest and horizontal (0°) configuration is second highest as shown in the Fig. 3. We could also observe deterioration in embedded inclined PZT patches, possibly due to the development of shear stresses. This behaviour was observed in all the three positions on the beam. Therefore, the repeatability of the inclined PZT patches in comparison to other orientations (namely, horizontal and vertical) is not attainable. The main reason for poor performance in 45° orientation is that the d_{31} & d_{33} effects act against one another due to their opposing sign (see Table 2).

Fig. 3 Comparison of FFT voltages with different excitation frequencies for different PZT positions. **a** At 0.25 L. **b** 0.50 L of the beam
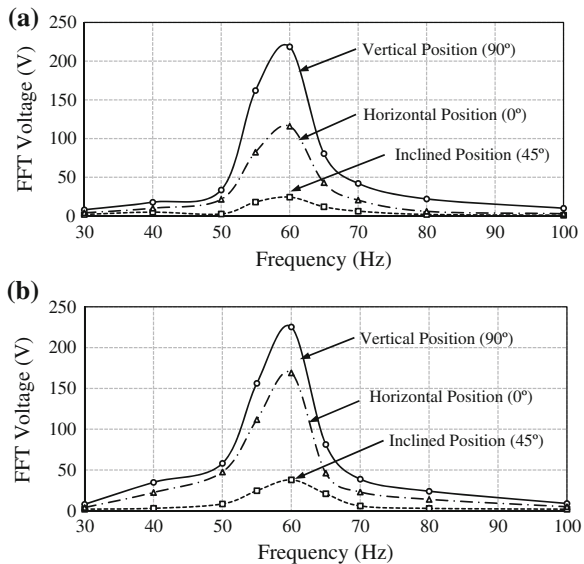
4 Conclusions

This study has presented the comparison of PZT patches for their sensitivity towards strain developed in RC structures. Mortars casting having embedded PZT patches were embedded in three different orientations, i.e. horizontal (0°), vertical (90°) and inclined (45°) on three different locations in the beam with equal spacing between them. It was found that the PZT patches are least sensitive in the inclined (45°) positions, whereas sensitivity is highest in vertical (90°) orientation. The opposing nature of d_{31} & d_{33} effects is accountable for this observation. Also, with continuous shaking the sensitivity in inclined piezos was found to be decreased, which indicated the deterioration in their packed structure. Hence, it is advised to ensure the orthogonal positions of sensors while using in embedded positions in real life structures.

References

1. Ikeda T (1990) Fundamentals of piezoelectricity. Oxford University Press, Oxford
2. Shanker R, Bhalla S, Gupta A (2011) Dual use of PZT patches as sensors in global dynamic and local EMI techniques for structural health monitoring. J Intell Mater Syst Struct 22 (16):1841–1856
3. Bhalla S, Soh CK (2004) Electro-mechanical impedance modelling for adhesively bonded piezo-transducers. J Intell Mater Syst Struct 15(12):955–972
4. Kaur N, Bhalla S (2014) Combined energy harvesting and structural health monitoring potential of embedded piezo concrete vibration sensors. J Energy Eng, American Society of Civil Engineers, (ASCE), in press, published online. doi:10.1061/(ASCE)EY.1943-7897.0000224
5. PI Ceramic (2013) Product information catalogue. Lindenstrabe, Germany. http://piceramic.de/fileadmin/FileDatabase/PI_Piezoelektrische_Aktoren_CAT128D.pdf. Accessed on 25th July 2014

Fundamental Mode Shape to Localize Delamination in Cantilever Composite Plates Using Laser Doppler Vibrometer

Koushik Roy, Saurabh Agrawal, Bishakh Bhattacharya and Samit Ray-Chaudhuri

Abstract The extensive usage of laminated composite plates in various industrial application and their often failure due to delamination encourage the researchers to focus on damage detection of these plates. This study mainly deals with structural damage detection of composite plates. Finite element models of composite plates have been developed and eigen analysis is carried out. Mode shape-based damage indices are proposed to identify delamination and its location. The difference in mode shapes corresponding to delaminated and healthy plates is found to be maximum at the location of damage. Experimental analyses have been performed on healthy as well as delaminated cantilever plates using three-dimensional laser Doppler vibrometer (LDV). The plates were scanned and the dynamic responses were recorded. The mode shapes were then estimated from the scanned response data. The experimental results are found to be in good agreement with that of the numerical illustration in identifying the damage location. The proposed methodology can thus be used in engineering and industrial applications to detect and localize damages in laminated composite plates.

Keywords Composite plates · Delamination · Fundamental mode shape · Laser doppler vibrometer

K. Roy (✉) · S. Ray-Chaudhuri
Department of Civil Engineering, Indian Institute of Technology Kanpur,
Kanpur 208016, India
e-mail: koushik@iitk.ac.in

S. Ray-Chaudhuri
e-mail: samitrc@iitk.ac.in

S. Agrawal · B. Bhattacharya
Department of Mechanical Engineering, Indian Institute of Technology Kanpur,
Kanpur 208016, India
e-mail: bishakh@iitk.ac.in

2621

1 Introduction

Advanced laminated composite plates are used widely now-a-days in engineering applications related to mechanical, aerospace and civil structures by virtue of their advantages in high specific stiffness, specific strength, improved fatigue resistance and superior damage tolerance capability. Due to continuous use and manufacturing defect, damage is evident in these plates in form of delamination, fatigue, fibre-breakage, matrix cracking, de-bonding etc. These defects can significantly affect the mechanical properties of the structure, resulting in degradation of overall structural performance in operating condition and sometimes lead to some unexpected catastrophic failure. The existing structural health monitoring techniques like ultrasonic scanning technique [1] are generally offline in nature. Besides, these conventional methods of structural fault diagnosis are also time-consuming, expensive and laborious.

Modal-based methods of damage identification are based on the fact that the modal parameters such as mode shape, modal damping and natural frequency are functions of the physical parameters like mass, stiffness and damping of the structure. Therefore, it can be assumed that the presence of damage may lead to alteration in some of the modal properties of the structure. The modal parameters that are generally used to detect structural damage are frequency response function (FRF), natural frequency, mode shape, mode shape curvature (MSC), modal flexibility, modal strain energy etc. It may be stated that not all these parameters are equally sensitive to predict the presence of damage in a structure. For example, changes in the mass of the structure and ambient temperature may generate uncertainties in the measured frequency changes. The intricacy of damage detection based on change in frequency can be overcome to some extent by using changes in the mode shapes and their curvature of the given structure. In general, mode shapes are more sensitive compared to natural frequency for detecting local damage. The mode shape curvature change due to damage has a local effect in nature, so it can be used to locate damage properly. The curvature mode shape methods [2] have good potential to identify damage type such as delamination. A brief literature review has been provided in the following paraggraph.

Ratcliffe and Bagaria [3] conducted an experimental study on laminated composite beams to detect delamination using mode shapes without any prior information regarding the reference model. Li et al. [4] conducted strain modal analysis of damaged plates to construct a couple of damage sensitive attributes for detection of plate delamination through simulation as well as experimental study. The amplitude difference of curvature mode shapes is also utilized to estimate the local stiffness loss due to damage. Araujo dos Santos et al. [5] showed the efficiency of displacement, rotation and curvature mode shape for damage localization in carbon fibre reinforced epoxy plates with the help of double pulse TV holography. The study found the differences in mode shape and its curvature are the best locator for any delamination. Qiao et al. [2] used the mode shape curvature-based techniques to detect delamination in composite plate by developing ULS from simulation as well as experimental measurements. The experimental set up consisted of one epoxy composite laminated plate with an embedded delamination using two different sets

of sensor measurement systems, namely, polyvinylidenefluoride sensors and scanning laser Vibrometer, where both systems included lead-zirconate-titanate actuators. The modal parameters were estimated for successful delamination and its extent. Fan and Qiao [6] proposed a strain energy-based method to localize and quantify damage of a fibre-reinforced plastic sandwich deck panel using a surface-bonded polyvinylidenefluoride sensor array. Very recently, Moreno-Garcia et al. [7] used mode shapes and its derivatives for delamination in laminated composites adopting a Ritz method-based techniques to differentiate the mode shape into its higher derivatives in order to avoid some numerical errors.

2 Fundamental Mode Shape as Damage Indices

Delamination in a composite plate leads to the degradation in plate stiffness. Hence, structural damage is closely correlated to mode shape. This study confines its focus only to the fundamental mode shape i.e. to the first eigen vector of the plate stiffness matrix. Pandey et al. [8] and Whalen [9] conducted some simulation studies on cantilever beams to show the effect of damage on mode shapes and found that the mode shape values and their derivatives show some signature patterns at the location of damage. In this study, their concept is extended to a cantilever plate, which is also flexural in nature like a cantilever beam.

For the illustration purpose, consider finite element model of a cantilever plate discretized into 20 elements with each node consisting of three degrees-of-freedom (DoFs). The global mass matrix and stiffness matrix are estimated assembling the element stiffness matrix of the plate. After this, a static condensation procedure [10] is applied to eliminate the dynamic DoFs associated with negligible mass moment of inertia. The stiffness matrix of the structure can be presented in such a way (as given in Eq. (1)) that the vertical translation DoF $\mathbf{w_z}$ and the rotational DoFs θ are segregated for the ease of eliminating the unwanted DoFs.

$$\begin{bmatrix} \mathbf{k_{ZZ}} & \mathbf{k_{Z\theta}} \\ \mathbf{k_{\theta Z}} & \mathbf{k_{\theta\theta}} \end{bmatrix} \begin{pmatrix} \mathbf{w_z} \\ \theta \end{pmatrix} = - \begin{bmatrix} \mathbf{m_{ZZ}} & \mathbf{m_{Z\theta}} \\ \mathbf{m_{\theta Z}} & \mathbf{m_{\theta\theta}} \end{bmatrix} \begin{pmatrix} \ddot{\mathbf{w}}_\mathbf{z} \\ \ddot{\theta} \end{pmatrix} \tag{1}$$

where $\mathbf{k_{zz}}$ and $\mathbf{k_{\theta\theta}}$ are the submatrices consisting of purely horizontal and rotational stiffness coefficients, respectively. The terms $\mathbf{k_{z\theta}}$ and $\mathbf{k_{\theta z}}$ represent the corresponding coupling terms. Also, $\mathbf{m_{zz}}$ and $\mathbf{m_{\theta\theta}}$ are the mass corresponding to the translational and rotational inertial forces, respectively, $\mathbf{m_{z\theta}}$ and $\mathbf{m_{\theta z}}$ are the corresponding coupling terms. As no rotational inertia forces are assumed to act upon the structure, $\mathbf{m_{\theta\theta}}$, $\mathbf{m_{z\theta}}$ and $\mathbf{m_{\theta z}}$ vanish. This leads the translational stiffness to take the following form:

$$\mathbf{k_z} = \mathbf{k_{zz}} - \mathbf{k_{z\theta}} \mathbf{k_{\theta\theta}^{-1}} \mathbf{k_{\theta z}} \tag{2}$$

To obtain the fundamental mode shape, the first eigen vector of the condensed stiffness is determined. Now to create a damage scenario, the flexural rigidity of one

element at the middle of the plate is reduced by 20 %. After that, the condensed stiffness matrix of this damaged plate is determined and the first eigen vector is estimated. The first eigen vectors of stiffness matrices corresponding to the stiffness of the healthy and delaminated plates are plotted in Figs. 1 and 2, respectively. Although there is a delamination at the mid location of the plate, Figs. 1 and 2 do not depict any visible mismatch from each other. Figure 3 shows the plots for difference in mode shape in forms of 3D surface plot. One can notice from Fig. 3 that the difference in mode shape attains maximum value at the mid location of the plate.

3 Experimental Study Using Laser Doppler Vibrometer

An experimental study has been carried out to demonstrate the efficiency of the fundamental mode shape in identifying damage location. The dynamic responses of healthy and delaminated composites are obtained from the laser Doppler vibrometer (LDV) in frequency domain.
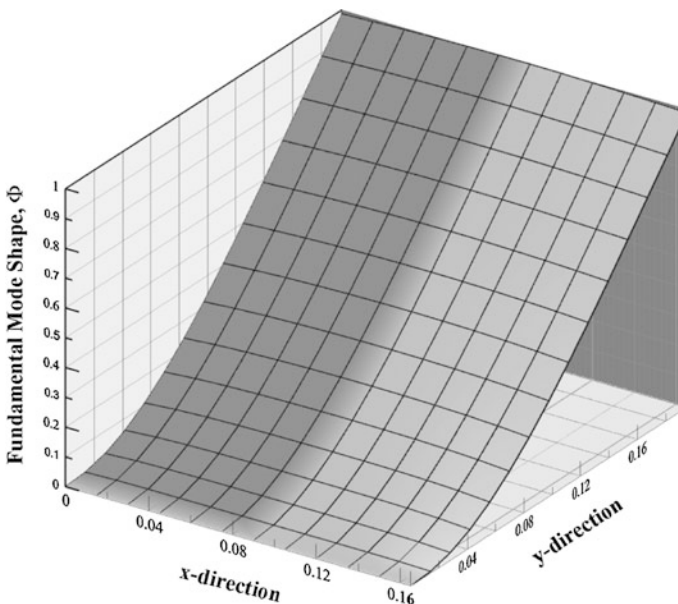
Fig. 1 Mode shapes of healthy plate from finite element analysis
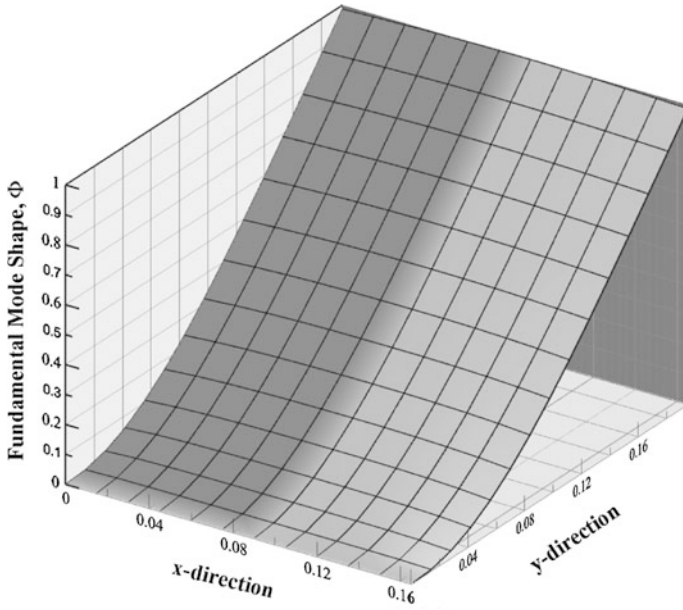
Fig. 2 Mode shapes of delaminated plate from finite element analysis
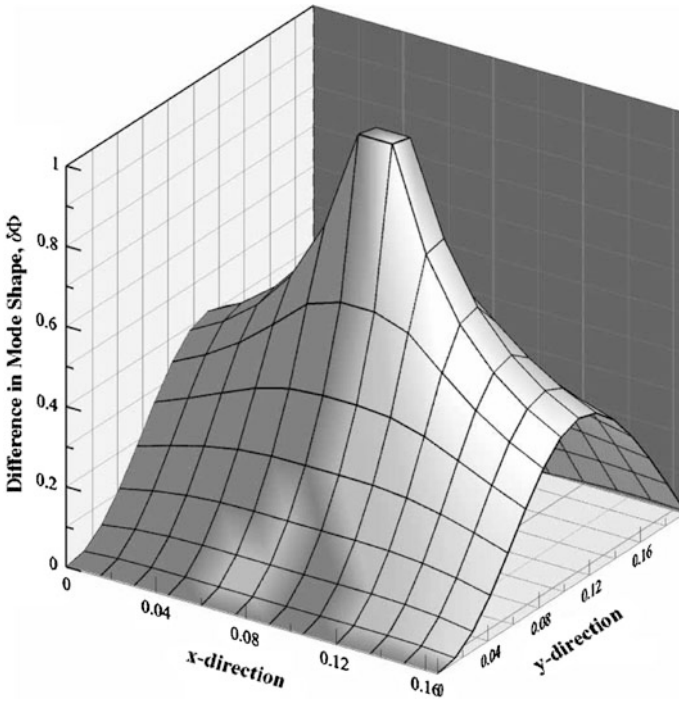
Fig. 3 Difference between mode shapes in form of 3D surface plot from finite element analysis

3.1 Experimental Setup

The test-bed set up majorly consists of an electrodynamic mass shaker and the composite plates to be tested. The shaker is attached to the plate at the center. The specimen is visible as video image on computer screen and the response data were recorded remotely with a sampling frequency of 2.56 kHz. Brief details of the shaker and laminated composite plates are provided in the following sections.

3.1.1 Laser Doppler Vibrometer

LDV is a laser-based non-contact vibration measurement system and it works on the principle of Doppler effect. It consists of three measuring scan heads; namely right, left and top head as shown in Fig. 4, which are capable of measuring the movements in all the three orthogonal directions yielding full information of the three dimensional responses of a vibrating surface [11]. The specification of LDV is provided in Table 1.

Fig. 4 Experimental set up: laser doppler vibrometer
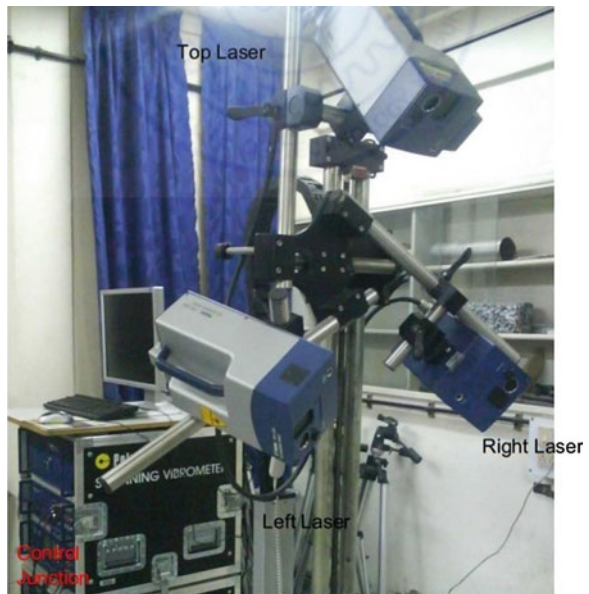
Table 1 Specifications of LDV

Minimum vibrational speed (mm/s)	0.005
Maximum vibrational speed (m/s)	10
Vibration measurement capacity (MHz)	30
Wavelength of He-Ne laser (nm)	633
Working distance (m)	0.5–50

3.1.2 Shaker

The electrodynamic shaker excites the plates with pseudo random noise of frequency ranging between 0 and 80 Hz. Signal generator card NI-671X was used to generate excitation to the shaker. The excitation signal was induced through input amplifier to the shaker via PSV software.

3.1.3 Composite Plates

Glass epoxy composite plates (0/90/0/90) with material properties given in Table 2 were used in the experiment. The plate is fixed at one edge with the help of a 20 mm × 190 mm clamp and other three edges are free. Two damage cases are considered to simulate two different damage scenarios. The plate was delaminated by inserting Teflon cloth between second and third plies of the plate, as shown in Figs. 5 and 6. Delamination at two locations are considered here. Figure 5 shows the

Table 2 Material properties of glass-epoxy laminate

Elastic modulus, E_1	28.45 GPa
Elastic modulus, E_2	2.14 GPa
Shear modulus, G_{12}	1.032 GPa
Poissons ratio, v_{12}	0.24
Density, (ρ)	1,670 kg/m^3

Fig. 5 Schematic diagram of delaminated composite plates for damage case I
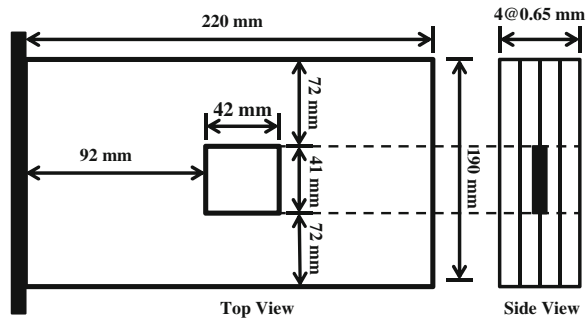
Fig. 6 Schematic diagram of delaminated composite plates for damage case II
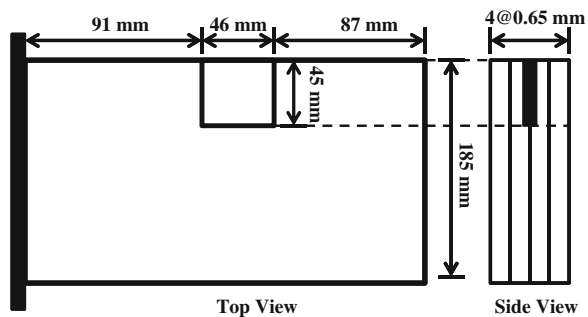
damage case I at the middle of the plate with an area of 42 mm × 41 mm and Fig. 6 shows the damage case II at one side of the plate with dimension 46 mm × 45 mm. The reason behind selecting Teflon as a delamination material is that it is almost frictionless, chemically stable and non-sticky. The composite plates are covered with a white coating for proper reflection of the laser ray from the specimen.

3.2 Data Acquisition

The PSV scanning vibrometer software [12] is used to store the video coordinates and the scan angles of the selected points on the scan area and also to carry out the polynomial interpolation for obtaining the complete modal surface. The data acquisition system has a frequency range of 0–1,000 Hz.

3.3 Test Procedure

2D and 3D alignments were performed to enable the PSV software to identify the any point in terms of X, Y and Z coordinates on the selected scan area on the plate with respect to the chosen coordinate system. Mesh grid should be created with the help of PSV software to define the nodal points. The data can be recorded from these points. In this experimental study, a mesh grid area of size 195 mm × 165 mm is recognized. The mesh grid area under consideration contains 15 × 12 points. Geometric scanning was performed at all 180 scan points with the help of three laser heads of the LDV to provide geometric information to the PSV software. Dynamic response of the plate from each and every nodal point was recorded in frequency domain with a sampling frequency of 2.56 kHz.

4 Results and Discussion

The mode shapes of the healthy and delaminated plates were recorded. The pseudo random excitation was not strong enough to excite the plates in higher modes. For this reason, only the fundamental mode was focused to identify the delamination. Results are presented for two damage cases as discussed earlier (see Figs. 5 and 6).

For damage case I, Figs. 7 and 8 provide the normalized fundamental mode shapes of the healthy and delaminated composite plates. One can notice from these figures that the difference in damaged and undamaged mode shapes is barely observable. Therefore, the difference between healthy and damaged mode shapes is plotted in Fig. 9 in form of a 3D surface plot. From this figure (Fig. 9), it can be observed that the magnitude of difference is maximum at the damage location. In order to investigate the sensitivity of the higher derivatives of mode shapes in
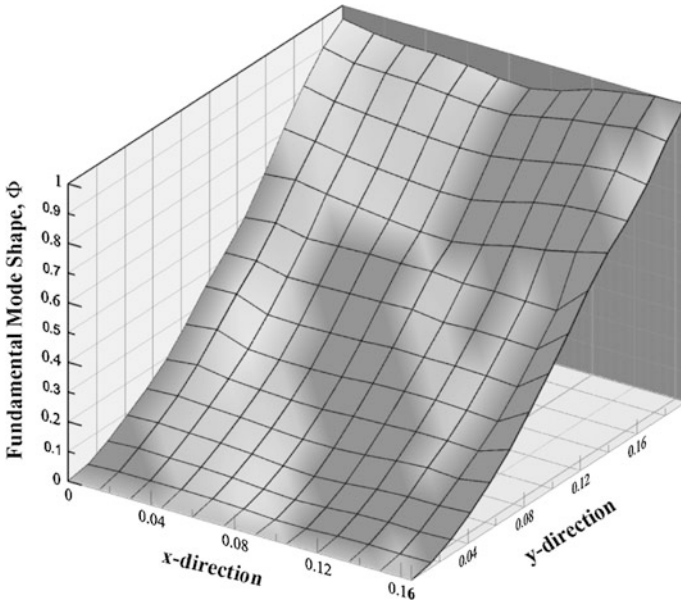
Fig. 7 Experimental mode shapes of healthy plate for damage case I
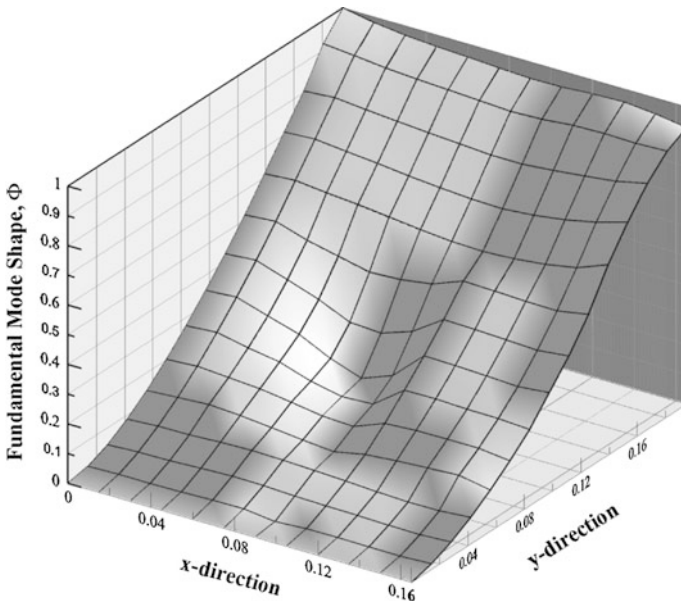
Fig. 8 Experimental mode shapes of delaminated plate for damage case I
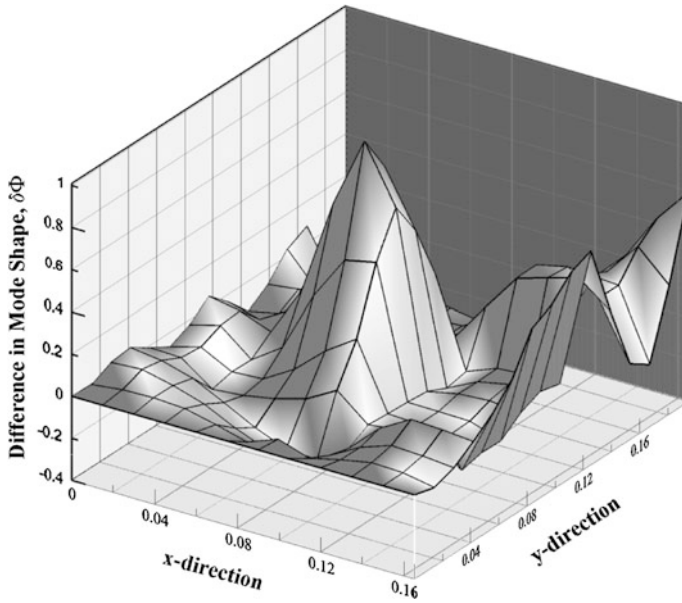
Fig. 9 Difference between experimental mode shapes for damage case I
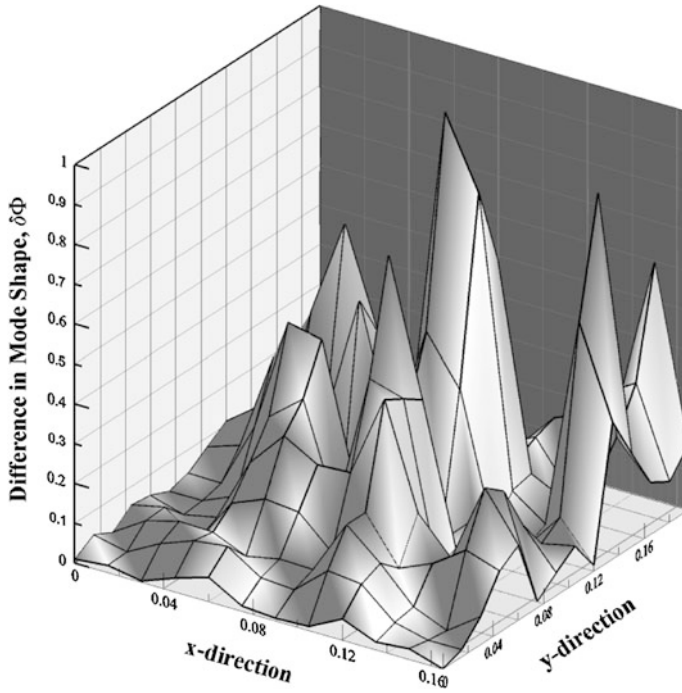
Fig. 10 Difference between experimental mode shape curvature for damage case I
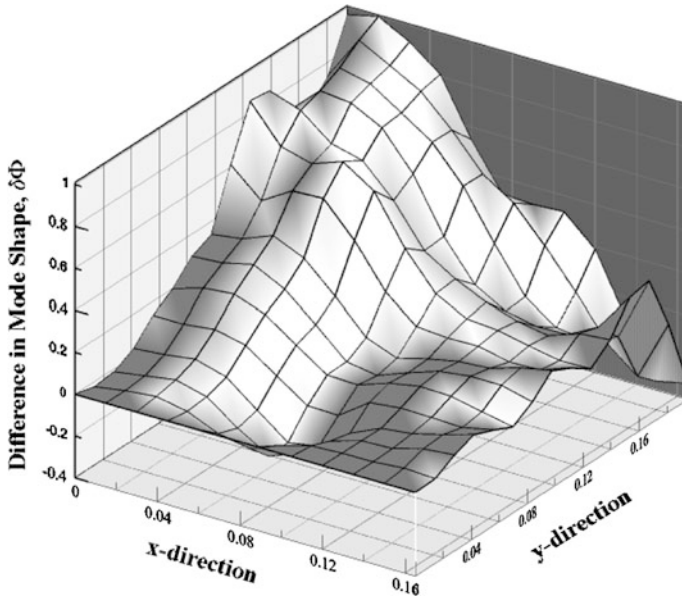
Fig. 11 Difference between experimental mode shapes for damage case II

damage localization, the difference in mode shape curvature is plotted in terms of 3D surface in Fig. 10. No decisive information can be extracted from Fig. 10 in identifying the zone of delamination.

For damage case II, the difference between healthy and damaged mode shapes is plotted in Fig. 11 in form of 3D surface plot. One can observe from this figure that the difference is more with a wide range of area (from the damage location to the nearest corner). The difference in mode shape curvature is plotted in terms of 3D surface plot in Fig. 12. However, Fig. 12 fails to detect damage location.

5 Conclusion

This work focuses on detecting delamination of composite plates at various locations using mode shape-based damage detection methodology. It has been found that the difference between mode shapes corresponding to delaminated and healthy plates attains maximum value at the location of damage for the delamination at the mid of the plate. However, for a localized delamination at the edge, the difference between mode shapes corresponding to delaminated and healthy plates is more with an area from the damage location to the nearest corner. For both damage cases, the difference between mode shape curvatures corresponding to delaminated and healthy plates cannot detect the location of delamination. Therefore, delamination in the plate can be identified by recognizing the spot having maximum difference of
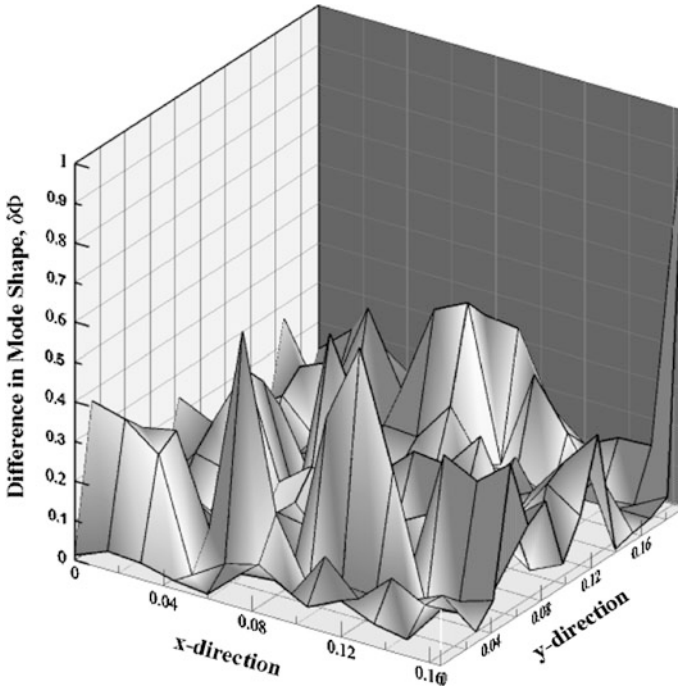
Fig. 12 Difference between experimental mode shape curvature for damage case II

fundamental mode shapes of the damaged condition from that of the undamaged one. The study thus demonstrates that the mode shape-based approach can broadly be applied to detect and localize damages in laminated composite plates.

References

1. Ben BS, Ben BA, Vikram KA, Yang SH (2013) Damage identification in composite materials using ultrasonic based lamb wave method. Measurement 460(2):904–912
2. Qiao P, Lu K, Lestari W, Wang J (2007) Curvature mode shape-based damage detection in composite laminated plates. Compos Struct 800(3):409–428
3. Ratcliffe CP, Bagaria WJ (1998) Vibration technique for locating delamination in a composite beam. AIAA J 36(6):1074–1077
4. Li YY, Cheng L, Yam LH, Wong WO (2002) Identification of damage locations for plate-like structures using damage sensitive indices: strain modal approach. Comput Struct 800 (25):1881–1894

5. Araujo dos Santos JV, Lopes HMR, Vaz M, Mota Soares CM, Mota Soares CA, de Freitas MJM (2006) Damage localization in laminated composite plates using mode shapes measured by pulsed TV holography. Compos Struct 760(3):272–281
6. Fan W, Qiao P (2012) A strain energy-based damage severity correction factor method for damage identification in plate-type structures. Mech Syst Signal Process 28:660–678
7. Moreno-Garcia P, Araujo dos Santos JV, Lopes H (2014) A new technique to optimize the use of mode shape derivatives to localize damage in laminated composite plates. Compos Struct 108:548–554
8. Pandey AK, Biswas M, Samman M (1991) Damage detection from changes in curvature mode shapes. J Sound Vib 1450(2):321–332
9. Whalen TM (2008) The behavior of higher order mode shape derivatives in damaged, beam-like structures. J Sound Vib 3090(3–5):426–464
10. Clough RW, Penzien J (1993) Dynamics of Structures. McGraw-Hill, New York
11. Kumar P (2010) Application of 3D laser doppler vibrometer for damage dection in composite plates. Master's thesis, IIT Kanpur
12. Polytec (2007) Advancing measurement by light. Psv scanning vibrometer software. version 9.0. http://www.polytec.com/int/products/vibration-sensors

Efficiency of the Higher Mode Shapes in Structural Damage Localization

Gourab Ghosh and Samit Ray-Chaudhuri

Abstract Detection of damage in an early stage can help in avoiding sudden failure of a structure. Vibration-based methodologies are currently very popular among the researchers due to their immense potential of providing continuous health monitoring. In this work, the efficiency of the higher mode shapes has been investigated for localizing damage in a structure. To achieve this goal, both numerical and experimental studies have been performed. For the numerical study, a ten-storey shear building has been modeled and the damage scenarios have been simulated by reducing the storey stiffness. For the experimental study, impact hammer tests have been performed on a small-scale three-dimensional six-storey steel frame model. To simulate the damage scenarios, cross-sections of the frame elements (beams and columns) have been reduced. From both numerical and experimental studies, it has been observed that the efficiency of higher mode shapes in damage localization is location dependent. Therefore, further research work is needed to circumvent this location dependency of higher mode shapes for use in damage localization.

Keywords Higher mode shapes · Structural damage localization · Frame structure

1 Introduction

Detection of damage in an early stage is always advantageous for avoiding any undesirable failure of a structure. Now-a-days, vibration-based methods are gaining popularity due to their potential of providing continuous health monitoring at a reasonable cost and consuming less time as compared to the conventional methods.

G. Ghosh (✉) · S. Ray-Chaudhuri
Department of Civil Engineering, Indian Institute of Technology Kanpur,
Kanpur 208016, Uttar Pradesh, India
e-mail: gourabg@iitk.ac.in

S. Ray-Chaudhuri
e-mail: samitrc@iitk.ac.in

In this work, the focus is on the mode shape-based damage localization methodology, which is a kind of vibration-based method.

From the comprehensive reviews presented by [1–4], a good understanding of the various vibration-based damage detection methodologies (i.e., about type and working principle) can be made. For the last few decades researchers are particularly interested about the potential of mode shape-based methods in damage localization. Pandey et al. [5] first used the curvature mode shapes for localizing a structural damage. It was shown by Abdo and Hori [6] that the changes in the derivative of the mode shapes are more sensitive to damage in comparison to the mode shapes. Whalen [7] concluded that higher order mode shape derivatives are more sensitive to damage in comparison to the mode shapes. Zhu et al. [8] used the change in slope of the fundamental mode for detecting damage in a shear building. A mathematical basis was proposed (using perturbation approach) by Roy and Ray-Chaudhuri [9] for establishing a correlation between a structural damage and change in fundamental mode shapes and its derivatives. It is clear from the aforementioned literature that the efficiency of the higher mode shapes has not been thoroughly investigated for localizing damage in a frame structure. In this work, both numerical and experimental studies have been performed to achieve the goal.

2 Numerical Study

A ten storey shear building model with uniform mass ($m_1 = m_2 = \cdots = m_{10} = 1 \times 10^5$ kg) and stiffness ($k_1 = k_2 = \cdots = k_{10} = 2 \times 10^8$ N/m) along the height has been modeled in MATLAB [10]. To simulate a damage scenario, stiffness has been reduced by 10 % at a desired storey level. In Fig. 1 a schematic diagram of the shear building is shown. The damage scenarios considered are shown in Fig. 2.

2.1 Results and Discussions

Case-A Here, stiffness was reduced at the 2nd storey level to simulate the damage condition. The plots of the undamaged and damaged mode shapes, their difference and derivatives are shown here for the second and third modes. From Fig. 3, the following observations can be made: (i) a jump from the 1st storey to the 3rd storey centering the 2nd storey (Fig. 3b); (ii) maximum slope at the 2nd storey (Fig. 3c); (iii) zero crossing, i.e., change in the sign of the curvature at the 2nd storey (Fig. 3d). These patterns are in good agreement with the damage signature proposed by Roy and Ray-Chaudhuri [9] for locating damage at the 2nd storey level. Similar patterns can be observed for the third mode from Fig. 4, respectively. Thus, these two modes are effective in localizing the damage at the 2nd storey level.
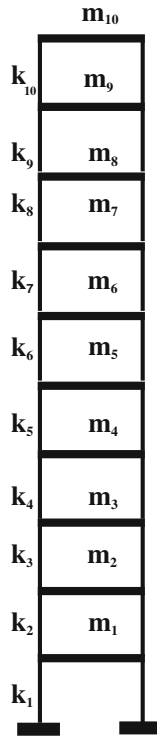
Fig. 1 Schematic diagram of the shear building
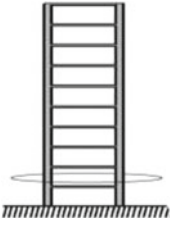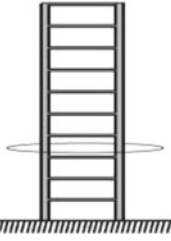
Case	Damage Description	Figure
Case A	Damage at 2nd storey	
Case B	Damage at 4th storey	

Fig. 2 Description of damage scenarios
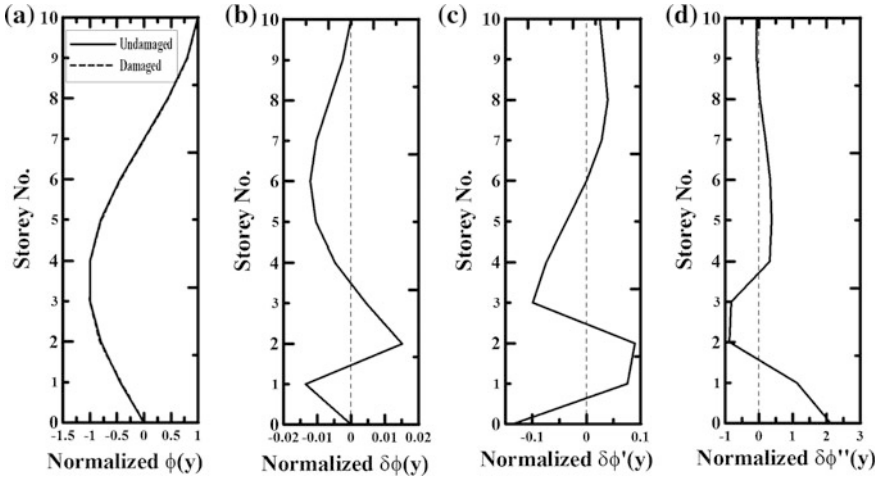
Fig. 3 Plot of the **a** second mode shape and changes in, **b** mode shape, **c** slope of mode shapes and, **d** curvature of mode shapes obtained from numerical study (Case-A)
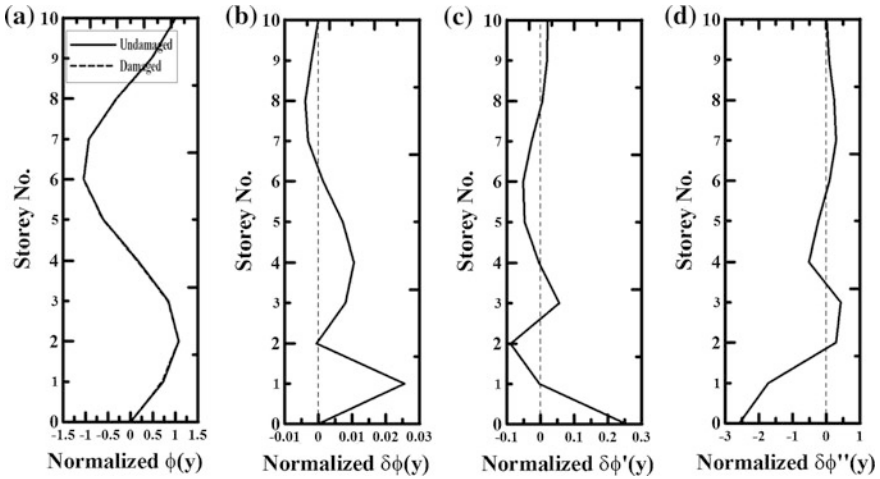
Fig. 4 Plot of the **a** third mode shape and changes in, **b** mode shape, **c** slope of mode shapes and, **d** curvature of mode shapes obtained from numerical study (Case-A)

Case-B Here, the damage scenario was simulated at the 4th storey level in the same manner described earlier. The mode shapes and their derivatives are plotted here for the second and third modes. Here also, the third mode effectively localize the damage at the 4th storey level using the same patterns proposed by Roy and Ray-Chaudhuri [9] (Fig. 6). But from Fig. 5, the following observations are made: (i) no jump is observed at the 4th storey (Fig. 5b); (ii) no steep slope is observed at the 4th
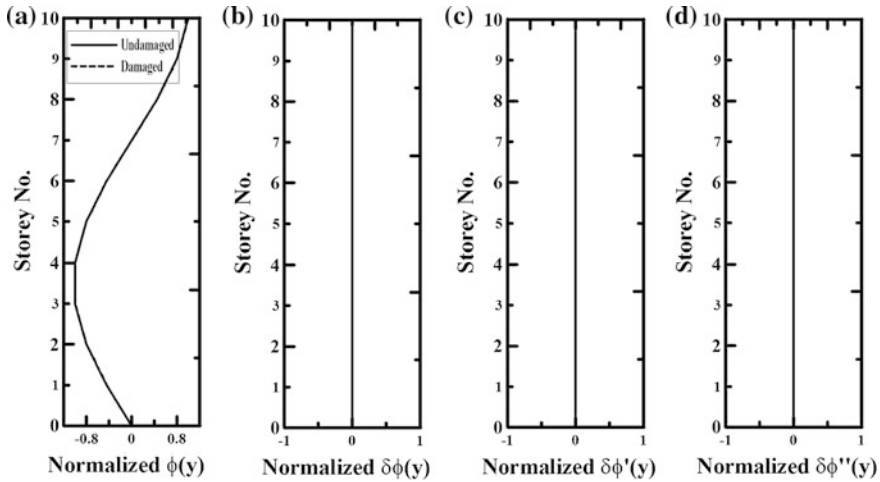
Fig. 5 Plot of the **a** second mode shape and changes in, **b** mode shape, **c** slope of mode shapes and, **d** curvature of mode shapes obtained from numerical study (Case-B)
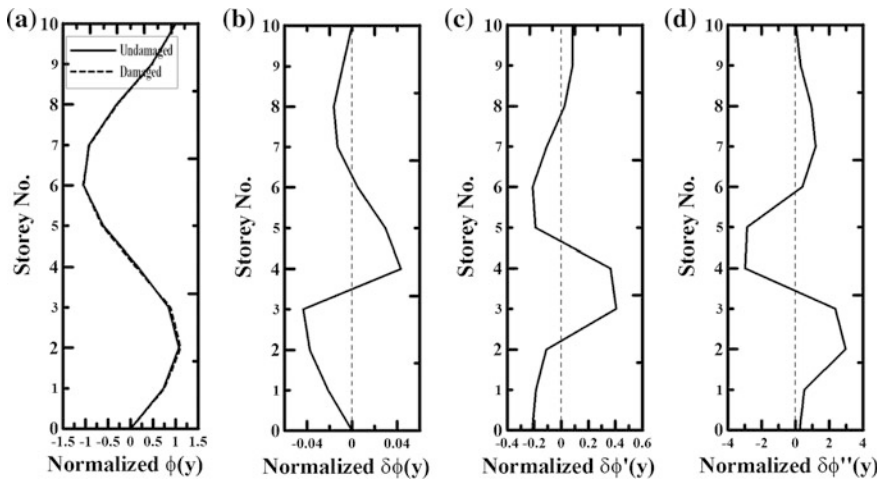
Fig. 6 Plot of the **a** third mode shape and changes in, **b** mode shape, **c** slope of mode shapes and, **d** curvature of mode shapes obtained from numerical study (Case-B)

storey (Fig. 5c); (iii) no zero crossing is observed at the 4th storey (Fig. 5d). Thus, the second mode fails to localize the damage at the 4th storey level following the damage signatures of the fundamental mode.

3 Experimental Study

In this study, impact hammer tests have been used to evaluate the dynamic char-acteristics (frequency and mode shape) of a six-storey three-dimensional steel frame model.

3.1 Model

A schematic diagram of the frame model is shown in Fig. 7. Dimension of the steel frame is 200 mm × 200 mm × 780 mm. Two steel beams of cross sectional dimension 8 mm × 8 mm and two aluminium plates of cross sectional dimension 40 mm × 5 mm are placed along perpendicular directions. Cross sectional dimensions of the steel columns are 10 mm × 10 mm. Strong column-weak beam approach has been followed to design the frame model having uniform distribution of mass and stiffness over the stories. In Fig. 8 a photograph of the undamaged structure is shown.
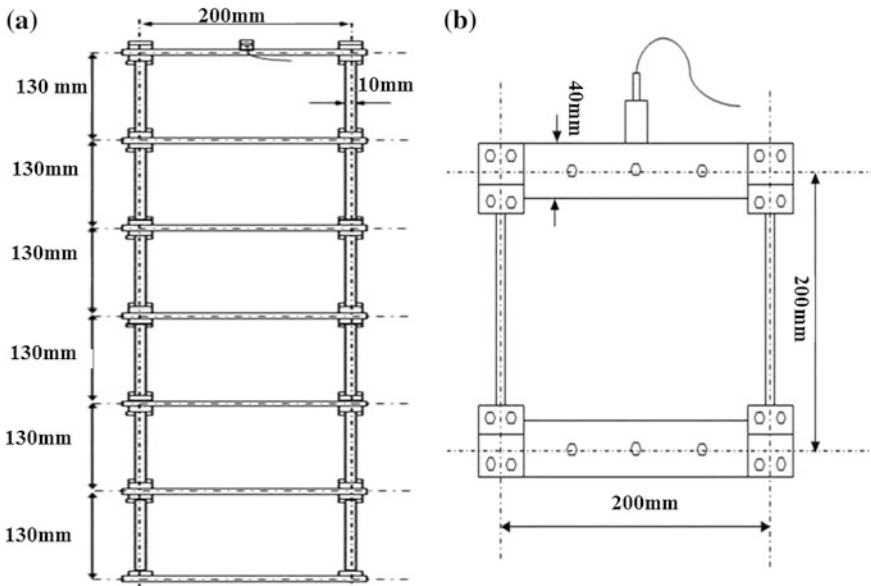
Fig. 7 Schematic diagram of the experimental model, **a** elevation **b** plan
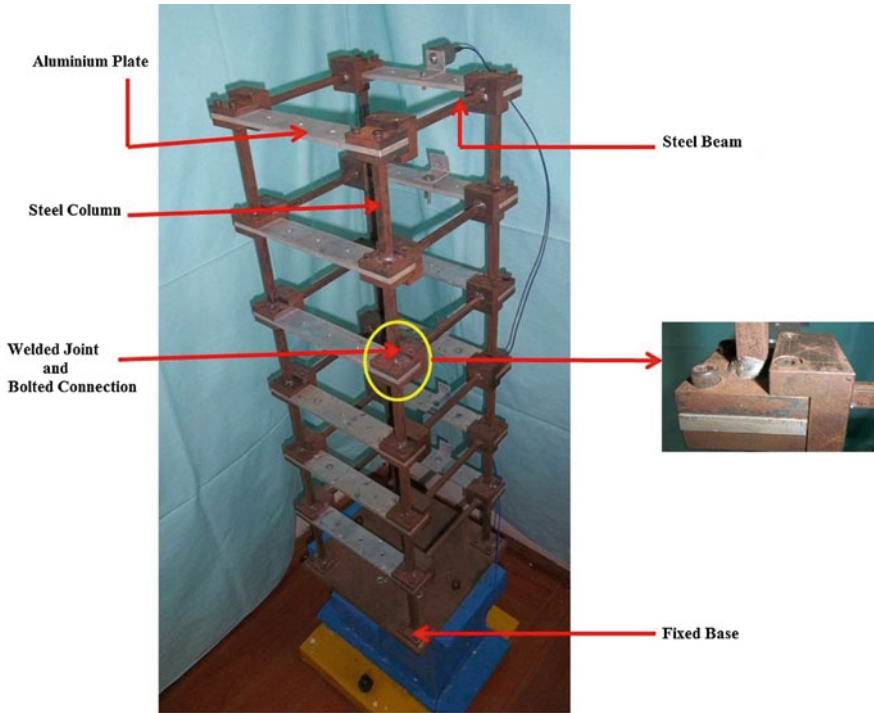
Fig. 8 Snapshot of the undamaged structure

3.2 Damage Scenarios

Based on the location of frame elements (beam, column), two damage scenarios (Fig. 9) were considered to study the effectiveness of higher mode shapes in damage localization.

Case-I To simulate damage, cross sections of the steel beams at the 2nd storey level were reduced to 6 mm × 6 mm and 3 mm depth notches were created at two ends. In Fig. 10 the damaged model is shown.

Case-II To simulate this damage scenario, the cross sections (thus, stiffness) of two columns between the 3rd and 4th storey were reduced to 7 mm × 7 mm. The damaged columns were placed along the direction of hitting.
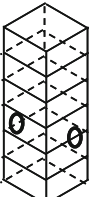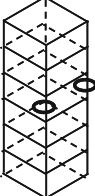
Case	Damage Description	Figure
Case-I	2nd storey beam damaged	
Case-II	Column damaged between 3rd and 4th storey	

Fig. 9 Various damage scenarios
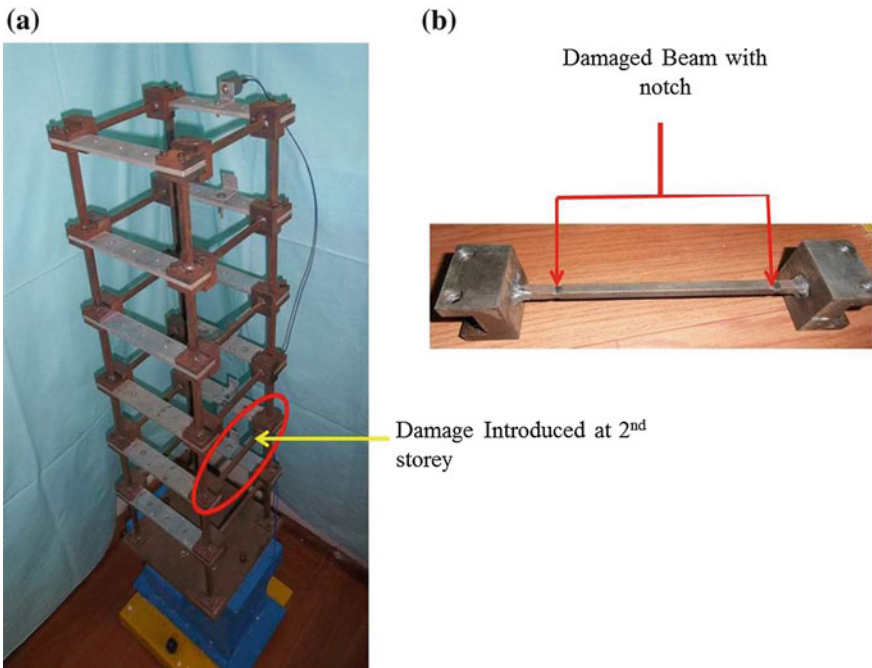
Fig. 10 Snapshot of the damaged structure (Case-I: beam damaged at the 2nd storey) **a** damage location, **b** damaged beam

3.3 Instrumentation

The instruments used for the test purpose are: (i) a PCB086D20 [11] type short-sledge impulse hammer (sensitivity of 0.23 mV/N) for impulse, (ii) PCB393B04 [11] seismic, miniature (50 gm), ceramic flexural ICP accelerometer (sensitivity of 1 V/g) for measuring acceleration response, and (iii) a 4 channel FFT Agilent-35670A Dynamic Signal Analyzer [12] for data acquisition.

3.4 Test Procedure

The whole test setup is shown in Fig. 11. The accelerometer has been placed on the top floor with the help of a L-shaped plate along the hitting direction (Fig. 12). The impact force has been applied at each storey to calculate the FRFs (frequency response function) (taking average of 10 readings) at each floor.
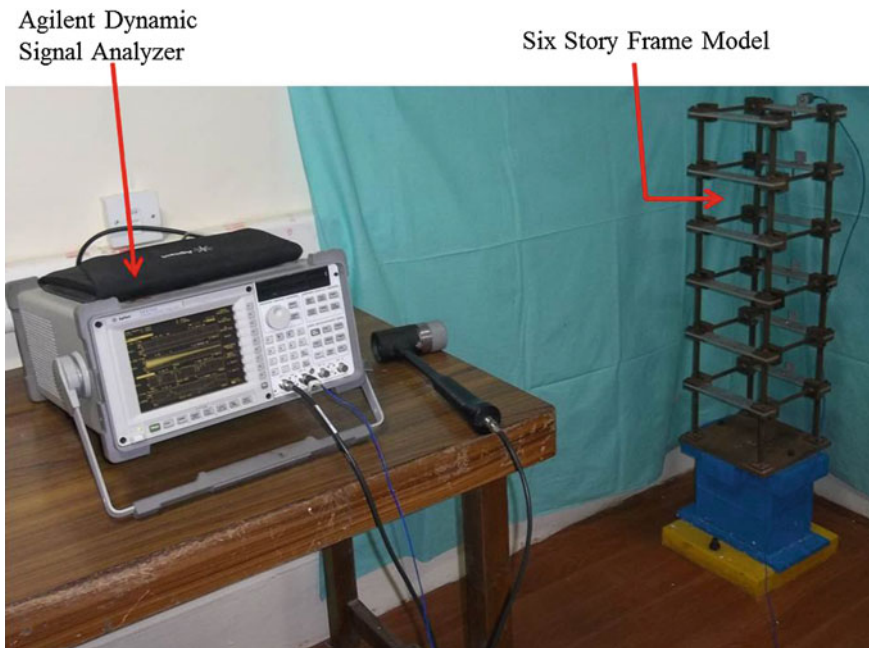
Fig. 11 Experimental setup showing model and signal analyzer

Fig. 12 Orientation of the accelerometer and direction of hitting with impact hammer
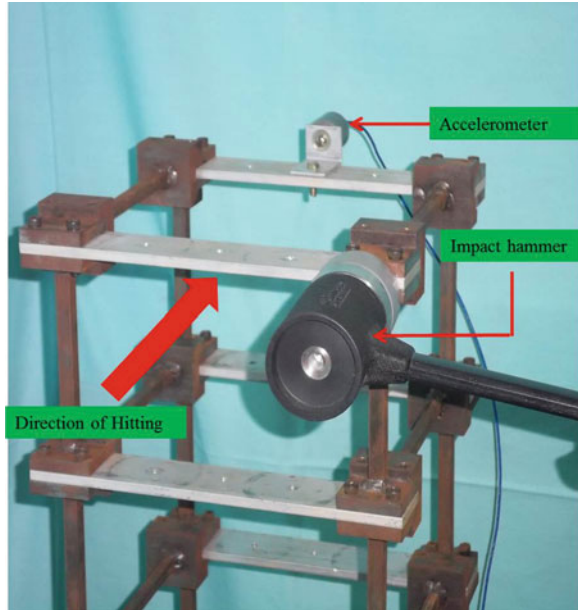
3.5 Experimental Data Analysis

A wire frame model of the experimental frame has been created in the ME'scopeVES [13] software. Then the mode shapes of the model have been obtained by analyzing the recorded FRFs (using global polynomial curve fitting method). The mode shapes have been normalized in such a way that the highest value is equal to unity. Their derivatives have been calculated using finite difference method in MATLAB [10].

4 Experimental Results

Here, efficiency of only the second mode shape in localizing damage is discussed, as the third mode could not be extracted from the experimental study (owing to high frequency of the model).

Case-I The normalized plot of the undamaged and damaged second mode shapes, and their derivatives are shown in Fig. 13. From this figure, following observations can be made: (i) there is no jump between the 1st and 3rd storey centering the 2nd storey in Fig. 13b, (ii) in Fig. 13c, steep slope is not observed at the 2nd storey level and (iii) also in Fig. 13d, zero crossing is noticed between the 2nd and 3rd storey instead of at the 2nd storey level. Thus, the damage location can not be predicted in this case using the damage signatures of the fundamental mode shape.
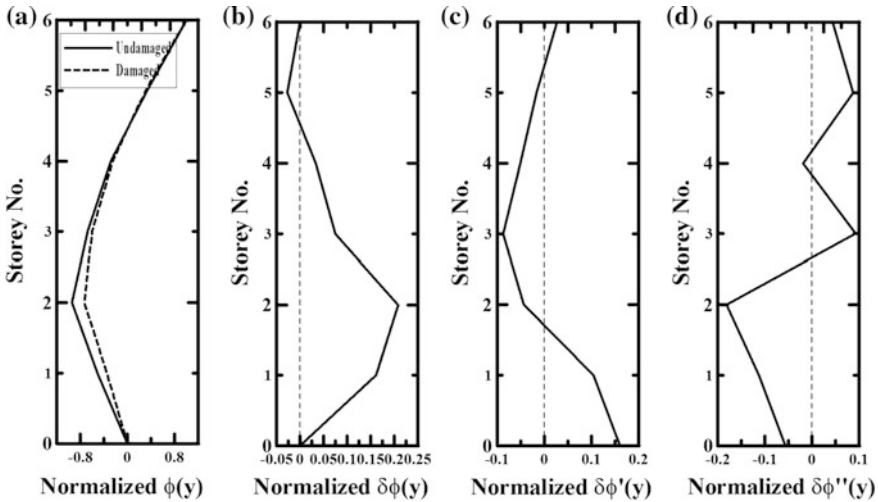
Fig. 13 Plot of the **a** second mode shape and changes in, **b** mode shape, **c** slope of mode shapes and, **d** curvature of mode shapes obtained from experimental study (Case-I)

Case-II In Fig. 14, the normalized plot of the undamaged and damaged second mode shapes, and their derivatives are shown. Here, (i) a jump occurs between the 3rd and 4th storey (Fig. 14b), (ii) maximum slope occurs between the 3rd and 4th storey (Fig. 14c), and (iii) a zero crossing, i.e., change of sign of curvature can be observed between the 3rd and 4th storey (Fig. 14d). These patterns are good indicator for localizing the column damage between the 3rd and 4th storey.
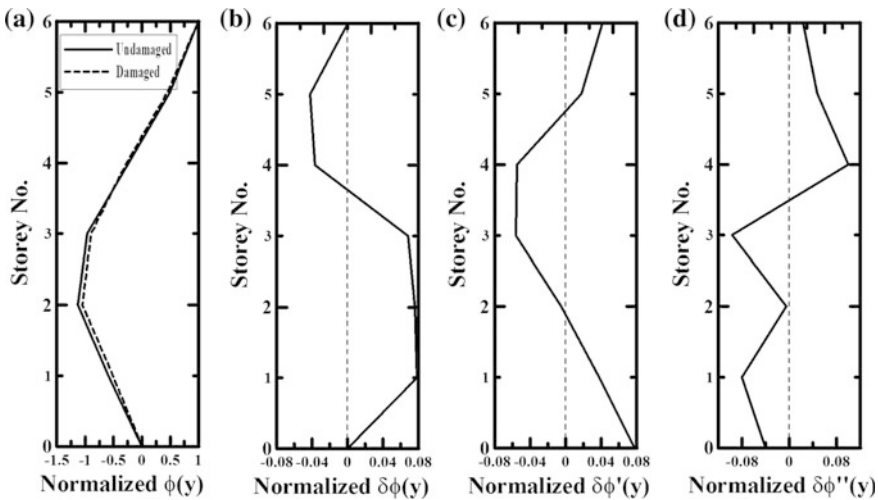
Fig. 14 Plot of the **a** second mode shape and changes in, **b** mode shape, **c** slope of mode shapes and, **d** curvature of mode shapes obtained from experimental study (Case-II)

5 Conclusions

Now-a-days, mode shape-based damage detection methodologies are gaining popularity among researchers due to their appealing nature and potential of providing continuous health monitoring at a reasonable cost. In this work, the efficiency of the higher mode shapes has been investigated for localizing damage in a structure. To achieve the goal, a numerical study has been performed considering a ten-storey shear building model and simulating damage condition by reducing the stiffness at different stories. The results indicate that the efficiency of the higher modes is location dependent. Subsequently, an experimental study has been performed by considering a small-scale three-dimensional six-storey steel frame model and simulating damage condition by reducing the cross-sections of the frame elements (beams and columns). It has been found that the experimental results are in good agreement with the numerical ones. Further research work can be pursued in order to get rid of the location dependency of the higher modes in localizing damage.

References

1. Doebling SW, Farrar CR, Prime MB, Shevitz DW (1996) Damage identification and health monitoring of structural and mechanical systems from changes in their vibration characteristics: a literature review. Technical report, Los Alamos National Lab, New Mexico
2. Salawu OS (1997) Detection of structural damage through changes in frequency: a review. Eng Struct 190(9):718–723
3. Alvandi A, Cremona C (2006) Assessment of vibration-based damage identification techniques. J Sound Vib 2920(1):179–202
4. Yan YJ, Cheng L, Wu ZY, Yam LH (2007) Development in vibration-based structural damage detection technique. Mech Syst Signal Process 210(5):2198–2211
5. Pandey AK, Biswas M, Samman MM (1991) Damage detection from changes in curvature mode shapes. J Sound Vib 1450(2):321–332
6. Abdo MAB, Hori M (2002) A numerical study of structural damage detection using changes in the rotation of mode shapes. J Sound Vib 2510(2):227–239
7. Whalen TM (2008) The behavior of higher order mode shape derivatives in damaged, beam-like structures. J Sound Vib 3090(3):426–464
8. Zhu H, Li L, He XQ (2011) Damage detection method for shear buildings using the changes in the first mode shape slopes. Comput Struct 890(9):733–743
9. Roy K, Ray-Chaudhuri S (2013) Fundamental mode shape and its derivatives in structural damage localization. J Sound Vib 3320(21):5584–5593
10. MATLAB version 8.0.0.783 (R2012b) (2012) The MathWorks Inc. Natick, Massachusetts

11. PCB Piezotronics. (2013) PCB Piezotronics Inc, 3425 Walden Avenue Depew, New York, 14043-2495, USA
12. Technologies Agilent (2013) Agilent. Agilent Technologies Inc, Santa Clara
13. ME'scopeVES (2013) ME'scopeVES5.0. Vibrant Technology Inc, 5 Erba Lane, Suite B, Scotts Valley, California, 95066

Author Index

Subject Index